Proceedings of the annual meeting of the French Society of Astronomy & Astrophysics

Editors
A. Siebert, K. Baillié, E. Lagadec, N. Lagarde, J. Malzac, J.-B. Marquette, M. N'Diaye, J. Richard, O. Venot

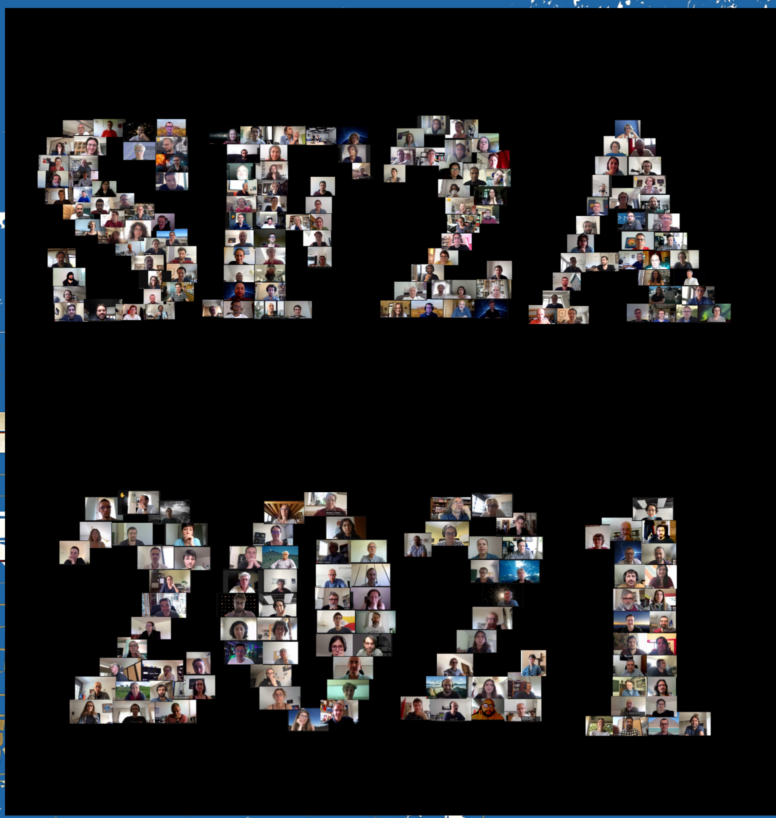

Credit: Nadège Lagarde

CarbonFreeConf

June 7-11, 2021

Sponsored by
cnrs INSU

Proceedings of the annual meeting of the French Society of Astronomy & Astrophysics
Actes de conférence des journées annuelles de la société Française d'Astronomie et d'Astrophysique

Publisher : Société Française d'Astronomie et d'Astrophysique (SF2A)
http://www.sf2a.eu

Edited by : A. Siebert, K. Baillié, E. Lagadec, N. Lagarde, J. Malzac, J.-B. Marquette, M. N'Diaye, J. Richard, O. Venot

Contents

Foreword

E. Lagadec, President of the SF2A

The French Society of Astronomy and Astrophysics (*Société Française d'Astronomie et d'Astrophysique* - SF2A) usually holds its annual meeting every spring. It is a great opportunity for all members of the French community to gather, exchange about different projects and work together on making our community stronger. Unfortunately, we have all gone through difficult times in 2020 and 2021 due to the sanitary crisis. The 2020 meeting was held online and limited to the general assembly and a career session, always important for the non-permanent members of our community. For 2021, the sanitary situation was still complicated, but together with the SF2A council, we decided it was very important to hold a meeting, and we decided to go online. The 2020 and 2021 meetings were scheduled in Paris, and the Local Organising Committee, chaired by Paola Di Matteo had already done a great job at preparing it, but the uncertainty was too important to prepare an in-person meeting. We wish to warmly thank Paoloa Di Matteo and the 2020 and 2021 LOCs for the great work achieved to end up having no meeting in Paris. Thank you Paola Di Matteo, Misha Haywood, Kevin Baillié, Danielle Briot, Sylvain Cnudde, Florence Durret, Guillaume Hébrard, Frédéric Royer, Zakaria Meliani, Jaqueline Plancy and Stéphane Thomas.

The meeting was thus held online, and we were soon to face an important challenge: organise an online meeting and make sure the community enjoys it after more than a year of online meetings. On the bright side, having an online meeting made it simple to host more parallel sessions than during in-person meeting, where the main limitation is the number of available rooms. But that meant we had to find a platform enabling exchanges, to record meetings etc.. while keeping the registration fees as low as possible. Quentin Kral offered us to be beta-testers for his CarbonFreeConf platform. Carbonfree is designed to organise online meetings, which should be more and more frequent with the climate crisis we are facing. We thus felt it was a good opportunity to use this service, offered at its cost price by Quentin Kral. I want to warmly thank him for that and his amazing reactivity before, during and after the meeting. It was quite some work for us, but at the end it worked well, and we hope it will be useful for online meetings in the future. The call for contributions to organise parallel sessions received a lot of answers, which allowed us to propose a very rich program, with meetings of the different *Programmes Nationaux* and *Actions Spécifiques* of INSU-CNRS and scientific meetings proposed by community members. We also received some very interesting "societal" proposals, such as the future of French historical observatories, discussions between scientists and journalists, sociological studies of observatories, well-being of students and post-docs, and inequalities between men and women.

The meeting, called "*Semaine de l'astrophysique française*", or "*Journées de la SF2A*" (and just "SF2A" by many colleagues) included the general assembly of our society, plenary sessions aimed at a large audience of professionals, and 27 parallel sessions dedicated to various scientific and community issues and also the young researcher and thesis prize talks. It was a great success, with more than 800 registered participants, and a great attendance for all the meetings, especially the societal ones. It confirmed us that the 2021 SF2A meeting was much needed, and that societal issues are very important to our community. SF2A meetings offer a unique place for such discussions to occur, and we hope it will continue in the future and that it will be important for the well-being of our community as a whole.

During the plenary sessions, representatives of INSU (G. Perrin), CNES (P. Laudet) and of the "*sections*" of CNAP (D. Mourard), CNRS (B. Mosser) and CNU (L. Rezeau) presented an update on the current situation of astrophysics in France. The discussion about careers is always important for students and post-docs, even if the small number of positions can be depressing.

The last news from large observatories were given by B. Devost for CFHT and M. Cirasuelo for ESO. The different *Programmes Nationaux* and *Actions Spécifiques* of INSU-CNRS proposed excellent speakers presenting the latest results from Gravity/MATISSE at the VLTI, Insight on Mars, tensions about the Cosmic Microwave Background, sample returns from asteroids, the potential of pulsar timing networks for the detection of gravitational waves, the Parker Solar Probe, open access to scientific data and an update on the study of molecules in molecular clouds. The SF2A council also proposed some talks about "hot topics" such as the Great Dimming of Betelgeuse, news about the Perseverance Rover on Mars and Astronomy in Africa. We also decided to have discussions about three very important topics during the plenary sessions:

- The preservation of our night sky via a presentation by Piero Benvenuti of the IAU action to preserve dark and quiet skies for astronomy and humanity.
- Well-being for PhD students and post-docs by Natalie Webb, an important topic for the most precarious in our community, even more after almost two year of pandemics.
- Men-women inequalities in astronomy, with a full session in plenary to introduce the parallel session. This is a very important topic for SF2A, and we have formed a commission to work on it. The talks were presented by Isabelle Kraus, specialist of the topic and VP of the Strasbourg University. Guy Perrin presented the INSU situation and actions that will be conducted.

Because of the pandemics, we could not organise in-person ceremonies for the SF2A prize laureates. They were thus invited to give talks during the plenary sessions, so we want to warmly thank:

- Anaëlle Maury, *Prix Jeune Chercheur 2020* laureate
- Doogesh Kodi Ramanah, *Prix de Thèse 2020* laureate
- Alexandre Santerne an his team for the project *Detection and Follow-Up of Exoplanets by Amateur Astronomers*, *Prix Gémini 2020 de la collaboration pro-amateur* laureate
- Matthieu Béthermin, *Prix Jeune Chercheur 2021* laureate
- Lisa Bugnet, *Prix de Thèse 2021* laureate
- Marc Delcroix and Ricardo Hueso for the project *Collaborative Amateur-Professional project for the detection and characterisation of impacts on Jupiter*, *Prix Gémini 2021 de la collaboration pro-amateur* laureate

Finally, we held our general assembly where the moral and financial reports were presented. A vote from the members will complement these presentations by the end of 2021.

Afternoons were dedicated to parallel workshops covering all branch of astronomy. These 27 workshops were selected among propositions from the *Programmes Nationaux* and *Actions Spécifiques*, but also from individual members of the society. These workshops thus covered the interests of our whole community, in good accordance with the topicality of the field.

Every year, the *Découvrir l'Univers* Prize is awarded during the SF2A. It was awarded to the class of Mireille Jarlut at the*Ecole Maternelle Thérèse Roméo* in Nice for a very touching work to explain the day/night alternation and gravity to very young pupils. Congratulations to everyone!

The SF2A council wants to warmly thanks CNRS-INSU for its financial support, which made the organisation of the meeting possible.

I would like to thank all the members of the SF2A board who were all very active for preparing the meeting, with a special and warm thank to all the always happy and fast-answering members of the *SAV*:

Kevin Baillié, Quentin Kral, Nadège Lagarde, Julien Malzac, Jean-Baptiste Marquette, Mamadou N'Diaye, Johan Richard, Arnaud Siebert, Olivia Venot. They all made this meeting a success. Next year we should finally meet in person, and I think many people are excited about it.. so see you in 2022 in Besançon!

Eric Lagadec, President of the SF2A

List of participants

ABRIL MELGAREJO Valentina (e-mail: vl.abril57@uniandes.edu.co)
ACEBRON Ana (e-mail: anaacebronmunoz@gmail.com)
ACERO Fabio (e-mail: fabio.acero@cea.fr)
ACUÑA Lorena (e-mail: lorena.acuna@lam.fr)
ADAMI Christophe (e-mail: christophe.adami@lam.fr)
AGHANIM Nabila (e-mail: nabila.aghanim@ias.u-psud.fr)
AHUIR Jeremy (e-mail: jeremy.ahuir@cea.fr)
AIZAWA Sae (e-mail: sae.aizawa@irap.omp.eu)
ALAGUERO Antoine (e-mail: antoine.alaguero@gmail.com)
ALECIAN Evelyne (e-mail: evelyne.alecian@univ-grenoble-alpes.fr)
ALEXANDROVA Olga (e-mail: olga.alexandrova@obspm.fr)
ALI-DIB Mohamad (e-mail: mma9132@nyu.edu)
ALLEN Mark (e-mail: mark.allen@astro.unistra.fr)
ALQEEQ Soboh (e-mail: soboh.al-qeeq@lpp.polytechnique.fr)
ÁLVARO Joaquín (e-mail: jalvaro@spainportugal-eps.org)
AMARD Louis (e-mail: l.amard@exeter.ac.uk)
AMODEO Stefania (e-mail: stefania.amodeo@astro.unistra.fr)
AMSIF Kader (e-mail: kader.amsif@cnes.fr)
ANDERSON Sarah (e-mail: sarah.anderson@univ-fcomte.fr)
ANDRE Nicolas (e-mail: nicolas.andre@irap.omp.eu)
ANDREU Audrey (e-mail: audrey.andreu@etu.u-bordeaux.fr)
ANGONIN Marie-Christine (e-mail: m-c.angonin@obspm.fr)
ANSARINEJAD Behzad (e-mail: behzad.ansarinejad@gmail.com)
ANTAO David (e-mail: davidantao@net-c.com)
ANTIER Sarah (e-mail: s.b.antier@uva.nl)
ANTOINE Cailleau (e-mail: antoine.cailleau@astromecca.fr)
APPOURCHAUX Thierry (e-mail: thierrya@neuf.fr)
ARENOU Frédéric (e-mail: Frederic.Arenou@obspm.fr)
ARENTSEN Anke (e-mail: anke.arentsen@astro.unistra.fr)
ARNOUTS Stephane (e-mail: stephane.arnouts@lam.fr)
ARSENAULT Robin (e-mail: rarsenau@eso.org)
ARTHUR Léna (e-mail: arthur@apc.in2p3.fr)
ARTIGUE Romain (e-mail: romain.artigue@ipsa.fr)
ASTOUL Aurelie (e-mail: a.a.v.astoul@leeds.ac.uk)
ATEK Hakim (e-mail: hakim.atek@iap.fr)
ATTIA Omar (e-mail: omar.attia@unige.ch)
AUBERT Dominique (e-mail: dominique.aubert@astro.unistra.fr)
AUCHÈRE Frédéric (e-mail: frederic.auchere@ias.u-psud.fr)
AUFORT Grégoire (e-mail: gregoire.aufort@lam.fr)
AULANIER Guillaume (e-mail: guillaume.aulanier@obspm.fr)
AUNAI Nicolas (e-mail: nicolas.aunai@lpp.polytechnique.fr)
AUSSEL Hervé (e-mail: herve.aussel@cea.fr)
AYCOBERRY Emma (e-mail: emmaaycoberry@gmail.com)
BABUSIAUX Carine (e-mail: carine.babusiaux@univ-grenoble-alpes.fr)
BACMANN Aurore (e-mail: aurore.bacmann@univ-grenoble-alpes.fr)

BAILLIÉ Kevin (e-mail: kevin.baillie@obspm.fr)
BALLERINI Giulio (e-mail: giulio.ballerini@oca.eu)
BALLET Jean (e-mail: jballet@cea.fr)
BALLET Romuald (e-mail: ballet.romuald@gmail.com)
BANERJEE Bihan (e-mail: banerjeebihan@gmail.com)
BARATOUX David (e-mail: david.baratoux@ird.fr)
BARBAN Caroline (e-mail: caroline.barban@obspm.fr)
BARJOT Kevin (e-mail: kevin.barjot@obspm.fr)
BARMA Judhajit (e-mail: judhajitiiser@gmail.com)
BARNIER Samuel (e-mail: s.h.barnier@gmail.com)
BARRET Didier (e-mail: didier.barret@irap.omp.eu)
BARREY Eric (e-mail: eric.barrey@free.fr)
BARROY Pierre (e-mail: pierre.barroy@u-picardie.fr)
BARTHELEMY Alexandre (e-mail: alexandre.barthelemy@iap.fr)
BARUTEAU Clément (e-mail: clement.baruteau@irap.omp.eu)
BASA Stephane (e-mail: stephane.basa@lam.fr)
BASALGÈTE Romain (e-mail: romain.basalgete@obspm.fr)
BASILLAIS Baptiste (e-mail: baptiste.boutin-basillais@u-bordeaux.fr)
BASKEVITCH Claire (e-mail: claire.baskevitch@latmos.ipsl.fr)
BAUDOZ Pierre (e-mail: pierre.baudoz@obspm.fr)
BEAUMONT Sophie (e-mail: sbeaumont@irap.omp.eu)
BEHAR Etienne (e-mail: etienne.behar@irf.se)
BELKACEM Kevin (e-mail: kevin.belkacem@obspm.fr)
BELLOTTI Stefano (e-mail: stefano.bellotti@irap.omp.eu)
BELMONT Gérard (e-mail: gerard.belmont@lpp.polytechnique.fr)
BEN LASSOUED Anis (e-mail: anisbenlassoued68@gmail.com)
BENSEGUANE Selma (e-mail: selma.benseguane@univ-lyon1.fr)
BERGER Jean-Philippe (e-mail: jean-philippe.berger@univ-grenoble-alpes.fr)
BERGEZ-CASALOU Camille (e-mail: camille.bergezcasalou@gmail.com)
BERNE Olivier (e-mail: olivier.berne@gmail.com)
BERTEAUD Joanna (e-mail: berteaud@lapth.cnrs.fr)
BERTRAND Etienne (e-mail: etienne.bertrand17@yahoo.fr)
BERTRAND Guy (e-mail: guy.bertrand@obspm.fr)
BERTRAND Tanguy (e-mail: tanguy.bertrand@obspm.fr)
BETHERMIN Matthieu (e-mail: matthieu.bethermin@lam.fr)
BÉZARD Bruno (e-mail: Bruno.Bezard@obspm.fr)
BIANCHI Eleonora (e-mail: eleonora.bianchi@univ-grenoble-alpes.fr)
BIGIOLI Azzurra (e-mail: azzurra.bigioli@kuleuven.be)
BITEAU Jonathan (e-mail: biteau@in2p3.fr)
BIZOUARD Marie Anne (e-mail: marieanne.bizouard@oca.eu)
BLANC Michel (e-mail: michel.blanc@irap.omp.eu)
BLANCO Leonardo (e-mail: blanle@eso.org)
BLIND Nicolas (e-mail: nicolas.blind@unige.ch)
BLONDIN Stéphane (e-mail: stephane.blondin@lam.fr)
BOCCALETTI Anthony (e-mail: anthony.boccaletti@neuf.fr)
BOCCAS Maxime (e-mail: mboccas@eso.org)
BOHM Torsten (e-mail: torsten.boehm@irap.omp.eu)
BOIN Tristan (e-mail: tristan.boin@etudiant.univ-rennes1.fr)
BOISSE Isabelle (e-mail: isabelle.boisse@lam.fr)
BOISSIER Samuel (e-mail: samuel.boissier@lam.fr)
BOISSON Catherine (e-mail: catherine.boisson@obspm.fr)
BOLDRINI Pierre (e-mail: boldrini@iap.fr)
BOMMIER Véronique (e-mail: V.Bommier@obspm.fr)
BONFAND Mélisse (e-mail: melisse.bonfand-caldeira@u-bordeaux.fr)
BONFILS Xavier (e-mail: xavier.bonfils@gmail.com)

BONNAIRE Tony (e-mail: tony.bonnaire@ias.u-psud.fr)
BONNASSIEUX Etienne (e-mail: etienne.bonnassieux@unibo.it)
BONNE Lars (e-mail: lbonne@usra.edu)
BONNEAU Daniel (e-mail: daniel.bonneau@oca.eu)
BONNEFOY Mickael (e-mail: mickael.bonnefoy@univ-grenoble-alpes.fr)
BONNET Guillaume (e-mail: guillaume.bonnet@lam.fr)
BONTEMPS Sylvain (e-mail: sylvain.bontemps@u-bordeaux.fr)
BOONKONGKIRD Chotipan (e-mail: B.Chotipan@gmail.com)
BORDIER Emma (e-mail: emma.bordier@eso.org)
BORG Janet (e-mail: borgjanet@gmail.com)
BOSMA Albert (e-mail: bosma@lam.fr)
BOSNJAK Zeljka (e-mail: Zeljka.Bosnjak@fer.hr)
BOT Caroline (e-mail: caroline.bot@astro.unistra.fr)
BOTTI Thierry (e-mail: thierry.botti@osupytheas.fr)
BOUCHE Nicolas (e-mail: nicolas.bouche@univ-lyon1.fr)
BOUCHET François (e-mail: bouchet@iap.fr)
BOULENGER Vincent (e-mail: vincent.boulenger@ipsa.fr)
BOULEY Sylvain (e-mail: sylvain.bouley@gmail.com)
BOUQUETY Axel (e-mail: a.bouquety@gmail.com)
BOURDAROT Guillaume (e-mail: guillaume.bourdarot@univ-grenoble-alpes.fr)
BOURGOIN Adrien (e-mail: adrien.bourgoin@obspm.fr)
BOURIAT Simon (e-mail: simon.bouriat@spaceable.org)
BOURNAUD Frédéric (e-mail: Frederic.bournaud@cea.fr)
BOURRIER Vincent (e-mail: vincent.bourrier@unige.ch)
BOUSCASSE Laure (e-mail: bouscasse@iram.fr)
BOUVIER Jerome (e-mail: jerome.bouvier@univ-grenoble-alpes.fr)
BOUY Herve (e-mail: herve.bouy@u-bordeaux.fr)
BRANCO Adrian (e-mail: adrian.branco@gmail.com)
BRAU-NOGUÉ Sylvie (e-mail: sylvie.brau-nogue@irap.omp.eu)
BRETON Sylvain (e-mail: sylvain.breton@cea.fr)
BRIOIS Christelle (e-mail: christelle.briois@cnrs-orleans.fr)
BRIONNE Mark (e-mail: mark.brionne@cnrs-orleans.fr)
BRIOT Danielle (e-mail: danielle.briot@obspm.fr)
BRON Emeric (e-mail: emeric.bron@obspm.fr)
BROUILLET Nathalie (e-mail: nathalie.brouillet@u-bordeaux.fr)
BROUSSAT Jean-Jacques (e-mail: jjbroussat@amtdata.com)
BRUN Allan Sacha (e-mail: sacha.brun@cea.fr)
BRUNN Valentin (e-mail: valentin.brunn@etu.umontpellier.fr)
BUCCIANTINI Luca (e-mail: luca.bucciantini@cnrs-orleans.fr)
BUCHLIN Éric (e-mail: eric.buchlin@universite-paris-saclay.fr)
BUGA Mihaela (e-mail: mihaela.buga@astro.unistra.fr)
BUGNET Lisa (e-mail: lbugnet@flatironinstitute.org)
BUIL Christian (e-mail: christian.buil@wanadoo.fr)
BULNES Manuela (e-mail: manolibulnes@gmail.com)
BURGARELLA Denis (e-mail: denis.burgarella@lam.fr)
BUSSCHAERT Clotilde (e-mail: cbusschaert@hotmail.fr)
CABANAC Rémi (e-mail: rcabanac@irap.omp.eu)
CABRAL Nahuel (e-mail: nahuel.cabral@univ-lyon1.fr)
CABRIT Sylvie (e-mail: sylvie.cabrit@obspm.fr)
CADIOU Corentin (e-mail: c.cadiou@ucl.ac.uk)
CALMELS Cyprien (e-mail: cyprien.calmels@etu.uca.fr)
CALORE Francesca (e-mail: calore@lapth.cnrs.fr)
CAMBRÉSY Laurent (e-mail: laurent.cambresy@astro.unistra.fr)
CANAMERAS Raoul (e-mail: rcanameras@mpa-garching.mpg.de)
CANTALLOUBE Faustine (e-mail: faustine.cantalloube@lam.fr)

CARASSOU Sébastien (e-mail: sebastiencarassou974@gmail.com)
CARINOS Emile (e-mail: emile.carinos@laposte.net)
CARLEY Eoin (e-mail: eoincarley@gmail.com)
CARMONA Andres (e-mail: andres.carmona@univ-grenoble-alpes.fr)
CAROTENUTO Francesco (e-mail: francesco.carotenuto@cea.fr)
CARPY Sabrina (e-mail: sabrina.carpy@univ-nantes.fr)
CARRASCO Nathalie (e-mail: nathalie.carrasco@latmos.ipsl.fr)
CASAMIQUELA Laia (e-mail: laia.casamiquela-floriach@u-bordeaux.fr)
CASOLI Fabienne (e-mail: fabienne.casoli@observatoiredeparis.psl.eu)
CASTELLANI Florent (e-mail: florent.castellani@irap.omp.eu)
CATALA Claude (e-mail: claude.catala@observatoiredeparis.psl.eu)
CAUX Emmanuel (e-mail: emmanuel.caux@irap.omp.eu)
CAVALIE Thibault (e-mail: thibault.cavalie@u-bordeaux.fr)
CENSIER Benjamin (e-mail: benjamin.censier@obs-nancay.fr)
CERUTTI Benoît (e-mail: benoit.cerutti@univ-grenoble-alpes.fr)
CHAABOUNI Henda (e-mail: henda.chaabouni@cyu.fr)
CHABERT Benjamin (e-mail: benjamin.chabert@obspm.fr)
CHANGEAT Quentin (e-mail: quentin.changeat.18@ucl.ac.uk)
CHANTEREAU William (e-mail: william.chantereau@astro.unistra.fr)
CHAPILLON Edwige (e-mail: edwige.chapillon@u-bordeaux.fr)
CHARBONNEL Corinne (e-mail: corinne.charbonnel@unige.ch)
CHARBONNEL Stéphane (e-mail: scharbonnel949@gmail.com)
CHARDIN Jonathan (e-mail: jonathan.chardin@astro.unistra.fr)
CHARLOT Stephane (e-mail: charlot@iap.fr)
CHARLY Pinçon (e-mail: charly.pincon@uliege.be)
CHARNAY Benjamin (e-mail: benjamin.charnay@obspm.fr)
CHARPINET Stephane (e-mail: stephane.charpinet@irap.omp.eu)
CHATAIN Audrey (e-mail: audrey.chatain@lmd.ipsl.fr)
CHAUVIN Gael (e-mail: gael.chauvin@univ-grenoble-alpes.fr)
CHAVEROT Guillaume (e-mail: guillaume.chaverot@unige.ch)
CHEN Siyuan (e-mail: siyuan.chen@cnrs-orleans.fr)
CHIAVASSA Andrea (e-mail: andrea.chiavassa@oca.eu)
CHINGAIPE Peter Marley (e-mail: peter.chingaipe@oca.eu)
CHITARRA Olivia (e-mail: olivia.chitarra@universite-paris-saclay.fr)
CHOLLET Lucas (e-mail: lucas.chollet@ipsa.fr)
CHOQUET Elodie (e-mail: elodie.choquet@lam.fr)
CHU Aline (e-mail: chu@iap.fr)
CIESLA Laure (e-mail: laure.ciesla@lam.fr)
CLAEYSSENS Adélaïde (e-mail: adelaide.claeyssens@univ-lyon1.fr)
CLAVEL Maïca (e-mail: maica.clavel@univ-grenoble-alpes.fr)
CLÉNET Yann (e-mail: yann.clenet@obspm.fr)
CLERC Nicolas (e-mail: nicolas.clerc@irap.omp.eu)
CODIS Sandrine (e-mail: sandrine.codis@cea.fr)
COGNARD Ismael (e-mail: icognard@cnrs-orleans.fr)
COHEN-TANUGI Johann (e-mail: johann.cohen-tanugi@umontpellier.fr)
COLEIRO Alexis (e-mail: alexis.coleiro@u-paris.fr)
COLLIN-ZAHN Suzy (e-mail: suzy.collin@obspm.fr)
COLOM Pierre (e-mail: pierre.colom@obspm.fr)
COLOMBAN Lucas (e-mail: lucas.colomban@cnrs-orleans.fr)
COMBES Francoise (e-mail: francoise.combes@obspm.fr)
COMMERCON Benoit (e-mail: benoit.commercon@ens-lyon.fr)
CONF Carbonfree (e-mail: admin@carbonfreeconf.com)
CONSEIL Emmanuel (e-mail: econseil@gmail.com)
CONSEIL Simon (e-mail: s.conseil@ip2i.in2p3.fr)
CONTINI Thierry (e-mail: thierry.contini@irap.omp.eu)

CORBEL Stéphane (e-mail: stephane.corbel@cea.fr)
CORNU David (e-mail: david.cornu@observatoiredeparis.psl.eu)
CORP Laurent (e-mail: laucorp@wanadoo.fr)
CORREIA Jean-Jacques (e-mail: jean-jacques.correia@univ-grenoble-alpes.fr)
CORTES-ZULETA Pia (e-mail: pia.cortes@lam.fr)
COSCAS Gabriel (e-mail: coscas.gabriel@gmail.com)
COTTALORDA Eric (e-mail: eric.cottalorda@oca.eu)
COTTIN Herve (e-mail: herve.cottin@lisa.u-pec.fr)
COUTENS Audrey (e-mail: audrey.coutens@irap.omp.eu)
COX Pierre (e-mail: pierre.cox@iap.fr)
COZZANI Giulia (e-mail: giuliacozzani@hotmail.it)
CREEVEY Orlagh (e-mail: orlagh.creevey@oca.eu)
CRIDA Aurélien (e-mail: crida@oca.eu)
CRINQUAND Benjamin (e-mail: benjamin.crinquand@univ-grenoble-alpes.fr)
CROVISIER Jacques (e-mail: jacques.crovisier@obspm.fr)
CRUZALEBES Pierre (e-mail: pierre.cruzalebes@oca.eu)
CSENGERI Timea (e-mail: TIMEA.CSENGERI@u-bordeaux.fr)
CUBY Jean-Gabriel (e-mail: jean-gabriel.cuby@lam.fr)
CUELLO Nicolas (e-mail: nicolas.cuello@univ-grenoble-alpes.fr)
CUILLANDRE Jean-Charles (e-mail: jc.cuillandre@cea.fr)
CUMENAL Didier (e-mail: cumenald@wanadoo.fr)
CVETOJEVIC Nick (e-mail: nick.cvetojevic@gmail.com)
D'HENDECOURT Louis (e-mail: ldh@ias.u-psud.fr)
DABAN Jean-Baptiste (e-mail: jean-baptiste.daban@obs-mip.fr)
DAGONEAU Nicolas (e-mail: dagoneau@apc.in2p3.fr)
DAHANI Souhail (e-mail: sdahani@irap.omp.eu)
DALAL Shweta (e-mail: shweta.dalal@iap.fr)
DALLIER Richard (e-mail: richard.dallier@subatech.in2p3.fr)
DAVOIGNEAU Jean (e-mail: jean.davoigneau@culture.gouv.fr)
DAZZI Pietro (e-mail: pietro.dazzi@cnrs-orleans.fr)
DE LA NOË Jérôme (e-mail: jerome.delanoe@sfr.fr)
DE LAVERNY Patrick (e-mail: laverny@oca.eu)
DEAL Morgan (e-mail: morgan.deal@astro.up.pt)
DEBRAS Florian (e-mail: florian.debras@irap.omp.eu)
DECELLE Aurélien (e-mail: adecelle@ucm.es)
DECOURCHELLE Anne (e-mail: anne.decourchelle@cea.fr)
DEFRÈRE Denis (e-mail: denis.defrere@kuleuven.be)
DEHEUVELS Sébastien (e-mail: sebastien.deheuvels@irap.omp.eu)
DELAHAYE Franck (e-mail: franck.delahaye@observatoiredeparis.psl.eu)
DELAVOIS Antony (e-mail: antony.delavois@lmd.ipsl.fr)
DELCAMP Simon (e-mail: simon.delcamp@univ-grenoble-alpes.fr)
DELCROIX Marc (e-mail: delcroix.marc@free.fr)
DELDEM Marc (e-mail: marc.deldem@free.fr)
DELEUIL Magali (e-mail: magali.deleuil@lam.fr)
DELORME Philippe (e-mail: philippe.delorme@univ-grenoble-alpes.fr)
DEMARTINO Matthew (e-mail: mcdemart@ucsc.edu)
DEMES Sandor (e-mail: sandor.demes@univ-rennes1.fr)
DEMYK Karine (e-mail: karine.demyk@irap.omp.eu)
DENNEFELD Michel (e-mail: dennefel@iap.fr)
DERRIERE Sébastien (e-mail: sebastien.derriere@astro.unistra.fr)
DESMARS Josselin (e-mail: josselin.desmars@obspm.fr)
DESROUSSEAUX Benjamin (e-mail: benjamin.desrousseaux@gmx.fr)
DETHIER William (e-mail: william.dethier@univ-grenoble-alpes.fr)
DHOUIB Hachem (e-mail: hachem.dhouib@cea.fr)
DI FOLCO Emmanuel (e-mail: edifolco@u-bordeaux.fr)

DI MATTEO Paola (e-mail: Paola.dimatteo@obspm.fr)
DÍAZ Rodrigo (e-mail: rdiaz@unsam.edu.ar)
DITZ Patrick (e-mail: patrick.ditz@wanadoo.fr)
DOLE Herve (e-mail: herve_dole@yahoo.com)
DONATI Jean-Francois (e-mail: jean-francois.donati@irap.omp.eu)
DOUGADOS Catherine (e-mail: catherine.dougados@univ-grenoble-alpes.fr)
DOUSPIS Marian (e-mail: marian.douspis@ias.u-psud.fr)
DOUTÉ Sylvain (e-mail: sylvain.doute@univ-grenoble-alpes.fr)
DOYEN Guillaume (e-mail: guillaume.optics@gmail.com)
DRANT Thomas (e-mail: thomas.drant@latmos.ipsl.fr)
DROSSART Pierre (e-mail: pierre.drossart@iap.fr)
DUBOIS Julien (e-mail: julien.dubois@univ-grenoble-alpes.fr)
DUBOIS Yohan (e-mail: dubois@iap.fr)
DUBREUIL Pierre (e-mail: pierre.dubreuil@gmail.com)
DUC Pierre-Alain (e-mail: pierre-alain.duc@astro.unistra.fr)
DUCROT Elsa (e-mail: educrot@uliege.be)
DUDOK DE WIT Thierry (e-mail: ddwit@cnrs-orleans.fr)
DUMONT Thibaut (e-mail: thibaut.dumont@unige.ch)
DUMUSQUE Xavier (e-mail: xavier.dumusque@unige.ch)
DUPOURQUÉ Simon (e-mail: sdupourque@irap.omp.eu)
DUPUIS Hadrien (e-mail: hadrien.dupuis@orange.fr)
DUROCHER Arnaud (e-mail: arnaud.durocher@cea.fr)
DURRET Florence (e-mail: durret@iap.fr)
DURRIVE Jean Baptiste (e-mail: jdurrive@protonmail.com)
DURST Clémence (e-mail: clemence.durst@oca.eu)
DUTREY Anne (e-mail: anne.dutrey@u-bordeaux.fr)
EL FAKHIRI Abdeladim (e-mail: abdeladim.elfakhiri@gmail.com)
EL HADI Kacem (e-mail: kacem.elhadi@lam.fr)
EL MELLAH Ileyk (e-mail: ileyk.elmellah@univ-grenoble-alpes.fr)
ELBAZ David (e-mail: david.elbaz@cea.fr)
ELLIEN Amaël (e-mail: a.r.j.ellien@uva.nl)
ESCOFFIER Stephanie (e-mail: escoffier@cppm.in2p3.fr)
ESPINASSE Mathilde (e-mail: mathilde.espinasse@cea.fr)
EZZIATI Meriam (e-mail: meriam.ezziati@lam.fr)
FALGARONE Edith (e-mail: edith.falgarone@ens.fr)
FAMAEY Benoit (e-mail: benoit.famaey@astro.unistra.fr)
FARCY Marion (e-mail: marion.farcy@univ-lyon1.fr)
FARGETTE Naïs (e-mail: nfargette@irap.omp.eu)
FARRENS Samuel (e-mail: samuel.farrens@cea.fr)
FAUROBERT Marianne (e-mail: marianne.faurobert@oca.eu)
FEAUTRIER Nicole (e-mail: Nicole.Feautrier@obspm.fr)
FEAUTRIER Philippe (e-mail: philippe.feautrier@univ-grenoble-alpes.fr)
FENSCH Jérémy (e-mail: jeremy.fensch@ens-lyon.fr)
FERLET Roger (e-mail: ferlet@iap.fr)
FERNÁNDEZ-ALVAR Emma (e-mail: Emma.Fernandez-Alvar@oca.eu)
FERRARI Chiara (e-mail: chiara.ferrari@oca.eu)
FICHET DE CLAIRFONTAINE Gaëtan (e-mail: gaetan.fichetdeclairfontaine@obspm.fr)
FICOT Audrey (e-mail: audrey.ficot@numericable.fr)
FIGON Patrick (e-mail: patrick.figon@osupytheas.fr)
FINLEY Adam (e-mail: adam.finley@cea.fr)
FLAGEY Nicolas (e-mail: nflagey@me.com)
FOGLIZZO Thierry (e-mail: foglizzo@cea.fr)
FOIN Martin (e-mail: martin.foin@univ-grenoble-alpes.fr)
FOUCHET Thierry (e-mail: thierry.fouchet@obspm.fr)
FOUCHEZ Dominique (e-mail: fouchez@cppm.in2p3.fr)

FOUQUÉ Pascal (e-mail: Pascal.Fouque@irap.omp.eu)
FOUREZ Julien (e-mail: julien.fourez@fr.thalesgroup.com)
FRAIX-BURNET Didier (e-mail: didier.fraix-burnet@univ-grenoble-alpes.fr)
FRÉOUR Laurane (e-mail: laurane.freour@eleves.ec-nantes.fr)
FREUNDLICH Jonathan (e-mail: jonathan.freundlich@astro.unistra.fr)
FROMENT Clara (e-mail: clara.froment@cnrs-orleans.fr)
FURTAK Lukas (e-mail: furtak@iap.fr)
GALÁRRAGA-ESPINOSA Daniela (e-mail: daniela.galarraga@universite-paris-saclay.fr)
GANGLER Emmanuel (e-mail: emmanuel.gangler@clermont.in2p3.fr)
GANNOUNI Bahaeddine (e-mail: bahaeddine.gannouni@cea.fr)
GANS Bérenger (e-mail: berenger.gans@universite-paris-saclay.fr)
GARCIA Rafael (e-mail: rgarcia@cea.fr)
GARCIA MARIN Satur (e-mail: saturhelena@orange.fr)
GARDE Olivier (e-mail: o.garde@wanadoo.fr)
GATKINE Pradip (e-mail: pgatkine@caltech.edu)
GATTANO César (e-mail: cesar.gattano@aiub.unibe.ch)
GAUDEL Mathilde (e-mail: mathilde-gaudel@orange.fr)
GAUTHIER Gaetan (e-mail: gaetan.gauthier@lpp.polytechnique.fr)
GAVAZZI Raphael (e-mail: gavazzi@iap.fr)
GAZAGNES Simon (e-mail: sgazagnes@gmail.com)
GIAMMICHELE Noemi (e-mail: noemi.giammichele@irap.omp.eu)
GIARD Martin (e-mail: martin.giard@irap.omp.eu)
GILLET Nicolas (e-mail: nicolas.gillet@astro.unistra.fr)
GIRARD Julien (e-mail: jgirard@stsci.edu)
GIRARD Julien (e-mail: julien.girard@cea.fr)
GKOTSINAS Anastasios (e-mail: anastasios.gkotsinas@univ-lyon1.fr)
GODARD Amélie (e-mail: amelie.godard@univ-rennes1.fr)
GODARD Jean-Paul (e-mail: jean-paul.godard@cegetel.net)
GOLDMAN Bertrand (e-mail: bertrand.goldman@isunet.edu)
GONZALEZ Ezequiel (e-mail: ezequiel.gonzalez@community.isunet.edu)
GONZALEZ Jean-François (e-mail: Jean-Francois.Gonzalez@ens-lyon.fr)
GORCE Adelie (e-mail: adelie.gorce@gmail.com)
GORI Pierre-Marie (e-mail: pierre-marie.gori@oca.eu)
GOTZ Diego (e-mail: diego.gotz@cea.fr)
GOUIFFES Christian (e-mail: christian.gouiffes@cea.fr)
GOUIN Céline (e-mail: celine.gouin@ias.u-psud.fr)
GOURDON Franck (e-mail: franck.gourdon@oagc.fr)
GOUYOU BEAUCHAMPS Sylvain (e-mail: gouyoub@cppm.in2p3.fr)
GRANIER Camille (e-mail: camille.granier@oca.eu)
GRAPPIN Roland (e-mail: roland.grappin@lpp.polytechnique.fr)
GRATIER Pierre (e-mail: pierre.gratier@u-bordeaux.fr)
GRESSIER Amélie (e-mail: amg.gressier@gmail.com)
GRIESSMEIER Jean-Mathias (e-mail: jean-mathias.griessmeier@cnrs-orleans.fr)
GRITON Léa (e-mail: lea.griton@irap.omp.eu)
GRONOFF Guillaume (e-mail: guillaume.p.gronoff@nasa.gov)
GROUSSIN Olivier (e-mail: olivier.groussin@lam.fr)
GRY Cecile (e-mail: cecile.gry@lam.fr)
GUÉRARD Jean (e-mail: jean.guerard@saf-astronomie.fr)
GUERIN William (e-mail: william.guerin@inphyni.cnrs.fr)
GUERLET Sandrine (e-mail: sandrine.guerlet@lmd.ipsl.fr)
GUETH Frederic (e-mail: gueth@iram.fr)
GUILET Jérôme (e-mail: jerome.guilet@cea.fr)
GUILLARD Pierre (e-mail: guillard@iap.fr)
GUILLEMOT Lucas (e-mail: lucas.guillemot@cnrs-orleans.fr)
GUINOT Axel (e-mail: guinot@apc.in2p3.fr)

GUITTON Thomas (e-mail: thomas.guitton@ipsa.fr)
GUPTA Sakshi (e-mail: sg20rs057@iiserkol.ac.in)
GURURAJAN Gayathri (e-mail: gayathri.gururajan@lam.fr)
HABART Emilie (e-mail: emilie.habart@ias.u-psud.fr)
HADID Lina (e-mail: lina.hadid@lpp.polytechnique.fr)
HALLE Anaelle (e-mail: anaelle.halle@obspm.fr)
HAMERS Adrian (e-mail: hamers@mpa-garching.mpg.de)
HAMMER Francois (e-mail: francois.hammer@obspm.fr)
HARA Nathan (e-mail: nathan.hara@unige.ch)
HAROUN Karim (e-mail: karim.haroun@etu.univ-lyon1.fr)
HAUBOIS Xavier (e-mail: xhaubois@eso.org)
HAYWOOD Misha (e-mail: misha.haywood@obspm.fr)
HÉBRARD Guillaume (e-mail: hebrard@iap.fr)
HEIDARI Neda (e-mail: heidari_n@ymail.com)
HENAREJOS Philippe (e-mail: philippe.henarejos@cieletespace.fr)
HENNEBELLE Patrick (e-mail: patrick.hennebelle@cea.fr)
HERPIN Fabrice (e-mail: fabrice.herpin@u-bordeaux.fr)
HILL Vanessa (e-mail: vanessa.hill@oca.eu)
HIRSH Kieran (e-mail: kieran.hirsh@univ-lyon1.fr)
HMIDDOUCH Said (e-mail: hmiddouch.said@gmail.com)
HOCDÉ Vincent (e-mail: vincent.hocde@gmail.com)
HOFFMANN Leopoldo (e-mail: hofbre@gmail.com)
HOUDAYER Pierre (e-mail: pierre.houdayer@obspm.fr)
HOUDEBINE Eric (e-mail: eric_houdebine@yahoo.fr)
HOYER Sergio (e-mail: sergio.hoyer@lam.fr)
HU Dangning (e-mail: dangning.hu@outlook.com)
HUBER Guillaume (e-mail: guillaume.h35@gmail.com)
HUBY Elsa (e-mail: elsa.huby@obspm.fr)
HUE Vincent (e-mail: vince.hue.fr@gmail.com)
HUERTAS-COMPANY Marc (e-mail: marc.huertas@obspm.fr)
HURTADO Norma (e-mail: norma.hurtado@gmail.com)
IBATA Rodrigo (e-mail: rodrigo.ibata@astro.unistra.fr)
ISHIDA Emille (e-mail: emille.ishida@clermont.in2p3.fr)
ISSAUTIER Karine (e-mail: karine.issautier@obspm.fr)
JAIN Rashi (e-mail: r.jain@unistra.fr)
JAMES Tomin (e-mail: Tomin.James@obspm.fr)
JAUZAC Mathilde (e-mail: mathilde.jauzac@durham.ac.uk)
JAVELLE Thomas (e-mail: thomas.javelle.pro@gmail.com)
JEANNEAU Alexandre (e-mail: alexandre.jeanneau@univ-lyon1.fr)
JIMENEZ Xavier (e-mail: xavier.jimenez@ens-lyon.fr)
JOBLIN Christine (e-mail: christine.joblin@irap.omp.eu)
JOLLY Antoine (e-mail: jolly@lisa.ipsl.fr)
JONCOUR Isabelle (e-mail: isabelle.joncour@univ-grenoble-alpes.fr)
JOSSELIN Eric (e-mail: eric.josselin@umontpellier.fr)
JOUVE Laurene (e-mail: laurene.jouve@irap.omp.eu)
JUBIER Xavier (e-mail: xjubier@free.fr)
JULLO Eric (e-mail: eric.jullo@lam.fr)
KAMMOUN Elias (e-mail: ekammoun@irap.omp.eu)
KENCHINGTON Harry-Dean (e-mail: harry-dean.kenchingtongoldsmith@anu.edu.au)
KERVAZO Mathilde (e-mail: mathilde.kervazo@univ-nantes.fr)
KERVELLA Pierre (e-mail: pierre.kervella@obspm.fr)
KHLAT Lucie (e-mail: lucie.khlat@lam.fr)
KIEFER Flavien (e-mail: flavien.kiefer@obspm.fr)
KIEOKAEW Rungployphan (e-mail: rkieokaew@irap.omp.eu)
KILBINGER Martin (e-mail: martin.kilbinger@cea.fr)

KLEIN Baptiste (e-mail: baptiste.klein@physics.ox.ac.uk)
KLEIN Karl-Ludwig (e-mail: ludwig.klein@obspm.fr)
KLUSKA Jacques (e-mail: jacques.kluska@kuleuven.be)
KNÖDLSEDER Jürgen (e-mail: jknodlseder@irap.omp.eu)
KODI RAMANAH Doogesh (e-mail: ramanah@nbi.ku.dk)
KÖNIG Pierre-Cécil (e-mail: pkonig@eso.org)
KORDOPATIS Georges (e-mail: georges.kordopatis@oca.eu)
KOSKAS Remy (e-mail: remy.koskas@obspm.fr)
KOUTCHMY Serge (e-mail: koutchmy@iap.fr)
KOUTROUMPA Dimitra (e-mail: dimitra.koutroumpa@latmos.ipsl.fr)
KOZHIKKAL Musfar Muhamed (e-mail: musfar-muhamed.kozhikkal@cnrs-orleans.fr)
KRAL Quentin (e-mail: quentin.kral@gmail.com)
KRALJIC Katarina (e-mail: katarina.kraljic@lam.fr)
KRETZSCHMAR Matthieu (e-mail: matthieu.kretzschmar@cnrs-orleans.fr)
LAFAYE Marc (e-mail: marc.lafaye.astro@gmx.fr)
LAGACHE Guilaine (e-mail: guilaine.lagache@lam.fr)
LAGADEC Eric (e-mail: eric.lagadec@oca.eu)
LAGAGE Pierre-Olivier (e-mail: pierre-olivier.lagage@cea.fr)
LAGARDE Nadège (e-mail: nadege.lagarde@utinam.cnrs.fr)
LAI Olivier (e-mail: olivier.lai@oca.eu)
LAIGLE Clotilde (e-mail: laigle@iap.fr)
LALLEMENT Manon (e-mail: manon.lallement@universite-paris-saclay.fr)
LAMAREILLE Fabrice (e-mail: fabrice.lamareille@ipsa.fr)
LAMBERTS Astrid (e-mail: astrid.lamberts@oca.eu)
LAMY Jérôme (e-mail: jerome.lamy@laposte.net)
LAMY Laurent (e-mail: laurent.lamy@obspm.fr)
LANÇON Ariane (e-mail: ariane.lancon@astro.unistra.fr)
LANGAN Ivanna (e-mail: langan.annavi@gmail.com)
LANGLOIS Maud (e-mail: maud.langlois@univ-lyon1.fr)
LANUSSE Francois (e-mail: francois.lanusse@cea.fr)
LANZIERI Denise (e-mail: denise.lanzieri@cea.fr)
LASKAR Jacques (e-mail: jacques.laskar@obspm.fr)
LAUGIER Romain (e-mail: romain.laugier@kuleuven.be)
LAURENT Philippe (e-mail: philippe.laurent@cea.fr)
LAVAIL Alexis (e-mail: alexis.lavail@physics.uu.se)
LAVAUX Guilhem (e-mail: guilhem.lavaux@iap.fr)
LAVIRON Adrien (e-mail: adrien.laviron@csnsm.in2p3.fr)
LAVORENTI Federico (e-mail: federico.lavorenti@oca.eu)
LAVRAUD Benoit (e-mail: benoit.lavraud@u-bordeaux.fr)
LE BOUQUIN Jean-Baptiste (e-mail: jean-baptiste.lebouquin@univ-grenoble-alpes.fr)
LE BRUN Amandine (e-mail: amandine.le-brun@obspm.fr)
LE CONTEL Olivier (e-mail: olivier.lecontel@lpp.polytechnique.fr)
LE DÛ Pascal (e-mail: ledu@shom.fr)
LE FLOC'H Emeric (e-mail: emeric.lefloch@cea.fr)
LE GAL Romane (e-mail: romane.legal@irap.omp.eu)
LE GOUELLEC Valentin (e-mail: valentin.le.gouellec@gmail.com)
LE GUEN Patrice (e-mail: patrice.leguen@laposte.net)
LE LAIN Matthieu (e-mail: matthieulel@gmail.com)
LE MIGNANT David (e-mail: david.lemignant@lam.fr)
LE PETIT Franck (e-mail: Franck.LePetit@obspm.fr)
LE PONCIN-LAFITTE Christophe (e-mail: christophe.leponcin@obspm.fr)
LE SAUX Arthur (e-mail: al598@exeter.ac.uk)
LE VAN SUU Auguste (e-mail: Auguste.Levansuu@osupytheas.fr)
LEBOULLEUX Lucie (e-mail: lucie.leboulleux@univ-grenoble-alpes.fr)
LEBOUTEILLER Vianney (e-mail: vianney.lebouteiller@cea.fr)

LEBRE Agnès (e-mail: agnes.lebre@umontpellier.fr)
LEBRETON Yveline (e-mail: yveline.lebreton@obspm.fr)
LECLERC Aurelia (e-mail: aurelia.leclerc@univ-grenoble-alpes.fr)
LECLERCQ Floriane (e-mail: floriane.leclercq@unige.ch)
LECONTE Jeremy (e-mail: jeremy.leconte@u-bordeaux.fr)
LEDU Pascal (e-mail: cielocean29@gmail.com)
LEHOUCQ Roland (e-mail: lehoucq@cea.fr)
LEIBACHER John (e-mail: john.leibacher@universite-paris-saclay.fr)
LEKIC Anica (e-mail: anica.lekic@ipsa.fr)
LELLOUCH Emmanuel (e-mail: emmanuel.lellouch@obspm.fr)
LEMAY Damien (e-mail: damien.lemay@globetrotter.net)
LEMIERE Anne (e-mail: alemiere@apc.in2p3.fr)
LEMOINE Martin (e-mail: lemoine@iap.fr)
LÉNA Pierre (e-mail: pierre.lena@obspm.fr)
LENAIN Jean-Philippe (e-mail: jlenain@in2p3.fr)
LESAGE Nelly (e-mail: nelly.lesage@humanoid.fr)
LESUR Geoffroy (e-mail: geoffroy.lesur@univ-grenoble-alpes.fr)
LEVRIER François (e-mail: francois.levrier@ens.fr)
LHOUSSAINE Romain (e-mail: romain.lhoussaine@gmail.com)
LIGI Roxanne (e-mail: roxanne.ligi@oca.eu)
LILENSTEN Jean (e-mail: jean.lilensten@univ-grenoble-alpes.fr)
LIMOUSIN Marceau (e-mail: marceau.limousin@lam.fr)
LIQUE Francois (e-mail: francois.lique@univ-rennes1.fr)
LIZEE Thomas (e-mail: thomas.lizee@astro.unistra.fr)
LOH Alan (e-mail: alan.loh@obspm.fr)
LOMBARDO Simona (e-mail: simona.lombardo@lam.fr)
LOMBART Gael (e-mail: glombart@leparisien.fr)
LOPEZ Arturo (e-mail: alopezariste@gmail.com)
LOUIS Corentin (e-mail: corentin.louis@dias.ie)
LOUTFI Amal (e-mail: loutifi.amal@gmail.com)
LOUVET Fabien (e-mail: fabien.louvet@cea.fr)
LOUYS Mireille (e-mail: mireille.louys@unistra.fr)
LUASHVILI Anna (e-mail: anna.luashvili@obspm.fr)
LUC Poirier (e-mail: luc.poirier@oca.eu)
MADDEN Suzanne (e-mail: suzanne.madden@cea.fr)
MAGGI Pierre (e-mail: pierre.maggi@astro.unistra.fr)
MAGRI Julie (e-mail: julie.magri@unilim.fr)
MAHLER Guillaume (e-mail: guillaume.mahler@durham.ac.uk)
MAILLARD Vincent (e-mail: vincent.maillard@obspm.fr)
MAIRE Anne-Lise (e-mail: almaire@uliege.be)
MAKSIMOVIC Milan (e-mail: milan.maksimovic@obspm.fr)
MALAVASI Nicola (e-mail: nicola.malavasi@universite-paris-saclay.fr)
MALBET Fabien (e-mail: Fabien.Malbet@univ-grenoble-alpes.fr)
MÂLIN Mathilde (e-mail: malinmathilde@gmail.com)
MALLIA Franco (e-mail: francomallia@tin.it)
MALZAC Julien (e-mail: julien.malzac@irap.omp.eu)
MANICK Rajeev (e-mail: rajeev.manick@univ-grenoble-alpes.fr)
MARCHAUDON Aurélie (e-mail: aurelie.marchaudon@irap.omp.eu)
MARCOWITH Alexandre (e-mail: Alexandre.Marcowith@umontpellier.fr)
MARET Sébastien (e-mail: sebastien.maret@univ-grenoble-alpes.fr)
MARICHALAR Pascal (e-mail: pascal.marichalar@cnrs.fr)
MARIN Frédéric (e-mail: frederic.marin@astro.unistra.fr)
MARINI Paolo (e-mail: paolo-linkedin@nicealias.com)
MARQUETTE Jean-Baptiste (e-mail: jean-baptiste.marquette@u-bordeaux.fr)
MARTIN Guillermo (e-mail: guillermo.martin@univ-grenoble-alpes.fr)

MARTINACHE Frantz (e-mail: frantz.martinache@oca.eu)
MARTINOD Marc-Antoine (e-mail: ma.martinod@gmail.com)
MARTINS Fabrice (e-mail: fabrice.martins@umontpellier.fr)
MARTIOLI Eder (e-mail: edermartioli@gmail.com)
MARY David (e-mail: david.mary@unice.fr)
MASSON Adrien (e-mail: adrien.masson@obspm.fr)
MASSON Sophie (e-mail: sophie.masson@obspm.fr)
MASVIEL Jean-Pierre (e-mail: jp.masviel@orange.fr)
MATHIAS Philippe (e-mail: Philippe.Mathias@irap.omp.eu)
MATHIS Stephane (e-mail: stephane.mathis@cea.fr)
MATHUR Savita (e-mail: smathur@iac.es)
MATTER Alexis (e-mail: Alexis.Matter@oca.eu)
MAUDUIT Emilie (e-mail: emilie.mauduit@universite-paris-saclay.fr)
MAUROGORDATO Sophie (e-mail: Sophie.Maurogordato@oca.eu)
MAURY Anaëlle (e-mail: anaelle.maury@cea.fr)
MAZZILLI CIRAULO Barbara (e-mail: Barbara.Mazzilli-Ciraulo@observatoiredeparis.psl.eu)
MÉHEUT Héloïse (e-mail: heloise.meheut@oca.eu)
MEI Simona (e-mail: mei@apc.in2p3.fr)
MELCHIOR Anne-Laure (e-mail: Anne-Laure.Melchior@observatoiredeparis.psl.eu)
MELIANI Zakaria (e-mail: zakaria.meliani@obspm.fr)
MELISSE Jean-Paul (e-mail: jean-paul.melisse@u-bordeaux.fr)
MELLIER Yannick (e-mail: mellier@iap.fr)
MENARD Francois (e-mail: francois.menard@univ-grenoble-alpes.fr)
MERCIER Wilfried (e-mail: wilfried.mercier@irap.omp.eu)
MERLE Thibault (e-mail: tmerle@ulb.ac.be)
MERTENS Florent (e-mail: florent.mertens@gmail.com)
MEUNIER Nadège (e-mail: nadege.meunier@univ-grenoble-alpes.fr)
MICHEL Patrick (e-mail: michelp@oca.eu)
MICHEL-DANSAC Leo (e-mail: leo.michel-dansac@univ-lyon1.fr)
MICHOULIER Stéphane (e-mail: stephane.michoulier@univ-lyon1.fr)
MIDAVAINE Thierry (e-mail: thierry.midavaine@saf-astronomie.fr)
MIGNON-RISSE Raphaël (e-mail: raphael.mignon-risse@apc.in2p3.fr)
MILLI Julien (e-mail: julien.milli@univ-grenoble-alpes.fr)
MILLOUR Florentin (e-mail: fmillour@oca.eu)
MIRABEL Felix (e-mail: felix.mirabel@cea.fr)
MIROUH Giovanni (e-mail: gm0027@surrey.ac.uk)
MIVILLE-DESCHÊNES Marc-Antoine (e-mail: marc-antoine.miville-deschenes@cnrs.fr)
MODOLO Ronan (e-mail: ronan.modolo@latmos.ipsl.fr)
MONDELIN Maëlie (e-mail: maelie.mond@gmail.com)
MONTARGÈS Miguel (e-mail: miguel.montarges@observatoiredeparis.psl.eu)
MONTILLAUD Julien (e-mail: julien.montillaud@univ-fcomte.fr)
MORALES SERRANO Sara (e-mail: sara.morales@esa.int)
MORAUX Estelle (e-mail: estelle.moraux@univ-grenoble-alpes.fr)
MOREAU Francois (e-mail: francois.moreau@osupytheas.fr)
MORIN Julien (e-mail: julien.morin@umontpellier.fr)
MORISSET Christophe (e-mail: chris.morisset@gmail.com)
MOSSER Benoit (e-mail: benoit.mosser@obspm.fr)
MOTTE Frederique (e-mail: frederique.motte@univ-grenoble-alpes.fr)
MOTTEZ Fabrice (e-mail: fabrice.mottez@obspm.fr)
MOUILLET David (e-mail: david.mouillet@univ-grenoble-alpes.fr)
MOURARD Denis (e-mail: denis.mourard@oca.eu)
MOUTOU Claire (e-mail: claire.moutou@irap.omp.eu)
MULATO Lionel (e-mail: lionelmulato@gmail.com)
MUNOZ SARDANETA Maria Minerva (e-mail: minerva.munoz@lam.fr)
MURDOCH Naomi (e-mail: naomi.murdoch@isae.fr)

MUSSET Sophie (e-mail: sophie.musset@esa.int)
N'DIAYE Mamadou (e-mail: mamadou.ndiaye@oca.eu)
NARDETTO Nicolas (e-mail: Nicolas.Nardetto@oca.eu)
NEBOT Ada (e-mail: ada.nebot@astro.unistra.fr)
NEICHEL Benoit (e-mail: benoit.neichel@lam.fr)
NEINER Coralie (e-mail: coralie.neiner@obspm.fr)
NENON Quentin (e-mail: q.nenon@gmail.com)
NESVADBA Nicole (e-mail: nicole.nesvadba@oca.eu)
NEVEU Stephane (e-mail: stephane.neveu@saf-astronomie.fr)
NEZRI Emmanuel (e-mail: emmanuel.nezri@lam.fr)
NG-GUIHENEUF Cherry (e-mail: cherrywyng@gmail.com)
NGUYEN Gautier (e-mail: gautier-mahe.nguyen@intradef.gouv.fr)
NIEMIEC Anna (e-mail: anna.niemiec@durham.ac.uk)
NOLL Anthony (e-mail: anoll@irap.omp.eu)
NORAZ Quentin (e-mail: quentin.noraz-73@hotmail.fr)
NOVAK Jerome (e-mail: jerome.novak@obspm.fr)
NOYELLES Benoît (e-mail: benoit.noyelles@univ-fcomte.fr)
NUNEZ Arturo (e-mail: arturo.nunez@cea.fr)
OCVIRK Pierre (e-mail: pierre.ocvirk@astro.unistra.fr)
OMONT Alain (e-mail: omont@iap.fr)
OUAZZANI Rhita-Maria (e-mail: rhita-maria.ouazzani@obspm.fr)
OUDART Nicolas (e-mail: nicolas.oudart@latmos.ipsl.fr)
PACAUD Florian (e-mail: fpacaud@astro.uni-bonn.de)
PAGANI Laurent (e-mail: laurent.pagani@obspm.fr)
PAILLOU Philippe (e-mail: philippe.paillou@u-bordeaux.fr)
PALACIOS Ana (e-mail: ana.palacios@umontpellier.fr)
PALAKKATHARAPPIL Dinil Bose (e-mail: dinilbose@oca.eu)
PALMERIO Jesse (e-mail: jesse.palmerio@obspm.fr)
PANEK Emilie (e-mail: emipanek918@gmail.com)
PANNETIER Cyril (e-mail: cyril.pannetier@oca.eu)
PANTIN Eric (e-mail: eric.pantin@cea.fr)
PANTOLMOS George (e-mail: george.pantolmos@univ-grenoble-alpes.fr)
PARENTI Susanna (e-mail: susanna.parenti@ias.u-psud.fr)
PARIAT Etienne (e-mail: etienne.pariat@obspm.fr)
PAUGNAT Hadrien (e-mail: hadrien.paugnat@obspm.fr)
PAULIN-HENRIKSSON Stéphane (e-mail: stephane.paulin-henriksson@u-bordeaux.fr)
PAUMARD Thibaut (e-mail: thibaut.paumard@obspm.fr)
PECONTAL Emmanuel (e-mail: emmanuel.pecontal@univ-lyon1.fr)
PEIRANI Sébastien (e-mail: speirani@oca.eu)
PELLEGRIN Theo (e-mail: theo.pellegrin@obspm.fr)
PELLO Roser (e-mail: roser.pello@lam.fr)
PERALTA Raphaël (e-mail: raphael.peralta@cea.fr)
PEREZ Marie (e-mail: marie.perez@cnrs.fr)
PERLBARG Anne-Charlotte (e-mail: anne-charlotte.perlbarg@obspm.fr)
PERRAUT Karine (e-mail: karine.perraut@univ-grenoble-alpes.fr)
PERRET Emmanuelle (e-mail: emmanuelle.perret@astro.unistra.fr)
PERRI Barbara (e-mail: barbara.perri@kuleuven.be)
PERRIN Clement (e-mail: clement.perrin@univ-nantes.fr)
PERRIN Guy (e-mail: guy.perrin@cnrs-dir.fr)
PERRIN Zoe (e-mail: zoe.perrin@latmos.ipsl.fr)
PERROT Clément (e-mail: clement.perrot@obspm.fr)
PERSSON Moa (e-mail: moa.persson@irap.omp.eu)
PETIT Antoine (e-mail: antoine.petit@astro.lu.se)
PETIT Jean-Marc (e-mail: jean-marc.petit@normalesup.org)
PETIT Pascal (e-mail: ppetit@irap.omp.eu)

PETIT Quentin (e-mail: quentin.petit.1@u-bordeaux.fr)
PETIT Thomas (e-mail: petittom@gmail.com)
PETRUCCI Pierre-Olivier (e-mail: pierre-olivier.petrucci@univ-grenoble-alpes.fr)
PETTORINO Valeria (e-mail: valeria.pettorino@me.com)
PFISTER Hugo (e-mail: hugo.pfister@nbi.ku.dk)
PHILIPPE Louarn (e-mail: philippe.louarn@irap.omp.eu)
PICOUET Vincent (e-mail: vp2376@columbia.edu)
PIERI Matthew (e-mail: matthew.pieri@lam.fr)
PILLEPICH Annalisa (e-mail: pillepich@mpia.de)
PINTO Rui (e-mail: rui.pinto@cea.fr)
PIRLOT Paul (e-mail: paul.pirlot@univ-rennes1.fr)
PITOUT Frédéric (e-mail: frederic.pitout@irap.omp.eu)
PLANTE Julien (e-mail: julien.plante@obspm.fr)
PLOTNIKOV Illya (e-mail: illya.plotnikov@irap.omp.eu)
POINTECOUTEAU Etienne (e-mail: etienne.pointecouteau@irap.omp.eu)
POIRIER Nicolas (e-mail: nicolas.poirier@irap.omp.eu)
POMMIER Mamta (e-mail: mamtapan@gmail.com)
POSTI Lorenzo (e-mail: lorenzo.posti@astro.unistra.fr)
POTIER Axel (e-mail: axel.q.potier@jpl.nasa.gov)
POUILLY Kim (e-mail: kim.pouilly@univ-grenoble-alpes.fr)
POURCELOT Raphaël (e-mail: raphael.pourcelot@oca.eu)
POUTEAU Yohan (e-mail: yohan.pouteau@univ-grenoble-alpes.fr)
POVEDA Mathilde (e-mail: mathilde.poveda@lisa.ipsl.fr)
PROUST Dominique (e-mail: dominique.proust@obspm.fr)
PUECH Mathieu (e-mail: mathieu.puech@obspm.fr)
QUINTIN Erwan (e-mail: erwan.quintin@irap.omp.eu)
RAFALIMANANA Alohotsy (e-mail: alohotsy.rafalimanana@oca.eu)
RAMAMBASON Lise (e-mail: lise.ramambason@cea.fr)
RAYNAUD Raphaël (e-mail: raphael.raynaud@cea.fr)
REBOUL Henri (e-mail: henri.reboul@umontpellier.fr)
REBOUL-SALZE Alexis (e-mail: alexisreboulsalze@gmail.com)
RECIO-BLANCO Alejandra (e-mail: arecio@oca.eu)
REESE Daniel (e-mail: daniel.reese@obspm.fr)
REMY Benjamin (e-mail: benjamin.remy@cea.fr)
RÉVILLE Victor (e-mail: victor.reville@irap.omp.eu)
REY Maxime (e-mail: maxime.rey@univ-lyon1.fr)
REYLÉ Céline (e-mail: celine@obs-besancon.fr)
REZEAU Laurence (e-mail: laurence.rezeau@sorbonne-universite.fr)
RICHARD Johan (e-mail: johan.richard@univ-lyon1.fr)
ROBERT Vincent (e-mail: vincent.robert@obspm.fr)
ROBIN Annie (e-mail: annie.robin@obs-besancon.fr)
ROBITAILLE Jean-François (e-mail: jean-francois.robitaille@univ-grenoble-alpes.fr)
ROBUTEL Philippe (e-mail: philippe.robutel@obspm.fr)
ROCCI Pier-Francesco (e-mail: pierfrancesco.rocci@gmail.com)
ROCHAIN Serge (e-mail: srochain@gmail.com)
ROGGERO Noemi (e-mail: noemi.roggero@univ-grenoble-alpes.fr)
ROLAND Timothé (e-mail: timothe.roland@univ-fcomte.fr)
ROMEUF David (e-mail: david.romeuf@univ-lyon1.fr)
ROQUES Françoise (e-mail: francoise.roques@obspm.fr)
ROSDAHL Joakim (e-mail: karl-joakim.rosdahl@univ-lyon1.fr)
ROTH Ilaria (e-mail: rothilaria@gmail.com)
ROUSSELOT Lionel (e-mail: tesse.lionel@free.fr)
ROUSSELOT Philippe (e-mail: phil@obs-besancon.fr)
ROYER Frédéric (e-mail: frederic.royer@obspm.fr)
ROZIER Simon (e-mail: simon.rozier@astro.unistra.fr)

SADH Mradumay (e-mail: mradumay137@gmail.com)
SADIBEKOVA Tatyana (e-mail: tatyana.sadibekova@cea.fr)
SAEZ CASARES Iñigo (e-mail: inigo.saez-casares@obspm.fr)
SAILLENFEST Melaine (e-mail: melaine.saillenfest@obspm.fr)
SAINT-MARTIN Arnaud (e-mail: arsaintmartin@gmail.com)
SALOME Philippe (e-mail: philippe.salome@observatoiredeparis.psl.eu)
SANSBERRO Inès (e-mail: inespacesideral@gmail.com)
SANTERNE Alexandre (e-mail: alexandre.santerne@lam.fr)
SARAZIN Marc (e-mail: msarazin@eso.org)
SAUNIERE Lucas (e-mail: lucasauniere@orange.fr)
SAUTY Christophe (e-mail: christophe.sauty@obspm.fr)
SAUVAGE Jean-François (e-mail: sauvage@onera.fr)
SCHIRMER Thiebaut (e-mail: thiebaut.schirmer@ias.u-psud.fr)
SCHMIEDER Brigitte (e-mail: brigitte.schmieder@obspm.fr)
SCHNEIDER Benjamin (e-mail: benjamin.schneider@cea.fr)
SCHULTHEIS Mathias (e-mail: mathias.schultheis@oca.eu)
SEIGNOVERT Benoit (e-mail: benoit.seignovert@univ-nantes.fr)
SELSIS Franck (e-mail: franck.selsis@u-bordeaux.fr)
SERVILLAT Mathieu (e-mail: mathieu.servillat@obspm.fr)
SHUNTOV Marko (e-mail: shuntov@iap.fr)
SICARD Angélica (e-mail: angelica.sicard@onera.fr)
SIEBERT Arnaud (e-mail: arnaud.siebert@astro.unistra.fr)
SKAF Nour (e-mail: nour.skaf@obspm.fr)
SOL Helene (e-mail: helene.sol@obspm.fr)
SOLA Elisabeth (e-mail: elisabeth.sola@astro.unistra.fr)
SORCE Jenny (e-mail: jenny.sorce@univ-lyon1.fr)
SOUBIRAN Caroline (e-mail: caroline.soubiran@u-bordeaux.fr)
SOUBKIOU Abderahmane (e-mail: abdousoubkiou@gmail.com)
SOUCAIL Geneviève (e-mail: gsoucail@irap.omp.eu)
SOULAIN Anthony (e-mail: anthony.soulain@gmail.com)
SOULU Frédéric (e-mail: frederic.soulu@univ-lorraine.fr)
SPIGA Aymeric (e-mail: aymeric.spiga@sorbonne-universite.fr)
SPITLER Laura (e-mail: lspitler@mpifr-bonn.mpg.de)
STASINSKA Grazyna (e-mail: grazyna.stasinska@obspm.fr)
STCHERBININE Aurélien (e-mail: aurelien.stcherbinine@ias.u-psud.fr)
STEE Philippe (e-mail: philippe.stee@oca.eu)
STEINHAUSSER Asma (e-mail: asma.steinhausser@mnhn.fr)
STOLARCZYK Thierry (e-mail: thierry.stolarczyk@cea.fr)
STOLL Veronique (e-mail: veronique.stoll@obspm.fr)
STROTTNER Xavier (e-mail: leonberx@hotmail.fr)
STRUGAREK Antoine (e-mail: antoine.strugarek@cea.fr)
SUAREZ Olga (e-mail: olga.suarez@oca.eu)
SULIS Sophia (e-mail: sophia.sulis@lam.fr)
TALBI Dahbia (e-mail: dahbia.talbi@umontpellier.fr)
TALLON Michel (e-mail: mtallon@obs.univ-lyon1.fr)
TALLON-BOSC Isabelle (e-mail: bosc@obs.univ-lyon1.fr)
TANGA Paolo (e-mail: paolo.tanga@oca.eu)
TANIMURA Hideki (e-mail: hideki.tanimura@ias.u-psud.fr)
TARRICQ Yoann (e-mail: yoann.tarricq@u-bordeaux.fr)
TASCA Lidia (e-mail: lidia.tasca@lam.fr)
TASSE Cyril (e-mail: cyril.tasse@obspm.fr)
TEDROS Jean (e-mail: tedros.jean@gmail.com)
TEINTURIER Lucas (e-mail: lucas.teinturier@hotmail.fr)
TERRIER Régis (e-mail: terrier.regis@gmail.com)
TERRY Jean-Noël (e-mail: jnterry@free.fr)

TESSORE Benjamin (e-mail: benjamin.tessore@univ-grenoble-alpes.fr)
THELIE Emilie (e-mail: emilie.thelie@astro.unistra.fr)
THEUREAU Gilles (e-mail: theureau@cnrs-orleans.fr)
THIBEAULT Christian (e-mail: ChristianThibeaultNB@gmail.com)
THOMAS Guillaume (e-mail: guillaume.thomas.astro@gmail.com)
THOMASSON Benjamin (e-mail: benjamin.thomasson@univ-grenoble-alpes.fr)
THOMSON-PARESSANT Keegan (e-mail: keegan.thomson-paressant@obspm.fr)
THOUVENY Nicolas (e-mail: nicolas.thouveny@univ-amu.fr)
THUILLOT William (e-mail: William.Thuillot@obspm.fr)
TIBALDO Luigi (e-mail: luigi.tibaldo@irap.omp.eu)
TKACHENKO Yevhen (e-mail: eugen.tkachenko@latmos.ipsl.fr)
TOBON VALENCIA Vanesa (e-mail: vanesa.tobon-valencia@fresnel.fr)
TOMMASINI Augustin (e-mail: august1.tommasini@gmail.com)
TRANIN Hugo (e-mail: hugo.tranin@irap.omp.eu)
TRAVEN Gregor (e-mail: gregor.traven@astro.lu.se)
TREBITSCH Maxime (e-mail: m.trebitsch@rug.nl)
TRESSE Laurence (e-mail: laurence.tresse@lam.fr)
TRESSOL Jeanlouis (e-mail: jltressol@gmail.com)
TREYER Marie (e-mail: marie.treyer@lam.fr)
TRISTRAM Matthieu (e-mail: tristram@ijclab.in2p3.fr)
TROTIGNON Roland (e-mail: roland.trotignon@wanadoo.fr)
TUCKEY Philip (e-mail: philip.tuckey@obspm.fr)
TURBET Martin (e-mail: martin.turbet@unige.ch)
TURPIN Damien (e-mail: damien.turpin@cea.fr)
URTADO Olivier (e-mail: ourtado@gmail.com)
VAKILI Farrokh (e-mail: farrokh.vakili@oca.eu)
VALDIVIA Valeska (e-mail: valeska.valdivia@cea.fr)
VALEILLE-MANET Maxime (e-mail: maxime.valeille-manet@etu.u-bordeaux.fr)
VAN DER SWAELMEN Mathieu (e-mail: mvds.amt@orange.fr)
VAN DRIEL Wim (e-mail: wim.vandriel@obspm.fr)
VARNIERE Peggy (e-mail: varniere@apc.in2p3.fr)
VASSEUR Serge (e-mail: hipparcos@outlook.com)
VAUBAILLON Jeremie (e-mail: vaubaill@imcce.fr)
VAUGLIN Isabelle (e-mail: isabelle.vauglin@univ-lyon1.fr)
VENOT Olivia (e-mail: olivia.venot@lisa.ipsl.fr)
VERGANI Susanna (e-mail: susanna.vergani@obspm.fr)
VERILHAC Daniel (e-mail: daniel.verilhac@free.fr)
VETOIS Jacques (e-mail: jacquesvetois@numericable.fr)
VIEVARD Sebastien (e-mail: sebastien.vievard@gmail.com)
VIGAN Arthur (e-mail: arthur.vigan@lam.fr)
VILLA VÉLEZ Jorge Andrés (e-mail: jorge.villa@lam.fr)
VILLANUEVA Lopez (e-mail: lopezvilla3@gmail.com)
VILMER Nicole (e-mail: nicole.vilmer@obspm.fr)
VINATIER Sandrine (e-mail: sandrine.vinatier@obspm.fr)
VINCENT Frederic (e-mail: frederic.vincent@obspm.fr)
VIOU Cedric (e-mail: cedric.viou@obs-nancay.fr)
VITRAL Eduardo (e-mail: vitral@iap.fr)
VOISIN Guillaume (e-mail: guillaume.voisin@obspm.fr)
VOLONTERI Marta (e-mail: martav@iap.fr)
WAKELAM Valentine (e-mail: valentine.wakelam@u-bordeaux.fr)
WEBB Natalie (e-mail: natalie.webb@irap.omp.eu)
WEISS Natacha (e-mail: n.pestel@laposte.net)
WULLAERT Patrick (e-mail: wullaert_chatillon@hotmail.com)
ZAMBRANA PRADO Natalia (e-mail: natazp@hotmail.com)
ZAMORANO VITORELLI André (e-mail: andre.zamoranovitorelli@cea.fr)

ZARKA Philippe (e-mail: philippe.zarka@obspm.fr)
ZHANG Yun (e-mail: yun.zhang@oca.eu)
ZYANE Khalil (e-mail: zyanek.83@gmail.com)

Session 0

SF2A Plenary session

SF2A 2021
A. Siebert, K. Baillié, E. Lagadec, N. Lagarde, J. Malzac, J.-B. Marquette, M. N'Diaye, J. Richard, O. Venot (eds)

ASTROPHYSICS IN AFRICA FOR DEVELOPMENT

D. Baratoux[1, 2] and the AFIPS, RISE 5A and MATERNA teams

Abstract. Africa is probably the continent with the most assets for Astrophysics and Planetology: skies without light pollution, meteorites and meteorite impact craters, and geological records of the ancient Earth and of origin of life. Outside of South Africa, however, there are still few African scientists working in these fields. This situation can be explained by the dependence of African researchers on the priorities of external (international) funding together with structural weaknesses of national public funding. Aware of these assets and challenges, a community of African astronomers and planetary scientists is involved in increasingly ambitious projects and is distinguished by original scientific works that highlight the African scientific heritage. This article will highlight some of the recent activities carried out in collaboration between African and European scientists in astrophysics and planetary sciences: the on-going AFIPS network (African Initiative for Planetary and Space Science) and AWA project (Astrophysics and Planetary Science in West Africa), and the Africa-Europe RISE 5A (Astronomy and Astrophysics Arising Across Africa) proposal for staff mobility between the two continents. The focus will also be placed on specific achievements, such as the 2 stellar occultation campaigns in Senegal in connection with the NASA's space program in Senegal, and the launch of the first popular science magazine on astronomy in Francophone Africa. Through these achievements, we will show the impact of these activities on African youth and emphasize the role that African astronomers play in the scientific and cultural development of their countries.

Keywords: Africa, Development, Education

1 Introduction

Astronomy is not the first scientific discipline that naturally comes to mind when one evokes the African continent, which faces many challenges concerning health, agriculture, the consequences of climate change, the exploitation of resources and the environment. However, Astronomy is the oldest science, with its 5000 years of history, as evidenced by the "stone observatories" such as the great megalithic circles (Nabta Playa, in Egypt, Stonehenge in the United Kingdom). Astronomy has largely contributed to the development of humanity, to its knowledge, and to its technological development (Astronomy and Astrophysics Survey Committee et al. 2001; Fabian 2010; Pović et al. 2018; Valls-Gabaud & Boksenberg 2009). It is also the only science where amateurs play an active and very significant role, and where collaborations between professionals and amateurs are often at the forefront of the discipline (Mousis et al. 2014). Because of the universal subjects it deals with, it is a science that favors the links between the academic world and society. Astronomy questions our origins and our place in the universe, and, to address these questions, rely on mathematics, physics, and chemistry. Astronomy can be cited as an example of multi-, trans and inter-disciplinarity. It is also a science that arouses many vocations for scientific careers among young people. For all these reasons, astronomy must be considered as essential to the sustainable development of human societies. The existence of curricula in astronomy at various levels (from primary schools to universities) and the practice of research in astronomy shall not depend on the economic development of a country, under the pretext that its applications do not seem as immediate as in other fields.

Many young Africans are fascinated - as elsewhere in the world - by the observation of the sky during their childhood, and wonder about the origin of the stars and the functioning of the universe. Often isolated, and with few opportunities to feed this passion for science, their thirst for learning can dry up. In contrast with these

[1] Université Félix-Houphouët-Boigny, Abidjan, Côte d'Ivoire
[2] Géosciences Environnement Toulouse, University of Toulouse, CNRS & IRD, Toulouse, France

unfavorable conditions, Africa is probably the continent with the most assets for astrophysics and planetary science: skies without light pollution (Netzel & Netzel 2018), meteorites and meteorite impact craters (Reimold & Koeberl 2014), geological records of the ancient Earth and of the origin of life. Outside of South Africa, which is the host of a major part of the Square Kilometre Array (SKA) project, there are still few African scientists working in astronomy or planetary sciences. This situation can be explained by the dependence of African researchers on international funding and the priorities of these funding bodies, and on the other hand, by the structural weakness of national public funding, which guarantees a certain academic freedom. Conscious of these assets, a community of astronomers and planetary scientists is involved in increasingly ambitious projects and is distinguished by original scientific works that highlight the African scientific heritage. Over the last few years, the extraordinary motivations of African astronomers and regular meetings with astronomers outside Africa, and in particular with European and American researchers, had indeed led to a number of new projects and initiatives that illustrate the growing dynamics of the continent in this field. In 2017, the launch of the "African Initiative for Planetary and Space Sciences" (Baratoux et al. 2017a,b), which can now be followed at `https://africapss.org`, contributed to break the isolation of some African astronomers and planetary scientists and brought more researchers from countries where astronomy is practiced at the highest level to engage with their African colleagues for the scientific development of their countries. The idea of this initiative was rooted in particular in the long-term collaboration between France and Morocco in the field of planetary science (Bouley et al. 2012; Ait Moulay Larbi et al. 2015; Chennaoui Aoudjehane et al. 2016). A few years later, the new projects and success stories mentioned below illustrate the growing interest for astronomy in Africa and the contributions of these initiatives to the sustainable Development of the continent.

2 Observations of occultations in Senegal in relations with missions of exploration of the Solar System

In 2018, Senegal enters the history of space exploration of the Solar System. For the first time, 21 Senegalese researchers, members of the Senegalese Association for the Promotion of Astronomy (ASPA), along with American and European researchers, participated in an astronomical observation campaign essential for the preparation of the flyby of the the most distant object ever explored by a human-made spacecraft: Arrokoth (Buie et al. 2020), in the framework of the New Horizons NASA mission, and following the exploration of Pluto. The deployment of telescopes in Senegal, to record the last observable stellar occultation by Arrokoth before the flyby, was also the occasion to produce a scientific documentary entitled “A la poursuite d’Arrokoth”, which is publicly available on the internet (Berger 2018). The impact of this observation campaign was beyond expectations, with several well-attended outreach events, exchanges between scientists and the public, and an audience of the entire team with the President of the Republic of Senegal (Fig. 1).

Two years later (September 2020), in the context of the Covid-19 pandemic, NASA decided to rely on the skills of the Senegalese astronomers, acquired during the deployment of telescopes in 2018, to pursue its occultation program. Maram KAIRE, president of ASPA, was appointed as the coordinator of a new campaign of astronomical observation. The necessary equipment was shipped by NASA to Senegal for a short period of time. The goal of this new deployment was to observe the stellar occultation by (15094) Polymele, an asteroid of Jupiter, which will be visited by the space probe Lucy (NASA), to be launched in October 2021. 14 telescopes were deployed in the region of Fatick (south-east of Dakar, Senegal) in order to attempt the recording of a few positive occultations. The telescopes were spatially distributed around the trajectory of the occultation. Good strategic decisions made by the team, taking in account the very difficult weather conditions in September 2020 (end of the rainy season), led to a successful observation of one chord.

To celebrate these achievements and the past activities of the president of ASPA, an asteroid, orbiting between Mars and Jupiter, now bears the name of Maram KAIRE - the first Senegalese scientist to receive this distinction. The Asteroid (35462) Maramkaire (by the WG Small Bodies Nomenclature 2021), a main belt asteroid, represents now a source of pride and of inspiration for the many students and young researchers in Senegal and beyond the borders of this country. A new observation campaign will take place in October 2021, in order to constrain the size and shape of the satellite of Jupiter Orus, again in preparation of its flyby by the Lucy spacecraft.

Through these missions, the participants had the opportunity to reinforce their skills in astronomy, but not only in astronomy. The preparation of the observation campaign was also an opportunity to approach notions of optics, mechanics, mathematics, physics. The instrumentation/software aspect is a key element of the training (Fig. 2). The success of these campaigns requires teamwork, with participants from different fields, with different positions (students, professors, engineers) who unite their motivations in the field during the training phases,

Fig. 1. The group of Senegalese, U.S.A and French astronomers in the front of the Presidential palace of Senegal, after an audience with the President of the Republic of Senegal, Macky Sall.

and during the final phase of night deployment of the telescopes on the Senegalese territory.

Fig. 2. Training session in the gardens of the Hôtel Royal Malango In Fatick. Participants are trained for telescope deployment and use of the software to record to the occultation using a GPS and camera. Credit : Senegalese Association for the Promotion of Astronomy.

3 Education and outreach

In parallel to these missions, the first Astronomy on-line magazine for French-speaking Africa, available at `https://lastronomieafrique.com/` has been launched, in the framework of a collaboration with ASPA, the Société Astronomique de France (SAF), and with other partners, including the SF2A. This on-line magazine presents astronomical phenomena that it is possible to observe from several capitals of African countries. It also connects African researchers with amateurs, and favors the dissemination of scientific knowledge in society.

A school has also been organized in May 2021 with the support of the Office of Astronomy for Development (OAD) of the International Astronomical Union. This school, entitled "Astronomy and Python" was an opportunity to train students with this programming language used in most scientific disciplines `https://astrosenegal.org/`. Here again, this experience illustrates how astronomy can be used to contribute to sustainable development. It is indeed unlikely that all of these students will become astronomers, but it is certain that most of them will now be able to use the Python language in their respective fundamental or applied research projects. The Python language is freely available, and used in many scientific and engineering fields. Learning Python through astronomy is an innovative educational experience that has given to the participants undeniable advantages for their future careers.

In the wake of the activities, the members of the AFIPS network have often contributed to the emergence of associations and events in several African countries, for instance, the launch of the Ivoirian Association for Astronomy (`https://lastronomieafrique.com/naissance-de-lassociation-ivoirienne-dastronomie-aia/`, the Mauritanian Association for Astronomy (`https://www.facebook.com/nmauritanienastronomie.astronomie.7`, the Days for Introduction to Astronomy in Togo, organized by the Togolese Association for Astronomy (`https://www.facebook.com/AstronomieTogo/`). These events, and many others, that we cannot mention here, together with institutional efforts and projects of astronomical observatories in several African countries (Pović et al. 2018) indicate a growing maturity, and favorable conditions for the emergence of high level academic research in astronomy and planetary sciences in Africa.

4 Conclusion and perspectives for Africa - Europe collaborations in Astronomy and Planetary Sciences

In this context, it appears timely to strengthen Africa-Europe collaborations in the field of astronomy and planetary sciences. For 2021 – 2022, a group of scientists in France, Senegal, Burkina Faso and Côte d'ivoire are funded by CNRS for a project entitled "Astrophysics and planetary Science in West Africa" (AWA) – this project focuses on astronomical observations of the solar systems (occultation campaigns), stellar and galatic physics, and search on existing and new meteorite impact craters in Africa (with a focus on the field of tectites in Côte d'Ivoire). A geophysical campaign of the potential meteoritic impact craters of Velingara will be organized by AWA in 2022. AWA will also strengthen existing collaborations between the University Ki-Zerbo of Ouagadougou and the Observatoire de la Côte d'Azur, which includes the co-supervision of PhD students between the two teams. AWA is co-funded by the French National Research Institute for Development (IRD) and the Agate project `https://agate-project.org/`. To implement the long-term vision for development of Astronomy on the continent, a group of African and European Astronomers are currently working on the preparation of large proposals, to be submitted to the Horizon Europe program in 2022. One of these proposals is entitled Astronomy and Astrophysics Arising Across Africa (RISE 5A) (Fig. 3). This proposal aims at offering new opportunities for staff and students exchanges between Europe and Africa. It is organized in 7 work packages, management (WP1), planetary sciences (WP2), stellar physics (WP3), Galactic and extragalactic science (WP4), instrumentation on and site testing (WP5), inclusion in astronomy (WP6), outreach dissemination on and communication (WP7).

This article of proceeding reports the efforts of large group of scientists including the members of the Africa Initiative for Planetary Science, the members of RISE 5A team, the members of the MATERNA (Mobility in Africa for Training, Education and Research: Network for Astrophysics) team, and the members of the different occultation campaigns in Senegal. The projects and achievements mentioned in this paper received funding from the French National Research Institute for Sustainable Development, the Centre National de la Recherche Scientifique (France), the Ministry of Research, Higher education and Innovation of Senegal, the French embassy in Dakar, the Organization of Women in Science, and the Agate Project. The University Cheikh Anta Diop (Sénégal), The Université Félix Houphouët-Boigny (Côte d'Ivoire), The University Jospeh Ki-Zerbo (Burkina Faso), the University of Côte d'Azur, and the University of Toulouse III Paul Sabatier are particular acknowledged for constant institutional support. The support of the Hôtel Royal Malango in Fatick for the occultation campaigns in Senegal is greatly appreciated. Marc Buie, Anne Verbiscer and all the scientists of the New Horizon and Lucy teams (NASA) are acknowledge for exceptional support for the achievement of occultation campaigns in Senegal, which include in particular the shipment of the necessary equipment and necessary guidance.

Fig. 3. Flyer summarizing the goal and groups involved in the RISE 5A (Astronomy and Astrophysics Arising Across Africa) project. Bottom left panel photography: Salma SYLLA MBAYE, first Senegalese PhD student in Astronomy, with her supervisor François COLAS from the Paris Observatory, and Marie Teuw NIANE, former Ministry of Higher Education Research and Innovation of Senegal, during the 2018 occultation campaign in Senegal. Credit : The RISE 5A team.

References

Ait Moulay Larbi, M., Daassou, A., Baratoux, D., et al. 2015, Earth, Moon, and Planets, 115, 1

Astronomy and Astrophysics Survey Committee, Board on Physics and Astronomy, Space Studies Board, Commission on Physical Sciences, Mathematics, and Applications, & National Research Council. 2001, Astronomy and Astrophysics in the New Millennium (Washington, D.C.: National Academies Press), pages: 9839

Baratoux, D., Chennaoui-Aoudjehane, H., Gibson, R., et al. 2017a, Eos

Baratoux, D., Chennaoui-Aoudjehane, H., Gibson, R., et al. 2017b, Eos

Berger, Y. 2018, A la poursuite d'Arrokoth

Bouley, S., Baratoux, D., Vaubaillon, J., et al. 2012, Icarus, 218, 115

Buie, M. W., Porter, S. B., Tamblyn, P., et al. 2020, The Astronomical Journal, 159, 130

by the WG Small Bodies Nomenclature, I. A. U. 2021, WGSBN Bulletin, Tech. Rep. Volume 1, #1

Chennaoui Aoudjehane, H., El Kerni, H., Reimold, W. U., et al. 2016, Meteoritics & Planetary Science, 51, 1497

Fabian, A. 2010, Astronomy & Geophysics, 51, 3.25

Mousis, O., Hueso, R., Beaulieu, J.-P., et al. 2014, Experimental Astronomy, 38, 91

Netzel, H. & Netzel, P. 2018, Journal of Quantitative Spectroscopy and Radiative Transfer, 221, 300

Pović, M., Backes, M., Baki, P., et al. 2018, Nature Astronomy, 2, 507

Reimold, W. U. & Koeberl, C. 2014, Journal of African Earth Sciences, 93, 57

Valls-Gabaud, D. & Boksenberg, A. 2009, Proceedings of the International Astronomical Union, 5, 4

OPEN ACCESS TO SCIENTIFIC DATA: EXCERPTS FROM THE INSU PROSPECTIVE

C. Bot[1], F. André[2], M. Allen[1], F. Bonnarel[1], A. Chambodut[3], S. Galle[4], F. Genova[1], M. Gérin-Laslier[5], F. Huynh[6], H. Pedersen[7], V. Stoll[8] and J. Vergne[3]

Abstract. Data is at the heart of the scientific method at INSU, the French national institute for Universe Sciences. INSU disciplines were engaged in data sharing and data management long before political acceptance to Open Science and the definition of FAIR principles (Findable, Accessible, Interoperable, Reusable). This early involvement brought us to the leading edge of data sharing. Open access to scientific data was therefore a natural topic for the first INSU inter-displinary prospective organized in 2019-2020. The discussion was organized on different points: the FAIR context, scientific data management and services, data models and metadata standardisation, and the certification of data repositories (CoreTrustSeal). The current paper provides an excerpt from the discussions, conclusions and recommendations, with an intended bias toward astronomy and astrophysics. The aim is to trigger interest and give extra motivation to read the full online document with the conclusions from the prospective on open access to scientific data.

Keywords: open science, data sharing, FAIR, data models, metadata, certification

1 Introduction

INSU (Institut National des Sciences de l'Univers) is the French national institute of CNRS on Universe Science and includes 4 different research domains pertaining to Earth Science as well as Astronomy and Astrophysics. In 2019-2020, INSU organized its first inter-displinary prospective exercise among these different disciplines.

Data is at the heart of research in all INSU disciplines and we are today at the forefront of data sharing, thanks to a long history of involvement, long before Open Science was a hot topic. Therefore, open access to scientific data was easily identified as one of the inter-disciplinary challenges to be discussed as part of the INSU prospective. A workshop on these questions was organized in Strasbourg in January 2020. A recording of the discussions (in French) is available online*. The conclusions and recommendations that stemmed from the prospective are gathered in an online document†. The current paper aims at summarizing some of these discussions and recommendations, with a bias on those pertaining to astronomy and astrophysics. The intent is to trigger interest for researchers in these fields and give some additional motivation to read the full document.

Let's step back. Why are researchers interested and willing to invest time on Open Science and share data? Open Science for scientific data is a "hot topic", with numerous political demands. One pragmatic incentive to share data is that it is now becoming mandatory in some contexts (e.g. for data obtained as part of H2020, ERC or ANR projects). Another motivation for data sharing is more general: it gives trust, shows reliability and accountability. Last but not least, sharing data opens new research fields.

[1] Observatoire Astronomique de Strasbourg, Université de Strasbourg, CNRS, Observatoire astronomique de Strasbourg (ObAS), UMR 7550, 67000 Strasbourg, France
[2] Observatoire Midi-Pyrenees, Toulouse, France
[3] Université de Strasbourg, CNRS, Institut Terre et Environnement de Strasbourg, ITES UMR 7063, Strasbourg F-67084, France
[4] Université Grenoble Alpes, CNRS, IRD, Grenoble-INP, IGE, 38000 Grenoble, France
[5] LERMA, Observatoire de Paris, PSL Research University, CNRS, Sorbonne Universités, 75014, Paris, France
[6] Institut de Recherche pour le Développement, Marseille, France
[7] Univ. Grenoble Alpes, Univ. Savoie Mont Blanc, CNRS, IRD, IFSTTAR, ISTerre, 38000 Grenoble, France
[8] Observatoire de Paris, PSL Research University, Paris, France

*http://www.canalc2.tv/video/15656
†https://extra.core-cloud.net/collaborations/ProspectiveTransverseINSU2020/Defi-14/Documents%20partages/defi14_final.pdf

2 FAIR context

Key concepts of data sharing and open science have been condensed in the acronym FAIR (Wilkinson et al. 2016), which stands for Findable, Accessible, Interoperable and Reusable. These FAIR principles describe criteria that should be met for data to be open. The FAIR concept is evolving in a larger context with a lot of developments at different levels happening now. The European commission is providing a strong support to EOSC (European Open Science Cloud European Open Science Cloud 2018). At the international level, the Research Data Alliance (RDA) provides a neutral forum to discuss all aspects of data sharing and there is a French RDA node. At the national level, CNRS published a roadmap for open science (Centre National pour la Recherche Scientifique 2019) and the ministry for research and education have a national plan for open science (Ministère de l'Enseignement supérieur, de la Recherche et de l'Innovation 2018). The prospective exercise highlighted that it is important to participate in activities like EOSC to make sure that what comes out of these initiatives will meet the needs of our communities and that our major services will be included.

At the heart of FAIR principles, the idea is to do science more efficiently. Yet sharing data requires a significant work at the level of each discipline. In practice, this means being on the same page as far as formats, metadata or exchange protocols are concerned. Astronomy was a pioneer on these aspects with the Virtual Observatory standards. An example of such standards, the provenance data model, is being presented by Servillat (2020) in this same volume. Today, data sharing is in the mindset of all disciplines. FAIR is a revolution but one has to keep in mind that it comes at a cost. One of the out-coming messages of the prospective is that not all data is intended to be FAIR. The consequence is that priorities have to be set for which data should be FAIR. Data from research infrastructures (European Strategy Forum on Research Infrastructures 2018) should be FAIR, as well as the ones from National Services (SNO- Services Nationaux d'Observation) or data associated to publications. For other data sets, there is a need to put priorities and think about whether these data should be FAIR or not and for how long. Inter-disciplinary data sharing also has a cost and a recommendation from the prospective was to start with use cases and existing frameworks (e.g. gravitational waves).

3 Management of scientific data and services

The discussion on scientific data management was done by considering two distinct yet complementary categories: data managed by data sharing platforms, observatories or infrastructures on the one hand, and any other datasets on the other hand (long tail, data attached to publications, data outside SNOs, non-digital data).

Data management is a key aspect of sharing data and enabling open science. In order for scientific data to be used and used again, one has to assign metadata and use inter-operability standards and frameworks. In this work, scientists, software engineers and documentalists have complementary roles. In France and for INSU, data management is done through two research infrastructures working (CDS -Centre de Données de Strasbourg- for astronomy and DataTerra for earth system) and the structure of OSUs (Observatoires des Sciences de l'Univers) and national services (SNOs). Recommendations made by the prospective are that this national structure within INSU is an asset and it should be used to suggest EOSC services that suit our usage. Another recommendation is that there is a need for a support of infrastructures, to favor thematic repositories. Finally, to avoid the risk of duplication of data at different places, repositories should be federated by harvesting metadata.

For data outside observatory services (long tail, non-digital data, ...), the issue is the deterioration of data with time, even if data is associated to a publication (Pepe et al. 2014). Data management is the responsibility of data producers. One of the difficulties to take care of these data is to have sustainable funding (for times longer than the time of the project). One proposition is to have overheads on projects (around 10%), especially for projects which would require a lot of data management on timescales larger than the project duration. Another proposition from the prospective is to put priorities on long tail data sets but that the description should be done beforehand for all data sets. We also recommended to do an inventory of data services in order to guide researchers and document the need for a long tail repository. Lastly, scientists should continue to develop their culture on data management (e.g. how important it is to attach metadata on the provenance to data) and there will be data correspondents or referents within each observatory (OSU).

4 Complimentary professions and skills

Among the different questions we asked ourselves during the prospective on open access to scientific data, professions and skills were a recurring discussion item. Data sharing involves different people with different skills (researchers, engineers, documentalists, information science specialists, legal experts, ...). New professions are arising (data analyst, data architect, data steward, data scientist, ...) and the definition of these jobs are not always clear or unequivocal. A recommendation is hence to do an analysis of the different professions needed to take care of data. There is a need to identify, recognize and value professions associated to data management and data preservation. A recommendation was made to recognize skills related to data. Working on data is a specific work that is complementary to works on algorithms or on infrastructures and IT systems.

5 Data description, formats

Standards for formats and metadata are central to interoperability. Standardisation in astronomy and astrophysics came very early compared to other disciplines. A good example is the FITS standard, which enabled an easy exchange and usage of astronomical images, spectra, ... This approach widened and formalized through the concept of Virtual Observatory and the creation of the International Virtual Observatory Alliance (IVOA), where standards for the virtual observatory are defined. Today, 45 standards exists for formats, protocols, and data models, covering different aspects of FAIR principles for different types of data. The IVOA framework is seen as the way to do interoperability and to open data in practice. In France, the Action Specifique Observatoire Virtuel (ASOV[‡]) is coordinating the French involvement and sharing good practices. Community training on these topics is important at all levels.

6 Certification of data repositories and services

All actors want to be assured that the structure giving access to their data is permanent, robust and has appropriate data management practices. Certification is the way to prove openly the trustworthiness. To do so, data repositories and services follow a set of principles gathered in the acronym TRUST: Transparency, Responsability, User Community, Sustainability, Technology (Lin et al. 2020). This certification applies to the repository, not the data quality nor its value to the community. For scientific services, the best suited certification is CoreTrustSeal[§]. Currently, in France, only two services have this certification: SISMER (sea data, Ifremer) and CDS. The prospective highlighted that the certification process involves governance. Auto-evaluation is a useful process, even if the service does not submit the certification.

7 Conclusion

Open science and data sharing are key aspects that are of interest across all INSU disciplines. The prospective organized by INSU was an occasion to discuss and reflect on the FAIR context, management of scientific data and services, and data models and meta-data harmonization. One of the overarching messages was that science should be at the heart of the process and should be the engine of evolution and strategic choices. All conclusions and recommendations are available online at `https://extra.core-cloud.net/collaborations/ProspectiveTransverseINSU2020/Defi-14/SitePages/Accueil.aspx`.

References

Centre National pour la Recherche Scientifique. 2019, Feuille de Route du CNRS pour la Science Ouverte

European Open Science Cloud. 2018, Strategic Implementation Plan

European Strategy Forum on Research Infrastructures. 2018, Strategy Report on Research Infrastructures

Lin, D., Crabtree, J., & Dillo, I. e. a. 2020, Sci Data, 7, 144

Ministère de l'Enseignement supérieur, de la Recherche et de l'Innovation. 2018, Plan national pour la science ouverte

Pepe, A., Goodman, A., Muench, A., Crosas, M., & Erdmann, C. 2014, PLoS ONE, 9, 8

Servillat, M. 2020, in Proceedings of the Annual meeting of the French Society of Astronomy and Astrophysics

Wilkinson, M., Dumontier, M., & Aalbersberg, I. e. a. 2016, Sci Data, 3, 160018

[‡] `http://www.france-ov.org`

[§] `https://www.coretrustseal.org`

SF2A 2021
A. Siebert, K. Baillié, E. Lagadec, N. Lagarde, J. Malzac, J.-B. Marquette, M. N'Diaye, J. Richard, O. Venot (eds)

THE GREAT DIMMING OF BETELGEUSE AS SEEN BY THE VLT/VLTI

M. Montargès[1], E. Cannon[2], E. Lagadec[3], A. de Koter[2,4], P. Kervella[1], J. Sanchez-Bermudez[5,6], C. Paladini[7], F. Cantalloube[8], L. Decin[2,9], P. Scicluna[7], K. Kravchenko[10], A. K. Dupree[11], S. Ridgway[12], M. Wittkowski[13], N. Anugu[14,15], R. Norris[16], G. Rau[17,18], G. Perrin[1], A. Chiavassa[3], S. Kraus[15], J. D. Monnier[19], F. Millour[3], J.-B. Le Bouquin[18,20], X. Haubois[7], B. Lopez[3], P. Stee[3] and W. Danchi[17]

Abstract. Between November 2019 and April 2020, the second nearest red supergiant Betelgeuse experienced an historic drop in brightness, called the 'Great Dimming' of Betelgeuse. Here we summarize the findings of our spatially resolved observations with the European Southern Observatory's VLT/VLTI. The VLTI/GRAVITY interferometric measurements indicate that between January 2019 and February 2020 the angular diameter of the star in the K-band continuum did not change significantly. The VLT/SPHERE images show an obscuration of the Southern hemisphere of the star. Using additional optical photometric observations from the AAVSO, we conclude that the 'Great Dimming' of Betelgeuse is best explained by both a cool photospheric patch, and a dusty cloud in the line of sight. The former may have triggered the latter.

Keywords: Stars: individual: Betelgeuse, supergiants, Stars: mass-loss, Stars: imaging, Techniques: high angular resolution

1 Introduction

Betelgeuse (α Ori) is the protoypical red supergiant (RSG) star. Located at 222^{+48}_{-34} pc (Harper et al. 2017; Joyce et al. 2020), it is the second closest RSG, and probably the most observed. Like most RSGs, it is

[1] LESIA, Observatoire de Paris, Université PSL, CNRS, Sorbonne Université, Université de Paris, 5 place Jules Janssen, 92195 Meudon, France
[2] Institute of Astronomy, KU Leuven, Celestijnenlaan 200D B2401, 3001 Leuven, Belgium
[3] Université Côte d'Azur, Observatoire de la Côte d'Azur, CNRS, Laboratoire Lagrange, Bd de l'Observatoire, CS 34229, 06304 Nice cedex 4, France
[4] Anton Pannenkoek Institute for Astronomy, University of Amsterdam, 1090 GE, Amsterdam, The Netherlands
[5] Max Planck Institute for Astronomy, Königstuhl 17, 69117, Heidelberg, Germany
[6] Instituto de Astronomía, Universidad Nacional Autónoma de México, Apdo. Postal 70264, Ciudad de México, 04510, México
[7] European Southern Observatory, Alonso de Cordova 3107, Vitacura, Santiago, Chile
[8] Aix Marseille Université, CNRS, LAM (Laboratoire d'Astrophysique de Marseille) UMR 7326, 13388, Marseille, France
[9] School of Chemistry, University of Leeds, Leeds LS2 9JT, UK
[10] Max Planck Institute for extraterrestrial Physics, Giessenbachstraße 1, D-85748 Garching, Germany
[11] Center for Astrophysics, Harvard & Smithsonian, 60 Garden Street, Cambridge, MA 02138, USA
[12] NSF's National Optical-Infrared Astronomy Research Laboratory, PO Box 26732, Tucson, AZ 85726-6732, USA
[13] European Southern Observatory, Karl-Schwarzschild-Str. 2, 85748, Garching bei München, Germany
[14] Steward Observatory, 933 N. Cherry Avenue, University of Arizona, Tucson, AZ, 85721, USA
[15] University of Exeter, School of Physics and Astronomy, Stocker Road, Exeter, EX4 4QL, UK
[16] Physics Department, New Mexico Institute of Mining and Technology, 801 Leroy Place, Socorro, NM 87801, USA
[17] NASA Goddard Space Flight Center, Exoplanets & Stellar Astrophysics Laboratory, Code 667, Greenbelt, MD 20771, USA
[18] Department of Physics, Catholic University of America, Washington, DC 20064, USA
[19] Department of Astronomy, University of Michigan, Ann Arbor, MI, 48109, USA
[20] Univ. Grenoble Alpes, CNRS, IPAG, 38000 Grenoble, France

a semi-regular variable with primary and secondary periods of $\sim 400-420$ and ~ 2100 days respectively (Stothers 2010). During the last months of 2019, as it was heading towards its February 2020 light minimum, the brightness of the star decreased rapidly (Guinan et al. 2019). It reached its historic minimum in the visible with $V = 1.614 \pm 0.008$ mag, on 7-13 February 2020 (Guinan et al. 2020 and Fig. 1).

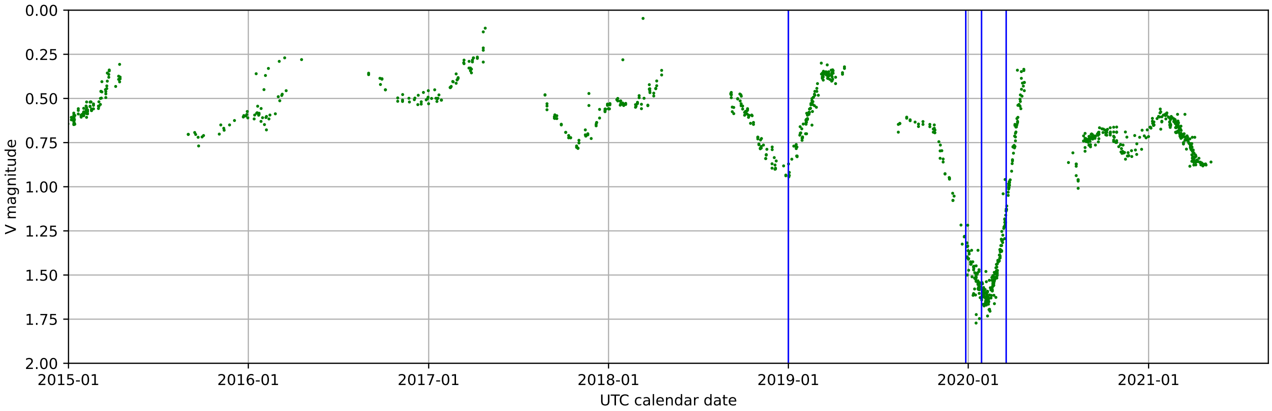

Fig. 1. V band light curve of Betelgeuse between 2015 and 2021 from the American Association of Variable Star Observers (AAVSO) measurements. The blue vertical lines correspond to the dates of the VLT/SPHERE-ZIMPOL images.

2 Observations and data reduction

Betelgeuse was observed a year before the 'Great Dimming' with VLTI/GRAVITY (Gravity Collaboration et al. 2017) in the compact configuration of the auxiliary telescopes (A0-B2-D0-C1), and with VLT/SPHERE (Beuzit et al. 2019), respectively on 20$^{\text{th}}$ January 2019, and 1$^{\text{st}}$ January 2019. The SPHERE observations were performed with two of its sub-units. The infra-red dual imaging and spectrograph (IRDIS, Dohlen et al. 2008) in its sparse aperture masking mode (SAM, Cheetham et al. 2016) was used to supplement the GRAVITY measurements with short baseline points sampling the inner part of the first lobe of the visibility function. The Zurich Imaging Polarimeter (ZIMPOL, Schmid et al. 2018) obtained spatially resolved images of the photosphere in the visible domain, using the P2 polarimetric mode. During the 'Great Dimming', the observations were obtained on 14$^{\text{th}}$ February 2020 with VLTI/GRAVITY, 27$^{\text{th}}$ December 2019 with VLT/SPHERE-IRDIS, and 27$^{\text{th}}$ December 2019 (before the light minimum), 28$^{\text{th}}$ January 2020 (at the light minimum), and 18$^{\text{th}}$, 19$^{\text{th}}$ and 21$^{\text{st}}$ March 2020 (after the light minimum) with VLT/SPHERE-ZIMPOL.

The details on the data reduction, calibration and description is available in Montargès et al. (2021).

3 VLTI/GRAVITY and VLT/SPHERE-IRDIS: angular diameter measurements

We estimated the angular diameter of the star, as a change in size could be linked to the physical reason for the 'Great Dimming' event. This parameter is also a mandatory input of the models developed in Sect. 4.

We fitted the first lobe observations in the K band continuum ($2.22-2.28$ μm for GRAVITY with the exclusion of several weak atomic and molecular lines, and Cnt_K2 filter for IRDIS) with a uniform disk (UD) model. We obtained the angular diameters values of $\theta_{\text{UD}} = 42.61 \pm 0.05$ mas (reduced $\chi^2 = 26.5$) before the Dimming, and $\theta_{\text{UD}} = 42.11 \pm 0.05$ mas (reduced $\chi^2 = 46.3$) during the Dimming. An attempt to fit the data with a power-law limb-darkened disk gave similar reduced χ^2 values without significant changes to the angular diameter.

The difference in angular diameter is within the variations observed over the previous decades (Ohnaka et al. 2009), and far from the 30% variation that would be required to explain the 'Great Dimming'.

4 VLT/SPHERE-ZIMPOL: spatially resolving the photosphere

4.1 The VLT/SPHERE-ZIMPOL image series

The pre-dimming image (January 2019) shows an almost spherical photosphere with a slight elongation in the North-East to South-West direction. The three images acquired during the Dimming (December 2019, January 2020, and March 2020) are much different with a Southern hemisphere that appears obscured or hidden. In Sect. 4.3 and 4.4 we model these observations using a cool photospheric patch and a dusty clump, respectively.

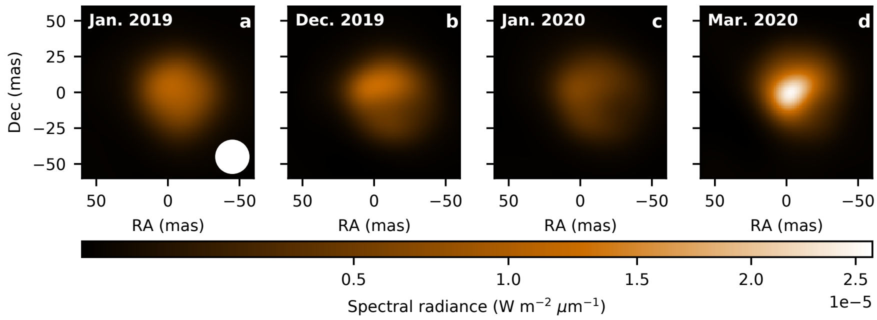

Fig. 2. VLT/SPHERE–ZIMPOL observations of Betelgeuse after deconvolution in the Cnt_Hα filter. North is up; east is left. The beam size of ZIMPOL is indicated by the white disk in panel a. We used a power-law scale intensity with an index of 0.65 to enhance the contrast. a: January 2019. b: December 2019. c: January 2020. d: March 2020. The Cnt_Hα filter (one of ZIMPOL's filters) is centred at 644.9 nm.

4.2 Estimation of the pre-dimming circumstellar extinction

Previous observations of Betelgeuse have revealed that it is surrounded by a dusty circumstellar envelope (eg. Verhoelst et al. 2009; Kervella et al. 2011). Before looking at the 'Great Dimming', we estimated the extinction caused by this circumstellar dust. We estimated the parameters of a Cardelli extinction law (Cardelli et al. 1989) that would be required to reproduce our VLT/SPHERE-ZIMPOL photometry and the contemporary American Association of Variable Stars Observers (AAVSO) measurements in January 2019 (pre-dimming). Further details on this modeling are available in Montargès et al. (2021). In the following results, the Cardelli extinction law with $R_V = 4.2$ and $A_V = 0.65$ is always implemented in order to focus on the effect of the Dimming.

4.3 Modeling: a photospheric cool patch

To reproduce the ZIMPOL images (Fig.2), we first constructed a stellar disk with a cool patch, using Phoenix spectral energy distributions (SEDs, Lançon et al. 2007). The cool patch was defined by three parameters: its center position on the stellar disk (x_p, y_p), and its size r_p. The modeling details are available in Montargès et al. (2021). The best-match parameters are summarized in Table 1. The images are shown in Fig. 3. We wish to emphasize that the goal was not to estimate precisely the effective temperature of the photosphere and of the patch, but to rather assess the compatibility of the model with the 'Great Dimming'.

4.4 Modeling: radiative transfer with a dusty clump in the line of sight

To test the dust clump hypothesis we used 3D radiative transfer simulations produced with the code Radmc3D (Dullemond 2012). In the following the x axis is oriented West to East, the y axis is South to North and z axis points towards the observer. In front of the star, we put a spherical dust density centred at (x_c , y_c , z_c), with r_c as its radius, and constant dust density ρ_0. We adopted a canonical silicate composition for the dust ($MgFeSiO_4$, Jaeger et al. 1994; Dorschner et al. 1995). We set the grain size to have maximum absorption of the dust clump in the visible; ranging from 0.18 to 0.24 μm. The modeling details are available in Montargès et al. (2021). Unfortunately, the procedure did not converge towards simulations reproducing the images for

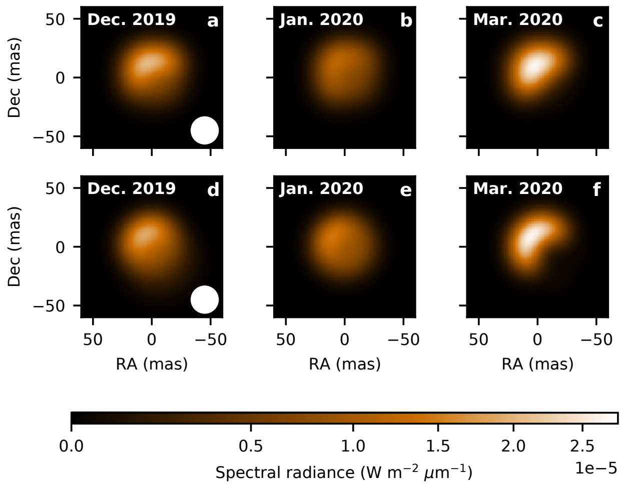

Fig. 3. Best matching models for the ZIMPOL images in the Cnt_Hα filter (644.9 nm). The upper images correspond to the cool spot PHOENIX model, the lower images to the dusty clump RADMC3D simulations.

Table 1. Result of the match between the synthetic cool patch PHOENIX models and the ZIMPOL observations

Parameter	December 2019	January 2020	March 2020
x_p (mas)	-7.1	-2.4	-28.4
y_p (mas)	-14.2	-2.4	-35.6
r_p (mas)	23.7	19.0	45.0
T_{hot} (K)	3,700	3,700	3,700
T_{cool} (K)	3,400	3,400	3,200
$\log \mathcal{L}$	-8.8×10^6	-5.5×10^7	-4.0×10^7

January and March 2020. Instead, we tuned the parameters manually to obtain best guesses. The results are summarized in Table 2, and the images are shown in Fig. 3.

5 Discussion

Both the cool photospheric patch model and the dusty clump simulations are able to reproduce the morphology of the ZIMPOL images. However, the SED of both type of models fail to properly reproduce the near infrared AAVSO measurements (Fig. 4). The cool patch models reproduce better these measurements. However, it should be noted that while the parameter space exploration is complete for the cool photospheric patch models, it is not the case for the dusty clump simulations. Indeed, we did not consider other grain size distributions, nor did we explore alternative dust compositions, since we were mostly interested in reproducing the visible obscuration. Therefore, we considered both type of models being equally able to match the observations, since with more time and more computation resources, we could have likely found a more favorable dust model.

Comparison with other observations of this event obtained with various techniques are performed in Mon-

Table 2. Result of the match between the RADMC3D clump simulations and the ZIMPOL observations

Parameter	December 2019	January 2020	March 2020
x_c (au)	-1.9	-0.8	-1.9
y_c (au)	-3.0	-0.6	-1.8
z_c (au)	12.5	20.0	20.0
r_c^{in} (au)	6.5	5.0	4.5
ρ_0^{in} (g cm^{-3})	3.2 $\times 10^{-19}$	4.0 $\times 10^{-19}$	2.0 $\times 10^{-18}$

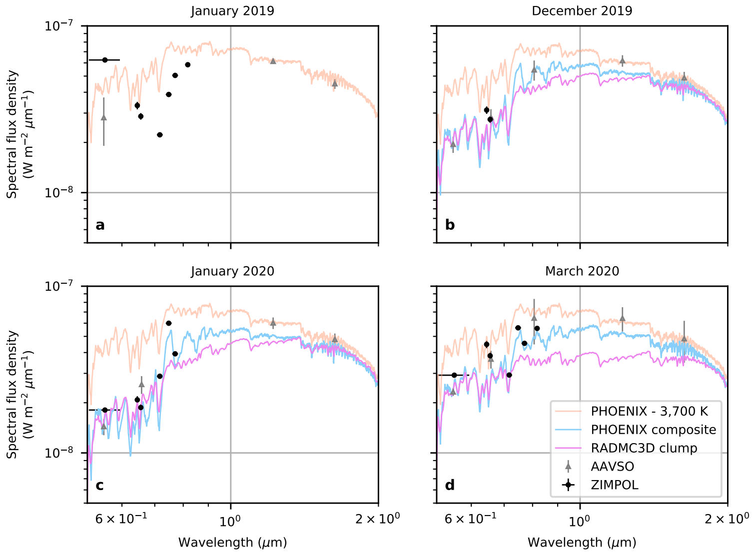

Fig. 4. Observed photometry and modeled SEDs for Betelgeuse before (a), and during the 'Great Dimming' (b, c, and d). The black dots correspond to the ZIMPOL photometry, the gray triangles to the AAVSO measurements. The orange curve represents the SED of a PHOENIX 15 $M_\odot$ RSG with $T_{eff} = 3700$ K. The blue curve corresponds to the best matching PHOENIX cool patch model, and the purple curve to the best dusty clump RADMC3D simulation.

targès et al. (2021).

6 Conclusion

We presented observations of Betelgeuse obtained before and during its 'Great Dimming' in 2019-2020. The VLTI/GRAVITY interferometric observations and VLT/SPHERE-IRDIS sparse aperture masking measurements showed that the angular diameter of the star did not change. The VLT/SPHERE-ZIMPOL spatially resolved imaging of the photosphere revealed that the Southern hemisphere of the star was obscured.

Using PHOENIX model atmospheres to build a composite synthetic image of the stellar surface, we tested the hypothesis of a cool photospheric patch as the cause of the Dimming. We also build a dusty clump simulation using the radiative transfer code RADMC3D. Both scenarios are able to reproduce the morphology and the photometry of the event. In agreement with observations by other teams, with other techniques, and to fit the 'Great Dimming' within the general pulsation pattern of Betelgeuse, we conclude that both events happened consecutively. A cool patch formed on the photosphere perhaps consistently with the primary light curve period and the periodic outflow velocity, that caused dust to form from plasma ejected months before in the line of sight. This caused an unusual light minimum for the red supergiant.

This 'Great Dimming' calls for a more frequent monitoring of the photosphere and close circumstellar environment of nearby RSGs that can be spatially resolved.

MM thanks the council of the SF2A for the invitation to present these results at the plenary session of the meeting. Based on observations collected at the European Southern Observatory under ESO programs 0102.D-0240(A), 0102.D-0240(D), 104.20UZ, and 104.20V6.004. We acknowledge with thanks the variable star observations from the AAVSO International Database contributed by observers worldwide and used in this research. This project has received funding from the European Union's Horizon 2020 research and innovation program under the Marie Skłodowska-Curie Grant agreement No. 665501 with the research Foundation Flanders (FWO) ([PEGASUS]^2 Marie Curie fellowship 12U2717N awarded to M.M.). EC acknowledges funding from the KU Leuven C1 grant MAESTRO C16/17/007. LD and MM acknowledge support from the ERC consolidator grant 646758 AEROSOL. SK acknowledges support from the ERC starting grant 639889 ImagePlanetFormDiscs. The material is based upon work supported by NASA under award number 80GSFC17M0002. We are grateful to the ESO staff for their fast response in accepting the DDT proposal and carrying out the observations. The authors would like to thank Betelgeuse for having undergone this peculiar event more than 700 years ago in the appropriate solid angle. This work has made use of the SPHERE Data Center, jointly operated by OSUG/IPAG (Grenoble), PYTHEAS/LAM/CeSAM (Marseille), OCA/Lagrange (Nice) and Observatoire de Paris/LESIA (Paris).

This research has made use of the Jean-Marie Mariotti Center `Aspro` and `SearchCal` services*. We used the SIMBAD and VIZIER databases at the CDS, Strasbourg (France)†, and NASA's Astrophysics Data System Bibliographic Services. This research made use of GNU Parallel (Tange 2018), IPython (Pérez & Granger 2007), Numpy (van der Walt et al. 2011), Matplotlib (Hunter 2007), SciPy (Virtanen et al. 2020), Pandas (pandas development team 2020; Wes McKinney 2010), Astropy‡, a community-developed core Python package for Astronomy (Astropy Collaboration et al. 2013), and Uncertainties§: a Python package for calculations with uncertainties.

References

Astropy Collaboration, Robitaille, T. P., Tollerud, E. J., et al. 2013, A&A, 558, A33

Beuzit, J. L., Vigan, A., Mouillet, D., et al. 2019, A&A, 631, A155

Cardelli, J. A., Clayton, G. C., & Mathis, J. S. 1989, ApJ, 345, 245

Cheetham, A. C., Girard, J., Lacour, S., et al. 2016, in Society of Photo-Optical Instrumentation Engineers (SPIE) Conference Series, Vol. 9907, Optical and Infrared Interferometry and Imaging V, ed. F. Malbet, M. J. Creech-Eakman, & P. G. Tuthill, 99072T

Dohlen, K., Langlois, M., Saisse, M., et al. 2008, in Society of Photo-Optical Instrumentation Engineers (SPIE) Conference Series, Vol. 7014, Ground-based and Airborne Instrumentation for Astronomy II, ed. I. S. McLean & M. M. Casali, 70143L

Dorschner, J., Begemann, B., Henning, T., Jaeger, C., & Mutschke, H. 1995, A&A, 300, 503

Dullemond, C. P. 2012, RADMC-3D: A multi-purpose radiative transfer tool, astrophysics Source Code Library

Gravity Collaboration, Abuter, R., Accardo, M., et al. 2017, A&A, 602, A94

Guinan, E., Wasatonic, R., Calderwood, T., & Carona, D. 2020, The Astronomer's Telegram, 13512, 1

Guinan, E. F., Wasatonic, R. J., & Calderwood, T. J. 2019, The Astronomer's Telegram, 13341, 1

Harper, G. M., Brown, A., Guinan, E. F., et al. 2017, AJ, 154, 11

Hunter, J. D. 2007, Computing In Science & Engineering, 9, 90

Jaeger, C., Mutschke, H., Begemann, B., Dorschner, J., & Henning, T. 1994, A&A, 292, 641

Joyce, M., Leung, S.-C., Molnár, L., et al. 2020, ApJ, 902, 63

Kervella, P., Perrin, G., Chiavassa, A., et al. 2011, A&A, 531, A117

Lançon, A., Hauschildt, P. H., Ladjal, D., & Mouhcine, M. 2007, A&A, 468, 205

Montargès, M., Cannon, E., Lagadec, E., et al. 2021, Nature, 594, 365

Ohnaka, K., Hofmann, K.-H., Benisty, M., et al. 2009, A&A, 503, 183

pandas development team, T. 2020, pandas-dev/pandas: Pandas

Pérez, F. & Granger, B. E. 2007, Computing in Science and Engineering, 9, 21

Schmid, H. M., Bazzon, A., Roelfsema, R., et al. 2018, A&A, 619, A9

Stothers, R. B. 2010, ApJ, 725, 1170

Tange, O. 2018, GNU Parallel 2018 (Ole Tange)

van der Walt, S., Colbert, S. C., & Varoquaux, G. 2011, Computing in Science Engineering, 13, 22

Verhoelst, T., van der Zypen, N., Hony, S., et al. 2009, A&A, 498, 127

Virtanen, P., Gommers, R., Oliphant, T. E., et al. 2020, Nature Methods, 17, 261

Wes McKinney. 2010, in Proceedings of the 9th Python in Science Conference, ed. Stéfan van der Walt & Jarrod Millman, 56 – 61

*Available at http://www.jmmc.fr

†Available at http://cdsweb.u-strasbg.fr/

‡Available at http://www.astropy.org/

§Available at http://pythonhosted.org/uncertainties/

SF2A 2021
A. Siebert, K. Baillié, E. Lagadec, N. Lagarde, J. Malzac, J.-B. Marquette, M. N'Diaye, J. Richard, O. Venot (eds)

PROVENANCE OF ASTRONOMICAL DATA

M. Servillat[1]

Abstract. In the context of Open Science, provenance has become a decisive piece of information to provide along with astronomical data. Provenance is explicitly cited in the FAIR principles, that aims to make research data Findable, Accessible, Interoperable and Reusable. The IVOA Provenance Data Model, published in 2020, puts in place the foundations for structuring and managing detailed provenance information, from the acquisition of raw data, to the dissemination of final products. The ambition is to provide for each astronomical dataset a sufficiently fine grained and detailed provenance information so that end-users understand the quality, reliability and trustworthiness of the data. This would ensure that the Reusable principle is respected.

Keywords: Provenance, Astronomy, Virtual Observatory

1 Introduction

The idea behind Open Science[*] is to allow scientific information, data and outputs to be more widely accessible (Open Access) and more reliably harnessed (Open Data) with the active engagement of all the stakeholders (Open to Society). Open Science is defined as "an inclusive construct that combines various movements and practices aiming to make multilingual scientific knowledge openly available, accessible and reusable for everyone" (UNESCO 2021). The aim is "to increase scientific collaborations and sharing of information for the benefits of science and society, and to open the processes of scientific knowledge creation, evaluation and communication to societal actors beyond the traditional scientific community" (UNESCO 2021).

Open science is a policy priority for the European Commission[†] and the standard method of working under its research and innovation funding programmes as it improves the quality, efficiency and responsiveness of research. One of the ambition of this policy is to build a European Open Science Cloud (EOSC), i.e. an environment that cuts across borders and scientific disciplines to store, share, process and reuse research digital objects (like publications, data, and software) that are Findable, Accessible, Interoperable and Reusable (FAIR).

In the astronomy domain, the FAIR principles (Wilkinson et al. 2016) have been a matter of concern since more than 20 years, primarily within the International Virtual Observatory Alliance[‡] (IVOA), that provides standards to foster interoperability and enable the production of Open Data. Several astronomical research infrasctructures are involved in the European Horizon 2020 ESCAPE project[§] (European Science Cluster of Astronomy & Particle physics ESFRI research infrastructures) that brings together the astronomy, astroparticle and particle physics communities and puts together a cluster with aligned challenges of data-driven research.

The Virtual Observatory ecosystem already provides robust solutions to Find and Access astronomical data in an Interoperable way. However, the Reusable principle is more subjective and requires dedicated rich metadata to demonstrate the quality, reliability and trustworthiness of the data. Detailed and structured provenance information is then key information to provide along with the astronomical data.

In this context, and with the implication of several members of the French ASOV (*Action Spécifique Observatoire Virtuel*), a series of meetings and workshops took place over the last years to model provenance information (Servillat et al. 2020b) and implement related tools (Servillat et al. 2021c). A provenance management system has then been proposed for astronomical facilities (Servillat et al. 2021b).

[1] Laboratoire Univers et Théories, Observatoire de Paris, Université PSL, CNRS, Université de Paris, 92190 Meudon, France; e-mail: mathieu.servillat@obspm.fr

[*] See the dedicated UNESCO web page: https://en.unesco.org/science-sustainable-future/open-science

[†] See the dedicated EU web page: https://ec.europa.eu/info/research-and-innovation/strategy/strategy-2020-2024/our-digital-future/open-science_en

[‡] https://www.ivoa.net

[§] https://projectescape.eu

2 Requirement for structured provenance

There are clear advantages to retain provenance information as structured, machine-readable data, in particular in the context of Open Science:

- **Quality / Reliability / Trustworthiness** of the products: the simple fact of being able to show its provenance is sufficient to give more value to a product, and if the provenance information is detailed, the value is higher.
- **Reproducibility requirement** in many projects: provenance details are essential to be able to rerun each activity (maybe testing and improving each step); Having this information, it may not be necessary to keep every intermediate file that is easily reproducible (hence a possible gain on storage space and costs).
- **Debugging**: with detailed provenance, it is not necessary to restart from scratch, as one can locate in the provenance graph the faulty parts or the products to be discarded, and reprocess only from the identified failing steps.

We often realize too late that there are missing elements or links in the provenance. The capture of the provenance should thus be as detailed as possible. It should also be as naive as possible: provenance should trace what happened, which is different to the workflow approach where one anticipates what should happen. The good practice would thus be to record provenance events directly when they occur, with the relevant links to what happened before, and not considering what will happen after.

3 A Provenance data model

The IVOA validated in April 2020 a Provenance Data Model (Servillat et al. 2020b) to structure the provenance information. It is based on the World Wide Web Consortium (W3C) PROV core concepts of Entity, Activity and Agent (Moreau et al. 2013) with a dedicated set of classes for the activity description (e.g. method, algorithm, software) and the activity configuration (e.g. parameters).

Provenance is related by definition to the origin of a product (where does it come from?), but also the path followed to generate this product (what has been done?). Provenance is thus seen as a chain of activities and entities, used and generated. With the core data model, basic objectives are achieved: use of unique identifiers, traceability of the operations, connection with contacts for further information, citation or acknowledgement. By following the full IVOA data model, more advanced questions are answered: What happened during each activity? How was the activity tuned to be executed properly? What kind of content is in the entities?

The data model is a basis for the development of tools and services, see e.g.: Servillat et al. (2021a); Sanguillon et al. (2021); Landais et al. (2021); Servillat et al. (2020a); Sanguillon et al. (2020).

The data model and related implementations provide a standard formalism to write and exchange the provenance information. This is illustrated in Figure 1, where the `voprov` Python package¶ was used to generate a graph of three activities, executed with the OPUS job manager (Servillat et al. 2021a).

4 Provenance in practice

4.1 Full provenance

It is tempting to limit the provenance information to a list of keywords associated to a data product. However, the full provenance is to be seen as a global graph of activities and entities up to the raw data, which cannot be embedded in the entities themselves. This consideration led to the development of an advanced provenance management system, with the concepts of capture "inside" (i.e. during the execution of a processing pipeline), storage of all provenance events in a central database, and visualization and exploration of the full provenance through database queries (for more details, see Servillat et al. 2021b).

To ease the capture of provenance inside a pipeline, a Python package, `logprov`‖, is in development along with the pipelines and science tools developed for the Cherenkov Telescope Array (CTA). This capture tool

¶ https://github.com/sanguillon/voprov

‖ https://github.com/mservillat/logprov

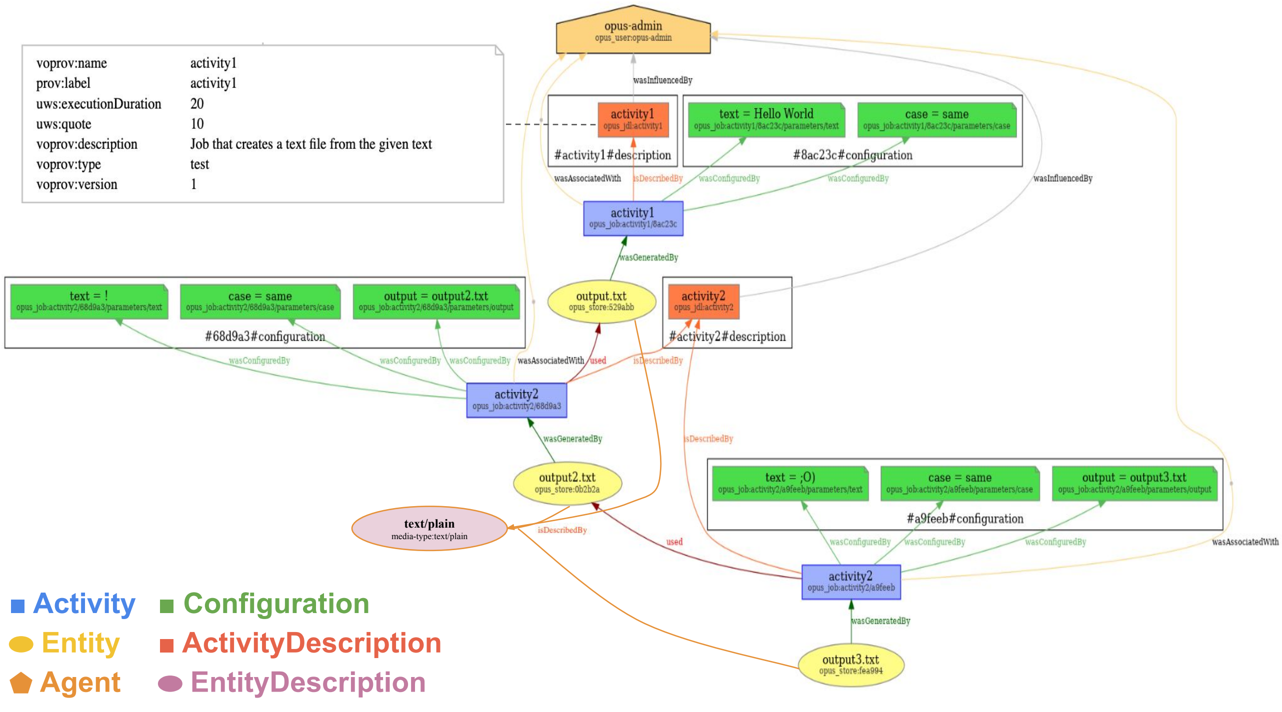

Fig. 1. Example of an IVOA Provenance graph using the main concepts of the IVOA Provenance Data Model (Servillat et al. 2020b). The graph shows a sequence of 3 activities. Each activity performs an operation for which the description and the configuration are available and explicit.

was initially implemented for `gammapy`** and its high level interface. The usage of `logprov` requires to insert decorators before the Python functions or classes one wish to trace. Provenance events are then written to a structured log. In addition, a definition file of the activities can be added to record more detailed descriptions of the activities and entities. To make this capture efficient, it is highly recommended to structure the code and pipelines in well defined functions, with identified inputs and outputs (i.e. not contained in local variables, but globally accessible).

4.2 Last-step embedded provenance

Along with the definition of the full provenance, the idea of an optimized subset of provenance that could be embedded in an entity has emerged. We defined the last-step provenance as a minimal list of keywords that gives information on the last activity (general process/workflow, software versions, contacts...), including links to used and generated entities (Servillat et al. 2021c). Such a list is a restriction of the full provenance information, that can be stored in a file header (e.g. using the FITS file format) or a flat table.

The last-step provenance is composed of attributes that refer to several items in a provenance graph basic template. For example, the entity itself is described by attributes like `entity_id`, `entity_location`... The template graph is shown in Figure 2. The main node in the graph is the entity that transports this last-step provenance, which is attached to the activity that generated the entity. The context is provided by attributes that describe the entity (e.g. `entity_content_type`) and the activity (e.g. `software_name`, `software_version`, `software_docurl`), and parameters that configure the activity. The activity may be part of a general workflow, itself described, and maybe linked to an instrument. Finally, the identifiers of used entities, and the generated ones during the same process allow for the exploration of the previous, or next, or parallel steps. By resolving those identifiers and combining chained last-step provenance records, one could thus explore or reconstruct the full provenance.

** https://github.com/gammapy/gammapy

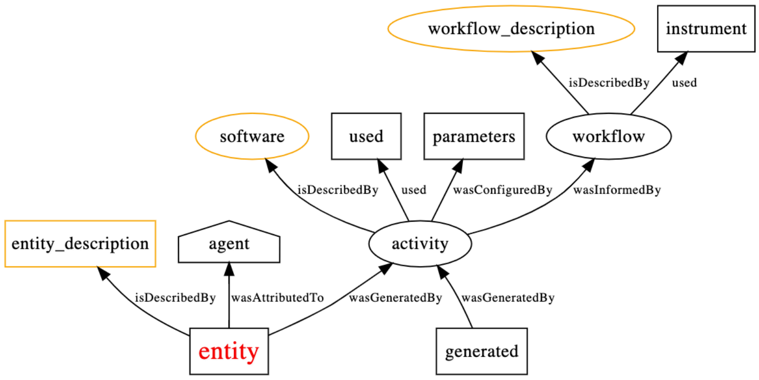

Fig. 2. Provenance graph template that defines the prefixes of last-step provenance attributes.

4.3 *Provenance access protocols*

Two access protocols are being discussed within IVOA, in order to be able to query the provenance information:

- **ProvSAP**: a Simple Access Protocol that returns a W3C PROV file from a regular GET query on an HTTP endpoint, where the main argument is ID with the identifier of the entity or activity for which the provenance graph is queried. This system is for example implemented in the OPUS job manager (Servillat et al. 2021a) and in other tools (Sanguillon et al. 2020).
- **ProvTAP**: IVOA Table Access Protocol (TAP) using a schema based on the IVOA Provenance data model (Bonnarel et al. 2019). It's a reverse mechanism to locate data through queries on its provenance. This approach also enables queries to test the data quality, based on the analysis of parameters of activities.

The solutions developed here for provenance management (full provenance capture and storage, last-step embedded provenance, and provenance access protocols) thus provide several efficient and standardized approaches that can be adapted to various astronomy projects of different sizes.

We acknowledge support from the ESCAPE project funded by the EU Horizon 2020 research and innovation program (Grant Agreement n.824064). Additional funding was provided by the INSU (Action Spécifique Observatoire Virtuel, ASOV), the Action Fédératrice CTA at the Observatoire de Paris and the Paris Astronomical Data Centre (PADC).

References

Bonnarel, F., Louys, M., Mantelet, G., et al. 2019, in ASP Conf. Ser., Vol. 523, ADASS XXVII, ed. P. J. Teuben, M. W. Pound, B. A. Thomas, & E. M. Warner, 313

Landais, G., Servillat, M., Bonnarel, F., et al. 2021, in ASP Conf. Ser., Vol. TBD, ADASS XXX, ed. J.-E. Ruiz & F. Pierfederici, TBD

Moreau, L., Missier, P., Belhajjame, K., et al. 2013, PROV-DM: The PROV Data Model, W3C Recommendation

Sanguillon, M., Arrabito, L., Boisson, C., et al. 2021, in ASP Conf. Ser., Vol. TBD, ADASS XXX, ed. J.-E. Ruiz & F. Pierfederici, TBD

Sanguillon, M., Bonnarel, F., Louys, M., et al. 2020, in ASP Conf. Ser., Vol. 522, ADASS XXVII, ed. P. Ballester, J. Ibsen, M. Solar, & K. Shortridge, 545

Servillat, M., Aicardi, S., Cecconi, B., & Mancini, M. 2021a, in ASP Conf. Ser., Vol. TBD, ADASS XXX, ed. J.-E. Ruiz & F. Pierfederici, TBD

Servillat, M., Boisson, C., Lefaucheur, J., et al. 2020a, in ASP Conf. Ser., Vol. 522, ADASS XXVII, ed. P. Ballester, J. Ibsen, M. Solar, & K. Shortridge, 199

Servillat, M., Bonnarel, F., Boisson, C., et al. 2021b, in Provenance and Annotation of Data and Processes, ed. B. Glavic, V. Braganholo, & D. Koop (Cham: Springer International Publishing), 244–249

Servillat, M., Bonnarel, F., Louys, M., , & Sanguillon, M. 2021c, in ASP Conf. Ser., Vol. TBD, ADASS XXX, ed. J.-E. Ruiz & F. Pierfederici, TBD

Servillat, M., Riebe, K., Boisson, C., et al. 2020b, IVOA Provenance Data Model Version 1.0, IVOA Recommendation

UNESCO, Director-General, A. A. 2021, UNESCO Circular Letter: Draft text of the UNESCO Recommendation on Open Science, `https://unesdoc.unesco.org/ark:/48223/pf0000378381`

Wilkinson, M. D., Dumontier, M., Aalbersberg, I. J., et al. 2016, Scientific Data, 3

PULSAR TIMING ARRAYS AND GRAVITATIONAL WAVES : THE FIRST STEPS TOWARDS DETECTION?

G. Theureau[1,2,3], S. Babak[4], A. Berthereau[1], A. Chalumeau[1,4], S. Chen[1,2], I. Cognard[1,2], M. Falxa[4], L. Guillemot[1,2] and A. Petiteau[4]

Abstract. PTA (Pulsar Timing Array) experiments use the natural clock properties of pulsars as a detector of gravitational waves. In practice, perturbations in the regularity of pulse arrival times are analysed and a quadrupole signature is sought that spatially correlates all the measurements amongst the pulsars. The PTAs are sensitive in the frequency domain ranging from 10^{-9} to 10^{-6} Hz, which targets in particular the population of supermassive binary black holes. In January of this year, the US consortium NANOGrav announced the first detection of a common signal across all the pulsars in the network, but without showing evidence for spatial coherence, closely followed by the other two consortia, Australia (PPTA) and Europe (EPTA). I will review these results, focusing on the methodology and on the analysis of foregrounds, and I will detail the astrophysical constraints expected in the years to come.

Keywords: pulsars, gravitational waves, black-holes, galaxy formation

1 Introduction

In France, Pulsar Timing Array (PTA) activities are hosted in two laboratories, LPC2E and APC, and are closely connected to the Nançay Radio Observatory where the dedicated instrumentation is developed and the timing observations are performed at high cadence with the decimetric Nançay Radio Telescope (NRT). There are also connexions with people in Femto-ST and Geoazur, for the link to clock metrology and Solar System Ephemerides. This long term program has been jointly supported for many years by PNCG, PNHE and Paris Observatory Scientific Council and has also received recently funding from DIM-ACAV+ and ANR. This year, there has been a renewed interest for PTA experiments, with the publication and forthcoming press releases by the North American consortium NANOGrav in January 2021 (Arzoumanian et al. (2020)) announcing that they found "possible first hints of low-frequency gravitational wave background". Indeed what happened is that the three international consortia, European Pulsar Timing Array (EPTA), Parkes Pulsar Timing Array (PPTA) and NANOGrav, contemporaneously and independently detected a red noise component shared by all the pulsars in their respective timing array (see respectively: Chen et al. (2021, submitted), Goncharov et al. (2021) and Arzoumanian et al. (2020)). As we will see, this signal has the main caracteristics in amplitude and spectral index of what we expect from the emission of a Super Massive Binary Black Hole population, but the three groups are still missing the detection of a spatial correlation of the signal, which would be the irrefutable proof that it is indeed of gravitational origin. Note that there are also other identified sources of gravitational background emission in the PTA frequency range, which are e.g. the emission from a network of cosmic string loops (Kibble (1976), Sanidas et al. (2012)), relic emission produced by quantum fluctuations of the gravitational field in the inflationary era (Caprini et al. (2010)), or the signature of a first-order phase transition in the primordial universe (Lasky et al. (2016); Grishchuk (2005)). At the time of the SF2A 2021 conference, more that three dozen of articles about the interpretation of this "possible" gravitational wave signal have been submitted to astro-ph since the first claim early this year.

[1] Université d'Orléans, CNRS, LPC2E UMR7328, F-45071 Orléans, France
[2] Observatoire de Paris, PSL University, CNRS, Université d'Orléans, USN, 18330 Nançay, France
[3] Université PSL, CNRS, Université de Paris, LUTh, 92190 Meudon,France,
[4] Université de Paris, CNRS, APC, F-75013 Paris, France

At the world wide level, continental PTA consortia are organised under a common umbrella organisation named the International Pulsar Timing Array. In addition to the three founding groups mentioned above, the Indian consortium InPTA recently formed and joined the collaboration, and one expects the South Africa and China to join as well in the coming years. There are eight radio telescopes presently participating in the data collection. Five in Europe : Effelsberg (Germany), WSRT (Netherlands), SRT (Italy), Lovell (United Kingdom) and NRT (France) ; one in Australia : Parkes, and two in North America : Arecibo and Green Bank. Arecibo recently collapsed and is being replaced by contributions from VLA and CHIME. GMRT (India) has started a high precision timing programme 3 years ago and MeerKAT (South Africa) has been gathering high quality data since 2.5 years and both are preparing their own first release to participate in the common effort. China will join with three radio telescopes : QTT, JRT and the giant FAST.

The PTA experiment has a long history. The first reference is certainly from Sazhin (1978), who proposed that "ultralong gravitational waves" could be detected by their perturbation on electromagnetic pulses propagation. A bit more than a year later, Detweiler (1979) showed that given published pulsar data, one can set an amplitude upper limit of 10^{-11} to the energy density of a stochastic gravitational wave background with periods 1 year. In 1982, Hellings & Downs (1983) further updated this limit and for the first time they calculated the expected spatial correlation of the signal as a function of the angular separation of pulsar pairs. PTA science was born.

2 Pulsar Timing Arrays: principles

What do pulsar timers measure exactly ? We measure at the telescope a series of pulsations with an observed period P due to the rotation of the neutron star, and we observe a variation δP of this period or of rotation frequency $\delta\nu$ with time. The integration of this $\delta\nu$ all along the signal pathway from the pulse emission to its reception is called the timing residual.

$$r(t) = \int_0^t \frac{\nu(t') - \nu_0}{\nu_0} dt' \tag{2.1}$$

In practice we assume that we know sufficiently well the pulsar, its environment, the material present along its line of sight and the Earth motion, that we can model any Doppler shift and dispersion of the signal, so that only the unknown, e.g. the gravitational perturbation we are looking for, remains. One writes:

$$\frac{\nu(t) - \nu_0}{\nu_0} = \frac{1}{2} \frac{\hat{n}^i_\alpha \hat{n}^j_\alpha}{1 + \hat{n}_\alpha . \hat{k}} \Delta h_{ij} \tag{2.2}$$

where $\hat{n}_\alpha$ is the direction of the pulsar i or j, $\hat{k}$ is the direction of a gravitational source, and $\Delta h_{ij} = h_{ij}(t_p) - h_{ij}(t_E)$ is the wave amplitude difference at the pulsar location (t_p) and at the Earth (t_E).

Let us summarize: the Earth and the distant pulsar are considered as free masses whose position responds to changes in the local metric of space time. The passage of a gravitational wave produces fluctuations in the arrival times of the individual pulses, so that with timing uncertainties dt ($\sim$100 ns), a cadence of a few days and total observation time spans T ($\sim$25 years), PTA are sensitive to amplitudes $\sim dt/T \sim 1.3\ 10^{-16}$ and to frequencies $f \sim 1/T \sim 10^{-9}$ - 10^{-6} Hz (see Fig. 1, left panel).

3 The recent results by NANOGrav, PPTA and EPTA

3.1 *A first detection of the stochastic background?*

Fig. 1 (right panel) shows the free spectrum of the PTA residuals along gravitational wave frequencies, as measured respectively by NANOGrav (blue violins, from Arzoumanian et al. (2020)) and EPTA (orange violins, from Chen et al. (2021, submitted)). The power is measured in frequency bins centered successively on $1/T$, $2/T$, ... N_{bin}/T, where T is the total time span covered by the PTA observations. The EPTA has longer time series, thus it reaches lower frequency bins. The full lines show the actual power law describing the red noise fitted from respectively the lowest 5 (NANOGrav) and 30 (EPTA) frequency bins. The European results show a shallower spectral index (-0.39 vs -1.26) and a bit higher amplitude (e.g. 2.95 10^{-15} vs 1.92 10^{-15}, at fixed α = -2/3) with respect to NANOGrav. Both experiments use completely independent data. They use also different analysis pipelines, different MCMC samplers and different models for Solar System Ephemerides uncertainties. Considering our own results from the EPTA analysis, we obtained a robust estimation of the significance of the common red noise detection by comparing bayesian evidences for different models. The Bayes factor is around 1000 in favor of a common red noise or gravitational wave background, with respect to a simple model considering only individual pulsar timing noise. By comparison, the false detection resulting from a clock reference error or a Solar System Ephemerides bias is granted a Bayes factor of respectively 5 and 100 only with respect to the simple model.

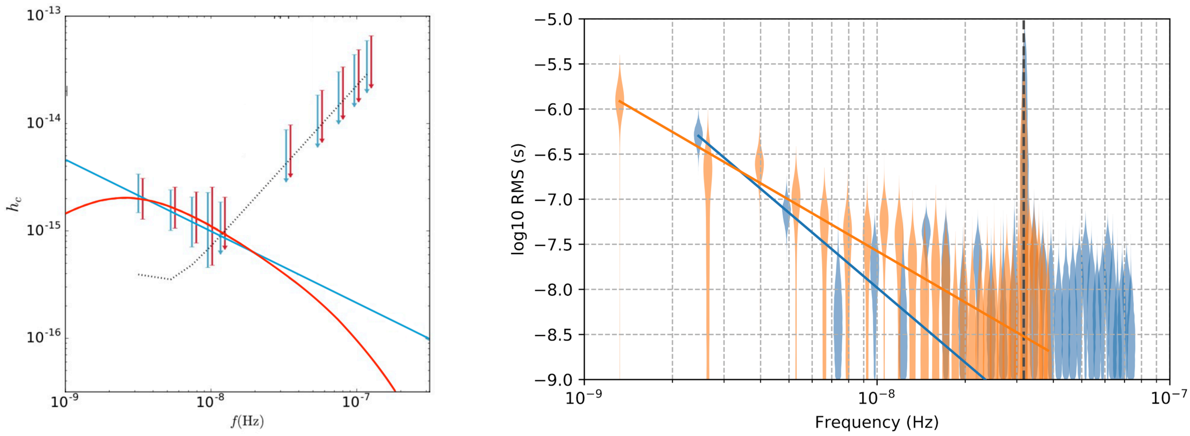

Fig. 1. Left: We illustrate here the principles of PTA stochastic gravitational wave background detection. On the vertical axis, hc is the strain amplitude and the frequencies along the horizontal axis range from 10^{-9} to 2 10^{-7} Hz. The blue line shows the expected power law spectrum $h_c(f) = A(f/yr^{-1})^{\alpha}$ with slope α = -2/3 for a population of super massive black hole binaries with circular orbits and energy loss dominated by gravitational emission. The red curve shows the same spectrum for a more realistic population, including eccentricity of the orbits and energy loss contribution from interactions with central stars and gas. The dotted line shows the PTA sensitivity curve. Above $\sim 10^{-8}$ Hz, the signal is not detected and PTA measurements only provide us with an upper limit. At lower frequencies instead, the signal is detected and one could even start to differentiate the two models of population. **Right:** We show here the recent PTA measurement from Arzoumanian et al. (2020) (red violins, NANOGrav) and Chen et al. (2021, submitted) (blue violins, EPTA). Below $\sim 10^{-8}$ Hz, we actually detect a clear signal in the form of low frequency correlated noise in the timing residuals. Straight full lines represent the respective fitted power law to the lowest 5 (NANOGrav) and 30 (EPTA) frequency bins.

In Fig. 2 (left), one compares the measured power law parameters (common red noise amplitude and index) from PTA experiments to the prediction from astrophysical models. These models describe a population of Super Massive Black Hole Binaries emitting low frequency gravitational waves in the context of hierarchical galaxy and large scale structure formation in a ΛCDM universe (prediction from Middleton et al 2021). One considers here the astrophysical parameters describing: the galaxy stellar mass function, the galaxy pair fraction, the merger time scale, the black-hole to bulge mass ratio, the binary BH eccentricity and the galaxy central stellar density. Among those, it is the merger rate, the merger time scale and the normalization of BH-bulge mass relation, which will be the first parameters to be constrained by a sensitivity limit or a robust detection of the GW background.

3.2 *An essential diagnostic: the spatial correlation of the signal*

However, the quadrupole nature of gravitational wave emission implies that the Earth term of the stochastic signal is necessarily spatially correlated between all pulsars and follows a well defined signature. Hellings & Downs (1983) showed that the overlap reduction function, which depends both on the sky position of the sources and on the antenna pattern (i.e. the relative position of the pulsars in the array) writes in a unique way as a function of the pulsar angular separations. This signature is an essential diagnostic. Let us emphasise here that **up to now, none of the PTA experiments has detected such a spatial correlation**, which would be the actual smoking gun of a gravitational wave background (see Fig. 2, right panel, for the NANOGrav result). **So no-one can yet claim a detection**. In order to get a detection, each consortium needs to extend its data set:

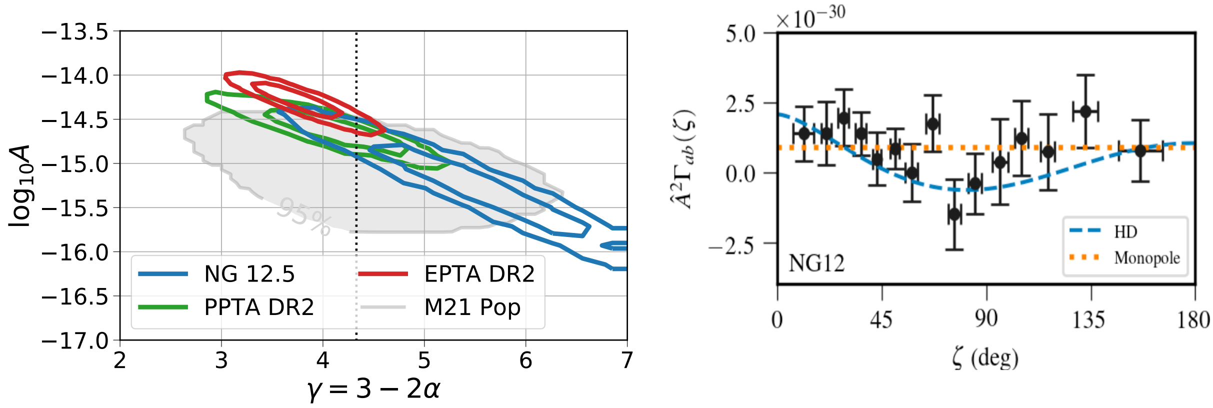

Fig. 2. Left: Contour plot corresponding to the posterior chains for the common-spectrum amplitude and spectral index obtained by the three regional consortia (NANOGrav in blue, EPTA in red, PPTA in green). The vertical dotted line corresponds to the spectral index expected for the emission from a population of Super Massive Black Hole Binaries in circular orbits. The grey area is obtained from Middleton et al. (2021) and shows the 95% confidence contour from astrophysical model predictions for the same population. **Right:** Hellings & Downs (HD) angular correlation measured from the NANOGrav 12.5 years sample (Arzoumanian et al. (2020)). The blue curve shows the expected quadrupolar signature. The orange horizontal line shows the fit of a monopole expected e.g. from clock reference systematics.

NANOGrav and PPTA to have essentially longer time spans, EPTA to add more pulsars in the analysis (i.e. include at least 25 pulsars instead of the 6 best timers only) in order in particular to better sample the spatial correlation. The data set should be completed and analyzed by mid-2022. After that, the full combination of the international data set will bring the ultimate confirmation, allowing to enhance both sensitivity and sky coverage.

3.3 Dealing with foregrounds and systematics

Of course, there are plenty of foreground noises that need to be characterised and correctly modelled before being able to access the GW signal in the timing residuals. Those noises are of different nature. We need to consider first the white or time un-correlated noise in each pulsar residual time series. Its origin can be instrumental (e.g. receiver gain instability, calibration uncertainty) or astrophysical (e.g. pulse jitter, related to the statistics of emission in the pulsar magnetosphere). We then have to deal with various time correlated or "red" noises that mimic or hide the gravitational emission signature at low frequencies. These ones come primarily from the dispersion measure (DM) variations (a secular change in electron content along the line of sight due to the relative motion of the Earth and the pulsar) and from long term variations of the neutron star rotation (either due to small bodies gravitational perturbations, variations in radiated energy or series of micro-glitches, presence of an unknown long orbital period companion). The former is chromatic with observed radio frequency and can be distinguished from the latter by using multi-band or multi-telescope observations. It can be modeled by a simple power law, but often requires custom modelization to take into account peculiar events (e.g. a lense effect due to a plasma bubble along the line of sight) or secondary variations due to multi-propagation changes or scintillation. The intrinsic or rotation noise is specific to each pulsar and can span a wide range of amplitudes. Fig. 3 shows an example of single pulsar noise analysis, with posterior plots for amplitude and spectral indices of both intrinsic red noise and chromatic DM noise.

Finally, Solar System planetary Ephemerides (SSE) play a crucial role in the timing process as they are used to transpose the timing residuals measured at the telescope to the barycentre of the Solar System (SSB), i.e. to correct for the Roemer delays. Any inaccuracy in such Roemer delays will impact all the pulsars of the array and will induce a spatial correlation that insidiously mimics the imprint of a GW background. To deal with this, the various consortia carefully compare the results from different SSE solutions (using JPL - Folkner & Park (2018) - , INPOP - Fienga et al. (2019) - or PMOE - Li et al. (2008)) and some have developed their own bayesian model of SSE uncertainties to be included in the full GW analysis. The difficulty is that SSE are built from space probe data to optimize the measurements of planets' positions, orbital velocities and masses,

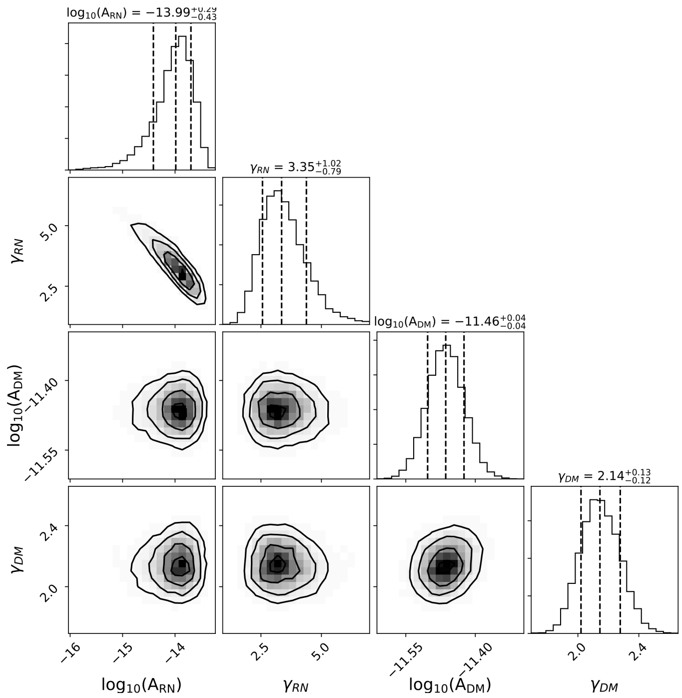

Fig. 3. Posterior distribution of intrinsic red noise (RN) and chromatic noise (DM) for the EPTA pulsar PSR J1600-3053. Each red noise component is modelled with a power law as $S \sim A^2(f/1yr^{-1})^{-\gamma}$. Courtesy of Aurélien Chalumeau (PhD student at LPC2E, Chalumeau et al 2021 in prep)

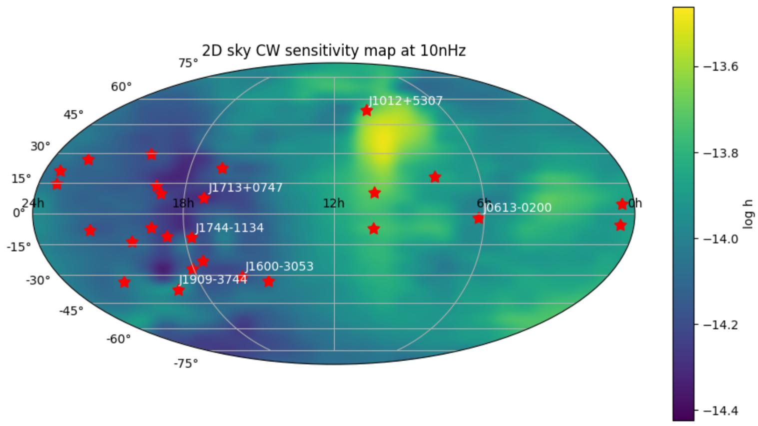

Fig. 4. 2D sky continuous wave sensitivity map at the fixed frequency of 10 nHz, derived from the analysis of EPTA first data release (Desvignes et al. (2016)), extended with 9 years of recent wide band NRT data. Red stars show the positions of the EPTA pulsars. The color scale denotes the span in strain hc in logarithmic scale. Courtesy of Mikel Falxa (PhD student at APC, Falxa et al 2022 in prep)

but not to accurately constrain the position of the SSB.

3.4 The search for individual sources

One expects that PTA measurements will also detect in the near future a few nearby or massive individual binary black-holes, which will show up as continuous wave sources at a single frequency or as a series of harmonics depending on the degree of eccentricity of their orbit. Such a detection is expected to occur as a second step, most probably after the first characterisation of the stochastic background from the whole population. Even without a detection, one can build a whole sky sensitivity map for each frequency bin, given the sky distribution and timing characteristics of the pulsars used in the array. A preliminary such map is shown on Fig. 4, for the GW frequency f = 10 nHz, given the current EPTA pulsar sample (2nd data release, courtesy of Mikel Falxa, PhD student at APC laboratory).

4 Conclusion

To summarize, all PTA consortia have developed independently a complete methodology to properly analyse the pulsar timing residuals and disentangle potential GW emission from various instrumental or astrophysical noise components affecting individual pulsars, as well as consistently taking into account uncertainties coming from SSE systematics. They all detect in their independent data sets the presence of a common process, which is comparable in amplitude and spectral index to the signal expected from a population of Super Massive Black Hole Binaries. However, these convergent results have to be considered with care, since the essential diagnostic of a spatial correlation following Hellings & Downs (1983) signature has not been successful yet. These results are preliminary, based on a sub-sample of available data. The next two years should bring a definitive and robust answer with the extension of the respective data sets and hopefully the global pooling of IPTA data, bringing the ultimate confirmation with much better sensitivity than the separate programmes.

The Nançay radio Observatory is operated by the Paris Observatory, associated to the French Centre National de la Recherche Scientifique (CNRS) and the Université of Orléans. We acknowledge financial support from "Programme National de Cosmologie and Galaxies" (PNCG), and "Programme National Hautes Energies" (PNHE) funded by CNRS/INSU-IN2P3-INP, CEA and CNES, France. We acknowledge financial support from Agence Nationale de la Recherche (ANR-18-CE31-0015) and from "Domaine d'Intérêt Majeur de la Région Île de France" (DIM-ACAV+), France.

References

Arzoumanian, Z., Baker, P. T., Blumer, H., et al. 2020, ApJ, 905, L34

Caprini, C., Durrer, R., & Siemens, X. 2010, Phys. Rev. D, 82, 063511

Chen, S., Caballero, N., Guo, Y., et al. 2021, submitted, MNRAS

Desvignes, G., Caballero, R. N., Lentati, L., et al. 2016, MNRAS, 458, 3341

Detweiler, S. 1979, ApJ, 234, 1100

Fienga, A., Deram, P., Viswanathan, V., et al. 2019, Notes Scientifiques et Techniques de l'Institut de Mécanique Celeste, 109

Folkner, W. M. & Park, R. S. 2018, IOM 392R-18-004

Goncharov, B., Shannon, R. M., Reardon, D. J., et al. 2021, On the evidence for a common-spectrum process in the search for the nanohertz gravitational wave background with the Parkes Pulsar Timing Array

Grishchuk, L. P. 2005, Physics Uspekhi, 48, 1235

Hellings, R. W. & Downs, G. S. 1983, ApJ, 265, L39

Kibble, T. W. B. 1976, Journal of Physics A Mathematical General, 9, 1387

Lasky, P. D., Mingarelli, C. M. F., Smith, T. L., et al. 2016, Physical Review X, 6, 011035

Li, G. Y., Zhao, H. B., Xia, Y., Zeng, F., & Luo, Y. J. 2008, in IAU Symposium, Vol. 248, A Giant Step: from Milli- to Micro-arcsecond Astrometry, ed. W. J. Jin, I. Platais, & M. A. C. Perryman, 560–562

Middleton, H., Sesana, A., Chen, S., et al. 2021, MNRAS, 502, L99

Sanidas, S. A., Battye, R. A., & Stappers, B. W. 2012, Phys. Rev. D, 85, 122003

Sazhin, M. V. 1978, Soviet Astronomy, 22, 36

SF2A 2021
A. Siebert, K. Baillié, E. Lagadec, N. Lagarde, J. Malzac, J.-B. Marquette, M. N'Diaye, J. Richard, O. Venot (eds)

CMB IN (RELATIVE) TENSION

M. Tristram[1]

Abstract. With Planck's CMB measurements, we have achieved high precision on the ΛCDM cosmological parameters with no need for model extensions. Many measurements are consistent with the predictions of the ΛCDM model fitted to Planck data. However, when compared to some cosmological probes, the CMB data exhibits some deviations which have been examined extensively for the last few years. We will describe the stability of the CMB results with respect to the fit of cosmological models and review the main so-called "tensions".

Keywords: cosmology: observations, cosmic background radiation, cosmological parameters, methods: data analysis

1 Introduction

The Planck satellite mission provided accurate measurements of the Cosmic Microwave Background radiation on the entire sky which gives powerful constraints on the Universe's content and geometry. Indeed, statistics from the measured CMB anisotropies can be compared to model predictions allowing the free parameters from specific cosmological models to be determined. The current standard model (so-called ΛCDM) can be described by 6 parameters in its simplest version but fits accurately the current cosmological observations.

In this model, we assume purely adiabatic, nearly scale-invariant perturbations at very early times, with curvature-mode (scalar) power spectrum parameterized by a power law $\mathcal{P}(k) = A_s\,(k/k_0)^{n_s-1}$, where A_s is the initial super-horizon amplitude for curvature modes and n_s i s the primordial index for scalar perturbations taken to be constant. The late-time parameters, on the other hand, determine the linear evolution of perturbations after they re-enter the Hubble radius: $\Omega_\mathrm{b}h^2$ the baryon density today, $\Omega_\mathrm{c}h^2$ the cold dark matter density today, H_0 the Hubble constant characterising the expansion of the Universe today, and τ the reionization optical depth.

With the current CMB measurements, the 6 parameters from the ΛCDM model are known at better than percent level with the exception of the reionization optical depth τ (Planck Collaboration VI 2020).

Planck provided the community with angular power spectra of CMB anisotropies in temperature (the so-called TT power spectrum) but also in polarisation (EE power-spectrum) and in cross-correlation temperature-polarization (TE power spectrum) (Planck Collaboration V 2020). Beyond the CMB anisotropies, Planck was also able to provide the first full-sky measurement of the gravitational amplitude through the lensing of CMB photons integrated along the line of side (so-called lensing power spectrum or $\phi\phi$).

Power spectra are plotted in Fig. 1. The uncertainties of the TT spectrum are dominated by sampling variance, rather than by noise or foreground residuals, at all scales below about $\ell = 1800$, the scale at which the CMB information is essentially exhausted within the framework of the ΛCDM model. The TE spectrum is about as constraining as the TT one, while the EE spectrum still has a sizeable contribution from noise.

From CMB data, the constraints obtained on the cosmological parameters are both consistent between the different mode (TT, TE, EE, as shown in Fig. 2) and stable with time (over the last decade). Moreover, the impact of the major instrumental systematic effects have been shown to be lower than 0.5σ of the published statistical uncertainties (Planck Collaboration VI 2020).

The ΛCDM model provides a good fit to the CMB data as well as to other astrophysical observations indicating that we have a good understanding of the physics to model cosmic history. Moreover, with the increase of sensitivity achieved by Planck, we have been able to constrain extensions from the standard model

[1] Université Paris-Saclay, CNRS/IN2P3, IJCLab, 91405 Orsay, France

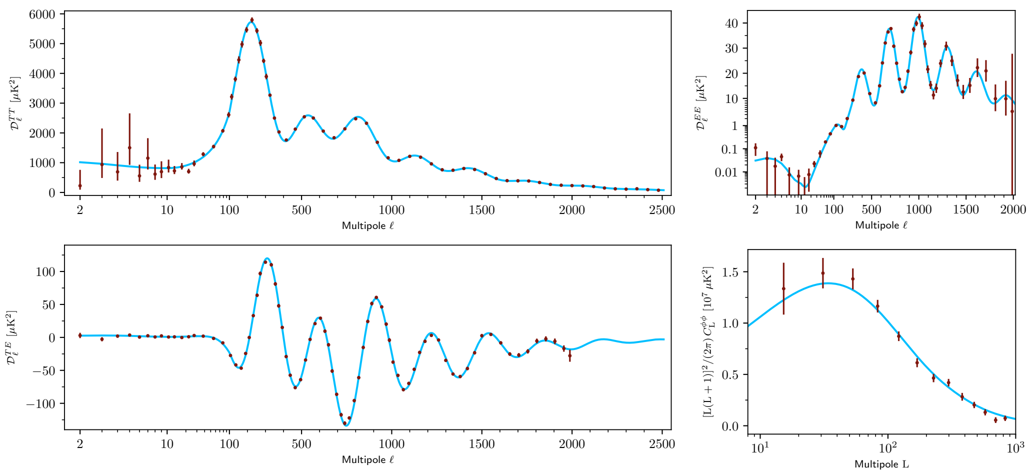

Fig. 1. Planck CMB power spectra for the temperature (top left), the temperature-polarization cross-spectrum (bottom left), the E-mode of polarization (top right), and the lensing potential (bottom right). The blue lines show the best-fitting ΛCDM model. *Extracted from* (Planck Collaboration I 2020).

with high precision (see Table 5 in Planck Collaboration VI 2020). This includes in particular: the flatness of the spatial hyperspaces; the neutrino masses; the number of relativistic species at decoupling; the running of power-laws for matter power spectra.

Nevertheless, despite these successes, some puzzling tensions have been highlighted after the Planck 2018 release and discussed in the literature since then. The most popular ones are as follows:

- the amplitude of lensing deduced from the CMB power spectra A_L which is inferred to be higher than the ΛCDM prediction,
- the Hubble constant H_0 from the inverse distance ladder which is discordant with measures of the distance scale from the nearby supernovae,
- the amplitude of the fluctuations σ_8 predicted by Planck which sits high compared to cosmic shear and cluster count inferred values

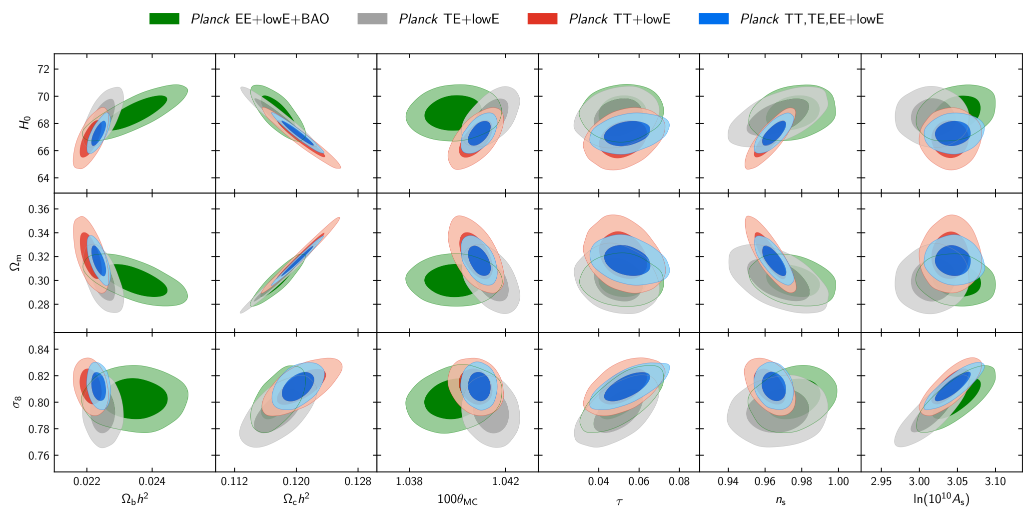

Fig. 2. Constraints on parameters of the base-ΛCDM model from the separate Planck EE, TE, and TT high-ℓ spectra combined with low-ℓ polarization (lowE), and, in the case of EE also with BAO, compared to the joint result using Planck TT,TE,EE+lowE. *Extracted from* (Planck Collaboration VI 2020).

2 The lensing amplitude A_L

Weak lensing enters the prediction of the CMB spectrum through a convolution of the unlensed spectrum with the lensing potential power spectrum. The effect of lensing is a smearing of the acoustic peaks as well as a redistribution of power towards the high multipoles (above $\ell \sim 3000$).

As originally proposed in Calabrese et al. (2008), a phenomenological parameter, A_L, that rescales the lensing potential, is introduced, allowing an internal check of the consistency of the lensing effect with the cosmology. Indeed, measuring a value of A_L deviating from one indicates either a problem with the model (modification of the gravity), or residual systematics in the data.

When estimated with the $\phi\phi$ power spectrum, this allows the measurement of the significance of the detection of the CMB lensing and compare to the ΛCDM prediction ($A_L = 1$). In Planck Collaboration VI (2020), the Planck lensing measurements is perfectly compatible with the model:

$$A_L = 1.011 \pm 0.028 \quad \text{(Planck } \phi\phi)$$

The lensing amplitude can also be estimated from the CMB anisotropies by looking for the impact on the angular power spectra. Since its first release, the Planck Collaboration has a reported a value of the A_L parameter that is discrepant with one by more than 2σ. The results from the different power spectra (TT, TE, EE) are barely compatible (see left panel in Fig. 3 and Planck Collaboration VI 2020). Moreover, as already discussed in Couchot et al. (2017), the fitted value depends on the CMB likelihood used. Indeed, the three different likelihoods used on Planck 2018 data (PR3*) give:

$$A_L = 1.243 \pm 0.096 \qquad \text{(TT+lowE [Plik])} \tag{2.1}$$

$$A_L = 1.246 \pm 0.095 \qquad \text{(TT+lowE [CamSpec])} \tag{2.2}$$

$$A_L = 1.160 \pm 0.075 \qquad \text{(TT+lowE [Hillipop])} \tag{2.3}$$

Even if there is still some tension at about 2σ, this indicates that the A_L deviation from unity is sensitive to the details of the likelihood implementations and in particular to the modelling of the foregrounds. Using the last release of Planck maps (PR4*, Planck Collaboration Int. LVII 2020), and with a more complete description of the low multipoles in polarisation, one can recover even lower estimates of A_L (Tristram et al. 2021) with similar uncertainty reinforcing the impact of systematic residuals in Planck 2018 data.

Ground-based telescopes measuring CMB anisotropies (such as ACT or SPT3g) recover A_L compatible with unity (see right panel in Fig. 3):

$$A_L = 1.01 \pm 0.11 \qquad \text{(ACT, Aiola et al. 2020)} \tag{2.4}$$

$$A_L = 0.98 \pm 0.12 \qquad \text{(SPT3g, Dutcher et al. 2021)} \tag{2.5}$$

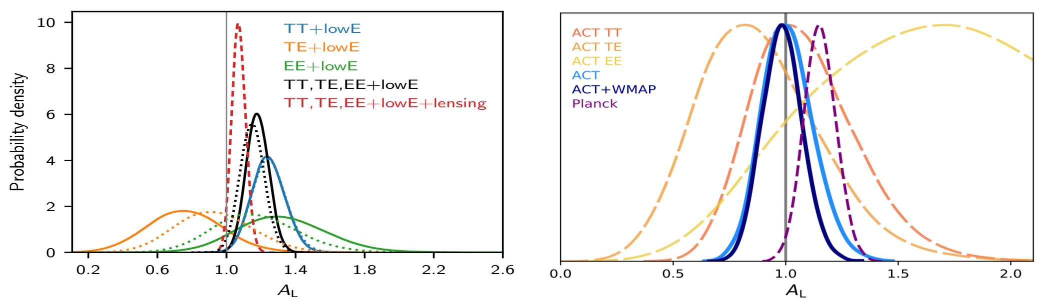

Fig. 3. Constraints on the value of the consistency parameter A_L. **Left:** Results using various combinations of Planck data. When only power spectrum data are used, $A_L > 1$ is favoured at about 3σ. The dotted lines show equivalent results for the CamSpec likelihood. *Extracted from* Planck Collaboration VI (2020). **Right:** Results as measured by ACT, by the individual TT, TE and EE spectra from ACT, and ACT combined with WMAP. The Planck measurement is shown for comparison. *Extracted from* Aiola et al. (2020).

*available at `http://pla.esac.esa.int`

3 The Hubble constant H_0

With the reduction of the uncertainties on the estimation of the Hubble constant, a notable discrepancy arises between the local measurements at the very lowest redshifts and the indirect measurements from the early Universe. There have been, and remain still, many studies around this significant tension which can reach up to 5σ.

Figure 4 shows a compilation of the results (in the left panel) as well as a summary of the tension between early Universe and local distance measurements (in the right panel). So called "early Universe" measurements do include CMB but also the Baryon Acoustic Oscillations (BAO) in combination with primordial element abundances whereas "local measurements" refer to distances of Type IA supernovae using different calibrations such as the Cepheid (Riess et al. 2021) or the Tip of the Red Giant Branch (Freedman et al. 2020).

As discussed in Linder (2021), it is difficult for early measurements to result in a large value of H_0. Indeed, CMB data tightly constrain H_0 within ΛCDM models. Combining CMB with another cosmic probe, such as Baryon Acoustic Oscillation (BAO) or Type Ia Supernovae (SNIa), breaks the degeneracy for models where the dark energy equation of state differs from -1 but still indicates a value of H_0 lower than 70.

On the contrary, the local measurements differ by about 2σ depending on the calibration method. The impact of the environment of the SNIa in the Cepheids is debated as a potential explanation for such variations as well as potential extinction by extra-galactic dust Mortsell et al. (2021).

New independent measurements from strong lensing time delays seem to show a transition between low and high H_0 values (Millon et al. 2020; Liao et al. 2020) but currently the sample is still small and the results may depend on the lensing object more than reported.

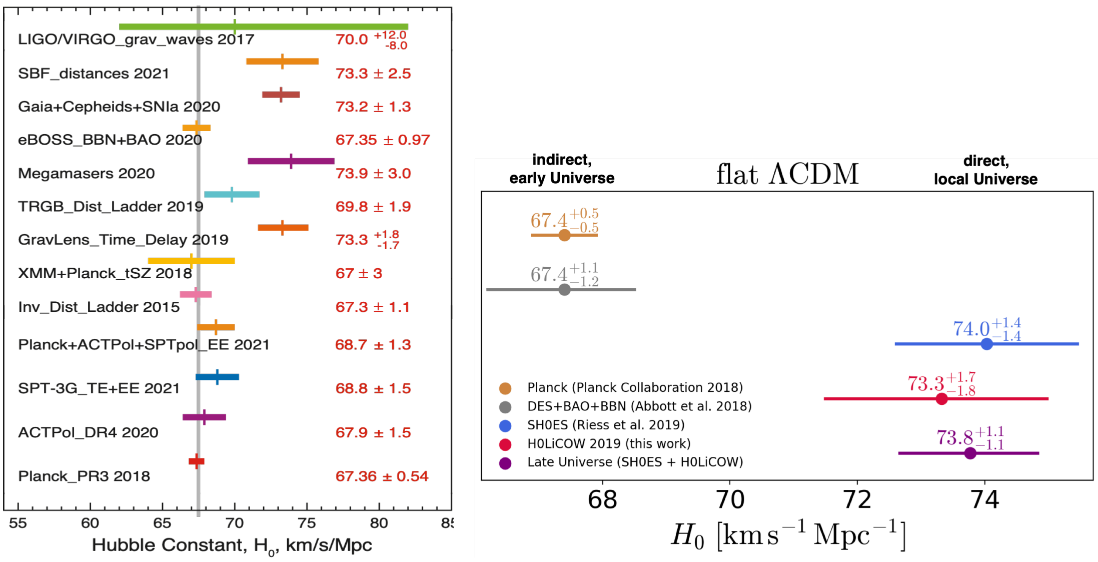

Fig. 4. Left: Hubble constant results from distance ladder determinations (labeled HST Key Project, Cepheids+SNIa, Distance Ladder, TRGB Dist Ladder), indirect CMB measurements (WMAP9, Planck PR3, both of which combine CMB with other data), BAO in combination with baryon abundance (BAO+D/H), the thermal SZ effect (CHANDRA+tSZ, XMM+Planck tSZ), strong gravitational lensing (Gravlens Time Delay) and gravitational waves (LIGO/Virgo grav waves). *Extracted from* LAMBDA (`https://lambda.gsfc.nasa.gov`). **Right:** Comparison of H_0 constraints for early- and late-Universe probes in a flat ΛCDM cosmology. The early-Universe probes shown here are from Planck (orange; Planck Collaboration VI 2020) and a combination of clustering and weak lensing data, BAO, and big bang nucleosynthesis (grey; Abbott et al. 2018). The late-Universe probes shown are the latest results from SH0ES (Riess et al. 2019, blue;) and H0LiCOW (red; Wong et al. 2019). When combining the late-Universe probes (purple), we find a 5.3σ tension with Planck. *Extracted from* Wong et al. (2019).

4 The amplitude of fluctuations σ_8

From both galaxy cluster counts as well as weak lensing from distant galaxies through large scale structure (also called "cosmic shear"), one can constrain the amplitude of fluctuations σ_8 (or equivalently $S_8 = \sigma_8(\Omega_m/0.3)^{0.5}$) and compare to the prediction from the ΛCDM model fitted on CMB data.

In Planck 2015, using cluster counts, Planck Collaboration XXIV (2016) reported a value of σ_8 between 2 and 3σ lower than the primary CMB results depending on the mass bias prior. Salvati et al. (2018) showed that using a more recent value of the reionization optical depth τ (Planck Collaboration Int. XLVII 2016), tension was released so that CMB results and combined tSZ results on σ_8 agree within 1.3σ (see left panel of Fig. 5). This was then confirmed with the 2018 Planck data (Planck Collaboration VI 2020) in which the subset of clusters used as a sample for cosmological constraints has been significantly increased (from 439 in 2015 to more than 1000 in 2018).

Cosmic shear measurements available from several collaborations originally found a modest tension with the Planck ΛCDM cosmology, preferring lower values of Ω_m and σ_8. However, the last release of the Dark Energy Survey (DES-Y3, DES Collaboration et al. 2021) found no significant evidence of inconsistency with Planck CMB at 0.7-1.5σ despite the significantly improved precision of both (see right panel of Fig. 5).

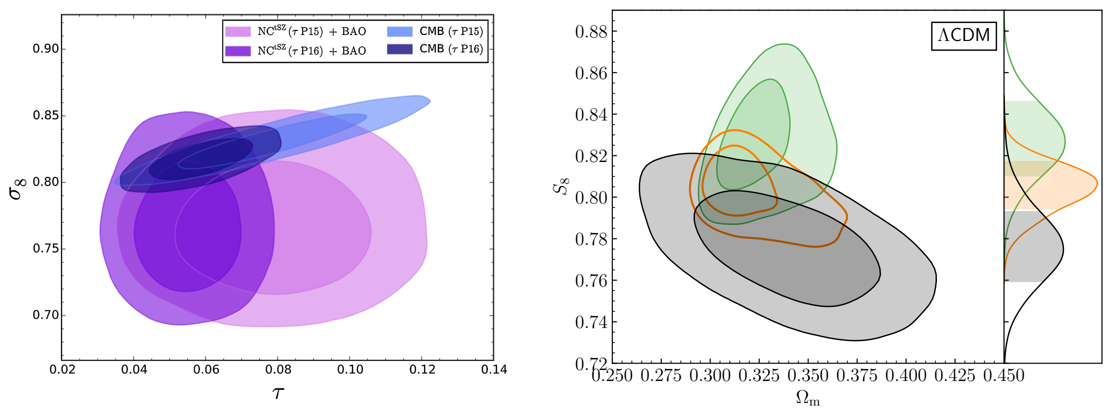

Fig. 5. Left: Two-dimensional probability distributions for τ and σ_8 for various values of optical depths. We compare results for SZ number counts alone (pink and purple) and for CMB data alone (blue and light blue). *Extracted from* Salvati et al. (2018). **Right:** A comparison of the marginalized parameter constraints in the ΛCDM model from the Dark Energy Survey with predictions from Planck CMB data (no lensing; green). We show the fiducial 3x2pt (solid black) and the combined Y3 3x2pt and Planck (orange) results. *Extracted from* DES Collaboration et al. (2021).

5 Conclusions

We have shown here that constraints from CMB data (essentially Planck) are robust and stable: with time (from WMAP to the last release of Planck); for the various spectra (the anisotropies TT, TE, EE and the lensing $\phi\phi$); with respect to extensions to the simple ΛCDM model, when adding extra parameters one at a time. There are many measurements that are consistent with the predictions of the ΛCDM model fitted to Planck data. The remaining areas of discordance have been discussed in this paper.

Internal consistency (amplitude of lensing A_L) As we have seen, the value of A_L is sensitive to choices made in the Planck CMB likelihoods and the tension is significantly reduced with the latest Planck release (PR4). Ground-based measurements are fully compatible with ΛCDM predictions. There is no evidence for new physics or statistical fluctuations. However, if the remaining impact of $A_L \neq 1$ on ΛCDM parameters is negligible, it can play a role in allowing model extensions as for example the reionization history, the curvature (Ω_k), or the sum of the neutrino masses ($\sum m_\nu$).

Expansion rate (Hubble constant H_0) CMB data gives tight constraints on the Hubble constant in the context of the ΛCDM. The constraints are also compatible for dark energy models when combined with BAO data. In both cases, it is very hard for "early Universe" data to result in a value of H_0 higher than 70, even in the case of model extensions (such as non-flat Universe, or when fitting neutrino masses). In order for the CMB data to match $H_0 > 70$, one needs to rely on very exotic models such as non-standard thermal history or radiation, existence of early dark energy (e.g. Poulin et al. 2019), or non-standard neutrino interactions (e.g. Kreisch et al. 2020). Local measurements show large variations depending on the first distance ladder which suggest there is still some physics to be understood in order to reach precision at the percent level on H_0. Independent measurements coming from time delay with strong lensing might help to further understand the current situation but the sample is still small. Measurements from gravitational waves are also interesting to consider but the need for a detected electromagnetic counterpart in order to estimate the redshift makes it difficult to increase the number of samples.

Amplitude of matter fluctuations (σ_8 or S_8) The estimation of the fluctuation amplitude σ_8 with CMB data shows a large degeneracy with the dark energy sector. However, even in the case of models with free dark energy equation of state (wCDM), the last release of DES data (DES Collaboration et al. 2021) finds all three independent data set combinations (DES 3x2pt; BAO, RSD, and SNe Ia; and Planck CMB) to be mutually consistent within ΛCDM. Tension with the estimation from cluster counts was also released after updating the value of the reionization optical depth τ while increasing the sample of clusters used for cosmology.

Given the uncertainties on cosmological parameters (at the percent level for most of them), error bars on the observational data need to be very accurate and to include systematic effects. Systematics arise from the instrument but can also be of astrophysical origin (such as the Galactic emissions for the CMB). In order to propagate correctly the systematics up to the cosmological parameters, one need reliable Monte-Carlo simulations. From those, one can extract the remaining bias from residual systematic effects (if there is one) but also estimate the increase of the uncertainties, including the correlation between the different effects involved. For Planck data, a huge effort has been made in the last release (PR4, Planck Collaboration Int. LVII 2020) to provide Monte-Carlo simulations associated to the released data and including all relevant systematic effects of Planck. However, CMB simulations make use of fixed template for foregrounds as we still miss a realistic stochastic description of the foregrounds.

References

Abbott, T. M. C., Abdalla, F. B., Annis, J., et al. 2018, MNRAS, 480, 3879
Aiola, S., Calabrese, E., Maurin, L., et al. 2020, J. Cosmology Astropart. Phys., 2020, 047
Calabrese, E., Slosar, A., Melchiorri, A., Smoot, G. F., & Zahn, O. 2008, Phys. Rev. D, 77, 123531
Couchot, F., Henrot-Versillé, S., Perdereau, O., et al. 2017, A&A, 597, A126
DES Collaboration, Abbott, T. M. C., Aguena, M., et al. 2021, arXiv e-prints, arXiv:2105.13549
Dutcher, D., Balkenhol, L., Ade, P. A. R., et al. 2021, Phys. Rev. D, 104, 022003
Freedman, W. L., Madore, B. F., Hoyt, T., et al. 2020, The Astrophysical Journal, 891, 57
Kreisch, C. D., Cyr-Racine, F.-Y., & Doré, O. 2020, Phys. Rev. D, 101, 123505
Liao, K., Shafieloo, A., Keeley, R. E., & Linder, E. V. 2020, The Astrophysical Journal, 895, L29
Linder, E. V. 2021, arXiv e-prints, arXiv:2105.02903
Millon, M., Galan, A., Courbin, F., et al. 2020, Astronomy & Astrophysics, 639, A101
Mortsell, E., Goobar, A., Johansson, J., & Dhawan, S. 2021, arXiv e-prints, arXiv:2105.11461
Planck Collaboration I. 2020, A&A, 641, A1
Planck Collaboration Int. LVII. 2020, A&A, 643, A42
Planck Collaboration Int. XLVII. 2016, A&A, 596, A108
Planck Collaboration V. 2020, A&A, 641, A5
Planck Collaboration VI. 2020, A&A, 641, A6
Planck Collaboration XXIV. 2016, A&A, 594, A24
Poulin, V., Smith, T. L., Karwal, T., & Kamionkowski, M. 2019, Phys. Rev. Lett., 122, 221301
Riess, A. G., Casertano, S., Yuan, W., et al. 2021, The Astrophysical Journal, 908, L6
Riess, A. G., Casertano, S., Yuan, W., Macri, L. M., & Scolnic, D. 2019, The Astrophysical Journal, 876, 85
Salvati, L., Douspis, M., & Aghanim, N. 2018, A&A, 614, A13
Tristram, M. et al. 2021, in prep.
Wong, K. C., Suyu, S. H., Chen, G. C.-F., et al. 2019, Monthly Notices of the Royal Astronomical Society, 498, 1420

SF2A 2021
A. Siebert, K. Baillié, E. Lagadec, N. Lagarde, J. Malzac, J.-B. Marquette, M. N'Diaye, J. Richard, O. Venot (eds)

WELL-BEING IN FRENCH ASTROPHYSICS

N. A. Webb[1], C. Bot[2], S. Charpinet[1], T. Contini[1], L. Jouve[1], F. Koliopanos[1], A. Lamberts[3], H. Meheut[3], S. Mei[4], I. Ristorcelli[1] and G. Soucail[1]

Abstract. It has become clear that early career astrophysics researchers (doctoral researchers, post-docs, etc) have a very diverse appreciation of their career, with some declaring it the best job that you can have and others suffering from overwork, harrassment and stress from the precarity of their job, and associated difficulties. In order to establish how astrophysics researchers, primarily in France, experience their career, we sent out a survey to understand the impact that their job has on their well-being. 276 people responded to the survey. Whilst around half of the respondents expressed pleasure derived from their career, it is clear that many (early career) researchers are suffering due to overwork, with more than a quarter saying that they work in excess of 50 hours per week and 2% in excess of 90 h per week. Almost 30% professed to having suffered harrassment or discrimination in the course of their work. Further, whilst only 20% had suffered mental health issues before starting their career in astrophysics, ∼45% said that they suffered with mental health problems since starting in astrophysics. Here we provide results from the survey as well as possible avenues to explore and a list of recommendations to improve (early) careers in astrophysics.

Keywords: careers, well-being

1 Introduction

Astrophysics is an exciting subject that attracts many young people, as there are many rewards to be had in research in this field, such as enjoying intellectual challenges, interacting with knowledgeable and fascinating colleagues, the possibility to be creative and discover new things and travelling, to name but a few. However, in recent years a general feeling of discouragement has been observed in a significant fraction of doctoral researchers and post-docs (e.g. Woolston 2019; Auerbach et al. 2018). In some, the feelings are tending towards distress, which can lead to terrible consequences.

To understand the situation in France, we put in place an anonymous survey using the platform *Framaforms*. The survey was open from 29th March - 3rd May 2021 and the questions were provided in English and French. It was announced via the French national astronomy and astrophysics society (SF2A) newsletter, in French astrophysics laboratories, as well as a couple of Swiss/Canadian institutes and some French nuclear and particle physics institutes with groups working on astrophysics. The questionnaire covered five main areas, namely general questions about work, such as favourite aspects of astrophysics research, the number of hours worked, perceived external constraints and future plans for remaining in the field. We also asked about relationships with colleagues, notably any issues concerning harassment or discrimination. We questioned about mental health issues, both before and since working in astrophysics. We requested suggestions for improvements that could be made as well as positive feedback and finally we inquired about some demographics, such as the respondents age, position, country where they are working, nationality and gender. None of the questions were obligatory. The results and a discussion are presented in the following sections, taking into account the small number statistics and eventual bias. Our aim was to identify reasons for any suffering, identify improvements that can be made, propose solutions to laboratories, doctoral schools and gouverning bodies and ultimately improve the PhD, post-doc and career experience.

[1] IRAP, Université de Toulouse, CNRS, CNES, Toulouse, France
[2] CDS, Université de Strasbourg, CNRS, Observatoire astronomique de Strasbourg, UMR 7550, 67000 Strasbourg, France
[3] Université Côte d'Azur, Observatoire de la Côte d'Azur, CNRS, Laboratoire Lagrange, Laboratoire Artémis, France
[4] Université de Paris, CNRS, Astroparticule et Cosmologie, F-75013 Paris, France

2 Results from the survey

276 people responded to the survey, but as none of the questions were obligatory, not everyone responded to each question. 57.8% of respondents identified as male, 40.6% as female and 1.6% identified as other. The survey was open to anyone from planetary science/astrophysics or connecting areas, but targeted doctoral researchers and post-docs. As a result, the majority of the respondents were doctoral researchers (108 respondents) and post-docs (99 respondents). 9 respondents were undergraduates and 62 in a permanent position (27 with (teaching) duties and 35 with no formal duties). The large majority of respondents (232) worked in France, with only 46 working outside of the France. Two thirds (190 people) were French and one third (86 people) were of a different nationality.

When asked about what was the best aspect of the job, almost all respondents replied that they enjoyed the intellectual challenge (243 people), discovering new things (209), the independence they had in their work (192) and interacting with colleagues (188). About half of the respondents enjoyed the creativity of their work (147 respondents), travelling (119) and sharing their discoveries (114 people). Less people cited the University/academic environment as their preferred aspect of their job (97 people), 54 appreciated the fact that their acquired skills will be useful for a future position, 39 cited the social life and just 6 evoked their salary as one of their favourite things. Other things that were occasionally cited were the prestige of the position, the international environment and supervising students.

Figure 1 shows the number of hours worked per week estimated by the respondents. In France, the working week is 35 hours and doctoral researchers sign a contract stipulating this volume. 44% of respondents felt external pressure to work outside legal hours, whilst 49% did not feel that pressure (7% did not know whether they felt external pressure). 55% felt that they should work outside of legal hours (37% that they shouldn't and 8% did not know). The reasons cited as to why long hours were worked were to be competitive/obtain a permanent position, because they enjoyed working more hours, because they can't achieve the work required without working longer hours, they are unable to *switch off*, they felt that more work is expected from post-doc/PhDs than permanent staff and some felt that as others work outside legal hours, so should they.

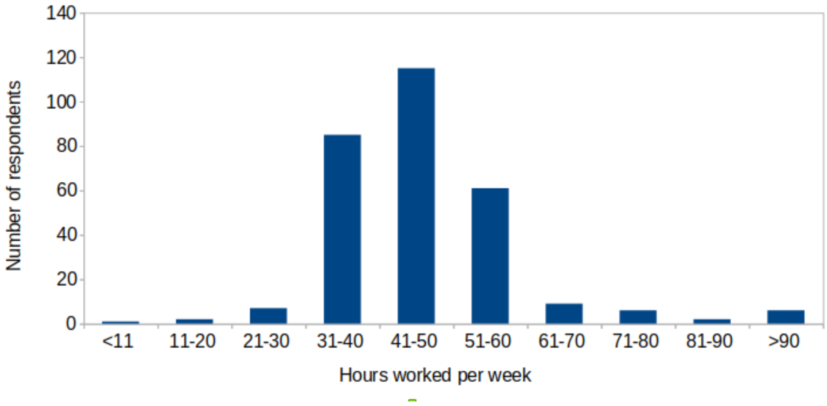

Fig. 1. The number of hours worked per week by the respondents.

With regards to job satisfaction, more than half agreed with the statement *Research is the best job that you can have* and almost three quarters felt that *their work gave them a sense of purpose* and just over a half agreed that *they looked forward to going to work every day.* 61% felt *well integrated in their institute.*

With regards to work-life balance, 62% said that they got sufficient sleep most nights. 35% felt that their life was balanced with respect to work, outside activities and sleep. 55% were satisfied with their living conditions and 48% were satisfied with their financial situation. 54% felt that the environment in which they work inspires them, 61% agreed that senior colleagues are there for them when needed and 48% agreed that they handle setbacks and disappointments in their work well. Just 36% agreed that they were satisfied with their career progression. 64% planned to stay in academia, with 11% planning to leave and 25% unsure. However, when asked if they would stay in academia if they were guaranteed a permanent position, 81% said they would stay, 5% said that they would leave and 14% were unsure. Difficulties cited were precarity (most highly cited), the geographical instability due short term contracts, the pressure felt to publish both frequently and high impact papers, feeling undervalued, the general disregard for well-being in the domain, supervisors with (very) poor management skills, difficulties in competing with child-free colleagues, a perception that people in positions of power may misuse their privilege, a lack of information provided for non-academic areas of research (how to access resources, etc) and the large amount of bureaucracy, especially when entering a new institute.

With regards to people's living situations, 13 people said that they had taken on a second job to supplement their salary and 30 people were struggling with debt. 23 post-docs had children or family members to care for, while 6 doctoral researchers had family members to care for. 20 doctoral researchers and 35 postdocs were living apart from their partners and/or children. 10 permanent staff were also living apart from their partners and/or children. 30% of the women were living apart from their partners and/or children but only 18% of men.

29% of the people responding to the survey had experienced harassment or discrimination since working in the domain. A further 4% were unsure whether they had experienced harassment or discrimination. Only 26% of those that had experienced harassment or discrimination reported the incident(s). Reasons why the incidents were not reported were because the respondents were embarrassed by the situation (20%), they didn't feel that someone would listen (37%), they felt that other people have worse problems (25%), they didn't know where to go for help (16%) or due to a language barrier (2%). The types of harassment or discrimination encountered are shown in Figure 2. Respondents who chose *other* cited discrimination based on nationality, discrimination based on hierarchy, discrimination due to having kids (or not), language discrimination and discrimination due to research subject. Whilst the data is incomplete for the gender of respondents having experienced gender discrimination, 32 were female, 2 male and 0 other.

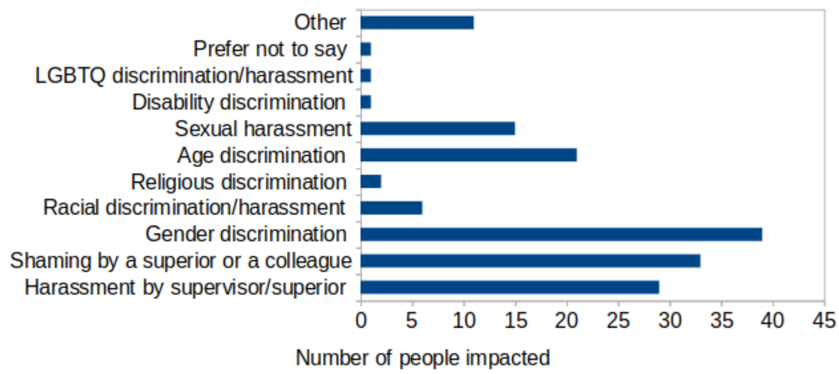

Fig. 2. The nature of the different types of harassment/discrimination encountered by respondents and the number of people experiencing the different types of incidents. Respondents who chose *other* cited discrimination based on nationality, hierarchy, due to having kids (or not), language discrimination and discrimination due to research subject.

We asked how often people felt overwhelmed by their situation at work over the course of the last year. 10% felt overwhelmed all of the time and 34% had often felt overwhelmed. Just 6% had not felt overwhelmed at all over the last year. Of those that felt overwhelmed all of the time, none of them were permanent staff. 43% of all respondents agreed that they were happy with their health and well-being.

Concerning mental health, 20% of respondents stated that they suffered from depression or other mental health problems before starting in research, however since starting their career, 44% of respondents suffer from depression or other mental health problems. The types of health issues suffered by the respondents both before starting research in astrophysics and since starting are given in Figure 3 . 41% have sought help for these issues. The other 59% have not sought help because they were embarrassed by the situation (15%), they didn't feel that someone would listen (13%), they felt that other people have worse problems (51%), they didn't know where to go for help (12%) or due to a language barrier (not speaking the local language, 9%). The problems experienced since starting astrophysics have caused some of the respondents to turn to alcohol abuse (23 people), drug abuse (8 people), other substance abuse (2 people), disordered eating (32 people), self-harm (9 people) and one suicide attempt in an aim to deal with their problems.

We also questioned about possible solutions. 81% of respondents agreed that PhD and post-doc supervisors should get training in supervision and 73% agreed that academic staff in general should get training in mental health issues, while 76% felt that more discussion of well-being should take place. Other suggestions from respondents included, longer temporary contracts (> 3 years), mentoring or general help to construct a future either in or out of research, improving relations between permanent and temporary staff, improving communication by having more open discussion on working hours, racism, sexism, etc, providing a realistic outlook about

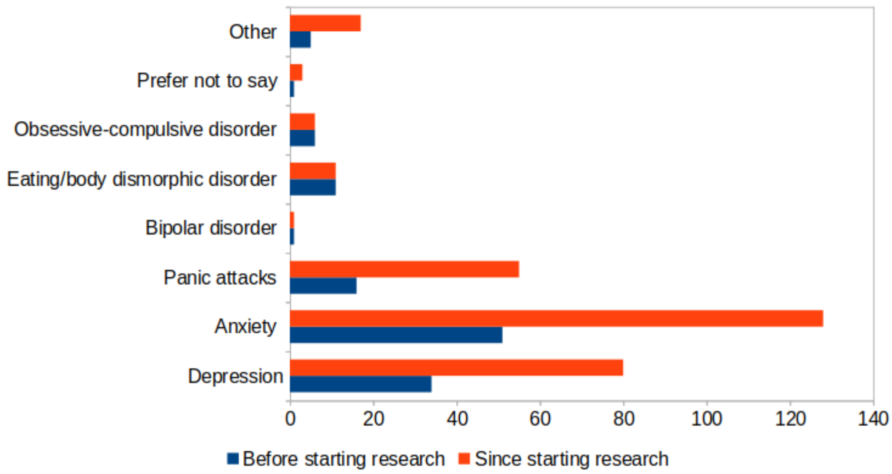

Fig. 3. The nature of the different mental health issues suffered by respondents and the number of people experiencing them, before starting in astrophysics research (blue) and since starting in the domain (red). Respondents who chose *other* cited post-traumatic stress syndrome, burnout, gender dysphoria, sleep disorder and imposter syndrome.

research jobs etc before the PhD, improving the welcome and provision of information for new hires, providing information on how to access psychological support (in English), improving transparency in decisions made and minimising (or helping with) administrative tasks.

Finally, we also asked about the most positive experiences in astrophysics research. These were plentiful and included: publishing work, international connections, international recognition, launching satellites/instruments, making new discoveries, attending international conferences, working abroad, getting a PhD, doing outreach, teaching, collaborating, interdisciplinary work, meeting people, learning, supervising, receiving constructive feedback, having scientific discussions, observing, changing domains, having great ideas, having proposals accepted, promotions, press releases and sharing success and contributing to big projects.

3 Discussion

Whilst the majority of respondents were male, the percentage of female respondents (see Section 2) was far in excess of the number of female astrophysicists in France (∼25%). This is a well known phenomenon, where more women than men respond to online surveys e.g. Cull et al. (2005). Women may also feel more concerned by the topics discussed, enhancing the percentage of respondents, as more women than men have suffered from gender discrimination (see Section 2) and more of the women stated that they suffered from depression and/or mental health issues (54% of the women that responded) compared to 34% of men that responded, similar to numbers found by Evans et al. (2018). 100% of those who replied to the gender question as 'other' also stated that they suffered from depression and/or mental health issues.

68% of respondents worked significantly in excess of the legal number of hours per week prescribed in France, primarily due to external pressure. These were almost all non-permanent staff, the same group that felt that they were either often or constantly overwhelmed. The proportion of men and women working more than the number of legal hours was similar. It is clear that working in excess of 90 hours per week leaves no time for any other activity during the week outside of work, sleeping and eating, which is clearly unhealthy. However, only a third of those working long hours were the same people that felt that they did not get enough sleep, indicating that it was often not long working hours that reduced sleep. Stress could be a factor preventing people from sleeping. The pressure felt to publish and/or be competitive/obtain a permanent position were frequently cited in the reasons for working long hours. The figures indicate that temporary staff are working longer hours than permanent staff, putting them more at risk of poor (mental) health.

One of the major sources of stress is the precarity in astrophysics research, as seen from the number of people that plan to leave academia, but would stay, if they could be guaranteed a job. Precarity was also the most highly cited difficulty encountered in astrophysics, along with related issues such as geographical instability. However, a fifth of respondents would not definitely stay in academia even if they were guaranteed a permanent job. Of those that are definitely planning to leave, one third had experienced harassment or discrimination in astrophysics or had experienced mental health issues since starting, which could explain part of their motivation. A further third is due to precarity issues, leaving a final third who are leaving for other reasons.

The number of people suffering with mental health issues since starting their career in astrophysics has more than doubled compared to prior to starting their career. This is a startling rise, but numbers recorded are commensurate with the study of graduate students in biosciences at the University of Berkeley (Evans et al. 2018) only slightly higher than in other studies e.g. Woolston (2019) who polled >6000 doctoral researchers from all subjects in various countries around the world or the study by Auerbach et al. (2018) carried out by the *World Health Organisation* that revealed that 31% of students showed signs of major depression, general anxiety disorder or panic disorder etc, in the previous 12 months. It is clear that there is a major problem, not just in France, but all over the world and this needs to be resolved to restore people's mental health and well-being. The problem needs to be tackled at the source and many of the suggestions proposed or agreed on by the respondents could go someway to help, namely training PhD and post-doc supervisors in supervision and training academic staff in mental health issues, along with more open discussion on well-being, working hours, racism, sexism, sexual harrassment, bullying, etc. Lengthening temporary contracts and providing mentoring or general help to construct a future either in or out of research could also help (see Section 4).

Finally, this survey was planned for release on March 30th 2020, but was delayed for a year because of the outbreak of the COVID-19 pandemic. It is clear that the unprecedented situation over the year before releasing the survey has added stress to everyone's lives and thus had an impact on well-being and mental health. It is difficult to fully decorrelate the impact of the COVID-19 pandemic on the long-term well-being. However, has evident from other publications (e.g. Woolston 2019; Auerbach et al. 2018) and our own observations, suffering in (early career) research has been prevalent for many years before the COVID-19 pandemic outbreak and the pandemic appears to have simply exacerbated existing problems.

4 Recommendations

Following the survey and numerous discussions amongst the authors of this paper, a dedicated workshop on the issue at the 2021 French National Astronomy meeting, along with further discussions with other groups which aim to improve well-being in astrophysics, we have drawn up a list of recommendations for institutes, masters programmes/doctoral schools and gouverning bodies. Some of the points may seem minor, but implementing the recommendations would go a long way to helping people feel included, accepted and happy in their job. We are aware that some of these recommendations have been put into place in some institutes, or some specific areas, but applying them across the board could help significantly to improve the day to day life of our colleagues.

During our discussions, it became clear that there is a lot of help and information already available, but it is often dispersed, making access complicated. We propose a single, highly visible webpage (e.g. as a part of the SF2A webpages) which regroups all of the relevant information (well-being, support for harassment, mental health support, etc) so colleagues and organisations know where to locate it. In addition, a working group is being put into place to help maintain the webpage and help implement current and future recommendations.

4.1 Recommendations at the institute level

A common source of stress for younger colleagues on short term contracts is that they are frequently required to move institutes, often in different countries where they don't necessarily speak the local language, and this requires a lot of administrative activities with many papers to fill out, often available in the local language only. This makes a short and simple job, long and complicated. Providing paperwork in English would facilitate this aspect. Further, a lot of new recruits find that no provision for an office space, a computer or other basics have been organised at their arrival. Putting these things into place in advance and introducing the new arrivals to key people immediately, can make new arrivals feel welcome and appreciated. Further, providing information booklets (with information on opening a bank account, finding an appartment, organisation within the institute, how to access the intranet, mailing lists, etc) along with introductory meetings (introducing key people, key structures, etc) will also help their integration. Up to date information on the local website (in English) and mailing lists (with specific mailing lists for students and post-docs) would also facilitate integration. More (non-)scientific events should be organised to facilitate colleagues meeting and creating a team spirit. This would also help bridge the perceived gap between permanent and temporary staff. Institute messages should ideally be written in the local language as well as English to be inclusive, as part of an effort to reinforce inclusivity.

Many (international) mentor programmes exist, but institutes should also provide a mentoring programme to be able to provide local information (recruitment possibilities in the area, specificities for applying for local jobs, applying for funding etc). Whilst finding mentors in an institute with a broad knowledge of working in astrophysics within France and abroad as well as working in industry, for example, will be difficult to find, having a pool of mentors identified (and their expertise) would mean that colleagues will know who to consult about which issue. Regular or occasional mentoring should be provided. Open discussion of common problems encountered (e.g. imposter syndrome, well-being, hours worked, racism, sexism, etc) are recommended. This could be through a weekly or bimonthly coffee or dedicated seminars, for example.

Not all students and post-docs will stay in academia. More information should be provided to younger colleagues on moving to other domains and to remove the perceived stigma that leaving academia is shameful. Institutes should aim to keep contact with previous researchers that have moved into industry. They could be invited once a year, perhaps during the PhD day, to provide information on finding jobs outside of academia.

4.2 Recommendations for masters programmes and doctoral schools

Several respondents to the survey felt that they did not have a clear picture about their chances of getting a permanent job in astrophysics before deciding to start a PhD and as a result felt that they wouldn't have chosen such a career path if they had had a proper understanding of the requirements. Masters programme should therefore provide information to all students spelling out the difficulties, to allow students to take an informed decision, however, labouring the point can be a source of stress to others. Doctoral schools should also try to form alumni associations, if one does not already exist at that particular University, so that current students can contact previous students to get feedback and tips on staying in research or moving into industry. More talks/information should also be provided about bad practice (supervisors requiring replies to emails late at night or at the weekend, long working hours, etc). In general, we recommend that the training during Masters and PhD programmes should take into account the fact that the majority of the students will not work in academia over the long term.

4.3 Recommendations for gouverning bodies

To avoid the stress of frequently changing jobs, and losing friends, support networks, etc, post-doc positions could be increased in length (ideally beyond three years). Where possible, post-doc salaries should be harmonised and provide for an evolution of the salary over the time the post-doc is employed. This could be done for example through salary recommendations when applying for national funding, if it is not yet implemented.

Everyone working in astrophysics should be trained in well-being, harassment, discrimination etc. This will enable them to be aware of problems and be familiar with the language associated with these issues. This training should be obligatory and done using online courses with tests, which need to be passed every few years. A proto-type demonstrator is currently being drawn up, to provide a basis for a nationally deployed platform. Every institute should have a clearly identified person that is properly trained to deal with harassment. This person should not be the direct superior of anyone within the institute to avoid a conflict of interest.

5 Conclusions

Through this short paper, we aimed to share results from our survey and provide some discussion and recommendations that could help improve the day to day lives of colleagues. By being aware of the problems and implementing solutions, we can all help to improve our colleagues lives and make our environment a better place to work in and above all preserve the (mental) health of all.

We thank the people that answered the survey, those who will take on board what has been said and those that will help improve research careers in the future. We are grateful to Benoît Mosser for insightful discussion and helpful comments on this paper. We acknowledge *Framaforms, Topcat* and *Excel* in the production of this work. We remember our colleagues that departed too soon, your memory will help us strive towards a better tomorrow.

References

Auerbach, R. P., Mortier, P., Bruffaerts, R., et al. 2018, Journal of Abnormal Psychology, 127, 623

Cull, W., O'Connor, K., Sharp, S., & Tang, S. 2005, Health Services Research, 40, 213

Evans, T., Bira, L., Beltran Gastelum, J., Weiss, L. T., & Vanderford, N. L. 2018, Nature Biotechnology, 36, 282

Woolston, C. 2019, Nature, 575, 403

Session 1

Atelier général du PNP

EVIDENCE FOR SCALLOPED TERRAINS ON 67P

A.Bouquety[1], O. Groussin[1], L. Jorda[1], A. Séjourné[2], F. Costard[2] and S. Bouley[2]

Abstract. The Rosetta mission of the European Space Agency (ESA) provided detailed data of the surface of the nucleus of comet 67P/Churyumov-Gerasimenko (hereafter 67P). In a previous study we performed a comparative morphometrical analysis on two depressions in the Ash region. The results indicated that these depressions are either shaped by the sublimation and/or by landslides. We continued the analysis on this kind of depression at the cometary scale. We analysed 131 depressions on 67P, exclusively located on the fine particle deposit (FPD) unit, and compared them with thaw depressions on Earth and Mars. The studied depressions have the same morphometrical characteristics than their planetary counterpart. They have the same area/perimeter evolution and present the same slope asymmetry that is characteristics of obliquity driven insolation. This study allowed to highlight that the depressions on 67P are analogs with thaw depressions on Earth and Mars. Moreover, we proved that the FPD is thicker (4.7 m) than predicted in models. The FPD layer is similar to an icy-rich planetary permafrost, in a cometray periglacial system where cometary thaw depressions are shaped by sublimation.

Keywords: 67P, Morphometry, Scalloped terrain, Comparison

1 Introduction

The Rosetta mission provided detailed data of the surface of the nucleus of comet 67P/Churyumov-Gerasimenko. The analysis of these data, and especially the images of the Narrow Angle Camera (NAC) from the Optical Spectroscopic and Infrared Remote Imaging System (OSIRIS instrument; (Keller et al. 2007)), revealed the morphological diversity of the nucleus surface (El-Maarry et al. 2019). Among these morphologies, depressions have been observed in several regions (Fig.1, left panel).

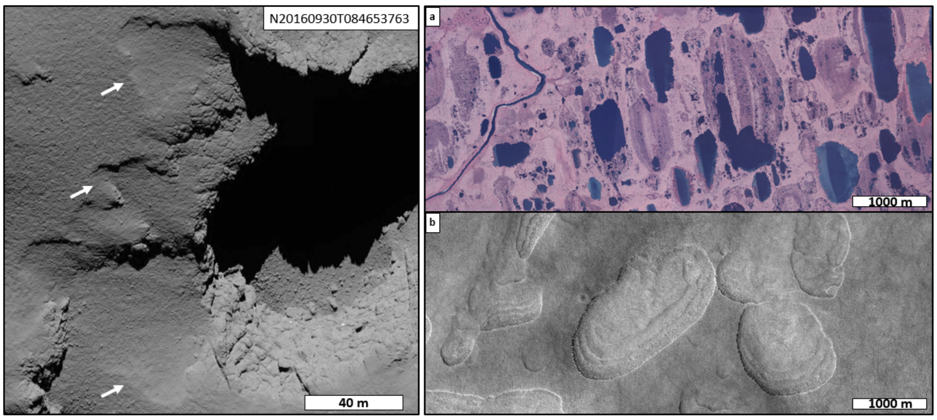

Fig. 1. Left: Example of studied depression located on Ma'at region (NAC image, 1 m/pixel). The white arrows indicate the depressions. **Right:** Example of thaw depressions. (a) Thermokarstic lakes in Alaska on Earth (Digital Orthophoto Quadrangle DOQ, 5 m/pixel). (b) Scalloped terrain in Utopia planitia on Mars (HiRISE image, 50 cm/pixel).

[1] Aix Marseille Univ, CNRS, CNES, LAM, Marseille, France
[2] GEOPS, Univ. Paris-Sud, CNRS, Université Paris-Saclay, Rue du Belvédère, Bât. 504-509, 91405 Orsay, France

The origin of these structures remains unclear and several hypotheses have been proposed: (1) the depressions could be indicative of scarp retreat (Vincent et al. 2016; El-Maarry et al. 2017), (2) they mark the location of future cliff collapses (Pajola et al. 2016), and (3) they are seasonal structures shaped by the changes induced by perihelion approach (Groussin et al. 2015). In a previous study, we studied two of these depressions, located in the Ash region, by a comparative morphometrical analysis (Bouquety et al. 2021). We observed that the two depressions grew by several meters during the last perihelion passage, and that this growth is not necessarily linked with cliff collapses. Thus, in that case, the sublimation of ices certainly played a key role in shaping these depressions. On Earth and Mars, there are similar depressions with the same shape and geometry that are controlled by thaw processes. These depressions are called thermokarstic lakes on Earth and scallops depressions on Mars (Fig.1, right panel).

On both planets, these periglacial structures result from the degradation of an ice rich permafrost (Costard & Kargel 1995; Morgenstern et al. 2007; Séjourné et al. 2011). Due to their processes and morphological similarities, we decided to compare the depressions observed on 67P's surface with thermokarstic lakes on Earth and scallops depressions on Mars to constrain their origin.

2 Data and method

We used the same method as in Bouquety et al. (2021). This comparative morphometrical analysis (CMA) allows to study surface features via a morphological and geometrical approach, with a great level of detail, in order to build an interplanetary database which can be used for comparison. All our measurements were made with the ArcGIS software. In order to perform the comparison, we established, from literature, a list of parameters and criteria that can be applied on Earth, Mars and 67P. For each depression we measured 10 parameters: the length, width, area, perimeter, depth, slope (max, min, mean), elongation and the circularity index(Ulrich et al. 2010; Séjourné et al. 2011; Morgenstern et al. 2011; Niu et al. 2014). Based on different dataset and their associated DTM (Earth: DOQ/3DEP; Mars: HiRISE/HiRISE DTM; 67P: NAC/SPC method Jorda et al. (2016)), we measured a total of 432 depressions, namely 200 on Mars (Utopia planitia), 101 on Earth (Arctic coastal plain) and 131 on the whole 67P's surface. The database which was used for the comparison contains 4320 exploitable parameters values (Fig.2).

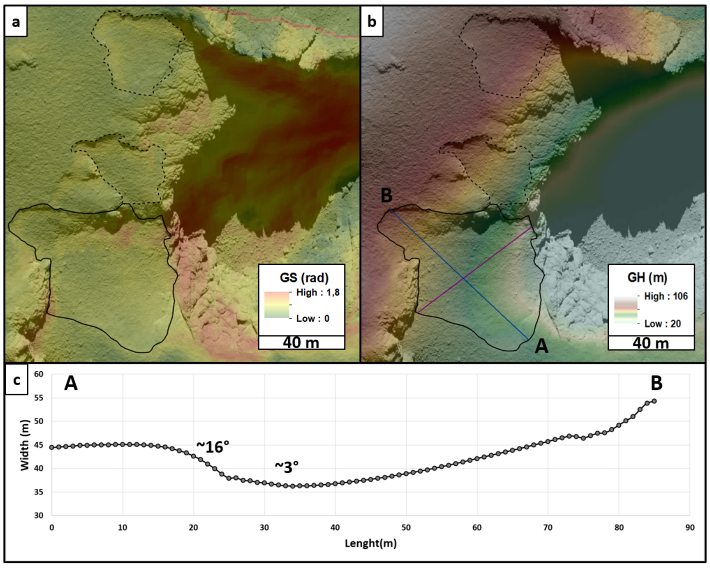

Fig. 2. Example of measurement. (a) Gravitational slopes and (b) gravitational height draped on NAC images. (c) Topographic profile extracted from gravitational height.

3 Results and interpretations

The depressions are distributed all over the comet. Among the 19 regions of the comet, 12 have at least one depression. The depression are exclusively located in terrains covered by fine deposit particules (FDP), and seems to be present in all topographical contexts (flat terrain, cliff edge).The highest depression densities are located on the body, where FPD covers the majority of the region (Thomas et al. (2018); Fig.4, left panel).

The analysis also revealed that the set of measured parameters is consitent with the references known in the litterature. Remarkably, all the measured parameters on 67P depressions are included in the range that characterized scallops terrains on Mars and thermokarstic lakes on Earth (Ulrich et al. 2010; Séjourné et al. 2011; Morgenstern et al. 2011; Niu et al. 2014). Moreover, depressions from 67P follow the same area/perimeter trend as scallops on Mars and thermokarstic lakes on Earth (Fig.3).

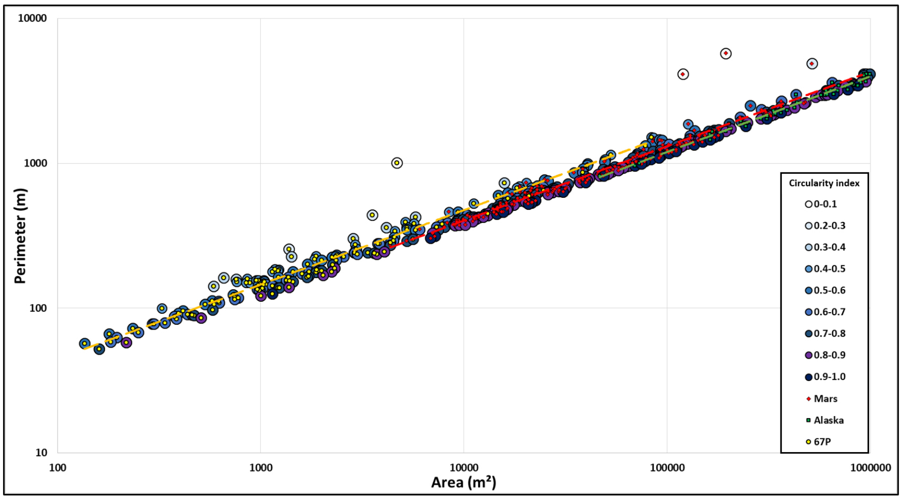

Fig. 3. Area versus perimeter for all the measured depressions on 67P, Mars and Earth. The points in shade of blue indicate the circularity index for each depression and the colored shape inside the body that the depression come from.

Finally, more than 90% of 67P depressions topographic profiles show a slope asymmetry (Fig.2c). This slope asymmetry have been observed on thermokarstic lakes on Earth and scallops on Mars and interpreted to be characteristic of depressions shaped by the obliquity-driven insolation (Morgenstern et al. 2007; Séjourné et al. 2011) These three results indicate that: (1) the depressions from 67P follow the same growth ratio than the scallops and the thermokarstic lakes while keeping their characteristic circularity, and (2) the sublimation induced by perihelion passages is the main erosion process that shaped these depressions on the comet (Bouquety et al. (2021)).

4 Discussions and conclusions

Our morphometrical analysis allowed to conclude that depressions on 67P are analogues to scalloped terrain on Mars and thermokarstic lakes on Earth. The FPD layer, on which depressions are formed, could be considered as an active layer where sublimation creates an erosion to shape the depressions. Despite the mean depth of the depressions (4.7 m), it was not possible to observe the underlying consolidated material. Thus, the depth of the depression is the minimum thickness of the FPD. We constructed a map of the minimum thickness of the FPD layer according to the region (Fig.4, right panel). This FPD layer is thicker than predicted in models (between few millimeters to 2 m; Hu et al. (2017); Oklay et al. (2017)).

This study bring evidence that the FPD could be considered as an active layer, icy rich, similar to a planetary permafrost, where sublimation occurred, and that this layer contains enough water ice to explain the surface erosion.

References

Bouquety, A., Jorda, L., Groussin, O., et al. 2021, Astronomy & Astrophysics, 649, A82

Costard, F. & Kargel, J. 1995, Icarus, 114, 93

El-Maarry, M. R., Groussin, O., Keller, H. U., et al. 2019, Space Science Reviews, 215

El-Maarry, M. R., Groussin, O., Thomas, N., et al. 2017, Science, 355, 1392

Groussin, O., Sierks, H., Barbieri, C., et al. 2015, Astronomy & Astrophysics, 583, A36

Hu, X., Shi, X., Sierks, H., et al. 2017, Monthly Notices of the Royal Astronomical Society, 469, S295
Jorda, L., Gaskell, R., Capanna, C., et al. 2016, Icarus, 277, 257
Keller, H. U., Barbieri, C., Lamy, P., et al. 2007, Space Science Reviews, 128, 433
Morgenstern, A., Grosse, G., Günther, F., Fedorova, I., & Schirrmeister, L. 2011, The Cryosphere, 5, 849
Morgenstern, A., Hauber, E., Reiss, D., et al. 2007, Journal of Geophysical Research, 112
Niu, F., Luo, J., Lin, Z., Liu, M., & Yin, G. 2014, Arctic, Antarctic, and Alpine Research, 46, 963
Oklay, N., Mottola, S., Vincent, J.-B., et al. 2017, Monthly Notices of the Royal Astronomical Society, 469, S582
Pajola, M., Oklay, N., Forgia, F. L., et al. 2016, Astronomy & Astrophysics, 592, A69
Séjourné, A., Costard, F., Gargani, J., et al. 2011, Planetary and Space Science, 59, 412
Thomas, N., Maarry, M. E., Theologou, P., et al. 2018, Planetary and Space Science, 164, 19
Ulrich, M., Morgenstern, A., Günther, F., et al. 2010, Journal of Geophysical Research, 115
Vincent, J.-B., Oklay, N., Pajola, M., et al. 2016, Astronomy & Astrophysics, 587, A14

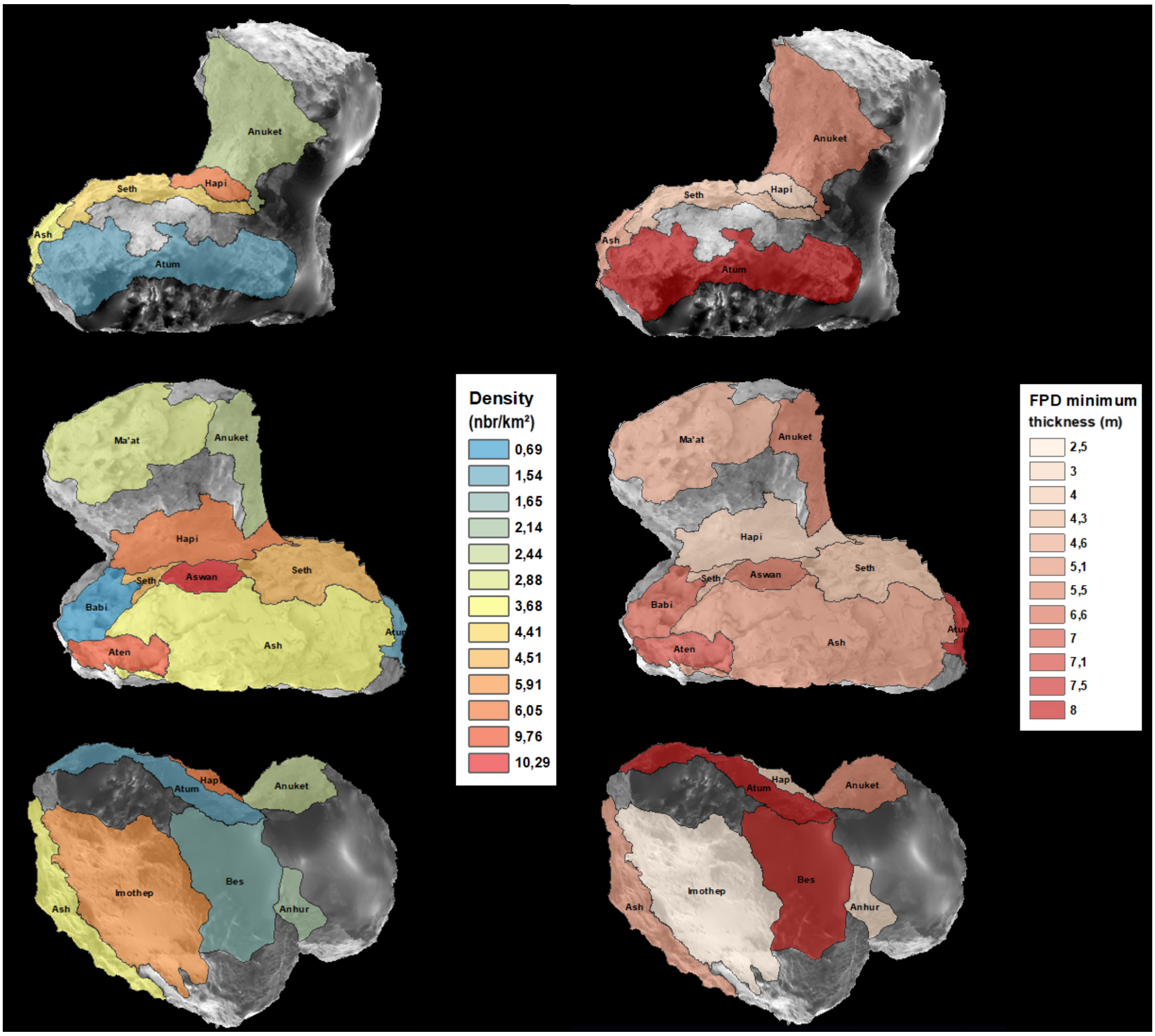

Fig. 4. Left: Density map of the measured depression according to the region. **Right:** Minimum thickness of the FPD layer calculated from the mean depth values of the depression according to the regions.

SF2A 2021
A. Siebert, K. Baillié, E. Lagadec, N. Lagarde, J. Malzac, J.-B. Marquette, M. N'Diaye, J. Richard, O. Venot (eds)

MOLECULAR HYDROGEN IN CO_2-DOMINATED ATMOSPHERES OF TERRESTRIAL EXOPLANETS : IMPACT ON THE PHOTOCHEMICAL FORMATION OF WATER

T. Drant[1], N. Carrasco[1], Z. Perrin[1], L. Vettier[1], S.-M. Tsai[2] and K. Heng[3]

Abstract. As for the rocky planets of the Solar System, the atmosphere of terrestrial exoplanets is affected by volcanic outgassing. Significant emissions of molecular hydrogen are expected in the early stage of their evolution. In the upper atmosphere, molecular hydrogen becomes photochemically active along with CO_2. Laboratory experiments conducted highlight a significant formation of water which strongly depends on the concentration of molecular hydrogen.

Keywords: atmosphere, terrestrial exoplanet, photochemistry

1 Introduction

Volcanic emissions are known to impact the composition of the atmosphere and its evolution by photochemistry. This explains the need to consider them in photochemical models as done by Hu et al. (2012) or James & Hu (2018). Recent modelling of volcanic outgassing by Liggins et al. (2020) shows that a few percent of molecular hydrogen is expected in early CO_2 or N_2 atmospheres. The exact mixing ratio of H_2 in the atmosphere depends on surface parameters : surface pressure, redox state of the mantle, volcanic flux of the planet.

The hypothesis of a CO_2-H_2 atmosphere has been introduced by Ramirez et al. (2014) as a possible scenario for the early Martian atmosphere. The presence of CO_2 with high amounts of H_2 in the atmosphere would lead to a significant radiative effect through collision-induced absorption of light (Ramirez & Kaltenegger 2017). The photochemistry of these CO_2-H_2 early atmospheres is the focus of the present study. Laboratory experiments are conducted to understand the photochemical processes occurring in these atmospheres.

2 Experimental method

The PAMPRE (French acronym for aerosol production in micro gravity by reactive plasma) experimental setup is used to simulate photochemical processes occurring in the upper atmosphere. A CO_2-H_2-N_2 mixture is injected in the reactor chamber with a flow rate of 55 sccm (standard cubic centimeter per minute). The mixing ratio of carbon dioxide is set at 0.7 and the H_2 to N_2 abundance ratio is varied in two experiments : 0.5% of H_2 for the first scenario and 5% of H_2 for the second scenario. The mixing ratio of H_2 is changed to highlight its role in the photochemistry of these early atmospheres. A rotary vane vaccum pump is connected to the reactor chamber creating a continuous flow which stabilizes the pressure at 1 hPa. Experiments are conducted at room temperature. A radio-frequency (RF) capacitively coupled plasma discharge is used to initiate dissociation reactions with electron impact (Szopa et al. 2006). The chemical evolution of the mixture within the reactor is monitered using the EQP200 Hiden quadrupole mass spectrometer.

[1] LATMOS, CNRS, Guyancourt, France
[2] Department of Physics, University of Oxford, Oxford, England
[3] CSH, University of Bern, Bern, Switzerland

3 Experimental results

The only parameter changed in both scenarios is the mixing ratio of molecular hydrogen. The first scenario with 0.5% of molecular hydrogen shows a formation of oxygen and water by photochemistry (Fig. 1). The formation of oxygen is dominant with an intensity around 18,000 counts/s measured by the mass spectrometer at a permanent regime. This production of oxygen is expected in these CO_2-dominated atmospheres from the photolysis of the main gas and the combination of atomic oxygen. The second scenario with 5% of molecular hydrogen shows a significant and dominant formation of water with an intensity of 34,000 counts/s reached at a permanent regime (Fig. 2). These two different scenarios highlight the importance of H_2 in the chemistry of these atmospheres. These results indicate that the formation of water increases with the concentration of molecular hydrogen.

Similiar to the formation of oxygen, the formation of water starts with the photolysis of carbon dioxide and the production of the $O(^1D)$ radical (R1).

$$\mathrm{CO_2 + h\nu \longrightarrow CO + O(1D)} \quad \mathrm{(R1)}$$

The $O(^1D)$ radical then reacts with molecular hydrogen to produce the OH radical (R2). This reaction highlights the role of molecular hydrogen in the formation of water. H_2 is a reactant which means that the production rate of OH is higher in the second scenario with 5% of H_2 in the mixture.

$$\mathrm{O(^1D) + H_2 \longrightarrow OH + H} \quad \mathrm{(R2)}$$

The products of (R2) can then react with a stable abundant molecule M (CO_2 or N_2) to form water (R3).

$$\mathrm{OH + H + M \longrightarrow H_2O + M} \quad \mathrm{(R3)}$$

The OH radical generated by (R2) can also react with the abundant molecular hydrogen (R4) or another OH radical (R5) to produce water as identified by Fleury et al. (2015) for the case of the early Earth.

$$\mathrm{OH + H_2 \longrightarrow H_2O + H} \quad \mathrm{(R4)}$$

$$\mathrm{OH + OH \longrightarrow H_2O + O} \quad \mathrm{(R5)}$$

4 Conclusions and perspectives

Laboratory experiments simulating low pressure chemistry show that the production rate of water increases with the mixing ratio of H_2. This suggests the presence of water vapor in early CO_2-H_2 atmospheres of terrestrial exoplanets. The chain of reactions leading to the production of water vapor could also occur in an H_2-dominated atmosphere and contribute to the formation of liquid water. This needs to be further explored using a photochemical model.

References

Fleury, B., Carrasco, N., Marcq, E., Vettier, L., & Maattanen, A. 2015, ApJL, 807
Hu, R., Seager, S., & Bains, W. 2012, ApJ, 761
James, T. & Hu, R. 2018, ApJ, 867
Liggins, P., Shorttle, O., & Rimmer, P. 2020, EPSL, 550
Ramirez, R. & Kaltenegger, L. 2017, ApJL, 837
Ramirez, R., Kopparapu, R., Zugger, M., et al. 2014, Nat. Geos., 7
Szopa, C., Cernogora, G., Boufendi, L., Correia, J., & Coll, P. 2006, PSS, 54

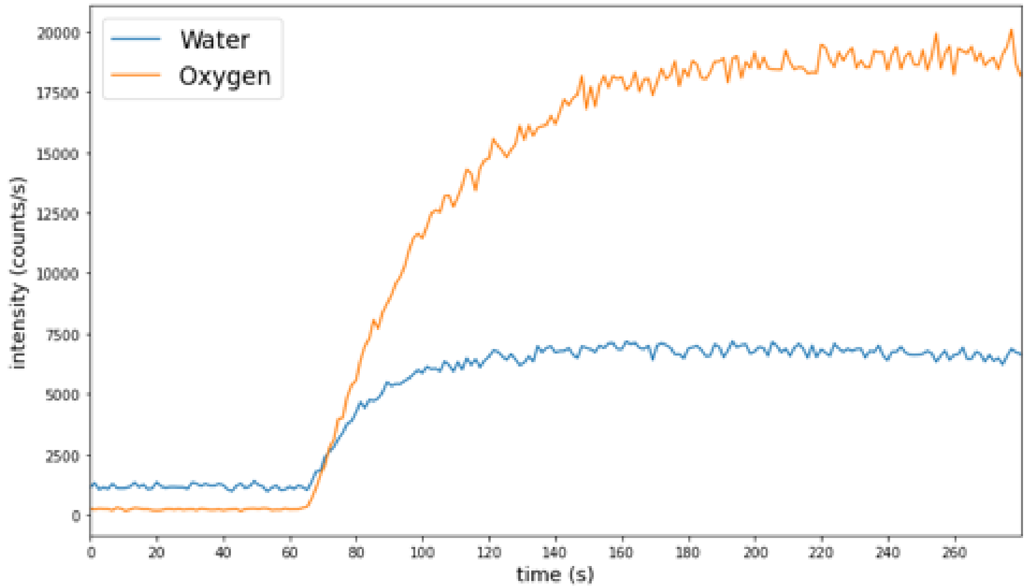

Fig. 1. Temporal evolution of the intensity (in counts/s) measured by the mass spectrometer for water (blue curve) and oxygen (orange curve). This first scenario is associated with 0.5% of molecular hydrogen in the mixture.

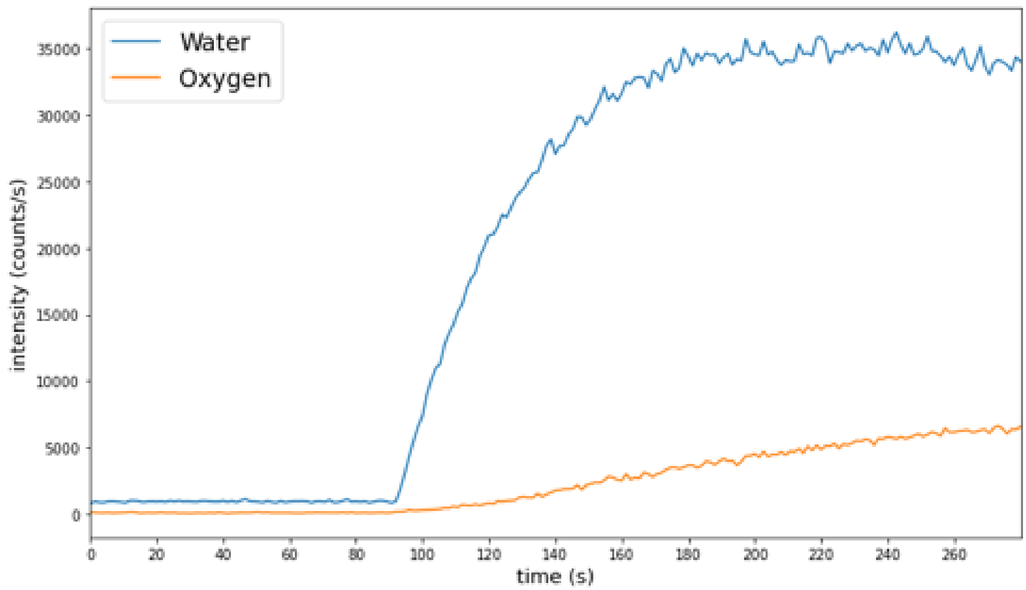

Fig. 2. Temporal evolution of the intensity (in counts/s) measured by the mass spectrometer for water (blue curve) and oxygen (orange curve). This second scenario is associated with 5% of molecular hydrogen in the mixture.

SF2A 2021
A. Siebert, K. Baillié, E. Lagadec, N. Lagarde, J. Malzac, J.-B. Marquette, M. N'Diaye, J. Richard, O. Venot (eds)

A NEW GENERATION OF STATISTICAL METHODS FOR EXOPLANET DETECTION WITH RADIAL VELOCITY

N. C. Hara[1]

Abstract. Radial velocities are essential to estimate the mass of exoplanet, and have the potential to detect Earth-like planets around Sun-like stars. However, radial velocity data are corrupted by instrumental systematics and complex stellar noises, which currently inhibit the detection of Earth analogs. We present new statistical and computational tools for the analysis of time-series, which show greater detection power than previous methods. We then discuss the scientific impact of the improvement of radial velocity precision.

Keywords: Exoplanets, radial velocity, statistics

1 Introduction

Since the discovery of the first extra-solar planets around a pulsar in 1992 Wolszczan & Frail (1992), and a Solar type star in 1995 Mayor & Queloz (1995) over four thousands exoplanets have been detected. Most of these detections have been obtained by two techniques: transits, which consist in searching for periodic dimming of the stellar light, indicating that a planet passes between the observer and the star, and radial velocities (or RV), where one searches for periodic variations of the star velocity along the line of sight. As of sept. 6 2021, over seven hundred planets have been discovered thanks to the RV technique.

RVs are essential for several reasons. First, they provide a direct measurement of the planetary projected mass. Combined with the planetary radius, a mass measurement yields the density and surface gravity, which are essential to study internal structures and planetary atmospheres (Batalha et al. 2017). One of the core science cases of the space mission PLATO is to provide a population of exoplanets with known masses, and thus, unlike Kepler (Borucki et al. 2011) will focus on bright stars, and aims at a 10% precision on the mass of planets. Secondly, RVs provide a crucial insight on the architecture of planetary systems. As the orbital period grows, the transit probability decreases. The RVs detection bias is less strong in that parameter space, they were used in particular to study giant planet demographics beyond the ice line Rosenthal et al. (2021); Fulton et al. (2021). Furthermore, transit surveys do not allow the detections of planetary systems with high mutual inclination such as HD 158259 (Hara et al. 2020). Finally, RVs cannot be circumvented for the detection and characterisation of Earth-like planets, as primary detection technique or follow-up of transit candidates. Instruments such as NIRPS and ESPRESSO (Pepe et al. 2021) are conceived with the goal of detecting Earth-like planets in the habitable zone (as a detection technique or to validate transit detections). The atmosphere of these planets will be probed either with transit spectroscopy, or direct imaging for objects within 15 parsecs from the Sun, and this for the best case scenarios of PCS (Kasper et al. 2021), LUVOIR[*], and HabEx[†] (Bouchy et al. 2017).

An Earth-mass planet in the habitable zone of a K dwarf produces a RV signal of the order of tens of centimeters per second, and the last generation spectrograph ESPRESSO demonstrated a stability of 25 cm/s. However, stellar features (granulation, plages and faculae) cause complex, poorly modelled radial velocity signals of the order of at least 50 cm/s (1 m/s for the Sun), which are added to potential instrument systematics (see Hara 2017). As low frequency noises, stellar and instrumental effects are particularly problematic in a parameter space where RV has an excellent potential: small planets at long periods. If not mitigated, these effects inhibits detections of terrestrial planets in the habitable zone of K and G stars, and population studies of planets of Saturn mass and below with periods ($\gtrsim 300$ d)

[1] Observatoire de Genève, Chemin de Pegasi 51, 1290, Versoix, Switzerland
[*] `https://asd.gsfc.nasa.gov/luvoir/resources/`
[†] `https://www.jpl.nasa.gov/habex/documents/`

2 Radial velocity data

Radial velocities are acquired as follows: the observer takes spectra of a star at different epochs. If the star has a non-zero velocity in the direction of the line of sight, the spectra will be shifted in frequency thanks to the Doppler effect. From this shift, one extracts the radial velocity. If a planet orbits the star, this one has a reflex motion so that the radial velocity of the star exhibits a periodic pattern at the orbital period. In Fig. 1, we show as an example 190 RV measurements of HD10180 made with the HARPS spectrograph (Lovis et al. 2011), which have a typical nominal uncertainty of 0.6 m/s, but in practice there are other sources of astrophysical and instrumental noise, showing complex structures (e. g. Saar & Donahue 1997; Meunier et al. 2010; Dumusque et al. 2015).

In the case where several planet orbit the star, if the gravitational interaction between the planets can be neglected on the observation timespan – which is true most of the time – the RV signals of the different planets add up. Searching for planets in radial velocity essentially comes down to a classical time series analysis problem: finding parametric periodic signals in an unevenly sampled timeseries, embedded in complex noises.

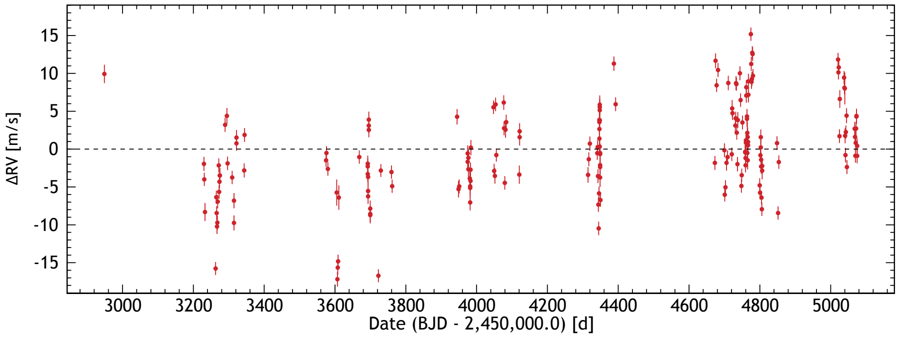

Fig. 1. 190 HARPS radial velocity measurements of HD10180 (Lovis et al. 2011).

3 New statistical tools

3.1 Detection criterion

Exoplanet d etections are typically claimed based on the computations of a statistical significance metric, which often are either the "Bayes factor" (e. g. Gregory 2007; Tuomi 2011; Díaz et al. 2016) or a $p-$value associated to a periodogram (e. g. Baluev 2008, 2009; Zechmeister & Kürster 2009). If the significance is greater than a certain thresold, a detection is claimed. In Hara et al. (2021b), we define a new metric called the true inclusion probability (TIP) (Hara et al. 2021b). The TIP is defined as the probability to have a planet whose frequency lies in a certain frequency interval. We then define the probability of absence of a planet as the False inclusion probability (FIP) = 1 - TIP.

In Fig. 2, we show a comparison of the different detection criteria. We generate a thousand mock RV datasets and, for different metrics, compute the number of false detections and missed detections as the detection threshold varies. The x axis of Fig. 2 shows the number of false detections, and the y axis shows the sum of false and missed detections. The FIP (in purple) shows a smaller number of missed detections for a given number of false detections, and it can be mathematically proven that, provided an accurate model of the data, the FIP outperforms other detection criteria. However, stellar and instrumental noises models might be inaccurate. To further test the reliability of detections, one can test whether the candidate planetary signals have a constant phase, amplitude and frequency – as they should exhibit – or display significant variations, indicating a non planetary origin of the signal (Hara et al. 2021a).

3.2 Numerical methods

The classical tool to model stellar activity is Gaussian processes. Manipulating them requires heavy computations, in particular matrix inversions. For some forms of the noise models, the computations can be brought from $O(N^3)$ to $O(N)$, which is the principle behind the CELERITE package (Foreman-Mackey et al. 2017).

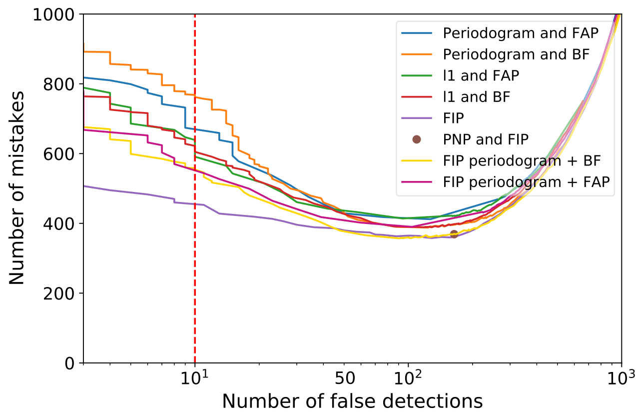

Fig. 2. Number of mistakes as a function of the number of false detections (log scale) for the different detection methods. The data corresponds to a simulation of 1000 datasets, where a random number of planets (0,1 or 2) are injected with, white and correlated noise. Mistakes are defined as the sum of missed and false detections. See Hara et al. (2021b) for details.

In Delisle et al. (2020), the CELERITE model is generalised to a wider class of noise models, which can in particular model simultaneously instrumental and stellar effects.

3.3 Extracting velocities

The previous techniques concern the time series of radial velocity. In those, the information contained in the spectrum is reduced to the RV as well as a few activity indicators. While planets affect identically all the spectral lines as a pure Doppler shift, activity and instrumental effects might have different effects depending on the wavelength. To exploit fully this property, one has to analyse the time series of spectra, which is the approach taken in Cretignier et al. (2021).

As we can see in Fig. 3, the map of spectra residuals after YARARA (bottom) is significantly cleaner than before its application (upper panel). Different recipes in YARARA allows a strong mitigation of the impact of cosmics, telluric and micro-telluric effects (e.g. Cunha et al. (2014)), ghosts (Dumusque et al. 2021) and HARPS detector stitching (Dumusque et al. 2015).

4 Conclusion

By combining the new processing of the spectra with the new numerical tools and detection criteria, we are able to significantly improve the capabilities of the radial velocity method to detect terrestrial planets in the habitable zone. To test our methods, we applied them to a hundred bright stars of the HARPS spectroscopic data, showing a nominal precision of 0.7 - 1 m/s. We are able to retrieve with high confidence three new candidate signals with minimum masses below 2 $M_\oplus$ and periods greater than 30 days, while there was only one known so far (τ ceti h, Feng et al. 2017). This analysis is still in progress. We have seen in section 1 that RVs are essential for mass measurements, probing outer regions and for the detection of planets in the habitable zone. It will play for instance a major role in the follow-up of the PLATO photometric mission. With the improvements made and further refinements, the use of RV for demographics studies will gain in precision and give access to Neptunes beyond the ice line., and eventually the detection and characterisation of terrestrial planets in the habitable zone.

This work has been carried out within the framework of the NCCR PlanetS supported by the Swiss National Science Foundation

References

Baluev, R. V. 2008, MNRAS, 385, 1279

Baluev, R. V. 2009, MNRAS, 393, 969

Batalha, N. E., Kempton, E. M. R., & Mbarek, R. 2017, ApJ, 836, L5

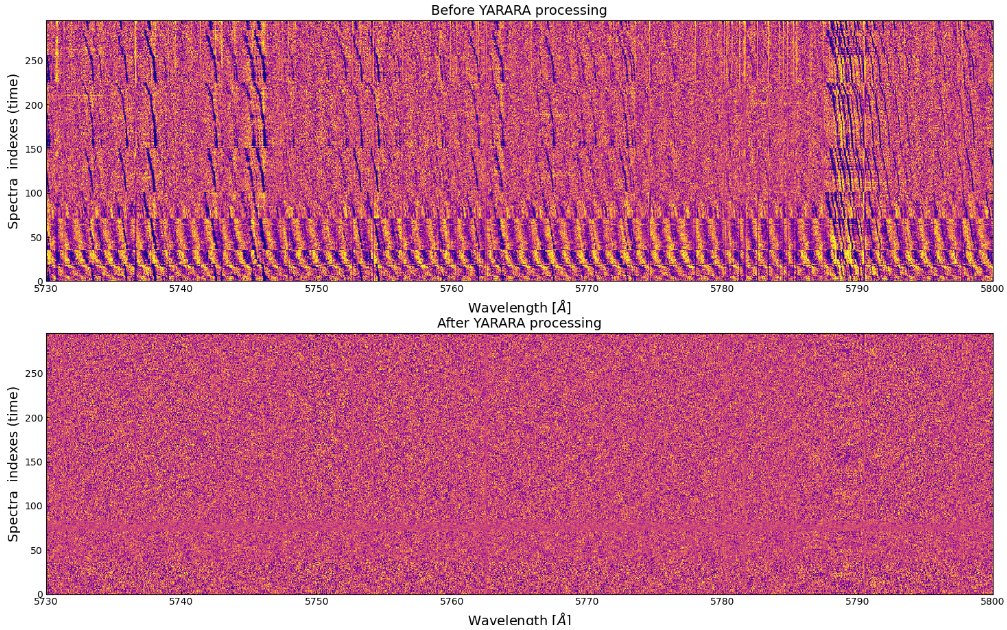

Fig. 3. Stacked HARPS spectra represented in color code (1 row is one spectrum for alpha Cen B) **Top:** Spectra before YARARA corrections. Spectra are suffering from interference patterns on two observational seasons (from index 0 to 71). **Bottom:** Residual river diagram after YARARA correction.

Borucki, W. J., Koch, D. G., Basri, G., et al. 2011, The Astrophysical Journal, 736, 19
Bouchy, F., Doyon, R., Artigau, É., et al. 2017, The Messenger, 169, 21
Cretignier, M., Dumusque, X., Hara, N. C., & Pepe, F. 2021, arXiv e-prints, arXiv:2106.07301
Cunha, D., Santos, N. C., Figueira, P., et al. 2014, A&A, 568, A35
Delisle, J. B., Hara, N., & Ségransan, D. 2020, A&A, 638, A95
Díaz, R. F., Ségransan, D., Udry, S., et al. 2016, A&A, 585, A134
Dumusque, X., Cretignier, M., Sosnowska, D., et al. 2021, A&A, 648, A103
Dumusque, X., Pepe, F., Lovis, C., & Latham, D. W. 2015, ApJ, 808, 171
Feng, F., Tuomi, M., Jones, H. R. A., et al. 2017, AJ, 154, 135
Foreman-Mackey, D., Agol, E., Ambikasaran, S., & Angus, R. 2017, AJ, 154, 220
Fulton, B. J., Rosenthal, L. J., Hirsch, L. A., et al. 2021, ApJS, 255, 14
Gregory, P. C. 2007, MNRAS, 381, 1607
Hara, N. C. 2017, PhD thesis, Observatoire de Paris
Hara, N. C., Bouchy, F., Stalport, M., et al. 2020, A&A, 636, L6
Hara, N. C., Delisle, J.-B., Unger, N., & Dumusque, X. 2021a, arXiv e-prints, arXiv:2106.01365
Hara, N. C., Unger, N., Delisle, J.-B., Díaz, R., & Ségransan, D. 2021b, arXiv e-prints, arXiv:2105.06995
Kasper, M., Cerpa Urra, N., Pathak, P., et al. 2021, arXiv e-prints, arXiv:2103.11196
Lovis, C., Ségransan, D., Mayor, M., et al. 2011, A&A, 528, A112
Mayor, M. & Queloz, D. 1995, Nature, 378, 355
Meunier, N., Desort, M., & Lagrange, A.-M. 2010, A&A, 512, A39
Pepe, F., Cristiani, S., Rebolo, R., et al. 2021, A&A, 645, A96
Rosenthal, L. J., Fulton, B. J., Hirsch, L. A., et al. 2021, ApJS, 255, 8
Saar, S. H. & Donahue, R. A. 1997, ApJ, 485, 319
Tuomi, M. 2011, A&A, 528, L5
Wolszczan, A. & Frail, D. A. 1992, Nature, 355, 145
Zechmeister, M. & Kürster, M. 2009, A&A, 496, 577

SF2A 2021
A. Siebert, K. Baillié, E. Lagadec, N. Lagarde, J. Malzac, J.-B. Marquette, M. N'Diaye, J. Richard, O. Venot (eds)

DUST GRAINS SHATTERING IN PROTOPLANETARY DISCS: COLLISIONAL FRAGMENTATION OR ROTATIONAL DISRUPTION?

S. Michoulier[1] and J.-F. Gonzalez[1]

Abstract.
Coagulation of dust grains into large aggregates still remains poorly understood. Grain porosity appears to be a promising solution to allow the grains to survive and form planets. Furthermore, dust shattering was considered to come only from collisional fragmentation, but a new process was introduced, rotational disruption. We wrote a C++ code to model grain growth and porosity evolution to study the final outcome of grains under the two shattering processes. When considering a disc model that reproduces observations, we point out that rotational disruption is negligible compared to the fragmentation and radial drift in almost all cases, and can therefore be neglected for commonly used values of fragmentation threshold and viscosity in 3D hydrodynamic simulations.

Keywords: protoplanetary discs, planet formation, dust, coagulation,

1 Introduction

In the theory of planetary formation, growth of sub-μm to mm dust aggregates in protoplanetary discs into planetesimals is hampered by theoretical problems commonly known as the radial drift barrier and the fragmentation barrier, preventing dust grains to survive and lately create planets. A promising solution to overcome these barriers is to consider intrinsic dust properties, namely grain porosity. For a given mass, fluffy grains have a larger collisional cross-section allowing them to grow faster, while staying coupled to gas at larger sizes, assuring their survival in the disc.

Recently, rotational disruption of porous dust grains was proposed as another possible barrier and has been investigated by Tatsuuma & Kataoka (2021) in the framework of protoplanetary discs. They found that grains can be disrupted by the gas-flow torque when aggregates tend to be highly porous, before they can decouple from the gas, when very compact grains subject to stronger radial drift are not.

We have developed a simple 1D C++ code to understand the behaviour of porous grains under the influence of different physical processes such as gas drag and grain growth. We incorporate the physics of a simplified rotational disruption model based on Tatsuuma & Kataoka (2021) in our code. We studied the behaviour of dust grains to understand in which case each shattering process, fragmentation due to collision between grains or rotational disruption dominates.

2 Theoretical background

To model protoplanetary discs, we adopt the commonly-used formulation in power-law of gas disc. For a stationary disc, two indices p and q can be defined to express the surface density profile $\Sigma_{\rm g} \propto R^{-p}$ and temperature profile $T_{\rm g} \propto R^{-q}$ as a function of the distance to the star R, assuming a vertically isothermal profile for the gas. We choose here to use a model of disc that reproduces observations. The star mass is set to $M_{\rm star} = 1\ \mathrm{M}_\odot$, the disc mass to $M_{\rm disc} = 0.01\ \mathrm{M}_\odot$. Inner, outer and reference radii of the disc are $R_{\rm in} = 10$ AU, $R_{\rm out} = 300$ AU and $R_0 = 1$ AU. Finally $p = 1$, $q = 1/2$ and the disc aspect ratio at R_0 is $\frac{H_{\rm g,0}(R)}{R_0} = 0.0283$.

[1] Univ Lyon, Univ Lyon1, Ens de Lyon, CNRS, Centre de Recherche Astrophysique de Lyon, UMR5574, F-69230, Saint-Genis-Laval, France

2.1 Growth and fragmentation model of dust grains

In this study, we focus on the evolution of porous aggregates. To model grain growth, we consider a locally mono-disperse mass distribution where collisions between identical grains occur. Grains collide with a relative velocity $v_{\rm rel}$ due to the gas turbulence transmitted to the dust by drag. $v_{\rm rel}$ can be expressed as:

$$v_{\rm rel} \propto \sqrt{\alpha}\frac{\sqrt{\rm St}}{1+{\rm St}}c_{\rm g}. \tag{2.1}$$

Here, $c_{\rm g}$ is the gas sound speed and α is the turbulent viscosity parameter defined by Shakura & Sunyaev (1973). To express the coupling between gas and dust, we define the Stokes number ${\rm St} = \tau_{\rm s}/t_{\rm K}$ as the ratio between the stopping time $\tau_{\rm s}$, i.e. the time needed for a grain to reach the gas velocity, and the keplerian orbital time $t_{\rm K}$. Depending on the value of St, grains behave differently, and three situation can be distinguished. If ${\rm St} \ll 1$, dust grains are typically small and well coupled to the gas. Thus, grains orbit at the sub-keplerian velocity of the gas. If ${\rm St} \gg 1$, dust grains are large enough to be almost completely decoupled from the gas, orbiting at a keplerian velocity. However, when ${\rm St} \approx 1$, dust grains have an intermediate size and gas drag is important. Therefore, the gas friction applied on the grains force them to slow down and they radially drifts toward the star due to the loss of angular momentum to be accreted onto the star. This is the radial drift barrier. Lastly, to model fragmentation of dust aggregates, we use the model developed by Kobayashi & Tanaka (2010) and Garcia (2018) where the loss of mass is also a function of the fragmentation threshold $v_{\rm frag}$.

2.2 Porosity evolution model

To take into account grain porosity, we use a reformulated and simpler version of the algorithm derived by Garcia (2018) and Garcia & Gonzalez (2020) based on the model of Suyama et al. (2008), Okuzumi et al. (2009), Okuzumi et al. (2012) and Kataoka et al. (2013). Details are presented in Garcia & Gonzalez (2020).

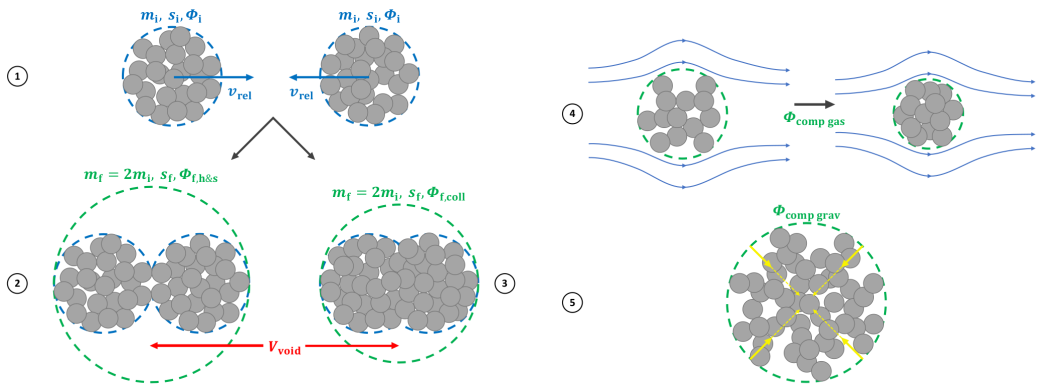

Fig. 1. Left: 1) Two identical grains collide with each other with a relative velocity $v_{\rm rel}$. 2) In the "hit & stick regime", grains simply stick together, a new volume of void is formed. 3) In the collisional compression regime, the new grains suffer internal restructuring. **Right:** 4) Grains can be compressed by the surrounding gas flow. 5) Massive grains can also be compressed by their own self-gravity.

A dust aggregate is a collection of n monomers considered to be compact spheres of mass m_0, size a_0 and intrinsic density $\rho_{\rm s}$. We define the filling factor $\phi = \rho/\rho_{\rm s}$ as the ratio between the mean internal density and the intrinsic density of the monomers which compose the aggregate. The mass m of the aggregate of size s and mean internal density ρ can be computed as followed:

$$m = \rho V = \rho_{\rm s}\phi\frac{4\pi}{3}s^3. \tag{2.2}$$

Depending on the mass of the grain, two regimes of expansion or compression drive the evolution of the aggregate. In the "hit & stick" regime (see figure 1 left), grains are small and coupled to the gas. For each collision, the mass doubles and a new volume of void is captured. When grains grow, the kinetic energy at impact increases and collisional compression appears. As $v_{\rm rel}$ depends on the Stokes number, the final filling factor takes a different expression in each drag regime (see Garcia & Gonzalez 2020). Independently of collisions, grains can also suffer static compaction (see figure 1) due to either gas flow or self-gravity (Kataoka et al. 2013).

2.3 Rotational disruption

This year, Tatsuuma & Kataoka (2021) presented a new barrier to dust growth: the rotational disruption barrier. Rotational disruption has already been investigated for interstellar medium dust or cometary dust, but not in the case of protoplanetary discs. We suppose that our grains are always in a steady-state angular velocity regime to be able to compute the angular velocity ω_c, considered to be driven only by the gas-flow torque. We also consider a relatively weak turbulent gas, as strong turbulence has unknown effects on disruption due to non trivial gas flow. To compute when a grain is rotationally disrupted in our simulations, we derive first the tensile stress S of a grain and we compare it to the tensile strength Smax derived by Tatsuuma et al. (2019). For more details, the full calculation is presented in Tatsuuma & Kataoka (2021).

3 Results

To study the effect of disruption, we choose to investigate the effect of the monomer size a_0 with various turbulent viscosity parameters α to compute when icy grains are disrupted. We choose two different monomer sizes: $a_0 = 0.1$ and $1\ \mu$m (Güttler et al. 2019). We restrict our study to icy grains with an intrinsic density of $\rho_s = 1000$ kg.m^{-3} and a surface energy of $\gamma_s = 0.1$ J.m^{-2}, because it is a very common species in discs. As the critical rolling displacement is uncertain, we choose, like Tatsuuma & Kataoka (2021), $\xi_{\rm crit} = 8$ Å. For the fragmentation threshold, we choose the typical value of $v_{\rm frag} = 15$ m.s^{-1}. Since turbulence is a key parameter for $v_{\rm rel}$, we choose a wide range of turbulence parameters $\alpha = 10^{-2}, 10^{-3}, 10^{-4}$ and 10^{-5}. As a first step, we run simulations where the grains are in fixed positions to derive when they are disrupted.

A higher turbulence leads to rotational disruption at smaller sizes compared to lower turbulence, where sizes of tens of meter can be reached in a much wider region for aggregates with monomers of 0.1 μm (figure 2). In fact, stronger turbulence leads to higher collisional velocities between grains, making collisional compaction start earlier during their growth. For $a_0 = 0.1\ \mu$m, we can see a slope change close to the star on both panels of figure 2, extending to larger radii when α is smaller, which is due to the gas flow static compression driving the grain evolution when the collisional compression is less efficient at low turbulence. With the left panel of figure 2, we can clearly see that aggregates made of bigger monomers are more susceptible to be disrupted at smaller sizes, as shown by (Tatsuuma & Kataoka 2021). Interestingly, the computed relative velocity $v_{\rm rel}$ between grains just before the disruption remains rather unaffected by the monomer size. For a given α, the difference is only of a few m.s^{-1} as shown in the right panel of figure 2. At an intermediate turbulence of $\alpha = 10^{-3}$, both barriers appear to be in a tight competition.

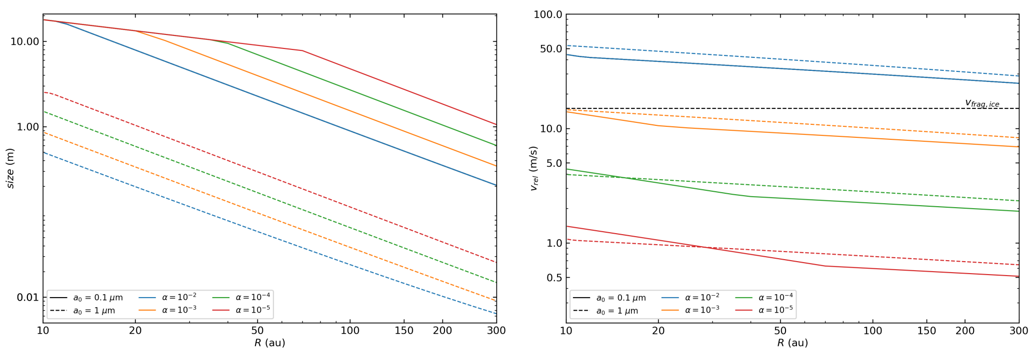

Fig. 2. Left: Maximum grain size before disruption for different α viscosity parameters and monomer sizes a_0 with icy grains. **Right:** Maximum relative velocity between gas and dust before disruption for different α viscosity parameters and monomer sizes a_0 with icy grains. The black dashed line correspond to the typical fragmentation threshold of ice.

Until now, we did not take into account the grains spatial evolution on the disc as orbital position was kept fixed. As we mentioned above for high turbulence ($\alpha = 10^{-2}$), fragmentation is the dominant process (figure

3). The grains start to grow from the monomer size, then slowly drift as St increases, then $v_{\rm rel}$ increases and rapidly exceeds the fragmentation threshold. An equilibrium between growth and fragmentation is reached, maintaining grains in a range of size big enough to allow efficient radial drift and finally get accreted onto the star. For $\alpha = 10^{-4}$ (not shown), neither rotational disruption nor fragmentation destroy aggregates. Very weak turbulence reduces the growth efficiency of fluffy grains too heavily. As the growth rate is smaller, grains are not able to reach in time either the fragmentation barrier or the disruption barrier. The growth rate of meter-sized aggregates is high enough to reach the disruption barrier before grains get accreted for an intermediate turbulence of $\alpha = 10^{-3}$. On figure 3, we plot with dashed lines the trajectory of grains if disruption was not taken into account. For $\alpha = 10^{-3}$, rotational disruption dominates, as grains crossed the disruption limit before exceeding the fragmentation threshold. Nevertheless, the maximum size reached by grains with or without disruption is the same, between 10 and 20 meters.

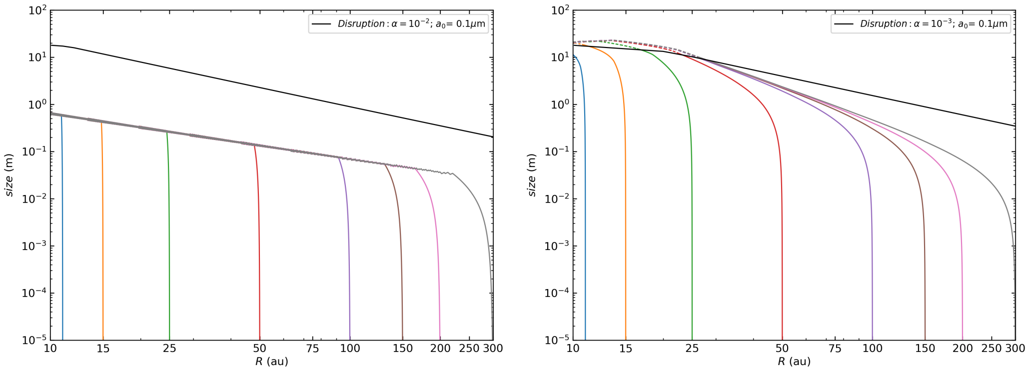

Fig. 3. Evolution of icy grains for three viscosity parameters $\alpha = 10^{-2}, 10^{-3}, 10^{-4}$ and $a_0 = 0.1\ \mu$m

4 Conclusions

We investigate dust grain shattering in protoplanetary discs to understand if rotational disruption is an important process in aggregate evolution. Using our growth and porosity evolution model, we showed that disruption is a marginal barrier and plays a role in a restricted range of parameters $\alpha \approx 10^{-3}$ and $v_{\rm frag} > 10$ m.s^{-1}. For higher turbulence or lower fragmentation threshold, collisional fragmentation rules, while for low turbulence, radial drift prevails. Thus, we can neglect in most cases rotational disruption as it is not the main process of dust grain shattering. Nevertheless, further investigation has to be done. It would be interesting to understand the effect of using different materials such as silicates, another abundant species in protoplanetary discs. The different material properties could change grain evolution significantly.

We would like to thank the SF2A and the PNP workshop for letting us presenting our work to the "journées de la SF2A 2021". Figures in the results section were made using the *matplotlib* library (Hunter 2007).

References

Garcia, A. 2018, Theses, Université de Lyon
Garcia, A. J. L. & Gonzalez, J.-F. 2020, Monthly Notices of the Royal Astronomical Society, 493, 1788
Güttler, C., Mannel, T., Rotundi, A., et al. 2019, Astronomy & Astrophysics, 630, A24, arXiv: 1902.10634
Hunter, J. D. 2007, Computing in Science & Engineering, 9, 90
Kataoka, A., Tanaka, H., Okuzumi, S., & Wada, K. 2013, Astronomy and Astrophysics, 557, L4
Kobayashi, H. & Tanaka, H. 2010, Icarus, 206, 735
Okuzumi, S., Tanaka, H., Kobayashi, H., & Wada, K. 2012, The Astrophysical Journal, 752, 106
Okuzumi, S., Tanaka, H., & Sakagami, M.-a. 2009, The Astrophysical Journal, 707, 1247
Shakura, N. I. & Sunyaev, R. A. 1973, Astronomy and Astrophysics, 24, 337
Suyama, T., Wada, K., & Tanaka, H. 2008, The Astrophysical Journal, 684, 1310
Tatsuuma, M. & Kataoka, A. 2021, arXiv:2101.04910 [astro-ph], arXiv: 2101.04910
Tatsuuma, M., Kataoka, A., & Tanaka, H. 2019, The Astrophysical Journal, 874, 159, arXiv: 1902.08356

SF2A 2021
A. Siebert, K. Baillié, E. Lagadec, N. Lagarde, J. Malzac, J.-B. Marquette, M. N'Diaye, J. Richard, O. Venot (eds)

AN ATMOSPHERIC ORIGIN FOR A HCN-DERIVED POLYMER ON TITAN

Z. Perrin[1], N. Carrasco[1], A. Chatain[1], L. Jovanovic[1], N. Ruscassier[2], L. Vettier[1] and G. Cernogora[1]

Abstract. Titan's haze is strongly suspected to be an HCN-derived polymer, but despite the first in situ measurements by the ESA-Huygens space probe, its chemical composition and formation process remain largely unknown. To investigate this question, we simulated in the laboratory, the atmospheric haze formation process. We synthesized analogues of Titan's haze, named Titan tholins, in an irradiated N2–CH4 gas mixture, mimicking Titan's upper atmosphere chemistry. HCN was monitored in situ in the gas phase simultaneously with the formation and evolution of the haze particles. We show that HCN is produced as long as the particles are absent, and is then progressively consumed when the particles appear and grow. This work highlights HCN as an effective precursor of Titan's haze and confirms the HCN-derived polymer nature of the haze.

Keywords: HCN-polymers, microphysical evolution

1 Introduction

The largest satellite of Saturn, Titan, has a thick atmosphere based on N_2 and CH_4. The photochemistry of N_2 and CH_4 leads to the formation of complex organic molecules, up to the formation of solid aerosols, observed under the appearance of an orange opaque haze by the Voyager 1 and Cassini/Huygens missions.

In-situ measurements by the Huygens probe (Israël et al. 2005), and laboratory experiments synthesizing Titan-like aerosols (called tholins), have revealed HCN as one of the main chemical signatures extracted from aerosols. This nitrile compounds has been detected in the gaseous phase, in Titan's atmosphere.

The objective of this work is to study in the laboratory if HCN is indeed a precursor to aerosol formation. Laboratory experiments were conducted using a dusty plasma reactor (Szopa et al. 2006) simulating the photochemistry of the Titan atmosphere, and initiating the formation of Titan-like organic aerosols (tholins) and associated gas-phase chemistry. In the present work, we simultaneously study the temporal evolution of HCN in the gas phase and the formation and growth of Titan tholins.

2 Context

2.1 *Literature citations*

During its passage near Titan, the IRIS infrared spectrometer on board the Voyager 1 spacecraft detected nitrile compounds, including HCN, in its atmosphere (Liang et al. 2007). The latter is formed by EUV photochemistry based on methane and nitrogen.

Titan is also surrounded by an organic photochemical haze, which has been probed by the DISR, ISS, and UVIS instruments aboard the Cassini/Huygens space mission (Liang et al. 2007; Tomasko et al. 2008). The production of these haze nanoparticles starts in the upper atmosphere at 1000 km altitude (Waite et al. 2007). After their formation, they slowly sediment towards the surface of Titan during several years (Lavvas et al.

[1] LATMOS Laboratory, CNRS, University Paris-Saclay, 78280 Guyancourt, France
[2] LGPM Laboratory, Centrale-Supélec, University Paris-Saclay, 91190 Gif-sur-Yvette, France

2011) and are suspected to undergo chemical and microphysical evolution processes during their descent (Lavvas et al. 2012).

Their chemical composition was studied by the Huygens spacecraft during its landing through the atmosphere of Titan in January 2005 (Israël et al. 2005). HCN was found to be one of the main chemical signatures extracted from the aerosols after their pyrolysis and analysis by gas chromatography coupled to Mass spectrometry. Laboratory experiments have confirmed the possible contribution of HCN to Titan aerosols. Pyrolysis of Titan aerosol analogs, combined with GC-MS analyses identified HCN as a systematic pyrolytic fragment (Coll et al. 2013; Morisson et al. 2016; Khare et al. 1984), but Titan tholins were also found to be more complex than pure HCN polymers (Vuitton et al. 2010; Bonnet et al. 2013). This converging evidence points to a probable polymeric HCN derivative structure for Titan aerosols.

2.2 Experimental simulation

Titan aerosol analogues are formed using the PAMPRE experiment (Szopa et al. 2006). PAMPRE is a reaction chamber, where a cold capacitively coupled radio frequency plasma is ignited at low pressure (0.9 mbar). A gas mixture of 95% N_2 and 5% CH_4 is injected into the reactor. Then a discharge is initiated, photolysing methane and nitrogen, and simulating photochemistry on Titan.

In this work, the gas flow rate was optimised to increase the residence time of the gas mixture in the reactor as much as possible. The chemical growth of the solid particles is thus favoured, making it possible to simultaneously follow the formation and evolution of the particles, as well as the co-evolution of the gas mixture composition.

3 Results

3.1 Morphology analysis of tholins by scanning electron microscopy

The formed samples were observed by scanning electron microscopy (SEM field emission gun).

Different stages of growth are observed in the images. In the first stage, the so-called primary nanoparticles coagulate with each other and form aggregates (Fig.1). These aggregates continue to grow into single spherical grains of 1.5 µm in diameter (Fig. 1). Subsequently, these micrometric spherical grains evolve by agglomerating.

3.2 Time evolution of the gas phase by mass spectrometry

The evolution of the N_2 - CH_4 gas phase allowing the production of organic polymers (tholins), is observed by quadrupole mass spectrometry, particularly for the masses corresponding to methane (m/z=16) and hydrogen cyanide (m/z=27).

Several phases are highlighted in the experiment (Fig. 2). Different phases of methane consumption (Fig. 2, red curve), with distinct decreasing slopes (on the logarithmic scale), associated in a first time with the ignition of the plasma discharge, in a second time with the formation of the primary nanoparticles, and in a third time with the agglomeration and growth of these nanoparticles. Finally, the stationary state is reached, by an equilibrium between particle growth and methane consumption.

In parallel, HCN is first produced, depending on the dissociation of the major components. Then it is progressively consumed in two distinct steps, in correlation with the appearance of the powders and their growth (Fig. 2, blue curve).

3.3 Figures

4 Conclusions

For conclusion, the observations made, highlight that the HCN formed during the simulation of Titan's photochemistry, is one of the precursors of Titan-like aerosols formed at low flows, interacting since their formation

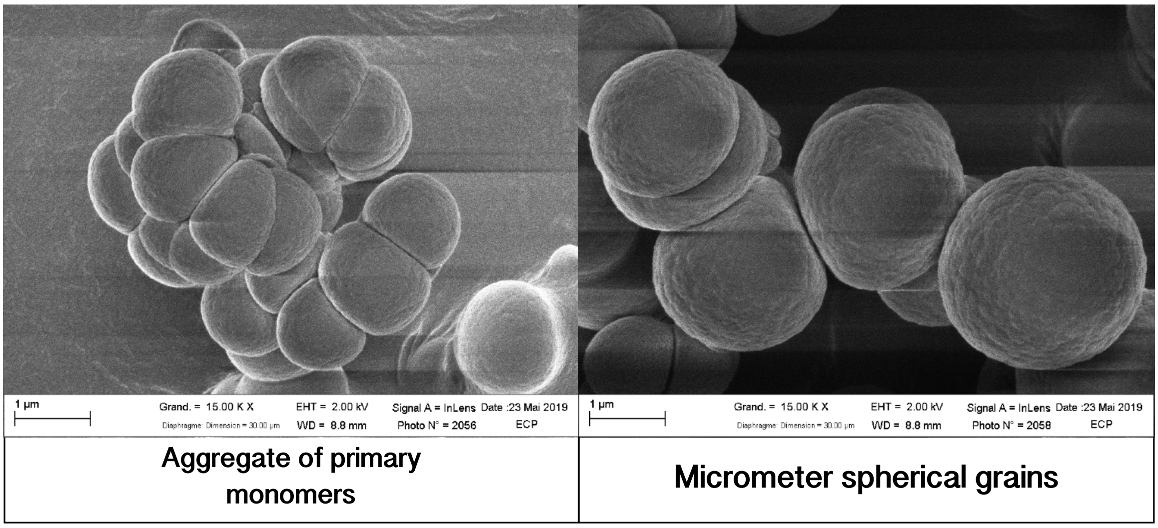

Fig. 1. SEM pictures of sample

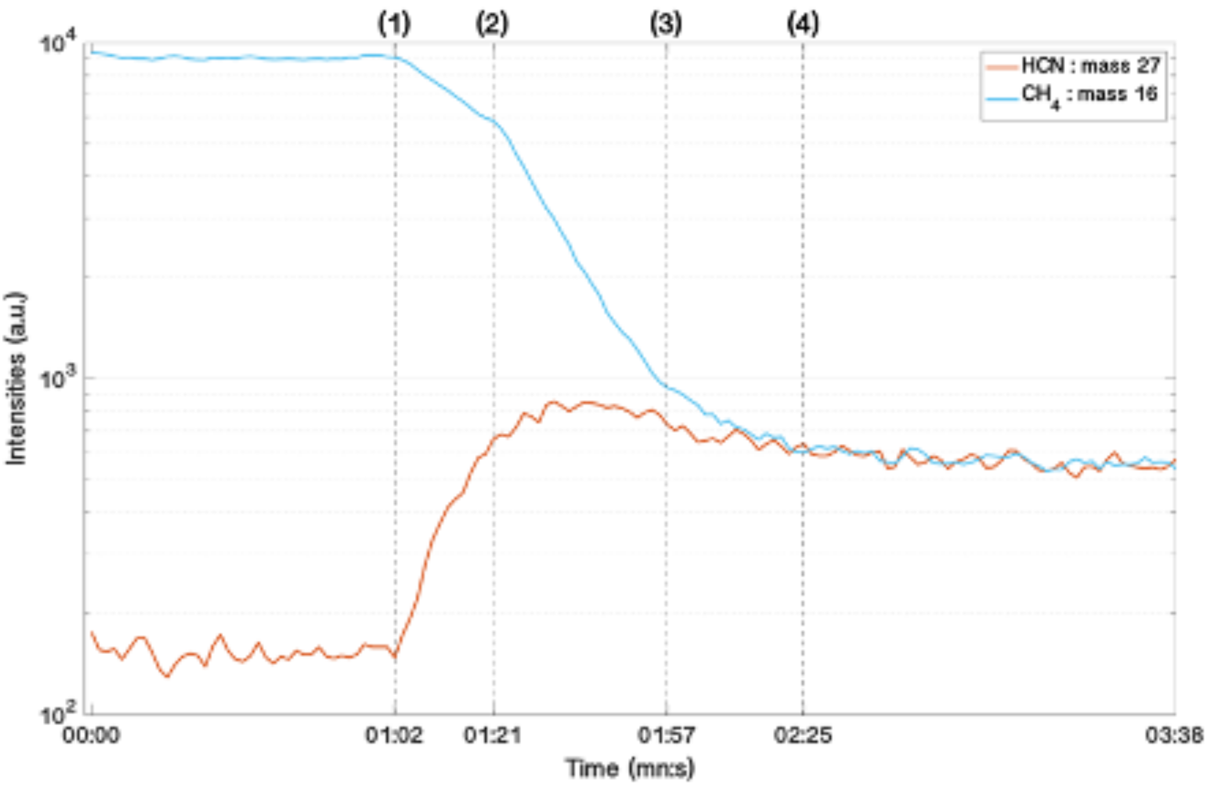

Fig. 2. Time evolution of the masses m/z 16 (CH4), 27 (HCN) of the gas phase present during the experiment

and then during their growth (Perrin et al. 2021).

This assumption is also made in the microphysical evolution model of aerosols residing in Titan's atmosphere by (Lavvas et al. 2012), where the predicted aerosol growth is similar in some respects, to that observed experimentally in this study.

N.C. thanks the European Research Council for funding via the ERC Prim- Chem project (grant agreement No. 636829).

References

Bonnet, J.-Y., Thissen, R., Frisari, M., et al. 2013, International Journal of Mass Spectrometry, 354-355, 193
Coll, P., Navarro-González, R., Szopa, C., et al. 2013, Planet. Space Sci., 77, 91
Israël, G., Szopa, C., Raulin, F., et al. 2005, Nature, 438, 796
Khare, B. N., Sagan, C., Thompson, W. R., et al. 1984, Advances in Space Research, 4, 59
Lavvas, P., Sander, M., Kraft, M., & Imanaka, H. 2011, ApJ, 728, 80
Lavvas, P., Yelle, R. V., Koskinen, T., et al. 2012, 2012, P24C
Liang, M.-C., Yung, Y. L., & Shemansky, D. E. 2007, ApJ, 661, L199
Morisson, M., Szopa, C., Carrasco, N., Buch, A., & Gautier, T. 2016, Icarus, 277, 442
Perrin, Z., Carrasco, N., Chatain, C., & et al. 2021, Processes, 9, 965
Szopa, C., Cernogora, G., Boufendi, L., Correia, J. J., & Coll, P. 2006, Planet. Space Sci., 54, 394
Tomasko, M. G., Doose, L., Engel, S., et al. 2008, Planet. Space Sci., 56, 669
Vuitton, V., Bonnet, J.-Y., Frisari, M., et al. 2010, Faraday Discussions, 147, 495
Waite, J. H., Young, D. T., Cravens, T. E., et al. 2007, Science, 316, 870

SF2A 2021
A. Siebert, K. Baillié, E. Lagadec, N. Lagarde, J. Malzac, J.-B. Marquette, M. N'Diaye, J. Richard, O. Venot (eds)

THE NAROO DIGITIZATION CENTER

V. Robert[1,2], J. Desmars[1,2], A.-C. Perlbarg[1,2], V. Lainey[2] and J.-E. Arlot[2]

Abstract. The New Astrometric Reduction of Old Observations NAROO center is built at Paris Observatory, Meudon, and is dedicated to the measurement of astro-photographic plates and the analysis of old observations. The NAROO digitizer consists of a granite based Newport-Microcontrol open frame air-bearing XY positioning table, a scientific sCMOS camera, and a telecentric optical system. The plate holder assembly is suited for mounting glass plates up to 350-mm square. The machine positioning stability is better than 15 nm, its repeatability is better than 40 nm. With real photographic plate data, we are able to produce measurements with an accuracy better than 65 nm.

The renewed interest about photographic plates concerns the expansion of the database of transient objects evolving in time, since digitization now makes it possible to measure images with a high level of accuracy and to identify all the available objects. The information extracted from such materials can be of an astrometric, photometric, and spectroscopic nature, when not purely imaging, with consequences in planetology, near-Earth asteroid risk assessment, astrophysical phenomena, and general relativity, to mention but a few. Through our scientific program in the Gaia era, we detail examples of current and upcoming uses for the community. We invite researchers to use our facilities and digitize their collection by answering our call for proposals.

We will present first results of mass digitizations and scientific application to the Galilean system using Gaia-eDR3 reference star catalog, and first results of NEA precoveries. We will also give details for the researchers to use our facilities and digitize their collection by answering our Call for Proposals.

Keywords: instrumentation: high angular resolution, techniques: image processing, digitization, photograhic plate

1 Introduction

The renewed interest about photographic plates concerns the expansion of the database of transient objects evolving in time, since digitization now makes it possible to measure images with a high level of accuracy and to identify all the available objects. The information extracted from such materials can be of an astrometric, photometric, and spectroscopic nature, when not purely imaging, with consequences in planetology, near-Earth asteroid risk assessment, astrophysical phenomena, and general relativity, to mention but a few.

Studying the dynamics of Solar System bodies, in particular, requires astrometric observations sampled over a long time span to quantify the long period terms which may help to analyze the evolution of the motion. Searching for old data is obviously useful for this purpose, and since we have demonstrated that a precise digitization and a new astrometric reduction of old photographic plates could provide very accurate positions (Robert et al. 2011, 2015, 2016), researchers involved in various scientific topics began to (re-)consider such materials. As a consequence, the Paris Observatory decided to acquire such an instrument and to build a scientific community for its exploitation, creating the New Astrometric Reduction of Old Observations NAROO program.

2 The NAROO center

The NAROO center is a unique place dedicated to the sub-micrometric analysis of old astro-photographic plates, fort scientific purposes only.

[1] Institut Polytechnique des Sciences Avancées IPSA, 63 bis Boulevard de Brandebourg, 94200 Ivry-sur-Seine, France
[2] IMCCE, Observatoire de Paris, PSL Research University, CNRS UMR 8028, Sorbonne Universités, UPMC, Univ. Lille 1, 77 avenue Denfert- Rochereau, 75014 Paris, France

Fig. 1. Logo of the NAROO center.

2.1 Hardware

Figure 2 shows the NAROO digitizer as of April 2020. The machine consists of a granite-based Newport-Microcontrol open-frame and air-bearing XY positioning table, with a plate holder assembly suited for mounting glass plates up to 350 mm squared. The NAROO machine is able to process almost all known transparent photographic plate materials automatically.

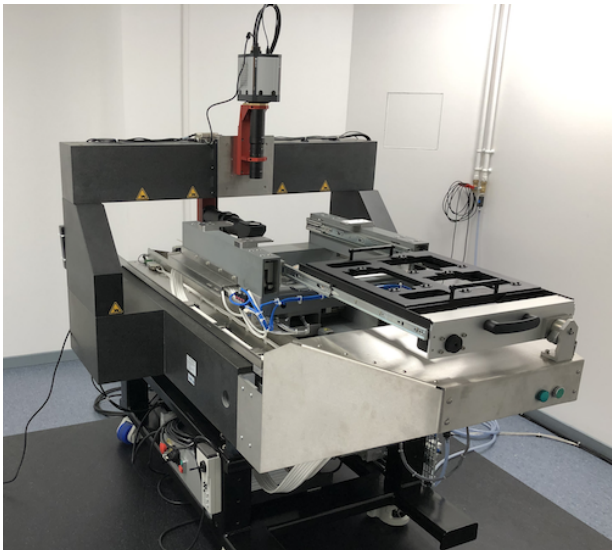

Fig. 2. NAROO machine at the Paris Observatory, Meudon.

The granite base measures 1.3 m × 1.3 m × 0.2 m. It is mounted on dynamic feet to compensate for the building and environment vibrations. The position of the XY-table is read by Heidenhain encoders with an accuracy better than 2 nm. The linearity and orthogonality of XY-axes were calibrated by Newport-Microcontrol using a laser interferometer. The local XY-table positioning was measured by the manufacturer with a capacitance up to 7 nm. The repeatability, how closely the XY-table can return to an initial position following movement over the entire XY-axes, was also measured by the manufacturer with a capacitance up to 40 nm. In order to reach and maintain a high geometric and radiometric accuracy, the digitizer is placed in an overpressure, air-conditioned, ISO-5 clean room, at a temperature of 20°C ± 0.1°C and a relative humidity of 50% RH ± 5% RH.

The optical unit consists of an Andor Neo sCMOS Camera, mounted on a VST VS-TCM-130/S telecentric 1:1 objective. This system is attached to the Z-axis above the XY-table. The photographic plates are illuminated from below with light emitting diodes (LEDs), controlled by a high-precision DC power supply. We paid particular attention to the complete optical system which was specifically designed by the instrumentation pole of the Paris Observatory to evenly illuminate the plate and avoid vignetting. The 2D sCMOS Camera generates images with 2560 by 2160 pixels of 6.5 µm by 6.5 µm. The maximum dynamic range is 30,000:1. Each frame results in a 16-bit FITS file with 11 MB disk space. For instance, the digitization of a classical 5 by 7 inch Kodak plate requires about 1.2 GB of disk space, while that of a 350 mm squared Schmidt plate is up to 5.9 GB.

2.2 Digitization process

Most of the NAROO functions are computer controlled. Depending on their size, one or several photographic plates are put inside a plate holder that is mounted on the XY-table. At the beginning of each digitization process, the supports are automatically put into focus, with the emulsion facing up, by clamping the plate holder upward against the counterpressure rack. The illumination is set to 3/4 of the saturation on the plate's sky background by adjusting the DC power supply unit to the LED. The plate is automatically digitized in step-and-stare mode with steps corresponding to user-defined moves in the X and Y directions. The local XY-table position is read by the Heidenhain encoders and inserted into the image header. After the plate digitization is complete, the XY-table automatically returns to its home position, and the plate holder is unclamped in anticipation of a new cycle. As a final product of digitization, an overall mosaic FITS image of the whole photographic plate is generated from the individual images with or without overlapping.

The time needed to digitize a single classical 5 by 7 inches Kodak plate with about of 120 individual images is 5 min, taking into account the overall movement from the XY-table home position and return. That of a complete Schmidt plate with about 550 individual images is 22 minutes.

3 Scientific program - First results

The information extracted from photographic plates are of an astrometric, photometric, and spectroscopic nature, when not purely imaging. Robert et al. (2021) provided details of current and upcoming scientific programs, in which the NAROO center is involved, as examples for the community and to possible interactions. Anyway, results of the first mass digitizations will be published soon.

3.1 USNO Galilean plates

A set of about 550 plates of the United States Naval Observatory USNO was digitized with the NAROO machine. These plates are observations of the Jovian system realized by Dan Pascu between 1967 and 1998 (Pascu 1994). They result in about of 2650 original observations. One should note that we previously measured these observations with the DAMIAN machine in 2010 (Robert et al. 2011), and we provided equatorial positions for the Galilean satellites using UCAC2 reference stars (Zacharias et al. 2004). Nevertheless, the complete results and positions were never published.

This previous work allowed us to make various comparisons with the new NAROO measurements, 10 years later. We compared both DAMIAN and NAROO measurements, we compared both UCAC2 and Gaia-eDR3 (Arénou 2020) star catalogs for the references, and obviously different planetary and satellite ephemerides. First, our results show that the NAROO machine provides the best digitizing accuracy. In fact, the satellites residuals over 30 years show that the DAMIAN machine was affected by a mean random error of 4.4 mas, that is to say about of 210 nm. Then, combining the NAROO digitizations and Gaia stars will provide the best accuracy for old observations, since the mean residuals are decreased by about of 10 mas, that is to say about of 30 km, by comparison with the first measurements.

The intersatellite positions of the USNO Galilean observations, over 30 years, are about of 30 mas versus 100 mas with the very first measurements by Dan Pascu. The equatorial positions of the USNO Galilean observations, over 30 years, are about of 55 mas, that is to say 165 km.

3.2 OCA asteroid precoveries

A PhD was started at the NAROO center in 2020 because we thought that dynamics of small Solar System bodies could benefit from long-term astrometry provided by the NAROO machine. In particular, we thought that photographic plates realized at the Observatoire de la Côte d'Azur OCA could be a source of old observations of Potentially Hazardous Asteroids PHA of the XXth century since the collection was exactly realized for the detection of new asteroids. They could have been observed even if it was not the purpose of the original observation. And we found several precoveries of PHAs in the collection, and the analysis is still in progress. As an example, Figure 3 shows the precovery in 1982 of asteroid 2006 SU49. The precovery is 24 years before the official discovery.

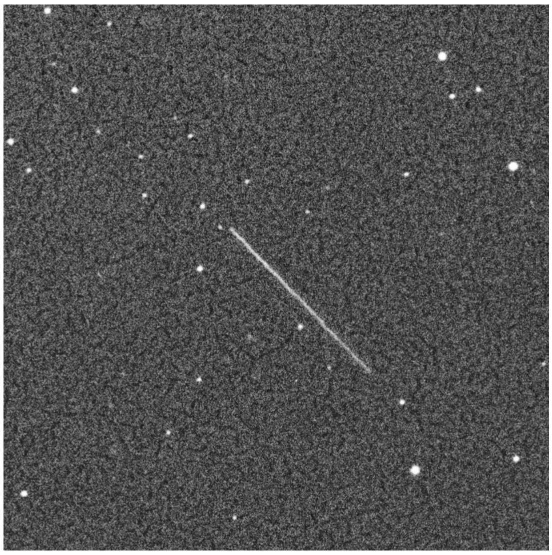

Fig. 3. Precovery in 1982 of asteroid 2006 SU49.

4 Call for Proposals

The value of a new analysis of old photographic plates has been demonstrated, and the community is beginning to worry about the use and preservation of such materials for science. As recommended by the resolution B3 of the XXX IAU General Assembly in 2018, the preservation, digitization, and scientific exploration of the plates must be realized. Plate collections of the Paris Observatory and other French and international institutions are being digitized to provide data spanning more than one century for our works. Corresponding results will be presented in upcoming papers. Digitized raw data will also be available for the community.

The NAROO machine is available for researchers to digitize their own collections for scientific purposes, since digitization time is reserved for external users. A call for proposals is being issued every six months via our project website `https://omekas.obspm.fr/s/naroo-project/`.

The NAROO program was supported by the DIM-ACAV of Ile-de-France region, PSL Research University, the Programme National GRAM and the Programme National de Planétologie (PNP) of CNRS/INSU with INP and IN2P3, co-funded by CNES.

References

Arénou, F. 2020, Newsletter, AF Gaia

Pascu, D. 1994, in Galactic and Solar System Optical Astrometry, ed. L. V. Morrison & G. F. Gilmore, 304

Robert, V., de Cuyper, J. P., Arlot, J. E., et al. 2011, MNRAS, 415, 701

Robert, V., Desmars, J., Lainey, V., et al. 2021, A&A, 652, A3

Robert, V., Lainey, V., Pascu, D., et al. 2015, A&A, 582, A36

Robert, V., Pascu, D., Lainey, V., et al. 2016, A&A, 596, A37

Zacharias, N., Urban, S. E., Zacharias, M. I., et al. 2004, AJ, 127, 3043

Session 2

Atelier général du PCMI

EXPERIMENTAL STUDY OF X-RAY PHOTON-INDUCED DESORPTION FROM METHANOL CONTAINING ICES AND ITS ASTROPHYSICAL IMPLICATIONS

R. Basalgète[1], R. Dupuy[2], G. Féraud[1], C. Romanzin[3], X. Michaut[1], L. Philippe[1], J. Michoud[1], L. Amiaud[4], A. Lafosse[4], J-H. Fillion[1] and M. Bertin[1]

Abstract. Detections of gas phase methanol CH_3OH in the cold regions of protoplanetary disks are still poorly understood. The role of X-rays, emitted from the central young stellar object (YSO), to explain these observations is still an open question. X-ray photodesorption, which is the desorption of molecules from interstellar ices, induced by its X-ray irradiation, is a potential candidate to explain the observed CH_3OH abundances. We have experimentally studied this process in the soft X-ray range near the O K-edge ($\sim$ 560 eV) on CO or H_2O-rich ices containing methanol. The X-ray photodesorption spectra of the desorbing molecules are found to be well-correlated with the ice X-ray absorption spectrum. X-ray photodesorption yields, which represent the efficiency of a X-ray to desorb a given molecule, are found to be strongly dependent on the ice composition. X-ray photodesorption of CH_3OH is efficient (with a yield of $\sim 10^{-2}$ molecule/photon at 565 eV) when CH_3OH is embedded in CO-rich ices. When embedded in H_2O-rich ices, the X-ray photodesorption of CH_3OH is not detected. This was assumed to be due to the X-ray induced-chemistry. Consequently, X-ray photodesorption should participate into explaining the presence of gas phase CH_3OH only beyond the CO snowline of protoplanetary disks.

Keywords: X-ray photodesorption, laboratory astrophysics, interstellar ices, complex organic molecules, protoplanetary disks

1 Introduction

The recent gas phase detection of methanol CH_3OH in the cold regions of the TW Hya protoplanetary disk is not fully understood so far (Walsh et al. 2016). This molecule is expected to accrete and/or form on interstellar ices that populates these regions. These ices originate from the condensation of gas phase molecules and from catalytic formation on the surface of cold (T<100 K) dust grains. They are mainly composed of H_2O, CO and CO_2 (Boogert et al. 2015) but can also contain more complex molecules such as CH_3OH. Therefore, the presence of CH_3OH in the gas phase of these cold regions implies that a non-thermal process should eject it from the ices into the gas phase. It is expected that UV photons and/or cosmic rays coming from various sources could trigger the ejection of methanol from the icy dust grains into the gas phase and participate in the overall gas-to-ice ratio of these cold regions (Dartois et al. 2020; Öberg et al. 2009; Cruz-Diaz et al. 2016; Bertin et al. 2016). Recent studies have shown that X-rays, emitted from various sources, such as the central Young Stellar Object (YSO) in the case of protoplanetary disks, could also participate in the desorption of molecules from interstellar ices (Dupuy et al. 2018; Ciaravella et al. 2020), a process known as X-ray photodesorption. The efficiency and the significance of this process for methanol-containing ices is still an open question. We have recently studied X-ray photodesorption from methanol-containing ices in the 525-570 eV range by coupling the ultra-high vacuum SPICES set-up to the SEXTANTS beamline of the SOLEIL synchrotron facility in Paris-Saclay. Pure methanol ices and mixed ^{13}CO:CH_3OH and H_2O:CH_3OH ices were formed on a rotatable copper substrate and irradiated at 15 K by X-rays while the photodesorbing neutral species were probed in the gas phase by mass spectrometry. This allowed to derive quantitative X-ray photodesorption yields (expressed in

[1] LERMA, Sorbonne Univ., Observatoire de Paris, CNRS, 75014 Paris, France
[2] Fritz-Haber Institute of the Max Planck Society, Berlin, Germany
[3] ICP, Univ Paris Saclay, CNRS, 91405 Orsay, France
[4] ISMO, Univ Paris Saclay, CNRS, 91405 Orsay, France

molecule desorbed by incident photon, displayed as molecule/photon in the following) that are representative of the efficiency of X-rays to desorb a given molecule. The copper substrate is also electrically insulated from its sample holder by a Kapton foil, which allows a measurement of the drain current generated by the escape of electrons from the ice surface after X-ray absorption, referred to as the Total Electron Yield (TEY) in the following. The critical influence of several parameters on the X-ray photodesorption yields, such as the ice composition (mainly the influence of CO and H_2O molecules) and the incident photon energy, allows to shed light on the chemical and physical mechanisms at play in these X-ray irradiated organic ices. The main results of these findings, from Basalgète et al. 2021a and Basalgète et al. 2021b, will be presented in the next sections.

2 Experimental results

2.1 Photodesorption spectra

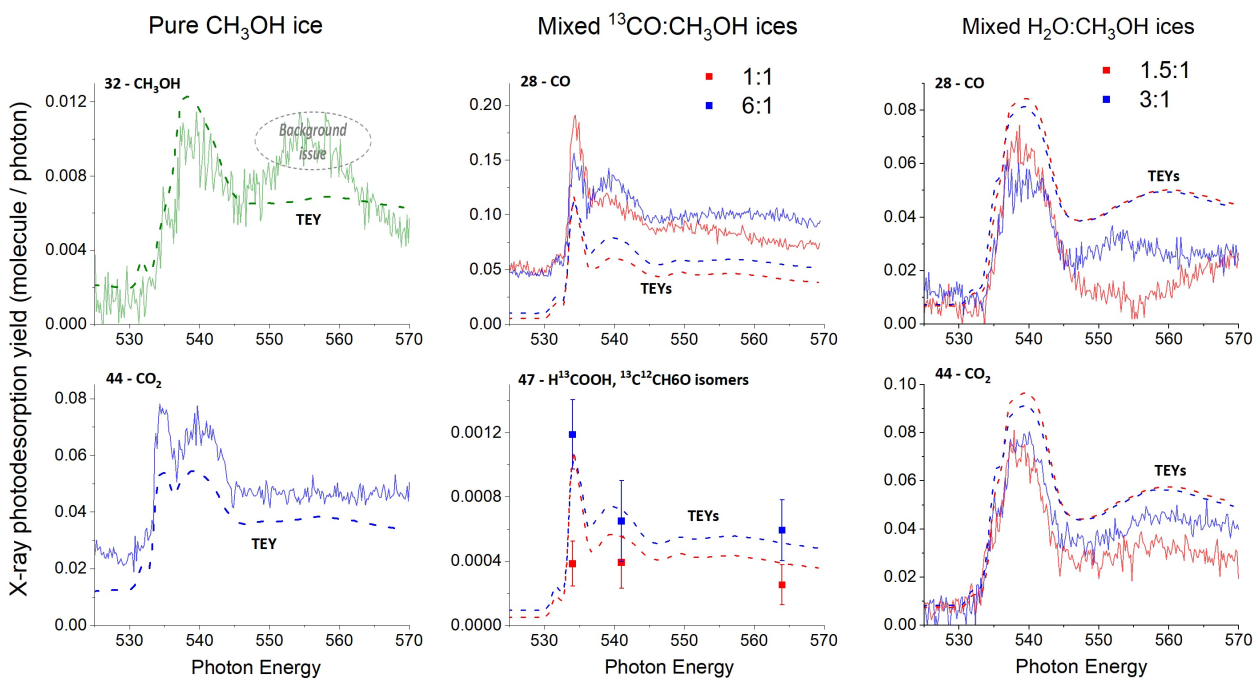

Fig. 1. X-ray photodesorption yields (solid noisy lines and squares with error bars) as a function of the incident photon energy, from pure methanol ice (left panels), mixed $^{13}CO:CH_3OH$ ices (middle panels) and mixed $H_2O:CH_3OH$ ices (right panels). In dashed lines is also displayed the Total Electron Yield (TEY) measured simultaneously during the irradiations. These data are adapted from (Basalgète et al. 2021a,b)

In Figure 1, we present some examples, from Basalgète et al. 2021a and Basalgète et al. 2021b, of molecules detected as photodesorbing in the gas phase during the X-ray irradiation of the ices tested : pure methanol ices and mixed $^{13}CO:CH_3OH$ and $H_2O:CH_3OH$ ices. We also displayed the Total Electron Yield (TEY) in dashed lines. The TEY is a direct measurement of the drain current escaping the ice after the X-ray absorption. It is due to the release of an Auger electron ($\sim$ 500 eV) in the ice after relaxation of the core excited states of oxygen-bearing molecules, which thermalizes within the ice, ionizing the surrounding molecules and creating secondary low energy electrons that escapes the ice surface. The TEY is proportional to the X-ray absorption cross section of the molecules present in the ice. Its energy features are typical of the X-ray absorption structure of the molecules studied and can be directly compared to X-ray spectroscopy studies (Püttner et al. 1999; Parent et al. 2002; Wilson et al. 2005; Laffon et al. 2006). As one can see in Figure 1, there is a good correlation between the TEYs and the photodesorption spectra of the molecules detected for each ice tested. This shows that the photodesorption process is well-correlated with the X-ray absorption profile of the ice and this implies that the X-ray photodesorption yields are strongly dependent on the ice composition and the incident photon energy.

2.2 X-ray photodesorption of methanol and ice composition

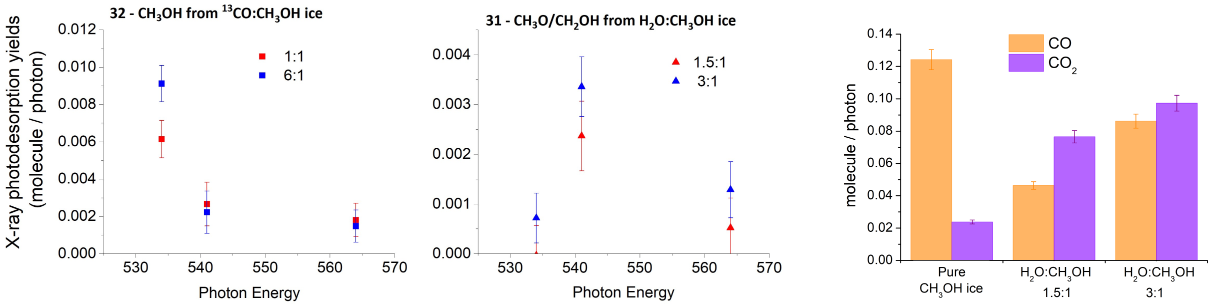

Fig. 2. X-ray photodesorption yield of CH_3OH (mass 32) from mixed $^{13}CO:CH_3OH$ ices (left panel) and of CH_2OH and/or CH_3O radical (mass 31) from mixed $H_2O:CH_3OH$ ices (middle panel) as a function of the incident photon energy. Right panel: comparison of CO and CO_2 X-ray photodesorption yields at 565 eV from pure CH_3OH ice and mixed $H_2O:CH_3OH$ ices. These results are taken from Basalgète et al. 2021b.

X-ray photodesorption of CH_3OH from mixed $^{13}CO:CH_3OH$ ices is detected in our experiments with a yield of the order of 10^{-2} molecule/photon (see left panel of Figure 2). However, when methanol is mixed in water ice, the X-ray photodesorption of CH_3OH is not detected anymore (with a detection upper limit of 5×10^{-4} molecule/photon) and we observe instead the photodesorption of radicals that could be attributed to either CH_3O or CH_2OH (see middle panel of Figure 2). These results can be nicely explained as a consequence of the chemistry induced by X-rays in the ice. This has been studied in the case of mixed methanol-water ices by Laffon et al. 2010. In their work, they observed the appearance and disappearance of NEXAFS peaks around the C K-edge in X-ray irradiated $H_2O:CH_3OH$ ices and they deduced a corresponding chemical reaction network that can be summarized as followed and in which the radical OH is playing a major role:

$$\mathrm{H_2O} \xrightarrow{(h\nu,e^-)} \mathrm{OH} + \mathrm{H} \tag{2.1}$$
$$\mathrm{CH_3OH} + \mathrm{OH} \longrightarrow \mathrm{CH_3O/CH_2OH} + \mathrm{H_2O} \tag{2.2}$$
$$\mathrm{CO} + \mathrm{OH} \longrightarrow \mathrm{CO_2} + \mathrm{H} \tag{2.3}$$

When comparing this chemical network to our X-ray photodesorption yields, a good agreement can be found. In fact, we do not observe the X-ray photodesorption of CH_3OH when it is mixed in water ice, which can be explained by the fact that it is chemically destroyed by reacting with OH. Instead, we observe the photodesorption of the products of this reaction which can be attributed to either CH_3O or CH_2OH radical. Moreover, when comparing the X-ray photodesorption yields at 565 eV of CO and CO_2 between pure CH_3OH and mixed $H_2O:CH_3OH$ ices (see right panel of Figure 2), we see that the X-ray photodesorption yield of CO_2 is higher than the one of CO in the case of mixed $H_2O:CH_3OH$ ice. In the case of pure methanol ice, we observe the opposite. These observations could be explained by the last reaction of the chemical network presented above, in which CO is reacting with OH to form CO_2 only in the case of mixed $H_2O:CH_3OH$ ice. X-ray photodesorption from methanol-containing ices is thus well correlated with the X-ray induced chemistry happening at the ice surface.

2.3 Implications for protoplanetary disks

YSOs (Class I, Class II, and Class III) have been shown to be X-ray emitters in the range of 0.1–10 keV (Imanishi et al. 2003; Ozawa et al. 2005; Giardino et al. 2007) with a typical luminosity of 10^{30} erg.s^{-1}. This X-ray radiation field can reach regions of protoplanetary disks that are shielded from VUV photons (Agundez et al. 2018; Walsh et al. 2015), and can originate from the central star and also from other surrounding young stars inside an YSO cluster, thus irradiating the disk out of its plane (Adams et al. 2012). Moreover, the stellar winds and the magnetic field structure produced by the YSO can reduce the cosmic-ray flux incident on the protoplanetary disk (Cleeves et al. 2013) such that, in some regions, the X-ray flux may be dominant over the other sources of irradiation. In that sense, our experimental results clearly show that X-ray photodesorption from interstellar ices in these regions should participate in the enrichment of the gas phase with molecules of astrochemical interest. As it has been demonstrated in the previous sections, this process is strongly dependent on the ice composition and should produce different outcomes depending on the region considered. In the regions where the surface temperature of the ices is below 20 K, regions in which the ices are expected to have an upper CO-rich phase with some traces of CH_3OH, X-rays should photodesorb COMs such as methanol, formic acid, dimethyl ether and/or ethanol in the gas phase. In the regions where the surface temperature of the ices is between 100 K and 20 K, regions in which the ices are expected to have an H_2O-rich phase with some traces of CH_3OH, X-ray photodesorption of the previous COMs is quenched and X-ray photodesorption of radicals such as CH_3O or CH_2OH should be observed.

3 Conclusions

X-ray photodesorption from methanol-containing ices is a process capable of explaining the presence of CH_3OH and other COMs (such as formic acid, dimethyl ether and/or ethanol) in the gas phase of the cold regions of protoplanetary disks, beyond CO snowlines. Experimentally, X-ray photodesorption of CH_3OH from H_2O-rich and CH_3OH-poor ices is not detected. Our results allows to better understand the presence of COMs such as CH_3OH in the gas phase of protoplanetary disks as a function of the ice composition and the incident X-ray energy. The experimental yields derived could also be incorporated in disk modeling.

This work was done with financial support from the Region Ile-de-France DIM-ACAV+ program and by the European Organization for Nuclear Research (CERN) under the collaboration Agreement No. KE3324/TE. We would like to acknowledge SOLEIL for provision of synchrotron radiation facilities under Project Nos. 20181140, and we thank N. Jaouen, H. Popescu and R. Gaudemer for their help on the SEXTANTS beam line. This work was supported by the Programme National "Physique et Chimie du Milieu Interstellaire" (PCMI) of CNRS/INSU with INC/INP co-funded by CEA and CNES. Financial support from the LabEx MiChem, part of the French state funds managed by the ANR within the investissements d'avenir program under Reference No. ANR-11-10EX-0004-02, is gratefully acknowledged. We also acknowledge support from the ANR PIXyES project, grant ANR-20-CE30-0018 of the French "Agence Nationale de la Recherche".

References

Adams, F. C., Fatuzzo, M., & Holden, L. 2012, Publications of the Astronomical Society of the Pacific, 124, 913
Agundez, M., Roueff, E., Petit, F. L., & Bourlot, J. L. 2018, Astronomy & Astrophysics, 616, A19
Basalgète, R., Dupuy, R., Féraud, G., et al. 2021a, Astronomy & Astrophysics, 647, A35
Basalgète, R., Dupuy, R., Féraud, G., et al. 2021b, Astronomy & Astrophysics, 647, A36
Bertin, M., Romanzin, C., Doronin, M., et al. 2016, The Astrophysical Journal, 817, L12
Boogert, A. A., Gerakines, P. A., & Whittet, D. C. 2015, Annual Review of Astronomy and Astrophysics, 53, 541
Ciaravella, A., Muñoz Caro, G. M., Jiménez-Escobar, A., et al. 2020, Proceedings of the National Academy of Sciences, 202005225
Cleeves, L. I., Adams, F. C., & Bergin, E. A. 2013, The Astrophysical Journal, 772, 5
Cruz-Diaz, G. A., Martìn-Doménech, R., Muñoz Caro, G. M., & Chen, Y.-J. 2016, Astronomy & Astrophysics, 592, A68
Dartois, E., Chabot, M., Bacmann, A., et al. 2020, Astronomy & Astrophysics, 634, A103
Dupuy, R., Bertin, M., Féraud, G., et al. 2018, Nature Astronomy, 2, 796
Giardino, G., Favata, F., Micela, G., Sciortino, S., & Winston, E. 2007, Astronomy & Astrophysics, 463, 275
Imanishi, K., Nakajima, H., Tsujimoto, M., & Koyama, K. 2003, PASJ, 55, 29
Laffon, C., Lacombe, S., Bournel, F., & Parent, P. 2006, The Journal of Chemical Physics, 125, 204714
Laffon, C., Lasne, J., Bournel, F., et al. 2010, Physical Chemistry Chemical Physics, 12, 10865
Öberg, K. I., Garrod, R. T., van Dishoeck, E. F., & Linnartz, H. 2009, Astronomy & Astrophysics, 504, 891
Ozawa, H., Grosso, N., & Montmerle, T. 2005, Astronomy & Astrophysics, 429, 963
Parent, P., Laffon, C., Mangeney, C., Bournel, F., & Tronc, M. 2002, The Journal of Chemical Physics, 117, 10842
Püttner, R., Dominguez, I., Morgan, T. J., et al. 1999, Physical Review A, 59, 3415
Walsh, C., Loomis, R. A., Öberg, K. I., et al. 2016, The Astrophysical Journal, 823, L10
Walsh, C., Nomura, H., & van Dishoeck, E. 2015, Astronomy & Astrophysics, 582, A88
Wilson, K. R., Cavalleri, M., Rude, B. S., et al. 2005, The Journal of Physical Chemistry B, 109, 10194

SF2A 2021
A. Siebert, K. Baillié, E. Lagadec, N. Lagarde, J. Malzac, J.-B. Marquette, M. N'Diaye, J. Richard, O. Venot (eds)

ASTROCHEMISTRY DURING THE CLASS I PHASE: THE PROTOSTELLAR HERITAGE

E. Bianchi[1]

Abstract. Solar System is the result of a complex star formation process still far to be fully understood. Chemical complexity builds up at each step of this process, starting from simple molecules and ending up with prebiotic species, until the appearance of life on Earth. It is still unclear how the chemical complexity evolves during the process leading to the formation of a Sun and its planetary system and if the chemical complexity we observe nowadays is inherited from the early protostellar stages or, instead, if there is a complete chemical reset during the star formation process. A powerful way to start answering these questions is by comparing the observed astrochemical content in young protostars with that in comets and asteroids, i.e. with the most pristine known material from which our Solar System formed. Protoplanetary disks observations suggest that planets could start to form very early when the protostar is still embedded in a prominent envelope (less than 1 Myr). For this reason, young protostellar disks in the Class 0/I stage are the perfect laboratory where to study the initial conditions and the chemical content of planetesimal formation. I will show how we can explore the chemical composition of young protostellar systems through multiwavelenght observations using both single-dish telescopes and interferometer to sample the different spatial scales, from the infalling envelope ($\sim$ 10000 au) down to the planet formation region ($\sim$ 50 au).

Keywords: astrochemistry, star formation, large carbon chains

1 Introduction

How does chemical complexity change during the process leading to the formation of a Sun and its planetary system? Is the chemical richness of a solar-like planetary system partially inherited from the early stages or is there a complete chemical reset? Recent evidence suggests that the formation of planets probably begins already in young protostellar discs (Class I phase $\geq 10^5$ yr). Therefore, the study of their chemical compositions represents a key step in our understanding of the initial material available for the formation of the planets. The protostellar phase is characterized by the molecular complexity blooming: when the inner 100 au protostellar envelope are heated at temperatures larger than 100 K, dust mantles products thermally sublimate and enrich the chemical composition of the gas (the so-called hot-corino phase). In addition, dramatic changes in the molecular abundances are expected also because of a warm gas-chemistry at work. While hot-corinos in Class 0 sources are relatively well-known, very little has been done so far to study the overall composition of more evolved Class I sources (age $\sim 10^5$ yr), which represent the link between the protostellar stage and the planetary system formation.

I will focus on the chemical complexity observed in Class I protostars. In particular, I will show the results we have obtained from the ASAI (Lefloch et al. 2018) and SOLIS (Ceccarelli et al. 2017) IRAM Large Programs and, more recently from FAUST (Bianchi et al. 2020), the first ALMA Large Program focused on astrochemistry. Using deuterated molecules and complex organic molecules, I will compare the chemical richness observed in Class I protostars with those observed in younger Class 0 protostars and in comets, representing the most pristine material in our solar system. I will present the possible evolutionary trends in order to study the inheritance scenario. I will also report future perspectives on Class I protostar studies and molecular exploration for the advent of SKA.

[1] Univ. Grenoble Alpes, CNRS, IPAG, 38000 Grenoble, France

2 The IRAM Large Programs ASAI and SOLIS

SVS13-A is the first Class I protostar for which a complete census of iCOMs emission has been obtained thanks to the synergy of two IRAM Large Programs: ASAI (Astrochemical Survey At IRAM-30m; Lefloch et al. 2018) with the 30m antenna and SOLIS (Seeds Of Life In Space; Ceccarelli et al. 2017) with the NOEMA interferometer. Thanks to the ASAI high-sensitivity unbiased spectral survey of the 3, 2 and 1.3 mm bands, we detected and analysed several emission lines from deuterated species and iCOMs. The complementary high-sensitivity and high-spatial resolution interferometric maps from SOLIS provided information on the molecular gas spatial distribution, allowing a precise determination of gas physical conditions (see Fig. 1). Different tracers such as deuterated formaldehyde, thioformaldehyde, cyanoacetylene, methanol, methyl cyanide and, water were used to reconstruct the physical and chemical structure of the protostellar system (Codella et al. 2016; Bianchi et al. 2017, 2019a). In general, the measured deuteration show a chemical connection among the different evolutionary stages. Interestingly, methanol deuteration seems to decrease in SVS13 A with respect to younger Class 0 sources, possibly indicating chemical evolution. Beside deuterated species, emission from several iCOMs such as ketene, acetaldehyde, methyl formate, dimethyl ether and ethanol, revealed for the first time a rich hot corino chemistry towards the source (Codella et al. 2016; Bianchi et al. 2019b). The comparison between iCOMs abundance ratios in SVS13 A with those measured in younger Class 0 protostars brought to light several similarities, suggesting that chemical complexity is transferred from the Class 0 to the Class I stage.

3 The ALMA FAUST project

The prototypical Class I source L1551 IRS5 has been observed as part of the ALMA Large Program FAUST (Fifty AU Study of the chemistry in the disk/envelope system of Solar-like protostars; Bianchi et al. 2020). More specifically, FAUST is the first ALMA Large Program dedicated to astrochemical studies and it is designed to survey the chemical composition of a sample of 13 Class 0 and I protostars at the planet formation scale (from $\sim$ 1000 down to $\sim$ 50 au. We detected in L1551 IRS 5 several emission lines from iCOMs (see Fig. 2) such as methanol (CH_3OH) and its most abundant isopotologue (CH_2DOH), as well as methyl formate ($HCOOCH_3$) and ethanol (a-CH_3CH_2OH). Line emission is bright toward the north component (N), although a hot corino in the south component, cannot be excluded. The non-LTE analysis of the methanol lines towards N provides constraints on the gas temperature ($\sim$ 100 K), density ($n_{H_2} \geq 1.5 \times 10^8$ cm^{-3}) and emitting size ($\sim 0\farcs15$, i.e. $\sim$ 10 au in radius). The lines are predicted to be optically thick, the $^{13}CH_3OH$ line having an opacity > 2. The methyl formate and ethanol column densities relative to methanol are ≤ 0.03 and ≤ 0.015, respectively, compatible with those measured in Class 0 sources. Thus, FAUST observations towards L1551 IRS5 agree with little chemical evolution in hot corinos from Class 0 to I, as previously suggested by the ASAI and SOLIS results.

4 Evidences for chemical inheritance ?

A way to test the inheritance scenario is to compare the relative abundances measured in young Class 0/I protostars with those measured in Solar System comets. Such an example is given in Fig. 3, where the protostellar molecular abundance ratios are compared with those observed in the comet 67P/Churyumov-Gerasimenko (ROSETTA mission, e.g. Rubin et al. 2019). Molecular abundance ratios are normalized to methanol and isomers are added because the ROSETTA mass spectrometer is not able to distinguish among them. More specifically, Fig. 3 shows measurements of SVS13-A, L1551 IRS5 and Ser-emb17 (Class I hot corinos), as well as younger Class 0 sources (Ser-emb1, Ser-emb8, HH212, IRAS16293-2422, IRAS4A, IRAS2A). Once considered the uncertainties, some iCOMs show a good agreement (within a factor of 10) suggesting chemical inheritance from the early stages (see also Drozdovskaya et al. 2019). Future perspectives include, as a first step, observational efforts to chemically characterise a larger sample of protostellar sources. In this respect, the forthcoming results of dedicated Large Programs, such as FAUST (Bianchi et al. 2020), will represent a major step ahead. On the other hand, complementary observations at radio wavelengths, for example using JVLA and, in a near future, SKA will be fundamental to overcome several limitations related to (sub-) mm-observations, such as dust opacity. An enlightening example is represented by the protostellar disk in HH212 as observed by ALMA down to 10 au scales (Lee et al. 2019): the continuum emission shows a dark equatorial lane due to high dust opacity, plus a rich iCOMs gas, detected only on the surface disk layers. Either (i) molecular abundance dramatically decreases in the equatorial disk, or (ii) iCOMs detection is hampered by the high opacity continuum (see e.g. De Simone et al. 2020). A decrease of the flux of molecular lines towards the central regions has been also observed using ALMA in more evolved Class I disks (see e.g. ALMA-DOT, Garufi et al. 2021). Only interferometric observation in the cm-domain can unveil the gaseous composition of protostellar disks mid-plane, the most interesting region for planets formation.

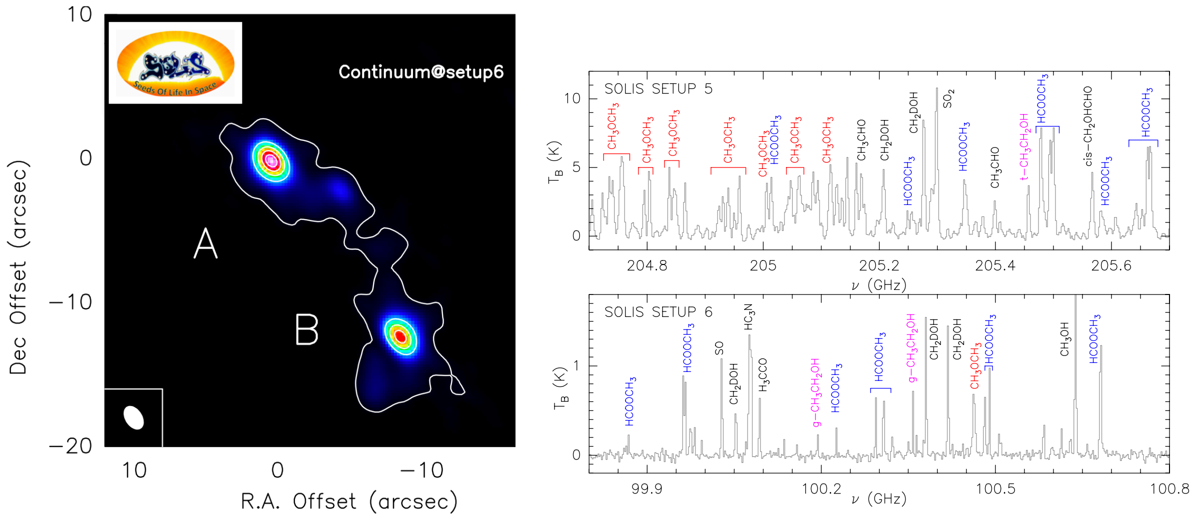

Fig. 1. Left: Continuum emission of the SVS13 system as observed by SOLIS NOEMA at 82 GHz. **Right:** Selected windows from SOLIS NOEMA observations, extracted towards the Class I protostar SVS13-A. Spectra show bright emission lines from several iCOMs including ethanol, methyl formate, acetaldehyde, dimethyl ether.

This project has received funding within the European Union's Horizon 2020 research and innovation programme from the European Research Council (ERC) for the project "The Dawn of Organic Chemistry" (DOC), grant agreement No 741002.

References

Bergner, J. B., Martín-Doménech, R., Öberg, K. I., et al. 2019, ACS Earth and Space Chemistry, 3, 1564

Bianchi, E., Ceccarelli, C., Codella, C., et al. 2019a, ACS Earth and Space Chemistry, 3, 2659

Bianchi, E., Chandler, C. J., Ceccarelli, C., et al. 2020, MNRAS, 498, L87

Bianchi, E., Codella, C., Ceccarelli, C., et al. 2017, MNRAS, 467, 3011

Bianchi, E., Codella, C., Ceccarelli, C., et al. 2019b, MNRAS, 483, 1850

Ceccarelli, C., Caselli, P., Fontani, F., et al. 2017, ApJ, 850, 176

Codella, C., Ceccarelli, C., Bianchi, E., et al. 2016, MNRAS, 462, L75

De Simone, M., Ceccarelli, C., Codella, C., et al. 2020, ApJ, 896, L3

Drozdovskaya, M. N., van Dishoeck, E. F., Rubin, M., Jørgensen, J. K., & Altwegg, K. 2019, MNRAS, 490, 50

Garufi, A., Podio, L., Codella, C., et al. 2021, A&A, 645, A145

Lee, C.-F., Codella, C., Li, Z.-Y., & Liu, S.-Y. 2019, ApJ, 876, 63

Lefloch, B., Bachiller, R., Ceccarelli, C., et al. 2018, MNRAS, 477, 4792

López-Sepulcre, A., Sakai, N., Neri, R., et al. 2017, A&A, 606, A121

Rodríguez, L. F., Porras, A., Claussen, M. J., et al. 2003, ApJ, 586, L137

Rubin, M., Bekaert, D. V., Broadley, M. W., Drozdovskaya, M. N., & Wampfler, S. F. 2019, ACS Earth and Space Chemistry, 3, 1792

Taquet, V., López-Sepulcre, A., Ceccarelli, C., et al. 2015, ApJ, 804, 81

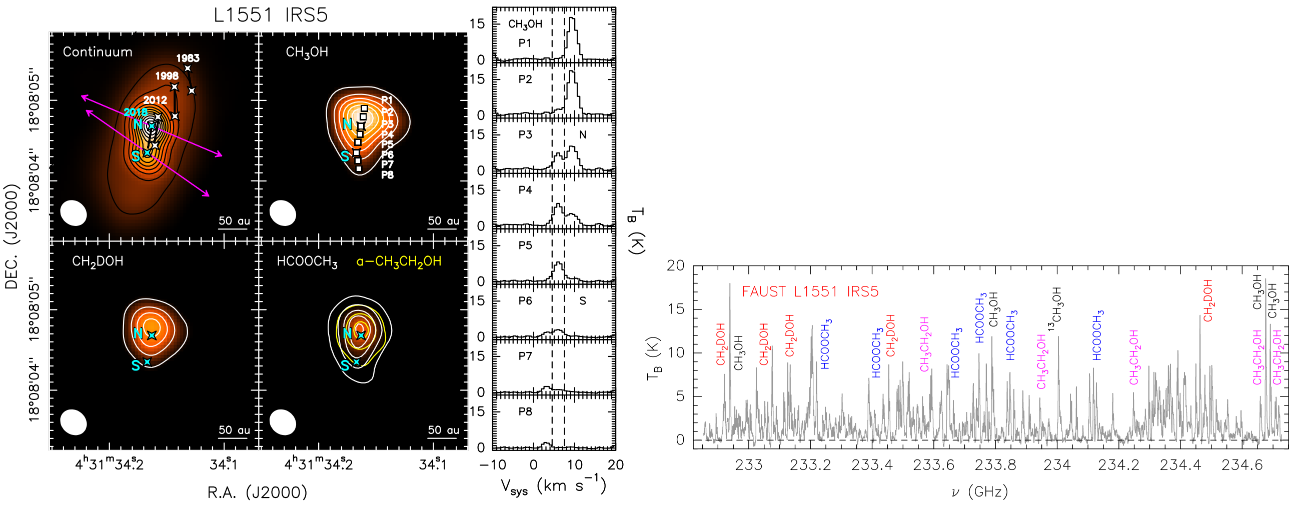

Fig. 2. Right panel: Dust and line emission as observed by FAUST towards the Class I protostellar system L1551 IRS5 (Bianchi et al. 2020). The white stars in the upper left panel indicate the positions of the binary system components (indicated as N, northern, and S, southern) measured from 1983 to 2018. The magenta arrows indicate the jet directions (Rodríguez et al. 2003). Emission from methanol and its deuterated isotopologue, methyl formate, and ethanol is detected on spatial scales comparable to our Solar System ($\sim$ 50 au). The ALMA beam is reported as a white ellipse in each panel. Maps show that iCOMs emission is present both in N and S, but it is brighter towards N, suggesting the presence of at least one hot corino. The white squares, labelled from P1 to P8, are the different positions where the spectra displayed on the right panels are extracted. The vertical dashed lines mark the systemic velocity inferred towards N (+7.5 km s1) and S (+4.5 km s1), respectively. **Right panel**: Observed line spectra (in T_B scale) towards the continuum peak position of the northern protostar N. The spectra show the chemical richness associated to the hot corino.

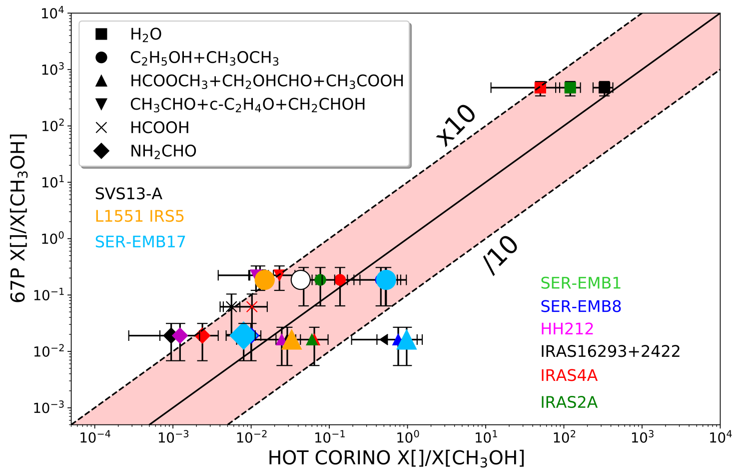

Fig. 3. Comparison of molecular abundance ratio of iCOMs observed in Class 0 and Class I hot corinos, including SVS13-A and L1551 IRS5, with those observed in the comet 67P/Churyumov-Gerasimenko (ROSETTA mission). Molecular abundance ratios are normalized to methanol and isomers are added because the ROSETTA mass spectrometer is not able to distinguish among them. Some molecular species, such as ethanol and dimethyl ether, show a striking agreement, within a factor of 10, suggesting chemical inheritance from the early stages. Measurements are from Rubin et al. (2019); Bianchi et al. (2017, 2019b, 2020); Bergner et al. (2019); Lee et al. (2019); Drozdovskaya et al. (2019); Taquet et al. (2015); López-Sepulcre et al. (2017).

CONSTRAINING THE DUST GRAIN ALIGNMENT MECHANISM(S) RESPONSIBLE FOR THE (SUB-)MILLIMETER DUST POLARIZATION OBSERVED IN CLASS 0 PROTOSTELLAR CORES

V. J. M. Le Gouellec[1,2], A. J. Maury[2,3] and C. L. H. Hull[4,5,6]

Abstract. With the aim of characterizing the role played by magnetic fields in the formation of young protostars, several recent studies have revealed unprecedented features toward high angular resolution ALMA dust polarization observations of Class 0 protostellar cores. Especially, the dust polarization has been found to be enhanced along the irradiated cavity walls of bipolar outflows, but also in region most likely linked with the infalling envelope, in the form of filamentary structure being potential magnetized accretion streamer. These observations allow us to investigate the physical processes involved in the Radiative Alignment Torques (RATs) acting on dust grains from the core to disk scales. Synthetic observations of non-ideal magneto-hydrodynamic simulations of protostellar cores implementing RATs, show that the ALMA values of grain alignment efficiency lie among those predicted by a perfect alignment of grains, and are significantly higher than the ones obtained with the standard RAT alignment of paramagnetic grains. Ultimately, our results suggest dust alignment mechanism(s) are efficient at producing polarized dust emission in the local conditions typical of Class 0 protostars. However, further study leading to a better characterization of dust grain characteristics, or additional grain alignment mechanisms, will be required to investigate the cause of strong polarized dust emission located in regions of the envelope where alignment conditions are not favorable. A new attempt aiming at a better characterization of the dust grain alignment mechanism(s) occurring in young star forming objects, is to investigate the chemistry going on in those cores, and see if the local physical conditions (irradiation, temperature) can reconcile both molecular line emission and dust polarization observations.

Keywords: ISM: jets and outflows – ISM: magnetic fields – polarization – stars: formation – stars: magnetic field – stars: protostars

1 Introduction

Protostellar formation is ruled by various competing dynamical processes. Once a prestellar core has undergone gravitational collapse, a protostar is formed; the so-called Class 0 phase corresponds to the stage when the protostar is accreting material from the surrounding envelope. During this phase, the magnetic field is thought to regulate the collapse of the envelope redistributing the angular momentum. A variety of mechanisms have been proposed to explain the removal of angular momentum from the rotating envelope, including binary formation via turbulent fragmentation (Offner et al. 2010), as well as the launching of jets and outflows. These processes are intimately linked with the magnetic field, which has the capability to extract angular momentum from the rotating core via magnetic braking, which in turn can suppress the formation of large disks at early times (Hennebelle & Ciardi 2009). In addition, magnetic field morphology in the inner core of protostars have been found to be affected by protostellar outflows, suggesting magnetic fields can be dynamically overwhelmed by the outflowing activity (Hull et al. 2017).

[1] European Southern Observatory, Alonso de Córdova 3107, Vitacura, Santiago, Chile
[2] AIM, CEA, CNRS, Université Paris-Saclay, Université Paris Diderot, Sorbonne Paris Cité, F-91191 Gif-sur-Yvette, France
[3] Harvard-Smithsonian Center for Astrophysics, Cambridge, MA 02138, USA
[4] National Astronomical Observatory of Japan, NAOJ Chile Observatory , Alonso de Córdova 3788, Office 61B, 7630422, Vitacura, Santiago, Chile
[5] Joint ALMA Observatory, Alonso de Córdova 3107, Vitacura, Santiago, Chile
[6] NAOJ Fellow

At the spatial scales now probed by ALMA, one can access to the magnetic field morphology of the inner regions of Class 0 protostellar cores. One way to characterize the morphology of magnetic fields is to observe the polarized thermal emission from dust grains. Indeed, since dust grains are not perfectly spherical, they tend to align themselves with the ambient magnetic field under some conditions via the action of Radiative Alignment Torques (RATs, (Lazarian & Hoang 2007; Andersson et al. 2015)). This linear polarization emanating from this dust grain population is orthogonal to the magnetic field component projected on the plane of the sky, and integrated along the line of sight. The aim of our work is to assess whether RATs are efficient at producing the polarized dust emission revealed by ALMA observations toward the interior of star forming cores, and if additional grain alignment mechanisms can occur. This requires a deep understanding of the physical conditions of these regions.

2 ALMA dust polarization observations

The recent ALMA observations of Class 0 envelopes revealed a variety of magnetic field morphology, toward specific regions of the core where the polarized dust emission was found to be strongly enhanced, namely the walls of the bipolar outflow cavities, filament-like structures that are potential magnetized accretion streamers, and core equatorial planes (Hull et al. 2017; Maury et al. 2018; Sadavoy et al. 2018a,b; Kwon et al. 2019; Takahashi et al. 2019; Le Gouellec et al. 2019; Hull et al. 2020). An example is shown if Figure 1, where we present ALMA observations of two Class 0 star forming cores located in the Serpens Main star forming region, Serpens Emb 8(N) and Serpens SMM1 (Le Gouellec et al. 2019). Serpens Emb 8(N), a low-mass protostellar core, exhibits enhanced polarized dust emission surrounding the two outflow lobes, suggesting an organized magnetic field. The core appears axisymmetric, and a powerful extremely high velocity (EHV) jet is launched from the central protostellar regions. Serpens SMM1 corresponds to a clump of cores, whose central one SMM1-a, is an intermediate-mass protostellar core, and launches a broad low-velocity outflow as well as an EHV jet of the redshifted side. The polarized dust emission is very different, with notably two crossing highly polarized filament-like structures to the South of the source. One is thought to correspond to an outflow cavity walls, while the other is more likely a streaming funnelling material to the central hot-corino.

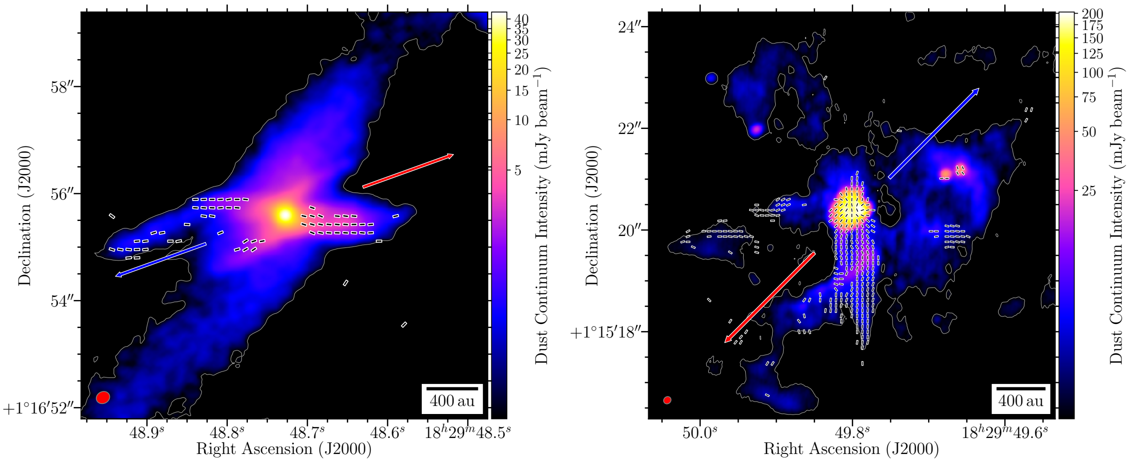

Fig. 1. Magnetic field around Serpens Emb 8(N) (left panel) and Serpens SMM1 (right panel) from (Le Gouellec et al. 2019). Line segments represent the magnetic field orientation. The color scale is the total intensity (Stokes I) of the thermal dust emission. The blue and red arrows represent the directions of the blueshifted and redshifted lobes of the bipolar outflow, respectively. The polarized emission is clearly enhanced along the outflow cavity walls visible here in the dust thermal emission.

3 Estimating the dust grain alignment efficiency

These highly polarized structures raised several questions concerning the grain alignment mechanism responsible for this grain alignment. The average level of fractional polarization $\mathcal{P}_{\rm frac}$ was high compared to what was expected from RATs, and the thermal emission is only polarized toward specific regions of the inner core. A solution has been to consider both the effects of interferometric filtering, and the impact of the disorganized component of the apparent magnetic along the line-of-sight, on the measurement of polarization fraction. To do so we applied the method developed in Planck Collaboration et al. (2020) for *Planck* observations, on a set of ALMA observations of Class 0 cores (Le Gouellec et al. 2020). The disorganized component of the apparent magnetic impacts the dispersion of polarization position angle in the plane of the sky $\mathcal{S}$, and the depolarization along the line-of-sight. The idea is that assuming this disorganized component is isotropic, one could correct its impact on the depolarization measured in the polarization fraction, multiplying $\mathcal{P}_{\rm frac}$ by $\mathcal{S}$.

As shown in Figure 2, we compare the values of $\mathcal{S} \times \mathcal{P}_{\rm frac}$ in the ALMA observations, with MHD models of protostars performed with collaborators with the state of-the-art RAMSES code, synthetically observed by the polarization radiative transfer code POLARIS (Reissl et al. 2016). Our analysis resulted in the discovery that the grain alignment efficiency is approximately constant across the three orders of magnitude in envelope column density probed by the ALMA observations. Thanks to these comparisons, we also found that the ALMA values of grain alignment efficiency are notably higher than what the classical RAT theory can produce, and are typically reaching values reproduced if we assume perfect alignment (PA) in our models. We concluded that a more detailed understanding of the dust grain characteristics and/or the proof that additional grain alignment mechanisms are occurring, will be required to complete our picture of dust polarization.

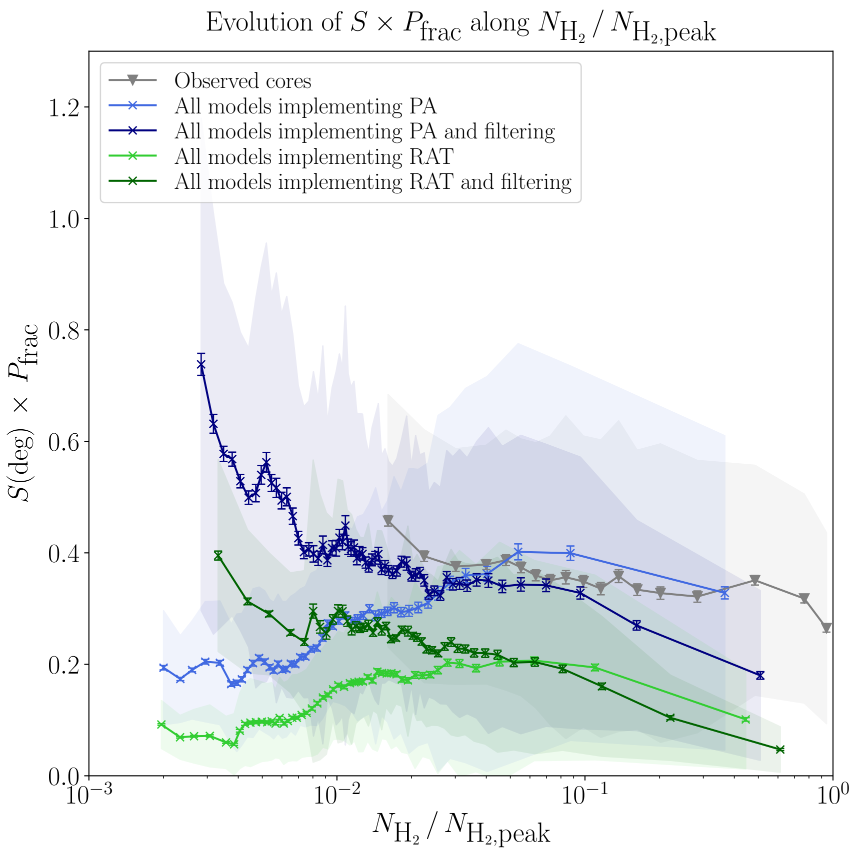

Fig. 2. Observed distributions of the mean values of $\mathcal{S} \times \mathcal{P}_{\rm frac}$ as a function of the column density $N_{\rm H_2}$ (normalized by its maximum value, $N_{\rm H_2,peak}$) of ALMA observations of Class 0 protostellar cores (triangles) and of MHD models (crosses) synthetically observed by the radiative transfer code POLARIS. The four lines representing the simulations correspond to results using RATs or perfect alignment (PA), both filtered and not filtered. The shaded areas represent the standard deviation of the Gaussian fit performed on each bin of points. The error bars correspond to these standard deviation values divided by the square root of the number of points in each bin. Taken from Le Gouellec et al. (2020).

4 Radiative transfer modelling of polarized dust emission

To reproduce the high level of grain alignment efficiency measured in ALMA observations, we developed further detailed MHD models to first reproduce the structures of the inner regions in Class 0 envelope, i.e. outflow cavity walls and filament-like accreting structures. Thanks to POLARIS, we can vary several parameters, linked to the dust grain characteristics (their size, shape and paramagnetic susceptibility) as well as to the local conditions of irradiation. The aim in to target the conditions that would reproduce the behavior of grains aligned by RATs. If RATs is responsible for the polarization we observe, we need to implement large grains (≥ 10 μm in size), super-paramagnetic grains (to ensure that a large fraction of grains rotate suprathermally), and high irradiation conditions (central luminosity ≥ 20 $L_\odot$) in our models of intermediate-mass protostellar cores to increase the grain alignment efficiency, which is still not entirely reproduced. This encourages us to investigate further mechanisms, such as mechanically aligned grains (Hoang et al. 2018), grain aligned with the radiation field anisotropy (Lazarian & Hoang 2007), and rotational disruption of grains (Hoang et al. 2019), in order to reconcile dust polarization observations and our knowledge of dust characteristics, grain alignment mechanisms, and local conditions, on the interior of protostars. An ultimate goal will be to compare these constrains on the environmental conditions in the interior of protostars with the results brought by the analysis of molecular emission lines detected toward these regions. Several molecules (like hydrocarbons chains such as C_2H or c-C_3H_2), whose chemical formation pathway requires significant irradiation have been detected toward outflow cavities. Qualitative comparisons between the polarized dust emission and the emission from such molecules could bring further clues on the characteristics of the aligned dust grains dust and magnetic fields of the inner regions of Class 0 protostellar cores.

References

Andersson, B.-G., Lazarian, A., & Vaillancourt, J. E. 2015, ARA&A, 53, 501
Hennebelle, P. & Ciardi, A. 2009, A&A, 506, L29
Hoang, T., Cho, J., & Lazarian, A. 2018, ApJ, 852, 129
Hoang, T., Tram, L. N., Lee, H., & Ahn, S.-H. 2019, Nature Astronomy, 3, 766
Hull, C. L. H., Girart, J. M., Tychoniec, Ł., et al. 2017, ApJ, 847, 92
Hull, C. L. H., Le Gouellec, V. J. M., Girart, J. M., Tobin, J. J., & Bourke, T. L. 2020, ApJ, 892, 152
Kwon, W., Stephens, I. W., Tobin, J. J., et al. 2019, ApJ, 879, 25
Lazarian, A. & Hoang, T. 2007, MNRAS, 378, 910
Le Gouellec, V. J. M., Hull, C. L. H., Maury, A. J., et al. 2019, ApJ, 885, 106
Le Gouellec, V. J. M., Maury, A. J., Guillet, V., et al. 2020, A&A, 644, A11
Maury, A. J., Girart, J. M., Zhang, Q., et al. 2018, MNRAS, 477, 2760
Offner, S. S. R., Kratter, K. M., Matzner, C. D., Krumholz, M. R., & Klein, R. I. 2010, ApJ, 725, 1485
Planck Collaboration, Aghanim, N., Akrami, Y., et al. 2020, A&A, 641, A12
Reissl, S., Wolf, S., & Brauer, R. 2016, A&A, 593, A87
Sadavoy, S. I., Myers, P. C., Stephens, I. W., et al. 2018a, ApJ, 859, 165
Sadavoy, S. I., Myers, P. C., Stephens, I. W., et al. 2018b, ApJ, 869, 115
Takahashi, S., Machida, M. N., Tomisaka, K., et al. 2019, ApJ, 872, 70

SF2A 2021
A. Siebert, K. Baillié, E. Lagadec, N. Lagarde, J. Malzac, J.-B. Marquette, M. N'Diaye, J. Richard, O. Venot (eds)

DYNAMICAL EFFECTS OF THE RADIATIVE STELLAR FEEDBACK ON THE H/H_2 TRANSITION

V. Maillard[1], E. Bron[1] and F. Le Petit[1]

Abstract. Molecular clouds are surrounded by an atomic layer where hydrogen is in atomic form (H) instead of molecular form (H_2). The depth where H_2 becomes more abundant than H is called the H/H_2 transition. This transition controls the fraction of molecular gas, which constitutes the mass reservoir for star formation, as evidenced by the Schmidt-Kennicutt law. Theoretical descriptions of this H/H_2 transition have been proposed in the case where the gas is assumed static (Sternberg et al. 2014). In star forming regions, however, Herschel and spatially-resolved ALMA observations (Joblin et al. 2018; Wu et al. 2018; Goicoechea et al. 2016) have revealed important dynamical effects at the PDR edges of molecular clouds, which could be explained by photo-evaporation (Bron et al. 2018) resulting in an advance of the ionization front into the neutral gas, or, equivalently, to neutral gas being advected through the PDR. We extend the analytic theory of the H/H_2 transition to include the dynamics of the gas induced by photo-evaporation and find its consequences on the total atomic hydrogen column density at the surface of clouds in presence of a strong UV field, and on the properties of the H/H_2 transition. We also include H_2 formation on grains, H_2 photodissociation, H_2 self-shielding and metallicity-dependence. The advection of gas through the H/H_2 transition caused by photo-evaporation reduces the width of the atomic region compared to static models. The atomic region may disappear if the ionization front velocity exceeds a certain value, leading the H/H_2 transition and the ionization front to merge. We provide analytical expressions to determine the total HI column density. Finally, we compared our results to observations of PDR illuminated by O-stars, for which we conclude that the dynamical effects are strong, especially for low-excitation PDRs. Some H_2 is then expected to be closer to the edge, in a hot and FUV-rich region, where H_2 lines are more intense. These lines will be the focus of upcoming James Webb Space Telescope (JWST) observations.

Keywords: galaxies: ISM, ISM: clouds, ISM: structure, ISM: dynamics, ISM: photon-dominated region (PDR), stars: formation

1 Introduction

In the atomic envelop surrounding a molecular cloud, the transition where molecular hydrogen turns into atomic hydrogen is called the H/H_2 transition, or the dissociation front (DF). It gives us information on the total fraction of molecular gas in a cloud where stars form through gravitational collapse of the gas. From transition models, one can get the total H I column density and the H_2 mass fraction which is linked to star-formation by the Schmidt-Kennicutt relations. Analytical models of the H/H_2 transitions are widely used to predict the column density of the atomic surface layer (Wong et al. 2009; Lee et al. 2012; Bialy et al. 2017). The most recent model of Sternberg et al. (2014) derived an analytic formula for the total H I column density for a cloud with one-dimensional planar geometry. In this analytic theory, the fluid is assumed to be static and the chemistry to be at a stationary state. However, Herschel observations of excited lines in strongly UV-illuminated galactic PDRs (Joblin et al. 2018; Wu et al. 2018) revealed dynamical effects. They indicate a thin compressed surface layer (10^{-3} pc) with a thermal pressure well above its environment at the edge of the PDR ($P_{\rm th} \sim 10^8\,{\rm K\,cm^{-3}}$). The gas thermal pressure was found to be strongly correlated to the UV field intensity, which was proposed to be a consequence of photoevaporation of the PDR. When a star illuminates a neutral cloud, its surface is heated and ionized by the radiation field. If the pressure in the H II region is not sufficient to contain the heated

[1] LERMA, Observatoire de Paris, PSL University, CNRS, Sorbonne Université, 92190 Meudon, France
e-mail: vincent.maillard@observatoiredeparis.psl.eu

gas (as for instance in blister H II regions), a photo-evaporation flow of ionized gas streams from the neutral cloud into the H II region, and the ionization front (IF) propagates into the neutral gas. This mechanism has been studied in the past by Bertoldi & Draine (1996) for neutral globules embedded in H II region. Numerical models of photo-evaporating PDRs with the time-dependent and dynamical *Hydra PDR Code* (Bron et al. 2018) reproduced the pressure structure and the correlation of the pressure with the UV radiation field. An extension of Sternberg et al. (2014) to include the effects of photo-evaporation is thus necessary. In this paper, we present a new semi-analytical theory of the H/H_2 transition to take into account the propagating IF. As in Störzer & Hollenbach (1998), we model this propagation with a constant advection velocity, and find the structure of the PDR by solving the stationary equation of the chemistry including advection.

2 Analytic overview

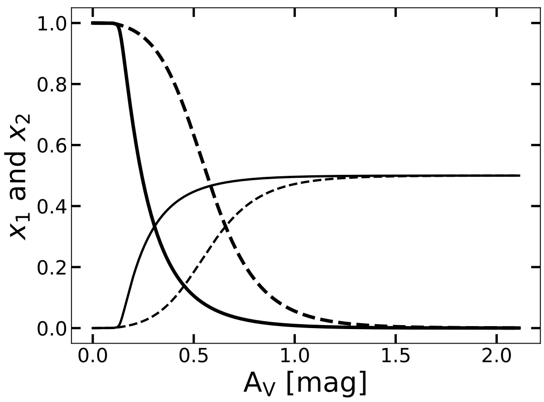

Fig. 1. Abundances of H and H_2 as functions of A_V for $G_0/n_H = 0.2$ cm^3. The dashed lines are obtained with $v_{IF} = 0$ km s^{-1} and the solid lines for a propagating IF with $v_{IF} = 0.79$ km s^{-1}. The radiation field comes from the left, where the gas is mostly atomic.

To take into account the propagation of the IF into the neutral gas with a velocity v_{IF}, we place ourselves in the frame of rest of the IF. In this reference frame, its propagation takes the form of an advection velocity of the neutral gas with an equal velocity in the opposite direction (towards the IF). We introduce the stationary state equation of the molecular hydrogen density $n(H_2)$, which gives its spatial profile as a function of the velocity v_{IF}, the FUV field intensity G_0 in Habing unit (Habing 1968; Draine 2011) and the uniform gas density n_H.

$$0 = R\, n_H\, n(\mathrm{H}) - G_0\, \mathcal{P}_0\, e^{-\sigma_g N}\, f_{\mathrm{shield}}(N(\mathrm{H_2}))\, n(\mathrm{H_2}) + v_{\mathrm{IF}}\, \frac{dn(\mathrm{H_2})}{dx}. \tag{2.1}$$

In this equation, there are three terms representing the processes taken into account in the stationary state. The first term represents the formation of H_2 on dust grains with a rate $R = 3 \times 10^{-17}\, Z'$ cm^3 s^{-1}, where Z' is the metallicity, defined as the ratio between heavy elements abundances in the cloud and in the solar photosphere. $n(\mathrm{H})$ is the density of atomic hydrogen. The second term is the photodissociation rate of H_2 by FUV photons (with $\mathcal{P}_0 = 3.3 \times 10^{-11}$ s^{-1}), which accounts for extinction both by dust with absorption cross-section $\sigma_g = 1.9 \times 10^{-21}\, Z'$ cm^2 and with N the hydrogen nuclei column density and by H_2 self-shielding, using the expression from Draine & Bertoldi (1996):

$$f_{\mathrm{shield}}(N(\mathrm{H_2})) = \frac{0.965}{(1 + y/b_5)^2} + \frac{0.035}{(1 + y)^{0.5}} \times \exp\left[-8.5 \times 10^{-4}\,(1 + y)^{0.5}\right], \tag{2.2}$$

with $N(H_2)$ the H_2 column density, $y = N(\mathrm{H_2})/5 \times 10^{14}$ cm^{-2}, $b_5 = b/1$ km s^{-1} and $b = 2$ km s^{-1} the Doppler broadening parameter. The last term of Eq.(2.1) represents the advection of the neutral H_2 with velocity v_{IF} because of the propagation of the IF. We solved Eq.(2.1) numerically and present results for an example case in Fig. 1 with (dashed lines, $v_{IF} = 0$ km s^{-1}) and without the advection term (solid lines, $v_{IF} = 0.79$ km s^{-1}). For these two cases, we see the abundances of H and H_2 as functions of A_V for a G_0/n_H ratio of 0.2 cm^3. The gas is mainly atomic on the illuminated side of the cloud (left), and becomes molecular deeper into the cloud (right).

Advection brings H_2 from its reservoir in the core of the cloud to the edge, acting like a formation term. We thus see on Fig. 1 that the H/H_2 transition is shifted closer to the edge of the cloud (to the left) and presents a sharper transition profile.

3 Results

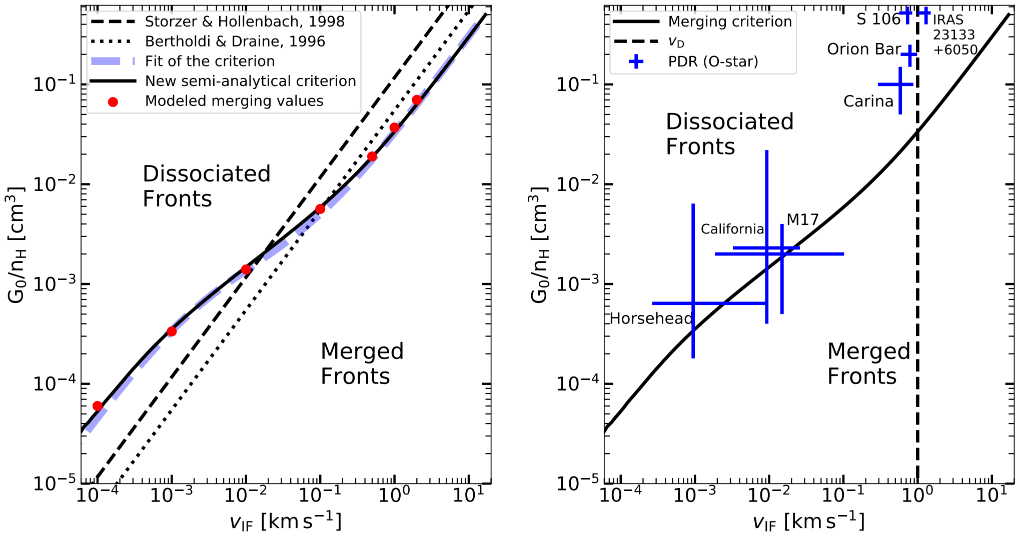

Fig. 2. Left: Frontier curves between the merged IF/DF regime and the unmerged regime. The black dotted line is the frontier derived by Bertoldi & Draine (1996), the black dashed line is the one of Störzer & Hollenbach (1998). The red circles are our results from a grid in the parameter space. The black line is our new semi-analytical frontier curve and the blue dashed line is a fit of a simpler analytical formula to this frontier curve. **Right:** Comparison between the merging frontier and deduced parameters $G_0/n_{\rm H}$ and $v_{\rm IF}$ for some observed PDRs illuminated by O stars. The vertical dashed bar at 1 km s^{-1} corresponds to the typical D-critical velocity from classical IF theory.

With a high-enough velocity, the atomic region disappears and we observe a merging (Bertoldi & Draine 1996) of the DF with the IF. When the IF propagates too fast in the medium, the DF cannot separate from the IF. We solved Eq.(2.1) for a grid of different $v_{\rm IF}$ and $G_0/n_{\rm H}$ ratio to determine critical values of $v_{\rm IF}$ above which fronts merging occurs for any $G_0/n_{\rm H}$. These computed critical values are presented as red circles in the left panel of Fig. 2. To the right of the frontier defined by these circles, the fronts are merged. Two expressions of the frontier curve were previously derived by Bertoldi & Draine (1996) (black dotted line) and Störzer & Hollenbach (1998) (black straight dashed line), under simplifying assumptions. We obtained a new semi-analytical derivation of the frontier curve (black solid line), that replicates correctly the curved shape of the numerical results. As this semi-analytical result is not reducible to a simple analytical expression, we found a simpler analytical fit to the results (blue dashed line), which expression is given below (Eq. 3.2). There are consequently two regimes (dissociated or merged fronts) for which we fitted the total atomic hydrogen column density $N_{\rm tot}({\rm H})$:

$$N_{\rm tot}({\rm H})\;\left[{\rm cm}^{-2}\right] = \begin{cases} N_{\rm stat}({\rm H}) + \frac{1}{1.5\,\sigma_g}\ln\left(1+\frac{v_{\rm IF}\,\sigma_{\rm g}}{2\,R}\right) & \text{for} \quad \frac{G_0}{n_{\rm H}} > \left(\frac{G_0}{n_{\rm H}}\right)_{\rm crit}(v_{\rm IF}, Z')\,, \\ N_{\rm stat}({\rm H}) + \frac{N_{\rm stat}({\rm H})}{\pi/2}\;\arctan\left(\sqrt{\frac{v_{\rm IF}/\sqrt{Z'}}{0.05\ {\rm km\,s^{-1}}}}\right) & \text{for} \quad \frac{G_0}{n_{\rm H}} < \left(\frac{G_0}{n_{\rm H}}\right)_{\rm crit}(v_{\rm IF}, Z')\,, \end{cases} \tag{3.1}$$

with $N_{\rm stat}({\rm H})$ is the total atomic hydrogen column density in the static case, taken from Sternberg et al. (2014) and the merging front criterion fit $(G_0/n_{\rm H})_{\rm crit}$ written as:

$$\left(\frac{G_0}{n_{\rm H}}\right)_{\rm crit}(v_{\rm IF},\, Z') = 1.5\cdot10^{-2}\;\;(1+Z')\left(\frac{v_{\rm IF}}{1.0\ {\rm km\,s^{-1}}}\right) + 4.5\cdot10^{-4}\;Z'^{\,2/3}\;\ln\left(1+\frac{v_{\rm IF}/\sqrt{Z'}}{1.0\cdot10^{-3}\ {\rm km\,s^{-1}}}\right). \tag{3.2}$$

The right panel of Fig. 2 compares our merging frontier (black solid line) and the typical value of the D-critical velocity (Kahn 1954; Draine 2011) for typical PDR conditions (black dashed line) to several observed PDRs illuminated by O-stars (blue crosses). The values of $v_{\rm IF}$ used were derived using classical IF theory (Draine 2011, Chap. 37). For high excitation PDRs with high $G_0/n_{\rm H}$ ratio, and as as expected from the IF theory, we see a saturation of $v_{\rm IF}$ at the black dashed line, which is the D-critical value from Kahn (1954). For low excitation PDRs, and despite the error bars, their $v_{\rm IF}$ seem to align with the merging criterion as if this one also acted as a saturation, preventing the PDRs from reaching the D-critical value. It can be a consequence of the fact that the IF cannot propagate faster that the DF. The dynamical effects are expected to be strong for low excitation PDRs. For high excitation PDRs, they will be of moderate importance, yet non negligible as concluded by Störzer & Hollenbach (1998).

4 Conclusions

To sum up, we built a semi-analytical model of the H/H_2 transition in a one-dimensional plane-parallel PDR illuminated by FUV radiation with advancing IF resulting from photo-evaporation. We investigated the stationary equilibrium state in the IF reference frame where its propagation translates into advection of neutral gas through the front. The advection locally acts as a formation term for H_2. /bf : Pour l'extinction, je n'aime pas appeler ce qu'on fait du transfert de rayonnement : Our radiative transfer for H_2 UV photodissociation takes into account not only the extinction by dust but also H_2 self-shielding. We obtained a simple set of analytical expressions allowing to compute the total H I column density $N_{1,\rm tot}$ in the presence of photo-evaporation. One simply needs to provide $v_{\rm IF}$, G_0, $n_{\rm H}$ and the metallicity. The advection of the gas through the IF induces a change in the location of the H/H_2 transition, which is closer to the IF compared to the static case. This effect reduces the width of the atomic region. If the IF velocity exceeds a certain value, the atomic region disappears. The DF and the IF then form a merged structure. Observations of PDRs illuminated by O-stars are close to the merging criteria, where the dynamical effects are strong. For this kind of objects, we expect $N_{1,\rm tot}$ to be much lower in the presence of photo-evaporation-induced advection than in a static situation, especially for low excitation PDRs. With the H/H_2 transition closer to the IF, more H_2 is expected to be located in a hotter, more FUV-rich region. One can then expect H_2 ro-vibrational lines to be more intense as collisions and UV-pumping will be more efficient. This effect could prove very important to understand the many H_2 ro-vibrational lines that will be observed by the upcoming JWST. The effects are expected to cause larger differences for low excitation PDRs, such as the Horsehead Nebulae.

This work was supported by the Programme National “Physique et Chimie du Milieu Interstellaire” (PCMI) of CNRS/INSU with INC/INP co-funded by CEA and CNES.

References

Bertoldi, F. & Draine, B. T. 1996, ApJ, 458, 222

Bialy, S., Bihr, S., Beuther, H., Henning, T., & Sternberg, A. 2017, ApJ, 835, 126

Bron, E., Agúndez, M., Goicoechea, J. R., & Cernicharo, J. 2018

Draine, B. T. 2011, Physics of the Interstellar and Intergalactic Medium

Draine, B. T. & Bertoldi, F. 1996, ApJ, 468, 269

Goicoechea, J. R., Pety, J., Cuadrado, S., et al. 2016, Nature, 537, 207

Habing, H. J. 1968, Bull. Astron. Inst. Netherlands, 19, 421

Joblin, C., Bron, E., Pinto, C., et al. 2018, A&A, 615, A129

Kahn, F. D. 1954, Bull. Astron. Inst. Netherlands, 12, 187

Lee, M.-Y., Stanimirović, S., Douglas, K. A., et al. 2012, ApJ, 748, 75

Sternberg, A., Le Petit, F., Roueff, E., & Le Bourlot, J. 2014, ApJ, 790, 10

Störzer, H. & Hollenbach, D. 1998, ApJ, 495, 853

Wong, T., Hughes, A., Fukui, Y., et al. 2009, ApJ, 696, 370

Wu, R., Bron, E., Onaka, T., et al. 2018, A&A, 618, A53

SF2A 2021
A. Siebert, K. Baillié, E. Lagadec, N. Lagarde, J. Malzac, J.-B. Marquette, M. N'Diaye, J. Richard, O. Venot (eds)

INVESTIGATING THE INTERSTELLAR MEDIUM STRUCTURE AND POROSITY TO IONIZING PHOTONS IN LOCAL PRIMITIVE GALAXIES

L. Ramambason[1] and V. Lebouteiller[1]

Abstract. Part of the ionizing continuum (Lyman continuum, LyC) produced by young stars can leak out of the host galaxy and ionize its surroundings. At high redshift, such LyC-leaking galaxies are among the best candidates to fully account for reionization (Robertson et al. 2013). However, direct measurements are extremely difficult as the LyC photons are easily absorbed by neutral gas on the observed line of sight. Instead, indirect tracers have been used to probe the structure of the interstellar medium (ISM) (e.g. Lyman alpha line, absorption lines) but such methods are also sensitive to line of sight selection effects. Using integrated emission lines in the optical and infrared domain mostly palliates viewing angle dependencies; it is a promising method to make the most of observations with current ground-based facilities (e.g., ALMA) and upcoming space missions (e.g., JWST) that will grant access to many spectroscopic tracers up to redshift above 7. However, a complex modeling step is much needed to take into account the available tracers originating in different phases and to consider a multi-component topology which matches the ISM signatures of known leaking galaxies (Ramambason et al. 2020). Such complex representative models are crucial to investigate morphology-dependent questions such as the impact of the metal and dust content on the gas distribution and mass in the different reservoirs and the porosity to ionizing radiation. Local low-metallicity galaxies, with quasi-primordial-like physical conditions and with numerous emission lines available, are ideal laboratories to benchmark this new method and explore its predictive power in high-redshift galaxies for which only a few tracers are often observed. To constrain the parameters of this representative galaxy model, we co-developped MULTIGRIS (Lebouteiller & Ramambason in prep.) a new Bayesian code using MCMC sampling. Among the various applications, MULTIGRIS can produce probability density functions of physical parameters, either primary (density, ionization parameter, stellar population age etc...) or secondary (ionizing photon escape fraction, dust mass, H2 mass etc...). I present here the first results obtained on the Dwarf Galaxy Survey (Madden et al. 2013), a sample of local, low-metallicity galaxies using combinations of Cloudy models (Ferland et al. 2017). We build upon previous results from Cormier et al. (2019) to quantify the larger porosity of the interstellar medium for low-metallicity galaxies, with the inferred topology having more density bounded regions, leading to photons escaping the HII regions. We explore dependencies of ionizing photons escape fraction on our model parameters and discuss promising line ratios for future local- and high-redshift studies.

Keywords: interstellar medium, emission lines, primitive galaxies, escape fraction

1 Introduction

Current observations available in the local and high-redshift universe are limited by spatial resolution and detection limit. Detailed studies of the ISM are especially challenging due the blending of emission arising from the different phases (e.g. H II regions, neutral atomic hydrogen and neutral molecular gas) into one single beam sight and potential multi-modal density distributions within a single ionization phase. To disentangle the contribution of each phase, we propose to use a representative topology which combines different sectors having different physical parameters. This approach is an intermediate step between simplistic geometries of classical photo-ionization/photo-dissociation code such as Cloudy (Ferland et al. 2017) and 3D radiative transfer codes and simulations which account for very complex gas distribution but have degrees of freedom that can hardly be constrained by observations. Our "topological" model introduces a layer of complexity which provide a more realistic picture of the multiphase ISM while keeping a relatively modest number of free parameters that

[1] AIM, CEA, CNRS, Université Paris-Saclay, Université Paris Diderot, Université de Paris, F-91191, Gif-sur-Yvette, France.

can be constrained with a only few emission lines. Similar approaches have successfully been used in previous studies (see Section 2) where the free parameters of models were tuned to match observation using frequentist methods (i.e., χ^2). We build on those results to develop a more general tool that will provide a new Bayesian framework to study the multiphase ISM and specifically some quantities of interest such as the LyC photons escape fraction.

2 Topological models

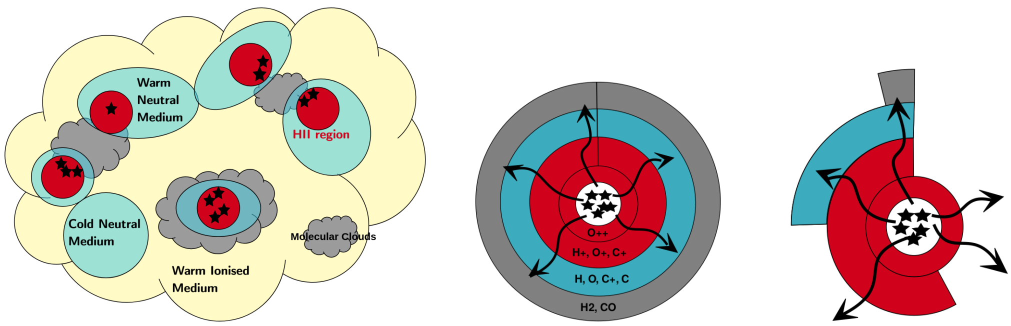

Fig. 1. Left: Schematic view of the main phases of the ISM. **Right**: Two possible representative topologies (1 sector and 4 sectors).

Topological models are refined multi-sector and multi-phase models representing the contribution of each phase (see Figure. 1) to the total emission. They were first introduced in Péquignot (2008) on a test case study on the proto-typical, low-metallicity galaxy IZw18. Figure 1 shows a schematic view of the multiphase ISM and two representative topologies with either one sector or 4 sectors stopping at different depths. Such models have been refined and successfully applied to local objects (e.g: Haro11: Cormier et al. 2012, IZw18: Lebouteiller et al. 2017, IC10: Polles et al. 2019), to sample of galaxies (e.g., DGS: Cormier et al. 2019) and resolved regions in the SMC/LMC (Lambert-Huygues et al. in prep.). The results from those studies indicate that the inclusion of density-bounded regions and non-unity PDR covering factor are necessary to reproduce the emission lines of most local objects. Such findings are at odds with UV observations which detect little to no LyC in the local universe. (e.g., Bergvall et al. 2006; Leitet et al. 2013; Borthakur et al. 2014; Leitherer et al. 2016). Results from Polles et al. (2019) indicate that the observed spatial scale drives the estimated porosity of the regions, with most clouds being matter-bounded at small scales while regions become more and more radiation-bounded at galactic scale. Using the best fitting model between 1-sector and 2-sectors configurations, Cormier et al. (2019) shows that the PDR covering factor varies with metallicity, lower metallicity leading to lower PDR covering factors. This might be suggestive of an increased porosity of the ISM at lower metallicity that might favor LyC photons escape. However a quantitative estimate of the amount photons leaking out of H II regions is yet to be determined as well as the physical mechanisms describing the variation of the escape fraction.

3 MULTIGRIS: a new Bayesian framework for ISM studies

MULTIGRIS (Lebouteiller & Ramambason in prep.) is a new Bayesian code designed to use emission lines to constrain the probability density functions (PDF) of various parameters from our topological models.

3.1 Grids of photo-ionization models

We use the photo-ionization and photo-dissociation code Cloudy c17.02 (Ferland et al. 2017) to create the models that will be combined as sectors around a representative cluster. Each model consists in a spherical shell of gas placed at a fixed inner radius of the incident radiation source wthin a single sector. We use a closed, spherical geometry which take into account the transmitted and reflected radiation. Radiative transfers are computed along each line of sight (1D) in a continuous way throughout the H II region, PDR and molecular zone. A detailed description of the grid will be presented in Ramambason et al. (in prep.). The models are then combined to create a representative topology in which the emission lines are computed as weighted linear combination of the emission line from each sector. Other physical quantities available in Cloudy can also be combined as long as they scale with luminosity and can be combined as linear function of sectors (e.g., gas masses in the different phases, number of ionizing photons Q...). We calculate the global escape fraction of photons for a given topology by using the ionizing continuum provided by Cloudy at each depth in the model.

3.2 *Bayesian framework*

MULTIGRIS can be used with different Monte Carlo samplers which will be described in the benchmark paper (Lebouteiller & Ramambason in prep.). For this study we run MULTIGRIS at order 0 which performs a nearest neighbour interpolation in the grid of Cloudy models. In the following example we used the SMC sampler from PyMC3 (Salvatier et al. 2016). We define the likelyhood of our data $P(d \mid \theta)$ by considering our suite of emission lines as independent identically distributed random variable (RV). Each RV can be chosen to follow either an asymmetric gaussian law centered on the measured value or an asymmetric StudentT law. In this study we consider use a Student-T distribution for each RV with a normality parameter ν=1. Hence the likelihood is given by:

$$\mathcal{L} = P(d|\theta) = \prod_{i=0}^{N} \mathcal{S}(\nu = 1, \mu = O_i, \sigma^2 = U_i^2), \tag{3.1}$$

where ν is the normality parameter of the Student-T distribution, N the number of emission lines with observed fluxes O_i and uncertainties U_i. For undetected lines with instrumental upper limit, the Student-T distribution is replaced by a half-Student-T likelihood with the same normality parameter ν. For lower and upper limits, the σ corresponds to the RMS of the signal and reflects the uncertainty on the limit itself.

3.3 *Example of application on the Dwarf Galaxy Survey*

On Figure 2, we show an example of the application of MULTIGRIS to the galaxy IZw18. For each galaxy, several configurations can be tested (i.e., with different number of sectors, different prior on the luminosity, metallicity etc...).

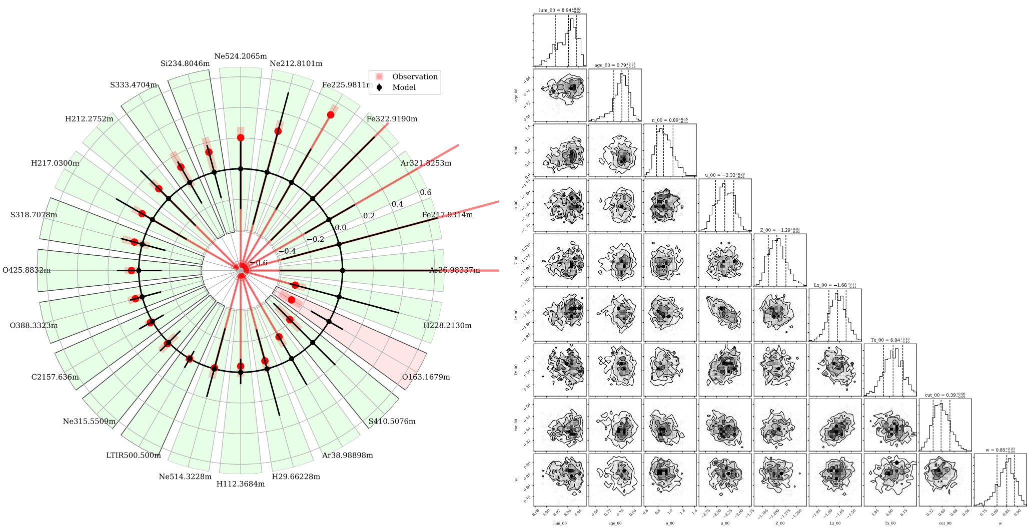

Fig. 2. Some diagnostic plots for galaxy IZw18, for a 3-sectors configuration. **Left**: Plot showing the agreement of predicted line fluxes with measured lines. Arrows represent instrumental upper limits. **Right**: Corner plot showing the PDF of primary parameter for one of the 3 sectors.

We applied MULTIGRIS to a sample of 38 compact, fully observed galaxies with at least three spectral lines detected among the 50 galaxies observed in the Herschel Dwarf Galaxy Survey (Madden et al. 2013). On Figure 3, we show the best models for each galaxy selected based on the Leave-One-Out cross validation (LOO) criterium (Vehtari et al. 2017) among 6 configurations having different number of sectors (1,2 or 3) and different model luminosity* (L=$10^7 L_\odot$ or $10^9 L_\odot$). Our results confirm the trend from Cormier et al. (2019) of increasing porosity of the ISM at low metallicity. We note that there seems to be a bimodality in our sample, with two branches of leaking and non-leaking galaxies clearly visible on the Kernel Density Estimate (KDE). The globally high escape fractions we find correspond to the fractions in the hypothesis that H II regions dominate the integrated spectrum of the galaxy, with in particular the diffuse ionized gas component and the neutral gas envelope being ignored for now. Those limits as well as other dependencies of the escape fraction will be further discussed in Ramambason et al. (in prep.).

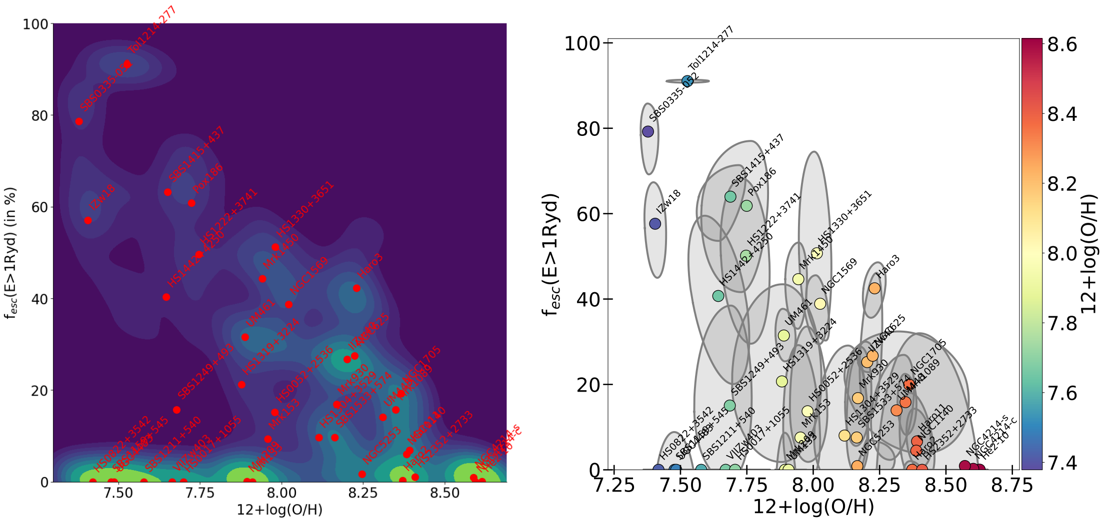

Fig. 3. Evolution of the inferred escape fraction from H II regions with respect to the inferred metallicity. **Left**: KDE representation, the red dots represent median values for each galaxy. **Right**: Skewed uncertainty ellipsis (SUE,Galliano et al. 2021) A SUE represents the 1σ contour of a 2 dimensional split-normal distribution adjusted to have the same three first moment as the underlying PDF.

References

Bergvall, N., Zackrisson, E., Andersson, B. G., et al. 2006, A&A, 448, 513

Borthakur, S., Heckman, T. M., Leitherer, C., & Overzier, R. A. 2014, Science, 346, 216

Cormier, D., Abel, N. P., Hony, S., et al. 2019, A&A, 626, A23

Cormier, D., Lebouteiller, V., Madden, S. C., et al. 2012, A&A, 548, A20

Ferland, G. J., Chatzikos, M., Guzmán, F., et al. 2017, Rev. Mexicana Astron. Astrofis., 53, 385

Galliano, F., Nersesian, A., Bianchi, S., et al. 2021, A&A, 649, A18

Lambert-Huygues et al., A. in prep.

Lebouteiller, V., Péquignot, D., Cormier, D., et al. 2017, A&A, 602, A45

Lebouteiller, V. & Ramambason, L. in prep.

Leitet, E., Bergvall, N., Hayes, M., Linné, S., & Zackrisson, E. 2013, A&A, 553, A106

Leitherer, C., Hernandez, S., Lee, J. C., & Oey, M. S. 2016, ApJ, 823, 64

Madden, S. C., Rémy-Ruyer, A., Galametz, M., et al. 2013, PASP, 125, 600

Péquignot, D. 2008, A&A, 478, 371

Polles, F. L., Madden, S. C., Lebouteiller, V., et al. 2019, A&A, 622, A119

Ramambason, L., Schaerer, D., Stasińska, G., et al. 2020, A&A, 644, A21

Ramambason et al., L. in prep.

Robertson, B. E., Furlanetto, S. R., Schneider, E., et al. 2013, ApJ, 768, 71

Salvatier, J., Wiecki, T. V., & Fonnesbeck, C. 2016, PeerJ Computer Science, 2, e55

Vehtari, A., Gelman, A., & Gabry, J. 2017, Stat Comput 27, 1413–1432

*The model luminosity is scaled with a free parameter to match the observed luminosity of each galaxy. Different model luminosities result in different geometry of the models.

SF2A 2021
A. Siebert, K. Baillié, E. Lagadec, N. Lagarde, J. Malzac, J.-B. Marquette, M. N'Diaye, J. Richard, O. Venot (eds)

THE FORMATION AND EVOLUTION OF DENSE FILAMENTS AND RIDGES

L. Bonne[1], S. Bontemps[2], N. Schneider[3], S. D. Clarke[3], D. Arzoumanian[4], R. Simon[3], Y. Fukui[5], K. Tachihara[4], T. Csengeri[3], R. Guesten[6] and the FEEDBACK consortium

Abstract. We confront two rather different star forming filaments: The Musca filament which forms isolated low-mass stars and the DR21 ridge which forms massive star clusters. Both regions are observed with several spectral lines, using the APEX, NANTEN2, IRAM 30m and SOFIA telescopes, that trace the gas from the ambient cloud into the dense filament/ridge. For both regions we find that the large scale kinematics are most likely explained by bending of the magnetic field which drives continuous inflow to the formed filament. For the DR21 ridge, it is additionally found that gravitational collapse takes over at a distance of ~1-2 pc from the ridge. The bending of the magnetic field in both sources would be the result of a large scale collision that initiates star formation in both regions.

Keywords: ISM kinematics, star formation, magnetic field, ISM structure

1 Introduction

Herschel observations highlighted that the majority of low-mass stars form in dense filaments (e.g. André et al. 2010), while the majority of high-mass stars form in the hubs where such filaments converge, in very massive filaments, so-called ridges, and in galactic bones (e.g. Jackson et al. 2010; Hill et al. 2011). The origin and evolution of these dense filaments is thus essential to understand the initial conditions of star formation. A comparison of low- and high-mass star forming filaments is also particularly interesting to understand how cores can overcome the typical Jeans mass such that high-mass stars can form. To address these questions, we studied the Musca filament, a prototype filament that can form low-mass stars, and the DR21 ridge which forms several clusters of massive stars. Both regions are presented in Fig. 1.

2 Asymmetric inflow driven by bending of the magnetic field

APEX observations show velocity gradients in $C^{18}O$(2-1) over the Musca filament, see Fig. 1, that are directly linked to the ambient cloud kinematics. This mass inflow fits with mid-J CO observations towards the filament that can be explained by filament accretion shocks that form the dense gas in the filament (Bonne et al. 2020b). The large-scale ^{12}CO(1-0) kinematics show that all the ambient gas of the Musca filament is blueshifted with respect to the filament and forms a 'V′-shape perpendicular to the filament, see Fig. 1. This velocity profile and more systematic kinematic asymmetries in Chamaeleon-Musca (Bonne et al. 2020a), suggest that star formation in Chamaeleon-Musca was initiated by a 50 pc scale HI cloud collision. This collision bends the magnetic field, as described in Inoue et al. (2018), that drives the inflow to the Musca filament.
For the DR21 ridge it was found that the ridge is gravitationally collapsing (Schneider et al. 2010). In the new larger maps, a V-shape is observed in the PV diagrams perpendicular to the ridge, similar to Musca, which becomes increasingly clear in tracers of the lower density ambient cloud such as [CII], see Fig. 1. In the

[1] SOFIA Science Center, USRA, NASA Ames Research Center, Moffett field, CA 94045, USA
[2] Laboratoire d'Astrophysique de Bordeaux, Université de Bordeaux, CNRS, B18N, allée Geoffrey Saint-Hilaire, 33615 Pessac, France
[3] I. Physikalisches Institut, Universität zu Köln, Zülpicher Str 77, 50937 Köln, Germany
[4] Aix Marseille Univ., CNRS, CNES, LAM, Marseille, France
[5] Department of Physics, Nagoya University, Chikusa-ku, Nagoya 464-8602, Japan
[6] Max-Planck-Institut für Radioastronomie, Auf dem Hügel 69, 53121 Bonn, Germany

denser gas tracers, the dynamics start to show indications of rapid gravitational acceleration at r $\sim$ 1 pc. As gravitational collapse of the cloud requires to pass through the bended magnetic field lines, this bending might play a substantial role in counterbalancing pure gravitational acceleration.

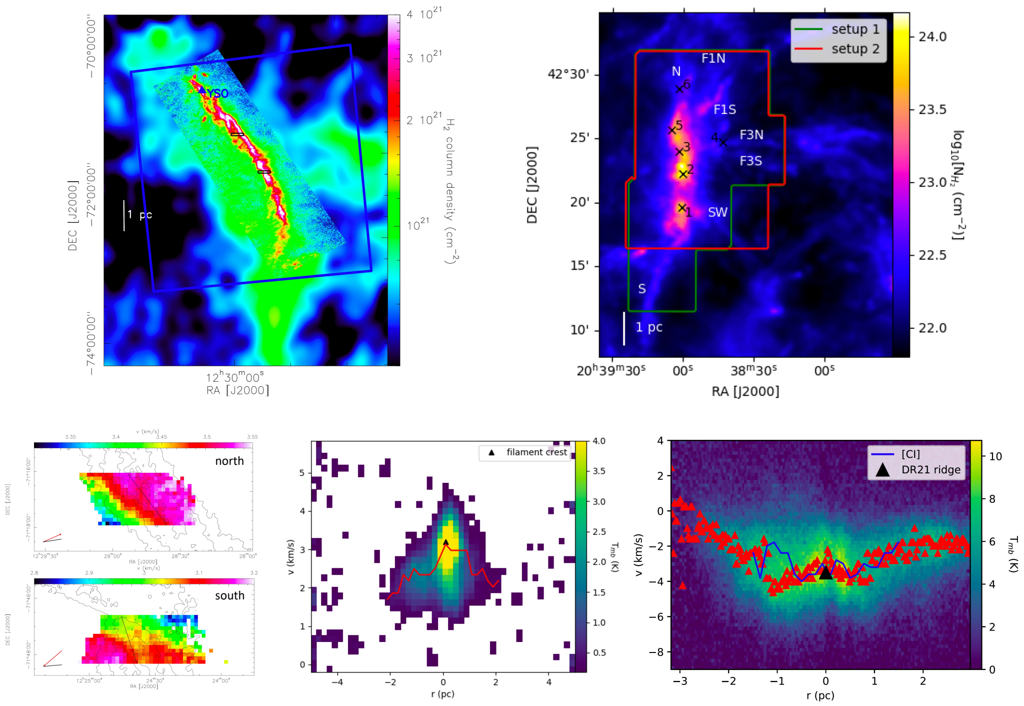

Fig. 1. Top left The column density map of the Musca filament with the NANTEN 2 (blue) and APEX (black) map size. **Top right** The same for the DR21 ridge with the IRAM 30m map sizes. **Bottom Left**: $C^{18}O$(2-1) velocity fields at two locations over the Musca filament (outlined by the contours). **Bottom middle**: The ^{12}CO(1-0) PV diagram perpendicular to the Musca filament. The red line follows the maximal intensity as a function of the radius. **Bottom right**: The same for the DR21 ridge constructed from [CII] observations from the FEEDBACK Legacy survey with the SOFIA telescope (Schneider et al. 2020).

3 Conclusions

The formation of the Musca filament and DR21 ridge appears to be triggered by a similar mechanism with an important dynamic role for the magnetic field in the mass collection on the filament. In the DR21 cloud, gravity becomes increasingly dominant at pc scales compared to Musca where gravity only takes over at $\sim$0.1 pc scale. This pc scale gravitational instability in the DR21 cloud increases the mass provision to centers of collapse where massive stars, orders of magnitude above the typical Jeans mass, can form.

This work is supported by the french ANR and the german DFG through the project "GENESIS" (ANR-16-CE92-0035-01/DFG1591/2-1). L.B. also acknowledges support from the Région Nouvelle-Aquitaine.

References

André, P., Men'shchikov, A., Bontemps, S., et al. 2010, A&A, 518, L102
Bonne, L., Bontemps, S., Schneider, N., et al. 2020a, A&A, 644, A27
Bonne, L., Schneider, N., Bontemps, S., et al. 2020b, A&A, 641, A17
Hill, T., Motte, F., Didelon, P., et al. 2011, A&A, 533, A94
Inoue, T., Hennebelle, P., Fukui, Y., et al. 2018, PASJ, 70, S53
Jackson, J. M., Finn, S. C., Chambers, E. T., Rathborne, J. M., & Simon, R. 2010, ApJ, 719, L185
Schneider, N., Csengeri, T., Bontemps, S., et al. 2010, A&A, 520, A49
Schneider, N., Simon, R., Guevara, C., et al. 2020, PASP, 132, 104301

SF2A 2021
A. Siebert, K. Baillié, E. Lagadec, N. Lagarde, J. Malzac, J.-B. Marquette, M. N'Diaye, J. Richard, O. Venot (eds)

SCATTERING TRANSFORMS FOR INTERSTELLAR ASTROPHYSICS AND BEYOND

F. Levrier[1], E. Allys[1], B. Régaldo-Saint Blancard[1], F. Boulanger[1], N. Jeffrey[1], S. Zhang[2], E. Bellomi[1], C. Colling[3], T. Marchand[2], S. Mallat[2] and P. Hennebelle[3]

Abstract. Scattering transforms are a set of novel tools that provide a general ensemble of statistical descriptors able to characterize the multi-scale geometry of images by encoding the couplings between oriented scales. They are inspired by the architecture of convolutional neural networks, but do not require any training stage. Their applications range from the statistical description of interstellar emission maps in total intensity and polarization, or that of large-scale structures in the cosmic web, to statistical denoising and component separation, through data augmentation. They are accessible thanks to two python packages.

Keywords: Interstellar medium, large-scale structure, statistics

1 Introduction

The complex filamentary patterns observed in the interstellar medium (ISM) are prime examples of highly non-Gaussian structures emerging from the non-linear interactions between a variety of physical processes at play (turbulence, gravity, magnetic fields, thermodynamics, ...). The large-scale filaments of the cosmic web in the non-linear regime set another example of such non-Gaussian structures. Our understanding of how these structures form and evolve now largely relies on the statistical analysis of observations and their comparison with numerical simulations, in order to assess physical processes and their interactions, across a vast range of spatial scales. The quantitive comparison of simulation results to sets of observational data therefore requires an adequate statistical description of non-Gaussian structures that goes beyond the power spectrum. Ideally, such a description would allow for a simple connection between statistical geometrical descriptors and physical properties of the systems under study.

2 Scattering transforms

Scattering transforms are a set of tools developed in the field of data science (Mallat 2012; Bruna & Mallat 2012), originally designed to reproduce and understand the results obtained by convolutional neural networks (CNN) in the field of supervised machine learning. They are based on a local, multi-scale description of images through wavelet transforms, using a discrete family of Morlet or bump-steerable wavelets, $\{\psi_{j,\theta}\}$ covering the entire Fourier plane through a set of scales (j) and angles (θ), together with non-linear operators aimed at coupling spatial scales.

2.1 Wavelet Scattering Transform (WST)

The WST implements a layered architecture of successive convolutions with these wavelets, followed by non-linear (modulus) operators. Although formally similar to a CNN, the WST only uses a few layers and the convolution kernels are not adapted, so that there is effectively no training stage. Combined with simple linear classifiers, the WST has been shown to achieve state-of-the-art results in various classification problems (e.g. Sifre & Mallat 2013). Typically, a 256×256 image may be adequately described by some ~ 1000 WST coefficients.

[1] Laboratoire de Physique de l'École Normale Supérieure, ENS, Université PSL, CNRS, Sorbonne Université, Université de Paris, 24 rue Lhomond, 75231 Paris Cedex 05, France
[2] DATA
[3] CEA

2.2 Reduced Wavelet Scattering Transform (RWST)

Images arising from physical processes are expected to exhibit some statistical regularity, which translates into regular patterns emerging when plotting their WST coefficients. The angular dependency of these coefficients may be modeled via simple trigonometric functions, resulting in the RWST, which typically reduces the number of necessary statistical descriptors by an order of magnitude - without any loss of informational content. The RWST model has been shown to apply equally well to ISM maps in total intensity (Allys et al. 2019) and in polarization (Regaldo-Saint Blancard et al. 2020).

2.3 Wavelet Phase Harmonics (WPH)

Another approach to describe statistical interactions across oriented scales in a given image lies in computing the covariance of different wavelet transforms $\mathrm{Cov}(I \star \psi_{j_1,\theta_1}, I \star \psi_{j_2,\theta_2})$. To ensure that this is non-zero, the "phase harmonics" operator $[z]^p : z = |z|e^{i\phi(z)} \mapsto |z|e^{ip\phi(z)}$ is applied to the wavelet transforms. It accelerates the phases to line them up for the different bandpasses. Thus altered, covariances yield statistical information on the couplings between scales (Mallat et al. 2019). The many different WPH coefficients may be used as a basis of generative models, starting from Gaussian random noise and performing a gradient descent constrained by the target WPH coefficients. This approach was used in the context of cosmological simulations of the large-scale structures of the Universe, demonstrating that WPH-constrained random realizations ("syntheses") present the same statistics (power spectra, probability density functions, bispectra, Minkowski functionals, ...) as the original image (Allys et al. 2020).

3 Application : denoising and component separation

The scattering transforms have been used to perform statistical component separation, given observational data $d = s + n$ that is the sum of a signal s and a noise n. Assuming that the statistics of the nuisance signal n are known, and that they are different from those of the target signal s, it is possible to obtain an estimate $\hat{s}$ of the signal through the minimization of a loss function $\mathcal{L}(s) \propto \sum_i ||\phi(s + n_i) - \phi(d)||$ where the n_i are different realizations of the noise. This was demonstrated on simulated polarization data and applied to observational data from *Planck* in the Chamaeleon-Musca molecular cloud (Regaldo-Saint Blancard et al. 2021).

A follow-up analysis has shown that such an approach may also be applied to the separation of Galactic thermal dust and cosmic infrared background (CIB) emission. Using a simulation of the CIB and 21 cm line emission as a proxy for a pure Galactic thermal dust emission map, a CIB-contaminated Galactic dust signal is built. The WPH statistics of the CIB map are used to generate multiple random realizations of the CIB, which are then used in the same way as in Regaldo-Saint Blancard et al. (2021) to statistically separate the Galactic dust from the total signal, effectively cleaning it from CIB contamination.

4 Conclusions

The WST, RWST, and WPH are novel statistical tools aimed at describing complex structures with non-Gaussian statistics such as appear in interstellar medium images. They provide sufficient statistics to serve as a basis for realistic generative models and for a metric to compare observational and simulation data sets. Finally, they usher in a new avenue towards statistical component separation, with potentially vast applications in astrophysics and cosmology. They are released for wide use through two public python packages, `PyWST` and `PyWPH`, available through `https://github.com/bregaldo`.

References

Allys, E., Levrier, F., Zhang, S., et al. 2019, A&A, 629, A115
Allys, E., Marchand, T., Cardoso, J. F., et al. 2020, Phys. Rev. D, 102, 103506
Bruna, J. & Mallat, S. 2012, CoRR, abs/1203.1513
Mallat, S. 2012, Communications on Pure and Applied Mathematics, 65, 1331
Mallat, S., Zhang, S., & Rochette, G. 2019, Information and Inference: A Journal of the IMA, 9, 721
Regaldo-Saint Blancard, B., Allys, E., Boulanger, F., Levrier, F., & Jeffrey, N. 2021, A&A, 649, L18
Regaldo-Saint Blancard, B., Levrier, F., Allys, E., Bellomi, E., & Boulanger, F. 2020, A&A, 642, A217
Sifre, L. & Mallat, S. 2013, in Proceedings of the IEEE Conference on Computer Vision and Pattern Recognition (CVPR)

SF2A 2021
A. Siebert, K. Baillié, E. Lagadec, N. Lagarde, J. Malzac, J.-B. Marquette, M. N'Diaye, J. Richard, O. Venot (eds)

HIERARCHY OF CLUMPS FRAGMENTS : A DEN FOR THE FORMATION OF LOCAL STAR-CLUSTERS USING A GRAPH THEORY-BASED APPROACH

B. Thomasson[1], I. Joncour[1] and E. Moraux[1]

Abstract. Young Stellar Objects (YSOs) form in molecular clouds from densest gas cores. Spatial distribution of YSOs features evidence of pristine multi-scale hierarchy through clusters and multiplicity, most probably inherited from their parental cloud on a larger scale. We design a graph theory-based approach to characterise the properties of fragmentation and apply it to Herschel multi wavebands observations of NGC2264. Spatial distribution of structures in NGC2264 revealed that hierarchical nested fragmentation is primary observed in the high density central part of NGC2264 and features a fractal law of fragmentation.

Keywords: fragmentation, NGC2264, stellar multiplicity, hierarchy, network

1 Introduction

Properties of local mini star-clusters (Joncour et al. 2018) are suspected to hint pristine imprints of star formation process, and highlighted two regimes of cloud fragmentation. In this work, we propose to check the existence of a hierarchical cascade of fragmentation in the NGC2264 molecular cloud, and assess its statistical properties. NGC2264 is an active star forming region located at 720pc (Cantat-Gaudin et al. 2018) which is composed of two massive hubs that incubate most of the YSOs (Rapson et al. 2014). Using Herschel multi-wave bands observation (Motte et al. 2010), five specific scales can be monitored associated to [8.4, 13.5, 18.2, 24.9, 36.3]" resolution. The massive dense clumps (MDCs) are extracted using the source extraction algorithm *getsf* on density maps (Men'shchikov 2021). The resulting physical spatial scale span from 5kAU to 30kAU, which are the scales where the fragmentation is suspected to occur (Joncour et al. 2018). In addition, we selected class 0/I YSOs from Rapson et al. (2014) observed by Spitzer in order to assess the final steps of the fragmentation process. As a result, 6 scales of fragmentation are available.

2 Network representation

The available 6 scales are organised in levels of fragmentation and we use them as reference to construct a directed network going from large scale to low scale, in which one node is a fragment (MDC or YSO) belonging to one specific level. Two nodes are connected if one of them is included into the other at 75% of its area. The nested node is considered as a child and the incubator node is considered as a parent. The last children are labeled sinks (see Figure 1) The resulting global network representing the whole data set (see Figure 2) is then composed of multiple components, which are independent sub-networks disconnected from each other. These components are identified as structures which can be hierarchical (number of sinks > 1), linear ($= 1$) or isolated ($= 0$) for which examples are given in Figure 1.

3 Hierarchy in NGC2264

Using the previous definitions, we extracted 151 structures for 81 YSOs and 414 MDCs. 10% of these structures are hierarchical and contain respectively 62% and 40% of YSOs and MDCs. Linear structures, however, represent 57% of the structure population with respectively 57% et 22% of YSOs and MDCs. Two striking properties are : 1) the presence of YSOs where fragments are located and 2) the dominance of hierarchical structures in terms of fragment number despite their under-representation (see Figure 2). In addition, hierarchical structures happens to be exclusive to densities above $3.10^{22} H_2/cm^2$, while there is a mix of hierarchical and linear below. Isolated structures are concerned for the less dense regions of the cloud ($< 10^{22} H_2/cm^2$).

[1] Univ. Grenoble Alpes, CNRS, IPAG, 38000 Grenoble, France

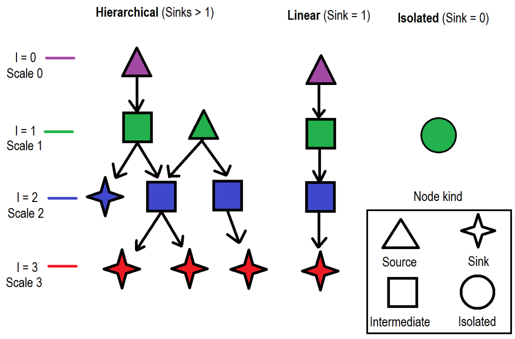

Fig. 1. Example of 3 types of networks to represent the data. MDCs and YSOs are represented as nodes along multiple levels of fragmentation. Nodes are labelled differently regarding of inheritance whether they possess parent or child. Each network component is labelled according to their number of sinks.

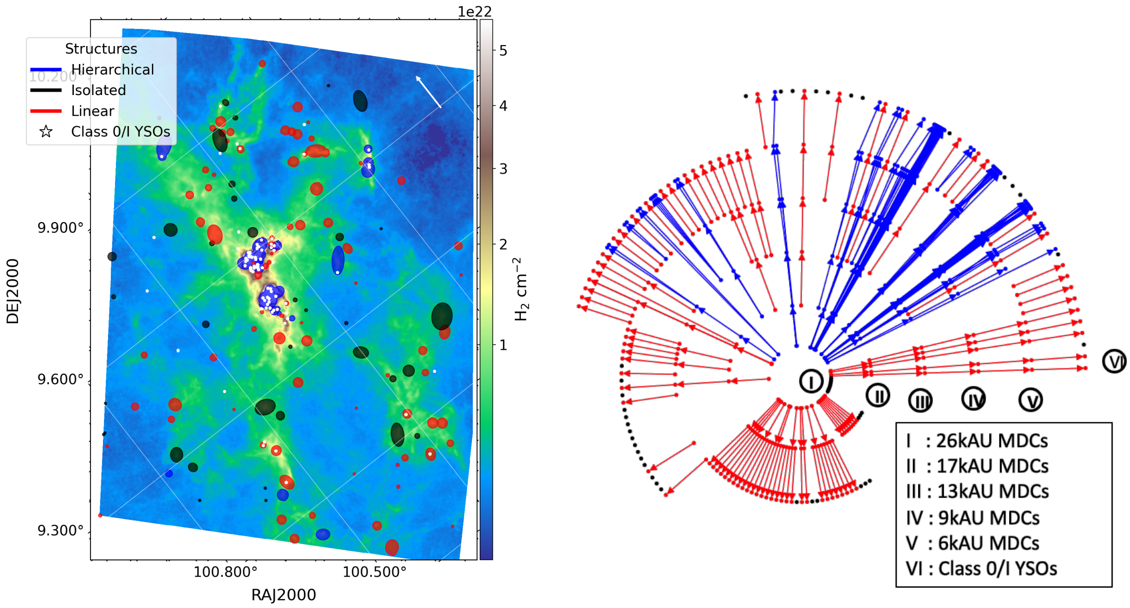

Fig. 2. Left: Map of NGC2264 overlapped with extracted structures. North is indicated by white arrow. Each structure type is represented with a color according to the legend. **Right:** Global network that represents all the fragments in NGC2264. The fragmentation cascade from the inner ring (high scale) to the outer ring (low scale). One structure is one component of the network. Color legend is the same as in the **Left** Figure.

4 Conclusion

Using Herschel 5 multi-wave bands data coupled with class 0/I observed by Spitzer (Rapson et al. 2014) of NGC2264, we designed a graph-theory based approach to describe and analyse the fragments extracted by *getsf* algorithm (Men'shchikov 2021). We were able to define hierarchical structures which assert their dominance in the densest regions of the cloud ($> 3.10^{22} H_2/cm^2$) and that contains half of the whole fragment population.

References

Cantat-Gaudin, T., Jordi, C., Vallenari, A., et al. 2018, Astronomy & Astrophysics, 618, A93
Joncour, I., Duchêne, G., Moraux, E., & Motte, F. 2018, Astronomy and Astrophysics, 620, A27
Men'shchikov, A. 2021, arXiv:2102.11565 [astro-ph]
Motte, F., Zavagno, A., Bontemps, S., et al. 2010, Astronomy and Astrophysics, 518, L77
Rapson, V. A., Pipher, J. L., Gutermuth, R. A., et al. 2014, The Astrophysical Journal, 794, 124

Session 3

Atelier général du PNHE

SF2A 2021
A. Siebert, K. Baillié, E. Lagadec, N. Lagarde, J. Malzac, J.-B. Marquette, M. N'Diaye, J. Richard, O. Venot (eds)

MULTI-WAVELENGTH PROBES OF THE FERMI GEV EXCESS

J. Berteaud[1], F. Calore[1] and M. Clavel[2]

Abstract. More than a decade after its discovery, the Fermi GeV excess is still an exciting subject of research. Thus far, an unresolved population of millisecond pulsars (MSPs) in the Galactic bulge shining in γ-rays is the favorite explanation to the excess, but other explanations exist. Data from the Fermi-LAT have been thoroughly studied and, in order to discriminate between the different hypotheses, a multi-wavelength approach is now needed. In a recent study, we demonstrated that if the GeV excess is caused by an MSP population, about a hundred of them could be detectable in X-rays in a region of $6^\circ \times 6^\circ$ about the Galactic center. The comparison with X-ray data allowed us to conclude that the MSP hypothesis is not excluded, as we found more than three thousand MSP candidates in a strictly conservative approach. The few hundred candidates, with good X-ray spectral knowledge and no optical counterpart, are promising MSP candidates.

Keywords: X-rays, γ-rays

1 Introduction

The Fermi Large Area Telescope (Fermi-LAT), launched more than a decade ago, has produced the most detailed γ-ray data to date. Its energy range and spatial resolution showed undeniable progress compared to its predecessor, EGRET. One objective of the Fermi-LAT was to investigate the composition of the dark matter (DM), and when an excess of γ rays around 2 GeV was detected in the direction of the Galactic center, the scientific community naturally got really excited. Straight away, this signal was interpreted as a possible sign of DM annihilation. However, after more than ten years of research, scientists now favor a more astrophysical explanation: an unresolved population of millisecond pulsars (MSPs) hiding in the Galactic bulge. These sources of γ-rays, because too faint, would not be resolved as point sources by the Fermi-LAT, but would contribute to the diffuse emission. The spectral shape of the excess, renamed "Fermi GeV excess" or "Galactic center excess", resembles the one of some globular clusters expected to host MSPs and its spatial morphology follows the stellar over-density of the Galactic bulge. The Fermi-LAT γ-ray data have been thoroughly studied in order to understand the Fermi GeV excess, and a multi-wavelength approach is now needed in order to discriminate between the different hypotheses. Therefore, in a recent work (Berteaud et al. (2021)), we studied the detectability of the MSP population in X-rays. With its unique high spatial resolution and low instrumental background, Chandra is an excellent instrument to detect X-ray sources in the 0.1-10 keV energy band, and therefore the perfect instrument to look for the MSP population in X-rays.

In the first section, we present our spatial and spectral modelling of the MSP population and in the second section, we study the detectability of our population by Chandra and compare our results to data.

2 MSP modelling

In order to assess the detectability of the Galactic Center MSP population by the Chandra X-ray space observatory, we started by modelling the MSP population using Monte Carlo simulation methods such as its spatial and γ-ray spectral properties match the ones of the Fermi GeV excess. Although only bulge MSPs are responsible for the excess, we also modelled disk MSP as they could represent an important source of foreground. Then, we used data of both X-ray and γ-ray detected MSPs to compute the X-ray emission of the population.

[1] Univ. Grenoble Alpes, USMB, CNRS, LAPTh, F-74940 Annecy, France
[2] Univ. Grenoble Alpes, CNRS, IPAG, F-38000 Grenoble, France

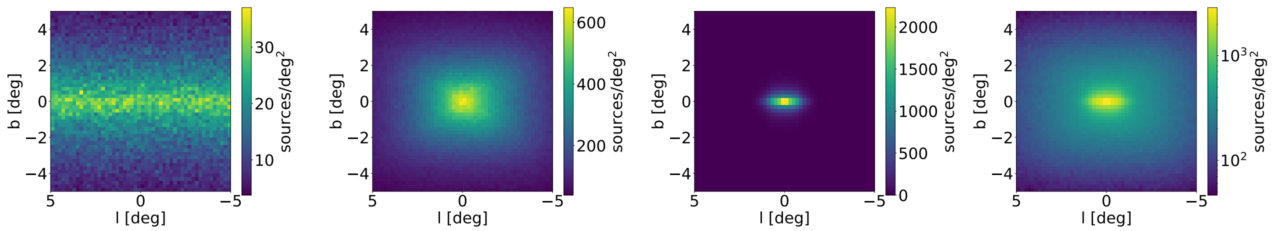

Fig. 1. From left to right, Galactic MSP density in the disk, the boxy bulge, the nuclear bulge and their sum as simulated/modelled by Berteaud et al. (2021).

2.1 Spatial modelling

MSPs can be found both in the disk and in the bulge of the Milky Way. Bartels et al. (2018) studied the spatial distribution of disk MSPs and they found the disk MSP number density to be given by a Lorimer disk profile:

$$n(r,z) = \frac{NC^{B+2}}{4\pi R^2 z_s e^C \Gamma(B+2)} \left(\frac{r}{R}\right)^B \times exp\left(-C\left(\frac{r-R}{R}\right)\right) exp\left(-\frac{|z|}{z_s}\right) \tag{2.1}$$

with best-fit parameters B = 3.91, C = 7.54, defining a vertical and radial profile, and $z_s = 0.76$ pc a scale height. The total γ-ray luminosity of the MSP disk population is 1.5×10^{37} erg/s. The bulge is made of a major component, the boxy bulge (BB), described by Cao et al. (2013):

$$n(x_{BB}, y_{BB}, z_{BB}) = K_0 \left(\left[\left[\left(\frac{x_{BB}}{x_0}\right)^2 + \left(\frac{y_{BB}}{y_0}\right)^2 \right]^2 + \left(\frac{z_{BB}}{z_0}\right)^4 \right]^{\frac{1}{4}} \right) \tag{2.2}$$

with $x_0 = 0.69$ kpc, $y_0 = 0.29$ kpc and $z_0 = 0.27$ kpc and K_0 being the modified Bessel function of the second kind. Here, (x_{BB}, y_{BB}, z_{BB}) refer to the Cartesian BB coordinates system. The z_{BB} axis is perpendicular to the Galactic plane and the x_{BB} axis is rotated 29.4° away from the Galactic center-Sun axis in the clockwise direction.

The γ-ray luminosity of MSPs from the boxy bulge adds up to 1.73×10^{37} erg/s. The other parts of the bulge are less bright, with 1.63×10^{36} erg/s for the nuclear stellar disk and 5.89×10^{34} erg/s for the nuclear stellar cluster. Both form the nuclear bulge (NB). Knowing the total γ-ray luminosity of each spatial component and the γ-ray luminosity function allows to deduce the total number of MSPs: 24009 for the disk and 30374 for the bulge . Fig. 1 shows the corresponding Galactic MSP density.

2.2 Spectral modelling

Bartels et al. (2018) also studied the γ-ray emission of disk MSPs and found that the best fit MSP γ-ray luminosity (L_γ, 0.1-100 GeV) probability density function can be described by a broken power-law:

$$\frac{dN}{dL_\gamma} \propto \begin{cases} \left(\frac{L_\gamma}{1erg/s}\right)^{-0.97} & L_\gamma \leq 10^{33.24} erg/s \\ \left(\frac{L_\gamma}{1erg/s}\right)^{-2.6} & L_\gamma > 10^{33.24} erg/s \end{cases} \tag{2.3}$$

We made use of this function for both the disk and bulge MSP simulations, although it was constructed from disk data. We have no reason to think the γ-ray luminosity function should be different in the disk and in the bulge. With a γ-ray luminosity and a position for each simulated pulsar, it is possible to calculate a flux. Using γ-ray data from Abdollahi et al. (2020) and X-ray data from Lee et al. (2018), we computed the γ-to-X (unabsorbed) flux ratio F_γ/F_X of 40 MSPs. We noticed a correlation between this quantity and the X-ray spectral index Γ of MSPs and used these 40 data points to fit a 2D probability density function, as can be seen in Fig. 2.

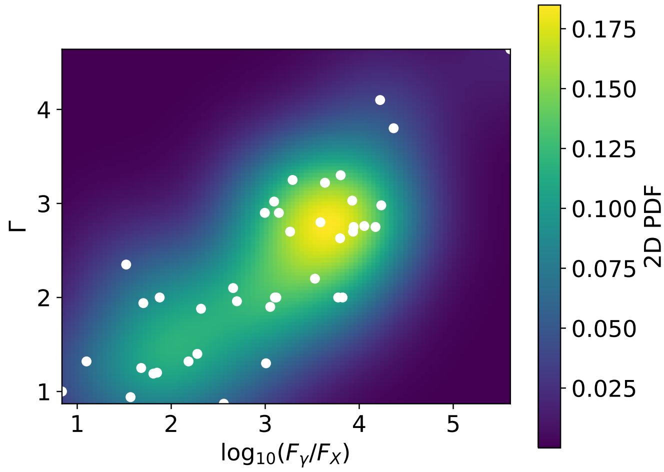

Fig. 2. 2D joint PDF (colored background) of $\log_{10}(F_\gamma/F_X)$ and X-ray spectral index Γ from the 40 MSPs observed in γ-rays and X-rays. Data are shown by the white dots. Figure from Berteaud et al. (2021).

3 Comparison with Chandra data

The current generation of X-ray telescopes is only able to detect the brightest sources, they have a detectability threshold, which means that not all of the 30347 simulated bulge MSPs could be detectable by Chandra. First, we used Chandra sensitivity data to compute the number of detectable MSPs in our simulation. On the other hand, not all Chandra detected sources are MSPs, so we had to make cuts on Chandra data to select only MSP candidates.

3.1 Detectability of the mock population

We selected a region of interest (ROI) of $6° \times 6°$ around the Galactic Center and computed the position dependent flux detection threshold of Chandra in this ROI. Then, for each MSP of the synthetic population, we compared its X-ray flux to the flux detection threshold at the source position. If its flux is larger, the MSP is said to be detectable by Chandra. Averaging over 100 Monte Carlo simulations, we found 95 ± 9 detectable MSPs, including 60 from the BB and 34 from the NB. Only one MSP from the disk is detectable on average. These results are illustrated in Fig. 3.

3.2 Candidate selection

For a meaningful comparison between the simulation and the data, we select from the Chandra catalog non-variable compact sources whose flux is larger than the flux detection threshold at the source position. With these minimal cuts we selected 6918 sources in our ROI. We reduced this number by excluding sources that cannot be MSP candidates using spectral and distance cuts. These cuts are based on the simulation, only taking into account detectable bulge MSPs as explained below.

Thanks to the X-ray spectral index Γ, we could calculate the X-ray flux of simulated MSPs in different energy bands, and we used these different fluxes to compute various flux ratios. For each of them, we obtained a minimal and a maximal value. Thanks to data collected by Chandra in these same energy bands, we could compute these ratios for the Chandra sources. If for one source, one of the ratios falls outside the minimal and maximal values allowed, this source is not considered as a candidate. If a ratio cannot be computed, the cut is not applied for this ratio.

From our simulation, we learned that detectable bulge MSPs are from 5.24 to 11.98 kpc away from us. These values define our distance cuts. To know the distance between us and the Chandra sources, we cross-matched the Chandra catalog with the Gaia eDR3 distance catalog by Bailer-Jones et al. (2021). If all potential matches of a Chandra source are outside our distance cuts, the source is not considered as a candidate.

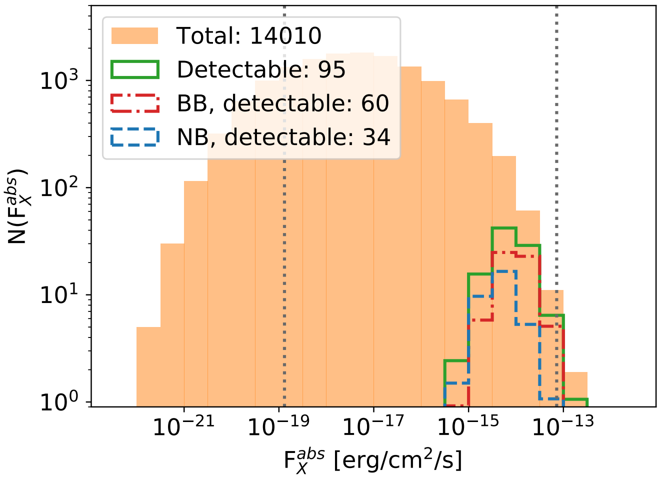

Fig. 3. X-ray energy flux distribution of the synthetic MSP population, averaged over 100 Monte Carlo simulations: Total MSPs in the ROI (orange filled), total detectable MSPs (green solid) including MSPs from BB (red dot-dashed), NB (blue dashed) and disk (not shown). The vertical dotted lines illustrate the validity range of our model extrapolation. Figure from Berteaud et al. (2021).

Applying these cuts allowed to reduce the number of candidates to about 3000, which is more than the hundred of detectable MSPs predicted by the simulation. Therefore the hypothesis is not excluded by the data and such a difference is not surprising knowing that our selection is for sure contaminated by other X-ray sources. From these more than 3000 candidates, we selected the most promising ones as follows: They should have a good spectral knowledge, so all flux ratios should be computable, and should have no Gaia counterpart, regardless of the distance, as optical counterparts of MSPs are known to be very faint. This further reduces the selection to about 300 promising MSP candidates.

4 Conclusion

The nature of the Fermi GeV excess is still to be demonstrated. We showed with Monte Carlo simulations that if it is caused by a population of MSPs, about a hundred of them could be detectable by Chandra in a ROI of $6° \times 6°$ about the Galactic Center. Unlike in γ-rays, the population wouldn't be completely unresolved in X-rays. Therefore, we looked for MSP candidates in Chandra data. Using simulation based cuts, we found more than 3000 candidates in a conservative approach, meaning that the MSP hypothesis as an explanation to the excess is not excluded. Moreover, we also selected about 300 promising sources among these candidates that have a good spectral knowledge and no optical counterpart. Our goal now is to use these candidates for follow-up studies, at radio wavelength for example.

This work was supported by the Programme National des Hautes Energies of CNRS/INSU with INP and IN2P3, co-funded by CEA and CNES

References

Abdollahi, S., Acero, F., Ackermann, M., et al. 2020, ApJS, 247, 33

Bailer-Jones, C. A. L., Rybizki, J., Fouesneau, M., Demleitner, M., & Andrae, R. 2021, AJ, 161, 147

Bartels, R. T., Edwards, T. D. P., & Weniger, C. 2018, MNRAS, 481, 3966

Berteaud, J., Calore, F., Clavel, M., et al. 2021, Phys. Rev. D, 104, 043007

Cao, L., Mao, S., Nataf, D., Rattenbury, N. J., & Gould, A. 2013, MNRAS, 434, 595

Lee, J., Hui, C. Y., Takata, J., et al. 2018, ApJ, 864, 23

DIPOLAR MAGNETIC FIELDS IN BINARIES AND GRAVITATIONAL WAVES

A. Bourgoin[1, 2], C. Le Poncin-Lafitte[1], S. Mathis[2] and M.-C. Angonin[1]

Abstract. The LISA mission will observe gravitational waves emitted from tens of thousands of galactic binaries, in particular white dwarf systems. These objects are known to have intense magnetic fields. Usually, these fields are not considered in the orbital or spins evolution of the dynamical system, as they are assumed for being too weak. It turns out that magnetic fields modify the orbits, in particular their geometry with respect to the observer. In this work, we revisit the issue and show how the magnetic fields, within the magnetostatic approximation, in a binary system generate secular drifts in the argument of the periastron, leading to modifications of the gravitational waveforms potentially detectable by LISA.

Keywords: white dwarfs, neutron stars, dipole magnetic fields, gravitational waves

1 Introduction

Laser Interferometer Space Antenna (LISA) is an ESA L class mission that aims at observing gravitational waves (GW) from space (LIS 2020; Amaro-Seoane et al. 2017) in the frequency band from below 10^{-4} Hz to above 10^{-1} Hz. Among the different sources of GW that LISA will observe are the galactic binaries. They comprise primarily white dwarfs (WD) but also neutron stars (NS) and stellar-origin black holes in various combinations. For LISA's frequency window, a typical orbital period for galactic binaries of WD and NS is ranging from tenth of hour to tenth of seconds corresponding to a semi-major axis distribution between 10^4 km to 10^6 km. Therefore, LISA will observe GW emitted by galactic binaries during the inspiral phase, just before merger which is detected by ground-based GW detectors such as LIGO, Virgo, KRAGA, and the future Einstein Telescope. LISA will thus bring precious information about the long term evolution of galactic binaries and their internal structure and equation of state.

It is expected that the galaxy is populated with approximately hundred millions of WD-WD systems and millions of NS-WD binaries (Nelemans 2009). These compact objects can have intense magnetic fields that may reach up to 10^9 G for WD and up to 10^{15} G for NS. White dwarfs with magnetic field ranging from 10^6 G to 10^9 G should represent around 20% of the total WD population while NS with magnetic field between 10^{14} G to 10^{15} G should represent around 10% of the total NS population (Ferrario et al. 2020). Therefore, a non-negligible amount of galactic binaries that LISA will observe can potentially be made of highly magnetized objects. Since then, the impact of the magnetic effects on the GW signal must be investigated. Indeed, the future data processing of the LISA mission will require that all observable physical effects be modeled with a sufficient accuracy in order to better understand the physics of these compact objects and to process the foreground noise coming from galactic binaries. Preliminary studies have focused on the monochromatic approximation only (Cornish & Littenberg 2007; LDC group 2018), that is to say the well-known Keplerian motion. However, it has been shown that a number of physical effects, such as the back reaction due to gravitational radiation (Nelemans 2009) or the dynamical tides (Fuller & Lai 2011, 2014; McNeill et al. 2020), can also have a significant impact for the time span of the LISA mission. Therefore, isolating and deriving the influence of magnetic effects on the orbital motion in order to assess their observability through the GW spectrum, is thus of a prime importance in the context of the future data processing of the LISA mission.

[1] SYRTE, Observatoire de Paris, PSL Research University, CNRS, Sorbonne Universités, UPMC Univ. Paris 06, LNE, 61 avenue de l'Observatoire, 75014 Paris, France
[2] AIM Paris-Saclay, CEA/DSM, CNRS, Université Paris Diderot, IRFU/SAp Centre de Saclay, F-91191 Gif-sur-Yvette Cedex, France

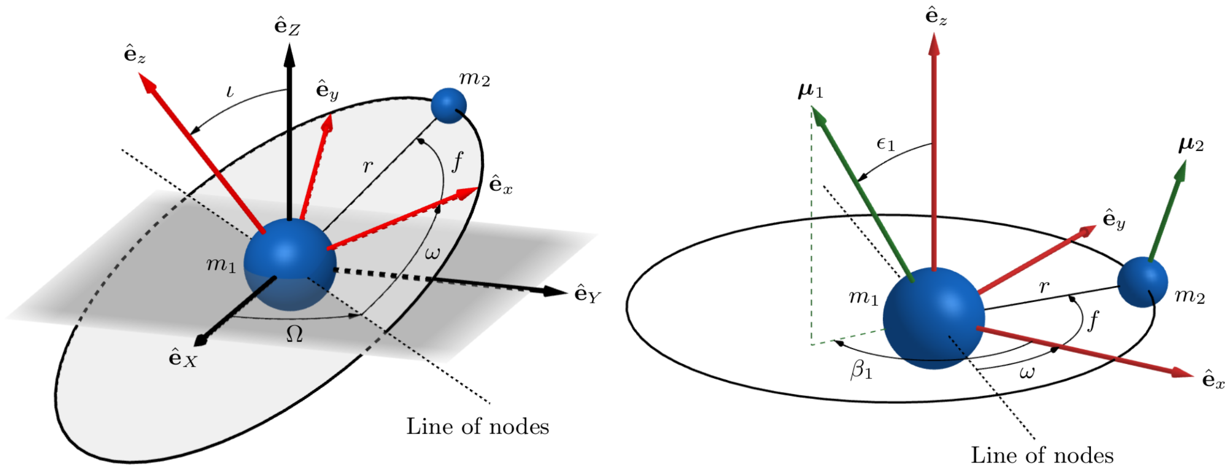

Fig. 1. Left: Orientation of the orbit frame $(\hat{\mathbf{e}}_x, \hat{\mathbf{e}}_y, \hat{\mathbf{e}}_z)$ in the center-of-mass frame $(\hat{\mathbf{e}}_X, \hat{\mathbf{e}}_Y, \hat{\mathbf{e}}_Z)$. The primary is shown at the center-of-mass of the binary system for simplicity. **Right:** Orientation of the magnetic moments in the orbit frame $(\hat{\mathbf{e}}_x, \hat{\mathbf{e}}_y, \hat{\mathbf{e}}_z)$. The obliquity ϵ_1 and the precession angle β_1 are represented for the primary only. The obliquity is a tilt between the normal to the orbital plane and the direction of the magnetic moments and the precession angle is the separation between the direction of $\hat{\mathbf{e}}_x$ and the projection of the magnetic moments on the orbital plane.

With this goal in mind, we explore the impact of dipolar magnetic fields on the orbital evolution of a binary system, within the magnetostatic approximation. We focus our attention on secular effects only, and we consider the case where the system has not reach equilibrium yet (i.e., that the magnetic torques acting on the magnetic moments do not cancel out). Then, the effect on the GW signal due to the magnetic perturbation is assessed.

2 Orbit and spins evolution considering magnetic interaction

We consider two condensed and well-separated bodies that are forming a binary system (cf., Fig. 1). The system consists of a first body (the primary) of mass m_1 and magnetic moment $\boldsymbol{\mu}_1$, and a second body (the secondary) of mass m_2 and magnetic moment $\boldsymbol{\mu}_2$. We consider a relativistic description of the point-mass dynamics up to 2.5 post-Newtonian (2.5PN) approximation (Lincoln & Will 1990; Blanchet 2014). In that sense we treat the dynamics of the binary system coherently with the loss of energy that is radiated away by gravitational waves. We also consider magnetic fields within the magnetostatic approximation which corresponds to the case of fossil fields that are frozen into the stars. In other words, we follow King et al. (1990) and assume that the internal currents that generate the magnetic field of the primary are not significantly distorted by the external field of the secondary and conversely. In addition, we consider that the magnetic fields of both stars are dominated by their dipole moments $\boldsymbol{\mu}_1$ and $\boldsymbol{\mu}_2$. Since internal currents are assumed to be stationary, the magnitude of the magnetic moments (i.e., $\mu_1 = |\boldsymbol{\mu}_1|$ and $\mu_1 = |\boldsymbol{\mu}_2|$) is taken to be constant during the motion so that we focus on their orientation only. We consider for simplicity that the direction of $\boldsymbol{\mu}_1$ and $\boldsymbol{\mu}_2$ are aligned with $\boldsymbol{S}_1$ and $\boldsymbol{S}_2$ being the spins of the primary and secondary respectively. In order to follow the evolution of the magnetic moments, we introduce two angles per stars, namely the obliquities ϵ_1 and ϵ_2, and the precession angles β_1 and β_2 (the angles are depicted in Fig. 1 for the primary only).

The methodology proceeds as follows. First, we adopt osculating elements within the method of variation of arbitrary constants in order to describe the orbital motion beyond the Keplerian approximation. We are thus dealing with a set of six first order differential equations describing changes of six Keplerian elements due to relativistic and magnetic terms. Obviously, the magnetic contribution depends on obliquities and precession angles of the magnetic moments. Therefore, we consider four additional differential equations describing changes in the orientation of $\boldsymbol{\mu}_1$ and $\boldsymbol{\mu}_2$. Secondly, in order to assess a long term secular description of the motions, the equations are averaged over the true anomaly (namely f in Fig. 1). This allows us to show that, on one hand, general relativity secularly affects the shape of the orbit (i.e., a the semi-major axis and e the eccentricity) and ω the argument of the periastron (see also Lincoln & Will (1990)). On the other hand, magnetism does affect the orientation of the orbit (i.e., ι the inclination, Ω the longitude of the node, and the argument of the periastron) but not the shape. Then, in order to solve for the secular evolution of the orbit, we first solve for the orientation of magnetic moments which can be mainly decoupled from the orbital motion. We show that the rate of precession of the magnetic moments are approximately given by

$$\dot{\beta}_1 \propto \frac{\mu_0}{4\pi}\frac{\mu_1\mu_2}{S_1}\frac{\cos\epsilon_{20}}{a^3(1-e^2)^{3/2}}, \qquad \dot{\beta}_2 \propto \frac{\mu_0}{4\pi}\frac{\mu_1\mu_2}{S_2}\frac{\cos\epsilon_{10}}{a^3(1-e^2)^{3/2}}, \tag{2.1}$$

where ϵ_{10} and ϵ_{20} are the initial value of the obliquities of the primary and secondary respectively, and where μ_0 is the vacuum permeability. We used the notation $S_1 = |\boldsymbol{S}_1|$ and $S_2 = |\boldsymbol{S}_2|$.

Then, the solutions for the orientation are then substituted within the orbital equations of motion which in turn are solved at first order in the perturbations. We show that the only angle which is secularly affected by magnetism is the argument of the periastron which presents a rate of precession that is approximately given by

$$\dot{\omega} \propto \frac{3\mu_0}{4\pi\sqrt{G}}\frac{\mu_1\mu_2}{m_1m_2}\frac{\sqrt{m_1+m_2}}{a^{7/2}(1-e^2)^2}\cos\epsilon_{10}\cos\epsilon_{20}, \tag{2.2}$$

where G is the gravitational constant.

Finally, after substituting the rate of precession of the argument of the periastron from Eq. 2.2 into the expression for the well-known GW mode polarizations h_+ and $h_\times$, we are able to assess the observability of magnetic effects by the future LISA mission. This is the subject of the following section.

3 Observing binary's magnetic effect in GW with LISA

The rate of precessions that have been derived in the last section are all proportional to the product of the magnitude of the magnetic moments of the primary and secondary. A rough estimate of the amplitude of the magnetic moments is assessed with $\mu = (2\pi/\mu_0)BR^3$ (see e.g., Pablo et al. (2019)), where R is the equatorial radius of the star and $B = |\mathbf{B}|$ is the magnitude of the magnetic field. Considering that magnetic fields can reach up to 10^9 G for the most magnetized WD and up to 10^{15} G for the most magnetized NS, we have the following rough estimates:

$$\mu_{\mathrm{WD}} \sim 10^{33}\ \mathrm{A}\cdot\mathrm{m}^2\left(\frac{R_{\mathrm{WD}}}{1\ R_\oplus}\right)^3\left(\frac{B_{\mathrm{WD}}}{10^9\ \mathrm{G}}\right), \qquad \mu_{\mathrm{NS}} \sim 10^{30}\ \mathrm{A}\cdot\mathrm{m}^2\left(\frac{R_{\mathrm{NS}}}{10\ \mathrm{km}}\right)^3\left(\frac{B_{\mathrm{NS}}}{10^{15}\ \mathrm{G}}\right). \tag{3.1}$$

Therefore, even though the magnetic fields can be several orders of magnitude stronger for highly magnetized NS than for highly magnetized WD, the magnetic moment can be higher for WD since it evolves as the cubic power of the radius and is only linear in the magnitude of the magnetic field (see also Wang et al. (2018)).

We thus consider a double WD system where the mass of the primary is $m_1 = 1.1\ M_\odot$ and the mass of the secondary is $m_2 = 0.4\ M_\odot$ such that the total mass is $m = 1.5\ M_\odot$. We consider a system with high magnetic moments at the level of $\mu_1 = 10^{33}$ A $\cdot$ m^2 and $\mu_2 = 5 \times 10^{32}$ A $\cdot$ m^2. In order to probe the LISA frequency window from 10^{-4} to 10^{-1} Hz, we assume initial values of the semi-major axis ranging from $a_0 = 10^6$ km to $a_0 = 10^4$ km, respectively. The dynamics of this system is modeled according to discussion of Sect. 2. From the dynamics, the GW mode polarizations are determined with Einstein's quadrupole formula. Finally, the relative errors generated by magnetism on h_+ and $h_\times$ are computed as follows:

$$\mathrm{err}(h_+) = \frac{|(h_+)_{\mathrm{GR+M}} - (h_+)_{\mathrm{GR}}|}{(h_+)_{\mathrm{GR+M}}}, \qquad \mathrm{err}(h_\times) = \frac{|(h_\times)_{\mathrm{GR+M}} - (h_\times)_{\mathrm{GR}}|}{(h_\times)_{\mathrm{GR+M}}}, \tag{3.2}$$

where $(h_+)_{\mathrm{GR+M}}$ is the mode polarization calculated accounting for both GR and magnetic dipole-dipole interaction while $(h_+)_{\mathrm{GR}}$ contains the gravitational contribution only. The same notation is used for $h_\times$.

The evolution of err(h_+) and err$(h_\times)$ are depicted in Fig. 2 for different values of the initial semi-major axis. It is seen that the fact of neglecting the magnetic dipole-dipole interaction can lead to errors of the level of 100% in a span of few days when the WD binary is in close orbit (i.e., for $a_0 = 10^4$ km).

4 Conclusions

In this work, we demonstrated that the dipole-dipole magnetic interaction within binary systems generates a secular drift of the argument of the periastron. The rate of the drift is proportional to the product of magnetic moments of the stars meaning that only a binary where both companions have very high magnetic moments have a chance to generate a secular drift sufficiently high for being observed by LISA. The only stars being

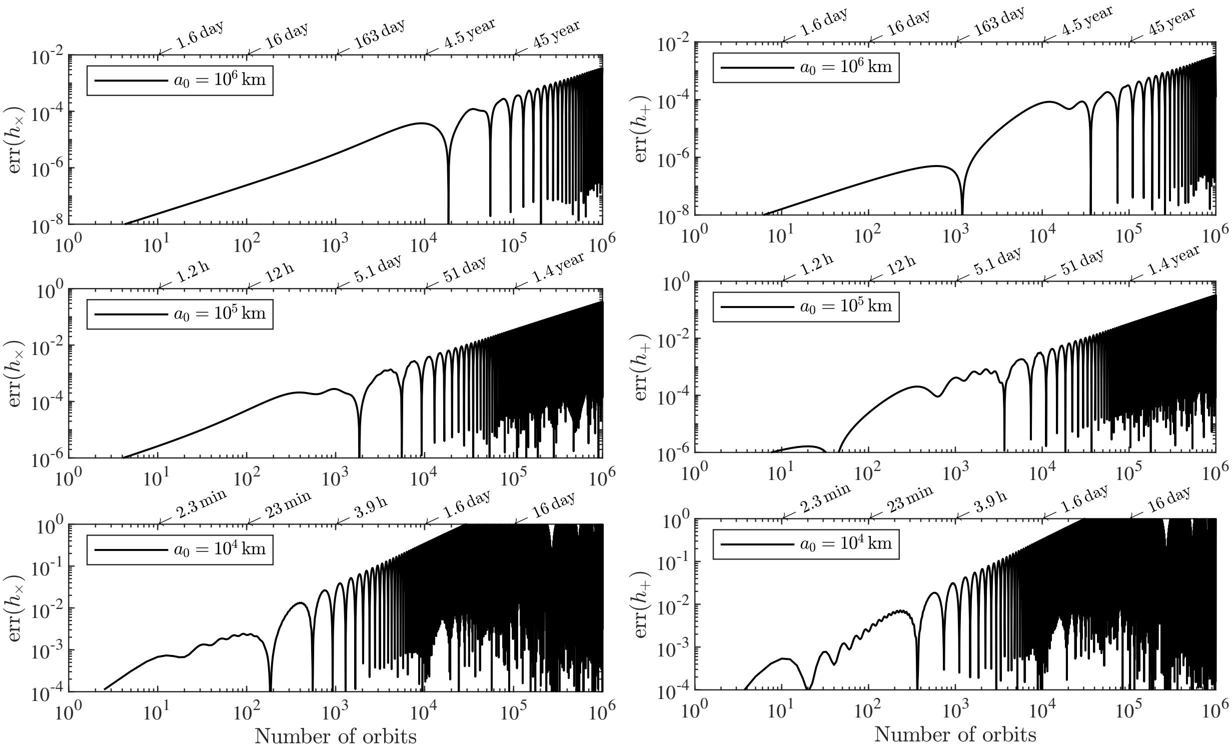

Fig. 2. Left: Relative errors caused by the fact of neglecting the dipole-dipole interaction in the computation of the mode polarization h_+. **Right:** Similar than left panel but for the mode polarization $h_\times$.

capable of such high magnetic moments are white dwarfs even though their magnetic fields are lower than for highly magnetized NS. For a binary of highly magnetized WD in a close orbit (i.e., the LISA high frequency part) not considering the magnetic effects can generate 100% errors in few days of observations. In this work, we neglected tidal effects for simplicity even though they could be important to account for while modeling the long term dynamics of binary systems. In addition, we assumed adiabatic magnetic fields but the more the orbit is shrinking the less the adiabatic hypothesis is accurate since internal currents might become distorted by external fields. In a future work, we aim at modeling binary systems in a coherent vision including tidal and magneto-hydrodynamics.

A.B. is grateful to CNES for financial support.

References

2020, The LISA collaboration, `https://www.lisamission.org/`

Amaro-Seoane, P., Audley, H., Babak, S., et al. 2017, arXiv e-prints, arXiv:1702.00786

Blanchet, L. 2014, Living Reviews in Relativity, 17

Cornish, N. J. & Littenberg, T. B. 2007, Phys. Rev. D, 76, 083006

Ferrario, L., Wickramasinghe, D., & Kawka, A. 2020, Advances in Space Research, 66, 1025

Fuller, J. & Lai, D. 2011, MNRAS, 412, 1331

Fuller, J. & Lai, D. 2014, MNRAS, 444, 3488

King, A. R., Frank, J., & Whitehurst, R. 1990, MNRAS, 244, 731

LDC group. 2018, Rev. 1

Lincoln, C. W. & Will, C. M. 1990, Phys. Rev. D, 42, 1123

McNeill, L. O., Mardling, R. A., & Müller, B. 2020, MNRAS, 491, 3000

Nelemans, G. 2009, Classical and Quantum Gravity, 26, 094030

Pablo, H., Shultz, M., Fuller, J., et al. 2019, MNRAS, 488, 64

Wang, J.-S., Peng, F.-K., Wu, K., & Dai, Z.-G. 2018, ApJ, 868, 19

SF2A 2021
A. Siebert, K. Baillié, E. Lagadec, N. Lagarde, J. Malzac, J.-B. Marquette, M. N'Diaye, J. Richard, O. Venot (eds)

COMCUBE: A CONSTELLATION OF CUBESATS TO MEASURE THE GRB PROMPT EMISSION POLARIZATION

A. Laviron[1], I. Cojocari[2], N. de Séréville[1], G. Fernandez[3], C. Hamadache[1], L. Hanlon[4], P. Laurent[2], J. Lommler[5], S. McBreen[4], A. Morselli[3], D. Murphy[4], H. Neves[6], U. Oberlack[5], R. Silva[6], V. Tatischeff[1], A. Ulyanov[4], V. Vitale[3] and P. von Ballmoos[7]

Abstract.
The precise mechanism for the prompt emission of gamma-ray bursts (GRBs) is still largely debated. Polarization measurements of the prompt gamma-ray emission could help model this phenomenon, and lead to a broader understanding of GRBs and astrophysical relativistic jets. COMCUBE is a project of the European programme AHEAD2020 aiming at the development of a Compton polarimeter CubeSat mission to measure the polarization of bright GRBs. The launch of a constellation of 6U CubeSats will allow the detection of several hundred GRBs per year and make possible a full-time monitoring of the gamma-ray sky for time-domain and multi-messenger astronomy. In addition, COMCUBE will accurately measure the polarization of the prompt emission of several GRBs per year. An extensive simulation work has been conducted to design the scientific payload, and is ongoing to quantify the sensitivity of the mission to GRBs and GRB polarization. Simultaneously, a reduced prototype of the Compton polarimeter is being developed. It uses double-sided silicon stripped detectors and inorganic scintillators read by SiPMs, and it should be tested during a stratospheric balloon flight in 2023.

Keywords: Gamma-ray burst, CubeSat, Polarization, gamma-ray astronomy

1 Introduction

In 1963, the USA, the USSR and Great Britain signed the Nuclear Test Ban Treaty, that forbids testing nuclear weapons underwater, in the atmosphere and in space. To make sure that USSR complied, the Vela space program was launched by NASA. It was composed of several pairs of satellites with embedded X- and gamma-rays detectors observing in the energy range from keV to a few MeV. In 1967, Vela 4 detected a very intense emission of gamma-rays, which was not located around the Earth nor the Sun, and showed an unexpected variability. It was the first observation of a gamma-ray burst (Klebesadel et al. 1973).

This phenomenon has been extensively studied in the next decades, and still is today. In the 1990's, the BATSE experiment onboard the CGRO spacecraft observed thousands of GRBs listed in Paciesas et al. (1999). It revealed that their location on the sky was isotropic and their duration distribution is bimodal, with a clear separation around two seconds. Longer GRBs are typically associated to powerful supernovae, and short GRBs to magnetar giant flares and binary neutron star mergers, which has been confirmed by Abbott et al. (2017) coincident observation of a short GRB and a gravitationnal wave event. In both cases, the gravitationnal collapse of an object or a system generates an accretion disk and an ultra-relativistic jet. This jet then interacts in the interstellar medium, which generates an afterglow emission, detectable from radio to TeV energies. The

[1] IJCLab, Orsay, France
[2] CEA-IRFU, Saclay, France
[3] INFN, Roma, Italy
[4] UCD, Dublin, Ireland
[5] Johannes Gutenberg Univ., Mainz, Germany
[6] LIP, Coimbra, Portugal
[7] IRAP, Toulouse, France

acceleration of particles in the jet is the source of the gamma-ray emission. The content of that jet and the physics driving the emission is still largely debated. Polarization measurements to probe GRB prompt emissions will rule out some models (Toma et al. 2009). It gives a better understanding of the jet mechanism, that points to the physics of the progenitor. In addition, it provides a direct measurement of the Lorentz invariance violation associated to vacuum birefringence (Laurent et al. 2011).

2 COMCUBE mission design

COMCUBE is a CubeSat constellation mission to measure the polarization of bright GRBs. A Compton telescope is embedded in each CubeSat, its role is to reconstruct the energy and direction of an incoming gamma ray by reconstructing a Compton interaction. By measuring, for each gamma ray, the position and energy deposit in both the tracker and the calorimeter, we can constrain the direction of the incoming gamma-ray to an event circle. If enough interactions are correctly reconstructed, the source is where all event circles intersect (see figure 1 left panel).

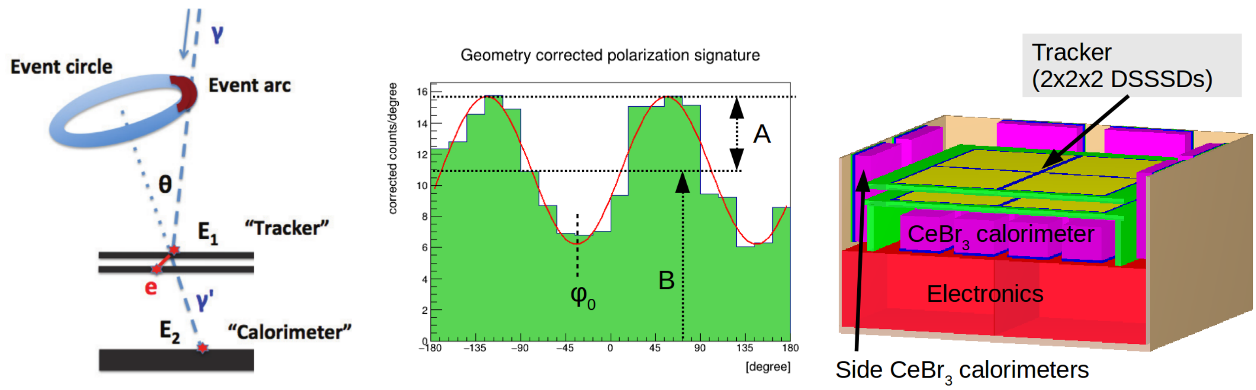

Fig. 1. Left: Scheme of a Compton telescope. **Middle:** Polarization signature (cosine squared modulation) in a Compton telescope (from simulations). The angle of polarization is ϕ_0 and the fraction of polarization is $\frac{A/B}{\mu_{100}}$, where μ_{100} is the amplitude of the modulation of a 100% polarized source. **Right:** 4U scientific payload of COMCUBE (6U).

This instrument is also sensitive to linear polarization through the azimuthal scatter angle of the Compton scattering, as shown in the Klein-Nishina differential cross-section for polarized photons :

$$\frac{d\sigma_{KN}}{d\Omega} = \frac{1}{2} r_e^2 \left(\frac{E'_\gamma}{E_\gamma}\right)^2 \left[\frac{E'_\gamma}{E_\gamma} + \frac{E_\gamma}{E'_\gamma} - 2 \ \sin^2 \ \theta \ \cos^2 \ \phi\right]$$

The polarization angle ϕ_0 is given by a minimum of the fitted cosine squared modulation, also called polarigram, represented in figure 1 middle panel. The polarization fraction is given by $\Pi = \frac{\mu}{\mu_{100}}$ with the amplitude $\mu = \frac{A}{B}$ (see A and B on figure 1 middle panel), and $\mu_{100}(< 1)$ the modulation of a 100% polarized source seen by the instrument.

To achieve our scientific goal, we designed the scientific payload from extensive numerical simulations using the MEGAlib software (Zoglauer et al. (2006)). It will be composed of two layers of four double-sided silicon stripped detectors (DSSSDs) for the tracker, and several calorimeter modules based on cerium bromide ($CeBr_3$ inorganic scintillator), integrated in a CubeSat. CubeSat units (U), defined as $10 \times 10 \times 10\,\mathrm{cm}^3$ in volume and 1.3 kg in mass, can be combined to form larger (2U, 3U, 6U) spacecrafts. COMCUBE instrument is $20 \times 20 \times 10\,\mathrm{cm}^3$ in size (4U) and will be embedded in a 6U spacecraft. Compared to the Compton telescope scheme (figure 1 left panel), we added calorimeters on all four sides to increase the sensitivity to polarization (see figure 1 right panel). A constellation of CubeSats, each containing its own Compton telescope, would allow all-sky monitoring, as well as time-of-arrival localization of transient with sub-degree accuracy for the brightest events, (see e.g. Werner et al. (2018) for the CAMELOT project).

3 COMCUBE performance simulations : preliminary results

Simulations are currently ongoing to better quantify the performances of our instrument. For a single 4U instrument, we simulated (so far) three long GRBs (1000 times each) from the 10 year catalog of GBM (Poolakkil et al. 2021), the secondary payload of the Fermi spacecraft. The background is assumed to be that of an equatorial low-Earth orbit at 550 km altitude. The considered GRB's peak fluxes are represented on the left of figure 2, over the peak flux distribution of the whole catalog. The two brightest ones (in red and green on figure 2 left panel) are detected with a signal to noise ratio SNR > 5 every time they are above the Earth horizon (we defined SNR $= \frac{S-B}{\sqrt{B}}$) where S is the signal (number of triggers of the GRB and the background), B is the expected background (number of triggers)). The SNR of the faintest one is represented in colorscale in the figure 2 right panel. This faint GRB is still detected frequently, mainly in the upper part of the sky near the zenith.

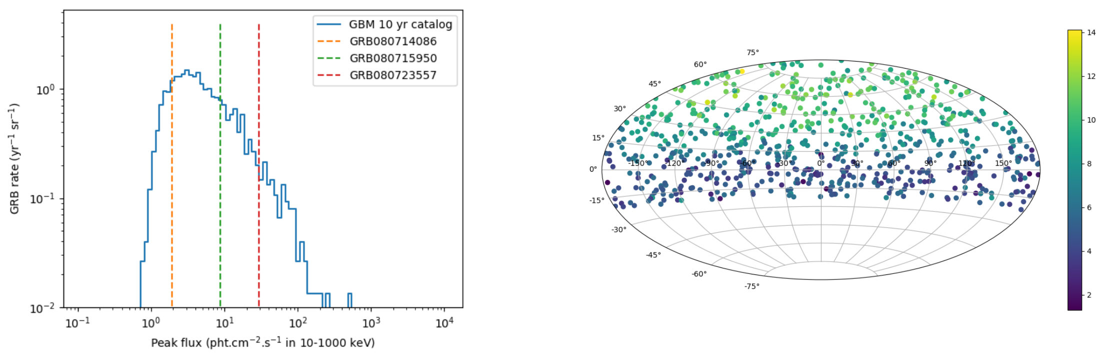

Fig. 2. Left: Histogram of the peak flux of GBM GRBs (blue) and the peak flux of the three GRBs simulated so far (yellow, green, red). **Right:** Map of the sky for the 1000 simulated GRBs of spectrum and peak flux that of GRB080714086. Each point represents a simulation, and its color the signal to noise ratio (see colorscale). The lower part of the sky has no point because it is located below the Earth horizon.

For polarization simulations, preliminary results are shown in figure 3 left and right panels. By using the BATSE or GBM catalog and 7 altitude sky bins of equal solid angle, we show on left panel that we expect to detect, on average, one GRB per year with a minimum detectable polarization at the 99% confidence level MDP_{99} ($\mathrm{MDP}_{99} = \frac{4.29}{\mu_{100} S}\sqrt{(S+B)}$, see e.g Weisskopf et al. (2010)). We obtain similar results from the BATSE and GBM catalogs. The simulated background from cosmic and atmospheric gamma rays is calculated with the MEGAlib background generator using 5 GV cutoff rigidity. We show on the left panel of figure 3 that it has a significant effect on GRB polarization measurements.

If we observe a same GRB with several instruments (figure 3 right panel), the data can be combined to perform a more precise polarization analysis. Thus, if we suppose that we have 4 CubeSats in low-Earth orbit, with a 20% downtime, we expect to measure 5 GRBs per year with a $\mathrm{MDP}_{99} < 30\%$.

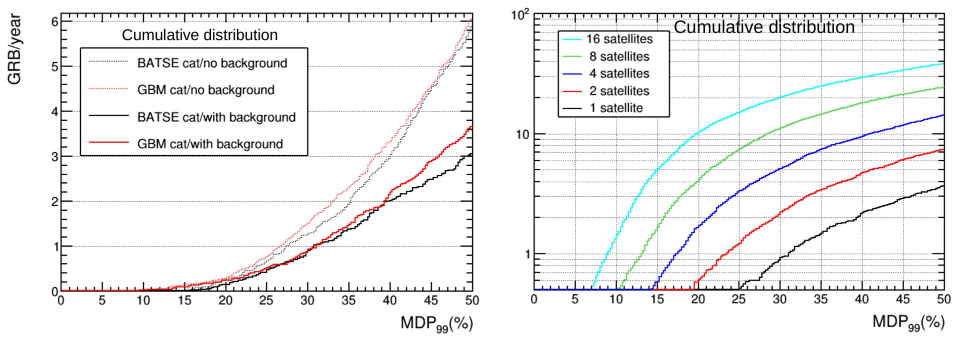

Fig. 3. Left: Number of GRB detected for one year in orbit as a function of the minimum detectable polarization achievable for the observation. **Right:** Number of GRBs observed in a year as a function of the minimum detectable polarization achievable for various numbers of CubeSats in orbit.

4 Compton telescope prototype status

A first prototype of the COMCUBE Compton telescope is being developed. Two kinds of detectors are studied. For the tracker, we developed double-sided silicon stripped detectors (DSSSD) and a low-noise readout electronics. These detectors are a single PN junction detector, of size 64 x 64 x 1.5 mm^3 with 32 strips on each side. For the calorimeter, we developed modules based on a single monolithic inorganic scintillating crystal of cerium bromide ($CeBr_3$), optically coupled to a pixelated photo-sensor. Since the scintillation light is emitted near the interaction position, the pixels closer to that position will receive more light. The position of interaction can then be reconstructed using machine learning algorithms. For more details, see Laviron et al. (2021). With these two building blocks, we assembled a first working prototype, shown on the picture figure 4 left panel.

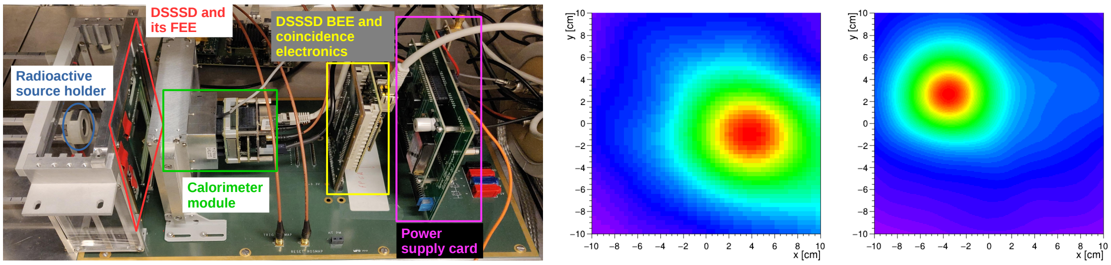

Fig. 4. Left: Picture of the first prototype with its main components. FEE and BEE stand respectively for Front-End Electronics (analog signal processing and digitization) and Back-End Electronics (data merging and communication with onboard computer) **Right:** Reconstructed images for two positions of the ^{137}Cs source. Source positions were $x, y = (36, -11)$ mm and $x, y = (-36, 23)$ mm.

One can see on figure 4 right panel, two Compton images obtained during preliminary tests with a ^{137}Cs radioactive source emitting 662 keV gamma rays. The source position was changed between the two acquisitions. We can see that it is well reconstructed. The energy resolution was 5.7 % at 662 keV.

5 Conclusions

COMCUBE is a constellation of CubeSats that will be able to measure the polarization of several GRB prompt emission per year. Simulations have been performed to design the instrument, and more simulations are ongoing to better quantify its performances. For one CubeSat, the chosen design is a 4U Compton telescope in a 6U spacecraft. The telescope is based on two layers of DSSSD detectors for the tracker and on $CeBr_3$ scintillating crystals coupled to SiPM arrays for the calorimeter. We have already built a minimal prototype and tested its imaging capabilities with success. We are building a 1U demonstrator for a stratospheric balloon flight in summer 2023 and we plan to further test the prototype with polarized gamma ray sources in the near future.

Acknowledgements: This paper is supported by European Union's Horizon 2020 research and innovation programme under grant agreement No 871158, project AHEAD2020.

References

Abbott, B. P., Abbott, R., Abbott, T. D., et al. 2017, The Astrophysical Journal, 848, L12
Klebesadel, R. W., Strong, I. B., & Olson, R. A. 1973, ApJ, 182, L85
Laurent, P., Götz, D., Binétruy, P., Covino, S., & Fernandez-Soto, A. 2011, Phys. Rev. D, 83, 121301
Laviron, A., Gourlaouen, V., Hamadache, C., et al. 2021, NIMA, 1007, 165379
Paciesas, W. S., Meegan, C. A., Pendleton, G. N., et al. 1999, ApJS, 122, 465
Poolakkil, S., Preece, R., Fletcher, C., et al. 2021, The Astrophysical Journal, 913, 60
Toma, K., Sakamoto, T., Zhang, B., et al. 2009, ApJ, 698, 1042
Weisskopf, M. C., Elsner, R. F., & O'Dell, S. L. 2010, Space Telescopes and Instrumentation 2010: Ultraviolet to Gamma Ray
Werner, N., Řípa, J., Pál, A., et al. 2018, in Society of Photo-Optical Instrumentation Engineers (SPIE) Conference Series, Vol. 10699, Proceedings of the SPIE, 106992P
Zoglauer, A., Andritschke, R., & Schopper, F. 2006, New A Rev., 50, 629

THE BEST BROTHS ARE COOKED IN THE OLDEST PANS: REVISITING THE ARCHIVAL HST/FOC OBSERVATIONS OF QUASARS

F. Marin[1], T. Barnouin[1] and E. Lopez-Rodriguez[2]

Abstract. The Faint Object Camera (FOC) aboard the Hubble Space Telescope (HST) observed 26 individual active galactic nuclei (AGNs) in ultraviolet imaging polarimetry between 1990 and 2002. Tremendous progresses have been made thanks to those high spatial resolution, high signal-to-noise ratio observations, such as the identification of the location of hidden active nuclei and the three dimensional arrangement of polar material within the first hundred of parsecs around the central core. However, not all AGN observations have been reduced and analyzed, and none in a standardized framework. In this lecture note, we present our project of downloading, reducing and analyzing all the AGN HST/FOC observations that were achieved using a consistent, novel and open-access reduction pipeline. We briefly present our methodology and show the first, preliminary result from our reduction pipeline: NGC 1068.

Keywords: Instrumentation: polarimeters, Methods: observational, Polarization, Astronomical data bases, Galaxies: active, Galaxies: Seyfert

1 Introduction

Ultraviolet (UV) observations allowed to make a huge leap forward in the field of astrophysics. UV pictures of the cosmos are rather different from the familiar collection of stars and galaxies seen at optical wavelengths. Main sequence stars become dimmer, since they emit most of their bolometric luminosity in the visible or near-infrared bands. Newly formed high-mass stars, producing UV radiation and violent stellar winds, light up instead. Similarly, irregular or spiral (young) galaxies and elliptical (old) galaxies become more visible because of the extra-production of UV light. Indeed, young galaxies experiment strong star formation, leading to large UV fluxes. In the case of old galaxies, UV photons are mainly produced by dying stars that have shed their cool outer layers in the post-red-giant phase of their evolution, revealing their small, hot cores (Code & Welch 1979; Davidsen 1993). It follows that UV astronomy can probe the evolution of stars and galaxies, in the early and late stages of their evolution. Those observations are essential to understand how the Universe has evolved from its origins to nowadays.

The Hubble Space Telescope (HST) was the first major space telescope to reveal the near, mid and far UV spectrum of the sky, though other UV instruments have flown on smaller observatories such as GALEX, as well as sounding rockets and the Space Shuttle (Linsky 2018). Among the original instruments aboard the HST, the Faint Object Camera (FOC) was a particular device. It consisted of a long-focal-ratio, photon-counting imager capable of taking high-resolution images in the wavelength range 1150 – 6500 Å. When corrected by COSTAR, the field-of-view (FoV) and pixel size of the f/96 camera were 7" × 7" (512 × 512 format) and 0.014" × 0.014", respectively. But, most importantly, it was a polarimeter. The huge spatial resolution offered by the FOC, coupled to the very low instrumental polarization and excellent polarizing efficiencies of the polarizers in the f/96 relay made the FOC a unique instrument, the first to take UV polarimetric pictures in space. The FOC remained in operation from 1990 to 2002, when it was replaced by the ACS during Servicing Mission 3B.

[1] Université de Strasbourg, CNRS, Observatoire astronomique de Strasbourg, UMR 7550, F-67000, Strasbourg, France
[2] Kavli Institute for Particle Astrophysics and Cosmology (KIPAC), Stanford University, USA

2 The HST/FOC initiative

Scanning the HST/FOC database, we found that about 15% of the proposals in the FOC archives lack any exploitation. In addition, all the published observational campaigns do not follow the same reduction procedure. Methods vary widely from one group to another, making a rigorous analysis of the whole HST/FOC sample impossible. We thus decided to achieve a meticulous, systematically complete and consistent re-analysis of all raw HST/FOC imaging polarimetric AGN observations to enable science deferred or unachieved by many approved programs.

2.1 A new, generalized reduction pipeline

In order to standardize the reduction of the HST/FOC data, we followed the steps presented by Capetti et al. (1995a), Capetti et al. (1995b), Nota & et al. (1996) and Kishimoto (1999) among other authors. We dismissed zeroth-order corrections and focused on the most precise operations, always working with the raw data (POL0, POL60, POL120) and Stokes parameters (I,Q,U) to estimate and propagate errors. In methodological order, we import the raw data and select the region of interest using a Graham's scan algorithm (Graham 1972). This algorithm finds the convex hull of a set of n points in the plane with a complexity $O\,(n \log n)$, cropping out undesired values from the data matrix. We then deconvolve the images using the Richardson-Lucy deconvolution algorithm (Richardson 1972) for recovering the underlying image that has been blurred by the photo-diodes of the detector. After deconvolution, we compute errors using a squared zone of the image that is background dominated. This error is later quadratically propagated for any reduction operation on the data. This includes correlated error through re-sampling and smoothing. The next steps are data re-sampling, alignment and smoothing thanks to user defined kernels or image combinations. The Stokes parameters are computed using the standard Nota & et al. (1996)'s procedure, then we derive the polarization degree and angle. Celestial rotation is applied, we compute the proper units for both the total and polarized fluxes and display the results before saving everything into FITS files. A very detailed explanation of each of the aforementioned steps will be presented in the first paper of our series (Barnouin et al., in prep).

2.2 Preliminary result: NGC 1068

In order to test our pipeline, we decided to re-analyze the FOC data of NGC 1068. This is the most archetypal type-2 (edge-on) radio-quiet AGN and thus the best target for benchmarking. It possesses the largest database of radio-to-UV polarization measurements (Marin 2018a) and was even part of the original catalog of Carl Seyfert (Seyfert 1943). NGC 1068 was observed by the FOC on Feb 28, 1995 (5:33AM), program ID 5144. The dataset was obtained through the F253M UV filter centered around 2530 Å, together with the polarizing gratings POL0, POL60, POL120. The optical relay f/96 was selected to obtain a FoV of 7" × 7" and a pixel size of 0.014" × 0.014". It results in a 512 × 512 pixelated image of the source and its environment. Each polarizing grating acquired 3 500 seconds worth of observation for a total exposure time of 10 581 seconds (including the CLEAR and F253M filters).

Fig. 1 shows the total flux image of NGC 1068 obtained by Capetti et al. (1995b) with the Feb 28, 1995's observation. Fig. 2 presents the exact same observation processed through our standardized pipeline. Despite being larger and containing more polarimetric information, we intentionally cropped our figure to approximatively the same FoV (3.3 × 2.9 arcsec) than the figure from Capetti to make comparisons easier. Our figure is also polychromic. Apart from those visual details, the global flux mapping and polarization vector pattern are extremely similar between the two figures. It is reassuring, telling us that our method works smoothly. But striking differences also appear. First, we extracted much more information from the raw data in terms of polarization. For the same cut-off in signal-to-noise ratio in polarization (>20), we detect much more polarized pixels. Those pixels, mostly along the polar direction of the AGN symmetry axis, better highlight the half-opening angle of the outflows. This could be used to constrain the half-opening angle of the circumnuclear, dusty region if the winds fill the whole solid angle. The vectors also define the centro-symmetric shape of the polarization pattern with a greater precision than before, validating the approach taken by authors such as Gratadour et al. (2015) to reveal obscured regions by contrast. Finally, small details vary from Fig. 1 to Fig. 2, such as the position of the maximum polarization degree pixels and the presence of vectors misaligned with respect to the centro-symmetric pattern at the outskirts of the polar winds. It is too early to determine if this is due to scattering on a dust lane (Stalevski et al. 2017; Vollmer et al. 2018), background contamination by the host Marin (2018b) or the presence of parsec-scale magnetic fields Lopez-Rodriguez et al. (2020).

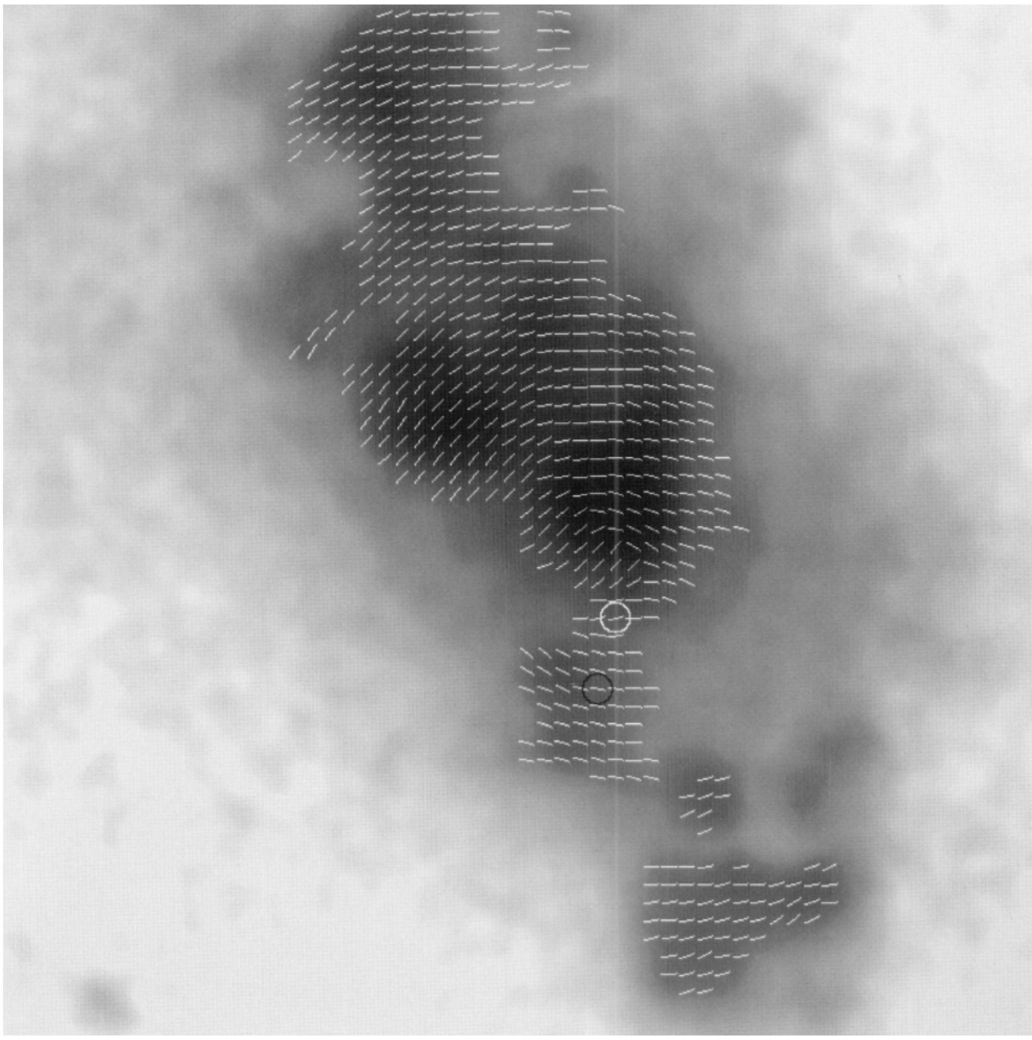

Fig. 1. Total flux image of NGC 1068 obtained by Capetti et al. (1995b). The polarization information is superimposed to the image using white vectors. The length of the vectors is fixed and does not represent the polarization degree value. The polarization position angle can be visualized thanks to the orientation of the vectors. No indication on the flux strength was provided by the authors. We only know that the darkest regions correspond to the brightest UV fluxes.

3 Conclusions

We have developed a new, standardized, consistent reduction pipeline to explore in great details the archives of the HST/FOC. Because 15% of the observations were never reduced, and because the rest has not been explored in a consistent way, we aim at producing a complete and generalized catalog with high-resolution images for the community. We expect new discoveries and refined conclusions on the geometry of the scattering regions in AGNs, the detection and location of hidden nuclei, the composition of the polar outflows (electrons, dust or a mixture of both) and novel constrains on the evolution of galaxies.

The authors would like to thank Dr. Makoto Kishimoto for his continuous help in establishing a robust and standardized reduction pipeline.

References

Capetti, A., Axon, D. J., Macchetto, F., Sparks, W. B., & Boksenberg, A. 1995a, ApJ, 446, 155
Capetti, A., Macchetto, F., Axon, D. J., Sparks, W. B., & Boksenberg, A. 1995b, ApJ, 452, L87
Code, A. D. & Welch, G. A. 1979, ApJ, 228, 95

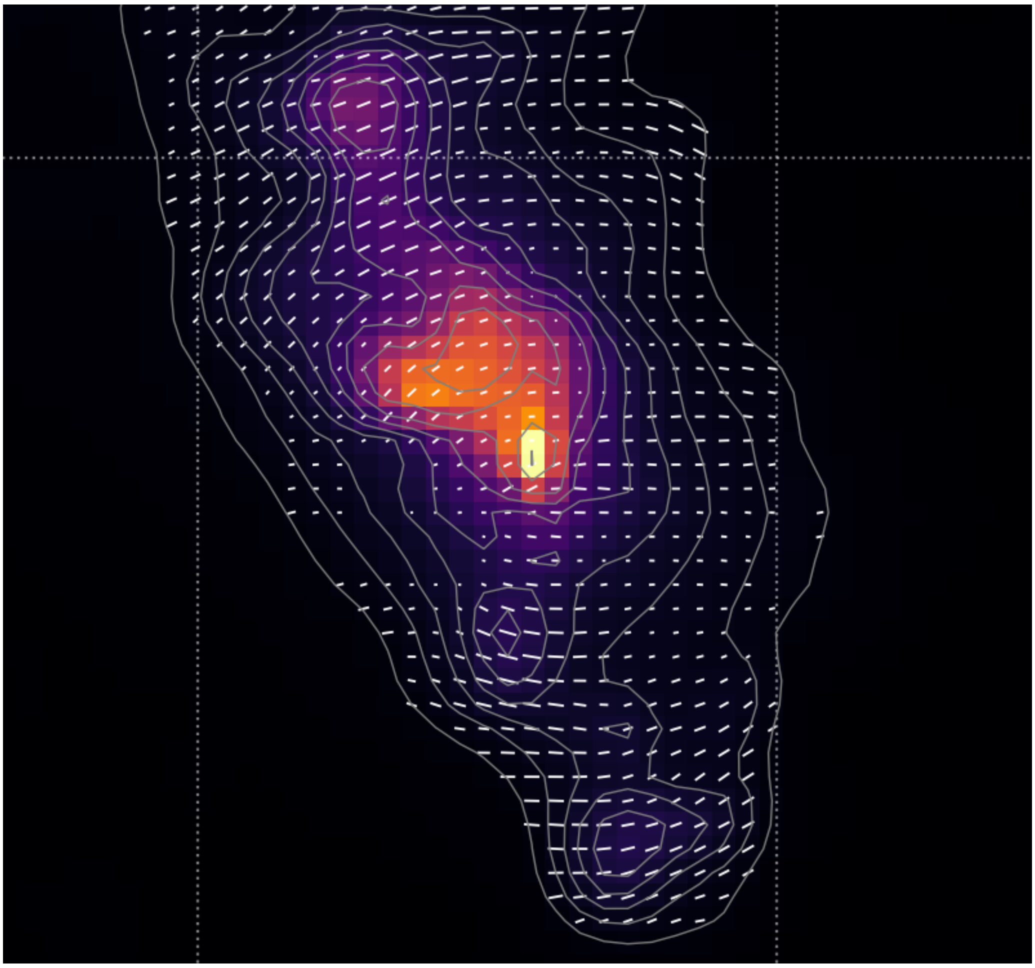

Fig. 2. Results from our re-analysis of NGC 1068. The total flux F_λ is linearly color-coded from black (no flux) to yellow (5.10^{-16} erg.s^{-1}.cm^{-2}.$\AA^{-1}$). The polarization information is superimposed to the image using white vectors. The linear polarization degree is proportional to the vector length while the polarization position angle is indicated by the orientation of the vector (a vertical vector indicating a polarization angle of 0°). North is up, East is left. A spatial bin corresponds to 0.1". The different contour levels highlight the various signal-to-noise ratios in total flux in decreasing order from the brightest region to the outskirts of the AGN (433, 399, 366, 332, 298, 265, 231, 197, 164, 130). We intentionally cropped our image to approximatively the same FoV than Capetti et al. (1995b)'s, see Fig.1.

Davidsen, A. F. 1993, Science, 259, 327
Graham, R. 1972, Information Processing Letters, 1, 132
Gratadour, D., Rouan, D., Grosset, L., Boccaletti, A., & Clénet, Y. 2015, A&A, 581, L8
Kishimoto, M. 1999, ApJ, 518, 676
Linsky, J. L. 2018, Ap&SS, 363, 101
Lopez-Rodriguez, E., Dowell, C. D., Jones, T. J., et al. 2020, ApJ, 888, 66
Marin, F. 2018a, MNRAS, 479, 3142
Marin, F. 2018b, A&A, 615, A171
Nota, A. & et al. 1996, Faint Object Camera Instrument Handbook v.7
Richardson, W. H. 1972, J. Opt. Soc. Am., 62, 55
Seyfert, C. K. 1943, ApJ, 97, 28
Stalevski, M., Asmus, D., & Tristram, K. R. W. 2017, MNRAS, 472, 3854
Vollmer, B., Schartmann, M., Burtscher, L., et al. 2018, A&A, 615, A164

SF2A 2021
A. Siebert, K. Baillié, E. Lagadec, N. Lagarde, J. Malzac, J.-B. Marquette, M. N'Diaye, J. Richard, O. Venot (eds)

A POSSIBLE INSTABILITY ORIGIN FOR THE FLARES IN SAGITTARIUS A*: LINKING SIMULATIONS AND OBSERVATIONS

R. Mignon-Risse[1], N. Aimar[2], P. Varniere[1, 3], F. Casse[1] and F. Vincent[4 4]

Abstract. While flares in the submm, near-IR and X-ray domains are regularly detected from Sagittarius A* (Sgr A*), the supermassive black hole at the center of our galaxy, no model has yet gained wide acceptance. Here we focus on structures originating from the wind of close-by massive stars or from the partial disruption of a comet/cloud/star and we study how instabilities occuring in those structures could produce an accretion burst and an associated observable flare.

Using NOVAs, composed of 3D general relativistic (GR) magneto-hydrodynamical (MHD) and GR ray-tracing codes, we aim to investigate how a post-disruption circularized annulus of gas hosts the development of the Rossby Wave Instability. We first show that the subsquent accretion event indeed produces an observable flare. Then, we look how this population of flares behaves with respect to SgrA* flares in the parameter space. In particular, we show how the annulus properties in terms of mass and spatial extent (partly inherited from its parent object, star or cloud) can reproduce the variety of observed flare shapes.

Keywords: Sagittarius A*, flare, submillimeter

1 Introduction

Theoretically, accreting Black Holes (BH) show us how matter behaves in a strong gravitational field. Observationally, they power among the most energetic accretion/ejection processes in the Universe, whose exact properties remain unknown. While not being as active as many supermassive BHs, the galactic supermassive BH Sgr A* offers a unique possibility for observing and understanding those objects: it has the largest angular size of any BH observable from Earth and it powers frequent (typically one per day) X-ray, near infrared and submm flares, i.e. sudden increases in brightness above the quiescent level, often at the same time or with a short delay. As the emission is estimated to originate from only a few gravitational radii from the BH (see e.g., GRAVITY Collaboration et al. 2018), those flares provide insights on the nearest region to the BH horizon.

The mechanism and the emitting process behind those flares remain debated, even though they are ubiquitous in the observations of Sgr A*. Indeed, a model should be able to reproduce the flare energetics as well as the lightcurve properties (duration, amplitude, shape. . .) and correlations between those properties over the electromagnetic spectrum. The typical duration is of the order of the orbital period and the amplitude can reach $\sim$70 times the quiescent level. Moreover, a single flare event can exhibit several local maxima before turning back to quiescence, something we will refer to as the flare "multiplicity". Overall, a model should account for the diversity of flare shapes observed while relying only on one physical phenomenon. We address in particular this problem here.

Estimates on the energetics of flares led to consider accretion of asteroids/comets as a possible explanation. These so-called partial/total tidal disruption events (hereafter, TDEs) may produce a ring-like structure of magnetized debris stream falling onto the BH (see Bonnerot & Stone 2021 and refs. therein). Such structures

[1] Université de Paris, CNRS, AstroParticule et Cosmologie, F-75013, Paris
[2] LESIA, Observatoire de Paris, Université PSL, CNRS, Sorbonne Universités, UPMC Univ. Paris 06, Univ. de Paris, Sorbonne Paris Cité, 5 place Jules Janssen, 92195 Meudon, France
[3] AIM, CEA, CNRS, Université Paris-Saclay, Université Paris Diderot, Sorbonne Paris Cité, 91191, Gif-sur-Yvette, France
[4] Observatoire de Paris/LESIA, 5 Place Jules Janssen, 92195 Meudon Cedex, France

would naturally give rise to the Rossby Wave Instability (RWI, Lovelace et al. 1999, see below). Indeed, the presence of an extremum of density in the ring-like structure will lead to the extremum in vortensity required by the RWI. In this study, we follow the RWI developing on this ring, building on previous studies (see Tagger & Melia 2006 and Falanga et al. 2007) that have shown it to match the flare duration, amplitude and modulation observed in several long flares (Bélanger et al. 2006). Our ultimate goal is to link the pre-flare properties (i.e. the ring and before that, the disrupted object) to the flare properties.

To that end, we use the NOVAs pipeline. NOVAs includes the GR-MHD version of the GR-AMRVAC code (Casse et al. 2017) which will allow us to expand in full GR the work done by Falanga et al. (2007) in pseudo-Newtonian gravity. More importantly, we will use NOVAs to produce synthetic observations with the GR ray-tracing code GYOTO* (Vincent et al. 2011). In fact, photons emitted close to the BH can reach the observer with a delay as large as half an orbital timescale at the LSO (Vincent et al. 2013), producing a secondary image (see also Casse et al. 2017 for the importance of including GR in the ray-tracing step of a BH disk). This two-steps process will allow us to obtain observables and to directly compare them with observations.

2 GRMHD simulations of the Rossby Wave Instability

The RWI is a good candidate to explain Sgr A* flares because it provides a natural mechanism to produce accretion bursts, as we will show now. Indeed, the RWI develops at the location of an extremum in vortensity (i.e. specific vorticity) or magneto-vortensity (Tagger & Varniere 2006), defined as (Tagger & Pellat 1999)

$$L_{\mathrm{B}} = (\nabla \times \mathbf{v})\,\frac{\Sigma}{B^2}, \tag{2.1}$$

where $\mathbf{v}$ is the velocity vector, Σ is the surface density and B is the magnetic field strength. When a post-TDE stream circularizes, it naturally develops an extremum in vorticity as the centrifugal acceleration builds the equilibrium around the density extremum. Thefore, the RWI will naturally develop on this ring and lead to an accretion burst, which was proposed earlier to produce an observable flare. The RWI has been studied in various astrophysical contexts because the aforementioned extremum is naturally present at the last stable orbit (LSO) of differentially-rotating disks, which makes it an elegant model for explaining the high-frequency quasi-periodic oscillations of microquasars (i.e. accreting stellar-mass BHs).

Here are the initial conditions of our simulations, consisting of a background disk with an additional ring structure. The background disk density profile follows a power-law of index $-3/4$, and the disk is initially threaded by a radial and vertical magnetic field with a plasma beta $\beta \gg 1$, consistent with a very weakly magnetized medium. On top of this background disk, the ring structure corresponds to an axisymmetric bump whose density is given by

$$\Sigma_{\mathrm{b}}(r) = \epsilon_{\mathrm{b}} \exp\left(- \left(\frac{r - r_{\mathrm{b}}}{\sigma_{\mathrm{b}}} \right)^2 \right) \tag{2.2}$$

where r is the radius with respect to the central BH. We consider simple ring properties such as its amplitude ϵ_{b}, its width σ_{b} and its position r_{b}. The bump vertical magnetic field is defined similarly. We explore ring magnetization levels from weakly magnetized ($\beta{\sim}5$) to fully magnetized ($\beta{\sim}1$). Those ring properties are inherited from the disrupted object mass, magnetization and angular momentum.

As shown in the density map of the left panel of Fig. 1, we see the RWI developing on the ring-like structure. Its behaviour agrees with the studies reported in the literature. Furthermore, as can be observed, the RWI leads to the formation of overdensities. The number of those overdensities is linked to the multiplicity of modes of the instability, which relies on local conditions (Varniere et al. 2019) and could possibly create several pics within a flare event (i.e. without the flux returning to the quiescent level). Hence, the number of pics would vary between different flares. In the simulation, we observe that the accretion is no longer axisymmetric and occurs via the episodic accretion of overdensities.

Then, we computed the frequency-integrated flux after the ray-tracing step and obtained the lightcurve displayed in the right panel of Fig. 1. For this work, we considered the frequency band $10^9 - 10^{15}$ Hz, covering the submm and near-infrared domains. We assume that the flares in those frequency bands arise from synchrotron

*Freely available at `http://gyoto.obspm.fr`

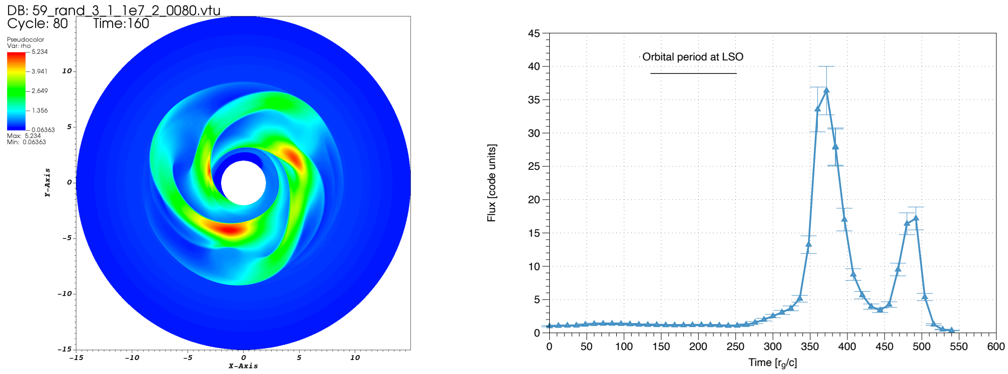

Fig. 1. Left: Density map of the RWI developing on the ring in the non-linear regime. **Right:** Corresponding light curve. Time has been expressed in r_g/c, where r_g is the gravitational radius and c is the speed of light.

emission with a κ distribution (with $\kappa = 5.5$). This lightcurve shows us that, as seen from an observer, the aforementioned accretion bursts indeed translate into a flare event. Moreover, the duration of this flare is roughly the orbital period, in agreement with the observational constraints.

3 Reproducing the flare variability

Left panel of Fig. 2 shows the concatenated lightcurve of Sgr A* in the K-band (2.2μm) as seen by VLT/NACO and Keck/NIRC2 (Fazio et al. 2018). As can be seen, flares have no typical shape: a Gaussian fit is not always satisfactory and they are not symmetric. A flare model should account for this.

Here, we investigate how the RWI can reproduce flare properties. Using the ring amplitude and width (i.e. the mass, magnetization and angular momentum of the disrupted object), we show in the right panel of Fig. 2 it is already possible to reproduce this variety of behaviors. All simulated flare durations are of the order of the orbital period at the LSO. This confirms the RWI as a good candidate to explain the variety of flare behaviors.

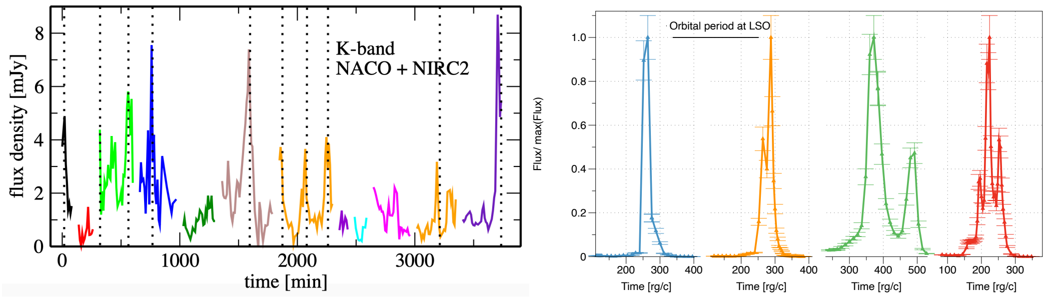

Fig. 2. Left: Concatenated lightcurve showing the near infrared flares of Sgr A* (Credits: Fazio et al. 2018 and Zhiyuan Li) exhibiting a variety of structures. More than one flux extremum can be seen in a single flare event. **Right:** Synthetic light curves reproducing the variety of observed flare shapes. We have varied the ring amplitude and witdh. For readability, fluxes are normalized by the maximal flux.

As briefly mentioned in the introduction, a single flare event can have a multiplicity of peaks (visible in the left panel of Fig. 2). A physical interpretation could be that multiple clumps have been accreted in a short amount of time, indicating that they could come from the same density structure. This is an additional constraint for a flare model, which we study next.

As shown in the right panel of Fig. 3, for a given set of parameters, the RWI is capable of reproducing qualitatively the multiplicity reported in the study of Hamaus et al. (2009) (left panel of Fig. 3). So far, varying the ring amplitude and width only, we get a flare multiplicity in the range [1;4] as it is the one that could be detected at those timescales, similar to the variety of multiplicities observed. Let us note though that, depending on the temporal resolution and the instrumental noise, detecting multiplicity within a flare can be challenging. Therefore, comparing the multiplicity of an observed flare with that of a synthetic flare - whose temporal resolution can be much finer - is not straightforward. Nonetheless, the presence of such multiple peaks confirms the relevance of the RWI model, as several overdensities formed by the instability get accreted.

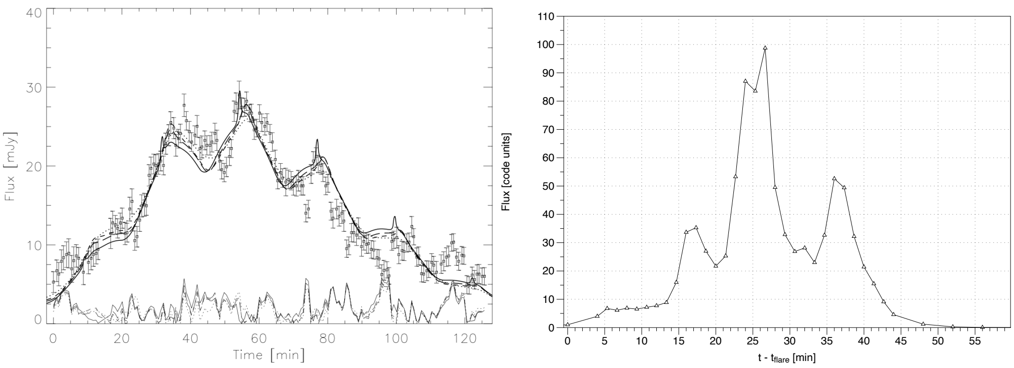

Fig. 3. Left: Observational light curve in the near-infrared range (credits: Hamaus et al. 2009). **Right:** Synthetic light curve of the frequency-integrated flux (in code units) reproducing qualitatively the multiplicity exhibited by the observational light curve. Time has been expressed in minutes for direct comparison with observations. Flare durations agree within a factor of two.

4 Conclusions

We followed the development of the Rossby Wave Instability on a ring-like structure following a TDE. As a first step we focused on the ring amplitude (in terms of magnetic fields and density), spatial width and position, whose combination points to the mass, magnetization and angular momentum of the disrupted object.

Our preliminary results show this model is able to produce a variety of flare behaviors and so-called "multiplicity" (i.e. number of peaks detected within a given flare) such as those observed in the flares of Sgr A*. While the presented lightcurves originate from spectra dominated by the submm emission, observable with the Very Large Array (VLA), our next step is to distinguish between this emission and the near-infrared emission to be then compared with the observations of GRAVITY. Furthermore, preliminary estimates on the dimensioned flux, to test the observability of our synthetic flares, are under study and confirm that they can reach the observed level (5 mJy in the GRAVITY band).

While we focus here on the flares of Sgr A* following a partial/total TDE, all the results presented here could be applied to other TDEs.

This work has been financially supported by LabEx UnivEarthS (ANR-10-LABX-0023 and ANR-18-IDEX-0001).

References

Bélanger, G., Terrier, R., Jager, O. C. d., Goldwurm, A., & Melia, F. 2006, J. Phys.: Conf. Ser., 54, 420
Bonnerot, C. & Stone, N. C. 2021, Space Sci Rev, 217, 16
Casse, F., Varniere, P., & Meliani, Z. 2017, Monthly Notices of the Royal Astronomical Society, 464, 3704
Falanga, M., Melia, F., Tagger, M., Goldwurm, A., & Bélanger, G. 2007, The Astrophysical Journal, 662, L15
Fazio, G. G., Hora, J. L., Witzel, G., et al. 2018, ApJ, 864, 58, arXiv: 1807.07599
GRAVITY Collaboration, Abuter, R., Amorim, A., et al. 2018, A&A, 618, L10
Hamaus, N., Paumard, T., Müller, T., et al. 2009, ApJ, 692, 902
Lovelace, R. V. E., Li, H., Colgate, S. A., & Nelson, A. F. 1999, The Astrophysical Journal, 513, 805
Tagger, M. & Melia, F. 2006, The Astrophysical Journal, 636, L33
Tagger, M. & Pellat, R. 1999, Astronomy & Astrophysics, arXiv: astro-ph/9907267
Tagger, M. & Varniere, P. 2006, The Astrophysical Journal, 652, 1457
Varniere, P., Casse, F., & Vincent, F. H. 2019, Astronomy & Astrophysics, 625, A116
Vincent, F. H., Meheut, H., Varniere, P., & Paumard, T. 2013, A&A, 551, A54, arXiv: 1301.1147
Vincent, F. H., Paumard, T., Gourgoulhon, E., & Perrin, G. 2011, Classical and Quantum Gravity, 28, 225011

A MULTI-WAVELENGTH STUDY OF THE TRANSIENT SKY

E. Quintin[1] and N.A. Webb[1]

Abstract. The last three decades have seen the development and launch of numerous X-rays observatories, providing a long temporal baseline to use to search for long term transients and to test new transient detection methods. We present a systematic study of the cross-correlation of 5 different X-rays source catalogs (4XMM-DR10, 4XMM-DR10 Stacked, CSC2, 2SXPS and XMM Slew 2), also taking into account upper limits in the case of non-detections, to search for X-ray sources that have varied over the last 30 years. We also use complimentary multi-wavelength data to identify the sources.

This method has already allowed us to find several variable Ultra Luminous X-ray sources (ULXs), changing-look AGNs, some Hyper Luminous X-ray sources and tidal disruption event candidates. Two major interests of such a method are the wealth of different variable sources that can still be uncovered in the archival data, and the future use of this method in the XMM-Newton pipeline to alert the community in quasi real time to sources undergoing strong variability. This will allow a prompt reaction and follow-up from the community, improving our knowledge of the X-ray transient sky.

Keywords: Methods: data analysis, Catalogs, X-rays: general

1 Introduction

1.1 Variable objects

A large number of astrophysical objects are characterized by some level of variability by their intrinsic luminosity, especially in the X-rays: stars, X-ray binaries, supernovae, ... This variability can either be short-term, meaning that it can be detected within the course of a single 100ks observation, or long-term, requiring multi-epochs observations to be detected.

Among those long-term variable objects, three of them are of particular interest:

- **Tidal Disruption Events (TDEs)**: TDEs (Rees 1988) happen when a star gets so close to a black hole that the tidal forces from the compact object overcome the star's self-gravity and destroy it, resulting in a bright flare lasting about three years (Komossa 2015) and decaying as a power-law, variable over three orders of magnitude in optical. The precise emission mechanisms are still poorly understood, due to the relatively small available sample (Gezari 2021), but are linked to the self-interaction of remaining debris from the disrupted star. One of the most puzzling aspect of TDEs is the lack of simultaneous X-ray and optical counterpart; some TDEs are found in the former wavelength, other in the latter, with no clear explanation for this dichotomy (Saxton et al. 2018). TDEs can also be used to detect otherwise faint black holes, such as Intermediate Mass Black Holes for instance (Greene et al. 2020), improving our knowledge of black holes across the entire mass spectrum.

- **Ultra Luminous X-ray sources (ULXs)**: ULXs (Kaaret et al. 2017) are sources with X-ray luminosities that exceed the Eddington luminosity for a $10M_\odot$ black hole, above 10^{39}erg.s^{-1}. In order for these sources to respect the Eddington limit while being this bright, they were first thought to harbour the elusive Intermediate Mass Black Holes (Colbert & Mushotzky 1999). However, their hard X-ray spectrum (Bachetti et al. 2013) and the discovery of coherent pulsation in M82 X-2 (Bachetti et al. 2014) lead to the conclusion that at least some of the ULXs are in fact neutron stars, in a super-Eddington accretions state. Those Pulsating ULXs (PULXs) are difficult to find, with only 7 of them known (Song et al. 2020). They all appear somewhat variable, on timescales of a few months and over two orders of magnitude, leading to the use of X-ray variability as a proxy to find PULXs candidates (Webb et al. 2014; Song et al. 2020).

[1] IRAP, Toulouse, France

- **Changing Look Active Galactic Nuclei (CLAGNs)**: CLAGNs are AGNs that undergo spectral changes between different observations. These changes are generally explained by a change in absorption due to clouds of dust traversing the line of sight; this translates into the appearance or disappearance of optical spectral lines, and changes in the soft X-ray component. Understanding these objects and their variability will help us improve our knowledge of the environment of black holes and thus their formation.

These three types of sources, while physically distinct, have some common aspects. They are rare; and as a consequence, the physical phenomena behind them are poorly understood. Thus, increasing the size of our samples might allow us to improve our knowledge of these phenomena.

1.2 Transient astronomy

To study all those events, a number of projects have been put into place in the field of time-domain astronomy: high return-rate optical campaigns with the Vera C. Rubin observatory (Ivezić et al. 2019), gravitational wave transients with the LIGO-Virgo-Kagra collaboration (Abbott et al. 2018), or multiple full-sky surveys in X-rays with eRosita (Predehl et al. 2007).

The *XMM-Newton* data processing pipeline, on the other side, has not been built with the direct objective of finding transient events. Indeed, a 1-year proprietary period ensures that the data from an observation is only available to its P.I. during this time. If a transient event was serendipitously observed in this field of view and was missed by the P.I., the community would need to wait at least a year for the data to be made public, and then wait for someone to find this transient and organize a follow-up observation. This means that the second observation, whether with *XMM-Newton* or as a part of a multi-wavelength follow-up, can only take place so late that the transient will most likely be already over.

It thus appears relevant to develop a way for the *XMM-Newton* data processing pipeline to automatically detect transient events and, with the prior agreement of the PI, publish this information in quasi-real time.

2 Our method

In order to detect transient events, one needs to get as many flux measurements for each source as possible. We have implemented different methods to reach this goal.

2.1 Cross catalog correlations

The first point of our method is to perform systematic cross-correlations between several X-ray catalogs. Indeed, comparing data from different epochs obtained with different instruments can reveal long-term variation in the flux of sources. We have selected 5 different catalogs from 3 instruments, with complementary properties, depicted in Table 1: 4XMM-DR10 (Webb et al. 2020), CSC 2.0 (Evans et al. 2020a), 2SXPS (Evans et al. 2020b), XMMSL2 (Saxton et al. 2008), 4XMM-DR10s (Traulsen et al. 2019). The first three are the basic catalogs for the observatories *XMM-Newton*, *Chandra* and *Swift* respectively, while the last two catalogs correspond respectively to the sources detected during the slews between each pointing of *XMM-Newton*, and to the sources only detected when stacking all overlapping *XMM-Newton* observations.

Catalog	Number of Sources	Sensitivity	Spatial resolution	Coverage
4XMM DR10	575 k	+	+	=
CSC 2.0	300 k	++	++	–
2SXPS	200 k	=	=	+
XMMSL2	30 k	–	–	++
4XMM DR10 Stacked	90k new sources	+	+	=

Table 1. A comparison between the major available X-ray catalogs, showing their respective strengths (shown with + or ++ signs) and weaknesses (shown with – signs).

The correlations were computed at first with pairs of catalogs, using the 3σ position errors and the TopCat software (Taylor 2005). We also took into account the astrometry error between catalogs; for this purpose, we looked at the distance distribution for all the matches between two catalogs, which should look like a Rayleigh distribution with an excess at long distances due to spurious associations, and took the peak of the Rayleigh distribution as an estimate of average astrometry error. This method was used for instance to estimate ROSAT's position errors (Boller et al. 2016).

Once the 2-by-2 correlations were computed, we merged them into Master Sources, that could group up to 5 catalogs and should correspond to unique astrophysical sources. We took a conservative approach, by rejecting any ambiguous associations, in order to avoid spurious correlations that would lead in the end to erroneous high variability.

We have then correlated these Master Sources with additional catalogs to provide multi-wavelength information, such as the *XMM-Newton* Serendipitous Ultraviolet Source Survey catalogue (Page et al. 2012) that contains all the sources detected by the Optical Monitor aboard *XMM-Newton*, or the galaxy catalog GLADE (Dálya et al. 2018).

2.2 Upper limits computations

Correlations between detected sources can help us retrieve a large number of data points; but non-detections also provide valuable information. Indeed, a known source in a given catalog that was observed but not detected by another telescope means that its flux was below the sensitivity level of the second telescope; this flux upper limit can sometimes be enough to conclude on the otherall variability of the source.

To this effect, we used the *RapidXMM* framework (Ruiz et al. 2021) to systematically compute *XMM-Newton* flux upper limits on every Master Source that lies in the *XMM-Newton* footprint, whether or not it was detected by it.

2.3 Quasi real-time transient alert system

Cross-catalog correlations and flux upper limits allow to enhance our knowledge of long-term evolution of X-ray sources. This can be used to dig into the 20 years of existing data, as will be shown in 3; it also allows to develop a real-time alert system, by comparing the existing Master Sources to the new detections and updating the variability of any matching Master Source. To assess the effectiveness of this method, we took two random months of *XMM-Newton* observations and sent alerts for any source with an overall 3σ variability of over a factor 3. We then identified by hand every alert, to estimate the rate of false positive alerts.

3 Results

3.1 Master sources catalog

The main outcome of our method is a catalog comprised of all Master Sources, that encompasses all 5 X-ray catalogs. This gives a total of 1 million Master Sources, 10% of them having sources in at least 2 different catalogs. An additional 325 000 *XMM-Newton* upper limits were computed using *RapidXMM*.

This method has generally allowed us to increase the long-term variability of the Master Sources, compared to those of their constitutive catalog sources, which is a confirmation of the effectiveness of our method. This large catalog, encompassing multi-wavelength and multi-epoch information, needs to be exploited in a systematic fashion. This work is still ongoing, and will be the object of a future publication; but several highly variable objects have already been uncovered, including a new highly transient ULX candidate.

3.2 NGC 7793 ULX-4

Using our method, we have discovered a new candidate pulsating ULX, NGC 7793 ULX-4 (Quintin et al. 2021). This source was only detected once by *XMM-Newton*, despite having been observed more than a dozen times. Its transient nature was revealed once the *Swift* detections, as well as both *Chandra* and *XMM-Newton* flux upper limits, were taken into account (see Figure 1). As explained in Section 1.1, variability is a hint at the presence of a neutron star and therefore possible pulsations, and we did manage to find a candidate pulsation in the X-ray signal at 3.4σ significance, making this ULX a candidate for the 8^{th} PULX.

3.3 Alert system early results

Our alert system was tested on the course of 2 random months of *XMM-Newton* data and revealed about one transient a day, with most of them being stellar flares or variable AGNs. Out of those alerts, about 75% of them are serendipitous detections, which confirms the usefulness of our method.

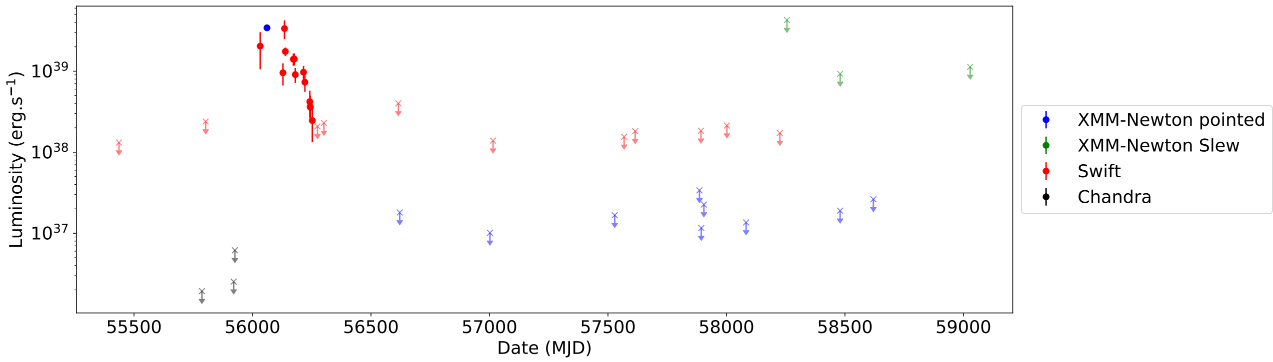

Fig. 1. Long-term multi-instrument lightcurve of NGC 7793 ULX-4, with detections depicted with dots and upper limits with downwards arrows. This reveals the transient nature of the object. Figure from Quintin et al. (2021).

4 Conclusions

Our work has been focused on improving the synergy between 5 existing X-ray catalogs by cross-correlating them and taking non-detections into account. This allows for a quasi-real time transient alert system, intended for the *XMM-Newton* data processing pipeline. The tests on two random months of data have confirmed the efficiency of this method, with a low number of false positives and a majority of serendipitous transients.

In the future, we intend to implement this code within the *XMM-Newton* pipeline, and anticipate the creation of synergy with both *LSST* and *Athena* data for a multi-wavelength study of transient events.

References

Abbott, B. P., Abbott, R., Abbott, T. D., et al. 2018, Living Reviews in Relativity, 21, 3

Bachetti, M., Harrison, F. A., Walton, D. J., et al. 2014, Nature, 514, 202

Bachetti, M., Rana, V., Walton, D. J., et al. 2013, ApJ, 778, 163

Boller, T., Freyberg, M. J., Truemper, J., et al. 2016, VizieR Online Data Catalog, J/A+A/588/A103

Colbert, E. J. M. & Mushotzky, R. F. 1999, ApJ, 519, 89

Dálya, G., Galgóczi, G., Dobos, L., et al. 2018, MNRAS, 479, 2374

Evans, I. N., Primini, F. A., Miller, J. B., et al. 2020a, in American Astronomical Society Meeting Abstracts, Vol. 235, American Astronomical Society Meeting Abstracts #235, 154.05

Evans, P. A., Page, K. L., Osborne, J. P., et al. 2020b, ApJS, 247, 54

Gezari, S. 2021, arXiv e-prints, arXiv:2104.14580

Greene, J. E., Strader, J., & Ho, L. C. 2020, ARA&A, 58, 257

Ivezić, Z., Kahn, S. M., Tyson, J. A., et al. 2019, ApJ, 873, 111

Kaaret, P., Feng, H., & Roberts, T. P. 2017, ARA&A, 55, 303

Komossa, S. 2015, Journal of High Energy Astrophysics, 7, 148

Page, M. J., Brindle, C., Talavera, A., et al. 2012, MNRAS, 426, 903

Predehl, P., Andritschke, R., Bornemann, W., et al. 2007, in Society of Photo-Optical Instrumentation Engineers (SPIE) Conference Series, Vol. 6686, UV, X-Ray, and Gamma-Ray Space Instrumentation for Astronomy XV, ed. O. H. Siegmund, 668617

Quintin, E., Webb, N. A., Gúrpide, A., Bachetti, M., & Fürst, F. 2021, MNRAS, 503, 5485

Rees, M. J. 1988, Nature, 333, 523

Ruiz, A., Georgakakis, A., Gerakakis, S., et al. 2021, arXiv e-prints, arXiv:2106.01687

Saxton, C. J., Perets, H. B., & Baskin, A. 2018, MNRAS, 474, 3307

Saxton, R. D., Read, A. M., Esquej, P., et al. 2008, A&A, 480, 611

Song, X., Walton, D. J., Lansbury, G. B., et al. 2020, MNRAS, 491, 1260

Taylor, M. B. 2005, in Astronomical Society of the Pacific Conference Series, Vol. 347, Astronomical Data Analysis Software and Systems XIV, ed. P. Shopbell, M. Britton, & R. Ebert, 29

Traulsen, I., Schwope, A. D., Lamer, G., et al. 2019, A&A, 624, A77

Webb, N. A., Coriat, M., Traulsen, I., et al. 2020, A&A, 641, A136

Webb, N. A., Cseh, D., & Kirsten, F. 2014, Publications of the Astronomical Society of Australia, 31, e009

MINING THE HIGH-ENERGY UNIVERSE: A PROBABILISTIC, INTERPRETABLE CLASSIFICATION OF X-RAY SOURCES FOR LARGE X-RAY SURVEYS

H. Tranin[1], N. Webb[1] and O. Godet[1]

Abstract. Serendipitous X-ray surveys have been proven to be an efficient way to find rare objects – tidal disruption events, galaxy clusters, binary quasars, etc. As X-ray astronomy slowly enters the era of Big Data, an automated classification of X-ray sources becomes increasingly valuable. I present a revisited Naive Bayes Classification of the X-ray sources in the *Swift*-XRT and *XMM-Newton* catalogues which amongst other objects identifies different types of AGN, stars and X-ray binaries – based on their spatial, spectral and variability properties at different timescales and their multiwavelength counterparts. An outlier measure is used to identify objects of other nature. I show the reliability of the method developed and demonstrate its suitability to data mining purposes. As an outlook, I introduce how the very small populations in some object classes can be enlarged using citizen science, with the development of a new platform designed for the classification of XMM sources by volunteers.

Keywords: catalogs, X-rays: general, X-rays: binaries, methods: statistical,

1 Introduction

Since its beginning in the 1960s, X-ray astronomy has known significant breathroughs pushing its limits in both sensitivity and angular resolution. To this day, sources detected by *Swift*-XRT, *XMM-Newton* and *Chandra* facilities are gathered in large X-ray catalogues totalling about 1 million X-ray sources, and most of them remain unstudied. This ever-growing number of sources illustrates how X-ray astronomy is progressively entering the era of Big Data. Nevertheless, an automatic, efficient and interpretable classification of X-ray sources adapted to these large surveys is still to be developed. Such a tool will be of great interest e.g. to perform data-mining studies in X-ray archives, to send an alert when observing a new rare and exotic object − changing-look AGN (LaMassa et al. 2015), ultraluminous and hyperluminous X-ray sources (e.g. Farrell et al. 2009), tidal disruption events (e.g. Lin et al. 2018)... and to enable population studies of such objects. Previous attempts to classify X-ray sources generally focused on small samples of a few thousand objects, using different classification techniques such as decision trees (Lin et al. 2012), random forest (Farrell et al. 2015) and exploring other machine learning methods (Arnason et al. 2020). They classify X-ray sources using their properties such as the location, X-ray hardness and spectral parameters, X-ray short-term and long-term variability and multiwavelength counterparts, but never all at the same time. While decision trees are easy to interpret but lack efficiency, machine learning methods are more accurate but often black-box. In this work – more detailed in Tranin et al. 2021 – we develop a probabilistic classifier for the *Swift* and *XMM-Newton* catalogues, 2SXPS (Evans et al. 2020) and 4XMM-DR10 (Webb et al. 2020), intended to reach a good trade-off between efficiency and interpretability, and taking advantage of all the previously mentioned source properties.

2 Method

In order to obtain optimal classification results, we first enriched the X-ray catalogues with additional data:

- We identified the best optical and infrared counterparts for each source, using the bayesian crossmatching algorithm Nway (Salvato et al. 2018) and catalogues of optical and infrared sources – among other Gaia EDR3 (Gaia Collaboration et al. 2021) and UnWISE (Schlafly et al. 2019). This enabled the computation of the X-ray to optical (resp. infrared) flux ratios.

[1] IRAP, Université de Toulouse, CNRS, CNES, 9 avenue du Colonel Roche, 31028 Toulouse, France

- We computed the long-term variability as the ratio between the maximum and the minimum flux gathering all X-ray detections among *Swift*, *XMM-Newton* and *Chandra* observations (Evans et al. 2010).
- We identified the galaxies potentially hosting the X-ray sources using a positional cross-correlation with the GLADE catalogue (Dalya et al. 2016), containing 2 billion galaxies, their distance and angular size and rather complete up to 300Mpc.
- We identified known AGN, stars, X-ray binaries (XRB) and cataclysmic variables (CV) by a positional cross-correlation with catalogues covering these types (notably Véron-Cetty & Véron 2010; Secrest et al. 2015; Kharchenko & Roeser 2009; Liu et al. 2006, 2007; Mineo et al. 2012; Ritter & Kolb 2015.

Last but not least, a sample of sources of sufficient quality was selected following these criteria: having at least one reasonable detection according to the catalogue quality flags; and having at least two of these qualities: 1) an optical counterpart, 2) an infrared counterpart, 3) a signal-to-noise ratio greater than 10 or an acquired spectrum and 4) several X-ray detections. This resulted in a sample representing ∼65% of each X-ray catalogue, e.g. about 138000 and 371000 sources for 2SXPS and 4XMM-DR10, respectively. In each catalogue, approximately 19000 AGN, 5000 stars, 500 X-ray binaries and 300 CV are previously identified sources, and they constitute the training sample. The rest constitutes the test sample to classify.

Category	Properties	α_t
Location	Galactic latitude, Gaia proper motion, Offset of the source to the host galaxy nucleus, X-ray luminosity from the host galaxy distance	7.5
Hardness	Hardness ratios, Exponent of the powerlaw spectral fit	3.2
Variability	$F_{\rm X,max}/F_{\rm X,min}$ in a single observation, $F_{\rm X,max}/F_{\rm X,min}$ between all observations	6.0
Flux ratios	(Optical) F_X/F_b, F_X/F_r, (Infrared) F_X/F_{W1}, F_X/F_{W2}	2.0

Table 1. Source properties used in the classification. α_t is the weighting coefficient of the category, fine-tuned to maximize classification performance.

The method we developed uses the distributions of about 15 source properties (detailed in Table 1 and split in four property categories) as probability densities to infer the source class. The distribution of each property and each class was modelled using a kernel density estimation (Sheather 2004) on the training sample. The result is illustrated in Figure 1 for two properties. Different properties characterizing the same category are combined by multiplying the likelihoods. The probability of a class C given the source properties is a weighted product of the likelihoods inferred from each property category, $L(t|C)$, multiplied by a prior representing the prior proportion of sources of class C (we used 66%, 25%, 7% and 2% for AGN, star, XRB and CV, respectively):

$$\mathbb{P}(C|data) = \frac{\mathcal{P}(C) \times \left(\prod_{t\in\{\text{categories}\}} \mathcal{L}(t|C)^{\alpha_t}\right)^{1/\sum_{t\in\{\text{categories}\}} \alpha_t}}{\sum_{C\in\{\text{classes}\}} \mathcal{P}(C) \times \left(\prod_{t\in\{\text{categories}\}} \mathcal{L}(t|C)^{\alpha_t}\right)^{1/\sum_{t\in\{\text{categories}\}} \alpha_t}} \quad (1)$$

where the coefficients α_t of each category were fine-tuned to optimize the f_1-score ($f_1 = 2/(1/recall + 1/accuracy)$) of the classification on one chosen class, which was XRB in our study. This fine-tuning was performed by a differential evolution algorithm (Storn & Price 1997) and the coefficients converged towards the values shown in Table 1. The location and variability information are thus the most discriminant to identify XRB. Following equation (1), our method is thus a revised version of the Naive Bayes Classifier (Murphy et al. 2006), allowing to compute the probabilities of each class and directly relate them to the values of the source properties. On top of that, the numerator of this equation depends on the frequency of sources at the same point of the parameter space, so we used it as an outlier measure (O.M.) which allows us to spot objects with exotic properties. We then evaluated the performance of the classifier by analyzing the recall and accuracy of each class in both the training and the test samples.

3 Results

When applied to the training sample, the classifier returned the results detailed in Table 2. Overall, more than 97% of sources are correctly classified, with a particularly good performance on AGN and stars having f_1-scores higher than 0.98. The optimization on X-ray binaries led to great results for this class as well, while CV

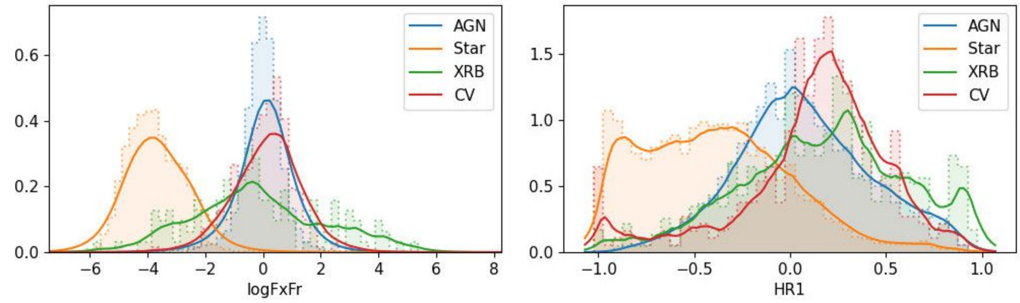

Fig. 1. Distributions of two properties in the reference sample of 2SXPS, and their kernel density estimation. **Left:** X-ray to r-band flux ratio. **Right:** Hardness ratio between soft and medium X-ray bands.

	AGN	Star	XRB	CV
→AGN	19515	82	25	191
→Star	44	4628	3	27
→XRB	140	18	326	17
→CV	9	9	2	124
recall (%)	99.0	97.7	91.6	34.5
precision (%)	97.0	98.6	90.7	85.5
f_1-score	.980	.981	.911	.492

	AGN	Star	XRB	CV
→AGN	18373	25	46	149
→Star	15	6197	10	12
→XRB	80	12	479	10
→CV	4	0	8	81
recall (%)	99.5	99.4	88.2	32.1
precision (%)	97.2	98.9	93.7	84.6
f_1-score	.983	.991	.909	.466

Table 2. Confusion matrices of the classifier applied to the 2SXPS (**left**) and the 4XMM-DR10 (**right**) training samples. The precision values are corrected for matching prior proportions.

are the most difficult to retrieve notably because of their diverse nature and the absence of detailed variability information in the enhanced catalogue. A detailed analysis of the XRB false positives revealed that most of them fall in one of these situations: they are an AGN in the background of a galaxy, a particularly variable AGN or star or their multi-instrument light-curve is not properly calibrated and thus shows a spurious variability. This diagnosis was easily obtained by looking at the sources' "probability tracks", a classification product showing the likelihoods of each class as given by each property (Figure 2).

According to the classification, the test sample is composed of about 80% of AGN, 17% of stars, 3% of XRB and 0.5% of CV. These proportions are in good agreement with the priors. A manual analysis of 200 sources revealed that more than 95% of AGN and stars were correctly classified, while sources classified as X-ray binaries contain about 50% of false positives because of the presence of objects of other nature and the reasons cited above. Enlarging the training sample is thus important for future progress, in order to refine XRB and CV types and represent rarer classes. Sources with a large outlier measure were also analyzed, showing a prevalence of spurious sources but also peculiar AGN and stars, XRB candidates, galaxy clusters and some transients.

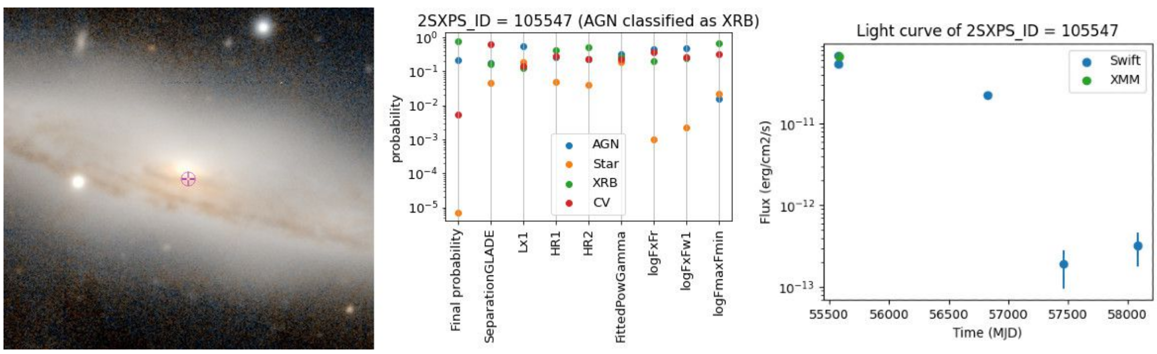

Fig. 2. 2SXPS J125801.1+013431, the central X-ray source of NGC 4845, known to host an AGN which underwent a tidal disruption event (Nikołajuk & Walter 2013). This source was wrongly classified as XRB. **Left:** PanSTARRS image of the galaxy and location of the source. **Middle:** Probability track of the source, showing the role of the variability ratio in the XRB probability. **Right:** X-ray light-curve from *Swift* and *XMM* detections.

4 Prospects

We developed a probabilistic, interpretable and efficient classification adapted to large X-ray surveys. After enhancing the *Swift* and *XMM-Newton* catalogues, we were able to classify more than 50% of their unknown sources. About 85-90% of these classifications proved to be reliable from a manual analysis, and each classification was made easy to interpret thanks to the classification products. Further research will address the applications of such a classification, and making a dynamic classification adapted to time-domain astronomy.

Besides, while AGN and stars are very well-classified, XRB and CV still show a lower performance which is at least partly due to their sparse and diverse training sample. In this context, enlarging the training samples e.g. using a citizen science approach is increasingly valuable. Citizen science takes advantage of the wisdom of crowds to ensure accurate classifications of samples as large as $\sim$100000 objects. Such experiments also proved to often lead to serendipitous discoveries. We thus launched CLAXSON (`http://xmm-ssc.irap.omp.eu/claxson`), a citizen science platform on which every volunteer can classify unknown X-ray sources after a discovery phase (quizz) and a training phase (classification of known sources and feedback). In order to classify a source, the user can examine its multiwavelength images and (when available) its spectrum and its short-term and long-term light curves. To this day, about 1000 unknown objects were classified more than 10 times thanks to 50 volunteers, who have a mean success rate of 82% in their classifications. Future work will therefore address the results of this experiment and evaluate its benefit in the field of X-ray classification.

This research has made use of several tools and services: Aladin sky atlas (`https://aladin.u-strasbg.fr/AladinLite/`) developed at CDS, Strasbourg Observatory, France (Bonnarel et al. 2000; Boch & Fernique 2014) ; TOPCAT version 4.8 (Taylor 2005).

References

Arnason, R. M., Barmby, P., & Vulic, N. 2020, MNRAS, 492, 5075
Boch, T. & Fernique, P. 2014, in ADASS XXIII, ed. N. Manset & P. Forshay, Vol. 485, 277
Bonnarel, F., Fernique, P., Bienaymé, O., et al. 2000, A&AS, 143, 33
Dalya, G., Frei, Z., Galgoczi, G., Raffai, P., & de Souza, R. S. 2016, VizieR Online Data Catalog, VII/275
Evans, I. N., Primini, F. A., Glotfelty, K. J., et al. 2010, ApJS, 189, 37
Evans, P. A., Page, K. L., Osborne, J. P., et al. 2020, ApJS, 247, 54
Farrell, S. A., Murphy, T., & Lo, K. K. 2015, ApJ, 813, 28
Farrell, S. A., Webb, N. A., Barret, D., Godet, O., & Rodrigues, J. M. 2009, Nature, 460, 73
Gaia Collaboration, Brown, A. G. A., Vallenari, A., et al. 2021, A&A, 649, A1
Kharchenko, N. V. & Roeser, S. 2009, VizieR Online Data Catalog, I/280B
LaMassa, S. M., Cales, S., Moran, E. C., et al. 2015, ApJ, 800, 144
Lin, D., Strader, J., Carrasco, E. R., et al. 2018, Nature Astronomy, 2, 656
Lin, D., Webb, N. A., & Barret, D. 2012, ApJ, 756, 27
Liu, Q. Z., van Paradijs, J., & van den Heuvel, E. P. J. 2006, A&A, 455, 1165
Liu, Q. Z., van Paradijs, J., & van den Heuvel, E. P. J. 2007, A&A, 469, 807
Mineo, S., Gilfanov, M., & Sunyaev, R. 2012, MNRAS, 419, 2095
Murphy, K. P. et al. 2006, University of British Columbia, 18, 60
Nikołajuk, M. & Walter, R. 2013, A&A, 552, A75
Ritter, H. & Kolb, U. 2015, Acta Polytechnica CTU Proceedings, 2, 21
Salvato, M., Buchner, J., Budavári, T., et al. 2018, MNRAS, 473, 4937
Schlafly, E. F., Meisner, A. M., & Green, G. M. 2019, ApJS, 240, 30
Secrest, N. J., Dudik, R. P., Dorland, B. N., et al. 2015, ApJS, 221, 12
Sheather, S. J. 2004, Statistical science, 588
Storn, R. & Price, K. 1997, Journal of global optimization, 11, 341
Taylor, M. B. 2005, in ADASS XIV, ed. P. Shopbell, M. Britton, & R. Ebert, Vol. 347, 29
Tranin, H., Godet, O., Webb, N., & Primorac, D. 2021, submitted to A&A
Véron-Cetty, M. P. & Véron, P. 2010, A&A, 518, A10
Webb, N. A., Coriat, M., Traulsen, I., et al. 2020, A&A, 641, A136

Session 4

Demain l'ELT! Quelle science dans quel contexte dans les années 2030

SF2A 2021
A. Siebert, K. Baillié, E. Lagadec, N. Lagarde, J. Malzac, J.-B. Marquette, M. N'Diaye, J. Richard, O. Venot (eds)

LISA AND SYNERGIES WITH ELT

M. Volonteri[1]

Abstract. LISA is a low-frequency gravitational wave experiment, which will have the ability to detect merging massive black holes with masses in the range $10^4 - 10^7$ solar masses. Some of these events are expected to have an electromagnetic counterpart, and multi-messenger observations can inform us on the physical conditions when and where massive black hole merge: the relative role of gas and stars in the dynamical evolution of binaries, constraining accretion physics – and how that differs from single massive black holes, the delay between galaxy and massive black hole mergers. Furthermore, if we can measure the redshift via electromagnetic observations we can constrain cosmological parameters, since gravitational wave measurements provide the luminosity distance. At variance with LIGO/Virgo, which can perform these cosmological tests only at low redshift, LISA has the capability of detecting massive black hole mergers out to high redshift. Since LISA's massive black holes have relatively low masses, the sources will be relatively faint: high-sensitivity telescopes, such as ELT, are expected to play a crucial role in characterizing these sources. I will discuss possible synergies between LISA and ELT in this context.

Keywords: massive black holes, gravitational waves, electromagnetic counterparts

1 Introduction

LISA is a ESA+NASA mission, planned for the mid-2030s. Laser Interferometers in space with 2.5 Mkm armlength and sensitivity at 10^{-4}-0.1 Hz gravitational wave (GW) frequency. The expected sources are massive black hole ($10^4 - 10^7$ solar masses) mergers, white dwarf binaries +other compact stellar-mass binaries, extreme mass ratio inspirals (e.g., 10^6 solar masses+ 1 solar mass black holes), plus backgrounds/foregrounds.

2 Multimessenger science with LISA

2.1 Tests of General Relativity; Measure cosmological parameters

Gravitational wave sources can be standard sirens: the measured parameter is the luminosity distance. If we measure the redshift of an electromagnetic counterpart we obtain cosmological parameters and constrain several models of modified gravity, to redshift >> than what LIGO/Virgo can do.

2.2 Properties of white dwarf binaries

See Baker et al. (2019).

2.3 Massive black hole/galaxy evolution

GWs provide accurate and precise measurement of black hole masses. Determine properties (e.g., mass, SFR) of the host galaxy to test how the relation between galaxies and massive black holes evolve with time.

2.4 Accretion physics in extreme conditions

Prior to merger: accretion in a circumbinary disc. Post merger: response of the accretion disc to sudden changes (mass, dynamics, kicks)

[1] Institut d'Astrophysique de Paris, Sorbonne Université, CNRS, UMR 7095, 98 bis bd Arago, 75014 Paris, France

3 Electromagnetic counterparts to MBH mergers

Massive black holes (MBHs) grow along with galaxies through accretion and MBH-MBH mergers. Over time they sweep the LISA band and shine as quasars when they accrete matter: detection possible in GW + Electromagnetic (EM) radiation. Several counterparts are predicted.

Pre-merger:

- Periodic variability;
- Spectral anomalies.

At merger:

- Burst at merger as gas plows in;
- Perturbed discs;
- Effect of recoils;
- Dual/single jet.

Sky localization improves with signal-to-noise ratio, implying that the error box decreases as we get closer to the merger proper, down to a fraction of a degree for the most favorable sources (Mangiagli et al. 2020).

LISA's MBHs have low mass, therefore the counterparts will be faint sources: ELT will be crucial for taking spectra (and obtain redshift, galaxy mass, SFR) and imaging (and ontain galaxy morphology)

4 Conclusions

There is rich multimessenger science with LISA waiting for us. Extragalactic sources are expected to be (relatively) faint: $10^4 - 10^7$ solar mass black holes in $10^8 - 10^{10}$ solar mass galaxies out to $z >> 3$. We need to measure redshift and properties of the sources: ELT is the best (if not only) telescope for the high-z sources. Synergies also with ATHENA, LSST, SKA are envisaged.

References

Baker, J., Haiman, Z., Rossi, E. M., et al. 2019, BAAS, 51, 123

Mangiagli, A., Klein, A., Bonetti, M., et al. 2020, Phys. Rev. D, 102, 084056

SF2A 2021
A. Siebert, K. Baillié, E. Lagadec, N. Lagarde, J. Malzac, J.-B. Marquette, M. N'Diaye, J. Richard, O. Venot (eds)

SUBMILLIARCSECOND ASTROMETRY OF EXOPLANETS AND BROWN DWARFS IN HIGH-CONTRAST IMAGING

A.-L. Maire[1], M. Langlois[2], P. Delorme[3], G. Chauvin[3], R. Gratton[4] and A. Vigan[5]

Abstract. Orbital monitoring of exoplanetary systems is fundamental for analyzing their architecture, dynamical stability and evolution, and mechanisms of formation. For directly-imaged exoplanets and brown dwarfs, high-precision relative astrometry is mandatory to measure precisely their slow orbital motion due to the wide separations to the stars ($>\sim$10 au) and their orbital parameters. Relative astrometry at the milliarcsecond level has been achieved with the first dedicated coronagraphic instruments on 8m telescopes (SPHERE, GPI) thanks to the high contrast and angular resolution that they deliver as well as optimized calibration procedures. The high-contrast imaging modes of MICADO, HARMONI, and METIS should achieve submilliarcsecond precisions at closer separations to the stars thanks to the gain in angular resolution and sensitivity provided by the ELT. We discuss the synergies of the ELT with radial velocity surveys, Gaia, GRAVITY+, and SPHERE+ for measuring the orbital plane, mass, and/or luminosity of exoplanets and brown dwarfs close to stars. Such measurements will allow for strong tests of their models of thermal evolution, which are affected by uncertainties in the modeling of the atmosphere and of the accretion process.

Keywords: exoplanets, brown dwarfs, high-contrast imaging, relative astrometry, ELT

1 Introduction

Most of the currently-known exoplanets are detected through indirect methods (radial velocities or RV, primary transits), which do not allow for measuring the light emitted by the planets and for characterizing their atmosphere. Several formation, evolutionary, and atmospheric models have been proposed to explain the extreme diversity of exoplanets in terms of architecture, mass, and composition, and because of uncertainties in the modeling (e.g., clouds, atmospheric opacities, the physics of the accretion process).

Exoplanet models remain poorly tested because it is not possible to measure with a single technique the mass, radius, and/or luminosity. Multitechnique approaches are required but the overlap between the exoplanet detection techniques is still small. The combination between RV and transits has been the most prolific for measuring the mass and radius of exoplanets but it is essentially limited to exoplanets close to the stars and strongly irradiated. Combining RV and high-contrast imaging would provide mass and luminosity measurements of exoplanets at separations beyond 1 au and colder exoplanets. However, the overlap between the techniques is still marginal, with RV biased toward mature exoplanets orbiting stars with low activity and high-contrast imaging biased toward young exoplanets because the thermal emission of exoplanets is larger for younger ages. Absolute astrometry is less sensitive to the stellar activity and can detect planets around young and old stars. This technique has provided very few detections so far because of stringent precision requirements (a few tens of a μas). However, this is expected to change with the exquisite precision of Gaia.

[1] Univ. Liège, 4000, Liège, Belgium
[2] Univ. Lyon 1, ENS Lyon, CNRS, Centre de Recherche Astrophysique de Lyon UMR5574, 9 av. Charles André, F- 69230, Saint-Genis-Laval, France
[3] Univ. Grenoble Alpes, CNRS, IPAG, 38000 Grenoble, France
[4] INAF-Astronomical Observatory of Padua, 35122 Padua, Italy
[5] Aix Marseille Univ., CNRS, CNES, LAM, Marseille, France

2 The ELT: an ideal instrument for submilliarcsecond astrometry of directly-imaged exoplanets and brown dwarfs

Thanks to its high angular resolution and sensitivity, the Extremely Large Telescope (ELT) will be an ideal instrument for high-precision astrometry in high-contrast imaging of exoplanets. Assuming a perfect calibration of the instrument systematics, the astrometric precision can be approximated as the ratio of the width of the point-spread function to the signal-to-noise ratio (Lindegren 1978). Assuming that the astrometric precisions of ∼1–2 mas achieved with SPHERE scale as λ/D with λ the observing wavelength and D the telescope diameter, we can expect the high-contrast imaging modes of the ELT's first-light instruments, MICADO, HARMONI, and METIS, to reach submilliarcsecond astrometric precisions of ∼0.2–0.5 mas. These higher astrometric precisions will be reached at closer separations to the stars compared to SPHERE, down to ∼2 au vs. down to ∼10 au.

Currently, MICADO is the only ELT instrument designed for high-precision astrometry for the study of the Galactic Center and stellar clusters (50 μas with a goal of 20 μas, see Clénet et al., this volume). However, high-contrast imaging of exoplanets requires a dedicated strategy to calibrate the position of the star (masked by coronagraphy) and the orientation of the field to the North (use of pupil-tracking observations to fix the stellar aberrations on the detector to calibrate them).

2.1 Synergies with RV surveys and Gaia

High-contrast imaging of exoplanets presents strong synergies with RV surveys and Gaia. A major result of high-contrast imaging surveys such as the SPHERE/SHINE survey (Desidera et al. 2021; Langlois et al. 2021; Vigan et al. 2021) is that giant exoplanets at separations beyond 10 au from solar-type stars are rare (about a few %). This result is coherent with the poor efficiency to form planets in wide orbits predicted for the planetary formation model by core accretion (which is the most accepted mechanism for forming the planet population detected at close separations with RV and transits). It also implies that alternative planetary formation models proposed to form planets in wide orbits such as the disk gravitational instability model occur rarely. The stars which were observed in these high-contrast imaging surveys were mostly selected based on age criteria and in some cases the presence of an infrared excess indicating the presence of a circumstellar disk. To improve the detection rates of high-contrast imaging surveys, the main path explored is to reach closer separations to the stars, where the bulk population of exoplanets is located. This requires to improve the performance at small angular separations of current instruments on 8m telescopes (e.g., SPHERE+, GPI2.0) or to build larger telescopes such as the ELT. A second approach is targeted imaging of stars showing indirect signs of the presence of long-period companions in RV or absolute astrometry. Such targeted surveys have shown detection rates of ∼30% (Currie 2020). For companions only detected in RV or from an astrometric acceleration trend, high-contrast imaging is valuable to measure their orbital inclination and mass. The least massive companions detected so far are in the brown dwarf regime, but the prospects are promising with the upcoming publication of the catalog of exoplanets detected by Gaia.

Another strong synergy between high-contrast imaging with RV surveys and Gaia deals with the characterization of the detected companions. The theoretical mass-luminosity-age relations used in high-contrast imaging to estimate the mass of the detected companions are poorly calibrated because we have very few empirical mass measurements of young and/or low-mass substellar companions. The thermal evolution of a substellar companion depends on the properties of its atmosphere (clouds, molecular opacities) and internal structure. The left panel of Fig. 1 shows that for given luminosity and age, the corresponding mass of a giant planet can vary significantly depending on the model used for the physics of the accretion. The right panel of Fig. 1 shows that the mass of a planet core strongly affects the mass-luminosity-age relation, with planets with more massive cores being brighter for a given age. Finally, Figure 2 illustrates the influence of the atmospheric model on the mass-luminosity-age relations.

2.2 Synergies with SPHERE+ and GRAVITY+

Strong synergies for exoplanet imaging exist between the ELT and the instruments SPHERE+ and GRAVITY+ planned in the VLT2030 roadmap (Boccaletti et al. 2020; Eisenhauer 2019, see also Paumard et al., this volume). SPHERE+ is an upgrade project for SPHERE to improve its high-contrast performance toward smaller angular separations to access closer physical separations to the stars. It will also improve the performance toward fainter stars to search for young giant protoplanets in a larger sample of the protoplanetary disks imaged with ALMA. SPHERE+ will be more suited than the ELT to complete large surveys and first characterizations of young

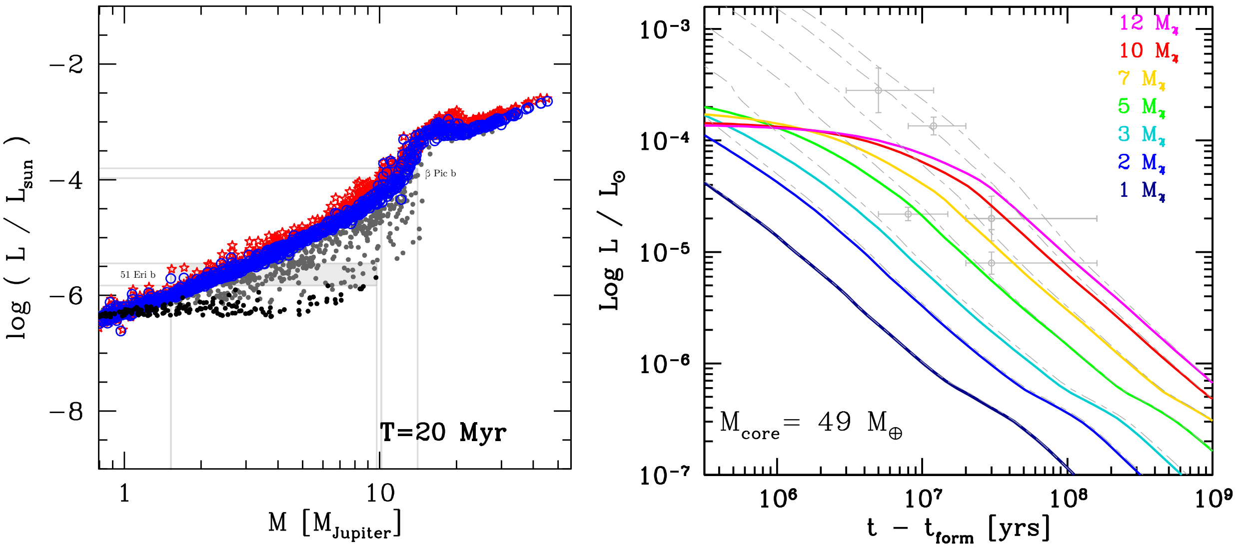

Fig. 1. Left: Bolometric luminosity of giant planets as a function of their mass for an age of 20 Myr for several accretion models differing by the efficiency of the accretion shock of the planetesimals onto the planetary core (from red: hot accretion to gray and black: cold accretion). Two known directly-imaged giant exoplanets are also shown (gray lines). Figure from Mordasini et al. (2017). **Right:** Bolometric luminosity of giant planets as a function of time after formation for several total planet masses (colors), a given core planet mass of 49 Earth masses, and a cold accretion model. The dotted-dashed curves show the predictions for a hot accretion model. Known directly-imaged planetary-mass companions are also shown (data points with error bars). Figure from Mordasini (2013).

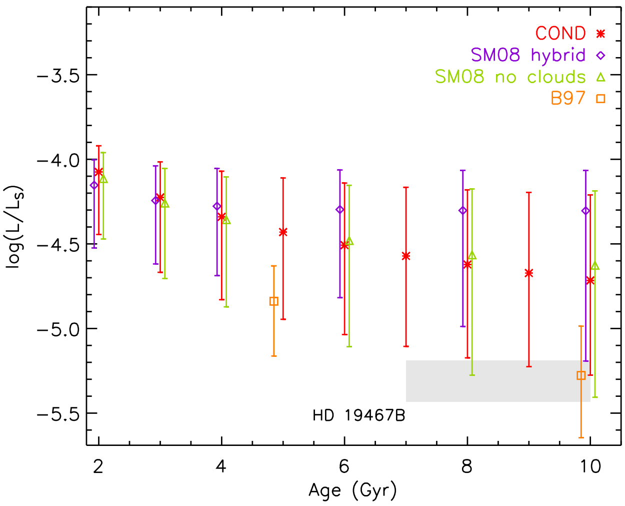

Fig. 2. Bolometric luminosity as a function of the age of the brown dwarf HD 19467B (gray area) compared to evolutionary tracks from the models COND (Baraffe et al. 2003), Saumon & Marley (2008) (for two cloud models, a cloudless model and a hybrid model designed to reproduce the L/T transition), and Burrows et al. (1997) using the companion mass measured from an RV-imaging-astrometry orbital fit and the theoretical hydrogen-burning mass limit (data points). Small horizontal offsets are applied to all models except for COND for clarity. Figure from Maire et al. (2020).

massive giant exoplanets at separations down to the snow line (~3 au). These planets will be ideal targets for a follow-up with the ELT to characterize their atmospheric and orbital properties more finely at higher spectral resolutions and astrometric precisions, respectively.

GRAVITY+ is an upgrade project for GRAVITY to extend its capabilities toward fainter science targets and achieve milliarcsecond astrometry over the entire sky. GRAVITY+ will be more suited than the ELT for a fine orbital characterization of known companions in particular mature giant exoplanets detected in RV surveys or with Gaia. GRAVITY has already allowed for the first imaging confirmation of an exoplanet discovered with RV, the giant exoplanet β Pictoris c (Nowak et al. 2020), which orbits the young star β Pictoris ($\sim$24 Myr). The orbit of β Pictoris c is inner to the orbit of the giant exoplanet β Pictoris b which was previously discovered with high-contrast imaging. GRAVITY requires a precise knowledge of the position of the planets because of the limited field of view of its dual-fiber mode (60 mas). However, RV cannot constrain the orientation of the orbital plane. The detection of β Pictoris c was possible by assuming that its orbit is coplanar with the orbit of β Pictoris b. To detect with GRAVITY+ other RV-detected exoplanets (which are found in mature systems), it will be critical to constrain their position in the field of view beforehand. This could be done with coronagraphic imaging, with SPHERE+ or MICADO, HARMONI, or METIS on the ELT. Alternatively, if the star shows an astrometric signature with Gaia, orbital predictions from joint fits of RV and Gaia data could be used.

3 Monitoring of the motion of substructures in circumstellar disks

Another major science case that will benefit from the improved astrometric precision of the ELT in high-contrast imaging is the monitoring of the slow motion of substructures (e.g., spirals, rings, shadows) in circumstellar disks to constrain the underlying production mechanism. For instance, spiral arms could be produced by a gravitational instability in the disk or by the gravitational interactions of a giant planet embedded in the disk. These scenarios predict different rotation speeds for the spiral arms. The rotational speed of the spiral arms of MWC 758 was measured using SPHERE images taken 4 years apart from each other and was shown to be compatible with a planet-driven scenario (Ren et al. 2020). Thanks to the ELT, monitoring of disk features will be feasible at higher spatial resolutions and precisions and for a larger sample of young protoplanetary disks in star-forming regions and fainter or less massive debris disks.

4 Conclusions

Thanks to its high angular resolution and sensitivity, the ELT will bridge the gap between the high-contrast imaging, RV, and/or astrometric techniques for the characterization of exoplanets beyond 1 au from the stars. The combination of these techniques is essential to break the degeneracies between the mass, luminosity, and age of the planets and to perform strong tests of the models of formation, evolution, atmosphere, and internal structure of exoplanets. The ELT will also be complementary to the VLT2030 instruments SPHERE+ for detailed follow-up characterization of newly-discovered young massive giant exoplanets and GRAVITY+ for first imaging snapshots of RV or Gaia exoplanets to constrain or refine the on-sky position for finer astrometric characterization.

A.L.M. acknowledges financial support from the European Research Council under the European Union's Horizon 2020 research and innovation program (Grant Agreement No. 819155).

References

Baraffe, I., Chabrier, G., Barman, T. S., Allard, F., & Hauschildt, P. H. 2003, A&A, 402, 701
Boccaletti, A., Chauvin, G., Mouillet, D., et al. 2020, arXiv e-prints, arXiv:2003.05714
Burrows, A., Marley, M., Hubbard, W. B., et al. 1997, ApJ, 491, 856
Currie, T. 2020, in Ground-Based Thermal Infrared Astronomy - Past, Present, and Future, 12
Desidera, S., Chauvin, G., Bonavita, M., et al. 2021, A&A, 651, A70
Eisenhauer, F. 2019, in The Very Large Telescope in 2030, 30
Langlois, M., Gratton, R., Lagrange, A. M., et al. 2021, A&A, 651, A71
Lindegren, L. 1978, in IAU Colloq. 48: Modern Astrometry, 197
Maire, A. L., Molaverdikhani, K., Desidera, S., et al. 2020, A&A, 639, A47
Mordasini, C. 2013, A&A, 558, A113
Mordasini, C., Marleau, G. D., & Mollière, P. 2017, A&A, 608, A72
Nowak, M., Lacour, S., Lagrange, A. M., et al. 2020, A&A, 642, L2
Ren, B., Dong, R., van Holstein, R. G., et al. 2020, ApJL, 898, L38
Saumon, D. & Marley, M. S. 2008, ApJ, 689, 1327
Vigan, A., Fontanive, C., Meyer, M., et al. 2021, A&A, 651, A72

Session 5

Atelier général ASHRA: bilan et prospective de l'interférométrie optique

Hα IMAGING OF PROTOPLANETS WITH THE SPECTRO-INTERFEROMETER FIRST AT THE SUBARU TELESCOPE

M. Lallement[1, 2], E. Huby[1], S. Lacour[1], K. Barjot[1], S. Vievard[2, 3], N. Cvetojevic[4], V. Deo[2], O. Guyon[2,3, 5], T. Kotani[3], F. Marchis[6], G. Martin[7] and G. Perrin[1]

Abstract. The Fibered Imager foR a Single Telescope (FIRST) is a spectro-interferometer installed on the Subaru Coronagraphic Extreme Adaptice Optics platform (SCExAO) at the 8-m Subaru Telescope, Hawaï. Its capability, unique in this field, is to perform visible spectroscopy at, and even below, the diffraction limit of a monolithic telescope thanks to the fibered pupil remapping technique. FIRST has already shown its capability to resolve binary stars, and upgrades in FIRST's setup are currently being carried out in order to detect and characterize companions much fainter than their host star. In particular, a new spectrograph was designed and integrated on the FIRST replica bench at the Paris Observatory for detecting the Hα signal emitted by young exoplanets accreting matter, i.e by protoplanets.

Keywords: Spectro-Interferometry, Optical design, Pupil remapping, Single-mode fibers, High contrast imaging, High angular resolution, Protoplanets, Hα imaging, Differential phase measurements

1 Introduction

Rewarded by a Nobel prize in 2019, the discovery of the first exoplanet 51 Pegasi b orbiting a main-sequence star was announced by Mayor & Queloz (1995) and launched the investigations on a large variety of exoplanets detection methods. As opposed to indirect detection deriving the presence of a planet thanks to the host star's properties, direct detection has allowed the exoplanet's light analysis of 53 exoplanets by August 2021 (`https://exoplanets.nasa.gov/`). Thanks to direct detection and spectroscopy of the planet light, it is possible to study the formation and evolution of exoplanets, through the characterization of their surface and atmosphere, eventually searching for biological markers of life. Direct imaging is performed with high angular resolution and high dynamic instruments to detect exoplanets that are 10^5 to 10^{10} times fainter than their host star in the visible according to Seager (2010). **Direct detection by adaptive optics and coronagraphy** reaches a factor 10^7 in star-exoplanet contrast but the angular resolution is generally limited to two times the telescope's diffraction limit, i.e. roughly 100 mas with a 10-m class telescope. At a distance of 140pc, it sets the limit at a minimum of 14 UA for the separation between the star and the planet. However, from indirect radial velocity and transit methods, Fernandes & Mulders (2019) infer that the distribution of gas giant planets is maximum around 1-4 UA from the host star, i.e at an angular distance of 7-28 mas at 140 pc. **FIRST performs direct detection by interferometry, down to the diffraction limit of the Subaru Telescope, that is 16 mas at 650nm, thus reaching the region where most giant planets might orbit, inaccessible to coronagraphic methods. Its principle is based on pupil remapping and spatial filtering by single mode fibers (SMF) detailled by Perrin et al. (2006) to reach the diffraction limit by turning a telescope into an interferometer .**

[1] LESIA, Observatoire de Paris, 5 place Jules Janssen, 92195 Meudon, France
[2] Subaru Telescope, National Astronomical Observatory of Japan, National Institutes of Natural Sciences (NINS), 650 North A'ohōkū Place, Hilo, HI, 96720, U.S.A.
[3] Astrobiology Center of NINS, 2-21-1, Osawa, Mitaka, Tokyo, 181-8588, Japan
[4] Observatoire de la Côte d'Azur, 96 Boulevard de l'Observatoire, 06300 Nice, France
[5] College of Optical Sciences, University of Arizona, Tucson, AZ 85721, U.S.A.
[6] Carl Sagan Center at the SETI Institute, 189 Bernardo Av., Mountain View, CA 94043, USA
[7] Univ. Grenoble Alpes, CNRS, IPAG, 38000 Grenoble, France

2 The FIRST instrument : Setup and on-sky results

In Hawaï, FIRST is installed at the Subaru telescope Nasmyth focus and regularly performs night sky observations. It benefits from two adaptive optics levels of correction (the AO188 and SCExAO respectively presented by Minowa et al. (2010) and Jovanovic et al. (2015)), providing a PSF with a Strehl ratio of $50-60\%$ at 750 nm. By stabilizing the wavefront and the fringes, SCExAO allows long exposures and the observation of 6.6 magnitude stars in the R band. A replica of FIRST is available at Paris Observatory in the LESIA laboratory. Fig. 1 presents the setups of FIRST version 1 (V1) and FIRST upgraded version 2 (V2) currently in development.

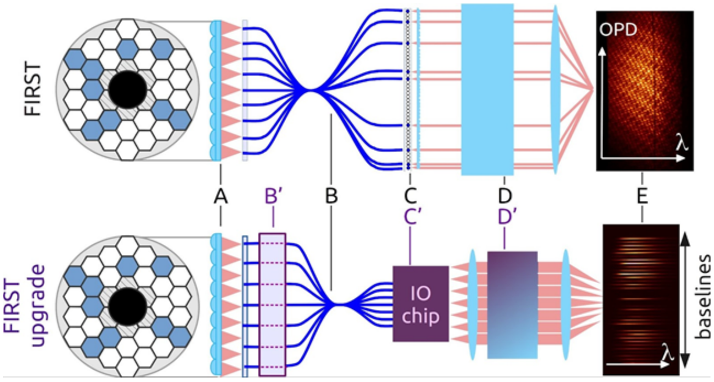

Top: FIRST's V1 setup. The pupil is sampled by a microlens array and subpupil fluxes are injected (**A**) into SMF (**B**). Fiber outputs are rearranged in a linear non-redundant configuration (**C**). The beams are spectrally dispersed (**D**) and recombined in a Young slits experiment way. **Bottom:** FIRST's V2 setup. Optical delay lines (**B'**) adjust optical path length differences, interferences take place into an integrated photonic chip (**C'**) for better accuracy and stability. The signal is then dispersed at higher resolution (**D'**), 2200 instead of 400.

Fig. 1.

The telescope's pupil is divided into 36 subpupils by a segmented mirror and the incident flux on each subpupil is injected into a SMF through a microlens. In FIRST V1, the remapping technique consists in arranging a set of nine fiber outputs into a non-redundant linear configuration (i.e each pair of subpupils is forming a unique baseline) and make them interfere (spatial modulation of the fringes). Only two sets of nine fibers are used for now but the whole telescope pupil could be used. As the remapping is linear, the interferometric signal can be spectrally dispersed by a prism in the orthogonal direction over the $650-900$ nm spectral band (resolving power of about 400). Until now, FIRST V1 performed closure phase measurements which reveal asymmetries in the target's intensity spatial distribution. With a contrast limited to 10^{-1}, FIRST V1 resolved and spectrally analysed the Capella binary star at the Shane Telescope of the Lick Observatory (Huby et al. 2013). In 2015, both components of the binary star Alpha Equu separated by 0.6 times the Subaru telescope diffraction limit have been detected (Huby in preparation). **FIRST V2's objective is to resolve exoplanets in addition to binary stars thanks to differential phase measurements at the Hα wavelength.**

3 A new scientific objective for FIRST : study gas giant formation mechanisms

FIRST V2's scientific objective is to understand gas giant formation process. Core accretion and gravitational instability are two formation models which differ when exoplanets are still very-young and accreting matter, i.e when they still are protoplanets ($\leq$ 4 Myrs). The first protoplanet discovered, PDS70b, has been imaged with SPHERE's extreme AO (Spectro Polarimetric High contrast Exoplanet REsearch) at the Very Large Telescope, Chile (Kepler & Benisty 2018). Haffert & Bohn (2019) confirmed the detection of PDS70b and revealed PDS70c by measuring a **signal in the $H\alpha$ line, a signature of matter accretion**, with the integral field spectrograph MUSE (Multi Unit Spectroscopic Explorer). These protoplanets are the only ones confirmed by $H\alpha$ imaging and can not constrain, validate or invalidate gas accretion mechanism in order to understand gas giant formation process. **The detection of a larger panel of protoplanets is required**. The interferometric analogue of $H\alpha$ imaging is the differential phase measurement used for example by Sturm et al. (Gravity Collaboration, 2019) to detect a gas mass orbiting the 3C273 Quasar. **$H\alpha$ differential phase measurement consists in the comparison between the measured phase at the $H\alpha$ and the continuum**. **FIRST is particularly suited to detect this $H\alpha$ signal by differential phase measurement** because it provides the capability to perform spectroscopy at an angular resolution of λ/D=17 mas at 140 pc (distance of the Taurus Molecular Cloud, the nearest star-forming region), thus probing the region where the giant planet distribution is supposed to be maximum. The contrast ratio is higher in the $H\alpha$ line region : on the order of 10^{-2} for a 1

Jupiter mass (M_{jup}) protoplanet accreting 10^{-7} M_{jup} per year. This contrast is achieved while having a 0.1° to 0.01° precision on the phase measurement reached through an increased SNR (thanks to the integrated optics chip and other upgrades) and better phase calibration (thanks to the differential phase technique). FIRST new spectrograph resolution is given by the $H\alpha$ signal width (0.3nm) and is about $656.3nm/0.3nm \approx 2200$ at the $H\alpha$ line. Table. 3 describes **FIRST instrumental upgrades needed in order to resolve protoplanets** by Hα differential phase measurements. In addition to contrast and the spectrograph's spectral resolution, the sensitivity of the instrument has to be enhanced.

	FIRST V1	**FIRST V2**
Angular resolution	8.5 mas	8.5 mas
Spectral resolution	400	2200
Sensibility in R band	6 mag	12 mag (PDS70)
Contrast	10^{-1}	10^{-2} - 10^{-3}
Measurement - Scientific target	Closure phase - Binary stars	$H\alpha$ differential phase - Protoplanets

Table 1. FIRST V1 performances & FIRST V2 instrumental upgrades

4 Optical design and performances of the R2200 spectrograph

The spectrograph is characterized by its spectral resolving power $R = \lambda/\delta\lambda$ which reflects its capability to resolve two wavelengths λ et $\lambda + \delta\lambda$ with $\delta\lambda$ the spectral resolution element. As the resolving power specification is 2200 at 656.3 nm (Hα), FIRST V1 prism is replaced by a grating in the FIRST V2 spectrograph design. The setup of the spectrograph comprises a source, a collimator, a grating, an imager and a camera. The spectrograph **source** is the V-groove in which are placed the **photonic chip fiber outputs**. The V-groove pitch is $p_{vg} = 127\mu m$, $N_s = 36$ fiber outputs are available and the fiber's numerical aperture is $NA_f = 0.12$. The total field is $y_0 = 4.45mm$. **The selected collimator is a Thorlabs 2x apochromatic microscope objective** TL2X SAP with a numerical aperture of $NA_o = 0.1$ (leading to a flux loss of about 10-15%) and a focal length $f'_{coll} = 100mm$. A **birefringent Wollaston prism** of separation $10' = 0.17°$ separates the two orthogonal linear polarisations in the X direction, as shown in Fig. 2, to avoid fringe blurring. The spectral band imaged is $\Delta\lambda = 783nm - 623nm = 260nm$ and is centered on $703nm$. The selected grating meets three specifications ; its diffraction efficiency η is maximal around the $H\alpha$ line (S1), η slightly depends on polarisation (S2) and is higher than 60% over the entire spectral band (S3). A **Volume Phase Holographic grating (VPH) with** 600 $lines/mm$ from Wasatch Photonic was chosen for the new spectrograph. This grating works in transmission and diffracts in the $m = 1$ mode. It offers higher diffraction efficiency maximum and stability over the spectral band and polarization. The imager's focal length depends on L, the detector's size in the dispersion direction and on $\alpha_{\lambda_{min}}$ and $\alpha_{\lambda_{max}}$, the incidence angles on the imager of two collimated beams associated with the extreme wavelengths of the spectral band ($623nm$ and $783nm$): $f'_{im} = L/(\tan\alpha_{\lambda_{min}} + \tan\alpha_{\lambda_{max}}) = 83mm$. **The imager choice was done thanks to the optical design software Zemax Optic Studio.** To reach the resolution of 2200 at $656.3nm$, the PSF RMS radius at this wavelength must be about $15\mu m$. A unique achromatic doublet of focal f'_{im} focuses the beam too rapidly so that the PSF radius remains too wide. The incident beam diameter on the imager is about $D = 30mm$ inducing that the numerical aperture of the imager has to be around $NA_i = \frac{1}{2*(83/30)} = 0.18$, which is small. **Two achromatic doublets arranged in a Lister configuration** (which compensates aberrations for low $NA \sim 0.25$) slowly focus the beams as the power of the doublets are reduced ($f'_{im1} = 150mm$ for the first doublet and $f'_{im1} = 80mm$ for the second). The camera for the spectrograph integration at the Paris Observatory is a **Andor Zyla sCMOS** with 2560*2160 pixels of $6.5\mu m$.**The resolving power is limited by the PSF RMS size.** Fig. 2 presents the spots diagram obtained on Zemax for different fibers in the V-groove. The resolving power is directly computed by a macro coded in Zemax. The resolving power is $R(\lambda) = \frac{\lambda}{s(\lambda)*FWHM(\lambda)}$ with $FWHM(\lambda)$ the spot diagram RMS diameter in the direction of dispersion (about $15\mu m$ at 656.3nm), $y(\lambda)$ is the ray position on the detector and $s(\lambda) = \frac{\delta\lambda}{\delta y}(\lambda)$ is the spectral dispersion in pm/μm. **The pixel size** px **and the Shannon criterion (two pixels are at least needed to sample one spot) also constrain the resolving power**. If $FWHM(\lambda)$ is smaller than two pixels, the spectrum is under-sampled. The resolving power is then computed with $FWHM(\lambda) = 2 * px$. Fig. 2 shows that with $px = 6.5\mu m$ the resolving power is 2210 at $656.3nm$. The camera at the Subaru telescope has a pixel size of $16\mu m$ for now, so with the same spectrograph, the resolving power will be limited to 1040.

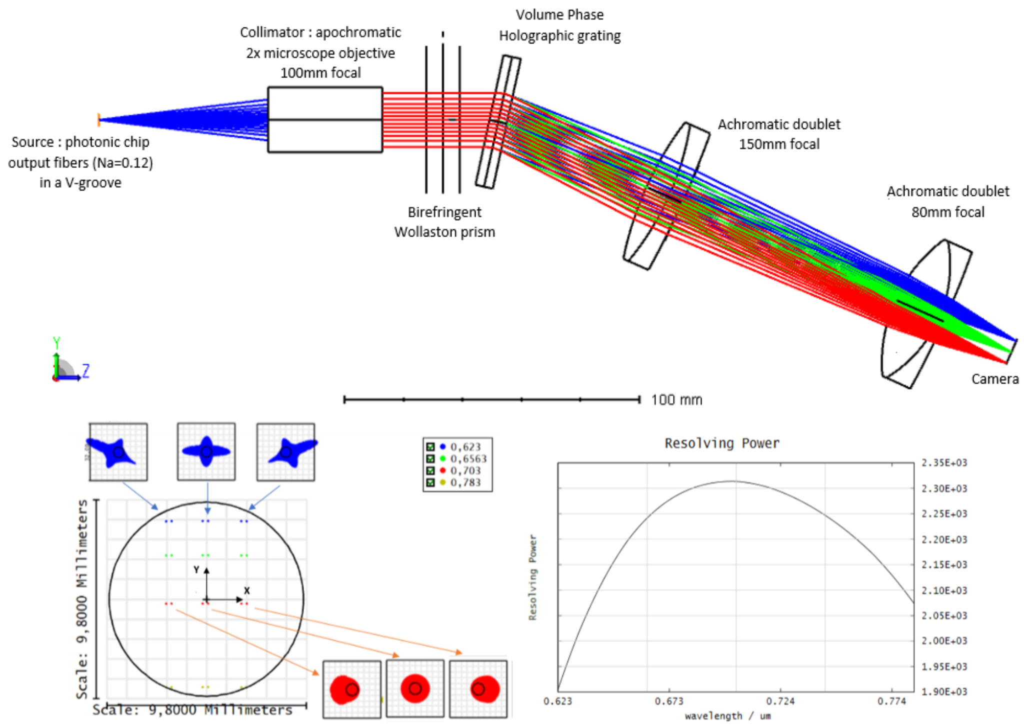

Fig. 2. Top: Optical design of FIRST new R2200 spectrograph on Zemax Optic Studio. **Left:** Spectrum positions on the detector for three fibers: at the v-groove ends and in the middle (X axis). Each fiber output produces two spectra, one for each linear polarization. The spectral dispersion follows the Y direction. **Right:** Resolving power as a function of wavelength (2210 @ 656.3nm) computed in Zemax according to the spot diagram RMS diameter.

5 Conclusions

This optical design of FIRST's new spectrograph meets the specification of a 2200 resolving power at the $H\alpha$ line with a 6.5μm pixel size and will allow the the measurement of the $H\alpha$ signal indicative of protoplanets' accretion phase. In August 2021, the spectrograph was integrated to the FIRST laboratory bench at Paris Observatory reaching a resolution of 3200 at the $H\alpha$ line. We think the alignement favoured smaller spots in the $H\alpha$ line, thus leading to a higher resolving power. Once the new setup is fully validated on laboratory data, it will be integrated to the FIRST instrument at the Subaru Telescope.

As a Master 2 intern working on this optical design for FIRST, I would like to thank the warm and welcoming team which supported me during those 6 months. I would also like to thank the SF2A organization for the conference week and particularly Frantz Martinache for giving me the opportunity to present this work.

References

Fernandes, R. B. & Mulders, G. D. 2019, ApJ, 874

Haffert, S. Y. & Bohn, A. J. 2019, A&A, 3, 749

Huby, E., Duchêne, G., Perrin, G., Marchis, F., & Lacour, S. 2013, A&A, 560

Jovanovic, N., Martinache, F., Guyon, O., et al. 2015, Publications of the Astronomical Society of the Pacific, 127, 890

Kepler, M. & Benisty, M. 2018, A&A, 617

Mayor, M. & Queloz, D. 1995, Nature, 378, 355

Minowa, Y., Hayano, Y., Oya, S., et al. 2010, in Adaptive Optics Systems II, Vol. 7736, International Society for Optics and Photonics, 77363N

Perrin, G., Lacour, S., Woillez, J., & Thiébaut, E. 2006, Monthly Notices of the Royal Astronomical Society, 373, 747

Seager, S. 2010, Exoplanet atmospheres (Princeton University Press)

Sturm, E., Dexter, J., & Pfuhl, O. Gravity Collaboration, 2019, A&A, 563, 657

A NEW LONGITUDINAL DISPERSION COMPENSATOR FOR OBSERVING AT LOW SPECTRAL RESOLUTION FROM 0.55 TO 2.45 MICROMETERS AT CHARA ARRAY

C. Pannetier[1], D. Mourard[1] and F. Cassaing[2, 3]

Abstract. The Center for High Angular Resolution Astronomy (CHARA), located in Mount Wilson, California, is an interferometric array of six telescopes feeding instruments observing from 0.55 to 2.45 µm. Since its first operations in 2003, it has been equipped with a Longitudinal Dispersion Compensator (LDC) that made possible observation at low spectral resolution and large spectral bands in the visible and near-infrared. To push the limiting magnitude and the quantity of interferometric data collection, CHARA has decided to replace the current LDC configuration with a more transmissive and performant one. This new solution will allow coordinated operations of the new generation instruments from 0.55 to 2.45 µm. I will present its design and expected performance.

Keywords: spectro-interferometry, group-delay, longitudinal dispersion, long baseline interferometry

1 Introduction

Ground-based stellar interferometers combine the light coming from telescopes separated by hundreds of meters. The highest distance between two telescopes of the Center for High Angular Resolution Array (CHARA) is 330 m. After being collimated in the Coudé train of each telescope, the light is propagated up to the focal laboratory where the spectro-interferometric instruments record dispersed interferometric fringes. However these inteferometric fringes are multiplied by a coherence envelop whose length increases with the spectral resolution of the instrument. High-contrast fringes are observed only at the center of this coherence envelop which position is called group-delay (GD). When the target is not at the zenith, an achromatic geometrical delay introduces an optical path difference between the electromagnetic fields coming from the different telescopes which translates to a non-null GD at the recombination focus. Classically, interferometers like CHARA use optical delay lines (MDL for main delay lines) to equalize the optical paths. However, when MDLs are filled with air, this equalization is chromatical and the GD is nulled only at a given wavelength (e.g. middle of H-band in Fig. 1a). An alternative, currently considered at MROI (Creech-Eakman et al. 2018), is to put these MDL under vacuum. Since 2003, CHARA uses longitudinal dispersion compensator (LDC) to compensate for the dispersion in the R-band where it is the most critical (Berger et al. 2003). A smart set of the thickness of these pieces of glass enables to null the GD at several wavelengths.

CHARA is preparing the arrival of several instruments since 2018. The instrument MIRCx (Kraus et al. 2018) is currently observing at spectral resolution as low as R=20 in H-band (1.45 − 1.75 µm). It is now able to record interferometric data simultaneously in H and J bands (1.15 − 1.3 µm), at least for R=44 (Labdon et al. 2020). The instrument MYSTIC (Monnier et al. 2018) also observes at R=20 in K-band (1.95 − 2.45 µm). Following these two instruments, the visible spectro-interferometer CHARA/SPICA (Mourard et al. 2017) should be commissioned in 2022 for observation in R-band (0.6 − 0.9 µm) at R=140. The development of the fringe-tracker SPICA-FT (Mourard et al. 2018) is in progress inside this instrument with the aim to stabilise the piston disturbance under 100 nm rms for allowing long exposures with the other instruments. To push the limiting magnitude of all the instruments and multiply the data collection with CHARA, a high performance

[1] Université Côte d'Azur, Observatoire de la Côte d'Azur, CNRS, Laboratoire Lagrange, Bd de l'Observatoire, CS 34229, 06304 Nice cedex 4, France
[2] DOTA, ONERA, Université Paris Saclay, F-92322 Chtillon, France
[3] Now at DTIS, ONERA, Université Paris Saclay, F-91123 Palaiseau, France

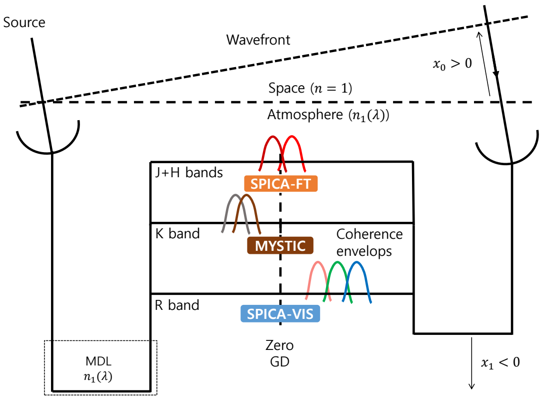

(a) Chromatical equalization using MDL. The fringe contrast is null in R and K bands and low in most of H-band.

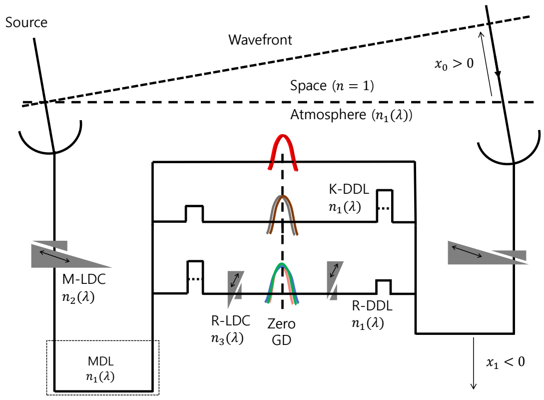

(b) Perfect compensation using MDL, DDL and LDC. The fringe-contrast is high for all instruments.

Fig. 1: Shift of the coherence envelops due to longitudinal dispersion and solutions to correct it.

fringe-tracking is necessary in H-band altogether with low dispersion on the whole observed wavebands. Yet, the current LDC is accountable for 1 magnitude loss in K-band and does not allow a coordinated and optimal operation of the new generation of instruments. The CHARA consortium decided to change the LDC for a more transmissive and complete solution that will enable, with the help of differential delay lines (DDL) in the different instruments, to compensate for the longitudinal dispersion from 0.6 to 2.45 µm, paving the way for very wide band coordinated operations.

We performed a numerical minimisation of the dispersion with all possible LDC configurations involving 340 glasses available in the main glass catalogs. Regarding our constrains in the CHARA optical path, we figured out a solution consisting in two stages of LDC made of SF66, whose transmission and dispersion laws garanty a SNR attenuation higher than 90 % from 0.6 to 1.9 µm and 47 % from 1.9 to 2.5 µm. We present here this solution.

2 Minimising the phase dispersion using LDCs

2.1 Phase dispersion minimisation

Tango (Tango 1990) paved the way for longitudinal dispersion compensation on a large waveband using LDC in the context of the SUSI interferometer (Davis 1994). The phase dispersion after propagation in the optical delay lines is a non-linear function of the wavenumber that can be approximated by a Taylor development around the central wavenumber of the concerned waveband. Doing that, the GD at the chosen wavenumber is the coefficient of the first degree of the polynomial and the terms of higher degree are contributors to the dispersion function which accounts for the chromatism of the GD on the large band. With this formalism, each additional LDC enables to null a coefficient of higher degree in the Taylor expansion.

Yet powerful and intuitive, this formalism is not perfectly adapted to our situation, as we need to correct with common glasses and individual differential delay lines the dispersion on four discontinuous wavebands. We developped a criteria of maximisation of the fringe contrast on the whole concerned waveband. A complete explanation of the criteria can be found in Pannetier et al. (2021) but here is a short demonstration.

For simplicity and because it is easy to generalise it to more telescopes, we study the case of a two-telescopes interferometer. We define **n** as the refractive index of all media (MDLs, DDLs, LDCs). All media are present in the two arms and **x** is the vectors of their thicknesses difference. The Phase-Delay (PD) between two arms at the wavenumber σ is:

$$\Phi(\mathbf{x}, \sigma) = 2\pi\sigma \sum_{k=1}^{n} n_k(\sigma) x_k \tag{2.1}$$

In the spectral channel S, the fringe contrast attenuation due to the chromatism of the PD is:

Table 1: Signal-to-noise attenuation in the four spectral bands where spectro-interferometers observe.

Band	R	J	H	K
Solution chosen for CHARA	0.90	0.93	0.94	0.47
Alternative solution using an infrared glass	0.92	0.99	0.99	0.99

$$C_S(\mathbf{x}) \simeq \exp\left(-Var_\sigma[\Phi(\mathbf{x},\sigma)]/2\right) \tag{2.2}$$

The maximisation of C over all the involved spectral channels S is obtained from the minimisation of the variance of the dispersion. Our criteria is quadratic in $\mathbf{x}$ so its minimisation gets a unique solution:

$$\mathbf{x}_0 = \mathbf{M}^{-1} \cdot \mathbf{d} \tag{2.3}$$

where $\mathbf{M}$ is the covariance matrix of all the dispersion laws and $\mathbf{d}$ is the achromatic GD to null.

Using this criteria, we tried out all the possible configurations involving one or two stages of LDCs made of glasses picked up within 340 of the main glasses catalogs (SCHOTT*, OHARA†, CDGM‡). All dispersion laws have been downloaded from ZemaxGlass package§. We figured out the ten best solutions in term of dispersion correction and used the signal-to-noise ratio (SNR) attenuation factor

$$\Gamma = TV^2$$

to conclude on the final performance taking into account both intensity transmission T and fringe contrast V^2.

3 The new Longitudinal Dispersion Compensator for CHARA

3.1 *Two stages of SF66-made LDCs*

Fig. 1b presents the setup of the solution we figured out. The DDLs in SPICA-VIS's and in MYSTIC's optical paths enable to null the average GD on these bands and on the H-band (using the MDL). Then, a first LDC stage (maximal thickness: 14 mm for 90 m of MDL) made of SF66 is placed in the common optical path to correct the dispersion residuals from J to K bands. A second LDC stage (maximal thickness: 9 mm for 90 m of ODL) made of the same material is placed in SPICA-VIS's optical path to correct the dispersion on this large band. The final fringe contrast is kept higher than 95% on the R, J and H bands and on half of the K-band. Fig. 2a presents the theoretical fringe contrast in the case of coordinated operations with the three main instruments in their low spectral resolution mode. Finally, we estimate in Table 1 that the SNR attenuation due to dispersion residuals and transmission loss from the LDC keeps higher than 90% in R, J and H bands and 47% in K-band when all instruments are observing simultaneously with their low spectral resolution mode.

3.2 *Using infrared glass for high SNR in the K-band*

SF66 absorbs 13% of the energy in the middle of the K-band (2.19 µm) and the dispersion residuals are responsible for a minimal fringe contrast of 78% in the two extreme spectral channels of the K-band. To further improve the K-band, the solution would be to remove the main LDC and to install a LDC made of an infrared glass like ZnSE in the optical path common to J, H and K bands, just after the first dichroic plate. Doing that, we get a high transmission in all spectral bands and the low dispersion residuals give fringe contrasts higher than 97% on the whole band. Fig. 2b presents the theoretical fringe contrast in the case of coordinated operations with the three new instruments dispersing with their low spectral resolution mode. We see in Table 1 that the final SNR attenuation is higher than 99% and 92% respectively in the infrared bands and in R-band. Unfortunatly, the current installation in CHARA focal laboratory doesn't allow to put a LDC at this position.

* https://www.schott.com/english/index.html
† https://www.oharacorp.com/
‡ http://cdgmglass.com/
§ Courtesy Nathan Hagen, https://github.com/nzhagen/zemaxglass

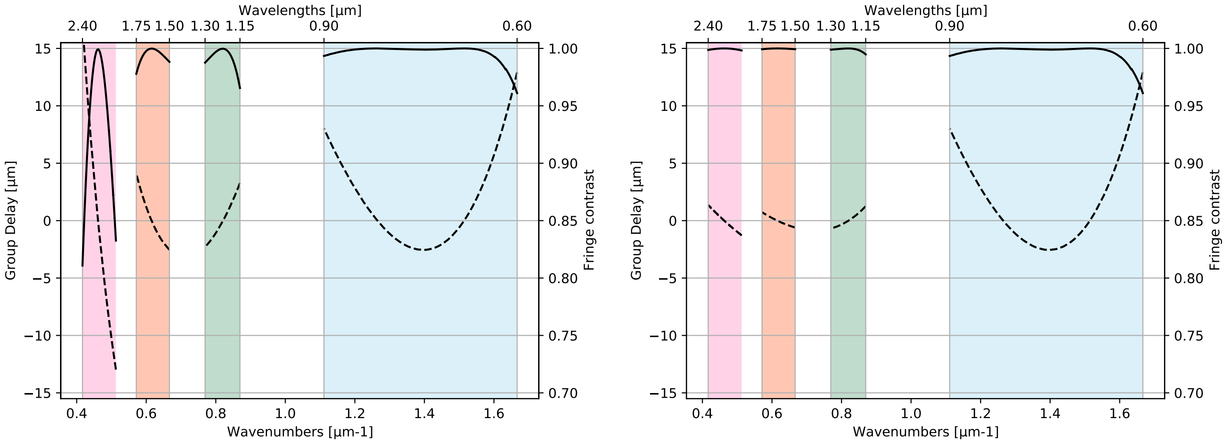

(a) Chosen solution with two LDC made of SF66.

(b) Solution involving a LDC made of infrared glass.

Fig. 2: Fringe-contrast (solid line) and GD (dashed line) after the dispersion minimisation using the two presented solutions during a coordinated operation with R=140 in R-band and R=20 in J, H and K bands.

4 Conclusion

We presented the best solution available in the current state of CHARA focal laboratory for maximising the overal SNR over the waveband $0.6 - 2.5$ µm for the in-coming generation of low spectral resolution spectro-interferometers SPICA, MIRCx and MYSTIC. The overall configuration finally garanties a SNR attenuation higher than 90 % from 0.6 to 1.9 µm and 47 % from 1.9 to 2.5 µm. Moreover, the low phase dispersion in the H-band will increase the performance of the SPICA-FT fringe-tracker, which is a critical condition for high performance with the observing instruments SPICA-VIS and MYSTIC.

References

Berger, D. H., ten Brummelaar, T. A., Bagnuolo, William G., J., & McAlister, H. A. 2003, in Society of Photo-Optical Instrumentation Engineers (SPIE) Conference Series, Vol. 4838, Interferometry for Optical Astronomy II, ed. W. A. Traub, 974–982

Creech-Eakman, M. J., Romero, V. D., Payne, I., et al. 2018, in Society of Photo-Optical Instrumentation Engineers (SPIE) Conference Series, Vol. 10701, Optical and Infrared Interferometry and Imaging VI, ed. M. J. Creech-Eakman, P. G. Tuthill, & A. Mérand, 1070106

Davis, J. 1994, in Very High Angular Resolution Imaging, ed. J. G. Robertson & W. J. Tango, Vol. 158, 135

Kraus, S., Monnier, J. D., Anugu, N., et al. 2018, in Society of Photo-Optical Instrumentation Engineers (SPIE) Conference Series, Vol. 10701, Optical and Infrared Interferometry and Imaging VI, ed. M. J. Creech-Eakman, P. G. Tuthill, & A. Mérand, 1070123

Labdon, A., Monnier, J. D., Kraus, S., et al. 2020, in Society of Photo-Optical Instrumentation Engineers (SPIE) Conference Series, Vol. 11446, Society of Photo-Optical Instrumentation Engineers (SPIE) Conference Series, 114460H

Monnier, J. D., Le Bouquin, J.-B., Anugu, N., et al. 2018, in Society of Photo-Optical Instrumentation Engineers (SPIE) Conference Series, Vol. 10701, Optical and Infrared Interferometry and Imaging VI, ed. M. J. Creech-Eakman, P. G. Tuthill, & A. Mérand, 1070122

Mourard, D., Bério, P., Perraut, K., et al. 2017, Journal of the Optical Society of America A, 34, A37

Mourard, D., Nardetto, N., ten Brummelaar, T., et al. 2018, in Society of Photo-Optical Instrumentation Engineers (SPIE) Conference Series, Vol. 10701, Optical and Infrared Interferometry and Imaging VI, ed. M. J. Creech-Eakman, P. G. Tuthill, & A. Mérand, 1070120

Pannetier, C., Mourard, D., Cassaing, F., et al. 2021, MNRAS, 507, 1369

Tango, W. J. 1990, Appl. Opt., 29, 516

Session 6

Atelier général du PNPS

SF2A 2021
A. Siebert, K. Baillié, E. Lagadec, N. Lagarde, J. Malzac, J.-B. Marquette, M. N'Diaye, J. Richard, O. Venot (eds)

NONLINEAR SIMULATIONS OF TIDES IN THE CONVECTIVE ENVELOPES OF LOW-MASS STARS AND GIANT GASEOUS PLANETS

A. Astoul[1] and A. J. Barker[1]

Abstract. In close two-body astrophysical systems, such as binary stars or Hot Jupiter systems, tidal interactions often drive dynamical evolution on secular timescales. Many host stars and presumably giant gaseous planets feature a convective envelope. Tidal flows generated therein by the tidal potential of the companion can be dissipated through viscous friction, leading to the redistribution and exchange of angular momentum within the convective shell and with the companion, respectively. In the tightest systems, nonlinear effects are likely to have a significant impact on the tidal dissipation and trigger differential rotation in the form of zonal flows, as has been shown in previous studies. In this context, we investigate how the addition of nonlinearities affect the tidal flow properties, and energy and angular momentum balances, using 3D nonlinear simulations of an adiabatic and incompressible convective shell. In our study, we have chosen a body forcing where the equilibrium tide (the quasi-hydrostatic tidal flow component) acts via an effective forcing to excite tidal inertial waves in a spherical shell. Within this set-up, we show new results for the amplitude of the energy stored in zonal flows, angular momentum evolution, and its consequences on tidal dissipation in the envelopes of low-mass stars and giant gaseous planets.

Keywords: star-planet interactions – tides – hydrodynamics – inertial waves – nonlinear simulations

1 Introduction

In tight stellar and exoplanetary systems, tidal interactions are a key process to understand orbital migration and circularisation, spin synchronisation, and possibly the low obliquities of the closest bodies (e.g. Mathis 2019; Ogilvie 2014). For low-mass stars and Hot Jupiter planets which feature a convective envelope, the dissipation of inertial waves restored by the Coriolis acceleration significantly contributes to the tidal dissipation. This is particularly true in the early stages of the life of rapidly rotating low-mass stars, as shown for example in Mathis (2015), Bolmont & Mathis (2016), and Barker (2020), and possibly may explain the rapid orbital expansion measured for Titan through resonant-locking of inertial modes in Jupiter (Lainey et al. 2020). Furthermore, for the most compact two-body systems, internal nonlinear fluid effects can become important (Barker et al. 2016), especially when considering the small-scales of inertial waves in spherical shells (Rieutord et al. 2001). This typically happens when the tidal amplitude parameter* ϵ is large, as for the ultra short-period Hot Jupiter WASP-19 b ($\epsilon \sim 0.05$, e.g. Ogilvie 2014). In Favier et al. (2014, denoted Paper I in the following), the authors performed a nonlinear numerical study of tidally-forced inertial waves in spherical shells. They found that the amplitude of the tidal dissipation could greatly differ from linear tidal response predictions (e.g. as in Ogilvie 2009) due to the inhomogeneous deposition of angular momentum which generates strong azimuthal zonal flows (see also Astoul et al. 2021). They also observed for some forcing frequencies unexpected evolution of the angular momentum, pushing the body away from synchronisation. Building upon their initial study, we have performed nonlinear hydrodynamical simulations of tidal waves in an adiabatic and incompressible convective envelope, but with different boundary conditions and tidal forcing. While they imposed a radial velocity through the outer boundary to force the tidal flow, we use an effective body force which accounts for the residual action of the large-scale non-wavelike tidal flow in exciting inertial waves (Ogilvie 2013), with stress-free impenetrable boundary conditions at the inner and outer boundaries. Within this more realistic set-up, we are able to separate wavelike and non-wavelike contributions in the nonlinear terms to elucidate the unphysical behaviour

[1] Department of Applied Mathematics, School of Mathematics, University of Leeds, Leeds, LS2 9JT, UK
*It is a measure of the ratio of the tidal gravity to the self-gravity at the surface of the perturbed body (e.g. Barker et al. 2016).

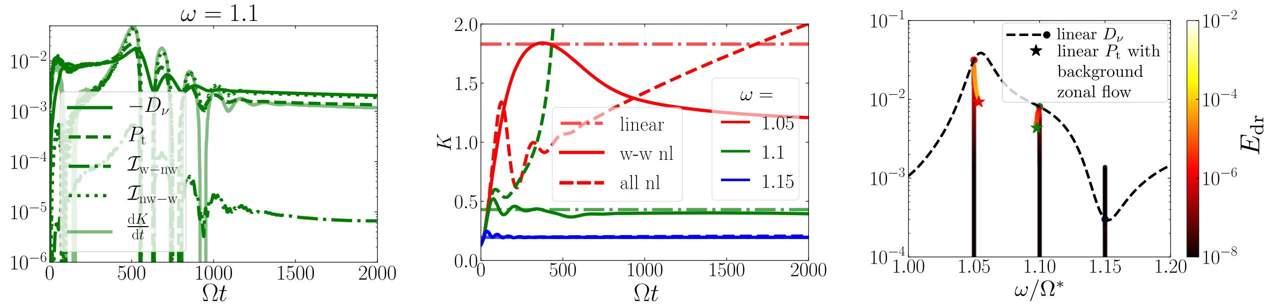

Fig. 1. Left: Terms in the energy balance (Eq. (2.3)) over time. **Middle:** Kinetic energy over time with or without the various nonlinear terms (nl). **Right:** Dissipation spectrum D_ν of wavelike-wavelike nonlinear simulations as a function of tidal forcing frequency in the fluid frame ω/Ω^*, where Ω^* is the modified spin rate due to the creation of zonal flows (see Paper 1 for a definition), also showing the energy in the differential rotation $\mathrm{E_{dr}}$. In the three panels, $C \approx 0.009$.

obtained for certain frequencies in Paper I. By removing the relevant nonlinearities that produce this unphysical behaviour (which should be less important than the ones we retain in reality), we present new results regarding the amplitude and spatial structure of kinetic energy, tidal dissipation, and azimuthal component of the velocity of inertial waves propagating in an adiabatic and incompressible convective shell.

2 Governing equations and energy balance for nonlinear tidal inertial waves

We model the outer convective envelope of our low-mass star or giant gaseous planet as an incompressible and adiabatic spherical shell as a first approach to treat the nonlinear hydrodynamic tidal response. The action of turbulent convection on tides is considered through a viscous term $\nu\Delta\boldsymbol{u}$ (e.g. Duguid et al. 2020, and references therein), where ν is the (constant) effective/turbulent viscosity and $\boldsymbol{u}$ is the total tidal flow. The flow $\boldsymbol{u}$ is decomposed into a large-scale non-wavelike component $\boldsymbol{u}_{\mathrm{nw}}$ (the equilibrium tide in this model) and a wave-like component $\boldsymbol{u}_{\mathrm{w}}$ (the dynamical tide, consisting of inertial waves) such that $\boldsymbol{u} = \boldsymbol{u}_{\mathrm{nw}} + \boldsymbol{u}_{\mathrm{w}}$ as in Ogilvie (2013, building upon earlier ideas reviewed in e.g. Zahn 2008). The equations of motion and continuity for tidally-forced inertial waves in the fluid frame are then:

$$\partial_t \boldsymbol{u}_{\mathrm{w}} + (\boldsymbol{u}\cdot\boldsymbol{\nabla})\boldsymbol{u} + 2\boldsymbol{\Omega}\wedge\boldsymbol{u}_{\mathrm{w}} = -\frac{\boldsymbol{\nabla}p_{\mathrm{w}}}{\rho} + \boldsymbol{f}_{\mathrm{t}} + \nu\Delta\boldsymbol{u}, \tag{2.1}$$

$$\boldsymbol{\nabla}\cdot\boldsymbol{u}_{\mathrm{w}} = 0, \tag{2.2}$$

which are solved together with stress-free and impenetrable boundary conditions on the inner and outer boundaries at radii $r = \alpha R$ and $r = R$, respectively, with α the radial aspect ratio and R the radius of the body. We have introduced $\boldsymbol{\Omega}$, the initial uniform rotation rate along the vertical axis, p_{w}, the reduced wavelike pressure, and ρ, the (uniform) mean fluid density. The effective tidal forcing is $\boldsymbol{f}_{\mathrm{t}} = -2\boldsymbol{\Omega}\wedge\boldsymbol{u}_{\mathrm{nw}}$, which takes into account the remaining action of non-inertial terms (here only the Coriolis acceleration) on the non-wavelike flow, since the equilibrium tide satisfies a quasi-hydrostatic equation of motion. The non-wavelike flow can be written $\boldsymbol{u}_{\mathrm{nw}} = \mathrm{Re}[C\ i\omega\boldsymbol{\nabla}\left[f(r)Y_2^2(\theta,\varphi)\right]\mathrm{e}^{-i\omega t}]$, where C is proportional to the tidal amplitude parameter ϵ (with a factor depending on the internal structure), ω is the tidal forcing frequency, $f(r)$ is a dimensionless radial function required for the scalar potential to satisfy Laplace's equation, and $Y_2^2(\theta,\varphi)$ is the dominant quadrupolar spherical harmonic function for colatitude θ and azimuth φ (Ogilvie 2013). Our approach considers the non-wavelike flow to be an imposed "background flow" to study the instantaneous tidal response (relative to tidal evolutionary timescales), as described in Barker & Astoul (2021). We use units of length and time equal to R and Ω^{-1}, respectively.

Taking the scalar product of Eq. (2.1) with $\rho\boldsymbol{u}_{\mathrm{w}}$ and integrating spatially, we obtain the energy balance for tidal inertial waves:

$$\partial_t\langle K_{\mathrm{w}}\rangle_V = \mathcal{I}_{\mathrm{nw-w}} + \mathcal{I}_{\mathrm{w-nw}} - D_\nu + P_{\mathrm{t}}, \tag{2.3}$$

where $\langle K_{\mathrm{w}}\rangle_V = \langle\rho|\boldsymbol{u}_{\mathrm{w}}|^2/2\rangle_V$ is the wavelike kinetic energy integrated over the volume V, $\mathcal{I}_{\mathrm{i-j}} = -\langle\rho\boldsymbol{u}_{\mathrm{w}}\cdot(\boldsymbol{u}_i\cdot\boldsymbol{\nabla})\boldsymbol{u}_j\rangle_V$, with $i,j\in\{\mathrm{w},\mathrm{nw}\}$, are the terms coming from the mixed (w-nw and nw-w) nonlinearities which transfer energy between the non-wavelike and wavelike flows, D_ν is the viscous dissipation of wavelike flows† and the energy injected into tidal waves by the forcing is $P_{\rm t} = \langle \boldsymbol{u}_{\rm w}\cdot\boldsymbol{f}_{\rm t}\rangle_V$. Note that $\mathcal{I}_{\rm i-i} = -\oint_{\partial V} K_{\rm i}\,\boldsymbol{u}_{\rm w}\cdot\boldsymbol{n}{\rm d}S = 0$ with $\boldsymbol{n}$ the unit normal vector to the bounding surface ∂V, using the divergence theorem along with the incompressible and impenetrable assumptions (which can also be applied to demonstrate that $\langle \boldsymbol{u}_{\rm w}\cdot\nabla p_w\rangle_V = 0$). One can also demonstrate that $\mathcal{I}_{\rm nw-w} = -\oint_{\partial V} K_{\rm w}\;\boldsymbol{u}_{\rm nw}\cdot\boldsymbol{n}{\rm d}S$, which does not necessarily vanish in our idealised spherical model. However, in a more realistic ellipsoidal model, the streamlines of the non-wavelike tidal flow in the bulge frame are expected to be tangential to the boundary so that $\boldsymbol{u}_{\rm nw}\cdot\boldsymbol{n} = 0$, cancelling $\mathcal{I}_{\rm nw-w}$ in that frame (see also Barker & Astoul 2021). The only physical nonlinear term expected to contribute to the energy exchange between inertial waves and the non-wavelike tidal flow is $\mathcal{I}_{\rm w-nw} = -\langle\rho\boldsymbol{u}_{\rm w}\cdot(\boldsymbol{u}_{\rm w}\cdot\boldsymbol{\nabla})\boldsymbol{u}_{\rm nw}\rangle_V$, namely Reynolds stresses involving correlations between wavelike flow components.

3 Analysis of nonlinear simulations

To solve Eqs. (2.1) and (2.2), we use the pseudo-spectral code MagIC‡ (e.g. Christensen et al. 2001) using Chebyshev polynomials in the radial direction and a spherical harmonic decomposition in the azimuthal and latitudinal directions, utilising the SHTns library for fast spherical harmonic transforms (Schaeffer 2013). In these initial simulations, the Ekman number is set to ${\rm Ek} = \nu/(\Omega R^2) = 10^{-5}$, the aspect ratio is $\alpha = 0.5$, and we vary the tidal forcing frequency ω and the tidal amplitude C. Our typical spatial resolution is $N_r = 97$ Chebyshev points in radius and spherical harmonics up to degree $l_{\rm max} = 85$. Further details about the simulations will be presented elsewhere.

In the left panel of Fig. 1, we display each term in the energy balance (Eq. (2.3)) for $C \approx 0.009$ and $\omega = 1.1$. The term $\mathcal{I}_{\rm nw-w}$ represents an unrealistic flux through the boundary which is not negligible compared to the tidal dissipation and tidal power $P_{\rm t}$, unlike the "physical" transfer term $\mathcal{I}_{\rm w-nw}$, which is very small here. This is especially true for low to moderate tidal amplitudes satisfying $C \lesssim 0.05$, but not for higher tidal amplitude (e.g. $C \sim 0.1$) where $\mathcal{I}_{\rm w-nw}$ can contribute more significantly. As a result, we have chosen to switch off nonlinear terms involving non-wavelike tides in the momentum equation, which is justified except for the highest tidal amplitudes considered ($C \lesssim 0.05$). Our choice is also motivated by the fact that the total angular momentum $\boldsymbol{L} = \langle\rho\boldsymbol{r}\wedge\boldsymbol{u}\rangle_V$ can be shown to evolve as:

$$\partial_t\boldsymbol{L} = -\oint_{\partial V}\rho(\boldsymbol{r}\wedge\boldsymbol{u})\boldsymbol{u}_{\rm nw}\cdot\boldsymbol{n}\;{\rm d}S. \tag{3.1}$$

Thus, $\boldsymbol{L}$ is not conserved in this model (as $\boldsymbol{u}_{\rm nw}$ is perfectly maintained) only because of the unphysical non-wavelike flux through the spherical boundaries, which drives the unexpected evolution of the total angular momentum as in Fig. 17 of Paper I.

We find that when all nonlinearities are included, the kinetic energy and tidal dissipation in our simulations are almost identical to those obtained in Paper I (after appropriate rescaling). In the middle panel of Fig. 1, we show that the kinetic energy including all nonlinearities highly departs from the linear prediction for $\omega = 1.05$ and 1.1, with the departure being somewhat less pronounced when considering only the wavelike-wavelike nonlinearity. In both cases this departure from linear predictions may strongly depend on whether wave attractors are produced (i.e. wave focusing along limit cycles) or to the presence of hidden large-scale flows (see Ogilvie 2009; Lin & Ogilvie 2021). When one or both of these features are present the linear dissipation is enhanced, as we can see in the right panel of Fig. 1. At the beginning of these simulations, kinetic energy and dissipation converge towards their linear values, and then evolve away for $\omega = 1.05$ and 1.1 due to the establishment of strong zonal flows indicated by the energy in the differential rotation (colorbar, see Paper 1 and Tilgner 2007, for a definition). Since the total angular momentum is conserved here (as $\boldsymbol{u}_{\rm nw}$ is perfectly maintained), a steady state is reached at the end of the simulation ($\max(\Omega t) = 5000$). The inhomogeneous deposition of kinetic energy (and angular momentum) near the rotation axis triggers cylindrical differential rotation from the pole to the equator as shown in Fig. 2 for the case with $\omega = 1.1$. The final dissipation of wavelike-wavelike nonlinear simulations can be neatly recovered by running new linear simulations with a background cylindrical differential rotation, using the zonal flows extracted from the associated nonlinear simulation (right panel of Fig. 1 using the flow shown in e.g. Fig. 2). We have therefore demonstrated that the effects of zonal flows on tidal waves

†The dissipation of the non-wavelike flow has been found to be negligible in our simulations since ν is small, as is also typically expected in reality.

‡`https://magic-sph.github.io/`

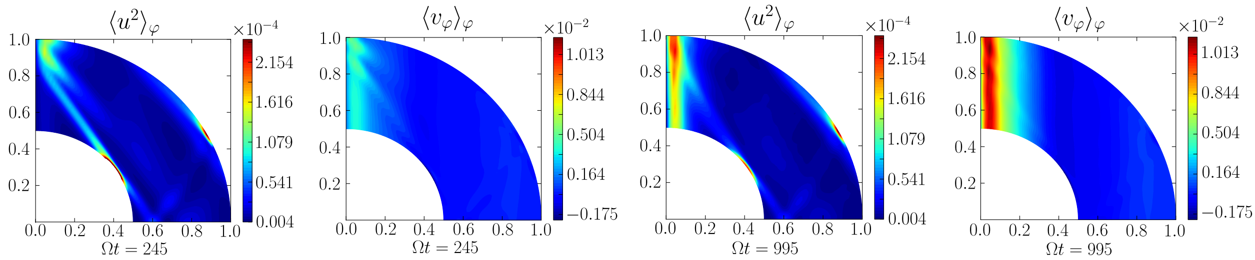

Fig. 2. Azimuthal average of the kinetic energy u^2 and azimuthal velocity v_φ at times $\Omega t = 245$ and $\Omega t = 995$ in one quarter of the meridional plane (due to equatorial and axial symmetry) for $\omega = 1.1$ and $C = 0.009$.

explains the departure of tidal dissipation rates in these simulations from linear theoretical predictions assuming uniform rotation.

4 Conclusions

We have performed new nonlinear hydrodynamical simulations of tidally-forced inertial waves in an incompressible and adiabatic convective shell. Our approach is different from that in Paper 1 by the use of (a more realistic) effective tidal body force to excite inertial waves, along with stress-free and impenetrable boundary conditions. Within this framework, we analysed in detail the energy transfer terms between wavelike and non-wavelike tidal flows, and demonstrated that an "unphysical" energy flux through the spherical boundaries was responsible for the unrealistic angular momentum evolution obtained in certain cases in Paper 1. We have removed the mixed wavelike-non-wavelike nonlinearities responsible, which can be further justified by scaling arguments (since wave-wave nonlinearities are predicted to dominate for short wavelength inertial waves). Differential rotation in the form of zonal flows is triggered inside the shell due to wavelike-wavelike nonlinearities and there are important departures from linear predictions as observed in Paper 1, though the differences here are less pronounced in the cases we have presented. Finally, we have also demonstrated that the departure of the nonlinear tidal dissipation from the linear prediction is explained by the zonal flows that are generated.

This research has been supported by STFC grants ST/R00059X/1 and ST/S000275/1. Simulations were undertaken using the MagIC software on ARC4 and DiRAC, part of the High Performance Computing facilities at the University of Leeds and Leicester.

References

Astoul, A., Park, J., Mathis, S., Baruteau, C., & Gallet, F. 2021, A&A, 647, A144
Barker, A. J. 2020, MNRAS, 498, 2270
Barker, A. J. & Astoul, A. A. V. 2021, MNRAS, 506, L69
Barker, A. J., Braviner, H. J., & Ogilvie, G. I. 2016, MNRAS, 459, 924
Bolmont, E. & Mathis, S. 2016, Celestial Mechanics and Dynamical Astronomy, 126, 275
Christensen, U. R., Aubert, J., Cardin, P., et al. 2001, Physics of the Earth and Planetary Interiors, 128, 25
Duguid, C. D., Barker, A. J., & Jones, C. A. 2020, MNRAS, 497, 3400
Favier, B., Barker, A. J., Baruteau, C., & Ogilvie, G. I. 2014, MNRAS, 439, 845
Lainey, V., Casajus, L. G., Fuller, J., et al. 2020, Nature Astronomy, 4, 1053
Lin, Y. & Ogilvie, G. I. 2021, arXiv e-prints, arXiv:2108.08515
Mathis, S. 2015, A&A, 580, L3
Mathis, S. 2019, in EAS Publications Series, Vol. 82, EAS Publications Series, 5–33
Ogilvie, G. I. 2009, MNRAS, 396, 794
Ogilvie, G. I. 2013, MNRAS, 429, 613
Ogilvie, G. I. 2014, ARA&A, 52, 171
Rieutord, M., Georgeot, B., & Valdettaro, L. 2001, Journal of Fluid Mechanics, 435, 103
Schaeffer, N. 2013, Geochemistry, Geophysics, Geosystems, 14, 751
Tilgner, A. 2007, Phys. Rev. Lett., 99, 194501
Zahn, J. P. 2008, in EAS Publications Series, Vol. 29, EAS Publications Series, ed. M. J. Goupil & J. P. Zahn, 67–90

SF2A 2021
A. Siebert, K. Baillié, E. Lagadec, N. Lagarde, J. Malzac, J.-B. Marquette, M. N'Diaye, J. Richard, O. Venot (eds)

GAS AND DUST EMISSION OF A PROTOPLANETARY DISC WITH AN ECCENTRIC JUPITER INSIDE A CAVITY

C. Baruteau[1], G. Wafflard-Fernandez[2], R. Le Gal[1], F. Debras[1], A. Carmona[2], A. Fuente[3] and P. Rivière-Marichalar[3]

Abstract. This conference proceeding summarises the results of our recently published work, where we investigated the observational signatures of a warm Jupiter that becomes eccentric after migrating into a low-density gas cavity in its protoplanetary disc. In this scenario, the wakes of the eccentric planet, and the fact that the gas in the cavity becomes eccentric, cause the formation of large-scale asymmetries in CO (3-2) integrated intensity maps as well as distortions of iso-velocity contours in CO (3-2) velocity maps inside the cavity. Both features are found to be detectable for an angular resolution and a sensitivity comparable to those achieved in ALMA disc gas observations. With too little dust left inside the cavity, the near-infrared polarized intensity and the sub-millimetre continuum emission mostly arise from outside the cavity and show no significant differences when the planet is eccentric or still circular inside the cavity.

Keywords: planetary systems: protoplanetary discs, planet-disc interactions, planets and satellites: formation, hydrodynamics, radiative transfer.

1 How did most warm Jupiters become eccentric?

The starting point of this work is the possible origins for the eccentricity of the warm Jupiters. These are the planets spotted by the red ellipse in the diagram shown in Fig. 1. They have a mass comparable to that of Jupiter, an orbital period longer than 100 days, and feature a substantial median eccentricity of approximately 0.25. A natural question is how most warm Jupiters acquired such level of eccentricity. In Debras et al. (2021), we have recently revisited the possibility that a massive planet could become eccentric during its early orbital evolution in its protoplanetary disc. We have found that the presence of a low-density gas cavity in the disc, carved for instance by stellar photoevaporation or disc magnetized winds, can grow the eccentricity of Jupiter-mass planets that migrated into the cavity to values as high as 0.3–0.4. Other mechanisms can grow the eccentricity of massive planets before or after the dissipation of the protoplanetary disc, and we refer the reader to the introductions of Debras et al. (2021) and Baruteau et al. (2021).

Cavities are often observed in protoplanetary discs. More frequently in the dust emission (such discs are commonly referred to as transition discs), but also in the gas emission (e.g., Carmona et al. 2017; Rivière-Marichalar et al. 2020). This suggests that the presence of a gas cavity could constitute a generic scenario to grow the eccentricity of massive planets (Debras et al. 2021). From the idea that warm eccentric Jupiters could indeed arise because of the presence of a gas cavity in their parent disc, we have investigated in Baruteau et al. (2021) what observational signatures such planets would entail in the gas and dust emission of their disc. The results of this work are briefly described below.

2 An eccentric warm Jupiter in a disc cavity

We carried out two-dimensional (2D) gas and dust hydrodynamical simulations modelling the interaction between a 2 Jupiter mass planet, its protoplanetary disc, and a 2 Solar mass star. The disc features a ∼30 au wide

[1] IRAP, Université de Toulouse, CNRS, UPS, Toulouse, France
[2] IPAG, Université Grenoble Alpes, CNRS, Grenoble, France
[3] Observatorio Astronómico Nacional, Madrid, Spain

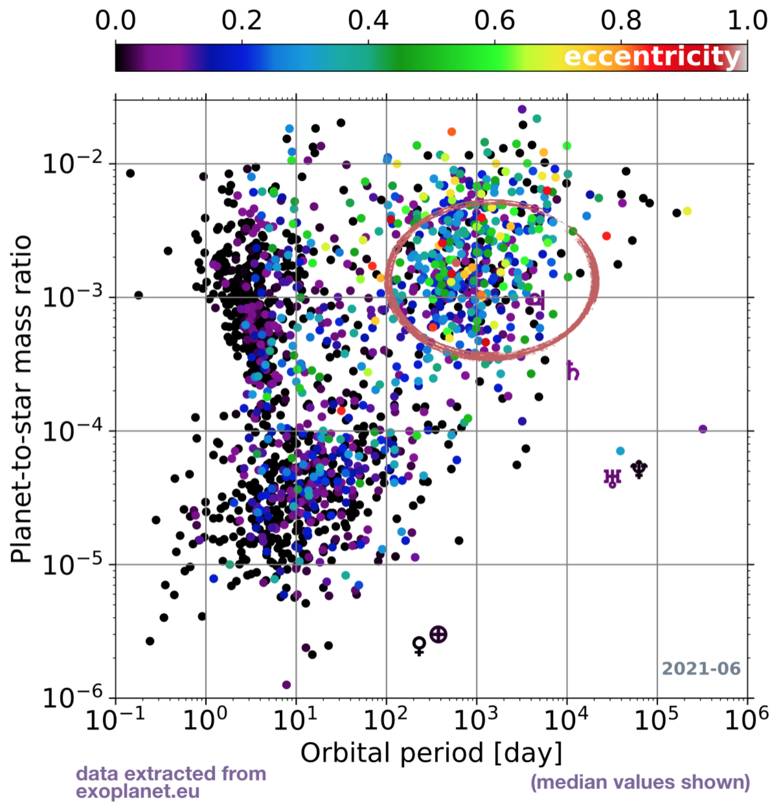

Fig. 1. Eccentricity of the exoplanets and the planets in the Solar System, as a function of planet-to-star mass ratio and orbital period (diagram updated from Debras et al. 2021). The red ellipse shows the group of planets commonly referred to as warm Jupiters.

cavity wherein the decrease in the gas surface density is maintained by a jump in the disc turbulent viscosity. All details about the physical model and numerical set-up can be found in Section 2 of Baruteau et al. (2021).

The planet starts its orbital journey slightly outside the cavity and progressively migrates into it. When the planet has drifted sufficiently far from the outer edge of the cavity, its eccentricity grows due to the dominance of the eccentric resonances of the disc-planet interaction. In our model, the planet reaches in about 4 Myr a near steady state eccentricity of approximately 0.25, which is close to the median eccentricity of the warm Jupiters. The top-left panel in Fig. 2 displays the gas surface density on a logarithmic scale when the planet has reached a near maximum eccentricity and is close to the apocentre of its orbit. We see that the gas density around the planet orbit displays strong asymmetries due to the shocks induced by the planet wakes (here, the gas density is about ten time smaller behind the planet along its orbit than in front of it). Asymmetries with a similar contrast in the gas density are obtained whether the planet is close to its apocentre, like in the figure, or at a different orbital phase of the planet.

To examine what implications our eccentric planet has on the gas and dust emission of its disc, we post-processed the results of the hydrodynamical simulations with gas or dust radiative transfer calculations. The disc is assumed to be located at 100 pc and to have a 30° inclination relative to the sky-plane (for further details about the radiative transfer calculations, like the inclusion of photodissociation by UV irradiation for the gas calculations, the reader is referred again to Baruteau et al. 2021).

First, for the gas we looked at the J=3→2 rotational line emission for several CO isotopologues in the sub-millimetre, and in the bottom row of panels in Fig. 2 we show results for ^{12}CO at the same time as the gas surface density in the top-left panel. The bottom-left image is obtained by adding white noise with a standard deviation of 1 mJy/beam in each simulated channel map, by collapsing the synthetic datacube along the spectral axis, and further convolving with a circular beam of full-width at half-maximum set to 0.″05. Both this noise level and angular resolution are comparable to those currently achieved in ALMA disc gas observations. The bottom-left image shows that the strong asymmetry caused by the planet eccentricity in the disc cavity manifests itself as

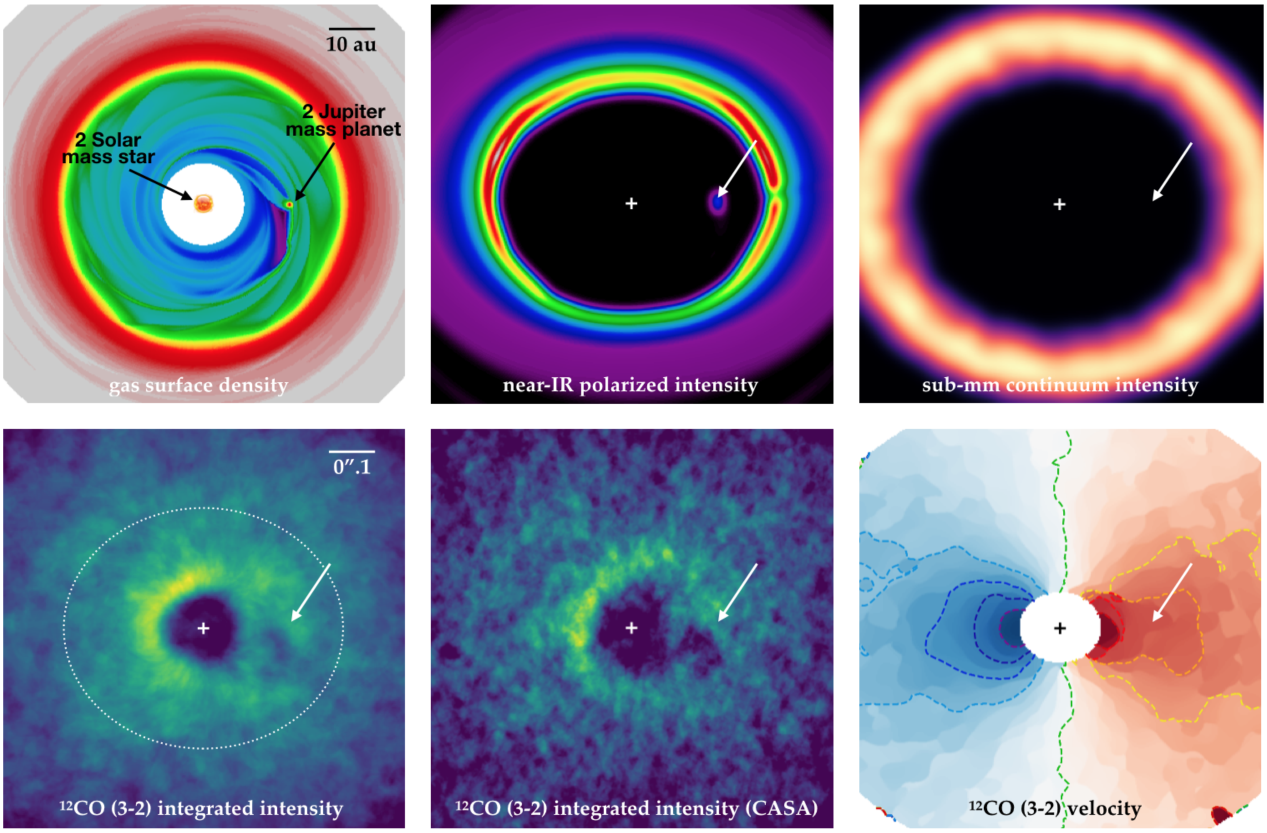

Fig. 2. Summary plot of the results presented in Baruteau et al. (2021). A 2 Jupiter mass planet reaches an eccentricity of about 0.25 after migrating into a ∼30 au wide gas cavity in its protoplanetary disc. Inside the cavity the gas becomes eccentric as well, and the planet gap is no longer annular but features a strongly asymmetric gas surface density (top-left panel). This has two main consequences: (i) the formation of a large-scale asymmetry in the ^{12}CO J=3→2 integrated intensity inside the cavity (bottom-left and bottom-middle panels), and (ii) the distortion of the iso-velocity contours inside the cavity in the ^{12}CO J=3→2 velocity map (bottom-right panel). However, the dust remains mostly outside the cavity on near-circular trajectories, and the dust emission thus shows no significant differences whether the planet is eccentric or still circular inside the cavity. This is illustrated with the polarized intensity at 1.04 μm (top-middle panel) and the dust continuum emission at 0.9 mm (top-right panel). See text for more details about the images. The white arrow spots the planet position in each synthetic image of the disc emission. All panels except the bottom-middle one are adapted from Baruteau et al. (2021).

a large-scale asymmetry in the ^{12}CO J=3→2 integrated intensity, and that this asymmetry could be detected by ALMA.

To strengthen this point, we post-processed the raw output of our gas radiative transfer calculation (synthetic datacube without added noise and beam convolution) with CASA `simalma`, assuming a 5h integration in the `alma.out21.cfg` array configuration, and a precipitable water vapour level of 0.7 mm. This leads to a $0\farcs055 \times 0\farcs043$ beam and a rms noise level (σ) of approximately 1.9 mJy/beam per channel map. Further 2σ clipping was applied to the synthetic data to obtain the final integrated intensity map displayed in the bottom-middle panel in Fig. 2. The image agrees well, overall, with the one obtained with simple white noise. This not only shows that our simple noise model is adequate to produce synthetic emission maps, but it also confirms that the large-scale asymmetry in the ^{12}CO J=3→2 integrated intensity is a feature detectable by ALMA, which could possibly spot the presence of an eccentric Jupiter inside a disc cavity.

The eccentricity of the gas inside the cavity also affects the morphology of the velocity map obtained from the synthetic gas emission. The bottom-right panel in Fig. 2 displays the velocity map for the ^{12}CO J=3→2 line emission at the same time as the other panels in the figure, and the dashed curves show a few iso-velocity contours. The contour levels are chosen symmetrical with respect to the zero line-of-sight velocity, shown in green. Despite the noise, an asymmetry can be clearly seen between contours of positive and negative line-of-sight velocities inside the cavity, which comes about because of the eccentricity of the gas in the cavity. This distortion of the iso-velocity contours constitutes another indirect, detectable signature of the presence of an eccentric Jupiter in a disc cavity.

Our hydrodynamical simulations calculated the orbital evolution of dust particles between 10 μm and 1 cm in size, which are found to quickly escape the disc cavity. Efficient radial drift due to a combination of gas drag and dust turbulent diffusion brings most of these particles near the outer edge of the cavity, which corresponds to a location where the gas pressure has a radial maximum. Around this location, both gas and dust have near-circular orbits, being too distant from the eccentric planet and gas inside the cavity. Consequently, the dust continuum emission in the sub-millimetre basically takes the form of an axisymmetric ring of emission around the edge of the cavity, as shown by the top-right panel of Fig. 2.

For computational reasons, we did not simulate the orbital evolution of dust with a size smaller than 10 μm. The near-infrared polarized intensity image in the top-middle panel in Fig. 2 is actually obtained by assuming that small (sub-micron) dust has the same spatial distribution as the gas *if* the Stokes number remains smaller than a threshold value of 10^{-4} (otherwise, the local dust density is set to 0). This condition is for the dust to be effectively well coupled to the gas: the low gas density inside the cavity implies indeed than even small, micron-sized dust particles have a Stokes number than can reach a few percent, which causes substantial radial drift due to gas drag and turbulent diffusion. With too little small dust expected inside the cavity, the polarized intensity signal mostly arises from outside the cavity, with the notable exception of the circumplanetary environment (spotted by the white arrow in the panel). Both the near-infrared polarized intensity and the sub-millimetre continuum emission show no significant differences whether the planet is eccentric or still circular inside the cavity.

3 Perspectives

In a nutshell, we have shown that the presence of an eccentric planet in a gas cavity could potentially be detected through a large-scale asymmetry in the CO emission inside the cavity. Other aspects of this work that could not fit in this proceeding, like for instance the fact that the optically thick CO emission outside the cavity takes the form of a four-lobed pattern of emission when the disc inclination is larger than about 30°, will be found in Baruteau et al. (2021).

We are currently working on extending this work in several ways. One is by simulating the same physical model in 2D with the multi-fluid hydrodynamical code `Fargo3D`, which has allowed us to include several dust fluids that model the evolution of small, (sub-)micron dust. Dust radiative transfer calculations using the dust density of these several dust fluids as input confirm that the near-infrared polarized intensity displays very little signal inside the cavity, as shown above. Another extension of this work is to simulate the same physical model in 3D. For now, we have been able to perform only one 3D gas-only simulation. It shows eccentricity growth for the planet in quite a similar way as in our 2D simulations, and, interestingly, we also observe the growth of the planet inclination. It will be interesting to investigate how large the inclination of a massive planet could grow as a result of disc-planet interactions in a gas cavity. Another interesting avenue for future work would be to test the predictions of our study to specific protoplanetary discs.

We thank the council members of the French Astronomical Society for keeping our annual meeting organized virtually.

References

Baruteau, C., Wafflard-Fernandez, G., Le Gal, R., et al. 2021, MNRAS, 505, 359

Carmona, A., Thi, W. F., Kamp, I., et al. 2017, A&A, 598, A118

Debras, F., Baruteau, C., & Donati, J.-F. 2021, MNRAS, 500, 1621

Rivière-Marichalar, P., Fuente, A., Le Gal, R., et al. 2020, A&A, 642, A32

SF2A 2021
A. Siebert, K. Baillié, E. Lagadec, N. Lagarde, J. Malzac, J.-B. Marquette, M. N'Diaye, J. Richard, O. Venot (eds)

LITHIUM ABUNDANCE DISPERSION IN METAL-POOR STARS

M. Deal[1], O. Richard[2] and S. Vauclair[3, 4]

Abstract. The formation and evolution of light elements in the Universe act as important cosmological constraints. The oldest stars of the Galaxy have long been assumed to display in their outer layers the primordial lithium abundance, although all studies of stellar physics proved that this abundance must have decreased with time. The primordial Li abundance deduced from the observations of the Cosmological Background is indeed larger than the maximum one observed in these stars. Recent observations gave evidence of a large Li abundance dispersion in very metal poor stars.

We address the general question of the lithium abundance dispersion obtained from observations of metal-poor stars, and more specifically of Carbon Enhanced Metal Poor stars rich in s-process elements (CEMP-s), and how the interplay of atomic diffusion and accretion of matter modifies the element abundances in these metal-poor stars. In particular, we focus on the hydrodynamic processes that could take place after accretion. We consider initial metallicities from [Fe/H]=−2.31 dex down to [Fe/H]=−5.45 dex.

We show that the observations of lithium dispersion, associated with carbon enrichment, are well accounted for in terms of accretion onto the metal-poor stars, with accreted masses smaller than a few Jupiter masses, when using a lithium initial abundance in accordance with the primordial lithium abundance obtained from latest Big Bang Nucleosynthesis results.

Keywords: stars: Population II, stars: abundances, accretion, diffusion, instabilities

1 Introduction

The observations of light elements in the Universe act as important cosmological constraints. For this purpose, their evolution over time must be precisely reconstructed through modelling. Among these elements, lithium plays a special role as it was the subject of numerous observations, in particular in the oldest stars of the Galaxy. For a long time the lithium surface abundances obtained for these old stars was assumed by some to be the primordial lithium abundance. The main argument for this assumption was the absence of dispersion on lithium abundances in the so-called "lithium plateau" stars (Spite & Spite 1982), which seemed incompatible with stellar lithium depletion. More recently, the evidence of a large lithium dispersion in the extremely metal-poor stars modified the landscape (Bonifacio et al. 2007; Cayrel et al. 2008; Sbordone et al. 2010). On the other hand, the primordial lithium abundance determined through Cosmological Microwave Background observations is 3 to 4 times larger than the present lithium surface abundances obtained in metal poor stars of the lithium plateau (Cyburt et al. 2016; Coc & Vangioni 2017) and led to the "lithium problem". However this gap between the primordial lithium and the lithium surface abundances of these old stars of the lithium plateau is expected if considering transport processes inside the stars and is qualitatively consistent with stellar modelling, as the surface lithium abundances decrease over time as shown since several decades (e.g. Michaud et al. 1984; Vauclair 1988; Proffitt & Michaud 1991; Vauclair & Charbonnel 1995; Richard et al. 2005; Vick et al. 2013). Recently, Deal & Martins (2021) showed that taking into account atomic diffusion, rotation-induced mixing, and penetrative convection in stellar models contributes to reconcile Big Bang Nucleosynthesis (hereafter BBN) primordial lithium with that of the plateau.

[1] Instituto de Astrofísica e Ciências do Espaço, Universidade do Porto, CAUP, Rua das Estrelas, PT4150-762 Porto, Portugal
[2] Laboratoire Univers et Particules de Montpellier, Université de Montpellier, CNRS, Place Eugène Bataillon, 34095 Montpellier, France
[3] Université de Toulouse; UPS-OMP; IRAP; Toulouse, France
[4] CNRS; IRAP; 14 av. Edouard Belin, F-31400 Toulouse, France

All these observations, from the lithium plateau to the extremely metal-poor stars, have to be reconciled, by deep studying of the possible lithium abundance evolution inside these stars. As a first step, we focused our study on the case of Carbon Enhanced Metal Poor stars rich in s-process elements (here after CEMP-s), for which many data are available. These stars are characterised by [Fe/H]$<$ 2 dex and [C/Fe]$>0.7-1$ dex (Beers & Christlieb 2005; Aoki et al. 2007). The abundance variations observed in these stars are generally explained in terms of accretion of the wind of stellar companions, especially Asymptotic Giant Branch stars (McClure & Woodsworth 1990; Stancliffe et al. 2007; Jorissen et al. 2016), taking into account the stellar structure and the thermohaline convection that take place after accretion. Thermohaline convection occurs when the thermal gradient is stable and the mean molecular weight gradient unstable. When a blob of matter falls towards the centre of the star, the heat gets in more quickly than the particles get out, and the blob keeps on sinking. This effect generates a mixing of chemicals in that region. Such an instability may occur in stars whenever heavy elements accumulation occurs on top of lighter ones. This is the case, for example, during the main-sequence phase after episodes of accretion (Vauclair 2004; Stancliffe et al. 2007; Théado et al. 2010; Garaud 2011; Deal et al. 2013, 2015; Wachlin et al. 2017, and reference therein).

Previous studies of such accretion scenarios from an AGB companion onto a main-sequence star showed their potentiality in explaining the formation of CEMP-s stars. They reproduce relatively well the surface abundances of these stars from the main sequence up to the red giant phase (Stancliffe et al. 2007; Stancliffe & Glebbeek 2008; Stancliffe 2009; Matrozis & Stancliffe 2016, 2017). However, the question of the lithium dispersion was not addressed, neither the effect of metallicity. These simulations were only done for $[\mathrm{Fe/H}]_{\mathrm{ini}} = -2.31$ dex. We extended our own study down to $[\mathrm{Fe/H}]_{\mathrm{ini}} = -5.45$ dex. We also considered a range of smaller accreted masses, which was not explored before, and we used more precise and up-to-date prescriptions for atomic diffusion and thermohaline convection. We focused our study on how such accretion processes modify the surface Li abundances. We took into account the stellar parameters of the primary star, the parameters of the AGB companion, the wind composition, the atomic diffusion and hydrodynamic processes that have important consequences on the final results. The full study is available in Deal et al. (2021).

2 Method

In order to explain the lithium dispersion also seen in CEMP-s star, we computed stellar models with the Montréal/Montpellier stellar evolution code (Turcotte et al. 1998; Richard et al. 2001), considering initial [Fe/H] between -2.31 and -5.45 dex and masses of 0.7, 0.75 and 0.78 $\mathrm{M}_{\odot}$. Atomic diffusion was taken into account, including radiative accelerations using the formalism of Burgers (1969). We included a parametrised turbulent diffusion coefficient calibrated to reproduce the Li plateau as described in Richard et al. (2005). We included the effect of thermohaline convection from recent 3D simulations (Brown et al. 2013). We considered accreted masses between 0.0038 and 4 $M_{♃}$ from AGB winds of 1, 2 and 3 $M_{\odot}$ companions (leading to accretion age of 5.83 Gyr, 0.748 Gyr and 0.27 Gyr, respectively). The chemical compositions and accretion ages of the AGB winds are taken from Stancliffe & Glebbeek (2008) and Campbell & Lattanzio (2008).

3 Lithium abundances in CEMP-s stars: comparison between models and observations

The lithium dispersion in CEMP-s is shown in Fig. 1 (grey squares) and goes from the plateau value (A(Li)=2.2 ± 0.2 dex) down to at least 1 dex. One must notice that about half of the observed lithium abundances are in fact upper limits, so that the real lithium abundance may still be smaller. In addition we have plotted the lithium surface abundance predicted by models of CEMP-s stars, for AGB companions of 2 and 3 $\mathrm{M}_{\odot}$ (see Deal et al. 2021 for the 1 $\mathrm{M}_{\odot}$ case). We see that our models correctly reproduce the lithium dispersion for accreted masses between 0.4 and 4 $M_{♃}$ (see middle and right panels of Fig. 1), both in terms of T_{eff} and surface [Fe/H]. We also show that the mass of the AGB companion, hence the chemical composition of the wind, has a strong impact on the accreted mass needed to induce a lithium depletion. We also show that the lithium dispersion occurs only when the proto-CEMP-s becomes a CEMP-s (i.e. [C/Fe]$>$ 0.7), as shown on the left panels of Fig. 1. This means that the scenarios that explain the lithium dispersion in CEMP-s stars can be different from the one(s) explaining C-normal metal poor stars.

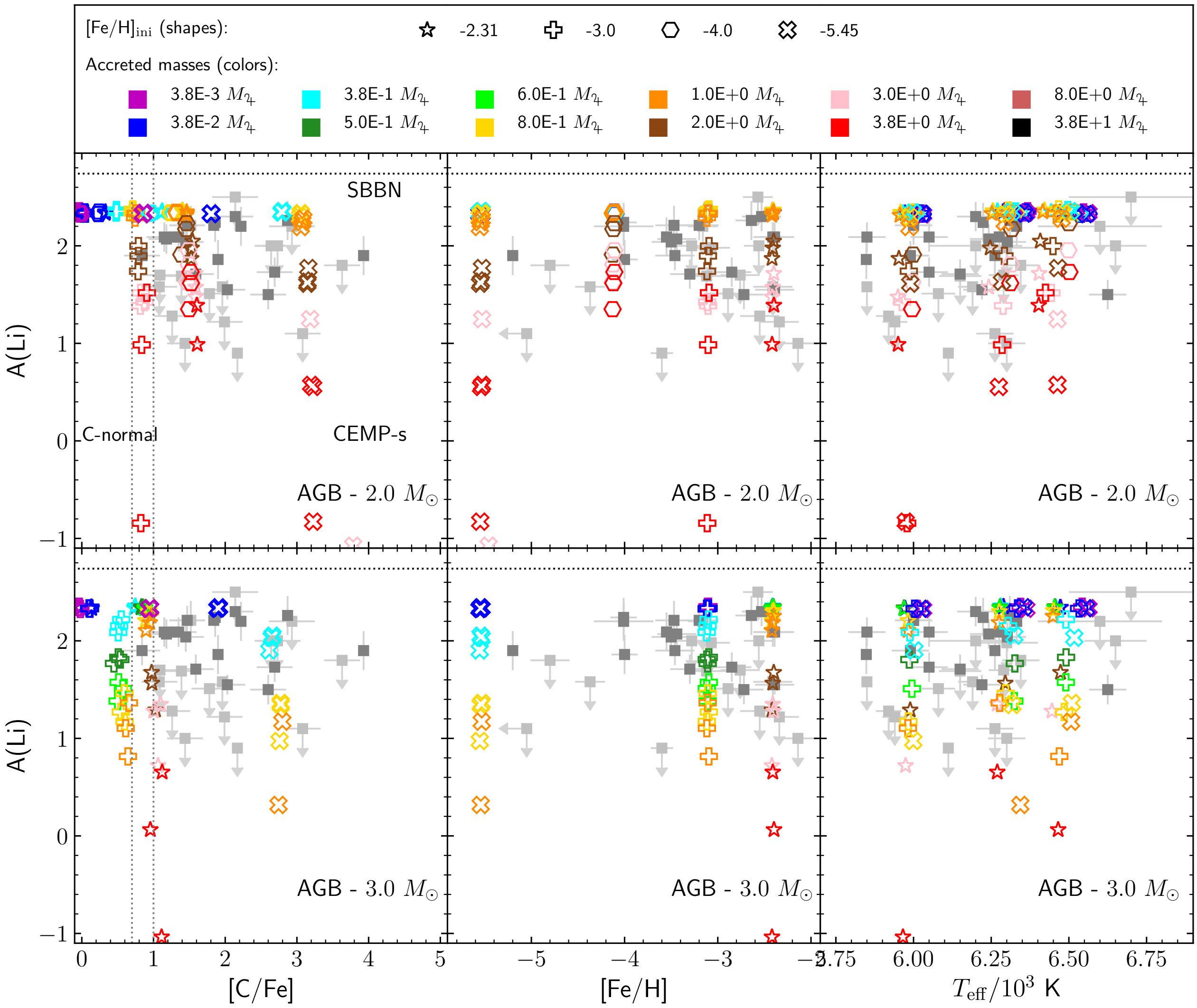

Fig. 1. Lithium surface abundances obtained in our models at the age of 12.5 Gyr. The various metallicities of the models are represented by the shapes of the open symbols and the accreted masses by their various colours. Each model includes an accretion episode of AGB wind at a specific age depending on the AGB mass (270 and 748 Myr for AGB stars of 3 and 2 $M_\odot$, respectively). The left column presents the Li results according to [C/Fe]. The vertical dotted lines correspond to [C/Fe]=0.7 and 1.0. The horizontal dotted lines are the BBN lithium abundance that has been used as the initial abundance in our computations. In the middle column, the lithium surface abundances are displayed as a function of [Fe/H] obtained in the same models at the same age. In the right column, the lithium surface abundances are displayed as a function of T_{eff}. The grey squares represent the observations, light-grey squares are upper limits. The observations are from the SAGA data base (`http://sagadatabase.jp/`: Suda et al. 2008, 2011, 2017; Yamada et al. 2013, and Matsuno et al. 2017).

4 Conclusions

We show that the observations of the lithium abundance dispersion in CEMP-s stars are well accounted for in terms of accretion of the winds of AGB companions. The needed accreted masses are smaller than those considered in previous studies. The initial lithium abundance value that we used in the models is in accordance with the primordial one, determined by cosmological observations. This also shows that the lithium dispersion observed in metal poor stars is linked to stellar interior processes, and that the so-called lithium problem is no more a problem when realistic treatments of the transport processes of chemical elements are taken into account in stellar models.

This work was supported by FCT/MCTES through the research grants UIDB/04434/2020, UIDP/04434/2020 and PTDC/FIS-AST/30389/2017, and by FEDER - Fundo Europeu de Desenvolvimento Regional through COMPETE2020 - Programa Operacional Competitividade e Internacionalização (grant: POCI-01-0145-FEDER-030389). MD is supported by national funds through FCT in the form of a work contract. We acknowledge financial support from the "Programme National de Physique Stellaire" (PNPS) of the CNRS/INSU co-funded by the CEA and the CNES, France.

References

Aoki, W., Beers, T. C., Christlieb, N., et al. 2007, ApJ, 655, 492
Beers, T. C. & Christlieb, N. 2005, ARA&A, 43, 531
Bonifacio, P., Molaro, P., Sivarani, T., et al. 2007, A&A, 462, 851
Brown, J. M., Garaud, P., & Stellmach, S. 2013, ApJ, 768, 34
Burgers, J. M. 1969, Flow Equations for Composite Gases
Campbell, S. W. & Lattanzio, J. C. 2008, A&A, 490, 769
Cayrel, R., Steffen, M., Bonifacio, P., Ludwig, H. G., & Caffau, E. 2008, in Nuclei in the Cosmos (NIC X), E2
Coc, A. & Vangioni, E. 2017, International Journal of Modern Physics E, 26, 1741002
Cyburt, R. H., Fields, B. D., Olive, K. A., & Yeh, T.-H. 2016, Reviews of Modern Physics, 88, 015004
Deal, M., Deheuvels, S., Vauclair, G., Vauclair, S., & Wachlin, F. C. 2013, A&A, 557, L12
Deal, M. & Martins, C. J. A. P. 2021, arXiv e-prints, arXiv:2106.13989
Deal, M., Richard, O., & Vauclair, S. 2015, A&A, 584, A105
Deal, M., Richard, O., & Vauclair, S. 2021, A&A, 646, A160
Garaud, P. 2011, ApJ, 728, L30
Jorissen, A., Van Eck, S., Van Winckel, H., et al. 2016, A&A, 586, A158
Matrozis, E. & Stancliffe, R. J. 2016, A&A, 592, A29
Matrozis, E. & Stancliffe, R. J. 2017, A&A, 606, A55
Matsuno, T., Aoki, W., Suda, T., & Li, H. 2017, PASJ, 69, 24
McClure, R. D. & Woodsworth, A. W. 1990, ApJ, 352, 709
Michaud, G., Fontaine, G., & Beaudet, G. 1984, ApJ, 282, 206
Proffitt, C. R. & Michaud, G. 1991, ApJ, 371, 584
Richard, O., Michaud, G., & Richer, J. 2001, ApJ, 558, 377
Richard, O., Michaud, G., & Richer, J. 2005, ApJ, 619, 538
Sbordone, L., Bonifacio, P., Caffau, E., et al. 2010, A&A, 522, A26
Spite, F. & Spite, M. 1982, A&A, 115, 357
Stancliffe, R. J. 2009, MNRAS, 394, 1051
Stancliffe, R. J. & Glebbeek, E. 2008, MNRAS, 389, 1828
Stancliffe, R. J., Glebbeek, E., Izzard, R. G., & Pols, O. R. 2007, A&A, 464, L57
Suda, T., Hidaka, J., Aoki, W., et al. 2017, PASJ, 69, 76
Suda, T., Katsuta, Y., Yamada, S., et al. 2008, PASJ, 60, 1159
Suda, T., Yamada, S., Katsuta, Y., et al. 2011, MNRAS, 412, 843
Théado, S., Bohuon, E., & Vauclair, S. 2010, in IAU Symposium, Vol. 268, Light Elements in the Universe, ed. C. Charbonnel, M. Tosi, F. Primas, & C. Chiappini, 427–428
Turcotte, S., Richer, J., Michaud, G., Iglesias, C. A., & Rogers, F. J. 1998, ApJ, 504, 539
Vauclair, S. 1988, ApJ, 335, 971
Vauclair, S. 2004, ApJ, 605, 874
Vauclair, S. & Charbonnel, C. 1995, A&A, 295, 715
Vick, M., Michaud, G., Richer, J., & Richard, O. 2013, A&A, 552, A131
Wachlin, F. C., Vauclair, G., Vauclair, S., & Althaus, L. G. 2017, A&A, 601, A13
Yamada, S., Suda, T., Komiya, Y., Aoki, W., & Fujimoto, M. Y. 2013, MNRAS, 436, 1362

SF2A 2021
A. Siebert, K. Baillié, E. Lagadec, N. Lagarde, J. Malzac, J.-B. Marquette, M. N'Diaye, J. Richard, O. Venot (eds)

OBSERVATIONAL APPEARANCE OF CIRCUMBINARY DISCS

K. Hirsh[1] and J.-F. Gonzalez[1]

Abstract. Binary companions are known to open large cavities in their circumbinary discs. Resolving a binary companion, however, remains a difficult observational problem and there exists a number of discs with observed cavities and as yet no resolved binary. An indirect detection method is therefore needed to infer the presence of a binary companion in these systems. As such we investigate the effect of a binary companion on the circumbinary disc in an attempt to find some signatures detectable in observations. We perform radiative transfer calculations on a suite of SPH simulations to create synthetic observations. We investigate the signal in the moment 1 and CO channel maps and develop a metric which aids in the inference of an otherwise undetected binary companion.

Keywords: accretion discs - binaries - radiative transfer - methods: numerical

1 Introduction

In Hirsh et al. (2020) we simulated a suite of circumbinary discs using the Smoothed Particle Hydrodynamics code `PHANTOM` (Price et al. 2018) in order to investigate the effects of the binary and disc properties on the cavity size. The reverse problem of inferring the presence of a binary companion from observations of a cavity also remains an open question, since there exists many systems displaying large cavities with no detected binary as yet (e.g: van der Marel et al. 2016; Canovas et al. 2018; Ubeira Gabellini et al. 2019). To this end we use the radiative transfer code `MCFOST` (Pinte et al. 2006, 2009) to compute synthetic moment 1 maps, as well as synthetic channel maps, of the simulated discs in Hirsh et al. (2020). We then examine these synthetic images to better understand how the presence a binary companion can be inferred from observations and we develop a metric to quantify the effect the binary has on the disc.

2 Definition of Asymmetry Metric

We define an metric to quantify the asymmetry in the disc. This is done by measuring the asymmetry in two opposite velocity CO channels by flipping the positive channel across the y-axis and subtracting from the negative channel (note that the choice of which branch to flip is arbitrary). The resulting images are show in Figure 1). We then define the asymmetry in the channel as the L2 norm of the flux in the subtracted image, normalised to the integrated flux in the positive channel. This is given by:

$$\aleph_c = \frac{\sqrt{\sum_{i,j} \Delta F_{ij}^2}}{F}, \tag{2.1}$$

where $\aleph_c$ is the asymmetry in channel c, ΔF_{ij} is the flux on pixel (i, j) in the subtracted image and F is the integrated flux. Normalising to the integrated flux gives a non-dimensional $\aleph_c$ that is insensitive to field of view and signal strength.

Figure 2 gives $\aleph_c$ for a disc with binary mass ratio $q = 0.1$, aspect ratio $H/R_{\rm in} = 0.05$, coplanar disc ($i = 0°$), and a number of binary eccentricities are shown. A local maximum is seen near the 0 velocity channel and have an increasing $\aleph_c$ at high velocity channels. Since $\aleph_c$ has only small variations in each channel we are free to take the average over all visible channels to get $\aleph$, the total disc asymmetry. This allows us to quantify the disc as a whole and has the advantage of allowing us to compare two discs even if part of one disc is obscured by removing the obscured channels from the average.

[1] Univ Lyon, Univ Claude Bernard Lyon 1, ENS de Lyon, CNRS, Centre de Recherche Astrophysique de Lyon UMR5574, F-69230, Saint-Genis-Laval, France

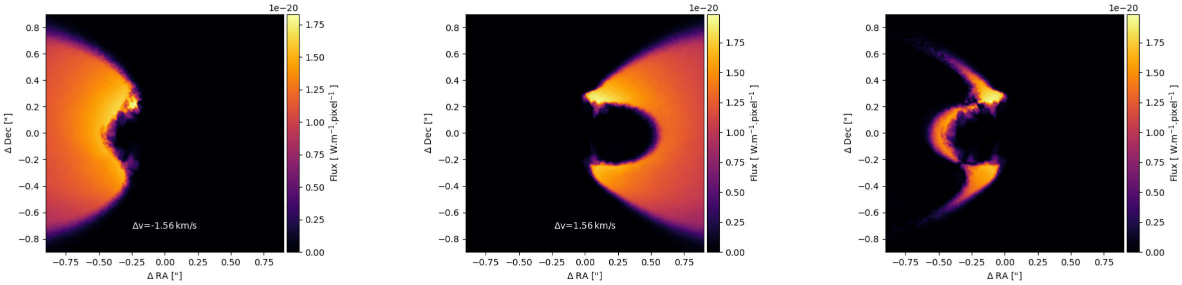

Fig. 1: Left and Middle: 2 channel maps with opposite velocities. Right: Flux differential between the two channels, the positive branch has been flipped horizontally and subtracted from the negative branch. Here the absolute value of the difference has been plotted to give $F_{\text{min}} = 0$.

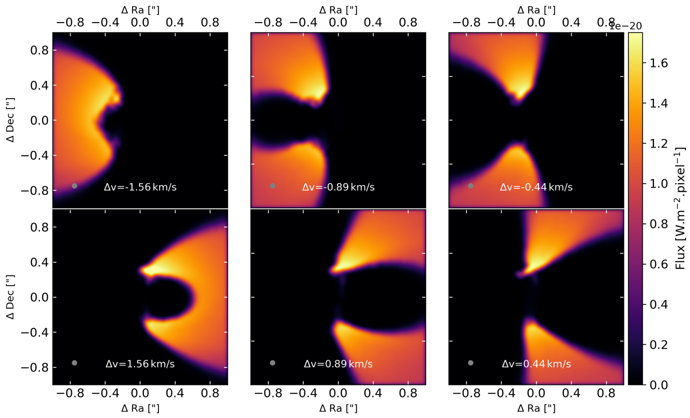

Fig. 3: A selection of CO channel maps of a coplanar disc with $(H/R)_{\text{in}} = 0.05$, surrounding a binary with $q = 0.1$, with an angle of 22.5° on the plane of the sky, after 1000 binary orbits. The top row shows only the negative branch and the bottom row shows the corresponding channels in the positive branch, highlighting the asymmetry in the disc.

2.1 Binary Eccentricity

Figure 3 shows a selection of CO channel maps for the disc in Figure 1. Large asymmetries are visible in opposite channels. We calculate $\aleph$ for this disc, as well as a suite of discs with increasing eccentricity up to $e = 0.9$, and for a single star disc with the same properties. The variation of $\aleph$ with eccentricity is shown in Figure 4, plotted with the single star disc for comparison. From this we can see that, with the exception of a circular binary, disc around binaries with $e > 0.4$ are more asymmetric than those around binaries with $e < 0.4$. Furthermore, even the least asymmetric circumbinary discs are roughly 3 times more asymmetric than a single star disc.

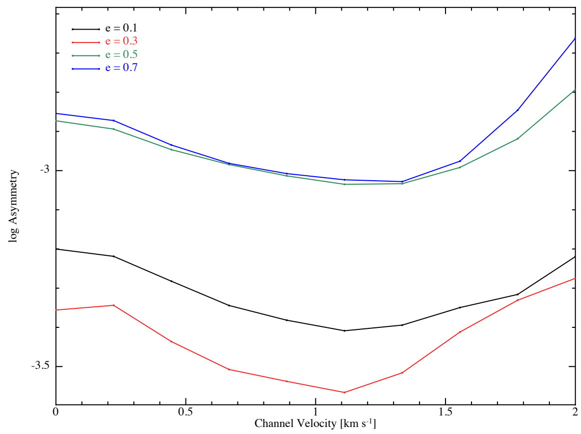

Fig. 2: Asymmetry metric $\aleph_c$ as a function of channel velocity.

2.2 Disc Scale Height

Figure 5 shows the dependence of $\aleph$ on disc scale height, with less viscous discs being more asymmetric. This is to be expected as viscosity acts to shrink and circularise the cavity (e.g: Artymowicz & Lubow 1994; Hirsh et al. 2020), thereby decreasing $\aleph$. This counteracts the dynamical effects from the binary which act to open a large, eccentric cavity, thereby increasing $\aleph$.

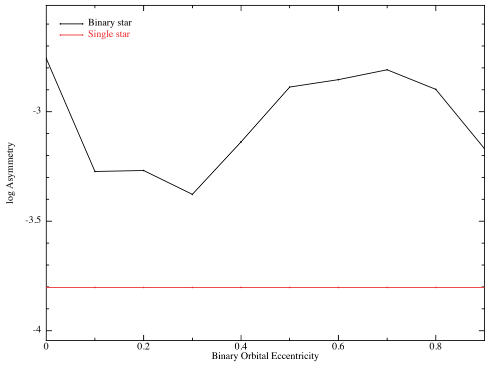

Fig. 4: Black line: Asymmetry as a function of binary orbital eccentricity for a coplanar disc with $(H/R)_{\text{in}} = 0.05$ surrounding a binary with $q = 0.1$ after 1000 binary orbits. Red line: Asymmetry of a single star disc with the same properties. Note that binary orbital eccentricity has no meaning for a single star disc, and this disc is only plotted as a horizontal line for ease of comparison with the suite of circumbinary discs.

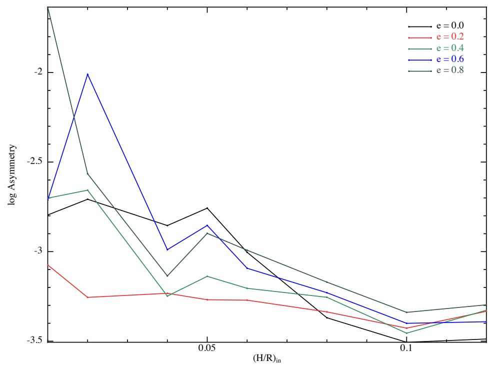

Fig. 5: Asymmetry as a function of disc aspect ratio for coplanar discs surrounding a binary with q = 0.1 after 1000 binary orbits. Different lines depict discs with different binary orbital eccentricities.

3 Moment 1 Maps

The top left panel of Figure 6 gives the moment 1 map for the disc described in Section 2, which shows the line of sight velocity of the material in the disc. Examining the $v = 0$ iso-velocity line, that is the line of the material which has no line of sight velocity, we see a twist inside the cavity. To investigate this peculiar shape we consider the effects of the radial and azimuthal components of the gas velocity in the plane of disc. We remove the radial component of the velocity by setting the $v_r = 0$ in the final output of the `PHANTOM` simulation before recomputing the moment 1 map with `MCFOST`. We then repeat this procedure, but keep the original v_r and instead set $v_\phi = v_{\text{k}}$, that is the azimuthal velocity is that of a Keplerian orbit. Finally, we force the velocity to be fully Keplerian, that is $v_r = 0$ and $v_\phi = v_{\text{k}}$. The effect of changing the radial and azimuthal velocity of the gas on the moment 1 map are also shown in Figure 6. When we remove the radial component of the velocity of the gas (top-right panel) this asymmetry largely vanishes, with the $v = 0$ line becoming much straighter. When we set the material to orbit with a Keplerian v_ϕ (bottom-left panel) the asymmetry remains. Finally, if we set the material on a purely Keplerian orbit (bottom-right panel) the shape resembles that of the observation with the radial velocity removed. This shows that the asymmetric shape of the moment 1 map is caused by the radial velocity of the material in the disc, while the deviations from Keplerian motion in the azimuthal direction have only a minor effect on the shape of the moment 1 map. The two most obvious sources of radial motion are binary-disc interactions and viscous accretion. Figure 7 compares the moment 1 maps of the fiducial disc with that of a disc with the same properties, but surrounding a single star. In the single star case the only source of radial motion is viscous accretion, and this is not strong enough to produce a twist in the moment 1 map. Therefore the source of the twist in the moment 1 maps of our discs is the companion.

4 Discussion

In defining $\aleph$, and while discussing the physical features present in the discs, we frequently refer to the positive and negative branches of the channel maps. It is important to stress that discussing these branches are unique to each individual disc. This is because which half of the disc appears in which branch is dependant on both the phase of the orbit and the position of the observer. For example, if the observer was positioned on the other side of the disc the positive and negative branches would be swapped. Therefore we caution the reader that a feature we see in, e.g., the positive branch is not constrained to only ever appear in the positive branch for all discs.

In this work we only investigated the dependence of $\aleph$ on binary orbital eccentricity and disc scale height.

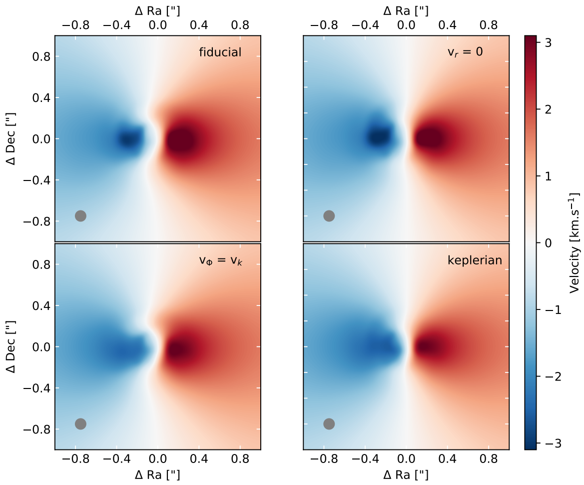

Fig. 6: Top left panel: Moment 1 map of a coplanar disc with $(H/R)_{\rm in} = 0.05$ surrounding a binary with $q = 0.1$, oriented with an inclination of 22.5° on the plane of the sky. Top right panel: Same, but with forcing $v_r = 0$. Bottom left panel: Same as top left, but with forcing $v_\phi = v_k$. Bottom right: Same as top left, but with forcing a fully Keplerian velocity.

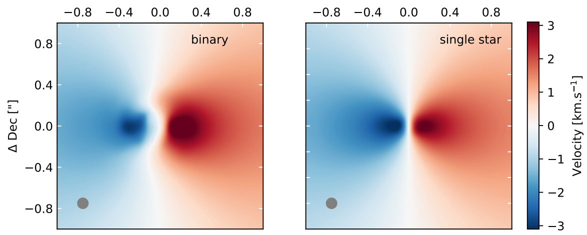

Fig. 7: Left panel: Moment 1 map of a coplanar disc with $(H/R)_{\rm in} = 0.05$ surrounding a binary with $q = 0.1$, oriented with an inclination of 22.5° on the plane of the sky (top left panel from Fig 6). Right panel: Moment 1 map of a disc with the same properties, but surrounding a single star.

In future work we will calculate $\aleph$ for all discs simulated in Hirsh et al. (2020), to investigate the dependence on binary-disc inclination and binary mass ratio. Beyond that performing this analysis on real observation, rather than the synthetic observations presented here, would allow us to test its validity in inferring the presence of a binary companion. Once confirmed this could be applied to transitional discs without a known companion to infer whether or not one is there.

5 Conclusion

We have generated a suite of synthetic observations of circumbinary discs, examining them to find signatures of the binary in these observations. We have also developed a metric to quantify the asymmetry, $\aleph$, in the channel maps and applied it to our synthetic CO channel maps. We found that the radial motion of the gas caused by binary-disc interactions leads to a twist in the moment 1 maps. Furthermore, single star discs have an asymmetry of $\log(\aleph) \sim -3.8$. The most symmetric circumbinary discs have a large scale height and low binary eccentricity. In these cases we find $\log(\aleph) \sim -3.5$. Conversely, thin discs around highly eccentric binaries can have asymmetries of $\log(\aleph) \sim -2$. It is important to note, however, that while a twisted moment 1 map, or an asymmetry of $\log(\aleph) \gtrsim -3.5$, do not constitute detections of a stellar companion, they do strongly hint towards their presence. As such, they can be used to identify systems that would make a good candidate for deeper observations with the intent of detecting a stellar companion.

References

Artymowicz, P. & Lubow, S. H. 1994, ApJ, 421, 651
Canovas, H., Montesinos, B., Schreiber, M. R., et al. 2018, A&A, 610, A13
Hirsh, K., Price, D. J., Gonzalez, J.-F., Ubeira-Gabellini, M. G., & Ragusa, E. 2020, MNRAS, 498, 2936
Pinte, C., Harries, T. J., Min, M., et al. 2009, A&A, 498, 967
Pinte, C., Ménard, F., Duchêne, G., & Bastien, P. 2006, A&A, 459, 797
Price, D. J., Wurster, J., Tricco, T. S., et al. 2018, PASA, 35, e031
Ubeira Gabellini, M. G., Miotello, A., Facchini, S., et al. 2019, MNRAS, 486, 4638
van der Marel, N., van Dishoeck, E. F., Bruderer, S., et al. 2016, A&A, 585, A58

SF2A 2021
A. Siebert, K. Baillié, E. Lagadec, N. Lagarde, J. Malzac, J.-B. Marquette, M. N'Diaye, J. Richard, O. Venot (eds)

MOBSTER: MAGNETO-ASTEROSEISMOLOGY OF HOT STARS WITH TESS

C. Neiner[1], J. Labadie-Bartz[2], C. Catala[1], K. Bernhard[3], D. M. Bowman[4], A. David-Uraz[5], S. Hümmerich[3], E. Paunzen[6] and M. E. Shultz[7]

Abstract. Magnetism has a strong impact on hot stars, including their internal structure. Therefore, performing magneto-asteroseismology provides valuable insight into hot stars and allows us to better constrain seismic models. However, only few magnetic pulsating hot stars have been identified and studied so far. Thanks to the TESS space mission, it is possible to find many magnetic hot stars including pulsating ones. The MOBSTER collaboration aims to identify magnetic candidates from TESS data, confirm and characterize their field with high-resolution spectropolarimetry, and ultimately perform magneto-asteroseismology on the most suitable targets.

Keywords: asteroseismology, stars: magnetic field, stars: chemically peculiar, stars: early-type, stars: oscillations, MOBSTER, TESS

1 Magnetic hot stars

About 10% of hot (OBA) stars are magnetic. Their fields are stable over decades, have typical polar field strengths of $\sim$3 kG at the stellar surface and usually a simple oblique dipolar configuration (Shultz et al. 2019). The fields are thought to be of fossil origin, i.e. a remnant from stellar formation (see Neiner et al. 2015, and references therein). In addition, a few A stars have been found to host ultra-weak magnetic fields (e.g. Blazère et al. 2016). These ultra-weak fields could be ubiquitous in OBA stars but are very difficult to detect with current instrumentation.

The presence of a magnetic field in a hot star has multiple consequences: in massive stars, wind particles escaping from the star are forced to follow magnetic field lines and can get trapped in a circumstellar magnetosphere (Petit et al. 2013). Moreover, in intermediate-mass stars, if the field is strong enough, it can create chemical enhancements at the stellar surface due to radiative diffusion along the field lines (Alecian & Stift 2010). In addition, if the star pulsates, the oblique magnetic field breaks the symmetry of the system and produces a splitting of the pulsation frequencies. The size of the frequency splitting is directly linked to the strength of the magnetic field, but the relative amplitude of the components of the split multiplet depends on the obliquity of the field with respect to the pulsation axis (Shibahashi & Aerts 2000). Knowing that a star is magnetic is thus crucial for pulsation mode identification. The field also modifies the period spacings of gravity-mode pulsations, which can then be used as a diagnostic of the strength of the internal magnetic field (Prat et al. 2020). Finally, above a fairly low strength the field inhibits mixing inside the star and there is thus no overshoot in magnetic stars (Zahn 2011).

As a consequence, magnetic hot stars are very interesting targets for asteroseismic studies. Magneto-asteroseismology indeed allows us to put additional constraints on seismic models and to extract more information about the internal structure of hot stars.

[1] LESIA, Paris Observatory, PSL University, CNRS, Sorbonne University, Université de Paris, 5 place Jules Janssen, 92195 Meudon, France

[2] Instituto de Astronomia, Geofísica e Ciências Atmosféricas, Universidade de São Paulo, Rua do Matão 1226, Cidade Universitària, 05508-900 São Paulo, SP, Brazil

[3] Bundesdeutsche Arbeitsgemeinschaft für Veränderliche Sterne e.V. (BAV), D-12169 Berlin, Germany

[4] Institute of Astronomy, KU Leuven, Celestijnenlaan 200D, B-3001 Leuven, Belgium

[5] Center for Research and Exploration in Space Science and Technology, and X-ray Astrophysics Laboratory, NASA/GSFC, Greenbelt, MD 20771, USA

[6] Department of Theoretical Physics and Astrophysics, Masaryk University, Kotlářská 2, 611 37 Brno, Czech Republic

[7] Department of Physics and Astronomy, University of Delaware, 217 Sharp Lab, Newark, Delaware, 19716, USA

2 Magnetic candidates from TESS

The inclination of the magnetic axis with respect to the rotation axis of the star produces rotational modulation of many observables, such as Hα, IR, and X-ray emission from the magnetosphere, UV resonance lines sensitive to the wind, polarization (Stokes) profiles, and light intensity. In the hotter stars the modulation of the light curve is due to varying column density of material in the magnetosphere along the line of sight as the star rotates, while in tepid stars it is due to the chemical elements accumulating in spots appearing on and disappearing from the visible half of the stellar surface. In both cases, rotational modulation of the light curve of a hot star is thus a good diagnostic of the presence of a magnetic field.

Using this property, three magnetic pulsating hot stars have been identified with Kepler2 (Buysschaert et al. 2018b). In addition, one hot magnetic pulsating star (HD 43317) was observed with CoRoT (Pápics et al. 2012; Briquet et al. 2013), and a few roAp stars with Kepler (e.g. Kurtz et al. 2011; Balona 2013). The BRITE constellation and associated BritePol spectropolarimetric program (Neiner & Lèbre 2014) observed some pulsating magnetic hot stars but those were already known from ground-based observations. Moreover, advanced seismic modelling has only been done for one such star so far (HD 43317, Buysschaert et al. 2018a) because of the small number of pulsation modes present in the other targets. It is therefore necessary to identify more magnetic pulsating hot stars.

The TESS mission observes most of the sky, with each target beeing observed for at least 28 days and up to 1 year depending on its coordinates (Ricker et al. 2015). The TESS data thus provide an excellent database to search for magnetic candidates through rotational modulation of their light curves. We cross-correlated our list of bright (V<10) magnetic candidates identified from TESS data with the list of chemically peculiar stars identified by Hümmerich et al. (2020) thanks to the characteristic 5200 Å flux depresssion observed in spectra from the LAMOST survey. We obtained 119 highly probable magnetic candidates. We plan to observe 48 of the 119 selected targets with high-resolution spectropolarimetry using ESPaDOnS at CFHT (Canada France Hawaii Telescope), with the aim to detect any magnetic field with a strength above 300 G. We consider that the remaining 71 stars are either less interesting from the seismic point of view or require too much observing time at CFHT. However, those 71 discarded targets are very likely magnetic stars as well. In addition, from the TESS data of the 48 selected magnetic candidates we identified 25 stars that show pulsational signals. These candidate magnetic pulsators are perfect targets for magneto-asteroseismology. Figure 1 shows an example of such a pulsating magnetic star, TYC 4766-330-1, which was indeed confirmed to be magnetic with ESPaDOnS at CFHT.

3 Spectropolarimetry

So far, the MOBSTER collaboration (David-Uraz et al. 2019) observed 21 of the 48 magnetic candidates with ESPaDOnS at CFHT. The data were analyzed with a Least-Squares Deconvolution technique (LSD, Donati et al. 1997) to extract magnetic signatures with a high signal-to-noise ratio. We obtained 20 clear magnetic detections, i.e. a 95% success rate in the confirmation of the presence of a magnetic field in these stars. The only non-magnetic star, TYC 2838-1789-1, is a spectroscopic binary (SB2) and had been flagged as dubious in Hümmerich et al. (2020). These very encouraging results show that our target selection process is very efficient, thanks to the combination of data from TESS and the LAMOST survey, and the vast majority of our magnetic candidates should indeed turn out to be newly discovered magnetic stars.

For the most interesting targets, i.e. those that are confirmed to be magnetic and show pulsational signal in the TESS data, we will acquire follow-up spectropolarimetric observations with the aim to obtain $\sim$20 spectropolarimetric measurements per star spread over their stellar rotation period, to fully characterize the magnetic configuration and strength. A first target, HD 86170, is scheduled for follow-up observations in the fall 2021 with NeoNarval at TBL (Télescope Bernard Lyot, Pic du Midi, France). Figure 2 shows the first spectropolarimetric observation of HD 86170 obtained with ESPaDOnS at CFHT in February 2021, indicating a clear magnetic signature.

Finally, the high-quality spectropolarimetric data will also be used to determine the stellar parameters (e.g. $T_{\rm eff}$, $\log g$, $v \sin i$, abundances) of the targets at the precision needed for seismic modelling.

4 Conclusions

The MOBSTER collaboration has set up a program to search for magnetic pulsating hot stars in the TESS data, with the goal to perform magneto-asteroseismology. The magnetic candidate selection process is very efficient,

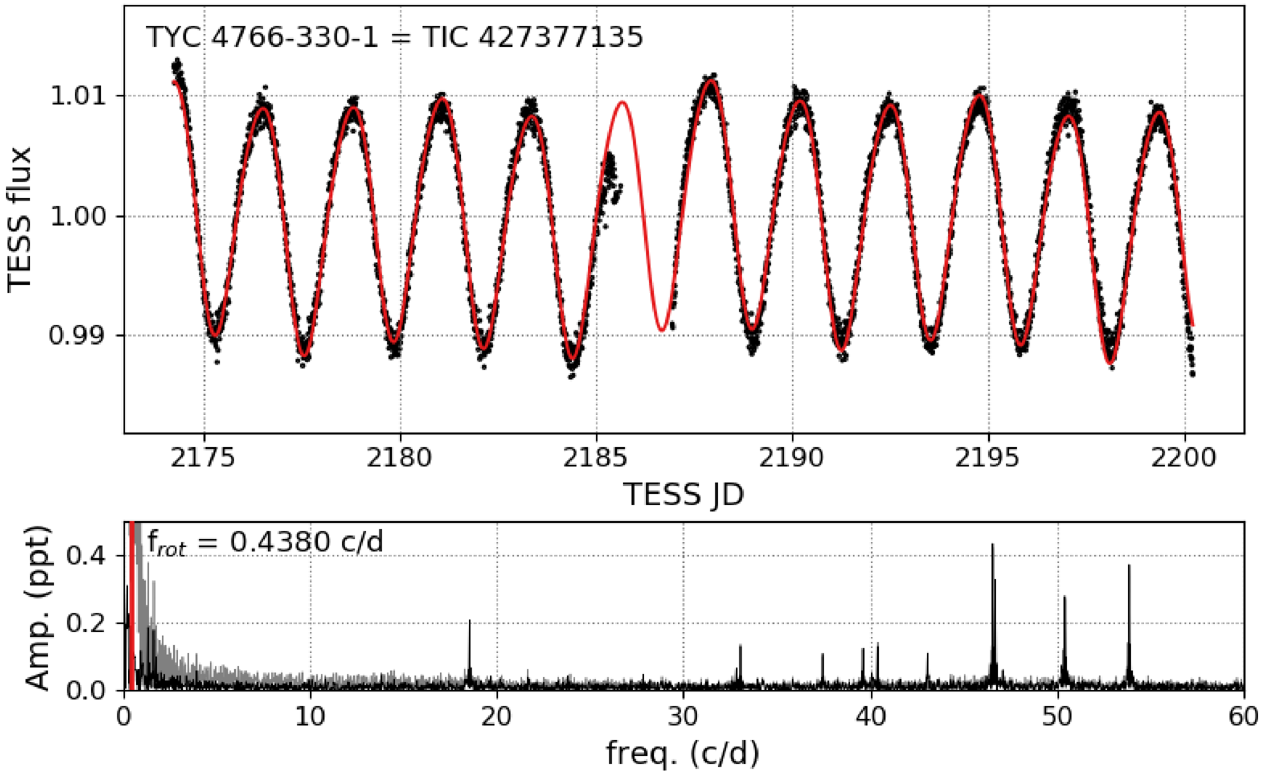

Fig. 1. Top panel: Light curve of TYC 4766-330-1 obtained by TESS in its sector 32 taken with a 10-min cadence, showing obvious rotational modulation. Bottom panel: Fourier transform (FT) of this light curve showing the original FT in grey and the FT after prewhitening for the rotation frequency (in red) and its first harmonic in black. Clear pulsational signal is present in the FT in addition to rotational modulation.

thanks to the combination of TESS and spectroscopic data, with 95% of the candidates confirmed to be magnetic so far using high-resolution spectropolarimetry at CFHT. Several very interesting magnetic pulsating targets have already been identified and will be the subject of follow-up spectropolarimetric observations at CFHT and TBL in the coming semesters to fully characterize their magnetic field. These results will be the starting point for magneto-asteroseismic modelling of hot stars by the MOBSTER collaboration.

This paper includes data collected by the TESS mission. Funding for the TESS mission is provided by the NASA's Science Mission Directorate. Based on observations obtained at the Canada-France-Hawaii Telescope (CFHT) which is operated by the National Research Council(NRC) of Canada, the Institut National des Sciences de l'Univers of the Centre National de la Recherche Scientifique (CNRS) of France, and the University of Hawaii. This work has made use of the SIMBAD database operated at CDS, Strasbourg (France), and of NASA's Astrophysics Data System (ADS). The material is based upon work supported by NASA under award number 80GSFC21M0002.

References

Alecian, G. & Stift, M. J. 2010, A&A, 516, A53
Balona, L. A. 2013, MNRAS, 436, 1415
Blazère, A., Petit, P., Lignières, F., et al. 2016, A&A, 586, A97
Briquet, M., Neiner, C., Leroy, B., Pápics, P. I., & MiMeS Collaboration. 2013, A&A, 557, L16
Buysschaert, B., Aerts, C., Bowman, D. M., et al. 2018a, A&A, 616, A148
Buysschaert, B., Neiner, C., Martin, A. J., et al. 2018b, MNRAS, 478, 2777
David-Uraz, A., Neiner, C., Sikora, J., et al. 2019, MNRAS, 487, 304
Donati, J. F., Semel, M., Carter, B. D., Rees, D. E., & Collier Cameron, A. 1997, MNRAS, 291, 658
Hümmerich, S., Paunzen, E., & Bernhard, K. 2020, A&A, 640, A40

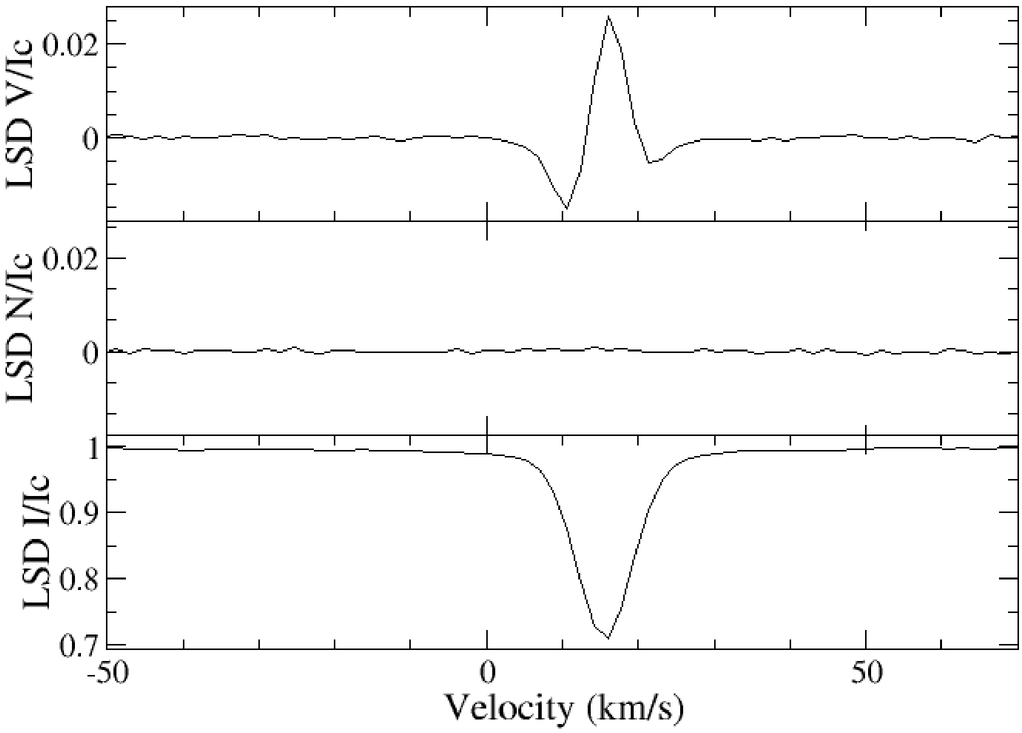

Fig. 2. ESPaDOnS observation of HD 86170 showing a clear magnetic detection in the LSD Stokes V profile (top), no detection in the null polarization used to check for spurious polarization signals (middle), and the LSD intensity line profile (bottom).

Kurtz, D. W., Cunha, M. S., Saio, H., et al. 2011, MNRAS, 414, 2550

Neiner, C. & Lèbre, A. 2014, in SF2A-2014: Proceedings of the Annual meeting of the French Society of Astronomy and Astrophysics, ed. J. Ballet, F. Martins, F. Bournaud, R. Monier, & C. Reylé, 505–508

Neiner, C., Mathis, S., Alecian, E., et al. 2015, in Polarimetry, ed. K. N. Nagendra, S. Bagnulo, R. Centeno, & M. Jesús Martínez González, Vol. 305, 61–66

Pápics, P. I., Briquet, M., Baglin, A., et al. 2012, A&A, 542, A55

Petit, V., Owocki, S. P., Wade, G. A., et al. 2013, MNRAS, 429, 398

Prat, V., Mathis, S., Neiner, C., et al. 2020, A&A, 636, A100

Ricker, G. R., Winn, J. N., Vanderspek, R., et al. 2015, Journal of Astronomical Telescopes, Instruments, and Systems, 1, 014003

Shibahashi, H. & Aerts, C. 2000, ApJ, 531, L143

Shultz, M. E., Wade, G. A., Rivinius, T., et al. 2019, MNRAS, 490, 274

Zahn, J.-P. 2011, in Active OB Stars: Structure, Evolution, Mass Loss, and Critical Limits, ed. C. Neiner, G. Wade, G. Meynet, & G. Peters, Vol. 272, 14–25

SF2A 2021
A. Siebert, K. Baillié, E. Lagadec, N. Lagarde, J. Malzac, J.-B. Marquette, M. N'Diaye, J. Richard, O. Venot (eds)

PROBING CORE OVERSHOOTING USING SUBGIANT ASTEROSEISMOLOGY

A. Noll[1], S. Deheuvels[1] and J. Ballot[1]

Abstract. Convective cores are the fuel reservoir of stars that are more massive than about $1.2\,M_\odot$. Their size therefore has a substantial influence on stellar evolution. However, several physical processes that remain poorly understood by theory can extend those convective cores. Observations are therefore required to help constrain them. We here show how we can use subgiant asteroseismology to indirectly constrain the main-sequence convective core extension. Indeed, subgiant stars exhibit mixed modes, whose dual nature as pressure and gravity modes allows us to probe the very core of the star. We therefore used the full Kepler data set to thoroughly model KIC10273246, using a method that we specifically tailored for subgiants. We obtained models that show a good statistical agreement with the observations, and found that adding overshooting significantly improves the quality of the seismic fit. We also found that having access to several g-dominated mixed modes provides a stronger constraint on the structure of the star, especially the Brunt-Väisälä frequency and the central density. This study paves the way of a more general study, which will include subgiants observed with Kepler and TESS.

Keywords: asteroseismology, convection, stars: evolution, stars: interiors, stars: individual: KIC10273246

1 Introduction

Convective cores are found in stars more massive than approximately $1.2\,M_\odot$ (e.g., Kippenhahn et al. 2012). As they are the fuel reservoirs of the star, their masses is of prime importance on stellar evolution: the bigger the core is, the more time the star spends on the main-sequence (MS). However, several physical processes are known to extend this core beyond the limit defined by the classical Schwarzschild (or Ledoux) criterion. Those can be, for instance, overshooting, rotational mixing or semi-convection. Unfortunately, those processes, and even more the way they interact are today poorly constrained by the theory. Therefore, one generally models the core extension, usually referred as *overshooting* regardless of the physical process, in a simplistic way. For instance, it is often modeled as a crude extension of the convective core, called step overshooting, on the distance $d_{\rm ov} = \alpha_{\rm ov} H_p$, H_p being the pressure scale length and $\alpha_{\rm ov}$ a free parameter.

Historically, constraints on the core extension have been obtained through the study of color-magnitude diagrams of clusters (e.g., Maeder & Mermilliod 1981). More recently, the study of eclipsing binaries also allowed to put constraints on this parameter (e.g., Claret & Torres 2018).In all cases, overshooting appears to be required in order to correctly reproduce the observations.

Over the last decade, the rapid progress of observation asteroseismology allowed to directly probe inside of the stars. Thanks to the data of the space missions CoRoT (Baglin et al. 2006), *Kepler* (Borucki et al. 2010) and now TESS (Ricker et al. 2014), oscillations have been detected in thousands of stars, which allowed unprecedented exploration of the stellar structure. Once again, overshooting have been a necessary ingredient to correctly model solar-like oscillators (e.g. Deheuvels et al. 2016), more massive slowly-pulsating (SPB) stars (e.g. Pedersen et al. 2021) and γ Doradus (Mombarg et al. 2021).

Asteroseismology of post-main-sequence stars is another way to place constraints on the MS core. Once the central hydrogen is totally exhausted at the end of the MS, the core becomes radiative and contracts until the hydrogen-rich layers above become hot enough to start hydrogen burning. The resulting core structure is therefore highly dependent on the properties of the former convective core. Moreover, interestingly, the stars starts to exhibit mixed modes. Those modes, which have a gravity (g) nature in the core and a pressure (p)

[1] IRAP, Université de Toulouse, CNRS, CNES, UPS, (Toulouse), France

nature in the envelope, allow a very fine probing of the structure of the star. These features make subgiant interesting targets to investigate the properties on MS convective cores. Thus, Deheuvels & Michel (2011) succesffuly constrained $\alpha_{\rm ov}$ by seismically modeling a star observed by CoRoT. In the present work, published in Noll et al. (2021), we use the high quality sesmic data from *Kepler* to model a subgiant star.

2 Choice of the target and observational properties

2.1 Choice of the target

In this study, we chose to focus on KIC10273246, a subgiant star observed during a total duration of 978 days by *Kepler*. Such a long duration of observation allows a high precision of the frequencies. Moreover, this star exhibits several "g-dominated" modes, i.e. modes that are mainly of gravity nature. We thus expected to obtain more precise information on the core as most of the energy and probing capacities of such modes are located in the central region of the star. Finally, early seismic analyses of this star (Campante et al. 2011; Creevey et al. 2012) indicate that it is massive enough to have had a convective core during the MS.

2.2 Observational properties

The luminosity of the star have been extracted using Gaia DR2 data (Evans et al. 2018) combined with a spectral energy distribution (SED) fit. We obtained $L = 5.74 \pm 0.17\, L_\odot$. The effective temperature and metallicity, from the spectroscopic modeling of Creevey et al. (2012), are respectively $6150 \pm 100\,$K and $-0.13 \pm 0.13\,$dex.

The oscillation frequencies have been extracted from the full *Kepler* light curve, following the method of Appourchaux et al. (2008). We obtained a large separation $\Delta\nu = 48.47 \pm 0.02\,\mu$Hz and a frequency of maximum power of the oscillations $\nu_{\rm max} = 843 \pm 20\,\mu$Hz.

3 Modeling method

To model the star, we carried out a forward modeling (i.e. trying to reproduce the observations with models) using the MESA v10108 stellar evolution code (Paxton et al. 2015) coupled with the ADIPLS stellar oscillation code (Christensen-Dalsgaard 2008). Microscopic diffusion has been taken into account (Burgers 1969). Radiative accelerations have been neglected. Overshooting has been modeled as a *step overshooting* (i.e. crude extension of the core). The surface effects were corrected using the cubic term of the prescription of Ball & Gizon (2014). The free parameters were the mass M, the age, the initial helium composition Y, the initial metallicity [Fe/H], the mixing-length parameter $\alpha_{\rm conv}$ and the overshoot parameter $\alpha_{\rm ov}$. All the rest of the physics is detailed in Noll et al. (2021).

Subgiant stars are notoriously difficult to model. This is mainly due to the very fast evolution of the frequencies of the g-dominated modes, which are highly impacted by the steep increase in the central density. Reproducing such modes by using a grid of stellar evolution models therefore requires extremely small steps in mass and age. Interpolation within the grid of models could alleviate this issue, however, if interpolation in age is doable for modes with degrees less than 2 (Li et al. 2020), it is difficult across tracks. Finally, the highly non-linear behavior of mixed modes prevents us from directly using traditional iterative optimization techniques.

We therefore used a dedicated approach in Noll et al. (2021), which consists in a nested optimization. This method is composed of two steps, the first being embedded within the second. The first part only deals with the mass and age as free parameters, the rest of the parameters being fixed. One can show that, when all other input parameters are fixed, the optimal mass and age of a model can be found only by reproducing the large separation $\Delta\nu$ and the frequency of a g-dominated mode ν_g (Deheuvels & Michel 2011). This allows to "easily" handle these two otherwise tedious parameters. This dedicated approach is nested in a more general step, in which we handle the other parameters, namely the metallicity, mixing-length parameter, initial helium composition and overshoot. For those parameters, we used more general techniques such as an optimization using a Levenberg-Marquardt algorithm (Press et al. 1992) and a grid. The former allowed us to retrieve more precise parameters, while the latter allowed a better exploration of the space parameters and determination of the modeling uncertainties.

4 Results

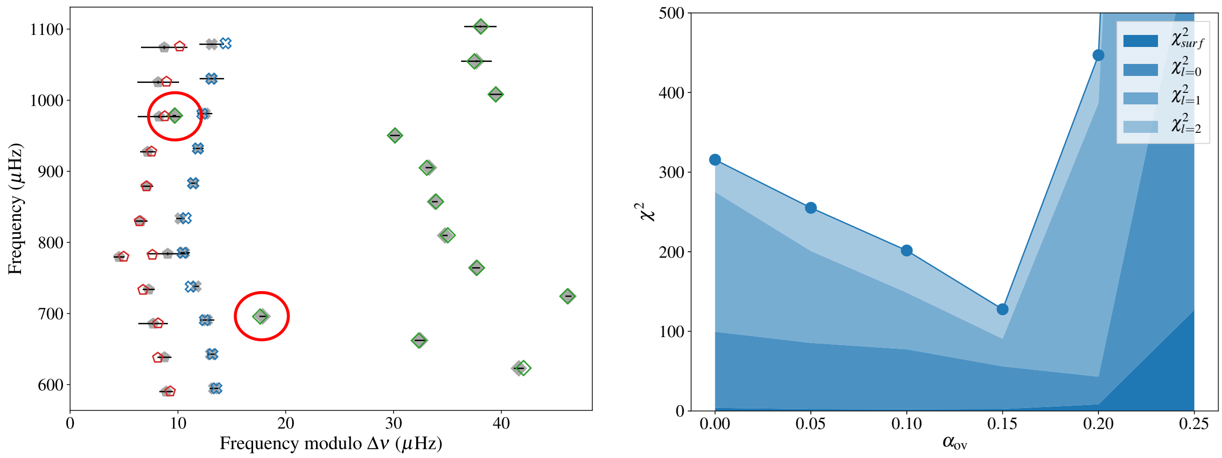

Fig. 1. Left: Echelle diagramme of the best model (in open symbols) and of the observations (in full symbols). Radial, dipolar and quadripolar frequencies are in blue, green and red, respectively. G-dominated modes are cercled in red. **Right:** χ^2 of the best models for every value of $\alpha_{\rm ov}$. The colored regions indicate the χ^2 contributions of surface observables and frequencies depending on their degrees.

4.1 General characteristics of the models

Using the nested optimization, we managed to obtain statistically satisfactory models of KIC10273246. Indeed, the best model, with $\alpha_{\rm ov} = 0.15$, has a reduced χ^2 of 3.2. We found the following characteristics : $M = 1.223 \pm 0.03\, M_\odot$, $R = 2.110 \pm 0.021\, R_\odot$, Age $= 3.89 \pm 0.25$ Gyr, [Fe/H] $= -0.073 \pm 0.01$, $\alpha_{\rm conv} = 1.739 \pm 0.089$ and $Y = 0.28 \pm 0.02$. Moreover, its luminosity and effective temperature are within the observational uncertainties. One can see in the left panel of Fig. 1 the échelle diagram of the best model, and the observations with the 3-σ uncertainties representend with black bars. It appears indeed that all the frequencies are well reproduced, even the g-dominated ones (circled in red) despite their high sensitivity to the age and mass of the model.

4.2 Constraints on $\alpha_{\rm ov}$

The right panel of Fig. 1 represents the χ^2 of the best models, for every value of $\alpha_{\rm ov}$. We can see that adding overshooting significantly improves the quality of the fit, with a χ^2 difference between the models without and with $\alpha_{\rm ov} = 0.15$ of 188. Modeling KIC10273246 therefore allowed us to constrain $\alpha_{\rm ov}$. One can also notice on this plot the colored regions below the curve, which represent the contributions of the frequencies to the total χ^2 according to their degree. We can see that the dipolar modes play a crucial role to favor models with overshoot. Indeed, g-dominated modes are mainly dipolar for such stars. So, this confirms the high probing potential of such modes.

Finally, we notice that a high overshoot $\alpha_{\rm ov} \geq 0.2$ strongly worsens the quality of the fit. This may be explained by the tight constraint on the central density ρ_c due to the g-dominated modes, as explained more in depth in Noll et al. (2021).

4.3 Constraints on the internal structure

We also investigated in Noll et al. (2021) the constraints that can be obtained from the mixed modes on the internal structure of the star. In particular, as KIC10273246 exhibits two g-dominated modes contrary to HD49385 which was studied in Deheuvels & Michel (2011). We showed that a second g-dominated mode allows to put strong constraints on the Brunt-Väisälä profile and especially on the part that is dominated by the chemical gradient in the H-burning shell. As this region is highly sensitive to the former MS core, subgiants with several g-dominated modes are therefore interesting targets to constrain overshoot.

5 Discussion and conclusion

During this detailed study of KIC10273246, we also tested the impact of the microscopic diffusion on the seismic modeling. Indeed, adding diffusion or not is a tricky question for stars in this mass range, as it may be competed by radiative accelerations in the envelope during the main sequence (Deal et al. 2018). We observed that adding microscopic diffusion allows to significantly improve the diffusion, as it indeed reduces the χ^2 by 71. We also observed no difference between the best model computed with and without radiative accelerations.

Additionally, a strong degeneracy between initial helium abundance Y and stellar mass M has been found during the modeling of the star. This degeneracy is the main contributor to the uncertainties on the stellar parameters. The mass-helium degeneracy, already known in main sequence (e.g., Lebreton & Goupil 2014), is therefore not lifted during the subgiant phase, in agreement with Li et al. (2020) .

Finally, the detection of a g-dominated quadrupolar mode which is split by rotation allowed us to constrain the core rotation of the star. Thus, we obtained a splitting of $0.53 \pm 0.03\,\mu$Hz. This value, close to the surface rotational modulation (around $0.5\,\mu$Hz, Campante et al. 2011), would indicate a low radial differential rotation, in agreement with Deheuvels et al. (2020).

In conclusion, this study showed the high interest that could represent the seismic study of subgiants to constrain the amount of overshooting in main-sequence convective cores. In the future, a similar method will be applied to other subgiant stars observed by *Kepler* (Noll et al., in prep.).

The authors thank the organizing committee for this great digital edition of the SF2A days and for giving the opportunity to present this work. We acknowledge support from from the project BEAMING ANR-18-CE31- 0001 of the French National Research Agency (ANR) and from the Centre National d'Etudes Spatiales (CNES).

References

Appourchaux, T., Michel, E., Auvergne, M., et al. 2008, A&A, 488, 705

Baglin, A., Auvergne, M., Barge, P., et al. 2006, in ESA Special Publication, Vol. 1306, The CoRoT Mission Pre-Launch Status - Stellar Seismology and Planet Finding, ed. M. Fridlund, A. Baglin, J. Lochard, & L. Conroy, 33

Ball, W. H. & Gizon, L. 2014, A&A, 568, A123

Borucki, W. J., Koch, D., Basri, G., et al. 2010, Science, 327, 977

Burgers, J. M. 1969, Flow Equations for Composite Gases

Campante, T. L., Handberg, R., Mathur, S., et al. 2011, A&A, 534, A6

Christensen-Dalsgaard, J. 2008, Ap&SS, 316, 113

Claret, A. & Torres, G. 2018, 859, 100

Creevey, O. L., Doğan, G., Frasca, A., et al. 2012, A&A, 537, A111

Deal, M., Alecian, G., Lebreton, Y., et al. 2018, A&A, 618, A10

Deheuvels, S., Ballot, J., Eggenberger, P., et al. 2020, A&A, 641, A117

Deheuvels, S., Brandão, I., Silva Aguirre, V., et al. 2016, A&A, 589, A93

Deheuvels, S. & Michel, E. 2011, A&A, 535, A91

Evans, D. W., Riello, M., De Angeli, F., et al. 2018, A&A, 616, A4

Kippenhahn, R., Weigert, A., & Weiss, A. 2012, Stellar Structure and Evolution

Lebreton, Y. & Goupil, M. J. 2014, A&A, 569, A21

Li, T., Bedding, T. R., Christensen-Dalsgaard, J., et al. 2020, MNRAS, 495, 3431

Maeder, A. & Mermilliod, J. C. 1981, A&A, 93, 136

Mombarg, J. S. G., Van Reeth, T., & Aerts, C. 2021, A&A, 650, A58

Noll, A., Deheuvels, S., & Ballot, J. 2021, A&A, 647, A187

Paxton, B., Marchant, P., Schwab, J., et al. 2015, ApJS, 220, 15

Pedersen, M. G., Aerts, C., Pápics, P. I., et al. 2021, Nature Astronomy

Press, W. H., Teukolsky, S. A., Vetterling, W. T., & Flannery, B. P. 1992, Numerical recipes in FORTRAN. The art of scientific computing

Ricker, G. R., Winn, J. N., Vanderspek, R., et al. 2014, in Society of Photo-Optical Instrumentation Engineers (SPIE) Conference Series, Vol. 9143, Space Telescopes and Instrumentation 2014: Optical, Infrared, and Millimeter Wave, 914320

AMPLITUDE OF THE PLUME-INDUCED SOLAR GRAVITY MODES: IMPLICATIONS REGARDING THEIR DETECTION

C. Pinçon[1]

Abstract. The observation of the low-frequency gravity oscillation modes in the Sun is expected to bring unprecedented constraints on the solar interior. However, despite several claims, their detection has not been confirmed yet. Within this context, theoretical estimates of their amplitude can help guide the observational strategies and the design of future measuring devices. In this short paper, we report the recent results of Pinçon et al. (2021) who considered the penetration of convective plumes at the top of the radiative interior as the driving mechanism, hence completing previous estimates. Accounting for the uncertainties in the plume modeling, the surface disk-integrated apparent mode radial velocity that would be measured with the GOLF instrument on the spacecraft SoHO is estimated on the order of 0.5 cm s^{-1} in the most plausible favorable case, which still requires about 25 years of observation for a robust detection.

Keywords: Sun – helioseismology – gravity modes

1 Introduction

Solar gravity modes have buoyancy as the restoring force: they thus can propagate in the central radiative zone of the Sun. As a consequence, the oscillation spectrum of the gravity modes contains information on the inner stratification of the Sun and thus appears very promising to constrain the microphysics used to build solar models, as for instance the opacity, the nuclear reaction rates, or the chemical mixture. The potential of combining these seismic constraints with the recent measurements of the neutrino flux produced by the CNO cycle in the nuclear solar core is even more promising (Borexino Collaboration et al. 2020; Salmon et al. 2021). It is expected for instance to give important insights into the solar metallicity problem (e.g., Buldgen et al. 2019). Moreover, the gravity modes have also the potential to inform us on the central rotation of the Sun, which will permit to put stringent constraints on the internal angular momentum redistribution and induced mixing processes during its whole past life. In addition, considering the Sun as a particular target to calibrate stellar evolution codes, the amount of information expected from the observation of the solar gravity modes represents a goldmine for the study of the stellar structure and evolution in general.

Nevertheless, although the detection of the solar gravity modes has already been claimed by several previous works, it has not been robustly confirmed yet (e.g., Appourchaux et al. 2010; Fossat et al. 2017; Schunker et al. 2018). Within this context, theoretical estimates of their amplitude can help implement new observational strategies and guide the design of future instruments dedicated to their search. While the current numerical simulations can provide interesting hints about the generation of gravity modes in stars, the values of their control parameters remain far from the expected stellar regimes (e.g., Dintrans et al. 2005; Alvan et al. 2014). A complementary approach then consists in studying the excitation mechanism from a semi-analytical point of view (e.g., Belkacem 2011). The previous models mainly considered the turbulent Reynolds stress in the convective envelope as the source of the gravity modes. Guided by numerical simulations of the envelope of the Sun to model the turbulent properties of the convective eddies, the most recent estimate of Belkacem et al. (2009) predicted GOLF apparent mode radial velocities close to about 0.5 cm s^{-1} for a typical mode frequency $\nu \sim 100$ μHz, which is at the limit of the detection with the current GOLF data. However, these previous estimates were incomplete since they did not account for the potential excitation of the gravity modes by the penetration of downward convective plumes into the top layers of the radiative zone, or penetrative convection.

[1] STAR Institute, Université de Liège, 19C Allée du 6 Août, B-4000 Liège, Belgium

This mechanism was shown to be very efficient in the Sun to generate very-low-frequency progressive gravity waves by Pinçon et al. (2016). The application to the case of gravity modes in a higher frequency range has been undertaken only recently by Pinçon et al. (2021). In this short paper, we briefly summarize their main results.

2 Analytical expression of the mean mode energy generated by penetrative plumes

Pinçon et al. (2021) could estimate the mean energy of the plume-induced gravity modes using three main assumptions. (1) The source term in the wave equation corresponds to the dynamical ram pressure exerted by an ensemble of incoherent penetrating plumes uniformly distributed over the sphere at the base of the convective region. (2) The plume Péclet number at the base of the convective zone is much higher than unity, meaning that the density contrast between the plumes and the surrounding is high at the top of the radiative region so that the buoyancy braking of the plumes when the penetrate into the stably-stratified radiative layers is very efficient. (3) The frequency range is comprised between 10 μHz and 100 μHz for the sake of the simplicity. Indeed, in this frequency range, the spatial behavior of the oscillation field can first be easily obtained using the JWKB asymptotic method; second, the mode damping is dominated by radiative diffusion and the mode lifetime is much larger than the mode period, which makes the coupling between the momentum and the heat equation tractable analytically using a two-timing method. Based on these assumptions, Pinçon et al. (2021) found that the mean energy over time of a mode with a radial order n, an angular degree ℓ, an azimuthal number m and an angular frequency $\omega_{n\ell m}$ is provided by the final expression

$$\langle E_{n\ell m} \rangle \approx \frac{\left[(\omega_{n\ell m} \Delta\Pi_\ell / \pi^2)\ \overline{L_{\mathrm{p}}}\ F_{\mathrm{d},\ell}\ e^{-\ell(\ell+1)b^2/2r_{\mathrm{b}}^2}\ \mathcal{C}_{n\ell m}\right]}{2\eta_{n\ell m}}\ , \tag{2.1}$$

where $\Delta\Pi_\ell$ is the asymptotic period spacing between two consecutive gravity modes of degree ℓ, $\overline{L_{\mathrm{p}}}$ is the mean plume kinetic luminosity at the base of the convective zone (at radius r_{b}), $F_{\mathrm{d},\ell} = V_{\mathrm{b}} k_{h,\mathrm{b}} / N_{\mathrm{t}}$ is the Froude number, with V_{b} the plume velocity, $k_{h,\mathrm{b}} = \sqrt{\ell(\ell+1)}/r_{\mathrm{b}}$ the horizontal wavenumber of the mode and N_{t} the value of the Brunt-Vaisala frequency at the top of the radiative zone, b is the plume radius, and $\eta_{n\ell m}$ is the damping rate per unit of time. Finally, the $\mathcal{C}_{n\ell m}$ term measures the temporal correlation between the plumes and the modes, and thus depends on the plume time evolution profile inside the penetration zone. Given the lack of knowledge on this question and its complexity, the authors considered the two limiting cases of an exponential and a Gaussian law, that is, in the form of $e^{-|t|/\tau_{\mathrm{p}}}$ and $e^{-t^2/\tau_{\mathrm{p}}^2}$ with τ_{p} the plume lifetime. In the considered frequency range, it can be shown that $\eta_{n\ell m} \ll \nu_{\mathrm{p}} \ll \omega_{n\ell m}$, where $\nu_{\mathrm{p}} = 1/\tau_{\mathrm{p}}$, and $\mathcal{C}_{n\ell m}$ reduces in the case of a Gaussian and and exponential plume time profile to, respectively,

$$\mathcal{C}^{\mathrm{G}}_{n\ell m} \approx 4\sqrt{\pi}\ \frac{\eta_{n\ell m}}{\nu_{\mathrm{p}}}\ \frac{\nu_{\mathrm{p}}^3}{\omega_{n\ell m}^3} \quad \text{and} \quad \mathcal{C}^{\mathrm{E}}_{n\ell m} \approx 16 \frac{\nu_{\mathrm{p}}^3}{\omega_{n\ell m}^3}\ . \tag{2.2}$$

In the considered frequency range, the temporal correlation is thus expected to be much smaller in the Gaussian case than in the exponential case, i.e. $\mathcal{C}^{\mathrm{G}}_{n\ell m} \ll \mathcal{C}^{\mathrm{E}}_{n\ell m}$, so does the mean mode energy.

3 Amplitude of the plume-induced solar gravity modes and concluding remarks

In order to compute Eq. (2.1), a standard calibrated solar model was used to estimate the structure parameters (e.g., $\Delta\Pi_\ell$, $\eta_{n\ell m}$, r_{b}, N_{t}). The plume width and velocity, b and V_{b}, were estimated using the turbulent model of plumes of Rieutord & Zahn (1995), and the plume lifetime was chosen around the turnover timescale of the convective eddies above the base of the convective zone such as predicted by the mixing length theory in the considered solar model. The result was then converted into a GOLF apparent mode radial velocity applying two multiplication factors: first, the mode mass that can be computed from the considered solar model using a pulsation code (e.g., Samadi et al. 2015); second, a visibility factor taking into account the effect of the limb darkening and the line-of-sight projection over the solar disk (e.g., Dziembowski 1977). For comparison, a theoretical detection threshold with the GOLF instrument as a function of the observation duration was estimated using the analytical development of Appourchaux et al. (2000) with a false alarm probability of 1%.

Without going into mode details, Pinçon et al. (2021) found that the result is very sensitive to the assumption made on the plume time evolution profile. In the case of a Gaussian time evolution, the gravity modes turn out to be undetectable because the temporal correlation between the plumes and the modes is definitely too small.

In the case of an exponential time evolution, the apparent mode radial velocity is estimated around 0.05 cm s^{-1} for $\nu \sim 100$ μHz, which is still one order of magnitude lower than the current GOLF detection threshold and the mode amplitude estimate considering the turbulent Reynolds stress as the driving mechanism by Belkacem et al. (2009). Considering uncertainties in the plume parameters, reasonable variations in their values in the most plausible favorable case (i.e., b and ν_{p} are multiplied by a factor of about 2) can lead to an increase of the apparent mode radial velocity to 0.4 cm s^{-1} at $\nu \sim 100$ μHz, which still requires at least 25 years of GOLF observation to be detected.

Overall, these estimates, considering the excitation both by turbulent pressure and penetrative convection, indicate that the solar gravity modes are currently at most at the limit of the detection with the GOLF instrument in the asymptotic frequency range. Nevertheless, it is worth mentioning that a large amount of data other than that provided by the GOLF instrument is available too and form an important source of information to be analyzed, as for instance the observations by the GONG and BiSON ground-based telescope networks. From a theoretical point of view, it will be also important in the future to reduce the large uncertainties in the amplitude modeling in order to make a relevant comparison (e.g., the plume time evolution profile at the base of the convective zone). Another point will be to extend this result to a higher frequency range around 100 μHz and 400 μHz. While this is challenging since it requires to fully accounting for the complex interaction between the modes and the turbulent convection (e.g., Belkacem 2011), the solar oscillation modes in this frequency range have the advantage to be mixed modes. These modes can propagate in the inner radiative zone, where they behave as gravity modes, but also in the external layers, where they behave as acoustic modes. The solar mixed modes thus represent particular target as their surface amplitude is expected to be higher than the pure gravity modes at lower frequencies that are evanescent in the external layers of the Sun.

The author warmly thanks T. Appourchaux, G. Buldgen, M.-A. Dupret and K. Belkacem for their active role in the investigation. This work was funded by a postdoctoral fellowship of Chargé de Recherche from F.R.S.-FNRS (Belgium).

References

Alvan, L., Brun, A. S., & Mathis, S. 2014, A&A, 565, A42

Appourchaux, T., Belkacem, K., Broomhall, A.-M., et al. 2010, A&A Rev., 18, 197

Appourchaux, T., Fröhlich, C., Andersen, B., et al. 2000, ApJ, 538, 401

Belkacem, K. 2011, Amplitudes of Solar Gravity Modes, ed. J.-P. Rozelot & C. Neiner, Vol. 832, 139

Belkacem, K., Samadi, R., Goupil, M. J., et al. 2009, A&A, 494, 191

Borexino Collaboration, Agostini, M., Altenmüller, K., Appel, S., et al. 2020, Nature, 587, 577

Buldgen, G., Salmon, S., & Noels, A. 2019, Frontiers in Astronomy and Space Sciences, 6, 42

Dintrans, B., Brandenburg, A., Nordlund, Å., & Stein, R. F. 2005, A&A, 438, 365

Dziembowski, W. 1977, Acta Astron., 27, 203

Fossat, E., Boumier, P., Corbard, T., et al. 2017, A&A, 604, A40

Pinçon, C., Belkacem, K., & Goupil, M. J. 2016, A&A, 588, A122

Pinçon, C., Appourchaux, T., & Buldgen, G. 2021, A&A, 650, A47

Rieutord, M. & Zahn, J.-P. 1995, A&A, 296, 127

Salmon, S. J. A. J., Buldgen, G., Noels, A., et al. 2021, A&A, 651, A106

Samadi, R., Belkacem, K., & Sonoi, T. 2015, in EAS Publications Series, Vol. 73, EAS Publications Series, 111–191

Schunker, H., Schou, J., Gaulme, P., & Gizon, L. 2018, Sol. Phys., 293, 95

THE DIPPER STAR POPULATION OF TAURUS SEEN WITH K2

N. Roggero[1], J. Bouvier[1], L. M. Rebull[2] and A. M. Cody[3]

Abstract. During the evolution of T Tauri stars and the formation of their planetary systems, accretion processes play a key role. However, the more complex interaction at the rim of the inner region of the disk is still not well understood. Some young stars exhibit recurrent, quite irregular flux dips in their photometry (dippers). These can be explained as extinction events by dusty material from the protoplanetary disk, which is finally accreted onto the star. In the magnetospheric accretion scenario, the magnetic field of a young star truncates the disk where the magnetic field pressure is equal to the ram pressure of the accreting material. If the temperature close to this distance is low enough to avoid dust sublimation, dust might be lifted above the disk plane and obscure the star. The dataset for this study consists of K2 light curves (C4 and C13) of the Taurus region, which was observed continuously for ∼80 days. The stars classified as dippers have spectral types K4-M6, consistent with studies in other regions, and the mass range goes down to the brown dwarf limit. The co-rotation radii can be derived to a few stellar radii, with temperatures at corotation < 1600 K, that indicates that in most cases dust could survive at corotation. Temperatures close to 1600 K give some constraints about the dust composition. Magnetospheric accretion can account for most of the light curves. However, for some dippers, also other phenomena might cause eclipses.

Keywords: protoplanetary disks, stars: pre-main sequence, stars: variables: T Tauri, accretion, accretion disks, techniques: photometric

1 Introduction

Classical T Tauri stars (CTTSs) are low-mass, pre-main-sequence stars. They are $\sim 10^6$ Myr old and are surrounded by a protoplanetary disk, from which they accrete gas and dust in its inner region. The star-disk interaction is regulated by the stellar magnetic field, which truncates the disk at distances < 0.1 AU and drives accretion along the magnetic field lines. CTTSs display a strong variability in both their spectra and their light curves. Many physical mechanisms have been proposed to explain this variability, such as accretion hotspots, accretion bursts, or occultations by dusty structures in the disk (e.g., Cody et al. 2014; Alencar et al. 2010; Bouvier et al. 2003). This talk focuses on a class of variable stars that show dips in their light curve, the so-called 'dippers' . The dips present an irregular shape and can be quasiperiodic or aperiodic. They are mostly of late spectral type (K to M) and seem to be fairly common among CTTSs, with occurrences of 20% to 40% of young stars. AA Tau was the first dipper studied in detail. Bouvier et al. (1999, 2007) proposed that the magnetic field lines, close to the truncation radius, could lift dust above the disk midplane, and that an observer would see dips in the light curve whenever the dust crossed the line of sight. The temperature in this region must be low enough for the dust to survive at this distance, and the inclination of the system sufficiently high for the observer to look through the dusty structure (Bodman et al. 2017). Photometric observations can thus help to better understand the accretion processes and the inner disk structure on scales that are still challenging to resolve directly with interferometry.

[1] Univ. Grenoble Alpes, CNRS, IPAG, 38000 Grenoble, France
[2] Infrared Science Archive (IRSA), IPAC, 1200 E. California Blvd., California Institute of Technology, Pasadena, CA 91125, USA
[3] SETI Institute, 189 N Bernardo Ave. Suite 200, Mountain View, CA 94043 USA

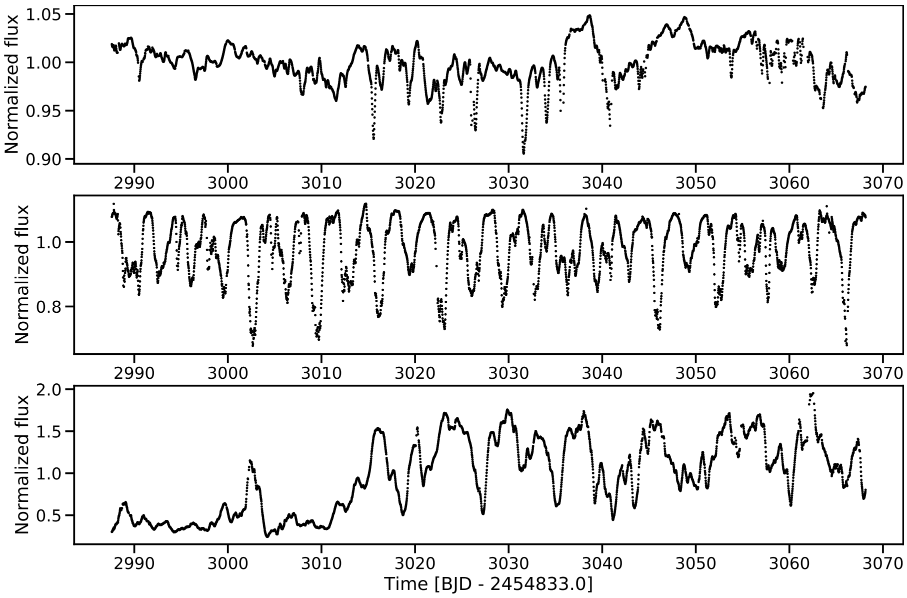

Fig. 1. Examples of an aperiodic dipper (HD 285893, top) a quasiperiodic dipper (JH223, center), and a dipper with a rather complex light curve (DK Tau, bottom).

2 Observations and data reduction

The Taurus region was observed nearly continuously with the Kepler satellite within the framework of the K2 mission (Howell et al. 2014), with a cadence of 29.4 min and a duration of ~ 80 days. The observation campaigns C13 (Mar - May 2017) and C4 (Feb - Apr 2015) delivered light curves for about 900 potential members. K2 data are challenging to reduce and several pipelines are available for this purpose. We compared different reduction pipelines and if the light curve did not present particular issues, we used the version with moving aperture as in Cody & Hillenbrand (2018) as default for consistency. The process to assess the membership of each star to the cluster is explained by Rebull et al. (2020). We attribute a higher-confidence membership to candidates which already appear as members in Luhman (2018). Finally, we searched for dippers in a sample of 156 members plus 23 possible members of Taurus.

3 Results

From the sample of members and possible members of Taurus, we identified 22 dippers, which are studied in more detail, and 12 additional dippers, which are dominated by another type of variability and display mostly aperiodic dips in their light curve (Roggero et al. 2021). This sums up to an occurrence of 20% among Taurus members, and of 30% among disked stars in the sample. This has to be considered as a lower limit to their true occurrence, due to both the observational limits (e.g., the system geometry) and the ephemerality of dippers. A majority of CTTSs might be a dipper at some point of its evolution.

Several properties of dippers are useful to gain information on the inner disk region and the star itself. All possible explanations for dippers converge on a dusty structure at the origin of the dips in the light curve. Thus, dip amplitude and dip width should provide hints on the geometry of this structure. At the same time, several other parameters allow to probe the different models. The hypothesis that the material provoking the occultation is corotating with the star can be probed by studying the dippers' periodicity, and comparing it to the stellar period. The temperature at the corotation radius should be below the dust sublimation temperature ($1500 - 1600\,\mathrm{K}$) and the viewing angle of the system can exclude certain dipper models.

3.1 Periodicities

For the aim of studying the periodicities of dippers, we used different algorithms: Lomb-Scargle periodogram (Rebull et al. 2020), CLEAN periodogram and wavelet analysis (Roggero et al. 2021). The latter method opens the possibility of time-resolved frequency analysis. Considering both the dipper sample studied in more detail and the dippers dominated by another variability (mostly cold stellar spots), the ratio of periodic to aperiodic dippers is of $\sim 1:1$. The periods are in the range of a few days, in accordance with the rotation periods of CTTSs, supporting the hypothesis of dust at corotation. In the case of the presence of both spots and dips in the light curve, the periods are slightly, yet not significantly different.

3.2 Dips' morphology

We identify dippers based on their light-curve morphology. This type of light curves presents irregularly shaped, sharp dips which can be aperiodic or quasiperiodic in their occurrence (Fig. 1). In order to study the dip morphology, we defined the dip amplitude as difference between the 90th and fifth percentile of flux of the detrended light curve. The amplitude of the dips can be influenced by, for example, the viewing angle, the height and the optical thickness of the dusty structure. We also defined a dip width as full width of half maximum of the detrended, phase-folded and then binned (that is, averaged) light curve (for more details, see Roggero et al. 2021). The dip width is a measure of the azimuthal extension of the occulting feature. We investigated whether dip width and dip amplitude correlate, as it might be expected following the model of the dusty disk warp (Bouvier et al. 1999), but we could not determine any correlation. However, we found a correlation between the dip width in units of phase and the dips' period, which was not found before (Roggero et al. 2021). It appears that the dip width increases with the period. This would imply that slow rotators are surrounded by azimuthally larger dusty warps. We speculate that large-scale magnetic fields might be at the origin of this correlation, by having a stabilizing effect on large warps.

3.3 Stellar parameters

We derived stellar luminosities by using photometric data from the literature, and effective temperatures by means of the conversion tables of Pecaut & Mamajek (2013). The resulting Hertzsprung-Russel diagram is shown in Fig. 2. We used the evolutionary models of Baraffe et al. (2015), as they include the lowest stellar masses. Almost all dippers of the sample have masses $< 1\,\mathrm{M}_\odot$, with the lowest ones close to the brown-dwarf limit. Despite the large uncertainties on their age, the stars are spread around the 1 Myr isochrone. These parameters can be used to derive the extent of the corotation radius as in:

$$R_{\mathrm{cor}} = \frac{P}{2\pi}^{\frac{2}{3}} (GM_*)^{\frac{1}{3}}. \tag{3.1}$$

The corotation radii are located at a few stellar radii, as expected for dippers. We can verify whether dust can survive at this distance from the star with the following approximation:

$$T_{\mathrm{cor}} = 2^{-\frac{1}{2}} T_{\mathrm{eff}} \left(\frac{R_*}{R_{\mathrm{cor}}}\right)^{\frac{1}{2}}. \tag{3.2}$$

For all dippers, the temperatures at corotation are below 1600 K, which is considered as an upper limit for dust sublimation. We also derived stellar inclinations following:

$$v \sin i = \sin i \frac{2\pi R_*}{P}. \tag{3.3}$$

This parameter is crucial to probe the different models proposed for dippers, as they depend on the viewing angle of the system. In fact, the dusty material has to cross the observer's line of sight in order to produce dips in the light curve; at the same time, dust is not supposed to be present close to the stellar poles. The inner disk wall first proposed by Bouvier et al. (1999) for AA Tau requires high inclinations $\sim 70°$, while the generalization of the magnetospheric accretion model (Bodman et al. 2017) can account, under certain conditions, for inclinations down to $\sim 50°$. Dusty disk winds, which have been invoked to explain dippers at low inclination, seem to be observable at rather high inclinations close to $\sim 70°$ (Vinković & Čemeljić 2020). The dippers of this sample are seen under moderate to high inclination, thus compatible with the generalized magnetospheric accretion model, but with few exceptions. We also retrieved inclinations of the outer disk from the literature, as observed at mm wavelengths. In general, the star has a higher inclination than the outer disk. This might be due, on one hand, to the high uncertainty on $\sin i$, which grows with the inclination. On the other hand, recent observations point out that misalignments between inner and outer disk might be pretty common among CTTSs.

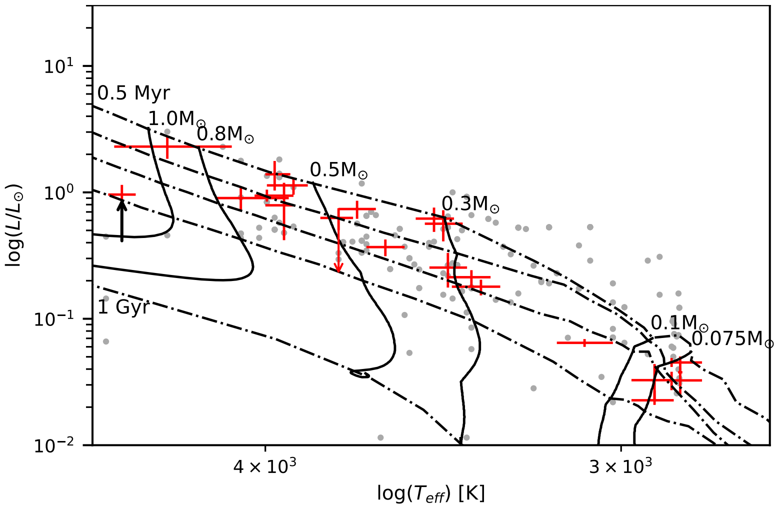

Fig. 2. Hertzsprung-Russell diagram of the studied sample of 22 dippers. The evolutionary tracks (solid lines) and the isochrones (dashed lines) are from Baraffe et al. (2015). Isochrones from top to bottom: 0.5, 1, 2, 5 Myr, and 1Gyr. The grey points represent other stars in Taurus as in Herczeg & Hillenbrand (2014). For the seek of readability, HD 285893 (spectral type F8) does not appear on this plot. All dippers are scattered around ~ 1 Myr and are fully convective, with the exception of LkCa 15 (indicated with an arrow).

4 Conclusions

We have searched for dippers in a sample of 156 + 23 Taurus members and found 22 dippers, with 12 additional dippers which display a different predominant variability. As a result, around 20% of Taurus members and 30% of disk-bearing stars in Taurus are dippers, as found also in surveys of other star-forming regions. This occurrence is a lower limit, due to the ephemerality of dippers and the observational constrains. The stars analyzed in this study are compatible with the presence of dust at corotation and magnetospheric accretion can account for most, but not all, dipper light curves. Future studies on this dipper sample will consider in more detail the cycle-to-cycle variation of the dips, which might provide a more complete picture of accretion and dust depletion on short time scales.

This project has received funding from the European Research Council (ERC) under the European Union's Horizon 2020 research and innovation programme (grant agreement No 742095; *SPIDI*: Star-Planets-Inner Disk-Interactions).

References

Alencar, S. H. P., Teixeira, P. S., Guimarães, M. M., et al. 2010, A&A, 519, A88
Baraffe, I., Homeier, D., Allard, F., & Chabrier, G. 2015, A&A, 577, A42
Bodman, E. H. L., Quillen, A. C., Ansdell, M., et al. 2017, MNRAS, 470, 202
Bouvier, J., Alencar, S. H. P., Boutelier, T., et al. 2007, A&A, 463, 1017
Bouvier, J., Chelli, A., Allain, S., et al. 1999, A&A, 349, 619
Bouvier, J., Grankin, K. N., Alencar, S. H. P., et al. 2003, A&A, 409, 169
Cody, A. M. & Hillenbrand, L. A. 2018, AJ, 156, 71
Cody, A. M., Stauffer, J., Baglin, A., et al. 2014, AJ, 147, 82
Herczeg, G. J. & Hillenbrand, L. A. 2014, ApJ, 786, 97
Howell, S. B., Sobeck, C., Haas, M., et al. 2014, PASP, 126, 398
Luhman, K. L. 2018, AJ, 156, 271
Pecaut, M. J. & Mamajek, E. E. 2013, ApJS, 208, 9
Rebull, L. M., Stauffer, J. R., Cody, A. M., et al. 2020, AJ, 159, 273
Roggero, N., Bouvier, J., Rebull, L. M., & Cody, A. M. 2021, A&A, 651, A44
Vinković, D. & Čemeljić, M. 2020, MNRAS

SF2A 2021
A. Siebert, K. Baillié, E. Lagadec, N. Lagarde, J. Malzac, J.-B. Marquette, M. N'Diaye, J. Richard, O. Venot (eds)

SCATTERING PROPERTIES OF DUST IN PLANET-FORMING DISKS: FIRST RESULTS FROM A MICROWAVE ANALOGY EXPERIMENT

V. Tobon Valencia[1], F. Ménard[2], A. Litman [1], J.-M. Geffrin [1], H. Tortel [1] and J. Milli [2]

Abstract.
The agglomeration process of dust in protoplanetary disks is a key element to understand the formation of planets. However, important information is still missing, e.g., the shape, structure and composition of the dust. Several ways to study the properties of these dust exist: observations, numerical simulations, and laboratory measurements. This paper is focused on laboratory measurements and simulations using the the microwave analogy. The phase function and degree of linear polarization of fractal-like aggregates and particles with rough surfaces are studied. Measurements and simulations show that each type of analogs has its own typical scattering properties. Future work will be focused on two more detailed studies of fractal-like aggregates and rough surfaces.

Keywords: microwave analogy, scattering properties, phase function, degree of linear polarization, analogs, rough surfaces, fractal-like aggregates, protoplanetary dust.

1 Introduction

The microwave analogy is a well-known method relying on the Scale Invariance Rule (SIR) that has been used to measure the scattering properties of objects that would otherwise be difficult to manipulate individually (Greenberg et al. 1961). The SIR states that the scattering properties of analog particles measured at a different wavelength are equivalent to those of the original particles of the same shape, as long as the refractive index and the size-to-wavelength ratio (or size parameter: $X = 2\pi r/\lambda$) are conserved.

The present work uses the SIR and the micro-wave analogy experiment at Institut Fresnel in Marseille to study the scattering properties of analogs of dust found in the Solar System and in planet-forming disks, the ultimate goal being to provide direct observational constraints on the first phases of planet assembly, when tiny solid particles start to grow and form larger bodies. Different studies have suggested that aggregates and particles with rough surfaces can be found in different astronomical environments like comets (Güttler et al. 2019) , debris disks (Milli et al. 2017), and protoplanetary disks (Min et al. 2016). However, the only way to directly measure the dust in these disks is through observations and analysis of the scattered light. For this reason the proper characterisation of the scattering properties of different type of particles is of utmost importance. This is the goal of the present study.

To reach this goal we have considered two types of analogs: fractal-like aggregates (aggregates with a finite number of monomers) and compact particles with rough surfaces (Renard et al. 2021). These analogs were produced by additive manufacturing where the possibility to control their shape, structure, and refractive index is unique, and a definite advantage over other measurement laboratory methods. In this paper, we summarize our first results on these protoplanetary dust analogs. We detail how they are produced, what the measurement conditions are, and the scattering results. In particular, the Intensity phase function and degree of linear polarization are presented, i.e., the elements S11 and -S12/S11 of the Mueller matrix, respectively. These measurements are compared to our numerical model (Voznyuk et al. 2015) to validate the method and highlight their distinctive features. The ultimate goal is to retrieve the particles' properties like the surface roughness, fractal dimension (D_f), porosity and others. These results are the first laboratory measurements of protoplanetary dust disks analogs with controlled structures using the microwave analogy.

[1] Aix Marseille Univ, CNRS, Centrale Marseille, Institut Fresnel, Marseille, France
[2] Univ. Grenoble Alpes, CNRS, IPAG, F-38000 Grenoble, France

2 Analogs

Two types of analogs were produced: fractal aggregates and compact particles with rough surfaces. To produce these analogs, a computer-aided design is followed by 3D printing. Virtual generation of fractal aggregates was based on the Diffusion Limited Aggregation software (DLA) developed by Wozniak et al. (2012). This software uses a particle-cluster aggregation scheme. All our aggregates are made of 74 monomers, each with a radius of 2.75 mm (overlapping of 10% between monomers), and a fractal prefactor of $k_0 = 1.593$. Five different fractal dimensions were printed $D_f = 2.8$, 2.5, 2.0, 1.7 and 1.5 with radius of gyration of 9.83 mm, 11.60 mm, 17.03 mm, 23.92 mm and 32.30 mm, respectively. Particles with rough surfaces were created from spheres of diameter 32.35 mm with a surface meshed with triangles. The distance between the center of the sphere and the vertex of each triangle were randomly modified to create the surface roughness. In total, five different surfaces were made with different levels of roughness.

Then, both types of analogs were printed using an additive manufacturing process named stereolithography (SLA). SLA works using a liquid acrylic resin that is photo-polymerized layer by layer by a UV laser. The resin used to print aggregates and rough surfaces had a refractive index of $1.7 + i0.03i$ (for more information see Renard et al. (2021)).

3 Measurement setup

Microwave analog measurements were performed in Marseille in the anechoic chamber of "Centre Commun de Ressources en Micro-Ondes". Wavelengths between 100mm and 16 mm (corresponding to frequencies of 3 GHz to 18 GHz) were used to measure all analogs. Emitter and receiver antennas worked at the same states of polarization, horizontal and then vertical; mixing these two polarizations non-polarised incident waves were obtained. The configuration that was used during measurements was a forward type configuration which corresponded to scattering angles (θ) from 0° to 130° (for more information see Geffrin et al. (2012)).

4 Results

The phase function S_{11} and the degree of linear polarization $-S_{12}/S_{11}$ were studied for both types of analogs. Measurements and finite element (FEM) simulations were compared for 16 different wavelengths from 100 to 16 mm. Here we present only four wavelengths: 60, 30, 20 and 16.7 mm.

For the fractal-like aggregates, results for the lowest, $D_f = 1.5$, and largest, $D_f = 2.8$, fractal dimensions are presented. They correspond to particles with an intermediate size parameter of $X_{int} = 6.77$ and $X_{int} = 2.06$, calculated with the radius of gyration of each aggregate at $\lambda = 30$ mm. The comparison of the scattering properties of the five fractal analogs will be published in Tobon Valencia et al. (2021).

The phase functions are illustrated in figure 1. Measurements and FEM simulations have the same behavior and amplitude levels. The difference between the phase function of the smallest and biggest fractal dimension is the number of lobes in the curves. For $D_f = 1.5$ there is one lobe while for $D_f = 2.8$ there are up to four lobes. In terms of the degree of linear polarization, shown in figure 2, there is also a difference between these two like-fractal aggregates. For $D_f = 1.5$ all four wavelengths have a Rayleigh-like behavior while for $D_f = 2.8$ the Rayleigh behavior is only present at $\lambda = 60$mm; the other three wavelengths have an oscillating behavior.

For the five particles with rough surfaces, only the roughest and smoothest ones are presented here. They also have an intermediate size parameter of $X_{int} = 3.4$. The full analysis of all particles will be published later. As can be seen in figure 3 the phase function of these two surfaces produce similar measurements of S_{11}. However, significant differences can be seen in $-S_{12}/S_{11}$, the linear polarisation. Figure 4 presents the differences between the degree of linear polarization of these two surfaces. The $-S_{12}/S_{11}$ parameter of the least rough surface has a more important amplitude of oscillation at all the scattering angles, compared to the roughest surface.

5 Conclusions

Simulations are in good agreement with measurements of phase functions and degrees of linear polarization for all four analogs, providing a cross-validation of these results. There are evident differences between aggregates of different fractal dimensions in both scattering properties: S_{11} and $-S_{12}/S_{11}$. In terms of rough surfaces, the degree of linear polarization is the scattering property with the most differences. In summary, the four analogs

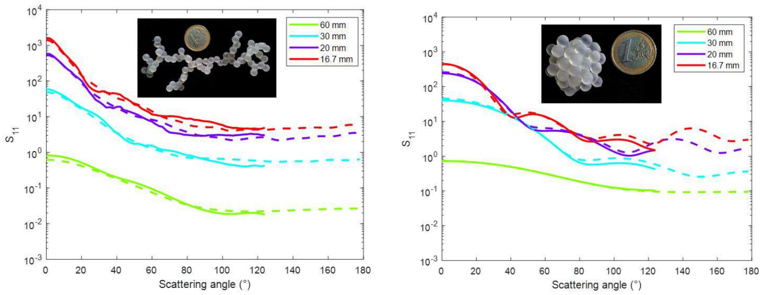

Fig. 1. Phase function of fractal-like aggregates for measurements (plain lines) and simulations (dashed line) at four different colours representing the wavelengths. **Left:** $D_f = 1.5$. **Right:** $D_f = 2.8$.

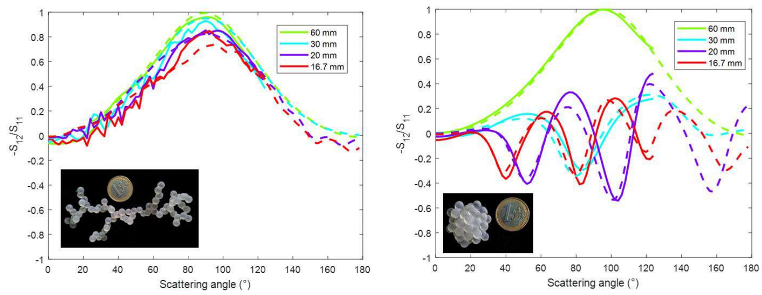

Fig. 2. Degree of linear polarization of fractal-like aggregates for measurements (plain lines) and simulations (dashed line) at four different colours representing the wavelengths. **Left:** $D_f = 1.5$. **Right:** $D_f = 2.8$.

studied here have different signatures. This is of essential importance for future comparisons of our analogs with protoplanetary dust.

The authors acknowledge the financial support of: PNPS, PNP, PCMI and CNRS-80|Prime.

References

Geffrin, J. M., García-Cámara, B., Gómez-Medina, R., et al. 2012, Nature Communications, 3

Greenberg, J. M., Pedersen, N. E., & Pedersen, J. C. 1961, Journal of Applied Physics, 32, 233

Güttler, C., Mannel, T., Rotundi, A., et al. 2019, 630, 1

Milli, J., Vigan, A., Mouillet, D., et al. 2017, Astronomy and Astrophysics, 599, 1

Min, M., Rab, C., Woitke, P., Dominik, C., & Ménard, F. 2016, Astronomy and Astrophysics, 585, 1

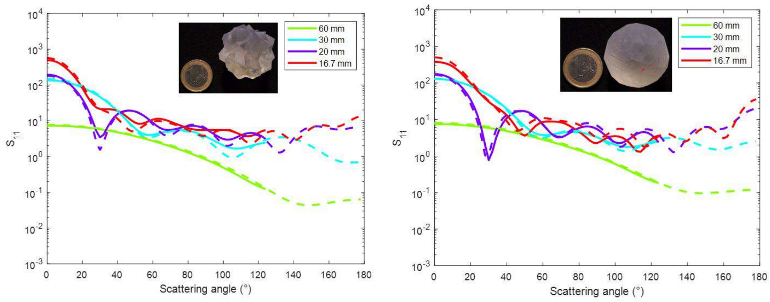

Fig. 3. Phase function of rough surfaces for measurements (full lines) and simulations (dashed line) at four different colours representing the wavelengths. **Left:** the roughest surface. **Right:** the smoothest surface.

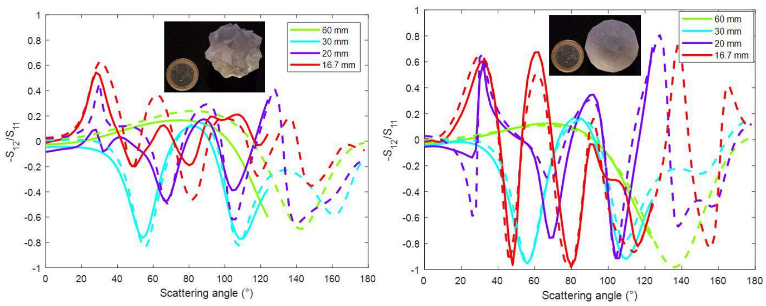

Fig. 4. Degree of linear polarization of rough surfaces for measurements (full lines) and simulations (dashed line) at four different colours representing the wavelengths. **Left:** the most rough surface. **Right:** the least rough surface.

Renard, J.-B., Geffrin, J.-M., Tobon Valencia, V., et al. 2021, Journal of Quantitative Spectroscopy and Radiative Transfer, 272

Voznyuk, I., Tortel, H., & Litman, A. 2015, IEEE Transactions on Antennas and Propagation, 63, 2604

Wozniak, M., Onofri, F. R., Barbosa, S., Yon, J., & Mroczka, J. 2012, Journal of Aerosol Science, 47, 12

ELECTRON THERMAL ESCAPE INSIDE THE SUN

V. Bommier[1]

The magnetic field vector observations in the solar photosphere systematically display a non-zero value of the divergence whatever the observation spatial resolution is. The vertical gradient is found on the order of 3 G km^{-1} when the horizontal gradient is found on the order of 0.3 G km^{-1} only. The difference is much larger than the measurement uncertainties. It must then be recalled that the quantity measured by interpretation of the Zeeman effect is the magnetic field $\vec{H}$. Four demonstrations can be found in Bommier (2020), also available at `https://doi.org/10.1051/0004-6361/201935244`. The magnetic field $\vec{H}$ is related to the divergence-free magnetic *induction* $\vec{B}$ by the law $\vec{B} = \mu_0(\vec{H} + \vec{M})$, where $\vec{M}$ is the magnetization. In plasmas like solar photosphere, magnetization results from plasma diamagnetism, which is due to spiral movement of charged particles about the magnetic field. However, the usually admitted value of the electron and charge density, although not directly determined, leads to very weak magnetization. It has to be remarked that in the solar interior the electron thermal velocity is 14 times larger than their escape velocity, and also 6 times larger than their escape velocity from protons. However, when the electron density decreases by escape, the proton keeping effect increases. The electron escape is however very slow and results in accumulation in surface layers. The order of magnitude of the observed magnetic field gradient is recovered from the height estimated decrease of the electron density and from $\mathrm{div}\vec{H} = -\mathrm{div}\vec{M}$. This model is presented in Bommier (2020). Such a structure is probably at play in solar type stars, with electric fields because protons do not escape. The solar and stellar MHD has to adapt to the fact that what is measured is $\vec{H}$ and not $\vec{B}$, which has to be related to the second Maxwell equation $\mathrm{curl}\vec{H} = \vec{j}$.

References

Bommier, V. 2020, A&A, 634, A40

[1] LESIA, Observatoire de Paris, Université PSL, CNRS, Sorbonne Université, Université de Paris, 5 place Jules janssen, 92195 Meudon, France, V.Bommier@obspm.fr

SEISMIC DIAGNOSIS FOR RAPIDLY ROTATING G-MODE UPPER-MAIN-SEQUENCE PULSATORS: THE COMBINED EFFECTS OF THE CENTRIFUGAL ACCELERATION AND DIFFERENTIAL ROTATION

H. Dhouib[1], V. Prat[1], T. Van Reeth[2] and S. Mathis[1]

Abstract. We generalise the traditional approximation of rotation (TAR) to take into account simultaneously the centrifugal deformation in a non-perturbative way and a general 2D differential rotation. We show how they affect the pulsation-period spacings between consecutive g-mode pulsations and we discuss their detectability using high-precision asteroseismic data.

Keywords: hydrodynamics, waves, stars: rotation, stars: oscillations

1 Introduction

The traditional approximation of rotation (TAR) is a treatment of the hydrodynamic equations of rotating and stably stratified fluids in which the horizontal projection of the rotation vector is neglected. This treatment makes it possible to preform intensive seismic forward modelling. This gives access to properties of chemical stratification and to the rotation rate near the convective core/radiative envelope interface of rapidly rotating intermediate-mass stars thanks to the high precision of space-based photometric observations (Aerts 2021). This approximation is applicable for low-frequency gravito-inertial waves (GIWs) propagating in strongly stratified zones of uniformly rotating spherical stars (Bildsten et al. 1996; Lee & Saio 1997). However, it has been generalised first to include the effects of general differential rotation (Mathis 2009; Van Reeth et al. 2018) and then to take the centrifugal acceleration into account for slightly deformed stars using a first-order perturbative approach (Mathis & Prat 2019; Henneco et al. 2021). Here, we generalise the TAR to take into account simultaneously the centrifugal deformation in a non-perturbative way and the general differential rotation.

2 Generalised TAR

Spheroidal geometry To account for the centrifugal deformation in a non-perturbative manner, we use the spheroidal coordinate system (ζ, θ, φ) proposed by Bonazzola et al. (1998) linked to the usual spherical one via a mapping, where ζ is the pseudo-radius, θ the colatitude and φ the azimuth.

To treat the wave dynamics in differentially rotating, strongly deformed stars, we first derive the complete adiabatic inviscid system of equations in spheroidal coordinates (we adopt the Cowling and the anelastic approximations). Then, by assuming the hierarchies of frequencies: $2\Omega \ll N$ and $\omega \ll N$ (where Ω is the angular velocity, N the Brunt-Väisälä frequency and ω the frequency of the waves in the rotating frame) and the resulting velocity scales ($|v^{\zeta}| \ll \{|v^{\theta}|, |v^{\varphi}|\}$), we built the generalised framework for the TAR. In fact, we derive the generalised Laplace tidal equation (GLTE) for the normalised pressure $w_{\omega^{\rm in}km}$ (the generalised Hough functions) by adopting the JWKB approximation where m is the azimutal order, k is the index of an eigenmode, $\Lambda_{\omega^{\rm in}km}$ are the eigenvalues, ν the spin parameter and $x = \cos\theta$ the reduced latitudinal coordinate

$$\begin{aligned}\mathcal{L}_{\omega^{\rm in}m}\left[w_{\omega^{\rm in}km}\right] = \omega\partial_x\left[\frac{1}{\omega}\frac{1}{\mathcal{B}(\mathcal{E}-\mathcal{F})}\left(\mathcal{E}+\frac{\nu^2\mathcal{C}^2}{\mathcal{B}}\right)\left(1-x^2\right)\partial_x\right]w_{\omega^{\rm in}km} - \frac{m\mathcal{F}}{\nu\mathcal{C}(\mathcal{E}-\mathcal{F})}\partial_x w_{\omega^{\rm in}km} \\ + \left(m\omega\partial_x\left(\frac{\nu\mathcal{C}}{\omega\mathcal{B}(\mathcal{E}-\mathcal{F})}\right) - \frac{m^2}{(\mathcal{E}-\mathcal{F})\left(1-x^2\right)}\right)w_{\omega^{\rm in}km} = -\Lambda_{\omega^{\rm in}km}(\zeta)w_{\omega^{\rm in}km}, \quad (2.1)\end{aligned}$$

[1] Département d'Astrophysique-AIM, CEA/DRF/IRFU, CNRS/INSU, Université Paris-Saclay, Université de Paris, F-91191 Gif-sur-Yvette, France
[2] Institute of Astronomy, KU Leuven, Celestijnenlaan 200D, 3001 Leuven, Belgium

where $\mathcal{B}$, $\mathcal{C}$, $\mathcal{D}$ and $\mathcal{E}$ are the coefficients that describe the geometry and the rotation. This equation allows us to derive the asymptotic frequencies of GIWs which is a great asset to perform detailed seismic modelling.

3 Application to 2D ESTER models

To implement our equations, we use the ESTER model (Espinosa Lara & Rieutord 2013) the most advanced 2D model of stellar structure and evolution that takes both the centrifugal and Coriolis accelerations into account.

Validity domain: The generalised TAR is applicable in all the space domain to early-type stars rotating up to $\Omega/\Omega_K = 0.2$ (Fig. 1, left panel). This formalism can be applied to all rapidly rotating bodies (stars of all types and planets) as long as we have a 2D model with access to the quantities that we used to solve the GLTE.

Period spacing pattern and detectability: The centrifugal acceleration and the differential rotation cause a shift in the period spacing pattern (Fig. 1, middle panel). In fact, the centrifugal effect is not important when assessed within the validity domain of the generalised TAR whereas the differential rotation effect is, theoretically, largely detectable using TESS and *Kepler* observations (Fig. 1, right panel). Despite their theoretical detectability, these effects will be subtle to detect in the real data because of their small amplitudes.

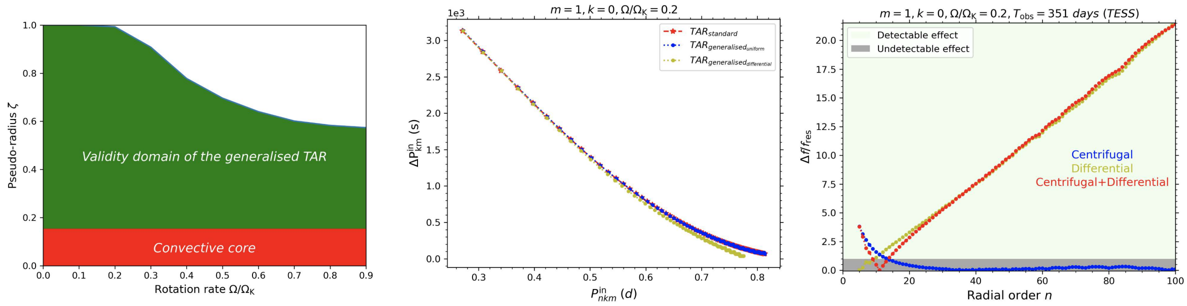

Fig. 1. Left: Validity domain of the generalised TAR for a $3\,M_\odot$ ESTER model. **Middle:** Period spacing pattern in the inertial frame. **Right:** Detectable radial orders n for a $\{k = 0, m = 1\}$ mode using TESS.

4 Conclusion

A new generalisation of the TAR designed for 2D stellar models like ESTER, which takes into account simultaneously the differential rotation and the centrifugal acceleration in a non-perturbative way, is derived. This generalisation allows us to study the detectability and the signature of the centrifugal effects on GIWs in differentially rotating deformed early-type stars which are theoretically detectable in asteroseismic data.

We thank the ESTER code developers for their efforts and for making their codes publicly available. We are also grateful to Pr. C.Aerts for helpful suggestions regarding our work. H.D., V.P. and S.M. acknowledge support from the European Research Council through ERC grant SPIRE No. 647383. H.D. and S.M. acknowledge support from the CNES PLATO grant at CEA/DAp. TVR gratefully acknowledges support from the Research Foundation Flanders (FWO) under grant agreement No. 12ZB620N.

References

Aerts, C. 2021, Rev. Mod. Phys., 93, 015001
Bildsten, L., Ushomirsky, G., & Cutler, C. 1996, ApJ, 460, 827
Bonazzola, S., Gourgoulhon, E., & Marck, J.-A. 1998, Phys. Rev. D, 58, 104020
Espinosa Lara, F. & Rieutord, M. 2013, A&A, 552, A35
Henneco, J., Van Reeth, T., Prat, V., et al. 2021, A&A, 648, A97
Lee, U. & Saio, H. 1997, ApJ, 491, 839
Mathis, S. 2009, A&A, 506, 811
Mathis, S. & Prat, V. 2019, A&A, 631, A26
Van Reeth, T., Mombarg, J. S. G., Mathis, S., et al. 2018, A&A, 618, A24

CHARACTERIZING THE STELLAR-SUBSTELLAR LIMIT: A STEP TOWARDS A BETTER UNDERSTANDING OF THE ULTRA-COOL DWARFS REVEALED BY GAIA

A. Ficot[1], C. Reylé[1], N. Lagarde[1], R. L. Smart[2] and A. J. Burgasser[3]

Abstract. Ultra-cool dwarfs (spectral type later than M7) serve as a link between stars and brown dwarfs which have not a sufficient mass to support the combustion of hydrogen. Although they are numerous in the Galaxy, they remain elusive due to their low luminosity and the modelling is still a chalenge. In this work we characterized 120 ultra-cool dwarfs revealed by *Gaia* for which spectroscopic monitoring have been obtained using various instruments of medium spectral resolution. Our results illustrate the impact of physics considered in atmospheric models on the characterization of these objects.

Keywords: stars: low-mass, ultra-cool dwarfs, brown dwarfs, spectroscopy

1 Analysis method

Thanks to its photometric and astrometric accuracy, the *Gaia* satellite (Gaia Collaboration et al. 2016) has revealed several tens of thousands of ultra-cool dwarfs (Reylé 2018; Smart et al. 2020; Scholz 2020). The spectroscopic follow-up has started for the closest ones. In order to confirm their spectral type and derive their effective temperature, we have compared our observed spectra with standard and synthetic spectra using the SpeX Prism Library Analysis Toolkit (*SPLAT,* Burgasser & Splat Development Team 2017).

The best fit is shown for four of our targets in Fig. 1 on the left panel. Spectral types are obtained from the best fit with a library of standard spectra (in blue). Effective temperature are obtained from the best fit with a grid of atmopshere models (in orange). For that, we have used five different grids computed from the recent atmosphere model *Bt-Settl* (Allard 2014) and *Drift* (Witte et al. 2011). They considere different physics: taking in count or not the results of radiation hydrodynamic simulations on the mixing length and considering different solar abundances (Asplund et al. 2009; Caffau et al. 2011; Grevesse et al. 1992).

2 Results

The spectral types we have obtained confirm the nature of our sample (excepted for a few low signal-to-noise spectra or bad pointing to a brighter, close star). The derived effective temperatures from the most recent *Bt-Settl* grid (Baraffe et al. 2015) are shown as a function of spectral type in Fig. 1 on the right panel (orange). Our work completes results of previous other studies (Schweitzer et al. 2003; Testi 2009; Rajpurohit et al. 2013; Pecaut & Mamajek 2013; López-Valdivia et al. 2019) (in gray on Fig. 1 on the right panel) to build the calibration relation $T_{\rm eff}$ vs spectral type.

As mentionned above, we also derive effective temperatures assuming different grids of synthetic spectra. Depending on the solar abundances assumed in the models, the variation of temperature can go up to 1000 K. If we now compare the models with different physics but same solar abondance, the variation is a little lower but can still go up to 600 K. These descrepancies are most important for the spectral type range M9 to L2, where the beginning of dust sedimentation in the atmosphere occurs and is a complex physic to model.

[1] Institut UTINAM CNRS UMR6213, Université Bourgogne Franche-Comté, OSU THETA Franche-Comté Bourgogne, Observatoire de Besançon, BP1615, 25010 Besançon Cedex, France
[2] INAF - Osservatorio Astrofisico di Torino, via Osservatorio 20, 10025 Pino Torinese (TO), Italy
[3] Center for Astrophysics and Space Science, University of California San Diego, La Jolla, CA 92093, USA

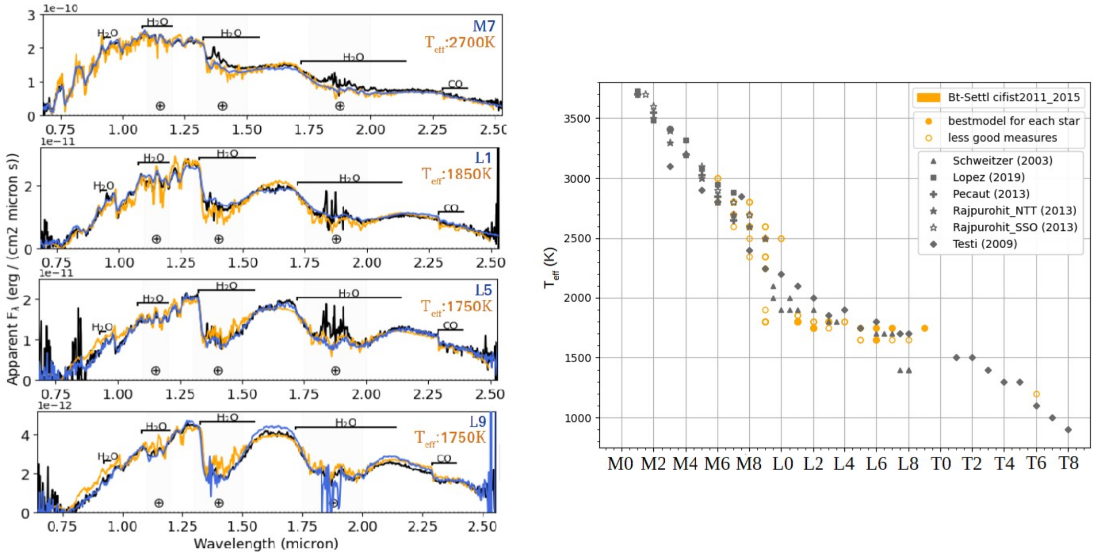

Fig. 1. Left: Comparison of four observed spectra (black) with the best fit by a standard spectral type (blue) and synthetic spectrum *BT-Settl*/cifist2011_2015 (Baraffe et al. 2015) (orange). **Right:** Effective temperature as a function of spectral type for our sample (orange) and previous other studies (gray). Markers are filled when this model shown here has the best χ^2.

3 Conclusions

This work is a first step towards a systematic analysis of a large numbers of brown dwarfs revealed by the Gaia satellite and will allow a better understanding of these stars that are difficult to characterize, the determination of stellar parameters being very sensitive to models atmosphere used. A better understanding of these objects is essential in the framework of future space missions, such as EUCLID which will detect more than hundreds of thousands of brown dwarfs, to the coldest and in the different populations of the Galaxy.

This study is a part of a work done during a master 2 internship at the institut Utinam, 25000 Besançon, France. Other figures are shown in the poster made during the sf2a days on `https://www.carbonfreeconf.com/website/139/posters`.

References

Allard, F. 2014, in Exploring the Formation and Evolution of Planetary Systems, ed. M. Booth, B. C. Matthews, & J. R. Graham, Vol. 299, 271–272

Asplund, M., Grevesse, N., Sauval, A. J., & Scott, P. 2009, ARA&A, 47, 481

Baraffe, I., Homeier, D., Allard, F., & Chabrier, G. 2015, A&A, 577, A42

Burgasser, A. J. & Splat Development Team. 2017, in Astronomical Society of India Conference Series, Vol. 14, Astronomical Society of India Conference Series, 7–12

Caffau, E., Ludwig, H. G., Steffen, M., Freytag, B., & Bonifacio, P. 2011, Sol. Phys., 268, 255

Gaia Collaboration, Prusti, T., de Bruijne, J. H. J., et al. 2016, A&A, 595, A1

Grevesse, N., Noels, A., & Sauval, A. J. 1992, in ESA Special Publication, Vol. 348, Coronal Streamers, Coronal Loops, and Coronal and Solar Wind Composition, ed. C. Mattok, 305–308

López-Valdivia, R., Mace, G. N., Sokal, K. R., et al. 2019, ApJ, 879, 105

Pecaut, M. J. & Mamajek, E. E. 2013, ApJS, 208, 9

Rajpurohit, A. S., Reylé, C., Allard, F., et al. 2013, A&A, 556, A15

Reylé, C. 2018, A&A, 619, L8

Scholz, R. D. 2020, A&A, 637, A45

Schweitzer, A., Gizis, J. E., Allard, F., & Hauschildt, P. H. 2003, in Brown Dwarfs, ed. E. Martín, Vol. 211, 403

Smart, R. L., Marocco, F., Caballero, J. A., et al. 2020, VizieR Online Data Catalog, J/MNRAS/469/401

Testi, L. 2009, A&A, 503, 639

Witte, S., Helling, C., Barman, T., Heidrich, N., & Hauschildt, P. H. 2011, A&A, 529, A44

SF2A 2021
A. Siebert, K. Baillié, E. Lagadec, N. Lagarde, J. Malzac, J.-B. Marquette, M. N'Diaye, J. Richard, O. Venot (eds)

ZEEMAN DOPPLER IMAGING OF TWO HOT STARS

L.L. Fréour[1], C. Neiner[1] and C.P. Folsom[2]

Abstract. Magnetic fields are known to exist in about 10% of hot stars on the main sequence. High-resolution data and the increase in computing power have enabled the development of new methods to map and characterize stars. Zeeman-Doppler-Imaging (ZDI) is one of them and it allows one to determine the magnetic topology at the stellar surface. Through a modelling of the intensity and polarized line profiles, ZDI aims at reconstructing the vectorial magnetic field at the stellar surface. We have acquired high-resolution spectropolarimetric observations for two hot stars: the Bp star V352 Peg and the early-B star i Car. Through a Least-Square Deconvolution, we extracted the intensity and mean Zeeman signature of thousands of spectral lines. We have established the presence of a magnetic field in both stars. Using a python ZDI code, we mapped and characterized their magnetic field, revealing two completely different configurations. While V352 Peg exhibits a strong, dipolar field with a polar field strength of ~ 9 kG, i Car shows a weaker field strength and a more complex, significantly toroidal, field topology.

Keywords: stars: chemically peculiar – stars: magnetic field – stars: individual: V352 Peg, i Car – techniques: spectropolarimetry

1 V352 Peg and i Car

V352 Peg is an α^2 CVn star, first detected as a photometrically variable star by the Hipparcos mission (Perryman et al. 1997). With an effective temperature of 11850 ± 180 K and a gravity of $\log g = 4.35$ (Stassun et al. 2019), V352 Peg is a hot star in the early main sequence stage. Its period is found to be $P_{\rm rot} = 2.63654 \pm 0.00008$ days (Fréour et al. 2021).

i Car has an effective temperature and gravity of 18900 ± 500K and $\log g = 3.94$ (Levenhagen & Leister 2006), being thus hotter and more evolved than V352 Peg. Its rotation period of $P_{\rm rot} = 22.24$ days (Neiner et al. 2021) is much longer than that of V352 Peg.

We have acquired 17 spectropolarimetric observations of V352 Peg between 2018 and 2019 and one archival observation from 2011 with the ESPaDOnS spectropolarimeter at CFHT, and 34 spectropolarimetric observations of i Car in 2015 obtained with HARPSpol at ESO.

2 Zeeman-Doppler Imaging (ZDI)

The ZDI method aims to reconstruct the vectorial magnetic field at the stellar surface by fitting Stokes profiles I and V obtained from spectropolarimetric observations. Using the code by Folsom et al. (2018), we fit the Stokes I and V profiles of the two stars and studied their magnetic configurations.

The Stokes I profiles of V352 Peg vary with the rotation phase of the star (Fig. 1). This is not the case for i Car. This variability is due to an inhomogeneous distribution of chemical elements at the stellar surface, typical of chemically peculiar stars. A clear magnetic signature is visible in the Stokes V profiles of both stars, showing rotational modulation due to the misalignment between the stellar rotation and magnetic axes as described by the oblique rotator model.

Using ZDI, we could characterise the magnetic configuration of V352 Peg and i Car as well as the distribution of the magnetic energies. We estimated the inclination angle and the obliquity angle of V352 Peg to be $i =$

[1] LESIA, Paris Observatory, PSL University, CNRS, Sorbonne University, Université de Paris, 5 place Jules Janssen, 92195 Meudon, France
[2] University of Tartu, Faculty of Science and Technology, Tartu Observatory, Estonia

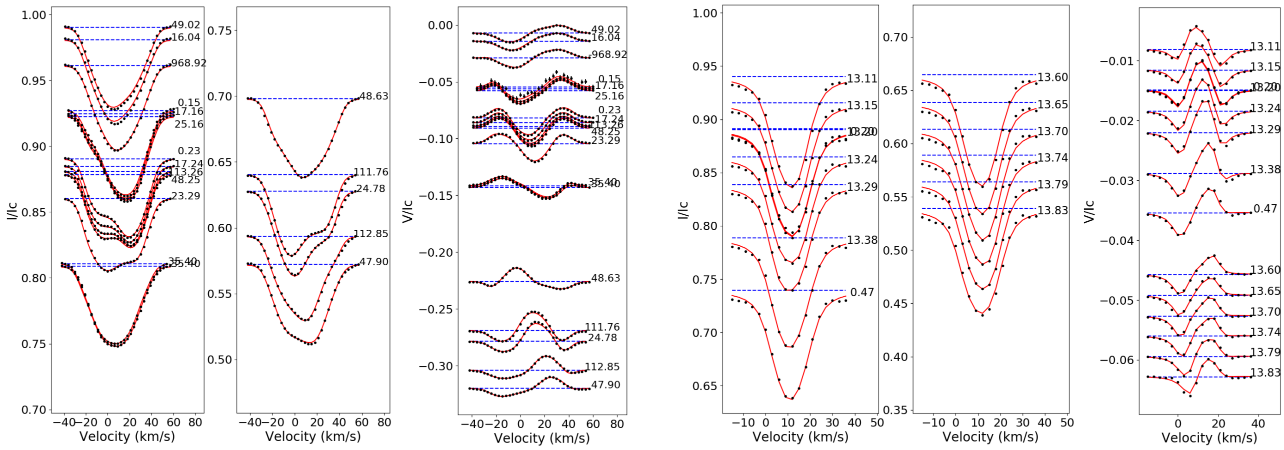

Fig. 1. Comparison between observed (black dots) and simulated (red lines) Stokes I (left 2 panels) and V (right) profiles of V352 Peg (left figure) and i Car (right figure). Taken from Fréour et al. (2021) and Neiner et al. (2021).

$62.5^{\circ}{}^{+4.0}_{-3.5}$ and $\beta = 100.5 \pm 4.0^{\circ}$. For i Car, we find $i = 54.2^{\circ}{}^{+3.6}_{-3.2}$ and $\beta = 137.5^{\circ}{}^{+4.2}_{-3.2}$. V352 Peg has a polar magnetic field strength of about 9 kG while it is only around 1 kG for i Car.

We also find differences in the distribution of the magnetic energies. While the magnetic field of V352 Peg is mainly poloidal (98.7%) and dipolar (91.6% of the poloidal field), the toroidal component of the magnetic field of i Car is dominant (71.5%) and the dipole percentage lower (76.3% of the toroidal field). The quadrupolar and octupolar components of the poloidal field (respectively 11.7% and 13.5%) of i Car contribute more to the total magnetic energy than in the case of V352 Peg (respectively 1.6% and 4.7%).

3 Conclusions

The results of our ZDI analysis show two clearly different magnetic configurations, highlighting the differences between the magnetic topology of a chemically-peculiar main-sequence star (V352 Peg) and a chemically-normal weaker-field star (i Car).

Based on observations obtained at the Canada-France-Hawaii Telescope (CFHT) which is operated by the National Research Council(NRC) of Canada, the Institut National des Sciences de l'Univers of the Centre National de la Recherche Scientifique (CNRS) of France, and the University of Hawaii. Based on observations obtained at the European Southern Observatory (ESO), Chile.

References

Folsom, C. P., Bouvier, J., Petit, P., et al. 2018, MNRAS, 474, 4956

Fréour, L. L., Neiner, C., Landstreet, J. D., Folsom, C. P., & Wade, G. A. 2021, MNRAS, submitted

Levenhagen, R. S. & Leister, N. V. 2006, MNRAS, 371, 252

Neiner, C., Fréour, L. L., Dalipi, R., Labadie-Bartz, J., & Folsom, C. P. 2021, MNRAS, in prep.

Perryman, M. A. C., Lindegren, L., Kovalevsky, J., et al. 1997, A&A, 500, 501

Stassun, K. G., Oelkers, R. J., Paegert, M., et al. 2019, AJ, 158, 138

SF2A 2021
A. Siebert, K. Baillié, E. Lagadec, N. Lagarde, J. Malzac, J.-B. Marquette, M. N'Diaye, J. Richard, O. Venot (eds)

THE CA II RESONANCE DOUBLET AND H$_\alpha$ FLUXES AS A FUNCTION OF STELLAR RADIUS: INDICATIONS FOR A TRANSITION IN DYNAMO MODES BETWEEN 0.500$R_\odot$ AND 0.330$R_\odot$.

E.R. Houdebine[1, 2]

Abstract. We report on the surface fluxes F_{HK} in the Ca II H & K lines and $F_{H\alpha}$ in the H$_\alpha$ line for 752 M dwarfs. Spectral sub-types range from M0.5 to M8.3. We plot the surface fluxes in these lines as a function of stellar radius and find that there is an important decrease between $0.500R_\odot$ and $0.330R_\odot$, i.e. spectral types dM1.2-dM3.4. This decrease is by a factor of 5.6 in F_{HK} for our sub-sample of low activity M dwarfs. Similar patterns are observed for our sub-sample of Me dwarfs, but with a somewhat smaller amplitude of 2.8. These radii correspond from partially convective early M dwarfs to approximately fully convective M dwarfs down to the Transition To Complete Convection (TTCC). We believe that we are observing the spectral signature of the progressive disapearance of the radiative core in M dwarfs, and therefore the progressive transition from an $\alpha - \Omega$ type of dynamo to an α^2 or/and $\alpha - \Omega$ type of dynamo.

Keywords: Stars: late-type dwarfs - Stars: Activity - Stars: Dynamo Mechanisms - Stars: Fundamental parameters

Ca II and H_α measures of the Equivalent Widths (EW) and surface fluxes.

Mullan & Houdebine (2020) investigated the Ca II line fluxes as a function of spectral type. They found an important decrease in surface fluxes between M1.1 and M8.3 for about 600 M dwarfs. However, spectral type is not the most appropriate parameter to diagnose the dynamo mechanisms since they depend on the stellar mass, and there is a scatter of about 5 in mass at a given spectral type. Therefore, we prefer here to invevestigate Ca II and H_α measures of the surface fluxes as a function of stellar radius for a stellar sample of 752 M dwarfs.

The method we used to measure the Ca II and H_α EWs have been described in Houdebine & Stempels (1997). The EWs are only a *relative* measure of the level of magnetic activity: they do not provide absolute measures of activity such as the surface fluxes ($ergs/s/cm2$) or the luminosities ($ergs/s$). We used the models of Allard et al. (2012). in order to transform the EWs into surface fluxes.

We found that most of the M dwarfs in our sample lie signicantly above the basal level, typically by a factor of 10 in F_{HK}. Therefore, we believe that most of our measures refer to the amount of non-thermal heating of magnetic origin in our sample of M dwarfs. Hence, the surface fluxes in the Ca II lines and H_α line are a direct measure of the amount of energy deposited by surface magnetic fields below 7000 K and between 7000 K and 8500 K repectively (e.g. Houdebine & Doyle 1994, Houdebine & Stempels 1997).

The Ca II lines: Low activity sub-sample

In order to plot our data as a function of radius, we choose bins with a width of $0.030R_\odot$. In Figure 1a, the mean value of F_{HK} for *each individual star* in our sample is plotted as a small dot. The mean values of F_{HK} for all stars in each of the 19 domains are plotted as large filled circles along with standard deviations in the mean.

Considering the scatter in the individual measures, which signicantly decreases as the radius decreases, the mean curve is remarkedly smooth. The mean curve is more or less flat between $0.711R_\odot$ and $0.605R_\odot$. Then the mean curve increases from $0.575R_\odot$ to $0.515R_\odot$. For stars with smaller radii, the mean curve shows a monotonic decrease in F_{HK} by a factor of 5.6 as we go from $\sim 0.500R_\odot$ to $\sim 0.330R_\odot$. At even smaller radii, the mean curve levels out between $\sim 0.330R_\odot$ and $\sim 0.100R_\odot$. These radii correspond on average to the spectral types M1.2 and M3.4.

[1] Université Paul Sabatier, OMP, CNRS, CNES, IRAP, F–31400 Toulouse, France
[2] Armagh Observatory & Planetarium, College Hill, BT 61 9DG, Northern Ireland

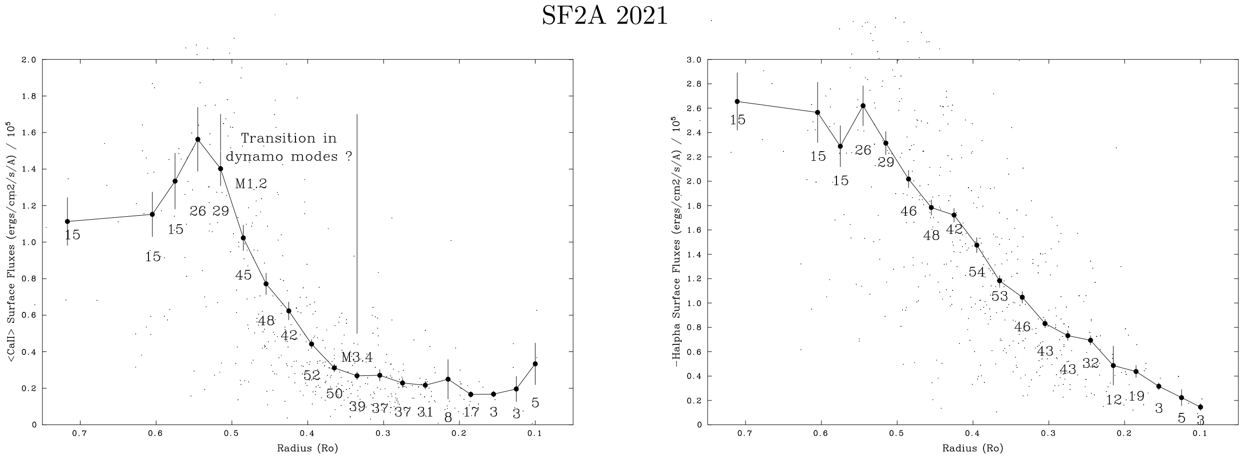

Fig. 1. Left: Values of the mean surface fluxes in the Ca II resonance doublet as a function of the mean stellar radius. The plotted uncertainties are a measure of the scatter of the measurements in each radius domain (3σ). The numbers plotted below each point indicate the number of stars in each sample. The curve first rises, then attains a maximum before it suddenly decreases markedly below $R_* < 0.500R_\odot$. This decrease continues down to $R_* \sim 0.330R_\odot$. The amplitude of the fall in surface fluxes is a factor of 5.6. We believe this transition reflects the internal effectiveness of the dynamo mechanisms in M dwarfs, and perheaps a progressive switch from an $\alpha\Omega$ type of dynamo and an α^2 or/and $\alpha^2\Omega$ types of dynamo ? **Right:** Values of the surface fluxes in the H_α line as a function of the mean stellar radius. The curve for H_α remains first rather constant down to the radius $\sim 0.500R_\odot$, then it decreases down to the smallest radii ($R_* < 0.100R_\odot$). The fall in surface fluxes has an amplitude of about a factor of 29 over a range of $\sim 0.400R_\odot$! This decrease is consistant with a decrease in column mass at about the transition region, i.e., with a decrease in activity levels starting approximately at $R_* \sim 0.500R_\odot$. Therefore the H_α line and Ca II line curves are more or less consistent in low activity M dwarfs.

The H_α line: Low activity sub-sample

The H_α line is an ambiguous diagnostic of magnetic activity in M dwarfs. However, it can provide some insights into the column density at the transition region when simultaneous Ca II line observations are available. For very low pressure chromospheres, the H_α line is absent in M dwarfs: there is no significant photospheric contribution (e.g. Houdebine & Stempels 1997). At first, if we consider low pressure chromospheres, the H_α line increases in absorption strength as the pressure increases. It reaches a maximum absorption which depends on the properties of the chromosphere. After reaching a maximum in absorption, it then "fills" in as the collisional control increases in the higher chromosphere. Eventually, it goes into emission, first in M(e) dwarfs (line filled in), and then in active dMe stars it is in emission: e.g. Houdebine & Stempels 1997. *Therefore, the H_α line is not a straightforward diagnostic of magnetic activity and the interpretation of the surface fluxes must be conducted with care.*

In dM stars, H_α is in absorption, and therefore has a negative EW, the plot in Fig. 1b plots -$F_{H\alpha}$ as a function of radius (same description as Fig. 1a). The curve of -$F_{H\alpha}$ in Fig. 1b is reminiscent of the F_{HK} curve in Fig. 1a. The curve from the radius $\sim 0.500R_\odot$ decreases down to the smallest radii ($R < 0.100R_\odot$). The decrease has an amplitude of about a factor of 29. This decrease is consistent with a decrease in column mass in the vicinity of the transition region, i.e., with a decrease in activity levels starting approximately at $R \sim 0.500R_\odot$.

Both the decreases in Ca II and H_α from $\sim 0.500R_\odot$ to $\sim 0.330R_\odot$ are consistent with a decrease in the level of magnetic activity between these radii. If one considers that in M1.2 dwarfs the stars possess a relatively large radiative core, which decreases continuously down to the TTCC at about M3.4, one can suggest that the observations point to a decrease in the efficiency of the dynamo mechanisms between these radii. We believe that we are observing the spectral signature of the progressive disapearance of the radiative core in M dwarfs, and therefore the progressive transition from an $\alpha - \Omega$ type of dynamo to an α^2 or/and $\alpha - \Omega$ type of dynamo.

References

Allard, F., Homeier, D., Freytag, B. 2012, RSPTA 370, 2765

Houdebine, E.R., Doyle, J.G. 1994, A&A 289, 169-184

Houdebine, E.R. & Stempels, H.C. 1997, A&A (Paper VI)

Mullan, D. J. & Houdebine, E. R. 2020, Astrophys. J., 891, 128 (MH20)

SF2A 2021
A. Siebert, K. Baillié, E. Lagadec, N. Lagarde, J. Malzac, J.-B. Marquette, M. N'Diaye, J. Richard, O. Venot (eds)

PROPERTIES OF THE IONISATION GLITCH: INSIGHTS FROM AN IONISATION REGION MODELLING

P. S. Houdayer[1], D. R. Reese[1], M.-J. Goupil[1] and Y. Lebreton[1,2]

Abstract. The work described here presents the first of two parts towards the development of a seismic method for obtaining unbiased estimates of the helium abundance in low-mass stars. This approach seeks to best exploit the information contained in the ionisation glitch by relying on a physically introduced model of the ionisation region. This model depends explicitly on quantities of interest (such as helium abundance) and thus aims to avoid both the reliance on ad hoc glitch modelling as well as the need for calibration, which are both part of the current methods. We present here how the model is conceived as well as some properties about the ionisation region structure that can be derived from it.

Keywords: stellar interior, ionisation, abundances, glitches, oscillations

1 Introduction

Asteroseismology, by combining information on resonant modes and a physical model of the star, provides strong constraints on internal stellar processes involved. The information thus obtained depends on what physics is included which may result in modelling biases. A well-known example is the mass/helium degeneracy first described in Lebreton & Goupil (2014) and based on a detailed seismic study of HD 52625. It highlights in particular the many mass-helium couples (M, Y) that satisfy the constraints provided by the oscillation frequencies, thus leading to a high degree of uncertainty on both quantities.

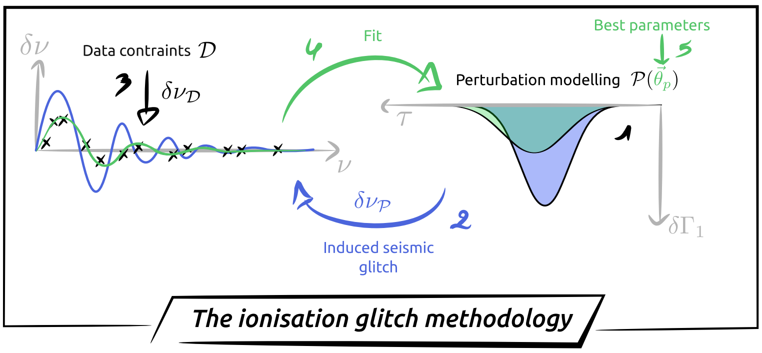

Fig. 1. Scheme of the ionisation glitch procedure. Based on a certain perturbation form $\mathcal{P}$ (1), we aim to find the induced signature (2) that best approximates the seismic constraints (3). The fit (4) thus provides the best parameterisation $\vec{\theta}_p$ (5) of $\mathcal{P}$ which gives information regarding the structure responsible for the observed signature.

Overcoming this issue may be achieved through an alternative approach that is the exploitation of the ionisation glitch (and whose procedure is schematised in Fig. 1). Rather than a whole stellar structure, this

e-mail: pierre.houdayer@obspm.fr
[1] LESIA, Observatoire de Paris, Université PSL, CNRS, Sorbonne Université, Université de Paris, 5 place Jules Janssen, 92195 Meudon, France
[2] Univ Rennes, CNRS, IPR (Institut de Physique de Rennes) – UMR 6251, 35000 Rennes, France

method only seeks to model a perturbation $\mathcal{P}$ with a given shape (examples of the first adiabatic exponent perturbation $\delta\Gamma_1$ can be found in Monteiro et al. (1994); Gough (2002); Monteiro & Thompson (2005)) in order to identify its signature in the oscillation frequencies. The information thus retrieved lies in the parameterisation $\vec{\theta}_p$ of this perturbation (cf Fig. 1). However, this approach presents two main flaws: first, one must assume the form of the perturbation $\mathcal{P}$ *a priori* and we might legitimately wonder about the consequences if the form of the actual perturbation differs from it. Secondly, if the information needed is not contained in $\vec{\theta}_p$, calibration on realistic models (Houdek & Gough 2011; Verma et al. 2014, 2019) becomes necessary to relate it to known physical quantities such as the helium abundance.

2 Ionisation region modelling

To address these difficulties, we derived a model of the ionisation region based on adequate assumptions for a mixture in an ionisation region (cf Fig. 2 with i designating the chemical species and r the ionisation states).

Isentropic region	Chemical equilibrium	Theoretical framework	Uniform abundances	Electroneutrality
$dS = 0$	$\mu_i^r + \mu_e - \mu_i^{r-1} = 0$		$\sum_r N_i^r = \text{cnst}$	$\sum_i \sum_r r N_i^r = N_e$

Fig. 2. Assumptions used to derive an expression of the first adiabatic exponent Γ_1

The analytical expression of the first adiabatic exponent Γ_1 resulting from these assumptions is found to depend on the density ρ, the temperature T and the helium abundance Y as illustrated in Fig. 3. The whole structure is determined through the integration of the hydrostatic equilibrium and Poisson's equation.

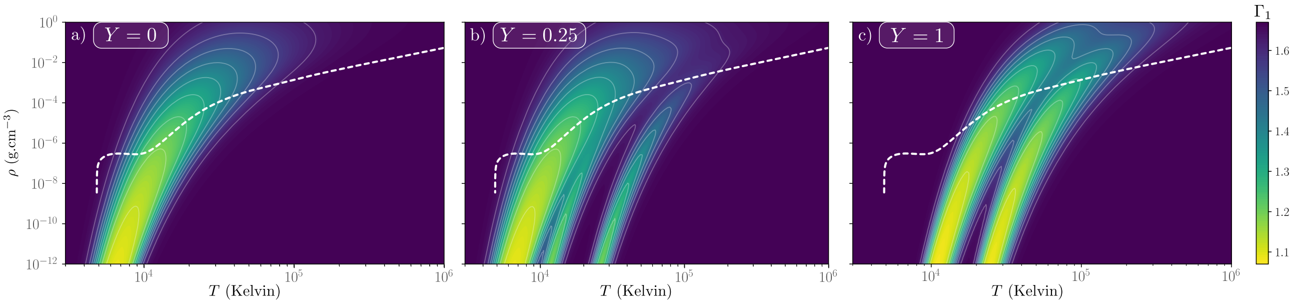

Fig. 3. $\Gamma_1(\rho, T, Y)$ as a function of density ρ and temperature T for multiple helium abundances. (a) : $Y = 0$, (b) : $Y = 0.25$, (c) : $Y = 1$. The dashed line present on each panel shows a relation $\rho(T)$ extracted from a realistic solar model.

The resulting model $\mathcal{M}$ can be parameterised by 3 quantities: the helium abundance at the surface Y_s, the electron degeneracy parameter in the convection zone ψ_{CZ} and a parameter controlling the position of the ionisation region ε. A forthcoming article (Houdayer et al. submitted) describes a method for exploiting the ionisation glitch by using a difference of these models $\delta\mathcal{M}$ instead of an ad hoc perturbation $\mathcal{P}$. The approach presented enables more elaborate perturbations to be considered as well as providing more direct access to the quantities of interest such as the helium abundance.

References

Gough, D. O. 2002, in ESA Special Publication, Vol. 485, Stellar Structure and Habitable Planet Finding, ed. B. Battrick, F. Favata, I. W. Roxburgh, & D. Galadi, 65–73

Houdek, G. & Gough, D. O. 2011, MNRAS, 418, 1217

Lebreton, Y. & Goupil, M. J. 2014, A&A, 569, A21

Monteiro, M. J. P. F. G., Christensen-Dalsgaard, J., & Thompson, M. J. 1994, A&A, 283, 247

Monteiro, M. J. P. F. G. & Thompson, M. J. 2005, MNRAS, 361, 1187

Verma, K., Faria, J. P., Antia, H. M., et al. 2014, ApJ, 790, 138

Verma, K., Raodeo, K., Basu, S., et al. 2019, MNRAS, 483, 4678

SF2A 2021
A. Siebert, K. Baillié, E. Lagadec, N. Lagarde, J. Malzac, J.-B. Marquette, M. N'Diaye, J. Richard, O. Venot (eds)

TESSIPACK: AN INTERACTIVE PYTHON-BASED TOOL TO FIND STELLAR VARIABILITY FROM TESS FFIS.

D. B. Palakkatharappil[1] and O. L. Creevey[1]

Abstract. TESS Transiting Exoplanet Survey Satellite (NASA exoplanet space mission) Full Frame Images (FFI) cover 85% of the sky with a cadence of 10 and 30 minutes. The light curves from the FFI can be used for studies of astrophysical phenomenon such as exoplanets, binaries, supernovae, etc. We developed a graphics-based python tool that combines various available pipelines (`Eleanor` and `LightKurve`) to generate a light curve from the FFIs. With this tool, one can interactively inspect the target pixel files and select aperture pixels to generate a light curve. Aperture selection helps to identify and remove the contamination on the light curve due to neighbouring sources. The tool is also integrated with Ds9 and the Gaia DR2 catalogue, with which we can inspect the environment of the target source. As a first example of the tool, we analyse a crowded young open cluster Collinder 69 using Gaia DR2 proper motions to identify members. We identify and present variable star cluster members comprising binaries and oscillating stars.

Keywords: TESS, FFI, variable stars, binaries

1 Introduction

The NASA Transiting Exoplanet Survey Satellite (TESS) was designed to search for exoplanets. It is an all-sky survey that covers 85 % of the sky. TESS not only provides short cadence (SC) data in 2 minute intervals for ∼200,000 targets and 20 second intervals for 1000 pre-selected targets, but also Full Frame Images (FFI) with 30- (Cycles 1 and 2) and 10- (Cycles 3 and 4) minute cadence. TESS has already confirmed 129 exoplanets, however the light curves from TESS can be used to study various other physical phenomena such as stellar rotation, flares, binaries, oscillations, and comets.

2 `tessipack`

The SC data is processed by the Science Processing Operations Center pipeline which extracts photometry and astrometry for each target star after removing the systematic errors. For FFI images only raw pixel correction is done. There are a number of packages available to obtain corrected light curves from FFI such as `TESScut` (Brasseur et al. 2019), `Eleanor` (Feinstein et al. 2019), and `lightKurve` (Lightkurve Collaboration et al. 2018). But none of the packages allows the user to select custom apertures interactively. `tessipack` is a publicly* available package that enables the user to interact directly with the pixels to obtain an optimal light curve and check for contamination of nearby stars.

`tessipack` acquires target pixel files (TPFs) with square target masks of 13 pixels on each side and a square background mask of 31 pixels on each side using the `Eleanor` and `lightKurve` packages. The optimal aperture of the target source can be defined interactively, and a systematic-error-corrected light curve can be obtained. Defining custom apertures improves the light curve, as seen in the light curve of the Gaia DR2 3337966050361143168 source (Fig. 1 top panel). Custom apertures also help to identify contamination from a nearby source: In Fig. 1 lower panel, a nearby source (blue custom aperture) contaminates the light curve of a non-variable star Gaia DR2 DR23336171308083686528 (red default aperture for given coordinates). `tessipack` allows one to quickly confirm the origin of the variability. A 1-minute demonstration video can be viewed on the conference site or here.

[1] Université Côte d'Azur, Observatoire de la Côte d'Azur, CNRS, Laboratoire Lagrange, Bd de l'Observatoire, CS 34229, 06304 Nice cedex 4, France
*`https://github.com/dinilbose/tessipack`

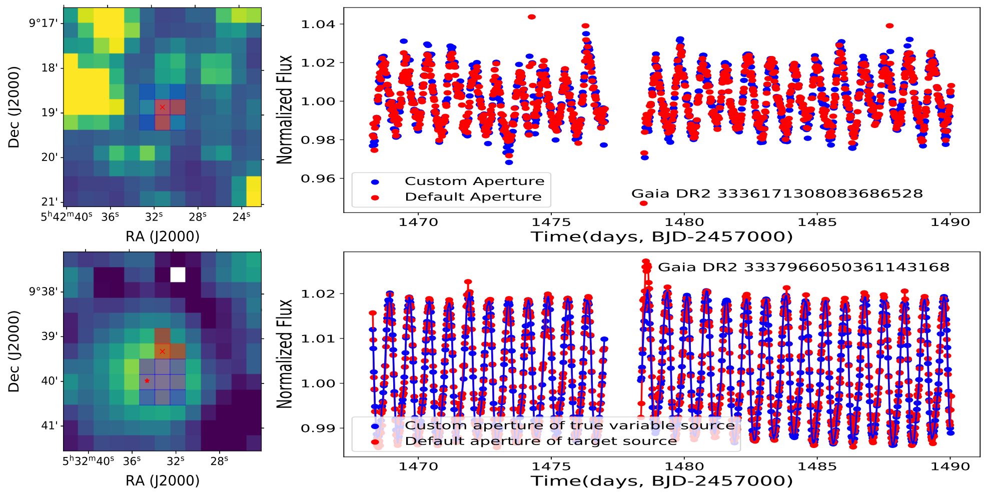

Fig. 1. Left: Custom (red) and default (blue) apertures overlayed over the TPFs. **Right:** Light curve obtained for Gaia DR2 3337966050361143168 (top) and Gaia DR2 DR23336171308083686528 (bottom, red only, see text for details).

3 Collinder 69

Collinder 69 is a young open cluster (6 Myr) at a distance of 400 parsecs. The 711 cluster members identified from Gaia DR2 (Cantat-Gaudin et al. 2018) were analysed using the `tessipack` package. We identified 44 variable stars and 30 candidate binary stars and these are shown in the colour-magnitude diagram (Fig. 2). The light curve of a variable star and a binary are shown in Fig 2b. The light curves and table of parameters are publicly accessible from github[†].

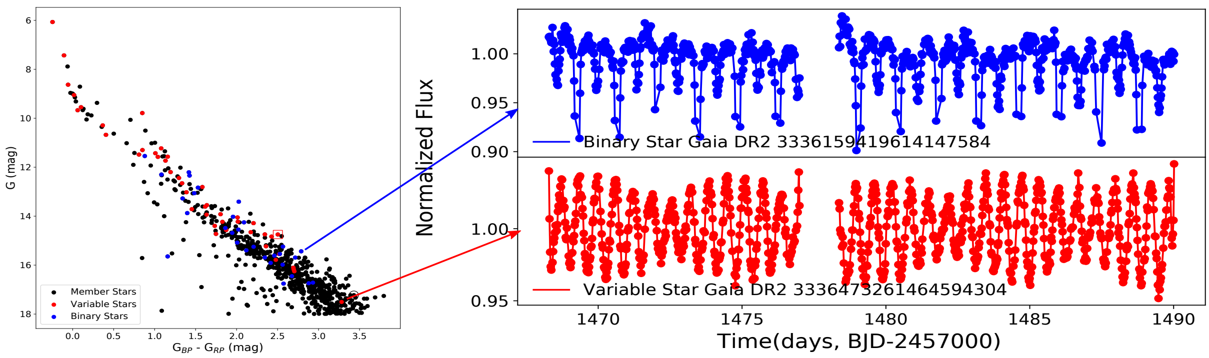

Fig. 2. Left: Color-magnitude diagram of Collinder 69 along with the identified variable source and binary stars. **Right:** Light curve of binary star Gaia DR2 3336159419614147584 and variable star Gaia DR2 3336473261464594304. The variable sources from Fig. 1 are shown as the red square (Fig. 1 top) and black open circle (Fig. 1 lower), respectively.

References

Brasseur, C. E., Phillip, C., Fleming, S. W., Mullally, S. E., & White, R. L. 2019, Astrophysics Source Code Library, ascl:1905.007

Cantat-Gaudin, T., Jordi, C., Vallenari, A., et al. 2018, Astronomy & Astrophysics, 618, A93

Feinstein, A. D., Montet, B. T., Foreman-Mackey, D., et al. 2019, Publications of the Astronomical Society of the Pacific, 131, 094502

Lightkurve Collaboration, Cardoso, J. V. d. M., Hedges, C., et al. 2018, Astrophysics Source Code Library, ascl:1812.013

[†]`https://github.com/dinilbose/tessipack/tree/main/examples/Collinder_69`

Session 7

Atelier général de l'AS SKA: SKA, son éclaireur français NénuFAR, et ses précurseurs

SF2A 2021
A. Siebert, K. Baillié, E. Lagadec, N. Lagarde, J. Malzac, J.-B. Marquette, M. N'Diaye, J. Richard, O. Venot (eds)

SCIENCE WITH SKA

F. Combes[1]

Abstract. Highlights are presented about the science to be done with SKA. as well as state of the art science already done today with its precursors (MeerKAT, ASKAP) and pathfinders (LOFAR, NenuFAR), with accent on the expected breakthroughs.

Keywords: SKA, galaxies, cosmology, pulsars, pre-biotic, molecules

1 The key scientific projects of SKA

Some of the main puzzles of cosmology are the nature of dark matter and dark energy, representing in total 95% of the content of the Universe. The dark energy is presently compatible within the uncertainties with a cosmological constant, but it is paramount to determine with greater precision whether its evolution with time is dynamic, and could be due to a fifth element, a quintessence, and new physics. The tools for making this diagnostic are the same as for many other dark energy probes, either from ithe ground or in space, with Euclid: the BAO (Baryon Acoustic Oscillations), playing the role of a standard ruler, measuring the expansion at differnt redshifts, the Weak Lensing (WL), or Redshift Space Distorsions (RSD), measuring the density and amplitude of large-scale structures to constrain the evolution of Ω and Λ. These tools will be exploited with optical tracers, and the novelty of SKA is to use radio tracers, and the HI-21cm line to identify galaxies. These tracers have different biases than the optical ones, and both studies are very complementary. Optically, the massive galaxies are early-type gathered in galaxy clusters, while the HI-rich galaxies are late-type in the field.

Another key project is to explore the Epoch of Reionization (EoR), likely to extend from z=20 to 6. If it is already possible to have some clues with present searches of galaxies and quasars at z>6, the inter-galactic medium will be uniquely explored by SKA, with the redshifted 21cm-HI line, as it is now with pathfinders and precursors. The large galaxy surveys made over the whole available sky, due to the wide field of view, will serve to determine uniquely the large-scale structures, and the galaxy formation and evolution.

Pulsars will be discovered in a huge number with SKA, exploring the whole Milky Way, while presently they are confined in the solar neighborhood. Milli-second pulsars are extremely precise clocks, which can be used to detect very long wavelength gravitational waves. Strong-gravity will be explored with pulsars and black holes

Cosmic magnetism is another key project, and in particular the formation of primordial magnetic fields will be tackled. Finally, the search for the origin of life, the mapping of the protoplanetary disks, and the search for pre-biotic molecules, will be carried out in synergy and complementarity with ALMA at higher frequencies.

All key projects with SKA have been developed in many whitepapers and conferences, (e.g., Carilli & Rawlings 2004; Carilli 2015).

2 Cosmology and galaxies

2.1 Dark sector and new physics

The state of the art constraints on the dark energy and the dark matter are obtained by combining all available data, from the SNIa standard candels, i.e. the Pantheon sample of 1048 SNIa between redshifts $0.01 < z < 2.3$ (Scolnic et al. 2018), and the 207 SN sample from DES-3yr (Abbott et al. 2019), with the BAO results from SDSS (Alam et al. 2021), and the CMB data (Planck Collaboration et al. 2020). The equation of state of

[1] Observatoire de Paris, LERMA, Collège de France, CNRS, PSL University, Sorbonne University, 75014, Paris, France

the dark energy can be written as the pressure proportional to the density P = w ρ, with w negative, and the variation of w(a)= w_0 + wa (1-a), where a is the characteristic radius of the Universe, a=1/(1+z). Since SNIa are difficult to observe at z>1, Inserra et al. (2021) propose to use and calibrate superluminous supernovae (SLSNe), which will allow to go farther and faster. The first results are promising, putting constraints in the w_0-wa diagram. With the enhanced precision acquired in the recent years, some tension has grown between observations and the standard ΛCDM model, suggesting the necessity of new physics (Smith et al. 2020). In particular the main tension occurs between the Hubble constant H_0= 73.48±1.66 km/s/Mpc measured locally with Cepheids or other indicators (Riess et al. 2018), and the Planck determination of 67.4± 0.5 km/s/Mpc. The discrepancy reaches 3.7σ. In radioastronomy, powerful masers (H_2O, OH..) allow to observe in VLBI the center of external galaxies, and their rotating circum-nuclear disk; measuring the velocities through the Doppler effect and monitoring through VLBI the gradient of maser poition with velocity, results in a precise distance indicator, as shown beautifully by the prototypical example of NGC 4258 (Greenhill et al. 1995). SKA will measure many more masers around AGN at various redshifts, and can give a complementary approach to the problem. Already Pesce et al. (2020) with megamasers confirm H_0 = 73.9±3 km/s/Mpc.

The most recent BAO and RSD results, including 147 000 quasars (Ata et al. 2018), and Lyα absorption surveys (Bautista et al. 2017), are compatible with a flat ΛCDM cosmology, and perfectly compatible with the Planck cosmological parameters (Bautista et al. 2021).

SKA-1 surveys of galaxies in the HI-21cm lines will be complementary and competitive with the optical ones from the ground and in space (Euclid). Surveys where galaxies are detected individually will be most useful for galaxy formation and evolution, they will detect 4 million galaxies up to z=0.2 in the all-sky survey, 2 million galaxies up to z=0.6 in the wide field, and 0.4 million in the deep field survey up to z=0.8 (of 50 square degrees area). For cosmology purposes, HI intensity mapping over 30 000 square degrees, and covering redshifts up to 3 will be more competitive (Maartens et al. 2015). Weak lensing in radio surveys up to redshift z=6 will consider a billion objects. One of the strong advantages of SKA-1 is the much larger volumes sampled, with respect to all other probes (Euclid, DESI, BOSS, Nancy-Grace-Roman...). The second phase SKA-2 will surpass all.

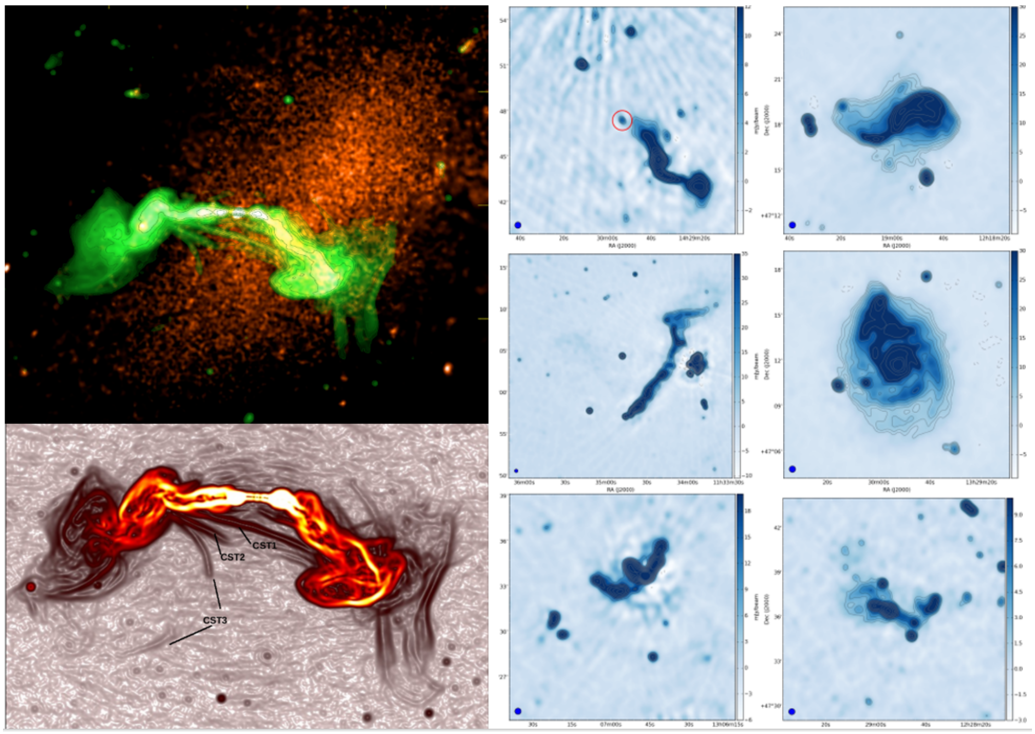

Fig. 1. Left: Radio continuum emission from ESO 137-006 detected by MeerKAT at 1030 MHz. Three collimated synchrotron threads (CSTs) between the radio lobes are indicated. The Sobel filter has been applied to the image, to better show these features (Ramatsoku et al. 2020). The upper panel shows that the galaxy is entering the Norma cluster, and its X-ray gas atmosphere (in red).. **Right:** Some radio images of nearby galaxies from the LOFAR Two-metre Sky Survey (LoTSS) (Shimwell et al. 2019).

2.2 Continuum and HI surveys

Simulations have been performed of wide-field images of the radio-continuum sky with SKA, detecting both the very numerous star-forming galaxies, with synchrtron emission coming from supernovae, and the stronger but less numerous radio AGN, of FRI and FRII types, the latter even less numerous but stronger (Jackson 2004). The AGN radio jets can be used easily as standard rods, constraining the cosmological parameters, by themsleves, and also through weak lensing.

For the all-sky survey at 1.4 GHz, in 2yrs of integration, SKA1 will achieve 3 μJy rms, and detect $\sim$4 galaxies per arcmin^2 (at more than 10σ), (Jarvis et al. 2015). The survey will be made with an excellent quality circular Gaussian beam from about 0.6 to 100", With almost uniform sky coverage of 3π str. This will provide a total of 0.5 billion radio sources, yielding weak lensing and Integrated Sachs Wolfe (WL, ISW) diagnostics. For the wide-field (5000 deg^2), with 2 μJy rms $\sim$6 galaxies per arcmin^2 are expected (at more than 10σ). For the deep-field (50deg^2) with 0.1 μJy rms, $\sim$20 galaxies per arcmin^2 will be detected, at more than 10σ.

Figure 1 shows some examples of radio images from the LOFAR Two-metre Sky Survey (LoTSS), and also how the precursor MeerKAT has discovered new features in typical radio-jets: collimated synchrotron threads, linking the radio lobes from the sides, in parallel to the radio jets, in ESO 137-006. This galaxy is moving inside the wind of the intra-cluster gas, entering the Norma cluster. The radio lobes are distorted and bent, and the threads look like relics of the previous radio jets, in previous episodes of ejection.

In HI-21cm surveys, SKA-1 will allow the imaging of substantial number of high-redshift galaxies for the first time (Staveley-Smith & Oosterloo 2015). While the present instruments are restricted to detect HI in individual galaxies only to the local Universe up to z=0.1, the very deep survey will permit the detection of galaxies at z=2, and even higher for SKA-2. A glance of what intensities could be detected is given by recent stacking to detect only "globally" some remote galaxies. With GMRT deep (117h) field, Bera et al. (2019) have stacked 445 blue galaxies between $0.2 < z < 0.4$, and obtained a detection at 7σ of M(HI) = 5 10 ^{9} M$_\odot$. Stacking the continuum to derive the star formation rate, they derive a depletion time of $\sim$ 9 Gyrs. From GAMA survey, imaged on DINGO-VLA, Chen et al. (2021) have stacked HI cubelets on a sample of 3622 galaxies, and obtained a clear detection, with FWHM of 60km/s.

3 Reionization

Intensity mapping is the only technique able to determine the global quantities searched for in the EoR. Continuum foregrounds are typically 1000 times brighter than the expected cosmological signal. The instrumental responses to bright foregrounds with extended and multiple sidelobes, forming a sea of confused signals, depending on their location on the field of view, are a challenge to understand and subtract away (Santos et al. 2015). The foregrounds to be eliminated produce a perturbing signal, which is not necessarily spectrally smooth (Switzer et al. 2015).

The LOFAR key project on EoR has observed more than 1000hours on selected clean fields, with the least possible foreground emission. However, even if the nominal sensitivity is reached to detect easily the expected signal, the confusion by foregrounds has prevented to draw any conclusion. Controlling the calibration, and cleaning for the sidelobes down to the low intensity level required is a long process. While in 2017, only 0.5% of data were understood and used (Patil et al. 2017), recently up to 5% of data has been understood and cleaned, resulting in an upper limit of the EoR signal two orders of magnitude above the expected signal. There still remains noise that could be due to residual emission from foreground sources or diffuse emission far away from the phase centre, polarization leakage, chromatic calibration errors, ionosphere, or low-level radiofrequency interference (Mertens et al. 2020)

4 Pulsars, Cosmic magnetism

4.1 Pulsars and gravitational waves

The large number of pulsars to be discovered by SKA, in combination with its exceptional timing precision, will revolutionize the field of pulsar astrophysics. SKA will provide a complete census of pulsars in both the Galaxy and in Galactic globular clusters (Cordes et al. 2004). In the Milky Way, about 30 000 pulsars should be present, and 10 000 milli-second ones. May be 20 000 pulsars will be detectable in the whole Galaxy (while today we know only pulsars in the solar neighborhood). Pulsars and compact objects will allow unique tests of the strong field limit of relativistic gravity and the equation of state at extreme densities.

Through monitoring these pulsars, which are extremely precise clocks, (up to 10^{-15} in relative), gravitational waves of long wavelengths, of the order of light-yrs, could be detected, and pulsars are the only way. The hope is to detect the merger of super-massive black holes, and also the primordial waves, signature of inflation (Janssen et al. 2015). A first preliminary detection has been claimed with present telescopes (Arzoumanian et al. 2020).

4.2 Fast Radio Bursts

Since their discovery by Lorimer et al. (2007), our knowledge of Fast Radio Bursts (FRB) have grown considerably: they have been detected in large numbers, especially with the wide-field instrument CHIME: 540 are known, and the occurence has been estimated at 800 per day on the whole sky (CHIME/FRB Collaboration et al. 2019). With SKA-MID, it will be possible to detect 100 FRB/yr, with precise localisation (Keane 2018). The nature of the FRB phenomenon is not yet clarified, although many repeaters have been detected, and one FRB has been associated with a Galactic magnetar, SGR 1935+2154 (Bochenek et al. 2020). Due to their surface magnetic fields larger than 10^{14} gauss, magnetars are the source of high-energy phenomena, where their magnetic energy decays. A florilege of theories have been proposed to explain the phenomena (Platts et al. 2019).

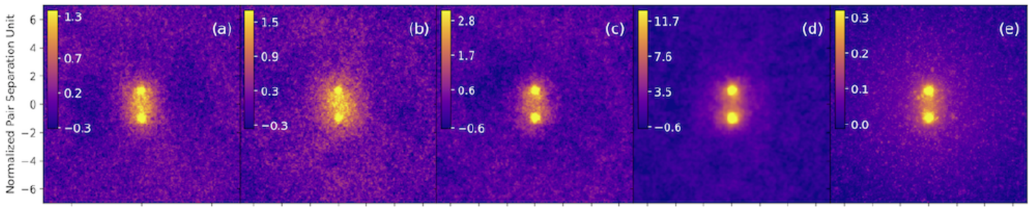

Fig. 2. Stacking radio and X-ray maps, around physically nearby pairs of luminous red galaxies (LRG). From left to right the columns are GLEAM 154 MHz, 118 MHz, 88 MHz, OVRO-LWA 73 MHz, and ROSAT combined band 0.1 -2.4 keV. The colour bars all have units of temperature in K, except the ROSAT maps which are in counts per second per arcmin^2 x10^4. From Vernstrom et al. (2021).

4.3 Magnetic Fields

Polarisation of radio emission, and Faraday rotation have been used intensively to determine the intensity and orientation of the magnetic field in spiral galaxies, at various depths according to the various wavelengths: either from the halo, or the disk, and different distributions have been obtained with respect to the spiral arms (Kierdorf et al. 2020). Turbulence due to star formation in spiral arms paradoxically reduces alignment, and frequent field reversals in the vertical direction contribute to distortions that are not yet well understood. LOFAR has been used in combination with VLA to determine the spectrum of the emission, separate thermal and non-thermal components, the magnetic field strength and the cosmic ray electron losses (Mulcahy et al. 2018).

All-sky survey of Faraday rotation will measure inter-galactic magnetic field, as well as inside galaxies. The mechanisms to generate the field are not yet settled, from inflation, phase transitions in the early Universe, and batteries to amplify the seeds. Normally the field is frozen in the ionized gas, but should dilute away in the expansion. When structures collapse, the field is amplified again (Johnston-Hollitt et al. 2015).

Searches have been done in diffuse filaments connecting clusters, at the cosmic web (15Mpc) scale, combining X-ray hot gas with eRosita with radio data from ASKAP/EMU Early Science (Reiprich et al. 2021). Missing baryons are searched for by studying the warm-hot gas in cluster outskirts and filaments. The bridge between two clusters is detected; it may contain known galaxy groupis, but not accounting for all the emission There are several clumps of warm gas falling into the clusters, compatible to what is observed in simulations.

LOFAR has also detected synchrotron emission in filaments between merging galaxies, with possible shocks re-accelerating the electrons (Govoni et al. 2019; Botteon et al. 2020), but these were only short scales. Now with GLEAM (the MWA survey), it is possible to search for longer filaments (see Figure 2). These are traced by Luminous red galaxies (LRGs), which are massive early-types residing in the center of galaxies clusters or groups. The first large-scale filament detection, has revealed a magnetic field of 30-60 nG, of intensity higher than previously believed, with electrons subject to more efficient shock acceleration (Vernstrom et al. 2021).

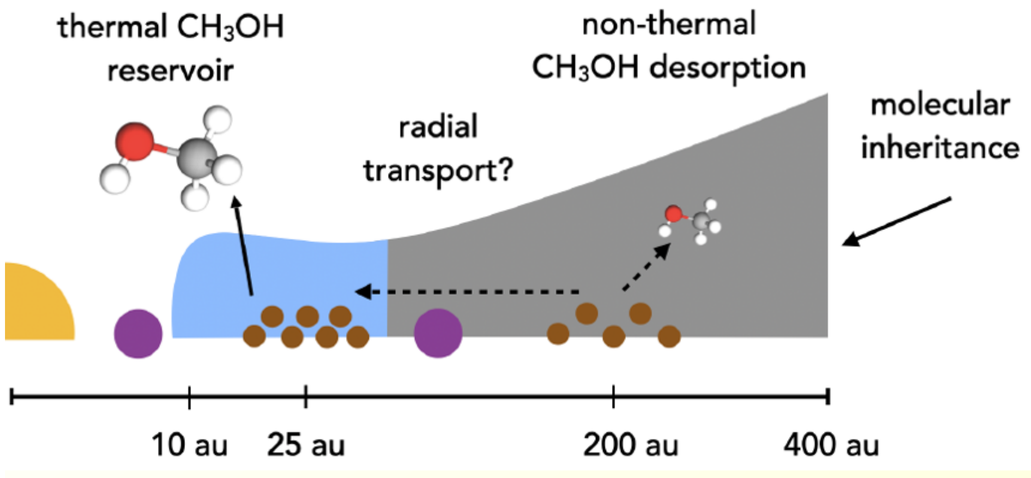

Fig. 3. Cartoon of a protoplanetary disk (HD 100546) showing the regions where CH_3OH is detected and the different physical and chemical mechanisms proposed (Booth et al. 2021).

5 Craddle for life

ALMA has made a breakthrough in the domain of the formation of planets and protoplanetary disks, in imaging with superb resolution resonant rings and gaps (Andrews 2020). Disks are formed first with gas and small-size dust grains, the latter agglomerating progressively in mm- and cm-sized grains before becoming planetesimals. These grains emit at longer and longer wavelengths, and SKA-1 will be the prefered instrument to detect cm to m-sized dust. At high resolution with 40mas beam, the nearest systems will be mapped with 4AU resolution, sufficient to determine the snow line (Hoare et al. 2015). Large exoplanets, of Jupiter-size, could be detected with their magnetic fields (Zarka et al. 2018). In synergy with ALMA, the detection of complex organic molecules (COM) could be carried out, such as the methanol CH_3OH, with deuterated species CH_2DOH, methanethiol CH_3SH, formamide NH_2CHO, and heavier pre-biotic molecules in Band 5, such as amino acids and sugars. In 1000h SKA1-mid could detect clearly α-alanine, with a hundred of lines, for a column density of 10^{13} cm^{-2} (Hoare et al. 2015).

Methanol has been detected in protoplanetary disks, and is thought to come from hydrogenation of CO on icy grains (cf Figure 3). Complex organic molecules have now been detected, which are key to form amino-acids, and pre-biotic molecules (Booth et al. 2021). These COM cannot form in situ, but must come from ices formed previously in dark interstellar clouds.

6 Conclusions

SKA-1 will help to tackle the main puzzles of cosmology: the nature of dark matter and dark energy, by using the common tools (BAO, WL, RSD) with high precision, and with tracers with different biases than optical surveys (radio continuum, HI in galaxies). With extragalactic masers, it will be possible to bring a complementary constraint to the H_0 problem, suggesting new physics.

With redshifted HI-21cm line, SKA will have a unique contribution to the Epoch of Reionization, and the birth of the first galaxies. With the timing of millisecond pulsars, SKA will make a breakthrough in probing strong ggavity, and detecting gravitational waves in the very low frequency regime (nanoHz), to search for primordial waves.

Our knowledge of magnetic genesis will considerably improve. SKA will work in synergy with ALMA to determine the physics of protoplanetary disks, and detect pre-biotic molecules.

All these key projects have begun to be tackled at very low frequency with the NenuFAR pathfinder in Nançay, where the first large programs are ES1: Cosmic Dawn; ES2: Exoplanets & Stars; ES3: Pulsars; ES4: Transients; ES5: Fast Radio Bursts; ES6: Planetary Lightning; ES7: Joint Jupiter studies; ES8: Cluster of galaxies & AGNs; and ES9: Cluster Filament & Cosmic Magnetism.

References

Abbott, T. M. C., Allam, S., Andersen, P., et al. 2019, ApJ, 872, L30

Alam, S., Aubert, M., Avila, S., et al. 2021, Phys. Rev. D, 103, 083533

Andrews, S. M. 2020, ARA&A, 58, 483

Arzoumanian, Z., Baker, P. T., Blumer, H., et al. 2020, ApJ, 905, L34

Ata, M., Baumgarten, F., Bautista, J., et al. 2018, MNRAS, 473, 4773

Bautista, J. E., Busca, N. G., Guy, J., et al. 2017, A&A, 603, A12

Bautista, J. E., Paviot, R., Vargas Magaña, M., et al. 2021, MNRAS, 500, 736

Bera, A., Kanekar, N., Chengalur, J. N., & Bagla, J. S. 2019, ApJ, 882, L7

Bochenek, C. D., Ravi, V., Belov, K. V., et al. 2020, Nature, 587, 59

Booth, A. S., Walsh, C., Terwisscha van Scheltinga, J., et al. 2021, Nature Astronomy

Botteon, A., van Weeren, R. J., Brunetti, G., et al. 2020, MNRAS, 499, L11

Carilli, C. 2015, in Advancing Astrophysics with the Square Kilometre Array (AASKA14), 171

Carilli, C. L. & Rawlings, S. 2004, New A Rev., 48, 979

Chen, Q., Meyer, M., Popping, A., & Staveley-Smith, L. 2021, MNRAS, 502, 2308

CHIME/FRB Collaboration, Amiri, M., Bandura, K., et al. 2019, Nature, 566, 230

Cordes, J. M., Kramer, M., Lazio, T. J. W., et al. 2004, New A Rev., 48, 1413

Govoni, F., Orrù, E., Bonafede, A., et al. 2019, Science, 364, 981

Greenhill, L. J., Jiang, D. R., Moran, J. M., et al. 1995, ApJ, 440, 619

Hoare, M., Perez, L., Bourke, T. L., et al. 2015, in Advancing Astrophysics with the Square Kilometre Array (AASKA14), 115

Inserra, C., Sullivan, M., Angus, C. R., et al. 2021, MNRAS, 504, 2535

Jackson, J. C. 2004, J. Cosmology Astropart. Phys., 2004, 007

Janssen, G., Hobbs, G., McLaughlin, M., et al. 2015, in Advancing Astrophysics with the Square Kilometre Array (AASKA14), 37

Jarvis, M., Bacon, D., Blake, C., et al. 2015, in Advancing Astrophysics with the Square Kilometre Array (AASKA14), 18

Johnston-Hollitt, M., Govoni, F., Beck, R., et al. 2015, in Advancing Astrophysics with the Square Kilometre Array (AASKA14), 92

Keane, E. F. 2018, Nature Astronomy, 2, 865

Kierdorf, M., Mao, S. A., Beck, R., et al. 2020, A&A, 642, A118

Lorimer, D. R., Bailes, M., McLaughlin, M. A., Narkevic, D. J., & Crawford, F. 2007, Science, 318, 777

Maartens, R., Abdalla, F. B., Jarvis, M., & Santos, M. G. 2015, arXiv e-prints, arXiv:1501.04076

Mertens, F. G., Mevius, M., Koopmans, L. V. E., et al. 2020, MNRAS, 493, 1662

Mulcahy, D. D., Horneffer, A., Beck, R., et al. 2018, A&A, 615, A98

Patil, A. H., Yatawatta, S., Koopmans, L. V. E., et al. 2017, ApJ, 838, 65

Pesce, D. W., Braatz, J. A., Reid, M. J., et al. 2020, ApJ, 891, L1

Planck Collaboration, Aghanim, N., Akrami, Y., et al. 2020, A&A, 641, A6

Platts, E., Weltman, A., Walters, A., et al. 2019, Phys. Rep., 821, 1

Ramatsoku, M., Murgia, M., Vacca, V., et al. 2020, A&A, 636, L1

Reiprich, T. H., Veronica, A., Pacaud, F., et al. 2021, A&A, 647, A2

Riess, A. G., Casertano, S., Yuan, W., et al. 2018, ApJ, 861, 126

Santos, M., Bull, P., Alonso, D., et al. 2015, in Advancing Astrophysics with the Square Kilometre Array (AASKA14), 19

Scolnic, D. M., Jones, D. O., Rest, A., et al. 2018, ApJ, 859, 101

Shimwell, T. W., Tasse, C., Hardcastle, M. J., et al. 2019, A&A, 622, A1

Smith, T. L., Poulin, V., & Amin, M. A. 2020, Phys. Rev. D, 101, 063523

Staveley-Smith, L. & Oosterloo, T. 2015, in Advancing Astrophysics with the Square Kilometre Array (AASKA14), 167

Switzer, E. R., Chang, T. C., Masui, K. W., Pen, U. L., & Voytek, T. C. 2015, ApJ, 815, 51

Vernstrom, T., Heald, G., Vazza, F., et al. 2021, MNRAS, 505, 4178

Zarka, P., Marques, M. S., Louis, C., et al. 2018, A&A, 618, A84

SF2A 2021
A. Siebert, K. Baillié, E. Lagadec, N. Lagarde, J. Malzac, J.-B. Marquette, M. N'Diaye, J. Richard, O. Venot (eds)

THE EARLY STAGE OF SOLAR-TYPE PROTOSTARS: THE MISSING EVIDENCE OF LARGE CARBON CHAINS

E. Bianchi[1], C.Ceccarelli[1], B. McGuire[2,3,4], A. Remijan[5], C. Codella[5], P. Caselli[6], N. Balucani[7], S. Spezzano[6] and E. Herbst[8,9]

Abstract. In the last few years a striking chemical diversity has been identified around Sun-like protostars. The vast majority of observations dedicated to the chemical exploration of these objects has been obtained via millimeter wavelength telescopes, where relatively light molecules, such as interstellar complex organic molecules or small carbon chains, have their peak of emission. In contrast, the lines of heavy molecules (e.g. chains and rings with more than seven C-atoms) at mm wavelengths are substantially weaker. Their observation would add a key piece to the overall puzzle as they might have a crucial role in the heritage of organic material from the pre- and proto- stellar phase to the objects of the newly formed planetary system, such as asteroids and comets. We report the first results obtained in a pilot study performed using the 100m Robert C. Byrd Green Bank Telescope (GBT) to observe several crucial C-bearing chains in the X and Ku bands (8–11.5 GHz and 14.0–15.4 GHz, respectively), in the two sources L1544 and IRAS16293-2422, which are considered the two archetypes of prestellar cores and protostars. This work paves the way for molecular exploration using SKA and it has inspired a new SKA user case, developed in the context of the Cradle Of Life working group activity.

Keywords: astrochemistry, star formation, large carbon chains

1 Introduction

The formation of a Solar-type planetary system starts with the collapse of a cold ($\leq$10 K) and dense ($\geq 10^5$ cm^{-3}) clump, called a prestellar core, in a molecular cloud. The evolution of the prestellar core into a protostar, a protoplanetary disk and, eventually, a planetary system, is also accompanied by the evolution of its chemical composition (e.g. Caselli & Ceccarelli 2012). Nowadays, we know that this evolution leads to protostars with a wide range of chemical composition, represented, for example, by hot corinos, which are enriched in interstellar complex organic molecules (hereinafter called iCOMs: e.g. Ceccarelli et al. 2007) and the WCCC (Warm Carbon Chain Chemistry) sources, which are enriched of unsaturated small carbon chains (fewer than about five C-atoms: e.g. Sakai & Yamamoto 2013). The origin of this chemical diversity is unclear and it may be related to environmental conditions at the epoch of icy dust mantles formation. (e.g. Sakai & Yamamoto 2013; Spezzano et al. 2017; Lefloch et al. 2018). Observational studies aimed at investigating the chemical inventories of Solar-type protostars have mainly been performed using (sub-)millimeter telescopes, where several relatively light molecules, like simple iCOMs or small C-chains, have their peak of emission. On the other hand, lines of heavy molecules (e.g. chains and rings with more than seven C-atoms) are quite weak at those wavelengths. For this reason, much less is known about the presence and evolution of heavy species. Even the relatively

[1] Univ. Grenoble Alpes, CNRS, IPAG, 38000 Grenoble, France
[2] Department of Chemistry, Massachusetts Institute of Technology, Cambridge, MA 02139, USA
[3] National Radio Astronomy Observatory, Charlottesville, VA 22903, USA
[4] Center for Astrophysics Harvard & Smithsonian, Cambridge, MA 02138, USA
[5] INAF, Osservatorio Astrofisico di Arcetri, Largo E. Fermi 5,50125 Firenze, Italy
[6] Max-Planck-Institut für extraterrestrische Physik, 85748 Garching, Germany
[7] Dipartimento di Chimica, Biologia e Biotecnologie, Università degli Studi di Perugia, 06123 Perugia, Italy
[8] Department of Chemistry, University of Virginia, Charlottesville, VA 22904, USA
[9] Department of Astronomy, University of Virginia, Charlottesville, VA 22904, USA

simple and abundant cyanotriacetylene (HC_7N) has only been detected in a handful of Solar-type prestellar cores and protostars (e.g. Gupta et al. 2009; Cordiner et al. 2012; Friesen et al. 2013; Jaber Al-Edhari et al. 2017). Yet, large C-carbon species might have a crucial role in the heritage of organic material from the pre- and proto- stellar phase to the objects of the newly formed planetary system, such as asteroids and comets (e.g. Mumma & Charnley 2011). Instructive results have been recently obtained towards the prestellar core TMC-1 by: (i) the GBT GOTHAM project (McGuire et al. 2020) and (ii) the Yebes QUIJOTE survey (Cernicharo et al. 2021). They reported the detection of cyclic hydrocarbons such as c-C_9H_8 (Burkhardt et al. 2021a) and o-C_6H_4 (Cernicharo et al. 2021). Interestingly, they also reported the detection towards different prestellar cores of benzonitrile (c-C_6H_5CN), suggesting that aromatic species are quite widespread at earlies stages (McGuire et al. 2018; Burkhardt et al. 2021a). In summary, these results confirm the presence of a complex carbon chemistry at work in Solar System precursors, calling for further observations of pre- and protostellar objects in different star forming regions. Despite the importance of large carbon species in the astrobiological context and its potential diagnostic power, only TMC-1 has been explored extensively so far. The present project fills this important gap in our knowledge, thanks to a survey of the archetype of prestellar cores and Class 0 protostars: L1544 and IRAS 16293-2422 (hereafter IRAS16293), respectively.

1.1 L1544 and IRAS 16293

L1544 (see e.g. the c-C_3H_2 map of Fig. 1) in the Taurus molecular cloud complex (d = 140 pc) is considered the prototype of prestellar cores, being on the verge of gravitational collapse (e.g. Caselli & Ceccarelli 2012). Its central high density ($\sim 10^6$ cm^{-3}) and very low temperature ($\sim$ 7 K) trigger the peculiar chemistry typical of cold and CO depleted gas (e.g. Caselli et al. 1999). In the external layers, however, different rich chemical processes take place which lead to the formation of iCOMs and carbon chains (e.g. Bizzocchi et al. 2014; Vastel et al. 2016; Punanova et al. 2018). Indeed, recent (single-dish) IRAM 30-m observations in the mm-window show the presence of small carbon chains such as HC_3N, c-C_3H_2, C_3H, C_4H, C_2O and C_3O over extended portions of L1544 (see Fig. 1 Vastel et al. 2014; Spezzano et al. 2017; Urso et al. 2019).

IRAS16293 is a Solar-type protostar in the ρ Ophiuchus star-forming region (d = 120 pc). Given its proximity and relatively large envelope, it has been the target of numerous studies at mm and submm wavelengths that have revealed its physical structure. IRAS16293 possesses a large envelope that extends up to 6000 au (Castets et al. 2001; Crimier et al. 2010) and that surrounds two protostellar objects separated by 600 au (Mundy et al. 1992; Jørgensen et al. 2016). From a chemical point of view, the IRAS16293 envelope is composed of: (i) the outer cold ($\sim$ 10–30 K) envelope, characterized by the presence of cyanopolyynes (HC_3N, HC_5N, Jaber Al-Edhari et al. 2017) and small carbon chains (as in L1544) such as c-C_3H_2, C_2H, C_3H, C_4H (Caux et al. 2011), and emitting narrow lines (FWHM$\sim$ 1–2 km s^{-1}); (ii) the hot corino, where the abundance of many molecules (in particular iCOMs) increases by orders of magnitude (e.g. Ceccarelli et al. 2000; Coutens et al. 2012; Jaber et al. 2014; Jørgensen et al. 2016, 2018) due to protostellar heating, which reaches the sublimation temperature of the icy grain mantles ($\sim$ 100 K). While the hot corino has been the subject of a large number of (mainly interferometric) observations to infer its chemical composition (e.g. Lykke et al. 2017; Persson et al. 2018 and references therein), not so much has been done to study the chemistry of the cold outer envelope.

2 Observations and first results

The spectra observed with the GBT are shown in Fig. 2, where the rms is typically $\sim$ 1–2 mK in a channel of $\leq$ 0.1 km s^{-1}. Observations have unveiled many complex C-chain species (C_4H, C_6H, HC_7N, HC_9N, C_3S, Bianchi et al. in prep). Both L1544 and IRAS16293 were observed in Ku band, between 13.9 and 15.41 GHz (see Fig. 2, right panel). Successively, given the richness of the observed spectra, we followed up L1544 to cover the full X-band (8 – 11.5 GHz). The first immediate result is that there is a chemical diversity between L1544 and the envelope of IRAS16293, evident from the spectra reported in Fig. 2 (right panel). In particular, in IRAS16293 the detected molecular species are formaldehyde (H_2CO) and c-C_3H. Instead in L1544, we detected several bright emission lines from heavy carbon-chain molecules. More specifically, we detected several transitions of c-C_3H, C_4H, C_6H with associated hyperfine structure, HC_3N, HC_5N and HC_9N (see Fig. 1, right panel), H_2CO, CCS, and C_3S. All the lines are well detected with a high signal to noise (S/N between 3 and 40). The analysis to dermine the physical parameters of the emitting gas, as well as the molecular abundances towards the sources is in progress. Our findings can be considered as part of a community effort aimed at exploring the carbon-chain and aromatic chemistry at cm wavelengths using GBT in different objects (see e.g. GOTHAM and the forthcoming ARKHAM results; McGuire et al. 2020; Burkhardt et al. 2021b). An open question is now to understand wheather the non-detection of heavy carbon species towards IRAS16293 indicates a lack of these species in the gas phase or instead, that they are located in a compact region around the protostar (inner 100-200 au), thus being heavily diluted in the GBT beam. Despite the importance of such observations to unveil the chemical processes occurring at large angular scales, the major limitation is the lack of angular resolution of the single-dish telescope, which prevents us from exploring the planet formation regions. In this respect, the GBT pilot project has inspired a scientific use case for the SKA interferometer.

3 Beyond GBT: exploring the planet formation region with SKA

A fundamental step ahead in Astrochemistry will be to use the SKA to study the C-chain reservoir at small angular scales, where planetary systems are forming. Recently, a SKA use case dedicated to this topic has been developed in the context of the Cradle Of Life working group activity. In particular, the proposed project will shed light on the origin of the chemical diversity observed in Solar-System precursors and on how it affects the composition of the forming planetary systems, thanks to the combination of high angular resolution and sensitivity provided by SKA. The project will be highly complementary to several astrochemical surveys at mm- and submm- wavelengths, performed with IRAM-30m (e.g., ASAI survey; Lefloch et al. 2018), IRAM-NOEMA (e.g., SOLIS; Ceccarelli et al. 2017) and ALMA (e.g., PILS, Jørgensen et al. 2016; FAUST, Bianchi et al. 2020), which obtained the chemical census of complex organic molecules in Solar System precursors. In this respect, the SKA project represents a major step forward. On the one hand, it will overcome several limitations related to mm-observations, such as dust opacity and line confusion, providing new insights on the envelope/disk protostellar structure. On the other hand, it will unveil a new chemistry of complex C-chain species, expected to play a major role in the emergence of life, acting as the backbone of relevant biological molecules, such as proteins.

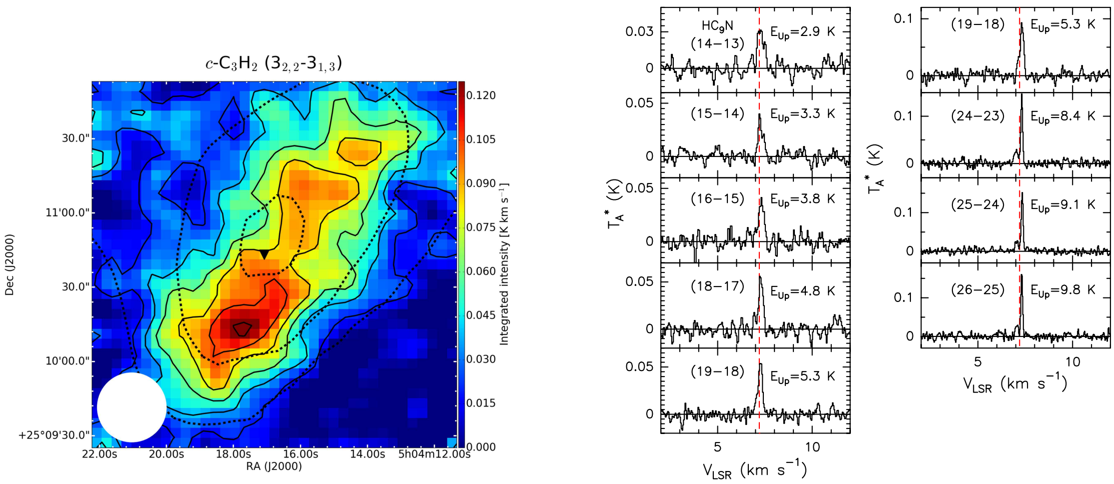

Fig. 1. Left: The prestellar core L1544 as observed with the IRAM 30-m (Spezzano et al. 2017). The map shows c-C_3H_2 integrated intensity emission at 3mm. **Right:** HC_9N transitions observed towards L1544 with the GBT. The vertical dashed lines mark the ambient LSR velocity (+ 7.2 km s^{-1}, Tafalla et al. 1998). The S/N is $\sim$ 15, and the lines are narrow with FWHM $\sim$ 0.08 km s^{-1}. The upper level energy of each transition is reported on the right inside each panel.

This project has received funding within the European Union's Horizon 2020 research and innovation programme from the European Research Council (ERC) for the project "The Dawn of Organic Chemistry" (DOC), grant agreement No 741002, and from the Marie Sklodowska-Curie for the project "Astro-Chemical Origins" (ACO), grant agreement No 811312. This work was supported by the PRIN-INAF 2016 "The Cradle of Life - GENESIS-SKA (General Conditions in Early Planetary Systems for the rise of life with SKA)".

References

Bianchi, E., Chandler, C. J., Ceccarelli, C., et al. 2020, MNRAS, 498, L87

Bizzocchi, L., Caselli, P., Spezzano, S., & Leonardo, E. 2014, A&A, 569, A27

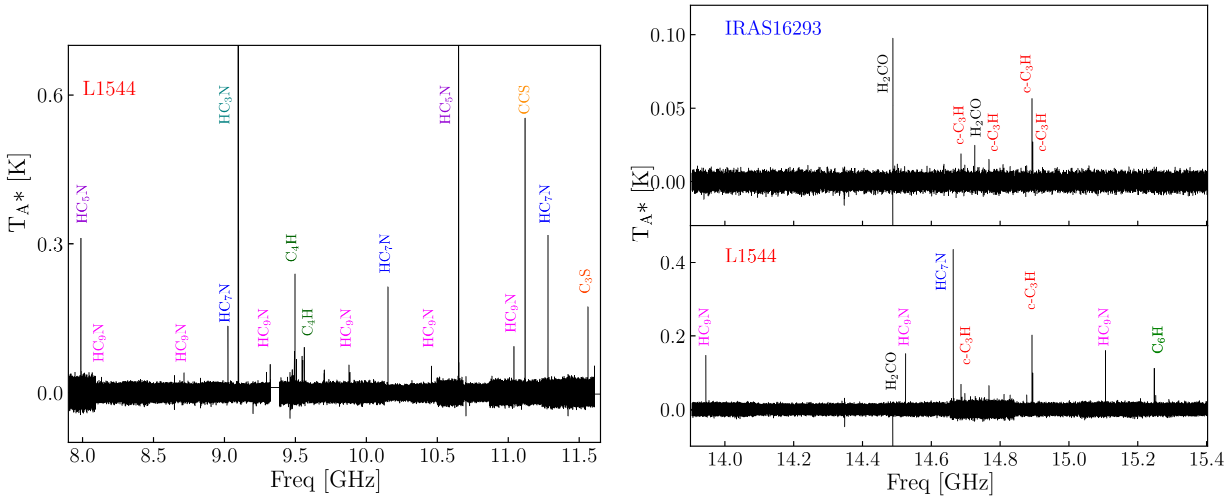

Fig. 2. Left: L1544 spectrum observed with the GBT in X-band. **R**ight: Spectrum observed with the GBT in Ku-band towars L1544 and IRAS16293-2224. The molecular species producing the emission lines are labelled in different colors. The y-axes is in antenna temperature.

Burkhardt, A. M., Long Kelvin Lee, K., Bryan Changala, P., et al. 2021a, ApJ, 913, L18

Burkhardt, A. M., Loomis, R. A., Shingledecker, C. N., et al. 2021b, Nature Astronomy, 5, 181

Caselli, P. & Ceccarelli, C. 2012, A&A Rev., 20, 56

Caselli, P., Walmsley, C. M., Tafalla, M., Dore, L., & Myers, P. C. 1999, ApJ, 523, L165

Castets, A., Ceccarelli, C., Loinard, L., Caux, E., & Lefloch, B. 2001, A&A, 375, 40

Caux, E., Kahane, C., Castets, A., et al. 2011, A&A, 532, A23

Ceccarelli, C., Caselli, P., Fontani, F., et al. 2017, ApJ, 850, 176

Ceccarelli, C., Caselli, P., Herbst, E., Tielens, A. G. G. M., & Caux, E. 2007, Protostars and Planets V, 47

Ceccarelli, C., Loinard, L., Castets, A., Tielens, A. G. G. M., & Caux, E. 2000, A&A, 357, L9

Cernicharo, J., Agúndez, M., Kaiser, R. I., et al. 2021, A&A, 652, L9

Cordiner, M. A., Charnley, S. B., Wirström, E. S., & Smith, R. G. 2012, ApJ, 744, 131

Coutens, A., Vastel, C., Caux, E., et al. 2012, A&A, 539, A132

Crimier, N., Ceccarelli, C., Maret, S., et al. 2010, A&A, 519, A65

Friesen, R. K., Medeiros, L., Schnee, S., et al. 2013, MNRAS, 436, 1513

Gupta, H., Gottlieb, C. A., McCarthy, M. C., & Thaddeus, P. 2009, ApJ, 691, 1494

Jaber, A. A., Ceccarelli, C., Kahane, C., & Caux, E. 2014, ApJ, 791, 29

Jaber Al-Edhari, A., Ceccarelli, C., Kahane, C., et al. 2017, A&A, 597, A40

Jørgensen, J. K., Müller, H. S. P., Calcutt, H., et al. 2018, A&A, 620, A170

Jørgensen, J. K., van der Wiel, M. H. D., Coutens, A., et al. 2016, A&A, 595, A117

Lefloch, B., Bachiller, R., Ceccarelli, C., et al. 2018, MNRAS, 477, 4792

Lykke, J. M., Coutens, A., Jørgensen, J. K., et al. 2017, A&A, 597, A53

McGuire, B. A., Burkhardt, A. M., Kalenskii, S., et al. 2018, Science, 359, 202

McGuire, B. A., Burkhardt, A. M., Loomis, R. A., et al. 2020, ApJ, 900, L10

Mumma, M. J. & Charnley, S. B. 2011, ARA&A, 49, 471

Mundy, L. G., Wootten, A., Wilking, B. A., Blake, G. A., & Sargent, A. I. 1992, ApJ, 385, 306

Persson, M. V., Jørgensen, J. K., Müller, H. S. P., et al. 2018, A&A, 610, A54

Punanova, A., Caselli, P., Feng, S., et al. 2018, ApJ, 855, 112

Sakai, N. & Yamamoto, S. 2013, Chemical Reviews, 113, 8981

Spezzano, S., Caselli, P., Bizzocchi, L., Giuliano, B. M., & Lattanzi, V. 2017, A&A, 606, A82

Tafalla, M., Mardones, D., Myers, P. C., et al. 1998, ApJ, 504, 900

Urso, R. G., Palumbo, M. E., Ceccarelli, C., et al. 2019, A&A, 628, A72

Vastel, C., Ceccarelli, C., Lefloch, B., & Bachiller, R. 2014, ApJ, 795, L2

Vastel, C., Ceccarelli, C., Lefloch, B., & Bachiller, R. 2016, A&A, 591, L2

SF2A 2021
A. Siebert, K. Baillié, E. Lagadec, N. Lagarde, J. Malzac, J.-B. Marquette, M. N'Diaye, J. Richard, O. Venot (eds)

FUTURE DEVELOPMENTS AND ENERGY MANAGEMENT: AN ANALOG POINT OF VIEW

B. Censier[1] and S. Bosse[1]

Abstract. Antenna arrays overcome single dishes limitations at a high energetical price. Analog based solutions for energy efficiency are presented, with the general concept of an adaptative instrument.

Keywords: energy, radiotelescope, array, electronics, RF, analog, frontend

1 Introduction

While single dishes are limited by both mechanical aspect and the fundamental diffraction limit, antenna arrays theoretically break those limitations, giving access to survey speed, but it implies lots of instrumented channels with a corresponding financial and energetical cost. The effective access to FoV is conditionned by the ability of computing enough array beams inside the single element FoV. There is thus a new practical feasability limit which is essentially linked to electronics and computing costs.Given the quest for ever better performances on one hand, and the global energetical and financial world context on the other hand, there is obviously a need for making those instruments more sober if one wants to see them built and operated succesfuly. In this context, the emphasis on operating cost reduction for phase I in the SKA Observatory Development Program (SODP) [SKA observatory (2021)] is not surprising. Several margins for improvements are identified in the following, ranging from low level electronics to global optimization of the instrument, with an important potential impact on digital backends consumption.

2 Energy consumption on aperture arrays

2.1 Some definitions

The *frontend* part consists in RF instrumentation at the antenna scale. The *station backend* part at the station scale, consists in digitization, channelizing and beamforming. The *central backend* part at the full array scale, consists in correlation and imaging features. The first 2 parts are generally on site while the central backend is centralized off site.

2.2 SKA I low numbers

SKA I Low is 58% of 1 km^2 in size: 512 stations with 256 antennas, 38 m diameter each, for a total of 131072 antennas over 578000 m^2. On-site consumption is expected at 3.3 MW (frontend + station backend), it represents an electricity cost of 5.2 Meuros per year and some thousands of CO2 tons. While the SKA projections don't separate frontend and station backend, an educated guess would be about 0.35 MW for frontend (1.35W/channel) and 2.95 MW for station backend (11W/channel). Off-site science processing centre (SPC) account for an additional 1.9 MW. The total consumption for SKA I low would then be 5.2 MW, with a share of 7% from frontend, 57% from station backend, and 36% for central backend. A consumption of 3.3 MW on site is about the dimensionning of a diesel train engine, which is technically feasible but expensive and not straightforward on a remote site. Despite some solar panels, there will be some MW dissipated through diesel generators each night and part of the day in support, with a corresponding high electricity bill and carbon emissions. The share could be different in other frequency bands, which is discussed in the following section.

[1] Nançay radioastronomy station (USN Nançay), Observatoire de Paris, CNRS/INSU, F-18330 Nançay, France

2.3 Power consumption vs. frequency

A simple toy model is used where antennas are positionned on a regular grid of periodicity $lambda2$, λ being the observation wavelength. Each antenna is fitted with 2 electronic channels dissipating 1W each. The density of antennas per unit surface is $\frac{4}{\lambda^2}$, the density of electronic channels is twice. With 1 W per channel, we thus have a density of dissipated power P_{surf} in W/m^2 expressed as $P_{surf} = \frac{8}{\lambda^2}$. At 100 MHz $P_{surf} \approx 1$ W/m^2, a 1 km^2 geometrical aperture has a total power consumption of the order of 1 MW. At 1 GHz, $P_{surf} \approx 100$ W/m^2 and the kilometer square total power is of the order of 100 MW. That's about the dimensioning of a transatlantic liner engine, once again technically feasible, but representing a financial and logistical nightmare for a radiotelescope, which concretely prevents it to be built. Nevertheless important progresses have been made with respect to that baseline estimation, with microelectronics development in Nançay allowing to reduce this consumption by a factor of 4. There are several possibilities to decrease it further, down to a more reasonable range of less than 10 MW, as will be shown in the following sections.

2.4 Power consumption on existing/projected instruments

The power consumption per surface for LOFAR LBA and HBA, SKA I low and Nenufar are summed up in figure 1 for both analog frontend (dots) and station backend (crosses). The quadratical trend in frequency is well followed by frontend systems, with SKA I low being above the 1W/channel reference essentially because of design choices like optical conversion included in the frontend. The Nenufar frontend is also above that reference, but it includes analog beamforming features: groups of 19 antennas are beamformed analogically before digitization as a single channel. The corresponding reduction of digitizing need can been seen in the figure of Nenufar's backend consumption, which is only about 0.02 W/m^2 with respect to the area effectively covered by a single digital channel. The effective consumption per digitized channel is around 5W, but the antennas grouping decrease it to an apparent $5/19 = 0.26$ W/antenna. The same effect can be seen on LOFAR HBA figures, with higher consumption on older technologies following the progress made in computing energy efficiency in the last decade.[TOP500 project team (2021)] Antennas grouping with analog beamforming is here a first example of a possible analog design choice having substantial impact on the digital part and the overall energy consumption. It comes to the price of reducing the field of view, but this loss may be recovered at low energetical price as will be shown in the following.

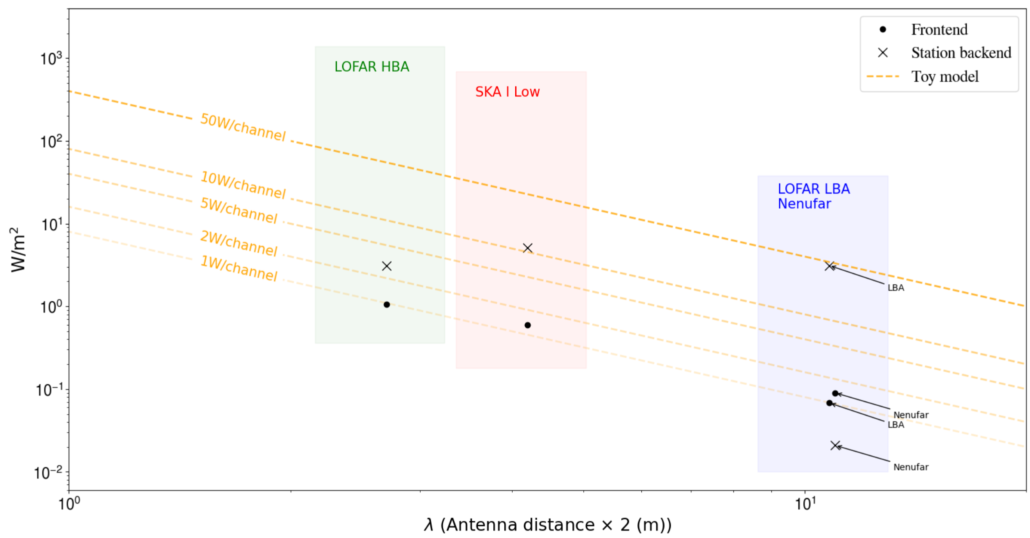

Fig. 1. Power consumption per instrumented meter square as a function of average distance between antennas, for both analog frontend (dots) and station backend (crosses), on LOFAR LBA (10 - 100 MHz) and HBA (120-240 MHz), SKA I low (50 - 350 MHz) and Nenufar (10-100 MHz). The orange dashed line is the toy model at 1 W/channel presented in section 2.3

3 Analog solutions for energy management

3.1 Integrated circuits optimization

Including energy consumption as yet another specification is pulling the R&D work towards energy optimized solutions, as can be illustrated by the work done in Nançay within the framework of the Aperture Array Integrated Receiver project (AAIR), focusing on GHz dense aperture array. The GHz scale implies 100 MW power scale (see 2.3) for 1 km^2, which makes it practically not feasible. Nevertheless this band is particularly important given the HI line, and GHz aperture arrays would unlock survey speeds 3 to 10 times higher than SKAmid dishes [Wijnholds & Jongerius (2013)]. The motto behind aperture array for SKA mid frequencies was "the billion galaxies survey machine", this band has thus pulled several efforts toward power consumption reduction. The EMBRACE demonstrator [Torchinsky et al. (2016)] was a 64m^2/4608 antennas dense aperture array, operating succesfuly between 500 MHz and 1.5 GHz from 2011 to 2017 in Nançay. Its integrated analog frontend has been designed in Nançay, including low noise amplifier (LNA), signal conditioning and analog beamforming through integrated beamformer chips. The power consumption was 1.2 W/channel, and has been decreased to 300 mW/channel 6 years after with further optimizations on a new AAIR prototype tile. This brings a GHz km^2 aperture array to a 25 MW power consumption scale. An additional factor of 2 reduction should be straightforward, bringing a km^2 down to 10 MW. Additional optimizations at the whole instrument scale are needed to really make it an energy efficient system, as will be presented in following sections.

3.2 Analog/digital load balance

Analog based solutions may also have an impact on the consumption of the digital part. In the simplest example, digitizing a group of beamformed antennas is paid in reduction of the FoV, but this FoV loss can be recovered at a marginal cost by adding more analog beams. The splitting of the RF signal several times allows to get several independent beams in parallel. This solution has already been demonstrated on several applications, and has a big impact on the main power sink for systems like SKA I low, namely the station backend. Analog beamforming may be seen as a pre processing stage reducing the burden on the following digital stages. It may also have a radical impact on the central backend, as illustrated in a study [Wijnholds & Jongerius (2013)] considering 2 scenarii for a full 1 km^2 SKA low : "AA low" with 911 stations of diameter 35m (about 250 antennas), and "alternative AA low" with 280 stations of diameter 75m (about 1000 antennas). The larger stations in the alternative scenario implies a FoV loss, which is recovered by generating 4 beams. We thus have 2 equivalent systems with respect to performances. Results show beamforming requirements are logically quadrupled. An analog beamforming system would accomodate those 4 beams without problems. Most impressively requirements on imaging as a whole are reduced by a factor ≈ 250. The AA low original scenario would dissipate 8.5 MW for imaging, while the alternative scenario only dissipates 34 kW. This is mainly due to the fact that imaging computing power requirements (taking into account w-projection only)[Cornwell et al. (2012)][Perley & Clark (2003)] falls like D_s^{-4} as the station diameter D_s increases, and like N_s^2 as the number of stations N_s decreases, while it scales linearly with respect to the number of RF analog beams. There is thus an enormous potential for power reduction on the whole chain working with analog beamforming. The SKA observatory (SKAO) has settled the design of SKA I low somewhere between the two scenarii presented here, with 512 stations of 256 antennas each and no analog beamforming. It should be noted however that RF channel splitting allows for instrument upgrade without major modifications, some additional instrumentation being installed for more independent RF channels. Also if the remaining 40% surface for a full km^2 is to be installed, their positions may be determined with those optimizations in mind.

3.3 RFI and input dynamics

Input dynamics has the biggest influence on frontend consumption, and it is dimensionned with respect to the maximum emission on site, instruments are thus systematically designed for a maximum frontend consumption. The maximum dynamic range of incoming RFI is most often around 6 orders of magnitude or more, implying 14 bits or so digitization, whereas a few bits may be sufficient to describe the astrophysical signal, and frontend electronics having to run in a regime dissipating up to ten times more than with a minimal input dynamics. There is thus an interest in mitigating the strongest RFIs on site *before* the digitization step, formitigating nonlinear intermodulation effects which are not correctible after digitization, reducing the required coding depth, and the frontend power consumption. Several methods for RFI mitigation already exist, but their digital nature and/or lack of automatization makes them unable to scale at SKA level. We thus need an almost autonomous system, with low energetical consumption, that could both detect and mitigate the strongest RFI signals analogically. For SKA we also add the constraint that additional features should be added to the existing instrumentation without deep modifications. The best instrument for RFI detection being the scientific instrument itself, one can design additional RF analog beams that are dedicated to RFI detection. Splitting the analog signal at each antenna, we create an additional RF channel, then beamformed analogically, with a pointing direction that may be updated regularly, so that a RFI dedicated beam scans the sky in parallel to the main astrophysical channel. In SKA I low, this can be done in existing "smart box" gathering signals from 16 antennas, giving a ≈ 20 degrees FWHM beam. With such a resolution, and a 1 ms integration time (sufficient for the biggest emissions), the whole sky can be scanned in 200 ms by regularly updating the beamforming weights. Since independent from the science beam, the RFI dedicated beam may have specific settings for RFI detection, e.g. a larger input dynamics and lower sensitivity. When an emission at a given beam pointing is found to be above a pre determined threshold, the RFI dedicated beam is fixed on target, and the RFI signal may be re injected out of phase in the main astrophysical path. That way the RFI emissions is mitigated in the analog part, keeping the input dynamics requirements in a reasonable range. The simplicity, autonomy and low consumption constraints are met thanks to integration of an almost closed loop analog system with a simple thresholding scheme. Several analog beams dedicated to RFIs may be generated, so that multiple source can be corrected for for in parallel.

3.4 Adaptive instrument

Designing electronics is basically defining a set of components, their values and the connections between them. If the circuit connections are defined, and the value of each component is a free parameter, meeting the specifications means optimizing a given cost function (aggregating specifications and constraints) with respect to all those free parameters. Through controllable integrated components receiving digital commands on a few bits, one may thus design a kind of programmable, or configurable frontend electronics, with free parameters being values for several active sources and impedances throughout the circuit. This is the heart of the Smart-AAIR project following AAIR, with the goal of optmizing a cost/perfomance ratio, by dynamically considering a set of specifications for each observation or each type of observations, thus using only the necessary resources for a given goal. This implies to model the complex relations between low level parameters at the electronic board level (impedances, voltages, currents) and high level parameters (sensitivity, dynamics, power consumption), with high dimensionnality and non linearities, and simulations being difficult and very time consuming on some parameters like input dynamics. Since we want dynamic modeling, we need a solution for measurement based, accurate and fast modeling of that relation, both for direct modeling (getting the performances associated with a set of low level parameters) and inverse modeling (getting the optimal low level parameters with respect to given performance goals). Machine learning is particularly suited to those constraints and we already tested the use of neural networks in Nançay, the first stage being a validation on simulated data. [Censier & Bosse (2020)]. Relatively small networks are showned to be sufficiently accurate (at the 0.1 dB level or less) for both direct and inverse modeling, with execution times ranging from microseconds to milliseconds on an unoptimized laptop where simulations may take days. This opens the possibility for dynamic modeling without any prior hypothesis, and optimizing low level parameters with respect to both performances goals and environmental constraints like energy provision and RFI. This concept thus has a link with all the sections above, for example, some RFI dedicated beam(s) (see section 3.3) would be a rich source of dynamic informations about the electromagnetic environment, and could be taken into account in the optimization. We are currently setting up a measurement bench for training the network directly on measured data, using a S-AAIR prototype board with 8 controllable low level parameters.

References

Censier, B. & Bosse, S. 2020, URSI GASS, Rome, Italy

Cornwell, T. J., Voronkov, M. A., & Humphreys, B. 2012, ser. SPIE Conference Series, 8500

Perley, R. & Clark, B. 2003, EVLA memo, 63

SKA observatory. 2021, SKAO official document

TOP500 project team. 2021, TOP500 website

Torchinsky, S., Olofsson, A. O. H., Censier, B., & et al. 2016, Astronomy & Astrophysics, A77

Wijnholds, S. & Jongerius, R. 2013, IEEE AfriCon / URSI BEJ Meeting

EXPLORING THE COSMIC DAWN WITH NENUFAR

F.G. Mertens[1,2], B. Semelin[1] and L.V.E. Koopmans[2]

Abstract. The exploration of the Cosmic Dawn, the period of the Universe during which the first stars and galaxies were formed, is one of the last frontiers of modern astronomy and cosmology. The redshifted 21-cm line emission from neutral hydrogen is a unique probe and can open this era for astrophysical and cosmological studies. The tentative detection of the 21-cm global signal by the EDGES team at $z \sim 17$ underlines the need for an interferometric detection of this signal to discriminate between the numerous models trying to explain this unexpected discovery. The NenuFAR Cosmic-Dawn Key-Science Program aims to perform this detection in the redshift range $z \sim 15 - 31$ with a novel SKA precursor, the NenuFAR radio telescope located at the Station de Radioastronomie de Nançay and that started operating in 2019. Due to its compactness it is particularly sensitive to the large scale of the 21-cm signal. Only 100 hours of observation are needed to reach the level of the most extreme models, while 1000 hours are needed for the more standard models. Observations have already started, accumulating to almost 500 hours on the North Celestial Pole field. In this contribution, we introduce the project, our first results and the developments in calibration and RFI mitigation specific to this new instrument.

Keywords: cosmology: dark ages, reionization, first stars; cosmology: observations; techniques: interferometric; methods: data analysis

1 Introduction

The observation of the 21-cm line of neutral hydrogen is the most promising method to study the Cosmic Dawn and Epoch of Reionization (EoR) in detail. Its detection can inform us about the timing and mechanisms of the formation of the first stars, as well as the impact on the physics of the interstellar medium and the intergalactic medium (IGM) of the radiation emitted by these first sources of light. Many observational programs are underway to detect it. The so-called "global" experiments, such as EDGES [*] (Bowman et al. 2018), aim at detecting the 21-cm signal average in the sky. In addition to the global signal, spatial fluctuations in the brightness temperature of the 21-cm signal can be detected by radio-interferometric imaging, using interferometers such as NenuFAR [†] (Zarka et al. 2020), LOFAR [‡] (van Haarlem et al. 2013), MWA [§] (Tingay et al. 2013), HERA [¶] (DeBoer et al. 2017), and in a near future SKA [‖] (Koopmans et al. 2015). The power spectrum of the image cube thus obtained allows in particular to characterize the fluctuations of the spin temperature, of the hydrogen density, and of the ionization fraction, on scales ranging from a few arc minutes to a few degrees.

The tentative detection reported by the EDGES team of an absorption spectrum at redshift $z \sim 14 - 21$ (Bowman et al. 2018), in the range where the Cosmic Dawn is predicted, has unexpected features. This observed absorption signal (-500 mK $\pm$ 200 mK, 99 % IC) is considerably deeper than expected (Fraser et al. 2018). Standard models predict a maximum absorption of the order of -200 mK and, to explain this observation, a new process must be introduced, either by supercooling the Inter Galactic Medium (IGM) gas (Barkana 2018,

[1] LERMA, Observatoire de Paris, PSL Research University, CNRS, Sorbonne Université, F-75014 Paris, France
[2] Kapteyn Astronomical Institute, University of Groningen, PO Box 800, 9700 AV Groningen, The Netherlands
[*] Experiment to Detect the Global Epoch of Reionization Signature, `https://loco.lab.asu.edu/edges`
[†] New Extension in Nançay Upgrading LOFAR, `https://nenufar.obs-nancay.fr`
[‡] Low-Frequency Array, `www.lofar.org`
[§] Murchison Widefield Array, `www.mwatelescope.org`
[¶] Hydrogen Epoch of Reionization Array, `https://reionization.org`
[‖] Square Kilometre Array, `www.skatelescope.org`

e.g.) or by an additional source of background radiation more intense than the CMB (Fialkov & Barkana 2019, e.g.). A confirmation is still needed, that could come from the SARAS2 experiment (Singh et al. 2017), and the EDGES detection might just be an artefact (Singh & Subrahmanyan 2019), but if true, this detection would have dramatic implications for our understanding of the physical processes that occurred during the Cosmic Dawn.

The global spectrum alone cannot distinguish between the different models explaining the signal observed by EDGES, an additional constraint is thus necessary. This may come from an interferometric detection, which will hold more information than the global signal. The different models also predict a power spectrum of the signal at 21-cm much more intense than the standard models predict which makes a detection much more accessible to the current instruments, and in first place by NenuFAR (see Figure 1). We present here the effort by the NenuFAR Cosmic Dawn Key Project team to observe this signal with NenuFAR.

2 The NenuFAR Cosmic Dawn Project

NenuFar is a new radio telescope being installed at the Station de Radioastronomie in Nançay (France). In its final specifications, it will consist of 96 mini-arrays (MAs) included in a 400 m diameter disk and each composed of 19 dual polarized antennas. The compactness of the instrument, offering a large effective collecting area and short baselines, gives it a high sensitivity at large spatial scales, making it ideal to detect the 21-cm signal from the Cosmic Dawn. The NenuFAR Cosmic Dawn project is one of the early scientific Key Project (KP) of the NenuFAR telescope and aims at detecting this signal in the frequency range $40 - 85$ MHz ($z \sim 15 - 31$). This exciting goal is challenged by the difficulty of extracting the feeble 21-cm signal buried under astrophysical foregrounds orders of magnitude brighter and contaminated by numerous instrumental systematics. We estimate that $\sim$100h of observation are required to reduce the thermal noise to a level suggested by some non-standard models (Barkana 2018), and $\sim$1000h for more standard models (see Figure 1). The project has been allocated more than 1000h of observations which started in September 2020 and will continue until early 2022. The target is the North Celestial Pole field (NCP) which is also one of the main target of the LOFAR-EoR project.

In these early stages of this new instrument, many components are still being installed or upgraded. Mid 2019, 52 MAs had been installed and new MAs are being added gradually. The remote MAs, which will provide when completed angular resolution down to 4 arcmin at 85 MHz, are also still in the process of being installed. Three of the 6 planned remote MAs are in operation at the time of writing. A new correlator (NICKEL) based on the COBALT2 LOFAR correlator (Pandey et al. 2020), increasing the instantaneous bandwidth and spectral resolution of the imaging mode, is also fully operational since mid-2020.

3 Early Observation Phase

In the first two semesters of the early science phase, before the availability of the NICKEL correlator and in preparation for later observations, we observed with NenuFAR a total of 340 hours on the North Celestial Pole field. The LaNewBa correlator available at that time offered only an instantaneous bandwidth of $\sim$ 3.1 MHz and repeated observations were necessary to cover the full $30 - 85$ MHz bandwidth. Our goal in this first phase of observation was to build a Galactic and extragalactic model of the NCP field, assess potential technical issues and repeat observations to refine observing strategy for the second phase.

Radio interferometric observations are affected by numerous effects which need to be precisely corrected or accounted for to produce science ready data. After data transfer to the LOFAR-EoR cluster 'Dawn' and pre-processing, the processing pipeline consists, in essence, of (1) Radio Frequency Interference (RFI) flagging with AOFlagger, (2) Calibration on three directions: NCP field, Cygnus A and Cassiopeia A, applying the solution of the NCP field and subtracting the contributions from Cygnus A and Cassiopeia A, (3) imaging using WSClean (Offringa et al. 2014), (4) power-spectra using the Lofar-EoR PS pipeline (Mertens et al. 2020).

Emphasis was given in this first phase on data quality assessment. Besides looking at standard RFI flagging statistics, we also used the technique of near field imaging (Paciga et al. 2011) to locate potential sources of local RFI in the field. Several were identified and reported with this technique.

The other aim of this first phase was to build a broadband Galactic and extragalactic sky model of the NCP field. All the observing nights of the NCP field have been processed and combined to form wide-field Stokes I and V images cubes. Figure 2 shows wide-field Stokes I images of the North Celestial Pole field at four frequency ranges. In these images, the field around the NCP is confusion limited, but we also observe many 3C radio sources at distances up to 50 degrees from the NCP. At the highest frequency, we could detect, and

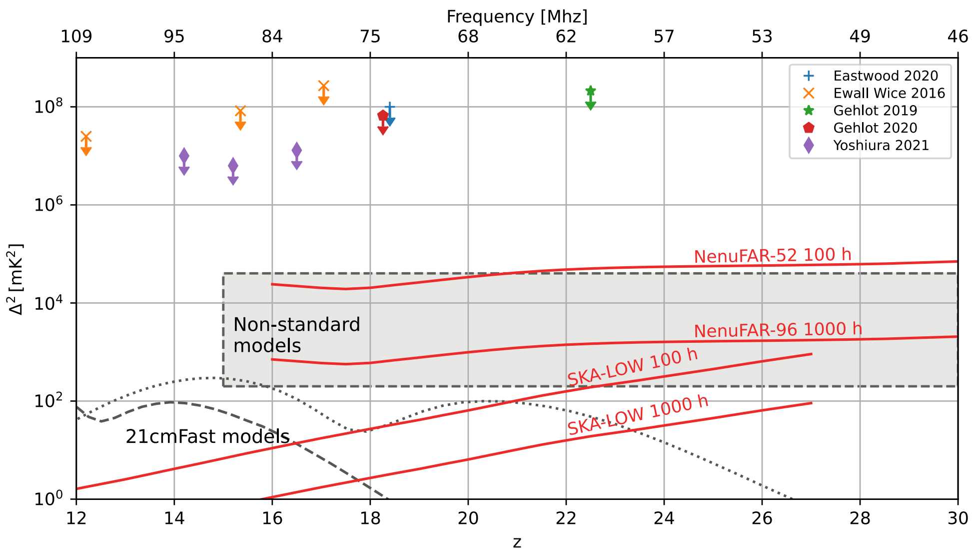

Fig. 1. Upper limits on the 21 cm power spectrum at 95% confidence (2σ) from various experiments from $12 < z < 30$, spanning the Cosmic Dawn, and at $k \gtrsim 0.1\text{Mpc}^{-1}$. Forecasted thermal noise limited 2σ sensitivity curves for the NenuFAR and SKA telescopes are also plotted for a 100 hour and 1000 hour integration

cross-identify with catalogs, almost 200 sources inside the 20 degrees FoV of the beam-corrected image with an intrinsic flux higher than 2 Jy/PSF ($\sim$2 time the confusion noise standard deviation). The Galactic diffuse emission is also clearly visible at all frequencies and shows striking similarity with an image obtained at higher frequency (122 MHz) with the AARTFAAC system (Gehlot 2019). We also produced Stokes I angular power spectra of the NCP field for all observed subbands. The galactic diffuse emission dominates on $\ell < 100$ (steep angular power spectrum index) while the confusion limited compact sources dominate the smaller scales (flat

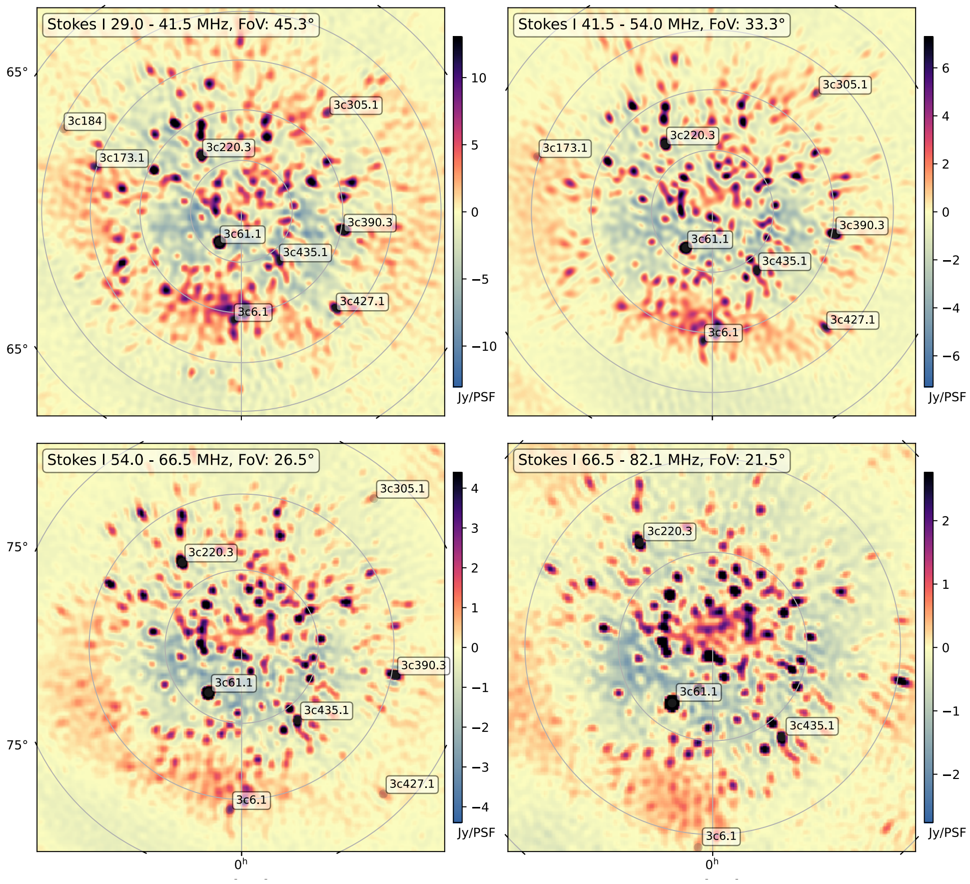

Fig. 2. Wide-field Stokes I image of the North Celestial Pole field at four frequency ranges. The images are cleaned and produced using Briggs weighting. Integration time from top-left to bottom right is: 14h (rms noise: 161 mJy/PSF), 14h (rms noise: 80 mJy/PSF), 15h (rms noise: 56 mJy/PSF) and 12h (rms noise: 60 mJy/PSF). Both compact as well as Galactc diffuse emission are seen in these images.

spectra). For the former, we observe an angular power spectrum index $\alpha \sim -2.5$ for the frequencies > 50 MHz which is consistent with previous observations of the NCP at other frequencies. The temperature spectral index is observed to be $\beta \sim -2.8$ for $\ell > 100$.

4 Phase 2: Observations and First Results

During the second phase of observation, we aim to reach the 1000h of observations on the NCP field required for the detection of the Cosmic Dawn's signal. A total of ∼500h have already been accumulated between July 2020 and June 2021 but which did not include yet the longer baselines. With the new NICKEL correlator narrowband RFI are now more optimally flagged which improved the data quality considerably. The availability of new remote additional MAs will also provide higher angular resolution required for an important milestone in the project which is to build a higher resolution and deeper sky model of the NCP field. This will then be used to improve our calibration, and allow for more accurate sky model subtraction with direction-dependent calibration. The first remote station is available since the beginning of October 2020 and commissioning observations have already been taken in this configuration.

Combining all our October observations, we produced a preliminary image cube at a resolution up to ∼15 arcsec. Artefacts are still present in these images due to direction-dependent effects and the yet-limited uv-coverage. The quality of these images will improve once later remote stations are integrated into the array.

5 Summary

The NenuFAR Cosmic Dawn project aims at detecting the 21-cm signal from the Cosmic Dawn with the new NenuFAR telescope. The signal may be more intense than previously thought which may be the sign of exciting new science. In a first phase of observation programme, with limited capacity of the telescope, we build a preliminary sky model of the NCP field with a peculiar emphasis on assessing data quality, thus providing important feedback for operating the telescope. The second phase started in July 2020 and we aim to reach the 1000 hours of observations which may be required for the detection of the signal by early 2022.

References

Barkana, R. 2018, Nature, 555, 71

Bowman, J. D., Rogers, A. E. E., Monsalve, R. A., Mozdzen, T. J., & Mahesh, N. 2018, Nature, 555, 67

DeBoer, D. R., Parsons, A. R., Aguirre, J. E., et al. 2017, PASP, 129, 045001

Fialkov, A. & Barkana, R. 2019, MNRAS, 486, 1763

Fraser, S., Hektor, A., Hütsi, G., et al. 2018, Physics Letters B, 785, 159

Gehlot, B. 2019, PhD thesis, University of Groningen

Koopmans, L., Pritchard, J., Mellema, G., et al. 2015, in Advancing Astrophysics with the Square Kilometre Array (AASKA14), 1

Mertens, F. G., Mevius, M., Koopmans, L. V. E., et al. 2020, MNRAS, 493, 1662

Offringa, A. R., McKinley, B., Hurley-Walker, N., et al. 2014, MNRAS, 444, 606

Paciga, G., Chang, T.-C., Gupta, Y., et al. 2011, MNRAS, 413, 1174

Pandey, V. N., Koopmans, L. V. E., Tiesinga, E., Albers, W., & Koers, H. U. A. 2020, in Astronomical Society of the Pacific Conference Series, Vol. 527, Astronomical Society of the Pacific Conference Series, ed. R. Pizzo, E. R. Deul, J. D. Mol, J. de Plaa, & H. Verkouter, 473

Singh, S. & Subrahmanyan, R. 2019, ApJ, 880, 26

Singh, S., Subrahmanyan, R., Udaya Shankar, N., et al. 2017, ApJ, 845, L12

Tingay, S. J., Goeke, R., Bowman, J. D., et al. 2013, PASA, 30, e007

van Haarlem, M. P., Wise, M. W., Gunst, A. W., et al. 2013, A&A, 556, A2

Zarka, P., Girard, J. N., Tagger, M., & Denis, L. 2020, in 2020 URSI General Assembly and Scientific Symposium

Session 8

Atelier général du PNST: le soleil et l'héliosphère

SOLAR-CYCLE VARIATIONS OF INTERNETWORK MAGNETIC FIELDS

M. Faurobert[1] and G. Ricort[1]

Abstract. Small-scale magnetic fields in the quiet Sun contain in total more flux than active regions and represent an important reservoir of magnetic energy. But the origin and evolution of these fields still remain largely unknown. We present a study of the solar-cycle and center-to-limb variations of the magnetic-flux structures at small scales in the solar internetwork. We used Hinode SOT/Spectropolarimetric data from the irradiance program from 2008 to 2016 and applied a deconvolution to the intensity and polarization profiles to correct them from the smearing due the Point Spread Function of the telescope. Then we performed a Fourier spectral analysis of the spatial fluctuations of the magnetic-flux density in 10"x10" internetwork regions spanning a wide range of latitudes. At low and mid latitudes and away from the active latitudes present at solar maximum, the power spectra do not vary significantly with the solar cycle. At high latitudes variations in opposition of phase with the solar cycle are observed at granular scales. Whatever the latitude the power of the magnetic fluctuations at scales smaller than 0.5" remain constant throughout the solar cycle. These results are in favor of a small-scale dynamo that operates in the internetwork.

Keywords: solar magnetism, high resolution, solar cycle

1 Introduction

The internetwork (IN) refers to the regions of the solar surface that are outside of active regions and the magnetic network. It has been shown that IN magnetic fields bring large amounts of magnetic flux at small scales to the solar surface and may play an important role in the heating of the chromosphere. A very thorough review of the numerous and sometimes contradictory observational investigations of the quiet Sun magnetism is presented in Bellot Rubio & Orozco Suárez (2019). Many high resolution spectro-polarimetric observations have shown that IN magnetic fields emerge at the solar surface on the form of magnetic loops with various sizes and lifetimes. State-of-heart simulations show that magnetic loops are a consequence of the interaction of convective flows with the magnetic field.

However, as noted in Bellot Rubio & Orozco Suárez (2019), the origin of IN magnetic fields is still debated. Are they due to the recycling of decaying active regions or generated by the solar dynamo in the deep convection zone? Alternatively they may be produced by a local dynamo operating at the solar surface. In this paper we address this issue by investigating the spatial structuring of IN magnetic flux and whether it varies according to the latitude and the global solar cycle. Using synoptic data from the Hinode irradiance program between 2008 and 2016, we obtain maps of the longitudinal magnetic flux density on a wide range of latitudes. We correct these maps from the smoothing effect of the Point Spread Function (PSF)of the telescope and from a time-varying defocus, then we select a set of 162 (10"x10") IN regions between the equator and $\pm 70°$. We perform a Fourier analysis of the unsigned magnetic-flux spatial fluctuations in these regions and examine the solar-cycle variations of their Fourier power spectra at various latitudes,

2 Principal component analysis of the Stokes profiles and deconvolution

Following Quintero Noda et al. (2015) we work on the spectral dimension of the Stokes parameters and not on the spatial dimensions. We write the Stokes profiles at each pixel as a linear combination of an orthonormal

[1] University Cote d'Azur, Lagrange Laboratory. Parc Valrose. 06108 Nice Cedex 2. France

basis of eigenfunctions $\Phi_i(\lambda)$ that are obtained through a principal component analysis of the observed profiles $S_p(\lambda, x, y)$,

$$S_p(\lambda, x, y) = \sum_{i=1}^{n_\lambda} (\omega_i(x, y) * PSF(x, y))\Phi_i(\lambda) + N(x, y), \tag{2.1}$$

where the star operator denotes the convolution and $N(x, y)$ is some additive noise. The scalar product of the observed Stokes profiles with any of the eigenfunctions gives

$$< S_p(\lambda, x, y), \Phi_k(\lambda) >= \omega_k(x, y) * PSF(x, y) + N(x, y). \tag{2.2}$$

Therefore the maps of the coefficients of the linear combination obtained from the observed Stokes profiles are affected by the same convolution with the PSF as the profiles. We recover the coefficients ω_k by applying a PSF deconvolution to the observed ω_k-maps, and we reconstruct the Stokes profiles using the linear combination of the eigenfunctions with the ω_k coefficients. We find that 8 principal components are sufficient to account for the variability of the observed profiles. The method also allows an efficient filtering of the noise that is mainly projected on less significant principal components.

For our long-term study we chose to deal with the Stokes I and V profiles only, linear polarization profiles in the irradiance data of Hinode are much more noisy and their quality is degrading after 2013. We do not use any sophisticated inversion method to recover the magnetic field components from the Stokes profiles but rather implement the simple and robust center-of-gravity method, which was first introduced by Semel (1970) and later extensively tested by Uitenbroek (2003) by comparison with the magnetic flux in 3D magnetohydrodynamical simulations of the magneto-convection in the solar photosphere.

In the center-of-gravity method the line-of-sight component of the magnetic field is derived from the wavelengths λ_+ and λ_- of the centroid of the right- and left-circularly polarized line components $I \pm V$,

$$\lambda_\pm = \frac{\int \lambda(I_{cont} - (I \pm V))d\lambda}{\int (I_{cont} - (I \pm V))d\lambda}, \tag{2.3}$$

where I_{cont} denotes the continuum intensity. The longitudinal magnetic component is then obtained from the relation

$$B_{LOS} = \frac{\lambda_+ - \lambda_-}{2} \frac{4\pi mc}{eg_L\lambda_0^2}, \tag{2.4}$$

where g_L is the line effective Landé factor and m and e are the mass and electric charge of the electron (in MKSA units), respectively. When the magnetic structure is not resolved by the instrument, Eq. (2.4) gives the longitudinal apparent flux density, that is, the magnetic flux density averaged over the pixel area. We remark that because the wavelengths $\lambda_\pm$ are obtained from a ratio of observed intensities, they should not be greatly affected by a possible aging of the detectors or calibration issues. Figure1 shows the magnetic flux map of an IN region at disk-center in 2014 before and after deconvolution. The sharpening effect of the deconvolution leads to higher flux densities in the corrected map.

3 Fourier power spectra of the magnetic flux density

We use one run of the irradiance program HOP79 per year from 2008 to 2016. For each year we have selected 162 IN regions of 10" x 10" located along the polar axis from the north to the south pole. The original pixel size of the data is 0.1475" x 0.32 ", we performed bilinear interpolations of the images to get a square pixel of 0.16" that is the size of the camera pixel. Figure 2 shows the mean unsigned magnetic flux in the selected regions in 2008 (solar minimum) and in 2014 (solar maximum). We observe no significant latitudinal variation nor variation between the solar minimum and maximum, except at some active latitudes in 2014.

We computed the 2D Fourier spectra of the IN unsigned flux density after dividing each selected region in four subregions of 32 px x 32 px (5" x 5") , we then further averaged the spectra over 9 IN regions at close latitudes. We then obtain 18 power spectra spanning latitudes between $\pm 70°$. Out of disk-center the radial averages of the 2D spectra are computed over elliptical bands instead of circular bands to account for the shortening of the images in the radial direction due to the projection effect. As the mean value of the unsigned flux density varies very little with the latitude and time we show spectra normalized by the mean unsigned flux density in the regions.

Figure 3 shows the normalized power spectra at disk-center and at high latitudes in 2008, 2009, 2013 and 2014 together with the one-sigma bars computed on the 9 regions used for the averaging. We observe no significant

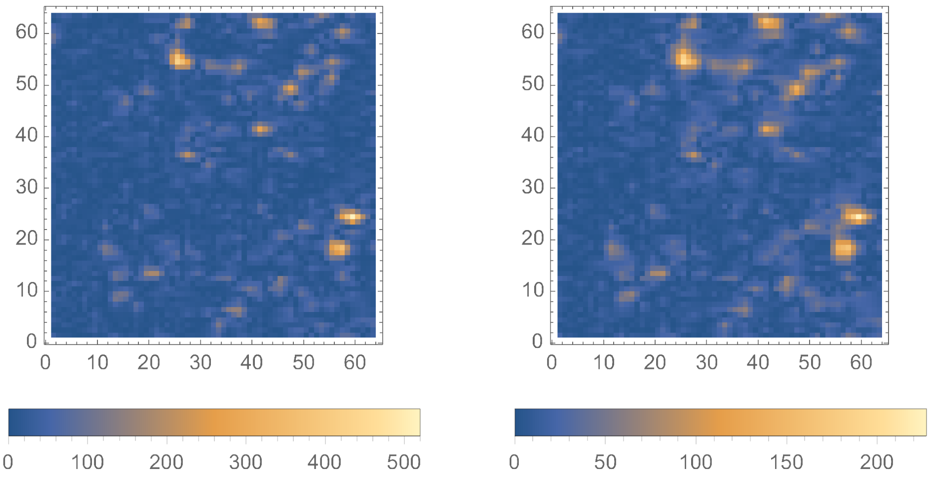

Fig. 1. Maps of the unsigned longitudinal magnetic flux density in a selected IN region. The axis are in pixels of 0.16". Left: after deconvolution, right: before deconvolution.

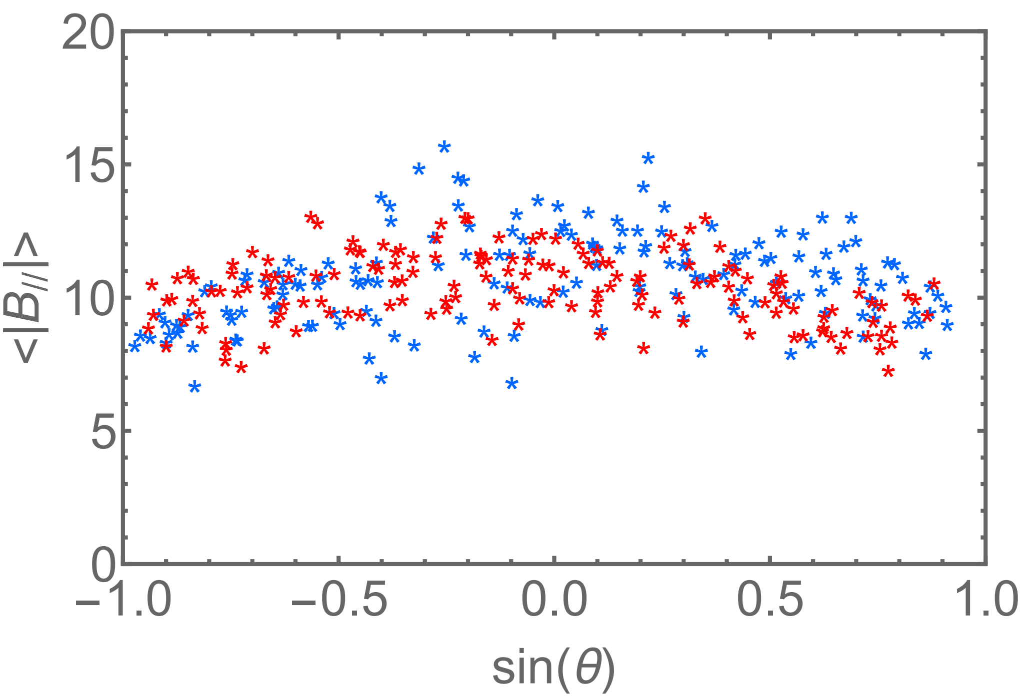

Fig. 2. Mean unsigned magnetic flux density in Mx/cm^2 in the selected IN regions in 2008 (red symbols) and in 2014 (blue symbols) as a function of the sinus of their latitude.

variation of the power spectra at disk-center but at high latitudes the power at low spatial frequencies (scales between 5" and 0.5") decreases significantly at the maximum of the solar cycle. We observed that the minimum of the cycle takes places in 2009 at the North pole, and in 2008 at the South pole. We observe no variation at spatial frequencies larger than 2 arcsec^{-1} (scales smaller than 0.5"), this is also true at all the latitudes of our data sets.

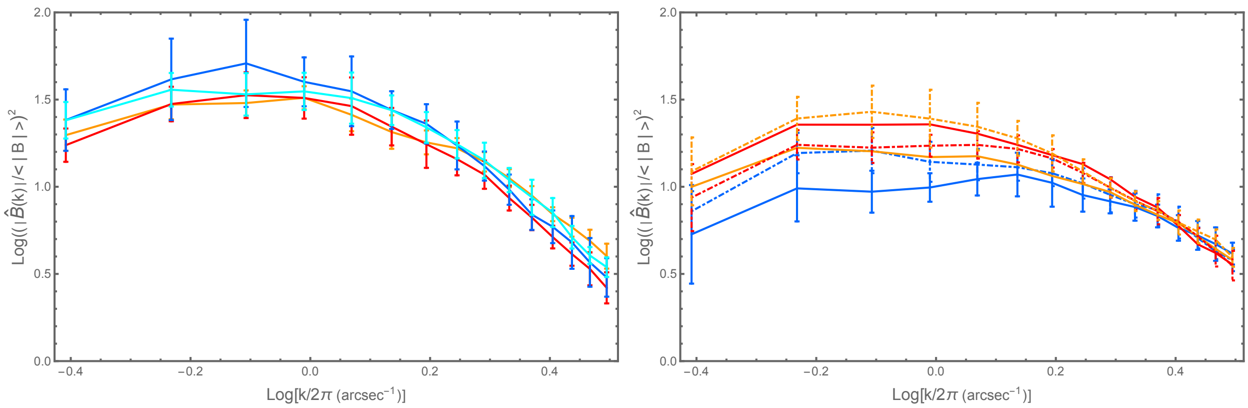

Fig. 3. Left: Normalized power spectra at disk-center in 2008 (red curve), 2009 (orange), 2013 (light blue), 2014 (blue). **Right:** Normalized power spectra at high latitudes. Full lignes: $-70°$, dot-dashed curves: $+70°$. In 2008 (red), 2009 (orange), 2014 (blue). The bars show one standard deviation computed on 9 IN regions at close latitudes.

4 Conclusions

We recall that the longitudinal flux reflects different magnetic components at disk center and high latitudes. At disk center the line of sight is vertical so we observe vertical fields, whereas at high latitudes it is inclined on the solar surface so we observe mainly the horizontal fields of the selected IN regions. As the heliocentric angle is larger at high latitude we also observe higher layers of the photosphere. It has been shown that magnetic fields in the IN have a more uniform distribution of field inclinations than network and other strong-field regions and that the inclination increases with height.

Our study shows that vertical fields in the IN at low latitudes do not vary significantly with the solar cycle, at least on the spatial scale that we could investigate, between 0.3 " and 5 ". The horizontal fields observed at high latitudes show variations in opposition of phase with the solar cycle, except at scales smaller than 0.5" , where the power spectra remain constant.

At scales smaller than 0.5" the power spectra of the IN longitudinal magnetic flux density are constant whatever the latitude, indicating the presence of a time-independent magnetic component. The time-independence of the spectra is a strong indication that the mechanism at the origin of IN fields is not, at least not directly, correlated to the global dynamo.

It is difficult to compare our observational results with the numerical simulations of Rempel (2014, 2018) because we measured the unsigned longitudinal flux and not the magnetic energy. In the simulations the magnetic energy power spectrum at disk-center has a broad maximum at small spatial scales on the order of 500 km to 1000 km. In our data, the power spectra have a broad maximum at sub-granular spatial scales on the order of 900 km, this is consistent with the simulations.

References

Bellot Rubio, L. & Orozco Suárez, D. 2019, Living Reviews in Solar Physics, 16, 1

Quintero Noda, C., Asensio Ramos, A., Orozco Suárez, D., & Ruiz Cobo, B. 2015, A&A, 579, A3

Rempel, M. 2014, ApJ, 789, 132

Rempel, M. 2018, ApJ, 859, 161

Semel, M. 1970, A&A, 5, 330

Uitenbroek, H. 2003, ApJ, 592, 1225

SPECTRAL EVOLUTION OF ALFVÉNIC TURBULENCE

R. Grappin[1], A. Verdini[2] and W.-C. Müller[3]

Abstract. A correct description of solar wind acceleration relies critically on a good understanding of the turbulent cascade in the solar wind. However, no cascade theory is presently able to reproduce the variability of the observed spectral indices in the large scale range of the spectrum (Grappin et al. 1991; Chen et al. 2013). We propose here to test numerically the possibility that expansion is at the origin of some of the still not understood spectral properties, and focus on the scaling of the Elsasser spectra $E_{\pm}$, especially with strong Alfvénicity. We use 3D MHD simulations, with moderate ratio B_0/b_{rms}, with and without expansion. We find that with zero expansion, small-scale pinning of the dominant and subdominant spectra lead to (unobserved) different indices for the two Elsasser spectra, while with expansion, one finds nearly equal spectral exponents, as observed, and a slow spectral steepening with distance, thus leading naturally to the observed variability of spectral indices.

Keywords: Solar Wind, MHD, Turbulence, Alfvénicity, expansion

1 Introduction

Turbulence in the solar wind above sub-ion scales shows large variations of spectral properties with wind bulk speed and Alfvénicity at a given distance (Chen et al. 2013), and as well with heliocentric distance (Chen et al. 2020; Grappin et al. 1991). Attempts to interpret large-scale turbulence in terms of known MHD turbulence theories includes weak isotropic cascade ((Iroshnikov 1964; Kraichnan 1965), later IK), strong Kolmogorov cascade (K41), or more recently small-scale Alfvénic cascade (Boldyrev 2005). It appears difficult to reconcile the variety of observed indices with the precise predictions of the above mentioned theories: -3/2 for IK and small-scale Alfvénic cascade, -5/3 for K41.

However, the above mentioned theories don't take into account the expansion of the plasma due to the mean radial flow. We want here to test whether we recover or not the above mentioned properties when solving the 3D MHD equations including expansion (Grappin et al. 1993; Dong et al. 2014), and compare the result both with standard 3D MHD simulations and with the above mentioned solar wind spectral properties. We hope this will help to prove that expansion cannot be neglected in describing the turbulent cascade in the solar wind.

The expansion rate is measured by the expansion parameter ϵ which is the ratio of the initial nonlinear time $t_{NL} = 1/(k_0 u)$ of large eddies over the expansion time $t_e = R_0/U_0$ where R_0 is the initial heliospheric distance (here 0.2 AU) and U_0 the (assumed constant) average bulk solar wind speed.

In both the non-expanding and expanding cases, spectral evolution is followed during 10 nonlinear times. In the expanding case, during this time, the transverse plasma sizes will increase by a factor 5, corresponding to the heliospheric distance R varying from 0.2 to 1 AU.

2 Definitions, parameters and Initial conditions

We first define the two Elsasser variables $z_{\pm}$:

$$z_{\pm} = u \mp sign(B_0)\delta B/\rho^{1/2} \tag{2.1}$$

[1] Laboratoire de Physique des Plasmas (LPP), CNRS, Observatoire de Paris, Sorbonne Université, Université Paris Saclay, Ecole Polytechnique, Institut Polytechnique de Paris, 91120 Palaiseau, France

[2] Università di Firenze, Dipartimento di Fisica e Astronomia, Firenze, Italy; INAF, OAA, Firenze, Italy

[3] Technische Universität Berlin, ER 3-2, Hardenbergstr. 36a, D-10623 Berlin, Germany; Max-Planck/Princeton Center for Plasma Physics

where $\delta B = B - B_0$ denotes the fluctuating magnetic field. The z_+ and z_- denote respectively the amplitude of the outward and inward propagating Alfvén waves. The energies of the two Elsasser fields are $E_\pm = (1/2)z_\pm^2$. The Alfvénicity or normalized cross helicity is measured by

$$\sigma_c = (E_+ - E_-)/(E_+ + E_-) \tag{2.2}$$

We consider the following initial conditions for the homogeneous runs: magnetic and velocity fluctuation $b_{rms} = u_{rms} = 1$, a mean magnetic field B_0 between 1 and 5 times b_{rms}. The domain is elongated along the mean field with aspect ratio equal to B^0/b_{rms} (fig.1a shows a case where $B_0 = 2$). The initial turbulent Mach number is $\delta u_{rms}/c_s$= 0.12, where c_s is the sound speed.

In the expanding case (see Montagud-Camps et al. (2018)), the initial domain is elongated along the radial with an aspect ratio equal to 5, so that at the end of the computation the aspect ratio is unity, thus allowing more efficient nonlinear couplings at that time (fig.1b). The initial mean magnetic field has an small angle with the radial direction: $\vec{B_0}(t = 0) = B_0[1, 0.2, 0]$, such that at the end of the run it makes a 45^0 angle with the radial. In most runs, we set B_0=2, but similar results are obtained with $B_0 = 1$ or 3.

Time t is normalized by the initial nonlinear time, the relation between distance and time is:

$$R = R^0(1 + \epsilon t) \tag{2.3}$$

where $\epsilon = \frac{U^0/R^0}{k^0 u_{rms}} = 0.4$ is the ratio between the non-linear time and the linear expansion time.

Initial kinetic and magnetic fluctuations autocorrelation isocontours follow ellipsoids with the same aspect ratio as that of the simulation domain. The reduced 1D initial spectra $E_+(k)$ and $E_-(k)$ have the same initial spectral index, with the excitation being concentrated on first 32 modes in the expanding case, and the first 8 modes in the homogeneous case. Note that in the zero expansion case, we will consider spectra depending on $k_\perp$, i.e. the average of $E(k_y)$ and $E(k_z)$ spectra, while in the case with expansion we will consider spectra depending on k_x, corresponding to the radial component of the wavevector.

3 Results

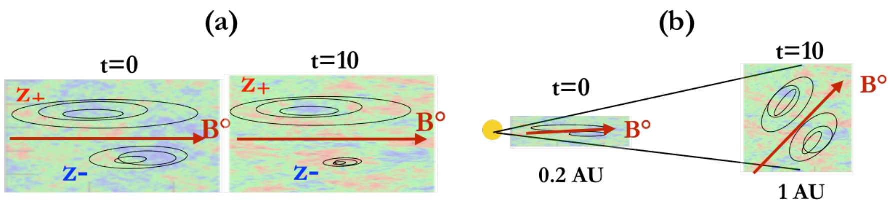

Fig. 1. Sketch of the evolution of the plasma volume: (a) Standard simulation; (b) simulation with expansion, Ox denoting the direction parallel to the radial; the domain expands in directions Oy and Oz as time/distance increase.

Fig. 2 shows $E_+(k)$ and $E_-(k)$ spectra, and the geometric mean $\sqrt{E_+E_-}$ at t=10, for five runs, with two values of the initial spectral index m_0, -5/3 and -1, and several values of σ_c^0. All runs show "pinning" of the $E_\pm$ spectra at dissipative scales, that is, spectra join there, i.e., cross helicity is zero at those scales. Cross helicity nevertheless remains at large scales. In the homogeneous case (top row), this leads to different spectral scalings for E_+ and E_-: the dominant E_+ spectrum is steeper than the E_- spectrum, i.e., $|m_+| > |m_-|$. However, this is not so in the expanding case (bottom row): E_+ and E_- spectra indeed separate, but the growth of cross helicity is limited by a secondary large-scale pinning effect, due clearly to expansion. In the following we choose to compute $E_\pm$ spectral indices ($m_\pm$) in the range $4 \leq k \leq 10$ (and we will call this range the inertial range) due to the reasonable constancy of indices in this range.

We first consider in fig. 3 some examples of the time evolution of m_+, the dominant spectrum index, varying again m^0 and σ_c^0, with the homogeneous runs in left panels (a), and runs with expansion right (b). We find (first panel) that the final scaling is quasi-independent of the initial scaling in non-expanding runs, which is expected, while on the contrary, in the expanding case (last two panels right), *the final scaling depends strongly on its initial value.*

Fig. 4 shows the evolution of the two $E_\pm$ spectral indices $m_\pm$ in different cases. The three left panels show runs without expansion with growing initial cross helicity from left to right, with two runs per panel, $m_0 = -1.2$

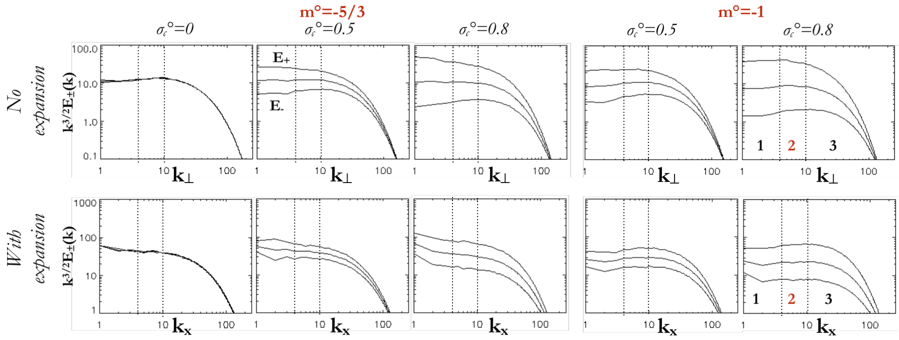

Fig. 2. Final (t=10) spectra: E_+, E_- and geometric mean $\sqrt{E_+(k)E_-(k)}$, with inertial range indicated by dotted lines (k=4 and k=10). Top raw: zero expansion runs; bottom raw: runs with expansion. Spectra are compensated by $k^{-3/2}$.

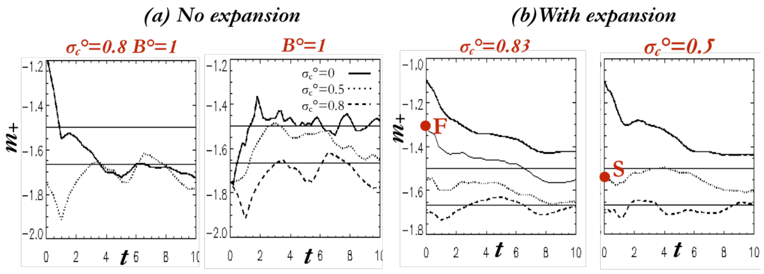

Fig. 3. Time evolution of the spectral index of the dominant energy ($E_+(k)$) illustrating the difference between the evolution (a) without and (b) with expansion, varying the initial index m_+^0 and cross helicity σ_c^0. Straight lines mark $m_+ = -1.5$ and -5/3.

(solid line) and $\simeq -5/3$ (dotted). Right panels show runs with expansion, all with large σ_c^0 (0.83) and different starting indices (an arrow is added to indicate the direction of motion). One sees for the non-expanding runs that the m_-, m_+ trajectories starting from $m_0 = -1.2$ and from $m_0 = -5/3$ join together close to the diagonal $m_+ + m_- = -3$, with the final attractor moving with growing σ_c^0 along the diagonal away from the central point $m_\pm = -3/2$ when σ_c^0 grows. This is the prediction of the weak isotropic turbulent regime (Grappin et al. (1983)). On the contrary, the four right panels (b) illustrate the formation of quasi-equal indices $m_\pm$ in the expanding case, with, again, the final index depending strongly on its initial value, confirming our earlier conclusion from fig. 3.

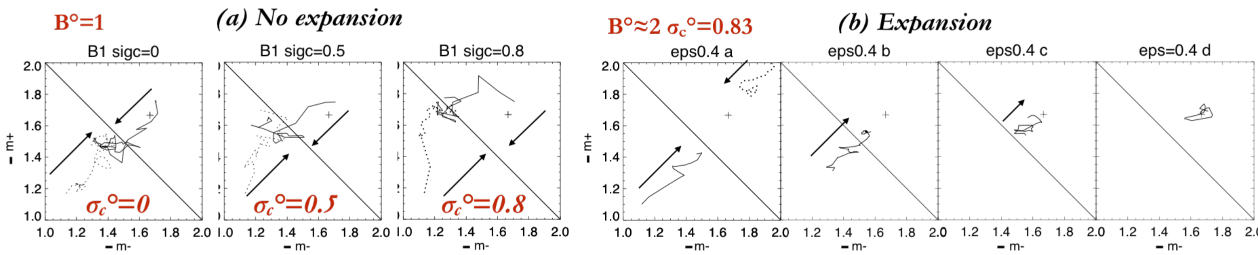

Fig. 4. Hodograms showing the evolution of the two spectral indices $m_\pm$ vs time, again illustrating the difference between (a) the zero expansion and (b) runs with expansion. Arrows indicate the direction of evolution. The cross represents $m_\pm = -5/3$ and the diagonal the line $m_+ + m_- = -3$.

Fig. 5 compares the $E_\pm$ spectra observed during the first four months of the Helios 2 mission (top row) with those obtained from simulations with expansion (bottom row). The bottom panels show spectra averaged within the following subsets, from left to right: *slow* streams close to the Sun and then far from Sun, *fast* streams close to the Sun and far from Sun. Helios data thus show the two properties remarked previously in our simulations with expansion: (i) the two E_+ and E_- spectra have comparable spectral indices; (ii) the "final" (close to Earth) scalings depend on the "initial" (close to Sun) scalings, considering the two subsets made of the fast (or highly Alfvénic) streams and slow (or mildly Alfvénic) streams. In our simulations, the corresponding test runs are denoted respectively run F and run S (see fig. 3).

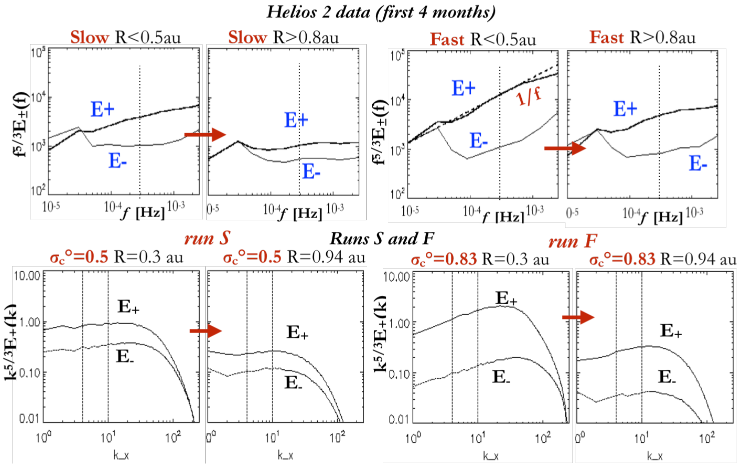

Fig. 5. Comparing $E_\pm(k)$ spectra (compensated by $k^{-5/3}$), respectively (a) in Helios data (top raw) and (b) in simulations with expansion (bottom). From left to right, Helios data show spectra averaged successively in slow streams close and far from the Sun, then in fast streams. Simulation data show spectra with low cross helicity close and far from the Sun, then the same with high cross helicity (see curves marked with S and F in fig. 3b).

4 Conclusions

We have considered here simulations of Alfvénic turbulence, with and without expansion. Our simulations show that 3D MHD simulations with expansion of the plasma volume (EBM) are able to reasonably reproduce the evolution of $E_\pm$ spectra in the inner heliosphere, as (i) similar indices for the two spectra, (ii) spectral indices varying slowly with distance, (iii) spectra becoming steeper with distance.

On the contrary, zero expansion simulations with cross helicity are dominated by the spectral pinning at dissipative scales, which leads to different spectral indices for the two E_+ and E_- spectra, similar to that found in IK weak isotropic turbulence as generalized to Alfvénic turbulence by Grappin et al. (1983).

The interpretation of this quasi-isotropic behavior in a regime with non zero mean field, thus basically anisotropic, requires further analysis. This is true as well of the slow evolution observed here in the expanding case which is reminiscent of the freezing of shock waves found analytically with expansion (Grappin et al. 1993).

We thank Victor Montagud-Camps for useful remarks when reading the manuscript. This work was granted access to the HPC resources of IDRIS under the allocation 2020-A0090407683 made by GENCI.

References

Boldyrev, S. 2005, The Astrophysical Journal, 626, L37
Chen, C., Bale, S., Bonnell, J. W., et al. 2020, The Astrophysical Journal Supplement Series, 246, 0
Chen, C., Bale, S., Salem, C. S., & Maruca, B. A. 2013, The Astrophysical Journal, 770, 125
Dong, Y., Verdini, A., & Grappin, R. 2014, The Astrophysical Journal, 793, 118
Grappin, R., Léorat, J., & Pouquet, A. G. 1983, ASTRONOMY AND ASTROPHYSICS, 126, 51
Grappin, R., Velli, M., & Mangeney, A. 1991, Annales Geophysicae, 9, 416
Grappin, R., Velli, M., & Mangeney, A. 1993, Physical Review Letters, 70, 2190
Iroshnikov, P. S. 1964, Soviet Astronomy, 7, 566
Kraichnan, R. 1965, Physics of Fluids, 8, 1385
Montagud-Camps, V., Grappin, R., & Verdini, A. 2018, The Astrophysical Journal, 853, 153

SF2A 2021
A. Siebert, K. Baillié, E. Lagadec, N. Lagarde, J. Malzac, J.-B. Marquette, M. N'Diaye, J. Richard, O. Venot (eds)

HOW WILL SOLAR MAGNETISM EVOLVE?

Q. Noraz[1], S. Brun[1] and A. Strugarek[1]

Abstract. In solar-type stars, magnetic field is generated and sustained through an internal dynamo. This process is mainly determined by the combined action of turbulent convective motions and differential rotation profile. It can sometimes lead to cyclic magnetic reversals, like the 11 years cycle of the Sun, and ranging from a few years to a few tens of years in other solar-like stars. The understanding of what control these cycles is of major importance to decipher how the solar dynamo works and could evolve.

Recent 3D numerical simulations of solar-like stars show that different regimes of differential rotation can be characterized with the Rossby number. In particular, anti-solar differential rotation (fast poles, slow equator) may exist for high Rossby number (slow rotators). As the rotation of stars is slowing down during their main-sequence, we may wonder how the magnetic generation through dynamo process will be impacted if our Sun evolve toward this regime. In particular, can slowly rotating stars have magnetic cycles?

We present a numerical multi-D study with the STELEM and ASH codes to understand the magnetic field generation of solar-like stars under various differential rotation regimes, and focus on the existence of magnetic cycles.

We find that short cycles are favoured for small Rossby numbers (fast rotators), and long cycles for intermediate (solar-like) Rossby numbers. Slow rotators (high Rossby number) are found to produce only steady dynamo with no cyclic activity in most cases. Magnetic cycles can be produced with anti-solar differential rotation only if the alpha effect is fine tuned for this purpose.

Keywords: solar-like star, solar-type star, anti-solar, differential rotation, convection, solar dynamo

1 Introduction

Observations of the Sun show us two interesting and intertwined features. First, the magnetic activity of the Sun is characterised by a magnetic cycle of 22 years. It is usually shown in a magnetogram evolution *vs.* latitude illustration, so-called *butterfly diagram* (Hathaway 2015). Second, the helioseismic inversions show that the convective zone is differentially rotating, i.e. that not all latitudes rotate at the same speed. In particular, the Sun has a fast equator and slow poles, in a so-called solar differential rotation (DR) profile (Thompson et al. 2003). The latter is believed to be at the heart of large-scale dynamo action.
We know that the Sun has gone through different rotational phases during its lifetime. In particular, stars will start to slow down, losing angular momentum when they enter the main sequence (MS). This rotation influences the dynamo process that creates and sustains the stellar magnetic field. This field will then shape and magnetize the wind of the star, which is next responsible for the mass loss and magnetic breaking. Finally, this characterises the angular momentum loss, and this physical loop leads stars with similar masses to converge towards a similar rotational evolution, described by Skumanich's law (see Skumanich 1972; Vidotto 2021, and references therein). Further using ZDI techniques, the stellar magnetic field has been observed to decrease as a function of the Rossby number(See et al. 2019). This number is dimensionless and quantify the time-scale of convection over rotation. It allows us to characterise the structure and internal dynamics of stars. Indeed, recent 3D global and hydrodynamic simulations have shown that different DR regimes exist as a function of the fluid Rossby number $Ro_{\rm f} = \tilde{\omega}/2\Omega_*$, with $\tilde{\omega}$ the *rms.* vorticity (Brun et al. 2017, see also Gastine et al. 2014). For weak Rossby number, which are fast rotators, the DR profile will be highly constrained by its rotation. This is the Taylor-Proudman constraint making the angular velocity invariant along the rotation axis. For

[1] Département d'Astrophysique/AIM, CEA/IRFU, CNRS/INSU, Univ. Paris-Saclay & Univ. de Paris, 91191 Gif-sur-Yvette, France

intermediate Rossby, we find the characteristic profile of the Sun with a fast equator and slow poles. Finally, it has been shown that so-called "anti-solar" rotation profiles (slow equator and fast poles) are possible for high Rossby numbers (slow rotators). As the rotation of stars decreases during their main-sequence, we may wonder if such a rotational regime could happen in the case of solar-type stars and more particularly for the Sun.How would the dynamo mechanism be affected? In general, can slowly rotating stars have magnetic cycles?

2 Anti-solar DR in kinematic mean-field dynamos

The dynamo mechanism is the ability of a plasma to create and maintain a magnetic field against its ohmic dissipation. A dynamo loop can be understood as illustrated in Figure 1. In a mean-field approach, one can start by considering the magnetic field in the meridional plane of the star, called the *poloidal field*. The latter will be sheared by the differential rotation into a horizontal magnetic field, called *toroidal field*. This process is called the Ω-effect. This toroidal component can then be transformed back into a poloidal field, for example by the α-effect. This effect characterizes the turbulent convection in a so-called $\alpha\Omega$ dynamo. To transform the toroidal field back into a poloidal one, another mechanism is possible, called Babcock-Leighton (BL) (Babcock 1961 and Leighton 1969). This latter characterises the influence of Coriolis force on the emerging toroidal structures. These structures are though to move up through the convective zone, and to be tilted at their surface emergence by this rotational effect. In such BL flux-transport dynamo models, meridional circulation (MC) can be used to link dynamically the two sources of the magnetic field (poloidal and toroidal). More generally and for all dynamo model, if the final poloidal polarity is opposite to the initial one, a cyclic activity can occur.

We first reproduce solar reference models, using the STELEM code in a 2D kinematic approach, prescribing a solar DR profile for $\alpha\Omega$ and BL models. After reproducing well the magnetic solar features observed in its cyclic activity, we then construct an anti-solar DR profile and apply it on both reference models. A cyclic magnetic activity emerges in the $\alpha\Omega$ dynamo model, which is not the case in the BL dynamo where the dynamo becomes stationary. It is therefore interesting to ask why this cyclic activity is lost. To do so, we move the location of the poloidal field generation in the solar and anti-solar DR $\alpha\Omega$ models, and analyse the impact on cyclic magnetic activity. We thus move the α-effect location up, from the tachocline into the convection zone (CZ). We finally reach the surface, where the poloidal generation term is located in the BL dynamo model.

All configurations illustrated in Figure 1 has been explored, and its conclusions has been confirmed. Indeed we note that the cyclic activity for anti-solar DR regime is lost as soon as the alpha effect is no longer spread enough on the tachocline, *i.e.* when the poloidal field generation moves in the CZ, appart from the radial shear of the DR. For the solar DR regime, the cyclic activity is preserved all along the convection zone. Furthermore, we note that the cycle period is longer for deeper locations and larger radial extensions of the α-effect. See more details and Figures in Noraz et al. (2022) submitted to A&A.

3 How stellar dynamos are characterised with the Rossby number?

In parallel, we used the ASH code (Brun et al. 2004) to conduct a systematic study in the 3D regime, using global MHD simulations of turbulent stellar dynamo, where convection and DR profiles are no longer prescribed and emerge self-consistently (Brun et al. 2022 submitted to ApJ). Based on a series of 15 simulations of solar-type stars, we cover 4 bins of rotation and mass, and thus different effective Rossby numbers.

First, we find rotational transitions as a function of the fluid Rossby number, similar to what was found in hydrodynamic cases of Brun et al. (2017). Indeed, solar-like DR profiles emerge for intermediate fluid Rossby numbers Ro_{f}, while anti-solar-like profiles appear when the Rossby number exceeds 1. Moreover the Lorentz force feedback strongly constrains the rotation profiles for the lowest Rossby numbers, bringing some DR close to a solid rotation profile when the DR-quenching is maximum.

Second, we also observe magnetic transitions as a function of the fluid Rossby number, similar to what was found in the work of Strugarek et al. (2017), and illustrated in Figure 2. For low Rossby number, generally fast rotators, we note the emergence of short cycles with period ranging around a couple of years. These cycles result from a dynamo located near the equator and in the upper part of the convective zone (CZ), and which dynamics seem to follow well the *Parker-Yoshimura rule*. It is potentially this type of mechanism that could be at the origin of the quasi-biennial oscillation observed on the Sun Fletcher et al. (2010). For intermediate Rossby (typically around the solar value), we observe decadal magnetic cycles resembling the solar 11-years cycle. They result from a deeper-seated dynamo located at the base of the CZ, governed by a non-linear

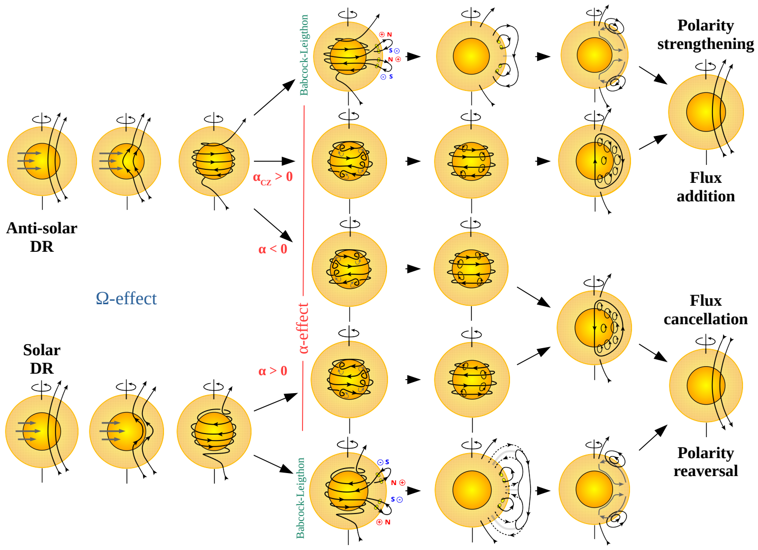

Fig. 1. The different steps for $\alpha\Omega$ and BL dynamo models in various geometrical configurations. They start on the left side with differential rotation (DR) performing the Ω-effect. It is represented on the first three columns, for anti-solar DR on the top, and the solar one on the bottom (see horizontal grey arrows). The next part (three next columns) illustrates the Babcock-Leighton mechanism on the first and last rows, while the three middle rows illustrate the α-effect For BL models, we represent the polarity of star-spots (red and blue), current sheet (light grey lines) and the meridional circulation (darker grey arrows), respectively on columns 4, 5 and 6. For the α-effect, column 4 illustrates orientation of cyclonic motions with grey arrows. Finally the last columns conclude the dynamo loop, with the presence of a cyclic activity when the final poloidal polarity is opposed to the initial one (bottom), or being stationary otherwise (top). The layout of this Figure is inspired from Sanchez et al. (2014), and soon published in Noraz et al. (2022, A&A).

feedback mechanism between the DR profile and the large-scale magnetic field. Indeed, we observe a cyclic energy exchange between the two energy reservoirs, resulting from a magnetic DR-quenching. Finally, when we transit towards high Rossby number (with $Ro_{\rm f} > 1$), models become anti-solar and all dynamos lose their cyclic activity, thus becoming stationary. We also note an increase in the toroidal magnetic field generation located at the bottom of the convective zone. These results are compatible with what we find in the mean field dynamo approach discussed in the previous section.
We then compare these simulations with observations by calculating the unsigned flux at the top of each model. We find flux from 10^{24} to 10^{25} Mx, which is in good agreement with the values observed on the Sun (Schrijver & Harvey 1994). Next, if time-averaged unsigned flux generally decreases as the Rossby increases, our models deviate drastically from this behaviour when Rossby becomes greater than one. This highlight a potential change of behaviour for this regime, possibly observed by Brandenburg & Giampapa (2018), that needs to be investigated further with additional high Rossby dynamo models. Finally, we perform a spectral decomposition of the magnetic field at the top of simulations, and observe no drastic drop in large-scale dynamo modes for the high Rossby regime (>1). As proposed by Metcalfe & van Saders (2017), such a drop could then have led to a less efficient wind braking (see how the Alfvén radius evolve in Finley & Matt 2017), which could have motivated and explained a *gyrochronology-break*. However, we do not find such collapses in the sample of simulations studied here. See more details and Figures in Brun et al. (2022).

4 Conclusions

In conclusion, we performed a numerical multi-D study through different DR regimes, focusing especially on their impact on the cyclic magnetic behaviour for stellar dynamos. This allows us to postulate the following scenario:
In its youth, the Sun had a relatively fast rotation in the first part of the main sequence. This resulted in a differential rotation profile strongly constrained by magnetic DR-quenching, and accompanied by a yearly-varying surface magnetic cycle. Subsequently, the decrease of its rotation rate brought the Sun into an intermediate Rossby range. This led its DR into its current regime, bringing out the emergence of the well known decadal

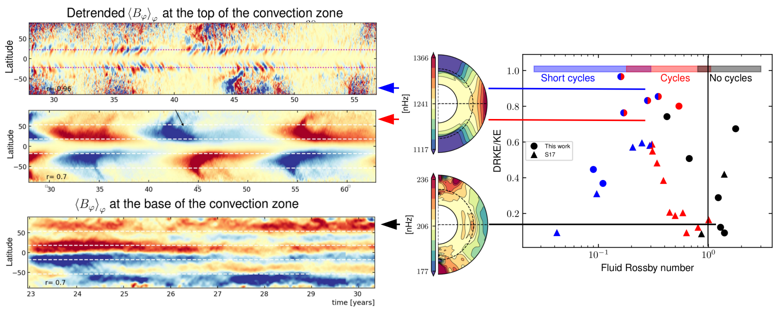

Fig. 2. Summary of the dynamo states found in our study. **Left:** Typical dynamo states on time-latitude representation of $\langle B_\phi \rangle$. The bottom panel represents a stationary dynamo found in anti-solar regimes. The middle one represents a deep decadal cyclic dynamo found around the solar regime. Both panels illustrate the toroidal magnetic component at the base of the CZ. The upper panel illustrates a surface and shorter dynamo in the same model, after filtering the longer cycle. **Middle:** Associated DR profiles achieved in the models. **Right:** Ratio between the differential rotation and total kinetic energies as a function of the Rossby number. Circles represent model of our study, while triangles represent the ones of Strugarek et al. (2017). Short cycles (blue) are found for low Rossby numbers, long decadal Sun-like cycles (red) appear for intermediate Rossby, and only stationary dynamo (dark) are found for high Rossby numbers (anti-solar DR).

cycle observed today. Finally, a quick calculation using the Skumanich's law show that the Sun's fluid Rossby number could possibly reach the value of 1 before the end of the MS. Then the Sun will be likely to change its DR regime toward an anti-solar DR (fast poles - slow equator), and finally to lose the cyclic character of its dynamo.

Indeed, most of the models of this study seem to show that stellar dynamos become stationary under this particular DR regime. However, we have found that a cyclic dynamo can still exist in anti-solar DR for particular alpha effect profiles (see also Karak et al. 2020). The detection of a cool main-sequence star in such a regime would therefore be a strong constraint to characterise the basis of the dynamo mechanism within our Sun. More generally, understanding stellar rotation and magnetism is of major importance for the data analysis of future missions, such as PLATO.

We acknowledge partial financial supports by: DIM-ACAV+ ANAIS2 project, ERC Whole Sun Synergy grant #810218 and STARS2 starting grant #207430, INSU/PNST, Solar Orbiter and PLATO CNES funds. We thank GENCI via project 1623 for having provided the massive computing resources needed to perform this extensive study.

References

Babcock, H. W. 1961, The Astrophysical Journal, 133, 572
Brandenburg, A. & Giampapa, M. S. 2018, The Astrophysical Journal, 855, L22
Brun, A. S., Miesch, M. S., & Toomre, J. 2004, The Astrophysical Journal, 614, 1073
Brun, A. S., Strugarek, A., Varela, J., et al. 2017, The Astrophysical Journal, 836, 192
Finley, A. J. & Matt, S. P. 2017, The Astrophysical Journal, 845, 46
Fletcher, S. T., Broomhall, A.-M., Salabert, D., et al. 2010, The Astrophysical Journal, 718, L19
Gastine, T., Yadav, R. K., Morin, J., Reiners, A., & Wicht, J. 2014, MNRAS: Letters, 438, L76
Hathaway, D. H. 2015, Living Reviews in Solar Physics, 12, 4
Karak, B. B., Tomar, A., & Vashishth, V. 2020, Monthly Notices of the Royal Astronomical Society, 491, 3155
Leighton, R. B. 1969, The Astrophysical Journal, 156, 1
Metcalfe, T. S. & van Saders, J. 2017, arXiv:1705.09668 [astro-ph], arXiv: 1705.09668
Sanchez, S., Fournier, A., & Aubert, J. 2014, The Astrophysical Journal, 15
Schrijver, C. J. & Harvey, K. L. 1994, Sol. Phys., 150, 1
See, V., Matt, S. P., Folsom, C. P., et al. 2019, The Astrophysical Journal, 876, 118
Skumanich, A. 1972, ApJ, 171, 565
Strugarek, A., Beaudoin, P., Charbonneau, P., & Brun, A. S. 2017, 4
Thompson, M. J., Christensen-Dalsgaard, J., Miesch, M. S., & Toomre, J. 2003, ARAA, 41, 599
Vidotto, A. A. 2021, Living Reviews in Solar Physics, 18, 3

SF2A 2021
A. Siebert, K. Baillié, E. Lagadec, N. Lagarde, J. Malzac, J.-B. Marquette, M. N'Diaye, J. Richard, O. Venot (eds)

ADDING A TRANSITION REGION IN GLOBAL MHD MODELS OF THE SOLAR CORONA

V. Réville[1], S. Parenti[2], A. S. Brun[3], A. Strugarek[3], A. P. Rouillard[1], M. Velli[4], B. Perri[5] and R. F. Pinto[3]

Abstract. Global MHD simulations of the solar corona are an essential tool to investigate long standing problems, such as finding the source of coronal heating and the mechanisms responsible for the onset and propagation of coronal mass ejections. The very low atmospheric layers of the corona, are however, very difficult to model as they imply very steep gradients of density and temperature over only a few thousand kilometers. In this proceedings, we illustrate some of the benefits of including a very simple transition region in global MHD models and the differences in the plasma properties, comparing with in situ data of the Parker Solar Probe.

Keywords: Solar wind, corona, MHD

1 Introduction

The new generation of inner heliosphere exploration spacecraft, Parker Solar Probe (PSP) and Solar Orbiter, has incentivized the development of ever more precise global MHD models of the solar corona. Over the past 10 years, many progresses have been made, including for instance Alfvén wave turbulence as the main process responsible for coronal heating and solar wind acceleration (Sokolov et al. 2013; van der Holst et al. 2014; Downs et al. 2016; Réville et al. 2020). The main objective of these models is to reproduce both in situ and remote sensing measurements, hence predicting accurately the thermal structure of the corona and the solar wind acceleration process. The lowest layers of the solar atmosphere, the chromosphere and the transition region, are however very challenging to model as the density and temperature vary on orders of magnitude over very short distances, in respect of the domain size of global models. In this work, we perform two similar runs of our model WindPredict-AW (Réville et al. 2020), with and without a transition region. We compare with in situ data of the first Parker Solar Probe perihelion and compute synthetic AIA images, illustrating the differences and the benefits of the transition region in the model.

2 Run description

The two simulations are based on the setup described in (Réville et al. 2020). The coronal heating is provided by two populations of turbulent Alfvén waves (parallel and anti-parallel to magnetic field) excited from the inner boundary. Table 1 sums up all the parameters of the two simulations. In the first simulation (Run 1) the inner boundary is located at $1.005R_\odot$, i.e. after the transition region estimated between 1000 and 2000 km above the surface ($1.001 - 1.003R_\odot$). The base density is fixed at $n = 2 \times 10^8$ cm^{-3}. The amplitude of the velocity perturbations generating Alfvén waves is 30 km/s. In the second run, we place the inner boundary conditions below the transition region, at $r = 1.0002R_\odot$. We increase the base density by a factor 100 compared to the first run. Although the precise profile of plasma density remains poorly known in the transition region

[1] IRAP, Université Toulouse III - Paul Sabatier, CNRS, CNES, Toulouse, France
[2] Université Paris-Saclay, CNRS, Institut d'Astrophysique Spatiale, 91405, Orsay, France
[3] AIM, CEA, CNRS, Université Paris-Saclay, Université Paris Diderot, Sorbonne Paris Cité, F-91191 Gif-sur-Yvette, France
[4] UCLA Earth, Planetary and Space Sciences department, CA, USA
[5] KU Leuven, CmPA, Mathematics, Belgium

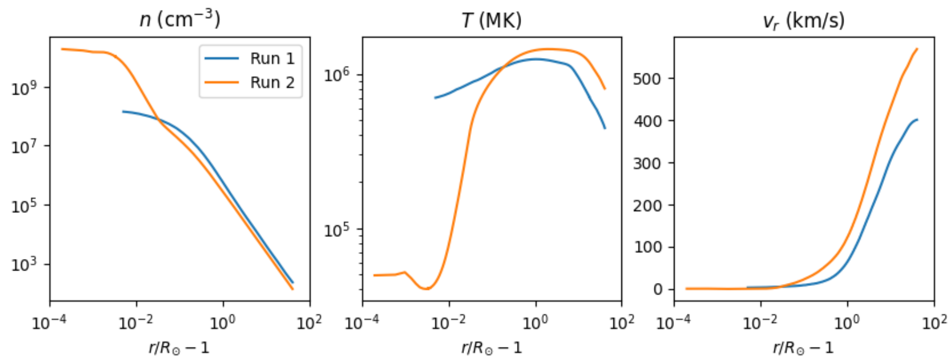

Fig. 1. Profiles of the solar wind corresponding toi the source of PSP's measurements on November 9th 2018. One can clearly see the strong density and temperature gradients corresponding to the (broadened) transition region. We see also the temperature minimum at the top of the chromosphere induced by radiative cooling.

and the chromosphere, this value is likely below expected chromospheric density. Increasing more this value does however make the simulation more difficult to run, while not changing significantly the coronal properties. The input Poynting flux is $F_w = \rho_\odot v_{A,r} \delta v^2$, which on average gives $\langle F_w \rangle = \sqrt{\rho_\odot/4/\pi} \langle B_{r,\odot} \rangle \delta v^2$. Both set of parameters are set to ensure that the average input Alfvén wave energy flux remain similar (see Table 1).

Run	$r_{\min}$	$n_\odot$ (10^8 cm^{-3})	$\delta v_\odot$ (km/s)	$\langle F_w \rangle$ (erg.cm^{-2}/s)	$\dot{M}$ ($M_\odot$/yr)	Grid
1	1.005	2	30	83500	2.15 $\times 10^{-14}$	196x96x192
2	1.0002	200	10	92800	2.3 $\times 10^{-14}$	256x160x320

Table 1. Simulation parameters

The magnetic field at the inner boundary is kept fixed using an ADAPT magnetogram of November 6th 2018 at 12:00 UTC. This period corresponds to the first perihelion of Parker Solar Probe (see, e.g., Réville et al. 2020). It is the same for both simulations and we use a projection of this field on the first 15 spherical harmonics, which smoothes the photospheric radial field. For the second run, we had to increase the radial and angular resolution, to better resolve the strong density and temperature gradients. This is essential because the thermal conduction is aligned with the magnetic field and small numerical errors in the field direction can create strong (numerical) thermal instabilities. The global mass loss of the two simulations is reported in table 1 and is similar in both cases.

Figure 1 shows the profile of the two solar wind solutions on the path connecting PSP to the Sun on November 9th. We see the structure of the TR for Run 2 and the much stronger gradients of density and temperatures. The minimum temperature for Run 2 is around 40000K. For numerical purposes, the transition region is artificially broadened using the technique described in (Lionello et al. 2009). We see that Run 2 produces a denser, hotter, and faster wind in this coronal hole.

3 In situ data

In Figure 2, we compare the in situ measurements predicted by both models for the first perihelion of Parker Solar Probe. The red curve (Run 1) has been already published in (Réville et al. 2020). The black curve (Run 2) shares very similar properties with the red curve. The polarity of the magnetic field is very consistent in both models, which means that they predict the same sources for the solar wind. The main differences come from the predicted amplitude of wind velocities and densities. The second run shows more contrast between slow and fast wind and is generally above the red curve when PSP is connected to a coronal hole (for instance between November 1st and November 14th), and below when crossing the current sheet (e.g. around November 15th). Interestingly, while the first model offers a better match with the data close to perihelion, the second works best after November 15th and PSP switching from one equatorial coronal hole (CH 1) to another (CH 2, see Figure 3 and Réville et al. 2020).

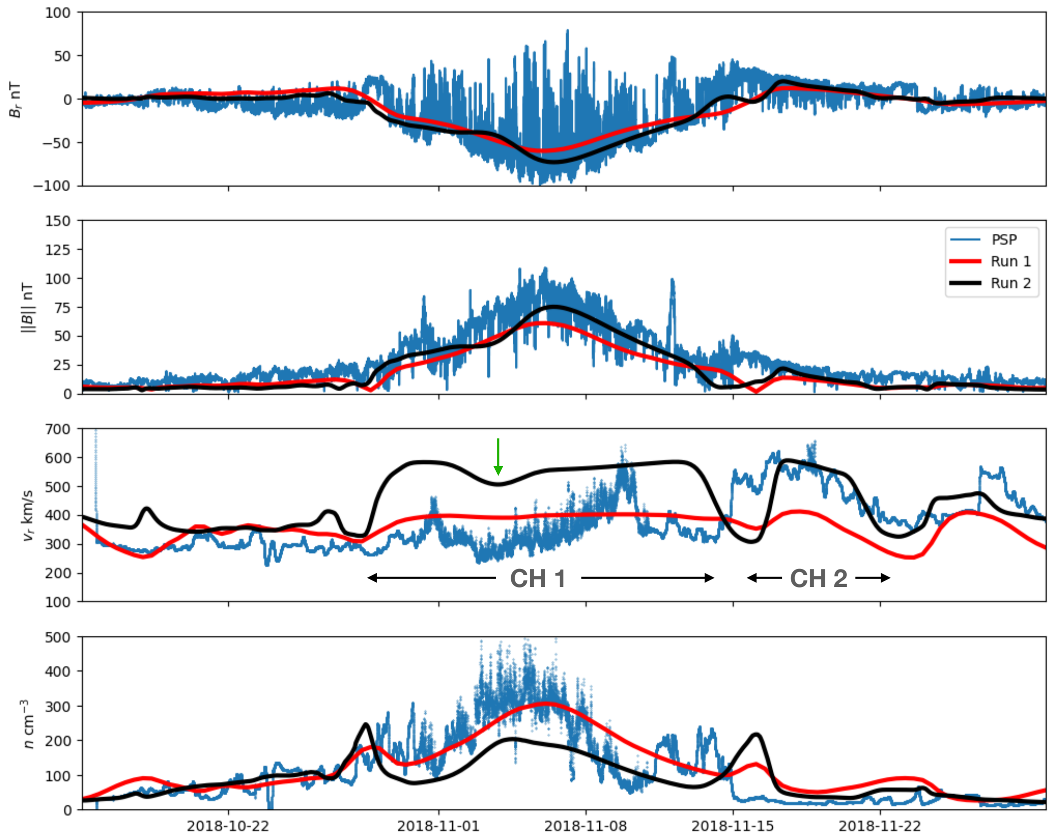

Fig. 2. Comparison of classical MHD quantities obtained along the trajectory of PSP in the simulations and the real data. Magnetic fields measurements (top and second panels) have been obtained thanks to the FIELDS instrument. Radial velocities and densities (third and fourth panels) are integrated moments of the Faraday cup (SWEAP/SPC).

The second model, however, shows speed variations inside the same coronal hole (green arrow in Figure 2), consistently with the data. This could be due to the higher resolution of Run 2, which allows to distinguish between the core and the boundary of the coronal hole at which PSP was connected. Note that both models have fast wind speed (≥ 600 km/s) above polar regions. Yet, in general, the solution with the transition region do provide more contrast and features in the simulated in situ data.

4 Remote sensing measurements

We now turn towards synthesized remote sensing measurements. More specifically, in the first row of Figure 3, we reproduce the UV emissions that would be measured by SDO/AIA with the 193 $\mathring{A}$ channel. This filter yields information on the thermal structure of the solution in the low corona between 1 and 2 MK. First, we see the effect of the higher resolution. Although the same structures are visible, especially the coronal holes in dark, the image for Run 2 is smoother. The two coronal holes in the right (labelled CH 1 and CH 2) are the source of the plasma measured by PSP between November 1st and November 14th (CH 1) and after November 15th (CH 2). We note that both CH 1 and CH 2 are larger in Run 2 than in Run 1, which may explain the variation in the velocity observed in the data and better reproduced by Run 2.

More generally we see more contrast and stronger EUV emissions in Run 2. During PSP E1, a small active region has been emerging, and is identified in the synthetic measurements of Figure 3 by the AR 1 label. We note that the AR is visible in the synthetic measurements only for Run 2. The reason can be understood looking at the middle and bottom panels of Figure 3. We clearly see that, although the temperature is similar in both runs, there is an increased density at the active region in Run 2. The presence of the transition region provides the density reservoir necessary to the equilibrium of small magnetic loops. Hence, as noted in several

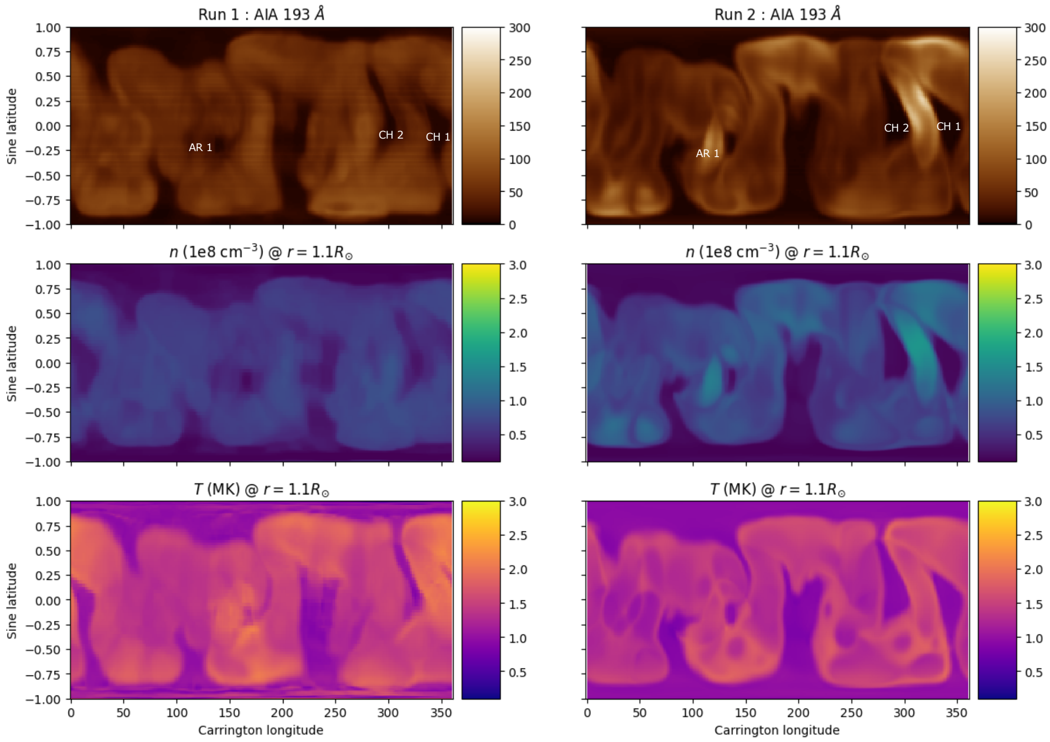

Fig. 3. Top panel: AIA 193 Å emission synoptic maps (integrated along the line of sight). Middle panel: synoptic map of the density at $1.1R_{\odot}$. Bottom panel: synoptic map of the temperature at $1.1R_{\odot}$.

previous investigations (see, e.g. Bradshaw & Cargill 2013; Cargill et al. 2015), the TR is essential to reproduce the thermal properties of active regions.

5 Conclusions

In these proceedings we have discussed the effect of adding a transition region in a global, Alfvén wave driven, coronal MHD model. The lowest layers of the solar atmosphere bring more contrast between the closed and open regions of the solar atmosphere and can in particular create a less dense and faster wind coming from equatorial coronal holes. The transition region is also essential to render correctly the density properties of small magnetic structures such as active regions as seen by EUV instruments such as SDO/AIA.

Numerical simulations have been supported by the GENCI program (grant A0090410293) and were made on Jean Zay machine (IDRIS). Parker Solar Probe was designed, built, and is now operated by the Johns Hopkins Applied Physics Laboratory as part of NASA's Living with a Star (LWS) program (contract NNN06AA01C). This work utilizes data produced collaboratively between AFRL/ADAPT and NSO/NISP.

References

Bradshaw, S. J. & Cargill, P. J. 2013, ApJ, 770, 12

Cargill, P. J., Warren, H. P., & Bradshaw, S. J. 2015, Philosophical Transactions of the Royal Society of London Series A, 373, 20140260

Downs, C., Lionello, R., Mikić, Z., Linker, J. A., & Velli, M. 2016, ApJ, 832, 180

Lionello, R., Linker, J. A., & Mikić, Z. 2009, ApJ, 690, 902

Réville, V., Velli, M., Panasenco, O., et al. 2020, ApJS, 246, 24

Sokolov, I. V., van der Holst, B., Oran, R., et al. 2013, ApJ, 764, 23

van der Holst, B., Sokolov, I. V., Meng, X., et al. 2014, ApJ, 782, 81

STUDY OF THE UPPER IONOSPHERE DURING THREE INTENSE STORMS MARCH 17-18, JUNE 22-23, OCTOBER 7-8, 2015 USING DATA FROM SWARM SATELLITES

K. Zyane[1], A.Bounhir[1] and Z.Benkhaldoune[1]

Abstract. We know that understanding the behavior of the earth's ionosphere during geomagnetic storms and especially the origin of positive (increase in electron density Ne compared to calm) and negative (decrease in Ne compared to calm) storms is an important task to accomplish in space weather. In this context, we compared the electron density Ne and neutral density Dn data provided by SWARM satellites, during three intense geomagnetic storms on 2015; March 17-18, June 22-23, October 7-8, with those of calm days in order to understand the origins of positive (+) and negative (-)storms at the level of the ionospheric region F and especially above the plasma peak. At the start of the main phase of these storms, the Earth's ionosphere simultaneously marked a (+) storm on the day side and a (-) storm on the night side, where the Bz component of the interplanetary magnetic field (IMF) is directed towards the south, and Ey of the interplanetary electric field (IEF) is directed towards the evening. This confirms that these two phenomena which affected the ionosphere at the start of this phase are mainly due to the prompt penetration electric fields (PPEF) due to the leakage of the convective electric field towards low latitudes. Later during the end of the main phase and the start of the recovery phase and when Bz experienced a long southward turn, the (+) storm persisted on the night side and appeared more intense along the day side (except for the October storm where the flanks experienced a (-) storm throughout this period). During this stage the density of the neutrals Dn marked an increase from the poles towards the equator which is more important in the northern hemisphere than in the southern one. This leads us to suggest that the laste (+) storm is probably due to two other mechanisms than the PPEF, which are the disturbance dynamo electric fields (DDEF) and the disturbances of the thermospheric circulation generated by joule heating caused by the penetration of high-energy particles from solar winds toward polar areas. While the thermosphere/ionosphere coupling leads to a flow of plasma to areas where loss rates are high, meaning that (-) storms are more likely to be attributed to a change in neutral compositions.

Keywords: SWARM mission, Geomagnetic storm, ionosphere, electron density, neutral density, prompt penetration electric field PPEF, disturbance dynamo electric field DDEF.

1 Introduction

We use Swarm satellite data to analyze the ionospheric response to three geomagnetic storms of the year 2015 (March 17-18, 2015, June 22-23, 2015 and October 7-8, 2015) which belong to three different seasons and ranked among the 10 largest geomagnetic storms of the 24th solar cycle. Although negative storms are usually explained by changes in thermospheric composition((Fuller-Rowell et al. 1994; Werner & Prölss 1995)), positive storms remain less certain. At present, there is still debate about the main drivers that generate positive ionospheric storms;(Huang et al. (2005); Tsurutani et al. (2008)), dynamic disturbance electric fields (Goncharenko et al. (2007); Lu et al. (2008); Balan et al. (2010)) rapidly penetrating electric fields (Blanc & Richmond (1980); Huang et al. (2005); Tsurutani et al. (2008)), the increase in neutral composition Blanc & Richmond (1980); Fuller-Rowell et al. (1994); Huang et al. (2005); Tsurutani et al. (2008)), as well as the plasmaspheric downward fluxes (Danilov (2013)). Therefore, the study of the ionospheric effects of geomagnetic storms remains among important scientific tasks. In this article, we use data from the Swarm mission to provide further contributions in our understanding of ionospheric storms in general and especially the behavior of upper ionosphere storms.

[1] High Energy Physics and Astrophysics Laboratory, Cadi Ayyad University, Marrakech, Morocco

2 Results and discussion

To study the impact of a geomagnetic storm on the entire terrestrial globe, we used all availible data from Swarm satellites that we have represented in figures 2 (March), 4 (June) and 6 (October). On the other hand to complete our study we used data of the interplanetary medium. We extracted the geophysical parameters from the OMNIWeb data services (`http://omniweb.gsfc.nasa.gov`) as shown in figures 1 (March), 3 (June) and 5 (October). For the March geomagnetic storm the SWA satellite was flying in the upstream 19.68 LT area on the night side just after sunset, and 7.68 LT in the daytime side, just after sunrise. According to figure2, we notice that there is a big increase of Ne and of two peaks of the equatorial anomaly compared to the day side which suggests that, although SwA flies over the night side according to local time, The ionosphere of this part is still under the effect and the conditions of the day and vice versa. These reasons are considered in our analysis at the start of the main phase for the geomagnetic storms of Mars, June and October. The Earth's ionosphere simultaneously marked a (+) storm ((-) storm) in the day (night) side at almost all mid and low latitudes, such that the Bz component of the interplanetary magnetic field IMF is directed towards the south and the Ey component of the IEF interplanetary electric field is directed towards the evening. This confirms that these two phenomena which affected the ionosphere at the start of this phase are caused mainly by the leakage of the prompt penetration electric field (PPEF) due to undershielding (Kelley et al. (2003); Huang et al. (2005); Manoj et al. (2008, 2013)). This field is directed towards the east (west) in the day (night) side which results in an ExB drift of plasma towards the high (low) altitudes where the loss rate is low (high) which leads to a (+) storm ((-) storm). During this period Dn marked an increase from the poles towards the equator with a favorite from the northern hemisphere (NH).

The return of Bz to the north leads to overshielding(Wolf et al. 2007; Kikuchi et al. 2010; Wei et al. 2011) which prevents the electric field of magnetospheric convection from entering towards mid and low latitudes. The ionosphere during these turns marked a (-) storm in the day side at these latitudes and a (+) storm in the night side except for the October storm where the night side has always exhibited a (-)storm. These storms are probably attributed to the rapid northward Bz reversal of the IMF which leads to a zonal electric field reversal resulting in a downward (upward) ionospheric plasma ExB drift in the day (night) side where the recombination phenomenon is high (low) (Fejer et al. (1979); Gonzales et al. (1979); Kikuchi et al. (2000); Rastogi & Patel (1975)). On the other hand, the intense ionospheric (-) storm on the day side at the level of the zone of the equatorial anomaly coincides with the arrival of the increase of Dn ($Dn > 1.610^{-12} Kg^{-3}$) in this zone, that is to say say the arrival of warm longitudinal thermospheric winds from the poles towards the equator, which are probably accelerated and intensify the loss phenomenon (Lee et al. (2002); Liu et al. (2014); Mikhailov & Schlegel (1998); Richmond & Matsushita (1975)). but the (-) storm on the night side for the October storm is probably explained either by the low amplitude of Bz during this storm compared to the other two storms, or by a seasonal effect.

During the end of the main phase and the start of the recovery phase for the storms of March and June, IMF Bz experienced a long southward turn and IEF Ey marked a long return towards the evening. The ionosphere on the day side experienced a (+) storm over almost all latitudes, which intensified later. On the other hand, the ionosphere on the night side marked a (+) storm at mid and low latitudes and a (-) storm in other latitudes. (+) Although the storm in the night side is clearly not associated with the PPEF. Astafyeva et al. (2016) analyzed the EEJ obtained from magnetic data from SWARM satellites during the June storm and show that this second storm (+) in the day side is not associated with the PPEF. This suggests that this simultaneous (+) storm in both sides is caused by other mechanisms. The analysis of Dn during this period shows the displacement of its increase from the poles towards the equator where it reached its maximum and exceeded $2.510^{-12} Kg^{-3}$ at the level of low and equatorial latitudes. This means that longitudinal thermospheric winds are directed towards the equator, and were generated by joule heating at the level of the poles because of the entry of the interplanetary particles of high energy. These winds can bring with them charged particles by the thermospheric-ionospheric coupling. This leads us to suggest that these types of storms in this area are probably due to the auroral disturbance dynamo electric field DDEF (Blanc & Richmond (1980); Richmond et al. (2003); Maruyama et al. (2005)). For the October storm both sides marked a (-) storm, this is probably explained by the same reasons mentioned before.

3 Conclusions

According to the analysis of interplanetary data especially Bz from IMF and Ey from IEF, in comparison with the variation of the electron density Ne and the density of neutrals of SWARM satellites during the three previous ionospheric storms, we can notice that:

- In the day side
  - Ionospheric first (+) storms are due to the prompt penetrating electric field PPEF, while the late (+) storms are probably due to disturbance dynamo electric fields DDEF as well as to the disturbance of the circulation of neutrals by thermospheric/ionospheric coupling.
  - Ionospheric (-) storms are mainly due to the large amplitude northward Bz inversion as well as to the change in neutrals compositions.
- In the night side
  - ionospheric (+) storms are probably mainly due to DDEF and the disturbance of neutrals circulations.
  - Ionospheric (-) storms are due in addition to changing neutral compositions to PPEF at first.

References

Astafyeva, E., Zakharenkova, I., & Alken, P. 2016, Earth, Planets and Space, 68, 1

Balan, N., Shiokawa, K., Otsuka, Y., et al. 2010, Journal of Geophysical Research: Space Physics, 115

Blanc, M. & Richmond, A. 1980, Journal of Geophysical Research: Space Physics, 85, 1669

Danilov, A. 2013, Advances in Space Research, 52, 343

Fejer, B. G., Gonzales, C., Farley, D., Kelley, M., & Woodman, R. 1979, Journal of Geophysical Research: Space Physics, 84, 5797

Fuller-Rowell, T., Codrescu, M., Moffett, R., & Quegan, S. 1994, Journal of Geophysical Research: Space Physics, 99, 3893

Goncharenko, L., Foster, J., Coster, A., et al. 2007, Journal of atmospheric and solar-terrestrial physics, 69, 1253

Gonzales, C., Kelley, M., Fejer, B. G., Vickrey, J., & Woodman, R. 1979, Journal of Geophysical Research: Space Physics, 84, 5803

Huang, C.-S., Foster, J. C., & Kelley, M. C. 2005, Journal of Geophysical Research: Space Physics, 110

Kelley, M. C., Makela, J. J., Chau, J. L., & Nicolls, M. J. 2003, Geophysical Research Letters, 30

Kikuchi, T., Ebihara, Y., Hashimoto, K., et al. 2010, Journal of Geophysical Research: Space Physics, 115

Kikuchi, T., Lühr, H., Schlegel, K., et al. 2000, Journal of Geophysical Research: Space Physics, 105, 23251

Lee, C.-C., Liu, J.-Y., Reinisch, B. W., Lee, Y.-P., & Liu, L. 2002, Geophysical research letters, 29, 12

Liu, J., Liu, L., Nakamura, T., et al. 2014, Journal of Geophysical Research: Space Physics, 119, 7716

Lu, G., Goncharenko, L., Richmond, A., Roble, R., & Aponte, N. 2008, Journal of Geophysical Research: Space Physics, 113

Manoj, C., Maus, S., & Alken, P. 2013, Journal of Geophysical Research: Space Physics, 118, 5919

Manoj, C., Maus, S., Lühr, H., & Alken, P. 2008, Journal of Geophysical Research: Space Physics, 113

Maruyama, N., Richmond, A., Fuller-Rowell, T., et al. 2005, Geophysical Research Letters, 32

Mikhailov, A. & Schlegel, K. 1998, 16, 602

Rastogi, R. & Patel, V. 1975, 82, 121

Richmond, A. & Matsushita, S. 1975, Journal of Geophysical Research, 80, 2839

Richmond, A., Peymirat, C., & Roble, R. 2003, Journal of Geophysical Research: Space Physics, 108

Tsurutani, B., Verkhoglyadova, O., Mannucci, A., et al. 2008, Journal of Geophysical Research: Space Physics, 113

Wei, Y., Wan, W., Pu, Z., et al. 2011, Journal of Geophysical Research: Space Physics, 116

Werner, S. & Prölss, G. 1995, Kleinheubacher Berichte, 38, 143

Wolf, R., Spiro, R., Sazykin, S., & Toffoletto, F. 2007, Journal of Atmospheric and Solar-Terrestrial Physics, 69, 288

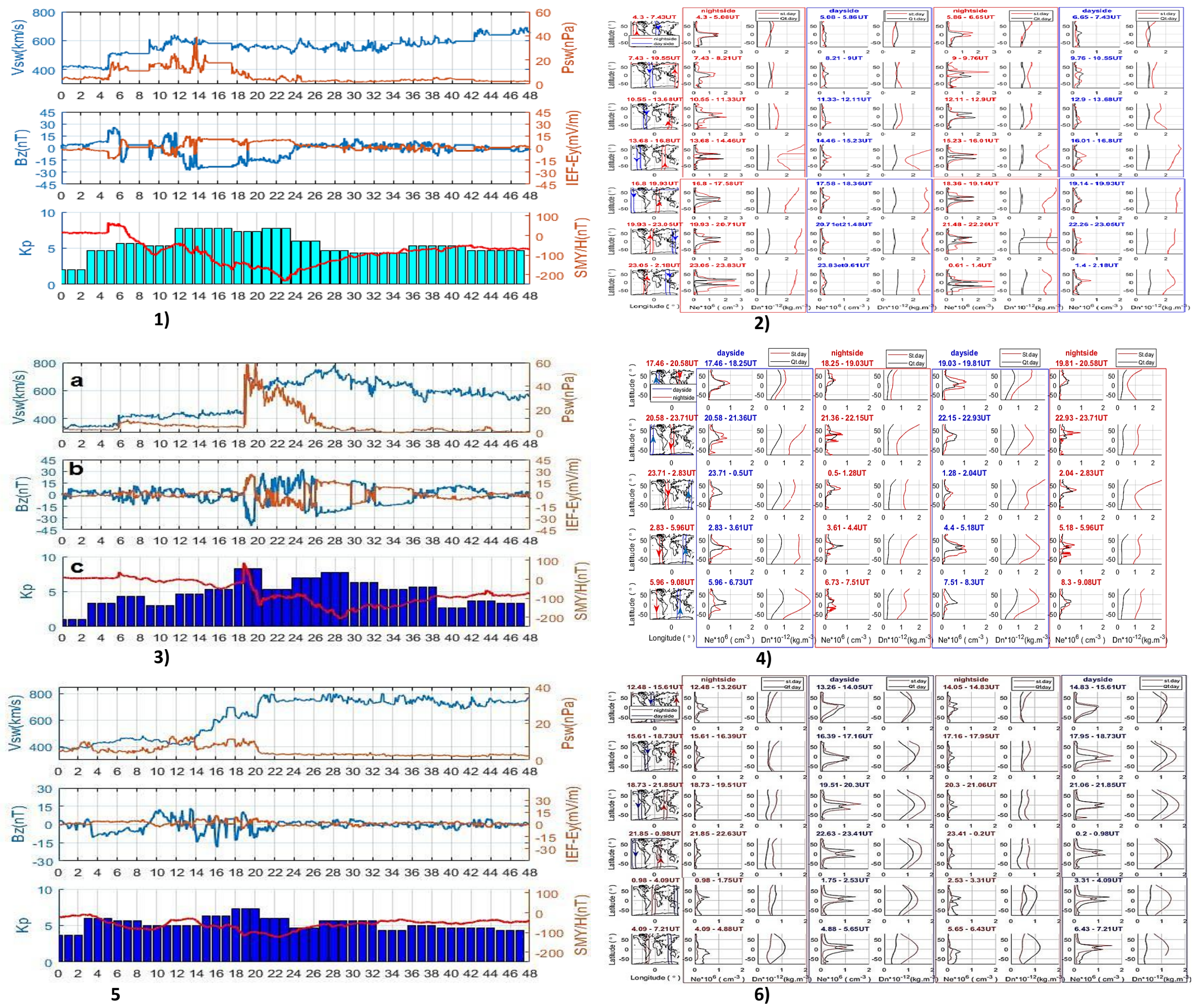

Fig. 1. *1,3et5:the Variation of interplanetary and geophysical parameters during the three geomagnetic storms of March, June and October 2015. a - solar wind speed (Vsw, blue) and solar wind pressure (Psw, red); b - component Ey of the interplanetary electric field (IEF Ey, red) and component Bz of the interplanetary magnetic field (IMF Bz, blue) in GSM coordinates; c - the kp index (green bars) and the SYM-H geomagnetic activity index (red). 2,4 and 6 represent Results of Swarm A (SWA) of 3 successive storms in the night orbit (red curves) and on the orbit of the day (blue curves) .the data of the electron density Ne (in* cm^{-3}*) and the density of neutrals Dn (in* $kg.m^{-3}$*) of the night are represented in two successive columns in a red frame, while the same parameters of the day are framed by a blue frame. The values of these two storm day parameters (red curves) are compared to the calm day values (black curves). The time in UT of the start and end of the satellite trajectories is indicated in red for the night side and in blue for the day side.*

PREDICTING THE HEIGHT OF THE SOLAR CYCLE 25 THROUGH POLAR REGIONS ACTIVITY

S. Koutchmy[1], E. Tavabi[2], J.-C. Noëns[3], O. Wurmser[4] and B. Filippov[5]

Abstract. We describe and discuss the reasons why we believe the forthcoming solar cycle (SC) 25 will be significantly higher than what was predicted by NASA in 2019.

Keywords: solar cycle prediction, cycle 25, polar regions activity, polar faculae, macro-spicules, polar mini ejections

1 Introduction

The solar activity through the sunspot number (SN) modulates geomagnetism, CMEs, flares, SEPs and associated disturbances. The prediction of the height of the forthcoming SC (expressed by the SN) is since 2019 the subject of many studies. They are mainly based on statistical and/or mathematical and/or Heuristic methods, taking parameters from the analysis of past cycles; they leaded to a predicted SC 25 similar to the low height preceding SC 24, sometimes significantly lower, indeed. Some predictions uses solar activity parameters justified by the solid belief that the solar activity is fully governed by a dynamo mechanism occurring inside the Sun. The most popular dynamo model being the Babcock-Leighton model describing the transformation of a general dipolar field of the rotating Sun into a toroidal field through the differential rotation visualized near the surface. The regeneration of the dipolar field is another aspect of the model that is left not well understood. Several puzzling features like the M- regions, the active longitudes, the occurrence of long- live big single sunspots, the cyclonic and the widely distorted behavior of extended interacting active regions, the occurrence of Coronal Holes not predictable by dynamo effect, the polar regions cycles and/or recurrences, and finally the large dispersion of heights of SN cycles etc. are however the subject of hot debates. More important for practical obvious reasons is the prediction of the solar cyclesin advance Nandy (2021)

2 Observations, discussion and conclusion

It has been naively suggested (following the Ohl's law) that the Polar Regions activity, with the occurrence of recurrent geo-activity in the years around the solar minimum of SC n is rather correlated with the height of the n+1 SC. Accordingly the height of the following SC could be predicted; additionally, there is now a growing consensus on the key role of polar magnetic fields as seeds for the SC Makarov et al (1987).

We looked at the activity of Polar Regions using proxies: i/ density of polar faculae from visually evaluated HMI of SDO mission W-L filtergrams; ii/ numbers of cool ejection events from a 15 Years survey of the Pic du Midi CLIMSO $H\alpha$ observations Noëns et al. (2000); iii/ averaged extensions of the 304 shell in Polar Regions related to the polar CHs macro- spicules activity. Time variations of these 3 parameters qualitatively point to a SC 25 that could reach high levels, of order of 2 times the height of the SC 24, in contrast with the moderate height predicted by the SC 25 Prediction Panel of NASA and NOAA (Chair: Doug Biesacker). The reason of this discrepancy is not clear. We better wait the occurrence of the double maximum of SC 25 in 2025-26 to

[1] Institut d'Astrophysique de Paris, 98 bis Bd Arago, CNRS and Sorbonne University
[2] Physics Department, Payame Noor University (PNU), 19395-3697, Tehran, I. R. of Iran
[3] Obs. Pic du Midi, Association des O.A., France
[4] Association des O.A., France
[5] Pushkov IZMIRAN, Moscow region, Fed. Russia

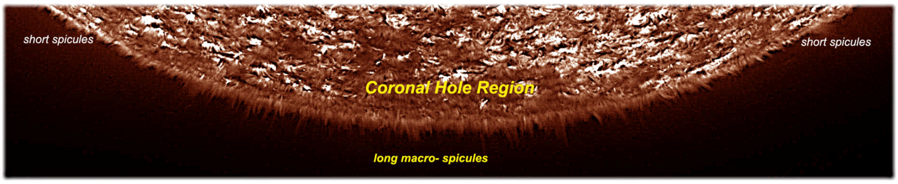

Fig. 1. Partial frame reconstructed image of a typical polar region at time of minimum activity to demonstrate the "abnormal" thickness of the 304 emissions (due to the HeII resonance line formed around 50 000K) in this polar region. Such extensions were measured during more than 1 solar cycle in both the South and the North regions. Extensions are believed to be due to many ejection events in nearly radial directions called macro-spicules, in contrast to spicules seen everywhere, including regions outside the coronal hole regions. AIA filtergrams of the NSO NASA mission were used after summing original frames for 10 min.

go further with the interpretetion. Another interesting parameter seemingly related to this topic is the definite observation of the chromospheric prolateness (ovalisation) in the Years of the minimum of 2018- 2020 that was discovered in the Years 1998- 2020 (before SC 23) and that was not well measured in 2010- 11 (before SC 24). In rather "cool" spectral lines, the smoothed upper edge of the solar chromosphere is prolate in the North-South direction at the epoch of minimum solar activity Filippov et al. (2000).

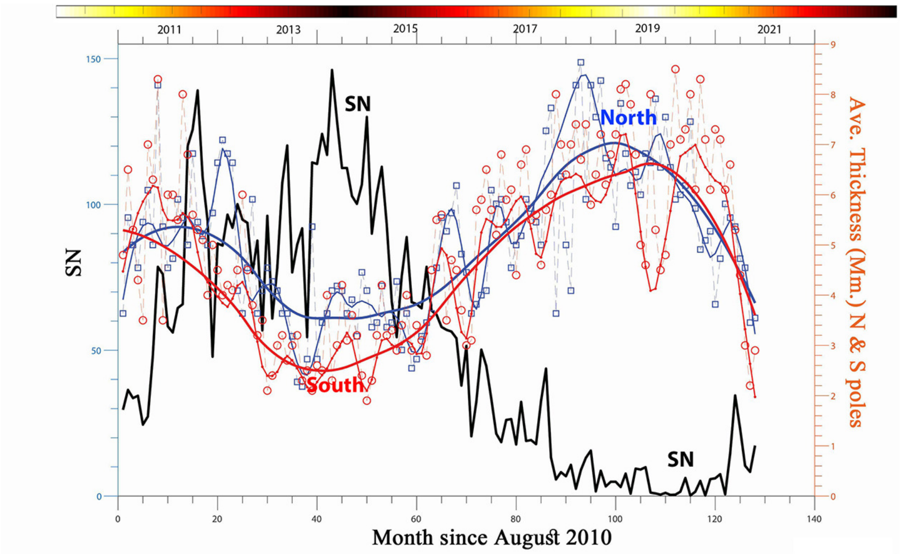

Fig. 2. Variations of the apparent "thicknesses" of the transition region polar regions shells as measured using the 304 emissions (He II) from AIA images of the SDO mission-NASA. Both the North (N) in blue and the South (S) in red poles are showing an extended shell ofmacro-spicules activity at Years of the solar minima but during the last period around 2019, an enhanced activity is recorded suggesting that the next SC 25 will be high. In black line the SN during the same period of time.

Acknowledgements. We acknowledge the HMI and AIA/SDO mission of NASA consortium for the easy access of calibrated data.

References

Filippov, B. Koutchmy, S. Vilinga, J. (2000) Solar Phys. 196, 311- 320;(2007) Astron. Astrophys. 464, 1119

Noëns J.C., Wurmser O., 2000, Astrophysics and Space Science, 273, 17

Makarov, V.I., Leroy, J.L., Noëns, J.C., 1987, Soviet Astronomy, 31, 560

Nandy, D. (2021) Solar Phys., in press

INTERHEMISPHERIC ASYMMETRY OF THE EQUATORIAL IONIZATION ANOMALY IN THE AFRICAN SECTOR OVER 3 YEARS

A. Loutfi[1,2], F. Pitout[1] and A. Bounhir[2]

Abstract. The electron density in the topside ionosphere recorded by the Langmuir probes on board the Swarm satellites has been systematically analyzed to determine the climatology of the Equatorial Ionization Anomaly (EIA) in the African sector over 3 years. Observations show strong seasonal variations, with the electron density being lower around the June solstice compared to the rest of the year. We have noticed the so-called semi-annual anomaly: the electron density is higher around equinox than around solstice. For solstice seasons, the asymmetries in the electron density with respect to the magnetic equator are stronger at the December solstice than at the June solstice. For equinox seasons, we can notice equinoctial symmetry in all local time sectors, meaning that the same trend is observed for both equinoxes with or without symmetrical crests.

Keywords: Ionosphere, electron density, Swarm, EIA.

1 Introduction

Several studies have investigated the interhemispheric asymmetries of the mid-latitude ionosphere, including the asymmetries of the latitudinal positions and densities of EIA crests. Moreover, the significant longitudinal variations of the EIA interhemispheric asymmetry have been studied in previous works (Lin et al. 2007; Luan et al. 2015). Despite all these studies, the interhemispheric asymmetry of the topside ionosphere needs to be further investigated. We present the first comprehensive study carried out in the Africa sector. Data used in this study were collected during the declining solar cycle (2014-2016) from Swarm satellite A. Langmuir Probes (LP) on aboard Swarm satellites allow to estimate the ambient electron density (Ne) of the ionospheric plasma (Friis-Christensen et al. 2008) at 460 km altitude. To study the seasonal variability of the ionospheric electron density, we have selected all Swarm A satellite passes that cross a rectangle of -60°S, 60°N in magnetic latitude and -7.88°-4°W and -7.88°+4°W in geographic longitude.

2 Seasonal variability of ionospheric electron density.

Figure 1 shows seasonal variability of the latitudinal distribution of the ionospheric plasma density at the mid- and low-latitude regions at around 7.866° W meridian sector (±4° longitude intervals) of all data available for different local time sector over 3 years (2014-2016). At first glance, we can see that the ionospheric electron density is very low at night and the lowest values are mainly found at the June solstice in most local times. We can also often see a hemispheric asymmetry in the electron density distribution. This asymmetry could find its origin in the asymmetry of the magnetic field itself (Barlier et al. 1974). For solstice seasons, the average Ne values indicate the existence of two different EIA asymmetries: Ne is higher in the northern (southern) hemisphere than in the southern (northern) one in the December solstice (June solstice). The overall electron density at low latitude is smaller around June solstice than December solstice. This is explained by the smaller Sun-Earth distance around June (Su et al. 1998). We also note that differences are larger during day time than night time.For equinox seasons, we can notice the so-called equinoctial symmetry in all local time sectors,

[1] IRAP, Universite Toulouse III, CNRS, CNES, Toulouse, France.
[2] Oukaimeden Observatory, Laboratoire de Physique des Hautes Energies et Astrophysique, FSSM, Cadi Ayyad University, Marrakech, Morocco.

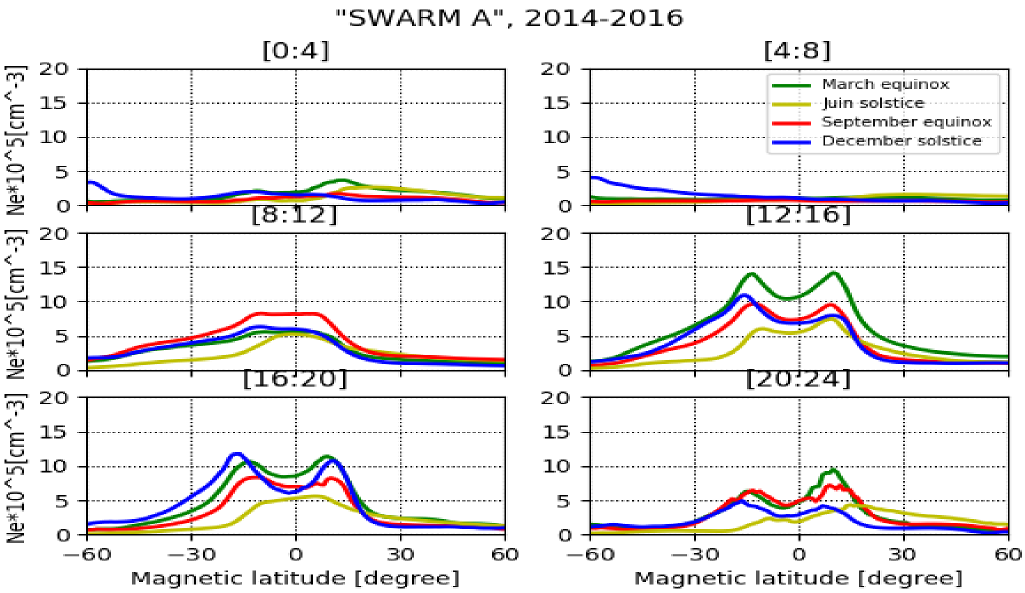

Fig. 1. The seasonal variation of the ionospheric plasma density structure at the mid- and low-latitude regions at around 7.866° W meridian sector (±4° longitude intervals) in different local time sectors.

meaning that the same trend is observed for both equinoxes with or without symmetrical crests. This features of the equinoctial symmetry is in good accordance with the result reported by Bailey et al. (2000). Still around equinoxes, EIA crests asymmetry is observed from 20 LT to 04 LT where the northern hemisphere crest density is higher than the southern one. The average of the electron density in March equinox is greater than the September one except from 8 LT to 12 LT where the opposite is observed for the single crest ionospheric density. A mechanism for this latter equinoctial asymmetry has been studied using CTIP (Coupled Thermosphere Ionosphere Plasmasphere model). The model results reproduce the observed equinoctial asymmetry and suggest that the asymmetries are caused by the north-south imbalance in energy imput into the thermosphere and ionosphere. This imbalance is due to the slow response of the thermosphere arising from the effects of the global thermospheric circulation (Bailey et al. 2000). From comparing the average electron density at equinox and solstice seasons, we have noticed the semi-annual anomaly: the electron density is higher at the equinoxes than at the solstices. This is in accordance with the observations made by the Hinotori satellite (Bailey et al. 2000).

3 Conclusions

The seasonal variability of the ionospheric electron density around 460 km altitude has been studied using 3 years (2014-2016) of Swarm satellite data in the African sector. Observations show strong seasonal variations, with the electron density being lower around the June solstice compared to the rest of the year. We have noticed the semi-annual anomaly: the electron density is higher around equinoxes than around solstices.

This project is financially supported by Campus France through the French-Moroccan bilateral program "PHC Toubkal 2019" (grant number: 41409WJ). The European Space Agency is acknowledged for providing the Swarm data. The official Swarm website is http://earth.esa.int/swarm, and the server for Swarm data distribution is ftp://swarm-diss.eo.esa.int.

References

Bailey, G., Su, Y. Z., & Oyama, K.-I. 2000, Annales Geophysicae, 18, 789

Barlier, F., Bauer, P., Jaeck, C., Thuillier, G., & Kockarts., G. 1974, Journal of Geophysical Research, 79(34), 5273–5285.

Friis-Christensen, E., Lühr, H., Knudsen, D., & Haagmans, R. 2008, Advances in Space Research, 41(1), 210–216.

Lin, C. H., Liu, J. Y., Fang, T. W., et al. 2007, Geophys. Res. Lett.,34, L19101,

Luan, X., Wang, P., Dou, X., & Liu, Y. C.-M. 2015, J. Geophys. Res. Space Physics, 120 , 3059–3073,

Su, Y., Bailey, G., & Oyama, K. 1998, Annales Geophysicae 16, 974–985

THE NAROO DIGITIZATION CENTER

V. Robert[1, 2], J. Desmars[1,2], A.-C. Perlbarg[1,2], V. Lainey[2], J.-E. Arlot[2] and J. Aboudarham[3]

Abstract. The New Astrometric Reduction of Old Observations NAROO center is built at Paris Observatory, Meudon, and is dedicated to the measurement of astro-photographic plates and the analysis of old observations. The NAROO digitizer consists of a granite based Newport-Microcontrol open frame air-bearing XY positioning table, a scientific sCMOS camera, and a telecentric optical system. The plate holder assembly is suited for mounting glass plates up to 350-mm square. The machine positioning stability is better than 15 nm, its repeatability is better than 40 nm. With real photographic plate data, we are able to produce measurements with an accuracy better than 65 nm.

The renewed interest about photographic plates concerns the expansion of the database of transient objects evolving in time, since digitization now makes it possible to measure images with a high level of accuracy and to identify all the available objects. The information extracted from such materials can be of an astrometric, photometric, and spectroscopic nature, when not purely imaging, with consequences in planetology, near-Earth asteroid risk assessment, astrophysical phenomena, and general relativity, to mention but a few.

We will present first research possibilities for Solar photographic plates to be digitized and analyzed. We will also give details for the researchers to use our facilities and digitize their collection by answering our Call for Proposals.

Keywords: instrumentation: high angular resolution, techniques: image processing, digitization, photograhic plate

1 Introduction

The renewed interest about photographic plates concerns the expansion of the database of transient objects evolving in time, since digitization now makes it possible to measure images with a high level of accuracy and to identify all the available objects. The information extracted from such materials can be of an astrometric, photometric, and spectroscopic nature, when not purely imaging, with consequences in planetology, near-Earth asteroid risk assessment, astrophysical phenomena, and general relativity, to mention but a few.

Studying the dynamics of Solar System bodies, in particular, requires astrometric observations sampled over a long time span to quantify the long period terms which may help to analyze the evolution of the motion. Searching for old data is obviously useful for this purpose, and since we have demonstrated that a precise digitization and a new astrometric reduction of old photographic plates could provide very accurate positions (Robert et al. 2011, 2015, 2016), researchers involved in various scientific topics began to (re-)consider such materials. As a consequence, the Paris Observatory decided to acquire such an instrument and to build a scientific community for its exploitation, creating the New Astrometric Reduction of Old Observations NAROO program.

[1] Institut Polytechnique des Sciences Avancées IPSA, 63 bis Boulevard de Brandebourg, 94200 Ivry-sur-Seine, France
[2] IMCCE, Observatoire de Paris, PSL Research University, CNRS UMR 8028, Sorbonne Universités, UPMC, Univ. Lille 1, 77 avenue Denfert- Rochereau, 75014 Paris, France
[3] LESIA, Observatoire de Paris, PSL Research University, CNRS UMR 8109, Sorbonne Universités, Université de Paris, 5 place Jules Janssen, 92195 Meudon, France

2 Solar activities

The Paris Observatory owns about 100,000 photographic plates of the Sun, mostly observed in Hα, Ca II K center line wavelength, and continuum (near Ca II K line). These observations were made from 1870 to 1999 with photographic plates, while new observations are still being realized today using digital recording, with a recent update in 2018 (Malherbe & Dalmasse 2019).

Using the NAROO machine with older photographic plates of the Sun will allow us to tackle the problem of morphology and topology of various Solar features. The overall accuracy of the NAROO machine is ideal to measure the best possible location of the contours of filaments. Obviously, this will not be done for all filaments in all observations, but it will be possible to digitize the boundaries of filaments involved in strong flares to deduce the behavior of the magnetic field leading to them. This work can be achieved quite easily as we can benefit from filament detections (Fuller et al. 2005) and time tracking (Bonnin et al. 2013) to identify the photographic plates and digitize them in the collection.

Another application of the NAROO program deals with the exact determination of the boundaries of active regions (AR). First, we could analyze digitizations to determine the place between two opposite polarities, called the neutral line, where filaments can appear. Then, it will allow us to accurately study the extension of an AR and its evolution in time, which gives clues to the strength of the underlying magnetic field. Lastly, and probably the most prospective scientific application, is the fact that it will help us to precisely determine, at various altitudes, the shape of the ARs, giving 3D information on the magnetic field extension and evolution.

3 Call for Proposals

The value of a new analysis of old photographic plates has been demonstrated, and the community is beginning to worry about the use and preservation of such materials for science. As recommended by the resolution B3 of the XXX IAU General Assembly in 2018, the preservation, digitization, and scientific exploration of the plates must be realized. Plate collections of the Paris Observatory and other French and international institutions are being digitized to provide data spanning more than one century for our works. Corresponding results will be presented in upcoming papers. Digitized raw data will also be available for the community.

The NAROO machine is available for researchers to digitize their own collections for scientific purposes, since digitization time is reserved for external users. A call for proposals is being issued every six months via our project website `https://omekas.obspm.fr/s/naroo-project/`.

The NAROO program was supported by the DIM-ACAV of Ile-de-France region, PSL Research University, the Programme National GRAM and the Programme National de Planétologie (PNP) of CNRS/INSU with INP and IN2P3, co-funded by CNES.

References

Bonnin, X., Aboudarham, J., Fuller, N., Csillaghy, A., & Bentley, R. 2013, Sol. Phys., 283, 49

Fuller, N., Aboudarham, J., & Bentley, R. D. 2005, Sol. Phys., 227, 61

Malherbe, J. M. & Dalmasse, K. 2019, Sol. Phys., 294, 52

Robert, V., de Cuyper, J. P., Arlot, J. E., et al. 2011, MNRAS, 415, 701

Robert, V., Lainey, V., Pascu, D., et al. 2015, A&A, 582, A36

Robert, V., Pascu, D., Lainey, V., et al. 2016, A&A, 596, A37

Session 9

Atelier général du PNCG: machine learning for the study of galaxies and cosmology

UNSUPERVISED CLASSIFICATION OF CIGALE GALAXY SPECTRA

J. Dubois[1], D. Fraix-Burnet[1], J. Moultaka[2], D. Burgarella[3] and P. Sharma[3]

Abstract. The goal of the work presented is to gain a thorough understanding of the unsupervised classification of galaxies' spectra using the Fisher-EM discriminative latent subspace Gaussian mixture technique to assess its physical relevance as well as to characterise the effect of the noise on the process. We simulated a sample of 11 475 optical spectra of galaxies with 496 monochromatic fluxes using the CIGALE tool. The integrated completed likelihood (ICL) criterion in Fisher-EM is used to determine the statistical model and the optimal number of clusters. The analysis was run numerous times to ensure that the results were reliable. The optimal classification obtained contains 12 clusters and is very robust against noise down to a signal-to-noise ratio (SNR) of 3. The distribution of the parameters used for the simulation shows excellent discrimination between classes. This study yields two conclusions valid at least for the Fisher-EM algorithm. Firstly, the unsupervised classification of spectra of galaxies is both reliable and robust to noise. Secondly, such analyses can extract the useful physical information contained in the spectra and build highly meaningful classifications. In an epoch of data-driven astrophysics, it is important to trust unsupervised machine learning approaches that do not require unavoidably biased training samples.

Keywords: Methods: data analysis – Methods: statistical – Galaxies: statistics – Galaxies: general – Techniques: spectroscopic

1 Introduction

Whether it be classifications based on morphological properties of galaxies, their spectra, or spectral features, the idea of classifying galaxies is not new and several studies were previously published on the matter (Kennicutt (1992), Dobos et al. (2012), Wang et al. (2018), Siudek et al. (2018)). Here we present a new, fully data-driven, and machine-learning-based approach for classifying galaxy spectra using the unsupervised classification method Fisher-EM (Bouveyron & Brunet (2011)). In this work, we have applied Fisher-EM on a large sample of optical galaxy spectra simulated using the spectral energy distribution (SED) fitting code CIGALE (Burgarella et al. (2005), Noll et al. (2009), Boquien et al. (2019)). We were able to assess the physical relevance of the method and the effect of noise on the process. We here provide a highlight of the most important results. In 2.1, we present the discriminative ability of the method in regards to the galaxies' physical properties. In 2.2, we show the robustness of the method against the presence of noise. A paper with a thorough description of the data, method, and results was submitted to A&A, and is undergoing the reviewing process at the time of writing.

2 Highlights of the classification

2.1 Discrimination of the galaxies' physical properties

The classification was performed on the sole basis of the spectra. The optimal classification contains 12 classes and is shown in Fig. 1 (left and center panel). As seen in the left panel, the dispersion of the spectra in the classes is relatively small, showing good homogeneity of the classes. Perhaps the most interesting result lies in the center panel, which shows that some of the galaxies' physical parameters in the classes (see Boquien et al. (2019) for more information about those parameters) are precisely discriminated. A linear discriminant analysis (LDA) shows that the most segregated parameters are the age of the galaxy T_{main}, the metallicity, the fraction of stars issued from a late burst of star formation f_{burst}, and the age of the late burst T_{burst}.

[1] Institut de Planétologie et d'Astrophysique de Grenoble, 38400 Saint-Martin d'Hères, France. email: julien.dubois@univ-grenoble-alpes.fr

[2] Institut de Recherche en Astrophysique et Planétologie, 31028 Toulouse, France

[3] Laboratoire d'Astrophysique de Marseille, 13013 Marseille, France

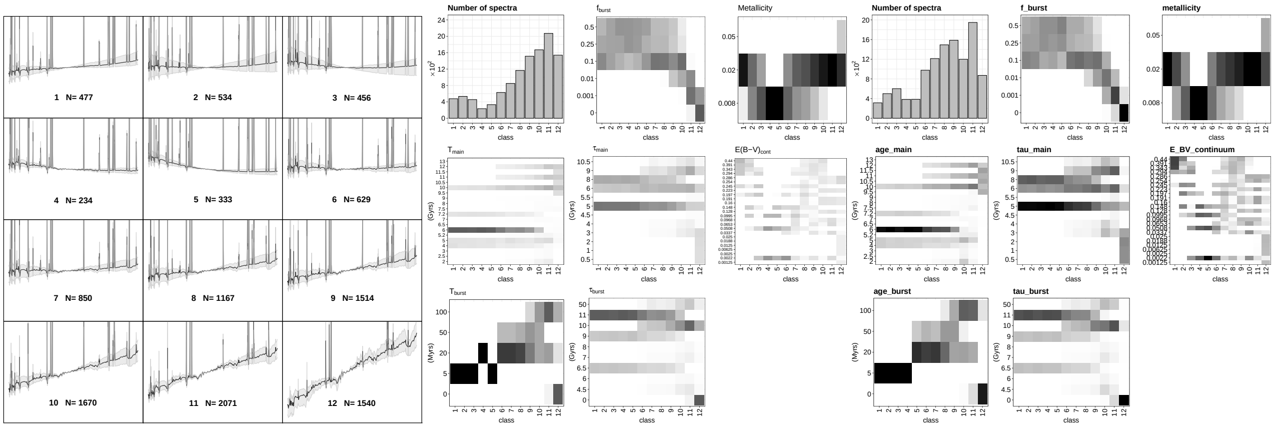

Fig. 1. Left: 12-clusters classification of the noiseless spectra. Mean spectra (in black) and their dispersion (in grey) for every class of the 12-clusters classification. The dispersion corresponds to the 10% and 90% quantiles for each monochromatic flux. **Center:** 12-clusters classification of the noiseless spectra. *Top left:* number of spectra contained in each class. *All others:* heatmaps of the relevant CIGALE input parameters among the 12 classes on noiseless spectra. All possible parameter values are represented on the y-axis, and the class index on the x-axis. The in-class densities of the parameter values are illustrated in the form of a heatmap, where a dark square equates to a density of 1, and white of 0. The classes are sorted by ascending average T_{main}. **Right:** Same but for spectra with an added noise of SNR=20.

2.2 Robustness against noise

The analysis was done multiple times with different levels of noise, characterised by their signal-to-noise ratio (SNR). The method showed consistent results for SNRs as low as 3. An example for SNR=20 is shown in the right panel of Fig. 1. At SNR=1, the optimal number of clusters drastically decreases down to 5 due to the loss of information, but the method is still capable of providing a certain degree of discrimination.

3 Conclusions

The study shows that the unsupervised classification algorithm Fisher-EM applied on thousands of CIGALE galaxy spectra yields a classification that is both robust against the initialisation of the algorithm and the noise. Very importantly, the classification is very discriminating with respect to the physical properties of the galaxies. Our findings provide considerable motivation to investigate the atlas presented in Fraix-Burnet et al. (2021) in greater depth and to apply it to larger samples. The interesting prospect is to incorporate galaxies at higher redshifts to investigate the classification's evolution over time using a fully data-driven procedure.

References

Boquien, M., Burgarella, D., Roehlly, Y., et al. 2019, A&A, 622, A103

Bouveyron, C. & Brunet, C. 2011, arXiv e-prints, arXiv:1101.2374

Burgarella, D., Buat, V., & Iglesias-Páramo, J. 2005, MNRAS, 360, 1413

Dobos, L., Csabai, I., Yip, C.-W., et al. 2012, MNRAS, 420, 1217

Fraix-Burnet, D., Bouveyron, C., & Moultaka, J. 2021, Astronomy and Astrophysics, in press

Kennicutt, Robert C., J. 1992, ApJS, 79, 255

Noll, S., Burgarella, D., Giovannoli, E., et al. 2009, A&A, 507, 1793

Siudek, M., Małek, K., Pollo, A., et al. 2018, arXiv e-prints, arXiv:1805.09905

Wang, L.-L., Luo, A. L., Shen, S.-Y., et al. 2018, MNRAS, 474, 1873

CLASSIFICATION OF COSMOLOGICAL MODELS FROM THE INTERNAL PROPERTIES OF DM HALOS BY USING MACHINE LEARNING

R. Koskas[1] and J. M. Alimi[1]

Abstract. We are interested in detecting the cosmological imprint on properties of present dark matter halos by using Machine Learning methods. We analyse the halos formed in Dark Energy Universe Simulations using several dark energy models (ΛCDM, Quintessence Ratra Peebles), whose parameters were chosen in agreement with both CMB and SN Ia data. Their resulting halos are thus extremely close from one cosmological model to another. However, we have shown that machine learning techniques can be implemented to determine the cosmological model in which each halo was formed: we associate to each present day halos from ΛCDM and RP CDM ellipsoidal mass and shape profiles, defined to efficiently keep track of the matter distribution anisotropies and, then, we experimentally show that those quantities allow a properly trained learning device to find the dark energy model of the Universe within which these halos have grown. Training our device on 40,000 halos of 10^{13} and 10^{14} solar masses, we can correctly classify more than 70% of the halos in the test set. We also study the misleading ML methodological biases, "Clever Hans effects", and the way to fix them.

Keywords: dark energy, machine learning, decision tree, numerical simulations, dark matter halos

1 Introduction

Dark Energy Universe Simulations (Alimi et al. 2010; Rasera et al. 2010; Alimi et al. 2012; Reverdy et al. 2015) is a set of high performance N-body cosmological simulations. From one simulation to another, several dark energy models are assumed, e.g. the dynamical Ratra Peebles (RP) CDM model and the fiducial ΛCDM. We will use in this proceedings the 648 $h^{-1}Mpc$ simulation containing $N = 2048^3$ particles. For each cosmological model, all cosmological parameters are chosen to form a CMB (Spergel et al. 2007) and SN Ia (Kowalski et al. 2008) compatible n-uplet. As a consequence, we study only **realistic** models (Alimi et al. 2010), which are extremely close one to each other - any halo of the ΛCDM Universe strongly overlap its $RPCDM$ counterpart. Therefore, natural questions emerge: **is there any cosmological imprint in the difference between the halos of the two Universes?** In other words, **does the internal structure of halos embed cosmological information ?** Our goal is to extract information about the cosmology (dark energy model) from the matter distribution and the dynamical state of the simulated halos. Whereas a conventional objective would consist in exhibiting a mean behaviour, *i.e.*a quantity whose the average value on a large population simulated halos change significantly (more than 1σ) with the dark energy model, our objective is here more predictive: we want to infer the cosmology from only the internal properties of each individual halo. To be more specific, **each halo is described by a common set of chosen quantitative attributes; we then aim at training an AI to associate to each set of attributes, the dark energy model of the Universe in which the corresponding halo has grown. This is a classification task**. Furthermore, by changing the set of chosen attributes, we will select those that are the most significant from a cosmological point of view.

2 Halo properties computation

For a correct description of a halo, it is necessary to capture the spatial distribution of the matter in it, that is to say its profile. Because DM halos are triaxial ellipsoids rather than isotropic (Despali et al. 2016), a

[1] Laboratoire Univers et Théories, CNRS UMR 8102, Observatoire de Paris, PSL University

thorough profile characterisation requires local density measures - The parameter free Delaunay Tessellation Field Estimator (Cautun & van de Weygaert 2011) provides the local density δ at each particle locus. That allows to remove subhalos. For each density δ_a in a sequence of pre-chosen "points of measure" $(\delta_a)_a$, we consider the δ_a isodensity shell $\mathcal{S}_a = \{k \mid |\frac{\delta(\mathbf{x}^k)}{\delta_a} - 1| \leq 0.1\}$ and we observe (Jing & Suto 2002) that it is approximately an ellipsoid $(\mathcal{E}_a)$ clearly non spherical. Its parameters are computed through the diagonalization the mass tensor of the particles forming the shell $\mathcal{S}_a$: $(M_{ij}^{\mathcal{S}_a})_{1\leq i,j\leq 3} = \langle x_i x_j\rangle_{\mathcal{S}_a} - \langle x_i\rangle_{\mathcal{S}_a}\langle x_j\rangle_{\mathcal{S}_a}$. Finally, in each fitted ellipsoid $\mathcal{E}_a$, one computes the quantities that will describe halo's structure and its dynamics (the set of attributes) namely the enclosed mass $\mathcal{M}_a$ (which is thus a multiple of the particle mass m_p), the length of $\mathcal{E}_a$ axis, the velocity dispersion σ_a^V,... and so on (Koskas & Alimi 2021).

3 Machine learning

Our objective is now to train an AI to associate to a sequence $(\mathcal{M}_a, \mathcal{E}_a, \sigma_a^V, ...)_a$ the dark energy model (fiducial or RP) of the Universe in which the corresponding halo was formed. We use for this propose an ensemble of decision trees , aggregated by gradient boosting (Friedman 2002). However, the use of Machine Learning algorithms induces specific subtle spurious effects. As, we use N-body simulations where all the particles have the same elementary mass m_p and because we have chosen realistic models, Ω_m and thus m_p are different from one dark energy model to another. Now, the $\mathcal{M}_a$'s belong to $m_p^{RP}\mathbb{N}$ or $m_p^{\Lambda}\mathbb{N}$, which do not intersect. So, if the machine detects that all first-cosmology halo masses in the train set are multiple of the same elementary mass (that the machine should determine) and that all second-cosmology halo masses are multiple of another base mass, then the machine will also be able to classify the halos of the test set (simply by looking if their masses are multiple of m_p^{Λ} or m_p^{RP}). In other words, data contain cosmological information of purely arithmetical nature, which would not be reproduced in a real Universe (continuous fields). It is a typical Clever Hans effect. **This kind of effects has been carefully hunted and corrected in order to obtain physically reliable results.** See (Koskas & Alimi 2021) for the way we altered the train set to avoid it.

4 Results and conclusions

Once trained, our AI can be tested individually on each halo in the test set and determines the cosmological model with a 71% probability of success. This result is essentially achieved by using ellipsoidal profile approach rather than the spherical one, and only with mass $(\mathcal{M}_a)$, and shape attributes $(\mathcal{E}_a)$. Those are therefore the most cosmologically impregnated properties of the halos. In Koskas & Alimi (2021) we further discuss the required precision on the attributes for the AI to be predictive. We also explain why velocity dispersion measurements are not sufficient to classify the halos.

As a conclusion, it is possible to read in the halo structure the dark energy model. To do so, one has to finely describe the mass profile through local density computation and **ellipsoidal** approximation for iso-densities. Supposing isotropy when determining the mass profile considerably lowers the result. Also, it is crucial to understand **how** the resulting engine works. In particular, one has to check that the classification is achieved only by **physical** means, ignoring any cosmological clue coming from the numerical nature of the simulation, so that the engine would work for a real Universe.

References

Alimi, J.-M., Bouillot, V., Rasera, Y., et al. 2012, IEEE Computer Soc. Press, CA, USA, SC2012, Article No 73

Alimi, J.-M., Füzfa, A., Boucher, V., et al. 2010, MNRAS, 401, 775

Cautun, M. C. & van de Weygaert, R. 2011, Astrophys Source Code Library

Despali, G., Giocoli, C., & et al, M. B. 2016, MNRAS, 466, 181

Friedman, J. H. 2002, Comput. Stat. Data Anal., 38, 367

Jing, Y. P. & Suto, Y. 2002, Astrophys. J., 574, 538

Koskas, R. & Alimi, J.-M. 2021, in preparation

Kowalski, M., Rubin, D., Aldering, G., et al. 2008, Astrophysical J, 686, 749

Rasera, Y., Alimi, J.-M., Courtin, J., et al. 2010, in AIP proc. 'Invisible Universe International Conference'

Reverdy, V., Alimi, J.-M., Bouillot, V., et al. 2015, IJHPCA, 29, 249

Spergel, D. N., Bean, R., Doré, O., et al. 2007, ApJS, 170, 377

Session 10

Inégalités femmes/hommes en astronomie

SF2A 2021
A. Siebert, K. Baillié, E. Lagadec, N. Lagarde, J. Malzac, J.-B. Marquette, M. N'Diaye, J. Richard, O. Venot (eds)

IMPACT OF THE COVID-19 CRISIS ON THE FRENCH ASTRONOMY COMMUNITY

L. Leboulleux[1], F. Cantalloube[2], É. Choquet[2], E. Huby[3] and G. Singh[4]

Abstract.
The world-wide Coronavirus Disease 2019 (COVID-19) pandemic spread in France from the beginning of 2020. This has led the government to implement lockdown and curfews and thus change work practices to limit the spread of the virus in the workplace and during commutes. In the field of research in astronomy and astrophysics and mainly during the first lockdown, researchers were encouraged or constrained to work from home, which impacted all their research activities (observations, conferences, experiments, teaching...). This unprecedented situation was likely to cause several negative side effects on the astronomical research community such as isolation, poor concentration, loss of motivation and meaning, mental health problems due to work-life imbalance and physical issues do to the inadequate home office space. On the other hand, the situation also had positive outcomes (reduction in the hectic pace of work, avoidance of travel time, increased family time, the convening of inter-laboratory seminars, access to international conferences for all...). In addition to these global effects, environmental and social factors may have also lead to different sensitivities from the crisis. To quantitatively and qualitatively assess the impact of the covid-19 pandemic consequences on our activities, we conducted a survey intended for the members of the French Astronomical Society of Astronomy and Astrophysics (SF2A). This paper presents an analysis of the 258 responses we received for this survey, specifically about the impact of the sanitary crises on the physical and mental health of individuals, professional relationships and workload, scientific production (e.g. publications and applications), and events that take place online (e.g. meetings and conferences). In particular, we identify groups of people particularly impacted by this crisis: women, precarious researchers, parents and expatriates. Based on these results, we also propose recommendations for the community to revive scientific interactions in the post-COVID-19 era while offsetting its most deleterious effects on vulnerable groups and maintaining its positive effects such as the consequent reduction of the carbon footprint of research.

Keywords: SF2A, socio-demographic survey, covid-19 pandemic, gender, parenthood, job security, early-career researchers

1 Introduction

The global coronavirus 2019 (COVID-19) pandemic spread in France from the beginning of 2020 and prompted various governmental decisions: three lockdowns (March 17-May 11, 2020; October 30-December 15, 2020; and April 3-May 3, 2021), curfews during and between lockdowns, border closures, interruption of social and cultural activities, significant changes in working conditions, long-term school and university closures, and shift to distance learning with limited childcare options. This situation had an impact on the health, work and personal lives of individuals, and astronomical research was not excluded.

Academy is a unique work environment with characteristics like long-distance work-related travels (mainly for field experiments, conferences and collaborations), short-term work contracts (3 years or less) sometimes in foreign countries, a significant amount of time spent applying for grants and job applications, as well as

[1] Univ. Grenoble Alpes, CNRS, IPAG, 38000 Grenoble, France
[2] Aix Marseille Univ, CNRS, CNES, LAM, Marseille, France
[3] LESIA, Observatoire de Paris, Université PSL, CNRS, Université de Paris, Sorbonne Université, 5 place Jules Janssen, 92195 Meudon, France
[4] National Research Council of Canada, Herzberg Astronomy and Astrophysics, 5071 West Saanich Road, Victoria BC V9E 2E7, Canada

Table 1. Gender and position demographics of the survey participants.

Gender	
Man	62.8%
Woman	34.9%
Non binary person	0.4%
Not disclosed	1.9%

Current position	
Permanent researcher or professor	59.3%
Post-doctoral researcher	19.8%
PhD candidate	10.9%
Engineer or technician	5.8%
Master student	1.9%
Emeritus	1.9%
Other staff	1.1%

specific metrics to evaluate the research quality (e.g. number of peer-reviewed publications, amount of funding received, observation/computation time granted, responsibilities in large projects). Several studies about the impact of the sanitary crisis on research communities have been conducted so far, whose results point out the effect on gender inequities, particularly due to unequal work-life balance and children home-schooling. First of all, the lockdown impacted differently publication rates of men and women, with an increase for men and a decrease for women. If Viglione (2020); King & Frederickson (2021) conducted an overview of the publication gender gap due to the pandemic, this phenomenon has been measured in specific subfields or journals, such as in general health and medicine (Beverly 2021), in ophthalmology (Nguyen et al. 2021), in publications related to COVID-19 (Lerchenmüller et al. 2021), or in the Elsevier journals (Squazzoni et al. 2020). In particular, it has also been observed in astronomy within the Italian astronomical community by Inno et al. (2021). Among women, young career female scientists appear as a particularly impacted group (Gewin 2020), in addition with mothers and women of color: Staniscuaski et al. (2021) measured this gender- and motherhood-based effect in the Brazilians academic system and Fulweiler et al. (2021) points out the intersection with ethnicity and race. COVID-19 did not only impact publication rates, but also academic job stability, particularly for women (Gewin 2020), the access to permanent positions for mothers (Cheng 2020), mental health, particularly for women and post-doctorate researchers (Beverly 2021; Woolston 2020a,b).

In line with the studies led in other fields of research and/or countries, we aim to understand the impact of the pandemic on the French astronomical research community, which has its own scientific culture (e.g. academic system, career path, job opportunities). This motivated the survey and its analysis presented in this paper, where we intend to gauge the impact of the pandemic on the French astronomy research workforce and to emphasize the practices to maintain in the after-crisis era and the other to implement to counterbalance the negative side effects of the sanitary crisis.

This study is based on a survey intended for the French community of researchers in Astronomy and Astrophysics, aiming to grasp the impact of the sanitary crisis on the scientific production (e.g. number of publications, grant applications, observing/computing proposals) and well-being (e.g. work-life balance, interactions with colleagues, mental and physical health) during the COVID-19 crisis. This survey was made of 38 questions divided in different sections (general demographics, parenthood, physical and mental health, day to day working activities, scientific publications, applications, online events, professional interactions, and post-COVID-19 inclination) and communicated by the SF2A conference committee during the French Astronomy Week in June 2021. The survey can be read in the Appendix A. We gathered a total of 258 valid answers that we analyzed to collect the general characteristics of the respondents, presented in section 2, and to identify specific problematics to pay attention to and the most vulnerable groups based on demographic data (gender, expatriate situation, job stability, parenthood) (see section 3). From the results, in section 4, we formulate a set of recommendations to better prepare the post-crisis scientific activities, before concluding in section 5.

2 General demographics

The survey was open during and after the French Astronomical Society SF2A annual conference that took place virtually in early June 2021. Among the $\sim$ 700 SF2A members, we collected 258 answers to our survey. The table 1 summarizes some of the demographics of the respondents.

The respondents panel consists of 162 men, 90 women, one non-binary person, and 5 people preferred not to disclose their gender. The women ratio can be compared to other measures made on the French astronomical community, such as Bot & Buat (2020) (23% of female permanent researchers and professors in astronomy in France, 22% according to Berné & Hilaire (2020), and the ratio evolution is also studied in Suarez (2021)), Pommier (2021) (22% of women in permanent position in astronomy in Europe), and `https://www.iau.org/administration/membership/individual/distribution/` (26% of women among the french IAU members). These percentages indicate that the survey panel over-gathers women respondents (a phenomenon already observed in Leboulleux et al. 2020) and the ratio of 34.9% should be taken with caution.

Table 1 also indicates the distribution of the participants among different professional positions. The main categories correspond to permanent researchers and professors (153 participants), post-doctoral researchers (51) and PhD candidates (28). The percentages of engineers, ITAs, and other staff members are clearly lower than the actual ratio in a French research institute, which is probably due to the fact that SF2A is mainly targeted at researchers. Belonging to one category or another has an impact on the experience of the covid-19 crisis, as it correlates with different situations such as job stability and with different age groups (Woolston 2020a; Webb 2021).

Among the respondents, 20.9% indicate working in a foreign country, 77.5% are working in France, and 1.58% preferred not to disclose. Expatriation can impact the personal experience of lockdown and COVID-19 crisis due to general isolation and mental vulnerability. It raises further challenges for expatriates including complex access and understanding of news and government decisions due to the language and media barriers, inability to meet family members and friends in their home countries due to travel restrictions and closed borders, home sickness, helplessness towards disparities between the gravity of covid-related events in their current country of residence and home countries, more complex access to medical facilities over the locals, and increased violence and racism due to misinterpretation of the covid-related events.

Among the respondents, 52.7% indicated they have no children, while 47.3% have at least one child. According to other studies, parenthood is also a discrimination criterion in academia, so we chose to take it into account and analyse it in this survey. Generally speaking, Cheng (2020) indicates that women with children are less likely than their male peers to ever obtain a tenure-track position and Berné & Hilaire (2020) discusses the gender-related impact of parenthood on the scientific performance for French researchers. Those effects were emphasized during the covid-19 pandemic: Crook (2020) describes parenthood in British academia during the Covid-19 pandemic, and Fulweiler et al. (2021) and Staniscuaski et al. (2021) focus on the impact of the crisis on scientific productivity and mental health of women and women of color with children. It should also be noted here that most parents are permanent staff (92.5% of parents are researchers, professors, emeritus, engineers or ITAs) and usually older than 30 years old (98.3% of parents are above 30 years old), which creates a correlation between different factors.

3 Observations and outputs

In this section, we present the main results of the survey, and we focus on the impact of the sanitary crisis on the individual physical and mental health (section 3.1), on the work environment and professional interactions (section 3.2), on the scientific production in terms of publications and applications (section 3.3), and on the virtual communication tools used to carry on working (section 3.4).

3.1 Physical and mental health

As of June 30 2019, more than 5.5 millions confirmed cases of Covid-19 infection have been reported in France*, which correspond to 8% of the overall population. As a comparison, 11.6% of the survey respondents have been hit by the virus with symptoms, 0.4% without symptoms (ie. one person), and 22.5% do not know if they got the virus.

As a side effect of the disease, the pandemic has had an impact on the physical and mental health of individuals. This is mainly due to the lack of an appropriate work setup (e.g. stable internet connection, ergonomic computer equipment, desk and chair, efficient computing power, separate room to work), the movement restrictions due to severe lockdown sometimes in small apartments (e.g. physical and cultural activities, holidays, family and friends interactions, social events with colleagues), the reduced access to medical care (e.g. virtual consultations with physicians, canceled surgery), and to the overall uncertainty, stress and anxiety due to the global situation and affected family members and friends. Figure 1 presents the feedback of the respondents on the impact of the sanitary crisis on their physical and mental health. In terms of physical health, 60% of the respondents declare a slight to very negative impact, 24.4% declare no impact, and 15.5% declare a positive

*www.santepubliquefrance.fr

impact. In terms of mental health, 65.6% of them declare a slight to very negative impact (skewed to very negative), 17.4% declare no impact, and 17.1% felt a slight to very positive impact. This shows that the sanitary crisis seem to present a more negative impact on mental health. Expatriates are the most concerning category, with more than 70% of slight to very negative impact (18.5% very negative, 25.9% negative, 25.9% slightly negative). Parents are less but still very affected (49.8% of negative impact, mostly slightly negative), probably partly due to a lower social isolation and a correlation with the fact that most parents occupy permanent positions that decreases their stress due to an uncertain future or prompt moving, even if other sources of stress (home-schooling, children future...) remain. Indeed, in terms of job position, the most vulnerable categories correspond to the post-doctoral researchers (72.5% of slight to very negative impact, including 25.5% of very negative impact) and the PhD candidates (89.3% of slight to very negative impact, including 17.9% of very negative impact), in addition with the master thesis students (all 3 students declare slight from very negative impact on their mental health). Eventually, no clear trend could be identified in terms of the gender of the participants. It should be noted here that some of the mentioned categories are correlated, which makes the identification of stress causes complex. For instance, 76% of expatriates are non permanent staff and only 14% of parents are expatriates.

Finally, we measure the feeling of isolation among participants: overall, 45.7% answered they felt isolated during the lockdown and 51.9% answered they did not. The most concerned categories are, once again, expatriates (63.0% felt isolated), PhD candidates (75.0%), and postdoctoral researchers (64.7%).

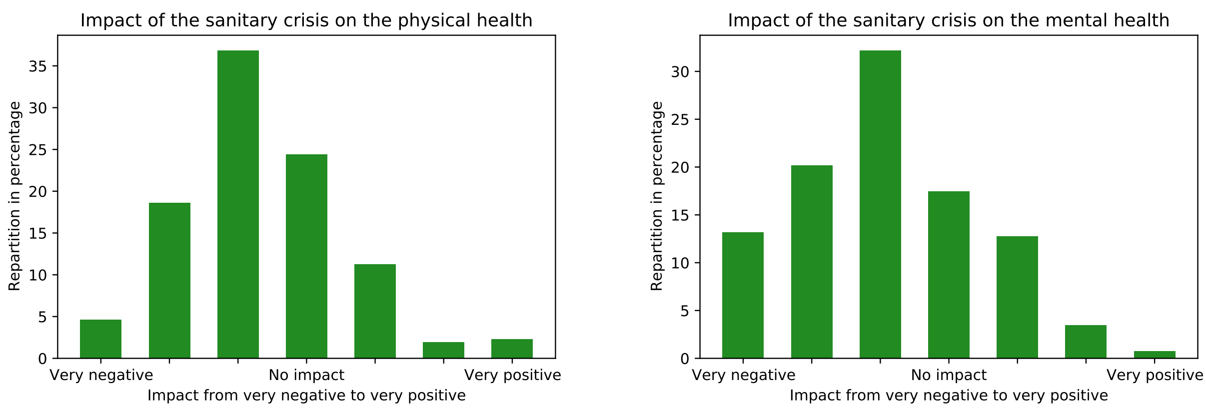

Fig. 1. Qualitative impact of the sanitary crisis on the physical and mental health. **Left:** Histogram of participant answers to the impact of the sanitary crisis on their physical health. **Right:** Histogram of participant answers to the impact of the sanitary crisis on their mental health.

3.2 Work environment

Due to lockdown and isolation, teams and collaborators could not meet and all social and professional interactions shifted to online meetings and email discussions. This evolution impacted the relationships between colleagues and collaborators. Fig. 2 (left) illustrates this effect: 82.8% of participants felt their professional relationships evolved negatively, 11.8% felt no evolution, 5.3% felt they improved. Informal discussions on professional or various topics were almost reduced to zero (no more common lunch time or coffee breaks), although these convivial conversations are essential to exchange even casual information within a group, or discuss and generate new ideas, even if some of these discussions shifted online.

In particular, a sane student-supervisor relationship is crucial to maintain since it corresponds to a strong hierarchy between individuals from the most and the least vulnerable groups. The survey indicates that this relationship follows the trend of the general professional relationships, with a better perception from the student perspective (60.4% felt a negative impact, 32.1% no impact, 7.55% a positive impact) than from the supervisor one (81.8% felt a negative impact, 13.5% no impact, 4.71% a positive impact).

The survey also collected the feeling of the participants towards the evolution of the workload with the sanitary crisis. As illustrated on Fig. 2 (right), 6.7% of participants felt their workload decreased with the pandemic, 36.5% felt no impact, and 57.3% felt an increase of their workload.

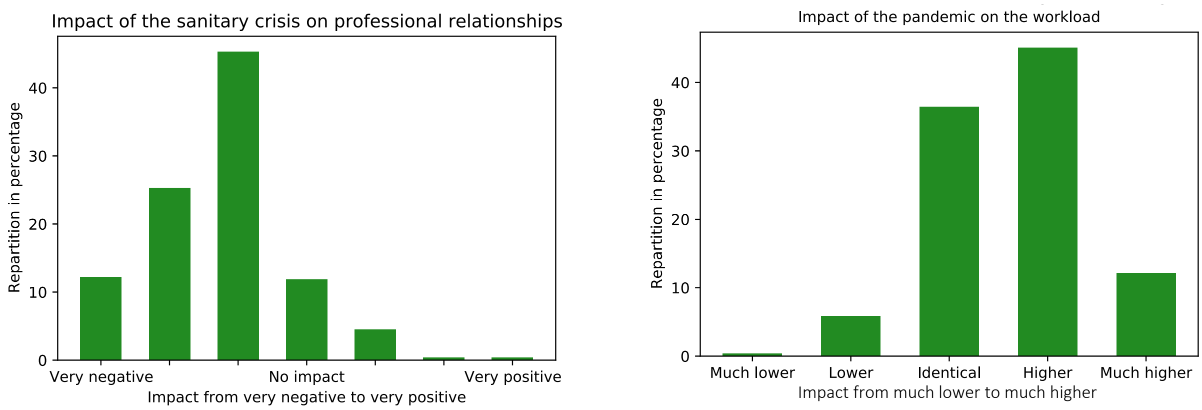

Fig. 2. Qualitative impact of the sanitary crisis in the work environment. **Left:** Histogram of participant answers to the impact of the sanitary crisis on their relations to colleagues. **Right:** Histogram of participant answers to the impact of the sanitary crisis on their workload.

3.3 *Scientific production*

While we acknowledge that the number of publications does not reflect the scientific quality and productivity of a researcher, this metric has been used in other fields as an indicator to assess the impact of the pandemic on research and and is also often taken into account for career development when it comes to hiring, promotions or grants. In particular, various articles have measured the differential publication rate between men and women during the sanitary crisis, pointing out a gender-based inequity in facing work-life balance challenges, with more resources for men and more mental, home, and family load for women. In particular, it has been shown that with the lockdown, publications by men have increased while publications by women have decreased (Kreeger et al. 2020; King & Frederickson 2021; Squazzoni et al. 2020; Lerchenmüller et al. 2021; Mahmoudi 2021; Nguyen et al. 2021; Staniscuaski et al. 2021).

Similarly, the survey participants provided their number of first author publications in 2019 and 2020. We put a threshold at 10 and computed the average number of publications per year, visible in Fig. 3 (purple columns, identical in the three plots). The average number of publications decreased by 1.36% between 2019 and 2020, which is negligible. However, this evolution depends on the participant category: if we consider the participant gender, men publication rate increased by 4.89% while women publication rate decreased by 8.79%, and we can also notice that in 2019 women already tended to publish less than men (see Fig. 3 top left). Expatriates tend to publish more than non-expatriates and their publication rate increased by 7.36% while it decreased by 4.42% for non-expatriates (see Fig. 3 top right). Similarly, parents tend to publish slightly more than non-parents, but their publication rate decreased by 11.4% between 2019 and 2020 while it increased by 9.85% for non-parents (see Fig. 3 bottom). In terms of status, PhD, postdoctorate, and emeritus researchers saw their publication rates increase (78.6%, 37.2%, and 13.3%), permanent researchers and professors saw it decrease (10.6%), and engineers did not change their publication rate. This can once again be related to the fact that permanent researchers tend to have children at home, while young career researchers do not, most of them even living alone.

In addition to the number of publications, the number of grant and job applications can be insightful: they impact the scientific productivity and so the long-term career, and are an indicator of the job stability. Therefore, the impact of the pandemic should be measured and taken into consideration to adapt the system to the situation (Oleschuk 2020).

In the survey, we measured the evolution of the average number of grant proposals (NP, ANR, ERC, etc.), of job applications (postdocs, fellowships, tenure tracks, permanent positions, etc.), and of proposals for observing time and supercomputing time. Fig. 4 shows that grant proposals increased by 3.62%, job applications by 10.8%, and observation and heavy simulation time proposals decrease by 10.8%. The increase of job applications shows a lack of confidence in the future and a high instability of the job market, while the decrease of observation and simulation times is probably due to the shutdown of several telescopes during the lockdown. Once again, these evolutions depend on the participant category and particularly affected women (+19.7% of job applications and −22.1% of observation and simulation tool proposals, vs +6.41% and −4.93% for men).

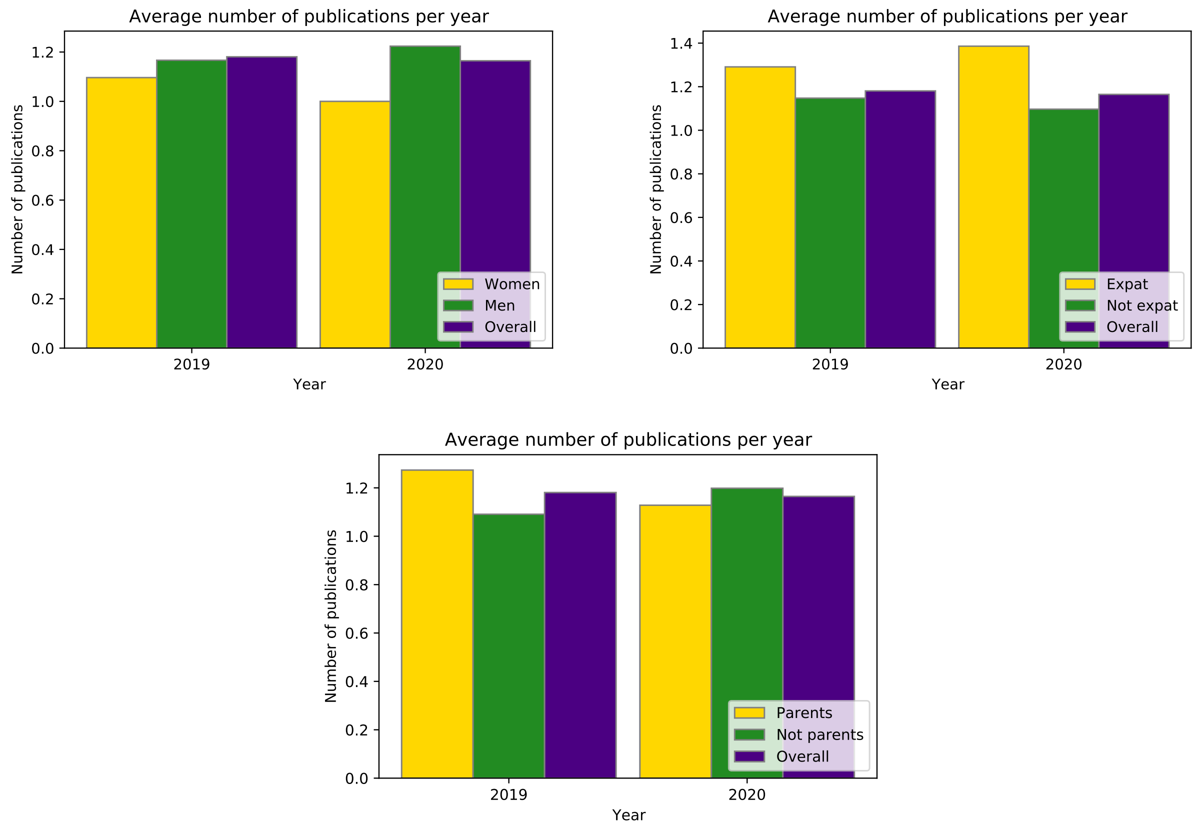

Fig. 3. Number of first author publication in 2019 and 2020 for different categories. **Top left:** Average number of publications in 2019 and 2020 for women (yellow), men (green), and overall (purple). **Top right:** Average number of publications in 2019 and 2020 for expatriates (yellow), non-expatriates (green), and overall (purple). **Bottom:** Average number of publications in 2019 and 2020 for parents (yellow), non-parents (green), and overall (purple).

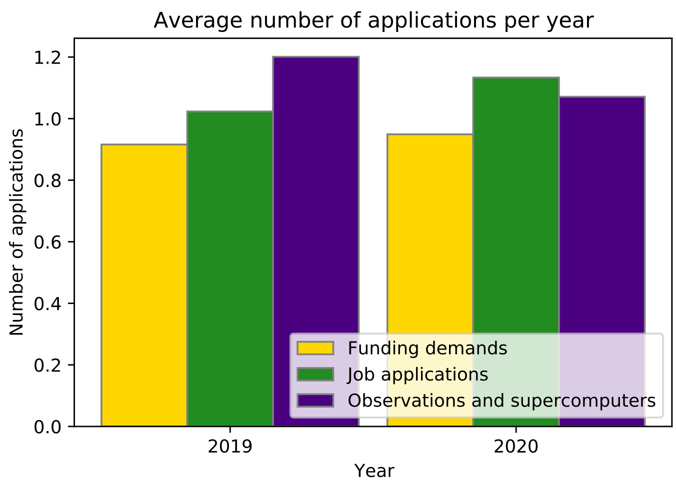

Fig. 4. 2019 and 2020 average numbers of funding demands (yellow), job applications (green), and observation and supercomputer simulation time proposals (purple).

Overall, 65.1% of concerned participants felt the Covid-19 crisis had a slight to very negative impact on their scientific production, 24.2% felt no impact, and 10.7% felt a positive impact on their scientific production.

3.4 Communication

Another effect of the pandemic on the astronomical research community is the cancellation of meetings, seminars, workshops and conferences. They were often replaced by online events based on tools that were sometimes used beforehand (Zoom, BigBlueButton, Gathertown...), in an effort to keep teams unified despite the pandemic and the distance. These many changes made it difficult to track the number of events, but survey participants were given the opportunity to share their feelings about the number of events online, plotted on Fig. 5 (left): 6.72% of them think there were too few events, 36.0% think there were enough events, and 57.3% think there were too many events.

This feeling of being overwhelmed by the number of online events echoes what has been called "zoom fatigue", i. e. the difficulty to focus for a long time during online events. Fig. 5 (right) indicates how this zoom fatigue has been experienced by the community: 68.9% reported an issue with concentration, 20.2% were not impacted by the switch to online events, and 10.85% prefer this new form of communication.

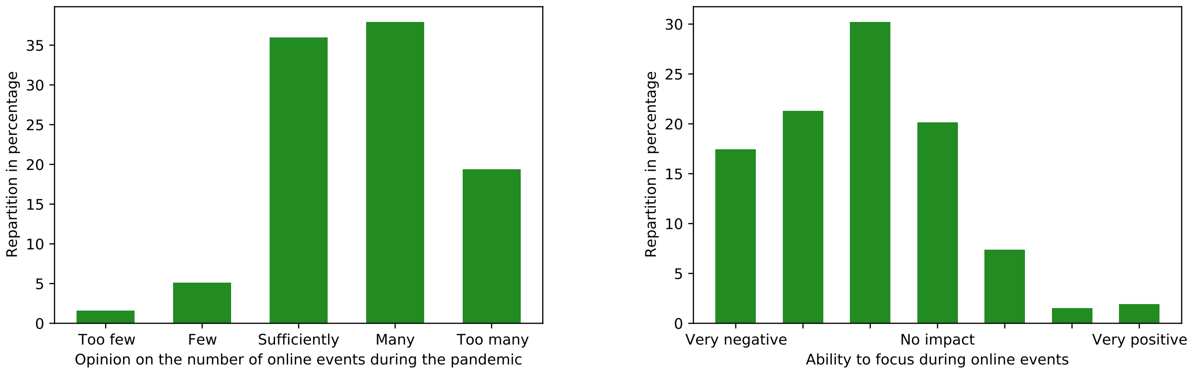

Fig. 5. Qualitative feeling about online events during the sanitary crisis. **Left:** Histogram of participant answers to the number of online events during the pandemic. **Right:** Histogram of participant answers to their ability to focus during online events (or zoom fatigue).

4 Recommendations of actions to be taken

To most people, the pandemic is experienced as a trauma and should be considered as so by institutions and individuals. This trauma is personal but also professional since it will have a long-term impact on careers, in particular for the following categories of people: non permanent researchers (PhD candidates and postdoctoral researchers), women, expatriates, and parents. These categories already suffer from discriminations in the field of astronomy that increased with the pandemic. Efforts to create a benevolent, diverse, and inclusive community should increase to compensate for the effects of the sanitary crisis.

These efforts need to be undertaken at different scales and in this section we provide some examples of actions that would support individuals, especially the most vulnerable ones, during and after the pandemic. We acknowledge the implication of the survey participants who proposed some of the recommendations below. Some actions have also been formulated in other articles for other fields of research (Gewin 2020; Kreeger et al. 2020; Oleschuk 2020; Fulweiler et al. 2021; Staniscuaski et al. 2021; Woolston 2021), and some have already been put in place, showing a high implication and support from laboratories during the crisis.

- **Individual well-being:** This pandemic had a high impact on mental health and well-being, particularly for precarious and expatriate people (see Fig. 1). We encourage to not assume or negatively judge one other experience and reaction to the crisis since they can be impacted by numerous factors. A psychological support would help some individuals, in particular PhD candidates who are highly vulnerable and can hardly afford one by themselves.

- **Student-supervisor relationship:** The frequency of interactions, preferably on-site instead of online, could be temporarily increased to maintain or rebuild a stable relationship. Clarifying without increasing expectations would also enable to minimize stress for all. In addition, educational activities can be organized, dedicated to both students and supervisors: to students concerning workload, rights, or mental health, and to supervisors to raise awareness towards mental health, vulnerability, or difficulties faced by under-represented groups.

- **Team building:** Maintaining a social link within a team is particularly crucial for vulnerable individuals or to welcome new team members. It can be done with dedicated communication channels (for instance Slack) and/or a virtual chat room open at any time for frequent informal exchanges or coffee breaks.

- **Administrations:** The instability of the situation and the variations of governmental constraints can be complex to apprehend, mainly for non-french speakers. Individuals could be helped by a clarification of rules by lab administrations or team managers. Support from administrations and institutions would also help precarious individuals to stay at home despite an opposite wish from the supervisor, or to reallocate fundings, duties and services.

- **Hardware and software work conditions:** All individuals do not have proper or equivalent work conditions at home. Young-career researchers tend to live in a one to two room apartment, without an optimal work material such as a wired connection, a large screen and a comfortable chair and desk. Help from the institute to check the access to research resources, provide proper tools, and optimize home-office conditions is greatly appreciated. In addition, an access to particular software tools dedicated to work, teaching, or social interactions would help home-working people.

- **Home-office:** If people were not used to home-office before the pandemic (63.6% of survey participants were never home working, see Fig. 6), they are willing to modify this habit: only 14.3% of people wish to remain fully on site, and the majority prefers to work from home between one and three days a week.

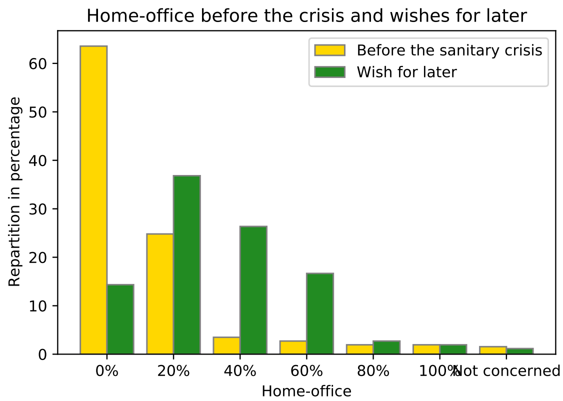

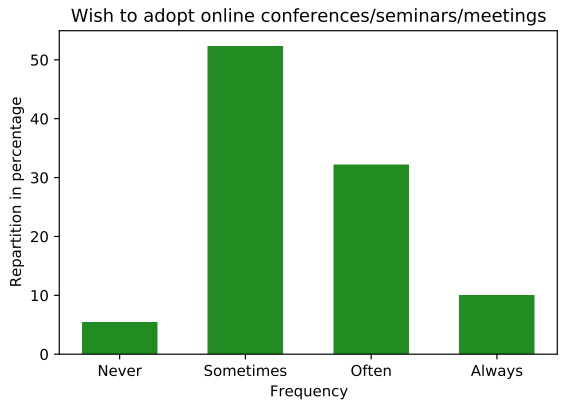

Fig. 6. Change of habits regarding teleworking and online events. **Left:** Histogram of participant answers to their fraction of home-office before the crisis (yellow), and their whishes for later (green). **Right:** Histogram of participant answers regarding their wish for the frequency of online events after the crisis.

- **Workload:** People generally felt their workload increased during the pandemic (see Fig. 2), with longer and more frequent meetings, longer preparations for teaching duties, and a different work-life balance (domestic labor, children home-schooling, eldercare, etc.). Individual workloads within small teams or projects could be maintained below a certain threshold and adapted to each one's living conditions. For instance, there could be an identification of supports to partially reallocate teaching duties and services from people with caregiving demands or junior researchers to colleagues with more flexibility.

- **Privacy respect:** In addition with the previous point, the workload and meetings should not exceed conventional work hours. This would limit work-life mixing and minimize negative effects on mental health, but it would also enable parents to participate to conferences and meetings without having to leave and miss events or information. It is also crucial to take into account the fact that people can be attached to different time zones when organizing online events, which could lead to shortening events.

- **Online events:** Even if survey participants felt generally overwhelmed by the number of online events and by the zoom fatigue (see Fig. 5), they are in huge majority willing to maintain some online events after the sanitary crisis (5.43% of participants refuse online events, 52.3% wish to adopt them sometimes, 32.2% often, 10.1% always, see Fig. 6). The selection could be done on the duration of the event (one-day or shorter events gathering people from different regions or countries can be done online), on the audience (the implication of new members among a network is easier if face-to-face), or hybrid options can even be considered: alternating online and on site events or proposing an online option to all face-to-face events. To fight zoom fatigue and the increased number of events, it is also important to select most necessary events and to focus on the planned topic and program.

- **Online event tools:** In addition to Zoom, different online event platforms have been made possible, with various security options, and should be advertised: BigBlueButton, MS Teams, Jitsi, Element/Matrix, or Renavisio. CarbonFreeConf[†](Kral 2021) also consists in a unique platform gathering multiple tools for a complete online conference with a Carbon compensation.

- **Meetings:** In addition to what has been proposed above, for online meetings (except for very large events) the camera could be turned on to facilitate interactions and face recognition. Seeing faces also help people with some disabilities. For privacy purposes, some online meeting tools even enable to blur backgrounds.

- **Conferences and seminars:** The pandemic has proven the possibility to organize online workshops and conferences at very different scales. As a side effect, these events have very lower Carbon footprint and financial cost than on site events, which can encourage young-career scientists or individuals with no financial support to attend them. It can also motivate people with disabilities and parents that avoid having to find an accommodation for their children. Therefore, we encourage online options to be developed even for on site conferences, possibly divided in half days instead of full days to avoid zoom fatigue and to remain open to several time zones. However, informal moments (coffee breaks, session gaps, evenings, etc.) could be maintained and adapted. Platforms like Gathertown can also be taken advantage of to maintain these social interactions despite the distance. A few on-site conferences, more rare, could also be kept when considered as not fully replaceable by online events.

- **Parenthood:** Due to school closures, parents have been highly impacted by the pandemic. It is important to acknowledge their situation and work conditions by increasing duty and deadline flexibility, removing the caregiving stigma, removing or reallocating some services, in particular when non essential (editing, reviewing, some teaching or night observations...) between colleagues, and remaining benevolent when confronted to colleague parenthood-due situations (children in meetings or conferences, task delay, etc.). Including parenthood status in activity reports and applications would also enable to reduce the discrimination they tend to face, mainly for women and young-career scientists.

- **Teaching:** During the lockdowns, online teaching has been negatively experienced by both students and professors and would better be avoided as much as possible. In addition, as mentioned above, during a lockdown, a reduction or redistribution of the teaching duty could be helpful for staff members encountering difficulties managing their duties, for instance when they have children at home.

- **Publications:** With the impact of the crisis on publication rates, in particular for vulnerable groups, journal editors have a crucial role in counterbalancing the long-term effect of the pandemic. Solutions could be to reduce fees for young-career scientists and women, to invite women, parents, and early-career researchers to write review articles, and to prioritize submissions from vulnerable groups, while extending deadlines for reviews and revisions.

- **Job market:** 2020 and 2021 have been a very unstable period for career opportunities and fundings, mainly for women (see Fig. 4). As already implemented in some institutions, a first solution consists in to systematically extend short-term contracts (PhD candidates, postdoctorate researchers, etc.) to provide a stable environment during the crisis, for instance since moving opportunities have become complicated with the border closure.

[†]https://www.carbonfreeconf.com

- **Proposals and applications:** To compensate for the effect of the pandemic on under-represented and vulnerable groups, offer vocabulary could be modified to be more inclusive to parents, women, non-binary people, and young-career scientists. In addition, these groups could be encouraged and supported by their institutions with possible mentoring to apply for positions, promotions, fellowships, grants, and prizes. Eventually, extending pr postponing deadlines (for non-essential scholarships) by a few months to a year would let people the most affected by the crisis apply safely. Eventually, some grants could specifically target under-represented groups like women, expatriates, young-career scientists, or parents.

- **Evaluation committees:** Funding organizations and evaluation committees could also consider or continue considering disparities between individuals during the crisis and more generally in the field. This requires shifting institutional norms and updating evaluation criteria to include under-represented groups, for instance by acknowledging other activities (teaching, outreach, implication in social activities, parenthood, etc.), mainly when judging 2020 and 2021 scientific performance (see the COVID-19 CV Matrix in Arora et al. (2020)). The jury can also set quotas for fundings, prizes, hirings, and leadership positions. Eventually, boards themself should be as diverse as possible, with at least 30% of women.

- **Learn from the pandemic:** measuring the impact of the pandemic and its side effects on the astronomical research community, in particular on underrepresented groups, is crucial to understand its trauma and improve its recovery, the well-being of its members, and the robustness of the community to possible future crises. This requires feedbacks from individuals to their laboratories and institutions, surveys, data collections and analyses like this one at different scales, and output spreading.

- **Sharing experiences:** A last recommendation we wish to formulate is the importance of sharing our experiences of the pandemic. The COVID-19 experience has been unprecedented so far and has a huge impact on isolated people. Many people have doubted themselves, questioned their own reactions to the situation. However, the problem has never been individual but global. It is time to share our experiences and see that each of us has never been alone. Several ways of communication could be used, such as a safe zone professional groups in institutions, Slack with a dedicated channel for vulnerable groups, or dedicated sessions in conferences.

5 Conclusions

In this paper, we have presented some of the effects of the pandemic on the french astronomical research community, collected with a survey conducted among the SF2A society. Concerning health, the most dramatic result concerns mental health and isolation, with 65.6% of participants negatively impacted by the pandemic, meanly PhD candidates and postdoctorate researchers. The lockdown also negatively affected professional relationships (82.8% of participants felt a negative evolution) and increased the workload of participants (57.3% felt an increase of the workload), particularly problematic during this year of mental isolation and uncertainty, combined with an increase of the family care for parents. The scientific production have also been impacted by these disturbed work conditions, number of publications evolving differently with the gender, the parenthood and the expatriation. The job market also appears highly unstable (+10.8% of job applications between 2019 and 2020), particularly for women (+19.7%), as did the demands of access to observations and supercomputer resources (−10.8% overall, −22.1% for women). Eventually, with the switch to online events (meetings, seminars, workshops, conferences), several side effects appear : the zoom fatigue (experienced by 68.9% of participants), ie. the difficulty to focus in front of a screen, and the feeling of too many events, some of them having been pointed out as useless or unefficient.

All categories have not been impacted equally by these different effects, and under-represented or vulnerable groups are particularly victims of the pandemic: women, expatriates, parents, and precarious individuals (PhD candidates and postdoctorate researchers). A special attention should be brought to their work conditions when looking for solutions to compensate for the effect of the crisis on research and careers and to go on improving the community environment. This is taken into account in the actions we propose in this paper, which focus on the overall wishes of the community (partial switch to online events, home-working...), on the well-being of all community members (team building, formations, work conditions...), and on equity in terms of scientific production and access to positions, grants, and tools. We acknowledge that several of the actions we mentioned have already been put in place thanks to high support and flexibility of many institutions or organizations.

Some of the recommendations should have positive side-effects. First, as mentioned earlier, they should create a more diverse and inclusive community, under-represented and vulnerable groups having been particularly impacted by the pandemic. For example, switching some events online should increase the access to conferences for more people, like young-career researchers with less financial resources, parents who do not need to find childcare accommodations, people with physical or other disabilities, etc. Modifying success criteria, defined for an outdated traditional research workforce (white people, men, non-disabled people...) and prioritizing under-represented groups for applications and publications can only make the community overall more diversed and inclusive. Another side-effect of these recommendations is their impact on the environment, in a period where the climate crisis imposes a fast and efficient ecological transition for all activities, including research (Cantalloube et al. 2020; Ligozat et al. 2020; Stevens et al. 2020; Zwart 2020; Mariette et al. 2021; Glausiusz 2021). The academic activity has a particularly high carbon footprint due to air travels (conferences, meetings, on-site observations) and the community wish to partially switch to online events will reduce its carbon footprint.

Some limitations of our study can be pointed out. In particular, more factors than gender, parenthood, expatriation, and precarity impact the COVID-19 experience, like race and ethnicity, and mental and physical disabilities (Crook 2020; Oleschuk 2020; Fulweiler et al. 2021; King & Frederickson 2021; Staniscuaski et al. 2021). Some intersecting factors should also be considered: on other studies (fields and/or countries), mothers and black women are by far more impacted by the pandemic than fathers and other gender and race categories. In addition, to measure the effect of the crisis on the scientific production, Inno et al. (2021) mentions considering only publications from March to May, where the lockdown was the hardest and the knowledge on the virus was the most uncertain. Given these remarks, the study we present here could and should be improved in the future, even if we recommend to later focus on developing solutions, compensations, improvements, and adaptations, at all the community scales (individuals, teams, laboratories, collaborations, national organizations, journal editions, etc.).

A Survey: Impact of environmental/social factors on scientific production during the covid-19 pandemic

We propose this survey, intended for the French community of researchers in Astronomy and Astrophysics, in order to better grasp the impact of the sanitary crisis on the scientific production (number of publications, grants application etc.) and well-being (work-life balance, relationship with colleagues etc.) during the covid crisis. The aim of this survey is to better prepare the post-covid scientific activities under the constraints given by the pandemic situation.

- **Demographic information:**
  1) Gender

     (Woman/Man/Non binary person/Other/Prefer not to disclose)
  2) Are you an expatriate?

     (Yes/No/Prefer not to disclose)
  3) Age range

     (Less than 20/21-25/26-30/31-35/36-40/41-45/46-50/51-55/56-60/61-65/More than 66)
  4) Current position

     (Master thesis student/PhD candidate/Postdoctorate researcher/Permanent researcher or professor/ Emeritus/Engineer and ITA/Other staff)
  5) Year of doctoral graduation

     (All options until 2021/Not concerned/Prefer not to disclose)
  6) Number of dependent children

     (0/1/2/3/4/More than 5)
- **Parenthood:**
  7) How many days of parental leave did you take in 2019 ? (excluding parental leave after birth)

     (0/1-5/6-10/11-15/16-20/More than 20/Not concerned)
  8) How many days of parental leave did you take in 2020 ? (excluding parental leave after birth)

     (0/1-5/6-10/11-15/16-20/More than 20/Not concerned)

9) Did you receive assistance and support with childcare during lockdowns/school closures? (partner, parent etc.)

(Yes 100%/Yes 75%/Yes 50%/Yes 25%/No/Not concerned)

- **Health (physical and mental):**

10) Have you contracted the coronavirus?

(Yes with symptoms/Yes without symptoms/Do not know/No)

11) What is the impact of the covid crisis and of home-office on your physical health (more physical activities, more or less back pain, joint pain, circulation problems, more or less migraines / headaches, vision problems etc.)?

(Very negative/Negative/Somewhat negative/No impact/Somewhat positive/Positive/Very positive)

12) What is the impact of the covid crisis on your mental health (more sleeping time, more personal time, less stress, insomnia, anxiety, burn-out, depression/breakdown)?

(Very negative/Negative/Somewhat negative/No impact/Somewhat positive/Positive/Very positive)

13) Did you feel isolated during the confinement?

(Yes/No/Prefer not to say/Not concerned)

- **Day to day working activities:**

14) Did the lockdown prevent you from performing critical tasks for your research (access to optical benches, experiments, observations)?

(Not at all/A little/A lot/Very much/Completely/Not concerned)

15) How do you feel about the workload during the health crisis compared to before?

(Much higher/Higher/Identical/Lower/Much lower/Not concerned)

- **Scientific publications:**

16) Number of publications in 2019 (peer-reviewed and SPIE proceeding, as a 1st author)

(0/1/2/3/4/5/6/7/8/9/More than 10/Not concerned)

17) Number of publications in 2020 (peer-reviewed and SPIE proceeding, as a 1st author)

(0/1/2/3/4/5/6/7/8/9/More than 10/Not concerned)

18) How do you feel about the impact of the health crisis on your scientific production?

(Very negative/Negative/Rather negative/No impact/Rather positive/Positive/Very positive/Not concerned)

- **Applications:**

19) How many grant proposals have you submitted (NP, ANR, ERC, etc.) in 2019?

(0/1/2/3/4/5/6/7/8/9/More than 10/Not concerned)

20) How many grant proposals have you submitted (NP, ANR, ERC, etc.) in 2020?

(0/1/2/3/4/5/6/7/8/9/More than 10/Not concerned)

21) How many job applications have you submitted in 2019 (post-doc, fellowship, tenure track, permanent position...)?

(0/1/2/3/4/5/6/7/8/9/More than 10/Not concerned)

22) How many job applications have you submitted in 2020 (post-doc, fellowship, tenure track, permanent position...)?

(0/1/2/3/4/5/6/7/8/9/More than 10/Not concerned)

23) How many proposals for observation time, simulation time on supercomputers, or any other tools needed for your work have you submitted in 2019?

(0/1/2/3/4/5/6/7/8/9/More than 10/Not concerned)

24) How many proposals for observation time, simulation time on supercomputers, or any other tools needed for your work have you submitted in 2020?

(0/1/2/3/4/5/6/7/8/9/More than 10/Not concerned)

- **Conferences (face-to-face or virtual):**

25) Number of participations in international conferences and workshops in 2019 (face-to-face or virtual)?

(0/1/2/3/4/5/6/7/8/9/More than 10/Not concerned)

26) Number of participations in international conferences and workshops in 2020 (face-to-face or virtual)?

(0/1/2/3/4/5/6/7/8/9/More than 10/Not concerned)

27) Number of talks given in international conferences and workshops in 2020 (face-to-face or virtual)?

(0/1/2/3/4/5/6/7/8/9/More than 10/Not concerned)

28) Number of invitations to give a seminar in 2019 (face-to-face vs. virtual)?

(0/1/2/3/4/5/6/7/8/9/More than 10/Not concerned)

29) Number of invitations to give a seminar in 2020 (face-to-face vs. virtual)?

(0/1/2/3/4/5/6/7/8/9/More than 10/Not concerned)

30) How do you feel about your ability to focus during online events (conferences, workshops, seminars) throughout the health crisis?

(Very negative/Negative/Rather negative/No impact/Rather positive/Positive/Very positive/Not concerned)

31) How do you feel about the numbers of online events throughout the health crisis?

(Too few/Few/Sufficiently/Many/Too many/Not concerned)

- **Professional relationships:**

32) For students: How do you feel about the impact of the covid crisis on your relationships with your supervisor(s)?

(Very negative/Negative/Somewhat negative/No impact/Somewhat positive/Positive/Very positive/ Not concerned)

33) For supervisors: How do you feel about the impact of the covid crisis on your relationships with your student(s)?

(Very negative/Negative/Somewhat negative/No impact/Somewhat positive/Positive/Very positive/ Not concerned)

34) How do you feel about the impact of the covid crisis on your relationships with your colleagues/work team?

(Very negative/Negative/Somewhat negative/No impact/Somewhat positive/Positive/Very positive/ Not concerned)

- **Post-covid:**

35) Were you doing home-office before the covid crisis?

(100% home-office/80% home-office/60% home-office/40% home-office/20% home-office/0% home-office/Not concerned)

36) How would you envision your working habits to evolve after the covid crises in terms of home-office vs. presence at the institute?

(100% home-office/80% home-office/60% home-office/40% home-office/20% home-office/0% home-office/Not concerned)

37) Would you like to adopt online conferences/seminars/meetings more often?

(Always/Often/Sometimes/Never/No opinion/Not concerned)

38) Any remarks or suggestions to improve the situation (conferences, meetings, observations, supervision, teaching, administration...)?

This work benefited from the help of Olivier Berné (Institut de Recherche en Astrophysique et Planétologie, Université de Toulouse, CNRS, CNES, UPS, Toulouse, France) whom we thank for his help and advices. It also received full support from the SF2A committee that the authors sincerely thank for its help and implication during the preparation and the spread of the survey.

References

Arora, V. M., Wray, C. M., O'Glasser, A. Y., Shapiro, M., & Jain, S. 2020, Proceedings of the National Academy of Sciences, 117, 24032

Berné, O. & Hilaire, A. 2020, Nature Astronomy, 4, 296

Beverly, E. 2021, Journal of osteopathic medicine, 121

Bot, C. & Buat, V. 2020, in SF2A proceedings

Cantalloube, F., Milli, J., Böhm, C., et al. 2020, Nature Astronomy, 4, 826

Cheng, S. 2020, Job Market Paper

Crook, S. 2020, Women's History Review, 29, 1226

Fulweiler, R., Davies, S., Biddle, J., et al. 2021, PLoS Biol, 19(3): e3001100

Gewin, V. 2020, Nature, 583, 867

Glausiusz, J. 2021, Nature, 589, 155

Inno, L., Rotundi, A., & Piccialli, A. 2021, in EGU General Assembly Conference Abstracts, EGU General Assembly Conference Abstracts, EGU21–3231

King, M. M. & Frederickson, M. E. 2021, Socius, 7, 23780231211006977

Kral, Q. 2021, SF2A proceedings

Kreeger, P., Brock, A., Gibbs, H., et al. 2020, PLoS computational biology, 16, e1008370

Leboulleux, L., Choquet, É., Huby, E., Singh, G., & Cantalloube, F. 2020, in Bulletin of the American Astronomical Society, Vol. 52, 0209

Lerchenmüller, C., Schmallenbach, L., Jena, A. B., & Lerchenmueller, M. J. 2021, BMJ Open, 11

Ligozat, A.-L., Névéol, A., Daly, B., & Frenoux, E. 2020, PLoS Computational Biology, 16, e1008148

Mahmoudi, M. 2021, Future Science OA, 7, FSO651, pMID: 33432271

Mariette, J., Blanchard, O., Berné, O., & Ben Ari, T. 2021, arXiv e-prints, arXiv:2101.10124

Nguyen, A., Trinh, X., Kurian, J., & Wu, A. 2021, Graefe's Archive for Clinical and Experimental Ophthalmology, 259

Oleschuk, M. 2020, Canadian Review of Sociology/Revue canadienne de sociologie, 57

Pommier, M. 2021, in SF2A proceedings

Squazzoni, F., Bravo, G., Grimaldo, F., et al. 2020, SSRN Electronic Journal

Staniscuaski, F., Kmetzsch, L., Soletti, R. C., et al. 2021, Frontiers in Psychology, 12, 1640

Stevens, A. R. H., Bellstedt, S., Elahi, P. J., & Murphy, M. T. 2020, The imperative to reduce carbon emissions in astronomy

Suarez, O. 2021, in SF2A proceedings

Viglione, G. 2020, Nature, 581, 365

Webb, N. 2021, SF2A proceedings

Woolston, C. 2020a, Nature, 585, 309

Woolston, C. 2020b, Nature, 583, 645

Woolston, C. 2021, Nature, 593, 613

Zwart, P. 2020, Nature, 819–822

SF2A 2021
A. Siebert, K. Baillié, E. Lagadec, N. Lagarde, J. Malzac, J.-B. Marquette, M. N'Diaye, J. Richard, O. Venot (eds)

WOMEN'S HISTORY IN ASTRONOMY OR FEMININE HISTORY OF ASTRONOMY: MUCH UNKNOWN CONTRIBUTIONS

I. Vauglin[1]

Abstract. Historically, women have had very little place in science and it is sad to see that nowadays things have not improved much. Recent studies confirm that stereotypes die hard: according to an international study in 2015 by the L'Oréal Foundation and Opinion Way (with 6035 respondents), 67% of Europeans begin their answer to the question "How would you describe a scientist?", first by: "He is a man". And this frightening proportion: for 89% of them, women would be good at everything except science!... The prejudices are really tenacious because, there are always been women scientists for a very long time but society has not kept the memory of them and their work had often been attributed to men. We would like to remind or put the light on some of these women astronomer who worked in astronomy since ancient times.

A way to give back to Cleopatra what belongs to Cleopatra!

Keywords: women in science, astronomy, gender equality

1 Introduction

Astronomy is one of the oldest science and it's quite easy to find a long list of famous astronomers, male astronomers. But it's really rare to find such lists including famous female astronomers. Yet, over the centuries, they have been numerous. Who remembers or has ever heard the name of Aglaonice of Thessaly, Sophie Brahé, Nicole-Reine Lepaute or Annie Cannon? There are many many other women but society has simply forgotten them, ignored them although their contributions are outstanding. It's time to give them the place and notoriety they should always have had. Even today, women in science do not benefit in many aspects from the same conditions as their male colleagues. The Femmes et Astro commission of SFA2 works to promote gender equality into the french astronomers community and decided to organise a session dedicated to gender inequalities in astronomy. In this perspective, it's important first of all to rise awareness that the problem is a long-standing issue and is still present nowadays. We would like to improve the visibility of women astronomers whose work has marked the history of astronomy. Of course, we are far to be exhaustive and we present here only very few of these women astronomers who significantly contributed to the progress of astronomy over the centuries.
This presentation has been made on behalf of the SF2A 'Femmes et Astro' commission.

2 Some historical women figures in astronomy

We must keep in mind that women had to overcome a lot of obstacles if they wanted to study and do science. At a time when only boys could study, the access to education was reserved for a very small number of privileged women, who were educated thanks to the open-mindedness and the goodwill of a father, a husband or a brother. Even then, special conditions were needed to keep track of their work. There is therefore in this (very incomplete) list an important bias on the major contributions of a lucky few women, often with exceptional intelligence, whereas there probably existed a much larger number of anonymous "little hands".

If we try to find their marks, we realise that the list of women scientists is long. With the overview, very far from being exhaustive, limited to the field of astronomy, we realize that women have widely participated to the progress of knowledge.

[1] Univ Lyon, Univ Lyon1, ENS-Lyon, CNRS, Centre de Recherche Astrophysique de Lyon UMR5574, F-69230, Saint-Genis-Laval, France

2.1 Antiquity and the Middle-Ages

Living in the 23rd century BC in the Sumerian city of Ur, **Enheduanna** was *High Priestess of the Moon Goddess of the city.* From her temple, she performed astronomical observations of the moon?s phases and planets positions, one of the activities falling in her duty. Daughter of the King Sargon I of Akkad, she is probably the oldest author whose name and a significant part of her work had come down to us (37 cuneiform tablets found, mainly poems). So, she is perhaps the oldest female writer known today.

Jumping forward in time, we meet **Aglaonike of Thessaly**, living in the 2nd century BC in the misogynistic greek society. Nonetheless her father allowed her to study Babylonian astronomy and she can be considered as the first women astronomer. According to the testimony of Plutarch, she "knew the cause of complete eclipses of the Moon and predicted the moment when it happens to the Moon to enter the shadow of the Earth". Thus, she had understood the phenomenon of eclipses, knew the Saros cycle but these skills led her to be regarded as a witch because of her apparent control of the phenomena... This has been too often the burden of many female scientists in the past, considered as dangerous by most of the others !

Hypatia of Alexandria (350 or 370 - 415) was a brilliant mathematician and philosopher, one of the most famous of the past. Aware of the intelligence of his daughter, her father Theon of Alexandria educated her in mathematics and philosophy. Highly educated, very intelligent and wise, Hypatia succeeded her father at the head of the Academy where a large number of people came from far away to attend her classes. Convinced of the heliocentric system, pagan, defending the separation between science and religion, she displeased to many religious persons and was savagely murdered by Christian's fanatic led by the bishop Cyril in 415.
Hypatia's death marks the beginning of the decline of science which lasts during the medieval period. Access to science was even more difficult for women; only convents offered them protective and cultural environnement allowing them to study scientific writings and to use their skills, like Hildegard of Bingen could.

2.2 Domestic helpers and calculators of the Renaissance

We have to wait until the 16th century to find a breakthrough (for an improvement), which begins with **Sophia Brahe** (1559-1643, Denmark), unknown sister of the well-known astronomer Tycho Brahe. Self-educated, Sophie Brahe showed such a talent that her brother Tycho eventually considered her as his assistant. She was the first of a long list of domestic helpers. None of these talented and devoted women would ever be paid for their work... Sophia Brahe assisted her older brother with making astronomical measurements. The many results attributed to Tycho Brahe were in fact the result of a joint effort with Sophia. In particular, the precision of their observations of Mars' position allowed Kepler to find the three laws describing the orbits of planets.

At that time, women were still excluded from education and knowledge because an educated woman was still considered as dangerous for men thus impossible to marry. In these conditions, very few women have benefited from an education thanks to the good will of their father, brother or husband, and often also thanks to their widowhood. Among them, we can mention the Polish **Maria Cunitz** and **Catherina Hevelius** and the Prussian **Maria Kirch**. Those three women carried out remarquable works in collaboration with their husband and/or son but also published alone their own work (like *Urania propitia* by Maria Cunitz which had an impact at the European level).

The conditions were really difficult during this period for female scientists because they were always mocked as seen through for instance Molière's plays *"Les femmes savantes"* or *"les précieuses ridicules"*. We will stop on **Jeanne Dumée** (1660-1706, Paris) who took advantage of the "salons" (gathering distinguished guests around noble clever ladies) to expose the Copernican theses that she defended with conviction. Independent and convinced, she went further in her manuscript *Entretiens sur l'opinion de Copernicus touchant à la mobilité de la Terre* by writing: "... since between the brain of a woman and that of a man there is no difference, I wish my book could give them some emulation...". She really was ahead of her time! Just like **Mary Somerville** (1780-1872, Scotland), a very brilliant mathematician, who studied without telling her parents. They married their daughter to prevent her from doing science. Widow of Mr. Greig in 1807, she finally has the possibility to pursue her intellectual interests and could study the Celestial Mechanics of Laplace, that she translated in English. By the way, Laplace told her "Only three women have understood me. It is you, Mrs Somerville, Caroline Herschel and a Mrs Greig of whom I know nothing". Besides that, she defended women's rights (we understand her!) and signed in 1868 a petition calling for women's right to vote !

Totally devoted to her brother's work, **Caroline Herschel** (1750-1848, Silesia) is the sister of the famous William Herschel. Her unknown contribution to her brother's work of is however remarkable because she helped him to build his telescopes, to polish the mirrors, to make long night observations and she discovered alone eight comets, she doubled the number of known nebulae, she made the first attempt to represent the Milky Way. The magnitude of her work is such that she receives in 1828 the gold medal of the Royal Astronomical Society, first woman (and the only one for 170 years!) to receive this distinction.

Some others brilliant mathematician women have been called calculators. This is the case of **Emilie du Chatelet** (1706-1749, France) whose intellectual capabilities allowed her to study mathematics, physics, mechanics, chemistry and astronomy. Outstanding mathematician, she mastered analytic geometry and infinitesimal analysis which allowed her to understand Newton's *Philosophiae Naturalis Principia Mathematica*, of which she made the first translation in 1745 which is still a reference. She is unfortunately more criticised for her way of living and her friendship with Voltaire than known for the importance of her scientific works.

A few years later, **Nicole-Reine Lepaute** (1723-1788, France) was another very gifted mathematician whose contributions were remarkable: she began calculating the tables of oscillations of the pendulum for her husband, a clockmaker. This work led her to meet Lalande and Clairaut, with whom she made the tremendously difficult calculations necessary to accurately predict (to the month!) the return of Halley's comet in 1759, taking into account the influence of Jupiter and Saturn on its trajectoire. But in 1760, Lalande fell out with Clairaut who published without mentioning Lepaute's contribution his *Théorie des comètes*. Reine continued her work with Lalande calculating the ephemerides, among others, for the transit of Venus in 1761, the elements of the comet of 1762 and the annular eclipse of April 1, 1764.

2.3 The 19th century: from Harvard computers to professionals

As observing facilities improved, the data to be processed and calibrated became increasingly numerous. Women were hired to carry out these long, tedious and repetitive tasks that required patience and precision, while being paid very little. A group of women has had an immense contribution to stellar spectroscopy but they are simply called the Harvard computers or Pickering's harem. Indeed, from 1875 onwards, E. Pickering, Harvard Observatory director, hired women to process the phenomenal quantity of stellar spectra recorded by the new telescopes. He even encouraged his colleagues to do the same, writing "women are able of doing as much good routine work as men... and for the same amount of money, three to four times as many female assistants can be employed" (sic!). Paid less than a secretary, these 80 or so women processed more than 390,000 stellar spectra, but were never called astronomers, just computers.
So please, try to remember the names of at least some of them: **Williamina Fleming** the first, initially Pickering's servant, she set up a classification of stars according to the prominence of hydrogen lines based on more than 10,000 spectra; **Antonia Maury** the rebel, an astronomy graduate from Vassar College, who got angry with Pickering because she wanted her name to appear in publications. She created a system of luminosity classes based on the width of the stellar lines, a system adopted by the International Astronomical Union (IAU); **Annie Cannon** who classified 350 000 stars (!), she rearranged the Fleming's classification to adopt a sequence more logical to her: O B A F G K M, the first fondamental attempt of stars' classification based on the strength of the Balmer absorption lines. These seven spectral types are still the basis of any study of stellar physics. Her tremendous work has been of primary importance for the understanding of stellar evolution, but Harvard University, without shame, gives her a position of astronomer at the age of 75 years!
We cannot omit **Cecilia Payne-Gaposchkin** who proves that spectral types are related to the temperature of stars. By a step further, she came to the conclusion that stars are composed mainly of hydrogen. But her idea went against the consensus of the time. Henry Russell dissuaded her from publishing her result which he did not believe. Five years later, Russell published an article in which he said that hydrogen is the major component of stars, just forgetting to mention that this idea was first that of Cecilia ...
The colossal work carried out by Pickering's women included that of **Henrietta Leavitt**, as exceptional as she was discreet. Undisputed expert in stellar photometry, she rigorously studied stars of the Small Magellanic Cloud and founded a new category of variable stars, the Cepheids. Her great discovery was to highlight a relationship between the period and luminosity of these variable stars and to understood what this implied. With her 'Period-luminosity relationship of Cepheids', Henrietta Leavitt has given a way to reach the depth of the universe. In 1908, she published her results in the Annals of the Astronomical Observatory of Harvard College and confirmed in 1912 that Cepheid Variables of greater intrinsic luminosity have longer periods. Using the P-L relationship, Edwin Hubble will obtain the distance of the Andromeda galaxy in 1925. When a colleague want to nominated her for the 1926 Nobel Prize for her discovery, she had been dead for 4 years ...

2.4 The 20th century: finally women researchers with a position

In France, **Edmée Chandon** was the first woman to have a "real" position as astronomer. She obtained a degree in mathematics in 1908, and this position in 1911 at Paris' Observatory. The second woman "astronomer" of France is Calixtina Bac who obtains a position at Lyon Observatory in 1912.
The number of women astronomers has increased steadily since then but we are still far from parity in astronomy: the International Astronomical Union counted only 18% of female astronomers in 2019. I would like to mention three of them whose remarkable careers are also indicative of the difficulties women have still faced just to work in the last century.

Fig. 1. Some exceptional female scientists of the 20th century: Katherine Johnson, Maryam Mirzakhani, Margaret Burbidge, Vera Rubin, Tatiana Proskouriakoff

The English **Margaret Burbidge** (1919-2020) obtained her degree in astronomy in 1939 at the University College London and because of the Second World War, she had to take charge of the UCL. But when men returned after the war, she found herself back in a position of second assistant. Margaret apply in 1946 to observe at Mount Wilson. This was refused because the observatory was forbidden to women... She had to wait until 1955 to have access to Mount Wilson and only as an "assistant" to her husband, even though she was the one making the observations! In 1957, Margaret publishes with her husband, W. Fowler and F. Hoyle an impressive article Burbidge et al. (1957), called B2FH, which demonstrates that all but the lightest elements are synthesised by nuclear reactions within stars. Margaret does not stop at this success and received many awards including the gold medal of the Royal Astronomical Society with her husband in 2005.

The American **Vera Rubin** (1928-2016), another great lady of astronomy, had the unfortunately classic fate of women scientists: she is one of those pioneers whose fame is inversely proportional to the importance of her work. She demonstrated that the galaxies seem to be heading towards an unknown point, which will be called the Great Attractor. Her article is refused. She then showed that the Universe is not homogeneous, galaxies gathering in vast clusters. Her results were ignored for twenty years before being widely confirmed. In 1964, she applied for telescope time at Mount Palomar, but women were still not allowed to make observations there... Tenacious, one year later, Vera created a small revolution by becoming the first woman to obtain the right to make observations at the observatory. With H. Ford, she studied the rotation curve of spiral galaxies and demonstrated an anomaly: far from the center of their galaxy, the stars rotate much faster than they should if gravitational force was due only to luminous matter. Their results gave a proof of the existence of the dark matter predicted by Zwicky. Throughout her life as an astronomer, Vera Rubin had to face difficult conditions because she was a woman. She often denounced *"the way girls are brought up, and it starts very early"*; she worked her life long against the unconscious mechanisms, conveyed by education and society, which lead to the persistence of gender inequalities. She was fond of reminding us that *"half of the world's neurons belong to women"*.

The Irish **Jocelyn Bell** (1943-) built during her thesis, with the help of some PhD students, the 2048 antennas radio telescope which she needed to observe quasars. Two months later, she records a strange signal that returns every 23h56 min. She had just discovered the first pulsar but her thesis director, A. Hewish, laughed at her. Finally convinced, Hewish published an article in Nature but Jocelyn is only 2nd author Hewish et al. (1968)... In 1974, the Nobel Prize was given to her thesis director alone. A very lively controversy broke out, led by Fred Hoyle and other colleagues, scandalised by the fact that the person who had made the discovery was not associated with this prestigious prize. Because she was merely a student or because she is a woman? Jocelyn Bell never complain about it but she has invested in improving the status and number of women with academic positions in physics and astronomy.

3 20th and 21st centuries: the (non) recognition and Matilda effect

We have seen that women have always contributed to the progress of astronomy, their work has led to major and even capital advances. However, their presence has been largely ignored by society and their work has received very little recognition. The problem is that it continues to be so. If we refer to the Nobel Prize, since its creation in 1901, only 57 women have been laureates (out of 958), which represents 5.9 % of all Nobel Prize winners. For physics, chemistry and medicine or physiology prize, the proportion of women is even lower as there have been 23 women awarded for 620 laureates, which is only 3.7 % of the Nobel Prize winners.
Today, it's usually recognised that several women should have received the Nobel Prize but that only their male colleagues or husbands were rewarded without associating her. This is the *Mathilda effect*, it refers to the recurrent denial or the systematic minimisation of the contribution of women scientists to research, their work being attributed to their male colleagues. The most blatant cases of unjustly ignored women scientists are: **Lise Meitner** for the discovery of nuclear fission in 1938 (her colleague Otto Hahn received alone the award for their joint work); **Nettie Maria Stevens** discovered the role of X-Y chromosomes in the determination of the sex of the embryo (the director of her laboratory received the Nobel Prize for this discovery); **Rosalind Elsie Franklin** for her discovery of the double helix structure of DNA (her colleagues Crick and Watson had access to her research without her knowledge, they received the Nobel Prize without her. The second on the structure of viruses, Klug receive the prize in 1982 but Rosalind is dead since 1958); **Jocelyn Bell Burnell** as said above her thesis' director awarded the Nobel Prize alone); **Esther Lederberg** for the replication of bacterial culture (her husband alone received the Nobel Prize!); **Daisy Dussoix** discovered the phenomenon of restriction enzymes (her thesis director received the Nobel Prize without mentioning her).

Fig. 2. "Forgotten" Nobel Prize winners: Rosalind Franklin, Lise Meitner, Netty Stevens, Esther Lederberg, Daisy Dussoix, Jocelyn Bell

Mathematicians do perhaps worse with the Fields Medal: in 83 years of existence, the Iranian **Maryam Mirzakhani** (1977-2017), winner in 2014 is the only one woman who has been awarded for 60 men, that's a very little 1.7 %... In mathematics people often think that there have been no female mathematicians in history, ignoring the work of Maria Gaetana Agnesi (1718-1799, published at the age of 30 "Analytical Institutions"), of Ada Lovelace (1815-1852, 1st algorithm to calculate Bernouilli numbers), Sofia Kovalevskaïa (1850-1891, Equations of motion of the spinning top), Emmy Noether (1850-1891, Noether's theorem), Betty Holberton (1917-2001, programming the ENIAC), Karen Uhlenbeck (1942- , differential calculus, 1st woman Abel prize in 2019) and so many others...
It took the movie "Hidden figures" for people to realize that the success of the Apollo missions owes much to women, even black women in segregationist state like for example Katherine Johnson, Dorothy Vaughan or Mary Jackson.

Another example in another field? Everyone knows JF Champollion for having deciphered hieroglyphs but **Tatiana Proskouriakoff** who made the breakthrough for Maya glyphic decipherment is totally unknown. Would she remained so invisible if she had been a man? We can at least ask ourselves the question.

4 Concluding remarks and hope!

We just gave a short overview of female astronomers from Antiquity to present days and the major contributions they left. The history of women in science is a story of exclusion. Girls were excluded from schools and women were denied access to high schools and universities until very recently, all over the world. Only few exceptional women managed to go through a mountain of difficulties to became scientist but even with these conditions, society has ignored them, forgotten them. Sometimes worse, their work has been attributed to their male colleagues.

Conditions are now changing, there is a trend towards greater gender equality in many countries. We would like that the girls will henceforth get rid of gender bias and will choose science in large numbers. Society needs their talents to solve the immense challenges we face!

References

Baudet, J. 2010, Curieuses histoires des dames de la science, eds. Jourdan

Bernardi, G. 2016, The unforgotten sisters - female astronomers and scientists before Caroline Herschel, eds. Springer

Burbidge, M., Burbidge, G. R., Fowler, W.A. & Hoyle, F. 1957, Reviews of Modern Physics, vol. 29, no 4, 547

Hewish, A., Bell, S. J., Pilkington, J. D. H., Scott, P. F., Collins, R. A. 1968, Nature 217 (5130), 709

Nazé, Y. 2008, L'astronomie au féminin, eds. Vuibert

Vauglin, I. 2021, Mémoires de l'Académie des Sciences, Belles-Lettres et Arts de Lyon, vol. 20, 125

GENDER IN PERMANENT RECRUITMENT IN ASTRONOMY IN FRANCE

O. Suarez[1]

Abstract. The question of equity in the access to research positions between men and women is frequently raised. This is especially important in astronomy, where the percentage of women researchers is weak. This work presents the data of recruitment by gender, using the official reports from the CNRS (*Centre National de la Recherche Scientifique*), CNAP (*Corps National des Astronomes et Physiciens*) and CNU (*Conseil National des Universités*) corresponding to the astronomy sections in the last 15 years. The statistical analysis is in progress and it does not seem to show a recruitment bias in function of gender for the CNRS (section 17) and CNAP (section Astronomy).

Keywords: gender, recruitment, astronomy

1 Introduction

The disequilibrium between the number of men and women working in research in astronomy in France has been evidenced by several authors (Berné & Hilaire 2020; Bot & Buat 2020). The aim of this study is to understand if there is a bias in the recruitment of permanent researchers that could have an influence in this difference. The final goal is to help the astronomical community to act over the origin of this inequality, at the moment where it is produced, to help to balance the women and men ratios in research in astronomy.

2 Results

This works presents the data of recruitment to access permanent positions in France in the last 10-20 years, from the moment when the information of recruitment by gender started to be available. Data have been obtained from the section rapports of CNAP (`http://cnap.obspm.fr/`), the social rapports of the CNRS (`https://drh.cnrs.fr/le-bilan-social-et-parite/`), the section 17 rapports of the CNRS (`http://section17.obspm.fr`), the demographic files of the CNU, the rapport of demography of university teachers and professors (`https://www.enseignementsup-recherche.gouv.fr`), and the recruitment archive in section 34 of the CNU (`http://www-cnu34.irap.omp.eu/`). In Figure 1 we present the number of candidates, recruitments and success rate for women and men in the public examinations to access a research position in astronomy.

To give a global probability of accessing a permanent position for women and men, one should consider each candidate's average number of applications. We have extracted this information from the average of each candidate's applications of to the CNAP examination between 2016 and 2019. These results show that each woman applies an average of 2.55 times to a position and each man applies an average of 2.72 times. Taking this into account by multiplying the success rates by this factor for each gender, we obtain the corrected global rate (Fig. 2). This rate should better represent the percentage of success of a candidate in earning a permanent position in astronomy in France.

3 Conclusions

The global success rate does not show apparent advantages in recruitment in favour of neither men or women. The CNU seems biased towards men recruitment. A statistical analysis in ongoing and is necessary to confirm these preliminary results. If this is confirmed, it would mean that the majority of the astronomy recruitments in France are not be gender biased and equity prevails. The actions to reach an equilibrium in number of women and men in astronomy should be thus tackled before the recruitment moment, starting by trying to inspire young girls to get involved in science.

[1] Observatoire de la Côte d'Azur, Nice, France

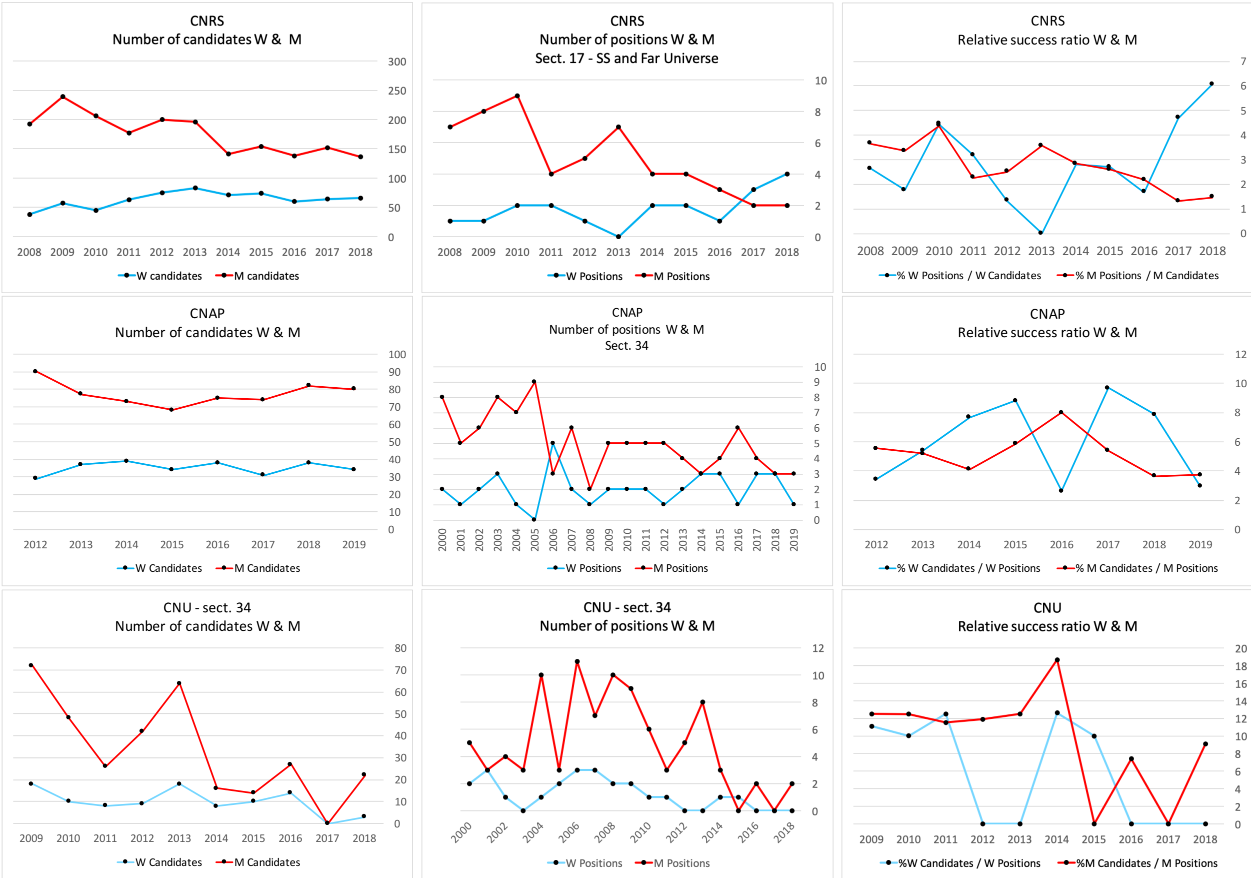

Fig. 1. Left column: Number of women and men candidates for the CNRS, CNAP and CNU positions. **Center column:** Number of positions obtained by women and men for CNRS, CNAP and CNU. **Right column:** Relative success rate for women and men for CNRS, CNAP and CNU positions.

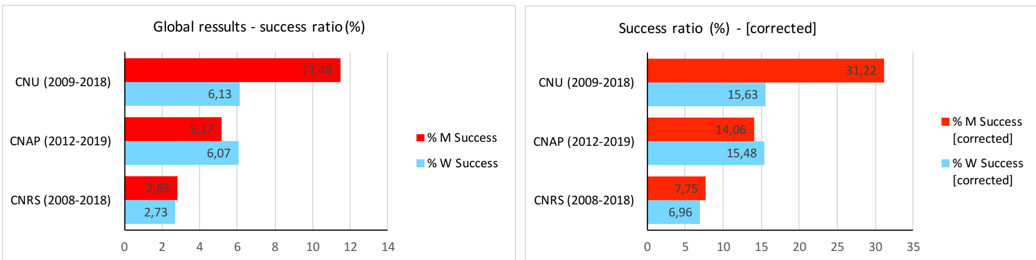

Fig. 2. Left: Global ratio of access to permanent positions. **Right:** Global ration of access to permanent positions corrected from the average of presentations of each candidate

References

Berné, O. & Hilaire, A. 2020, Nature Astronomy, 4, 296
Bot, C. & Buat, V. 2020, Rapport SF2A.

Session 12

Cinquième réunion des utilisateurs des télescopes français

TBL DIRECTORS' REPORT

R. Cabanac[1] and P. Mathias[1]

Abstract. Latest news on Telescope Bernard Lyot are given in this communication.

Keywords: Telescope, Instrumentation, Spectropolarimetry, Observations

1 Pic du Midi latest news

1.1 New science buildings: Dauzère and SPIP extension

Erection of Dauzère building and TBL extension for SPIP started in spring 2021. Fig 1 shows a top view of the extension that shall home the vacum chamber for TBL primary coating. TBL tower level 0 was relevelled with a concrete slab (grey area on Fig. 1). The aea is ready for SPIP enclosure.

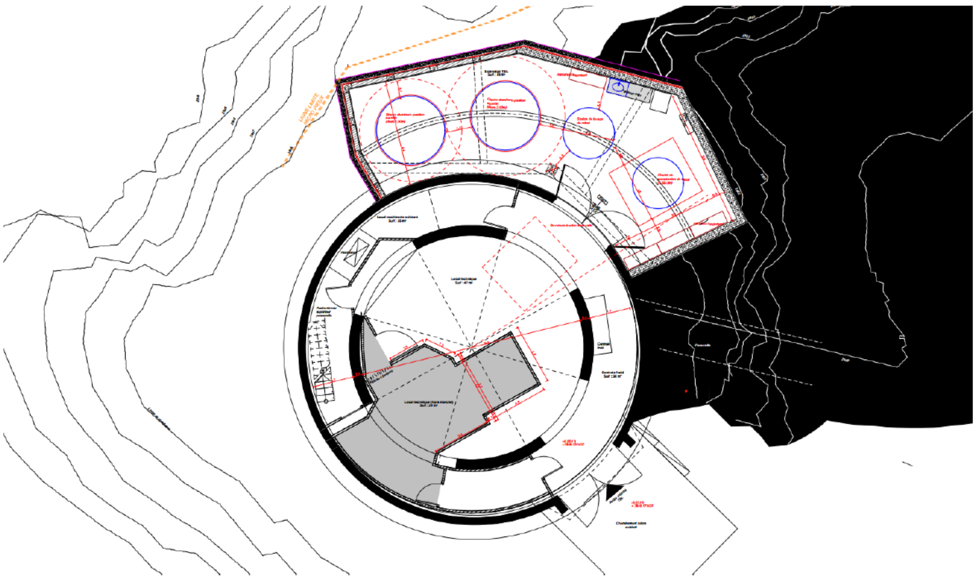

Fig. 1. Top view of the plan of TBL/SPIP extension started in spring 2021. This extension will home the vacuum chamber for primary Al coating.

Pic du Midi was granted funding of 1.15 million euros (under Contrat Plan Etat Région 2021, project Observ'Occ) for the developing the new bonnet VISION (Lopez Ariste S12 communication). The new bonnet will allow to use Neo-Narval and SPIP instruments simultaneously at TBL cassegrain focus. Other developments at Pic du Midi include a new building construction Dauzère, with 30 beds, conference room, central control room, network room (completion expected 2023), a new coronagraph in replacement of CLIMSO. A new T50 (in replacement of the T60) and refurbishing of T1M to serve the training sessions of new European Research School TESS (first Masters trainees expected in Fall 2022.)

[1] IRAP, OMP, Université de Toulouse, CNRS, CNES, UPS, (Toulouse), France.
ORCID of the author: http://orcid.org/0000-0001-6679-2600

2 TBL administrative news

2.1 *TBL new status: pro/con*

TBL has changed its administrative status from USR 5026 to SNO in 2016. We have now a few years to review the impact of the change. The most positive impact is that management by OAR831 OMP has added lots of flexibility in organising staff missions at the summit. The Pic du Midi Team of electronics experts and telescope operators are fully trained on TBL observations. Unfortunately this positive impact does not compensate the loss of budget of 50 000 euros/year since 2015, which has a very significant impact on our ability to maintain TBL infrastructure, small components, and fluids. The users should be aware that TBL reliability may decrease in a close future because of our lack of funds. Finally, the directors' interim will end on Aug. 31st, 2021. A new director has yet to be nominated. Needless to say, that this is the most urgent task that the community as large must focus on.

2.2 *TBL Staff*

TBL runs in full service mode with 8 telescope operators and 6 electronics experts. In the coming 2 years, three essential TBL staff will retire, and 2 staff working closely for TBL. The cryogenic expert among the operator, the head of electronics team at TBL and senior expert, the head of the mechanical workshop in Tarbes, and the technical director of Pic du Midi. If any of those positions are not replace one to one, TBL be have to reduce its offer (number of night, higher cost of maintenance, etc.)

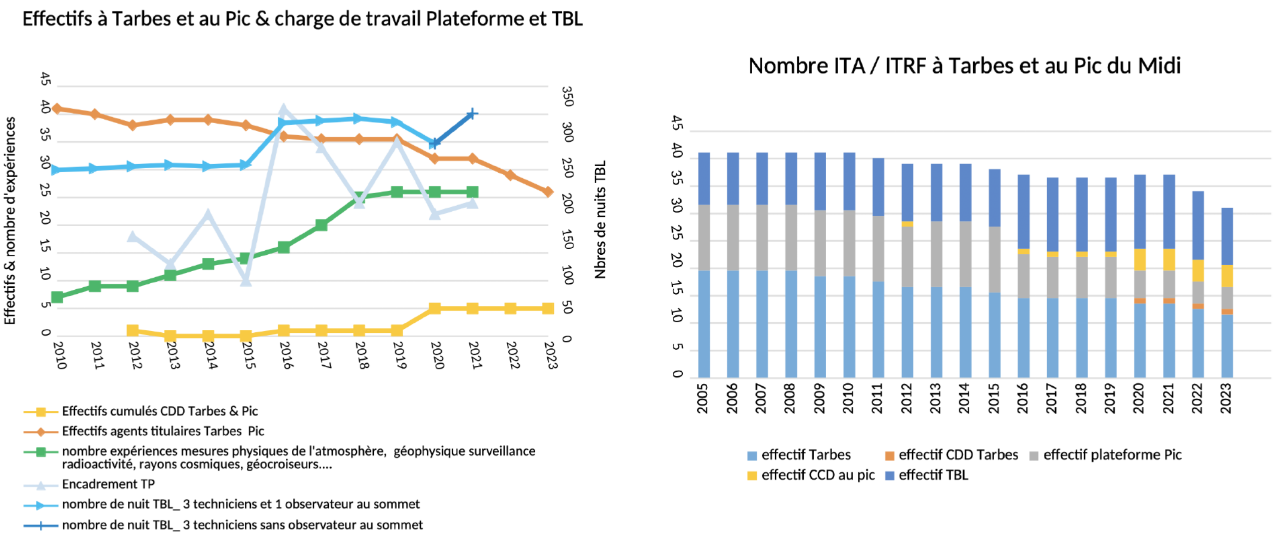

Fig. 2. Recent evolution of Pic du Midi and TBL workload and staff replacement. **Left:** number of experiment (green) number of TBL nights (blue), student training session (grey), number of permanent staff (orange), number of short term staff (yellow). **Right:** Histogramme of staff number between 2005 and 2023: TBL staff (dark blue) in Tarbes (lgiht blue) Pic du Midi platform (grey) short term (orange and yellow).

2.3 *TBL service observing*

During the period 2016-2021, full service mode required 3 full time equivalent (CNAP astronomers) for support and queue preparation and qualité control. The service observations were performed by 80 volunteers from the Observateurs Associés TBL association, 25 PhD or post-doc, 72 Masters Students, and 10 astronomers. Since May 2020 (Covid-19 sanitary crisis), service observations are completely performed by TBL operators. Remote observations are possible for Neo-Narval. The new direction will have to review observation management on a regular basis. It seems important to allows young astronomers to train on telescope observing. Keeping that option for TBL is easy.

3 Observations statistics

Semestre	PNPS	PNP	PCMI	PNCG	Opticon	Divers
2016A	6	1	1	0	1	0
2016B	7	0	1	0	1	0
2017A	6	0	1	0	1	1
2017B	5	2	1	2	0	0
2018A	7	0	0	2	1	0
2018B	8	0	0	0	0	0
2019A	10	0	0	0	0	1
2019B	7	0	0	1	0	0
2020A	9	0	0	2	0	1
2020B	11	1	0	0	1	2
2021A	9	0	0	0	0	2

Sem.	A		B		C	
h %	Alloc.	Réal	Prog	Réal	Prog	Réal
2016A	171	68.3	124	52.3	7	900.0
2016B	150	202.4	75	88.2	95	168.4
2017A	139	131.4	91	151.1	39	218.3
2017B	396	86.3	194	82.5	76	55.3
2018A	307	59.5	137	54.2	10	5.0
2018B	316	109.8	234	66.4	35	98.7
2019A	300	57.7	300	19.1	35	0.0
2019B	332	28.3	148	22.7	2	0.0
2020A	202	44.2	198	39.7	351	20.3
2020B	234	42.4	219	18.3	319	26.5

Fig. 3. The two tables sumarise observational statistics. **Left:** proposal distribution among PN in the past five years. **Right:** completion rate of A, B, C classes, firs column are the number TAC allocated hours, second column is completion rate in percent of allocated hours.

Technical losses: 2019B: Neo-Narval integration and commissioning 3 months, 2020A: CoVid-19: 2-month close down, 2020B: Primary coating, 2 weeks (Fabry-Perot upgrade during the same period), 2021B and 2022A: expect SPIP integration and commissioning.

4 TBL Publication record

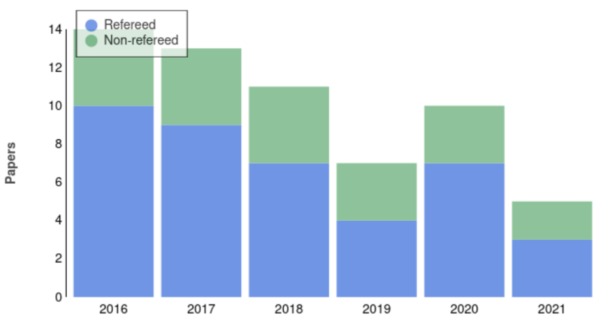

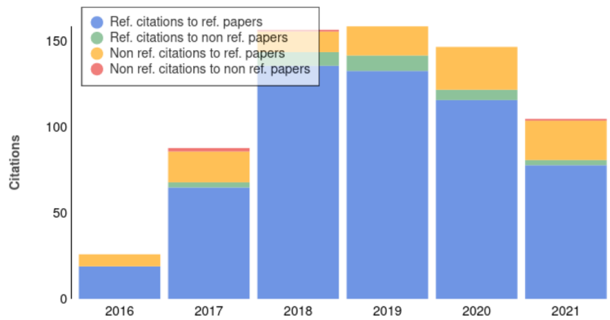

Fig. 4. Publication record at TBL over the past five years (data from ADS). **Left**: publication number refereed (blue), non-refereed (green). **Right**: number of citations.

5 Future developments

During this National Telescope Users Meeting (Session 12) you will hear of the latest development on Neo-Narval (instrument stability, DRS) from Arturo Lopez Ariste, and an update on SPIrou Pyrénéen (SPIP) from Claire Moutou. I briefly mention that Neo-Narval is now fully operational, the arrival of the new Fabry-Perot from Geneva in spring 2021, allow us to track the behaviour of the spectrograph in the thermal enclosure. A day-to-day stability of ¡ 2m/s in radial velocity is monitored with jumps from one night of 30-50 m/s. Those jumps are correlated with the TBL tower temperature from sunrise on. DRS is getting close to its final version with a good measure of absorption line equivalent with, some remanent errors on the wavelength calibration polynomial and magnetic field measurements are different from Narval Libre-Esprit by ca. 10%, this difference is not yet understood.

SPIP integration and arrival has shifted a bit from original plans. The expected arrival is now scheduled as follows: Sept. 2021, spectrograph enclosure, Spring 2022 (SPIP polarimetre), end of 2022 (SPIP Spectrograph). A few weeks are expected for integration and commissioning.

6 Final words

R. Cabanac wishes to add that he enjoyed the past 14 years serving the French astronomical community as director of TBL (with an halt in 2017-2018 when Eric Josselin took the lead), he will still be in Tarbes and will continue to serve Pic du Midi as science director and co-Director of OMP in Bigorre.

HD207897 B: A DENSE SUB-NEPTUNE TRANSITING A NEARBY AND BRIGHT K-TYPE STAR

N.Heidari[1,2 3], I. Boisse[3], SOPHIE team and others

Abstract. We present the discovery and characterization of a transiting sub-Neptune orbiting with a 16.20-day period around a nearby (28 pc) and bright (V= 8.37) K0V star HD207897 (TOI-1611). This discovery is based on photometric measurements from the Transiting Exoplanet Survey Satellite (TESS) mission and radial velocity (RV) observations from the SOPHIE, Automated Planet Finder (APF) and HIRES high precision spectrographs. We used EXOFASTv2 for simultaneously modeling the parameters of the planet and its host star, combining photometry and RVs data to determine the planetary system parameters. We show that the planet has a radius of 2.50 ± 0.08 R_E and a mass of either 14.4 ± 1.6 M_E or 15.9 ± 1.6 M_E with nearly equal probability; the two solutions correspond to two possibilities for the stellar activity period. Hence, the density is either 5.1 ± 0.7 g cm^{-3} or $5.5^{+0.8}_{-0.7}$ g cm^{-3}, making it one of the relatively rare dense sub-Neptunes. The existence of such a dense planet at only 0.12 AU from its host star is unusual in the currently observed sub-Neptune ($2 < R_E < 4$) population. The most likely scenario is that this planet has migrated to its current position.

Keywords: planets and satellites: detection, techniques: photometric, techniques: radial velocities

1 Introduction

The NASA *Kepler* and *TESS* Mission have discovered a large number of planets of intermediate size, with radii between Earth and Neptune, also known as sub-Neptunes. Since the size of planets is directly dependent on physical mechanisms in formation and evolution, the absence of sub-Neptunes in our solar system and their abundance among exoplanet population has raised numerous fundamental questions.

Here, we announce the detection and characterization of a sub-Neptune orbiting a bright (V=8.4) K0 star using TESS photometry data and SOPHIE, APF, and HIRES RVs.

2 Observations

2.1 Photometry

TESS observations of HD207897 were taken on five sectors divided into two continuous periods from sectors 18-20 and 25-26, with a total time span of 131 days. After observations of sector 18 were completed, the MIT's Quick Look pipeline detected the signature of two transits of HD207897 b at a period of 16.20 d, and an alert was issued 19 December 2019 by the TESS Science Office. No transits occurred during sector 19 as the sole transit fell in the data gap between the two orbits. After observations of sector 20 were downlinked, the Science Processing Operations Center (SPOC; Jenkins et al. 2016) at NASA Ames Research Center conducted a transit search detected two transits of HD207897 b at a signal-to-noise ratio (S/N) of 23.3. Two additional transits were observed and detected in sector 25, and one more occurred during sector 26. A multi-sector search of sectors 18-26 by the SPOC detected 7 transit events of HD207897 b in total, at an S/N of 34.3 and an average depth of 913.7±21.1 ppm.

[1] Department of Physics, Shahid Beheshti University, Tehran, Iran.
[2] Laboratoire J.-L. Lagrange, Observatoire de la Côte d'Azur (OCA), Université de Nice-Sophia Antipolis (UNS), CNRS, Campus Valrose, 06108 Nice Cedex 2, France.
[3] Aix Marseille Univ, CNRS, CNES, LAM, Marseille, France.

We used 2-minutes photometry data which was extracted with the Pre-search Data Conditioned Simple Aperture Photometry (PDC-SAP) pipeline provided by the TESS team. The normalized and detrended light curve is shown in Figure 1.

To look for any periodic signals in the data, we used the transit-least-squares (TLS) algorithm (Hippke & Heller 2019). We found a prominent periodic signal occurring every 16.20 d with a S/N of 43, with false alarm probability (FAP) below 0.01 %.

2.2 *High-resolution spectroscopy*

HD207897 had been monitored between 2012 to 2020 by the SOPHIE spectrograph (Perruchot et al. 2008). The observations were performed using high-resolution mode with a simultaneous Thorium-Argon (Th-Ar) or Fabry perot calibration lamp, allowing us to monitor the instrumental drift. We collected 68 spectra with an exposure time ranging from 1000 to 1500 s and a median signal-to-noise ratio (S/N) of 97.7 per pixel at 550 nm. The mean RVs uncertainty is also 1.7 m s^{-1}.

We also observed this satr using the Keck I telescope and HIRES spectrometer (Vogt 1994) from 2003, and additional RVs were collected for eleven months beginning on 2020 Jan 21. Thirty-seven RVs were collected using the B5 decker (0.87" x 5.0") resulting in a resolution of 50,000. The median exposure time was 231 s, an average signal-to-noise ratio per pixel of 220, and internal uncertainty of 1.04 m/s.

Morover, from the summit of Mt. Hamilton at Lick Observatory, we collected 23 more RVs of HD207897 using the Levy Spectrograph on the APF from 2 Jun 2020 until 28 Feb 2021. Twenty-three RVs were collected having a median exposure time of 1200s, a signal to noise per pixel of 86, and internal uncertainty of 3.0 m/s. With resolution of 100,000, this slit-fed spectrograph uses the iodine-cell technique to calculate RVs descended from.

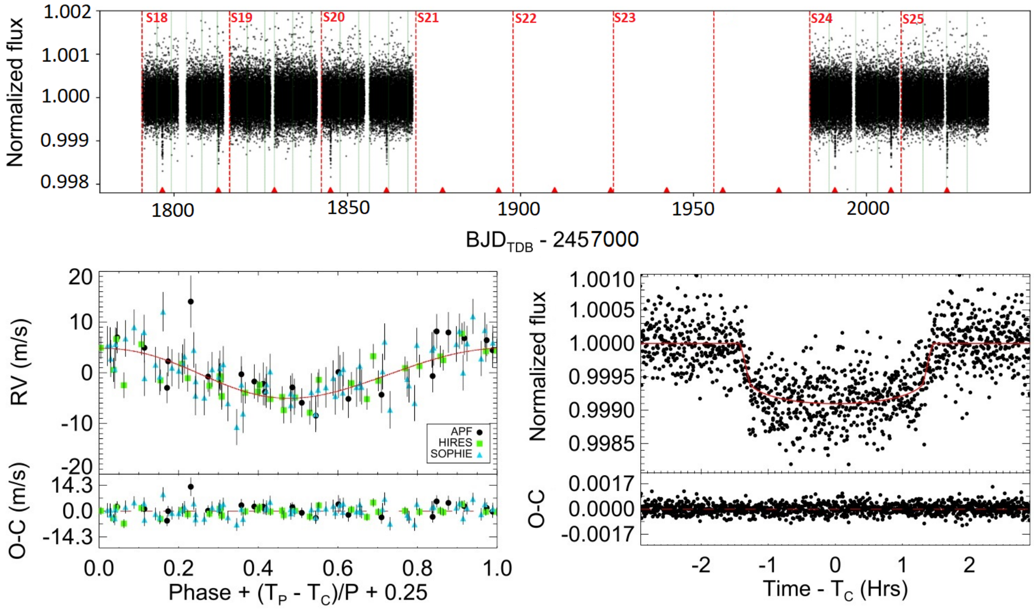

Fig. 1. Top: The Full PDC-SAP (2-minute) TESS light curve after detrending. **Left:** Phase-folded SOPHIE, APF, and HIRES RVs of HD207897 b at the period of 16.20 d. **Right:** TESS Phase-folded light curve.

3 Radial velocity data analysis

The data are extract by Doppler shifted method. After removing a drift, we investigated the footprints of the planet by searching for periodic signals. To do so we used the Data and Analysis Center for Exoplanets (DACE, Delisle et al. 2016) web platform and computed periodograms for RVs (Fig. 2).

The RVs periodogram displays a clear peak at 16.20 d with a value below 0.1 % false alarm probability (Baluev 2008). Moreover, there is no corresponding peak in the periodogram of activity indicators, which shows that this periodic signal is likely due to a planet and not due to stellar activity, Figure 2.

Table 1. Median values and 68% confidence interval for HD207897 b and its host star.

Parameter	Units	Activity on 35.9 d (Prob. = 46%)	Activity on 37.6 d (Prob. = 54%)
M_*	Mass (M_{sun})	$0.801^{+0.036}_{-0.031}$	$0.800^{+0.036}_{-0.030}$
R_*	Radius (R_{sun})	$0.779^{+0.019}_{-0.018}$	$0.779^{+0.019}_{-0.018}$
P	Period (days)	16.202157 ± 0.000085	$16.202159^{+0.000085}_{-0.000083}$
ρ_P	Density (cgs)	$\mathbf{5.52}^{+0.82}_{-0.73}$	$\mathbf{5.05}^{+0.77}_{-0.69}$
R_P	Radius ($R_\oplus$)	$2.505^{+0.081}_{-0.077}$	$2.501^{+0.082}_{-0.078}$
M_P ...	Mass ($M_\oplus$)	**15.9**$\pm$1.6	**14.4**$\pm$1.6
a	Semi-major axis (AU)	$0.1164^{+0.0017}_{-0.0015}$	$0.1163^{+0.0017}_{-0.0015}$

Moreover of the planet signal, there is also two signals at 35.9 d and 37.6 d in RV residuals. The estimated rotational period of star using extracted $\log(R'_{HK})$ from SOPHIE spectra, is 37 ± 7 d. Also, there is a peak at 36 d in periodogram of CRX activity indicator. So, it is likely the signals at 35.9 d and 37.6 d are due to stellar rotational period.

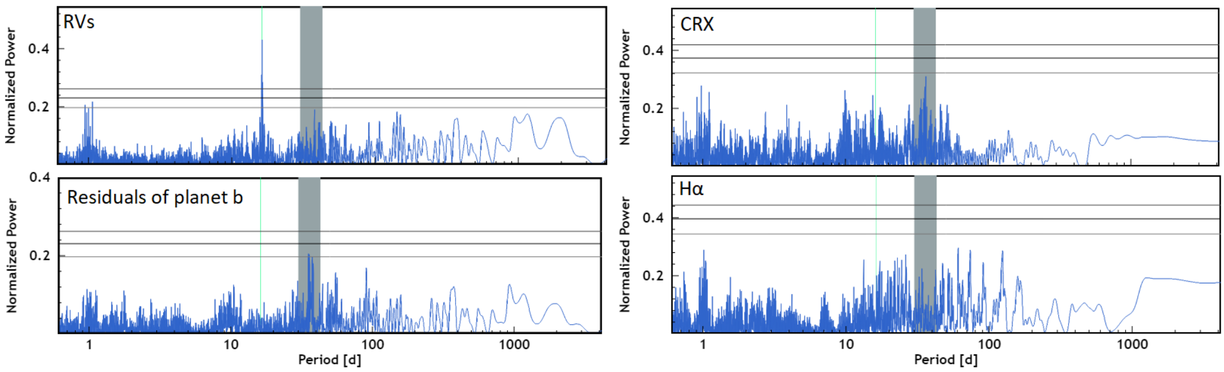

Fig. 2. Left: RVs and residual of RVs after Keplerian fit on 16.20 d. **Right:** CRX and $H\alpha$ index. The cyan vertical line marks the position of highest peak at RVs periodogram at 16.20 d. Horizontal lines indicate 0.1, 1, 10 % FAP level, from top to bottom, respectively. Also, the grey vertical strip is highlighting the position of the estimated rotational period of star.

4 Joint modeling of RV and photometry

To explore all the parameters of the system, including both the host star and the planet, we modeled simultaneous and self-consistent the photometric observations and RV measurements using the Fast Exoplanetary fitting package (EXOFASTv2, Eastman et al. 2019).

As we showed in Sect. 3, the signals at 35.9 and 37.6 d are likely to be due to the stellar rotation periods. Since these signals affect slightly the mass estimate of the planet, we considered them as an additional keplerian fit in our global analysis. We did not fix the period and let EXOFASTv2 find the best activity period between 35.9 and 37.6 d signals. After EXOFASTv2 converged, we saw a bimodality in the posterior distribution for the stellar activity periods, so we present the final median posterior distributions values of both the most probable solutions in Table 1. We also report their calculated probabilities based on the area of the posterior distributions. The probability of the most likely values is 54% and the less likely values are 46%.

5 Discussion and Summary

In this paper, we detected and characterized a sub-Neptune orbiting around HD207897, with a period of 16.202161 ± 0.000083 d, using TESS photometry data along with SOPHIE, HIRES, and APF RVs observations. We found the planet has a mass of 14.4 ± 1.6 M_E with probability of 56 % (or 15.9 ± 1.6 M_E with probability of 46 % based on bimodal results of stellar activity period) and a radius of 2.5 ± 0.08 R_E, which translates into a high density of 5.1 ± 0.7 g cm^{-3} (or $5.5^{+0.8}_{-0.7}$ g cm^{-3}). We used the same mass and radii bounds as Otegi et al.

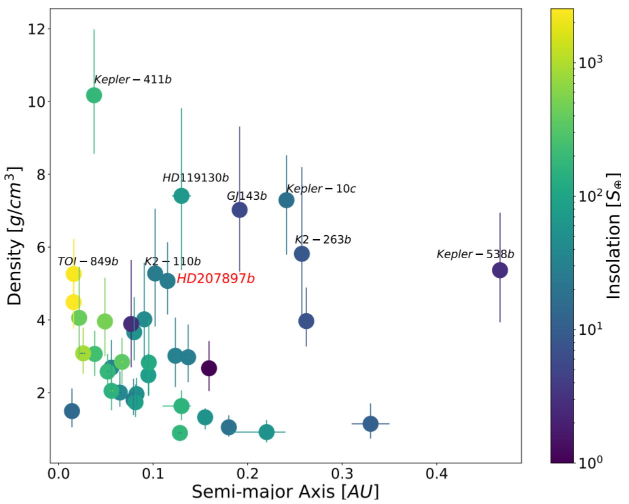

Fig. 3. The density-semi major axis diagram for HD207897 b and other sub-Neptune sized planets ($2 < R_{\rm E} < 4$) with known semi-major axis, luminosity and accurate mass and radius (Otegi et al. 2020). Dots are colored with planet insolation in Earth unit.

(2020) on NASA Exoplanet Data Archive* (December 5th, 2020) and plotted in Fig 3, all the sub-Neptune sized planets ($2 < R/R_{\rm E} < 4$) with semi-major axis and luminosity determined.

How can HD207897 b and other similar planets with such a high density exist at a close distance from their host star? One possibility could be that the planet has lost most of its volatile elements by evaporation, but for the case of HD207897 b with an orbital period of 16.20 d and receiving an incident flux of F=26.3 $\rm F_E$ it is not a satisfactory answer. Indeed, even if we consider an extreme evaporation process (Lecavelier Des Étangs 2007), the mass-loss of the planet would be just 0.1 $\rm M_E$ during the entire lifetime of the star, which cannot account for its high density. HD207897 b is unlikely to have formed in situ. According to Schlichting (2014) the maximum isolation mass that can form at a distance of a = 0.12 AU is only $\sim$ 0.06 $\rm M_E$, assuming the minimum mass solar nebula (MMSN); a disk surface density $\sim$ 41 times larger than the solar nebula would be required to form a planet as massive as HD207897 b at this distance. Two possible scenarios can however be considered, both consistent with the MMSN: either the material from the outer region migrated and formed the planet HD207897 b or the formation of HD207897 b occurred far out of the disc and the planet subsequently migrated to its current location. The second scenario could have been triggered by another planet in this system. The hint of long-term trend on RVs allows for the presence of another planet. The high occurrence rate of long-period giant planets ($mass > 0.3M_{\rm J}$) in the systems harboring small planets (planets with mass/radius between Earth and Neptune) (Schlecker et al. 2020) can also support such a scenario.

References

Baluev, R. V. 2008, Monthly Notices of the Royal Astronomical Society, 385, 1279

Delisle, J.-B., Ségransan, D., Buchschacher, N., & Alesina, F. 2016, Astronomy & Astrophysics, 590, A134

Eastman, J. D., Rodriguez, J. E., Agol, E., et al. 2019, arXiv preprint arXiv:1907.09480

Hippke, M. & Heller, R. 2019, A&A, 623, A39

Jenkins, J. M., Twicken, J. D., McCauliff, S., et al. 2016, in Software and Cyberinfrastructure for Astronomy IV, Vol. 9913, International Society for Optics and Photonics, 99133E

Lecavelier Des Étangs, A. 2007, Astronomy & Astrophysics, 461, 1185

Otegi, J., Bouchy, F., & Helled, R. 2020, Astronomy & Astrophysics, 634, A43

Perruchot, S., Kohler, D., Bouchy, F., et al. 2008, 7014, 70140J

Schlecker, M., Mordasini, C., Emsenhuber, A., et al. 2020, Astronomy & Astrophysics

Schlichting, H. E. 2014, The Astrophysical Journal Letters, 795, L15

*https://exoplanetarchive.ipac.caltech.edu/

SF2A 2021
A. Siebert, K. Baillié, E. Lagadec, N. Lagarde, J. Malzac, J.-B. Marquette, M. N'Diaye, J. Richard, O. Venot (eds)

THE MAGNETIC EVOLUTION OF YOUNG SUNS

S. C. Marsden[1], C. Neiner[2] and I. A. Millburn[1]

Abstract. Magnetic fields are one of the main drivers of the evolution of solar-type stars. They affect everything from the rotational evolution of the star through to the habitability of orbiting exoplanets. In this project we are attempting to help understand how the magnetic dynamos of young Suns evolve from chaotic variability to the regular magnetic cycles that we see on our own Sun today. To do this, in 2018 we started a monitoring campaign using the NARVAL, and more recently NEONARVAL, spectropolarimeters on the Téléscope Bernard Lyot to observe five of the brightest young Suns. As of mid-2021 we have so far obtained two to four epochs of spectropolarimetric data on each of our targets and from these have created preliminary maps of the stellar magnetic topologies. So far two of our targets have shown magnetic polarity reversals that could indicate developing cycles, with one of the targets showing a strong link between the differential rotation measured from its brightness features and that measured from its magnetic features.

Keywords: stars: solar-type, stars: pre-main sequence, stars: imaging, stars: magnetic fields, starspots

1 Introduction

Sun-like stars can be broadly defined as having an internal structure similar to that of our own Sun. Such stars would have an inner radiative zone, which in the Sun rotates as a solid body, and an outer convection zone, which in the solar case rotates differentially, with the equator rotating faster than the poles. It is this difference in rotation between the Sun's radiative and convective zones that drives the solar dynamo. This dynamo creates a regular magnetic activity cycle in the Sun with an $\sim$11 year cycle of increasing/decreasing sunspots and magnetic polarity reversals every $\sim$22 years.

But what of young solar-type stars? When young these stars rotated much more rapidly, up to 100 times the current solar rate (i.e. Gallet & Bouvier 2015), which was thought to have driven a powerful magnetic dynamo (Gudel 2007). There is some evidence that the magnetic dynamo in these stars operates differently to that of today's solar dynamo. Unlike today's Sun young solar-type stars appear to have a more chaotic dynamo with measurements of the magnetic activity, taken from Calcium HK observations, showing high levels of variability and no real regular cycles (i.e. Baliunas et al. 1995). Young solar-type stars also show large regions of near-surface azimuthal magnetic field (field wrapped around the star's rotation axis) (i.e. Marsden et al. 2006, 2011a; Waite et al. 2011). This is something not seen on the Sun, with most of the solar azimuthal field confined to the tachocline layer between the solar radiative and convection zones, with this interface layer thought to be the seat of the solar dynamo. This may not be the case for young Suns.

Magnetic fields are directly linked to the rotational evolution of solar-type stars (Gallet & Bouvier 2015). The study of magnetic field generation on young, rapidly-rotating solar-type stars is of importance in understanding not only the history of our own Sun, and its impact on our Earth, but more generally in understanding how the magnetic dynamo operates under different conditions. Thus in 2018 we started a project aimed at studying the magnetic fields on young Suns using the NARVAL, and more recently the NEONARVAL, spectropolarimeters on the Téléscope Bernard Lyot (TBL) at Pic du Midi. We chose to monitor five of the best young Sun candidates to map their magnetic fields and look for evidence of changes in their magnetic fields that may indicate the development of emerging cycles on such stars.

[1] Centre for Astrophysics, University of Southern Queensland, Toowoomba, Queensland 4350, Australia
[2] LESIA , Paris Observatory, PSL University, CNRS, Sorbonne University, Université de Paris, 5 place Jules Janssen, 92125 Meudon, France

2 Targets and Observations

The five targets chosen are some of the brightest (V $\sim$ 5.1 to 7.9) young solar-type stars known: AF Lep, 111 Tau, V1358 Ori, EK Dra, and V889 Her. Based on GAIA DR2 data (Gaia Collaboration 2018) and the Baraffe et al. (2015) stellar evolution models, these stars range in age from around 30 to 50 Myrs and have masses from $\sim$1.0 to 1.2 $M_{\odot}$. All the stars are rapid rotators with rotational periods ranging from $\sim$1 to 3.6 days (Marsden et al. 2006; Hackman et al. 2016; Mittag et al. 2018). As part of our project, each star has been observed $\sim$10 to 20 times at nearly yearly epochs in Stokes V using NARVAL or NEONARVAL for (as at mid-2021) two semesters (2018B and 2019B) for AF Lep and V1358 Ori, three for 111 Tau (2018B, 2019B, and 2020B) and four semesters (2018A, 2019A, 2020A, and 2021A) for both EK Dra and V889 Her. For some of the targets previous magnetic maps exist; AF Lep - Millburn et al. (in prep.), V1358 Ori - Hackman et al. (2016), 111 Tau - Waite et al. (2015), EK Dra - Waite et al. (2017), and V889 Her - Marsden et al. (2006); Jeffers & Donati (2008); Jeffers et al. (2011), that will also be used to compare to our observations.

3 Magnetic Maps of Young Suns

The (NEO)NARVAL spectropolarimetric observations of the targets have been reduced using the standard TBL data reduction pipeline and then using the technique of Zeeman Doppler Imaging (ZDI) using ZDIpy (Folsom et al. 2018) to produce magnetic maps of all the targets. Examples of preliminary maps from our TBL observations produced for one of our targets, the late-F star 111 Tau, are given in Fig. 1.

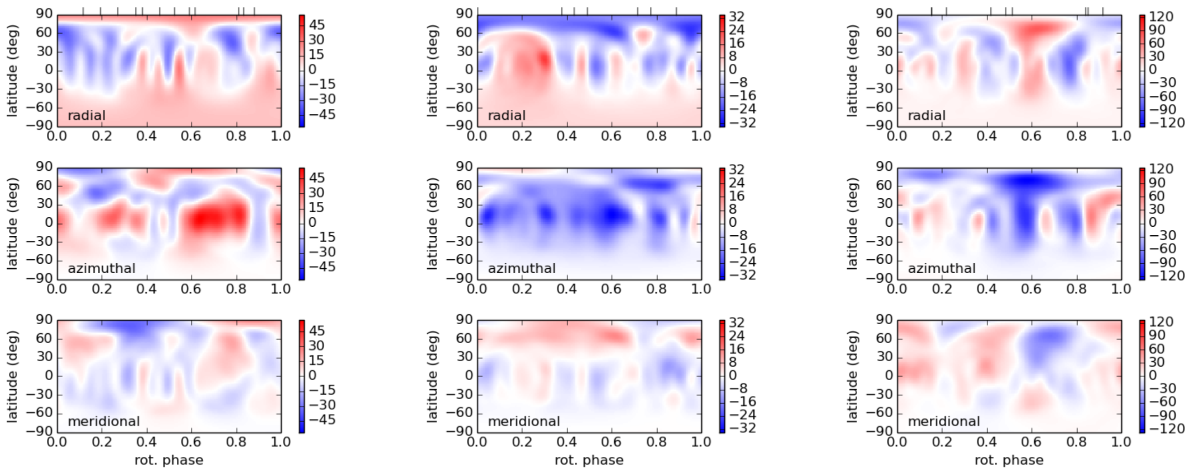

Fig. 1. Preliminary magnetic maps of 111 Tau from Nov/Dec 2018 (left), Dec 2019 (centre), and Dec/Jan 2020/21 (right). The top row shows the radial magnetic field, the middle row the azimuthal field, and the bottom row the meridional magnetic field. The scale bars are in Gauss, with the ticks at the top of the plots showing the phases of observations.

Fig. 1 shows that for 111 Tau the dominant polarity of the radial field around the northern pole has changed from positive in 2018 to negative in 2019 and then to a more mixed polarity in 2020/21. However, the polarity in the southern hemisphere appears to remain unchanged (predominantly positive) at all epochs. At the same time the azimuthal magnetic field changed from a mixed polarity (with possibly dominant positive regions) in 2018 to a more negative polarity field in both 2019 and 2020/21. These could potentially be indications of a nascent cycle starting to form on this young Sun.

Our magnetic maps can also determine the geometry of stellar magnetic fields, e.g. the amount of poloidal or toroidal field, the axisymmetry of the field, and the amount of field contained in the dipolar, quadrupolar, etc., components. These are important indicators that will be used to study the dynamo in our stars.

4 Polarity Reversals

One of the key features of the Sun's 22 years magnetic cycle is the reversal of the dominant magnetic polarity in each hemisphere every $\sim$ 11 years. Thus one of the key observational quantities to measure from our magnetic maps is the location of the magnetic dipole at each epoch. This can more clearly show a magnetic polarity reversal than trying to determine this just from looking at the magnetic maps. An example of the location of the positive dipole on another late-F star, AF Lep, taken from both our (NEO)NARVAL observations and other datasets obtained for the star, is shown in the left-hand side of Fig. 2.

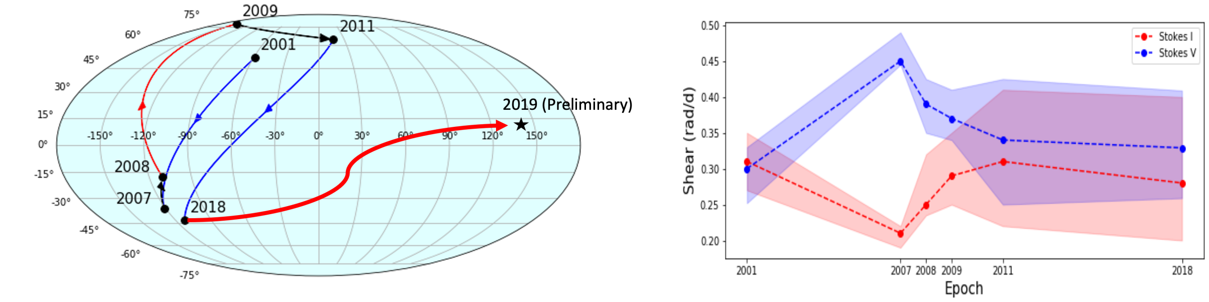

Fig. 2. Preliminary location of the positive dipole for AF Lep (left) and the preliminary variations in the level of surface differential rotation from both the brightness features (Stokes I) and the magnetic features (Stokes V) for the same star (right). These are from both our TBL observations and previously obtained datasets (Millburn et al. in prep.).

Fig. 2 (left) shows that AF Lep has undergone at least three (and potentially four) polarity reversals during the ∼20 years of observations. If this is a regular cycle (yet to be determined) it would indicate a magnetic cycle approximately half the length of the Sun's 22 year magnetic cycle, or possibly even shorter.

5 Spot Maps of Young Suns

As our targets are mostly fast rotators with $v\sin i$ values of ∼20 km/s or more (with the exception of 111 Tau with a $v\sin i$ of 16 km/s), we can also use the observations to map the location of the spot/brightness features on the stellar surface. Again we use the ZDIpy mapping code and map both dark and bright features. An example of the preliminary spot maps for AF Lep for three epochs (one from the TBL and two from previous observations) are given in Fig. 3.

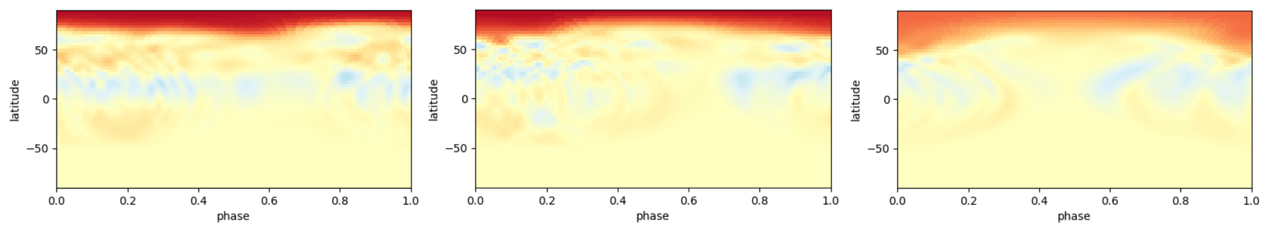

Fig. 3. Preliminary spot maps of AF Lep from 2001 (left), 2008 (centre), and our 2018 TBL observations (right), with brown features indicating dark spots, yellow the photosphere and blue features being bright spots (Millburn et al. in prep.).

Fig. 3 shows that AF Lep always maintains a polar spot feature (with possibly varying intensity), similar to other young, rapidly-rotating stars, but the amount and location of lower latitude features potentially varies. We plan to investigate if the location of lower latitude features is linked to the magnetic features on the star.

6 Surface Differential Rotation

Differential rotation (DR), where the equatorial regions of a star rotate faster than the polar regions, is thought to be a key driver of the magnetic dynamo. Thus measuring the level of DR on our stars, and any variability of the values such as that seen on other young solar-type stars (i.e. Collier Cameron & Donati 2002; Donati et al. 2003), can provide another window into the operation of the stellar dynamo. Through the imaging process, for both magnetic and spot maps, we can measure the level of surface DR on our star by incorporating a solar-like DR law into the imaging process. We use a simplified solar-like law:

$$\Omega(\theta) = \Omega_{\rm eq} - d\Omega \sin^2(\theta)$$

where $\Omega(\theta)$ is the rotation rate at latitude θ, $\Omega_{\rm eq}$ is the equatorial rotation, and $d\Omega$ is the shear between the equator and the poles (the differential rotation). The values of $\Omega_{\rm eq}$ and $d\Omega$ are treated as free parameters and varied to find the best fit to the data as described in Petit et al. (2002). This is done for both the brightness (Stokes I) and magnetic (Stokes V) features with preliminary results for AF Lep being shown in the right panel of Fig. 2.

Fig. 2 (right) shows that, as seen on other young solar-type stars (i.e. Donati et al. 2003; Marsden et al. 2011b; Waite et al. 2015), the level of DR measured from the magnetic features is usually higher than that from the brightness features. This has been interpreted as being due to the brightness and magnetic features being anchored at different depths in the stellar convection zone (Donati et al. 2003) and would show that unlike the Sun, the level of DR varies with depth in the convection zone. This could indicate that the dynamo in young stars is operating throughout the convection zone rather than being confined to the interface layer, as in the solar case. Also, although these results are preliminary it appears that changes in AF Lep's DR from the brightness features is mirrored by changes in the DR measured from the magnetic features. These could give insights into the dynamics of the stellar convection zone and hence the stellar dynamo.

7 Conclusions

One of the key questions in understanding the generation of stellar magnetic fields in how stars like the Sun go from chaotic variability to the regular cycle seen on our Sun today. One of the main windows we have on the operation of stellar dynamos is through the mapping of stellar magnetic fields. Thus our TBL project has set out to study the magnetic fields of five of the brightest young Suns to look for evidence of emerging dynamos in these stars. So far we have obtained two to four epochs of spectropolarimetric observations on the stars. Our preliminary analysis shows at least two of our stars (AF Lep and 111 Tau) have magnetic polarity changes reminiscent of magnetic cycles, with AF Lep showing multiple polarity reversals when combined with previous data. Also, preliminary analysis of the DR of AF Lep shows an intriguing relationship between the level of DR measured from the magnetic features compared to that from the brightness features. Further observations and study of these young stars will enable us to provide new insights into the operation of the powerful stellar dynamo at this important phase of stellar evolution as well as improving our understanding of the impact the infant Sun may have had on the developing Solar system.

We would like to thank the staff at the TBL for their excellent work in obtaining the observations used. This work made use of the SIMBAD database operated at CDS, Strasbourg, France and NASA's Astrophysics Data System Bibliographic Services.

References

Baliunas, S. L., Donahue, R. A., Soon, W. H., et al. 1995, ApJ, 438, 269
Baraffe, I., Homeier, D., Allard, F., & Chabrier, G. 2015, A&A, 577, A42
Collier Cameron, A. & Donati, J.-F. 2002, MNRAS, 329, L23
Donati, J.-F., Collier Cameron, A., & Petit, P. 2003, MNRAS, 345, 1187
Folsom, C. P., Bouvier, J., Petit, P., et al. 2018, MNRAS, 474, 4956
Gaia Collaboration. 2018, A&A, 616, A1
Gallet, F. & Bouvier, J. 2015, A&A, 577, A98
Gudel, M. 2007, Living Reviews of Solar Physics, 4, 3
Hackman, T., Lehtinen, J., Rosén, L., Kochukhov, O., & Käpylä, M. J. 2016, A&A, 587, A28
Jeffers, S. V. & Donati, J.-F. 2008, MNRAS, 390, 635
Jeffers, S. V., Donati, J.-F., Alecian, E., & Marsden, S. C. 2011, MNRAS, 411, 1301
Marsden, S. C., Donati, J.-F., Semel, M., Petit, P., & Carter, B. D. 2006, MNRAS, 370, 468
Marsden, S. C., Jardine, M. M., Ramírez Vélez, J. C., et al. 2011a, MNRAS, 413, 1922
Marsden, S. C., Jardine, M. M., Ramírez Vélez, J. C., et al. 2011b, MNRAS, 413, 1939
Mittag, M., Schmitt, J. H. M. M., & Schröder, K.-P. 2018, A&A, 618, A48
Petit, P., Donati, J.-F., & Collier Cameron, A. 2002, MNRAS, 334, 374
Waite, I. A., Marsden, S. C., Carter, B. D., et al. 2011, MNRAS, 413, 1949
Waite, I. A., Marsden, S. C., Carter, B. D., et al. 2015, MNRAS, 449, 8
Waite, I. A., Marsden, S. C., Carter, B. D., et al. 2017, MNRAS, 465, 2076

SF2A 2021
A. Siebert, K. Baillié, E. Lagadec, N. Lagarde, J. Malzac, J.-B. Marquette, M. N'Diaye, J. Richard, O. Venot (eds)

HIGH PRECISION ABUNDANCES OF FGK STARS WITH (NEO)NARVAL

L. Casamiquela[1], C. Soubiran[1] and Y. Tarricq[1]

Abstract. Chemical abundances of low-mass FGK stars probe the physical processes which drive evolution in the Milky Way. Chemical elements that remain unaltered in the stellar atmosphere through the lifetime of a star are those useful for these type of studies because we assume that the chemical information of the star's birthplace is recorded in its photosphere. Open Clusters are useful for this purpose because they provide ages and distances with good precision. (Neo)NARVAL is among the best instruments to obtain such abundances because of its high resolution and large wavelength coverage.

Keywords: stars: abundances, techniques: spectroscopic, open clusters and associations: general

1 Introduction

To advance towards a broader understanding of the chemical evolution of the Milky Way, detailed element abundances from high-quality spectroscopic data and precise ages are needed. Well studied open clusters (OCs) are frequently been used for this purpose because their age and distances are very precise compared to field stars. Our aim in the latest years has been to obtain detailed and highly precise chemistry of a large sample of open clusters Casamiquela et al. (2017, 2019, 2020). We present here two results which came out of this effort. In Sect. 3 we analyse the chemical homogeneity of three clusters in our sample. OCs have long been thought to be chemically homogeneous(e.g. Friel et al. 2002) as a result of the hypothesis that the cloud from which the cluster was formed was uniformly mixed. Thanks to the good precision in the abundances, our results show some chemical inhomogeneities at the level of 0.02-0.03 dex. In Sect. 4 we investigate the dependency of different abundance ratios with cluster age. The fact that not all chemical elements are produced in the same way or in the same timescale across cosmic times implies that some combinations of elements may have strong dependences on stellar age (see e.g. Nissen 2015; Delgado Mena et al. 2019; Jofré et al. 2020). These have been dubbed as chemical clocks, and can be informative for chemical evolution models to help to understand the variables that control it, like supernovae yields, the star formation rate, or feedback mechanisms.

2 Sample and method

We gathered high signal-to-noise spectra of more than 300 stars in 47 different clusters, from archival data and own observations. Our final sample contains data from the following instruments: UVES@VLT, FEROS@2.2mMPG, HARPS@3.6mESO, HARPS-N@TNG, FIES@NOT, ESPaDOnS@CFHT, ELODIE@1.93mOHP, NARVAL@TBL (several observing programs in 2018 and 2019), and recently in NeoNARVAL@TBL during semesters 2020A and 2020B.

We use the tool iSpec (Blanco-Cuaresma et al. 2014; Blanco-Cuaresma 2019) to perform a spectroscopic analysis to the obtained spectra, normalised and previously homogenised in terms of wavelength coverage and spectral resolution. An example of a NARVAL spectrum can be found inf Fig. 1. Our pipeline uses iSpec to derive precise radial velocities, and also stellar atmospheric parameters and individual line abundances of 25 chemical species using spectral synthesis fitting. Finally, we perform a strictly line-by-line differential analysis of twin stars, which allows to reach a high precision in abundances typically below 0.02 dex. Details of the pipeline are explained in detail in Casamiquela et al. (2020).

[1] Laboratoire d'Astrophysique de Bordeaux, Univ. Bordeaux, CNRS, B18N, allée Geoffroy Saint-Hilaire, 33615 Pessac, France

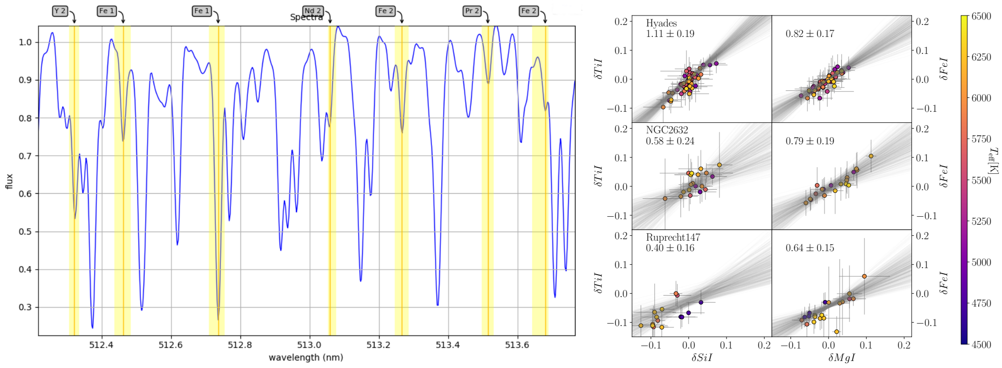

Fig. 1. Left: example of a normalised spectrum from NARVAL, where some of the used lines for the abundance computations are highlighted. Right: abundances of Ti versus Si, and Fe versus Mg for stars in the Hyades, Praesepe (NGC 2632) and Ruprecht 147.

3 Chemical homogeneity

We investigated the level of chemical homogeneity of three of our clusters (the Hyades, Praesepe and Ruprecht 147), the ones for which we have the largest number of stars. We obtain large amplitudes in all chemical species, compared with our uncertainties, and dispersions of the order 0.02-0.03 dex in the Hyades. Moreover, very significant correlations are found for almost all pairs of elements with low dispersions (see an example in Fig. 1). This is a sign of internal chemical inhomogeneity (Casamiquela et al. 2020). Our analysis confirms the previous study by Liu et al. (2016) for 16 stars in the Hyades, including now three times more stars, and two additional clusters.

4 Chemical clocks

Using the sample of clusters inside a 1 kpc bubble around the Sun, we find 19 different combinations of elements $[X_1/X_2]$ that have strong correlations with age in our metallicity range($-0.2 < [Fe/H] < 0.2$). Particularly we find that all combinations involve elements produced via the *s*-process (Casamiquela et al. 2021). We find that Y, Zr and Ba (which have a large contribution to the *s*-process) always produce correlations when combined with α-elements. In Casamiquela et al. (2021) we investigate the validity of the abundance-age relations outside the local bubble. We see that a larger scatter introduced when using the full sample of clusters (half of them farther than 1 kpc). We interpret this as a hint that the chemical clocks may not be as universal as thought, but instead they probably have a dependence on the spatial volume analyzed.

We acknowledge support from "programme national de physique stellaire" (PNPS) and from the "programme national cosmologie et galaxies" (PNCG) of CNRS/INSU. We acknowledge the support of the scientific cooperation program ECOS-ANID Number 180049. L.C. acknowledges the support of the postdoc fellowship from French Centre National d'Etudes Spatiales (CNES)

References

Blanco-Cuaresma, S. 2019, MNRAS, 486, 2075
Blanco-Cuaresma, S., Soubiran, C., Heiter, U., & Jofré, P. 2014, A&A, 569, A111
Casamiquela, L., Blanco-Cuaresma, S., Carrera, R., et al. 2019, MNRAS, 490, 1821
Casamiquela, L., Carrera, R., Blanco-Cuaresma, S., et al. 2017, MNRAS, 470, 4363
Casamiquela, L., Soubiran, C., Jofré, P., et al. 2021, arXiv e-prints, arXiv:2103.14692
Casamiquela, L., Tarricq, Y., Soubiran, C., et al. 2020, A&A, 635, A8
Delgado Mena, E., Moya, A., Adibekyan, V. Z., et al. 2019, arXiv e-prints
Friel, E. D., Janes, K. A., Tavarez, M., et al. 2002, AJ, 124, 2693
Jofré, P., Jackson, H., & Tucci Maia, M. 2020, A&A, 633, L9
Liu, F., Yong, D., Asplund, M., Ramírez, I., & Meléndez, J. 2016, MNRAS, 457, 3934
Nissen, P. E. 2015, A&A, 579, A52

Session 13

Atelier collaboration Amateurs-Professionels

SF2A 2021
A. Siebert, K. Baillié, E. Lagadec, N. Lagarde, J. Malzac, J.-B. Marquette, M. N'Diaye, J. Richard, O. Venot (eds)

JUPITER AND SATURN IMPACT DETECTION PROJECT AN EXAMPLE OF A COLLABORATIVE AMATEUR-PROFESSIONAL PROJECT

M. Delcroix[1], R. Hueso[2] and Impact Team[3]

Keywords: Impact, Jupiter, collaboration, amateur, professional

1 Background and observations

Impacts of objects in the atmosphere of gaseous planets can be observed directly, in the form of luminous flashes caused by the combustion of the bodies at the time of entry into the atmosphere, or indirectly, by the traces of these combustion (dark traces, high in the atmosphere and thus brilliant in the absorption bands of methane).

Jean-Dominique Cassini followed the evolution of a complex dark spot on Jupiter throughout December 1690, a potential sign of an impact trace reminiscent of those left 3 centuries later by the fragments of comet P/Shoemaker-Levy 9.This last exceptional event was observed before the impacts, with the break-up of the comet into 21 bodies, during with the corresponding flashes, and after with traces visible for several months. The next impact was discovered as a trace 15 years later by Australian amateur Anthony Wesley (Hueso 2010).Then as described in Hueso & Delcroix (2018), 6 collisions have so far been discovered exclusively by amateurs in the form of flashes (see Fig. 1) in June and August 2010, September 2012, March 2016, May 2017 and finally August 2019. While the fragments of P/Shoemaker-Levy 9 were of the order of km in size, the 2010 trace came from a body of the order of hundreds of m, and the flashes (of 1 to 2s duration) between 10 and 20m.

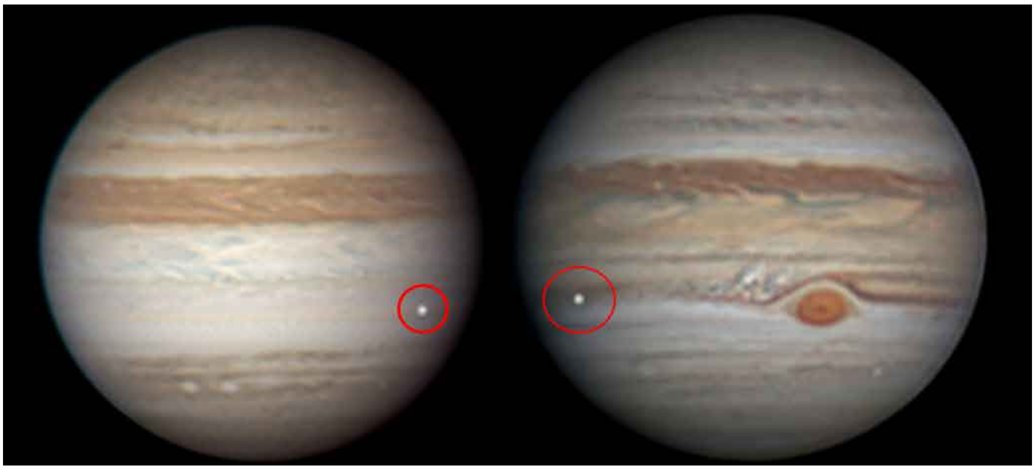

Fig. 1. First and sixth (and last) impact flashes discovered respectively by Anthony Wesley on June 3rd 2010, by looking at the screen during capture, and by Ethan Chappel on August 17th 2019, thanks to the use of the DeTeCt project software after the observation session.

[1] French Astronomical Society, Paris, France
[2] Física Aplicada I, Escuela de Ingeniería de Bilbao, UPV EHU, Bilbao
[3] 109 amateur astronomers from 20 different countries

2 DeTeCt project and software

Following the first amateur discoveries, the planetology team in Bilbao (RH) started in 2010 the development of a software to analyse video for impact flashes. In 2012, MD took over the development (DeTeCt software, see Fig. 2 on the left) to extend the objectives to the estimation of the frequency of the detected impacts, using the logs of the acquisition software used during the captures to date and characterise them, and generating an analysis log. This development has also been punctually supported by the Bilbao team thanks to Europlanet funding, and now counts 27 000 lines of code. It is shared on GitHub.

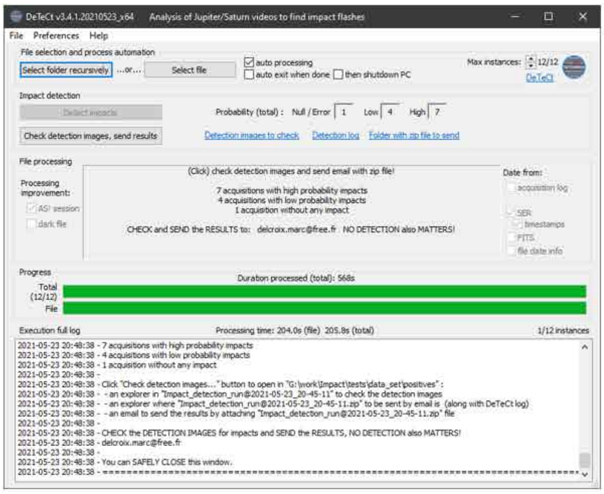

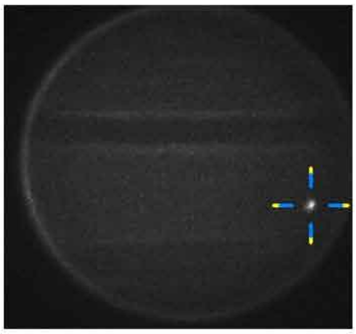

Fig. 2. On the left, the latest version of the DeTeCt software (regularly updated by MD). Right, detection image generated by the software (on the video of C. Go showing the June 2010 impact).

Video analysis works in two ways: A differential photometry algorithm looks for a localised and temporary increase in brightness over the frames that could be caused by an impact flash. A detection image is generated, consisting of each pixel's maximum value minus its average value over the entire video, to highlight a potential impact flash (see Fig. 2 right). The amateur himself analyses the results and detection images and sends them to the project (MD). The project confirms the results and takes them into account with a second consolidation software. The project web page (`http://http://www.astrosurf.com/planetessaf/doc/project_detect.php`) is automatically updated, showing the participation of each amateur, and the calculated estimate of the impact frequency for the planets Jupiter and Saturn (Delcroix 2017).

3 Project results

During its 9 years of existence, 109 participants from 20 countries (mainly in Europe, but also from the American continent, South Africa and Australia) have contributed to the project. Apart from contributions from the T1M at the Pic du Midi (F. Colas with amateurs) and Hampton University (K. Sayanagi), all of the contributions come from amateurs.

The data go back to 2003, and the 165,000 Jupiter videos which were analysed represent the equivalent of 6 full months of observation. Out of the 6 flashes detected, one (the last one in 2019) was only detected thanks to DeTeCt, and would have been missed without the use of the software, which demonstrates the interest of the project.

These data allow us to estimate the frequency of impacts on Jupiter at 13 impacts per year. As the data on Saturn, which is less observed, are much less numerous (28 days of observations), the estimate is currently that the impact frequency is less than 26/year (no impacts have been observed there so far, apart from suspicious traces in the rings observed by Cassini).

The calculated impact frequency for Jupiter is consistent with estimates made by other methods (see Fig. 3).

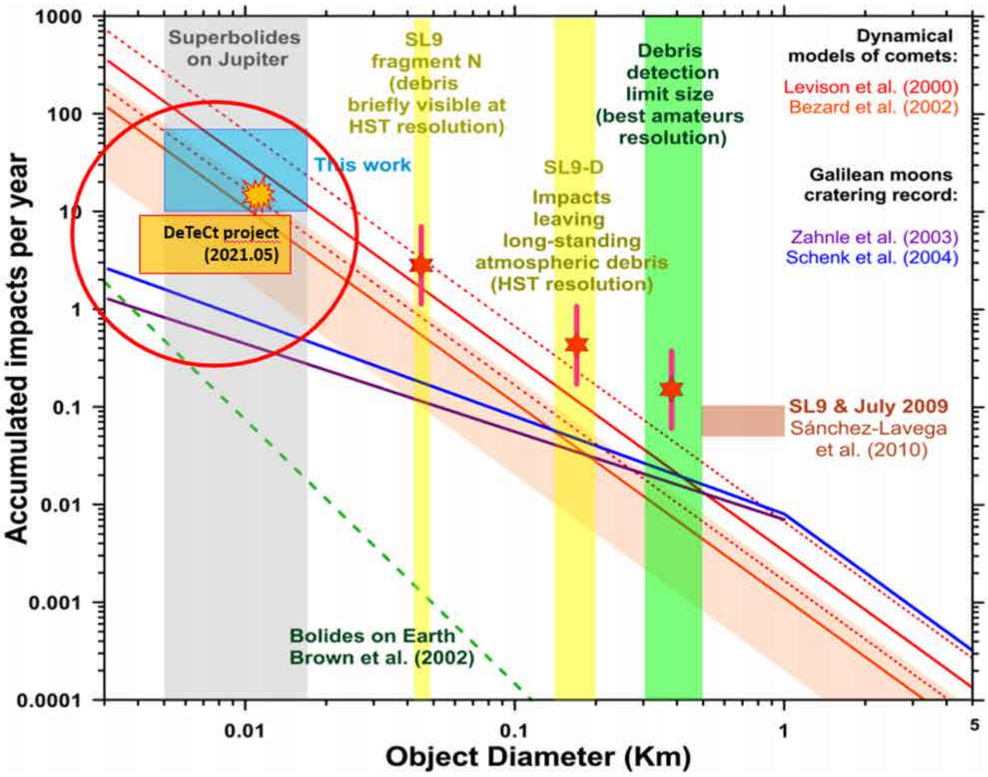

Fig. 3. Estimates by different methods of impact frequencies on Jupiter as a function of impacting body size from Hueso & Delcroix (2018).

4 Scientific value

The study of the light curves derived from amateur observations of impact flashes makes it possible to determine the energy released by the phenomenon by integrating the light intensity during the event (see Hueso (2013), Hueso (2018)). This enables us to estimate the size of the impacting body according to its possible density (which can range from a low-density comet-like body to an iron-like asteroid). On a quality observation such as the one shown in Figure 4, Sankar (2020) could identify simulations of impact light curves (varying as a function of angle of incidence and density) that best reproduce the observation showing the fragmentation of the body in the atmosphere.

These studies contribute to a better understanding of the population of small bodies crossing the Jovian orbit, and of the age of the surface of Jovian satellites as a function of their cratering. This project is a fine demonstration of the contribution of the amateur astronomy community to professional studies.

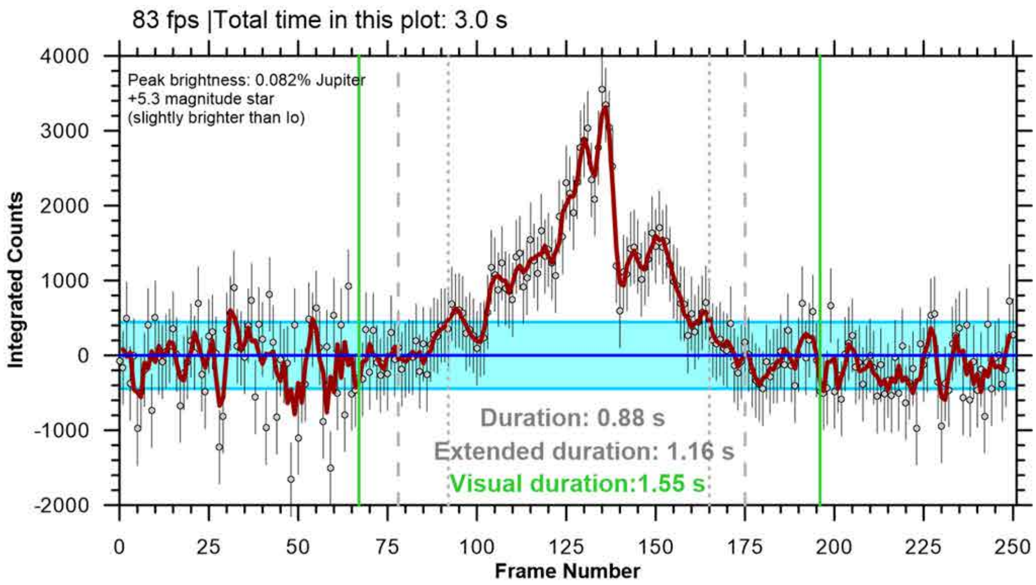

Fig. 4. Light curve of the flash discovered by E. Chappel with DeTeCt, from Sankar (2020). The quality of the observation makes it possible to distinguish secondary flashes.

5 Acknowledgements

We want to thank all amateur astronomers participating to the project.

References

Delcroix, M. e. a. 2017, European Planetary Science Congress

Hueso, R. & Delcroix, M. e. a. 2018, Astronomy and Astrophysics, 617, A68

Hueso, R. e. a. 2010, The Astrophysical Journal Letters, 721, 129

Hueso, R. e. a. 2013, Astronomy and Astrophysics, 560, A55

Hueso, R. e. a. 2018, J. Space Weather Space Climate, 8, A57

Sankar, R. e. a. 2020, Monthly Notices of the Royal Astronomical Society, 493, Issue 4, 4622

ATELIER ETN - WORKSHOP VIRTUAL - HUB SPAIN AND PORTUGAL 15-05-2021

S. García Marín[1,2], J. Álvaro[3,4], I. Garate Lopez[5,6], G. Gilli[4,7], R. Hueso[6], A. Leroy[2,8] and I. Ordóñez Etxeberria[5,9]

Abstract. The Federation of Astronomical Associations of Spain, the Spanish Society of Astronomy, and the Spain & Portugal Regional hub of the Europlanet Society, organized on 15 May 2021 a virtual workshop on the use of the Europlanet Telescope Network for amateur astronomers. The Europlanet Telescope Network is one of the activities of the ongoing Europlanet 2024 Research Infrastructure, and it aims to provide accesibility to professional and amateur astronomers to different telescopes on solar system and exoplanet research topics. After two sessions focused on the presentation of the general characteristics of the network and the closest telescopes, as well as on the writing of funding applications, the 1.23 m telescope of the Calar Alto Observatory was used remotely during the nighttime session to observe two comets, an exoplanet's transit, and Saturn with some of its satellites.

Keywords: Europlanet Telescope Network, virtual workshop, Solar System, amateur astronomer

1 Introduction

One of the activities of the Europlanet 2024 Research Infrastructure project is the Europlanet Telescope Network (ETN), a program to fund access and costs of use to a network of telescopes for observations of Solar System objects and exoplanets. One of the goals of the network is to widen the participation of amateur astronomers in professional and amateur (Pro-Am) collaborations. However amateur astronomers have little to no experience in the subtleties of writing proposals. To counteract this disadvantage the Europlanet Society, through its Spain & Portugal regional hub, together with the Federation of Astronomical Associations of Spain and the Spanish Society of Astronomy decided to organize a workshop on the use of the ETN and on the writing of funding applications. It was held on May 15, Saturday, in order to reach a larger number of attendees and was conducted in Spanish to better communicate with the participants, many of whom are not fluent in foreign languages.

2 Europlanet Telescope Network

The ETN is a network of almost twenty small telescopes scattered all over the world. Although Europlanet does not provide observing time (this should be requested directly to the observatory, preferably before applying for funding), it provides funding for costs associated to observation nights at the telescopes and reimburses travel, accommodation, and per diem of the observer. Proposals eligible for funding are evaluated by an external comittee and eligible topics are those of scientific interest in planetary science (planets, asteroids, comets, exoplanets...).

[1] Société d'Astronomie Populaire de la Côte Basque (SAPCB)
[2] Société Astronomique de France (SAF)
[3] Federación de Asociaciones Astronómicas de España (FAAE)
[4] Spain & Portugal Regional Hub of the Europlanet Society
[5] Comisión Pro-Am de la Sociedad Española de Astronomía (SEA)
[6] Dpto. de Física Aplicada, Euskal Herriko Unibertsitatea (UPV/EHU)
[7] Instituto de Astrofísica e Ciências do Espaço (IACE)
[8] Uranoscope de l'Ile de France
[9] Planetario de Pamplona

3 Agenda and results of the Workshop

The workshop was a virtual event with three live sessions, one in the morning, one in the afternoon and one observation session during the evening/night. In the first one, we presented the telescope network, emphasizing on the closest ones (the 1.23 m of Calar Alto, the IAC80 on Teide and the 1.06 m of Pic du Midi de Bigorre), and we summarized the Pro-Am collaborations or activities carried out by Europlanet and by the Spanish Society of Astronomy, to which the amateurs could contribute. In the afternoon session, we focused on the access to the network and on the process of writing the funding applications, highlighting the potential of amateur proposals and the necessary scientific approach for a successful proposal. The night session was organized around observations of objects previously proposed by the participants. These were the transiting exoplanet WASP-14b (Fig. 1 left), the comets C2021A1 and C2017K2 (Fig. 1 right, top and center), and Saturn and 6 of its moons (Fig. 1 right, bottom). We operated the Calar Alto Observatory's 1.23 m telescope remotely from home.

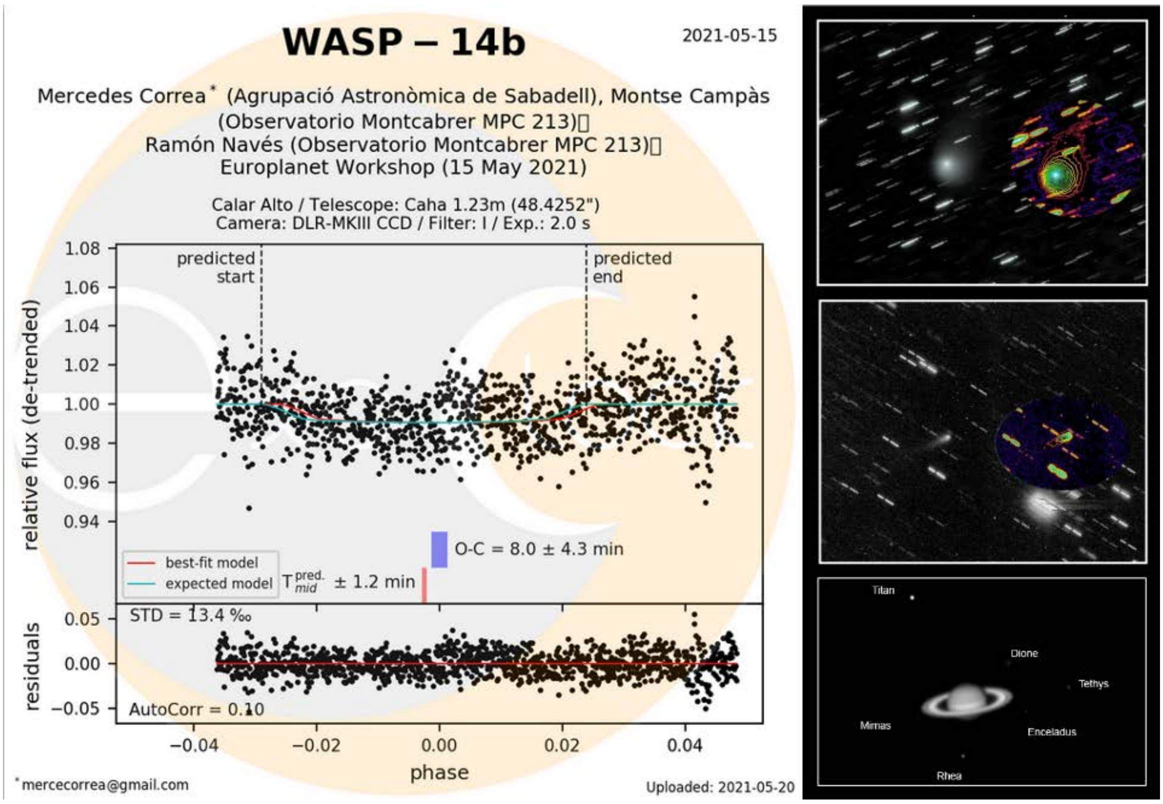

Fig. 1. Left: Lightcurve of exoplanet WASP-14b based on 2 seconds exposures. **Right:** Comet C/2017K2 (top), comet C/2021A1 (center), and Saturn with six moons (bottom). Cometary images are stacks of 25 (top) and 21 (center) exposures of 2 minutes with brightness isolines represented in color in the insets. Saturn was observed with a single shot of 0.01 seconds near dawn. All the data was analyzed by participants of the workshop.

4 Conclusions

The workshop was a great success and Europlanet intends to replicate it in other countries by adapting it to the local amateur community and the language of the country. However, we encourage amateur communities (if interested) to contact the corresponding regional hub of the Europlanet Society to speed things up.

More information at: `https://www.europlanet-society.org/europlanet-2024-ri/telescope-network/`

Europlanet 2024 RI has received funding from the European Union's Horizon 2020 research and innovation program under grant agreement No 871149. We are very grateful to the Calar Alto Observatory for their good disposal and technical support.

SF2A 2021
A. Siebert, K. Baillié, E. Lagadec, N. Lagarde, J. Malzac, J.-B. Marquette, M. N'Diaye, J. Richard, O. Venot (eds)

POLARIMETRIC CORONAGRAPHY TO RECORD THE INITIATION OF CMES

S. Koutchmy[1], F. Sèvre[1], S. Rochain[2], J.-C. Noëns[3] and F. Pitout[4]

Abstract. A new type of polarimetric coronagraph is proposed for permitting citizen Astronomers and Amateurs involved in $H\alpha$ and coronal observations using the Pic du Midi (PdM) Observatory Facilities (so-called CLIMSO) to apprehend and analyze the dynamical processes inside the solar corona. It includes relevant for economic reasons observations of the initiation phase of Coronal Mass Ejections (CMEs) and of recurrent geo-active quasi-polar coronal holes (CHs).

Keywords: coronagraphy, polarimetry, solar corona activity, CMEs, white-light coronal ejections

1 Introduction

The solar activity of the coronal levels modulates different components of the solar wind, CMEs, flares, solar energetic particles (SEPs) and associated disturbances initiated in 3D magnetic separatrices and in open regions. It is today parts of the Space Weather studied before in the frame of solar-terrrestrial relationships. Important investment are planned for developing the Space Weather. So the next decades will see new facilities to cover observations of the dangerous for many Critical Economic reasons (including the survival of sensitive Space Systems) of i/ Coronal Mass Ejections (CMEs) and disturbances especially numerous during the Years of sunspot maximum; ii/ Geoactive recurrent fast events from CHs related to X-ray jet activity from open regions. The important phase of the initiation process at the origin of CMEs is still mysterious: filament eruptions, prominence destabilization, rising coronal cavity inside the hot corona, flares and explosions of active regions coronal enhancement and loops of the low corona, EUV (EIT) coronal waves, arch system interactions with subsequent magnetic reconnections, restructering in singularities of the 3D magnetic separatrices, etc. are suggested. The sophisticated X-EUV space-borne routine instruments will provide coronal temperature sensitive images taken in different coronal emission lines. Unfortunately, no direct measurements of coronal mass storage and motions in the very inner corona and higher can be done in Space. Only a K-coronograph extracting the pB intensities in white-light (WL) can provide this diagnostic related to electro densities. Today advanced commercially available components permit to define a miniature but performing instrumental set-up offering appropriate for advanced Amateurs opportunity to take part in this important routine and exciting research.

2 A prototype: discussion and conclusion

It is proposed to use a new adapted coronagraph to perform this study in the frame of the association called O.A. (Observateurs Associés) of the Pic du Midi Observatory to generously collect data up to 3 solar radii, by recording polarized WL images like it is well done at the MLSO for a long time using sophisticated pB rather large coronagraphs. Note that i/ p is the measured effective linear polarization ratio of the observed total intensities B see Fig. 1; ii/ B is the total intensity observed at ground around the Sun; it includes both the instrumental and the sky background see Koutchmy et al (1990) of very low polarization ratio. ; the superposed K-corona intensities are well polarized in the tangential to the solar limb directions but with a variable amount in both the radial and the tangential directions see Fig. 1. This 2-parts externally occulted instrument will take

[1] Institut d'Astrophysique de Paris, 98 bis Bd Arago, CNRS and Sorbonne University
[2] Association des O.A., Obs. Pic du Midi, France
[3] Pic du Midi Observatory, Bagnères de Bigorre and Association des O.A.
[4] IRAP - CNRS and Univ. Toulouse 3 - France

advantage of the excellent large equatorial mount already in use in the big dome of PdM for the ”CLIMSO” cluster of coronagraphs that routinely analyze the very inner corona. The instrumental parameters of this new instrument we call ”2APC” (Amateur Advanced Polarimetric Coronagraph) are preliminary outlined based on the available space of the mount. The distance between the External Occulter (EO) system see Aime (2020) and the doublet lens of the entrance aperture (effective pupil is of 38 mm diameter aperture) is 6 m. The newly available polarimetric CMos 6 Mpx polarimetric camera (Sony chip) will be used to reach a large multiplexing gain compared to the parameters of the former PdM K-coronometer that was used in the 70ies see Noëns et al. (2000). The first results of laboratory measurements performed with a prototype of the instrument (so-called technological model put on an optical bench) behind a specially designed artificial WL Sun (AS) put at the focus of a 20 cm aperture collimator lens lead to the definition of a model of the inner K-corona around the AS to permit the optimization of the instrumental parameters. We simultaneously plan to work on the software of the polarimetric camera, including its fast recording part to damp the fluctuating sky background Koutchmy et al (1990) and the polarimetric calibration parts to extract the tangentially polarized intensities. Excellent data available from the analysis of solar total eclipses are used as reference. Observations at Pic du Midi could start in 2022-23, well before the forthcoming solar maximum of 2025-26.

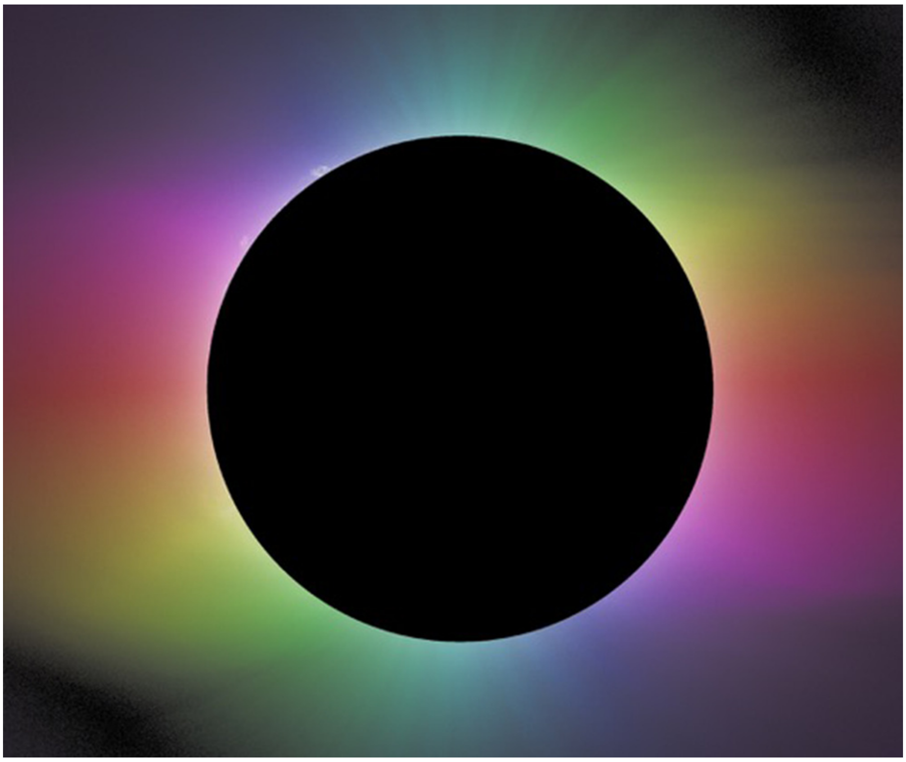

Fig. 1. Map of pB (intensities coded with different color intensities to show as well the directions of polarization observed during the solar total eclipse of 2019. Note the directions of p everywhere in tangential to the limb directions and also the low polarization ratio observed on the prominence at NE. Picture provided by David Elmore-private comm.

Acknowledgements. We thank the support given at the Institut d’Astrophysique de Paris (CNRS and Sorbonne University) for performing optical tests using an artificial Sun put in the basement facilities.

References

Aime, Cl. (2020), Fresnel diffraction of multiple disks on axis-Application to coronagraphy, Astron. Astrophys. 637, A16

Koutchmy, S. Smartt, R. et al (1990) Real-time image processing and data handling for ground-based and spaceborne coronal observations, Proc. SPIE 1235, Instrumenation in Astron. VII; doi: 10.1117/12.19149

Noëns J.C. and J-L. Leroy (1981), Measuring Electron Density in coronal active regions,Solar Phys. 73, 81-87

SF2A 2021
A. Siebert, K. Baillié, E. Lagadec, N. Lagarde, J. Malzac, J.-B. Marquette, M. N'Diaye, J. Richard, O. Venot (eds)

MAKING ADAPTIVE OPTICS AVAILABLE TO ALL: A CONCEPT FOR 1M-CLASS TELESCOPES.

O. Lai[1], S. Kuiper[2], N. Doelman[2,3], M. Chun[4], D. Schmidt[5], F. Martinache[1], M. Carbillet[1], M. N'Diaye[1] and J.–P. Rivet[1]

Abstract. Adaptive optics is challenging for smaller telescopes (0.5∼2m) due to the small isoplanatic angle, small subperatures and high correction speeds needed at visible wavelengths, requiring bright stars for guiding and thus severely limiting the sky coverage. To enable large sky coverage we can correct the turbulence which is common to the entire field we are trying to capture, which is achieved by the technique of GLAO (Ground Layer Adaptive Optics). The turbulence is measured by averaging wavefront measurements in multiple directions. The corrective element can either be a deformable lens or a small adaptive secondary mirror. The motivation to develop such a compact and robust AO system for small telescopes is two-fold: On the one hand, schools and universities often have access to small telescopes as part of their education programs. Also researchers in countries with fewer resources could also benefit from well engineered and reliable adaptive optics on smaller telescopes for research and education purposes. On the other hand, amateur astronomers and enthusiasts might want improved image quality for visual observation and astrophotography.

Keywords: adaptive optics, wide field imaging, GLAO

1 Introduction

Adaptive optics is a technique which is now mature for large telescopes but a number of challenges have hindered our ability to apply this technology for general use, especially for amateur telescopes and astrophotography. Atmospheric phase disturbances increase with decreasing wavelength, and most amateur astronomers are more interested in visible wavelengths (e.g. most nebulas have their strongest emission lines in that part of the spectrum, commercially available large format CCD or CMOS cameras are sensitive at those wavelengths) but adaptive optics in the visible is challenging. In particular for 1-2 m class telescopes, SCAO (single conjugate adaptive optics with only one reference source) imposes severe limitations for sky coverage:

Due to the small physical size of the subapertures on the primary mirror and the high frame rate, the limiting magnitude is bound to be small (around 5∼8, depending on the telescope diameter and the order of the system).

Because the isoplanatic field is very small in the optical domain, the quality of the correction will rapidly decrease further away from the guide star.

Therefore the parts of the sky where adequate correction is possible is limited to tens of arcseconds around some thousands of bright stars or planets. To enable large sky coverage we first recognize that we cannot correct the entire volume of turbulence above the telescope or in a direction where there is no source to illuminate the wavefront perturbation we are trying to correct. The next best thing we can do is to correct the turbulence which is common to the entire field we are trying to capture. This is achieved by the technique of GLAO (Ground Layer Adaptive Optics), whereby a deformable mirror, conjugated to the telescope pupil is used to correct only the ground layer turbulence. This is obtained by averaging wavefront measurements in multiple directions. The corrected wavefront will be limited by the residuals of the free atmosphere turbulence, so resulting images will in general not be diffraction limited but will show a substantial improvement in FWHM.

[1] Université Côte d'Azur, Observatoire de la Côte d'Azur, CNRS, Laboratoire Lagrange, Nice, France
[2] TNO, Leiden, Netherlands
[3] Leiden Observatory, Leiden, Netherlands
[4] Institute for Astronomy, University of Hawaii, Hilo, HI96720, USA
[5] National Solar Observatory, Boulder, CO, USA

2 Motivation to develop AO on 1-2 m class telescopes

The concept we propose opens whole new fields of applications on smaller telescopes and potentially makes adaptive optics accessible to whole new communities: On the one hand, schools and universities often have access to small telescopes as part of their education programs. Furthermore researchers in c ountries with fewer resources would also benefit from well engineered and robust adaptive optics on smaller telescopes, by improving their performance and exposure to advanced optics. On the other hand, amateur astronomers and enthusiasts would be enthusiastic for improved image quality for visual observation and astrophotography. Implementing readily accessible adaptive optics in astronomy clubs would also likely have a significant impact on citizen science.

2.1 VWFWFS: Very Wide Field WaveFront Sensor concept

Every single source in the field contributes to measurement at pupil. Wide fields are required to gather more light and homogenise the flux (as the optical averaging is done on the wavefront sensor and is flux weighted).

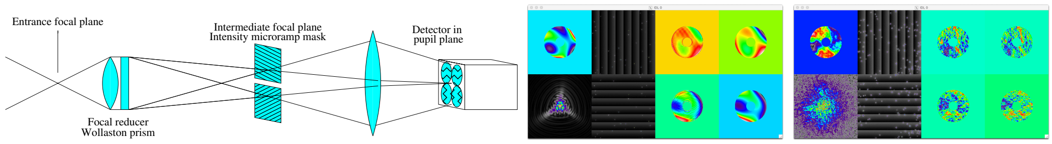

Fig. 1. Left: schematic concept of the VWFWFS, with a mask in the focal plane, introducing an optical differentiation operation, and measurement in the pupil plane. **Middle & Right:** example of reconstructed wavefront derivatives for low order aberrations and a turbulent wavefront respectively.

2.2 Expected performance

End to end Monte Carlo simulations using realistic star field (Besancon Model) with more than 400 sources show a gain of ~ 2 in FWHM and Strehl.

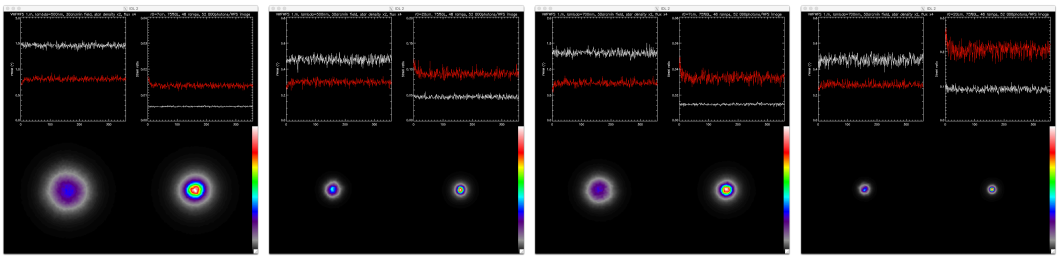

Fig. 2. Strehl and FWHM, White, no correction; red, correction; from left to right: $\lambda = 500$nm, r_0=7cm and r_0=20cm; $\lambda = 700$nm, r_0=7cm, r_0=20cm. In all cases the wavefront sensor has 11×11 subapertures, collecting 2×10^5photons per integration (at 500Hz) over a 30' field of view. Lower row shows corrected and uncorrected PSFs on same scale.

3 Conclusions and future work

Adaptive secondary mirrors are becoming available for smaller telescopes using a new actuator technology developed by TNO. A lab demonstrator is currently being planned and telescope tests are being considered for the C2PU 1m telescope and the UH-2.2m imaka AO system. Simulations show that good sky coverage is possible with a 30' field on a 1m telescope, but large fields require large optics and the optimal field size depends on the telescope size and the application. For a 1m class telescope aimed at astrophotography, 100% sky coverage may not be necessary, since many interesting fields and nebulae can be found near the galactic plane with high star densities. Commercially available large format detectors for amateur telescopes (e.g. ZWO ASI6200MM, based on Sony IMX455 CMOS with 9576x6388 pixels of 3.76µm retails for $4000) cover fields of 10x10 arcminutes with 0.1" pixels; thus for such a system, a 10 arcminute field of view for the wavefront sensor may be more than adequate and only needs a small number of pixels (40×40) read out at 500Hz.

FIRST RESULTS OF THE ANALYSIS OF SOME SPECTRA OF THE AMATEUR SCIENTIFIC PROGRAMME OF THE OBSERVERS ASSOCIATED WITH THE BERNARD LYOT TELESCOPE

A. Lekic[1,2,3], Q. Barussaud[1,4], O. Fayet[1,4], H. Holland[1,4], H. Quénéa[1,4], G. Le Faou[1,4], T. Guitton[1,2], L. Capitaine[1,2], C. Gac[1,2], F. Bellière[1,2] and L. Saunière[1,2]

Abstract. We present here the results of an amateur-professional collaboration between the members of the OATBLs (from an inter-school project IPSA/Ecole Polytechnique) and the support astronomers of the OMP and the TBL (Telescope Bernard Lyot) at Pic du Midi. This poster follows the first results presented in Nice in 2019.

Keywords: stars, metallicity, spectroscopy, polarimetry, Zeeman, Doppler

1 The OATBLs and News from TBL : installation of Neo-Narval

Since 2016, the OATBLs have been filling in the duty observer roster, in addition to the statutory staff, if the schedule cannot be filled. Since 2018, the amateur programme focuses on the study of high metallic stars. Some tools and programs are made by members to process the data. The OATBL association is made up of people from different backgrounds. Most are retired and some are students or employees. In 2020 and 2021, an inter-school project has been set up to work on the data. We present here the first results of this collaboration between Ecole Polytechnique and IPSA. Since September 2019, the Narval instrument, which was coupled to the TBL, has been replaced by its successor : Neo-Narval. This instrument provides radial velocity stabilisation $v < 3m/s$ of the Narval/TBL spectrograph. It will also make it possible to study the links between stellar activity and magnetism around exoplanet host stars. In order to organise the data, a new way of structuring them has been introduced using fits files containing everything the instrument produces as output : observation conditions and data in two related extensions.

2 First results: $H\alpha$ line study and Doppler effect

The OATBL has been actively working for two years now on the analysis of the spectra obtained with Narval and Neo Narval since its installation and start-up. The amateur scientific programme of the OATBL consists of 36 spectra, part of which were obtained with Neo-Narval. In the framework of an inter-school project between IPSA and the Ecole Polytechnique, 10 students were able to help the OATBL by analysing a set of 11 spectra from this programme. Moreover, the OATBL and students checked that the Doppler shift on the lines of these spectra corresponds for each star, within the measurement errors, to that obtained in the literature. This shows that the adjustment made by the students of the inter-school project inside OATBL association, is correct. Only two stars stand out from the crowd by their different Doppler coefficient values, due to the multiplicity of their stellar system.

[1] OATBL
[2] IPSA
[3] SAF
[4] École Polytechnique

Nom	Type de décalage	k mesuré	Vélocité radiale mesurée en km/s	k tabulé	Vélocité radiale tabulée km/s	Erreur relative
4cam	*redshift*	$8,38 \times 10^{-5}$	25,14	$7,51 \times 10^{-5}$	22,5	11,6 %
30lmi	*redshift*	$4,28 \times 10^{-5}$	12,84	$4,60 \times 10^{-5}$	13,7	6,9 %
c Her	*blueshift*	$-10,60 \times 10^{-5}$	-31,8	$-10,51 \times 10^{-5}$	-31,5	0,8 %
f UMa	*blueshift*	$-0,15 \times 10^{-5}$	-0,45	$-0,03 \times 10^{-5}$	-0,10	400 %
hd23193	*redshift*	$7,89 \times 10^{-5}$	23,68	$9,11 \times 10^{-5}$	27,3	13,4 %
hd28204	indéterminé	$-5,32 \times 10^{-5}$	-15,95	$3,30 \times 10^{-5}$	9,9	261 %
hd99747	*blueshift*	$-3,34 \times 10^{-5}$	-10,01	$-3,18 \times 10^{-5}$	-9,54	5,0 %
hd169885	*blueshift*	$-1,37 \times 10^{-5}$	-4,11	$-1,23 \times 10^{-5}$	-3,7	11,4 %
hd179143	indéterminé	$-0,91 \times 10^{-5}$	-2,73	$0,92 \times 10^{-5}$	2,76	199 %
hd200407	*blueshift*	$-2,06 \times 10^{-5}$	-6,17	$-2,60 \times 10^{-5}$	-7,8	20,8 %
hr4021	*redshift*	$4,27 \times 10^{-5}$	12,80	$3,6 \times 10^{-5}$	10,8	18,6 %

Fig. 1. Doppler Effect : Measured VS. Tabulated Coefficients

3 First results: Doppler-Zeeman effect, link with polarisation and magnetic field

The inter-school project has shown that it is unfortunately difficult, if not impossible, to obtain correct magnetic field values by studying the Zeeman effect alone. Indeed, despite the high resolution of Neo-Narval, the Zeeman effect is hardly visible even on the Fe I and Fe II lines, which are nevertheless sensitive to it. The lines are not resolved and an important Doppler effect is added to the Zeeman splitting, which makes it almost impossible to obtain the magnetic field by this means. Thus, the students, together with the OATBL, decided to focus on the set of 3 spectra of high metallicity stars obtained by Neo-Narval. Polarisation is the orientation of the electromagnetic field of the light received by the detector. When the star has a stronger or weaker magnetic field, information on the polarisation of the light can be obtained from its spectrum and the value of the star's magnetic field can be determined by knowing the Stokes parameters (I, V, Q and U). A python code was developed by the students to find the intensity I, and the intensity V of the circular component as well. Extracting I and V from the data cube allowed the students and the OATBL, using a fairly simple formula $Bcos\theta = \frac{4\pi mc}{eg_c}\frac{IV}{\lambda^2 \frac{dI}{d\lambda}}$, to propose longitudinal magnetic field values for several lines and for the three high-metallicity stars. The analysis of the results is still in progress but there is for the moment a weak correlation between the expected values from the literature and the magnetic fields found. It is likely that the method of measuring the offset between the centres of the polarised lines, an important value for tracing the magnetic field, is at the origin of these magnetic fields that differ from the expected values. The order of magnitude, however, seems to be appropriate.

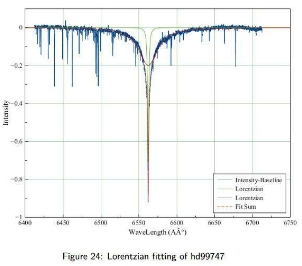

(a)

Étoile hd141675
(type A3m)

λ_{th} (en Å)	B cos ϑ (en G)
6609, 11	313, 92
4520, 22	2862, 67
5328, 53	3365, 81
6456, 24	2542, 28
5260, 25	2708, 93

Étoile hd127381
(type B1/B2V)

λ_{th} (en Å)	B cos ϑ (en G)
4520, 23	763, 10
5001, 95	808, 50
5328, 53	483, 06
6546, 24	159, 78
6667, 99	442, 90
6750, 15	8, 93

(b)

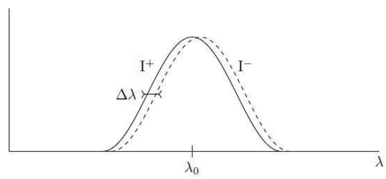

(c)

Fig. 2. Lorentzian Fitting (a), Values of B-field obtained (b) , Circular polarisation profiles (c)

4 Conclusion : Prospects for further analysis of the spectra of the OATBL science program

The possibility that a Stark effect influences the structure of the lines of these stars, in particular the Balmer line, is being studied in the literature by the association. Is there a correlation between metallicity and the parameter of this line? What about the magnetic field strength ? Is there a link between metallicity and magnetic field strength? Do these stars have exoplanets around them ? Is there a link between metallicity and the existence of exoplanets taking into account an average magnetic field strength ? These are some questions that the OATBL and all the members who are involved in the analysis of these stars would like to answer.

2021 GEMINI TABLE OF THE AMATEUR PROFESSIONAL COLLABORATIONS

T. Midavaine[1]

Abstract. For this third workshop dedicated to Amateur Professional Collaborations organized in the "Journées de la SF2A", here is the update of the data base of the all the known topics with the latest information gathered in the GEMINI table. For this third workshop in the online organisation of "2021 Journées de la SF2A" this release allows authors and participants to introduce the latest inputs related to the topics they are involved in or even create new lines. This is an important action in the frame of the GEMINI partnership between SAF and SF2A.

Keywords: citizen science, amateur-professional, pro-am collaborations, astronomy

1 Introduction

Thanks to the two very successful workshops hold during the "Journées de la SF2A" 2018 in Bordeaux (Midavaine 2018), then 2019 in Nice (Midavaine & Herpin 2019a), SF2A and SAF decided to organize this third workshop in the frame of their partnership. The 2021 online organisation of this workshop allows a wide participation both for authors and attendance. This annual meeting gives the opportunity to share on a poster this table gathering all the Amateur Professional Collaboration topics and to update it with the latest data to release here in the proceedings the version AA of the table.

2 The Amateur-Professional Collaboration Topics Table

0 years ago I consolidated a data base in an Excel file gathering the panorama of astronomical topics for amateurs willing to do science. It was first published on the Club Eclipse web site * then in "l'Astronomie" (Collectif 2009) and in 2019 during the IAU meeting (Midavaine & Herpin 2019b). This 2021 version AA of the data base classifies amateur activities breakdown in five headlines:

- Object discovery : the most fascinating task for amateurs is the ability to discover new objects,
- Object surveillance: one amateur strength, thanks to the observer numbers spread over all the Longitudes and the quotidian weather diversity range,
- Observation campaign : mobilization of observers on astronomical events for data acquisition,
- Data gathering : Thanks to methodologies, digital imaging and processing, amateurs can provide reliable metrological data in five scales :
  - Astrometry
  - Photometry
  - Polarimetry (useful for few topics)
  - Spectroscopy
  - Time and datation

[1] Société Astronomique de France, 3 rue Beethoven, 75016 Paris, France
*Club Eclipse web site `http://astrosurf.com/club_eclipse`

- Exploitation of data base : this is a growing up field, thanks to dedicated web site gathering the overwhelming data collected by robotic instruments or space probes

Through the lines in column A, you have a review of all the potential topics from the closest like shooting stars, up to the farthest related to quasars or even cosmology! The columns are organized according to the above activity breakdown. It covers all the topics spread over a large range of required skillness from the beginners to start to do science up to the amateur experts, including the thema for amateur professional collaborations from data acquisition, up to scientific publishing. Here are some comments on the column contents:
Column B gives the minimum magnitude to reach to be able to perform the respective object discovery. You may notice this magnitude start from 6 with Nova discovery easily done every year with Digital Single Lens Reflex (DSLR) Camera with standard high aperture lens.
Column C gives the Surveillance program name or reference.
Column D gives the event for dedicated campaign to acquire data.
Column E : does the topic requires metrology ? These metrologies are quoted in the five following columns with the minimum useful accuracy required from the instrument, of course an improved one could be wished.
Column F: the waited accuracy in arc second for Astrometry.
Column G: the relative accuracy for Photometry.
Column H : the useful accuracy of Polarimetric ratio.
Column I : the waited Spectral resolution.
Column J: the Time accuracy (datation and sampling) in second for the above measurements or surveillance and event detection.
Column K you have the on line data base reference where amateur or citizen contribution is waited.
Column L : you have the "Castor" the name of the amateur focal point in France or abroad.
Column M: you have the "Pollux" the name of the professional focal point in France or abroad.
Column N : the name of an organisation or Society coordinating the topic.
Column O : the web site dedicated to the topic.
Column P : an e-mail address, this is often the e-mail address of the focal point or of the organisation.
And in column Q : the name of the conference gathering the actors on the field.

This table could be used in several ways. One of the purposes is to allow amateur astronomers, amateur observatories, amateur societies and scolarship projects to choose a topic and to define the fitted instrument setup. I quote in several colors the table cells to allow a quick access to any project :
Blue : the easiest topics for the beginner with small instrument,
then in Green : topics relying on a dedicated process methodology, a 200mm maximum telescope aperture is enough,
then in Orange : topics requiring large telescope 500mm aperture class with sensitive and accurate instruments to analyze and record signals and accurate amateur skillness. This is where Amateur Observatories and Amateur Mission Telescopes like T60 [†], Astroqueyras [‡] or TJMS [§] are meaningful referent organisation for these projects,
then in Purple : very challenging topics requiring heavy hardware with involvement of thousands of hours which is achievable for amateur dedicated instruments.

Therefore all the known amateur professional collaborations are quoted in this table. Some are old topics waiting to be awake. Some topics meet strong interest without professional involvement for it's historical perspective or pedagogic purpose. Another way to use this table is to take empty cells to wonder whether it could become a new active topic. Thanks to the papers and lectures from the communities, given all along the years, the file is updated at least once a year. Here is the version AA of the table released in 2021, this up date includes the latest data introduced during this workshop. Feel free to contact us for proposing new inputs for the 2022 update. Today it is in French, dedicated to the francophone community; an English worldwide version could be prepared through multi-country partnerships and with IAU as it was proposed in Bruxelles during the Amateur day of the 100th year IAU Symposium (Midavaine & Herpin 2019b).

[†] Association T60 Observatoire Midi Pyrénée web site `http://www.astrosurf.com/t60/`
[‡] Astroqueyras web site `https://www.astroqueyras.com/`
[§] TJMS web site `https://www.planete-sciences.org/astro/Le-Telescope-Jean-Marc-Salomon`

3 Conclusions

The SAF SF2A partnership is now running with the delivery of several productions meeting the amateur professional collaboration needs with

- This table update
- The organisation of the annual GEMINI Prize awarding the best Amateur Professional Collaboration through a call for candidates. The third GEMINI Prize will be launch beginning of 2022
- The GEMINI collaboration web portal ¶
- Prepare the proposal of a fourth Amateur Professional Workshop during the next Journées de la SF2A scheduled in June 2022 in Besançon.
- Prepare a third Photometry School

References

Collectif. 2009, in L'Astronomie, Vol. 123, 16

Midavaine, T. 2018, in SF2A-2018: Proceedings of the Annual meeting of the French Society of Astronomy and Astrophysics, ed. P. Di Matteo, F. Billebaud, F. Herpin, N. Lagarde, J. B. Marquette, A. Robin, & O. Venot

Midavaine, T. & Herpin, F. 2019a, in SF2A-2019: Proceedings of the Annual meeting of the French Society of Astronomy and Astrophysics, ed. P. Di Matteo, O. Creevey, A. Crida, G. Kordopatis, J. Malzac, J. B. Marquette, M. N'Diaye, & O. Venot

Midavaine, T. & Herpin, F. 2019b, in IAU 100 years, Amateur Day, Bruxelles, Belgium

¶Gemini web site `https://proam-gemini`

The Amateur-Professional Topics Table Version AA the 2021 update.

Objets	Découvertes	Suivi	Evenements	Métrologies	Astrométrie	Photomètrie	Polarisation	Spectroscop	Rés Tempor	Exploitation	Castor	Pollux	Organisation	site web	e mail	Conférence
Unités	Mag min				arcsec	Précision	Taux de Pol	P Résolution	seconde	sur Internet	Amateur référent	Professionnel réf	Association	astro-proam.com		
Météorites		Vigie-Ciel										Brigitte Zanda	Vigie-Ciel	Vigie-Ciel.org		Commission des météores SAF
Météores	-4	Fripon	Fragmentatio	Orbite, Impac	60				1		Karl Antier	Francois Colas	REFORME	https://www.fripon.org/	http://www.reforme-meteor.net	International Meteor Conference
Essaims d'étoiles filantes	1	Orbite	Sursaut	ZHR Radian	240				60		Karl Antier	J. Vaubaillon	IMO	www.imo.net	http://www.reforme-meteor.net	International Meteor Conference
Cratères d'impact terrestre										Google Earth		David Baratoux				
Aurores Boréales														www.spaceweather.com	wagner.d@uni-jena.de	
Night Glow																
Sprite																
Rayons Cosmiques																
Lune			TLP	Occultation Rasante			0.1	10	0.1	Moon zoo			ALPO, IOTA	users.aber.ac/atc/tlp/tlp.htm		
Impacts sur la Lune			flash										IMCCE	http://uranoscope.free.fr		
Lumière Cendrée								10				Luc Arnold				
Lumière Zodiacale										Stardust						
Planètes		Météorologie	Tempète, Occultation					100	1			SAF commission	ALPO	www.astrosurf.com/planetessaf/	delcroix.marc@free.fr	European Planetary Science Congress
Venus		Akatsuki									Christophe Pellier	Peralta	Akatsuki		coordinatewithakatsuki@gmail	European Planetary Science Congress
Mars		Météorologie	Tempete, nuages							planet four	Christophe Pellier		ISMO	http://www.mars.dti.ne.jp/~cmo/ISMO.html	chrispellier@sfr.fr	European Planetary Science Congress
Jupiter		Junocam	Impacts							missionjuno.swri.edu	Marc Delcroix		SAF	www.missionjuno.swri.edu/junocam/	delcroix.marc@free.fr	Commission des observations planétaires
Jupiter		Météorologie	évolutions formations atmosphériques								Christophe Pellier	Kévin Baillié	Jupos, IOPW	https://www.imcce.fr/recherche/campagnes-observations/impacts/impacts	kevin.baillie@observatoiredepa	European Planetary Science Congress
Saturne		Météorologie	Tempete								Marc Delcroix	Marc Delcroix	SAF, IOPW	http://pvol2.ehu.eus/pvol2/	delcroix.marc@free.fr	European Planetary Science Congress
Uranus, Neptune		Météorologie	Tempete								Marc Delcroix	Marc Delcroix	SAF, IOPW	http://pvol2.ehu.eus/pvol2/	delcroix.marc@free.fr	European Planetary Science Congress
Impacts sur les Planètes géantes		Impact							1		Marc Delcroix	Ricardo Hueso	Impact Team	http://www.astrosurf..com/planetessaf/doc/project_detect.php	delcroix.marc@free.fr	
Satellites de Planètes	21		Occultation	Phemu	0.04	0.1			0.1			Jean-Eudes Arlot,	IMCCE	www.imcce.fr/phemu09	Jean-Eudes.Arlot@obspm.fr	
Astéroides (orbites)	19	Position	Occultation		0.2	0.1			0.1	http://www.asteroidzoo.org/		Jerome Berthier	MPC	www.minorplanetcenter.net/iau/	mpc@cfa.harvard.edu	http://m1p.fr/sof/
Astéroides (objets)		CdR	Occultation			0.05		10	0.1	Asteroids@home		Benoit Carry, Eric	EAON, IOTA,	www.euraster.fr		ESOP
Astéroides longues périodes		CdR		14		0.1					Stéphane Fauvaud			http://hebe.astro.amu.edu.pl	sfauvaud@mail.com	
Satellites d'astéroides	CdR ou Occu	CdR	Occultation			0.01			0.1			Raoul Behrend	CdR-CdL	http://obswww.unige.ch/-behrend/page_cou.html		
Géocroiseurs AAA	19			Orbite, Impact				10	0.1	orbit@home		Mirel Birlan	EURONEAR	http://www.minorplanetcenter.org/iau/NEO/TheNEOPage.html		
Troyens			LUCY									Marc Buie		http://lucy.swri.edu/		
Objets Trans Neptuniens	20		Lucky Star		0.2	0.2		10	10			Bruno Sicardy	LESIA	http://lesia.obspm.fr/lucky-star/predictions/	Bruno.Sicardy@obspm.fr	
Objets de la bande de Kuiper				Myosotis				10				Francoise Roque				
Planète 9										Backyard Worlds: Planet 9						
Comètes	14		Sursaut, Fragmentation		0.2	0.2		100	1	Soho		Nicolas Biver	CBAT	www.cfa.harvard.edu/iau/mpc.html	cbatiau@eps.harvard.edu	Commission Comètes SAF
Comete 67P Tchouri			CdR								David Romeuf					
Objets du Système Solaire	18		Gaia-FUN-SSO		1	0.2						William Thuillot	IMCCE	https://gaiafunsso.imcce.fr/index.php	thuillot@imcce.fr	
Soleil Taches		Nbre Wolf					0.05	1000	0.1	Soho		Didier Favre	GEFOS	http://solardatabase.free.fr		Commission du Soleil SAF
Soleil Protubérances			Eruption, Eclipse				0.05	1000	0.1	Solar stormwatch	Franck Vessière	Pitout	Observateurs	www.climso.fr		liste astrosoleil
Soleil Couronne			Eclipse Totale 08/04/2024		0.1		0.001				Xavier Jubier	Serge Koutchmy			xjubier@free.fr	
Etoiles			Alertes GAIA	Temp Classe Spectrale				10		http://cdsportal.u-strasbg.fr/		Paolo Tanga		http://gsaweb.ast.cam.ac.uk/alerts/		
Etoiles à record				Mouvement p	0.1	0.1		10	10000	DASCH		CDS	D. Gray modèle des atmosphères			
Jumelles du Soleil	9															
Etoiles Doubles	11		Luhman 16		0.1	0.1		10	100000		A. Debackère	David Valls Gabau	WDS USNO	http://ad.usno.navy.mil/wds	dbrstars@gmail..com	Commission des étoiles doubles SAF
Binaires Spectroscopiques								1000				Daniel Bonneau				
Binaires à éclipses EA EW	12	Photometrique				0.01	0.1	10000	1000	VSX	Laurent Corp		AAVSO/VSX	Gerry Samolyk	astro.laucorp@orange.fr	
Etoiles Variables	10	CdL				0.1			100			Dominique Proust	AFOEV	http://astro.u-strasbg.fr/afoev	afoev@astro.u-strasbg.fr	International Meeting on Variable Stars
Céphéides		0	Maxima puls	Spectres				10000	300-3600	aavso.org/vsx		Denis Gillet, Philip	GRRR	http://www.aavso.org/vsx/index.php?view=search.top	Philippe.Mathias@irap.omp.eu	
RR Lyrae	14	GRRS	Maxima pulsation			0.01			300-900			Jean-Francois Le B	GEOS	http://rr-lyr.irap.omp.eu/	jean-francois.leborgne@irap.or	Workshop annuel à l'OHP
RR Lyrae ondes de choc				Spectres				10000			Benjamin Mauclair	Denis Gillet			bma.ova@gmal.com	
Delta Scuti						0.1									denis.gillet@osupytheas.fr	
Etoiles Be, Eruptives	12		Sursaut			0.1		1000	10000	BeSS		Coralie Neiner	ARAS	http://basebe.obspm.fr/basebe		Stages Spectro OHP Aude
Etoiles OB actives											Christian Buil		ARAS	www.astrosurf.com/buil/index.htm		
Etoiles Cataclismiques												Etienne Morelle		http://cbastro.org		
Etoiles Symbiotiques											Francois Teyssier		AAVSO		francois.teyssier@dbmail.com	
Nouvelles classes variables						0.001			100			Denis Gilet	GRE	Pulsating star		OHP
Ddisparitions d'étoiles		Vasco												https://ui.adsabs.harvard.edu/abs/2020arXiv200910813V/abstract		
Pulsars	10					0.1			0.01	einstein@home		Fabrice Mottez		http://einstein.phys.uwm.edu/		
Trous Noirs Galactiques																
Disques Stellaires										diskdetective.org			satellite WISE	http://www.diskdetective.org		
Planétes Extra Solaire		Vitesse radia	ExoClock			0.01		10000	10	planethunters.org		Alexandre Santern	transitsearch.	http://var2.astro.cz/ETD	http://brucegary.net	http://var2.astro.cz/ETD/
			WASP 184b									Guillaume Hebrard				
Super-Terres										https://exoplanetarchive.ipac.caltech.edu/		Jean-Philippe Beaulieu		http://exoplanet.eu		
Satellites de Planètes Extra Solaire						0.01			10			Jean Schneider, David Kipping		https://www.exoclock.space/project		
Vie extraterrestre										seti@home			SETI	seti@home		
Novae de la Voie Lactée	6					0.05			10000		Francois Teyssier	Steve Shore	CBAT	http://www.cbat.eps.harvard.edu/index.html	cbatiau@eps.harvard.edu	
Super Novae Voie Lactée	0	ASAS-SN									Emmanuel Conseil			http://www.cfa.harvard.edu/iau/cbat.html	skypub.com/supernovarace	
Remanents de SN					1		0.1	1000	100000			Agnés Acker				
Nébuleuses Planétaires	16			étoile centrale			0.1	600		HASH Database	Pascal Le Dû		Deep Sky Hu	http://planetarynebulae.net/	pascal.le.du@shom.fr	https://apn7.com/
Nebuleuse de Wolf-Rayet										Digital Sky Survey		Agnés Acker			agnes.acker@astro.unistra.fr	
Nébuleuses								1000								
Bulles cosmiques										Milky way project				www.milkywayproject.org		
Amas d'étoiles et asterisme	9					0.01		10		Milky way project		Jose Peña Institut d'Astronomie Mexico				
Amas Globulaires																
Voie Lactée										MilkyWay@Home				http://milkyway.cs.rpi.edu/milkyway/		
Galaxies naines																
Galaxie d'Andromède	Novae									PHAT				http://www.andromedaproject.org/		
Novae galaxies voisines	16	photométrique			0.1	0.1				http://www.rochesterastronomy.org/n	Emmanuel Conseil			http://econseil.blogspot.com/	econseil@gmail.com	
Amas d'etoiles galaxies voisines										http://www.projectstardate.org/						
Galaxies	green peas	Classification								Galaxy zoo :3D				www.galaxyzoo.org		
Galaxies à noyaux actifs				Variabilité AGN												
Micro Quasars												Katherine Blundell	Oxford			
Quasars	15		Sursaut			0.1		10	10000			Jean Schneider	Surveillance du Quasar Triple			
Supernovae	13 - 21	photometrie/s	Gaia Alerts		0.1	0.1		10	10000	www.rochesterastronomy.org/snimage	Emmanuel Conseil	Michel Dennefeld	TNS	https://wis-tns.weizmann.ac.il/	econseil@gmail.com	SNAude
Gamma Ray Burst	18	contrepartie	SVOM			0.1			10000			Bertrand Cordier	CEA	http://gcn.gsfc.nasa.gov		
Ondes Gravitationnelles	17	contrepartie	GRANMA KNC O4					2			Antoine Cailleau	Sarah Antier	IN2P3	https://grandma.lal.in2p3.fr/	sarah.antier@oca.eu	
Amas de Galaxies	20			Mesure de Z		0.5		10				Vincent Boucher			aapeteam@protonmail.com	
Filaments extragalactiques												David Valls Gabau	GEPI OBSPM			
Contres parties Neutrinos																
Lentilles Gravitationnelles										space_warps		Alain Klotz		https://www.zooniverse.org/project/space_warps		
Autres Objets																
Matière Noire												David Martinez-Delgado Max Plack Institute				
Energie noire																
Cosmologie						0.1		10		cosmology@home	Jean-Pierre Martin		SAF	http://www-cosmosaf.iap.fr/		SAF Commission Cosmologie
										www..zooniverse.org						Les Rencontres du Ciel et de l'Espace
Code Couleurs Sujets Coll Amateurs-Pro		Facile		Exigeant		Difficile		Challenge		boinc.berkeley.edu						
AA V3 Septembre 2021 Thierry Midavaine GEMINI			https://proam-gemini							scistarter.com						

Session 14

Transition environnementale : quel rôle pour la communauté astronomique?

SF2A 2021
A. Siebert, K. Baillié, E. Lagadec, N. Lagarde, J. Malzac, J.-B. Marquette, M. N'Diaye, J. Richard, O. Venot (eds)

ASTRONOMERS FOR PLANET EARTH: FORGING A SUSTAINABLE FUTURE

F. Cantalloube[1], L. Burtscher[2] and the Astronomers for Planet Earth collective

Abstract. The last few years have witnessed strong consequences of the on-going climate crisis in every part of the globe that are difficult to ignore. Taking advantage of their unique view over life in the universe and their privileged attention from the public, a group of professional astronomers, astronomy students and educators, gathered in late 2019 to form the international collective *Astronomers for Planet Earth* (A4E). A4E shares resources to inform, advocate and act on the necessary environmental transition to be undertaken, both with the astronomical community and the general public. As of today, A4E gathers more than 1331 members from more than 73 countries. In this communication we provide a description of A4E, list the main activities completed up to now and give an outlook to future developments.

Keywords: SF2A-2021, S14, environmental transition, climate crisis, astronomical community

1 Statement of the A4E collective

As astronomers, we do have tools and methods that we can use to defend climate science and debunk the misconceptions used by climate deniers and delayers to blur the sense of emergency. In addition, by exploring notions of habitability and by studying the atmospheres of other planets, we have a specific view on the uniqueness and fragility of ecosystems on planet Earth, even though we are not climate scientists. Many fundamental questions about the formation of stars within galaxies and planets remain unanswered, demonstrating the complexity of the emergence of life as we know it on Earth. Astronomy also brings to society images of the cosmos that can trigger a sense of wonder and empathy. Images of planet Earth itself highlight the thin atmosphere that protects, harbors and sustains life in all its wondrous forms, not all of which are yet revealed to our eyes. Astronomy is a source of inspiration for most humans. Astronomers therefore have privileged access to the general public and can use this advantage to make their voices heard in favour of the protection of planet Earth. Therefore, we believe that, as scientists working for the citizens of Earth, we have a role to play and a responsibility to communicate about the on-going climate and environmental crises.

Fig. 1. A4E logo

Astronomer for Planet Earth (A4E) is a volunteer network of current and former professional astronomers (including staff scientists and members of faculties, postdocs and PhD candidates), students in astronomy, educators, amateur astronomers, journalists and writers, working in institutes, observatories, universities, museums or planetariums, who are committed to advocate the science behind the climate crisis and associated climate justice and to take actions to fight against all arguments delaying climate action (e.g. denial, diversion, doomism, green dictature, individualism, competition, greenwashing, compromise etc.).

A4E is working in two directions, inside and outside the astronomical community. To provide the public with information: (i) sharing the astronomical perspective of Earth, (ii) explaining the science behind the climate change, and (iii) sharing information about solutions to the climate crises. To provide astronomers with tools: (i) establishing a community to share ideas and amplifying our voices, (ii) working together to identify opportunities for meaningful actions, and (iii) gathering resources to educate ourselves and others.

In addition, astronomers also have responsibilities with their high carbon footprint, mainly due to the nature of the field including running observatories in remote areas, running large simulations on supercomputers and frequent overseas travel to reach observatories or attend conferences all over the world. A4E therefore is pushing astronomical institutions, societies and observatories to adopt sustainable practices. The A4E collective wrote a white paper summarizing their statement, that can be found here.

[1] Aix Marseille Univ, CNRS, CNES, LAM, Marseille, France
[2] Leiden Observatory, The Netherlands

2 Means of communication

Communication within A4E members: When signing-up to become a member of Astronomers for Planet Earth, one can opt in to appear on our public partner page and choose to receive the newsletters (groups.io platform). Members can also join the dedicated Slack space, which gathers specific channels for projects (e.g. white paper, special session to conferences, proceeding writing), working groups (e.g. website, roadmap, regional discussions), general information about A4E (e.g. webinar series, resources, related conferences announcements) or topical discussions (e.g. emotional support, reduction of waste, food habits, reducing flights). Documents used for communication are shared and accessible to all members upon demand on a dedicated Google Drive and a dedicated member section of our future website. Finally, regular online meetings for members are organised to discuss the current and future A4E projects and each topical working group organises online meetings when needed. Note that we collaborate over almost all time zones and most of us have never met in person.

Communication within the astronomical research community: Inside the astronomical community, members can touch upon the topic and potentially present A4E during conferences; suggestions of introductory slides and posters are available in the Google Drive. In addition, A4E organised special sessions on sustainability during the meetings held by the various astronomical societies, such as the American Astronomical Society (AAS), the European Astronomical Society (EAS) or Astronomical Society of the Pacific (ASP). A4E provides support if members want to organize a dedicated workshop about sustainability at a national astronomical society meeting (e.g. French Astronomical Society, SF2A or Spanish Astronomical Society, SEA). At last, the A4E website provides numerous links towards other collectives, initiatives and organisations, at different levels in academia: institutes, institutions and observatories or national initiative such as Labo1point5 in France.

Communication with the general public: The main way of communicating is through regular social media such as Facebook and Twitter (more than 1100 followers) for short facts, and Vimeo and YouTube for videos. The collective is cooperating with other outreach organizations such as Astronomy on Tap and the Astrobites community, which gives space for members to discuss astronomy in the context of the environmental crises (see here). Various resources are shared on the A4E website and Google drive with ideas and suggestions to present, demonstrate and start discussions about the climate crisis, seen through the astronomical perspective.

3 Examples of actions led by A4E

Open Letter: A working group of A4E members recently wrote an Open Letter for astronomers to sign, calling on astronomy departments, institutions and societies to recognize the urgency of the climate crisis and to lead by example by improving institutional policies and practices to reduce the carbon footprint of researchers in astronomy. As of September 2021*, we gathered 2844 valid signatures from astronomers working in 80 countries across the globe, including current and former presidents of astronomical societies, two Nobel prize winners and has been endorsed by a number of well-known astronomical institutions.

Global climate strike 2021, making our stand: On 25th of September 2020, the organization Fridays for Future led a global climate strike. Astronomers for Planet Earth joined activists from all over the world and produced a video to encourage any individual to join the climate strike and take actions.

Webinar series: Regular 30min long webinars are organized with invited experts on various subjects relating astronomy and the environmental crises. The webinars are recorded via Zoom and made exclusively accessible to A4E members, then followed (about two weeks later) by a live Questions and Answers session with the speaker. The videos are then made publicly available on the dedicated YouTube channel.

EAS special session 2020 and 2021: During the annual European Astronomical Society (EAS) virtual meeting in 2020, A4E organized the very first Special and Lunch Sessions "Astronomy for Future: Development, global citizenship & climate action". These were among the best attended and most discussed of the conference. During EAS 2021, A4E organized a second Special and Lunch Sessions: "Astronomers for Planet Earth: Forging a Sustainable Future". The slides and recordings are available on a dedicated Zenodo repository and Youtube channel. One of the first actions of A4E was to write a letter to the EAS council urging them to take action and to install a sustainability working group. This call has been met with a lot of sympathy by the EAS council and the EAS sustainability working group has subsequently been created. Its aims are to advise EAS council on how to reduce the carbon emissions of the society (mostly generated at the EAS annual meeting) and to connect sustainability initiatives within Europe.

*On 2nd of July 2021, the European Astronomical Society hosted a press conference for this Open Letter to present its impact.

4 Conclusions and prospects for A4E

Many projects are on-going within A4E, such as updating the website, starting a blog, making new videos etc. In addition, we are preparing packages to support individual researchers and institutions to take immediate actions. This packages are meant to lower the time needed to implement these actions, while being homogeneous among institutions, and to keep track of the implemented initiatives and their results. More generally, we are working towards establishing A4E as an official organisation and are looking for funding resources. People who want to help with this process or know anyone who would like to contribute funds, please contact us.

As astronomers, we are immeasurably lucky to work in such a fascinating field. With our unique perspective on the universe, it is our responsibility to communicate, inside and outside our community, about the disastrous consequences of the anthropogenic climate crisis on our planet and our society. A4E aims at leading astronomy institutions towards sustainable working habits to cope with the environmental transition. It is also important to hear astronomers say the simple truth: there is no planet B.

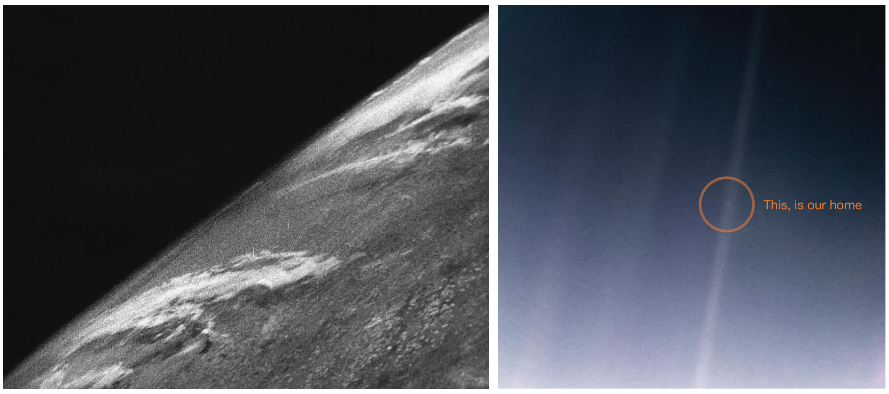

Fig. 2. Left: First photo of planet Earth from space (105 km altitude) taken in 1946. Credits: U.S. Army, White Sands Missile Range, Applied Physics Laboratory. Right: The emblematic *pale blue dot* picture highlights the sense of fragility of our planet, its place in the universe and the notion of distances in the solar system. Credits: NASA/JPL-Caltech.

A "Climate Issue" in Nature Astronomy 2020

After the successful special session "Astronomy for Future" organized during the virtual EAS annual meeting 2020, the journal Nature Astronomy proposed to summarize the contributions into several comments edited in a special September 2020 issue called The Climate Issue. The papers are kindly made freely available by Nature Astronomy and can be found at the following links:

- Burtscher et al., 'The carbon footprint of large astronomy meetings': `rdcu.be/b610r`
- Cantalloube et al., 'The impact of climate crises on astronomical observations': `rdcu.be/b610h`
- Flagey et al., 'Measuring carbon emissions at the Canada-France-Hawaii Telescope': `rdcu.be/b610f`
- Jahnke et al., 'An astronomical institute's perspective on meeting the challenges of the climate crisis': `rdcu.be/b610n`
- Portegies Zwart, 'The ecological impact of high-performance computing in astrophysics': `rdcu.be/b610i`
- Stevens et al, 'The imperative to reduce carbon emissions in astronomy': `rdcu.be/b610k`

B "Climate Issue" in Nature Astronomy 2021

After this first successful climate issue, a second edition was released on September 14th 2021.

- Burtscher et al., 'Forging a sustainable future for astronomy': `https://rdcu.be/cxPAG`
- Anderson & Maffey, 'Five steps for astronomers to communicate climate change effectively': `https://rdcu.be/cxPAR`
- Williams, 'The need for political advocacy in astronomy': `https://rdcu.be/cxPA0`

SF2A 2021
A. Siebert, K. Baillié, E. Lagadec, N. Lagarde, J. Malzac, J.-B. Marquette, M. N'Diaye, J. Richard, O. Venot (eds)

EXPONENTIAL AND FERMI'S PARADOX: LIMITS TO GROWTH

A. Crida[1]

Abstract. We now know that there are billions of (potentially habitable) terrestrial planets in the Milky Way, which only strengthens Fermi's paradox: why has no extraterrestrial civilization already conquered the Galaxy and visited Earth ? Such a conquest would be a natural consequence of an exponential development. However, every exponential phenomenon hits its limits at some point. The same should apply to the growth of the world Gross Domestic Product (GDP) and energy consumption (both being intimately linked), as numbers easily show.

A solution to Fermi's paradox is simply the limits to exponential growth. The fact that no little green man has visited us teaches us that we are soon to hit the limits (actually we already have). Meanwhile, the Covid-19 pandemic has shown that exponential phenomena require action before the situation becomes dramatic. Hence, simple maths and astronomy show that we need to stop with our exponential growth now.

Keywords: Exponential function, Fermi's paradox, growth

1 Fermi's paradox

Since 1995, more than 4000 exoplanets have been discovered, with a wide variety in mass, radius, orbital distance. From radial velocity studies (HARPS), Mayor et al. (2011) showed that about 14% of solar-type stars have a giant planet with an orbital period shorter than 10 years, and that more than half solar-type stars harbor at least one planet with an orbital period shorter than 100 days. From transit studies (*Kepler*) Bryson et al. (2021) estimate that the occurrence rate of terrestrial planets (between 0.5 and 1.5 Earth radius) in the habitable zone of solar type stars (between 4800 and 6300 K effective temperature) is of the order of 50%. This makes billions of such planets in the Milky Way, with the closest one probably within 6 parsecs of our Sun.

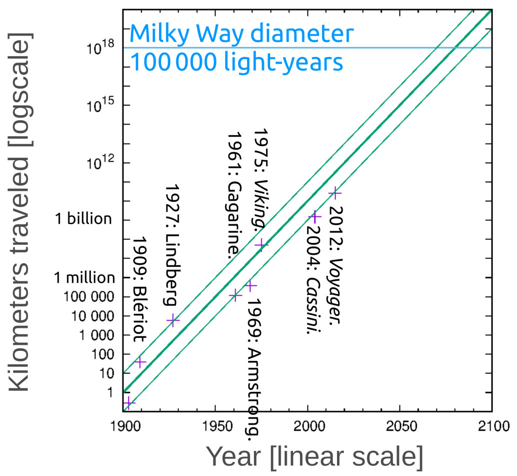

Fig. 1. Landmarks of the conquest of space showing the distance traveled increasing with time. Without using a logarithmic scale in the y-axis, the diagram would be impossible to read. The underlying trend corresponds to multiply the distance by 10 every 10 years, or equivalently double every 3 years.

Looking at the conquest of space, from the first plane which flew a few hundred meters to the crossing of the Channel by Blériot, man in space, man on the Moon, *Viking* on Mars, *Cassini* at Saturn, *Voyager II* leaving the heliosphere, one finds a roughly exponential growth of the distance flown, which is multiplied by ten every decade. Extrapolating this relation (see Figure 1), we should reach 100 000 light-years (the diameter of the Milky Way) by the end of the century. Obviously this won't happen: we all know that the speed of light, c, can not be overpassed, so that traveling 100 000 light-years in less than 100 years is not possible. This is a first example of a physical limit to an exponential development.

Nonetheless, even if we limit ourselves to exploring the universe at $c/10$, it should take only a million years to visit the Galaxy. This is just a snap on the Universe clock. Though our planet, and our civilization, did not appear early in the history of the Milky Way, other planets and civilizations must have appeared long ago. So why didn't others do it before?

[1] Université Côte d'Azur, Observatoire de la Côte d'Azur, UMR7293 Lagrange, 06300 Nice, France

2 The exponential function and limits

The exponential function is the solution to the simplest differential equation : $y' = ay$. Hence, many phenomena, in which the increase rate is proportional to the considered quantity, follow an exponential development. Using $e^{at} = 2^{t/T}$ where $T = \ln(2)/a \approx 0.7/a$, one can convert an exponential growth rate a into doubling time T, which is more visual and handy to conceive.

For instance, percentages describe exponential processes. To first order, a quantity that grows by $r\%$ per year doubles in $70/r$ years. The world Gross Domestic Product (the total amount of wealth produced per year) has doubled every 17 years since the industrial revolution in the mid XIX$^{\text{th}}$ century*, which corresponds to an average growth rate of 4% per year.

But it's not so easy to keep doubling. Takes a sheet of paper and fold it in two. You now have doubled its thickness. Do it again. The thickness is four times the initial one. Do it again, and again... Any guess of the thickness after 10 folds ? You won't get there, it's impossible to fold a normal A4 paper more than 7 times. If one could do it, it would only take 42 folds to reach the Earth-Moon distance ! Yes, $2^{42} \times 0.1\,\text{mm} \approx 4 \cdot 10^5\,\text{km}$.

Another well-known example is the tale of the waterlily that produces a new leaf from every leaf every night. If it covers half the lake in 30 days, how long will it take to cover the whole lake ? The simplest (linear) answer is "an other month", but the real answer is of course "one more day". What is less known is that doubling its area everyday, the waterlily would cover the entire Earth in less than two months...

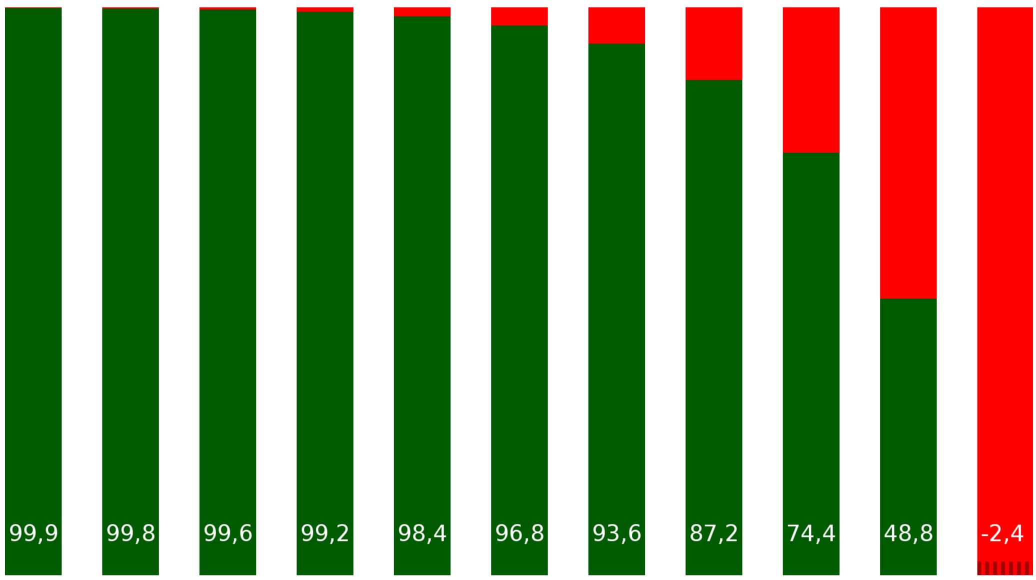

Fig. 2. Illustration of reaching the limits in an exponential development. A vertical bar represents 100, the total available for a quantity. Green (bottom) is the part left over, red (top) in the quantity used. Moving from left to right, the used quantity doubles every bar. At first, the green part is not affected, but it suddenly vanishes.

Finally, figure 2 illustrates why reaching the limits comes as a surprise. Say a quantity is limited to 100, and one takes initially 0.1 (leftmost column). Doubling the take to 0.2, what remains available hardly changes, decreasing from 99.9 to 99.8. The used quantity (in red in the figure) can keep doubling regularly many times without significantly affecting the available stock (in green). However, from the antepenultimate to the penultimate column, the rest drops by one third, from 74.4 to 48.8. One more doubling and there is nothing left.

While the behavior of the used quantity (in red) has not changed (doubling every time), the behavior of the available quantity (green) suddenly changes and collapses to zero. Similarly, folding a sheet of paper is easy, until the 6$^{\text{th}}$ fold and then it's impossible. After 31 days of quiet growth, the water lily finds itself blocked and asphyxiates the pond. Which brings us to the next section.

*As a consequence, the total amount of wealth produced in the XXI$^{\text{st}}$ century is already more than the total amount of wealth produced during all mankind history until and including year 2000 !

3 What about growth ?

Our economic growth has been an exponential phenomenon since the industrial revolution. But it relies on exploiting resources, and emitting waste. The capacity of the planet to provide resources and to absorb waste are finite. Hence, the limits are expected to be reached (Meadows et al. 1972, 1992, 2004, 2012). Let us focus on the energy demand, which is in linear relation with the GDP (e.g Parrique et al. 2019), and grows by 2% per year since 1990. The world total energy consumption was $5.67 \cdot 10^{20}$ J or 158 000 TWh in 2013. Increasing this number by 2% per year for 463 years multiplies it by 9600, and it reaches the whole energy the Earth receives from the Sun. In other words, if we move to renewable energies and keep our growth, we need to cover the entire planet by solar panels of 100% efficiency in a shorter time than what separates us from the Renaissance.

Assume we succeed. 1100 years later, we need the whole energy emitted by the Sun in all directions ! Very clearly, nuclear fusion plants on Earth can never provide this... Assume we manage to surround the Sun by ideal solar panels in a so-called Dyson-sphere ; 35 years later, we'll need an other star ! And 35 years later 2 new stars. In less than 3000 years, we will need all the stars of the Milky Way. Then what ?

An astrophysicist must conclude that growth can not be an everlasting phenomenon. And we see that the time scale is actually pretty short, comparable to human civilizations. So when should we stop ?

4 Exponential + delay = danger !

It is already well-known that we have overpassed the limits of Earth's capacity. But so far, so good, one could (almost) say. Unfortunately, the recent pandemic has taught us the hard way how acting too late against an exponential phenomenon can be a disaster.

In the case of the Covid-19 pandemic first wave, the development of the number of deaths was exponential, with a doubling time of 2.6 days in most countries. The way to stop the exponential propagation of the virus is the lock-down. But there is an average delay of two to three weeks between the time someone is infected by the coronavirus and the time the disease starts, develops, and eventually leads to death. Hence, after the lock-down, the number of casualties still grows exponentially, and eventually saturates in a month, as the last persons who got contaminated just before lock-down either heal or die. In every country, the final number of deaths after the first lock-down was about 80 times what it was at the moment of the lock-down. Because no one was ready to accept a lock-down when only a dozen people were killed, the final number of casualties reached several tens of thousands. Moving the time of the lock-down by only 2.6 days would have changed the number of victims by a factor 2.

In this case, in absence of tests, we could only see the consequences (the number of deaths), and act on the cause (the propagation of the virus). The delay between the cause and the consequence had disastrous effects.

Similarly, our emissions of greenhouse gases are following an exponential trend very similar to that of the world GDP and energy consumption. But the consequences of a stronger greenhouse effect (melt of polar caps and mountain glaciers, modifications of ecosystems, change in ocean currents, higher frequency of heat waves...) take decades to reach their final amplitude. We just start seeing the effects of the global warming, with more numerous and severe natural disasters. We are on the front of climate where we were on March 16, 2020 in France[†] on the front of Covid. To stop the exponential growth of our greenhouse gases emissions, action must be taken without delay.

5 Conclusion

The solution to Fermi's paradox is a *reductio ad absurdum* :

- Hypothesis (often implicit) : an everlasting exponential growth is possible without limits.
- Consequence : the conquest of the Milky Way is easy and quick.
- Contradiction : this has not been done by any of the billions of potentially habitable terrestrial planets in 12 billion years.
- Conclusion : the starting hypothesis is wrong, for some reason (e.g. energy resource limits).

[†]The lock-down started on March 17, 2020. Only 175 persons had then died from Covid-19.

Many other solutions have been proposed to Fermi's paradox in the litterature. Some are exotic, but most of them actually point to some specific limitation to the growth of a civilisation. Here, I have focused on the energy budget, which is clearly an upper limit. Anyway, if growth is limited, there is no way a civilization can leave its planetary system and communicate with, visit, or conquer planets around other stars. The paradox vanishes, but this teaches us a lesson : as our space conquest is progressing rapidly, we are soon to hit a wall.

Astronomy, because it forces to see the global picture, helps to understand that our planet is just a small pale blue dot and our civilization an epiphenomenon. With this in mind, it becomes clear that growth, which we consider as natural as the cycle of seasons because it dates back to the grand-parents of our grand-parents, is actually not granted. We have to imagine an other way of life, within the limits.

I thank the organisers of the S14 workshop "Transition environnementale: quel rôle pour la communauté astronomique ?".
Many thanks as well to the SF2A council for having allowed and encouraged this very interesting workshop to take place.
The oral presentation (in French) can be seen here (15 minutes) : https://vimeo.com/560589409 .
A longer, outreach version (still in French) is available there : https://www.youtube.com/watch?v=I3JkQ7quGG8 .

References

Bryson, S., Kunimoto, M., Kopparapu, R. K., et al. 2021, AJ, 161, 36

Mayor, M., Marmier, M., Lovis, C., et al. 2011, arXiv e-prints, arXiv:1109.2497

Meadows, D. H., Meadows, D. L., & Randers, J. 1992, Beyond the limits (Chelsea Green Publishing)

Meadows, D. H., Meadows, D. L., & Randers, J. 2004, The limits to Growth : the 30-years update (Chelsea Green Publishing)

Meadows, D. H., Meadows, D. L., Randers, J., & Behrens, W. W. 1972, The limits to Growth (Potomac Associates – Universe Books)

Meadows, D. L., Meadows, D. L., & Randers, J. 2012, Les limites à la croissance (dans un monde fini) : Le rapport Meadows, 30 ans après (Rue de l'échiquier – L'écopoche)

Parrique, T., Barth, J., Briens, F., et al. 2019, Decoupling debunked: Evidence and arguments against green growth as a sole strategy for sustainability. (European Environmental Bureau)

SF2A 2021
A. Siebert, K. Baillié, E. Lagadec, N. Lagarde, J. Malzac, J.-B. Marquette, M. N'Diaye, J. Richard, O. Venot (eds)

CARBONFREECONF: MITIGATE THE CARBON EMISSIONS OF ACADEMICS USING CARBON-NEUTRAL VIRTUAL PLATFORMS

Q. Kral[1]

Abstract. The carbon footprint of academics is not negligible and higher than average. This is in part due to academic conferences, implying many long-distance travels to present new research results. One way to thwart these carbon emissions would be to go virtual for most conferences, when possible. To do so, researchers need an easy way to set up their virtual conferences and manage their participants. Moreover, the platform they use should have all the necessary tools to share their research more readily. CarbonFreeConf was developed by a researcher for researchers with these goals in mind as we explain in further detail in these proceedings. In addition, virtual conferences organized with CarbonFreeConf are totally carbon-free as (the low) emissions produced during the conference (from streaming and computer energy usage) are compensated with already approved carbon removal technologies.

Keywords: carbon footprint, virtual conferences, environmental transition

1 Introduction

To reach our goals in terms of carbon emissions and maintain the state of the Earth (almost) as we know it (even though it is already a bit late as the mean temperature on Earth already increased by 1.1 degree compared to the pre-industrial era), the only way out is to cut down on CO_2 emissions very quickly. Every citizen should try to do it on its own scale and businesses should find ways to mitigate their emissions before finally (hopefully) reaching world-wide (strict) regulations in the coming years, which would lead to the end of the biggest issue we (and most other living species) face today! Researchers - especially those preaching to cut down on emissions - should be exemplary but numbers show that their carbon emissions are often greater than the rest of the population, mostly because they travel to distant places to present their research several times a year. Virtual conferences would help to reduce the carbon footprint of academics by a large factor (which depends on the research they carry out and their respective countries). CarbonFreeConf was developed to help researchers organize carbon-neutral virtual conferences (and cut-down on greenhouse gas emissions) in a few clicks providing all the tools necessary to get the most out of it. The study by Burtscher et al. (2020, see also a more succinct analyse on the CarbonFreeConf Blog) shows that the carbon footprint of virtual conferences is at least 1000 times smaller than that of in-person conferences. A cut of emissions by 3 orders of magnitude provides a strong motivation for multiplying ecologically minded conferencing.

2 The CarbonFreeConf platform

2.1 *History*

The idea of developing the CarbonFreeConf platform for the research community popped up in 2017, well before the start of the Covid-19 pandemics (although it is also useful in these complicated times we currently live in). One of the thoughts I had as a young researcher was that many conferences could be organized virtually (to cut down on carbon emissions, Burtscher et al. 2020) rather than having to move a whole community across continents every time we want to share our research (though some face-to-face meetings are still essential). However, to do so, we would need simple and efficient tools to be able to organize, plan, distribute and make

[1] LESIA, Observatoire de Paris, Université PSL, CNRS, Sorbonne Université, Univ. Paris Diderot, Sorbonne Paris Cité, 5 place Jules Janssen, 92195 Meudon, France

happen our virtual conferences in a few clicks. Another thought was that large virtual conferences still emit quite a lot of carbon in the atmosphere so we needed a way to offset these emissions. Both points are the essence of why CarbonFreeConf was developed.

2.2 The concept of CarbonFreeConf

CarbonFreeConf is a website where one can create a virtual conference in a few clicks (Fig. 1 left). It just needs a few inputs from the organizers, such as a title, and what the conference is about and it will then rely on those to make a (customizable) website for participants to register and see all what the conference has to offer (Fig. 1 right). The website lists the different sessions of the conference as well as their participants. Abstracts and Posters can be accessed easily as well as the conference program/timeline and some other useful tools (e.g., archived documents and video recordings). In addition, an admin panel is accessible to organizers to manage the participants (accept their talks, contact them, ...). Once a talk or poster is accepted, it can be added to the conference program automatically and it becomes visible on the conference website. Many tools are provided to make the conference/participants handling much simpler than one would expect. Based on the program, the platform then automatically creates virtual rooms for when the conference happens as well as some chat rooms for participants to discuss before and after the talks if, e.g., they did not have the opportunity to ask their questions, or want to network with their peers. At the end of the virtual experience, the carbon emissions produced by the conference are calculated (see our carbon calculator here) and offseted via companies using direct air capture methods (see more here).

2.3 Aims and perspectives

This platform was used for the first time on a large scale for the SF2A (Société Française d'Astronomie & d'Astrophysique) virtual conference in June 2021, which gathered more than 800 astronomers and it is now archived on the associated conference website accessible here (some talk recordings are public and posters are all accessible). The main goals of the platform are:

- Reduce our carbon footprint as researchers while still being able to efficiently share our research;
- Make it as simple as possible to organize a conference for up to 1000 participants (thanks to the automatic creation of a website, and tools for handling the program, the abstracts, networking, uploading posters (pdf and/or video), uploading slides, recording talks, ...). CarbonFreeConf also provides the virtual rooms for the conference itself as well as many chat rooms, tools for interactive questions & polls, ... so that researchers have it all in one place and do not have to spend time looking for that themself and trying to connect the different bricks together (which is often impossible as, e.g., Slack-type tools do not interact with abstract handling tools, or with website creation editors, ...).

After every conference, we gather feedback from the participants to improve the platform, which has already evolved substantially since June 2021. For instance, we are now proposing an hybrid version, where participants can either meet face-to-face or join the conference virtually (e.g., if they live too far or not want to disrupt their family life). We also added a parallel coffee-break room for each session (if activated by organizers) that can be joined at any moment as well as a timeline showing all the talks from the different sessions at a given time to not miss out on anything that could be of interest to you. We also added an interactive map of the conference showing the conference with all of its sessions and posters, which makes it easy to join the different rooms or see what sessions/posters are available and explore further what the meeting has to offer in a few clicks.

The hope is that this platform can help researchers meet their carbon emission abatement goals while still be able to efficiently share their research. To do so, CarbonFreeConf relies on the research community to go forward and let us know about their needs. If you would like to send feedback please contact us at admin@carbonfreeconf.com. One of the major outcomes of this platform is that talk recordings are archived for a long time and researchers can watch them when needed. It could become a very useful research library in the future that would be complementary to the classic literature. We plan to release an open-source version of the website in the future to make it easier to contribute and favoring an open research approach.

3 Conclusions

These proceedings presented a new way of carrying out conferences remotely (or in a hybrid fashion) using the CarbonFreeConf platform. This new platform aims to be simple to use and to provide all the tools needed to

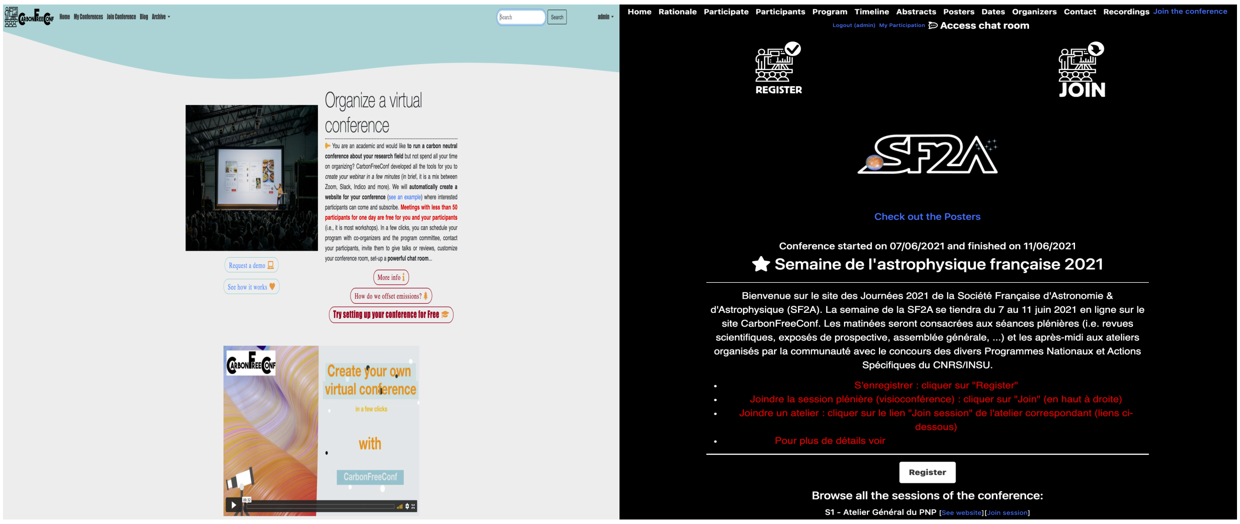

Fig. 1. Left: The CarbonFreeConf website to organize a virtual or hybrid conference in a few clicks. **Right:** Example of a customizable website created for a virtual conference in astrophysics (see it live here).

make the most out of each conference. The main goal is to cut down on carbon emissions when organizing conferences while still being able to share our research efficiently around the world. Research is primordial and we need more initiative to cut down on emissions on every aspect of our respective research fields!

Thanks to the SF2A organizers for using the CarbonFreeConf platform and all those who helped improve it so that we can now widely use it to share our research across the world!

References

Burtscher, L., Barret, D., Borkar, A. P., et al. 2020, Nature Astronomy, 4, 823

Session 15

Photonic technologies for astronomy: manipulating light at fundamental scales

V8: AN 8 BEAM MID-INFRARED HETERODYNE INSTRUMENT CONCEPT FOR THE VLTI

J.-P. Berger[1], G. Bourdarot[1] and H. Guillet de Chatellus[2]

Abstract. In this presentation we present the concept of an instrument, called V8, capable of combining all eight VLTI telescope coherently. Unlike all existing instruments the concept of V8 is based on mid-infrared heterodyne technologies. These have the potential to considerably simplify the infrastructure of a future large interferometric facility dedicated to planet formation studies such as the Planet Formation Imager. The overall concept and coarse layout of the instrument is presented and we discuss the requested technological building blocks.

Keywords: interferometry, mid-infrared, heterodyne, VLTI, instrumentation, photonics, QCD technologies

1 Introduction

From the birth of stars and planetary systems to supermassive black-holes, the recent observations of astronomical objects at the highest angular resolution have profoundly changed our vision of our surrounding universe. In this field, aperture synthesis with Very Long Baseline interferometry (VLBI) and optical infrared interferometry such as the Very Large Telescope Interferometer (VLTI) are currently the two techniques that provide the highest angular resolution achievable. With its shorter wavelength, infrared interferometry, still confined at 100m scale baseline, could be envisioned as one of the most promising technique to go even further. The extension of this technique to a large number (N$\geq$20) of telescopes and kilometric baselines would represent a major step for observational astronomy. Nevertheless, such an infrastructure, as proposed in the context of the Planet Formation Imager (PFI) initiative (Monnier et al. 2018) will also require challenging technological developments that cannot be extrapolated simply from existing instrumentation (Ireland et al. 2016).

In the current status of PFI, direct interferometry is the privileged option since it provides a major sensitivity gain in the short part of the mid-infrared spectrum (the 3-5 μm window) with respect to heterodyne. A fundamental quantum noise with a dramatically increasing effect at high frequencies explains its poor performance. However, this advantage is less strong in the N and Q mid-infrared bands.

Because it is less demanding on the infrastructure, and because the gain of direct interferometry at $\approx 10\mu$m is not so superior, heterodyne detection offers a still valuable and complementary path to address the problem of kilometric baseline and aperture synthesis with a large number of telescopes. In the past, through the pioneering work of maser inventor and Nobel Prize C.H. Townes and his team, heterodyne detection was the first technique able to combine 2 telescopes in the mid-infrared and to measure closure phases with 3 telescopes, on the Infrared Spatial Interferometer (ISI) in UC Berkeley (Hale et al. 2000; Danchi et al. 2003; Hale et al. 2004). ISI provided valuable scientific results well ahead of its time, anticipating the following generation of direct mid-infrared interferometric instruments such as MIDI and MATISSE. Despite the sensitivity disadvantage in the 10 μm regime by a few factors (and almost none in the Q band), its strength deserves to be further explored, particularly in the context of an array of several tenths of telescopes (Michael et al. 2020).

We present here the idea that mid-infrared heterodyne interferometry is currently the sole technique capable of combining all the eight VLTI telescopes with very limited infrastructure modifications. We describe a concept of a simple instrument, code-named V8 that would bring an unprecedented imaging capability at VLTI, albeit limited to bright sources. It relies on technological advances on many fields pushed by the world-wide interest in developing mid-infrared photonics technologies. Our overarching goal is to push technology towards a complete fiber-linked mid-infrared interferometric facility.

[1] Univ. Grenoble Alpes, CNRS, IPAG, 38000 Grenoble, France
[2] Univ. Grenoble Alpes, CNRS, LIPhy, 38000 Grenoble, France

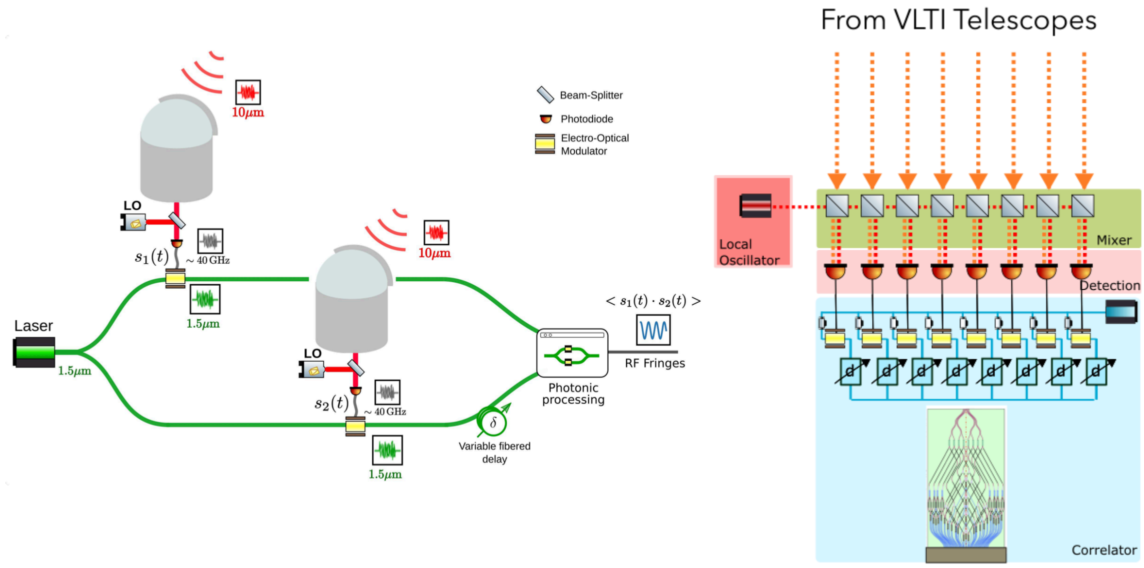

Fig. 1. Left: conceptual scheme of a two telescope heterodyne optical chain Right: schematic of the proposed V8 optical layout inside the VLTI laboratory with the first local oscillator-signal mixing stage, the detection stage and the photonics correlator.

2 The concept

Figure 1 shows a conceptual scheme of a two-telescope heterodyne instrument which forms the basis of our proposition. The incoming celestial light of each telescope interferes (is "mixed") with a local-oscillator on a high temporal bandwidth detector. Local-oscillators are synchronized in phase between the telescopes. In such a process, the mixed mid-infrared signal is down-converted to radio-frequencies signal that can be correlated with other telescopes'. Unlike the classical architecture inspired by radio interferometry, we do not digitize the beating signal but rather use it to modulate a stable laser in such a way that it acts as a carrier of the amplitude information and can be carried through fiber links. We refer to Bourdarot et al. in this conference for a description of this photonics scheme. Interference between the two arms of the fiber link allow a measurement of the correlation between the incoming electromagnetic fields to be made. This provides a direct measurement of the object spatial coherence.

3 The technological building blocks

Other industries such as sensing, telecommunications, time and frequency propagation have considerably pushed forward technologies since the ISI observatory. These developments have reach a sufficient maturity to deserve a thorough examination.

Detection The ISI used ≈ 3 GHz detectors corresponding to a ≈ 10000 spectral resolution power, which explains partly its limited sensitivity. Improving the detector bandwidth is the first way to increase the sensitivity of the heterodyne scheme as it allows a broader portion of the spectrum to be sampled. We are exploring with Laboratoire de Physique de l'Ecole Normale de Physique (LP-ENS) unipolar mid-infrared ($4\mu\mathrm{m} < \lambda < 12\mu\mathrm{m}$) detectors for a high speed operation up to room temperature Palaferri et al. (2018). These detectors are based on a quantum well absorbing medium embedded into a metallic metamaterial that provides strong sub-wavelength confinement. Such architectures increase the device responsivity and also the detector operating temperature thanks to a reduction of the thermally generated dark current. In addition, unipolar detectors have a unique property which is their very short excited carrier lifetime, on the order of few picoseconds, leading to a frequency bandwidth of several tens of GHz. Using a heterodyne setup made with two quantum cascade lasers, frequency response above 20 GHz have been already demonstrated (Palaferri et al. 2018; Gacemi et al. 2018).

Local oscillator The ISI used a CO_2 laser as a local oscillator (LO) which presents the interest of generating many lines in the 9-12 μm band that can be further enriched depending on the isotope used. In order to further increase the spectral coverage of an heterodyne setup mid-infrared frequency combs should be considered. However, only a few broad bandwidth mid-infrared lasers exist. As a consequence nonlinear frequency down-conversion is the privileged way to generate frequency combs in this spectral region. The specific constraint of the heterodyne interferometric technique requires to generate combs with line spacing corresponding to detector bandwidths which, in our particular case, should be of the order of a few 10GHz. There are currently no commercially available products. However, we note that several applications such as gas sensing, precision spectroscopy and kinetics chemical reactions monitoring require such light sources. With that in mind (Kowligy et al. 2020) have reported the first mid-infrared frequency combs with 10GHz repetition rate around a wavelength of 4 mic and have explored the extension to the 7-11 window using OP-GaP crystals as non-linear conversion material. Other technologies, based on QCL lasers are close to maturity and provide another path for mid-infrared frequency combs (Hugi et al. 2012).

The distribution of a phase-locked mid-infrared local oscillator is another challenge. We note that the recent work by Argence et al. (2015) has demonstrated the possibility to lock a mid-infrared QCL laser to an atomic clock located 47 km away thanks to the phase-controlled propagation of a near infrared ultra-stable laser. The adaptation of this scheme to long-baseline interferometry would not necessarily require the locking on an atomic clock since we are interested in relative phase stability.

Correlation and delay Radio interferometric arrays such as ALMA require correlation techniques that can handle several tens of telescopes with the maximum possible spectral bandpass and resolution. Dedicated electronic technologies are required, starting at the antenna end with high bandwidth digitizers, optical data links to the central correlator. As pointed out by (Ireland & Monnier 2014), the extrapolation of radio-techniques for a mid-infrared array such as PFI lead to not-yet available computing power requirements. Moreover, the perspective of having to deal with high bandwidth RF signals (several 10s of GHz) complicates further the matter. Finally, the bandwidth over frequency ratio being so different between the radio and the mid-infrared, it is highly likely that specific architectures would have to be conceived in order to retrieve the spectral information.

We revisited the idea of carrying an *analogical correlation* by converting the RF signal over to a stable telecom laser carrier using electro-optics modulators. Using off-the-shelf components, we demonstrated that the correlation between two telescopes could be done (Bourdarot et al. 2020). The main interest of this approach is that it provides a simple way to handle both high bandwidth signals (up to 50GHz), many telescopes and several spectral channels with telecom technologies (DWDM). In this conference Bourdarot et al. and in a forthcoming paper (Bourdarot et al. JOSA B under review) present in more detail our photonics analogical approach. The delay compensation can be achieved using commercially available discrete delay line that can generate delays of several 100s of meters and a continuous small range one. Indeed, since we are in this analogical correlation scheme we are limited neither by losses nor by chromatic dispersion.

Fringe tracking As for direct interferometry, heterodyne is subject to the adverse effects of atmospheric piston. This leads to a considerable shortening of the coherence time therefore reducing the integration capability, thus the sensitivity. The only currently known remedy is to stabilize the optical path by providing a dedicated sensor called "fringe tracker". In the context of an all-fibered array such a fringe tracker would need the development of broadband low-loss optical path compensators and dedicated photonics or direct beam combination techniques capable of handling the tens of telescope of the array.

4 V8 simplified layout, implementation and sensitivity

Until a proper way to distribute the local oscillator is demonstrated (this would increase the sensivity by a factor 4) we propose that the 8 beam heterodyne correlator could be entirely located inside the VLTI laboratory. Right of figure 1 shows a conceptual layout of such an instrument. The eight beams originating from the four Unit Telescopes and Auxiliary Telescopes would have to be brought back to the VLTI laboratory. A QCL-based mid-infrared local oscillator stabilized in frequency is distributed and interferes with the incoming celestial light onto the high-bandwidth unipolar detectors. As the laser is polarized, a specific care to the polarization state of the incoming signal would have to be taken. The resulting beating signals modulates the electro-optics modulators of the photonic correlator. We use an 8-beam photonics chip to ensure a pairwise correlation function using the same technique that we used for PIONIER and GRAVITY Benisty et al. (2009); Perraut et al. (2018).

Although the quantum noise still limits heterodyne sensitivity in the N band the gap between direct interferometry and heterodyne can be significantly reduced (and almost cancelled in the Q band). In order to quantify this difference we have compared MATISSE performances as advertised on the ESO official web pages with ISI performances and our putative heterodyne instrument V8. V8 improves on ISI by having state of the art high bandwidth detectors (25 GHz bandpass), better quantum efficiency (0.5) and an improved noise penalty (2) with respect to the one described in Hale 2000.

This analysis leads us to conclude that, despite the systematic better sensitivity of MATISSE with respect to ISI and V8, both heterodyne instruments fare globally well in terms of sensitivity by reaching limiting fluxes compatible with many sources in the southern hemisphere. This is particularly the case for Red Super Giants, Asymptotic Giant Branch stars and post AGB stars for which several tens are significantly brighter than the limits computed here. We note that coupling AT with UTs allows decent limiting fluxes per spectral channel to be obtained. Those are comparable with MATISSE's performance per spectral channel on the AT's.

Our conclusion is that a simple heterodyne instrument at VLTI would be perfectly capable of mapping tens of evolved sources and massive young embedded stars, even without a fringe tracker. Our scientific motivation to pursue this instrumental research avenue is therefore the trade between sensitivity and an incomparable mapping capability since V8 would sample 28 baselines instead of 6 with MATISSE.

5 Conclusion

We have presented a very preliminary concept of an 8 beam instrument that would use mid-infrared heterodyne interferometry to correlate the 8 VLTI telescope thus providing an unprecedented imaging capability at the VLTI. This proposition is based on state of the art technologies and will require further developments and demonstrations but based on expected performances we think it could lead to an actually well performing mid-infrared imager of bright sources while providing an excellent pathfinder for Planet Formation Imager technologies.

This work has been partially supported by the LabEx FOCUS ANR-11-LABX-0013. This work has been partially supported by CNRS-INSU CSAA and ASHRA.

References

Argence, B., Chanteau, B., Lopez, O., et al. 2015, Nature Photonics, 9, 456

Benisty, M., Berger, J.-P., Jocou, L., et al. 2009, Astronomy & Astrophysics, 498, 601

Bourdarot, G., Guillet de Chatellus, H., & Berger, J.-P. 2020, Astronomy & Astrophysics, 639, A53

Danchi, W. C., Townes, C. H., Fitelson, W., et al. 2003, in Interferometry for Optical Astronomy II, Vol. 4838 (International Society for Optics and Photonics), 33–44

Gacemi, D., Todorov, Y., Bigioli, A., Palaferri, D., & Sirtori, C. 2018, in 2018 43rd International Conference on Infrared, Millimeter, and Terahertz Waves (IRMMW-THz) (Nagoya: IEEE), 1–1

Hale, D. D. S., Bester, M., Danchi, W. C., et al. 2000, The Astrophysical Journal, 537, 998

Hale, D. D. S., Weiner, J., & Townes, C. H. 2004, USA, 490

Hugi, A., Villares, G., Blaser, S., Liu, H. C., & Faist, J. 2012, Nature, 492, 229

Ireland, M. J. & Monnier, J. D. 2014, in Optical and Infrared Interferometry IV, Vol. 9146 (International Society for Optics and Photonics), 914612

Ireland, M. J., Monnier, J. D., Kraus, S., et al. 2016, Edinburgh, United Kingdom, 99071L

Kowligy, A. S., Kowligy, A. S., Carlson, D. R., et al. 2020, Optics Letters, 45, 3677

Michael, E. A., Emadi, R., Moreno, E., et al. 2020, 11446, 114462O

Monnier, J. D., Kraus, S., Ireland, M. J., et al. 2018, Experimental Astronomy, 46, 517

Palaferri, D., Todorov, Y., Bigioli, A., et al. 2018, Nature, 556, 85

Perraut, K., Jocou, L., Berger, J. P., et al. 2018, Astronomy & Astrophysics, 614, A70

SF2A 2021
A. Siebert, K. Baillié, E. Lagadec, N. Lagarde, J. Malzac, J.-B. Marquette, M. N'Diaye, J. Richard, O. Venot (eds)

V8 CONCEPT AND PHOTONIC CORRELATION FOR MID-INFRARED INTERFEROMETRY

G.Bourdarot[1,2], J.-P. Berger[1] and H. Guillet de Chatellus[2]

Abstract. The recombination of a large number of telescopes over kilometric baselines in an infrared interferometric array, such as proposed in the Planet Formation Imager (PFI) initiative, requires the investigation of renewed interferometric architectures. In the mid-infrared, heterodyne interferometry represents a potential solution, appropriate for the recombination of a large number of telescopes and the practical transport of interferometric signals. A major challenge of heterodyne interferometry is the limitation in terms of detection bandwidth, which requires the development of detectors and correlators handling detection bandwidth up to tens of GHz. Here, we report on the status of our technological demonstration in this direction. We present an update of the concepts of photonic correlation, including both phase and amplitude modulation schemes, and their proof-of-principle demonstration in the laboratory. Together with the advent of new mid-infrared high bandwidth detectors and Quantum Cascade Lasers (QCLs), the current state of mid-infrared technologies could be applied to the simultaneous combination of the eight telescopes of the VLTI, so-called V8 concept. We describe the first step in this direction, with the development of mid-infrared test bench at 10.6 μm with 2 detection channels, including a QCL, commercial high-bandwidth detectors and a photonic correlator.

Keywords: Planet Formation Imager, Heterodyne Interferometry, VLTI, Photonic Correlation, QCL

1 Introduction

The development of an infrared interferometric array recombining a large number of telescopes over kilometric baselines represents a major step in observational astrophysics, in particular for the study and the image reconstruction of protoplanetary environments with milli-arcsecond (mas) and sub-mas resolution in the infrared, such as proposed in the Planet Formation Imager (PFI) initiative (Monnier et al. 2018; Ireland & Monnier 2014). In the mid-infrared, heterodyne interferometry, which consists in detecting the amplitude of the field (coherent detection) as a radio-frequency (RF) signal and in correlating these RFs signal between each pair of telescopes, offers a practical solution while relaxing the requirement on a hard infrastructure. In this perspective, the V8 concept (this work and Berger et al. in the same proceedings) proposes to take advantage of the scalability of heterodyne interferometry and of the current state of mid-infrared technologies to combine the 8 telescopes of VLTI simultaneously in the VLTI lab through an heterodyne combiner, which handles the correlation and the delay function on the heterodyne signal, in order to exploit the full imaging capability of VLTI. In the following, we complement the photonic correlation proposed in this perspective and present a preliminary 2 beams combiner at 10.6 μm dedicated to the validation of a complete detection and correlation chain.

2 Photonic correlation

The principles of photonic correlation consists in encoding a wide band RF signal through a photonic modulator on a optical carrier, typically at telecom wavelength, which is then transported and combined on a photodiode. The scheme that enables to extract the correlation product of the signal can be based either on phase modulation or amplitude modulation. In both cases, the signal that is extracted is proportional to the multiplication product of the two input RF channels integrated in time i.e. the correlation product of the input RF signals at one delay. This principle is very similar to the analog RF correlator implemented on the Infrared Spatial Interferometer (Hale et al. 2000).

[1] Univ. Grenoble Alpes, CNRS, IPAG, F-38000 Grenoble, France
[2] Univ. Grenoble Alpes, CNRS, LIPhy, F-38000 Grenoble, France

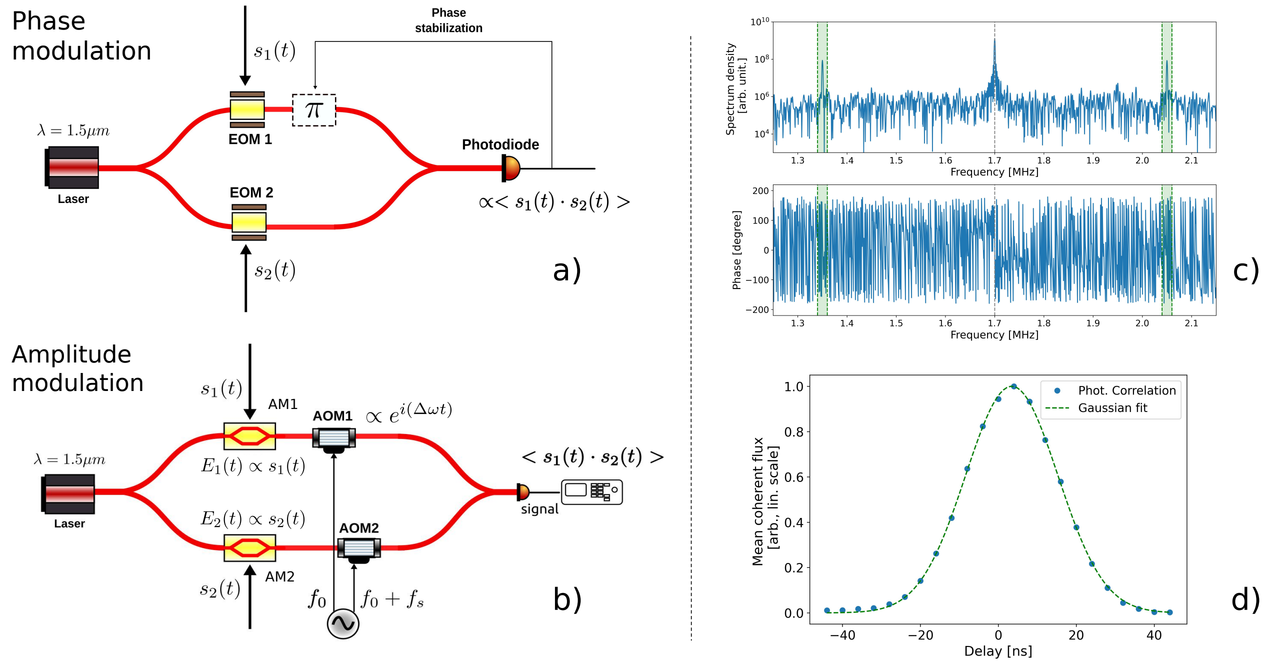

Fig. 1. a) : Phase modulation scheme (EOM : Electro-Optical Modulator) **b) :** Amplitude modulation scheme **c) :** Correlation of heterodyne signals in amplitude modulation (fringe peak in green area). **d) :** Coherence envelope of the correlated signals.

2.1 Photonic correlation in phase modulation

In the phase modulation scheme, the RF signal at the output of the rapid mid-infrared photodiode is encoded on the optical carrier through a phase modulator, placed at the level of each telescope. This signal then propagates in telecom fiber and is combined with an arm coming from an other telescope, which forms a Mach-Zehnder, as shown in Fig 1. The key idea of phase modulation consists in noticing that at a minimum or at a maximum of intensity of a Mach-Zehnder, the output intensity of the Mach-Zehnder varies as the square of the relative phase modulation between the arm. Since the phase modulation is proportional to the input RF signal, the output intensity contains the product term of the two input RF signals, which is the correlation product we seek to compute. A detailed description of the functioning principle as well as its experimental demonstration is given in Bourdarot et al. (2020). The stabilization of the Mach-Zehnder to a given functioning point (maximum or minimum of intensity) is an important constraint of this scheme. In the next section, we describe a second correlation scheme, based on *amplitude* modulation, which enables to relax the requirement on phase stabilization.

2.2 Photonic correlation in amplitude modulation

In the amplitude modulation, an amplitude modulator, on which is imposed the output RF signal of the heterodyne detection stage, is placed in each arm of the Mach-Zehnder, and used at the null of transmission. The optical field $E_k(t)$ in each arm (numbered k) after these two components is :

$$E_k(t) = E_0 e^{i\omega_0 t} e^{i\phi_k} \left(1 - e^{i\beta_k s_k(t)}\right) \approx -iE_0 \beta_k s_k(t) e^{i\omega_0 t + i\phi_k(t)} \tag{2.1}$$

where we have assumed that each modulator is at a minimum of intensity, with E_0 the amplitude of the optical carrier at telecom wavelength (carrier), ω_0 the angular frequency of the optical carrier, $\beta_k = \frac{\pi}{V_\pi}$ with V_π the half-voltage of the modulator, $s_k(t)$ the RF signals coming from the heterodyne stage, and $\phi_k(t)$ the phase perturbation in the fiber link. In addition, a fiber frequency shifter (Acousto-Optic Modulator abrev. AOM) can be placed downstream the amplitude modulator, and has the effect of shifting the central frequency of the optical field i.e. multiplying the electric field by $e^{i\Delta\omega_k t}$, with $\Delta\omega_k$ the angular frequency shift in arm k. The beating term at the output of the Mach-Zehnder (measured with a balanced detection for example) is finally :

$$I(t) = 4I_0 \mathrm{V}_i \beta_1 \beta_2 s_1(t) s_2(t) \cos\big((\Delta\omega_2 - \Delta\omega_1)t + \Delta\phi_{12}(t)\big) \tag{2.2}$$

with $I_0 = |E_0|^2$ and $\Delta\phi_{12}(t) = \phi_2 - \phi_1$. At the output of the correlator, the correlation product $\langle s_1(t)s_2(t)\rangle$ is thus encoded at a given (angular) frequency $(\Delta\omega_2 - \Delta\omega_1)$. In this way, the correlator does not require the stabilization to a given functioning point, but only a relative stabilization over the coherent integration time.

2.3 Experimental demonstration

Following the same methodology than in (Bourdarot et al. 2020), the amplitude modulation scheme was implemented with commercial fibred components, and enables to demonstrate the correlation of heterodyne signals that were previously registered and generated a posteriori with Arbitrary Waveform Generator (AWG). We measure the correlation fringes with a noise factor $> 90\,\%$, and we measure the coherence envelop of the incident signal by varying numerically the relative delay between each arm of the Mach-Zehnder. The results of this proof-of-principles are shown in Fig 1.

2.4 Extension to a large number of telescopes

The photonic correlation scheme described so far is adapted to the correlation of two channels. This scheme can be extended to the correlation of a larger number of telescopes. Different architectures can be envisioned, as in direct interferometry (Lebouquin et al. 2004). These beam combinations can be categorized in different type of flux encoding (spatial, temporal, static phase-shifting) and beam routing (pair-wise, all-in-one, hybrid), cf Fig. 2. In our photonic scheme, temporal techniques are favoured, as they are more suited to the temporal encoding of the fringes in the architecture presented so far, and to the integration of a metrology system in the same channel that the signal channel. In temporal techniques, all-in one combinations based on frequency multiplexing of the fringes, and pair-wise combination, are both compatible to the correlation of a large number of channels. Alternatively, direct-imager combiner, such as proposed in (Blanchard et al. 1999), could also be envisioned, but are less suited to the correlation of a large number of spectral channels, contrary to temporal techniques. These different techniques and the parallel with direct interferometry are summarized in Fig. 2.

3 Preliminary 2 channels heterodyne demonstrator at $10.6\,\mu$m

We propose the implementation of a 2 beam heterodyne combiner at $10.6\,\mu$m in order to demonstrate the detection and correlation architecture devised earlier, to produce a complete sensitivity analysis of this chain, and to validate in the laboratory the technological sub-systems required for V8. The current layout of the

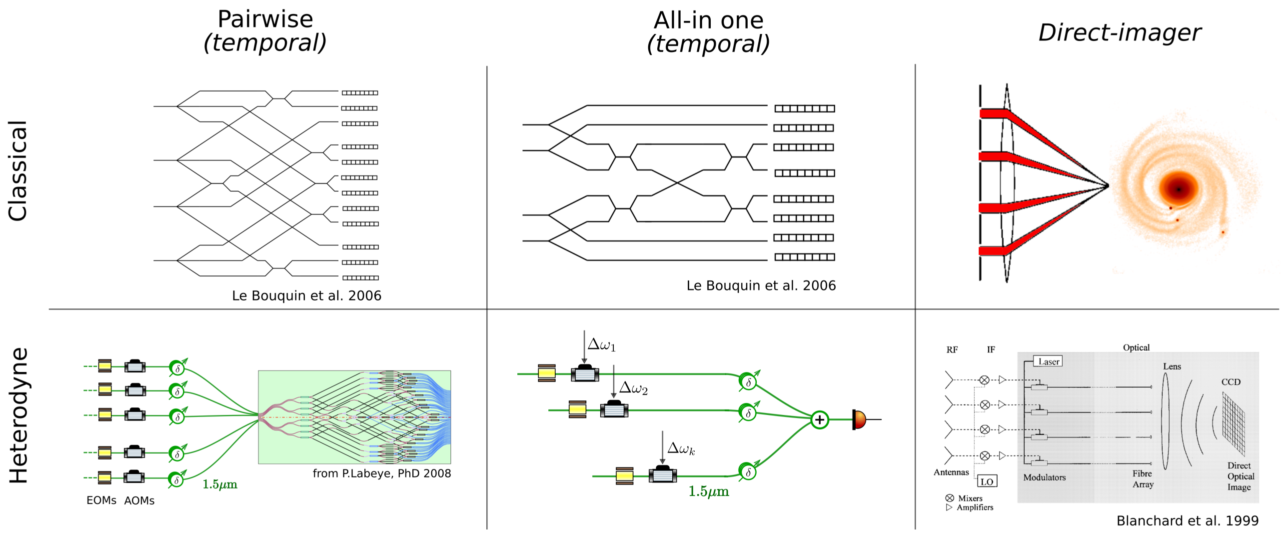

Fig. 2. Extension of the photonic correlation scheme to a larger number of telescopes.

demonstrator is shown in Fig. 3. In this demonstrator, the local oscillator (LO) is a Quantum Cascade Laser (QCL), splitted in two channels to two detectors, which naturally ensures the relative phase stability of the LO between the two channels. The signal channel can be either fed by a laser signal (e.g. the initial QCL) or an independent source (laser, black-body). The current detectors are commercial detectors (VIGO company, 1 GHz bandwidth) , and the correlator is a photonic correlator in amplitude modulation, identical to Sec 2.2. The demonstrator is currently under development, and is designed to observe an heterodyne interferometric signal on a black-body at 900K.

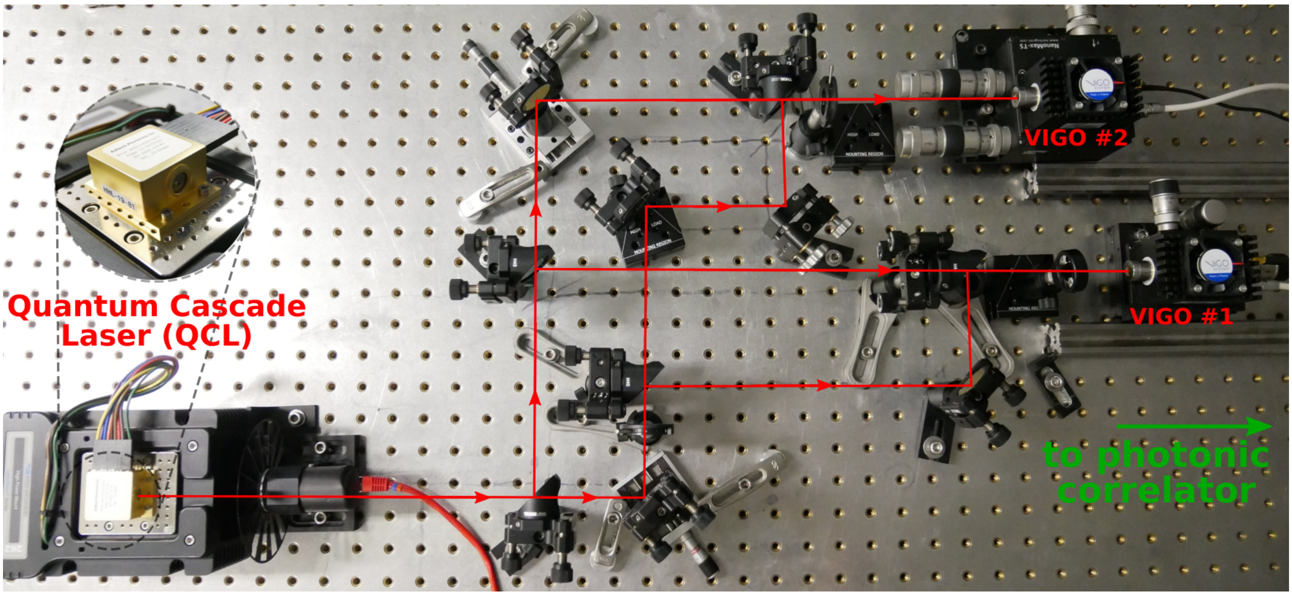

Fig. 3. Mid-infrared optics of the two beam heterodyne interferometric demonstrator at 10.6 μm.

4 Conclusions

The recombination of large number of telescope over kilometric baselines in the mid-infrared can benefit from the use of heterodyne interferometry. We complement the photonic correlation architecture proposed in this purpose with the introduction of amplitude modulation and the extension of this technique to the correlation of a larger number of telescopes. We present the preliminary implementation of a 2 channels heterodyne combiner at 10.6 μm whose goal is to validate the complete detection and correlation chain of our renewed heterodyne architecture, its sensitivity budget, and its essential technological blocks. Once demonstrated, this essential step could be scalable to the correlation of a larger number of telescopes and adaptable to existing infrastructures, in particular to the simultaneous correlation of the eight telescopes of VLTI in the mid-infrared, so-called V8 concept.

This work was partially funded by INSU-CNRS through the Commission Spécialisée Astronomie & Astrophysique (CSAA) and the Action Spécifique Haute Résolution Angulaire (ASHRA) co-funded by CNES. It was partially funded by LabEx FOCUS ANR-11-LABX-0013. We acknowledge the additional funding of Agence Nationale de la Recherche ("ANR FROST", ANR-14-CE32-0022).

References

Blanchard, P. M., Greenaway, A. H., Harvey, A. R., & Webster, K. 1999, Journal of Lightwave Technology, 17, 418

Bourdarot, G., Guillet de Chatellus, H., & Berger, J.-P. 2020, Astronomy & Astrophysics, 639, A53

Hale, D. D. S., Bester, M., Danchi, W. C., et al. 2000, The Astrophysical Journal, 537, 998

Ireland, M. J. & Monnier, J. D. 2014, in Society of Photo-Optical Instrumentation Engineers (SPIE) Conference Series, Vol. 9146, Optical and Infrared Interferometry IV, ed. J. K. Rajagopal, M. J. Creech-Eakman, & F. Malbet, 914612

Lebouquin, J.-B. J., Berger, J.-P., Labeye, P. R., et al. 2004, in SPIE, Vol. 5491, New Frontiers in Stellar Interferometry, ed. W. A. Traub, 1362

Monnier, J. D., Kraus, S., Ireland, M. J., et al. 2018, Experimental Astronomy, 46, 517

REVIVAL OF INTENSITY INTERFEROMETRY WITH MODERN PHOTONIC TECHNOLOGIES

W. Guerin[1], J.-P. Rivet[2], M. Hugbart[1], F. Vakili[2,3], E. S. G. de Almeida[2], A. Domiciano de Souza[2], G. Labeyrie[1], N. Matthews[1], O. Lai[2], P.-M. Gori[2], D. Vernet[4], J. Chabé[5], C. Courde[5], E. Samain[6], B. V. Castilho[7], A. M. Magalhaes[8], E. Janot-Pacheco[8], A. Carciofi[8], P. Bourget[9], N. Schuhler[9] and R. Kaiser[1]

Abstract. We present our project on the revival of intensity interferometry with modern photonic technologies, and more specifically with conventional optical telescopes. This original approach is complementary to the work currently done aiming at applying intensity interferometry to Cherenkov telescopes. We briefly summarize the results obtained so far.

Keywords: Intensity interferometry, Correlation function, η Carinæ

1 Introduction

The study of light intensity correlations, while being nowadays the daily bread of quantum opticians, was originally pioneered by R. Hanbury Brown and R. Q. Twiss for astronomy (Hanbury Brown & Twiss 1956). Indeed, they demonstrated that the intensity correlation function $g^{(2)}(r, \tau)$ (Guerin et al. 2018) provides information about the source: the amplitude of the "bunching peak", i.e., $g(r, \tau = 0) - g(r, \tau \to \infty)$, is proportional to the squared modulus of the visibility. This technique was called stellar intensity interferometry (SII), as opposed to amplitude (or direct or Michelson) interferometry, in which the visibility is measured by the contrast of the interference fringes. Direct optical interference is challenging as it requires a control of the optical paths to better precision than the wavelength. On the contrary, SII is relatively insensitive to the phase of the optical field and therefore much easier to implement. However, this simplicity has a price of lower sensitivity in comparison to direct inteferometry. Therefore, SII requires large collectors and has only so far been used with very bright stars (Hanbury Brown et al. 1974).

Nevertheless, for the last 15 years, there has been a growing interest in reviving SII, in particular in the context of the future Cherenkov Telescope Array (CTA) [see, e.g., (Dravins et al. 2013) and references therein]. Indeed, the number and size of baselines would be much greater than with any other interferometer, with an unprecedented collecting surface. Recently, successful measurements have been performed with other Cherenkov telescopes, namely the MAGIC array (Acciari et al. 2020) and the VERITAS array (Abeysekara et al. 2020).

Our team follows a complementary approach, which is to revive SII for optical telescopes (Rivet et al. 2018). Although the size and number of available telescopes will probably always be much smaller than with Cherenkov arrays, the optical quality of the telescopes provides several advantages. The seeing-limited point-spread function (PSF) (compared with a typical PSF of 0.1° of Cherenkov telescopes) allow us to use the

[1] Université Côte d'Azur, CNRS, Institut de Physique de Nice, France
[2] Université Côte d'Azur, Observatoire de la Côte d'Azur, CNRS, Laboratoire Lagrange, France
[3] Department of Physics, Shahid Beheshti University, G.C., Tehran, Iran
[4] Université Côte d'Azur, Observatoire de la Côte d'Azur, CNRS, UMS Galilée, France
[5] Université Côte d'Azur, Observatoire de la Côte d'Azur, CNRS, Laboratoire Géoazur, France
[6] SigmaWorks, Saint Vallier de Thiey, France
[7] Laboratório Nacional de Astrofísica, Brazil
[8] Instituto de Astronomia, Geofisica e Ciências Atmosféricas, Universidade de São Paulo, Brazil
[9] European Southern Observatory, Chile

best available detectors, yielding a better quantum efficiency ($>70\%$) and timing resolution (<500 ps), and to transport the light from the telescope focus to the detectors by optical fibers. It also allows us to use narrow-band filters (e.g., $\Delta\lambda \leq 1$ nm) to increase the coherence time, and select emission lines. In that configuration stray light from the sky background is negligible. In the future, this should also allow us to use integrated photonic components (Dinkelaker et al. 2021), for example for wavelength multiplexing (Lai et al. 2018). Finally, our setup is compact and transportable and can easily be adapted to any facility.

In this paper we briefly summarize the status of our project and the results obtained so far. Note that in parallel we are also contributing to the study on the use of Cherenkov telescope for SII (Gori et al. 2021).

2 Results

2.1 Experimental setup

Our setup is based on avalanche photodiodes (APDs) used in photon counting mode. Counting and correlations are performed in real time by a time-to-digital converter (TDC). In order to measure the zero-baseline $g^{(2)}(\tau, r = 0)$ correlation function, two APDs per channel are required, each one fed by the complementary outputs of a fibered 50:50 splitter. Special care is taken to avoid spurious correlations and crosstalk.

The inputs of the fibered splitters are connected to optical telescopes output ports through multimode graded index optical fibers (MMF) with 100 μm core diameter. Fig. 1 describes the optical interfaces we use to couple the fiber tips to the output beams of the telescopes. The converging beam issued by the telescope first passes through a dichroic beam splitter (DBS). The blue part of the light is reflected to a guiding CCD camera, through a neutral density filter (ND). The red part is transmitted to the collimating lens L_1. The collimated beam passes through a narrow-band filter ($\Delta\lambda = 1$ nm) to increase the coherence time or select an emission line. Then, a polarizing beam splitter (PBS) separates the light into two orthogonal linear polarization states denoted as "V" and "H" for the reflected and transmitted beams, respectively. An additional linear polarizing plate is placed in the path of the reflected beam to increase the extinction ratio, which would otherwise be significantly lower than for the transmitted beam. A converging lens L_2 is then used to efficiently inject the filtered light into the MMFs. The combination of the collimation and focusing lenses results in a focal reduction factor of 2.5. These coupling modules are made almost completely from standard off-the-shelf opto-mechanical components, requiring only a few custom mechanical adaptation parts.

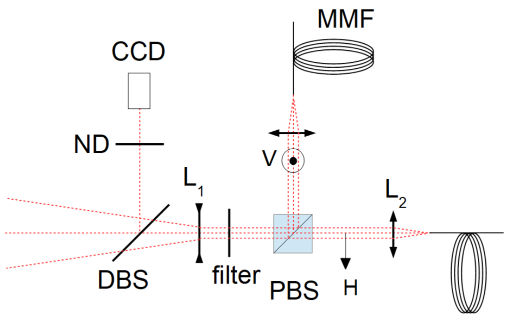

(a)

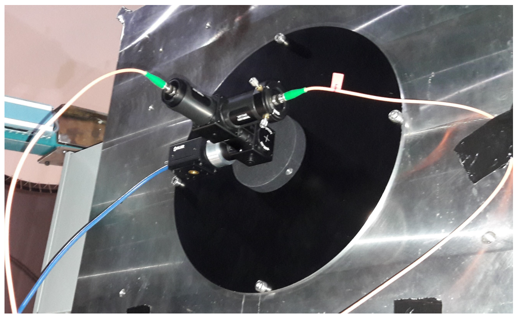

(b)

Fig. 1: (a) Scheme of the coupling module at the focus of the telescope, as it was in 2018-2019. The previous version only had one polarization channel and converging light on the filter; in the next version we have added a supplementary linear polarizer on the V channel to improve the purity of the polarization. (b) Picture of the coupling module at the Nasmyth focus of the SOAR telescope.

2.2 Temporal and spatial bunching with star light

Our first on-sky test of intensity correlation measurements were performed in February 2017 using a 1 m telescope of the C2PU facility (Observatoire de la Côte d'Azur, Calern site). For this initial experiment, we measured the temporal correlation function $g^{(2)}(\tau)$, yielding a zero-baseline calibration ($r = 0$). We obtained well-resolved bunching peaks on three different very bright stars (Arcturus, Procyon and Pollux) at $\lambda = 780$ nm. We could also estimate the injection efficiency into the MMF to be $\sim 66\%$ for average seeing conditions ($\sim 1.4''$) and check that the signal-to-noise (SNR) ratio was only limited by the photon statistics (Guerin et al. 2017). This means that we can always look at dimer objects at the cost of a longer integration time.

In October 2017 we duplicated the coupling module and performed a spatial SII experiment between the two C2PU telescopes separated by 15 m. We observed bunching peaks with two marginally resolved bright stars, Vega and Rigel, and also with a more complex, partially resolved target, the Capella binary, yielding a reduced visibility (Guerin et al. 2018).

2.3 Intensity interferometry on emission lines

The narrow spectral filtering is particularly well adapted to select emission lines allowing for the study of extended stellar atmospheres. This naturally includes Hα emission, but also lines at shorter wavelengths such as Hβ, or He lines, which are traditionally challenging to observe with direct interferometry. The use of such narrow filters is difficult in Cherenkov telescopes due to the large PSF and has so far been limited to $\Delta\lambda > 10$ nm. Therefore interferometry on emission lines at short wavelengths is a natural niche for SII with optical telescopes.

In August 2018 we have performed a run of observations on the very intense Hα emission line of P Cygni. We obtained normalized squared visibilities on the order of 0.3 to 0.5 for baselines between 12 and 15 m. These visibilities are related to the angular size of the emissive region. We used the radiative transfer code CMFGEN (Hillier & Miller 1998) to model the star. We tuned some parameters to reproduce a spectrum acquired independently, which then allowed us to compute the luminosity profile (and thus the physical size) of the star. The Hankel transform of this model profile can thus be adjusted to the visibility data with the distance of the star as the only free parameter. This procedure allowed us to determine P Cygni's distance with an uncertainty comparable with the best published values (Rivet et al. 2020).

2.4 Observations at SOAR

In April 2019 we had one allocated night (at full moon) on the 4.1 m Southern Astrophysical Research (SOAR) Telescope in Chile. It was a single-telescope experiment, yielding the temporal correlation function, like in (Guerin et al. 2017). The goal was mainly to demonstrate the transportability and adaptability of our setup. In order to adapt the setup from the C2PU telescopes (diameter 1.06 m, focal length 13 m) to the SOAR telescope (diameter 4.1 m, focal length 68.175 m) we only had to add a converging lens ($f = 200$ mm) at the input of the coupling module in order to reduce the global focal length. This was also the first time we performed simultaneous measurements with two polarization channels. It is interesting to note that all our equipment was carried in two suitcases only, emphasizing the simplicity and compactness of the setup.

The target was the Hα line of η Carinæ with a total observing time of only 3.5 hours due to a partly cloudy night. The average count rate was about 4.5×10^6 counts per second per detector on each polarization channel, with a significant defocussing not to saturate the detectors. The results for the two polarization channels are presented in Fig. 2. One can see that the widths and the heights are different on the two functions, and they do not agree with each other within the uncertainties. This is mainly due to the fact that each APD has a different jitter such that each detector pair has a different timing resolution. However, the area of the bunching peak should remain constant against differences in the detector jitter and thus we use the area as our observable.

The area under each peak is extracted from a Gaussian fit. We get $A_{\rm H} = 0.68 \pm 0.13$ ps and $A_{\rm V} = 0.60 \pm 0.13$ ps, with 1σ statistical uncertainties. The two areas are in agreement within the error bars, although we found out later that there is a systematic underestimation of the bunching area on the V-channel, estimated

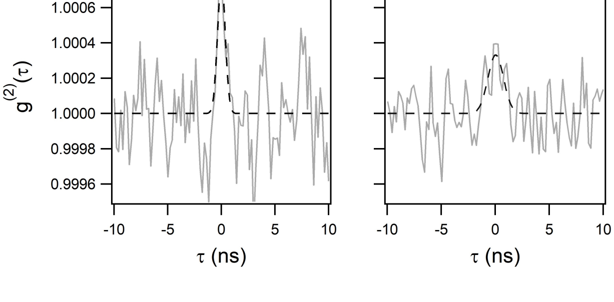

Fig. 2: Temporal intensity correlation functions measured on η Car in the night of 19/20 April 2019. (a) Horizontal polarization channel. (b) Vertical polarization channel. Dashed lines: Gaussian fits.

at $\sim 20\%$ by lab calibration. Half of this reduction can be attributed to the extinction ratio of the PBS, which can be as low as $1:20$ (while it's much better in transmission for the H channel). Indeed, 5% of orthogonal polarization induce a loss of coherence of 10%. The origin of the other missing 10% is not known with certainty but could be due to a slow tail in the timing response of one of the detectors. By correcting for this loss of contrast, and taking the weighted average of the two measurements, our final estimation of the bunching peak area is $A = 0.7 \pm 0.1$ ps.

To calculate the expected area of the bunching peak, we need to numerically compute the $g^{(2)}(\tau)$ function from a measured spectrum, as explained in (Rivet et al. 2020). Although the source is variable, we have checked that several spectra found in open data bases give very close results. We find an expected bunching area equal to $A_0 = 1.48$ ps, significantly higher than our measured value $A = 0.7 \pm 0.1$ ps. This indicates that the 4.1 m aperture of the telescope partially resolves the Hα-emitting region.

Since we know the telescope's aperture, we could compute the expected visibility, given a model for the shape of the emissive region. If there is only one free parameter in the model [like the distance in (Rivet et al. 2020), also using the spectrum to constrain the model], such measurement would allow us to fit this parameter. This is beyond the scope of this paper because η Car is a highly complex object and our measurement uncertainty is still relatively high, due to the short integration time and poor weather conditions.

3 Prospects

Recently, we have improved the optical quality of our coupling module and upgraded it with a tip-tilt correction, which will improve the average injection efficiency in the fibers. We have also performed some tests of superconducting nanowire single-photon detectors [SNSPDs, Zadeh et al. (2021)], which are very promising for SII. On the long term, the way to significantly increase the sensitivity is to perform multichannel measurements, and we start exploring the possible techniques to do it (Lai et al. 2018).

Another direction is to extend the number and size of available baselines. For that we plan to use a transportable 1 m telescope at Calern and the 1.5 m laser-ranging telescope, which is located 150 m away from the C2PU telescopes. We have already developed and tested a method to transfer the timing signal at this long distance with a few picosecond accuracy. We also plan to perform experiments using the Auxiliary Telescopes (ATs) of the VLTI (Chile), which have the strong advantage of being movable. The opto-mechanical adaption of our coupling module to the ATs has already been done. Initial on-sky tests with the ATs are provisionally scheduled for February 2022.

Finally, another (more speculative) goal is to search for laser-like emission (Johansson & Letokhov 2007).

We thank J. Elias, A. Tokovinin, and all the technical staff at SOAR for their help before and during our observing session. We acknowledge the financial support of the UCA-JEDI (ANR-15-IDEX-01), the Doeblin Federation (FR2800 CNRS), the OPTIMAL platform, the Région PACA (project I2C) and the French National Research Agency (project I2C No. ANR-20-CE31-0003).

References

Abeysekara, A. U., Benbow, W., Brill, A., et al. 2020, Nature Astronomy, 4, 1164

Acciari, V. A., Bernardos, M. I., Colombo, E., et al. 2020, MNRAS, 491, 1540

Dinkelaker, A. N., Rahman, A., Bland-Hawthorn, J., et al. 2021, Appl. Opt., 60, AP1

Dravins, D., LeBohec, S., Jensen, H., & Nuñez, P. D. 2013, Astropart. Phys., 43, 331

Gori, P.-M., Vakili, F., Rivet, J.-P., et al. 2021, MNRAS, 505, 2328

Guerin, W., Dussaux, A., Fouché, M., et al. 2017, MNRAS, 472, 4126

Guerin, W., Rivet, J.-P., Fouché, M., et al. 2018, MNRAS, 480, 245

Hanbury Brown, R., Davis, J., & Allen, L. R. 1974, MNRAS, 167, 121

Hanbury Brown, R. & Twiss, R. Q. 1956, Nature, 178, 1046

Hillier, D. J. & Miller, D. L. 1998, ApJ, 496, 407

Johansson, S. & Letokhov, V. S. 2007, New. Astron. Rev., 51, 443

Lai, O., Guerin, W., Vakili, F., et al. 2018, in Optical and Infrared Interferometry and Imaging VI, Vol. 10701, Proc. SPIE, 1070121

Rivet, J.-P., Siciak, A., de Almeida, E. S. G., et al. 2020, MNRAS, 494, 218

Rivet, J.-P., Vakili, F., Lai, O., et al. 2018, Exp. Astron., 46, 531

Zadeh, I. E., Chang, J., Los, J. W. N., et al. 2021, Appl. Phys. Lett., 118, 190502

SPECTRAL MULTIPLEXING IN INTENSITY INTERFEROMETRY

O. Lai[1], G. Labeyrie[2], W. Guerin[2], F. Vakili[1], R. Kaiser[2], J.–P. Rivet[1], M. Hugbart[2], N. Matthews[2], J. Chabé[3], C. Courde[3], E. Samain[3] and D. Vernet[4]

Abstract. Intensity Interferometry offers an interesting path forward for astronomical interferometry at very long baselines and at short wavelengths, all leading to extremely high angular resolution. Single photon counting detectors (and associated correlator technology) has evolved to allow a sensitivity gain of two orders of magnitude since the seminal experiments of Hanbury-Brown and Twiss in the 1960s, but sensitivity remains the challenge to make this technique widely useful: extremely high angular resolution requires high surface brightness by definition. The simplest way to increase the sensitivity of an intensity interferometer is to obtain multiple simultaneous correlation measurements at different wavelengths since these are uncorrelated and improve the SNR as $\sqrt{N}$, with N spectral channels. The first issue to address is the break-even point since the throughput of spectrographs can be low; for example a throughput of 50% requires at least 4 spectral channel to break even. The next issue we wish to address is one of reliability and ease of use as we intend to deploy these spectrographs at multiple locations. In this paper, we propose and compare three concepts, each with its advantages and drawbacks: a classical multimode fiber-fed spectrograph, a photonics lantern fed focal plane based concept and an integrated optics solution using photonics lanterns and an Arrayed Waveguide Grating Spectrograph. We hope to build a simple demonstrator of whichever concept we end up choosing for testing in the context of the I2C project.

Keywords: Intensity interferometry, photonics, White Dwarfs, AGN

1 Introduction

Intensity Interferometry (II) allows to reach places that are hard to reach with amplitude interferometry, such as extremely long baseline, short wavelengths or high precision polarisation studies. However, it suffers from a lack of sensitivity compared to amplitude interferometry because the bandpass has to be extremely narrow to detect single photons to be correlated, compared to the coherence length–spectral resolution relationship that amplitude interferometers can make use of for broadband or dispersed measurements. In II, the optical bandwidth has to be large enough to not degrade the timing resolution (it is inversely proportional to the time resolution of the intensity measurements), which is limited by the detector and the Time–to–Digital Converter (TDC, used to obtain the correlation measurements) jitter. TDCs have count rates of several million per second and the best detectors (Single Photon Avalanche Diodes, SPADs or SNSPDs) have a timing measurement jitter of tens to hundred of picoseconds. The electronic bandpass thus has to be smaller than the optical bandpass at optical wavelengths ($\Delta\lambda = \lambda^2/(c\tau_e)$); if the former is on the order of 50∼100 picoseconds, then the latter would be a limiting factor if smaller than 0.1Å . Once this condition is satisfied, it turns out that the SNR is independent of the actual optical bandpass (as long as it doesn't introduce spurious correlations and count rate is much greater than the dark counts (and sky), and is less than the saturation of the detector), because there are more photons to measure the correlation peak, but its absolute value decreased in equal measure.

The original Hanbury-Brown and Twiss experiments (Hanbury Brown et al. 1967) used photocathodes (the correlations were carried out in analog, continuous mode on the current of the photocathodes, and were limited by the electronics), and modern technologies have allowed to gain about two orders of magnitude in timing

[1] Université Côte d'Azur, Observatoire de la Côte d'Azur, CNRS, Laboratoire Lagrange, 06304 Nice Cedex 4, France
[2] Université Côte d'Azur, Université Nice-Sophia Antipolis, CNRS, InPhyNi, 06560 Valbonne, France
[3] Université Côte d'Azur, Observatoire de la Côte d'Azur, CNRS, UMR GéoAzur, France
[4] Université Côte d'Azur, Observatoire de la Côte d'Azur, CNRS, UMS Galilée, France

resolution (essentially better detectors such as SPADs and Digital Time correlators). However (and as already noted by Hanbury Brown et al. (1974)), the most efficient way to improve the sensitivity of II is to increase the number of independent spectral channels. While this is true, we note that 100 spectral channels only provides an improvement of 2.5 magnitudes. To be truly transformative and become a complementary to amplitude interferometry, thousands of channels will be needed (e.g. 5000 channels provides a gain of 4.8 magnitudes). Our current brightness range with 1–m class telescopes is around magnitude 3 to 4).

There are however difficulties in the implementation of spectral multiplexing in II. First is the issue of detectors; multipixel SPADs exist (for instance 8×1 linear arrays), but they are not readily available and difficult to interface to SNSPDs show more potential for multipixel arrays, but are not mature enough for hundreds of spectral channels. Another issue is the data storage and post-processing which becomes significant for thousands of spectral channels. Pair-wise real time processing (correlations) may be easier, but doesn't offer the same flexibility in terms of re-using the same data in different ways (e.g. filtering). Finally is the issue of implementation, namely how to disperse the light. We note in passing that it is not spectroscopy *stricto sensu* because although we disperse the light, all the spectral channels must contain the same (spatial and intensity) information to be able to be combined as independent variable. Nonetheless we will use a spectrograph to disperse the light and its throughput will be crucial as there is an effective break-even point below which the gain of multiple spectral channels is canceled by the throughput. If the throughput is 50%, then at least 4 spectral channels are needed to obtain any gain at all and if the throughput is 10%, then more than 100 spectral channels are needed to break even.

2 Astrophysical motivation

2.1 Existing facilities

As with the OHANA project (Perrin et al. 2006), a strong motivation for intensity interferometry is the possibility to retrofit interferometric capabilities to observatories or sites which were not designed with that purpose in mind. The reason why this is especially enticing is because there are many serendipitous hectometric to kilometric baselines between large (8∼10m) and extremely large (>20m) optical telescopes at major observatories. For instance, on Cerro Pachón in Chile, the Gemini South 8m telescope is 420m away from the 4m SOAR telescope and we note in passing that our Brazilian colleagues have access to both. At Las Campanas Observatory, the two 6.5m Magellan telescopes are 60 meters apart and the 24m Giant Magellan Telescope (GMT) will be built 1.7km away.

The summit of Mauna Kea hosts four 8∼10m class telescopes (Gemini North, Subaru and the two Kecks) as well as four 2∼4m class telescopes (UH88, UKIRT, IRTF, CFHT) aligned around the caldera in a semi-circle with an 800m diameter, providing good $u-v$ plane coverage. The 30m TMT will likely be built at the 13N site below the summit, 2.4km away, providing 40μarcsecond resolution.

Finally and maybe more conjecturally, the 39m ELT is currently being built on Cerro Armazones, 21km away from the four 8m VLT telescopes on Cerro Paranal. The geometric mean implies the sensitivity of a 25m diameter telescope but with a 5 μarcsecond resolution!

The expected resolution of these arrays is shown on Figure 1. We can also get a rough estimate of sensitivity of large arrays coupled interferometrically if we simply assume as a first approximation that the SNR is proportional to the collecting area, although this is not strictly true due to the geometrical ratio of different size telescopes as well as redundant baselines co-additions. Nonetheless under this assumption we then use our Calern results (Guerin et al. 2018) and normalize them for a SNR of 5 in one night of observing, and optimistically assuming 5000 spectral channels. The Ohana array would have a limiting magnitude of 11.2 and provide resolution between 0.25mas and 0.5mas (for 400nm to 900nm respectively). Adding the TMT would increase the limiting magnitude to 13.1 and with a resolution of 40 micro-arcseconds. Similar resolutions would be achieved by the GMT coupled with the Magellan telescopes, with a limiting magnitude of 12.3. Finally, the VLTs and the ELT, would provide a limiting magnitude of 13.6.

2.2 Astrophysical cases

Such resolutions on relatively bright objects at short wavelengths imply that the scientific applications will be focused on hot, compact, high surface brightness objects, such as White Dwarfs and X-ray binaries, as well as the BLR and accretion disk of active galactic nuclei (quasars and Seyfert 1 especially).

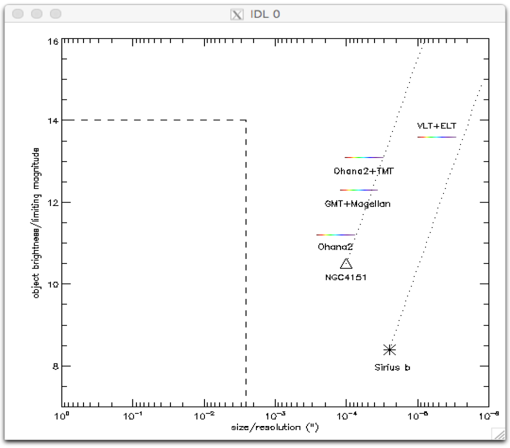

Fig. 1. Resolution versus expected sensitivity is shown for the various arrays with the spectrum showing the wavelength dependence. Sources below and to the left of the horizontal lines will be observable. The dashed rectangle on the left side of the plot shows the current limits of amplitude interferometry (although the limiting magntiude of VLTI is expected to increase to mag$_K \sim 18$ with the Gravity+ project). Also show on the plot is the brightness and expected size (or upper limit) of the closest know White Dwarf, Sirius-b (star), and of a Seyfert 1 nucleus (triangle), and the distance modulus extrapolation (dotted line) for such objects.

An upper limit of the apparent size of the nucleus of NGC 4151 was obtained by the Keck interferometer (Swain et al. 2003) with an 85m baseline in the near infrared (resolution ∼5mas). But if we consider that the size of an accretion disk should be on the order of 10^{-2}pc, at the distance of NGC4151 (19Mpc) this corresponds to an apparent size of 100μarcseconds; we note in passing that the K magnitude of the nucleus is ~ 9 while it is fainter in the visible (V∼12), so a compromise may be required in terms of resolution versus sensitivity for such objects, which we have plotted on Figure 1, as well as its distance modulus extrapolation for fainter, more distant objects. We can see that a Maunakea or Las Campanas intensity interferometer would be extremely well suited for the study of compact extragalactic sources.

The closest known White Dwarf, Sirius-b is expected to have a diameter on the order of 10^4km; at a distance of 8.6 light years, this translates to an apparent diameter of a few tens of μarcseconds, well within reach of the ELT–VLT baseline described above.

3 Spectral multiplexing

The first and simplest way to disperse the output of a multimode fiber and to couple it to a linear array of SPADs using a lenslet array. The dispersive element could be a prism (low-res), line grating (medium-res) or Volume Phase Holographic (VPH) grating (hi-res). Being fiber fed, the spectrograph can be made gravity invariant which helps with stability. Although simple in concept, the spectral resolution is limited unless such a spectrograph becomes large (we currently use a 1nm filter in front of the SPADs), making it sensitive to telescope environment (e.g. stability versus temperature). Such concepts are depicted on Figure 2.

An extension of this concept is to use a photonic lantern to split the multi-mode fiber into several single mode fibers which can be aligned in a pseudo-entrance slit in a V-groove. Although we currently do not have much experience with photonic lanterns, we suspect that they are preferable to adaptive optics due to the short wavelengths used in intensity interferometry. The main advantage here is in terms of compactness, since a single mode, bulk optics spectrograph can then be used. Furthermore a curved grating (and/or cross disperser) can be used to superpose the output of the different single mode fibers in the entrance slit onto the SPADs. Another advantage is that the optical parameters can be adjusted as new detectors become available and using 2D arrays, thousands of spectral channels appear feasible.

Finally, a fully integrated optics spectrograph is also worth mentioning since components exist and could in principle be duplicated or stacked into a very compact configuration. Figure 3 shows what such a device could look like: a multimode fiber is split into several single mode fibers (the exact number will depend on the D/r_0, or number of modes to be coupled into the spectrograph), each one feeding an Array Wave Guide (AWG) spectrograph; these devices are commercially available at near-IR wavelengths but nothing prevents an

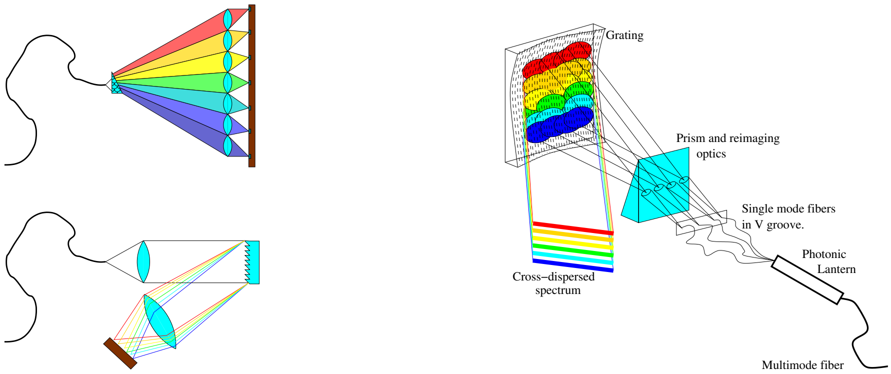

Fig. 2. Left: Conceptual spectrograph using a prism (left) or grating/VPH (right), fed by a multi-mode fiber. Although simple in design, the main issue with such concepts are the size and the stability. **Right**: Using a photonic lantern and a V-groove to align the single mode fibers into a pseudo slit, a single mode, bulk optics spectrograph can be used, allowing for a more compact design.

extension to shorter wavelengths. The monochromatic outputs of each AWG are then recombined (incoherently) using inverted photonic lanterns so that only one detector is required per wavelength.

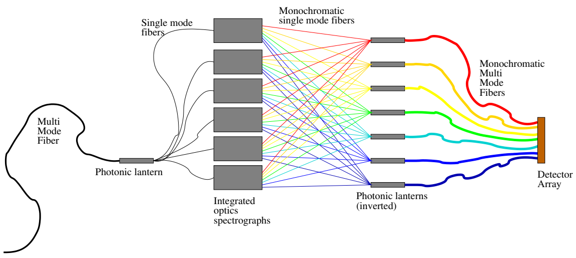

Fig. 3. Fully integrated optics spectrograph. See text for details.

The number of AWGs is determined by number of modes in the input photonic lantern and the number of inverse photonic lanterns is equal to the number of spectral channels, but we note that a custom device could integrate all these functions in a single optical chip. The main advantage here is that the beam never needs to come in or out of waveguides, the devices can be made very compact, and would be easy to maintain in temperature. We point out that a reliable, stable and completely autonomous device will be highly valuable when we try to operate several of these devices at telescopes kilometers away!

4 Conclusions

Intensity Interferometry seems very well matched to photonics techniques, especially to achieve double digit limiting magnitudes. As we pointed out, these high resolution spectrographs will need to be operated simultaneously (autonomously) many kilometers apart, requiring a high level of reliability and stability. We have started discussions to build a demonstrator for testing at the C2PU telescopes (Observatoire de la Côte d'Azur, Calern site), but we still need to find right level demonstrator between available technology (detectors, especially with SNSPDs becoming more attractive) and scalability. A sound first step would be to demonstrate that we can achieve an effective gain in sensitivity proportional to the square root of the number of spectral channels.

References

Guerin, W., Rivet, J. P., Fouché, M., et al. 2018, MNRAS, 480, 245
Hanbury Brown, R., Davis, J., & Allen, L. R. 1967, MNRAS, 137, 375
Hanbury Brown, R., Davis, J., & Allen, L. R. 1974, MNRAS, 167, 121
Perrin, G., Woillez, J., Lai, O., et al. 2006, Science, 311, 194
Swain, M., Vasisht, G., Akeson, R., et al. 2003, ApJ, 596, L163

SF2A 2021
A. Siebert, K. Baillié, E. Lagadec, N. Lagarde, J. Malzac, J.-B. Marquette, M. N'Diaye, J. Richard, O. Venot (eds)

THE HI-5 NULLING INSTRUMENT AND SCIFYSIM: AN END-TO-END SIMULATOR FOR INTEGRATED OPTICS BEAM COMBINERS

R. Laugier[1], D. Defrère[1] and A. Bigioli[1]

Abstract. By limiting the precision of the fringe visibility measurement, photon noise is a major obstacle to the capability of interferometers to detect exoplanets at the smallest angular separations. To circumvent this limitation, the SCIFY project aims to design, build and commission Hi-5: the first nulling instrument for the VLTI, operating in the L' band, a sweet spot for the detection of young giant exoplanets. Based on an integrated optics chip combining all four VLTI beams into a double Bracewell configuration, it will enable medium spectral resolution (R=2000) in the L' band of giant exoplanets between 5 and 50 mas from their star. The end-to-end simulator SCIFYsim is being developed to predict the performance of this new instrument in the presence of a wide variety of instrumental errors, like optical path difference residuals from fringe tracking, wavefront error at the injection, longitudinal dispersion, chromaticity of the combiner chip, and more. As it was designed for modularity, this simulator could also be used to study the performance of other types of integrated beam combiners operating in realistic conditions, like ABCD pairwise combiners, or the more elaborate kernel-nulling combiner envisioned for the VIKiNG project. I will present both the current state of the design of the high-contrast combiner Hi-5, and some of the features and early results of SCIFYsim.

Keywords: High contrast, nulling interferometry, long-baseline interferometry, simulations

1 The Hi-5 instrument

Hi-5 is a possible future visitor instrument for the VLTI led by the Institute of Astronomy of KU Leuven and mainly financed by the ERC project SCIFY. Its design is optimized for high contrast observation and the detection and characterization of young giant planets around nearby stars. It will leverage the long baselines of the observatory to do this down to unprecedented angular separations (5 to 50 mas) from their host stars. This challenging observing task can be achieved using nulling interferometry (Bracewell 1978) to work in a regime comparable to coronagraphy where on-axis light is treated in a special way, so that the corresponding photon noise does not affect significantly the scientific measurement.

Hi-5 will offer a spectral resolution of up to $R \approx 2000$ in the L' band (a sweet spot for the direct detection of young giant planets). It should probe uncharted territories in planet formation into shorter orbital period planets, inside the snow line of their system. It should also allow the detection and characterization of some giant exoplanets detected by radial velocity measurements.

The instrument will take advantage of the spatial filtering, stability, and compactness offered by single-mode waveguide integrated (i.e. photonics) beam-combiners, to implement one of the more recent and more complex beam-combiner architectures called Double Bracewell or Angel & Woolf, from the seminal paper (Angel & Woolf 1997). Future evolutions are already considered to leverage more advanced nulling techniques (Martinache & Ireland 2018), that are beyond the scope of current simulation tools (Den Hartog et al. 2003; Absil et al. 2006).

Much like a coronagraph, the performance of a nulling combiner is directly affected by the quality of the wavefront that feeds it. Therefore, predicting its performance requires, in addition to the simulation of the beam-combination device, the simulation of the adverse effects introduced — or partially corrected — by the interferometer's infrastructure and environment, which will be listed in section 3. SCIFYsim is the python-based end-to-end simulator designed to reproduce the complicated interactions between the beam combiner architecture and the various instrumental effects. While Hi-5 is currently in its design phase, the end-to-end simulator, here presented, stands as a guideline to determine and optimize the attainable performances and to provide a working ground for developing data reduction algorithms.

[1] Institute of Astronomy, KU Leuven, Celestijnenlaan 200D, 3001 Leuven, Belgium

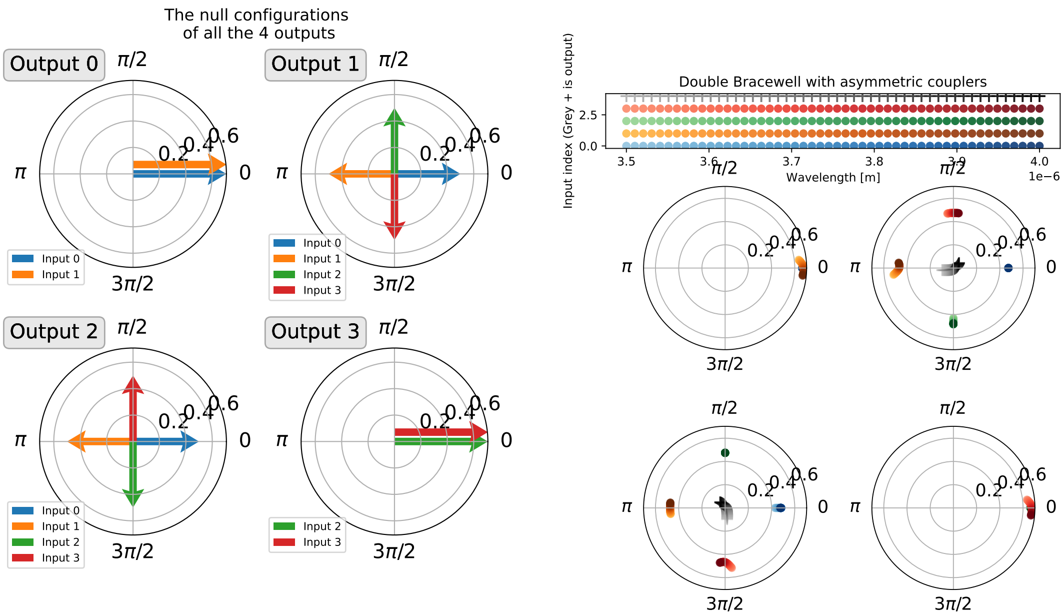

Fig. 1. Left: Graphical representation of achromatic combiner matrix. Right: representation of a chromatic combiner. Each row of the matrix corresponds to an output and is plotted on one complex plane graph. Each column of the matrix corresponds to an input and is plotted in a different color. Each wavelength channel is mapped to a luminance in the color scales. The outputs corresponding to cophased input are plotted in gray tones and its closeness to zero can informs us on the depth of the null.

2 Beam combination

The data flow in SCIFYsim is built around the beam combiner, which is implemented as the matrix of the complex amplitude transfer function of the photonics component. This matrix represents the transformation of the vector of complex amplitude injected into the input waveguides into the vector of complex amplitudes at the outputs.

The spectrograph module then computes the output intensity which is convolved with the spectroscopic PSF to generate the image on the pixels of the detector. The preliminary simulations bypass this step and assume that each wavelength channel is evenly distributed on a fixed number of pixels.

The sensor module computes the integration of light on each pixel, and incorporates readout noise, photon noise, and excess noise in the case of amplified sensors.

3 Aberrations

The main aberrations on the complex amplitude of the injected light are simulated through three independent processes detailed below.

First, for the injection, we assume that the effect of the atmospheric turbulence corrected by an adaptive optics system. The injection is in this case simulated independently for each telescope, using a sliding phase screen based on a spatially filtered Kolmogorov function. Figure 2 shows the simulation of this phasor at three wavelengths which is then interpolated at each spectral channel.

Secondly the simulation of the fringe-tracking residuals is based on a random time series generated on the basis of the temporal power spectrum of optical path differences (OPD) residual measurements taken with the GRAVITY fringe tracker.

Finally, the chromatic component of the OPD errors, arising from the correction of optical paths in delay lines that have different chromatic optical properties from the path atmosphere is split into two components. A static contribution depends on the pointing of the instrument and atmospheric conditions, will be corrected with variable thickness ZnSe plates. Another is dynamic, (called water vapor seeing) will be implemented in the same way as the geometric OPD as it can be measured with the GRAVITY fringe tracker. Both these

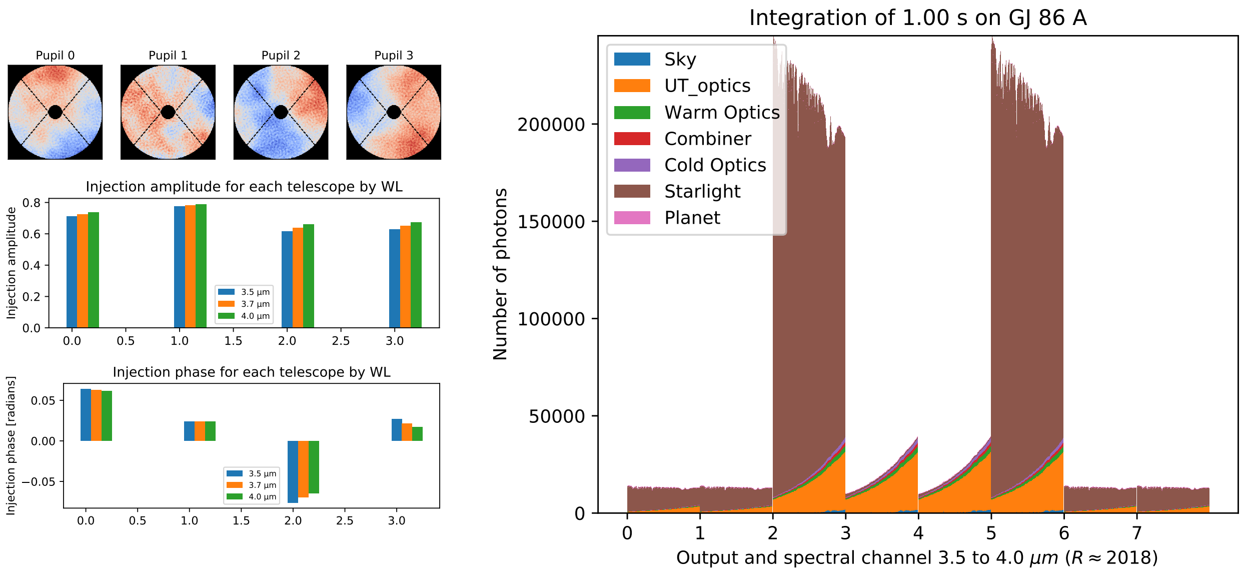

Fig. 2. Left: Detail of the simulation of the injection effect showing the pupil wavefront, and the resulting complex amplitude injected in different wavelength channels in amplitude and phase. The wavefronts are spatially filtered to emulate the effect of the adaptive optics system. **Right:** The decomposition of the (cumulative) contribution of each sources to the different outputs. Within each output, each of the 270 wavelength channel is represented side-by-side, increasing wavelength from left to right. The signal of interest on the two dark channels (3 and 4) is dwarfed by the main contributor: the UT thermal background.

chromatic effects are not considered for the results shown here.

The simulation includes a module simulating transmission and emission in a recursive chain including the sky, the coudé train, the warm optics, the combiner, and the cold optics. They feature a temperature, and a transmission law that is used to infer on the emissivity. If needed, all these sources can be propagated independently to obtain the detail of the contributions to the signal and background for each wavelength channel, as shown in Fig. 2.

Although polarization is not modeled vectorially in the simulator, we consider that the phase mismatch due to the chip birefringence is compensated a the inputs and the polarizations are split in the spectrograph (thus using twice the number of pixels), and we scale the signal accordingly.

4 Early results

The signal of interest produced in the differential output by an off-axis source is shown in Fig. 3. It is shown here as a broadband combination (the instrument will actually work independently in all wavelengths) and takes into account both the radial profile of the injection and the projection of the baselines for a target at a declination of $-50°$ near the meridian. As expected with the combination architecture, the fundamental pattern is the same as could be seen if Fig. 7 of Martinache & Ireland (2018). Depending on the order in which the telescopes are fed into the instrument, either of the three patterns can be chosen.

We use the simulator to generate a series of 100 DIT realizations to evaluate the leakage light and the standard deviation of instrumental noise as a function of the star's magnitude. Noise is then computed as the quadratic sum of the detector readout noise, the photon noise from thermal background and leakage light, and the instrumental noise. It is then adjusted by the number of pixels involved in the reading and the number of DIT used in an integration time.

The signal to noise ratio (S/N) can then be evaluated, assuming a certain position on the map, for any value of star and planet parameters. Here we chose to examine the mean S/R over the 270 spectral channels, therefore our capacity for spectral characterization of the target. An example is shown in Fig. 3 where two regimes can be identified. For bright stars, the noise is dominated by the instrumental noise and the temporal variability of the leakage light, especially at shorter wavelengths. For fainter stars, the noise is dominated by

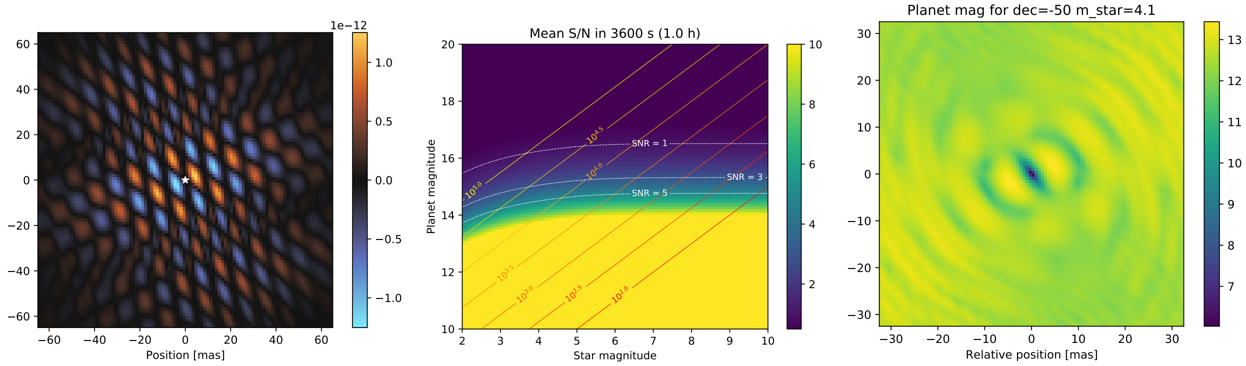

Fig. 3. Left: the broadband ($3.5 - 4\mu$m differential map of one considered configuration observing at declination -50deg. Units are arbitrary, and the optical axis is marked by a white star. While the fundamental pattern visible around the center would repeat to infinity, it is here limited in extent both by the transmission of the fiber injection, and by the bandwidth that produces a radial smearing. **Center:** the mean value of S/N in each spectral channel as a function of star and planet magnitude in the most sensitive region of the map. Diagonal lines indicate the corresponding contrast. **Right:** the sensitivity map around a magnitude 4.1 star. Combining the different wavelengths and pointings produces a smoothing of the sensitivity regions.

the thermal background of the optical train, especially at longer wavelengths.

In order to compute the detection performance, we follow the example given by Ceau et al. (2019) and establish a T_E test of detection. This test, while not the most powerful, provides realistic performance prediction in rejecting the null hypothesis (of the absence of detectable features) for an unknown detected signature. Here, we use a numerical approach to invert the P_{Det} function and obtain the magnitude of the fainter single planet that would be detected with a probability of 90%

These results are a first approximation as the figures for the input aberrations are not yet representative, and some features of the simulator are yet to be implemented.

5 Conclusion

Hi-5 will pioneer L-band photonics instruments and be the first to use photonics to deploy one of the advanced nulling architecture at a long-baseline interferometric facility. Details of the design, the performance evaluation, and yield estimation are in progress and will be described in coming peer-reviewed publications.

The simulator SCIFYsim was designed for flexibility. As it is articulated around the complex amplitude transfer matrix of arbitrary single mode photonic device with its output sent into a spectrograph, it can just as easily be used to simulate the behavior of instruments like GRAVITY, PIONIER, or even monolithic aperture devices like GLINT, opening the door to more complex architectures like VIKiNG (Martinache & Ireland 2018).

SCIFY has received funding from the European Research Council (ERC) under the European Union's Horizon 2020 research and innovation program (grant agreement No 866070).

References

Absil, O., Hartog, R. D., Gondoin, P., et al. 2006, 800, 787

Angel, J. R. P. & Woolf, N. J. 1997, The Astrophysical Journal, 475, 373

Bracewell, R. N. 1978, Nature, 274, 780

Ceau, A., Mary, D., Greenbaum, A., et al. 2019, Astronomy and Astrophysics, 630, 1

Den Hartog, R., Absil, O., Kaltenegger, L., et al. 2003, European Space Agency, (Special Publication) ESA SP, 399

Martinache, F. & Ireland, M. J. 2018, Astronomy and Astrophysics, 619, 1

REVEALING NEW WORLDS FROM DARKNESS: GLINT

M.-A. Martinod[1]

Abstract. Characterisation of exoplanets is key to understanding their formation, composition and potential for life. However, detecting their glint drown in the overwhelming star glare is challenging. Nulling interferometry, combined with extreme adaptive optics, is among the most promising techniques to address it and advance this goal. We present an integrated-optic nuller whose design is directly scalable to future science-ready interferometric nullers: the Guided-Light Interferometric Nulling Technology, deployed at the Subaru Telescope. It combines four beams and delivers spatial and spectral information. We demonstrate the capability of the instrument on-sky. These successes pave the way for future design enhancements: scaling to more baselines, improved photonic component and handling low-order atmospheric aberration within the instrument, all of which will contribute to enhanced sensitivity and precision.

Keywords: Nulling, interferometry, high contrast imaging, high angular resolution, GLINT, exoplanets, integrated-optics, photonics, adaptive-optics

1 Introduction

Despite more than 4800 detected exoplanets so far, few are detected within the habitable zone or the snow line (Fig. 1). The latter region is critical for studying the formation process of planetary systems where young Jupiter-like exoplanets are mainly located (Fernandes et al. 2019). However, most exoplanets have been discovered by indirect methods (such as transits or radial velocities), which tends to detect giant planets close to their host star, or by direct imaging (e.g. coronagraphy), which tends to detect planets far from their star. Accessing the intermediate scale where the snow line necessitates high angular resolution and high contrast capabilities.

The technique of nulling interferometry addresses both issues: it suppresses the overwhelming glare of the host star while preserving the light of the planet. This technique makes the on-axis starlight self-destructively interfere (Bracewell 1978) by setting a π radians phase shift. The light coming from an off-axis source carries another phase shift imposed by the non-axial angle of incidence. Thus, it does not destructively interfere inside the nulling interferometer and can be detected.

Unlike coronagraphs, the effective Inner Working Angle (IWA) of a nuller depends on the baseline B separating the apertures so that $IWA = \frac{\lambda}{2B}$ (Lay 2005). Furthermore, the spatial structure can still be resolved below the IWA at the expense of lower achievable contrast.

The primary observable is called the *null depth*, defined as the ratio of the intensity of destructive over constructive interference. It quantifies the degree of suppression of the light due to the spatial brightness distribution of the source.

The *Guided-Light Interferometric Nulling Technology* (GLINT) is the first nuller based on integrated-optics technology to perform light processing. It is deployed at the Subaru Coronagraphic Extreme Adaptive Optics system (SCExAO) (Guyon et al. 2011; Jovanovic et al. 2015), at the Subaru Telescope, which provides wavefront correction.

We present the instrument in Section 2 and its on-sky commissioning in Section 3 and the further upgrades and applications allowed by the use of integrated optics in Section 4.

[1] University of Sydney, 2006, Sydney, NSW, Australia

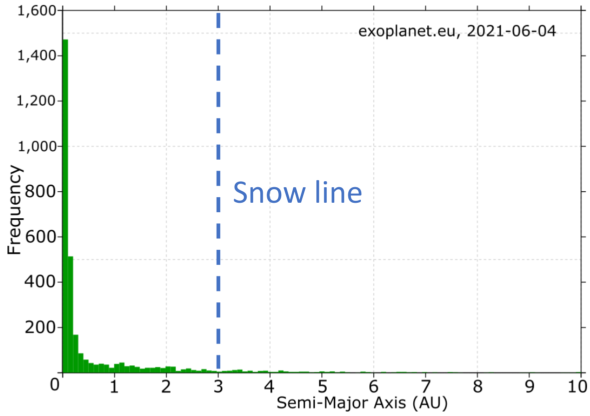

Fig. 1. Histogram of discovered of exoplanets with respect to the semi-major axis in AU. The vertical blue dashed-line is the snow-line for a Sun-like star.

2 Presentation of GLINT

GLINT and its commissioning in lab and on-sky have been extensively described in Martinod et al. (2021a). In a nutshell, GLINT is optimised for science by benefiting from the wavefront correction provided by the extreme adaptive optics system (AO) of SCExAO and being the first instrument able to cancel several baselines simultaneously. GLINT operates in the H band and disperses the light from 1400 to 1650 nm with a spectral resolution of 160 at 1.55 μm. GLINT combines up to 4 apertures, providing 6 non redundant baselines, spanning from 2.15 to 6.45 metres. The light processing is performed inside an integrated-optics component which has two functions. The first one is to coherently remap the 2D configuration of the aperture mask into a linear array. The second function is to combine the beams pair-wise with directional couplers and provides photometric outputs. The former delivers information about the injection for each aperture. The latter delivers two outputs per baseline in opposition of phase: one 'null' output carrying the destructive interference (in which the planet-light will be) and an 'antinull' output carrying the constructive interference (which mainly contains the starlight). The integrated-optic chip is designed with the Ultrafast Laser Inscription method (ULI) (Nolte et al. 2003; Gattass & Mazur 2008; Arriola et al. 2013; Gross & Withford 2015) which allows three-dimensional circuitry. The 16 outputs are spectrally dispersed on a CRED2 InGaAs camera, operating at 0.7 ms to 'freeze' the atmospheric turbulence.

The data processing relies on the *Numerical Self-Calibration* method described by Hanot et al. (2011) adapted for the case of multiple baselines and spectral dispersion. To sum up, this method models the statistical fluctuations of the measured null depth to determine the null depth of the source (called 'source null depth' hereafter) without a calibrator. The main advantage of such a method is a longer observing time of the object of interest. The disadvantages so far are the need for an extensive dataset ($>10^5$ frames) and a high signal-to-noise ratio per frame.

3 On-Sky commissioning

GLINT was deployed on-sky to determine the apparent angular diameters of α Bootis and δ Virgo.

α Bootis is a red giant branch star, with magnitude in H band of -2.81 mag and with published angular diameter measurements between 19.1 and 20.4 mas (Richichi et al. 2005) in K band. It is around 40% of the λ/D diffraction limit of the telescope in our band. The average seeing during the night of the 20th of June 2020 ranged between 0.3 and 0.5 arcseconds at 1600 nm, but with some significant wavefront error resulting from low-wind-effect and telescope vibrations. Data was acquired for 15 min at a frame rate of 1400 Hz for four baselines spanning from 2.15 to 5.68 metres.

δ Vir is also a red giant branch star, with a magnitude in H band of -1.05 mag and a measured angular diameter of 10.6 ± 0.736 mas in H band (Bourges et al. 2017), i.e. around 20% of the diffraction limit. The conditions of observation for the night of the 5th of July 2020 and the configuration of the acquisition were the same as for α Bootis.

For each star, the source null depth was determined with respect to the four baselines with the NSC method. The angular diameters of both stars were deduced from the fit of these four null depths by a uniform disk model that gave the expected null leakage given the stellar size.

The source null depth points of α Boo are an excellent match to the expected curve and yield parameters within the range of expected literature values (Fig. 2, left). The angular diameter found is 19.7 ± 0.1 mas with a reduced χ^2 of 52.0. The uncertainty has been rescaled by the square root of the reduced χ^2. The χ^2 is high because the error bars are derived only from statistical diversity in the data and do not account for systematics (for example, blurring due to seeing variations faster than the frame rate).

Similarly, the found diameter of δ Vir is 10.9 ± 0.1 mas with a reduced χ^2 of 11.2 where the uncertainty has been rescaled as before. The source null data points yield an excellent fit to the model (Fig. 2, right), which in turn is in agreement with literature expectations for this star (expected UD diameter of 10.6 mas). As for α Boo, the high χ^2 betrays the presence of systematic errors not taken into account in the measurement of the null depth.

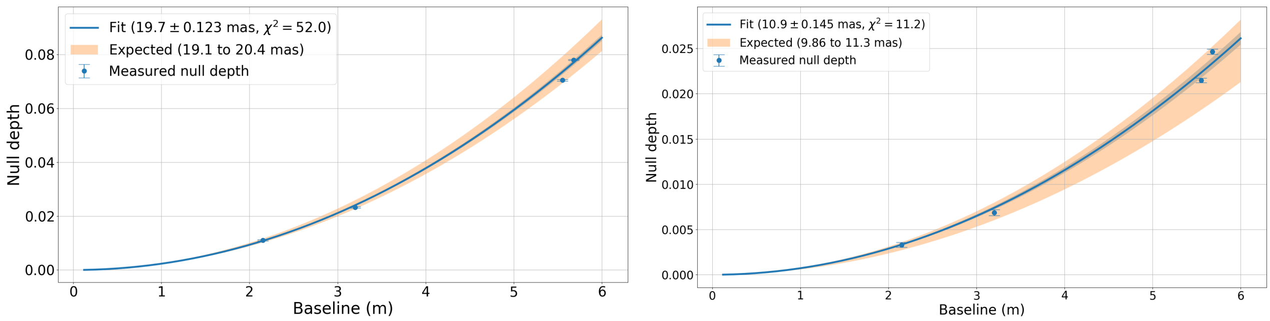

Fig. 2. Left: Variation of the source null depth of α Boo (blue dots) as a function of baseline together with the best-fit model (blue solid curve). The orange area highlights the expected range of null depth at 1550 nm for an expected UD diameter between 19.1 and 20.4 mas. Right: Source null depth of δ Vir (blue dots) with baseline together with the best-fit model (blue solid curve). The orange gives the expected range of null depth for a UD diameter between 9.86 and 11.3 mas. The error bars on both plots represent the standard deviation of the fitted value of the source null depth given by the covariance matrix of the fit of the histogram, rescaled by the reduced χ^2 of that fit.

4 Further upgrades and applications

The directional coupler is a chromatic device that limits the null depth to achieve the desired contrast of 10^{-5} to detect self-luminous exoplanets. In addition, extreme adaptive optics suffer from low-order aberrations (Vievard et al. 2020) which are sharp phase discontinuities across the telescope's spiders believed due to thermal effects. The pyramid wavefront sensor of SCExAO is blind to this effect, but GLINT is (Fig. 3). It shows the potential for a photonic instrument nuller also to be used as a wavefront sensor. These two elements are the main limiting factors of the performance of GLINT and will be addressed in a future upgrade with the replacement of the directional couplers by tricouplers.

The concept of the tricoupler could solve both issues as it provides an achromatic null depth and fringe-tracking capabilities while performing nulling. This all-in-one device is interesting as it is not affected by non-common-path errors and can be used as a wavefront sensor to enhance the wavefront correction of an AO system. Its application has been explored by Martinod et al. (2021b).

In a nutshell, a tricoupler where three parallel guides are at the points of an equilateral triangle provide interesting symmetry properties for a nuller. If the incident beams can be injected in anti-phase, then the intrinsic symmetry of the structure means that none of the light is able to couple into the central guide regardless of the wavelength. For nulling, this centre waveguide is exploited as the null channel. The outer waveguides will allow recovering the incoming beams' differential phase, thus feeding a fringe tracker or the AO system to stabilize the null depth. This ability will allow an AO system to correct low-order aberrations.

The simulations of a GLINT instrument with tricoupler performing fringe tracking instead of directional coupler presented by Martinod et al. (2021b) show a gain of the null depth by a factor of 45. This device, added to the NSC for data processing, would allow reaching the required contrast of 10^{-5} to image exoplanets.

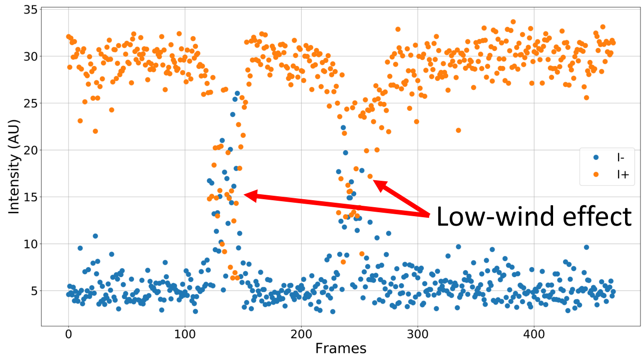

Fig. 3. Fluxes measured at the null (blue dots) and antinull (orange dots) outputs of the baseline of 5.55 metres. The events when the outputs swap are due to low-wind effect.

5 Conclusion

GLINT is the first nuller based on integrated-optic technology combining more than two apertures and providing spectral information. It successfully measured the diameter of stars which are respectively smaller than the half and the quarter of the diffraction limit of the telescope. It demonstrates the potential of this technology, associated with adaptive optics, to design instruments able to image and characterize exoplanets within the snow line. The use of integrated-optics device makes the concept easily scalable to bigger telescopes or long-baseline interferometry. The current limitations of GLINT have been identified and are being addressed with the investigation and the development of the photonic tricoupler which provides an achromatic signal and fringe-tracking capability.

M.A. Martinod acknowledges funding through the Australian Research Council Discovery Program DP180103413.

References

Arriola, A., Gross, S., Jovanovic, N., et al. 2013, Optics Express, 21, 2978

Bourges, L., Mella, G., Lafrasse, S., et al. 2017, VizieR Online Data Catalog, II/346

Bracewell, R. N. 1978, Nature, 274, 780

Fernandes, R. B., Mulders, G. D., Pascucci, I., Mordasini, C., & Emsenhuber, A. 2019, ApJ, 874, 81

Gattass, R. R. & Mazur, E. 2008, Nature Photonics, 2, 219

Gross, S. & Withford, M. J. 2015, Nanophotonics, 4, 20

Guyon, O., Martinache, F., Clergeon, C., et al. 2011, Society of Photo-Optical Instrumentation Engineers (SPIE) Conference Series, Vol. 8149, Wavefront control with the Subaru Coronagraphic Extreme Adaptive Optics (SCExAO) system, 814908

Hanot, C., Mennesson, B., Martin, S., et al. 2011, ApJ, 729, 110

Jovanovic, N., Martinache, F., Guyon, O., et al. 2015, PASP, 127, 890

Lay, O. P. 2005, Appl. Opt., 44, 5859

Martinod, M.-A., Norris, B., Tuthill, P., et al. 2021a, Nature Communications, 12, 2465

Martinod, M.-A., Tuthill, P., Gross, S., et al. 2021b, Appl. Opt., 60, D100

Nolte, S., Will, M., Burghoff, J., & Tuennermann, A. 2003, Applied Physics A: Materials Science & Processing, 77, 109

Richichi, A., Percheron, I., & Khristoforova, M. 2005, A&A, 431, 773

Vievard, S., Bos, S. P., Cassaing, F., et al. 2020, in Society of Photo-Optical Instrumentation Engineers (SPIE) Conference Series, Vol. 11448, Society of Photo-Optical Instrumentation Engineers (SPIE) Conference Series, 114486D

Session 16

Détecter et caractériser des exoplanètes en présence d'activité stellaire

SF2A 2021
A. Siebert, K. Baillié, E. Lagadec, N. Lagarde, J. Malzac, J.-B. Marquette, M. N'Diaye, J. Richard, O. Venot (eds)

STELLAR MAGNETIC ACTIVITY OF SOLAR-LIKE STARS ALONG THEIR EVOLUTION: IMPACT ON EXOPLANET HABITABILITY

S. Mathur[1, 2]

Abstract. Exoplanet search has been at the center of many space missions such as CoRoT, *Kepler*, TESS, and PLATO in a near future. In particular, a special attention is given to exoplanet that could be habitable. While this requires conditions on the planet orbit that depend on the spectral type of the host star, the level of the magnetic activity is key as it would have a non-negligible impact on the development of life, such as sweeping away the planet atmosphere. It is thus important to know how magnetic activity evolves during the lifetime of a star. In this review, I will show what we have learned on the magnetism of solar-like stars on the main sequence up to the red-giant branch. I will mostly focus on stars observed by the *Kepler* mission and for which surface rotation periods have been measured with photometric data. These studies will provide some insights, especially for the PLATO mission.

Keywords: Solar-like stars; Magnetic activity; Stellar evolution; Habitability of exoplanets; NASA *Kepler* mission

1 Introduction

The last decade, the search and discovery of exoplanet has undergone a leap forward with the space missions CoRoT (COnvection, Rotation, Transits Baglin et al. 2006), *Kepler* (Borucki et al. 2010), K2 (Howell et al. 2014), and TESS (Transiting Exoplanet Survey Satellite Ricker et al. 2015). More than 4,000 confirmed exoplanets are known*. However, the search for planets in the habitable zone is still on. While the "goldilock zone" depends on the spectral type of the host star, it is also important to take into account the radiation emitted by the latter. The NASA mission TESS has the goal to look for exoplanets in the habitable zone. Given that M dwarfs are the most numerous stars and that the the habitable zone is closer compared to G dwarfs, more focus is given to M dwarfs (e.g. Kostov et al. 2019; Günther et al. 2019; Bluhm et al. 2020; Gilbert et al. 2020; Van Eylen et al. 2021). Usually, those stars have higher X-ray and UV radiation compared to earlier type stars and the magnetic activity of stars needs to be studied in order to better assess the habitability and development of life on the exoplanets detected around them.

An interesting system is Proxima Centauri, the closest star to our Sun, which is an M dwarf hosting a super-Earth (Anglada-Escudé et al. 2016). The X-ray emission received by the planet is 400 times larger than for Earth but Bolmont et al. (2017) showed that for similar systems, the water loss could still be small enough to allow the planet to be habitable. In the same direction, Abrevaya et al. (2020) led experimental studies of flare impact on micro-organisms survival and measured viable counts that remained above the Level Of Detection up to 600 s after a flare. They found that a small part of a microbial population irradiated during a flare is able to survive.

Knowing the level of magnetic activity of the planet host star is thus important not only for different spectral types but also at different evolutionary stages. For a star like the Sun, stellar magnetic activity results from the interplay between rotation, convection, and magnetic field. Several models have been developed for the Sun that are based on dynamo theory. In one of the most common dynamo theory, called $\alpha\Omega$ dynamo, two different effects are taken into account to explain the changes in the magnetic field geometry: the Ω effect that

[1] Instituto de Astrofísica de Canarias (IAC), E-38205 La Laguna, Tenerife, Spain
[2] Universidad de La Laguna (ULL), Departamento de Astrofísica, E-38206 La Laguna, Tenerife, Spain
*https://exoplanets.nasa.gov/exoplanet-discoveries/

comes from the latitudinal differential rotation on the surface of the star and the α effect that is responsible for local twists of the magnetic field. The different models that have been developed are either 2- or 3-D and can be mean field, thin shell or distributed dynamos (e.g. MacGregor & Charbonneau 1997; Augustson et al. 2013; Brun & Browning 2017; Jouve et al. 2020). While a lot of effort has been undertaken to understand the detailed mechanisms responsible for the magnetic activity of stars, in particular to reproduce what is observed for the Sun, in this review, we will focus on the observations of magnetic activity of stars (from F to M-type) from the main sequence and as a function of age.

2 Proxies for Stellar Magnetic Activity

Stellar magnetic activity can be studied using different indexes. Chromospheric emission can be studied with spectroscopy with lines such as Ca HK or Hα. Other observations include X-ray and UV measurements. Flares and spots (or active regions) can also be studied with photometric data. Finally, it has been shown that magnetic activity of the Sun and solar-like stars affect the properties (frequency and amplitude) of the acoustic modes observed in those stars (e.g. Salabert et al. 2009; García et al. 2010; Kiefer et al. 2017; Santos et al. 2018; García & Ballot 2019). In the following subsections we will show examples of works done for some of those different types of observations.

2.1 Spectroscopic observations

Almost fifty years ago, a large spectroscopic survey was started at the Mount Wilson Observatory in order to study magnetic activity of solar-like stars through the chromospheric emission from the CaHK lines (Wilson 1978). This allowed the follow up of several hundreds of stars during several decades. Later on, more surveys were led such as at the Lowell observatory (e.g. Hall et al. 2007) or the SMARTS telescope (e.g. Metcalfe et al. 2010). HARPS spectra have also been used for more than 4,000 cool stars (Boro Saikia et al. 2018). These observations have shown that different types of variability can be observed with stars showing regular cycles, stars with flat variability, or stars with some variability but no regular patterns (e.g. Baliunas et al. 1995).

A clear relation between the activity cycle and the rotation period was also seen using these observations, where two branches appeared (also called the active and inactive branches). An interesting feature was that the Sun was just in between these branches making it peculiar compared to other solar-like stars (Böhm-Vitense 2007). However that position can be more or less obvious depending on the parameters considered (Brandenburg et al. 2017).

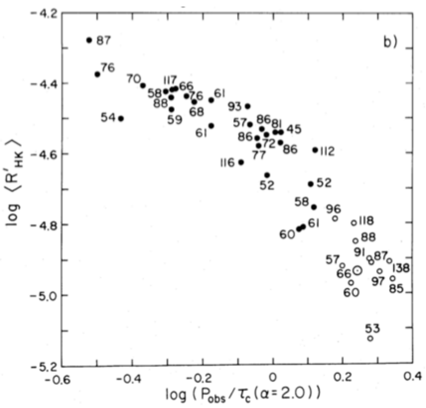

Fig. 1. Chromospheric activity index ($R'_{\rm HK}$) as a function of the Rossby number for stars observed with the Mount Wilson Observatory. The Sun is represented with the solar symbol. Extracted from Noyes et al. (1984).

One key parameter for magnetic activity and dynamo models is the Rossby number (Ro), which is the ratio between the rotation period and the convective turnover time. There are different ways of computing it (e.g. Noyes et al. 1984; Wright et al. 2011; Brun et al. 2017; Corsaro et al. 2021; Lehtinen et al. 2021) but as shown in Figure 1, in general there is a clear relation between the chromospheric activity index (R'_{HK}) and the Rossby number. When Ro increases the magnetic activity decreases. For stars on the main sequence, the increase of Ro is usually due to the increase of the rotation period, which means that the stars are older as known with age-rotation relations (Skumanich 1972; Barnes 2007). Mamajek & Hillenbrand (2008) looked into the activity-age relations using cluster data, obtaining a precision of ∼0.2 dex for stars younger than the Sun.

2.2 X-ray luminosity and Flares

X-ray luminosity measurements are also an interesting proxy for magnetic activity. X-rays are emitted from stellar coronae that are constituted of magnetic hot plasma. The heating of the corona appears to come from the magnetic activity of the star. Figure 2 shows the X-ray emission of a large sample of stars from M to G dwarfs as a function of Ro (Wright et al. 2018). Two regimes can be noted: the saturated and unsaturated regimes where the knee between the two is at Ro∼0.1. The unsaturated regime follows what is expected with the evolution of magnetic activity with rotation periods. The common explanation for these two regimes is based on the type of dynamo operating in the stars (Barnes 2003). For the low Ro, i.e. fast rotators, this is the "Convective" sequence while for the slower rotators, this is the "Interface" sequence. The fact that fully convective M dwarfs show a similar behavior is quite surprising suggesting that those stars have a similar dynamo to the one of partially convective stars.

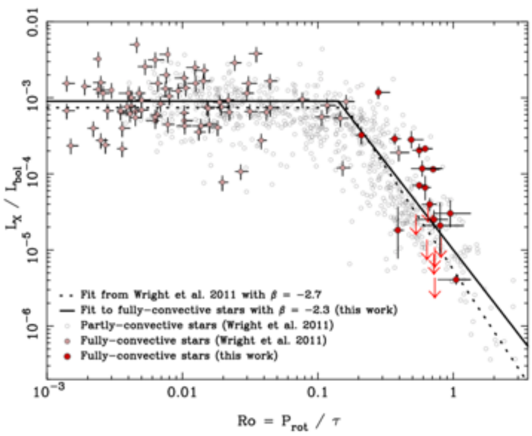

Fig. 2. X-ray luminosity as a function of the Rossby number. Partially convective stars are represented with grey circles and fully convective stars are represented with color symbols.Extracted from (Wright et al. 2018).

Flares are another manifestation of the magnetic activity of stars. The *Kepler* mission (even more with the very high cadence mode of TESS) has allowed us to study flares in a large number of stars, showing that stellar flares can be much more energetic than solar flares. Yang & Liu (2019) analyzed the *Kepler* providing a large flare catalog. By measuring the flare energy for 3,240 stars with 162,262 flare events, they found that the flare activity behaves very similarly to the X-ray luminosity as a function of the Rossby number. They also looked at differences with spectral types, showing that for hotter stars the flare energy decreases in such way that M dwarfs have more energetic flares.

2.3 Spectropolarimetric observations

Spectropolarimetric observations allow us to measure the magnetic field of stars. The Bcool[†] team has been leading a survey of spectropolarimetric observations at the NARVAL (Aurière 2003) and ESPaDOnS (Donati 2003) spectropolarimeters. By analyzing 170 solar-like stars observed for 7 years they measured the magnetic field from Stokes parameters. They studied the relation with ages, where ages were derived from the $R'_{\rm HK}$ relations. They found that the magnetic field also decreases when the star gets older (Marsden et al. 2014).

3 Recent results from *Kepler* photometric observations

Photometric observations, as done by the *Kepler* mission, not only provide information about transiting exoplanets but allows us to study different types of variability of the stars. With high-precision observations, we

[†]http://bcool.ast.obs-mip.fr/

can study stellar surface rotation thanks to the presence of spots or active regions that come in and out of view.

3.1 Measuring surface rotation and magnetic activity level

When a star is active, we can measure its rotation period through the modulation in the lightcurves. Several techniques can be used to measure that periodicity (Lomb-Scargle periodograms, Auto-correlation function, time-frequency analysis, Gaussian Processes...). With hundreds of thousands of stars observed by the *Kepler* mission, many studies were done to measure the surface rotation of stars (e.g. Reinhold et al. 2013; McQuillan et al. 2014; García et al. 2014; Santos et al. 2019; do Nascimento et al. 2020; Santos et al. 2021).

Since the measurement of a rotation period is related to the presence of magnetic features on the surface of a solar-like star, we can measure a proxy of magnetic activity with the standard deviation in the lightcurve. Several proxies have been used with *Kepler* data such as $R_{\rm var}$ (Basri et al. 2013) or $S_{\rm ph}$ (Mathur et al. 2014).

The most recent catalog of solar-like stars and subgiants contain rotation periods for more than 55,000 stars (Santos et al. 2021), constituting the largest catalog available so far. Rotation periods were obtained from the analysis of more than 160,000 stars observed with *Kepler* for up to 4 years by using a combination of auto-correlation function, wavelet analysis, and machine learning (Mathur et al. 2010; Ceillier et al. 2017; Breton et al. 2021). Figure 3 shows the distribution of the magnetic activity proxy $S_{\rm ph}$ as a function of effective temperature for main-sequence stars (top panel) and subgiants (bottom panel) showing that magnetic activity is higher for low-mass stars.

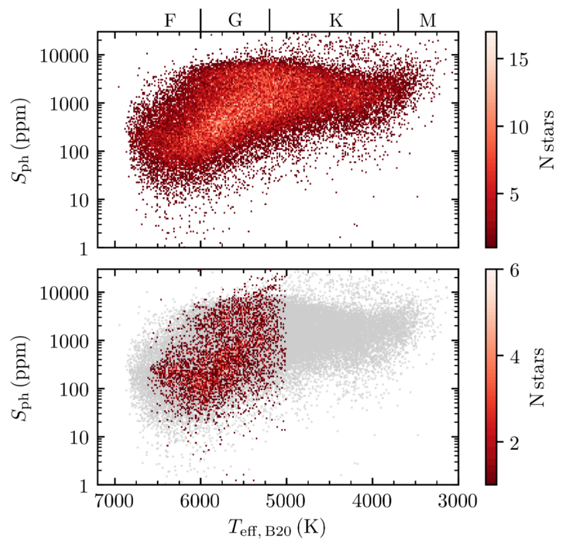

Fig. 3. Magnetic activity proxy $S_{\rm ph}$ vs $T_{\rm eff}$ for the *Kepler* targets with measured rotation periods color-coded with the number of stars: mains-sequence stars (top) and subgiants (bottom panel). Extracted from Santos et al. (2021).

3.2 Evolution of stellar magnetic activity

With such a large sample, we can start to study how the dynamics of solar-like stars evolve with age and as a function of other stellar parameters.

By cross-matching the sample of stars with measured rotation periods and metallicity from spectroscopic surveys, See et al. (2021) studied how the magnetic proxy $R_{\rm var}$ changed with metallicity. They compared their observations with stellar evolution models that included angular momentum transport. They found that the magnetic activity level is higher when the star is more metallic in agreement with the models.

That sample includes a subsample of stars with detection of acoustic modes (García et al. 2014) for which precise ages can be derived with asteroseismology. By comparing the observed rotation periods with *Kepler* with models including classical process for the angular momentum transport, van Saders et al. (2016) showed that the models predicted longer rotation periods than the observed ones, suggesting that the magnetic braking stops near the age of the Sun and that the Sun could be in a transition phase. Later, Metcalfe & van Saders

(2017) linked that transition to the peculiar position of the Sun in the activity cycle period as a function of rotation period where stars could go from one branch to the other during its evolution as shown by the dash lines in Figure 4. This theory assumes that the magnetic activity of the Sun will undergo a drastic decrease while the rotation period will remain unchanged for some time.

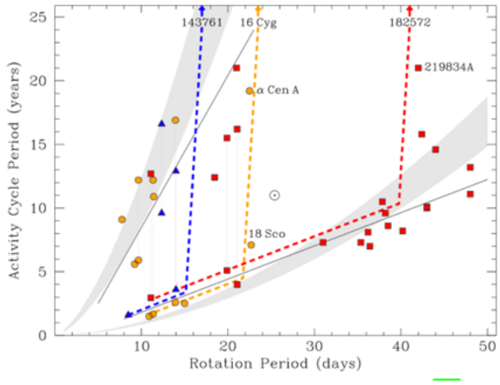

Fig. 4. Magnetic activity cycle period as a function of rotation period for different spectral types: K (blue triangles), G (yellow circles), and F (red squares). The Sun is represented with the solar symbol. The dash lines represent assumed evolutionary path of the stars. Extracted from Metcalfe & van Saders (2017) .

Finally, for red giants, rotation periods have been measured with the *Kepler* data for around 300 stars (Ceillier et al. 2017; Tayar et al. 2017). While some slow rotators are present, there are some fast rotators ($P_{\rm rot}$ < 50 days) and they still need to be taken cautiously as there could still be some contamination from a nearby star. However, magnetic fields for red giants have also been measured from spectropolarimetric observations (e.g. Aurière et al. 2008; Konstantinova-Antova et al. 2012) showing that these stars could still be magnetically active.

4 Conclusions

From different indexes for stellar magnetic activity, we saw that there is a saturation for low Ro (younger) stars and a decrease of magnetic activity after a given Ro value. There is also a dependence of the magnetic activity on spectral type: low-mass stars are more active. A metallicity dependence has also been seen where metal-rich stars have higher magnetic activity level.

From the analysis of the photometric data of *Kepler*, it seems that the magnetic braking is stalled after a given Rossby number. One question that remains unanswered is the following: is the Sun in transition?

The knowledge of the level of magnetic activity of planet-host stars is crucial to better define the habitability zone. While it starts to be taken into account, understanding the stellar magnetic activity of stars will have a direct impact on habitability (e.g. Gallet et al. 2017; Johnstone et al. 2021).

S. M. acknowledges support by the Spanish Ministry of Science and Innovation with the Ramon y Cajal fellowship number RYC-2015-17697 and the grant number PID2019-107187GB-I00.

References

Abrevaya, X. C., Leitzinger, M., Oppezzo, O. J., et al. 2020, MNRAS, 494, L69

Anglada-Escudé, G., Amado, P. J., Barnes, J., et al. 2016, Nature, 536, 437

Augustson, K. C., Brun, A. S., & Toomre, J. 2013, ApJ, 777, 153

Aurière, M. 2003, in EAS Publications Series, Vol. 9, EAS Publications Series, ed. J. Arnaud & N. Meunier, 105

Aurière, M., Konstantinova-Antova, R., Petit, P., et al. 2008, A&A, 491, 499

Baglin, A., Auvergne, M., Boisnard, L., et al. 2006, in COSPAR, Plenary Meeting, Vol. 36, 36th COSPAR Scientific Assembly, 3749

Baliunas, S. L., Donahue, R. A., Soon, W. H., et al. 1995, ApJ, 438, 269

Barnes, S. A. 2003, ApJ, 586, 464

Barnes, S. A. 2007, ApJ, 669, 1167
Basri, G., Walkowicz, L. M., & Reiners, A. 2013, ApJ, 769, 37
Bluhm, P., Luque, R., Espinoza, N., et al. 2020, A&A, 639, A132
Böhm-Vitense, E. 2007, ApJ, 657, 486
Bolmont, E., Selsis, F., Owen, J. E., et al. 2017, MNRAS, 464, 3728
Boro Saikia, S., Marvin, C. J., Jeffers, S. V., et al. 2018, A&A, 616, A108
Borucki, W. J., Koch, D., Basri, G., et al. 2010, Science, 327, 977
Brandenburg, A., Mathur, S., & Metcalfe, T. S. 2017, ApJ, 845, 79
Breton, S. N., Santos, A. R. G., Bugnet, L., et al. 2021, A&A, 647, A125
Brun, A. S. & Browning, M. K. 2017, Living Reviews in Solar Physics, 14, 4
Brun, A. S., Strugarek, A., Varela, J., et al. 2017, ApJ, 836, 192
Ceillier, T., Tayar, J., Mathur, S., et al. 2017, A&A, 605, A111
Corsaro, E., Bonanno, A., Mathur, S., et al. 2021, A&A, 652, L2
do Nascimento, J. D., J., de Almeida, L., Velloso, E. N., et al. 2020, ApJ, 898, 173
Donati, J.-F. 2003, in Astronomical Society of the Pacific Conference Series, Vol. 307, Astronomical Society of the Pacific Conference Series, ed. J. Trujillo-Bueno & J. Sanchez Almeida, 41
Gallet, F., Charbonnel, C., Amard, L., et al. 2017, A&A, 597, A14
García, R. A. & Ballot, J. 2019, Living Reviews in Solar Physics, 16, 4
García, R. A., Ceillier, T., Salabert, D., et al. 2014, A&A, 572, A34
García, R. A., Mathur, S., Salabert, D., et al. 2010, Science, 329, 1032
Gilbert, E. A., Barclay, T., Schlieder, J. E., et al. 2020, AJ, 160, 116
Günther, M. N., Pozuelos, F. J., Dittmann, J. A., et al. 2019, Nature Astronomy, 3, 1099
Hall, J. C., Lockwood, G. W., & Skiff, B. A. 2007, AJ, 133, 862
Howell, S. B., Sobeck, C., Haas, M., et al. 2014, PASP, 126, 398
Johnstone, C. P., Bartel, M., & Güdel, M. 2021, A&A, 649, A96
Jouve, L., Lignières, F., & Gaurat, M. 2020, A&A, 641, A13
Kiefer, R., Schad, A., Davies, G., & Roth, M. 2017, A&A, 598, A77
Konstantinova-Antova, R., Aurière, M., Petit, P., et al. 2012, A&A, 541, A44
Kostov, V. B., Schlieder, J. E., Barclay, T., et al. 2019, AJ, 158, 32
Lehtinen, J. J., Käpylä, M. J., Olspert, N., & Spada, F. 2021, ApJ, 910, 110
MacGregor, K. B. & Charbonneau, P. 1997, ApJ, 486, 484
Mamajek, E. E. & Hillenbrand, L. A. 2008, ApJ, 687, 1264
Marsden, S. C., Petit, P., Jeffers, S. V., et al. 2014, MNRAS, 444, 3517
Mathur, S., García, R. A., Régulo, C., et al. 2010, A&A, 511, A46
Mathur, S., Salabert, D., García, R. A., & Ceillier, T. 2014, Journal of Space Weather and Space Climate, 4, A15
McQuillan, A., Mazeh, T., & Aigrain, S. 2014, ApJS, 211, 24
Metcalfe, T. S., Basu, S., Henry, T. J., et al. 2010, ApJ, 723, L213
Metcalfe, T. S. & van Saders, J. 2017, Sol. Phys., 292, 126
Noyes, R. W., Hartmann, L. W., Baliunas, S. L., Duncan, D. K., & Vaughan, A. H. 1984, ApJ, 279, 763
Reinhold, T., Reiners, A., & Basri, G. 2013, A&A, 560, A4
Ricker, G. R., Winn, J. N., Vanderspek, R., et al. 2015, Journal of Astronomical Telescopes, Instruments, and Systems, 1, 014003
Salabert, D., García, R. A., Pallé, P. L., & Jiménez-Reyes, S. J. 2009, A&A, 504, L1
Santos, A. R. G., Breton, S. N., Mathur, S., & García, R. A. 2021, ApJS, 255, 17
Santos, A. R. G., Campante, T. L., Chaplin, W. J., et al. 2018, ApJS, 237, 17
Santos, A. R. G., García, R. A., Mathur, S., et al. 2019, ApJS, 244, 21
See, V., Roquette, J., Amard, L., & Matt, S. P. 2021, ApJ, 912, 127
Skumanich, A. 1972, ApJ, 171, 565
Tayar, J., Somers, G., Pinsonneault, M. H., et al. 2017, ApJ, 840, 17
Van Eylen, V., Astudillo-Defru, N., Bonfils, X., et al. 2021, arXiv e-prints, arXiv:2101.01593
van Saders, J. L., Ceillier, T., Metcalfe, T. S., et al. 2016, Nature, 529, 181
Wilson, O. C. 1978, ApJ, 226, 379
Wright, N. J., Drake, J. J., Mamajek, E. E., & Henry, G. W. 2011, ApJ, 743, 48
Wright, N. J., Newton, E. R., Williams, P. K. G., Drake, J. J., & Yadav, R. K. 2018, MNRAS, 479, 2351
Yang, H. & Liu, J. 2019, ApJS, 241, 29

SF2A 2021
A. Siebert, K. Baillié, E. Lagadec, N. Lagarde, J. Malzac, J.-B. Marquette, M. N'Diaye, J. Richard, O. Venot (eds)

CHARACTERISING THE INTERIOR STRUCTURES AND ATMOSPHERES OF MULTIPLANETARY SYSTEMS

L. Acuña[1], T. Lopez[1], M. Deleuil[1], O. Mousis[1], E. Marcq[2], T. Morel[3] and A. Santerne[1]

Abstract. The modelling of the internal structures of super-Earths and sub-Neptunes gives a valuable insight into their formation history and possible atmospheres. We present a planet model where the interior is coupled with the atmosphere within a Bayesian retrieval scheme. We take into account water in all its possible phases, including steam and supercritical phases, which is necessary for systems with a wide range of stellar irradiations. Our interior-atmosphere model calculates the compositional and atmospheric parameters, such as Fe and water content, surface pressures, scale heights and albedos. We analyse the multiplanetary systems K2-138 and TRAPPIST-1. From their individual composition, we derive a global increasing trend on the water content with increasing distance from the star in the inner region of the systems, while the planets in the outer region present a constant water mass fraction. This trend reveals the possible effects of migration, formation location and atmospheric mass loss during their formation history.

Keywords: Planets and satellites: interiors, Planets and satellites: composition, Planets and satellites: atmospheres, Planets and satellites: individual: K2-138, Stars: activity.

1 Introduction

Multiplanetary systems show a diversity in the composition of their planets, ranging from rocky super-Earths to volatile-rich sub-Neptunes. This variety in composition makes multiplanetary systems environments that are interesting for testing theories on planet formation and evolution. Two examples of multiplanetary systems of low-mass planets (M ¡ 20 $M_{\oplus}$) with different densities are TRAPPIST-1 (Gillon et al. 2016; Agol et al. 2021) and K2-138 (Christiansen et al. 2018; Lopez et al. 2019). In this work we present a homogeneous interior-atmosphere analysis of the planets in these two systems to unveil their compositional trends. We also discuss how interior structure and composition studies of low-mass planets can be impacted by stellar activity.

2 Interior-atmosphere analysis

2.1 Interior model

The interior structure model is initially presented in Brugger et al. (2016) and Brugger et al. (2017). It is a one-dimensional model that takes as input the total planetary mass, two compositional parameters and the surface pressure and temperature. The two compositional parameters are the core mass fraction (CMF) and water mass fraction (WMF), which are the mass of the core and the water layer, respectively, divided by the total mass of the planet. Along the one-dimensional grid, which represents the radius, we calculate the pressure $P(r)$, gravity $g(r)$, temperature $T(r)$ and density $\rho(r)$. We finally obtain as output the total planetary radius and the Fe/Si mole ratio.

The planet is stratified in three main layers: a Fe-rich core, a Si-dominated mantle and a water layer. Depending on the water phase, we use a different equation of state (EOS) that is valid under the pressure and temperature conditions of that phase. Brugger et al. (2016) and Brugger et al. (2017) implemented liquid and

[1] Aix Marseille Univ, CNRS, CNES, LAM, Marseille, France
[2] LATMOS/CNRS/Sorbonne Université/UVSQ, 11 boulevard d'Alembert, Guyancourt, F-78280, France
[3] Space sciences, Technologies and Astrophysics Research (STAR) Institute, Université de Liège, Quartier Agora, Allée du 6 Août 19c, Bât. B5C, B4000-Liège, Belgium

ice phases, which are valid for temperate planets. Nonetheless, many of the planets in multiplanetary systems are highly irradiated, having surface conditions that do not allow for the formation of liquid and ice phases. Therefore we update our interior structure model to include the supercritical phase (Mousis et al. 2020). We use an EOS that is valid for high-pressure, high-temperature conditions in supercritical phase from Mazevet et al. (2019).

In addition, we couple the interior with the atmosphere self-consistently. We use a one-dimensional, k-correlated model, described in Marcq (2012) and Marcq et al. (2017). The interface between the atmosphere and the interior, which is either the supercritical layer or the mantle, is situated at P = 300 bar. The atmospheric model calculates the thickness of the atmosphere, which contributes significantly to the total radius, with an EOS that is valid for water vapour conditions. Furthermore, the atmospheric model also obtains the outgoing longwave radiation (OLR) and Bond albedo, which enable us to estimate the temperature at the bottom of the atmosphere assuming radiative-convective equilibrium. The temperature at the bottom of the atmosphere is the input boundary condition for the interior. We developed an algorithm to couple self-consistently the interior and the atmosphere, described in Acuña et al. (2021). This implementation of the supercritical interior and atmosphere allows us to obtain smooth pressure-temperature profiles of the water layer (Fig. 1).

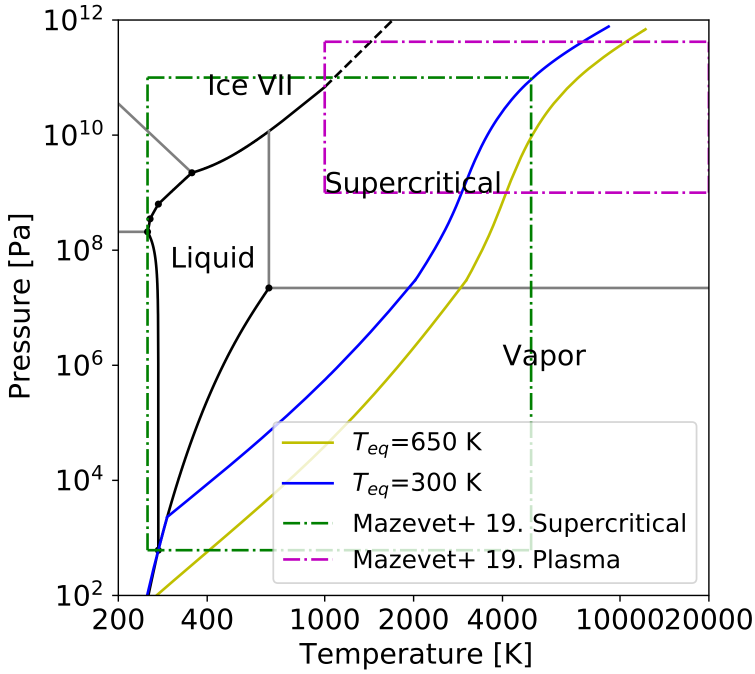

Fig. 1. Pressure-temperature profiles of the water layer for our interior-atmosphere model for highly irradiated planets. The two profiles correspond to two hypothetical planets with M = 15 $M_\oplus$ and 100% water composition for two different equilibrium temperatures. Green and magenta dashed-dotted boxes indicate the validity ranges of the supercritical EOS from Mazevet et al. (2019).

2.2 Observational parameters

We use a Bayesian MCMC scheme, described in Dorn et al. (2015) and Acuña et al. (2021), to obtain the non-observable parameters (CMF and WMF) and their uncertainties, while having as input the observables, which are the planetary mass and radius, and the Fe/Si mole ratio. The latter is estimated with the host stellar abundances, as defined in Sotin et al. (2007) and Brugger et al. (2017). For K2-138, we perform our own spectroscopic analysis to obtain refined planetary masses, stellar parameters and abundances (Acuña et al. in prep). In the case of TRAPPIST-1, we employ masses and radii reported in Agol et al. (2021) and the Fe/Si mole ratio estimated by Unterborn et al. (2018), Fe/Si = 0.76 ± 0.12. This estimate is obtained by selecting a sample of stars with similar metallicity to TRAPPIST-1 and available Fe and Si abundances.

3 Results

We observe that the WMF trend in K2-138 consists of an increasing gradient with increasing distance from the star (or incident flux) for the three inner planets, whereas the three outer planets have a constant WMF (a plateau). In addition, the outermost planet, K2-138 g, has a radius that is significantly larger than the radius we obtain with our interior-atmosphere modelling, assuming 100% water atmosphere. This indicates that the atmosphere of K2-138 g is composed of species that are more volatile than water, and therefore produce a more extended atmosphere than a water-dominated one. These species are H and He, which means that they have survived atmospheric loss due to XUV photoevaporation, while for the other planets in the K2-138 this is not the case. This WMF trend is also seen in TRAPPIST-1 (Fig. 2), where planets b to e have increasing WMF and planets f to g have a constant WMF of 15% approximately. TRAPPIST-1 d seems to be the exception to this trend. However, in Acuña et al. (2021) we discuss that this could be due to assuming that the water layer in TRAPPIST-1 d is in liquid phase. If CO_2 is mixed with water vapour in the atmosphere, this would not allow the presence of liquid water in TRAPPIST-1 d. Since the density of water vapour is lower than liquid water, a lower WMF is needed to account for the total density of the planet. This shifts downwards the position of TRAPPIST-1 d in Fig. 2, placing it between that of TRAPPIST-1 c and e (Acuña et al. 2021; Turbet et al. 2020)

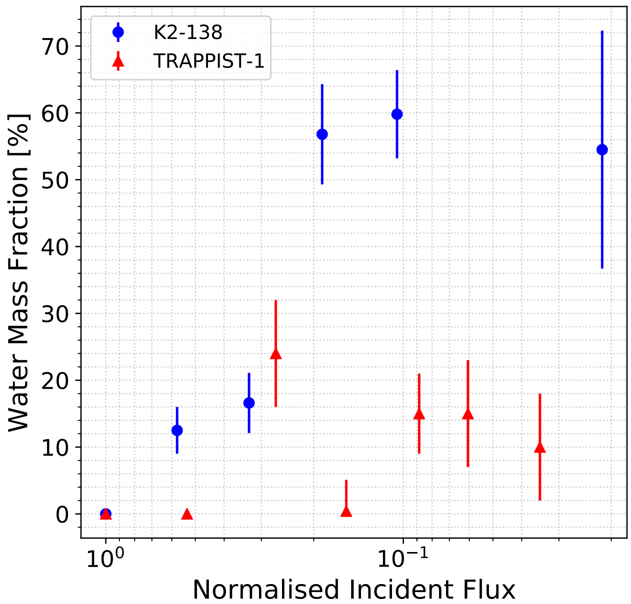

Fig. 2. WMF trend as a function of normalised incident flux for K2-138 and TRAPPIST-1. The incident flux is normalised with the flux of the innermost planet in each planetary system.

4 Discussion

The uncertainty in radius due to stellar activity for a Jupiter-size planet is 3% (Czesla et al. 2009), which translates into a larger uncertainty in the case of small planets. The uncertainty in radius necessary to distinguish a super-Earth from a sub-Neptune is 10% for planets with M ¿ 10 $M_{\oplus}$, 5% for masses between 5 and 10 $M_{\oplus}$, and less than 5% for planets less massive than 5 $M_{\oplus}$ (Wagner et al. 2011). Therefore, we need accurate stellar activity modelling to obtain radii within these uncertainties, especially for Earth-size planets. This requires observations of several stellar rotations and models for stellar granulation, star spots and faculae.

An example of the importance of modelling stellar activity is TRAPPIST-1. Interior structure models present a degeneracy between the composition of their volatile layer and the total mass of this layer. Transmission spectroscopy, which is affected by stellar activity, can break this degeneracy by revealing the chemical species in the atmosphere. In the case of TRAPPIST-1, Ducrot et al. (2018) used a photosphere and a low contribution of stellar spots at high temperature to model the stellar contamination in the transmission spectra. This contamination model could not account for the inverted water line seen in the data, whereas the contamination model of Zhang et al. (2018) reproduced the water line. This contamination model considered that more than 50% of the stellar surface was covered by faculae and spots, which enable the formation of water vapour.

5 Conclusions

Our interior-atmosphere model can be applied to low-mass planets of a wide range of irradiations, including temperate planets with liquid and ice conditions to highly irradiated ones. We perform a spectroscopic analysis to obtain refined planetary masses and stellar parameters and abundances for the multiplanetary system K2-138 (Acuña et al. in prep) and apply our interior-atmosphere model to their planets. We find that the K2-138 system presents a WMF trend of increasing water content with incident flux for the inner planets, while the outer planets show a constant water content (a plateau). This trend is also seen in TRAPPIST-1 (Acuña et al. 2021) and could be the result of several formation mechanisms, including atmospheric mass loss, migration and location of accretion in the protoplanetary disk.

In addition, we conclude that stellar activity affects both planetary radius and transmission spectroscopy measurements, which are essential to break the degeneracy present in our interior structure models. We need accurate stellar activity models, including granulation, faculae and spots in transit photometry and transmission spectroscopy to help us identify planetary structure and composition trends.

M.D. and O.M. acknowledge support from CNES

References

Acuña, L., Deleuil, M., Mousis, O., et al. 2021, A&A, 647, A53

Agol, E., Dorn, C., Grimm, S. L., et al. 2021, The Planetary Science Journal, 2, 1

Brugger, B., Mousis, O., Deleuil, M., & Deschamps, F. 2017, ApJ, 850, 93

Brugger, B., Mousis, O., Deleuil, M., & Lunine, J. I. 2016, ApJ, 831, L16

Christiansen, J. L., Crossfield, I. J. M., Barentsen, G., et al. 2018, The Astronomical Journal, 155, 57

Czesla, S., Huber, K. F., Wolter, U., Schröter, S., & Schmitt, J. H. M. M. 2009, A&A, 505, 1277

Dorn, C., Khan, A., Heng, K., et al. 2015, A&A, 577, A83

Ducrot, E., Sestovic, M., Morris, B. M., et al. 2018, AJ, 156, 218

Gillon, M., Jehin, E., Lederer, S. M., et al. 2016, Nature, 533, 221

Lopez, T. A., Barros, S. C. C., Santerne, A., et al. 2019, A&A, 631, A90

Marcq, E. 2012, Journal of Geophysical Research (Planets), 117, E01001

Marcq, E., Salvador, A., Massol, H., & Davaille, A. 2017, Journal of Geophysical Research (Planets), 122, 1539

Mazevet, S., Licari, A., Chabrier, G., & Potekhin, A. Y. 2019, A&A, 621, A128

Mousis, O., Deleuil, M., Aguichine, A., et al. 2020, ApJ, 896, L22

Sotin, C., Grasset, O., & Mocquet, A. 2007, Icarus, 191, 337

Turbet, M., Bolmont, E., Ehrenreich, D., et al. 2020, A&A, 638, A41

Unterborn, C. T., Desch, S. J., Hinkel, N. R., & Lorenzo, A. 2018, Nature Astronomy, 2, 297

Wagner, F. W., Sohl, F., Hussmann, H., Grott, M., & Rauer, H. 2011, Icarus, 214, 366

Zhang, Z., Zhou, Y., Rackham, B. V., & Apai, D. 2018, AJ, 156, 178

SF2A 2021
A. Siebert, K. Baillié, E. Lagadec, N. Lagarde, J. Malzac, J.-B. Marquette, M. N'Diaye, J. Richard, O. Venot (eds)

ROTATIONAL AND ORBITAL EVOLUTION OF STAR-PLANET SYSTEMS. IMPACT OF TIDAL AND MAGNETIC TORQUES.

J. Ahuir[1], A. Strugarek[1], A. S. Brun[1] and S. Mathis[1]

Abstract. The discovery of more than 4000 exoplanets during the last two decades has shed light on the importance of characterizing star-planet interactions. Indeed, a large fraction of these planets have short orbital periods and are consequently strongly interacting with their host star. In particular, several planetary systems are likely to host exoplanets undergoing a migration due to tidal and magnetic torques. We consider here the joint influence of stellar wind, tidal and magnetic star-planet interactions on the star's rotation rate and planetary orbital evolution. To this end, we have developed a numerical model of a circular and coplanar star-planet system taking into account stellar structural changes, wind braking and star-planet interactions, called ESPEM (Evolution of Planetary Systems and Magnetism). We present synthetic populations of star-planet systems and compare their distribution in orbital period and in stellar rotation period to the *Kepler* satellite data. We find that star-planet magnetic interactions significantly modify the distribution of super-Earths around slowly rotating stars, which improves the agreement between synthetic populations and observations. Tidal effects, on the other hand, shape the distribution of giant planets.

Keywords: star-planet interactions, stellar evolution, solar-type stars, stellar rotation

1 Introduction

Over the past two decades, many close-in exoplanets have been detected around a wide variety of host stars. These planets are likely to undergo migration throughout the evolution of the star-planet system, from their formation within a protoplanetary disk to the end of the host star's life. Once the disk is gone, the migration of a planet in close orbit can be triggered by two complementary physical mechanisms. On one hand, the presence of the planet induces tidal effects within the star. These lead to a deformation of the star in the direction of the companion which generates a large scale flow, the equilibrium tide (Zahn 1966a; Remus et al. 2012a), dissipated by tubulent friction in the stellar convective zone. The planet can also excite waves within its host star that will then be dissipated in the radiative (e.g., Zahn 1975; Goodman & Dickson 1998; Ahuir et al. 2021b) and the convective zone (e.g., Ogilvie 2013; Mathis 2015): this is the so-called dynamical tide. The dissipation of these flows induces an angle between the deformation of the star and the line connecting the planet to the center of the star, at the origin of a torque that can induce a planetary migration. On the other hand, the planet feels a drag force from the ambient stellar magnetized wind. This results in the propagation of Alfvén waves between the planet and the star, whose superposition forms stationary structures called *Alfvén wings* (Neubauer 1980). Such a connection between the two celestial bodies is conducive to exchanges of energy and angular momentum (e.g., Saur et al. 2013; Strugarek et al. 2015; Strugarek 2016; Strugarek et al. 2017). These two types of mechanisms then define characteristic orbits playing a determining role in the evolution of the system considered. Thus, a planet located below the co-rotation orbit (for which the orbital period is equal to the stellar rotation period) migrates towards its host star, whose rotation accelerates. Beyond this orbit, the planet moves away from the star, whose rotation slows down. We aim in this work to predict the orbital evolution of a planet throughout the structural, rotational and magnetic evolution of its host star, simultaneously taking into account tidal and magnetic torques, in order to understand the distribution of close-in planets observed.

[1] Département d'Astrophysique-AIM, CEA/IRFU, CNRS/INSU, Université de Paris, 91191 Gif-sur-Yvette, France

2 The ESPEM code

To account for the secular evolution of star-planet systems under the action of magnetic and tidal interactions, we use ESPEM (French acronym for Evolution of Planetary Systems and Magnetism ; see Benbakoura et al. 2019; Ahuir et al. 2021a), which is a numerical code computing the secular evolution of a star–planet system by following the semi-major axis of the planetary orbit as well as the stellar rotation rate. We assume a coplanar and circular orbit, and a synchronized planetary rotation, as the reservoir of angular momentum of the planet is less important than the one in its orbit (Guillot et al. 1996). The companion is considered as a punctual mass. We consider a two-layer solar-type star composed of a radiative core and a convective envelope, whose changes are monitored along the evolution of the system by relying on grids provided by the 1D stellar evolution code STAREVOL (e.g., Amard et al. 2019). Tidal dissipation is only considered in the stellar envelope in this work as a first step (Hansen 2012; Ogilvie 2013; Mathis 2015). The core is interacting with the envelope through internal coupling (MacGregor & Brenner 1991; MacGregor 1991), and the latter exchanges angular momentum with the orbit through tidal and magnetic interactions. Moreover, the whole system loses angular momentum through magnetic braking by the stellar wind (e.g., Weber & Davis 1967; Matt et al. 2015; Ahuir et al. 2020). Hence, the angular momentum of the planetary orbit, $L_{\rm orb}$, the stellar convective zone, L_c, and radiative zone, L_r, are evolved by the following system of equations:

$$\frac{dL_{orb}}{dt} = -\Gamma_{\rm tide} - \Gamma_{\rm mag} \tag{2.1}$$

$$\frac{dL_c}{dt} = \Gamma_{\rm int} + \Gamma_{\rm tide} - \Gamma_{\rm wind} + \Gamma_{\rm mag} \tag{2.2}$$

$$\frac{dL_r}{dt} = -\Gamma_{\rm int}, \tag{2.3}$$

where $\Gamma_{\rm int}$ is the internal torque, coupling the core and the envelope of the star, $\Gamma_{\rm wind}$ is the wind-braking torque, $\Gamma_{\rm tide}$ and $\Gamma_{\rm mag}$ are the tidal and magnetic torques between the star and the planet, respectively. A schematic global view of the system studied by ESPEM is provided in Figure 1.

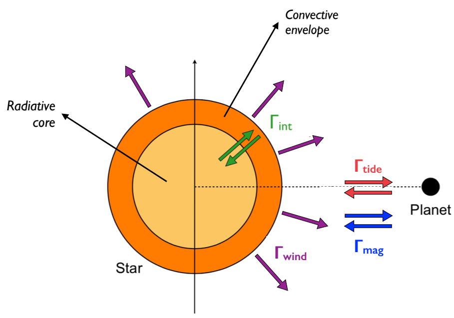

Fig. 1. Schematic view of the system and its interactions (adapted from Benbakoura et al. 2019). The radiative core (in yellow) and the convective envelope (in orange) exchange angular momentum (green arrows). Stellar wind carries away angular momentum from the envelope and spins the star down (purple arrows). Stellar rotation and planetary orbit are coupled through tidal (red arrows) and magnetic effects (blue arrows).

3 Secular evolution and planetary populations

We now seek to generate a synthetic population of star–planet systems from ESPEM, and then compare the resulting distributions with observations from the *Kepler* mission. To this end, we design a sample comprising 7000 ESPEM simulations that covers the set of possible configurations of compact star–planet systems. As we assume a bi–layer structure for the star, we consider stellar masses between 0.5 and 1.1 $M_\odot$ with a step of 0.1 $M_\odot$. Furthermore, to account for the rotational distribution of stars in open clusters (Gallet & Bouvier 2015) in our synthetic populations, we consider five initial rotation periods uniformly distributed between 1 and 10 days. The age of the system is sampled between 1 Myr and 10 Gyr to obtain 2000 uniformly distributed instants. Then to create our distribution only stellar ages corresponding to the main sequence phase are considered. Stellar masses, initial rotation periods and ages are then biased to reproduce the distribution in effective temperatures and rotation periods from the McQuillan et al. (2014, MMA14) sample, constituting until very recently the largest homogeneous database on the rotation of stars in the *Kepler* field involving F- to M-type stars. We then include various planets by choosing 40 initial semi-major axes between 5×10^{-3} and 0.2 AU, uniformly distributed in logarithm, as well as five planetary masses between 0.5 Earth masses and 5 Jovian masses, evenly spaced in logarithm. The corresponding initial orbital periods then range between 0.12 and 46 days, which allows to initially populate all orbital distances for which star–planet interactions can act effectively. From these initial conditions, we can generate three different populations of star-planet systems by evolving them by tidal effects only, or by taking into account magnetic effects for a planetary magnetic field B_p assumed equal to 1 and 10 G. Each planetary mass is weighted to reproduce the planetary radius distribution of the McQuillan et al. (2013, MMA13) sample, one of the very few studies to date combining the orbital period of detected exoplanets and the stellar rotation period of their host star. To do so, we rely on the probabilistic mass–radius relations proposed by Chen & Kipping (2017). For the sake of consistency, since our model does not deal with multi-planet interactions, we filter out multi-planetary systems from the MMA13 database, thus excluding 106 systems out of the 737 *Kepler* systems of interest (KOI) of the sample. We then compare the ESPEM-predicted orbital period and stellar rotation period distributions with observations of KOIs from the filtered MMA13 sample.

We find that that star-planet interactions shape the orbital distribution of exoplanets by depopulating low orbital periods. More precisely, magnetic interactions significantly affect the distribution of super-Earths around stars whose rotation period $P_{\rm rot}$ is higher than about 5 days. Compared to tidal-only simulations, this improves the agreement between synthetic populations and observations at orbital periods lower than $P_{\rm orb} = 1$ d (corresponding to an orbital distance of around 4.3 solar radii in the solar case, see Figure 2). Tidal effects, on the other hand, shape the distribution of giant planets. Hence, star–planet magnetic interactions play a key role in the migration of the less massive planets. Overall, the simultaneous consideration of magnetic and tidal effects shows a better agreement between synthetic populations and observations. The planetary magnetic field thus plays an important role in shaping the distributions. Indeed, an increase of B_p leads to an enhanced depopulation of the shortest orbital periods, bringing the ESPEM predictions closer to the *Kepler* distributions (see the left panels of Figure 2). Moreover, while values close to those observed in the Solar System (between 1 and 10 G) lead to an excess of planets at low orbital periods for the synthetic distributions, intense fields up to 4000 G have been predicted for hot Jupiters orbiting young stars, which significantly enhances the efficiency of the magnetic interactions (e.g., Hori 2021). Therefore, considering planetary fields stronger than 10 G may lead to an even better agreement. However, a large uncertainty about the value of the magnetic field of exoplanets remains to this day. Moreover, additional star-planet interactions, such as the dynamical tide in the stellar radiative zone (e.g., Guillot et al. 2014; Barker 2020; Ahuir et al. 2021b) or magnetic interactions in the unipolar regime (Laine et al. 2008; Laine & Lin 2012), could further depopulate short orbital periods. It is also possible that some of the planets we considered at the beginning of the evolution are simply not formed in the protoplanetary disk. These two avenues will be investigated in future work to account for the distribution of close-in planets observed in the *Kepler* field.

4 Conclusions

We designed synthetic populations of star-planet systems based on *Kepler* stellar distributions by taking into account for the first time magnetic and tidal effects simultaneously in their secular evolution. We found that magnetic interactions, after disk dissipation, significantly affect the distribution of super-Earths around slow rotators, improving the agreement between synthetic populations and observations, while tidal effects shape the distribution of giant planets. Our work shows that the observed populations must be carefully studied to derive constraints on planetary formation, because migration within the disk (not considered here) as well as magnetic and tidal interactions (post-disk) influence the evolution of close-in planets. Conversely, the observed distributions do not directly constrain the planetary distributions following the dissipation of the disk. This new description of the secular evolution of these systems is thus essential for instruments and missions to study exoplanets such as CHEOPS, TESS, PLATO, JWST and ARIEL.

The authors acknowledge funding from the European Union's Horizon-2020 research and innovation programme (Grant Agreements no. 776403 ExoplANETS-A, no. 647383 ERC CoG SPIRE and no. 810218 ERC Synergy WholeSun), INSU/PNST, INSU/PNP and the CNES-PLATO grant at CEA.

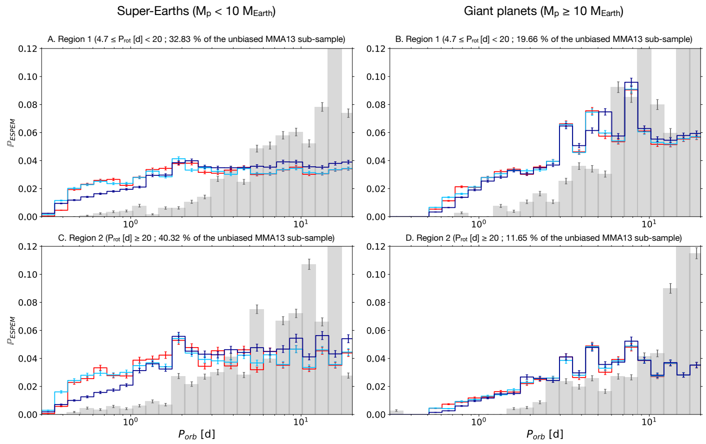

Fig. 2. Distribution of orbital periods for super-Earths (left column) and giant planets (right column). Each row corresponds to a population of middle-aged (Region 1, for which $4.7 \leq P_{\rm rot}$ $[d] < 20$), and old (Region 2, $P_{\rm rot} \geq 20$ d) star–planet systems. The letter d stands for days. The gray histogram corresponds to the distributions obtained with the unbiased MMA13 sample. The ESPEM distributions with $B_p = 0, 1, 10$ G are shown in red, light blue and dark blue respectively.

References

Ahuir, J., Brun, A. S., & Strugarek, A. 2020, A&A, 635, A170

Ahuir, J., Mathis, S., & Amard, L. 2021b, A&A, 651, A3

Ahuir, J., Strugarek, A., Brun, A. S., & Mathis, S. 2021a, A&A, 650, A126

Amard, L., Palacios, A., Charbonnel, C., et al. 2019, A&A, 631, A77

Barker, A. J. 2020, MNRAS, 498, 2

Benbakoura, M., Réville, V., Brun, A.-S., et al. 2019, A&A, 621, A124

Chen, J. & Kipping, D. 2017, ApJ, 834, 17

Gallet, F. & Bouvier, J. 2015, A&A, 577, A98

Goodman, J. & Dickson, E. S. 1998, ApJ, 507, 938

Guillot, T., Burrows, A., Hubbard, W. B., et al. 1996, ApJ, 459, L35

Guillot, T., Lin, D. N. C., Morel, P., et al. 2014, in EAS Publications Series, Vol. 65, EAS Publications Series, 327

Hansen, B. M. S. 2012, ApJ, 757, 6

Hori, Y. 2021, ApJ, 908, 77

Laine, R. O. & Lin, D. N. C. 2012, ApJ, 745, 2

Laine, R. O., Lin, D. N. C., & Dong, S. 2008, ApJ, 685, 521

MacGregor, K. B. 1991, in Proceedings of the NATO Advanced Research Workshop on Angular Momentum Evolution of Young Stars

MacGregor, K. B. & Brenner, M. 1991, ApJ, 376, 204

Mathis, S. 2015, A&A, 580, L3

Matt, S. P., Brun, A. S., Baraffe, I., et al. 2015, ApJ, 799, L23

McQuillan, A., Mazeh, T., & Aigrain, S. 2013, ApJ, 775, L11

McQuillan, A., Mazeh, T., & Aigrain, S. 2014, ApJS, 211, 24

Neubauer, F. M. 1980, Journal of Geophysical Research, 85, 1171

Ogilvie, G. I. 2013, MNRAS, 429, 613

Remus, F., Mathis, S., & Zahn, J.-P. 2012a, A&A, 544, A132

Saur, J., Grambusch, T., Duling, S., et al. 2013, A&A, 552, A119

Strugarek, A. 2016, ApJ, 833, 140

Strugarek, A., Bolmont, E., Mathis, S., et al. 2017, ApJ, 847, L16

Strugarek, A., Brun, A. S., Matt, S. P., et al. 2015, ApJ, 815, 111

Weber, E. J. & Davis, L. 1967, ApJ, 148, 217

Zahn, J.-P. 1966a, Annales d'Astrophysique, 29, 313

Zahn, J.-P. 1975, A&A, 41, 329

SF2A 2021
A. Siebert, K. Baillié, E. Lagadec, N. Lagarde, J. Malzac, J.-B. Marquette, M. N'Diaye, J. Richard, O. Venot (eds)

ANALYSING KEPLER STELLAR SURFACE ROTATION AND ACTIVITY WITH ROOSTER

S. N. Breton[1], A. R. G. Santos[2], S. Mathur[3, 4], R. A. García[1], L. Bugnet[5] and P. L. Pallé[3,4]

Abstract. It is crucial for our knowledge of stellar evolution to be able to efficiently determine stellar surface rotation periods in large stellar samples. Random forest (RF) learning abilities are exploited to automate the extraction of rotation periods in *Kepler* light curves. We train three different classifiers: one to detect if rotational modulation is present in the light curve; one to select the rotation period among estimates provided by ACF and wavelet analysis methods; and finally one to flag classical pulsators or close binary candidates that can bias our rotation-period determination. We test our machine learning pipeline, ROOSTER, on the *Kepler* K and M dwarf sample using the most up-to-date reference catalog. We show that we are able to detect rotational modulations with an accuracy of 94.2% and to retrieve final rotation periods with an accuracy of 95.3%. This value is raised to 99.5% after visually inspecting 25.2% of the stars. Over the two main analysis steps, the pipeline yields a global accuracy of 92.1% before visual checks, 96.9% after. The method is then applied to analyse the F and G stars observed by *Kepler*. The methodology presented here can be adapted to extract surface rotation periods for stars observed by other missions, like K2, TESS, and PLATO.

Keywords: Methods: data analysis – Stars: solar-type – Stars: activity – Stars: rotation – starspots

1 Introduction

Corotating dark spots and bright faculae on the stellar surface lead to brightness variations (e.g. Berdyugina 2005; Strassmeier 2009). Therefore, the long-term photometric surveys performed by a space instrument like *Kepler* (Borucki et al. 2010) provides ideal datasets to measure stellar surface rotation periods and build stellar rotation catalogs. These rotation catalogs can then be used to constrain gyrochronology models (e.g. Barnes 2003, 2007; Mamajek & Hillenbrand 2008; Meibom et al. 2011; García et al. 2014) in order to provide an estimate of the age of each considered target. Understanding the origin of the discrepancies between the different methods used to estimate stellar ages (for example between asteroseismology and gyrochronology) is a key issue in stellar physics (see e.g. Angus et al. 2015; van Saders et al. 2016). They are also of greatest interest to study the interplay between rotation and magnetic activity (e.g. Mathur et al. 2014) and yield information directly related to the dynamics at a given time for planetary system, which is crucial when considering star-planet interactions (e.g. Zhang & Penev 2014; Mathis 2015; Bolmont & Mathis 2016; Strugarek et al. 2017; Benbakoura et al. 2019). One of the main challenge that we face today on the observational side is finding efficient and reliable methods to analyse the large amount of collected data in large-scale surveys. Over the last years, automatic methods have been implemented to perform classification tasks related to stellar physics (e.g. Blomme et al. 2011; Armstrong et al. 2016; Bass & Borne 2016; Bugnet et al. 2019; Kuszlewicz et al. 2020; Audenaert et al. 2021). We focus here on the possibilities and outcomes offered by random forest classification methods to deal with stellar surface rotation in a photometric survey like the one completed by *Kepler*

[1] AIM, CEA, CNRS, Université Paris-Saclay, Université de Paris, Sorbonne Paris Cité, F-91191 Gif-sur-Yvette, France
[2] Department of Physics, University of Warwick, Coventry, CV4 7AL, UK
[3] Instituto de Astrofísica de Canarias, 38200 La Laguna, Tenerife, Spain
[4] Universidad de La Laguna, Dpto. de Astrofísica, 38205 La Laguna, Tenerife, Spain
[5] Flatiron Institute, Simons Foundation, 162 Fifth Ave, New York, NY 10010, USA

2 Analysing surface rotation with ROOSTER

The rotational analysis method combining the auto-correlation function (ACF; McQuillan et al. 2013) and the time frequency analysis of the wavelet power spectrum (WPS; Torrence & Compo 1998; Mathur et al. 2010; García et al. 2014) has shown to be the method able to provide the most complete and reliable set of rotation period estimates during the hare and hounds exercise performed by Aigrain et al. (2015). However, to be applied to the much larger sample of K and M stars, this required to perform a lot of visual inspections as it was done in Santos et al. (2019, hereafter S19). The rotation catalog of S19 was built after visually inspecting about 60% of the considered sample. The Random fOrest Over STEllar Rotation pipeline (ROOSTER, Breton et al. 2021) was designed to reduce the number of light curves and respective rotation diagnostics that have to be visually inspected when analysing large samples. ROOSTER is composed of three random forest (RF) classifiers. The first one is dedicated to assess the presence of a rotational modulation in the considered star. The second one selects the period linked to the rotational modulation among the different estimates yielded by the ACF/WPS rotational analysis. The performance of those classifiers have been assessed with the KM sample of S19. We obtain an accuracy of 94.2% and 95.3% for the first and second step, respectively. Designing a strategy that required the visual inspection of only 25.2% of the stars in the sample, a significant increase from what had to be done for S19, we were able to raise the score of the second classifier to 99.5%. The accuracy estimation over the two steps of analysis was therefore of 92.1% and 96.9%, before and after visual inspection, respectively. The last classifier of the ROOSTER framework is an auxiliary RF classifier which flags close-binary or classical-pulsator candidates, that is targets for which signals in the light curves can be confused with rotational modulation (see S19).

3 First outcomes from the new rotation catalog

Having been properly evaluated, ROOSTER abilities were exploited when analysing the FG main-sequence and subgiant sample of *Kepler* (Santos et al. 2021, hereafter S21). In total, 159,442 *Kepler* targets were analysed in S19 and S21, yielding rotation period $P_{\rm rot}$ and photometric magnetic activity index $S_{\rm ph}$ (see Mathur et al. 2014, for the definition) for 55,232 stars. For each spectral type, F, G, K and M, $P_{\rm rot}$ and $S_{\rm ph}$ values are represented together in the panels of Fig 1. In the four panels, the existence of a saturation regimes at high activity and short rotation period is apparent, particularly for G stars. Magnetic activity intensity then decreases as the star spins down due to stellar rotational braking. The rotation period for the slowest, less active rotators is difficult to constrain from the data collected by an instrument like *Kepler* due to the small amplitude of the long-term rotational modulation. This might explain why this region of the diagram is not populated with the data presented here. While G and K stars experience magnetic braking along their evolution, this mechanism is less efficient for earliest F-type stars, which explains why the F-star population present a larger proportion of fast rotators than coolers stars. The dynamo is also expected not to be very vigorous for those stars, hence the small $S_{\rm ph}$ values.

4 A look at the KOIs

ROOSTER was also used to perform an analysis of the stellar rotation of the *Kepler* Objects of Interests (KOIs Brown et al. 2011), that is to say, host stars of confirmed or candidate planetary objects. It is expected that magnetic activity can be triggered by star-planet magnetic interactions (e.g. Strugarek et al. 2019). Figure 2 shows the orbital period $P_{\rm orb}$-$S_{\rm ph}$ diagram for the confirmed planet-host stars. Due to *Kepler* detection biases (the transit method favours detection of planets with large radius and short orbital periods), it is expected that the Earth is situated in the bottom right corner of the figure with only a few other planets. No clear correlation pattern between $P_{\rm orb}$ and $S_{\rm ph}$ appears in this diagram.

5 Conclusions

Data analysis machine learning methods are increasingly relevant for astronomical purposes as we nowadays face the challenge of analysing data from surveys with hundreds of thousands of stars (or even millions, for an instrument like TESS). We showed here how exploiting the abilities of RF classifiers with the ROOSTER pipeline allowed us to significantly reduce the amount of visual inspections required to build the new *Kepler* FG main-sequence and subgiants catalog of S21. We commented on the first outcomes of the complete *Kepler*

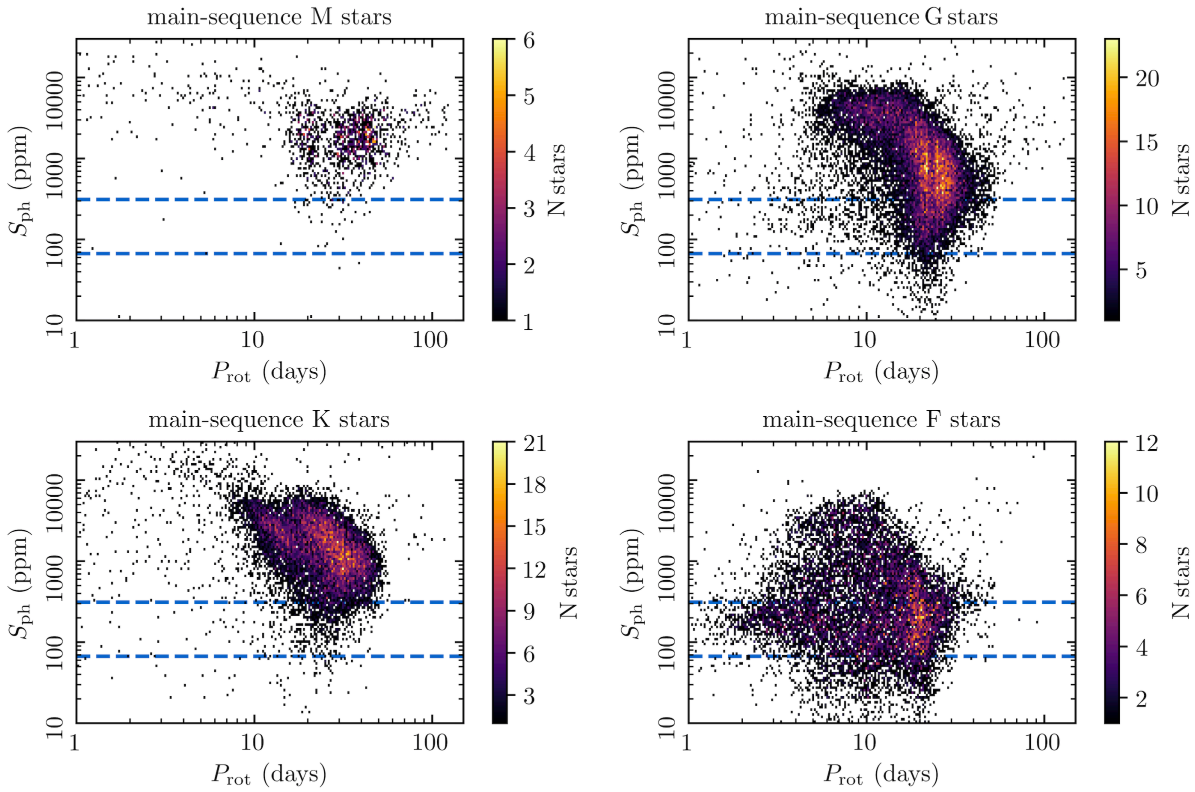

Fig. 1. Magnetic activity index S_{ph} as a function of the rotation period for M (*top left*), K (*bottom left*), G (*top right*) and F (*bottom right*) stars. Adapted from Santos et al. (2019, 2021).

FGKM catalog that is now available through the work of S19 and S21. In particular, we were able to show that the shape of the rotation period-magnetic activity diagram shape is significantly different depending on the spectral type of the considered population of targets. Finally, we emphasised that our first analysis of the confirmed planet-host stars did not reveal a particular relation between planetary orbital period and magnetic activity level. This preliminary work needs to be refined and extended to include a comparison with the *Kepler* sample without detected planet.

S.N.B. and R.A.G. acknowledge the support from PLATO and GOLF CNES grants. A.R.G.S. acknowledges the support from STFC consolidated grant ST/T000252/1 and NASA grant NNX17AF27G. S.M. acknowledges the support from the Spanish Ministry of Science and Innovation with the Ramon y Cajal fellowship number RYC-2015-17697. P.L.P. and S.M. acknowledge support from the Spanish Ministry of Science and Innovation with the grant number PID2019-107187GB-I00. This research has made use of the NASA Exoplanet Archive, which is operated by the California Institute of Technology, under contract with the National Aeronautics and Space Administration under the Exoplanet Exploration Program.

References

Aigrain, S., Llama, J., Ceillier, T., et al. 2015, MNRAS, 450, 3211

Angus, R., Aigrain, S., Foreman-Mackey, D., & McQuillan, A. 2015, MNRAS, 450, 1787

Armstrong, D. J., Kirk, J., Lam, K. W. F., et al. 2016, MNRAS, 456, 2260

Audenaert, J., Kuszlewicz, J. S., Handberg, R., et al. 2021, arXiv e-prints, arXiv:2107.06301

Barnes, S. A. 2003, ApJ, 586, 464

Barnes, S. A. 2007, ApJ, 669, 1167

Bass, G. & Borne, K. 2016, MNRAS, 459, 3721

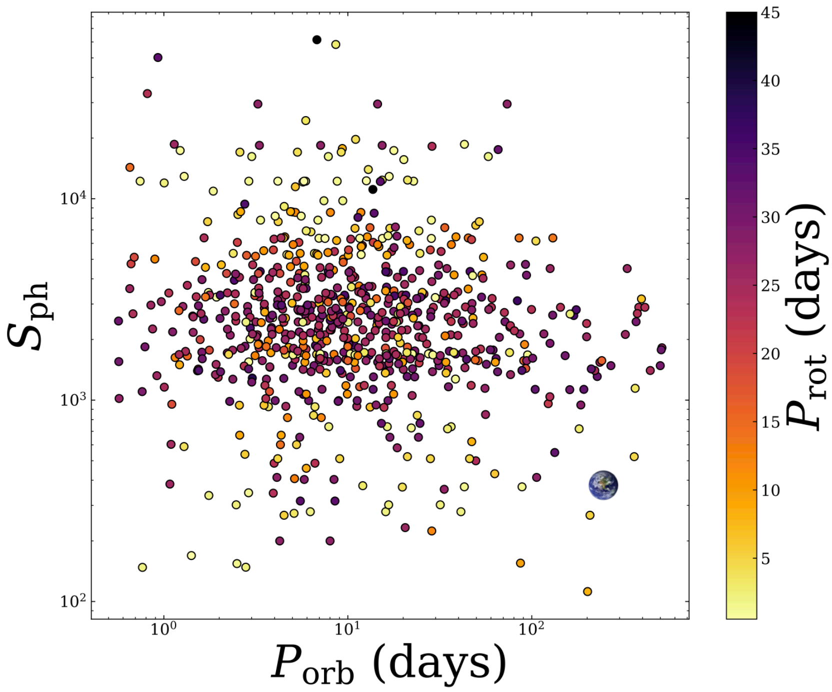

Fig. 2. Photometric magnetic activity index S_{ph} as a function of the orbital period P_{orb} of the confirmed KOIs. The surface rotation period of the star, P_{rot}, is color-coded.

Benbakoura, M., Réville, V., Brun, A. S., Le Poncin-Lafitte, C., & Mathis, S. 2019, A&A, 621, A124
Berdyugina, S. V. 2005, Living Reviews in Solar Physics, 2, 8
Blomme, J., Sarro, L. M., O'Donovan, F. T., et al. 2011, MNRAS, 418, 96
Bolmont, E. & Mathis, S. 2016, Celestial Mechanics and Dynamical Astronomy, 126, 275
Borucki, W. J., Koch, D., Basri, G., et al. 2010, Science, 327, 977
Breton, S. N., Santos, A. R. G., Bugnet, L., et al. 2021, A&A, 647, A125
Brown, T. M., Latham, D. W., Everett, M. E., & Esquerdo, G. A. 2011, AJ, 142, 112
Bugnet, L., García, R. A., Mathur, S., et al. 2019, A&A, 624, A79
García, R. A., Ceillier, T., Salabert, D., et al. 2014, A&A, 572, A34
Kuszlewicz, J. S., Hekker, S., & Bell, K. J. 2020, MNRAS, 497, 4843
Mamajek, E. E. & Hillenbrand, L. A. 2008, ApJ, 687, 1264
Mathis, S. 2015, A&A, 580, L3
Mathur, S., García, R. A., Ballot, J., et al. 2014, A&A, 562, A124
Mathur, S., García, R. A., Régulo, C., et al. 2010, A&A, 511, A46
McQuillan, A., Mazeh, T., & Aigrain, S. 2013, ApJ, 775, L11
Meibom, S., Barnes, S. A., Latham, D. W., et al. 2011, ApJ, 733, L9
Santos, A. R. G., Breton, S. N., Mathur, S., & García, R. A. 2021, ApJS, 255, 17
Santos, A. R. G., García, R. A., Mathur, S., et al. 2019, ApJS, 244, 21
Strassmeier, K. G. 2009, A&A Rev., 17, 251
Strugarek, A., Bolmont, E., Mathis, S., et al. 2017, ApJ, 847, L16
Strugarek, A., Brun, A. S., Donati, J. F., Moutou, C., & Réville, V. 2019, ApJ, 881, 136
Torrence, C. & Compo, G. P. 1998, Bulletin of the American Meteorological Society, 79, 61
van Saders, J. L., Ceillier, T., Metcalfe, T. S., et al. 2016, Nature, 529, 181
Zhang, M. & Penev, K. 2014, ApJ, 787, 131

SF2A 2021
A. Siebert, K. Baillié, E. Lagadec, N. Lagarde, J. Malzac, J.-B. Marquette, M. N'Diaye, J. Richard, O. Venot (eds)

SYNERGY BETWEEN STELLAR PHYSICS AND PLANETOLOGY, A PATHWAY FOR HIGH-RESOLUTION SPECTROSCOPY OF EXOPLANET ATMOSPHERE

A. Chiavassa[1], M. C. Maimone[1], M. Brogi[2] and J. Leconte[3]

Abstract.
Spectroscopy of exoplanet atmospheres at high-resolving powers is a determinant technique for remote atmospheric characterisation of exoplanet atmospheres. However, the non-stationary stellar spectrum affects the position and/of shift of line profiles and creates a non-negligible source of noise that can alter or even prevent detection. In this work, we present three examples of transmission and emission of HD 189733-b and 51 Pegasi b for which the correction for the stellar convection-related activity was included in the analysis. There is a significant improvement in planet detectability when removing the stellar spectrum with our method. Moreover, we briefly present a new approach based on realistic synthetic observations whose innovation and uniqueness is based on the use of 3D hydrodynamical simulations for the atmosphere of both the host star and the planet during the transit

Keywords: stars: atmospheres – Planets and satellites: individual (HD189733b) – Planets and satellites: individual (51 Peg) – Techniques: spectroscopic

1 Introduction

High-resolution spectroscopy (HRS) at resolving powers $R > 25000$ is a determinant technique for remote atmospheric characterisation of exoplanet atmospheres. HRS allows to partially resolve the molecular dense forest of lines and to robustly identify them by line-matching techniques such as cross-correlation. This technique already led to the detection of molecular (CO, H_2O, CH_4, HCN, TiO) and atomic (H, He, K, Na, Mg, Fe, Ti) species in a dozen exoplanets (e.g., Birkby 2018). Secondly, the Doppler shift experienced by the planet during its orbit allows to solve non-transiting systems (e.g., Brogi et al. 2012). Eventually, line shift and broadening is also important to constrain planetary atmospheric winds (Louden & Wheatley 2015; Brogi et al. 2016; Flowers et al. 2019).

HRS technique is currently performed with different infrared spectrographs mounted at large and medium-size telescope facilities and a bright future is forehead with the advent of visible and infrared ELT instruments HIRES (Marconi et al. 2021), METIS (Brandl et al. 2016), and HARMONI (Thatte et al. 2016), with a complete new window open in the field of the combination of high-dispersion spectroscopy with high contrast imaging (Snellen et al. 2015; Houllé et al. 2021).

In this context, the non-uniformity of the planet-hosting stars is a potential source of spurious signals, which can severely complicate the interpretation of exoplanet spectra (Chiavassa et al. 2017; Cegla et al. 2019; Chiavassa & Brogi 2019; Dravins et al. 2021). Stars are not smooth. Their photosphere is covered by a granulation pattern associated with the heat transport by convection (Nordlund et al. 2009), whose temporal and spatial variability depends on the stellar parameters. The related activity (in addition to other phenomena such as magnetic spots, rotation, dust, etc.) has an impact in stellar parameter determination (Bigot et al. 2011; Creevey et al. 2012; Chiavassa et al. 2012), radial velocity (Bigot & Thévenin 2008; Chiavassa et al. 2011; Allende Prieto et al. 2013), chemical abundances determinations (Asplund et al. 2005, 2009; Caffau et al. 2011), photometric colours (Chiavassa et al. 2018; Bonifacio et al. 2017), and on planet detection (Magic et al. 2015; Chiavassa et al. 2017).

[1] Université Côte d'Azur, Observatoire de la Côte d'Azur, CNRS, Lagrange, CS 34229, Nice, France
[2] Department of Physics, University of Warwick, Coventry CV4 7AL, UK
INAF - Osservatorio Astrofisico di Torino, Via Osservatorio 20, 10025, Pino Torinese, Italy
Centre for Exoplanets and Habitability, University of Warwick, Gibbet Hill Road, Coventry CV4 7AL, UK
[3] Laboratoire d'Astrophysique de Bordeaux, Univ. Bordeaux, CNRS, B18N, allée Geoffroy Saint-Hilaire, 33615 Pessac, France

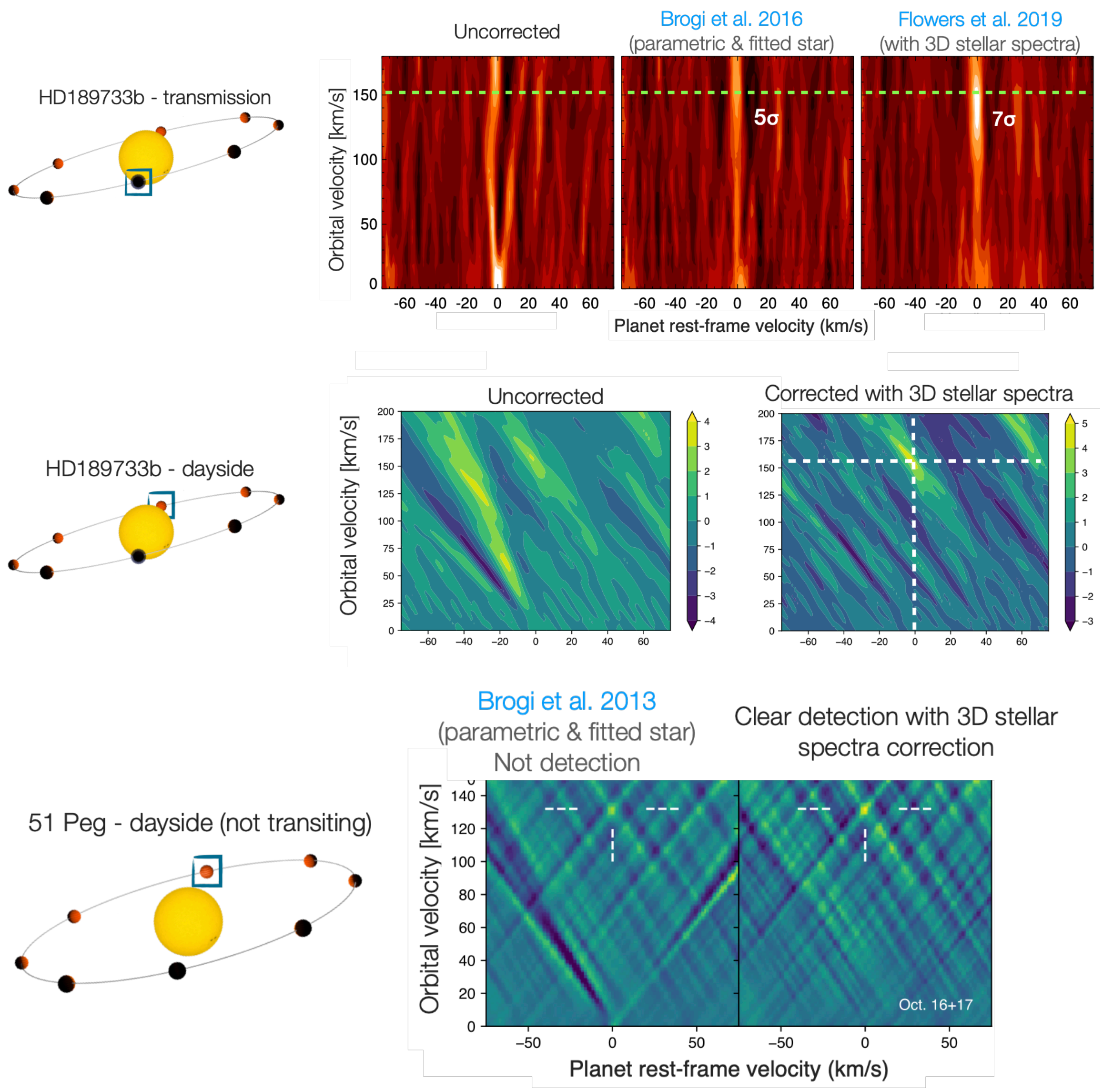

Fig. 1. Total cross-correlation signal, as a function of stellar removal applied to data, from carbon monoxide in transmission spectrum of HD 189733 b (*Top row*), HD 189733 b emission spectrum (*Central row*), and 51 Pegasi b (*Bottom row*). The dashed lines indicate the signal at expected planet maximum orbital velocity ($K_P \sim 151$ km s^{-1}). The leftmost sketch displays the configuration of the transit. The Images are from Chiavassa & Brogi (2019).

2 Method

The method used here is based on the pioneering detection of carbon monoxide with HRS cross-correlation (Snellen et al. 2010) with later improvements in several works (e.g., Brogi et al. 2012, 2013). One ultimate aim is the retrieval of exoplanetary temperatures and abundances (Brogi & Line 2019). In this context, the correction for the host star convection-related activity was included for the first time in Chiavassa & Brogi (2019), and we resume here few details concerning the stellar spectra used.

The stellar photosphere are simulated using non-local, three-dimensional, ab initio radiative hydrodynamical (RHD) simulations that cover a substantial portion of the Hertzsprung-Russell diagram (the Stagger-grid, Magic et al. 2013). Afterwards, we used the 3D pure-LTE radiative transfer code Optim3D (Chiavassa et al. 2009) to compute synthetic spectra from the snapshots of different stellar types. To account for center-to-limb distribution, we computed spectra for ten box tilting angles and four azimuths rotations. The constant resolving power used $\lambda/\Delta\lambda = 300\,000$ and the range covered is 22 850 to 23 900 Å, (for mote details, see Chiavassa et al.

2018; Chiavassa & Brogi 2019).

3 Time-differential high-dispersion spectroscopy of CO lines in the K band: three examples

3.1 Transmission spectrum of the exoplanet HD 189733 b

We present one example from Chiavassa & Brogi (2019) to which we point the reader for further details. Fig. 1 (*top row*) displays the significant contaminant stellar contamination (first panel). Brogi et al. (2016) achieved to pinpoint the CO planetary absorption at 5σ using parametric ad-hoc modelisation to account for the stellar correction, albeit with a remaining residual signal from the star (central panel). The use of 3D RHD synthetic spectra (rightmost panel) brought a much better correction and resulted in a unique and unambiguous identification of the planetary signal in CO alone (Flowers et al. 2019). This improvement is reflected into a refined inference on the rotational rate and wind speed of exoplanet HD 189733 b.

3.2 Emission spectra of HD 189733-b and 51 Pegasi b

A second example comes again from HD 189733-b during its orbital phases comprises between 0.38 and 0.48 and analyzed initially by de Kok et al. (2013). Fig. 1 (*central row*) shows that after a quantitative correction with 3D RHD stellar spectra, we recover the signal of the exoplanet in CO at a S/N=4.5, consistent with de Kok et al. (2013), and no stellar residual above the S/N = 3. Also in this case, the uncorrected signal by the stellar spectrum would be completely outshone by stellar residuals, preventing the detection.

The last example concerns the data described in Brogi et al. (2013) for 51 Pegasi b. Fig. 1 (*bottom row*) displays that when the stellar spectrum is removed, the planet remains the only unambiguous source detected. This results, detailed in Chiavassa & Brogi (2019), is a clear improvement from the non-detection originally reported by Brogi et al. (2013).

4 The future: coupling stellar and planet dynamics during transits

We are developing a new approach (Maimone 2021) based on realistic synthetic observations whose innovation and uniqueness is based on the use of 3D hydrodynamical simulations for the atmosphere of both the host star (Stagger-code, Nordlund et al. 2009) and the planet (hot jupiters grid computed with MITgcm, Parmentier et al. 2016) during the transit. This is done using an updated version of the post-processing radiative transfer code Optim3D (Chiavassa et al. 2009). The code takes into account, simultaneously, the stellar and planetary dynamics. They influence the shape, shift, and asymmetries of spectral lines, and not rarely of the same specie (Fig. 2). This new method will be used to interpret HRS data to extract extremely useful information either for the characterization of the stellar parameters and metallicity and for the planet dynamics and composition.

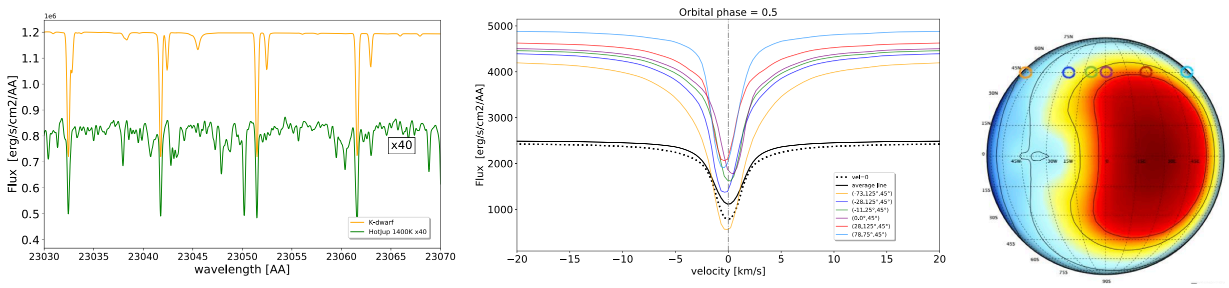

Fig. 2. *Right panel:* example of stellar (K dwarf from Chiavassa et al. 2018) and scaled hot jupiter with T_{eq}=1400 K (Parmentier et al. 2016) spectra in K band computed with the new version of Optim3D. Both objects show the same CO spectral features. *Central panel:* one particular hot jupiter CO line computed for different atmospheric regions. *Right panel:* Temperature map of the hot jupiter with highlighted areas (colored circles) used to compute CO lines in central panel.

With this tool in hands, we will have access to the whole comprehension of the transit phenomena with a large impact on different areas of astrophysics from exoplanets to stars: e.g., reliable study on the impact of stellar parameters and activity as well as a full characterization of the atmosphere of the planet, from molecular detection to the abundance of their elements.

This project has received funding from the European Research Council (ERC) under the European Union's Horizon 2020 research and innovation programme (grant agreement n∘ 679030/WHIPLASH).

References

Allende Prieto, C., Koesterke, L., Ludwig, H.-G., Freytag, B., & Caffau, E. 2013, A&A, 550, A103

Asplund, M., Grevesse, N., & Sauval, A. J. 2005, in Astronomical Society of the Pacific Conference Series, Vol. 336, Cosmic Abundances as Records of Stellar Evolution and Nucleosynthesis, ed. T. G. Barnes, III & F. N. Bash, 25

Asplund, M., Grevesse, N., Sauval, A. J., & Scott, P. 2009, ARA&A, 47, 481

Bigot, L., Mourard, D., Berio, P., et al. 2011, A&A, 534, L3

Bigot, L. & Thévenin, F. 2008, in Proceedings of the Annual meeting of the French Society of Astronomy and Astrophysics, ed. C. Charbonnel, F. Combes, & R. Samadi, 3

Birkby, J. L. 2018, Handbook of Exoplanets, Springer Nature, 16

Bonifacio, P., Caffau, E., Ludwig, H.-G., et al. 2017, Mem. Soc. Astron. Italiana, 88, 90

Brandl, B. R., Agócs, T., Aitink-Kroes, G., et al. 2016, in Society of Photo-Optical Instrumentation Engineers (SPIE) Conference Series, Vol. 9908, Ground-based and Airborne Instrumentation for Astronomy VI, ed. C. J. Evans, L. Simard, & H. Takami, 990820

Brogi, M., de Kok, R. J., Albrecht, S., et al. 2016, ApJ, 817, 106

Brogi, M. & Line, M. R. 2019, AJ, 157, 114

Brogi, M., Snellen, I. A. G., de Kok, R. J., et al. 2012, Nature, 486, 502

Brogi, M., Snellen, I. A. G., de Kok, R. J., et al. 2013, ApJ, 767, 27

Caffau, E., Ludwig, H.-G., Steffen, M., Freytag, B., & Bonifacio, P. 2011, Sol. Phys., 268, 255

Cegla, H. M., Watson, C. A., Shelyag, S., Mathioudakis, M., & Moutari, S. 2019, ApJ, 879, 55

Chiavassa, A., Bigot, L., Kervella, P., et al. 2012, A&A, 540, A5

Chiavassa, A., Bigot, L., Thévenin, F., et al. 2011, Journal of Physics Conference Series, 328, 012012

Chiavassa, A. & Brogi, M. 2019, A&A, 631, A100

Chiavassa, A., Caldas, A., Selsis, F., et al. 2017, A&A, 597, A94

Chiavassa, A., Casagrande, L., Collet, R., et al. 2018, A&A, 611, A11

Chiavassa, A., Plez, B., Josselin, E., & Freytag, B. 2009, A&A, 506, 1351

Creevey, O. L., Thévenin, F., Boyajian, T. S., et al. 2012, A&A, 545, A17

de Kok, R. J., Brogi, M., Snellen, I. A. G., et al. 2013, A&A, 554, A82

Dravins, D., Ludwig, H.-G., & Freytag, B. 2021, A&A, 649, A17

Flowers, E., Brogi, M., Rauscher, E., Kempton, E. M. R., & Chiavassa, A. 2019, AJ, 157, 209

Houllé, M., Vigan, A., Carlotti, A., et al. 2021, arXiv e-prints, arXiv:2104.11251

Louden, T. & Wheatley, P. J. 2015, ApJ, 814, L24

Magic, Z., Chiavassa, A., Collet, R., & Asplund, M. 2015, A&A, 573, A90

Magic, Z., Collet, R., Asplund, M., et al. 2013, A&A, 557, A26

Maimone, M. C. 2021, in Cambridge Workshop on Cool Stars, Stellar Systems, and the Sun, Cambridge Workshop on Cool Stars, Stellar Systems, and the Sun, 249

Marconi, A., Abreu, M., Adibekyan, V., et al. 2021, The Messenger, 182, 27

Nordlund, Å., Stein, R. F., & Asplund, M. 2009, Living Reviews in Solar Physics, 6, 2

Parmentier, V., Fortney, J. J., Showman, A. P., Morley, C., & Marley, M. S. 2016, ApJ, 828, 22

Snellen, I., de Kok, R., Birkby, J. L., et al. 2015, A&A, 576, A59

Snellen, I. A. G., de Kok, R. J., de Mooij, E. J. W., & Albrecht, S. 2010, Nature, 465, 1049

Thatte, N. A., Clarke, F., Bryson, I., et al. 2016, in Society of Photo-Optical Instrumentation Engineers (SPIE) Conference Series, Vol. 9908, Ground-based and Airborne Instrumentation for Astronomy VI, ed. C. J. Evans, L. Simard, & H. Takami, 99081X

SF2A 2021
A. Siebert, K. Baillié, E. Lagadec, N. Lagarde, J. Malzac, J.-B. Marquette, M. N'Diaye, J. Richard, O. Venot (eds)

THE IMPACT OF SURFACE FLOWS AT DIFFERENT SCALES: EXOPLANET DETECTABILITY IN RADIAL VELOCITY AND HIGH-PRECISION ASTROMETRY

N. Meunier[1] and A.-M. Lagrange[1, 2]

Abstract. It is now well accepted that stellar activity prevents the detection of Earth-like planets around solar type stars when using the radial velocity technique. Although the impact of dark spots and bright plages, through various processes, is now well modelled, surface flows at different time scales (granulation, supergranulation, meridional circulation) also lead to important radial velocity signatures due to their temporal variability but have been less studied. Those signatures are larger than an Earth-like signal. In this talk, we will focus on those flows, which we have studied based on our knowledge of the Sun and extended towards other stars. We will also show that a high-precision astrometric mission would not be strongly impacted by stellar activity for such planets.

Keywords: Stellar activity - Solar-type stars - Exoplanets - Convection - Radial velocity - Astrometry

1 Introduction

A large variety of stellar processes affects radial velocity (hereafter RV) temporal variations (see Meunier 2021, for a review). The best studied impact is due to the contrast of spots and plages, distorting the shape of the spectral lines as structures rotate (Saar & Donahue 1997). Another major effect is due to the inhibition of the convective blueshift in plages, which appears to be dominant for a star like the Sun (Lagrange et al. 2010; Meunier et al. 2010): this affects both short timescales (rotation) and long timescales (cycles). Surface flows at different scales also directly impact radial velocities. Granulation (and, at a larger scale, supergranulation) produces stochastic variabilities, following a specific power law with a plateau a long periods (Harvey 1984; Meunier et al. 2015), while pulsations mostly affect very short periods. Finally, meridional circulation is a large scale flow, mostly poleward in the solar case, but not yet observable for other stars, which also affects radial velocities if variable with time (Makarov 2010; Meunier & Lagrange 2020a). The inhibition of the convection leads to RV amplitudes up to a few m/s. The other aforementioned effects lead to RV variations with amplitudes typically in the 0.4-1 m/s range for old main-sequence FGK stars. They produce a barrier at the $\sim$1 m/s level. This is to be compared with the Earth signal, below 10 cm/s. Conversely, there are many less processes contributing to the stellar astrometric signal, which should not prevent to detect low mass planets if high precision can be reached (Lagrange et al. 2011).

2 Our approach

Our approach is twofold. First, we used our extensive knowledge of the Sun to better understand these different processes. We therefore developed reconstruction of the integrated signal based on solar observations (including with spatial resolution of the structures at the surface Lagrange et al. 2010; Meunier et al. 2010), then built a model validated in the solar case (Borgniet et al. 2015). This model was then extrapolated to other stars (Meunier et al. 2019). This allowed us to produce a very large amount of synthetic time series of radial velocities for FGK main old sequence stars, but also in photometry (Meunier & Lagrange 2019b), astrometry (Meunier et al. 2020) and chromospheric emission ($\log R'_{HK}$). This approach is complementary to others, such as RV

[1] Univ. Grenoble Alpes, CNRS, IPAG, F-38000 Grenoble, France
[2] LESIA, Observatoire de Paris, Université PSL, CNRS, Sorbonne Université, Univ. Paris Diderot, Sorbonne Paris Cité, 5 place Jules Janssen, 92195 Meudon, Franc

observations of the Sun as a star with HARPS-N (e.g. Collier Cameron et al. 2019), coordinated campaigns (Lopez et al. 2019), or more simple simulations (e.g. Desort et al. 2007; Dumusque et al. 2014).

Our simulations primarily include the contributions of spots and plages, and the inhibition of the convective blueshift (Meunier et al. 2019). We generated structures with a realistic spatio-temporal distribution, size and lifetime distributions and contrasts. Structures of different types are generated in a coherent way. The parameters cover F6-K4 stars with moderate activity level (young active stars are excluded at this stage because their parameters are less well constrained and different from the solar case). A second type of simulations takes pulsations, granulation and supergranulation into account. We performed a first simulation based on the proper number of granules and supergranules to check Harvey's law (Meunier et al. 2015), and later generated a large amount of time series based on their expected power law (Meunier & Lagrange 2019c, 2020b). The amplitude of the granular signal was scaled to the solar one with two different assumptions (low and high), with a dependence on spectral type. Supergranulation amplitude is also scaled to granulation. As for meridional circulation, we have so far only reconstructed the temporal variability in the solar case, based on the observations of Ulrich (2010), and extrapolated the amplitudes to other stars following numerical simulation prescriptions (Brun et al. 2017). Full synthetic simulations remain to be built.

We present here examples illustrating four important objectives on our approach: 1/ Predict the expected RV amplitudes for the different contributions; 2/ Understand correction method limitations; 3/ Quantify the impact on exoplanet mass characterisation, for example when performing an RV follow-up of transit detections, and compare them with high-precision astrometry; 4/ Quantify the impact on exoplanet detectability in RV, and compare them with high-precision astrometry.

3 Results

3.1 Predicting the expect RV amplitudes for the different contributions

The typical amplitude of magnetic activity (spots, plages, inhibition of the convective blueshift) is strongly dependent on the activity of the stars (average level and variability), with a rms (root-mean-square) RV between a few 0.1 m/s and several m/s (Meunier & Lagrange 2019a). Stellar inclination also impacts the amplitude. Simulations of granulation (Meunier et al. 2015) led to a solar rms of 0.8 m/s, a value larger than the observed one (0.4 m/s, Pallé et al. 1999), or from HD simulations (Sulis et al. 2020). The difference could be due some center-to-disk effects, or the use of a single spectral line in observations. The amplitude decreases from F to K stars. The supergranular signal shows variation with an rms between 0.3 and 1.2 m/s, in agreement with the solar observations of Pallé et al. (1999) in a single spectral line (0.7 m/s). The amplitude is expected to decrease from F to K stars, like granulation. Finally, our solar reconstruction of the large scale meridional circulation provided an amplitude in the 1-2 m/s range (Meunier & Lagrange 2020a). The variability is the highest for a star seen pole-on, and the sign of the variability reverses for a latitude around 30°, leading to a still important variability for a star seen edge-on. There may be a relation of the meridional circulation with the solar cycle, but possibly shifted in phase. Our extrapolation to FGK stars gave amplitudes in the 0.1-4 m/s range.

3.2 Understanding method limitations when correcting for stellar activity in RV

Many methods have been used to attempt to correct for the stellar contribution to RV variations, to be able to extract planetary signals. Some of them are based on proxy of stellar activity such as the $\log R'_{HK}$ indicator. A linear correlation between the two observables is often used, although it has been known to leave residuals: this correlation arises from the fact that both the inhibition of the convective blueshift in plages and the chromospheric emission are related to the same structures. The study of the synthetic time series (Meunier et al. 2019) allowed us to identify an effect leading to a non-linearity between RV and $\log R'_{HK}$, as the relationship is different between the ascending and descending phases of the cycles. This is due to the combination of two effects: due to the butterfly diagram of activity pattern, structures are on average at different distances from disk center during the cycle, while the chromospheric emission and the convective blueshift inhibition both depend on the position on the disk, but with different projection effects. We proposed a simple way to take this into account, by modeling the RV variability using a function of $\log R'_{HK}$ and of the phase of the cycle (providing an estimate of a cycle period can be made). We found that the rms of the residual could in such a case be indeed significantly improved with respect to the linear correction for some configurations. Some additional residuals remain, more stochastic, because at any given time, there is a dispersion in latitude of the plages. We conclude that this should degrade the detectability in RV. Transit detection with further mass characterisation in RV may be easier, as discussed in the next section.

3.3 Quantifying the impact on exoplanet mass characterisation in transit follow-up

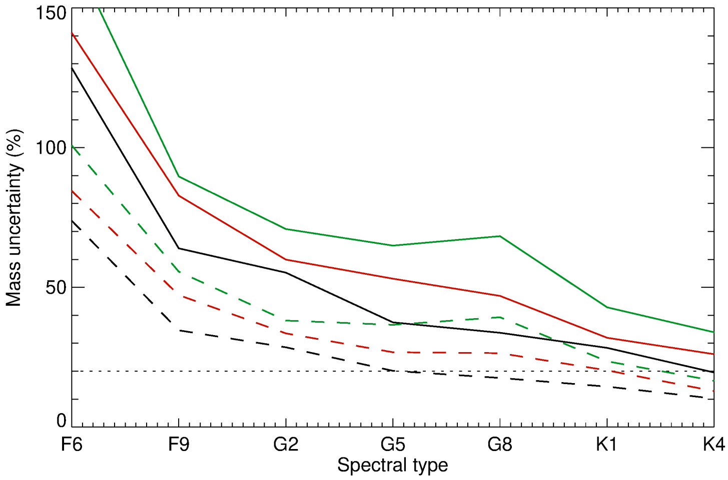

Fig. 1. Mass uncertainty for 1 M_{Earth} (solid) and 2 M_{Earth} (dashed), in the inner part of the habitable zone (black), middle (red) and outer part (green) versus spectral type, for a low level of granulation, supergranulation (both averaged over 1 h), spot, plages, and convective blueshift inhibition.

We used these synthetic time series to test the uncertainty on the mass estimation in a transit follow up. We focused on Earth-like planets in the habitable zone around solar-type stars, with masses of typically 1-2 M_{Earth}. The signal of the planet is first added to the synthetic stellar signal. We then assumed that the transit provides a precise estimate of the period and phase of the planet, and finally fitted the mass. The rms of the fitted mass on all realisations provided an estimate of the expected uncertainty on the mass. When considering the contributions due to pulsations, granulation, and supergranulation (Meunier & Lagrange 2020b), assuming 1-hour exposure time, we found that even with a very large amount of nights (>1000 over 10 years), the uncertainty for 1 M_{Earth} is above the 20% expected for PLATO, except for the lowest assumption for the stellar signal and K stars. The performance was slightly better for 2 M_{Earth}. The same computation made for the magnetic activity shows a worse performance, and again the uncertainty is always above 20%, as shown in Fig. 1. For the solar case and 1 M_{Earth} for example, the uncertainty is a factor 2 above 20%. By comparison, a high-precision astrometric mission with the performance of The Theia Collaboration et al. (2017) would allow to reach uncertainties of 20% or better (down to 10%) for a star at 10 pc, 1-2 M_{Earth} in the habitable zone, assuming 50 visits over 3.5 y and a noise of 0.2 μarcsec per measurement (Meunier et al. 2020).

3.4 Quantifying the impact on exoplanet detectability

We first estimated the mass of the detectable planet using a very simple analysis of the rms RV derived from these simulations and a threshold based on the performance of the best methods in the blind test performed in Dumusque et al. (2017). This showed that it was not possible to reach Earth mass planets in the habitable zone around solar-type stars (Meunier & Lagrange 2019a). To move further, a systematic analysis similar to that of Sect. 3.2 can be applied to detectability. Instead of assuming the period and phase of the planet found using its transits, a false alarm probability is computed on the time series, and peaks above this level in the periodogramme are considered to be detections. These detections are compared with the true parameters of the planet added to the stellar signal, which allows to estimate detection rates and false positive rates. Such blind tests on the pulsation-granulation-supergranulation time series, again with 1-hour exposure time, showed that the level of detection rates is low, typically 20% for G2 stars and 1266 nights over 10 years. Furthermore, there is a large amount of false positives, well above the 1% level. The signal is then dominated by supergranulation. The same blind tests made when considering the magnetic activity contribution (spots, plages, inhibition of the convective blueshift in plages) leads to worse performance (with a correction as in Sect. 3.2): preliminary results for G2 stars and 1 M_{Earth} show a detection rate around 2% only, and more than 60% false positives, most of them at low periods however. The false positive rate in the habitable zone is of the order of 2-5%. By comparison, the detection rates for astrometry, again based on the The Theia Collaboration et al. (2017) configuration, leads to very good detection rates: only 10 to 20% of the planets are missed. The level of false positive in the habitable zone is below 0.1% (Meunier et al. 2020).

4 Conclusion and perspectives

We conducted a very fruitful approach, based on complex and realistic synthetic time series and a systematic analysis of these time series. For the first time, many processes were taken into account. The detectability of long-period exoplanets is affected by all processes, in which surface flows play an crucial role. Blind tests show that the mass characterisation in transit follow-up is poor for FGK stars and Earth mass planets in the habitable zone, and their detectability with RV alone is low (including a high level of false positive). The performance is much better for high-precision astrometry, although the technical challenges of such a mission is still problematic. Future work will focus on combining all processes and on improving the RV simulations to provide more observables, in order to test more correction methods. It will indeed be necessary to improve correction techniques based on the knowledge of the physical processes to be able to control the residuals and reach lower mass planets.

References

Borgniet, S., Meunier, N., & Lagrange, A.-M. 2015, A&A, 581, A133

Brun, A. S., Strugarek, A., Varela, J., et al. 2017, Astrophys. J., 836, 192

Collier Cameron, A., Mortier, A., Phillips, D., et al. 2019, MNRAS, 487, 1082

Desort, M., Lagrange, A. M., Galland, F., Udry, S., & Mayor, M. 2007, A&A, 473, 983

Dumusque, X., Boisse, I., & Santos, N. C. 2014, ApJ, 796, 132

Dumusque, X., Borsa, F., Damasso, M., et al. 2017, A&A, 598, A133

Harvey, J. W. 1984, in Probing the depths of a Star: the study of Solar oscillation from space, ed. R. W. Noyes, & E. J. Rhodes Jr., JPL, 400, 327

Lagrange, A.-M., Desort, M., & Meunier, N. 2010, A&A, 512, A38

Lagrange, A.-M., Meunier, N., Desort, M., & Malbet, F. 2011, A&A, 528, L9

Lopez, T. A., Barros, S. C. C., Santerne, A., et al. 2019, A&A, 631, A90

Makarov, V. V. 2010, Astrophys. J., 715, 500

Meunier, N. 2021, arXiv e-prints, arXiv:2104.06072

Meunier, N., Desort, M., & Lagrange, A.-M. 2010, A&A, 512, A39

Meunier, N. & Lagrange, A. M. 2019a, A&A, 628, A125

Meunier, N. & Lagrange, A. M. 2019b, A&A, 629, A42

Meunier, N. & Lagrange, A. M. 2019c, A&A, 625, L6

Meunier, N. & Lagrange, A. M. 2020a, A & A, 638, A54

Meunier, N. & Lagrange, A. M. 2020b, A & A, 642, A157

Meunier, N., Lagrange, A. M., & Borgniet, S. 2020, A & A, 644, A77

Meunier, N., Lagrange, A.-M., Borgniet, S., & Rieutord, M. 2015, A&A, 583, A118

Meunier, N., Lagrange, A. M., Boulet, T., & Borgniet, S. 2019, A&A, 627, A56

Meunier, N., Lagrange, A.-M., & Cuzacq, S. 2019, A&A, 632, A81

Pallé, P. L., Roca Cortés, T., Jiménez, A., GOLF Team, & Virgo Team. 1999, in Astronomical Society of the Pacific Conference Series, Vol. 173, Stellar Structure: Theory and Test of Connective Energy Transport, ed. A. Gimenez, E. F. Guinan, & B. Montesinos, 297

Saar, S. H. & Donahue, R. A. 1997, Astrophys. J., 485, 319

Sulis, S., Mary, D., & Bigot, L. 2020, A&A, 635, A146

The Theia Collaboration, Boehm, C., Krone-Martins, A., et al. 2017, arXiv:1707.01348

Ulrich, R. K. 2010, Astrophys. J., 725, 658

SF2A 2021
A. Siebert, K. Baillié, E. Lagadec, N. Lagarde, J. Malzac, J.-B. Marquette, M. N'Diaye, J. Richard, O. Venot (eds)

EXAMINING TESS LIGHT CURVE TO SORT OUT SOPHIE PLANET CANDIDATE

N.Heidari[1,2 3] and I. Boisse[3]

Abstract. Since stellar activity is a dominant source of noise in both photometric and radial velocity (RV) surveys, a deeper understanding of its effects is essential for accurate exoplanet detection and characterization. Photometric data of Transiting Exoplanet Survey Satellite (TESS) offers us an opportunity to investigate the radial velocity jitters induced by stellar activities through photometric variabilities. In this project, we used the SOPHIE (1.93m-OHP) RV measurements and TESS photometry data in order to 1) evaluate the activity of the host star of the SOPHIE planet candidates; 2) investigate the likely activity-induced RV variations; 3) try to detect a new planet signal in photometry data. We present the result of our current analysis and how it can help for making an efficient observation planning for the future SOPHIE surveys.

Keywords: methods: data analysis, stars: activity, techniques: radial velocities, techniques: photometric

1 Introduction

It is well known that the presence of stellar activity can interfere with spectroscopic and photometric observations of exoplanets, leading to false detection or missing signals from the radial velocity (Rajpaul et al. 2015; Díaz et al. 2016). Stellar activity can also influence the accurate determination of exoplanet parameters (Barros et al. 2014). It is therefore quite important to identify and characterize the stellar activity in order to distinguish it -as accurately as possible- from the variations caused by exoplanets. Using simultaneous RV and photometric measurements delivers a wealth of information about the stellar activity, a key to evaluating the activity of host stars and having accurate data analysis. For this purpose, here, we used the SOPHIE RV measurements and TESS photometry data.

2 Activity induced RV variations

By analyzing the SOPHIE RV measurements and TESS photometry data, we successfully removed some false positives of SOPHIE planet candidates. As an example, in Fig. 1 top-left, we plotted the RVs periodogram of one of the SOPHIE targets which illustrates a significant peak with false alarm probability (FAP) of below 1 % at 5.9 d. The same peak was found in periodogram of bissector span. Our investigation in the TESS light curve shows that the star is very active. Moreover, the posterior distribution of stellar rotational period using the Gaussian Processes (GPs) model shows a peak at 12 d. Considering the star is very active and there is a corresponding peak in the activity indicator, it is likely that the RVs signal at 5.9 days is half of the rotational period peak at 12 d.

3 Detecting transit signals

Among the exoplanet population, transiting planets have a considerable impact. They can be characterized accurately in mass and in radius, hence giving access to their mean bulk composition.

[1] Department of Physics, Shahid Beheshti University, Tehran, Iran.
[2] Laboratoire J.-L. Lagrange, Observatoire de la Côte d'Azur (OCA), Université de Nice-Sophia Antipolis (UNS), CNRS, Campus Valrose, 06108 Nice Cedex 2, France.
[3] Aix Marseille Univ, CNRS, CNES, LAM, Marseille, France.

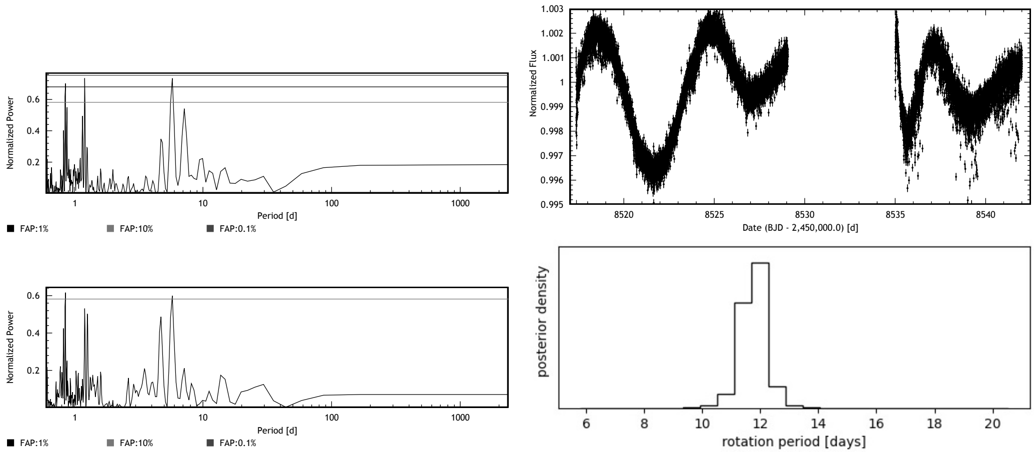

Fig. 1. Right: periodogram of RVs (*top*) and bissector span (*bottom*) of one of the SOPHIE targets. **Left:** TESS light curve of the target (*top*) and the posterior distribution of stellar rotational period using the Gaussian Processes (GPs) model (*bottom*).

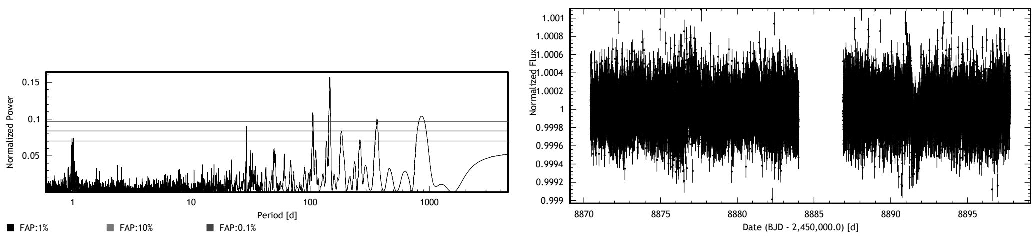

Fig. 2. Right: RVs periodogram of one of SOPHIE targets. **Bottom:** solo transit signature of the target in TESS light curve.

To detect such interesting planets, we searched the TESS light curve of the SOPHIE planet candidates. To do so, we used the transit-least-squares (TLS) algorithm (Hippke & Heller 2019), a method to investigate planetary transits taking into account the stellar limb-darkening and also the effects of planetary ingress and egress. In Fig. 2, we plotted a solo transit which we found in TESS light curve. An analysis of RV measurements shows us a strong peak with FAP of below 0.1 % at 147 d and a lot of other peaks everywhere in the periodogram (see Fig. 2 top). The solo transit can be the signature of each of these candidates. We have a plan to determine the phase of the RVs through combing with TESS photometric data to identify which candidate it might be. Moreover, TESS will re-observe this star in February and provide us more information about this system.

4 Conclusions and next work

In the target selection for the observation plan, it is necessary to define priority and have an observation strategy for each star. To do so, a better understanding of the star activity is essential. Such work will greatly help in evaluating the activity of stars and having accurate data analysis. We plan to continue this work with current and future SOPHIE and TESS observations.

References

Barros, S., Almenara, J., Deleuil, M., et al. 2014, Astronomy & Astrophysics, 569, A74

Díaz, R., Ségransan, D., Udry, S., et al. 2016, Astronomy & Astrophysics, 585, A134

Hippke, M. & Heller, R. 2019, A&A, 623, A39

Rajpaul, V., Aigrain, S., & Roberts, S. 2015, Monthly Notices of the Royal Astronomical Society: Letters, 456, L6

Session 17

Des galaxies à la toile cosmique : baryons et matière noire

SF2A 2021
A. Siebert, K. Baillié, E. Lagadec, N. Lagarde, J. Malzac, J.-B. Marquette, M. N'Diaye, J. Richard, O. Venot (eds)

CORED DARK-MATTER PROFILES IN $Z \simeq 1$ STAR FORMING GALAXIES

N. F. Bouché [1], S. Bera[1], D. Krajnović[2], E. Emsellem[3], W. Mercier[4], J. Schaye[5], B. Epinat[6], J. Richard[1], S. L. Zoutendijk[5], V. Abril-Melgarejo[6], J. Brinchmann[7], R. Bacon[1], T. Contini[4], L. Boogaard[5 8], L. Wisotzki[2], M. Maseda[6] and M. Steinmetz[2]

Abstract. We present a study of the dark-matter (DM) content of 9 $z \approx 1$ low mass SFGs (with $M_\star$ ranging from $10^{8.5}$ to $10^{10.5}$ $\mathrm{M}_\odot$) selected among the brightest [O II] emitters in the deepest Multi-Unit Spectrograph Explorer (MUSE) field to date, namely the 140hr MUSE Extremely Deep Field. We perform disk-halo decompositions on their [O II] emission line with a 3D parametric model using GalPaK$^{3\mathrm{D}}$. The disk-halo decomposition includes a stellar, DM, gas and occasionally a bulge component, and the DM component is made of a generalized α, β, γ profile. We find that the disk stellar masses $M_\star$ obtained from the [O II] disk-halo decomposition agree with the values inferred from the spectral energy distributions. We find that the rotation curves show diverse shapes, ranging from rising to declining at large radii, the DM fractions within the half-light radius $f_{\mathrm{DM}}(< R_{\mathrm{e}})$ are found to be 60% to 95%, extending to lower masses (densities) the results of Genzel et al. For isolated galaxies, same SFGs shows a strong preference for cored over cuspy DM profiles and the presence of DM cores occurs in galaxies with low stellar-to-halo mass ratio, $\log M_\star/M_{\mathrm{vir}} \approx -2.5$. The cored/cuspiness nature of the DM profiles is found to be a strong function of the recent star-formation activity, supporting feedback induced core formation in the Cold Dark Matter context.

Keywords: galaxies: evolution; galaxies: high-redshift; galaxies: kinematics and dynamics; methods: data analysis

1 Introduction

The universe's matter content is dominated by the elusive dark-matter (DM), which has yet to be discovered and understanding the nature and properties of DM on galactic scales remains one of the greatest challenges of modern physics and cosmology (see Bullock & Boylan-Kolchin 2017, for a review). The concept of DM became part of mainstream research only in the 1970s, when it was realized that galaxy rotation curves (RCs) became flat at large radii (e.g. Rubin & Ford 1970), which could not be explained within the standard Newtonian gravity framework, but instead implied the presence of an unobserved mass component attributed to a DM halo.

Understanding the relative distributions of baryons and dark matter in galaxies is still best achieved from a careful analysis of galaxies' RCs on galactic scales. At redshift $z = 0$, this type of analysis is mature with a wealth of studies published in the past 20-30 years, using a variety of dynamics tracers such as H I (e.g. de Blok & McGaugh 1997; de Blok et al. 2001) or a combination of H I & Hα as in the recent SPARC sample (Allaert et al. 2017; Katz et al. 2017; Li et al. 2020). In low surface brightness (LSB) galaxies, the DM profiles have shown to be consistent with a flat density inner 'core', contrary to the expectations from DM-only simulations that

[1] Univ Lyon, Univ Lyon1, Ens de Lyon, CNRS, Centre de Recherche Astrophysique de Lyon (CRAL) UMR5574, F-69230 Saint-Genis-Laval, France
[2] Leibniz-Institut für Astrophysik Potsdam (AIP), An der Sternwarte 16, D-14482 Postdam, Germany
[3] ESO, Karl-Schwarzschild-Strasse 2., D-85748 Garching b. München, Germany
[4] Institut de Recherche en Astrophysique et Planétologie (IRAP), Université de Toulouse, CNRS, UPS, F-31400 Toulouse, France
[5] Leiden Observatory, Leiden University, P.O. Box 9513, 2300 RA Leiden, The Netherlands
[6] Aix Marseille Univ, CNRS, CNES, LAM, Marseille, France
[7] Instituto de Astrofísica e Ciências do Espaço, Universidade do Porto, CAUP, Rua das Estrelas, 4150-762 Porto, Portugal
[8] Max Planck Institute for Astronomy, Königstuhl 17, 69117 Heidelberg, Germany

predicts steep central density profiles or 'cusp' (e.g. Navarro et al. 1997, NFW). It has long been recongnized that this cusp-core debate can be resolved within CDM with feedback processes (e.g. Navarro et al. 1996; Pontzen & Governato 2012).

At high redshifts, where 21cm observations are not yet available, it is very difficult to measure the DM content of high-redshift galaxies from the kinematics in the outskirts of individual star-forming galaxies (SFGs) using nebular lines (e.g. Hα), because of the exponential decrease in signal-to-noise (S/N). But thanks to the pioneering work of Genzel et al. (2017), disk-halo decompositions have proven to be possible at $z \simeq 2$ using deep (> 30 hr) near-IR integral field spectroscopy (IFS) on a small sample of six massive star-forming galaxies (SFGs) (see also Genzel et al. 2020; Rizzo et al. 2021).

Here, we perform a disk-halo decomposition in *individual* low-mass SFGs at intermediate redshifts ($0.6 < z < 1.1$) using the deepest (140hr) Multi-Unit Spectroscopic Explorer (MUSE Bacon et al. 2010) data obtained on the *Hubble* Ultra Deep Field (HUDF Bacon et al. 2021) and 3D algorithms such as GalPaK^{3D} (Bouché et al. 2015). Tthanks to the combination of 3D modeling approach and these extremely deep IFU data, rotation curves can be constrained up to 3 R_e in individual galaxies.

2 Data and Methodology

2.1 Sample

From the recent MUSE eXtremely Deep Field (MXDF) region of the HUDF (Bacon et al. 2021) We selected 9 [O II] emitters with the highest S/N per spaxel in [O II], with pixel S/N reaching $S/N_{pix} \sim 100$ in the central spaxel. These galaxies have redshifts ranging from 0.6 to 1.1, and have stellar masses from $M_\star = 10^{8.9}$ M$_\odot$ to $M_\star = 10^{10.3}$ M$_\odot$ with SFRs from 1 to 5 M$_\odot$ yr^{-1}. The stellar masses and SFR were determined from spectral energy distribution (SED) fits with the Magphys (da Cunha et al. 2015) software on the HST photometry.

2.2 Method

In order to measure individual RCs in the outskirts of individual SFGs, at radii up to 10-15 kpc (2-3 Re) where the S/N per spaxel falls below unity, we use the GalPaK^{3D} algorithm (Bouché et al. 2015) which compares 3D parametric models directly to the 3D data, taking into account the instrumental resolution and PSF*. Note this 3D algorithm GalPaK^{3D} allows to fit the kinematics and morphological parameters *simultaneously* and thus no prior information is required on the inclination †. The agreement between HST-based and MUSE-based inclinations is typically better than 7°(rms) for galaxies with $25 < i < 80$ as demonstrated in Contini et al. (2016) and with mock data-cubes (Bouché et al. 2021) derived from the Illustris "NewGeneration 50 Mpc" (TNG50) simulations.

For the morphology, the model assumes a Sérsic (1963) surface brightness profile $\Sigma(r)$, with Sérsic index n. The disk model is inclined to any given inclination i and orientation or positional angle (P.A). The thickness profile is taken to be Gaussian whose scale height h_z is $0.15 \times R_e$. For [O II] emitters, as in this analysis, we add a global [O II] doublet ratio r_{O2}.

For the kinematics, the velocity dispersion profile $\sigma_t(r)$ consists of the combination of a thick disk σ_{thick}, defined from the identity $\sigma_{thick}(r)/v(r) = h_z/r$ (Genzel et al. 2006; Cresci et al. 2009) where h_z is the disk thickness (taken to be $0.15 \times R_e$) and a dispersion floor, σ_0, added in quadrature (similar to σ_0 in Genzel et al. 2006, 2008).

We perform a disk-halo decomposition of the rotation curve $v(r)$ into the following components

$$v_c^2(r) = v_{dm}^2(r) + v_d^2(r) + v_g^2(r), \tag{2.1}$$

where v_{dm} is the DM component, v_d the disk component (stellar and molecular) and an atomic a gas v_g component. The mass profile in molecular gas and star are inherently degenerate without direct CO measurements, but given that the molecular gas fractions are typically 30-50% (e.g. Tacconi et al. 2018; Freundlich et al. 2019), this amounts to a systematic uncertainty of 0.1-0.15 dex on the disk component. The disk component v_d is modelled as a Freeman (1970) disk suitable for exponential mass profiles and most of our galaxies have stellar Sérsic indices $n_\star$ close to $n_\star \simeq 1$.

*See `http://galpak3d.univ-lyon1.fr`.

†The traditional $i - V_{max}$ degeneracy is broken using the morphological information, specifically the axis b/a ratio.

The DM component $v_{\rm dm}(r)$ is modelled as a Hernquist-Zhao profile following Di Cintio et al. (2014, hereafter DC14):

$$\rho(r;\rho_s,r_s,\alpha,\beta,\gamma)=\frac{\rho_s}{\left(\frac{r}{r_s}\right)^{\gamma}\left(1+\left(\frac{r}{r_s}\right)^{\alpha}\right)^{(\beta-\gamma)/\alpha}} \tag{2.2}$$

where r_s is the scale radius, ρ_s the scale density, and α,β,γ are the shape parameters, with β corresponding to the outer slope, γ the inner slope and α the transition sharpness. In simulations with supernova feedback (e.g. DC14, Tollet et al. 2016; Lazar et al. 2020), the shape parameters α,β,γ in Eq. 2.2 are a direct function of the disk-to-halo mass ratio $\log X\equiv\log(M_\star/M_{\rm vir})$. Here, we used the $\alpha(X),\beta(X),\gamma(X)$ parametrisation with $\log M_\star/M_{\rm vir}$ from DC14 (their Eq.3), and this DM profile $v_{\rm dm}(r)$ has three free parameters, namely $\log X, V_{\rm vir}$ and the concentration c_{-2} defined as $c_{{\rm vir},-2}\equiv R_{\rm vir}/r_{-2}$, where $R_{\rm vir}$ is the halo virial radius.

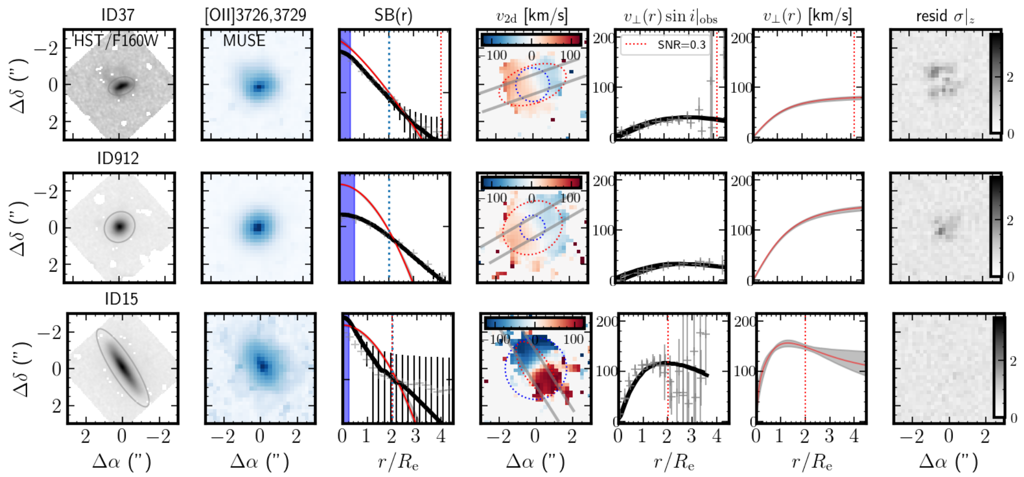

Fig. 1. Examples of 3D morpho-kinematics modelling. Each panel show the stellar continuum from *HST*/F160W, the [O II] flux map from MUSE, the [O II] surface brightness profile (SB(r)), the observed projected velocity field ($v_{2\rm d}$), the observed 1d velocity profile $v_\perp \sin i$, the intrinsic (i.e. deprojected, corrected for beam smearing) modeled rotation curve ($v_\perp$) using the model of (Persic et al. 1996).

3 Results

We find that the 3D approach allows to constrain RCs to $3R_{\rm e}$ in individual SFGs revealing a diversity in shapes with mostly rising and some having declining outer profiles (Fig. 1). The disk stellar mass $M_\star$ from the [O II] rotation curves is consistent with the SED-derived $M_\star$, except for two SFGs whose kinematics are strongly perturbed by a nearby companion (< 2"). With this sample of SFGs which have stellar masses (from $10^{8.5}{\rm M}_\odot$ to $10^{10.5}{\rm M}_\odot$), the DM fractions $f_{\rm DM}(<R_{\rm e})$ are high (60-90%) (Fig. 2a). These DM fractions complement the low fractions of the sample of Genzel et al. (2020), and globally, the $f_{\rm DM}(<R_{\rm e})-\Sigma_\star$ relation is similar to the $z=0$ relation (e.g. Courteau & Dutton 2015), and follows from the TFR. We wind that the DM concentrations are consistent with the $c_{\rm vir}-M_{\rm vir}$ scaling relation predicted by DM only simulations. Finally, DM cores are present in galaxies with high SFRs (Fig. 2b), supporting the scenario of SN feedback-induced core formation.

This study is based on observations collected at the European Southern Observatory under ESO programme 1101.A-0127. This work has been carried out in part thanks to the support of the ANR 3DGasFlows (ANR-17-CE31-0017), the OCEVU Labex (ANR-11-LABX-0060), the Programme National Cosmology et Galaxies (PNCG) of CNRS/INSU with INP and IN2P3, co-funded by CEA and CNES. R.B. acknowledges support from the ERC advanced grant 339659-MUSICOS.

References

Allaert, F., Gentile, G., & Baes, M. 2017, A&A, 605, A55

Bacon, R., Accardo, M., Adjali, L., et al. 2010, in Society of Photo-Optical Instrumentation Engineers (SPIE) Conference Series, Vol. 7735, Society of Photo-Optical Instrumentation Engineers (SPIE) Conference Series, 8

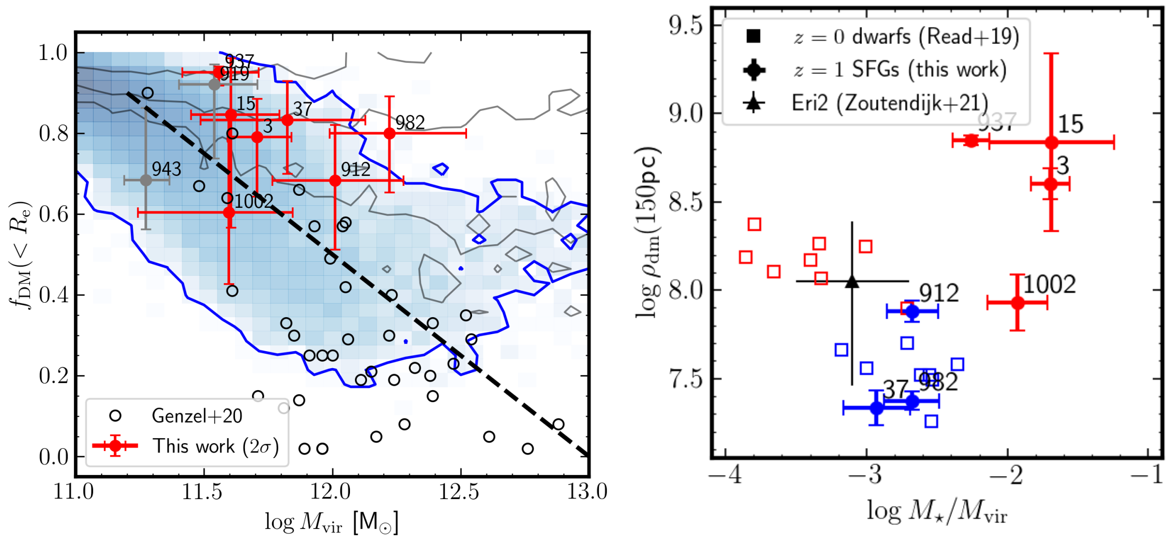

Fig. 2. Left: The DM fractions within the half-light radius $R_{\rm e}$, $f_{\rm DM}(< R_{\rm e})$, as a function of halo mass, $M_{\rm vir}$. The dashed line represent the downwards trend of Genzel et al. (2020). **Right:** The DM density at 150pc as a function of $\log M_\star/M_{\rm vir}$. The blue (red) solid circles with error bars (2σ) represent our SFGs with high (low) $\Sigma_{\rm SFR}$, respectively. The blue (red) open squares represent the $z \approx 0$ dwarfs from Read et al. (2019) whose SFR was truncated less (more) than 6 Gyrs ago.

Bacon, R., Mary, D., Garel, T., et al. 2021, A&A, 647, A107
Bouché, N. F., Carfantan, H., Schroetter, I., Michel-Dansac, L., & Contini, T. 2015, AJ, 150, 92
Bouché, N. F., Genel, S., Pellissier, A., et al. 2021, A&A, in press (arXiv/2101.12250)
Bullock, J. S. & Boylan-Kolchin, M. 2017, ARA&A, 55, 343
Contini, T., Epinat, B., Bouché, N., et al. 2016, A&A, 591, A49
Courteau, S. & Dutton, A. A. 2015, ApJ, 801, L20
Cresci, G., Hicks, E. K. S., Genzel, R., et al. 2009, ApJ, 697, 115
da Cunha, E., Walter, F., Smail, I. R., et al. 2015, ApJ, 806, 110
de Blok, W. J. G. & McGaugh, S. S. 1997, MNRAS, 290, 533
de Blok, W. J. G., McGaugh, S. S., & Rubin, V. C. 2001, AJ, 122, 2396
Di Cintio, A., Brook, C. B., Dutton, A. a., et al. 2014, MNRAS, 441, 2986
Freeman, K. C. 1970, ApJ, 160, 811
Freundlich, J., Combes, F., Tacconi, L. J., et al. 2019, A&A, 622, A105
Genzel, R., Burkert, A., Bouché, N., et al. 2008, ApJ, 687, 59
Genzel, R., Price, S. H., Übler, H., et al. 2020, ApJ, 902, 98
Genzel, R., Schreiber, N. M. F., Übler, H., et al. 2017, Nature, 543, 397
Genzel, R., Tacconi, L. J., Eisenhauer, F., et al. 2006, Nature, 442, 786
Katz, H., Lelli, F., Mcgaugh, S. S., et al. 2017, MNRAS, 466, 1648
Lazar, A., Bullock, J. S., Boylan-Kolchin, M., et al. 2020, MNRAS, 497, 2393
Li, P., Lelli, F., McGaugh, S., & Schombert, J. 2020, ApJS, 247, 31
Navarro, J. F., Eke, V. R., & Frenk, C. S. 1996, MNRAS, 283, L72
Navarro, J. F., Frenk, C. S., & White, S. D. M. 1997, ApJ, 490, 493
Persic, M., Salucci, P., & Stel, F. 1996, MNRAS, 281, 27
Pontzen, A. & Governato, F. 2012, MNRAS, 421, 3464
Read, J. I., Walker, M. G., & Steger, P. 2019, MNRAS, 484, 1401
Rizzo, F., Vegetti, S., Fraternali, F., Stacey, H., & Powell, D. 2021, MNRAS
Rubin, V. C. & Ford, W. Kent, J. 1970, ApJ, 159, 379
Sérsic, J. L. 1963, BAAA, 6, 41
Tacconi, L. J., Genzel, R., Saintonge, A., et al. 2018, ApJ, 853, 179
Tollet, E., Macci, A. V., Dutton, A. A., et al. 2016, MNRAS, 456, 3542

SF2A 2021
A. Siebert, K. Baillié, E. Lagadec, N. Lagarde, J. Malzac, J.-B. Marquette, M. N'Diaye, J. Richard, O. Venot (eds)

CHARACTERIZING THE BULK AND TURBULENT GAS MOTIONS IN GALAXY CLUSTERS

S. Dupourqué[1], E. Pointecouteau[1], N. Clerc[1] and D. Eckert[2]

Abstract. The most massive halos of matter in the Universe grow via accretion and merger events throughout cosmic times. These violent processes generate shocks at many scales and induce large-scale bulk and turbulent motions. These inject kinetic energy at large scales, which is transported to the viscous dissipation scales, contributing to the overall heating and virialisation of the halo, and acting as a source of non-thermal pressure in the intra-cluster medium. Characterizing the physical properties of these gas motions will help us to better understand the assembly of massive halos, hence the formation and the evolution of these large-scale structures. We base this characterization on the study of the X-ray and Sunyaev-Zel'dovich effect brightness fluctuations. Our work relies on three complementary samples covering a wide range of redshifts, masses and dynamical states of clusters. We present the results of our X-ray analysis for the low redshift sample, X-COP, and a subsample of higher redshift clusters. We investigate the derived properties according to the dynamical state of our clusters, and the possibility of a self-similar behaviour based on the reconstructed gas motions power-spectra.

Keywords: X-rays: galaxies: clusters, galaxies: clusters: intracluster medium, turbulence

1 Introduction

The baryonic content of galaxy clusters is largely dominated by the hot gas that constitutes the intracluster medium (ICM). The processes governing the growth, as well as the physics of the ICM, introduces perturbations at various scales within the gas. The resulting turbulent motions transport kinetic energy, which cascades to the dissipation scale and contributes to the virialisation of the halo through non-thermal heating of the ICM (e.g Vazza et al. 2018).

Direct measurements of these turbulent processes can be achieved using spatially resolved X-ray spectroscopy (Böhringer & Werner 2010; The Hitomi Collaboration 2016), and will be fully enabled in the future with the upcoming XRISM and Athena missions (XRISM Science Team 2020; Nandra et al. 2013). These turbulent processes are expected to induce fluctuations in the thermodynamic properties of the ICM, that should be detectable in the related observables (Simionescu et al. 2019). For instance, the X-ray surface brightness and Sunyaev-Zel'dovich distortion scale respectively with the squared density and pressure, integrated along the line of sight. Studies on the nearby Coma and Perseus clusters (Churazov et al. 2012; Zhuravleva et al. 2015; Khatri & Gaspari 2016) have demonstrated the feasibility of this approach in both X-ray and SZ, and was already extended to a small sample ($N = 10$) to derive statistical trends (Zhuravleva et al. 2018).

With this work, we aim at characterizing the X-ray surface brightness and SZ distortion fluctuations for a large cluster sample ($N > 150$) spanning a large range of redshifts, masses and dynamical states. This should allow us to better constrain the properties and impact of turbulence in the ICM, considering the assembly of massive halos.

2 Data

We rely on three cluster samples, built over the Planck (The Planck Collaboration 2014, 2016) and the Atacama Cosmology Telescope (ACT, Mallaby-Kay et al. 2021) cluster catalogues:

[1] IRAP, Université de Toulouse, CNRS, UPS, CNES, Toulouse, France
[2] University of Geneva

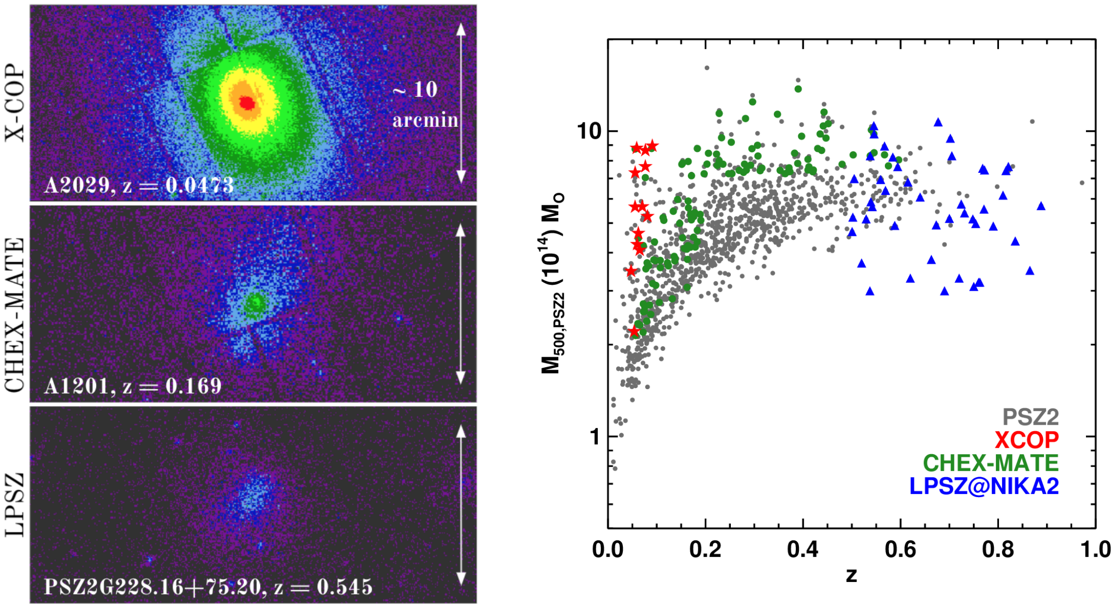

Fig. 1. Left: XMM-Newton image (0.7-1.2 keV band) of A2029, A1201 and PSZ2G228.16+75.20 which belong to X-COP, CHEX-MATE and LPSZ@NIKA2. **Right:** Distribution of the X-COP, CHEX-MATE and LPSZ@NIKA2 samples alongside the PSZ2 catalogue, in the mass-redshift plan.

- The XMM Cluster Outskirts Project (X-COP, Eckert et al. 2017), a SZ selected sample based on the Planck catalogue, designed to study the outer regions of 12 nearby ($z < 0.1$) galaxy clusters.
- The Cluster HEritage project with XMM-Newton (CHEX-MATE, The CHEX-MATE Collaboration 2021) : a SZ selected sample, based on the Planck catalogue, of 118 clusters designed to obtain an accurate vision of the statistical properties of the cluster population at low to intermediate redshifts ($0.1 < z < 0.5$).
- The NIKA2 SZ Large Program (LPSZ@NIKA2, Mayet et al. 2020), a SZ-selected sample from both Planck and ACT catalogues, including 50 intermediate to high redshift clusters ($0.5 < z < 0.9$) designed to perform evolution studies and cosmological analysis.

In this paper, we present our preliminary results on the full X-COP sample, and pilot sub-samples of 8 and 4 clusters for CHEX-MATE and LPSZ@NIKA2, respectively.

3 Method

3.1 *Mean profile determination*

To determine the mean X-ray surface brightness map, an analytical elliptical model is fitted on the photon count image. We first estimate the centroid of emission and the ellipticity using a principal component analysis in a region of $0.5R_{500}$, centred on the emission peak. Then we extract the total photon count in concentric elliptical annuli to obtain a radial surface brightness profile with a 10" binning. The parameter distributions of a β-Model (Cavaliere & Fusco-Femiano 1976) fitting this profile is determined using Bayesian inference, assuming that the number of counts in each annulus follows a Poisson distribution.

3.2 *Fluctuation map and 2D power spectrum*

The surface brightness image I is directly dependent on the 3D density profile n_e, which can be decomposed into a mean component n_0 and relative fluctuations δ:

$$I(x,y) = \int_{-\infty}^{+\infty} \Lambda(T) n_e^2(\vec{r})\, dz = \int_{-\infty}^{+\infty} \Lambda(T) n_0^2(\vec{r})(1+\delta(\vec{r}))^2\, dz \tag{3.1}$$

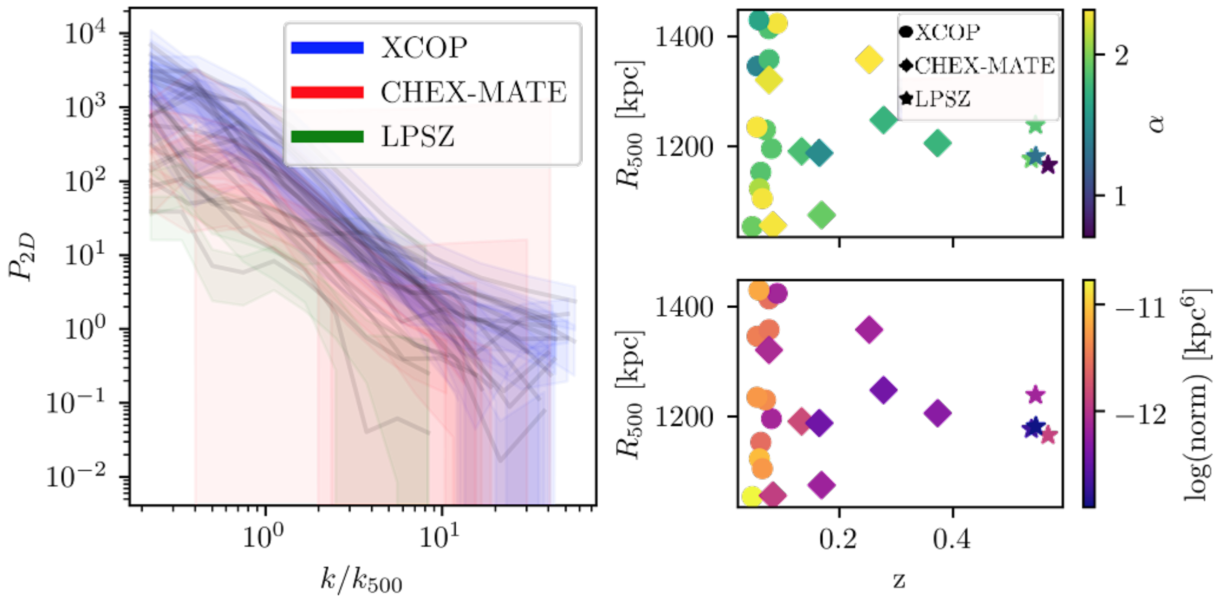

Fig. 2. Left: 2D power spectra, P_{2D} [kpc^4], for the set of clusters we are using (See. Sec. 2) plotted as a function of the normalized scale, k/k_{500}. The shaded envelopes correspond to the 1σ dispersion about each individual P_{2D}. **Right:** 3D power spectrum best-fit slope α (11/3 corresponds to a Kolmogorov cascade) and normalization in the R_{500}-z plane.

By linearizing for δ and dividing by the previously determined mean count image I_0, we obtain the map of surface brightness fluctuations, J (see Churazov et al. 2012):

$$J(x,y) = \frac{I(x,y)}{I_0(x,y)} = 1 + 2\int_{-\infty}^{+\infty} \eta(\vec{r})\delta(\vec{r})\,dz; \quad \eta = \frac{n_0^2(\vec{r})}{\int_{-\infty}^{+\infty} n_0^2(\vec{r})dz} \tag{3.2}$$

The associated power spectrum, latter referred to as P_{2D}, is defined as the squared complex modulus of $\mathcal{F}_{2D}\{J\}$, the 2D Fourier transform of the fluctuation map :

$$P_{2D}(k) = |\mathcal{F}_{2D}\{J\}(k)|^2 = \left|\int J(\vec{\rho})e^{-2i\pi\vec{k_\rho}\cdot\vec{\rho}}d^2\vec{\rho}\right|^2 \tag{3.3}$$

For each cluster, the power spectrum, P_{2D}, is computed following the method by Arévalo et al. (2012). It uses Mexican hat filtering at various scales and handles properly masked data (e.g., source exclusions, gaps, and borders effects). The uncertainties due to the shot noise was estimated by computing P_{2D} for 100 Poisson realizations of the image I_0. The power spectrum is also affected by the uncertainty related to the sample variance, which we consider in the following way : assuming that the velocity field is Gaussian, and as in this context, density fluctuations field are proportional to velocity fluctuations (Zhuravleva et al. 2014; Gaspari et al. 2014), the standard deviation of the 3D power spectrum, P_{3D}, is proportional to the power spectrum itself. As the projection operations from P_{3D} to P_{2D} are linear, we assume that the variance of P_{2D} follows the same law. We therefore added to the P_{2D} variance a term of $(P_{2D}/3)^2$.

3.3 Projection and fitting of the 3D power spectrum

To recover the properties of the inherent 3D density fluctuations power spectrum, we first express the previously obtained 2D power spectrum as a function of the P_{3D}. After introducing the power spectrum of the profile P_η, of the PSF $P_{\rm PSF}$, the power spectrum of the Poisson noise $P_{\rm Poisson}$ and by designating the 2D convolution with the $**$ operator, we can show that the observed P_{2D} is linked to the P_{3D} with the following dependence :

$$P_{2D}(k_x, k_y) = P_{\rm Poisson} + 4P_{\rm PSF}\int (P_\eta ** P_{3D})(x,y,z)\,dz \tag{3.4}$$

We use a simple power law representation, $P_{3D} = 10^A \left(k/k_{\rm ref}\right)^{-\alpha}$, where the normalization, 10^A [kpc^6], and slope, α, are free parameters. The pivot is set to $k_{\rm ref} = 10^{-3}{\rm kpc}^{-1}$. This model is projected using Eq. (3.4) and fitted against the measured P_{2D} for each individual cluster.

4 Preliminary results

The 2D power spectra, computed for our pilot sample, are shown in the left of Fig. 2, re-scaled to $k_{500} = 1/R_{500}$, and exhibit a strong power-law behaviour in this test sample. The spectra do not seem to vary significantly from one sample to another. Thus, we do not see any trend that could correlate with the redshift (though the statistics of our intermediate and higher redshift sub-samples are very limited). The best values of our fit of P_{3D} are displayed in the $R_{500} - z$ plane in Fig. 2, right panel. From this preliminary analysis, we do not see any particular trend of the normalization nor slope of P_{3D} with the characteristic size or redshift of our clusters. Nevertheless, as the error propagation has not yet been done on these quantities, we cannot draw any solid conclusion about these results.

5 Perspectives

We presented here a preliminary analysis of the power spectrum of brightness fluctuations for a sample of galaxy clusters. We will test models with higher levels of complexity for P_{3D} by including, for instance, the injection scale starting the underlying turbulent cascade. We plan to investigate the correlation to morphological indicators, reflecting the dynamical state of each of our clusters. We will pursue our study and extend it to the whole CHEX-MATE and LPSZ@NIKA2 samples. We plan to extend this work to the fluctuations of the SZ signal (directly related to the fluctuations of the ICM pressure), making use of the Planck, ACT and NIKA-2 data.

References

Arévalo, P., Churazov, E., Zhuravleva, I., Hernández-Monteagudo, C., & Revnivtsev, M. 2012, Monthly Notices of the Royal Astronomical Society, 426, 1793, publisher: Oxford Academic

Böhringer, H. & Werner, N. 2010, The Astronomy and Astrophysics Review, 18, 127

Cavaliere, A. & Fusco-Femiano, R. 1976, Astronomy and Astrophysics, 500, 95

Churazov, E., Vikhlinin, A., Zhuravleva, I., et al. 2012, Monthly Notices of the Royal Astronomical Society, 421, 1123

Eckert, D., Ettori, S., Pointecouteau, E., et al. 2017, Astronomische Nachrichten, 338, 293, arXiv: 1611.05051

Gaspari, M., Churazov, E., Nagai, D., Lau, E. T., & Zhuravleva, I. 2014, Astronomy and Astrophysics, 569, A67

Khatri, R. & Gaspari, M. 2016, Monthly Notices of the Royal Astronomical Society, 463, 655, arXiv: 1604.03106

Mallaby-Kay, M., Atkins, Z., Aiola, S., et al. 2021, arXiv:2103.03154 [astro-ph], arXiv: 2103.03154

Mayet, F., Adam, R., Ade, P., et al. 2020, EPJ Web of Conferences, 228, 00017, arXiv: 1911.03145

Nandra, K., Barret, D., Barcons, X., et al. 2013, arXiv:1306.2307 [astro-ph], arXiv: 1306.2307

Simionescu, A., ZuHone, J., Zhuravleva, I., et al. 2019, Space Science Reviews, 215, 24

The CHEX-MATE Collaboration. 2021, arXiv:2010.11972 [astro-ph], arXiv: 2010.11972

The Hitomi Collaboration. 2016, Nature, 535, 117

The Planck Collaboration. 2014, Astronomy & Astrophysics, 571, A29, publisher: EDP Sciences

The Planck Collaboration. 2016, Astronomy & Astrophysics, 594, A13, publisher: EDP Sciences

Vazza, F., Angelinelli, M., Jones, T. W., et al. 2018, Monthly Notices of the Royal Astronomical Society: Letters, 481, L120

XRISM Science Team. 2020, arXiv:2003.04962 [astro-ph], arXiv: 2003.04962

Zhuravleva, I., Allen, S. W., Mantz, A., & Werner, N. 2018, The Astrophysical Journal, 865, 53, publisher: IOP Publishing

Zhuravleva, I., Churazov, E., Arevalo, P., et al. 2015, Monthly Notices of the Royal Astronomical Society, 450, 4184, arXiv: 1501.07271

Zhuravleva, I., Churazov, E. M., Schekochihin, A. A., et al. 2014, The Astrophysical Journal, 788, L13, publisher: IOP Publishing

SF2A 2021
A. Siebert, K. Baillié, E. Lagadec, N. Lagarde, J. Malzac, J.-B. Marquette, M. N'Diaye, J. Richard, O. Venot (eds)

JELLYFISH GALAXIES IN MACS J0717.5+3745 AND THEIR LINK TO THE COSMIC WEB

F. Durret[1], S. Chiche[1], C. Lobo[2,3] and M. Jauzac[4,5,6,7]

Abstract. Galaxies in clusters undergo several phenomena, such as ram pressure stripping and tidal interactions, that can trigger or quench their star formation, and, in some cases, lead to galaxies acquiring unusual shapes and long tails, such as jellyfish galaxies. We searched for such objects in MACS J0717.5+3745, for which our large spatial coverage and abundant sampling of spectroscopic redshifts allowed us to pursue a detailed analysis in the cluster and its extended filament. We found 81 jellyfish galaxy candidates in a large region around MACS0717, that tend to avoid the densest regions of the cluster. An eight-magnitude optical and infrared catalogue covering the entire region allowed us to compute the best stellar population fits with LePhare through the GAZPAR interface for 79 jellyfish galaxies and for a control sample of 122 non-jellyfish galaxies. We find stellar masses in the range $10^9 - 10^{11}$ M$_\odot$, rather young stellar ages (more than half have an age smaller than 1.5×10^9 yrs), star formation rates (SFRs) in the $10^{-1} - 60$ M$_\odot$ yr^{-1} range and rather high specific star formation rates (sSFRs), with more than half of the sample having values larger than 10^{-9} yr^{-1}. The mean sSFR of the 79 jellyfish galaxy candidates is 3.2 times larger than that of star-forming non-jellyfish galaxies. Based on several arguments, the jellyfish candidates identified in MACS0717 seem to have fallen rather recently into the cluster.

Keywords: galaxy clusters, jellyfish galaxies

1 Introduction

Galaxies in clusters may be undergoing several phenomena, among which ram pressure stripping due to their interaction with the hot intracluster gas. Their gas may then be compressed and undergo intense star formation, in the galaxy itself as well as in filaments that can be stripped from them. They thus can acquire the shape of a jellyfish and their study can give indications on the cluster properties.

In our search for extensions and filaments around clusters of the DAFT/FADA and CLASH surveys, we have selected red sequence galaxies and drawn density maps (Durret et al. 2016). For the cluster MACS J0717.5+3745 (hereafter MACS0717) at redshift z=0.5458, we detected a very large extension covering 6.0×1.8 Mpc^2 including the cluster, and continued by a 3.2×2.1 Mpc^2 filament North-South extension. These extensions are in rough agreement with those found with a weak lensing analysis by Jauzac et al. (2012) and Martinet et al. (2016).

We exploit here a large set of spectroscopic and photometric data to search for jellyfish galaxies in MACS0717 and its extended filament, and to characterise their properties.

[1] Sorbonne Université, CNRS, UMR 7095, Institut d'Astrophysique de Paris, 98bis Bd Arago, 75014, Paris, France
[2] Departamento de Física e Astronomia, Faculdade de Ciências, Universidade do Porto, Rua do Campo Alegre 687, PT4169-007 Porto, Portugal
[3] Instituto de Astrofísica e Ciências do Espaço, Universidade do Porto, CAUP, Rua das Estrelas, PT4150-762 Porto, Portugal
[4] Centre for Extragalactic Astronomy, Durham University, South Road, Durham DH1 3LE, UK
[5] Institute for Computational Cosmology, Durham University, South Road, Durham DH1 3LE, UK
[6] Astrophysics Research Centre, University of KwaZulu-Natal, Westville Campus, Durban 4041, South Africa
[7] School of Mathematics, Statistics & Computer Science, University of KwaZulu-Natal, Westville Campus, Durban 4041, South Africa

2 Spatial distribution of jellyfish galaxies in MACS0717

2.1 The data

Our study is based on a large mosaic covering the entire cluster and its extended filament in the F606W and F814W filters. We also have a catalogue of over 600 spectroscopic redshifts, and a ground-based 8 magnitude catalogue in the optical and infrared that allows a stellar population analysis.

2.2 Selection of jellyfish candidates

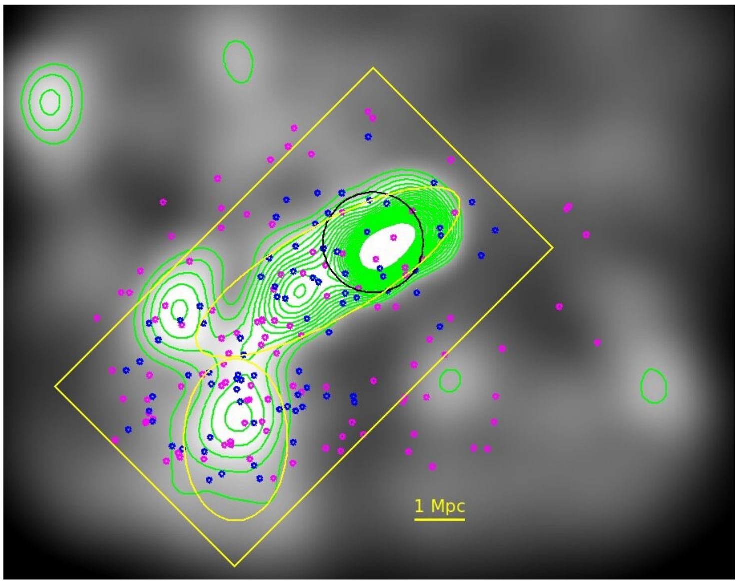

Fig. 1. Density map of red sequence galaxies from Durret et al. (2016), with green contours starting at 3σ above the background and spaced by 1σ. The black circle has a 1 Mpc radius around the cluster centre, the two yellow ellipses indicate the maximum extensions of the cluster (6.0×1.8 Mpc^2) and its filament (3.2×2.1 Mpc^2). The blue and pink points respectively show the positions of the jellyfish and non-jellyfish galaxies considered in the stellar population analysis.

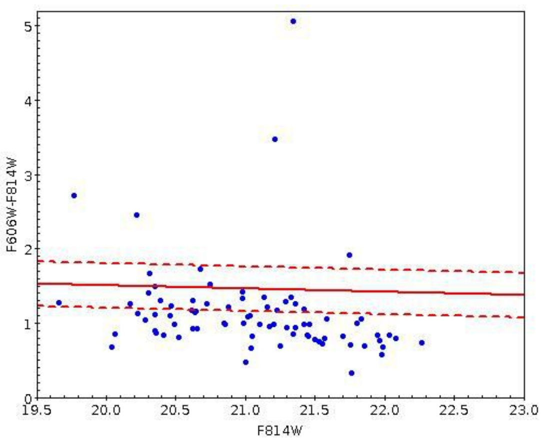

Fig. 2. F606W-F814W vs. F814W colour-magnitude diagram. The red line is the best fit to the red sequence, and the red dashed lines indicate the interval of ± 0.3 on either side of this line, in which red sequence galaxies were selected to build the density map shown in Fig. 1. The 81 jellyfish candidates are shown as blue points.

We looked at all the galaxies with a redshift within $\pm 4\sigma_v$ of the cluster redshift (σ_v being the cluster velocity dispersion). We eliminated galaxies with obvious gravitational interactions with a neighbour (within 50 kpc) and two of us selected jellyfish candidates by eye, classifying them between J=1 (least probable) and J=5 (most probable), following the classification proposed by Ebeling et al. (2014). Our catalogue of jellyfish candidates contains 81 galaxies. Their spatial distribution is shown in Fig. 1. We can note that the jellyfish tend to avoid the cluster centre and are spread over the entire region. In the colour-magnitude diagram that was used to select the red sequence galaxies used to build the density map, a large majority of the jellyfish galaxies are below the red sequence, confirming that they are mainly blue galaxies, as expected (see Fig.2).

3 Stellar populations

For 79 of the 81 jellyfish galaxies of MACS0717 we were able to obtain a stellar population fit with the LePhare software through the GAZPAR interface. A comparable fit was obtained for 122 non-jellyfish galaxies in the same redshift range as a control sample.

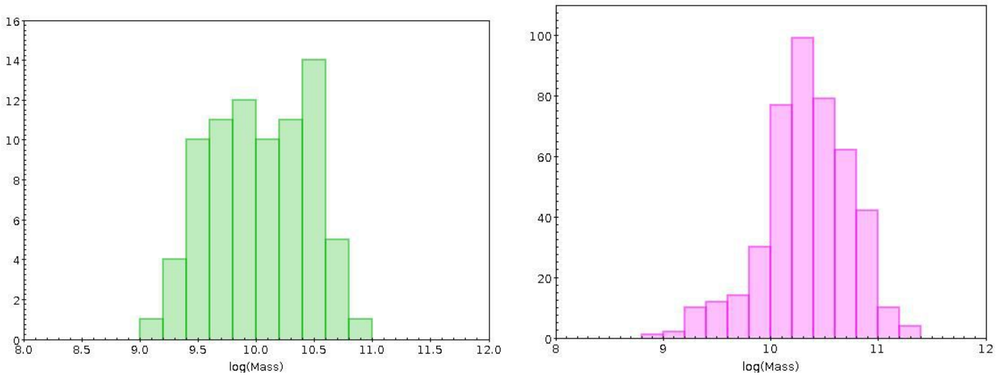

Fig. 3. Histograms of the galaxy stellar masses in jellyfish (left) and non-jellyfish (right) galaxies.

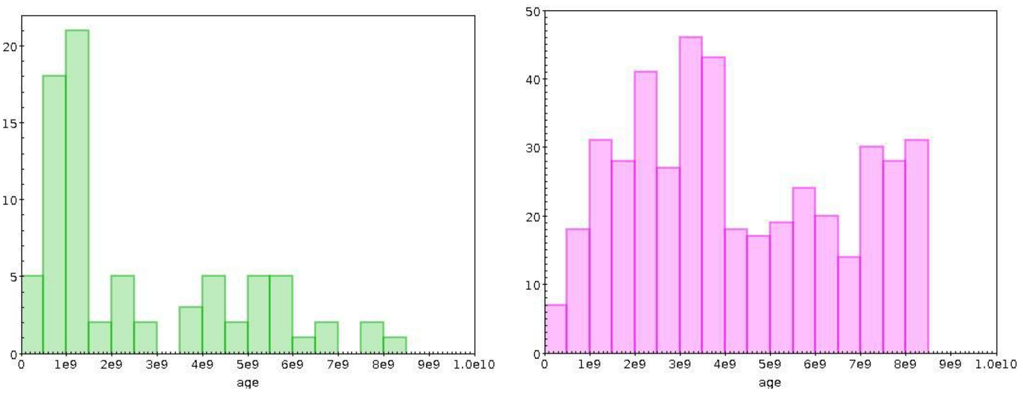

Fig. 4. Histograms of the galaxy stellar ages in jellyfish (left) and non-jellyfish (right) galaxies.

The histograms of the stellar masses, ages, star formation rates and specific star formation rates are shown in Figs. 3, 4, 5, and 6 respectively.

4 Main results and conclusions

Out of more than 600 galaxies with spectroscopic redshifts, we have found 81 jellyfish candidates.

The analysis of the stellar populations of 79 of these show that the best fit spectrum of all but two shows the Hα line, and more than half are fit with a spectrum that also includes the [OII]3727, Hβ, and [OIII]4959,5007 emission lines, in agreement with the general picture of jellyfish undergoing star formation. This is confirmed by the main quantities derived from the stellar population fits: the jellyfish galaxies have stellar masses in the

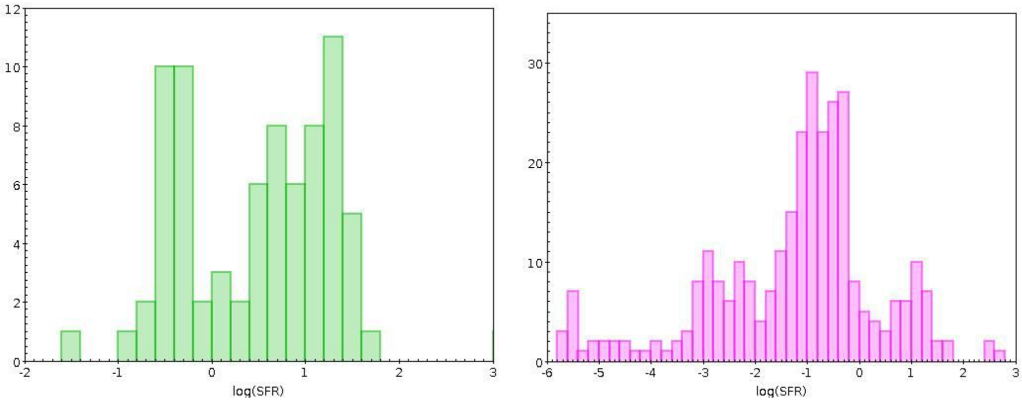

Fig. 5. Histograms of the galaxy star formation rates in jellyfish (left) and non-jellyfish (right) galaxies.

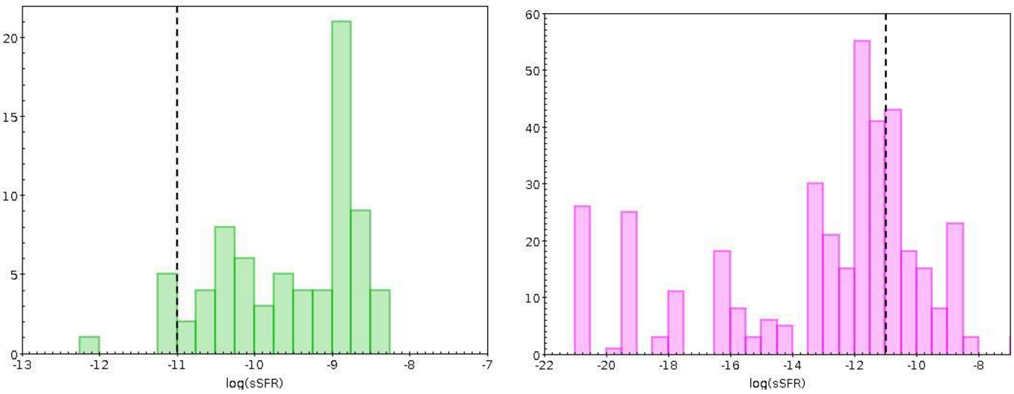

Fig. 6. Histograms of the galaxy specific star formation rates in jellyfish (left) and non-jellyfish (right) galaxies.

range $10^9 - 10^{11}$ $M_\odot$, rather young stellar ages (more than half have an age smaller than 1.5×10^9 yrs), star formation rates (SFRs) in the $10^{-1} - 60$ $M_\odot$ yr^{-1} range and quite high specific star formation rates (sSFRs), with more than half of the sample having values larger than 10^{-9} yr^{-1}. The mean sSFR of the 79 jellyfish galaxy candidates is 3.2 times larger than that of non-jellyfish galaxies.

We are now in the process of analysing the dynamical properties of the jellyfish galaxies in MACS0717 compared to the overall cluster dynamics, based on a plot as that of Mahajan et al. (2011), Figure 10. The result of this analysis, coupled with a comparable study for another cluster for which we have similar data, will be described in a forthcoming paper (Durret et al., in preparation).

A full description of the present work on MACS0717, together with the detection of 97 jellyfish candidates in 22 clusters covering the redshift range $0.2 < z < 0.9$ and the analysis of the stellar populations of 31 of them can be found in Durret et al. (2021).

F.D. acknowledges continuous support from CNES.

References

Durret, F., Chiche, S., Lobo, C., & Jauzac, M. 2021, A&A, 648, A63
Durret, F., Márquez, I., Acebrón, A., et al. 2016, A&A, 588, A69
Ebeling, H., Stephenson, L. N., & Edge, A. C. 2014, ApJ, 781, L40
Jauzac, M., Jullo, E., Kneib, J.-P., et al. 2012, MNRAS, 426, 3369
Mahajan, S., Mamon, G. A., & Raychaudhury, S. 2011, MNRAS, 416, 2882
Martinet, N., Clowe, D., Durret, F., et al. 2016, A&A, 590, A69

SF2A 2021
A. Siebert, K. Baillié, E. Lagadec, N. Lagarde, J. Malzac, J.-B. Marquette, M. N'Diaye, J. Richard, O. Venot (eds)

MODELS FOR DARK MATTER CORE FORMATION INDUCED BY FEEDBACK

J. Freundlich[1]

Abstract. Cold dark matter numerical simulations predict steep, 'cuspy' density profiles for dark matter haloes, while observations favour shallower 'cores'. The introduction of baryonic physics in simulations alleviates this discrepancy, notably as feedback-driven outflow episodes contribute to expanding the dark matter distribution. We present different theoretical models describing core formation in dark matter haloes. In the first one, small stochastic density fluctuations induced by stellar feedback in the interstellar medium dynamically heat up the halo, leading to the formation of a core. In the second one, sudden bulk outflows reorganise the halo mass distribution while it relaxes to a new equilibrium. In the third one, the combination of dynamical friction from incoming satellites with outflows speeds up core formation and enables the presence of cores early in the history of the universe.

Keywords: galaxies: evolution, galaxies: haloes, dark matter

1 Introduction

Within the cold dark matter (CDM) model of structure formation, 85% of the total matter content in the universe is assumed to be made of dark matter (DM), forming relatively diffuse haloes along the cosmic web. The remaining baryons, initially in the form of gas, can condense at halo centers, cool down, form stars, and lead to powerful *feedback* processes resulting from stellar evolution and active galactic nuclei (AGN). These feedback processes include stellar winds, radiation fields, supernova explosions, and AGN jets. They can heat up the surrounding gas and eject part of it.

The CDM model is extremely successful at describing the large scale structure of the universe, but it faces several challenges at galactic scales. In particular, CDM-only simulations predict steep, 'cuspy' central density profiles for DM haloes while observations favor 'cores' with a constant density towards the center (e.g., Oh et al. 2011). Within the CDM framework, the introduction of baryonic processes in simulations alleviates the tension by reproducing cored density profiles (e.g., Governato et al. 2012). However, hydrodynamical simulations do not necessarily isolate by themselves the physical mechanisms through which baryons affect the DM distribution. We propose here three different theoretical models describing core formation in DM haloes from first principles.

Baryons can affect DM through the gravitational potential in and around galaxies, where they locally dominate the mass budget. Baryons can lead to *adiabatic contraction* of the DM distribution when they accumulate towards the halo center and steepen its potential well (Blumenthal et al. 1986). Gas clumps or satellites can transfer part of their orbital energy to the DM background through *dynamical friction* (Chandrasekhar 1943) and thus dynamically heat the DM halo, which can contribute to core formation (El-Zant et al. 2001). Finally, *gas outflows* induced by the different feedback processes lead to mass and potential fluctuations that can also dynamically heat the DM distribution and form cores (Pontzen & Governato 2012).

2 Core formation from stochastic density fluctuations

Stellar feedback processes such as radiation, stellar winds and supernova explosions generate density fluctuations of variable size and amplitude in the different phases of the interstellar medium (e.g., Peters et al. 2017). Each of these fluctuations induces a small change in the gravitational potential, which can affect DM particles in the form of a force 'kick'. Each of these kicks is small, but their cumulative effect can induce the DM particles to slowly deviate from their initial trajectories, as in a diffusion process or two-body relaxation. As shown in El-Zant et al. (2016), this process can lead to DM core formation. It is illustrated in Fig. 1.

[1] Université de Strasbourg, CNRS UMR 7550, Observatoire astronomique de Strasbourg, 67000 Strasbourg, France

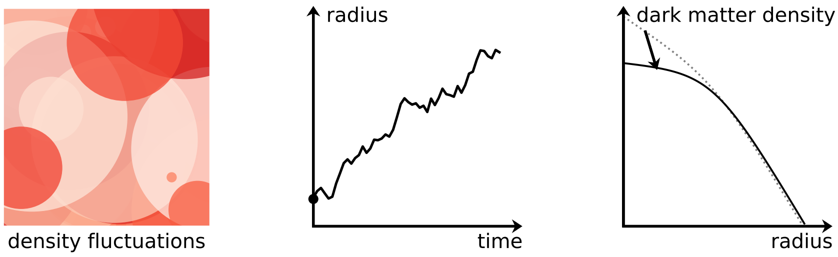

Fig. 1. Core formation from stochastic density fluctuations, as proposed in El-Zant et al. (2016): small density fluctuations of different size and amplitude resulting from feedback (left panel) induce 'kicks' to DM particles, slowly deviating them from their initial orbits as in a diffusion process (middle panel) and leading to DM core formation (right panel).

To describe this process, we assumed stochastic density fluctuations in a gaseous medium of mean density ρ_0 and Fourier-decomposed the density contrast $\delta(\vec{r}) = \rho(\vec{r})/\rho_0$ over a volume V,

$$\delta(\vec{r}) = \frac{V}{(2\pi)^3} \int \delta_{\vec{k}} e^{i\vec{k}.\vec{r}} d^3\vec{k}. \tag{2.1}$$

Each mode $\vec{k}$ induces a small force kick on the DM particles

$$\vec{F}_{\vec{k}} = 4\pi i \; G\rho_0 \; \vec{k} \; k^{-2} \; \delta_{\vec{k}}, \tag{2.2}$$

whose cumulative effect after a time T increases the velocity of the DM particles following

$$\langle \Delta v^2 \rangle = 2 \int_0^T (T-t) \, \langle F(0) F(t) \rangle \; dt, \tag{2.3}$$

from which we can derive an analytic expression for the relaxation time associated to the process (cf. El-Zant et al. 2016 and Freundlich et al. 2016 for more details, the latter providing a brief summary of the model).

This model and the resulting expression for the relaxation time were tested against collisionless simulations of a fiducial dwarf halo using the self-consistent field (SCF) method developed by Hernquist & Ostriker (1992). The potential fluctuations led to DM core formation within a timescale comparable to the relaxation time derived analytically (El-Zant et al. 2016). This model was also used to describe the effect of *fuzzy dark matter** halo fluctuations on collisionless stellar systems by Marsh & Niemeyer (2019) and El-Zant et al. (2020a,b).

3 Core formation from bulk outflows

Feedback episodes induced by stellar evolution and AGN can launch massive gas outflows (e.g., Förster Schreiber & Wuyts 2020). Suddenly removing part of the gravitational pull at the center of the halo leads to its expansion and can hence form a core. This is the basis for the DM core formation model presented in Freundlich et al. (2020a), hereafter referred to as *CuspCore* (cf. also Freundlich et al. 2019 for a brief summary and Dutton et al. 2016, Section 4, for a preliminary version of the model). It is illustrated in Fig. 2.

The *CuspCore* model assumes a two-stage process where (1) the gravitational potential first adjusts instantaneously to the sudden mass loss while the DM velocities remain frozen to their initial values and (2) the halo then relaxes to a new equilibrium with no dissipation and no energy exchange between shells enclosing a given DM mass. The energy of such a shell, initially at radius r_i, can be written as

$$E_i(r_i) = U(r_i; p_i) + K(r_i; p_i) \tag{3.1}$$

where $U(r; p_i)$ and $K(r; p_i)$ are parametric expressions for the potential and kinetic energies, K being set by Jeans equilibrium. Such expressions, depending on parameters p_i, are notably available for the 'Dekel-Zhao' profile introduced by Dekel et al. (2017) and Freundlich et al. (2020b). We assume the shell energy to be

$$E_t(r_i) = U(r_i; p_i) - \frac{Gm}{r_i} + K(r_i; p_i) \tag{3.2}$$

*Fuzzy dark matter (or ultralight axions) is an exotic proposed form of DM where particles are so light that their de Broglie wavelength is of the order of a kpc, inducing quantum phenomena (such as density fluctuations) at galaxy and halo scales.

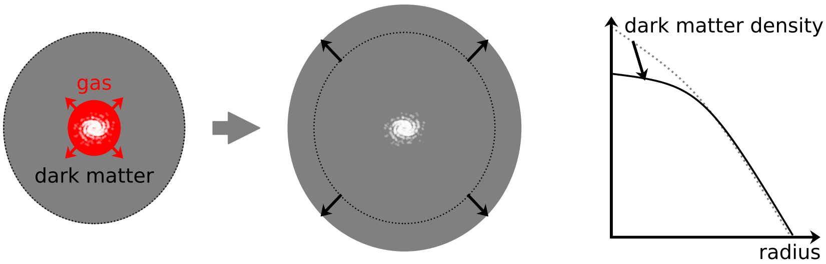

Fig. 2. Core formation from bulk outflows, as proposed in Freundlich et al. (2020a, *CuspCore* model): a sudden gas outflow instantaneously changes the gravitational potential at fixed velocities (left panel) and leads to halo expansion when the system relaxes to a new equilibrium (middle panel), thus leading to core formation (right panel).

right after a central mass loss m, and the system to subsequently relax to a new equilibrium where the shell initially at r_i has moved to r_f. Using the same parametric expressions for U and K, the final energy of the shell is written

$$E_f(r_f) = U(r_f; p_f) - \frac{Gm}{r_f} + K(r_f; p_f, m), \tag{3.3}$$

where parameters p_f describe the new mass distribution. Eqs. (3.1), (3.2), and (3.3) can be generalised to account for multiple halo components and a radius-dependent mass loss. The energy conservation assumption yields $E_f(r_f) = E_t(r_i)$ for each shell, which can be solved numerically to obtain the final parameters p_f. Radius r_f is indeed set for given parameters p_f, since the enclosed DM mass within each shell is conserved.

This model has been tested against successive outputs of cosmological zoom-in simulations, where it successfully predicted the evolution of the inner DM profile in about 75% of the cases, failing mainly in merger situations (Freundlich et al. 2020a). We are currently testing it using ideal N-body simulations, yielding an excellent agreement in the mass range where core formation occurs (François et al., in prep.).

4 Core formation from dynamical friction and AGN outflows

Recent observations have reported low DM fractions at the center of massive high-redshift galaxies (Wuyts et al. 2016; Genzel et al. 2017, 2020; Sharma et al. 2021), possibly indicating the presence of cored DM distributions three billion years after the Big Bang. To explain these early massive cores, we propose in Dekel et al. (2021) a hybrid scenario combining dynamical friction from merging satellites with AGN outflows when each of the two processes may not be sufficient by itself: dynamical friction first heats up the inner DM halo, which boosts the effect of AGN outflows with respect to core formation, as illustrated in Fig. 3.

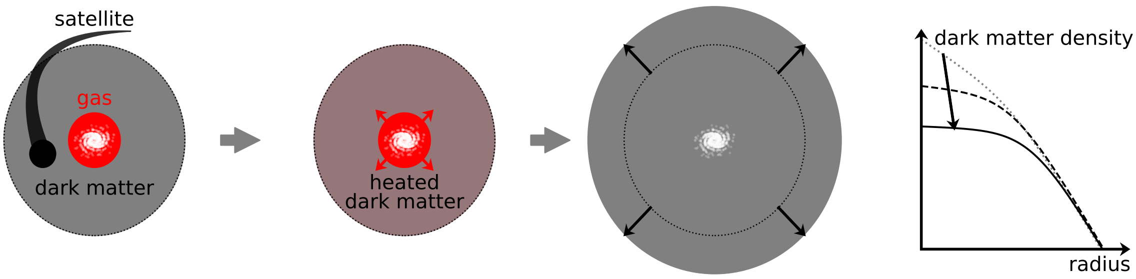

Fig. 3. Core formation from the combination of dynamical friction and AGN feedback, as proposed in Dekel et al. (2021): dynamical friction from a merging satellite (left panel) dynamically heats the DM halo (middle left panel), which increases the effect of the subsequent AGN outflow towards expanding the DM distribution and forming cores (right panels). Although not represented here, the energy deposited by dynamical friction can also contribute to expanding the DM distribution.

We first use analytical arguments and the *SatGen* semi-analytical model (Jiang et al. 2021) to assess the energy deposited in the halo through dynamical friction by single satellites, of different concentrations and orbits, and by a cosmological sequence of satellites. This energy heats up the halo and can already contribute to flattening its central cusp. If we assume an instantaneous energy deposition followed by relaxation to a new equilibrium and energy conservation for shells enclosing given DM masses, we can adapt the different steps of the *CuspCore* model (outlined in the previous Section) to describe how the DM halo can flatten from the heating. Namely, the transitional shell energy right after the energy deposition would be

$$E_t(r_i) = U(r_i; p_i) + K(r_i; p_i) + W(r_i), \tag{4.1}$$

where W is the energy input from dynamical friction, and the final shell energy

$$E_f(r_f) = U(r_f; p_f) + K(r_f; p_f, m), \tag{4.2}$$

where the energy input has been absorbed to transform the DM mass distribution. Again using the *CuspCore* model to describe the effect of a sudden bulk AGN outflow on the pre-heated or already-flattened halo, we show that the combination of dynamical friction and outflows enables particularly efficient core formation.

5 Conclusion

We presented three theoretical models for core formation in dark matter haloes induced by baryonic processes: a model invoking the small density fluctuations induced by stellar feedback in the interstellar medium, a model invoking bulk gas outflows, and a model invoking the combination of dynamical friction from merging satellites with AGN outflows in early massive galaxies. Each of these models provides a physical understanding of core formation within the cold dark matter framework, the predictions of the first two can be compared in certain situations despite their different formalism, and the different processes at stake may act in concert. We highlight that solutions to the cusp-core discrepancy invoking fundamental changes in the cosmological model have also been proposed.

The work presented here has been carried out in collaboration with A. El-Zant, F. Combes, A. Dekel, F. Jiang, S. Lapiner, A. Burkert, T. François, and B. Famaey.

References

Blumenthal, G. R., Faber, S. M., Flores, R., & Primack, J. R. 1986, ApJ, 301, 27
Chandrasekhar, S. 1943, ApJ, 97, 255
Dekel, A., Freundlich, J., Jiang, F., et al. 2021, arXiv e-prints, arXiv:2106.01378
Dekel, A., Ishai, G., Dutton, A. A., & Maccio, A. V. 2017, MNRAS, 468, 1005
Dutton, A. A., Macciò, A. V., Dekel, A., et al. 2016, MNRAS, 461, 2658
El-Zant, A., Shlosman, I., & Hoffman, Y. 2001, ApJ, 560, 636
El-Zant, A. A., Freundlich, J., & Combes, F. 2016, MNRAS, 461, 1745
El-Zant, A. A., Freundlich, J., Combes, F., & Halle, A. 2020a, MNRAS, 492, 877
El-Zant, A. A., Roupas, Z., & Silk, J. 2020b, MNRAS, 499, 2575
Förster Schreiber, N. M. & Wuyts, S. 2020, ARA&A, 58, 661
Freundlich, J., Dekel, A., & Jiang, F. 2019, in SF2A Proceedings, 477–480
Freundlich, J., Dekel, A., Jiang, F., et al. 2020a, MNRAS, 491, 4523
Freundlich, J., El-Zant, A., & Combes, F. 2016, in SF2A Proceedings, 153–156
Freundlich, J., Jiang, F., Dekel, A., et al. 2020b, MNRAS, 499, 2912
Genzel, R., Förster Schreiber, N. M., Übler, H., et al. 2017, Nature, 543, 397
Genzel, R., Price, S. H., Übler, H., et al. 2020, ApJ, 902, 98
Governato, F., Zolotov, A., Pontzen, A., et al. 2012, MNRAS, 422, 1231
Hernquist, L. & Ostriker, J. P. 1992, ApJ, 386, 375
Jiang, F., Dekel, A., Freundlich, J., et al. 2021, MNRAS, 502, 621
Marsh, D. J. E. & Niemeyer, J. C. 2019, Phys. Rev. Lett., 123, 051103
Oh, S.-H., de Blok, W. J. G., Brinks, E., Walter, F., & Kennicutt, Jr., R. C. 2011, AJ, 141, 193
Peters, T., Naab, T., Walch, S., et al. 2017, MNRAS, 466, 3293
Pontzen, A. & Governato, F. 2012, MNRAS, 421, 3464
Sharma, G., Salucci, P., & van de Ven, G. 2021, arXiv e-prints, arXiv:2105.13684
Wuyts, S., Förster Schreiber, N. M., Wisnioski, E., et al. 2016, ApJ, 831, 149

SF2A 2021
A. Siebert, K. Baillié, E. Lagadec, N. Lagarde, J. Malzac, J.-B. Marquette, M. N'Diaye, J. Richard, O. Venot (eds)

X-IFU/ATHENA VIEW OF THE MOST DISTANT GALAXY CLUSTERS IN THE UNIVERSE

F. Castellani[1], N. Clerc[1], E. Pointecouteau[1], Y. Bahé[2] and F. Pajot[1]

Abstract. The X-ray Integral Field Unit (X-IFU) on-board the second large ESA mission "Athena" will be a high spatial (5") and spectral (2.5eV) resolution X-ray imaging spectrometer, operating in the 0.2-12 keV energy band. It will address the science question of the assembly and evolution through cosmic time of the largest halos of matter in the Universe, groups and clusters of galaxies. To this end, we present an on-going feasibility study to demonstrate the X-IFU capabilities to unveil the physics of massive halos at their epoch of formation. Starting from a distant (z=2) group of galaxies ($M_{500} = 7\ 10^{13}\ M_{\odot}/h$) extracted from the HYDRANGEA cosmological and hydrodynamical numerical simulations, we perform an end-to-end simulation of X-IFU observations. From the reconstruction of the global, 1D and 2D quantities, we plan to investigate the various X-IFU science cases for clusters of galaxies, such as the chemical enrichment of the intra-cluster medium (ICM), the dynamical assembly of groups and clusters and the impact of feedback from galaxy and super-massive black hole evolution.

Keywords: clusters of galaxies, chemical enrichment, intra-cluster medium, numerical simulations

1 Introduction

Athena is the ESA second large mission of Cosmic Vision program, dedicated to study the Hot and Energetic Universe (Nandra et al. 2013). On-board Athena, the X-ray Integral Field Unit (Barret et al. 2016) (X-IFU) is a cryogenic imaging spectrometer composed by an array of 3168 superconducting Transition Edge Sensors (Smith et al. 2016) operated at 90mK. It will provide high spatial resolution (5" within an FoV of 5' equivalent diameter) and high spectral resolution (2.5eV FWHM up to 7 keV) observations in the 0.2-12 keV energy band. The X-IFU is reaching the end of its preliminary definition phase (phase B). In order to assess the specifications of its performance, we put in place feasibility studies of the core science objectives of Athena to be carried out by X-IFU (Pointecouteau et al. 2013; Croston et al. 2013).

2 Mock X-IFU observations

In the following we present the mock observation of a distant galaxy cluster (z=2, $M_{500} = 7\ 10^{13}\ M_{\odot}/h$) extracted from the numerical simulation of structure formation HYDRANGEA (Bahé et al. 2017). These cosmological simulations are based on the EAGLE simulations, and use the same implementation of several physical processes for the intra-cluster medium (ICM). Each gas particles forming the ICM is considered as an X-ray source and its emission is modeled as a thermal emitting fully ionised plasma with emission lines (model `vvapec` in XSPEC (Arnaud 1996)). The chemical abundances are in units of solar abundances as from Anders & Grevesse (1989). In addition to the cluster X-ray emission, our mock observations include realistic background contributions as non X-ray background (Lotti et al. 2014), cosmic X-ray background and foreground emission from the galaxy and the local bubble. Then, we make use of the end-to-end simulator SIXTE (Dauser et al. 2019) to produce an X-IFU event list. Following the methodology described in Cucchetti et al. (2018), we performed a 10^6 sec exposure time mock observation (Fig. 1 middle).

[1] IRAP, Univ. de Toulouse, CNRS, UPS, CNES, Toulouse, France
[2] Leiden Observatory, Leiden University, Leiden, the Netherlands

3 Reconstruction of the gas physical properties

With this mock observation our goal is to demonstrate the ability of X-IFU to recover the physical properties of the ICM, that is the density, temperature, entropy, pressure. Making use of X-IFU's exquisite spectral resolution we also aim at estimating our ability to recover the chemical abundances and abundance ratios. Our analysis is starting. We first plan to recover the 1D projected distribution assuming the spherical symmetry of the cluster. In the second step we will look into the 2D reconstruction of the aforementioned physical characteristics. This requires an adequate radial or 2D binning (for instance through Voronoi tessellation) maximising the signal with respect to the objectives (e.g., measurements of temperature, chemical abundances). The challenges reside in the relatively modest number of cluster counts with respect to these of the total background (astrophysical and instrumental). Disentangling the line emission from the continuum is another difficulty. The X-IFU's exquisite spectral resolution and field of view will be a decisive asset in our study.

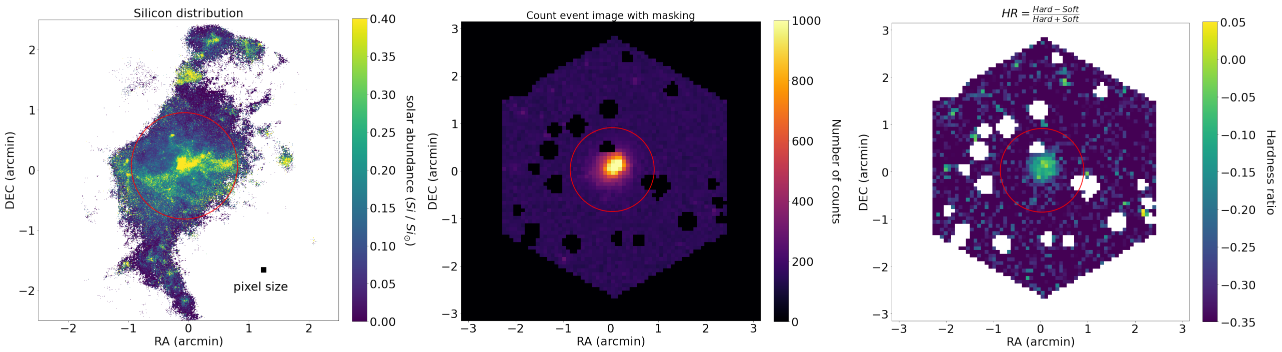

Fig. 1. Left: Emission-measure weighted map of the silicon abundances derived from the input simulated cluster gas particles. **Middle:** Count image of our mock X-IFU observation including astrophysical and instrumental background (detected point sources are masked). **Right:** Hardness ratio map from the count images derived in the 0.2-0.85 keV and 0.85-12 keV energy bands. The red circles shows the locus of R_{500}.

4 Perspectives

With this case study we will demonstrate the abilities of X-IFU to effectively observe and characterise the first massive haloes that have assembled an atmosphere of hot gas. The data analysis of our realistic mock observations will allow us to quantify the precision with which we can recover the physical properties of the ICM. Hence, it will tells us with which precision we could constraint the amount of energy deposited in the ICM through feedback processes by star formation in galaxies and the activity of their super-massive black holes, together with, what is the chemical enrichment state of the first massive formed halos.

F. Castellani acknowledges the financial support of CNES (Centre National d'Etudes Spatiales) and ADS (Airbus Defence & Space). We thank J. Schaye for his fruitful comments on this manuscript.

References

Anders, E. & Grevesse, N. 1989, Geochim. Cosmochim. Acta, 53, 197
Arnaud, K. A. 1996, in Astronomical Data Analysis Software and Systems V, Vol. 101, 17
Bahé, Y. M., Barnes, D. J., Dalla Vecchia, C., et al. 2017, MNRAS, 470, 4186
Barret, D., Lam Trong, T., den Herder, J.-W., et al. 2016, in SPIE, Vol. 9905, 99052F
Croston, J. H., Sanders, J. S., Heinz, S., et al. 2013, AGN feedback in galaxy clusters and groups
Cucchetti, E., Pointecouteau, E., Peille, P., et al. 2018, A&A, 620, A173
Dauser, T., Falkner, S., Lorenz, M., et al. 2019, A&A, 630, A66
Lotti, S., Macculi, C., Cea, D., et al. 2014, in SPIE, Vol. 9144, 91442O
Nandra, K., Barret, D., Barcons, X., et al. 2013, arXiv e-prints, arXiv:1306.2307
Pointecouteau, E., Reiprich, T. H., Adami, C., et al. 2013, The evolution of galaxy groups and clusters
Smith, S. J., Adams, J. S., Bandler, S. R., et al. 2016, in SPIE, Vol. 9905, 99052H

SF2A 2021
A. Siebert, K. Baillié, E. Lagadec, N. Lagarde, J. Malzac, J.-B. Marquette, M. N'Diaye, J. Richard, O. Venot (eds)

MASS RATIO EVOLUTION IN CLUSTERS BETWEEN HALOS AND SUB-HALOS

G. Mahler[2]

Abstract. Structure in our universe grow hierarchically, where small structures (stars and galaxies) assemble first and later on galaxies group and proto-clusters together in large potential wells to form clusters. Clusters of galaxies are the largest structure observable in our Universe and can contain more than hundreds of galaxies. We believe that every galaxy carries its own small halo of dark matter, and when they fall in a cluster part of that halo is stripped and diffused in the larger halo of the cluster. I will present here, how I am using the strong gravitational lensing effect in combination with IFU of cluster fields to answer questions on the evolution of the halos and sub-halos dark matter components. Indeed galaxies and their dark matter falling in the cluster and losing their dark matter to the profit of the cluster also called the sub-halos mass loss. In the future, I will use a large number of models spanning a wide range of redshifts (0.3 < z < 1.0) to show how cluster transfer their mass from their cluster members to their host halos.

Keywords: gravitational lensing, strong gravitational lensing, galaxy cluster, galaxy mass

1 Introduction

Clusters of galaxies are located at the nodes of the cosmic filaments and represent the densest structures of dark matter; their merging history and evolution shape the properties of their mass distribution. The density profiles of massive galaxy clusters show strong self-similarity up to z∼2 outside of cluster cores (McDonald et al. 2017), but depart from this self-similarity within cluster cores. While X-ray, SZ, and/ or weak lensing studies have been able to accurately probe the outer region of clusters, the inner core profile is much better probe with different methods such as strong lensing (e.g. Newman et al. 2009)

2 Methods

Simulations have shown that a large fraction of the mass from subhalos merge with the host and only up to about 20% of it remain within cluster member galaxies (Wu et al. 2013). This scenario implies that through their life the cluster sub-halos fraction mass can change. Building on such realization I gathered clusters from the South Pole Telescope catalog, see left panels Fig. 1. Adding mass evolution relation from simulation and modeling of a few clusters showing very peculiar subhalos mass fraction we are tempted to draw a relation between subhalos mass fraction and redshift evolution. To remove some biases and degeneracies among parameters during the strong lensing modeling, we can use dynamical information when available. Based on galaxy-galaxy strong lensing relation from Bolton et al. (2007). We can use the relation between velocity dispersion, with effective radius and mass Using this relation we are able to test this on cluster member galaxies under the assumption that the inner core of field elliptical is similar to the one of cluster member galaxies. To do so I used one of the most constrained cluster, Abell 370 (Lagattuta et al. 2019) due to its large spectroscopic coverage and well constrained strong lensing model.

3 Results and Conclusions

Fitting all of the cluster members spectra using PPFX (Cappellari 2017) fitting software. We were able to fit 119 different cluster member galaxies The depth of the data allowed to reach a faint cluster member galaxies 0.05 $L^\star$ Before investigating the spread in mass for cluster members we compared the dynamical mass to the

[1] Institute for Computational Cosmology, Durham University, South Road, Durham DH1 3LE, UK
[2] Centre for Extragalactic Astronomy, Durham University, South Road, Durham DH1 3LE, UK

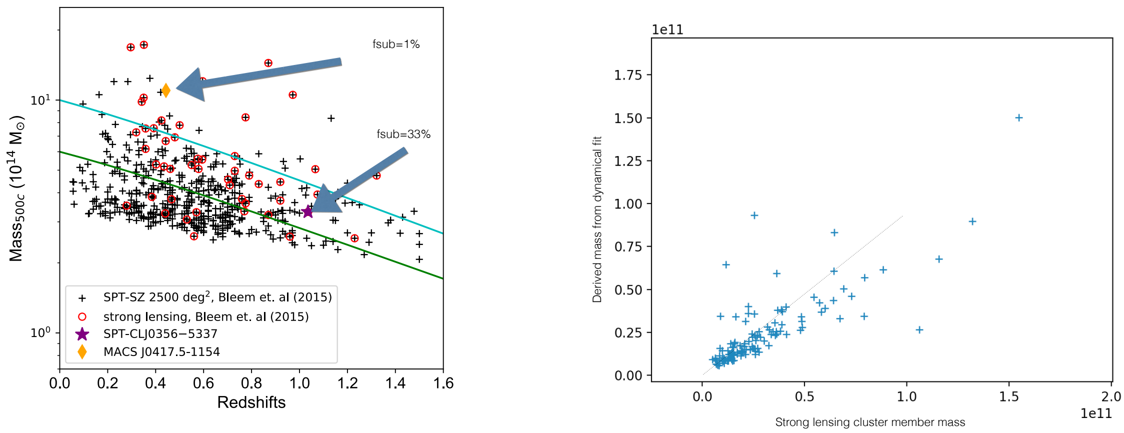

Fig. 1. Left: Mass redshift diagram of South Pole Telescope cluster sample from Bleem et al. (2015). Green and cyan line represents the mass evolution for clusters to guide the eye. The two arrow points toward cluster with very peculiar sub-halos mass fraction from Mahler et al. (2019, 2020) **Right:** Mass comparison between the mass derived from the strong lensing models optimized only using strong lensing constraints and the masses derived from the dynamical formula in Bolton et al. (2007)

mass directly directed from the strong lensing fit (See right panel Fig. 1) This figure show a nice correlation, however slightly biases in the 1:1 relation. Indeed it seems that the most massive galaxies fitted in the strong lensing minimization tends to be more massive that what predicted from their velocity dispersion. This could be due to the interplay between the cluster scale halo and the biggest cluster member galaxies. This might also be a hint for a non-constant mass-to-light ratio in our cluster. In the future, I will extend the sample of cluster used and try to directly inject the dynamical mass estimate in the cluster to model it.

Thank you for collaborators participation and discussion, especially JR and DJL. GM received funding from the European Union's Horizon 2020 research and innovation programme under the Marie Skłodowska-Curie grant agreement No MARACAS - DLV-896778.

References

Bleem, L. E., Stalder, B., de Haan, T., et al. 2015, ApJS, 216, 27

Bolton, A. S., Burles, S., Treu, T., Koopmans, L. V. E., & Moustakas, L. A. 2007, ApJ, 665, L105

Cappellari, M. 2017, MNRAS, 466, 798

Lagattuta, D. J., Richard, J., Bauer, F. E., et al. 2019, MNRAS, 485, 3738

Mahler, G., Sharon, K., Fox, C., et al. 2019, ApJ, 873, 96

Mahler, G., Sharon, K., Gladders, M. D., et al. 2020, ApJ, 894, 150

McDonald, M., Allen, S. W., Bayliss, M., et al. 2017, ApJ, 843, 28

Newman, A. B., Treu, T., Ellis, R. S., et al. 2009, ApJ, 706, 1078

Wu, H.-Y., Hahn, O., Wechsler, R. H., Behroozi, P. S., & Mao, Y.-Y. 2013, ApJ, 767, 23

SF2A 2021
A. Siebert, K. Baillié, E. Lagadec, N. Lagarde, J. Malzac, J.-B. Marquette, M. N'Diaye, J. Richard, O. Venot (eds)

THE EFFECT OF NODES AND FILAMENTS ON THE QUENCHING AND THE ORIENTATION OF THE SPIN OF GALAXIES

N. Malavasi[1], M. Langer[1], N. Aghanim[1], D. Galárraga-Espinosa[1] and C. Gouin[1]

Abstract. Filaments and clusters of the cosmic web have an impact on the properties of galaxies, such as star-formation, stellar mass, and angular momentum. We use the IllustrisTNG simulation, coupled with the DisPerSE cosmic web extraction algorithm, to test which is the galaxy property most affected by the cosmic web and, conversely, to assess the differential impact of clusters and filaments on a given galaxy property. Results show that star-formation is the quantity that shows the strongest variation with the distances from the cosmic web features, while the direction of the angular momentum of galaxies shows the weakest trends. The direction of the angular momentum of galaxies and its use to improve our detection of the cosmic web features could be the focus of futures studies benefitting from larger statistical samples.

Keywords: large-scale structure of the Universe – Galaxies: statistics – Galaxies: evolution

1 Introduction

Both galaxy clusters (Boselli & Gavazzi 2006, 2014) and filaments (Malavasi et al. 2017; Laigle et al. 2018; Kraljic et al. 2018; Bonjean et al. 2020) affect galaxy properties, with systems in these structures being more massive and less star-forming than elsewhere. In addition, filaments also affect the acquisition of angular momentum (spin) in galaxies. Galaxies are formed with their spin parallel to the filaments of the cosmic web (Codis et al. 2015) and progressively turn massive and align their spin perpendicularly to the filaments during their evolution while flowing towards the clusters (Aragón-Calvo et al. 2007; Hahn et al. 2007). In this work (based on Malavasi et al., 2021, under review) we explore which galaxy property (mass, SFR, spin) is the most affected by cosmic web structures (clusters and filaments) and is therefore better suited to improve the detection of cosmic web elements.

2 Data and Method

We exploit 275 818 galaxies from the $z = 0$ snapshot of the TNG300-1 box of the IllustrisTNG cosmological simulation (Nelson et al. 2019), with a side of ~ 300 Mpc, defined as subhaloes with $10^9 \leq M^*/M_\odot < 10^{12}$. The filaments of the cosmic web in the simulation have been detected by Galárraga-Espinosa et al. (2020) using the Discrete Persistence Structure Extractor (DisPerSE, Sousbie 2011). We focus on three galaxy distances from the cosmic web: distance from a galaxy to the axis of the closest filament ($d_{\rm fil}$), 3D distance from a galaxy to the closest node ($d_{\rm CP}$, only for galaxies with $d_{\rm fil}> 1$ Mpc), and distance from a galaxy to the node connected to the closest filament following the filaments ($d_{\rm skel}$, only for galaxies with $d_{\rm fil}< 1$ Mpc). A sketch of the three distances is shown in the left panel of Figure 1. We also focus on several galaxy properties: stellar mass M^*, SFR-related quantities (SFR, specific SFR, defined as sSFR = SFR/M^*, and fraction of quenched galaxies, i.e. having sSFR $\leq 10^{-11}$yr^{-1}, $f_{\rm Q}$), and spin-related quantities: the angle θ between the direction of the spin vector and the local direction of the filaments (limited to $0 \leq \theta \leq 90$ deg), the fraction of parallel ($\theta \leq 30$ deg, $f_\parallel$) and perpendicular ($\theta \geq 60$ deg, $f_\perp$) galaxies, the quantity $\cos(4\theta)$ (to separate between galaxies with spin either parallel or perpendicular to the filaments, $\cos(4\theta) > 0$, i.e. galaxies having an ordered relation between spin and filament direction, and galaxies with no relation between spin and filament direction, $\cos(4\theta) < 0$), and the fraction of ordered galaxies ($f_{\rm Ord}$).

[1] Université Paris-Saclay, CNRS, Institut d'Astrophysique Spatiale, 91405, Orsay, France

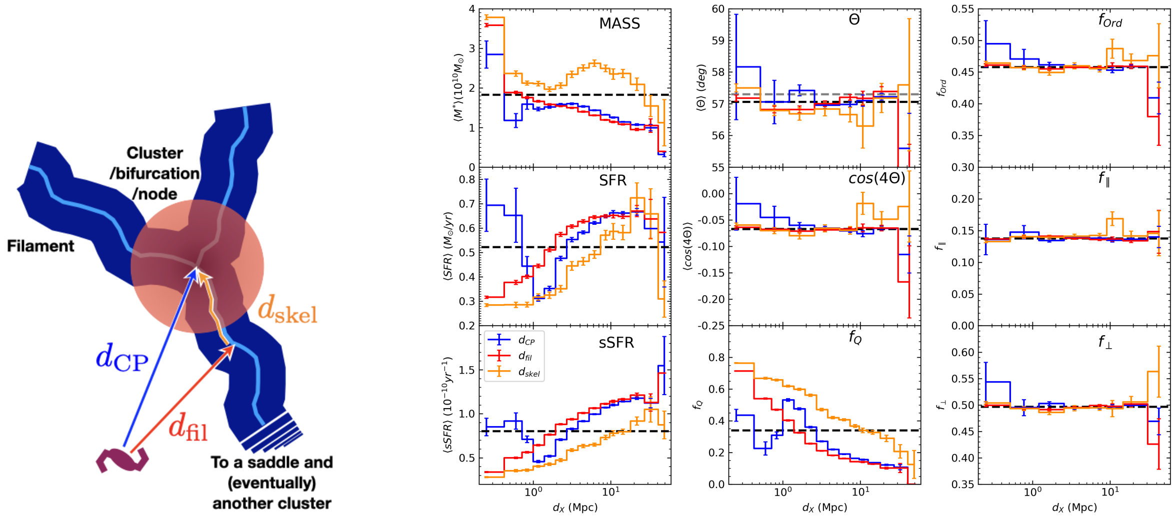

Fig. 1. Left: The three galaxy distances from the cosmic web: $d_{\rm fil}$, $d_{\rm CP}$, and $d_{\rm skel}$. **Right:** Distributions of $\langle M^* \rangle$, $\langle {\rm SFR} \rangle$, $\langle {\rm sSFR} \rangle$, $\langle \theta \rangle$, $\langle \cos(4\theta) \rangle$, $f_{\rm Q}$, $f_{\rm Ord}$, $f_{\parallel}$, $f_{\perp}$ in bins of $d_{\rm fil}$ (red), $d_{\rm CP}$ (blue), and $d_{\rm skel}$ (orange). The black dashed line in every panel is the average of each quantity in the full simulation box. For θ, the grey line is $\bar{\theta}$, computed given the expected distribution of this quantity.

3 Results and Conclusions

Figure 1 (right panel) shows the distributions of the considered quantities as a function of $d_{\rm CP}$, $d_{\rm fil}$, and $d_{\rm skel}$. We find that SFR-related quantities allow to distinguish between $d_{\rm fil}$ (proxy for the accretion onto filaments) and $d_{\rm CP}$ and $d_{\rm skel}$, proxies for the accretion onto nodes (further separated between the isotropic case and flowing inside the filaments). Mass and spin-related quantities seem to allow only for a distinction between $d_{\rm CP}$ and $d_{\rm fil}$ with respect to $d_{\rm skel}$. The distributions of SFR-related quantites are those that show the largest variation with respect to each distance, a further confirmation that they are the best tracers for $d_{\rm CP}$, $d_{\rm fil}$, and $d_{\rm skel}$. Spin-related quantities show the lowest amount of variation and are therefore the worse tracer. However, SFR-related quantities show also a large dependence on the local environment of galaxies, which may prevent their use as tracers to improve the detection of the cosmic web. On the other hand, spin related quantities are more robust with respect to the effect of local density. Although the strength of the signal of the recovered trends is lower, their use could provide a detection of the cosmic web in a way more independent from the local density.

This research has been supported by the funding for the ByoPiC project from the European Research Council (ERC) under the European Union's Horizon 2020 research and innovation programme grant agreement ERC-2015-AdG 695561.

References

Aragón-Calvo, M. A., van de Weygaert, R., Jones, B. J. T., & van der Hulst, J. M. 2007, ApJ, 655, L5
Bonjean, V., Aghanim, N., Douspis, M., Malavasi, N., & Tanimura, H. 2020, A&A, 638, A75
Boselli, A. & Gavazzi, G. 2006, PASP, 118, 517
Boselli, A. & Gavazzi, G. 2014, A&A Rev., 22, 74
Codis, S., Pichon, C., & Pogosyan, D. 2015, MNRAS, 452, 3369
Galárraga-Espinosa, D., Aghanim, N., Langer, M., Gouin, C., & Malavasi, N. 2020, A&A, 641, A173
Hahn, O., Carollo, C. M., Porciani, C., & Dekel, A. 2007, MNRAS, 381, 41
Kraljic, K., Arnouts, S., Pichon, C., et al. 2018, MNRAS, 474, 547
Laigle, C., Pichon, C., Arnouts, S., et al. 2018, MNRAS, 474, 5437
Malavasi, N., Arnouts, S., Vibert, D., et al. 2017, MNRAS, 465, 3817
Nelson, D., Springel, V., Pillepich, A., et al. 2019, Computational Astrophysics and Cosmology, 6, 2
Sousbie, T. 2011, MNRAS, 414, 350

INTERACTING GALAXIES HIDING INTO ONE, REVEALED BY MANGA

B. Mazzilli Ciraulo[1], A.-L. Melchior[1], D. Maschmann[1 3], I. Y. Katkov[2,3, 4], A. Hallé[1], F. Combes[1, 5], J. D. Gelfand[2,3, 6] and A. Al Yazeedi[2,3]

Abstract.
Interacting galaxies represent a fundamental tool for investigating the underlying mechanisms that drive galaxy evolution. In order to identify merging systems, high-resolution spectroscopic data are required, especially when the morphology does not show clear galaxy pairs. Here, we present a merging galaxy, MaNGA 1-114955, in which we highlighted the superimposition of two distinct rotating discs along the line of sight. We suggest that we are observing a pre-coalescence stage of a merger. Our results demonstrate how a galaxy can hide another one and the relevance of a multi-component approach for studying ambiguous systems.

Keywords: Galaxy: evolution – Galaxy: kinematics and dynamics – Galaxies: interactions – Techniques: spectroscopy – Methods: data analysis

1 Introduction

The improvement in data resolution has made it possible to highlight various observational signatures of mergers, such as colour change (Alonso et al. 2012), morphological disruption (Casteels et al. 2013), star formation enhancement (Patton et al. 2013), and merger-induced nuclear activity at low redshift for optical and mid-IR active galactic nuclei (AGN; Ellison et al. 2019). The presence of double nuclei (such as in NGC 3526; Sakamoto et al. 2014) is a clear signature of mergers as the existence of tidal tails (Mesa et al. 2014) and, alternatively, spectral features, such as double-peaked profiles in molecular gas emission lines, have also been interpreted as merger signatures (e.g. Greve et al. 2005; Weiß et al. 2005).

The galaxy merger studied here consists of a system at z = 0.09 which belongs to a sub-sample (Mazzilli Ciraulo et al., in prep.) created by cross-identifying the MaNGA data release (SDSS DR15, Aguado et al. 2019) and a catalogue gathering sources with detected double-peaked emission-line profiles in their central SDSS spectrum (Maschmann et al. 2020).

2 Unveiling a merger event through a multi-component decomposition

2.1 *Gas kinematics from the multi-component approach*

We developed a two-component fitting procedure that we applied to the main emission lines in all the binned spectra of the MaNGA data. We highlighted two components along the line of sight, separated by a velocity difference $\Delta V \sim 450$km s^{-1}. The first object is a galaxy with a fairly regular velocity field, whereas the second is detected in a smaller region of the field of view, shows a slightly stronger Hα line flux, and shows a velocity field counter-rotating with respect to the main object. The 2D maps are displayed on Fig. 1.

[1] LERMA, Sorbonne Université, Observatoire de Paris, Université PSL, CNRS, F-75014, Paris, France
[2] New York University Abu Dhabi, Saadiyat Island, PO Box 129188, Abu Dhabi, UAE
[3] Center for Astro, Particle, and Planetary Physics, NYU Abu Dhabi, PO Box 129188, Abu Dhabi, UAE
[4] Sternberg Astronomical Institute, M.V. Lomonosov Moscow State University, 13 Universitetsky prospect, Moscow, 119991, Russia
[5] Collège de France, 11 Place Marcelin Berthelot, 75005 Paris, France
[6] Center for Cosmology and Particle Physics, New York University, 726 Broadway, New York, NY 10003, US

2.2 *Consistent gas and star kinematics*

We found associated counterparts to the gaseous double-peaked structure in the stellar kinematics, using an analysis workflow based on the full spectral fitting technique NBursts. We spotlighted two stellar population components: One is regular, and the second is less prominent but is detected in the region where we see a second gas component as well.

2.3 *Figures*

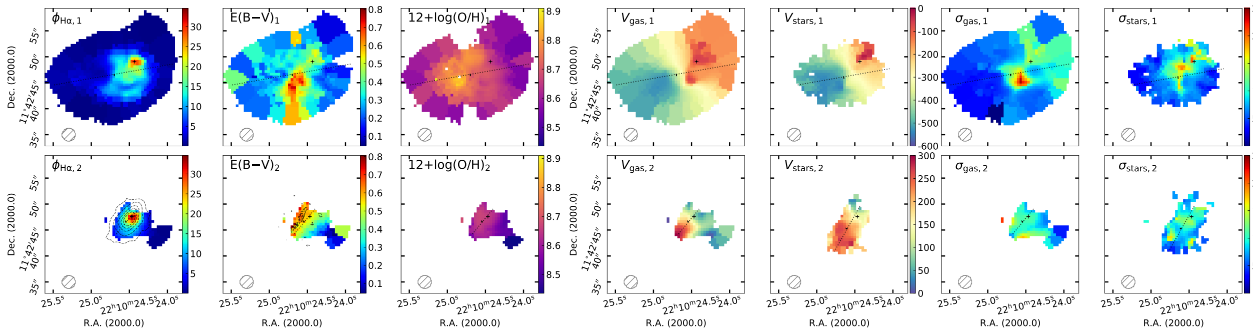

Fig. 1. The first and second rows show the maps for the first and second components detected in MaNGA data, respectively. **Left:** Gas properties derived from our fitting procedure. From left to right: Hα extinction-corrected flux (in erg s^{-1} Å^{-1} cm^{-2} per spaxel), extinction computed from the Balmer decrement, and oxygen gas-phase abundance derived using the O_3N_2 calibrator. The MaNGA PSF is displayed as a hatched grey circle in the bottom-left corner of the panels. **Right:** Kinematics of the gas and stars. First and second columns: respective ionised gas and stellar velocity fields (in km s^{-1}). The dotted black lines refer to the computed position angles. Third and fourth columns: respective velocity dispersion fields (in km s^{-1}) for the gas and the stars. As in the left panels, the black crosses indicate the position of the extinction-corrected Hα flux peak for the represented component.

3 Conclusions and remaining questions

Through the kinematics analysis of MaNGA 1-114955, we detected two separate components along the line of sight, both in gas and stars. We estimated a mass ratio of 9:1 between both objects. The second component shows an extended radio emission, that could be associated to the composite excitation of the gas observed within the system. The Hα-based star formation rate is under-estimated with respect to the one expected from the radio luminosity. From CO observations, we inferred an H_2 mass corresponding to 21% of the total stellar mass. These results are detailed in the A&A accepted paper Mazzilli Ciraulo et al. (2021). High-resolution CO observations are in progress to get the kinematics of the molecular gas.

References

Aguado, D. S., Ahumada, R., Almeida, A., et al. 2019, ApJS, 240, 23

Alonso, S., Mesa, V., Padilla, N., & Lambas, D. G. 2012, A&A, 539, A46

Casteels, K. R. V., Bamford, S. P., Skibba, R. A., et al. 2013, MNRAS, 429, 1051

Ellison, S. L., Viswanathan, A., Patton, D. R., et al. 2019, MNRAS, 487, 2491

Greve, T. R., Bertoldi, F., Smail, I., et al. 2005, MNRAS, 359, 1165

Maschmann, D., Melchior, A.-L., Mamon, G. A., Chilingarian, I. V., & Katkov, I. Y. 2020, A&A, 641, A171

Mazzilli Ciraulo, B., Melchior, A.-L., Maschmann, D., et al. 2021, arXiv e-prints, arXiv:2106.07060

Mesa, V., Duplancic, F., Alonso, S., Coldwell, G., & Lambas, D. G. 2014, MNRAS, 438, 1784

Patton, D. R., Torrey, P., Ellison, S. L., Mendel, J. T., & Scudder, J. M. 2013, MNRAS, 433, L59

Sakamoto, K., Aalto, S., Combes, F., Evans, A., & Peck, A. 2014, ApJ, 797, 90

Weiß, A., Downes, D., Walter, F., & Henkel, C. 2005, A&A, 440, L45

Session 18

Fast radio bursts : Atouts et perspectives pour la communauté

SF2A 2021
A. Siebert, K. Baillié, E. Lagadec, N. Lagarde, J. Malzac, J.-B. Marquette, M. N'Diaye, J. Richard, O. Venot (eds)

A MAZE IN(G) FRB MODELS

G. Voisin[1]

Abstract. For a substantial part of FRB history, the number of FRB models could easily rival the count of the recorded events. Although this has changed in the last few years with the arrival of new instruments and the multiplication of observation campaigns which, on the one hand, have dramatically increased the number of events, and on the other hand have reduced the number of viable models, there remains a quite amazing diversity of ideas and mechanisms. I will attempt to gather in some broad categories the current state of the art, and focus more particularly on those model that predict possible repetitions and, in some cases, periodicity.

Keywords: Stars: neutron, (Stars:) pulsars: general, Stars: magnetars, Stars: flare, Radio continuum: general

1 Introduction

The topic of this review are the so-called fast radio bursts (FRB). These are short bursts, lasting typically 1 - 100 ms, that have been observed from $\sim$ 100MHz (LOFAR) to few GHz (Effelsberg) in radio frequency. Their dispersion measure, that is the column density of free electrons encountered by the signal on its way, indicates an extra-galactic and even cosmological origin (except for one source known in our Galaxy). The extra-galactic origin has been confirmed by the association of a dozen sources with host galaxies (Bochenek et al. 2021). As a result, the source must be intrinsically extremely bright, with isotropic equivalent luminosities in the range of $10^{38} - 10^{46}$ ergs/s (Bochenek et al. 2020; Lu et al. 2020), peak spectral luminosity $10^{28} - 10^{36}$ erg/Hz (Bochenek et al. 2020) (see Fig. 1, left) and brightness temperature well in excess of 10^{30}K (Bochenek et al. 2020), implying a coherent radiation mechanism.

This paper focuses on these FRB sources that have been seen to repeat. Indeed the majority of known FRB sources gave (so far) single events*. Whether this results from two distinct classes of sources, or simply from the fact that some sources repeat much more often is unknown. However, there are indications that repeaters have distinctive spectro-temporal characteristics, which might be key to select the correct FRB model(s).

Thus, repeaters usually show narrow spectral occupancy (Kumar et al. 2020) i.e. $\Delta f \sim f/N$ where f is frequency and $N \sim$ a few, downward-drifting sub-pulses (e.g. Hessels et al. 2019) i.e. a sequence of a few pulses the frequency window of which drifts to lower frequencies (see Fig. 1, right). Substructures on the scale of $\sim 10\mu s$ have also been observed (e.g. Farah et al. 2018; Cho et al. 2020; Nimmo et al. 2020). Repetitions appear to follow a clustered, non-poissonian distribution in time (Connor et al. 2016; Lawrence et al. 2017), although it has been argued that the distribution may be poissonian if the analysis is restricted to active windows (Cruces et al. 2021). Note that these statistical considerations follow essentially from one source, FRB121102, which is the most frequent repeater thus far. Periodic activity windows have been evidenced in two sources, FRB160916 and FRB121102, with periods of $\sim$ 16 and $\sim$ 160 days, and duty cycle ~ 0.3 and ~ 0.5 respectively (see Collaboration et al. (2020) and Rajwade et al. (2020); Cruces et al. (2021) respectively). Polarisation of the signal is very highly linear (e.g. Michilli et al. 2018; Hilmarsson et al. 2021). No counter-part have so-far been detected, with the exception of the Galactic source FRB200824 (Bochenek et al. 2020), which was accompanied by X-ray flares of the associated magnetar. Rotation measure (RM), which measures the integral of the magnetic field parallel to the line of sight, has no clear trend: some are compatible with a RM

[1] LUTH, Observatoire de Paris, PSL Research University, CNRS, 5 place Jules Janssen, 92195 Meudon, France
*See the FRB catalog at `https://www.wis-tns.org/` and CHIME/FRB repeater catalog `https://www.chime-frb.ca/repeaters`

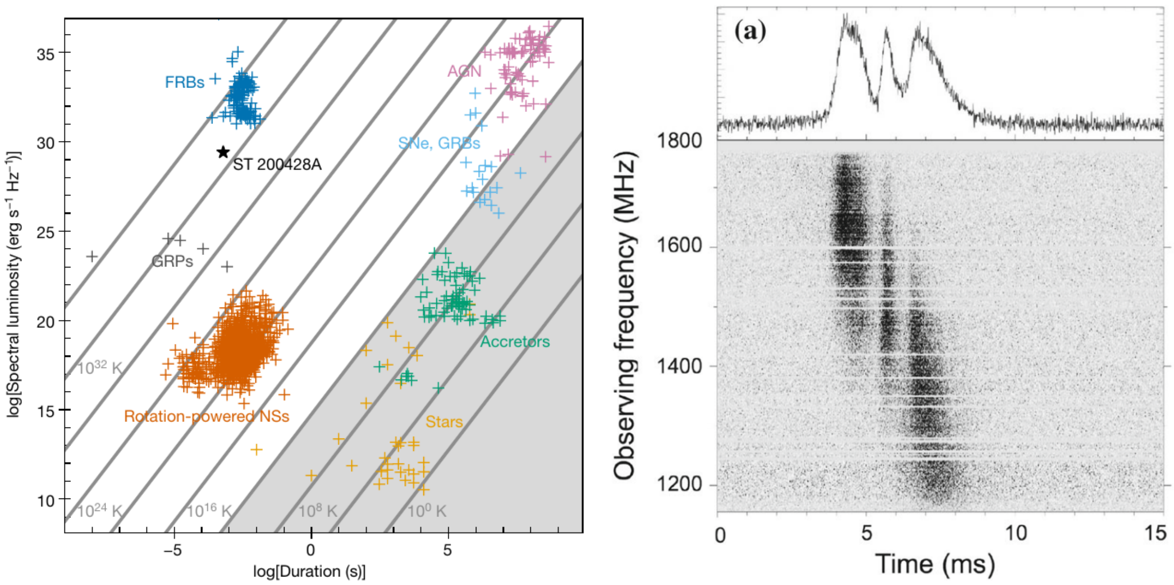

Fig. 1. Left: Equivalent isotropic spectral luminosity as a function of burst duration for sources in the centimetre-wavelength band. 'GRPs' stands for Giant Radio Pulses. ST 200428A correspond the burst from the galactic magnetar SGR 1935+2154, FRB200428, observed by STARE2. (more details in Bochenek et al. 2020). Right: An example of downward drifting subpulses from the loud repeater FRB121102 (from Hessels et al. 2019).

from the Galactic contribution alone or with a moderate intrinsic RM$\sim$ 200rad/m^2(Caleb et al. 2018), but we may note that the FRB121102 displays a very large value of $\sim 10^5$rad/m^2 (Michilli et al. 2018) which suggests a peculiar environment. Polarisation swing, the variation of polarisation angle through a burst, appears to be flat in most repeaters (e.g. Michilli et al. 2018; Hessels et al. 2019; Hilmarsson et al. 2021) with the exception of FRB180301 (Luo et al. 2020).

Currently, it is noteworthy that most modelling works focus on the characteristics of essentially three sources which we have already mentioned above. FRB121102 (Spitler et al. 2016, 2018; Josephy et al. 2019), which we may call the loud one due to the abundance of bursts observed, with sometimes 30 bursts/hour. It is also a particularly bright FRB, localised in a host galaxy 1Gpc away (Chatterjee et al. 2017; Tendulkar et al. 2017). It is also associated with a persistent radio counterpart (Marcote et al. 2017). It also has a periodic activity window spanning $\sim 60\%$ of the ~ 160day period (Rajwade et al. 2020; Cruces et al. 2021).

FRB180916 (Collaboration et al. 2020; Pleunis et al. 2021), that we may call the periodic one, because it is the first one for which a periodic activity window has been observed. Due to its relatively short period, ~ 16 days, it is better determined than the longer period of the loud FRB121102. Interestingly, recent LOFAR observations have shown that the $\sim$ 5-day activity window appears to start $\sim$ 3 days later in the LOFAR $100-190$MHz band than in the $400-800$Mhz CHIME/FRB band (Pleunis et al. 2021). It is located near a star-forming region in a galaxy 250Mpc away (Tendulkar et al. 2021; Marcote et al. 2020).

FRB200824, the Galactic one, is associated with magnetar SGR1935+2154 (Bochenek et al. 2020; Andersen et al. 2020). It is only known source of FRBs in our Galaxy. Only two consecutive bursts have been observed and it is therefore not strictly speaking a repeater. The bursts occurred during an X-ray outburst of the magnetar and are coincident with X-ray flares. Although it is somewhat dimmer than extra-galactic FRBs, it would be detected as such in a nearby galaxy, and is three orders of magnitude brighter than any other magnetar radio emission (see Fig.1). It is thus consistent with representing the low luminosity end of the FRB distribution.

The following focuses on models that involve a neutron star, usually a magnetar. These models represent the majority of the literature and are supported by the recent discovery of the Galactic FRB200428. Sec. 2 addresses models where the neutron star is necessary but not sufficient. One could see these models as challengers of the second category where magnetars are both necessary and sufficient, which we address in Sec. 3. In conclusion, Sec. 4, we direct the reader to other reviews that have been published in the recent years.

2 FRBs created by interaction of an object with a pulsar/magnetar

This category of models appeals to the interaction of neutron star with a third-party object, in particular asteroids. There are essentially two broad classes. In the first class, the energy powering FRBs comes from the neutron star magnetosphere/wind themselves, and an orbiting object is merely converting this energy into radiation. In the second class, the object is falling onto the neutron star and its gravitational energy is partly converted into FRBs. We see here why asteroids rather than larger objects can be appealing: it is easier to produce (frequently) repeating FRBs with small objects than with larger ones, as the number of objects can be larger, especially if the asteroids is destroyed in the process ! We note that in the current state of the literature these models appear as the main challengers, in terms of coarse bibliometric indicators, to the more discussed models where FRBs are produced by the neutron star alone (see Section 3).

2.1 Orbiting asteroid models

This model follows from the generalisation of a phenomenon known in the Solar system as Alfvén wings to the relativistic environment of neutron stars (Mottez & Zarka 2014). The source results from the interaction of an asteroid with the wind of a magnetar or a pulsar (Mottez et al. 2020; Decoene et al. 2020; Voisin et al. 2020). The object, immersed in the wind, forms a unipolar inductor and creates a plasma wake called Alfvén wings, because these perturbations are conveyed by Alfvén waves. As a result of the unipolar inductor phenomenon, a current flows along the wings and through the asteroid. Plasma instabilities may develop in the wings that convert the power carried by the current into coherent radiation through an unspecified mechanism. The available power is essentially limited by the wind power intercepted by the cross-section of the object, and modulated by a radio-conversion efficiency factor that one may take in the range $10^{-4} - 10^{-2}$ by analogy with similar phenomena in the solar system. An essential point is that, independently of the emission mechanism, the particles at the origin of the radiation are convected with the ultra-relativistic wind of the neutron star. As a result, any emission is highly collimated in a cone of apex $1/\gamma$, where γ is the Lorentz factor, which allows for bright pulses on a relatively cheap energy budget, visible at a large distance but unlikely to cross the line of sight of a nearby observer. Nonetheless, it has been shown that very young pulsars or magnetars (¡ 1000 years) are needed to provide sufficient power for distant FRBs such as the loud FRB121102 (Mottez et al. 2020). On the other hand, this mechanism should also produce fainter bursts with regular pulsar/magnetars.

One expects asteroids to be in belts or swarms, therefore one expects apparently random pulses every time an asteroid transits. Since the orbits of asteroids in such clusters is not strictly periodic due to many-body interactions and the very narrow beam of the emission one does not expect periodic repetition from a given asteroid. One caveat is that asteroid belts may reside too far from the source to produce strong enough FRBs. It has been proposed that asteroids may acquire very eccentric orbits thanks through Kozai-Lidov oscillations due to a distant black-hole companion(Decoene et al. 2020). In order to obtain a periodic active window, as seen in the repeater FRB180916, it has been proposed to cluster asteroids at 2:3 resonances of the orbit of a sub-stellar object (Voisin et al. 2020). A prediction of this model is that rare events may occur outside of the activity window.

2.2 Falling asteroids models

This model relies on the idea that a neutron star may occasionally cross an asteroid field surrounding a main-sequence star, which would provoke the collision of some asteroids with the neutron star, and FRBs (Geng & Huang 2015; Dai et al. 2016; Bagchi 2017; Smallwood et al. 2019; Liu et al. 2020; Dai 2020; Dai & Zhong 2020). Although the event is unlikely, these authors argue that it is sufficient to produce the observed FRB rate. An important element is that the neutron star should be a dead pulsar or magnetar rather than an active one, which considerably increases the reservoir of objects available (Geng & Huang 2015; Dai et al. 2016; Dai & Zhong 2020, e.g.). This is necessary to avoid evaporation of the asteroid by the intense high-energy radiations from the neutron star before it reaches the magnetosphere, which would prevent FRB production.

The scenario starts with an asteroid on a collision course with the NS. Past the Roche limit, the asteroid is torn apart into several pieces and continues its way until it reaches the magnetosphere. Each piece moving in the magnetic field of the neutron star creates a unipolar inductor electric field which locally accelerates electrons and positrons in the magnetosphere, producing coherent curvature radiation. The successive pieces may produce downward-drifting sub-pulses by the interplay of radius-to-frequency mapping Liu et al. (2020).

Coherent curvature radiation also explains the mostly linear polarisation seen in FRBs. The overall duration is connected to the size of the initial asteroid.

This mechanism may be adapted to produce periodic activity windows by assuming that the NS is in an eccentric orbit with a main-sequence star possessing a asteroid field. The NS then crosses the asteroid field when close enough to its periastron, and the width of the activity window is determined by the eccentricity of the orbit.

A variation of this model replaces the asteroid field+MS star by a white dwarf in an eccentric orbit around the NS. The white dwarf overflows its Roche lobe around periastron, and the material falls onto the neutron star similarly to asteroids. In order to produce the observed activity window, the material would have to reach very quickly (compared to the orbital period) the inner magnetospheric region of the NS, and it is unclear what may cause it to spiral so fast.

3 FRBs created from the magnetar/pulsar itself

The association of FRBs with magnetars is the most studied hypothesis in the literature. It was originally proposed by Popov & Postnov (2010) that a scaled-up version of magnetar flares might have a coherent radio counterpart visible at cosmological distances while the high energy component would be too faint for current instrumentation. To provide the necessary power, most (but not all, see below) models appeal to young magnetars with stronger magnetic and spin-down power. The abundance of such objects is sufficient to provide the observed FRB population (e.g. Metzger et al. 2017), possibly forming a rare sub-population of magnetars Lu et al. (2020); Margalit et al. (2020).

Interestingly, the theory of coherent radio counterpart to X-ray flares also originally followed from an analogy between type III solar flares and magnetars (Lyutikov 2002). Type III solar flares indeed associate X-ray emission with coherent radio emission with a fluence ratio of $F_R/F_X \sim 10^{-4}$. Such ratio has been observed in past radio emission from the galactic magnetar XTE J1810-197, and the recent observation of the Galactic FRB200428 seems to extend further this correlation, which therefore spans about 20 orders of magnitude (see Fig. 2, left). The accumulation of events, in particular from the loud FRB121102, allowed to compare the frequency and energy distributions of FRBs with those of magnetar bursts. This led some authors to argue in favour of the association between the two based on statistical similarity (e.g Wadiasingh & Chirenti 2020; Popov & Postnov 2010).

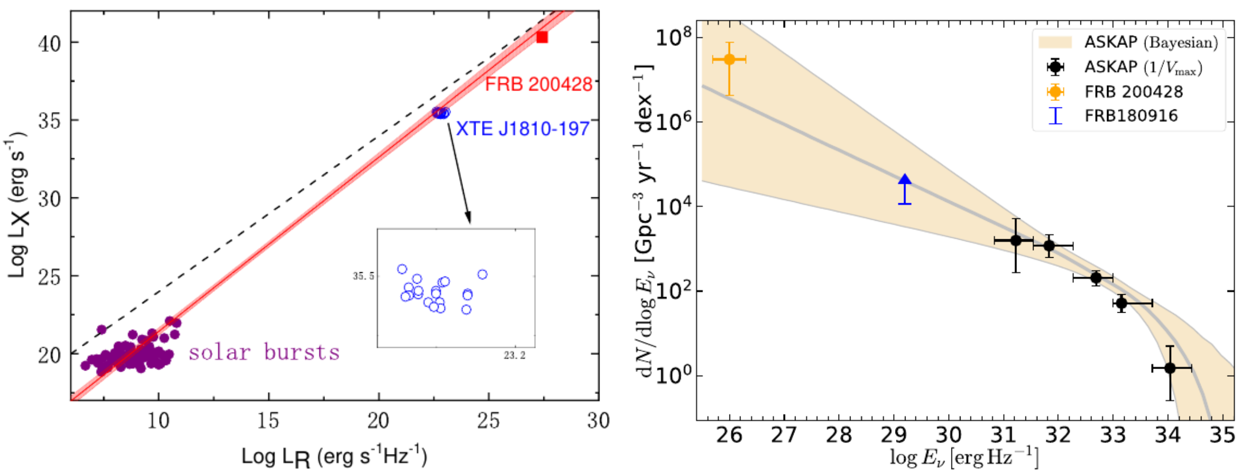

Fig. 2. Left: Relation X-ray vs radio isotropric equivalent luminosities of type III solar bursts, magnetar XTE J1810-197, and the Galactic FRB200428. The red line is a fit on this data. The dashed line is the Güdel-Benz correlation, which can only be used the gyrosynchrotron radio emissions, and does correspond to the data. (from Wang et al. 2021). Right: Volumetric rate of FRB events as a function of their specific energy E_ν (intrinsic energy released at frequency ν) at 1.4GHz. Black markers are ASKAP data. Orange marker is the Galactic FRB200428 observed by STARE2. Blue marker is a 90% confidence level lower limit on the contribution of the repeater FRB180916 derived from the CHIME/FRB data (Collaboration et al. 2020) (so at $\sim$ 600MHz instead of 1.4GHz). The silver lines show the mean and 68% confidence region of the bayesian fit performed on the ASKAP data alone (Lu & Piro 2019). (from Lu et al. 2020).

Energetically, one can show it is unlikely that rotation power suffices by itself, even for a very young pulsar (Metzger et al. 2017), which tends to discard this hypothesis and in particular the idea that FRBs would be a scaled-up version of the supergiant pulses of the Crab (Cordes & Wasserman 2016). On the other hand, dissipation of magnetic energy, as in magnetars (Thompson & Duncan 1996), appears to be sufficient even for normal magnetars (i.e. similar to the known Galactic objects) if efficiency is as high as $F_R/F_X \sim^{-2}$. Otherwise, decade to century old objects are needed. In the latter case, magnetar activity is expected to decrease measurably over a few years/decades, and DM/RM variations are expected from the young supernova remnant.

Practically, large bursts of energy are released by star-quakes, that is when the crust of the star, stressed by the huge magnetic field, eventually breaks releasing magnetic energy (Thompson & Duncan 1996). This in turn creates a large perturbation of the magnetosphere, eventually propagating into the wind zone†.

3.1 Magnetospheric models

These models assume that the radio emission is produced within the magnetosphere, and in this way they are the natural prolongation of the early papers on magnetar radio emission that pointed out a possible similarity to type III solar flares (Lyutikov 2002). It is indeed well established that the X-ray emission of Galactic magnetars comes from their magnetosphere, and therefore one may expect a putative radio counterpart to have the same origin. Recently, authors argued that the FRB rate from the Galactic FRB200428 was compatible with being the tail of the observed extragalactic FRB distribution (see Fig. 2, right). It follows from this argument that the Galactic FRB200428 is part of the same population of sources as other FRBs and, if one assumes magnetospheric radio emissions for magnetars, emissions of the general population are magnetospheric as well.

Several emission mechanisms have been proposed in the literature. The most commonly found is undoubtedly bunched curvature radiation, whereby bunches of electrons or positrons moving relativistically along field lines in the magnetosphere emit coherently provided that they share a common location both in position and velocity space. This mechanism has been recently shown to be able to provide a wide range of luminosities, from pulsars to FRBs (Cooper & Wijers 2021). However, this has also been criticised as an overly simplistic view of the plasma behaviour (Lyubarsky 2021), since it remains unclear how such coherent bunches could form, the model being being effectively a coherent addition of individual particle motion, and not a collective mode of the plasma. These authors advocate fast magnetosonic waves to convey the energy released in the star quake through the magnetosphere, arguing that such waves can eventually escape the magnetosphere. Other authors (Kumar & Bošnjak 2020) argue in favour of large-amplitude Alfvén waves conveying the energy outward until the plasma density is insufficient to sustain these waves. They then break into particle bunches radiating under the coherent curvature radiation mechanism. Some authors (e.g.) only refer to the pulsar emission mechanism, thereby assuming that the same mechanism that produces coherent emission responsible for pulsar radio emissions is likely to function as well in magnetars.

In this picture, the duration of a burst is naturally scaled with the magnetosphere light-crossing time, which is of the order of the millisecond. The occupied frequency band is not necessarily narrow, except if one relies on the Solar flare analogy (Lyutikov 2002), since type III flare have narrow spectral occupancy. However, the magnetosphere is particularly favourable to the phenomenon of radius-to-frequency mapping whereby emission frequency is connected to the altitude (or radius) of emission. This is due to the fact that all emission mechanisms scale either with the magnitude of the magnetic field or the radius of curvature of the local magnetic field (for curvature radiation) and both are monotonously decreasing with radius for simple magnetic geometry (e.g. dipole field). As a result, the spectral properties of the burst become geometric properties of the magnetosphere, similarly to the RVM model for radio pulsars (Radhakrishnan & Cooke 1969; Pétri 2017). Thus, by playing on the parameters of the magnetic field geometry, the line of sight, and the spin that makes the observer sweep through a given cross-section of the magnetosphere during a given burst, one can reproduce a broad range of temporal and spectral behaviours (Lyutikov 2020; Li & Zanazzi 2021). The sweep can also explain polarization swing.

In these models, an X-ray counterpart is expected with a luminosity ratio of $10^2 - 10^5$ compared to radio. This was seen for the Galactic FRB200428, but is undetectable with current instruments for extra-galactic sources. If future instruments were able to detect such counterparts, this would be a clear evidence in favour of the magnetar model. The fact that most X-ray bursts lack a radio counterpart may be interpreted in terms of

†In pulsars and magnetars, the wind zone is the zone beyond the light cylinder, while the magnetosphere is within. The light cylinder is the surface where an hypothetical plasma co-rotating with the star reaches the speed of light.

relative beaming Lu et al. (2020).

A variant is the low-twist magnetar model Wadiasingh & Timokhin (2019); Wadiasingh & Chirenti (2020); Wadiasingh et al. (2020). In this model, it is argued that the emission mechanism is the same as for pulsars. The originality is that, instead of appealing to young and powerful magnetars, this model appeals to old, slow stars. The argument is that old magnetars can have lower magnetospheric charge density unable to screen the onset of a highly efficient 'pulsar emission mechanism' when triggered by a star-quake pertubation.

3.2 Blast wave models

This model is derived from models for short gamma ray bursts (e.g. Lyubarsky 2014; Beloborodov 2017, 2020; Zhang 2020). It considers that, when a starquake occurs, its energy is conveyed through the magnetosphere by Alfvén waves, which eventually provoke magnetic reconnection near the light cylinder. Then, a plasmoid is ejected into the wind with a very high Lorentz factor, up to 10^5 (Beloborodov 2020). In addition, the wind is greatly enhanced during a quake episode due to intense magnetospheric perturbations, and a denser variable wind along with and a train of plasmoids may be produced. Some plasmoids may propagate at super-magnetosonic speeds within the previous ejecta and produce a strong shock wave. A cyclotron maser develops at the shock, responsible for coherent radio emission.

Emission is linearly polarized (e.g. Lyubarsky 2021), and weakly beamed due to the pancake-like shape of the plasmoid which occupies a broad solid angle as seen from the source while being relatively thin. Emission frequency scales with the local plasma frequency and therefore drops as the plasmoid propagates away from the star. It is argued that the duration of a burst at GHz frequency is compatible with a few milliseconds (Beloborodov 2017, 2020). Overall, FRBs should be seen in a wide frequency range, and an optical counterpart is expected in some models (Beloborodov 2020). So far optical follow-up observations gave only upper limits (Hardy et al. 2017; Tingay & Yang 2019; Kilpatrick et al. 2021).

3.3 Periodicity mechanisms

The intrinsic magnetar models summarised above predict repetitions without periodicity. We here examine present two additional complementary mechanisms compatible with the two observed periods.

Free precession results from the deformation of the star by the magnetic stress of the huge field of a magnetar (Levin et al. 2020; Zanazzi & Lai 2020). It is not so far observed in galactic magnetars, where it might be suppressed by superfluidity (Shaham 1977). Young magnetars, on the other hand, might be sufficiently hot to prevent superfluidity to set in, and allow precession with the required magnitude. One key prediction in this case is the rapid increase of the period over a few years.

In the frame of the low-twist model, for older magnetars, it has been proposed that periodicity might result from ultra-long spin periods (Beniamini et al. 2020).

Alternatively, it has been proposed that a magnetar might be in a close binary with a O/B star (Lyutikov et al. 2020). The wind of the companion enshrouds the magnetar, leaving only a relatively narrow corridor for radio emissions to escape the environment of the magnetar without excessive free-free absorption. Thus, the period is set by the orbit and the activity window by the width of the corridor. A key prediction is the variability of the activity window with frequency, due to the frequency dependence of absorption.

All three models have been suggested to explain the 3-day low-frequency lag of the repeater FRB180916 (Pleunis et al. 2021; Li & Zanazzi 2021).

4 Conclusions

A number of reviews on FRBs are a available in the literature. Let us mention the 'living theory catalog for fast radio bursts' (Platts et al. 2019)[‡] which is probably the most exhaustive listing of FRB models, including catastrophic events and non neutron-star scenarios. Observations are reviewed in particular in (Petroff et al. 2019, 2021). The review (Cordes & Chatterjee 2019) is probably the most advanced concerning propagation effects for FRBs. Let us use this opportunity to admit that propagation effects are one of the missing pieces of the current review, as this should be included in any model that aims at fully reproducing observations. There is also specialised review on emission mechanisms for FRBs, particularly related to blast waves and synchrotron masers (Lyubarsky 2021).

[‡]The catalog is available at `https://frbtheorycat.org/`.

References

Andersen, B. C., Bandura, K. M., Bhardwaj, M., et al. 2020, Nature, 587, 54, number: 7832 Publisher: Nature Publishing Group

Bagchi, M. 2017, The Astrophysical Journal, 838, L16, publisher: American Astronomical Society

Beloborodov, A. M. 2017, ApJ, 843, L26, _eprint: 1702.08644

Beloborodov, A. M. 2020, ApJ, 896, 142, _eprint: 1908.07743

Beniamini, P., Wadiasingh, Z., & Metzger, B. D. 2020, MNRAS, 496, 3390, _eprint: 2003.12509

Bochenek, C. D., Ravi, V., Belov, K. V., et al. 2020, Nature, 587, 59, bandiera_abtest: a Cg_type: Nature Research Journals Number: 7832 Primary_atype: Research Publisher: Nature Publishing Group Subject_term: Astronomical instrumentation;Compact astrophysical objects;High-energy astrophysics;Time-domain astronomy;Transient astrophysical phenomena Subject_term_id: astronomical-instrumentation;compact-astrophysical-objects;high-energy-astrophysics;time-domain-astronomy;transient-astrophysical-phenomena

Bochenek, C. D., Ravi, V., & Dong, D. 2021, The Astrophysical Journal Letters, 907, L31

Caleb, M., Keane, E. F., van Straten, W., et al. 2018, Monthly Notices of the Royal Astronomical Society, 478, 2046, aDS Bibcode: 2018MNRAS.478.2046C

Chatterjee, S., Law, C. J., Wharton, R. S., et al. 2017, Nature, 541, 58, aDS Bibcode: 2017Natur.541...58C

Cho, H., Macquart, J.-P., Shannon, R. M., et al. 2020, The Astrophysical Journal Letters, 891, L38

Collaboration, T. C., Amiri, M., Andersen, B. C., et al. 2020, arXiv:2001.10275 [astro-ph], arXiv: 2001.10275

Connor, L., Pen, U.-L., & Oppermann, N. 2016, MNRAS, 458, L89, _eprint: 1601.04051

Cooper, A. J. & Wijers, R. A. M. J. 2021, Monthly Notices of the Royal Astronomical Society, aDS Bibcode: 2021MNRAS.tmpL..84C

Cordes, J. M. & Chatterjee, S. 2019, Annual Review of Astronomy and Astrophysics, 57, 417

Cordes, J. M. & Wasserman, I. 2016, MNRAS, 457, 232, _eprint: 1501.00753

Cruces, M., Spitler, L. G., Scholz, P., et al. 2021, Monthly Notices of the Royal Astronomical Society, 500, 448

Dai, Z. G. 2020, ApJ, 897, L40, _eprint: 2005.12048

Dai, Z. G., Wang, J. S., Wu, X. F., & Huang, Y. F. 2016, ApJ, 829, 27, _eprint: 1603.08207

Dai, Z. G. & Zhong, S. Q. 2020, ApJ, 895, L1, _eprint: 2003.04644

Decoene, V., Kotera, K., & Silk, J. 2020, arXiv e-prints, 2012, arXiv:2012.00029

Farah, W., Flynn, C., Bailes, M., et al. 2018, arXiv:1803.05697 [astro-ph], arXiv: 1803.05697

Geng, J. J. & Huang, Y. F. 2015, ApJ, 809, 24, _eprint: 1502.05171

Hardy, L. K., Dhillon, V. S., Spitler, L. G., et al. 2017, Monthly Notices of the Royal Astronomical Society, 472, 2800, aDS Bibcode: 2017MNRAS.472.2800H

Hessels, J. W. T., Spitler, L. G., Seymour, A. D., et al. 2019, The Astrophysical Journal, 876, L23, publisher: American Astronomical Society

Hilmarsson, G. H., Spitler, L. G., Main, R. A., & Li, D. Z. 2021, publication Title: arXiv e-prints ADS Bibcode: 2021arXiv210712892H Type: article

Josephy, A., Chawla, P., Fonseca, E., et al. 2019, The Astrophysical Journal, 882, L18, aDS Bibcode: 2019ApJ...882L..18J

Kilpatrick, C. D., Burchett, J. N., Jones, D. O., et al. 2021, The Astrophysical Journal Letters, 907, L3

Kumar, P. & Bošnjak, Ž. 2020, Monthly Notices of the Royal Astronomical Society, 494, 2385

Kumar, P., Shannon, R. M., Flynn, C., et al. 2020, Monthly Notices of the Royal Astronomical Society, 500, 2525

Lawrence, E., Vander Wiel, S., Law, C., Burke Spolaor, S., & Bower, G. C. 2017, AJ, 154, 117, _eprint: 1611.00458

Levin, Y., Beloborodov, A. M., & Bransgrove, A. 2020, The Astrophysical Journal, 895, L30, aDS Bibcode: 2020ApJ...895L..30L

Li, D. & Zanazzi, J. J. 2021, The Astrophysical Journal, 909, L25, aDS Bibcode: 2021ApJ...909L..25L

Liu, Z.-N., Wang, W.-Y., Yang, Y.-P., & Dai, Z.-G. 2020, ApJ, 905, 140, _eprint: 2010.14379

Lu, W., Kumar, P., & Zhang, B. 2020, MNRAS, 498, 1397, _eprint: 2005.06736

Lu, W. & Piro, A. L. 2019, The Astrophysical Journal, 883, 40, aDS Bibcode: 2019ApJ...883...40L

Luo, R., Wang, B. J., Men, Y. P., et al. 2020, Nature, 586, 693, bandiera_abtest: a Cg_type: Nature Research Journals Number: 7831 Primary_atype: Research Publisher: Nature Publishing Group Subject_term: Compact astrophysical objects;Transient astrophysical phenomena Subject_term_id: compact-astrophysical-objects;transient-astrophysical-phenomena

Lyubarsky, Y. 2014, Monthly Notices of the Royal Astronomical Society, 442, L9

Lyubarsky, Y. 2021, Universe, 7, 56, number: 3 Publisher: Multidisciplinary Digital Publishing Institute

Lyutikov, M. 2002, The Astrophysical Journal Letters, 580, L65

Lyutikov, M. 2020, ApJ, 889, 135, _eprint: 1909.10409

Lyutikov, M., Barkov, M. V., & Giannios, D. 2020, The Astrophysical Journal, 893, L39, publisher: American Astronomical Society

Marcote, B., Nimmo, K., Hessels, J. W. T., et al. 2020, Nature, 577, 190

Marcote, B., Paragi, Z., Hessels, J. W. T., et al. 2017, The Astrophysical Journal Letters, 834, L8

Margalit, B., Beniamini, P., Sridhar, N., & Metzger, B. D. 2020, ApJ, 899, L27, _eprint: 2005.05283

Metzger, B. D., Berger, E., & Margalit, B. 2017, The Astrophysical Journal, 841, 14

Michilli, D., Seymour, A., Hessels, J. W. T., et al. 2018, Nature, 553, 182

Mottez, F. & Zarka, P. 2014, Astronomy and Astrophysics, 569, A86

Mottez, F., Zarka, P., & Voisin, G. 2020, Astronomy & Astrophysics, 644, A145, publisher: EDP Sciences

Nimmo, K., Hessels, J. W. T., Keimpema, A., et al. 2020, arXiv e-prints, 2010, arXiv:2010.05800

Pétri, J. 2017, Monthly Notices of the Royal Astronomical Society, 466, L73

Petroff, E., Hessels, J. W. T., & Lorimer, D. R. 2019, The Astronomy and Astrophysics Review, 27, 4

Petroff, E., Hessels, J. W. T., & Lorimer, D. R. 2021, Fast radio bursts at the dawn of the 2020s, Tech. rep., publication Title: arXiv e-prints ADS Bibcode: 2021arXiv210710113P Type: article

Platts, E., Weltman, A., Walters, A., et al. 2019, Physics Reports, 821, 1

Pleunis, Z., Michilli, D., Bassa, C. G., et al. 2021, The Astrophysical Journal Letters, 911, L3, publisher: American Astronomical Society

Popov, S. B. & Postnov, K. A. 2010, in Evolution of Cosmic Objects through their Physical Activity, ed. H. A. Harutyunian, A. M. Mickaelian, & Y. Terzian, 129–132, _eprint: 0710.2006

Radhakrishnan, V. & Cooke, D. J. 1969, Astrophysical Letters, 3, 225

Rajwade, K. M., Mickaliger, M. B., Stappers, B. W., et al. 2020, arXiv:2003.03596 [astro-ph], arXiv: 2003.03596

Shaham, J. 1977, The Astrophysical Journal, 214, 251, aDS Bibcode: 1977ApJ...214..251S

Smallwood, J. L., Martin, R. G., & Zhang, B. 2019, MNRAS, 485, 1367, _eprint: 1902.05203

Spitler, L. G., Herrmann, W., Bower, G. C., et al. 2018, The Astrophysical Journal, 863, 150, publisher: American Astronomical Society

Spitler, L. G., Scholz, P., Hessels, J. W. T., et al. 2016, Nature, 531, 202

Tendulkar, S. P., Bassa, C. G., Cordes, J. M., et al. 2017, The Astrophysical Journal, 834, L7, aDS Bibcode: 2017ApJ...834L...7T

Tendulkar, S. P., Gil de Paz, A., Kirichenko, A. Y., et al. 2021, The Astrophysical Journal Letters, 908, L12

Thompson, C. & Duncan, R. C. 1996, The Astrophysical Journal, 473, 322

Tingay, S. J. & Yang, Y.-P. 2019, The Astrophysical Journal, 881, 30, aDS Bibcode: 2019ApJ...881...30T

Voisin, G., Mottez, F., & Zarka, P. 2020

Wadiasingh, Z., Beniamini, P., Timokhin, A., et al. 2020, ApJ, 891, 82, _eprint: 1910.06979

Wadiasingh, Z. & Chirenti, C. 2020, ApJ, 903, L38, _eprint: 2006.16231

Wadiasingh, Z. & Timokhin, A. 2019, ApJ, 879, 4, _eprint: 1904.12036

Wang, F. Y., Zhang, G. Q., & Dai, Z. G. 2021, MNRAS, 501, 3155, _eprint: 1903.11895

Zanazzi, J. J. & Lai, D. 2020, ApJ, 892, L15, _eprint: 2002.05752

Zhang, B. 2020, Nature, 587, 45, number: 7832 Publisher: Nature Publishing Group

SF2A 2021
A. Siebert, K. Baillié, E. Lagadec, N. Lagarde, J. Malzac, J.-B. Marquette, M. N'Diaye, J. Richard, O. Venot (eds)

FAST RADIO BURSTS WITH CHIME

C. Ng[1] and the CHIME/FRB Collaboration

Abstract. A few days before SF2A 2021, the CHIME radio telescope released its first catalog which consists of over 500 FRB discoveries. In this article, we will review the CHIME/FRB project and discuss some of its highlight discoveries reported so far. We will end with a brief on-look at the next generation radio telescope facilities, which aim to improve localization capability of FRB surveys.

Keywords: Fast Radio Bursts, radio transient, radio telescope

1 Introduction

Since the first report of an extragalactic Fast Radio Burst (FRB) detection in 2007 (Lorimer et al. 2007), the origins of these bright, short-duration bursts of radio waves have been a highly contentious topic. Our knowledge of FRBs has been limited since only a few tens of cataclysmic FRBs were observed in this first decade. The FRB field has been revolutionized in the last few years, much of this is thanks to the hundreds of FRBs discovered by CHIME, the Canadian Hydrogen Intensity Mapping Experiment.

2 The CHIME/FRB system and its highlight discoveries

CHIME is a radio telescope located at the Dominion Radio Astrophysical Observatory (DRAO) in Penticton, British Columbia in Canada. CHIME has been built by students and researchers on the team. The construction took over three years and was completed in late 2017. It consists of four half-pipe like cylinders placed side by side, spanning an area of $100\,\mathrm{m}\times 80\,\mathrm{m}$. On each of the four focal lines is a linear array of 256 dual polarization clover-leaf antennas. This telescope design provides a much larger field-of-view (FOV) compared to a single dish radio telescope of comparable sensitivity. This is one of the reasons why CHIME has been such a game changer in the study FRBs: with the over 200-squared-degree FOV, CHIME has a proportionally higher chance in detecting FRBs bursting in *a priori* unknown location and time.

An overview of the CHIME data acquisition and real-time analysis pipeline can be found in CHIME/FRB Collaboration et al. (2018). To summarize, a Fast Fourier Transform (FFT)-based beamforming algorithm enables 1024 coherently pointed beams to be formed simultaneously to tile CHIME's FOV (Ng et al. 2017; Masui et al. 2019). We up-channelize the data to improve frequency resolution of our data to 24 kHz sampled at 0.983 ms to minimize the effect of intra-channel smearing. This intensity data output is searched for FRB signals using a tree-style dedipsersion algorithm called BONSAI, which covers a large parameters space up to a maximum dispersion measure (DM) of $13{,}000\,\mathrm{pc\,cm^{-3}}$. A ring buffer constantly stores a short window (up to 240 s) of the most recent baseband data, which allows us to trigger a baseband dump when a high signal-to-noise FRB candidate is detected. The localization of the bursts can then be refined during a subsequent offline analysis, as well as enable the extraction of any polarization information (Michilli et al. 2021). Below are some of the highlight discoveries CHIME has reported to-date.

2.1 A large population of FRBs

Within the first two months of operation, 13 new FRBs were reported by CHIME, providing proof that FRBs do exist at the relatively low frequency range of 400−800 MHz (CHIME/FRB Collaboration et al. 2019b). Between July 2018 and July 2019, CHIME has detected 536 FRBs (see Fig. 1), which formed the basis of its first Catalog release (CHIME/FRB Collaboration et al. 2021a).

[1] Dunlap Institute for Astronomy & Astrophysics, University of Toronto, 50 St. George Street, Toronto, ON M5S 3H4, Canada

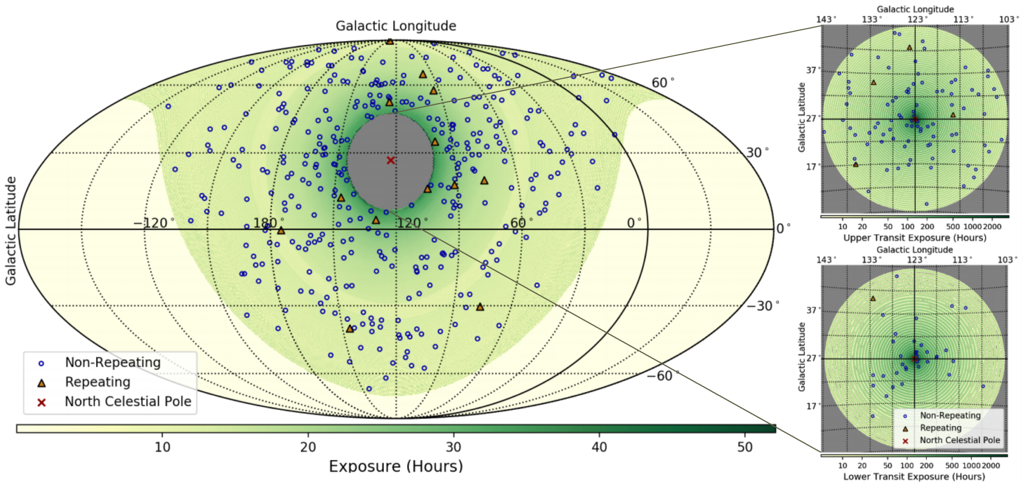

Fig. 1. The 536 FRBs reported in the CHIME Catalog 1. The colour scale represents the non-uniform exposure of CHIME as a function of sky position. The region around the North Celestial pole requires special treatment, since it is visible at CHIME twice a day at the upper (**top right panel**) and lower (**bottom right panel**) transients where the telescope sensitivity are very different. Figure adapted from CHIME/FRB Collaboration et al. (2021a).

From this FRB sample, we conclude that the FRB luminosity function is consistent with a power-law index of $\alpha = -1.40 \pm 0.11$, which is what is expected from an Euclidean sky distribution. The overall sky rate is 818 ± 64 /sky/day, considering FRBs with fluence ≥ 5 Jy ms, at DM $\geq 100\,\mathrm{pc\,cm^{-3}}$ and with scattering time $\tau_{600} \leq 10$ ms. There is no evidence for Galactic latitude dependence of the FRB sky distribution (Josephy et al. 2021), contrary to what was suggested in some of the earliest FRB literature. Furthermore, we detect significant correlation between the Catalog 1 FRBs and large scale structure of the Universe (Rafiei-Ravandi et al. 2021). We obtain a p-value of $\sim 10^{-4}$ after accounting for look-elsewhere effects in redshift and angular scale. This is observed to be true over a wide range of redshifts between $0.3 \leq z \leq 0.5$.

2.2 Repeating FRBs

The CHIME Catalog 1 also confirmed the existence of multiple FRB populations, notably one that consists of one-off, cataclysmic bursts and one that consists of repeating FRBs. We have compared the morphology of the one-off and the repeating FRBs. From Pleunis et al. (2021a), it is apparent that repeating FRBs have wider pulses and narrower emission bandwidths compared to the non-repeating population. We also note that no obvious differences are present in other parameters such as DM, scattering time, and the flux density. In order to facilitate quick follow-up observations by other telescope facilities, CHIME is now releasing any new and latest repeating bursts on a public server*.

Repeating FRBs are particularly interesting because it is easier to obtain more information of these bursts through re-observations. CHIME has thus far published 18 repeaters (CHIME/FRB Collaboration et al. 2019a,c; Fonseca et al. 2020). Fig. 2 gives a visual representation of the bursts occurrence of these 18 sources. Already by eye we can tell that they repeat on a range of cadence, although there is some level of clustering. Upon a more in-depth analysis, we find that one of the repeaters, FRB 20180916B (nicknamed R3 within the collaboration and in Fig. 2) has a 16.35-d periodic activity cycle (The CHIME/FRB Collaboration et al. 2021). The activity window lasts for roughly 4-d each time. One LOFAR team conducted simultaneously observations with CHIME and the upgraded Giant Metre Wavelength Radio Telescope (uGMRT). They have shown that the burst activity is systematically delayed toward lower frequencies by about 3 d from 600 to 150 MHz (Pleunis et al. 2021b). Furthermore, one other repeater FRB 20191221A shows sub-second periodicity among its multi-component profile (CHIME/FRB Collaboration et al. 2021b).

*`https://www.chime-frb.ca/repeaters`

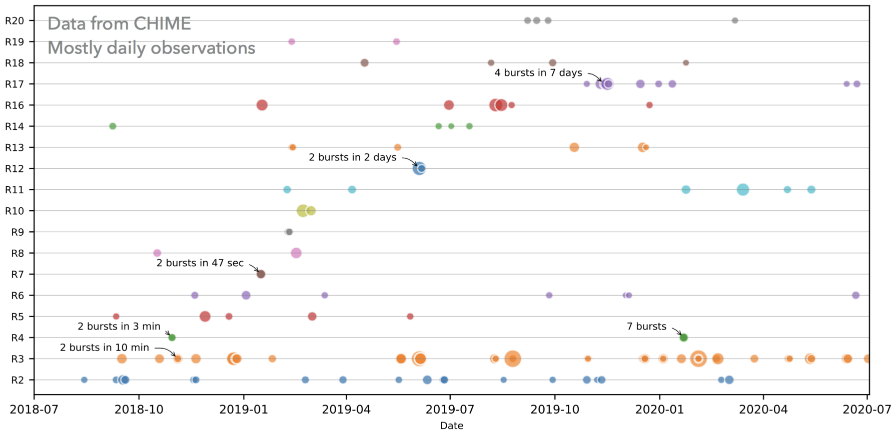

Fig. 2. The burst occurrence of the first 18 repeating FRBs discovered by CHIME. Figure by Shriharsh Tendulkar.

2.3 Galactic magnetar

Another important result CHIME obtained is the detection of an FRB from a Galactic magnetar. On April 28, 2020, CHIME detected an FRB from magnetar SGR 1935+2154 (CHIME/FRB Collaboration et al. 2020). This event was also noticed by the STARE2 collaboration (Bochenek et al. 2020). The energetics of this burst falls between the FRB and the Galactic pulsar population, potentially providing a path to close the existing energy gap. It is tempting to speculate that all FRBs are produced by magnetars. Indeed, a number of FRB emission models proposed involve magnetars (see, e.g. Metzger et al. 2017). However, some FRBs have now been localized to the outskirts of galaxies (see, e.g. Marcote et al. 2020), whereas Galactic magnetars are preferentially located near the Galactic plane. In addition, the morphology of this FRB from SGR 1935+2154 is somewhat atypical, and it would be premature to conclude that this burst can serve as a representative for all FRBs. Nonetheless, the importance of this discovery has been recognized by the Science magazine which has ranked it one of the most significant breakthroughs in 2020[†], second only to the discovery of the covid vaccine.

2.4 Low-DM FRBs

A few other CHIME FRBs have been localized to their host galaxies. One of them has been associated with M81, a spiral galaxy in the local volume at 3.6 Mpc (Bhardwaj et al. 2021a). The Precise team has further pin-pointed the FRB to be from a Globular Cluster (Kirsten et al. 2021). Another FRB has been found to be from NGC3252 (Bhardwaj et al. 2021b), a star-forming spiral galaxy at 20 Mpc. These two are the nearest localized FRBs so far, apart from the Galactic magnetar FRB mentioned in Section 2.3. These nearby FRBs are particularly interesting, since they allow easier multi-wavelength follow-up observations, and hence this sub-population might provide the best hope in uncovering the origin of FRBs.

3 Localization with outriggers and CHORD

While CHIME has been extremely successful in discovering a large number of FRBs, it lacks the required localization precision to pin-point the exact origin of these extragalactic bursts. The CHIME/FRB Outriggers project is being deployed which will provide baseline of the order of 1000 m and hence greatly improve localization capability. A prototype of the CHIME outrigger has been set up at the Algonquin Radio Telescope, and this system has detected and localized FRBs with a localization uncertainty of tens of milliarcseconds (Cassanelli et al. 2021), a significant improvement over CHIME alone.

Looking ahead, CHORD is a \$20 M experiment (Vanderlinde et al. 2019) whose budget has just been approved by the Canadian Research Council. CHORD will have ultra-wideband receivers covering 300 − 1500 MHz. It will have a highly sensitive core array consisting of 512 6-m dishes located right next to CHIME as well as multiple outrigger stations. CHORD is expected to provide both the large number of FRB detections as well

[†]https://vis.sciencemag.org/breakthrough2020/#/finalists/found:-elusive-source-of-fast-radio-bursts

as milliarcsecond localization capability. CHORD is expected to come online within the next few years and it is a promising instrument to pave the path to use FRB as cosmological probes.

4 Conclusion

The CHIME Catalog 1 consists of 536 FRBs including 18 repeaters. The FRB event rate as determined from the CHIME data is about 800 bursts/sky/day with an Euclidean distribution. FRBs appear to be correlated with galaxy large-scale structure over a wide redshift range. There is evidence that there are multiple FRB populations, notably one-off vs repeating FRBs. These two samples have different burst widths and emission bandwidth distribution. One of the repeaters shows periodicity in its activity cycle, and another one has sub-second periodicity within its multi-component profile. Furthermore, an FRB has been associated with a Galactic magnetar, while some low-DM FRBs have been identified with their host galaxies. The CHIME/FRB Outriggers Project is in progress and will provide better localization capability thanks to the longer baselines. The next step up will be enabled by the CHORD experiment, which is expected to discover thousands of FRBs with milliarcsecond localization, potentially allowing FRBs to be used as cosmological probes.

We are very grateful for the warm reception and skillful help we have received from the staff of the Dominion Radio Astrophysical Observatory, which is operated by the National Research Council of Canada. We acknowledge sup- port from the Canada Foundation for Innovation, the Natural Sciences and Engineering Research Council of Canada, the B.C. Knowledge Development Fund, le Cofinancement gouvernement du Quebec-FCI, the Ontario Research Fund, the CIfAR Cosmology and Gravity program, the Canada Research Chairs program, and the National Research Council of Canada. We thank Xilinx University Programs for their generous support of the CHIME project, and AMD for donation of test units.

References

Bhardwaj, M., Gaensler, B. M., Kaspi, V. M., et al. 2021a, ApJ, 910, L18

Bhardwaj, M., Kirichenko, A. Y., Michilli, D., et al. 2021b, arXiv e-prints, arXiv:2108.12122

Bochenek, C. D., Ravi, V., Belov, K. V., et al. 2020, Nature, 587, 59–62

Cassanelli, T., Leung, C., Rahman, M., et al. 2021, Localizing FRBs through VLBI with the Algonquin Radio Observatory 10-m Telescope

CHIME/FRB Collaboration, Amiri, M., Andersen, B. C., et al. 2021a, The First CHIME/FRB Fast Radio Burst Catalog

CHIME/FRB Collaboration, Amiri, M., Bandura, K., et al. 2018, ApJ, 863, 48

CHIME/FRB Collaboration, Amiri, M., Bandura, K., et al. 2019a, Nature, 566, 235

CHIME/FRB Collaboration, Amiri, M., Bandura, K., et al. 2019b, Nature, 566, 230

CHIME/FRB Collaboration, Andersen, B. C., Bandura, K., et al. 2019c, CHIME/FRB Detection of Eight New Repeating Fast Radio Burst Sources

CHIME/FRB Collaboration, Andersen, B. C., Bandura, K., et al. 2021b, Sub-second periodicity in a fast radio burst

CHIME/FRB Collaboration, Andersen, B. C., Bandura, K. M., et al. 2020, Nature, 587, 54

Fonseca, E., Andersen, B. C., Bhardwaj, M., et al. 2020, The Astrophysical Journal, 891, L6

Josephy, A., Chawla, P., Curtin, A. P., et al. 2021, No Evidence for Galactic Latitude Dependence of the Fast Radio Burst Sky Distribution

Kirsten, F., Marcote, B., Nimmo, K., et al. 2021, A repeating fast radio burst source in a globular cluster

Lorimer, D. R., Bailes, M., McLaughlin, M. A., Narkevic, D. J., & Crawford, F. 2007, Science, 318, 777

Marcote, B., Nimmo, K., Hessels, J. W. T., et al. 2020, Nature, 577, 190–194

Masui, K. W., Shaw, J. R., Ng, C., et al. 2019, ApJ, 879, 16

Metzger, B. D., Berger, E., & Margalit, B. 2017, ApJ, 841, 14

Michilli, D., Masui, K. W., Mckinven, R., et al. 2021, The Astrophysical Journal, 910, 147

Ng, C., Vanderlinde, K., Paradise, A., et al. 2017, in 2017 XXXIInd General Assembly and Scientific Symposium of the International Union of Radio Science (URSI GASS), 1–4

Pleunis, Z., Good, D. C., Kaspi, V. M., et al. 2021a, arXiv e-prints, arXiv:2106.04356

Pleunis, Z., Michilli, D., Bassa, C. G., et al. 2021b, ApJ, 911, L3

Rafiei-Ravandi, M., Smith, K. M., Li, D., et al. 2021, arXiv e-prints, arXiv:2106.04354

The CHIME/FRB Collaboration, Andersen, B. C., Bandura, K., et al. 2021, arXiv e-prints, arXiv:2107.08463

Vanderlinde, K., Liu, A., Gaensler, B., et al. 2019, in Canadian Long Range Plan for Astronomy and Astrophysics White Papers, Vol. 2020, 28

Session 20

L'observatoire dans son environnement social

OBSERVATORIES AND THEIR SOCIAL ENVIRONMENT: THE CASE OF PIC DU MIDI OBSERVATORY

R. Cabanac[1]

Abstract. The case of Pic du Midi Observatory is an interesting one. The end of its scientific operations were announced in 1993 by the French National Agency CNRS. But the observatory activities were saved by a national and international social reaction, triggering an original solution. The summit was parted into a scientific administration comprising Paul Sabatier University (Toulouse) and CNRS, and a public administration comprising the Regional government, and local cities and villages. The public administration was endowed with the task of maintaining buildings in a sustainable fashion with incomes from touristic visits of the Summit. This organisation turned to be very efficient. In 2021, Pic du midi Observatory is on a dynamic track, growing fast both touristically and science wise. This communication describes Pic du midi organisation in 2021 and the reasons that concurred towards it.

Keywords: observatory, history, social

1 Introduction

The observatory of Pic du Midi de Bigorre (2877 m, N 42°56'11", E 0°8'34") is the first high-altitude site in the world (1872). Its history flows throught two world wars, and a fair share of the emergence of the Modern World. Its meteo records span almost 150 years, including temperature, humidity, winds, and ozone measurements. This long history of science observations at Pic du Midi encompasses a broad range of disciplines, readers interested in Pic du Midi history may read Sanchez (2014); Davoust (2014). Among the numerous sciences that Pic du Midi hosted in his history, one may cite Meteorology, Geology, Glaciology, Atmospheric Sciences (Thunder, Sprites, Chemistry), Botanics, Studies of Cosmic Rays, Nuclear and Particle Physics, Medical Studies, Earth Magnetism, Radioactivity Studies, Lunar cartography, Small Planets and planetary observations, Studies of galaxies, Cosmology, Stellar Magnetism, Solar studies and Coronagraphy, Ethology, Ecology and most recently climate studies. This fantastic wealth of data gathering continues at its best in 2021 thanks to the contemporaneous organisation that emerged in the latest part of the twentieth century. We will describe here the way Pic du Midi works in 2021, describe how this organisation emerged, and conclude on a few ongoing emblematic projects for the future. (This communication is part of two, interested readers may look at the S22 communucation on Pic du Midi patrimony).

2 Pic du Midi in 2021

In 2021, the activities of Pic du Midi Observatory are shared between two independent administrations, one administration takes care of science, and the other is in charge of Education and Public Outreach (EPO) activities. The two partners have separate budgets, their management is independent and most of their activities are non-overlapping. This organisation turns out to be very efficient for fund raising, because each partner pursues distinct objectives. Hence, any funding administration knows when money is spent on the public side or the science side. Thanks to this clarification, over the past ten year, about 10 million euros were invested on various science projects, and similar amounts on public infrastructures.

[1] IRAP, OMP, Université de Toulouse, CNRS, CNES, UPS, (Toulouse), France.
ORCID of the author: http://orcid.org/0000-0001-6679-2600

2.1 Science

The science activities at Pic du midi are managed by the Observatoire Midi Pyrénées (OMP), component of the University of Toulouse 3 Paul Sabatier. The science staff is shared between CNRS (9 people) and the University (15 people). Pic du midi comprises 3 national services; the Telescope Bernard Lyot, the Atmosphere science platform (P2OA, European network Actris, ...), the Solar Corona service (coronagraph) and a national platform welcoming researchers and experiments at the summit all year round. In addition to national services, 3 telescopes are active (T1M, managed by IMCCE small planets team, T60 managed by OMP, Jean-Rösch telescope managed by IRAP) and geophysics experiments (GPS for tectonics, Bonner sphere neutron spectrograph of ONERA, fast cameras for Luminous transitory Events or sprites, ...). Apart from long-term experiments, numerous short-lived public or private experiments use Pic du Midi for its qualified staff and pristine observing conditions. Pic du midi astronomers are actively involved in teaching astronomical observation techniques to Master students all over France through training sessions with small telescopes and state-of-the-art instruments. The science future of Pic du midi is oriented towards a world-leading instrumental suite on the 2-m TBL, (i) a visible spectro-polarimetre and velocimeter Neo-Narval, (ii) IR spectro-polarimetre and velocimetre SPIP, and (iii) a new bonnet allowing observers to use both instruments simultaneously. The science goal is to study stellar magnetism as well as exo-planetary systems evolution from birth to death, in particular exo-Earths in habitable zone. In addition to the TBL, A new coronagraph in the making will be the largest in the world studying the solar polarised corona in highly-ionised species.

2.2 Public

150000 people visit the summit every year. The public administration comprises ca. 40 staff members and manages the public flow. The board of the public administration is composed of regional and local government members and the mayors of close by cities. The public administration runs a 25-bed hotel at the summit, a restaurant that equally serves tourists and science staff, and a tourist shop at the cablecar base. Thanks to a dynamic funding program, the public administration can invest every year in new outreach capabilities. As of 2021, the summit hosts a modern museum, a planetarium, a set of open terraces, connected history tablets lead visitors to a rich visit of the patrimonial summit. A wide variety of activities are offered to culturally diverse groups, from downhill skying, biking, sight-seeing, to science-oriented visits of the summit. Night visitors are led by an EPO professional, they can visit the science premises and star-gaze through small telescopes set on the terrace. An important duty of the public administration is to perpetuate the long-term science activities at Pic du Midi. Among its supporting activities, access to the summit from the skying resort, power and food supplies, and sanitary infrastructures are central to the observatory science capabilities. Among the on-going public projects are a museum at the nearby Tourmalet Pass (a well-known Tour de France stop) dedicated to night-sky protection and rehabilitation of a mountain refuge connected to the summit by cablecar to increase tourists night access.

3 The making of Pic 2000

Today idyllic situation has emerged from a much darker period of the 1990s. After a long period of prolific science activities over the XXth century, the Pic du Midi stalled in the 80s-90s leading the french funding agency CNRS to stop investments at the summit while redirecting investments to other international sites, until 1993 where the complete close down of the Pic du Midi Observatory was announced by CNRS. That announcement triggered a large support over France and international communities from scientists and public likewise. The OMP director Michel Blanc, the local MP and senator François Fortassin and State Prefect Jean Dussourd worked together to create an original solution to "save Pic du Midi". The public administration was born with the primary goal to perpetuate science activities at the summit by opening part of the premises to the public. More than 30 million euros were invested in a cable car and summit infrastructures. That was the beginning of a fruitful collaboration between University Paul Sabatier and a public administration. After a transition period when the old users and the new administration learned how to work with the other partner, a clear synergy emerged and science re-invented itself, creating citizen science projects fully relying on volunteers and sponsor (Fiducial) to run the coronagraph (responsible JC Noëns) years before the internet citizen science initiatives. The contract between University Paul Sabatier and the public administration runs over 30 years, ending in 2029. Partners are already working on new secure long-term contracts to pursue the successful adventure.

Fig. 1. Illustrations of activities at Pic du Midi. **Top left:** Museum, **Top right:** training session on astronomical observing techniques with Masters students of Toulouse, **Top right:** artist view of the future science building in the making (opening 2023) for science workshops, training sessions, centralised control of summit telescopes and experiments .

4 Projects for the future

Among projects that emerged because of the current management of the Pic du Midi, three are worth mentioning: The International Darksky Association Reserve, the new science building, and the UNESCO World Heritage project.

4.1 IDA reserve

The idea to preserve the pristine night sky of Pic to Midi through an International Darksky Association Reserve dubbed RICE in French for Réserve Internationale de Ciel Etoilé (https://picdumidi.com/en/discover-the-pic-du-midi/rice-en) was launched by François Colas (IMCCE, OPM), responsible of Pic du Midi T1M, immediately supported by University Paul Sabatier (OMP), and soon delegated to the Public administration that provided manpower and resources. The IDA reserve was the first of its kind in Europe in 2013. In 2021, the IDA reserve covers 700 km^2 of core area around Pic du Midi over ca. 200 nearby villages. The key-element to a successful future was to involve, from the beginning, institutional partners (mayors, MP, State), technical experts (Energy Supply administration responsible of developing public lighting for the area), and Pic du Midi partners (scientists, EPO experts). Over the past years, the RICE successfully replaced thousand of light points around Pic du Midi and launched campaigns of night sky protection leading many villages to switch-off public lights midnight to 5 am.

4.2 New building: Dauzère-Soler

Although, most of data gathering is today performed in an autonomous way (specially atmosphere science experiments), our capabilities to welcome researchers, astronomers and students is of the essence to a bright science future of Pic du Midi. This is the goal of a new building erected in 2021 (opening 2023) to allow ca. 30 scientists to stay at the summit for a few days. This new building will also provide a 40-seat conference room, technical rooms, a network room and a centralised control room to run all telescopes of the summit days and nights. A new dome is provisioned on the new building top, as well as a larger experiment area for atmosphere science experiments. The new building will allow workshops and training sessions for a large science community, opening a new domain of science activities at the summit.

4.3 UNESCO World Heritage

The Pic du Midi was the first high-mountain observatory to be built in the world, and one of the last pioneering site still active in the XXIst century. Its long science adventure and history of 150 years generated a rich patrimony. The fact that the summit is a connecting site between a larger public and scientists is very unique in the world today. All these characteristics argue for an outstanding universal value under criteria III and IV (https://whc.unesco.org/en/criteria/) for a nomination to UNESCO World Heritage. The public administration, the University Paul Sabatier and the State prefect work together to make that happen in the coming years. If the site is nominated, it will attract international visitors and preserve its science activities for the foreseeable future. Becoming a UNESCO World Heritage is a long two-step process. First, the site must join the French national indicative list. This shall happen in the late months of 2021, and then build a site management document detailing how partners will work together to protect the site. An important point of this UNESCO World Heritage is that science activities are at the heart of the outstanding universal value, they are what needs to be protected and developed, the summit historical artefacts are subject to evolve to support this universal science adventure.

5 Conclusions

After 150 years of science observations at Pic du Midi, our duty is to pass this extraordinary site to future generations in the best state possible to continue this Human adventure. Each year, tens of thousands of visitors can admire the panorama and learn about the science advances done at Pic du Midi. Maintaining such an high-mountain observatory is a difficult task, demanding dedication and hard work. Thanks to the dedication of the staff working at the summit, from both Science and Public Administrations, we are today is a good position to face this challenging task. Ongoing projects both on the science and public sides allows us to claim that the best is to come at Pic du Midi Observatory. Two conditions are mandatory to keep Pic du Midi future bright, one, visitors must continue to support the science activities and two, the funding agency CNRS and University Paul Sabatier must continue to invest in people at the summit. Until today, those two conditions were filled, let's hope that this will continue in the coming years!

References

Davoust, E. 2014, Pic du Midi: cent ans de vie et de science en haute montagne, 1st edn. (65500 Vic-en-Bigorre: MSN)

Sanchez, J.-C. 2014, Le Pic du Midi de Bigorre et son Observatoire, 1st edn. (BP 1503 29, rue Carrerot 64015 Pau: Editions CAIRN), www.editions-cairn.fr

SF2A 2021
A. Siebert, K. Baillié, E. Lagadec, N. Lagarde, J. Malzac, J.-B. Marquette, M. N'Diaye, J. Richard, O. Venot (eds)

REPORT FROM THE 2021 SF2A SESSION : "THE OBSERVATORY IN ITS SOCIAL ENVIRONMENT"

P. Marichalar[1], M. Boccas[2], R. Cabanac[3], P. Cox[4], E. Lagadec[5], J. Lamy[6], P. Léna[7], C. Moutou[8], F. Pitout[9] and A. Saint-Martin[10]

Abstract. This session was proposed and moderated by **Pascal Marichalar**, sociologist and historian at the CNRS French National Centre for Scientific Research (where he is a member of the Institute for Interdisciplinary Research on Social Issues). The session was not recorded in order to give free rein to discussions on subjects which can be touchy. The objective was to initiate a debate on the historical, political, economic, social and environmental stakes of the installation and operation of astronomical observatories on a territory - this both in the perspective of being able to continue the scientific work in the future, and with the objective of not reproducing the unequal relations with the local communities which are sometimes inherited from the past. Discussions were rich.

The starting point of the reflection was the following. Since 2014, protests have been taking place on the access road to the Mauna Kea volcano in Hawai'i in opposition to the Thirty Meter Telescope (TMT) project carried by an international consortium. The protesters, who at times numbered in the thousands, identifiy as kia'i (protectors) of the mountain, opposed not to astronomy per se, but to the logic of land grabbing and the way in which people and institutions from outside the island community decide the fate of these lands - whether for tourism, military development, real estate promotion, or scientific activity. They recall that Hawai'i was an independent nation whose monarchy was overthrown by a coup in 1893, with the support of the U.S. Navy, followed by unilateral annexation by the United States in 1898 (Hawai'i became the 50th U.S. state in 1959). One of the world's most important astronomical observation sites is thus at the center of political and social issues that reach far beyond it. In its 2021 convention, the American Astronomical Society CASCA announced that its support for the TMT (of which Canada is a potential partner) is now conditional on the Hawaiian population expressing its agreement. This important decision raises other questions, however, since under the current framework of Hawaiian government, there is no representative body of a native Hawaiian population, whose contours are themselves not clearly delineated.

The Mauna Kea conflict, which historical research shows is not new (the first protests against the development of astronomy on the mountain date back to the early 1970s), is a reminder that astronomical observatories are always built somewhere, even though site-testing campaigns usually insist on a site's remoteness from potentially disturbing human activity. The construction of an observatory supposes to mmake use (and take possession) of a parcel of land, sometimes of a significant surface (one thinks of the radio telescope arrays). This land is generally situated in a region which has remained preserved from the damage of human "development", because of an express will to protect the environment or because of a difficulty to exploit the environment (and often both together). In spite of the regular insistence on the "deserts" in which the observatories will be inserted, there is always a past and present human presence.

[1] IRIS - Campus Condorcet, Aubervilliers
[2] European Southern Observatory, Chile
[3] IRAP, Université de Toulouse, CNRS, CNES, UT3, Toulouse
[4] Sorbonne Université, UPMC Université Paris 6, CNRS, UMR 7095, Institut d'Astrophysique de Paris
[5] Université Côte d'Azur, Observatoire de la Côte d'Azur, CNRS, Laboratoire Lagrange
[6] CERTOP – UMR 5044 – Université Toulouse Jean Jaurès
[7] LESIA, Observatoire de Paris, PSL, CNRS, Sorbonne Université, Université de Paris
[8] Université de Toulouse, CNRS, IRAP
[9] IRAP, Université de Toulouse 3/CNES/CNRS
[10] Centre européen de sociologie et de science politique, Paris

The first block of interventions was centered on the case of Mauna Kea in Hawai'i.

Claire Moutou recounted some impressions of her experience as the resident astronomer of the Canada-France-Hawai'i Telescope, at a time when the first anti-TMT protests were taking place on Mauna Kea. While living there for several years allows for greater familiarity with local political and historical issues, it does not avoid uncomfortable situations where the "expat" astronomer comes to embody, for some, a history of conflict, dispossession and alienation.

Pascal Marichalar went back over the history of the access road to the volcano, from the first layout in the 1930s to the present day, showing how the question of accessibility to an astronomical observatory can be problematic. The astronomers want to be able to easily access their workplace, but are concerned about other mountain users who might come if the road is improved, and disrupt scientific activities. The opponents of the TMT recall that the road was built on "public lands trust" land that is supposed to be used for the benefit of the native Hawaiian population - finally, the road is left in an intermediate and dangerous state of progress that is not suitable for anyone.

The second block of interventions was centered on astronomical observatories in France. **Jérôme Lamy** described the history of the Toulouse Observatory in the 19th century, which was first set up at a distance from the city, but was overtaken by urbanization. The conceptions that astronomers had of their natural and social environment played a role in the way in which they occupied this space. Surrounded by an increasingly overwhelming city, Toulouse observers at the beginning of the 20th century envisaged an even greater distance - eventually heading to the Pic du Midi.

Rémi Cabanac described the recent history of the Pic du Midi Observatory. The site, at one time threatened by the budget cuts linked to the installation of telescopes abroad, succeeded in obtaining perennial financing by opening up to its regional environment. Contrary to what one might have thought, the activities of animation and use of the site are no longer thought of as detrimental to the astronomical activity, but have become on the contrary the condition of its functioning and of a relatively harmonious integration with the environment.

Arnaud Saint-Martin told the story of the first years of existence of the Haute-Provence Observatory, by making the link with the evolution of the conception of what an observatory should do (observatory of services, or of fundamental research). This history is also the one of the meeting between a remote rural environment and Parisian scientists, with perspectives on both sides on what the village of Saint-Michel (renamed Saint-Michel l'Observatoire) should become.

The third block of interventions was dedicated to observation abroad by French astronomers. **Eric Lagadec** evoked some of the projects he is part of to carry out astronomy in Africa with African astronomers. In particular, he mentioned stellar occultation campaigns in Senegal. These initiatives take as a starting point the inequality of academic and scientific means between France and many African countries without professional observatories, and aim to mitigate the effects by sharing resources, equipment, training and support to local initiatives.

Frédéric Pitout described his experience as an observing astronomer at the EISCAT ionospheric sounding and heating facilities in Tromsø and Spitsbergen (Norway). He told of the precautions to be taken in a context where electricity supply is scarce, where observations can have an effect on flights transiting through the local airport, and where the emission of radio waves has been the object of suspicion from some members of the local community, in the context of conspiracy theories but also of very real geopolitical tensions.

The fourth and final block of interventions focused on the case of Chile. Since the 1950s, this country has been invested by Western scientific powers for the development of astronomical observatories. The "convenio" governing the collaboration between ESO and Chile dates from 1964, and the first telescope at La Silla received its first light in 1969. The military coup of September 11, 1973 installed General Augusto Pinochet in power (he would remain in power until 1990). It was with Pinochet that at the end of the 1980s, the ESO negotiated to have access to a new piece of land on Cerro Paranal, where the VLT/VLTI would be built. In the 1990's, an important legal conflict almost caused the project to fail: a Chilean family claimed ownership of the land that Pinochet was not allowed to give up, there was indignation that ESO workers did not have the right to unionize, and the Chilean scientific community demanded preferential access to the telescopes, as was already the case for observatories managed by the United States. The agreement reached in the mid-1990s allowed the partnership to be redrafted on a sounder basis.

Pierre Léna shared his experience of the history of relations between ESO and Chile, from the 1970s to today, which he followed closely as one of the founding fathers of the VLT. **Pierre Cox**, as former director of ALMA, spoke about the importance of the ancient presence of the Atacameño people and the initiatives put in place by the ALMA observatory to value their culture rather than invisibilize them. **Maxime Boccas** explained the history of the recruitment policies of engineers and technicians by the ESO in Chile, and the concern to have a balance between "expats" and Chileans, less and less difficult to reach because of the development of higher education in the country, and truly competitive salaries.

At a time when Chile is beginning an unprecedented constitutional process, and as the construction of the ELT has begun on Cerro Armazones, the partnership between European astronomers and Chile seems to have reached a more egalitarian stage than in the past - but a lot still remains to be done, notably because of the blatant economic and social inequalities that still exist.

SF2A 2021
A. Siebert, K. Baillié, E. Lagadec, N. Lagarde, J. Malzac, J.-B. Marquette, M. N'Diaye, J. Richard, O. Venot (eds)

VALORISING THE SCIENTIFIC HERITAGE OF ABBADIA OBSERVATORY CASTLE

F. Pitout[1], R. Primout[2] and C. Davadan[3]

Abstract. We present a peculiar place in the French astronomical landscape: the Château Observatoire (literally observatory castle) Abbadia, home of Antoine d'Abbadie in the XIXth century. This place is particularly interesting because of the historical instruments is contains and Antoine d'Abbadie corresponded with many scientists and personalities of his time. Our goal is to preserve and promote the heritage of Abbadia and of his past owner. To do so, we have searched interesting old books in the castle's library, we have gone through the correspondence of Antoine d'Abbadie, archived in Bayonne, and we have designed activities based of this heritage. In addition, we organise teacher training sessions at Abbadia, mixing heritage and modern knowledge.

Keywords: astronomical heritage, instruments, correspondence

1 Introduction

Antoine d'Abbadie d'Arrast (1810-1897) was born in a very wealthy family, inherited quite young a fortune, and lived on unearned incomes his whole life. He had therefore all the time in the world to indulge his passions : travels, languages (he wrote French-Basque and French-Amharic dictionaries) and science (especially astronomy, geodesy, and geomagnetism). He had his house built in Hendaye in the Basque Country, in the south west of France. The Château Observatoire Abbadia, building of neogothic style (figure 1), was both his residence and his place of work (Delpech 2012; Briot 2016). During his life, Abbadie acquired many scientific books and journals which he kept in the castle library. In addition, he equipped is home and the surroundings with instruments. Astronomical and geomagnetic measurements were made and the results recorded in notebooks. Most of these documents are still at Abbadia and in a good general state of conservation, but they are not accessible to the public; worse: they were not all inventoried. We carried out this inventory work and set out to select the works that were of particular interest. In addition, Antoine d'Abbadie had epistolary exchanges with many scientists of his time. This rich correspondence, kept at the Bayonne Departmental Archives, has also been the subject of a selection which will be digitized. Finally, the instruments in the Observatory Castle have a heritage interest that should be enhanced. The final objective of the presented work is threefold: to bring a new perspective to Antoine d'Abbadie and his fascinating observatory castle; make this rich heritage accessible to the public; offer educational activities and resources for education and outreach (Primout 2018).

2 Instruments at Abbadia

2.1 Antoine d'Abbadie and the metric system

First of all, let us emphasize that Antoine d'Abbadie was convinced that the metric system, created shortly after the French revolution, should be adopted. Clocks in metric system can still be found at Abbadia (figure 2).

[1] IRAP/OMP; Toulouse, France
[2] DAAC, Bordeaux, France
[3] Académie des sciences, Hendaye, France

Fig. 1. Abbadia seen from the North (Wikimedia)

Fig. 2. Decimal clock with 100 ”minutes”, 100 ”seconds” and 4 quarters of a day (or ”quadrants”).

2.2 Astronomical instruments

Abbadie acquired several portable refractors he used during his trips but the main instrument of Abbadia is a so-called meridian telescope; the same model as those used for the ”Carte du Ciel” project, an international endeavour to map the celestial vault. Abbadia’s meridian telescope is the only of its kind as it is graduated in grads, not in degrees (figure 3). It is still used now and then for pro-am projects (Arlot et al. 2018).

Abbadia was also bored through to act as a structure for a huge refractor pointing towards the top of La Rune, the highest mountain in the Basque Country. Antoine d’Abbadie wanted to study the refraction properties of the atmosphere but he failed to obtain convincing results.

Fig. 3. Meridian telescope's circle graduated from 0 to 400 grads

His correspondence reveals that he was not only a user of his instruments, he was able to design them as well. He was in regular contact with opticians and other skilled and renowned makers across Europe who built lenses and other parts for him.

2.3 Geophysical instruments

Antoine d'Abbadie was also very interested in geophysics. He made countless magnetic measurements everywhere he went. He even invented and made built a brand new instrument capable of measuring both the magnetic inclination and declination. In the park around Abbadia, he set a few stones to which he installed his instruments, far away from metallic structures that could possibly interfere with his magnetic measurements.

He was also interested in the variations of the local gravity field. He installed a so-called "nadirane" in his lab: a device that consists of a long still pendulum able to detect variations of the vertical direction, mainly due to oceanic tides and seismic activity.

3 Books and correspondence

In his library (figure 4), Abbadie collated thousands of books from the XVIIIth and the XIXth centuries. Astronomers who were on duty after Antoine d'Abbadie completed the collection with more recent books, up to the middle of the XXth century. Besides, Antoine d'Abbadie corresponded with about 800 persons: astronomers, physicists, opticians, linguists, etc. All of this correspondence is kept in the local archive in Bayonne.

One of our main goal has been to go though all of this books and correspondence so as to identify what could be of interest for the public, for teachers, and for scientists. As a first step, we have selected 40 correspondents related to physics and astronomy. The corresponding letters were read and scanned; they teach us a lot on several matters. First, they tell us how scientists exchanged at this time: there were no international meetings to exchange ideas, very few journals in which to publish results, so scientist wrote letters to their peers. Second, they allow us to trace back the evolution of ideas and techniques. this is of particular interest for history of science. Last and incidentally, they are testament to the way people lived back then, the trouble and worries they could have, such as health and well-being.

Fig. 4. Abbadia's library (credit: B. Blanc)

4 Activities and teacher training sessions

To promote the heritage of Abbadia, we have imagined activities that can be done with the public or with students. Through those activities, the building of Abbadia can be discovered or the instruments and their use can be explained. Through the correspondence, astronomical notions can be tackled like the Polaris star and its "companion" which are evoked in a letter by the French astronomer Felix Tisserand.

5 Summary and perspectives

We have presented Abbadia and a glimpse of what can be found inside: the scientific instruments, the old books in the library, etc. We have also set path for (future) activities with students and the public. But, the heritage of Antoine d'Abbadie is not only his incredible home and the instruments he left behind him. It also resides in his writings, personal notes or correspondence. Not only do his writings reflects the exchanges he had with brilliant researchers of the XIXth century, which can be used as a starting points of many activities, but they also reveal the everyday life back in those days. So sociologically speaking, it is very rich as well.

As we were working on disseminating resources about Antoine d'Abbadie and Abbadia, we were approached by the University of Bordeaux to join a project aiming at scanning and valorising written heritage. This still is on-going and will lead to resources available at Gallica, the digital service of the French National Library in Paris.

We would like to thank the people in charge of the Archives in Bayonne who granted us access to the correspondence of Antoine d'Abbadie.

References

Arlot, J. E., Beauchamp, P., Garcia, S., & Ibarboure, S. 2018, in SF2A-2018: Proceedings of the Annual meeting of the French Society of Astronomy and Astrophysics, ed. P. Di Matteo, F. Billebaud, F. Herpin, N. Lagarde, J. B. Marquette, A. Robin, & O. Venot

Briot, D. 2016, L'Astronomie, 130, 38

Delpech, V. 2012, PhD thesis, Université de Pau, France

Primout, R. 2018, Master's thesis

Session 22

Quel futur pour le patrimoine astronomique français?

SF2A 2021
A. Siebert, K. Baillié, E. Lagadec, N. Lagarde, J. Malzac, J.-B. Marquette, M. N'Diaye, J. Richard, O. Venot (eds)

WHAT FUTURE FOR THE FRENCH ASTRONOMICAL PATRIMONY? THE CASE OF PIC DU MIDI

R. Cabanac[1]

Abstract. The Pic du Midi Observatory is not the oldest institution among the French historical astronomical observatories, neither does its buildings present any particularly fine architectural school, but Pic du Midi may be regarded as a very successful example of how to preserve historical patrimony. It welcomes tens of thousands of visitors each year with a rich Education and Public Outreach offer, and at the same time, continues science activities at their best. Pic du Midi operation is based on a world unique bimodal organisation. On the one hand, a science administration run by University Paul Sabatier is in charge of science activities, and on the other hand, a public administration is endowed with the task of maintaining buildings in a sustainable fashion with incomes from touristic visits. Thanks to this organisation, Pic du Midi preserves 150 year-long datasets and ancient instruments in many fields of science, allows thousands of visitors to meet with researchers, and learning state-of-the-art science in the doing. In 2021, Pic du midi Observatory is on a dynamic track, growing fast both touristically and science wise. Pic du midi started a major project to perpetuate patrimony: a UNESCO world heritage nomination under cultural and natural outstanding universal value criteria. This communication describes the patrimonial situation of the Pic du Midi in 2021. Interested readers may read the S20 communication on Pic du Midi.

Keywords: observatory, history, social, patrimony

1 Introduction

The observatory of Pic du Midi de Bigorre (2877 m, N 42°56'11", E 0°8'34") is the first high-altitude site in the world (1872). Its history flows throught two world wars, and a fair share of the emergence of the Modern World. Its meteo records span almost 150 years, including temperature, humidity, winds, and ozone measurements. This long history of science observations at Pic du Midi encompasses a broad range of disciplines, readers interested in Pic du Midi history may read Sanchez (2014); Davoust (2014). Among the numerous sciences that Pic du Midi hosted in his history, one may cite Meteorology, Geology, Glaciology, Atmospheric Sciences (Thunder, Sprites, Chemistry), Botanics, Studies of Cosmic Rays, Nuclear and Particle Physics, Medical studies, Earth Magnetism, Radioactivity Studies, Lunar cartography, Small Planets and planetary observations, Studies of galaxies, Cosmology, Stellar Magnetism, Solar studies and Coronagraphy, Ethology, ecology and most recently climate studies. This fantastic wealth of data gathering was produced over the years by rich historical ensemble of instruments, and has demanded summit building to cover most of the summit area. Observations and experiments continue at their best in 2021 thanks to the contemporaneous organisation that emerged in the latest part of the twentieth century. This organisation also offers a unique way to fund patrimony protection, which has become an almost insuperable task for French Universities because of the drastic under funding since 2010. We will describe here the way Pic du Midi works in 2021, with an emphasis on patrimonial management and conclude on the Pic du midi candidacy to UNESCO world heritage.

2 Pic du Midi: 150 years of sciences and more...

One of the most striking observations that a visitor can make when visiting Pic du Midi today is the mix of ancient buildings and domes with state-of-the-art contemporaneous infrastructures and instruments. Pic du

[1] IRAP, OMP, Université de Toulouse, CNRS, CNES, UPS, (Toulouse), France.
ORCID of the author: http://orcid.org/0000-0001-6679-2600

Midi is both a historical site and a living platform with many national services. The second peculiarity of Pic du Midi, is of course the very fact that thousands people can visit the observatory every year. A wide variety of Education and Public Outreach (EPO) activities are offered for all tastes, from concerts (Piano-Pic Festival, Rock at the summit, etc.) to downhill sports in all seasons, and of course a modern science museum reflecting the past and contemporaneous science activites ongoing at Pic du Midi, a planetarium located in Baillaud Dome (1909), a "HistoPad" tablet will allow interested visitors to discover what Pic du Midi looked like at different epochs since its foundation. The most fortunate visitors, staying one night at the summit, will follow an EPO professional through the science premises of Pic du Midi and discover what and how science observations are performed today. They will stargaze at night with small telescopes installed on the terrace and most important of all from a science perspective, they will participate to the funding of the observatory with their visit fees.

This visitor may figure that Patrimony at Pic du Midi comes in three categories, the first category is made of more traditional science records, books, photographs, old walls, domes and buildings dating back from 1880s to 2021, the second category is connected to the exceptional natural quality of the site that must be preserved, and the third category is connected to the so-called immaterial patrimony of Pic du Midi as a one of the world best example of high-mountain observatories fostering human science endeavour in modern history.

We will come back to Pic du Midi Patrimony in a later section, but let's summarize first Pic du Midi organisation allowing such wide variety of activities and patrimony protection.

Fig. 1. A concert at Pic du Midi.

3 Pic du Midi organisation in 2021

Since 2000, Pic du Midi summit is shared between two independent administrations. Readers interested in the making of such an organisation may read the communication of S20 on Pic du Midi in these proceedings. On the one hand, science activities at Pic du midi are managed by the Observatoire Midi Pyrénées (OMP), component of the University of Toulouse 3 Paul Sabatier. The science staff is shared between CNRS (9 people) and the University (15 people). On the other hand, Pic du Midi EPO activities are fully delegated to a public administration, comprising ca. 40 staff members. Apart from the aforementioned touristic activities, an important duty of the public administration is to perpetuate the long-term science activities at Pic du Midi. Among its supporting activities, access to the summit from La Mongie skying resort, power, water and food supplies, and sanitary infrastructures are central to the observatory science capabilities. The two administrations run separate budgets, their management is independent.

This bimodal organisation is very efficient for fund raising, because each partner pursues distinct objectives. Hence, any funding administration knows when money is spent on the public side or the science side. Thanks to this clarification, over the past ten years, about 10 million euros were invested on various science projects, and similar amounts on public infrastructures. In particular patrimony protection has profited from this.

4 Patrimony management at Pic du Midi

Management of the three categories of the Pic du Midi patrimony are covered by various partners.

4.1 Traditional patrimony: ancient science records, books and instruments

The Observatoire Midi Pyrénées created a Patrimony Commission endowed with four tasks: inventory, protection, restoration and valuation of patrimonial collections. At Pic du Midi, emblematic meteo records and other anthropogenic pollution, witnesses of long-term climate evolution, has been ongoing since 1870s, hundreds of photo-magnetograms of our Sun surface, numerous publications of particles physics that used Pic du Midi collider in the 1950s, hundreds of coronagraph time-lapses of Solar activity over many cycles, those examples are few among many that illustrate the richness of Pic du Midi science record patrimony. To this, one may add, old instruments, barometers, heliographs, old telescopes (The telescope of 60 cm, given by Italian jewish astronomer G Gentili to thank Pic du midi for hiding him during WW II, is 110 year-old).

Among its activities, The OMP Patrimony Commission has inventoried all Pic du Midi collections and stored most of them in University Libraries or public archives, deposited instruments in museums (ancient clocks in Dupuy Museum in Toulouse, instruments in Pic du Midi Museum). The commission also maintains links with science societies (Soc. Ramond de Carbonière, Bagnères de Bigorre, Soc. Astron. Toulouse), and institutional partners (PATSTEC mission; Université Fédérale de Toulouse). Finally OMP Patrimony Commission manages loans for exhibitions (Prototypes - Arts et Metiers, Fragments de Science Université Toulouse III , Train du Climat, virtual exposition Dauvillier, and virtual Explorer series Explorer, Héliographe de Campbell), organises public talks, training sessions for high-school teachers (Preac "science et société" de 2019 with a workshop entitled "Earth Physics: the Flat Earth)) and participates to national efforts for patrimony protections (ANR RESEED).

4.2 Natural site patrimony: Night sky protection

Another patrimony of Pic du Midi is the natural site quality highly suited for astronomical and environmental observations. Protecting the site quality is central to the future use of Pic du Midi for science. This protection was initiated by François Colas (IMCCE, OPM), responsible of Pic du Midi T1M, immediately supported by University Paul Sabatier (OMP), and soon delegated to the public administration that provided manpower and resources. The idea converge towards creating an International Darksky Association Reserve (RICE in French for Réserve Internationale de Ciel Etoilé: RICE) was launched by The IDA reserve was the first of its kind in Europe in 2013. In 2021, the IDA reserve covers 700 km^2 of core area around Pic du Midi over ca. 200 nearby villages. The key-element to a successful future was to involve, from the beginning, institutional partners (mayors, MP, State), technical experts (Energy Supply administration responsible of developing public lighting for the area), and Pic du Midi partners (scientists, EPO experts). Over the past years, the RICE successfully replaced thousand of light points around Pic du Midi and launched campaigns of night sky protection leading many nearby villages to switch-off public lights midnight to 5 am.

4.3 Immaterial patrimony: UNESCO World heritage

The Pic du Midi was the first high-mountain observatory to be built in the world, and one of the last pioneering site still active in the XXIst century. Its long science adventure and history of 150 years generated a rich patrimony. The fact that the summit is a connecting site between a larger public and scientists is very unique in the world today. All these characteristics argue for an outstanding universal value under criteria III and IV (https://whc.unesco.org/en/criteria/) for a nomination to UNESCO World Heritage. The public administration, the University Paul Sabatier and the State prefect work together to make that happen in the coming years. If the site is nominated, it will attract international visitors and preserve its science activities for the foreseeable future. Becoming a UNESCO World Heritage is a long two-step process. First, the site must join the French national indicative list. This shall happen in the late months of 2021, and the second step consist in building a site management plan detailing how partners will work together to protect the site. An important point of this UNESCO World Heritage is that science activities are at the heart of the outstanding universal value, they are what needs to be protected and developed, the risk of "fossilising" the site is null; the summit historical artefacts are expected to evolve to support this universal science adventure.

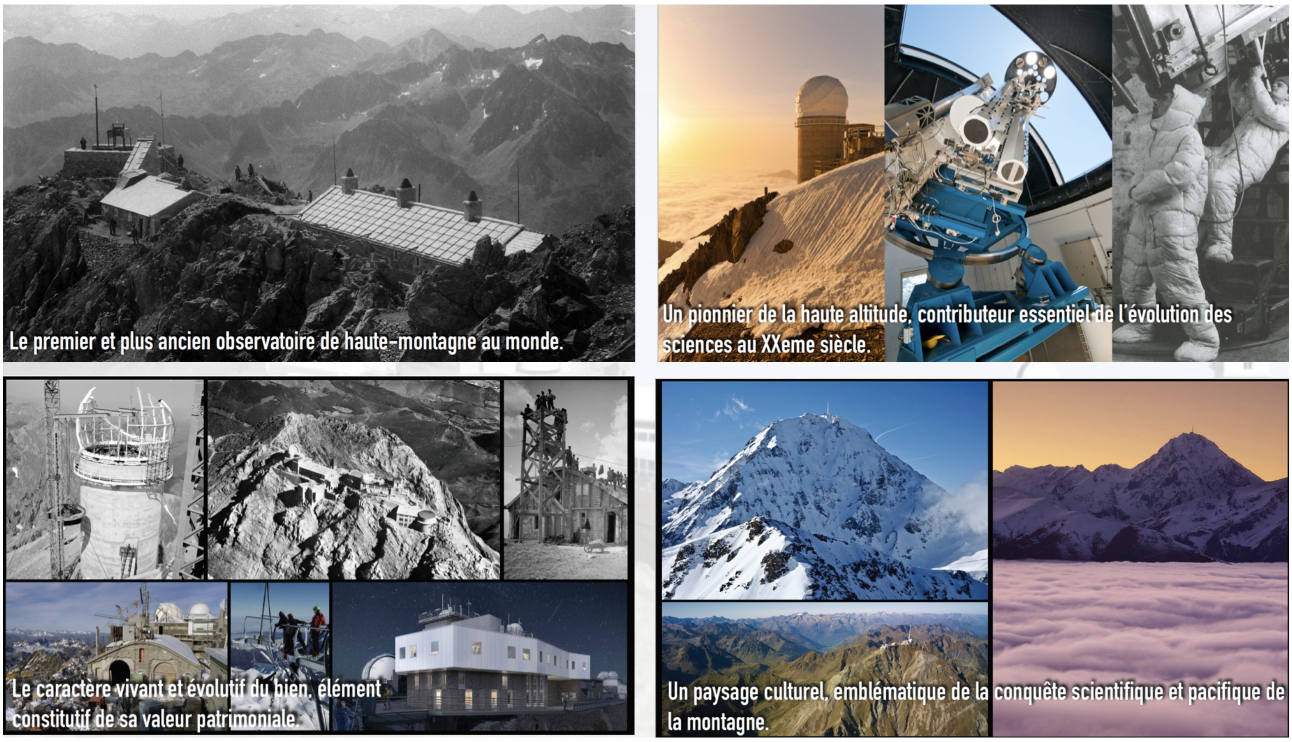

Fig. 2. Pic du Midi outstanding universal values for UNESCO world heritage patrimony candidacy.

5 Conclusions

In 2021, Pic du midi bimodal organisation is optimised for the site protection. Thanks to this very unique way of managing the observatory, we are confident that our generation can pass on future generations this extraordinary patrimony. Already rich of 150 years of science observations, ongoing projects both on the science and public sides allow us to claim that the best is to come at Pic du Midi Observatory. But this will only become a reality under two conditions, (i) visitors must continue to support the science activities, and (ii) the funding agency CNRS and University Paul Sabatier must continue to invest in people at the summit. Maintaining such an high-mountain observatory demands dedicated and expert staff at the summit. Until today, those two conditions were filled, let's hope this will continue in the coming years!

References

Davoust, E. 2014, Pic du Midi: cent ans de vie et de science en haute montagne, 1st edn. (65500 Vic-en-Bigorre: MSN)

Sanchez, J.-C. 2014, Le Pic du Midi de Bigorre et son Observatoire, 1st edn. (BP 1503 29, rue Carrerot 64015 Pau: Editions CAIRN), www.editions-cairn.fr

SF2A 2021
A. Siebert, K. Baillié, E. Lagadec, N. Lagarde, J. Malzac, J.-B. Marquette, M. N'Diaye, J. Richard, O. Venot (eds)

MONTPELLIER: 3 CENTURIES OF ASTRONOMY, 56 INSTRUMENTS IN THE NATIONAL CULTURAL HERITAGE AND A UNIVERSITY CONTEXT

H. Reboul[1]

Abstract. The astronomy heritage in Montpellier (France) expressed itself in an observatory and its instruments in the 18th century. During the 19th and 20th centuries the science gradually moved in the local science university. Even when outdated, these instruments were still cared for by the astronomy academics who were responsible or very involved for their preservation until 10 years ago. At the beginning of the 21st century, a team of volunteer academics assembled in the Science university of Montpellier 2, then under the guidance of a curator (conservateur d'État). During the next ten years, very significant progress were made: the astronomy collection was included in the national heritage inventory, it was stored in the official collections department store rooms, and 56 of these items were classified as national French heritage (Monument Historique) ; the 18th and 19th century instruments also benefited from restoration works. These instruments were regularly shown in exhibitions. But the astronomy collection was then significantly impacted by major budget cuts led by different administrative changes. In 2015, the merging of two of the three Montpellier universities amplified its isolation within a very large quantity of life science collections.

Keywords: Astronomical instruments, collections, university, cultural objectives, administration

1 Introduction

Astronomy in Montpellier has a long history of teaching, research and conversation among the general public; since the 17th century this continuity has been a dominant factor in the conservation of an instrumental ensemble remarkable for both its variety and its integrity. At the beginning of the 21st century, a few academic volunteers from different fields (including astronomy) have started to work on the preservation of these heritages.

2 Origins of Montpellier's astronomical heritage collection

In 1705 the King Lewis XIV issued a royal decree creating the "Société Royale des Sciences de Montpellier" (SRSM), which gave its unique status as "extension and part" of the Royal Academy of Sciences in Paris. The first official astronomy observatory was built on top of the Babote tower (Fig. 1a) between 1742 and 1745 (Faidit (1986), see also Faidit (1993)); the building itself was classified as national heritage monument in 1927. The 1770 Gregorian telescope (Fig. 1.b), '7 inches and 8 lines' (208 mm) (Faidit (1986)) was set up there in 1784. The legal status of the SRSM led to its disappearance during the French revolution in 1793, but when a "Science Faculty" was created in 1809, astronomy was one of its original seven chairs (Dulieu (1981)), and after 1812 the former instruments of the SRSM were made available to the Science Faculty (except two large quarter-circles of 3 feet rad. that are missing compared to the inventory of 1793).

This astronomy collection was augmented throughout the 19th century despite the missed opportunity of the great observatory that Urbain Le Verrier initially wanted to build in Montpellier (Faidit (2001)). The dome of the local botanic gardens (Fig. 3.a) was opened in 1879, together with the Foucault telescope built by Eichens (Fig.2.c) but was faced by a long-lasting protest from the local botanists (Fig. 3.b) and astronomers

[1] LUPM, Laboratoire Univers et Particules de Montpellier (UMR 5299), Université de Montpellier - Campus Triolet, Place Eugène Bataillon - CC 72 - 34095 Montpellier Cedex 05 FRANCE

often used other sites of observation until the building of the present campus in 1963 : it has its own observatory with two domes that currently house ten active telescopes, some dating as far back as 1873 (Fig. 2.d, e, f, h).

With the development of large "mission" observatories in the 20^{th} century, the Montpellier Astronomy Laboratory acquired instruments for the reduction of silver recordings (images and spectra) : Askania (Fig. 2.g), Challonge, Joyce, Hilger and Watts (digitized version), ... The ground based observation equipment for the 1966 and 1969 space "experiments" (by four members of the Montpellier laboratory) of "artificial comets" generated by rockets sent at 220 km alt. is also part of this collection.

3 Preservation of this heritage collection and its present perspective

In 1998 a new dynamic began to take shape within the Science University of Montpellier 2 (UM2). A large exhibition "Trésors de Science" was held in the city center, later reinstalled at the Agropolis Museum : it showcased a selection of the various heritage collections of the Science University and gave the opportunity to draw out the new astronomy collection' inventory despite their geographic dispersion in different buildings or store rooms within (or even far outside) the university campus.

In 2000 the collection was studied by the National inventory of the "Groupe du patrimoine astronomique" (Françoise Le Guet and Anthony Turner). In 2003 a secured store room was set up by volunteer academics at the Botany Institute (owned by the university UM2) in the city centre. In 2003 a University Collections Department (Service des Collections) was created at the UM2, with a curator at its head. In 2004, a photographic campaign of the astronomy instruments was carried out by the DRAC (Direction Régionale des Affaires Culturelles). In 2005 an association of volunteer academics was created under the aegis of the 1901 law, to enable them to work (even when retired) in the collection store rooms complying with the current regulations.

In 2005 the application for the classification of 56 astronomy items as national heritage collections was defended and granted at CSMH ("Commission Supérieure des Monuments Historiques") in Paris. In 2007, as part of the 12^{th} International Congress on the Enlightenment (Montpellier), in partnership with the science university library and with the county's archives, an exhibition showed books and instruments within the same showcase: they were thus exhibited as they were used during the 18^{th} century at the observatory, which was then a very rare occurrence. In 2008, the collections were described in an online database on the UM2's website (now `https://collections.umontpellier.fr/collections/astronomie`). From 2007 to 2010, all the 18^{th} and 19^{th} classified astronomy instruments were restored in Paris by a specialized conservation studio (they were granted the "Museum of France" award).

In 2010 the University Collections Team ("Service des Collections") became the Center for the Heritage Collections ("Pôle Patrimoine Scientifique"). Between 2012 and 2013 their budget was reduced by two thirds : for the astronomy collections, it then became inexistant. The access to the store room got more restricted and it then became very difficult to do useful work on these collections. In 2015 the merging of two universities (UM2: Sciences and Arts university, and UM1 : Medicine, Pharmacy and Law) led to that of the Center for the Heritage Collections ("Service du Patrimoine Historique") within the Heritage Collections Department of the university of Montpellier. In this particular framework, the astronomy collection with its distinctive features is lost within the very large series of life sciences specimens and more specifically the prestigious medical and anatomy collections of the Medical Faculty. Almost no information about the astronomy collection's loans for exhibitions nor about their transfers to other institutions leak through to the astronomy academics; unfortunately they have no opportunity to discuss these questions with the curators.

4 Conclusions

At the beginning of the 21st century the academics' incentive led to a significant progress on the university heritage collections ; it was a means of fulfilling the university usual missions which are to promote research, to teach, and to disseminate scientific culture. After ten very positive years (conservation, protection, restoration, heritage development) the astronomy collection of Montpellier finds itself excluded from the original target of this heritage strategy.

For astronomy collections the logistics of an observatory are essentially different to those of a university. The former strategy that was supported during the 1990ies both by the Culture, and the Higher Education Ministries seems to be a pertinent solution to our current problems. Because of the very small number of astronomy academics, the local scale alone is probably not the most pertinent to ensure this particular heritage's preservation: each site of conservation holds instruments that can be unique. A national (or higher?) supervision level seems to be the most relevant to ensure the future preservation of this astronomy collection, whose long history has to be told jointly by astrophysicists and curators. What remains to be found is a workable *modus vivendi* between them for the benefit of the astronomy collection of Montpellier.

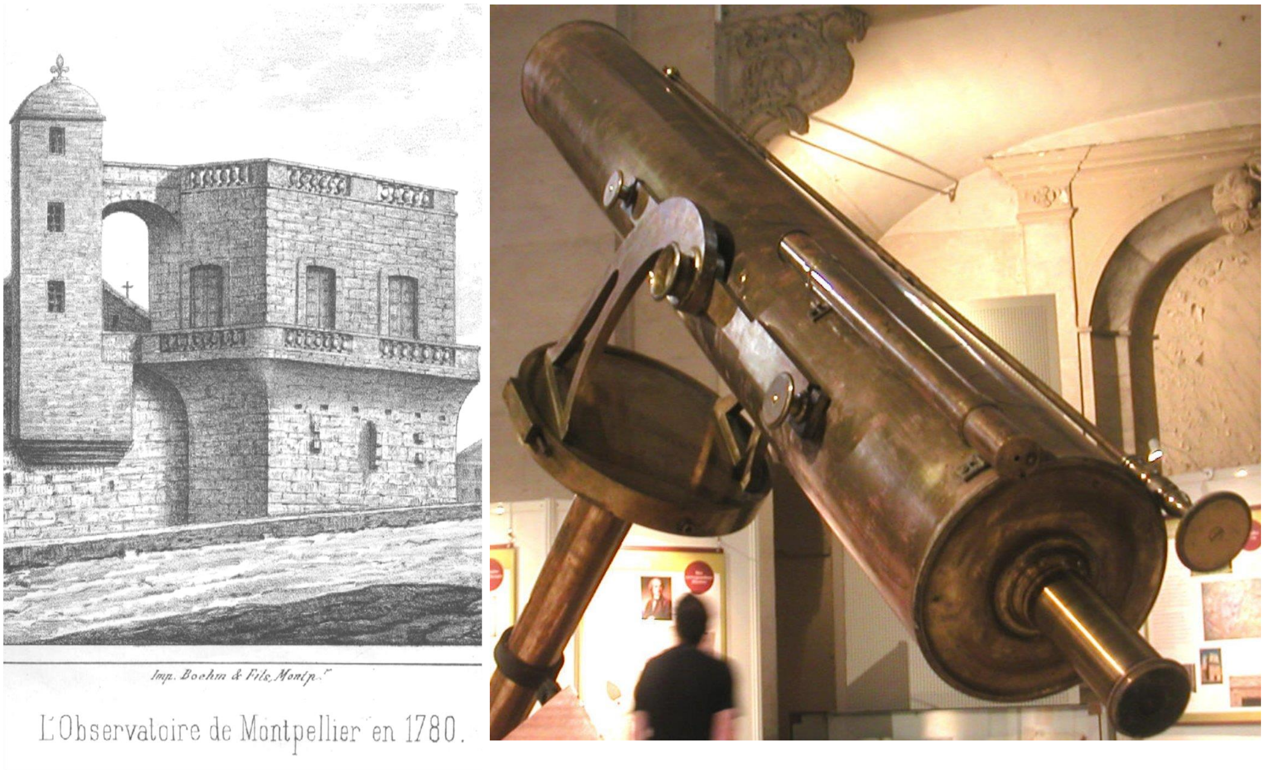

Fig. 1. a: Babote Observatory in 1780 (from Roche (1881)). **b:** Gregorian Nairne telescope, 1770 (here in 2007, before restoration, during the exhibition for the XII$^{\text{th}}$ International Enlightenment Congress in Montpellier)

=

References

Anonymous, 1883 'Registre des mathématiques' de 1883 à 2003, UM2-4144, Université de Montpellier

Dulieu, L., 1981 'La faculté des Sciences de Montpellier' Presses universelles.

Faidit, J.-M., 1986, 'L'Observatoire de la Babote', ISBN 2-9501264-0-5.

Faidit, J.-M., 1993, 'Les 'amateurs de sciences' d'une province et le ciel au XVIIIe siècle : Astronomie et Astronomes en Languedoc : approche d'histoire des sciences'. Thèse de l'université Montpellier III.

Faidit, J.-M., 2001, 'Le pavillon d'astronomie du jardin des plantes', ISBN 2-9516194-0-5.

Roche, E., 1881, 'Notice sur l'Observatoire de l'ancienne société des sciences de Montpellier', Mémoires de l'Académie des Sciences de Montpellier.

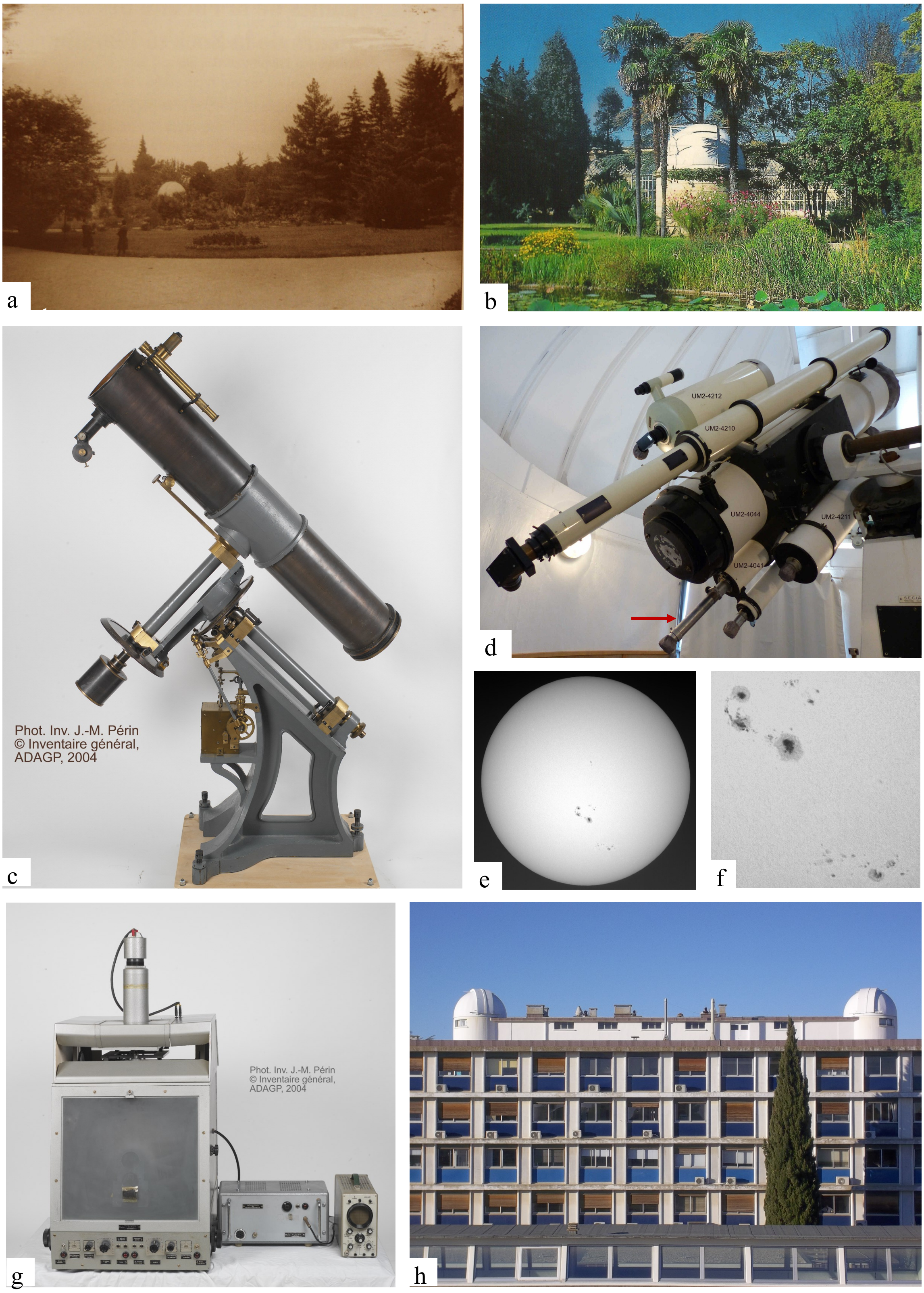

Fig. 2. **a:** dome of the "jardin des plantes", late XIX$^{\text{th}}$ century '(in (Faidit 2001), p. 29). **b:** *late* XX$^{\text{th}}$ century : photo from the cover of Faidit (2001). **c:** 1877 Foucault's telescope (20 cm instead of the envisaged 80 cm in Faidit (2001)) before restoration, MH. **d:** East dome content of the present observatory: the red arrow indicates the Secrétan-Eichens refractor of 1873 (national commission of the Venus transit of 1874); its MH classification is in progress, its equatorial mount has been preserved but its original Eichens clock mechanism with Foucault regulator probably 'is in Toulouse since the eclipse of Elche' (Anonymous (1883)) within the framework of the joint expedition of the FdS of Montpellier and Toulouse to Sfax and Elche for the eclipse of the sun of 28 May 1900). **e:** image of the sun obtained in 2012 with above Secrétan-Eichens refractor, then 139 years old (and a 2010 SBIG 11000M camera). **f:** detail of 5. **g:** Askania 1965 iris photometer. MH. **h:** Today FdS observatory (built in 1963).

Session 23

Relevés photométriques grand champ II

SF2A 2021
A. Siebert, K. Baillié, E. Lagadec, N. Lagarde, J. Malzac, J.-B. Marquette, M. N'Diaye, J. Richard, O. Venot (eds)

UNCOVERING THE VERY METAL-POOR TAIL OF THE THIN DISC

E. Fernández-Alvar[1], G. Kordopatis[1] and V. Hill[1]

Abstract. In this talk we present the results of the recent published study by Fernández-Alvar et al. (2021), consisted on the exploration of the rotational velocity distribution as a function of the metallicity of stars located towards the Galactic anticenter. The analyzed sample was observed as part of the Pristine survey, a photometric program devised to find the most metal-poor stellar populations in the Galaxy in order to understand the first Galactic formation processes. When combining metallicities obtained from the Pristine photometry with rotational velocities derived from proper motions several stellar structures emerge. The most intriguing one is the metal-poor tail of stars moving like the thin disc extended down to very low metallicities, [Fe/H] ~ -2. Fast rotators are also observed at even lower metallicities, $-3.5 <$ [Fe/H] < -2, but in a scarcer number. These recently discovered very and extremely metal-poor disc-like stars merit a dedicated spectroscopic follow-up to provide a complete chemical characterization to better constrain their origin. The clarification of their formation scenario will undoubtly shed light on the understanding of the first formation episodes of the Milky-Way.

Keywords: Galaxy: disc – Galaxy: kinematics and dynamics – Galaxy: abundances

1 Introduction

Chemo-dynamics of metal-poor stars encode key information to understand how our Galaxy formed. For this reason, several programs have been devised through the last decades in order to find and characterize these kind of objects. This is the case of the Pristine survey (Starkenburg et al. 2017). Pristine is a photometric survey whose strategy to observe metal-poor objects relies on the use of a filter centered in the CaII doublet H&K, at 3933 and 3968 Å, which is a spectral feature very sensitive to the stellar metallicity. The survey is carried out with the 3.6-meter optical/infrared Canadian-French-Hawaiian Telescop on the Mauna Kea Hawaiian Observatory. It already mapped around 12 millions of targets over 5000 square degrees on the sky. Its efficiency to detect extremely metal-poor stars has been largely probed (Youakim et al. 2017, Aguado et al. 2019). It aims to provide a comprehensive view of the metallicity distribution of the metal-poor Galaxy and an insight on the Galaxy build-up and structure. The metallicity sensitivity of Pristine photometry is used to derive a metallicity estimation for each target. The CaHK magnitude is combined with broad-band colours in a colour-colour space that separates out the temperature and metallicity effects. Then, metallicity estimates from a subsample of stars with an spectroscopic counterpart are used to derive a global metallicity calibration, as explained in detail in Starkenburg et al. (2017).

We aim to combine Pristine metallicities with the unprecedently accurate Gaia early third data release (EDR3 – Gaia Collaboration et al. 2021) astrometry. Our goal is to perform a chemo-kinematical analysis over the metal-poor Milky Way stellar populations observed with Pristine. All Pristine targets have Gaia proper motions measurements, but a very low fraction count with radial velocity measurements ($\sim$0.5%), preventing the full velocity characterization. However, in the direction towards the anticenter the rotational velocity, V_ϕ, is perpendicular to the line-of-sight. Consequently, V_ϕ does not depend on the radial velocity and only the proper motion measured along the galactic longitude direction, μ_ℓ, is required. Taking advantage of this fact, we are able to explore the V_ϕ and [Fe/H] distributions of stars observed by the Pristine survey towards the anticenter direction.

[1] Université Côte d'Azur, Observatoire de la Côte d'Azur, CNRS, Laboratoire Lagrange, Bd de l'Observatoire, CS 34229, 06304 Nice cedex 4, France

2 The rotational velocity and metallicity distribution towards the anticenter: statistical evidence of a very metal-poor thin disc.

We choose stars located at $(170 < \ell < 190, 20 < b < 40)^\circ$, the Pristine footprint region where the uncertainty of V_ϕ determined with the proper motion approximation is lower than 5 $\mathrm{km\,s^{-1}}$on average, as probed by evaluating a Gaia EDR3 mock catalogue (see Fernández-Alvar et al. 2021 for the detailed explanation). Figure 1 shows the resulting V_ℓ, derived from the Gaia EDR3 proper motions, as a function of the [Fe/H], estimated from Pristine photometry combined with Sloan Digital Sky Survey magnitudes (Starkenburg et al. 2017). Just a rough inspection of the distribution of stars on the V_ℓ vs. [Fe/H] plane reveals the presence of several structures. First, our stellar sample is mostly comprised by thin disc stars with metallicities close to solar and moving with velocities typical of the Local Standard of Rest (LSR), i.e., -238 $\mathrm{km\,s^{-1}}$* (Schönrich 2012). We see, however, that fast rotating stars are not restricted to the highest metallicity range but that there is a continuous extension down to the lowest metallicity values. This feature is surprising, since the thin disc distribution is expected to be metal-rich, with a negligible number of stars with metallicities lower than ~ -0.7 (e.g. Bensby et al. 2014).

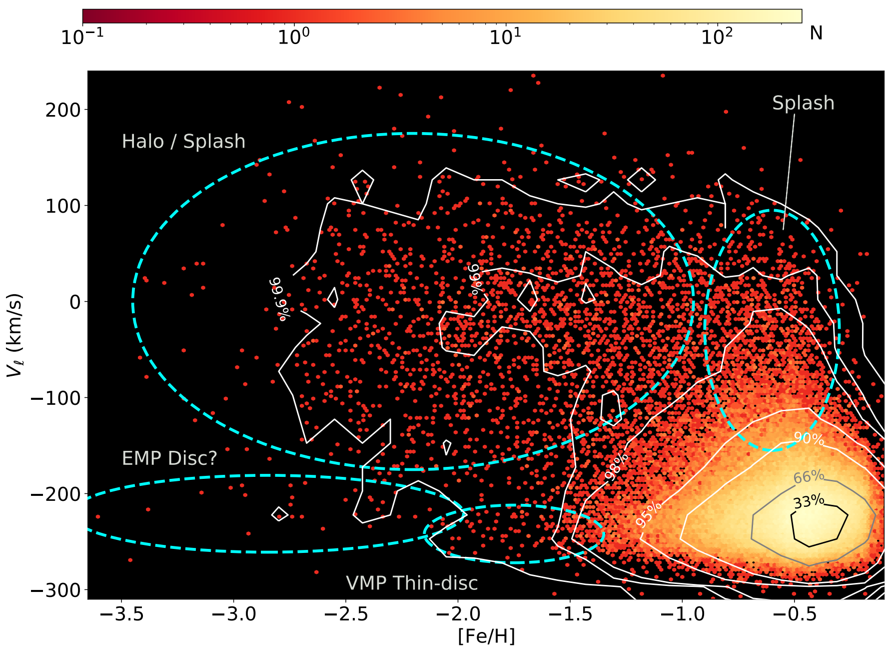

Fig. 1. V_ℓ as a function of [Fe/H], colour coded by density (the color code lower limit is set to 0.1 due to color contrast purposes). The density is measured in bins of 10 $\mathrm{km\,s^{-1}}$and 0.1 dex and contour lines show the 33, 66, 98, 99 and 99.9% of the cumulative distribution. The most evident stellar substructures are pointed out with annotated cyan ellipses: a presumed extremely metal-poor disc (EMP disc), the very metal-poor thin disc (VMP thin disc), the Splash, and the halo. Stars on prograde motion are those with $V_\ell < 0$, while stars on retrograde motion have $V_\ell > 0$.

Figure 1 also reveals that high metallicity stars show a velocity distribution which extends towards non-rotating velocities and even retrograde motions. This velocity tail is similar to the heated disc stellar population recently discovered (Fernández-Alvar et al. 2019, Di Matteo et al. 2019,Belokurov et al. 2020), the so-called *Splash*. Finally, stars with [Fe/H] < -1.5 are dominated by a stellar sample that resembles the classical kinematical stellar halo, with a velocity distribution centered around 0 $\mathrm{km\,s^{-1}}$with a large dispersion (Fermani & Schönrich 2013).

In order to distinguish more quantitatively the subyacent stellar populations based on their chemo-kinematical characteristics we fit the data with Gaussian Mixture Models†. This technique consists on a clustering algorithm that searches for the best number of gaussian components that reproduces a data set. We split our sample in

*In our reference system negative velocity values correspond to a prograde motion.
†We make use of the python module sklearn.mixture (Pedregosa et al. 2011)

metallicity bins and fit the V_ℓ data with Gaussian Mixture Models. We evaluate models comprised by one up to six gaussians.

For the metallicity range typically dominated by thin and thick disc stars, $-0.8 <$ [Fe/H] < -0.2 ‡, we obtained that a five-gaussian model is the one that best fit the data. Two of these gaussians are centered at values close to the typical rotational velocity of the LSR in the solar neighbourhood, $V_\phi \sim -238$ km s^{-1}. Other two gaussian components peak at velocities around those of thick disc stars, lagging prograde rotation respect to the thin disc (Recio-Blanco et al. 2014). These four gaussians are, thus, comprised by thin and thick disc stars. The fact that we need more than two gaussians to reproduce the two disc components is not completely surprising, since we already know that their velocity distributions are not perfect gaussians (e.g., Sharma & Bland-Hawthorn 2013, and references therein). Besides, it is also known that there is a velocity correlation with the metallicity, negative for the thin disc and positive for the thick disc as the metallicity increases (e.g. Kordopatis et al. 2017). Interestingly, there is need of an additional gaussian component to take into account for the non-rotating and retrograde stars, i.e., the *Splash*. As the metallicity decreases, the gaussian components shift toward higher velocity values, with those comprising velocities typical of the thick disc and the one counting for the *Splash* increasing in relative weight.

Noticible, at $-1.5 <$ [Fe/H] < -0.8 there is still a large contribution of stars moving with velocities typical of the thin disc. We verified whether such fast rotating stars at a metallicity range where the contribution of the thin disc should be very low could be an artifact, consequence of a problem in the metallicity calibration. Indeed, the comparison of photometric metallicities with those derived spectroscopically for the targets with a spectroscopic follow-up reveals large differences at metallicities between -1.5 and -0.8 approximately. In order to quantify the possible contamination of metal-rich stars at lower photometric metallicity bins we model a thin disc metallicity distribution function and how it is modified due to the error function of our metallicity calibration. This exercise shows that around 45% of our stars with photometric metallicities between $-1.5 <$ [Fe/H] < -0.8 are likely more metal-rich thin disc stars.

At lower metallicities, $-2 <$ [Fe/H] < -1.5, the best Gaussian Mixture Model fit is a two-gaussian model: one centered around -233 km s^{-1}(a velocity value closer to the LSR rotational velocity rather than the typical velocities of the thick-disc or the halo) and the other around -38 km s^{-1}. Interestingly, the estimated contamination in this metallicity bin is very low ($< 1\%$) and cannot take into account all the stars moving with thin-disc-like velocities. We also verified that errors in velocities are not the responsible for this feature. We performed a Monte Carlo simulation by calculating 1000 times the velocity taking into account the measurement errors in parallax and proper motions considering they follow a gaussian distribution. The best Gaussian Mixture Model fit for more than 90% of the simulations is the two-gaussian model. These verifications reinforce the statistical significance of this feature. At metallicities $-3.5 <$ [Fe/H] < -2 there is no significant evidence of a distinct kinematically thin disc stellar population, although there is still the presence of fast rotating stars.

3 Hypothetical formation scenarios.

This is not the first time that fast rotating stars with extremely low metallicities have been detected. The first one was the work by Sestito et al. (2019), who discovered that 26% of all known ultra metal-poor stars with radial velocities were confined to $z_{max} < 3$ kpc to the plane, and 5% moving in prograde circular orbits. Since then subsequent works confirmed these results and found evidence of extremely and ultra metal-poor stars moving with thick-disc-like velocities (Sestito et al. 2020, Di Matteo et al. 2019, Di Matteo et al. 2020; Venn et al. 2020; Carter et al. 2021; Cordoni et al. 2021). In particular, Di Matteo et al. (2020) compared the chemo-dynamical properties of stars from the ESO's Large Program "First Stars" with other stellar samples covering a metallicity range between [Fe/H] < -4 up to [Fe/H] ~ 0. This work showed that there is evidence of a kinematical disc and halo populations coexisting at every metallicity range.

Our work shows from an homogeneous data set that there is indeed statistical evidence of a kinematical disc and halo populations coexisting down to, at least, [Fe/H] ~ -2. Interestingly, our kinematical disc rotates more like the thin disc than a thick disc. Our sample is mostly confined at low z, what could be the reason why we are able to probe this fast rotating stellar population better than previous works.

The existence of fast rotators at such low metallicities is puzzling. From the theoretical point of view, stars with [Fe/H] < -2 are expected to form during the first couple of Gyr after the Big Bang (El-Badry et al. 2018), the epoch at which the Galaxy was assembling through the hierarchical merger of smaller systems.

‡ -0.2 is the upper limit up to which the Pristine metallicity calibration is reliable

Consequently, stars were expected to be pressure supported or heated into halo-like kinematics due to the impact of the mergers, preventing a disc configuration. However, some recent cosmological simulations predict that thin disc stars formed first, later evolving to a thicker configuration as a result of heating (Park et al. 2020). The existence of metal-poor stars moving like the thin disc could be explained as a fraction of stars formed in the early disc that succeded in maintaining their original motion without being heated. These stars would be characterized by high [α/Fe] ratios. Further investigation with cosmological simulations is needed to explore this scenario.

On the other hand, there are recent results of a two-infall chemical evolution model based on an inside-out formation scenario able to predict the formation of thin disc stars with metallicities down to [Fe/H] ~ -2 after the dilution of the second infall of gas (Spitoni et al. 2021). These stars should have lower [α/Fe] ratios compared with the scenario where they would have formed in the first stages of Galaxy formation. However, the two-infall model cannot explain the presence of kinematical disc stars with lower metallicities, [Fe/H] < -2. Further analysis of the chemical abundances of these stars is needed to clarify whether stars with metallicities higher and lower than [Fe/H] ~ -2 are belong to one or two different stellar populations.

4 Conclusions

In this talk we have presented the main results of the rotational velocity and metallicity distributions analysis of stars observed by the Pristine survey recently published in Fernández-Alvar et al. (2021). In this work we discovered statistical evidence of the existence of a very metal-poor ([Fe/H] > -2) stellar population moving with rotational velocities resembling the thin disc motion. This is not the first time metal-poor stars, even at lower metallicities ([Fe/H] < -4), moving in disc-like orbits had been detected, although without such fast rotating velocities. This is an exciting discovery with important implications regarding the first stages of star formation of the Milky Way. For this reason, it merits a detailed follow-up, in particular with spectroscopic stellar surveys that could allow a deeper chemo-dynamical characterization in order to clarify their formation scenario.

References

Aguado, D. S., Youakim, K., González Hernández, J. I., et al. 2019, MNRAS, 490, 2241
Belokurov, V., Sanders, J. L., Fattahi, A., et al. 2020, MNRAS, 494, 3880
Bensby, T., Feltzing, S., & Oey, M. S. 2014, A&A, 562, A71
Carter, C., Conroy, C., Zaritsky, D., et al. 2021, ApJ, 908, 208
Cordoni, G., Da Costa, G. S., Yong, D., et al. 2021, MNRAS, 503, 2539
Di Matteo, P., Haywood, M., Lehnert, M. D., et al. 2019, A&A, 632, A4
Di Matteo, P., Spite, M., Haywood, M., et al. 2020, A&A, 636, A115
El-Badry, K., Bland-Hawthorn, J., Wetzel, A., et al. 2018, MNRAS, 480, 652
Fermani, F. & Schönrich, R. 2013, MNRAS, 432, 2402
Fernández-Alvar, E., Fernández-Trincado, J. G., Moreno, E., et al. 2019, MNRAS, 487, 1462
Fernández-Alvar, E., Kordopatis, G., Hill, V., et al. 2021, arXiv e-prints, arXiv:2106.03406
Gaia Collaboration, Brown, A. G. A., Vallenari, A., et al. 2021, A&A, 649, A1
Kordopatis, G., Wyse, R. F. G., Chiappini, C., et al. 2017, MNRAS, 467, 469
Park, M. J., Yi, S. K., Peirani, S., et al. 2020, arXiv e-prints, arXiv:2009.12373
Pedregosa, F., Varoquaux, G., Gramfort, A., et al. 2011, Journal of Machine Learning Research, 12, 2825
Recio-Blanco, A., de Laverny, P., Kordopatis, G., et al. 2014, A&A, 567, A5
Schönrich, R. 2012, MNRAS, 427, 274
Sestito, F., Longeard, N., Martin, N. F., et al. 2019, MNRAS, 484, 2166
Sestito, F., Martin, N. F., Starkenburg, E., et al. 2020, MNRAS, 497, L7
Sharma, S. & Bland-Hawthorn, J. 2013, ApJ, 773, 183
Spitoni, E., Verma, K., Silva Aguirre, V., et al. 2021, A&A, 647, A73
Starkenburg, E., Martin, N., Youakim, K., et al. 2017, MNRAS, 471, 2587
Venn, K. A., Kielty, C. L., Sestito, F., et al. 2020, MNRAS, 492, 3241
Youakim, K., Starkenburg, E., Aguado, D. S., et al. 2017, MNRAS, 472, 2963

EXTRAGALACTIC GLOBULAR CLUSTERS WITH EUCLID AND OTHER WIDE SURVEYS

A. Lançon[1], S. Larsen[2], K. Voggel[1], J.-C. Cuillandre[3], P.-A. Duc[1], W. Chantereau[1], R. Jain[1], R. Sánchez-Janssen[4], M. Cantiello[5], M. Rejkuba[6], F. Marleau[7], T. Saifollahi[8], C. Conselice[9], L. Hunt[10], A. M. N Ferguson[11], E. Lagadec[12], P. Côté[13] on behalf of the Euclid Consortium

Abstract. Globular clusters play a role in many areas of astrophysics, ranging from stellar physics to cosmology. New ground-based optical surveys complemented by observations from space-based telescopes with unprecedented near-infrared capabilities will help us solve the puzzles of their formation histories. In this context, the Wide Survey of the *Euclid* space mission will provide red and near-infrared data over about 15 000 square degrees of the sky. Combined with optical photometry from the ground, it will allow us to construct a global picture of the globular cluster populations in both dense and tenuous environments out to tens of megaparsecs. The homogeneous photometry of these data sets will rejuvenate stellar population studies that depend on precise spectral energy distributions. We provide a brief overview of these perspectives.

Keywords: globular clusters ; surveys

1 Introduction

A refreshing wave of interest is currently pushing globular cluster science ahead, triggered by a growing body of stringent empirical constraints: new formation scenarios are needed to explain the abundance patterns seen among globular cluster stars; galaxy formation scenarios must explain a variety of globular cluster color distributions without endagering the scaling relations between cluster numbers and host galaxy properties; the relationships between globular clusters (hereafter GC), dwarf galaxy nuclei and ultra-compact galaxies remain to be elucidated; direct observations of star forming clumps at high redshift must find their place in the global picture of globular cluster histories. At the same time, GCs remain objects of reference, with comparatively simple stellar populations that can allow us to test our understanding of stellar evolution. For this purpose, at least at distances not yet accessible to detailed spectroscopic observations, homogeneous and deep photometry across the spectrum of stellar photospheres is a must.

The nearby future will see the launch of several astronomical telescopes into space, a few of which will focus on the near-infrared spectral range and thus complement large ground-based optical surveys that are rapidly

[1] Observatoire astronomique de Strasbourg, Université de Strasbourg, CNRS, UMR 7550, 67000 Strasbourg, France
[2] Department of Astrophysics/IMAPP, Radboud University, PO Box 9010, 6500 GL Nijmegen, The Netherlands
[3] AIM, CEA, CNRS, Université Paris-Saclay, Université Paris Diderot, Sorbonne Paris Cité, Observatoire de Paris, PSL University, F-91191 Gif-sur-Yvette, France
[4] UK Astronomy Technology Centre, Royal Observatory, Blackford Hill, Edinburgh, EH9 3HJ, UK
[5] INAF Osservatorio Astr. d'Abruzzo, Via Maggini, 64100 Teramo, Italy
[6] European Southern Observatory, Karl-Schwarzschild-Strasse 2, D-85748 Garching bei Munchen, Germany
[7] Institute fur Astro- und Teilchenphysik, Universität Innsbruck, Technikerstrasse 25/8, A-6020 Innsbruck, Austria
[8] Kapteyn Astronomical Institute, University of Groningen, PO Box 800, NL-9700 AV Groningen, the Netherlands
[9] Jodrell Bank Centre for Astrophysics, University of Manchester, Oxford Road, Manchester M13 9PL, UK
[10] INAF - Osservatorio Astrofisico di Arcetri, Largo E. Fermi 5, 50125 Firenze, Italy
[11] Institute for Astronomy, University of Edinburgh Royal Observatory, Blackford Hill, Edinburgh EH9 3HJ, UK
[12] Université Côte d'Azur, Observatoire de la Côte d'Azur, CNRS, Laboratoire Lagrange, 06304 Nice, France
[13] National Research Council of Canada, Herzberg Astronomy and Astrophysics Research Centre, Victoria, BC V9E 2E7 Canada

progressing across the globe. The *Euclid* space mission* and the *James Webb* Space Telescope† are next in line for launch. While the second will provide a variety of instruments for pointed observations of small fields of view, the first will operate in survey mode with wide-field cameras in the red part of the optical spectrum (VIS instrument) and in the Y, J, H bands of the near-infrared (NISP instrument). The pointed observations of the *James Webb* Space Telescope, later followed by those of the *Nancy Grace Roman* Space Telescope, will extend the volume in which Local Group clusters can be resolved into stars and will also transform our view of high-redshift structure formation. The *Euclid* mission has its place in between these extremes, and will draw a new picture of GC populations at intermediate distances, out to almost 100 Mpc.

Globular clusters are among the targets of the Legacy Science program of the *Euclid* mission plan (Laureijs et al. 2011), and their detection and study is being prepared as a dedicated work package of the Local Universe science working group within the Euclid Consortium. As a consequence of the requirements set by the primary science cases of *Euclid* (dark matter and cosmology studies via tracers such as weak lensing and galaxy clustering; Mellier, this conference), *Euclid* will observe a large part of the darkest skies (almost 15 000 square degrees; Scaramella et al. 2021), with a good spatial resolution ($\simeq 0.15''$ in VIS), a well-characterized point-spread function, and the deep uniform red and near-infrared photometry necessary for photometric redshift measurements. The need for photometric redshifts has led to unprecedented coordination efforts with ground-based optical surveys, in both the Southern and Northern hemispheres.

2 Taking advantage of *Euclid*'s survey specifications

Deep high-resolution observations of extragalactic GC populations obtained over the years with the *Hubble* Space Telescope (HST) have produced high-purity samples of GCs with information on their half-light radii out to about 30 Mpc (e.g. Jordán et al. 2005; Peng et al. 2006; Villegas et al. 2010), and GC candidate photometry out to typically 100 Mpc (e.g. in Coma; Harris et al. 2009; Saifollahi et al. 2021), exceptionally much farther (Alamo-Martínez et al. 2013). However, due to the small field of view of HST cameras, these data sets are not complete but rather restricted to the pointings selected by various observers for their specific purposes. Deep pointed observations from the ground have complemented the HST datasets, again for selected objects; notable examples are the early-type galaxies of the SLUGGS and MATLAS surveys, respectively at $D \leq 27$ Mpc and $D \leq 42$ Mpc (Brodie et al. 2014; Duc & the MATLAS Collaboration 2020). The widest ground-based surveys suitable for extensive GC studies have covered areas of order 10^2 square degrees and targeted the dense environments of nearby galaxy clusters such as Virgo (NGVS; Ferrarese et al. 2012) or Fornax (NGFS; e.g. Ordenes-Briceño et al. 2018; FDS; e.g. Cantiello et al. 2020). *Euclid* will cover almost 15 000 square degrees of sky, and this will allow us to characterize GCs around galaxies of all types in high- and low-density regions, as well as to locate GCs far away from their host (e.g. Jang et al. 2012; Mackey et al. 2019) or associated with extended halo substructures (e.g. Fensch et al. 2020). In these external regions dynamical timescales are longer than near galaxy centers, and the GCs are more direct tracers of galaxy assembly histories.

Before GCs can be studied, they must be found. Here, the spatial resolution of *Euclid*'s VIS camera will be an asset. Any catalog property that reveals the non-point-like nature of a source is instrumental in separating remote GCs from stellar contaminants, as was shown in previous studies from the ground (e.g. Powalka et al. 2016) or using a combination of ground-based and Gaia satellite data (Voggel et al. 2020). The typical 5 pc half-light diameter of a GC will match the VIS pixel size ($0.1''$) at a distance of 10 Mpc (Fig. 1). At a 30 Mpc distance, a cluster at the peak of the GC luminosity function ($M_{\rm VIS} \simeq -8$ AB mag with some dependence on color and environment‡) will have an apparent AB magnitude of about 24.4, and an expected signal-to-noise ratio above 20 in stacked VIS images (C. Laigle, private communication§). Its non-point-like nature will be detectable. The non-point-like nature of brighter clusters will be recognized up to distances of about 70 Mpc, and this limit will be pushed beyond 100 Mpc for ultra-compact dwarf galaxies (UCDs).

Within the first few Mpc, the grainy aspect of the semi-resolved outer parts of GCs will be a characteristic that the eye and trained machine-learning algorithms will recognize. At larger distances however, the separation between GCs and redshifted compact objects will require the analysis of colors; the ideal combination would include *Euclid* measurements in the red and near-IR parts of the spectrum, and optical and u-band data from

*`https://sci.esa.int/web/euclid`

†`https://www.jwst.nasa.gov/`

‡Based on Rejkuba (2012) and the $V - \mathrm{VIS_{AB}}$ indices of stellar population models.

§Based on simulations for point-sources, Nov. 2020

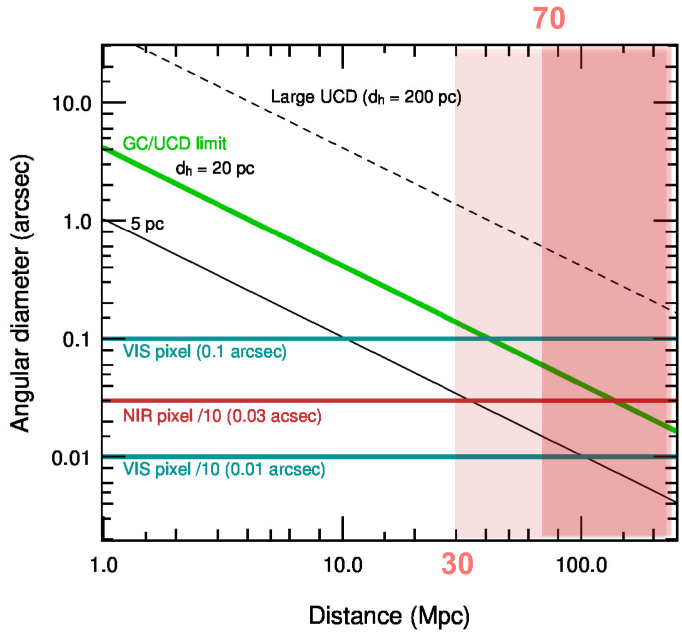

Fig. 1. Properties of globular clusters and ultra-compact dwarf galaxies as seen by the *Euclid* VIS and NIR cameras. The diagonal lines show the angular diameters that correspond to half-light diameters d_{h} typical of globular clusters or ultra-compact dwarf galaxies. Horizontal lines mark the VIS pixel size, and one tenth of the NIR and VIS pixel sizes. The shaded areas are representative of the limits to which GCs near the peak of the GC luminosity function (light shade), or bright clusters (dark shade) will be recognized as non point-like.

other surveys. Indeed, color-color diagrams that exploit the full photospheric emission spectrum of stellar populations are best suited for this exercise (one now commonly used combination is the uiK diagram; Muñoz et al. 2014). The photometric redshift pipelines that are being developed for the core science programs of *Euclid*, and that will use data from ground-based surveys via partnerships, will effectively help rejecting compact background galaxies. We also intend to implement dedicated searches that exploit morphology and colors simultaneously.

As already mentioned, *Euclid* represents a huge step forward in near-infrared photometry, not only by pushing the $5\,\sigma$ detection limit in Y, J, H to $\sim$ 24.4 AB mag (Scaramella et al. 2021) but also by ensuring an excellent uniformity over the sky. For the first time, GC spectral energy distributions that include near-infrared data will be comparable across samples, without the need for color transformations. This will give new perspectives to studies of the dependencies between the stellar populations of GCs and their environment. As both the ground-based sky surveys of the near future and the Euclid Consortium strive to improve absolute photometric calibrations, the new data sets will also provide the most accurate GC colors to date, which will allow a critical evaluation of population synthesis model predictions.

3 How many globular clusters?

Estimates of the number of GCs that *Euclid* catalogs will contain depend on the final footprint of the wide survey, on assumptions on GC specific frequencies and their luminosity distributions, and on a number of technical aspects related to the processing of the images with a pipeline designed primarily for the study of galaxies in the distant universe.

For a first estimate, we have used the NED-D catalog of galaxy distances (Steer et al. 2017), total optical magnitudes from the Simbad database at CDS[¶] and a conservative parametrization of the dependence of specific frequencies on galaxy luminosity based on Peng et al. (2008) and Georgiev et al. (2010). The number of GCs expected to lie within the *Euclid* footprint out to 35 Mpc is of several 10^5, and out to 70 Mpc it exceeds 10^6. How many of these will indeed be measured remains to be examined, using parameters such as galaxy inclination

[¶] `http://simbad.u-strasbg.fr/simbad/` and `http://cdsxmatch.u-strasbg.fr/`

and pipeline characteristics such as its ability to measure small sources near large host galaxies. Rule of thumb estimates suggest that permissive catalogs of GC candidates will contain a few 10^6 objects. Excluding the nearest 2 Mpc and the largest galaxies in the Virgo and Fornax galaxy clusters (the numerous GCs of which have been extensively studied), the numbers of robust GC candidates with high signal-to-noise photometry are expected to approach 10^5. Dedicated simulations are being designed to ascertain these preliminary values.

4 Conclusions

The Euclid Wide Survey will provide us with near-infrared photometry of unprecedented precision across vast parts of the sky. The combination of this information with uniform optical photometry from wide ground-based surveys promises a breakthrough in the study of globular clusters, in particular in fields that require reliable spectral energy distributions: the comparison between GC populations in various environments, the validation of stellar evolution models and stellar population synthesis models for these particular astronomical objects. Indeed, systematic errors and color transformation uncertainties had become a limiting factor that the new data will finally push out of the way.

Complete samples will serve to set up spectroscopic follow-up campaigns, leading to new dynamical studies of galaxy halos and of merging histories. In some areas, *Euclid* will open doors for deeper studies with pointed observations, for instance with the *James Webb* Space Telescope or the *Nancy Grace Roman* Space Telescope. This will be the case for instance for the study of GC populations associated with low surface brightness galaxies or galaxy sub-structures that Euclid may find, at distances of 100 Mpc and more, or for the study of the faint end of the GC luminosity function in various environments.

The EC acknowledges the European Space Agency and a number of agencies and institutes that have supported the development of Euclid, in particular the Academy of Finland, the Agenzia Spaziale Italiana, the Belgian Science Policy, the Canadian Euclid Consortium, the Cen- tre National d'Etudes Spatiales, the Deutsches Zentrum für Luft- und Raumfahrt, the Danish Space Research Institute, the Fundaçao para a Ciência e Tecnologia, the Ministerio de Economia y Competitividad, the National Aeronautics and Space Administration, the National Astronomical Observatory of Japan, the Netherlandse Onderzoekschool Voor Astronomie, the Norwegian Space Agency, the Romanian Space Agency, the State Secretariat for Education, Research and Innovation (SERI) at the Swiss Space Office (SSO), and the United Kingdom Space Agency (cf http://www.euclid-ec.org). A.L., P.-A.D., W.C., A.L. acknowledge financial support via grant ANR-19-CE31-0022 of the French Agence Nationale de la Recherche. This work has made use of the SIMBAD database and of the cross-match service operated at CDS, Strasbourg, France.

References

Alamo-Martínez, K. A., Blakeslee, J. P., Jee, M. J., et al. 2013, ApJ, 775, 20
Brodie, J. P., Romanowsky, A. J., Strader, J., et al. 2014, ApJ, 796, 52
Cantiello, M., Venhola, A., Paolillo, M., et al. 2020, IAU Symp., 351, 68
Duc, P.-A. & the MATLAS Collaboration. 2020, IAU Symp. 355 (in press), arXiv e-prints, arXiv:2007.13874
Fensch, J., Duc, P.-A., Lim, S., et al. 2020, A&A, 644, A164
Ferrarese, L., Côté, P., Cuillandre, J.-C., et al. 2012, ApJS, 200, 4
Georgiev, I. Y., Puzia, T. H., Goudfrooij, P., & Hilker, M. 2010, MNRAS, 406, 1967
Harris, W. E., Kavelaars, J. J., Hanes, D. A., Pritchet, C. J., & Baum, W. A. 2009, AJ, 137, 3314
Jang, I. S., Lim, S., Park, H. S., & Lee, M. G. 2012, ApJ, 751, L19
Jordán, A., Côté, P., Blakeslee, J. P., et al. 2005, ApJ, 634, 1002
Laureijs, R., Amiaux, J., Arduini, S., et al. 2011, arXiv e-prints, arXiv:1110.3193
Mackey, D., Lewis, G. F., Brewer, B. J., et al. 2019, Nature, 574, 69
Muñoz, R. P., Puzia, T. H., Lançon, A., et al. 2014, ApJS, 210, 4
Ordenes-Briceño, Y., Puzia, T. H., Eigenthaler, P., et al. 2018, ApJ, 860, 4
Peng, E. W., Jordán, A., Côté, P., et al. 2006, ApJ, 639, 95
Peng, E. W., Jordán, A., Côté, P., et al. 2008, ApJ, 681, 197
Powalka, M., Lançon, A., Puzia, T. H., et al. 2016, ApJS, 227, 12
Rejkuba, M. 2012, Ap&SS, 341, 195
Saifollahi, T., Trujillo, I., Beasley, M. A., Peletier, R. F., & Knapen, J. H. 2021, MNRAS, 502, 5921
Scaramella, R., Amiaux, J., Mellier, Y., et al. 2021, arXiv e-prints, arXiv:2108.01201
Steer, I., Madore, B. F., Mazzarella, J. M., et al. 2017, AJ, 153, 37
Villegas, D., Jordán, A., Peng, E. W., et al. 2010, ApJ, 717, 603
Voggel, K. T., Seth, A. C., Sand, D. J., et al. 2020, ApJ, 899, 140

THE SOLAR NEIGHBOURHOOD AS SEEN BY GAIA

C. Reylé[1]

Abstract. The *Gaia* astrometric space mission with all sky parallax measurements for about 1.5 billion objects offers the means to complete volume-limited samples with large distance limits. The *Gaia* Catalogue of Nearby Stars (GCNS) is a clean and well-characterized catalogue of objects within 100 pc of the Sun produced from the *Gaia* Early Data Release 3 (EDR3). It has 331 312 entries that is an increase by an order of magnitude with respect to the most complete nearby star census prior to the *Gaia* mission. We briefly show how the catalogue was constructed and why it was not possible before *Gaia EDR3*. Several scientific results were drawn from the catalogue, we here focus on the kinematics properties. We also give a short overview of the 10 pc sample, a by-product of the GCNS.

Keywords: Galaxy: solar neighbourhood, Galaxy: stellar content, parallaxes, kinematics

1 The Gaia Catalogue of Nearby Stars

The *Gaia* Catalogue of Nearby Stars Stars (hereafter GSS21, Gaia Collaboration et al. 2021b) is one of the scientific demonstration papers that have been issued at the same time of the third data release 3 (hereafter *Gaia* EDR3, Gaia Collaboration et al. 2021a) of the *Gaia* mission (Gaia Collaboration et al. 2016). The GCNS is an attempt to make a census of all stars within 100 pc of the Sun using *Gaia* EDR3 to find their distance, motion, magnitude and colour. Such catalogue is important since it provides a calibrating point where unbiased, homogeneous and precise data on all objects can be used to extend our nearby understanding to the whole Galaxy. The 100 pc limit has been chosen because one can expect to have all stars within this volume: GSS21 estimated a completness of 92% for all stars (up to the spectral type M9).

Such a task is not easy to do with the previous *Gaia* data release (hereafter *Gaia* DR2, Gaia Collaboration et al. 2018). It requires a very high astrometric precision, now reached with *Gaia* EDR3, to disentangle between false and true objects. Because *Gaia* measured parallaxes for 1.5 billion stars, even if a tiny proportion of them have a bad astrometric solution, they can scatter on the large parallax tails (both on the positive and negative sides, see Figure 1, left panel) and make more numerous spurious nearby stars than real ones.

Even with the improved astrometry in *Gaia* EDR3, it is not trivial to construct a volume limited catalogue. The simple cut in parallax, $\varpi > 10$ mas, is not enough. Spurious astrometric solutions remain, in particular in crowded regions or for binary stars (*Gaia* EDR3 has a single star astrometric solution). GCNS was constructed with a random forest classification using two training set of objects with "good" and "bad" astrometric solutions. Bad objects are selected with $\varpi < -8$ mas. Good objects are selected outside the Galactic plane, have consistent photometry in *Gaia* (G, $G_{\rm RP}$) and 2MASS (Skrutskie et al. 2006) bands (J, H, K_S), and $\varpi > 8$ mas. All features used for classification are astrometric. The procedure returns a probability of reliable astrometry.

In fine, 625 171 objects are rejected and 331 312 objects constitute the GCNS (see Section 2.1 in GSS21 for a complete description of the classification). A large part of rejected objects are in crowded regions or would have an absolute magnitude M_G around 15 (see figures 1 and 2 in GSS21), which is probably a contamination due to bad solutions for the faintest stars ($G = 20$), e.g. lowest signal-to-noise, near the 100 pc limit where $G = 20$ converts to $M_G = 15$. The same classification procedure have been applied in *Gaia* DR2. Figure 1, right panel, shows the parallax distribution for all objects and only good objects, in *Gaia* DR2 and *Gaia* EDR3. It illustrates that even this classification cannot remove all false entries in *Gaia* DR2(15 entries with $\varpi > 500$ mas remain in *Gaia* DR2, whereas *Gaia* EDR3 has only one, Proxima Centauri).

[1] Institut UTINAM CNRS UMR6213, Université Bourgogne Franche-Comté, OSU THETA Franche-Comté Bourgogne, Observatoire de Besançon, BP1615, 25010 Besançon Cedex, France

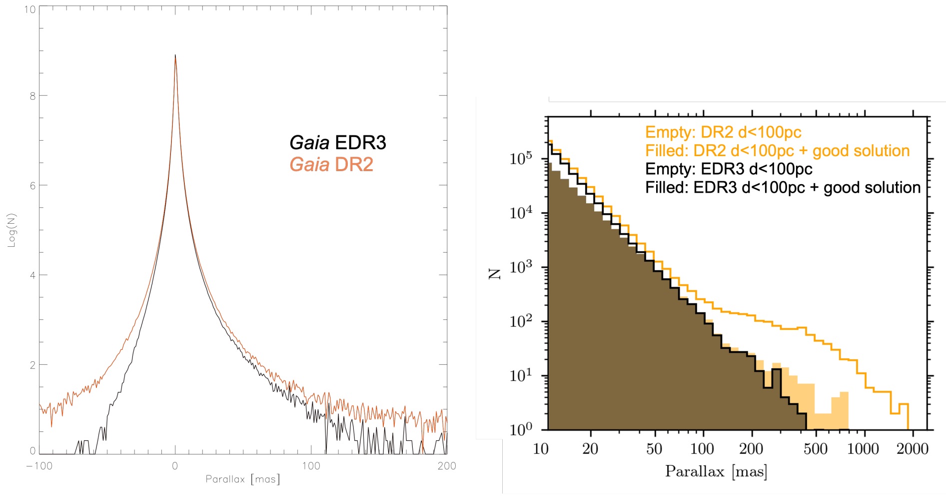

Fig. 1. Left: number of stars (in logarithmic scale) as a function of parallax in *Gaia* DR2 (orange) and *Gaia* EDR3 (black). Right: Zoom on the large parallax tail, showing the *Gaia* DR2 (orange) and *Gaia* EDR3 (black) content before (empty) and after (filled) the random forest classification.

Several examples of scientific exploitation of the GCNS are given in GSS21 (see their Section 5), on the luminosity function, the local kinematics, the Hyades cluster, the ultra-cool dwarfs, the white dwarfs, the unresolved and wide binaries. We here focus on the exploration of the local kinematical plane.

2 The local kinematics from GCNS

In the GCNS, 74 281 stars have a radial velocity in *Gaia* EDR3 (22% of the full GCNS). For those it was possible to compute the (U, V, W) cartesian velocities in the Galactic frame. The resulting Toomre diagram is shown in Figure 2, upper left panel.

Even in this very local sample, the kinematics plane is highly structured in the thin disc, probably due to dynamical effects attributed by several studies to resonance of the bar or linked to the spiral structure (Antoja et al. 2012; Monari et al. 2017; Hunt et al. 2018; Michtchenko et al. 2018).

The nearby halo is clumpy as well. Twelve stars with kinematics similar to *Gaia* Enceladus, a major event experienced by the Milky Way (Helmi et al. 2018) are highlighted in Figure 2, upper left panel. The most extreme star in the Toomre diagram is GJ 725 AB, a twin pair of chemically anomalous stars with a probable extragalactic origin (Reggiani & Meléndez 2018).

The orbital parameters were computed using the online tool Gravpot16*. The Galactic potential we used is a non-axisymmetric potential including the bar, developed by Fernandez-Trincado (2017)†. Gravpot16 is based on a Galactic gravitational potential driven by the Besançon Galaxy Model mass distribution. It includes an axisymmetric component (discs, stellar halo, dark halo, interstellar medium) whose potential computation is described by Bienaymé et al. (1987), and a non axisymmetric component (boxy bar, described in Robin et al. 2012) whose potential is computed via Pichardo et al. (2003) method.

Assuming a bar mass of 10^{10} $M_{\odot}$, a bar pattern speed of 43 km s^{-1} kpc^{-1}, a bar angle of 20°, we compute various orbital parameters: pericentric and apocentric distances, inclination, ellipticity, orbital energy, Jacobi constant, angular momentum, etc. We explore the orbital energy vs Jacobi constant plane‡ to define several groups, as proposed by Fernández-Trincado et al. (2020). It is shown in Figure 2, lower left panel.

We tentatively interpret this diagram. Most of the stars are in the disc and shown by the orange density-scaled region. The clump of twelve stars (blue dots) lies in the region expected for stars dynamically associated with *Gaia* Enceladus, being either merger stars or stars heated by the it. Sixty stars (orange squares) located

*https://gravpot.utinam.cnrs.fr/

†http://theses.fr/s108979

‡The Jacobi energy considers the bar pattern speed, potential energy, and kinetic energy. The total orbital energy is the kinetic plus potential energy.

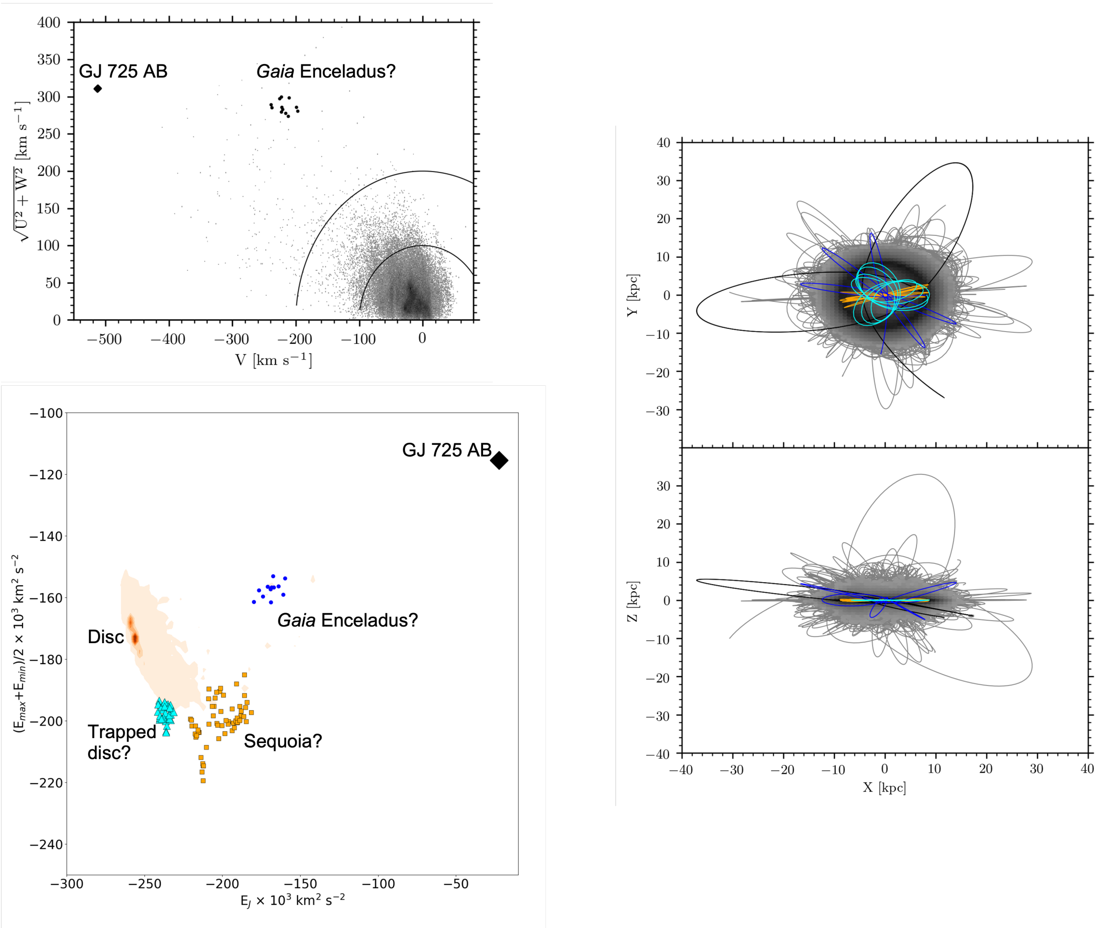

Fig. 2. Upper left: Toomre diagram for all the GCNS entries with a radial velocity in *Gaia* EDR3. The circles indicatively delineate thin-disc, thick-disc, and halo stars. Lower left: orbital energy vs Jacobi energy for all the GCNS entries with a radial velocity in *Gaia* EDR3. Courtesy of José G. Fernández-Trincado. Right: Orbits over 1 Gyr (forward), depicted on a face-on (top) and an edge-on (bottom) view. The colours refer to the objects highlighted on the left panel.

in the low-energy region could be associated to Sequoia, another major merger event (Myeong et al. 2019). The "hook" sample of 40 stars (cyan triangles) in the low-energy tail of the disc could be disc stars trapped in resonance with the bar structure. Further analysis of these groups should be done by cross-identification with spectroscopic surveys, or spectroscopic follow-up of the kinematical "outliers" for chemical characterisation.

Orbits are integrated over 1 Gyr, forward, in the referential frame of the Galaxy[§]. They are shown in Figure 2, right panel. The most numerous disc stars, such as the Sun, populate the circular orbits in the Galactic plane($Z = 0$). Halo stars have higher eccentricities and inclinations.The central part of the (X, Y) plane is populated by the orbits of stars coming from (or going to) the central regions of the Galaxy.

3 The 10 pc sample

As a by-product of the GCNS, we compiled all stars and brown dwarfs within 10 pc observable by *Gaia* and compare it with the GCNS as a quality assurance test. We further complement the list to get a full 10 pc census, including bright stars, brown dwarfs, and vetted exoplanets. The resulting catalogue contains 540 stars, brown dwarfs, exoplanets in 339 sytems, and is the as volume-complete as possible list from current knowledge (Reylé et al. 2021). The colour-absolute magnitude diagram is shown in Figure 3, coloured as a function of spectral type, superimposed with the GCNS (grey dots). It provides benchmark stars to define calibration samples, and to test the quality of the forthcoming Gaia releases.

[§]An animation of these orbits can be seen on `https://www.youtube.com/watch?v=k9pHGhNtyPk&ab_channel=ESAGaiaMission`

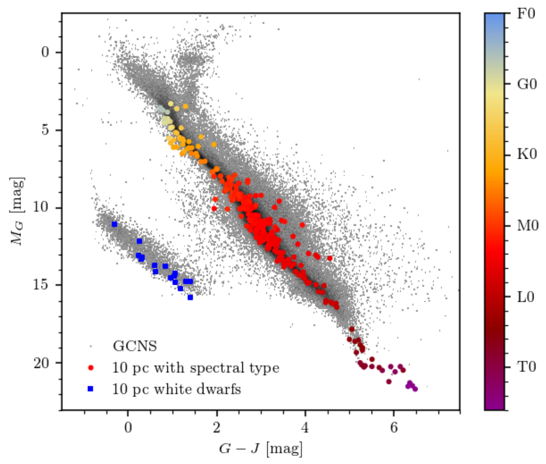

Fig. 3. Colour-absolute magnitude diagram of the 10 pc sample, superimposed on the GCNS (grey dots). The colour bar indicates the spectral type. White dwarfs are in dark blue. From Reylé et al. (2021).

4 Conclusions

The *Gaia* Catalogue of Nearby Stars offers a clean, homogeneous and precise sample of the 100 pc sphere, allowing a detailed kinematics study (but not only). It contains a large diversity of stars and show that our "today" neighbours are from all the parts of the Galaxy, including the innermost regions. The *Gaia* next data release in 2022 will provide radial velocities for over 50% of the GCNS, allowing the computation of more more orbits and charaterisation of nearby streams, but also astrophysical parameters for complementary chemical characterisation. It will also improve the astrometric solution of binary stars, and will allow to update the very nearby, 10 pc sample.

The *Gaia* Catalogue of Nearby Stars, the 10 pc catalogue, and outreach material can be found on `https://gucds.inaf.it/`.

References

Antoja, T., Helmi, A., Bienayme, O., et al. 2012, MNRAS, 426, L1
Bienaymé, O., Robin, A. C., & Creze, M. 1987, A&A, 180, 94
Fernandez-Trincado, J. 2017, PhD thesis, University Bourgogne-Franche-Comté, France, http://theses.fr/s108979
Fernández-Trincado, J. G., Chaves-Velasquez, L., Pérez-Villegas, A., et al. 2020, MNRAS, 495, 4113
Gaia Collaboration, Brown, A. G. A., Vallenari, A., et al. 2018, A&A, 616, A1
Gaia Collaboration, Brown, A. G. A., Vallenari, A., et al. 2021a, A&A, 649, A1
Gaia Collaboration, Prusti, T., de Bruijne, J. H. J., et al. 2016, A&A, 595, A1
Gaia Collaboration, Smart, R. L., Sarro, L. M., et al. 2021b, A&A, 649, A6
Helmi, A., Babusiaux, C., Koppelman, H. H., et al. 2018, Nature, 563, 85
Hunt, J. A. S., Hong, J., Bovy, J., Kawata, D., & Grand, R. J. J. 2018, MNRAS, 481, 3794
Michtchenko, T. A., Lépine, J. R. D., Pérez-Villegas, A., Vieira, R. S. S., & Barros, D. A. 2018, ApJ, 863, L37
Monari, G., Kawata, D., Hunt, J. A. S., & Famaey, B. 2017, MNRAS, 466, L113
Myeong, G. C., Vasiliev, E., Iorio, G., Evans, N. W., & Belokurov, V. 2019, MNRAS, 488, 1235
Pichardo, B., Martos, M., Moreno, E., & Espresate, J. 2003, ApJ, 582, 230
Reggiani, H. & Meléndez, J. 2018, MNRAS, 475, 3502
Reylé, C., Jardine, K., Fouqué, P., et al. 2021, A&A, 650, A201
Robin, A. C., Marshall, D. J., Schultheis, M., & Reylé, C. 2012, A&A, 538, A106
Skrutskie, M. F., Cutri, R. M., Stiening, R., et al. 2006, AJ, 131, 1163

Session 24

Stellar multiplicity / Multiplicité stellaire

SF2A 2021
A. Siebert, K. Baillié, E. Lagadec, N. Lagarde, J. Malzac, J.-B. Marquette, M. N'Diaye, J. Richard, O. Venot (eds)

MULTIPLE STELLAR EVOLUTION: A POPULATION SYNTHESIS ALGORITHM TO MODEL THE STELLAR, BINARY, AND DYNAMICAL EVOLUTION OF MULTIPLE-STAR SYSTEMS

A.S. Hamers[1]

Abstract. In recent years, observations have shown that multiple-star systems such as hierarchical triple and quadruple-star systems are common, especially among massive stars. They are potential sources of interesting astrophysical phenomena such as compact object mergers, leading to supernovae, and gravitational wave events. However, many uncertainties remain in their often complex evolution. Here, we present the population synthesis code *Multiple Stellar Evolution* (MSE), designed to rapidly model the stellar, binary, and dynamical evolution of multiple-star systems. MSE includes a number of new features not present in previous population synthesis codes: (1) an arbitrary number of stars, as long as the initial system is hierarchical, (2) dynamic switching between secular and direct N-body integration for efficient computation of the gravitational dynamics, (3) treatment of mass transfer in eccentric orbits, which occurs commonly in multiple-star systems, (4) a simple treatment of tidal, common-envelope, and mass transfer evolution in which the accretor is a binary instead of a single star, (5) taking into account planets within the stellar system, and (6) including gravitational perturbations from passing field stars. MSE, written primarily in the C++ language, will be made publicly available and has few prerequisites; a convenient PYTHON interface is provided. We give a short description of MSE and illustrate how to use the code in practice. We demonstrate its operation in a number of examples.

Keywords: binaries: general, stars: kinematics and dynamics, methods: statistical, gravitation,planets and satellites: dynamical evolution and stability, stars: evolution

1 Introduction

Multiple-star systems, stellar systems containing three or more stars, are common. They are usually arranged in a hierarchical configuration, since they would otherwise be short lived. The simplest hierarchical configuration occurs in triple systems in which two stars are orbited by a more distant, tertiary star. If the inner and outer orbits in such a configuration are initially mutually highly inclined, then the gravitational torque of the outer orbit can induce high-amplitude eccentricity oscillations in the inner binary, known as von Zeipel-Lidov-Kozai (ZLK) oscillations, which have important implications for a large variety of triple systems (von Zeipel 1910; Lidov 1962; Kozai 1962; see Naoz 2016; Shevchenko 2017; Ito & Ohtsuka 2019 for reviews). The dynamics become more complex for higher-order multiplicity systems. In hierarchical quadruples, secular evolution can be more efficient compared to triples (Pejcha et al. 2013; Hamers et al. 2015; Vokrouhlický 2016; Hamers & Lai 2017; Grishin et al. 2018a), and this can have implications for, e.g., short-period binaries (Hamers 2019), and Type Ia Supernovae (SNe Ia; Hamers 2018a; Fang et al. 2018). This trend carries over to higher-multiplicity systems (quintuples, sextuples, etc.), in which the likelihood for strong interactions due to secular evolution is even higher (Hamers 2020a).

Population synthesis codes, have been used extensively during the past several decades to study the evolution of predominantly binary stars (e.g., Whyte & Eggleton 1985; Portegies Zwart & Verbunt 1996; Izzard et al. 2009; Toonen et al. 2012). In particular, BSE (Hurley et al. 2002, hereafter HTP02), based on the rapid evolution algorithm SSE (Hurley et al. 2000, hereafter HPT00), has been an industry standard for nearly two decades. Also, BSE, and the SSE analytic stellar evolution tracks on which it is based, have formed the basis for many

[1] Max-Planck-Institut für Astrophysik, Karl-Schwarzschild-Str. 1, 85741 Garching, Germany

other codes. More recently, population synthesis codes have been developed that can model the evolution of triple stars taking into account both stellar/binary evolution, and gravitational dynamics (Hamers et al. 2013; Toonen et al. 2016). Current triple population synthesis codes face a number of limitations: mass transfer is not taken into account self-consistently, dynamics are often approximated, 'triple' interactions such as mass transfer from the tertiary onto the inner binary are not included, and objects are limited to be stars (i.e., planets cannot be included).

In these proceedings, we present a new population synthesis code, Multiple Stellar Evolution (MSE), aimed at modelling the stellar evolution, binary interactions (such as mass transfer and common-envelope, CE, evolution), and gravitational dynamics of multi-body systems. The core components of MSE are the stellar evolution fits of HPT00, several aspects of binary evolution adopted from HTP02, a self-consistent treatment of eccentric mass transfer, and accurate dynamical modelling using either secular or direct N-body integration. We briefly present the new evolution algorithm (Section 2; for more details, we refer to Hamers et al. (2021)) and give an example in Section 3. We conclude in Section 4.

2 The MSE algorithm

2.1 Dynamics

The MSE code models the evolution of an arbitrary number of stars in an initial hierarchical configuration. Gravitational dynamical evolution is taken into account via two methods: (1) secular (orbit-averaged) integration for sufficiently hierarchical systems, based on the formalism of Hamers & Portegies Zwart (2016); Hamers (2018b, 2020b), and (2) direct N-body integration for cases in which the secular approach breaks down using the algorithmic chain regularization code MSTAR (Rantala et al. 2020). The secular integrations include tidal evolution under the assumption of equilibrium tides (Hut 1981; Eggleton et al. 1998), where the efficiency of tidal dissipation is computed using the prescription of HTP02. The direct N-body integrations currently do not include additional acceleration terms that describe tidal evolution. However, collision detection is implemented. Both secular and direct N-body codes include post-Newtonian terms.

Often, the system is dynamically stable, and the secular approximation applies. However, evolutionary processes such as mass loss from stellar evolution can destabilise a system, or could void the validity of the secular approximation. In MSE, it is continuously checked whether the system is still stable using the stability criterion of Mardling & Aarseth (2001). However, other, less stringent conditions exist in which the secular approximation breaks down, namely when the secular time-scale becomes comparable to one of the orbital periods in the system (e.g., Antonini & Perets 2012; Luo et al. 2016; Grishin et al. 2018b; Lei et al. 2018; Hamers 2020b). The MSE code checks for this 'semisecular' regime by comparing the instantaneous time-scale for secular evolution to change the specific angular momentum of any orbit to the orbital period. If either a dynamical instability occurs or the semisecular regime is entered, MSE switches to direct N-body integration. Subsequently, the N-body system is analysed and if (and only if) a stable hierarchical (sub)configuration is identified for the entire system (this can include unbound objects), it will switch back to secular integration.

2.2 Stellar evolution

Stellar evolution in MSE is modelled using fast analytic fitting formulae to detailed stellar evolution models from HPT00. These tracks include information on large-scale parameters such as total mass, radius, luminosity, and global properties of the core (if present). Also included is mass loss due to stellar winds, and spin-down due to magnetic braking. Mass loss due to stellar winds is assumed to affect the orbits adiabatically, i.e., with $m_{\rm enc}a_i$ and e_i constant, where $m_{\rm enc}$ is the enclosed mass, and a_i and e_i are the orbital semimajor axis and eccentricity, respectively.

When stars evolve to become NSs or BHs, we assume that mass is lost instantaneously (i.e., the opposite from the adiabatic regime), and take into account the effect of the mass loss on all orbits in the system, assuming no interaction with the lost mass. We also take into account natal kicks for NSs and BHs, by adopting several models for sampling the velocity kick when compact objects are formed (see Hamers et al. 2021). In the default model, 'kick distribution model 1', the natal kick speeds are drawn from a Maxwellian distribution with dispersion $\sigma_{\rm kick} = 265\,{\rm km\,s^{-1}}$ for NSs, Hobbs et al. 2005) and $\sigma_{\rm kick} = 50\,{\rm km\,s^{-1}}$ for BHs.

2.3 Binary interactions

The MSE code includes a number of binary interactions. We check for the condition of Roche lobe overflow (RLOF) for all stars onto companions. If the companion is a single star, 'binary' mass transfer applies; otherwise, 'triple' mass transfer or triple CE could occur (see Section 2.4). In the binary case, details of the mass transfer process such as the mass transfer rate, aging/rejuvenation, and the conditions for unstable CE evolution are modelled using similar prescriptions as those used by HTP02. However, an important difference from HTP02 is the orbital response to mass transfer: HTP02 assumed that tides are always efficient enough to circularise the orbit at the onset of mass transfer. This assumption can break down in triple or higher-order systems, in which eccentricity can be excited secularly (e.g., Toonen et al. 2020). MSE includes the analytic model of Hamers & Dosopoulou (2019) to describe the orbital response to mass transfer in eccentric orbits. Unstable mass transfer can lead to CE evolution; this is taken into account in MSE by adopting the α_{CE}-λ prescription, similar to HTP02. Prescriptions for the outcomes of CE evolution are also adopted from HTP02. In close orbits, accretion of material from stellar winds onto companions can be important. MSE includes this process of wind accretion by adopting the Bondi-Hoyle-Lyttleton formalism (Hoyle & Lyttleton 1939; Bondi & Hoyle 1944).

2.4 Triple interactions

In some systems, an outer star can fill its Roche lobe around an inner companion consisting of two stars (in contrast to 'binary' mass transfer). This type of evolution, which can result in stable transfer onto the companion binary, or unstable 'triple CE' evolution, is still poorly understood. MSE models this phase by adopting a number of simplified prescriptions, motivated by more detailed simulations (de Vries et al. 2014; Comerford & Izzard 2020; Glanz & Perets 2021).

2.5 Fly-bys

The effects of passing stars in the field (i.e., low-density environments) are taken into account in MSE by sampling interloping stars during the simulation with a Monte Carlo approach. Based on the stellar density and relative velocity dispersion, perturbers are sampled that impinge on an 'encounter sphere' with a large radius. The effects of the perturber on the multiple system are then computed for impulsive encounters (the latter are most important in the field, although secular encounters dominate in dense stellar systems such as globular clusters, see, e.g., Heggie & Rasio 1996; Hamers & Samsing 2019).

3 Example system

We show an example system evolved with MSE involving RLOF and CE evolution in a stellar triple. In Fig. 1, we show the evolution of the masses (top row), orbital separations and stellar radii (middle row), and stellar types (bottom row). We also show important events during the evolution of the system in the form of a mobile diagram (Evans 1968) in Fig. 2. During the MS, high-amplitude ZLK oscillations are induced in the inner binary, but they are not sufficiently strong to induce interaction. As the $3\,\mathrm{M}_\odot$ primary star evolves to an AGB star, it fills its Roche lobe around its $2\,\mathrm{M}_\odot$ companion. The donor is then stripped of its envelope, and the core turns into a CO WD which is orbiting the companion (still an MS star) in a more compact orbit. In this example, we focus on the early evolution. However, at later times, the inner orbit could undergo further interaction (e.g., produce a cataclysmic variable).

4 Conclusions

MSE is a new population synthesis code which can be used to quickly model the stellar, binary, and gravitational dynamical evolution of hierarchical multiple systems with any number of stars. The gravitational dynamics are taken into account using either a secular approach (Hamers & Portegies Zwart 2016; Hamers 2018b, 2020b), or direct N-body integration (Rantala et al. 2020). Stellar evolution is taken into account by adopting the SSE fitting functions (HPT00), whereas binary interactions are modeled using semi-analytic models and prescriptions. New features of MSE in comparison to previous population synthesis codes include (1) an arbitrary number of stars, as long as the initial system is hierarchical, (2) dynamic switching between secular and direct N-body integration for efficient computation of the gravitational dynamics, (3) treatment of mass transfer in eccentric orbits, which occurs commonly in multiple-star systems, (4) a simple treatment of tidal, common-envelope, and

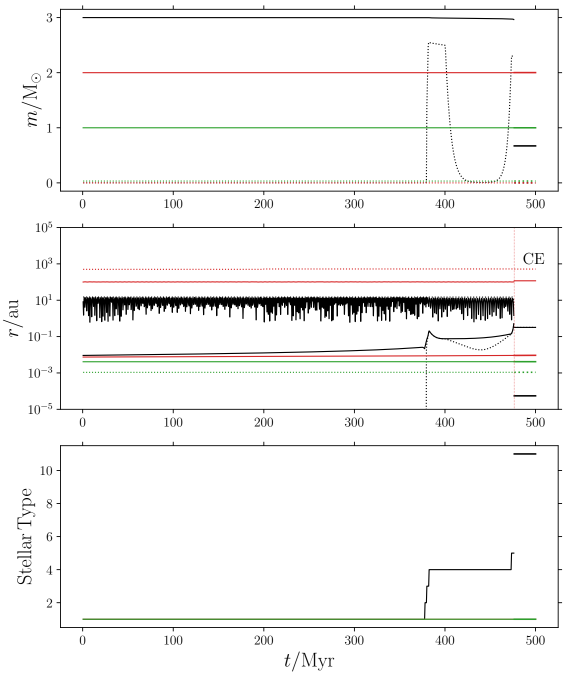

Fig. 1. Evolution of the masses (top row), orbital separations and stellar radii (middle row), and stellar types (bottom row) for the example triple system discussed in Section 3. In the top panel, the three masses are shown with solid black, red, and green lines, respectively. The convective core radii of the corresponding stars are shown with dotted lines. In the middle panel, the bottom solid lines show the stellar radii, with the same colours used as in the top panel. The black and red lines in the top and middle part of the panel show the orbital separations (solid: periapsis distances; dotted: semimajor axes) of the inner and outer orbits, respectively. The onset of a CE event in the inner binary is indicated. The bottom panel shows the evolution of the stellar types (see HPT00), with the same colours used as in the top panel.

mass transfer evolution in which the accretor is a binary instead of a single star, (5) taking into account planets within the stellar system, and (6) including gravitational perturbations from passing field stars. At the time of writing, MSE is part of a private repository on `GitHub`*. Access to this repository can be requested by contacting the author. In the future, the repository will be made publicly available.

A.S.H. thanks the Max Planck Society for support through a Max Planck Research Group.

References

Antonini, F. & Perets, H. B. 2012, ApJ, 757, 27
Bondi, H. & Hoyle, F. 1944, MNRAS, 104, 273
Comerford, T. A. F. & Izzard, R. G. 2020, MNRAS, 498, 2957
de Vries, N., Portegies Zwart, S., & Figueira, J. 2014, MNRAS, 438, 1909
Eggleton, P. P., Kiseleva, L. G., & Hut, P. 1998, ApJ, 499, 853
Evans, D. S. 1968, QJRAS, 9, 388
Fang, X., Thompson, T. A., & Hirata, C. M. 2018, MNRAS, 476, 4234
Glanz, H. & Perets, H. B. 2021, MNRAS, 500, 1921
Grishin, E., Lai, D., & Perets, H. B. 2018a, MNRAS, 474, 3547
Grishin, E., Perets, H. B., & Fragione, G. 2018b, MNRAS, 481, 4907
Hamers, A. S. 2018a, MNRAS, 478, 620
Hamers, A. S. 2018b, MNRAS, 476, 4139

*`https://github.com/hamers/mse`.

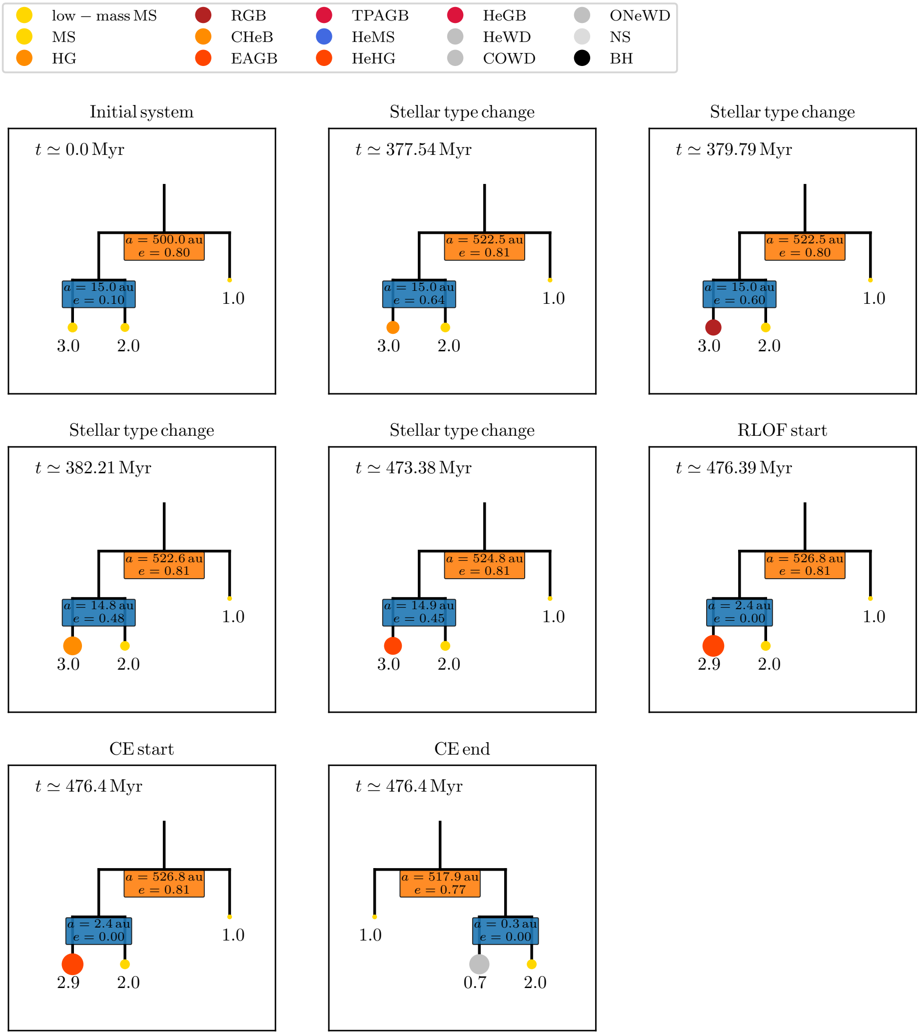

Fig. 2. Mobile diagrams for the example triple system discussed in Section 3. The title of each panel gives a description of the event that occurred. The semimajor axes and eccentricities are indicated at each orbit. Numbers next to stars show the masses of the objects (in $M_\odot$). The colours of the stars depend on the stellar type; see the legend at the top of the figure.

Hamers, A. S. 2019, MNRAS, 482, 2262
Hamers, A. S. 2020a, MNRAS, 494, 5298
Hamers, A. S. 2020b, MNRAS, 494, 5492
Hamers, A. S. & Dosopoulou, F. 2019, ApJ, 872, 119
Hamers, A. S. & Lai, D. 2017, MNRAS, 470, 1657
Hamers, A. S., Perets, H. B., Antonini, F., & Portegies Zwart, S. F. 2015, MNRAS, 449, 4221
Hamers, A. S., Pols, O. R., Claeys, J. S. W., & Nelemans, G. 2013, MNRAS, 430, 2262
Hamers, A. S. & Portegies Zwart, S. F. 2016, MNRAS, 459, 2827
Hamers, A. S., Rantala, A., Neunteufel, P., Preece, H., & Vynatheya, P. 2021, MNRAS, 502, 4479
Hamers, A. S. & Samsing, J. 2019, MNRAS, 487, 5630
Heggie, D. C. & Rasio, F. A. 1996, MNRAS, 282, 1064
Hobbs, G., Lorimer, D. R., Lyne, A. G., & Kramer, M. 2005, MNRAS, 360, 974
Hoyle, F. & Lyttleton, R. A. 1939, Proceedings of the Cambridge Philosophical Society, 35, 405
Hurley, J. R., Pols, O. R., & Tout, C. A. 2000, MNRAS, 315, 543
Hurley, J. R., Tout, C. A., & Pols, O. R. 2002, MNRAS, 329, 897
Hut, P. 1981, A&A, 99, 126
Ito, T. & Ohtsuka, K. 2019, Monographs on Environment, Earth and Planets, 7, 1
Izzard, R. G., Glebbeek, E., Stancliffe, R. J., & Pols, O. R. 2009, A&A, 508, 1359
Kozai, Y. 1962, AJ, 67, 591
Lei, H., Circi, C., & Ortore, E. 2018, MNRAS, 481, 4602

Lidov, M. L. 1962, Planet. Space Sci., 9, 719

Luo, L., Katz, B., & Dong, S. 2016, MNRAS, 458, 3060

Mardling, R. A. & Aarseth, S. J. 2001, MNRAS, 321, 398

Naoz, S. 2016, ARA&A, 54, 441

Pejcha, O., Antognini, J. M., Shappee, B. J., & Thompson, T. A. 2013, MNRAS, 435, 943

Portegies Zwart, S. F. & Verbunt, F. 1996, A&A, 309, 179

Rantala, A., Pihajoki, P., Mannerkoski, M., Johansson, P. H., & Naab, T. 2020, MNRAS, 492, 4131

Shevchenko, I. I. 2017, Part of the Astrophysics and Space Science Library book series (ASSL, volume 441), Vol. 441, The Lidov-Kozai Effect - Applications in Exoplanet Research and Dynamical Astronomy

Toonen, S., Hamers, A., & Portegies Zwart, S. 2016, Computational Astrophysics and Cosmology, 3, 6

Toonen, S., Nelemans, G., & Portegies Zwart, S. 2012, A&A, 546, A70

Toonen, S., Portegies Zwart, S., Hamers, A. S., & Band opadhyay, D. 2020, A&A, 640, A16

Vokrouhlický, D. 2016, MNRAS, 461, 3964

von Zeipel, H. 1910, Astronomische Nachrichten, 183, 345

Whyte, C. A. & Eggleton, P. P. 1985, MNRAS, 214, 357

SF2A 2021
A. Siebert, K. Baillié, E. Lagadec, N. Lagarde, J. Malzac, J.-B. Marquette, M. N'Diaye, J. Richard, O. Venot (eds)

ORBIT CHARACTERIZATION WITH HIPPARCOS AND GAIA

A. Leclerc[1], C. Babusiaux [1], T. Forveille [1] and X. Delfosse [1]

Abstract. Combining absolute astrometry with direct imaging or radial velocities allows to better constrain the masses of binary systems. The absolute astrometry data from the Hipparcos (1990-1993) and Gaia (2014-) satellites allow us to use the long period of time between the two missions to accurately characterize orbits. Moreover, the exploitation of the Hipparcos data prepares us to use the future Gaia data in the study of binary systems. We will present here a new tool that combines the data from these two satellites rigorously, together with direct imaging and radial velocities. This modular tool can use the Transit Data from Hipparcos, which should be used in cases where the secondary light affects the observations. We will also present an example of its use with the case of GL494.

Keywords: binaries, astrometry

1 Introduction

The combination of multiple observational methods for the characterization of binary systems is frequently used because it allows to determine the masses in a system with the fewest assumptions.
The absolute astrometry method uses the evolution of the position of a star to retrieve the 5 astrometric parameters that describe it the best. These 5 astrometric parameters (AP) are the position (α and δ), the parallax (π) and the proper motion of the star (μ_α and μ_δ).
When the light from the secondary is negligible compared to the light from the primary star, what is called the photocentre (the centre of light of the system) is located on the primary star. This photocentre is moving, due to the presence of the secondary, around the barycentre of the system: this motion is called the reflex motion. When the reflex motion is detected in astrometry, the orbital parameters of the binary system can be determined: the period of the system, the periastron time, which is the date when the photocentre is closest to the star, the eccentricity of the system, the semi major axis of the orbit of the photocentre, the inclination of the system and two angles that orientate the system: the longitude of the ascending node and argument of the periastron.
All these parameters can be adjusted with our new tool, using a gradient descent method implementing automatic differentiation thanks to the R package: TMB (Kristensen et al. 2016). The absolute astrometry data used in the tool are presented in section 2, and the method for the combination of Hipparcos and Gaia data is presented in section 3. An example of a study done with this tool, GL494 system, is presented in the section 4.

2 Absolute astrometric data

2.1 *Hipparcos data*

The Hipparcos mission took place in the 90's and two data reductions are available: the original reduction (ESA 1997) and the new reduction (van Leeuwen 2007).
The observations from Hipparcos are given unidimentionnaly along great circles defined by each rotation of the satellites, and are denoted by $\Delta\nu$. These observations are in fact residuals between the real position of the star and the position of the star modelised with the astrometric parameters published in the Hipparcos catalog. The residuals $\Delta\nu$, the observational epoch and informations on the orientation of the great circle that path through a certain observed star are given in the Intermediate Astrometric Data (IAD, Martin et al. 1997 and van Leeuwen & Evans 1998).

[1] Univ. Grenoble Alpes, CNRS, IPAG, 38000 Grenoble, France

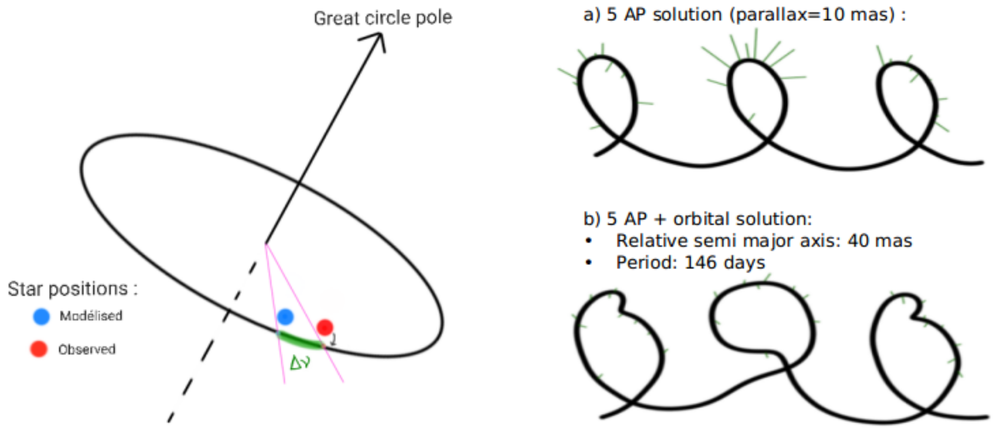

Fig. 1. Left: Projection on the great circle in green: residuals $\Delta\nu$. **Right:** Illustration of the astrometric solution, represented in black continuous line, and the residuals in green. **a:** 5 astrometric parameters solution. **b:** 5 astrometric parameters and orbital solution.

In the illustration in the right part of the figure 1 we plotted in green the residuals with significant size, but their orientation are chosen arbitrary. When comparing the size of the residuals between solution a and b we see that the residuals are minimized with the complete solution b * . It is important to notice that we have to be careful that the light of the secondary star does not affect Hipparcos detection in order to use the IAD. In Hipparcos, these systems where the secondary light impacts the data are listed in DMS-C (Double and Multiple System, with Component solution). In these cases, we can not use the IAD anymore and we have to use the Transit Data (TD, original reduction: Quist & Lindegren 1999 and new reduction: van Leeuwen 2007) from Hipparcos, that are also available in the reductions, and that contains additional light modulation informations. The other solutions from the DMS annex of Hipparcos are: G for acceleration solutions with 7 and 9 parameters, 0 for orbital solutions where the orbital parameters are estimated, V for the variability induced mover solution and X for stochastic solutions. All these solutions are described in ESA 1997.
An evaluation of the quality of the solution is also provided: the F2, which is a Gaussianized χ^2. When this one is higher than 2, there is a potential signal that describes the reflex motion of the photocentre.

2.2 *Gaia data*

The Gaia mission (Gaia Collaboration et al. 2016b) started in 2014 and it is still ongoing. The different data releases (DR1: Gaia Collaboration et al. 2016a, DR2: Gaia Collaboration et al. 2018 and eDR3: Gaia Collaboration et al. 2021) provide the 5 astrometric parameters that best adjust the observations, without taking into account an eventual multiplicity: the multiplicity will be taken into account in the DR3 release.
The scanning law of Gaia, that gives for each star the epoch of observation and the angle of scan of the satellite is also provided for each release.
The RUWE (Renormalised Unit Weight Error) of Gaia evaluates the quality of the 5 AP for each star: if this value is higher than 1.4, then the published AP are not good and we have to check that the signal comes from an astrometric signal and not a flux contamination. The evidence of a contamination is a high rate of the *ipd_frac_multi_peak* flag in Gaia eDR3. The only solutions for considering the Gaia data of these stars is to wait for Gaia to solve the system, or wait for the Gaia's full data to be released (DR4). When it is the case, the tool uses the 5 AP of each components. It happens that the solution of one or both of the components is an astrometric solution with 2 parameters (the positional parameters α and δ): in these cases, the tool uses the 2 AP available.

*Because the observations are unidimensional, the real position of the star is located somewhere in a perpendicular line at the end of the lines that represents the residuals. This is not represented here for the purpose of simplification.

3 The combination of Hipparcos and Gaia data

The principle used by the tool is that it combines all the observations available (from direct imaging and radial velocity), together with the absolute astrometry from Hipparcos and Gaia, by adjusting the residuals from Hipparcos (from the IAD or the TD) and the 5 AP from Gaia latest reduction (eDR3 at this moment). If the star is resolved by Gaia, the 5 AP of the components A and B are adjusted as described in the section 2.2.
The illustration of this principle is represented in the figure 2, with Hipparcos and Gaia in the same reference frame. The reference frame chosen in the tool is the Hipparcos frame.

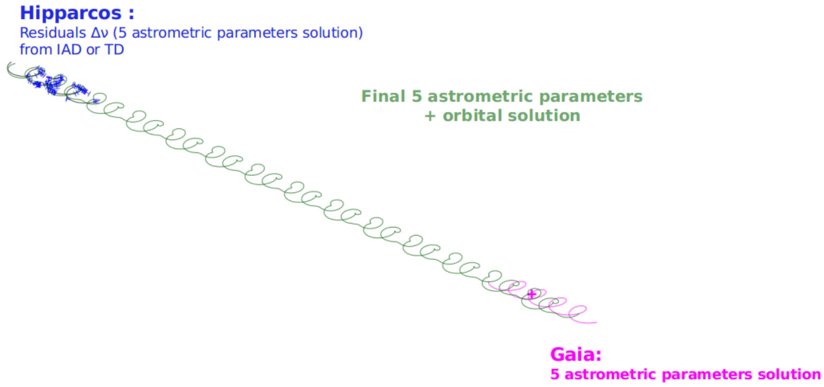

Fig. 2. Illustration of the principle of the combination of Hipparcos and Gaia data in the tool.

The principle of the Gaia's frame rotation is to put the Gaia's positions and proper motions in the Hipparcos proper motion reference frame as described in Lindegren et al. 2018, Brandt 2018 and Kervella et al. 2019. The errors on the positions, the proper motions and the parallaxes are also increased, and the difference between the zero parallax of Hipparcos and Gaia is taken into account. The values used for the rotation of Gaia eDR3 are given in Fabricius et al. 2021.
The method consists then in the adjustment of a 5 AP solution with the Hipparcos epoch as reference. This solution is then propagated at the Gaia epoch while taking into account the radial velocity of the source: the new solution is then called the AP_G. The Gaia AP published cannot be compared with the propagated solution AP_G, because in the Gaia AP, the 5 AP tries to describe a more complex motion: the one of the barycentre and an additional reflex motion. However, since we are adjusting the orbital solution, we can predict where the two companions are at the time Gaia observed. Thanks to the epochs of observations and the orientation of the satellite provided in the scanning law, we can simulate Gaia's residuals corresponding to the reflex motion, and then deduce the 5 AP solution that would have been observed by Gaia and compared it with the Gaia AP published through a χ^2 using a covariance matrix.

4 Example case: GL494

This star is a variable star studied in direct imaging by Bowler et al. (2020) and in radial velocity by Tal-Or et al. (2019). The relative orbit is well covered with 16 observations,and an estimation of the magnitude difference in K band is also provided: $\Delta m_K = 4.27 \pm 0.02$. The 65 observations available in radial velocity are very impacted by the stellar variability.

For this system, the magnitude difference between the two stars is significant so the light of the secondary star in negligible. Gaia does not resolve the system and the RUWE value is 4.19: the signal contained in Gaia is due to the reflex motion of the primary star, so we can use the 5 AP published. There is also a proper motion anomaly detected by Kervella et al. (2019), a solution type in the Original Reduction of Hipparcos that detected an acceleration (7 parameters solution), and an F2 with a value of 2.32 in the New Reduction of Hipparcos, that indicates that the simple 5 AP solution is not sufficient and that there is a reflex motion signal.

Here is represented the adjustment of the direct imaging data with the IAD from Hipparcos and Gaia's 5 AP solution from eDR3. The radial velocity data are not used because of the variability but but we will check their agreement with the adjustment after.

The parameters determined with this new adjustment are compatible with the parameters published by Bowler et al. (2020). This adjustment is represented in the figure 3 together with the observations. For Hipparcos, the new residuals are represented.

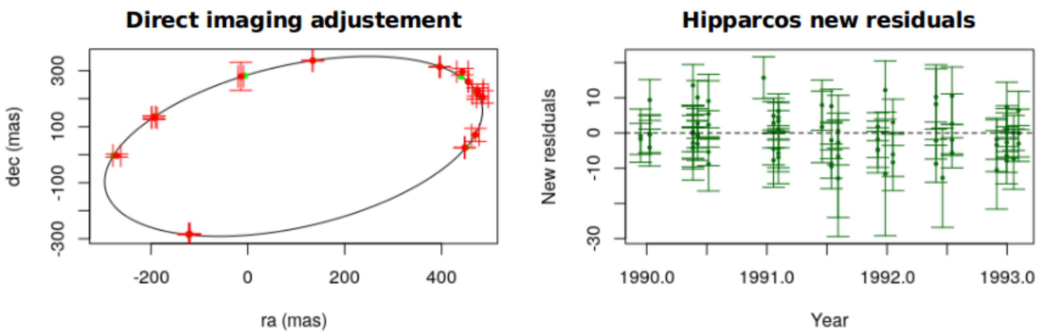

Fig. 3. Left: Direct imaging adjustment: The observations are represented in red, the relative orbit from the adjustment is the continuous line in black and the real epoch of observations are the green dots. **Right:** The new Hipparcos residuals are represented in green. They are the residuals from the new 5 AP determined from the adjustment.

The observations in radial velocity are also in good agreement with the adjustment from the relative and absolute astrometry data, and the variability is responsible of the noise around the adjustment. Finally, what is new here is the estimation of the individual masses of the system, that will be published soon.

5 Conclusion

Here we have introduced our new tool that combines the available absolute astrometric data from Hipparcos and Gaia together with complementary observations such as radial velocity and relative astrometric data. For now, the tool have been tested on several stars as well as on simulated data and it allows us to identify the advantages and disadvantages of it. The first advantage is obviously that it is a realistic approach that adjust all the observations available together, and the second is that it is the closest method that will be used with the future Gaia full data. The disadvantage is that this method work only on well-constrained orbit, and so, it need enough data. The expertise on the Transit Data offers to study also resolved stars by Gaia, and this topic will be a part of an upcoming article, together with the presentation of the tool, and the study of several interesting stars such as GL494.

References

Bowler, B. P., Blunt, S. C., & Nielsen, E. L. 2020, AJ, 159, 63
Brandt, T. D. 2018, ApJS, 239, 31
ESA. 1997, The Hipparcos and Tycho Catalogues, ESA SP-1200
Fabricius, C., Luri, X., Arenou, F., et al. 2021, A&A, 649, A5
Gaia Collaboration, Brown, A. G. A., Vallenari, A., et al. 2018, A&A, 616, A1
Gaia Collaboration, Brown, A. G. A., Vallenari, A., et al. 2021, A&A, 649, A1
Gaia Collaboration, Brown, A. G. A., Vallenari, A., et al. 2016a, A&A, 595, A2
Gaia Collaboration, Prusti, T., de Bruijne, J. H. J., et al. 2016b, A&A, 595, A1
Kervella, P., Arenou, F., Mignard, F., & Thévenin, F. 2019, A&A, 623, A72
Kristensen, K., Nielsen, A., Berg, C. W., Skaug, H., & Bell, B. M. 2016, Journal of Statistical Software, 70, 1
Lindegren, L., Hernández, J., Bombrun, A., et al. 2018, A&A, 616, A2
Martin, C., Mignard, F., & Froeschle, M. 1997, A&AS, 122, 571
Quist, C. F. & Lindegren, L. 1999, A&AS, 138, 327
Tal-Or, L., Trifonov, T., Zucker, S., Mazeh, T., & Zechmeister, M. 2019, MNRAS, 484, L8
van Leeuwen, F. 2007, Astrophys. Space Sci. Lib., 350
van Leeuwen, F. 2007, A&A, 474, 653
van Leeuwen, F. & Evans, D. W. 1998, A&AS, 130, 157

SF2A 2021
A. Siebert, K. Baillié, E. Lagadec, N. Lagarde, J. Malzac, J.-B. Marquette, M. N'Diaye, J. Richard, O. Venot (eds)

A YOUNG STELLAR QUADRUPLE WITH NON-COPLANAR ORBITS

T. Merle[1], S. Van Eck[1], A. Jorissen[1], M. Van der Swaelmen[2] and K. Pollard[3]

Abstract. Stars form in clusters and associations; some of the multiple systems born in such environments will remain gravitationaly bound for their entire life. Multiplicity is thus an inherent property of stellar populations. Recent large spectroscopic surveys have harvested many spectroscopic multiple systems with two and three components but those with four components (SB4) remain comparatively very rare. Here we report on the preliminary properties of the first SB4 found within a cluster: HD 74438, located in the close-by young open cluster IC 2391. It is the youngest (43 My) SB4 discovered so far. Identified in the context of the Gaia-ESO Survey, this system benefited from HRS/SALT, HERCULES/UCMJO spectroscopic follow-up and archival observations from ESO. We show that the system consists of a 2+2 bound hierarchical stellar system, *i.e.* two SB2 gravitationaly bound. We derived orbital and astrophysical parameters for the two inner pairs and found that their orbits are non-coplanar. The outer pair is characterized by a preliminary orbit of 6 y with an eccentricity of 0.5. The non-coplanarity of the two inner pairs sheds light on secular evolution of quadruple systems that can lead to merger end-points of stellar evolution in multiples.

Keywords: stars: individual: HD 74438 – binaries: close – binaries: spectroscopic – techniques: radial velocities

1 What do we known about HD 74438 before the discovery of its quadruple nature?

Identifying multiple stars in clusters is fundamental because the evolution of stars are well-understood only for single stars, and their study can reveal important clues on the formation of stars and its interplay with its environment. Monitoring radial velocities (RV) of stars allow to identify spectroscopic binaries (SB), *i.e.* binary stars with orbital period lower than a few 10^4 d (~ 20 y). Quadruple hierarchical systems in a 2+2 or 3+1 configurations are challenging objects because of the complexity of their dynamics (Hamers et al. 2015; Hamers 2019). But these rare objects offer unique opportunity to study tidal interactions between the components.

The *Gaia*-ESO Survey (Gilmore et al. 2012; Randich et al. 2013) is a ground based multi-object spectroscopic large public survey targetting 10^5 stars in all stellar populations until $V = 20$ to complement RV and chemical composition characterization of a fraction of stars observed by the ESA space mission *Gaia* (Gaia Collaboration et al. 2016, 2018b). It was not designed to monitor RV variables but allow Merle et al. (2017, 2020) to discover hundreds of SB1 and SB2, a ten of SB3 and one SB4 candidate, the latter being the subject of this proceedings.

HD 74438 system is born in the young IC 2391 cluster, one of the closest open clusters to the Sun, located at 146^{+8}_{-7} pc in the Vela constellation and aged of 43^{+15}_{-7} My (Randich et al. 2018; Gaia Collaboration et al. 2018a). The RV of the system is compatible with the cluster's mean RV of 14.8 ± 0.7 km s^{-1}and its membership is reliable (Platais et al. 2007). By intrinsic brightness and color, Pasinetti Fracassini et al. (2001) provides a radius of 1.8 R$_\odot$. Bochanski et al. (2018) reported a higher radius of 2.76 ± 0.27 R$_\odot$, a mass of 2.11 ± 0.07 M$_\odot$ as well as an age of 759 My, more than 15 times older than the parent cluster. Contrary to Siegler et al. (2007) who reported no sign of binarity, Platais et al. (2007) noticed that this system should be a triple because it lies 0.9 mag above the cluster's main sequence, but they did not detect the presence of several RV components in the CCF. In addition, this system appears well above the fitted isochrone of the main sequence of IC 2391 cluster as well as the binary sequence taken with $q = 0.8$ (Randich et al. 2018).

[1] Institut d'Astronomie et d'Astrophysique, Université Libre de Bruxelles, Brussels, Belgium
[2] INAF – Osservatorio Astrofisico di Arcetri, Largo E. Fermi 5, 50125, Firenze, Italy
[3] Department of Physics and Astronomy, University of Canterbury, Private Bag 4800,Christchurch 8120, New Zealand

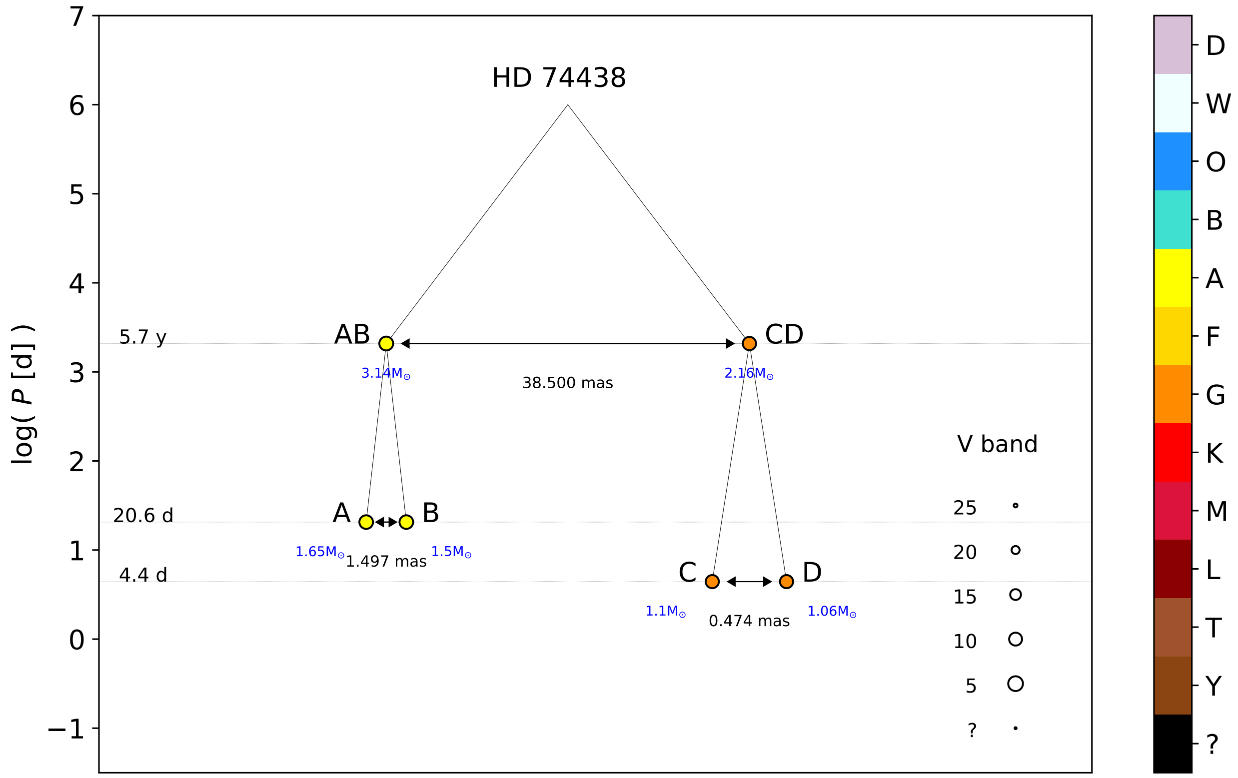

Fig. 1. The hierarchical 2+2 quadruple stellar system HD 74438 discovered in the Gaia-ESO Survey. The full characterization of the architecture and the orbital parameters were obtained thanks to several follow-up with HRS/SALT, HERCULES/UCMJO and ESO archival data from GIRAFFE. The astrophysical parameters are still preliminary.

2 What are the orbital and astrophysical parameters of HD 74438?

We obtain follow-up spectroscopic observations of this SB4 with high resolution spectroscopy on HRS/SALT* in South Africa (Crause et al. 2014) and HERCULES/UCMJO† in New Zealand (Hearnshaw et al. 2002, 2003). They are complemented with GIRAFFE observations at medium resolution retrieved in the ESO archive‡ and taken $\sim$ 10 years before the GES. Such medium resolution does only allow to resolve the two brightest components. RVs of the time series spectra are analyzed to find orbital solutions of the two SB pairs. The preliminary orbital parameters for the two inner orbits were reported by Merle et al. (2019). The inclinations on the sky of the AB and CD pairs are 52° and 86° respectively, making the two inner orbits not coplanar. The mutual inclinations are not reachable with spectroscopy alone (see Sect. 4). The architecture of the system and the main preliminary orbital parameters are displayed on Fig. 1.

The astrophysical parameters were derived using HRS/SALT spectra taken on 2018-10-14 and 2018-12-31 because they show four well-separated components at the highest resolution. Because this system belongs to a young cluster, we assumed solar metallicity and main sequence components (*i.e.* [Fe/H] $= 0$ and $\log g = 4.5$). The radiative transfer code Turbospectrum (Plez 2012) was used, with Kurucz's model atmosphere grid§. (Kurucz 1991). We built a grid of synthetic spectra on the wavelength region [3 850 − 5 500] Å combining four models with temperatures ranging from 4 000 to 10 000 K (with a step of 250 K) shifted at the RV of each component. The composite model that best fits the four components is taken to be the one with the smallest standard deviation on the residuals distributions. The best combined synthetic spectrum together with its

*Southern Africa Large Telescope
†University of Canterbury Mt John Observatory
‡`http://archive.eso.org`
§`http://kurucz.harvard.edu/grids.html`

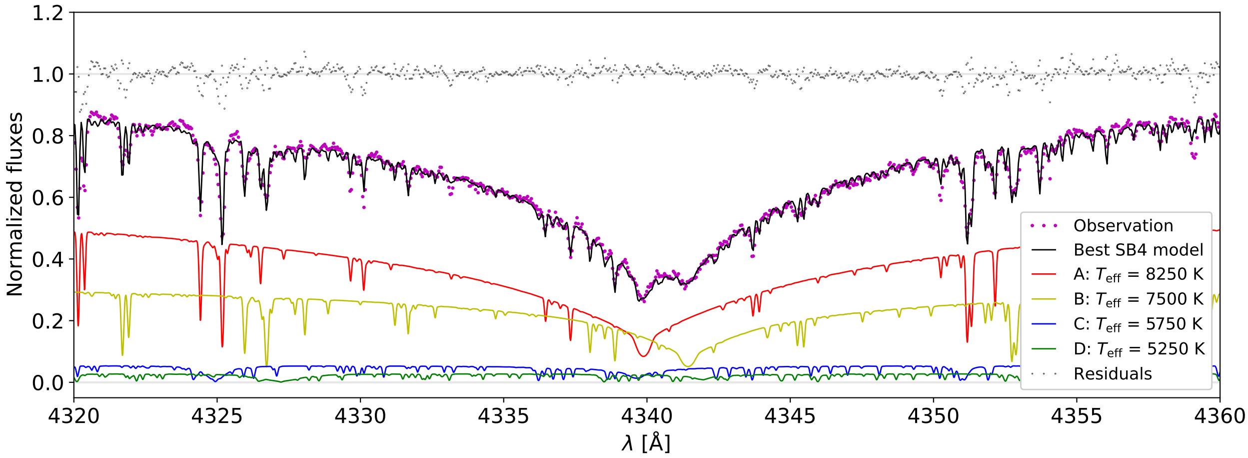

Fig. 2. Display around Hγ of the observed composite spectrum (magenta dots) taken on night 2018-12-31 with HRS/SALT, when the four components were well separeted and resolvable. The best fitted SB4 composite model is shown in black and the residuals in grey, shifted around $y = 1$ for clarity. The individual spectra are also shown and color-coded as given in the legend; they give an idea of the contribution of each component to the total flux.

individual components is compared to the 2018-12-31 observed spectrum on Fig. 2 as an illustration of the fit. Once the effective temperatures are derived for each component, we derived their spectral type using conversion table from Gray & Corbally (2009, Appendix B3). Determination of masses and luminosities were performed by using stellar evolution models (PARSEC, Bressan et al. 2012) with solar metallicity $Z = 0.0147$. We first select three isochrones corresponding to the most recent age determination of the parent cluster: $t = 43^{+15}_{-7}$ My (Randich et al. 2018). The masses and luminosities are interpolated at the spectroscopic temperatures on the main sequence for each component. Radii are also deduced. The spectroscopic masses and spectral type are displayed on Fig. 1. The spectroscopic mass ratio for each orbit is also determined. Combining orbital and astrophysical parameters, we can also deduce the inclinations and the separations of the three orbits: the two inner and the outer ones. The periods satisfied the dynamical stability criterion for a 2+2 architecture (Naoz 2016). The consolidated orbital and astrophysical parameters for each component will be available soon (Merle et al., submitted).

3 What is so special with the spectroscopic quadruple system HD 74438?

HD 74438 turns out to be especially interesting because:

- It belongs to a very young (43 Myr) and nearby (146 pc) open cluster, IC 2391 (Randich et al. 2018), so its age is known;
- It has the shortest outer orbital period when compared to other quadruples in clusters reported in the MSC (Tokovinin 2018);
- It is one of the rare SB4 systems with non-coplanar inner orbits (as inferred from the inclinations derived from the spectroscopic masses);
- The CD subsystem has a higher eccentricity than SB2s of similar spectral types and periods, as seen in the eccentricity–period diagram from the SB9 catalogue (Pourbaix et al. 2004);
- According to Fig. 2 of (Geller et al. 2013) giving the circularization period (derived from population synthesis simulations) as a function of the cluster age, all systems with $P_{\rm orb} \leq 8$ d in clusters of the age of IC 2391 should be circularized, which is not the case of the CD pair of HD 74438, calling for an eccentricity-pumping mechanism.

To date, less than 10 SB4 are reported in the literature, and when the inclinations are known, they turn out to be nearly co-planar.

4 What's next?

To fully characterize this SB4 system, one needs the orientation of the orbits on the sky that will allow to determine the mutual inclinations between the inner orbits and the outer one. Spectroscopy alone cannot afford the longitudes of ascending nodes of the three orbits, and astrometery with Gaia/ESA and/or interferometry with PIONIER/ESO is required to constrain these parameters. Characterizing such systems are indeed important as they might be one kind of progenitors of type Ia supernovae. Recent simulations demonstrated that quadruple systems with 2+2 architecture undergoing secular evolution could produce SNIa at an higher rate compared to triples when inner binaries merge (Fang et al. 2018).

References

Bochanski, J. J., Faherty, J. K., Gagne, J., et al. 2018, VizieR Online Data Catalog, J/AJ/155/149

Bressan, A., Marigo, P., Girardi, L., et al. 2012, MNRAS, 427, 127

Crause, L. A., Sharples, R. M., Bramall, D. G., et al. 2014, in Proc. SPIE, Vol. 9147, Ground-based and Airborne Instrumentation for Astronomy V, 91476T

Fang, X., Thompson, T. A., & Hirata, C. M. 2018, MNRAS, 476, 4234

Gaia Collaboration, Babusiaux, C., van Leeuwen, F., et al. 2018a, A&A, 616, A10

Gaia Collaboration, Brown, A. G. A., Vallenari, A., et al. 2018b, A&A, 616, A1

Gaia Collaboration, Prusti, T., de Bruijne, J. H. J., et al. 2016, A&A, 595, A1

Geller, A. M., Hurley, J. R., & Mathieu, R. D. 2013, AJ, 145, 8

Gilmore, G., Randich, S., Asplund, M., et al. 2012, The Messenger, 147, 25

Gray, R. O. & Corbally, Christopher, J. 2009, Stellar Spectral Classification

Hamers, A. S. 2019, MNRAS, 482, 2262

Hamers, A. S., Perets, H. B., Antonini, F., & Portegies Zwart, S. F. 2015, MNRAS, 449, 4221

Hearnshaw, J. B., Barnes, S. I., Frost, N., et al. 2003, in Astronomical Society of the Pacific Conference Series, Vol. 289, The Proceedings of the IAU 8th Asian-Pacific Regional Meeting, Volume 1, ed. S. Ikeuchi, J. Hearnshaw, & T. Hanawa, 11–16

Hearnshaw, J. B., Barnes, S. I., Kershaw, G. M., et al. 2002, Experimental Astronomy, 13, 59

Kurucz, R. L. 1991, in NATO Advanced Science Institutes (ASI) Series C, Vol. 341, NATO Advanced Science Institutes (ASI) Series C, ed. L. Crivellari, I. Hubeny, & D. G. Hummer, 441

Merle, T., Van der Swaelmen, M., Van Eck, S., et al. 2020, arXiv e-prints, arXiv:2002.02275

Merle, T., Van Eck, S., Jorissen, A., et al. 2017, A&A, 608, A95

Merle, T., Van Eck, S., Pollard, K., et al. 2019, Mem. Soc. Astron. Italiana, 90, 424

Naoz, S. 2016, ARA&A, 54, 441

Pasinetti Fracassini, L. E., Pastori, L., Covino, S., & Pozzi, A. 2001, A&A, 367, 521

Platais, I., Melo, C., Mermilliod, J.-C., et al. 2007, A&A, 461, 509

Plez, B. 2012, Turbospectrum: Code for spectral synthesis

Pourbaix, D., Tokovinin, A. A., Batten, A. H., et al. 2004, A&A, 424, 727

Randich, S., Gilmore, G., & Gaia-ESO Consortium. 2013, The Messenger, 154, 47

Randich, S., Tognelli, E., Jackson, R., et al. 2018, A&A, 612, A99

Siegler, N., Muzerolle, J., Young, E. T., et al. 2007, ApJ, 654, 580

Tokovinin, A. 2018, ApJS, 235, 6

Session 25

Simuler la formation des galaxies et de leurs étoiles

SF2A 2021
A. Siebert, K. Baillié, E. Lagadec, N. Lagarde, J. Malzac, J.-B. Marquette, M. N'Diaye, J. Richard, O. Venot (eds)

GINEA AND DYABLO

D. Aubert[1] and A. Durocher[2]

Abstract. GINEA (Groupe d'investigation numérique pour l'exascale en astrophysique) is an initiative of numerical astrophysicists dedicated to the development of future astrophysics simulation codes. During the Exascale era, the next generation of supercomputers, massively parallel and hybrid, will provide significant challenges to the current generation of simulation codes. Prototypes and code evolutions are being investigated and discussed worldwide to prepare for the advent of these machines. Within GINEA such investigations are conducted with the new Dyablo AMR hydrodynamics code, developed at the CEA. Thanks to the hardware agnostic library Kokkos, Dyablo is currently able to run on multi-GPU architectures with promising performances and parallel scaling. The features of Dyablo are presented as well as the objectives of GINEA.

Keywords: numerical simulations, high-performance computing

1 Introduction

The near future of High Performance Computing (HPC) is often referred to as the 'Exascale Era' due to the upcoming generation of super-computers that aim at being able to reach a computing power of one *Exaflop* , i.e. 10^{18} floating point operations per second. Corresponding to a few times the performance of the current most powerful machines, this threshold should be passed in the next few years. For example, *Frontier*, the next flagship of U.S. supercomputing is expected to reach this level of computing power and will be delivered before the end of 2021. Likewise, Euro-HPC *, a European Union joint initiative, is expected to install several computers with Exascale abilities in the next few years. Of course, numerical astrophysics, and notably fields that are driven by numerical simulations, should benefit from such an evolution. Many codes display high level of parallelization that are able to harness the processing power provided by thousands, if not tens or hundreds of thousands, cores, to simulate astrophysical processes highly resolved in time and space with large dynamical ranges.

However, the advent of the Exascale era relies on a few paradigms that come with their share of challenges such as :

- an increase in the number of CPUs being made available. Load balancing can be more difficult to optimize leading to parallelized codes with performances unable to scale with the number of cores. The available memory per core has also a tendency to decrease, simply forbidding some applications to be done. Finally, a large number of computing units often imply significant I/Os, putting high stresses on storage systems.

- hybrid computing. Supercomputers rely more and more on co-processing devices such as graphics processing units (GPUs). These devices can provide significant boosts in computing power, but rely on parallelization or memory handling paradigms that can significantly differ from the ones applied to standard CPUs. In practice, some current codes are found to be unable, by design, to benefit from them.

[1] Observatoire Astronomique de Strasbourg, Université de Strasbourg, CNRS UMR 7550, 11 rue de l'Université, 67000 Strasbourg, France
[2] IRFU, CEA, Université Paris-Saclay, 91191 Gif-sur-Yvette, France
*https://eurohpc-ju.europa.eu/

- new architectures. For example, the last few years have seen the emergence of ARM architectures for CPUs, disputing the previous dominance of x86 processors and it is expected that the future flaships of the Euro-HPC Joint initiative will rely on such technology. It's not clear yet how existing codes will behave on such chips and more generally it illustrates how changes in architectures and/or devices is an obstacle to the long-term development and support of scientific applications that uses HPC installations.

It should be noted that this ever changing landscape is also nurtured by the rise of new actors such as the field of artificial intelligence or High Performance Data Analysis (HPDA). Their specifications can differ from the ones required by the more traditional actors of supercomputing (such as numerical simulations) and a convergence of the requirements, techniques and methods of these different field has to be expected. Such convergence will inevitably lead to changes in the current standard solutions for numerical astrophysics.

2 GINEA : Groupe d'Investigation Numerique pour l'Exascale en Astrophysique

GINEA is group of scientists from French laboratories that aims at defining, implementing and prototyping future astrophysical simulation codes tailored for the Exascale Era. These codes are expected to be massively parallel, hybrid and compatible with multiple architectures. More importantly such codes should be maintainable with a relative ease and capable of long-term evolution, as it is difficult to anticipate today what will be the standards (methods, hardware,...) of the Exascale era and beyond. In addition, GINEA also aims at pushing for a collaborative development between GINEA numerical astrophysicists, computational scientists and software engineers. This strategy should provide solid foundations, professional standards for code engineering, thus ensuring long-term support and code evolutions.

These future exascale codes should also answer the challenges specific to astrophysical situations. Among the desirable features, one can list the ability to deal with :

- the coupling of multiple physics such as gravity, hydrodynamics, radiative transfer, thermo-chemistry, MHD, etc..
- heterogeneous data with often combined eulerian (grid-based) and lagrangian (particle-based) descriptions
- great dynamics of length and time scales, which inevitably lead to load-balancing and memory issues
- production of large amount of data. For example, a large simulation project can produce petabytes of data, i.e. equivalent to several years of state-of-the art observational surveys.

The GINEA initiative started in November 2019, at the Maison de la Simulation and this first meeting led to the declared intent of looking at ways to have prototypes and platforms for new simulation codes with the aforementioned capabilities. As of today, GINEA gathers about 20 computer scientists and numerical astrophysicists from CEA, CNRS and Universities, as well as collaborators in foreign institutions, with a majority coming from the RAMSES code (Teyssier 2002) community. It benefits from support by 4 National Programs (PNCG, PCMI, PNPS, PNHE), reflecting the scope of our fields of research in astrophysics. In practice, (virtual) meetings are regularly organised on a monthly basis to discuss about numerical techniques and strategical choices about code design. Most importantly such meetings are also dedicated to updates about the developments made at the CEA on the adaptive mesh refinment code DYABLO, described in the following section.

3 DYABLO

DYABLO is an adaptive mesh refinement (AMR) hydrodynamics simulation code, initially designed by P. Kestener at the CEA, and currently developed by A. Durocher as well as M. Delorme on a different fork dedicated to physics of the Sun. DYABLO is a 2D/3D parallel code, capable of being deployed on many cores in distributed memory (MPI) and shared memory systems (OpenMP). The code is also able to benefit from GPUs parallel devices (Nvidia/CUDA) and it can be run in hybrid configurations, e.g. on multiple CPU nodes equipped with GPUs. This versatility in terms of parallelisation is made possible by relying on the C++ KoKKos[†] library (Edwards et al. 2014), which provides means of high-level development for multiple parallel

[†]https://github.com/kokkos/kokkos

architectures and in an agnostic and optimized way. Kokkos therefore provides portability to Dyablo, even for architectures that may arise in the future as long as they are supported by the library.

The AMR structure is currently managed by the PABLO CPU-only library[‡] but the development of a portable (CPU/GPU) custom AMR library is currently near completion. The Dyablo AMR strategy can be either cell-based or block-based, both having their own pros and cons in terms of e.g. parallel performance and memory consumption on GPUs. In terms of physics, the code currently implements a MUSCL-Hancock hydrodynamics, as well as a static gravity. The inclusion of self-gravity and particles (e.g. for collisionless dark matter, stars, tracers) is currently under study. In terms of design, the code, written in C++, aims at being modular to ease e.g. the addition of future astrophysics modules. Finally, it should be noted that beyond astrophysics, Dyablo is written as a generic platform for parallel AMR simulation, hence the emphasis on modularity and high-level templates.

Since the code is still in development, performance assessments should be taken with caution. Nevertheless, preliminary benchmarks on 3D Sedov Blast waves (256^3 + 2 refinement levels, equiv. 1024^3) already show an acceleration factor of a few using a Jean-Zay (IDRIS) V100 GPU for Dyablo compared to Ramses deployed on 40 cores on the same Jean-Zay nodes. Likewise weak scaling appears satisfactory up to 256 GPUs on the same test-case. Obviously, these promising results will have to be revisited on more demanding astrophysical test-cases. Only then full confidence would be claimed about the potential of Dyablo as a generic and performant astrophysics simulation code for exascale machines.

4 Conclusions and Prospects

The AMR code Dyablo is currently in heavy development and while initial benches are very promising, a long way remains until a fully functional code for state-of-the art astrophysical productions. In particular, fundamental choices about code design (esp. regarding the AMR data structure) are being currently discussed to implement functionalities related to particles and to self-gravity. For example, the introduction of particles or the use of a multigrid solver for self-gravity may require significant changes in the way Dyablo handles the AMR tree to achieve good performance, especially on GPU accelerators. The GINEA group is thus a place to discuss the priorities in terms of features and performances, to decide for the best route to be taken for a future simulation framework useful for state-of-the exascale astrophysics. Beyond that, once this framework (Dyablo or an evolution from Dyablo) has been settled, numerical astrophysicists will have to adopt it and expand it by adding the astrophysical modules required for their specific science. That will be the task of the GINEA initiative for the months and years to come.

This work has been supported by the Programmes Nationaux Cosmologie et Galaxies (PNCG), Hautes Energies (PNHE), Physique Stellaire (PNPS) and Milieu Interstellaire (PCMI).

References

Edwards, H. C., Trott, C. R., & Sunderland, D. 2014, Journal of Parallel and Distributed Computing, 74, 3202 , domain-Specific Languages and High-Level Frameworks for High-Performance Computing

Teyssier, R. 2002, A&A, 385, 337

[‡]https://optimad.github.io/PABLO/doxy/html/index.html

SF2A 2021
A. Siebert, K. Baillié, E. Lagadec, N. Lagarde, J. Malzac, J.-B. Marquette, M. N'Diaye, J. Richard, O. Venot (eds)

THE ROLE OF COSMIC RAY FEEDBACK IN THE EVOLUTION OF GALAXIES

M. Farcy[1], J. Rosdahl[1] and Y. Dubois[2]

Abstract. Cosmic rays are charged particles accelerated in supernova shocks, exerting pressure on gas and heating it. As these effects can alter both the star formation and the multiphase structure of galaxies, they are likely an important feedback channel in galaxy evolution. Using Radiation-Magneto-Hydrodynamics simulations of three isolated and idealised disk galaxies of different masses, we investigate the impact of cosmic ray feedback on galaxy evolution. We find that cosmic rays have a mild effect in reducing star formation, by at most a factor two, and with decreasing efficiency in increasingly massive galaxies. At any galaxy mass however, cosmic ray pressure support increases galactic outflows, which are also much colder than when cosmic rays are excluded. We find that both the increase in outflows and their temperature are sensitive to the adopted cosmic ray diffusion coefficient, revealing the importance of the detailed modelling of cosmic ray propagation.

Keywords: galaxy evolution, cosmic rays

1 Introduction

Feedback is an essential but still not fully understood component of galaxy formation and evolution. Without any feedback, gas accreted into galaxies would cool rapidly and be converted into stars much more efficiently than what is observed. It is a long-standing challenge in theoretical astrophysics to reproduce observations, such as the galaxy mass function or the stellar mass to halo mass relation. If invoking only the energetic feedback of supernova (SN) explosions, simulated galaxies tend to contain too many stars, because the SN energy is radiated away too quickly to efficiently clear away dense gas and delay or suppress star formation. It has been shown that SN feedback by itself remains inefficient in producing fully realistic simulated galaxies, not only in terms of star formation regulation (see e.g Hopkins et al. 2011), but also in reproducing the temperature and metallicity content of gas in the interstellar medium (ISM) and circumgalactic medium (CGM) (see e.g Schaye et al. 2015), or the scaling of mass-loading factors with galaxy velocity. With time, and as numerical capabilities increase, more and more feedback sources have been investigated, such as radiation pressure, stellar winds, photoionisation heating, active galactic nuclei and cosmic rays. In particular, cosmic rays are highly regarded as being able to both play a role in regulating star formation in galaxies as well as the multiphase structure of the ISM and CGM.

Cosmic rays (CRs) are energetic charged particles, mainly consisting of protons with energy around a few GeV. Produced and accelerated in SN shock waves, they are advected with gas and diffused along magnetic field lines. Moving from dense star-forming clouds to more diffuse regions, they provide an important non thermal pressure gradient in galaxies and heat the gas through hadronic collisions and streaming losses. These effects combined have the potential to disrupt ISM clouds and hence alter the star formation rate. They can also help driving gas away from the galaxy, impacting the CGM and its observational properties. Here, we present a study of three isolated galaxies of different masses, combining supernova feedback, radiation and cosmic ray feedback together in radiation-magneto-hydrodynamics (RHMD) simulations, to know if and to what extent CRs contribute to regulate galaxy evolution.

[1] CRAL, Université Lyon1, CNRS UMR 5574, Ens de Lyon, 9 avenue Charles André, 69561, Saint-Genis-Laval, France
[2] Institut d'Astrophysique de Paris, CNRS UMR 7095, UPMC Univ. Paris VI, 98 bis boulevard Arago, 75014 Paris, France

2 The effects of cosmic rays

We use the Ramses code (Teyssier 2002) to perform simulations of disk galaxies embedded in dark matter halos of 10^{10}, 10^{11} and 10^{12} $M_\odot$ respectively. The initial conditions for all our simulations are generated using the MakeDisk code (Springel et al. 2005). For each galaxy, we have a set of two runs, with and without cosmic ray feedback. The galaxies are evolved for 500 Myr, with a maximum cell resolution of 9 pc for the two smaller dwarf galaxies, and 18 pc for the most massive one. More details about the galaxies can be found in Rosdahl et al. (2015) and Dashyan & Dubois (2020), and we adopt a very similar setup. To give a brief overview, the simulations have been performed using the Ramses-rt version of the code (Rosdahl & Teyssier 2015) to account for the propagation of hydrogen and helium-ionising radiation and its interactions with the gas via radiative pressure and photo-ionisation. An initial toroidal magnetic field of 1 μG in strength is evolved using the Fromang et al. (2006) MHD solver. Cosmic rays are modelled as a non-collisional relativistic fluid, following the advection-diffusion approach implemented by Dubois & Commerçon (2016) and Dubois et al. (2019), with a constant diffusion coefficient $\kappa = 10^{28}$ cm^2/s. Gas is converted into stellar populations with a local star formation efficiency by the thermo-turbulent model of Federrath & Klessen (2012). The star particles, representing stellar populations, then trigger individual SN explosions between 3 and 50 Myrs after their birth, following the mechanical feedback method described in Kimm & Cen (2014) and Kimm et al. (2015). When CRs are included, 10% of the energy from each SN explosion (i.e. 10^{50} ergs) is put into non thermal cosmic ray energy.

2.1 Star formation rate

Fig. 1 shows the stellar mass produced in our three galaxies as a function of time, with and without cosmic ray feedback. Each galaxy includes an initial distribution of stellar particles, which contribute to the baryonic mass, but never explode as supernova, and hence do not provide any feedback. We exclude these initial stellar particles from Fig. 1 to show only the stellar mass formed since the start of the run. By exerting their pressure on gas, CRs tend to smooth the gas distribution in the ISM, and reduce the number of star-forming clumps. By the end of the 500 Myr runtime, they suppress the total amount of stars formed by a factor two for the dwarf galaxies. For a galaxy as massive as our Milky-Way (i.e. with a halo mass of 10^{12} $M_\odot$), they are not efficient enough at the ISM scale to affect the star formation at any time. This can be explained by the stronger gravitational potential of the massive galaxy, which reduces the CR feedback efficiency to make any significant disruptions in the ISM.

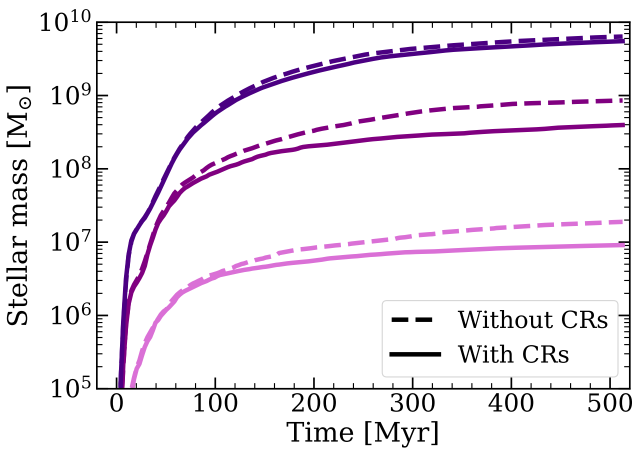

Fig. 1. Cumulative formation of stars in the three galaxies. The three sets of two curves correspond to each galaxy being simulated with (solid) and without (dashed) CRs, by order of increasing galaxy mass from light to dark purple. Cosmic ray feedback efficiency in suppressing the star formation decreases with galaxy mass.

2.2 Outflows

Cosmic rays also have the ability to impact galactic outflows and the properties of the CGM. In Fig. 2, we show the time evolution of the flux of outflowing gas crossing parallel planes located 10 kpc from the disks. For each galaxy, we show the total amount of outflows in black before and decompose it into its cold ($T < 10^4$ K), warm ($10^4 \leq T < 10^5$ K) and hot ($T > 10^5$ K) components in blue, green, red respectively. Solid lines represent the cases with CR feedback included, while the dashed lines show the counterpart runs without CRs. At any galaxy mass, including CRs clearly enhances the amount of outflows, by at least a factor 2, compared to runs where the outflows are generated only by SN feedback. This is the direct consequence of the extra pressure support cosmic rays provide, helping to drive more gas away from the galactic disks. Additionally, their energy is dissipated much less efficiently than the thermal energy of gas, so that they can in practice hold it on longer timescales. Moreover, the energy lost by CRs is injected directly into the gas, which increases the thermal pressure more than it decreases the cosmic ray one, since the gas has a harder equation of state. Combined with the fact that cosmic ray pressure decreases less quickly upon adiabatic expansion than the thermal pressure does, all of this explains why CRs can energise winds and maintain outflows more efficiently than with (largely thermalised) SN feedback only.

Another consequence of CRs is a change in the temperature of the outflowing gas. Without CR feedback, the outflows are dominated by hot gas, especially for the two most massive disks. With CRs included, the outflows become dominated by the warm phase, and even gas with temperature below 10^4 K appears in the outflows.

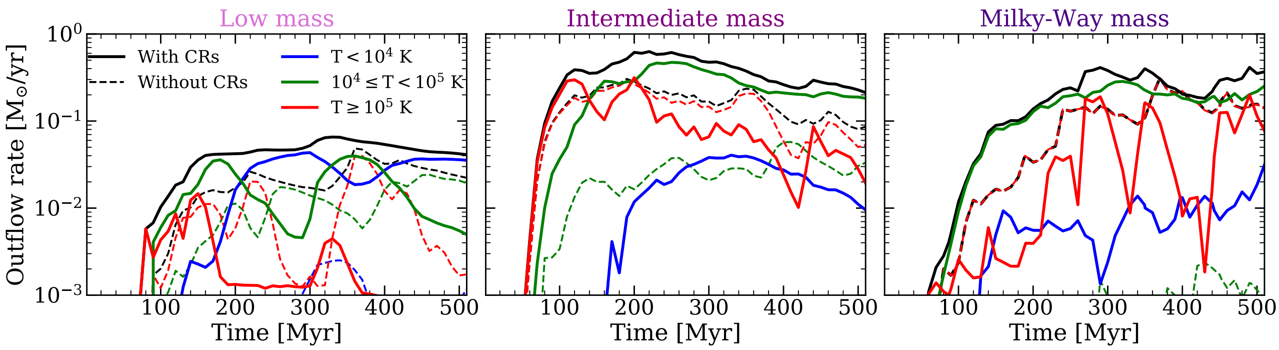

Fig. 2. Mass outflow rate of gas as a function of time, measured 10 kpc from the disks, with increasing galaxy mass from left to right. Each panel shows two sets of 4 curves for one galaxy, one set for a run with cosmic ray feedback (solid lines) and another set without (dashed lines). Black curves show the total rate of outflowing gas, while blue, green, red lines show how it separates into the cold, warm and hot phases. At any galaxy mass, adding CRs leads to stronger and colder outflows.

3 Sensitivity of the results to the diffusion coefficient

Our understanding of CR transport is limited by a number of uncertainties, making the study of their role in shaping galaxies model-dependant. This is especially true for the diffusion coefficient κ, which regulates the transport of the cosmic ray energy away from their production sites. Hence the value of κ can alter how CRs affect galaxy evolution. Theoretically or observationally, the diffusion coefficient is not well constrained. Some empirical constraints exist, from gamma-ray emission or spallation products measured in the Milky-Way. While κ is usually determined to be around a few 10^{28} cm^2/s, values at least ten times larger or smaller are still well within the realm of possibility.

In Fig. 3, we show the evolution of the mass outflow rate, measured at 10 kpc, when varying the diffusion coefficient from 10^{27} to 3×10^{29} cm^2/s in our most massive galaxy. Globally, the higher the diffusion coefficient, the larger the outflow rate, even if this increase becomes less and less significant for the highest values. For the lowest value adopted, $\kappa = 10^{27}$ cm^2/s, the amount of outflowing gas is actually lower than in the counterpart run without cosmic ray feedback. This is the consequence of CRs remaining trapped in the disk, with the pressure they exert sufficient to start pushing gas from the midplane, but not enough to completely overcome the gravitational potential of the disk. As the diffusion coefficient increases, larger cosmic ray pressure and

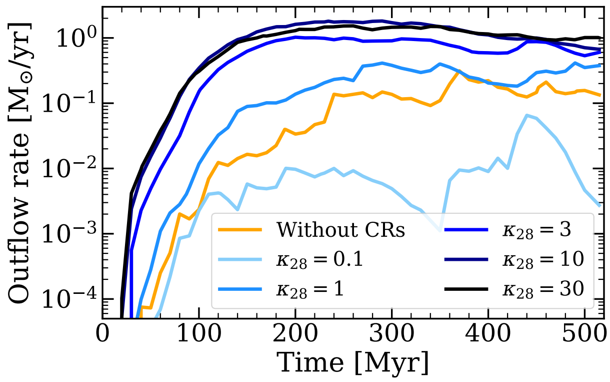

Fig. 3. Mass outflow rates for the Milky-Way mass galaxy. The orange curve corresponds to the run without cosmic ray feedback. From light blue to black, we increase the diffusion coefficient (expressed in units of 10^{28} cm^2/s). Globally, increasing its value increases the outflow rate. If it is very low, there is actually less gas outflowing than in the counterpart run without CRs. In the most extreme case of the largest diffusion coefficient, the outflow rate stops increasing.

velocities make it is easier to remove more and more material out of the galaxy up to larger distances. In the most extreme case of $\kappa = 3 \cdot 10^{29}$ cm^2/s, CRs escape the galaxy so quickly that they do not apply their pressure gradually. Consequently, we do not measure a net increase of outflows anymore.

4 Conclusions

We perform simulations of three idealised galaxies in dark matter halos with masses from 10^{10} to 10^{12} M$_\odot$, with radiation, a magnetic field, mechanical feedback from supernovae and with or without cosmic rays. Our results show that cosmic ray feedback has as an effect similar to SNe in reducing star formation, and that this effect decreases with galaxy mass. Additionally, the pressure support provided by CRs helps driving gas away from all our galaxies. They dramatically change the temperature of these outflows, which are dominated by gas between 10^4 and 10^5 K, while much hotter with SN feedback only and without cosmic rays. Pushing this gas more gently than supernovae, they also allow for outflows colder than 10^4 K to be found at large distances from the disks. However, changing the diffusion coefficient can alter quite significantly the amount of outflowing gas. In our Milky-Way mass galaxy, a diffusion coefficient $\kappa = 10^{27}$ cm^2/s is too low to render CRs dynamically relevant in driving more gas away from the disk than the counterpart run without CRs. Generally, increasing the diffusion coefficient increases the total outflow rate, but in the most extreme case where $\kappa = 3 \times 10^{29}$ cm^2/s, CRs escape so quickly that the flux of outflowing gas slowly starts to drop. A better understanding of CR propagation remains essential to determine their role in shaping galaxies and their CGM environment, bringing us a step closer to understanding galaxy evolution.

References

Dashyan, G. & Dubois, Y. 2020, A&A, 638, A123
Dubois, Y. & Commerçon, B. 2016, A&A, 585, A138
Dubois, Y., Commerçon, B., Marcowith, A., & Brahimi, L. 2019, A&A, 631, A121
Federrath, C. & Klessen, R. S. 2012, ApJ, 761, 156
Fromang, S., Hennebelle, P., & Teyssier, R. 2006, A&A, 457, 371
Hopkins, P. F., Quataert, E., & Murray, N. 2011, MNRAS, 417, 950
Kimm, T. & Cen, R. 2014, ApJ, 788, 121
Kimm, T., Cen, R., Devriendt, J., Dubois, Y., & Slyz, A. 2015, MNRAS, 451, 2900
Rosdahl, J., Schaye, J., Teyssier, R., & Agertz, O. 2015, Monthly Notices of the Royal Astronomical Society, 451, 34
Rosdahl, J. & Teyssier, R. 2015, MNRAS, 449, 4380
Schaye, J., Crain, R. A., Bower, R. G., et al. 2015, MNRAS, 446, 521
Springel, V., Di Matteo, T., & Hernquist, L. 2005, MNRAS, 361, 776
Teyssier, R. 2002, A&A, 385, 337

SF2A 2021
A. Siebert, K. Baillié, E. Lagadec, N. Lagarde, J. Malzac, J.-B. Marquette, M. N'Diaye, J. Richard, O. Venot (eds)

FORMULATION OF EVOLUTION OF SUPERMASSIVE BLACK HOLE MASS

M. M. Kozhikkal[1], S. Chen[1], G. Theureau[1], M. Volonteri[2], M. Habouzit[3] and A. Sesana[4]

Abstract. Supermassive black holes (SMBH) with mass greater than 1 million solar masses are found in the core of most massive galaxies in the local Universe. The relationship between the mass of the spheroidal component of the host galaxy and that of their central BH known as the BH-bulge mass relationship has been widely studied. We present a new phenomenological BH-bulge mass relationship with redshift evolution and compare it to the population of BHs produced by six large-scale cosmological simulations. We compare the growth of BHs with redshift in Illustris, Horizon-AGN, SIMBA, TNG100, TNG300, and EAGLE.

Keywords: black hole physics - galaxies: formation - galaxies: evolution - methods: numerical

1 Introduction

Supermassive Black Holes (SMBH) in the centre of galaxies show fast-moving gas revolving around them that are being pulled in by the gravitational field of the black hole. Most of the massive galaxies in the local Universe host a SMBH, including our own Milky Way. The mass of the SMBH is strongly correlated with the mass of the bulge of the host galaxy. This relation has been studied widely due to its significance for the study of galaxy and central black hole co-evolution. Observations allow us to measure this correlation.

One of the important applications of this relation is its key role in calculating the gravitational wave background (GWB) from a population of merging Supermassive Black Hole Binaries (SMBHBs). SMBHBs are formed when two SMBHs start to coalesce, often after the merger of their host galaxies. As the binary components get close at sub parsec scale, more distortion happens in spacetime and produces gravitational waves until they merge. All the existing SMBHBs together form a stochastic GWB emission. The spectral energy distribution of the GWB in the frequency range ($10^{-9} - 10^{-6}$Hz) can be expressed using a formalism that depends on the BH-bulge mass relation (Chen et al. 2019). Pulsar Timing Arrays (PTAs) use radio telescopes to search for this GWB as a common signal by timing an array of millisecond pulsars each acting as an independent arm of a galactic-scale detector*.

Observations have investigated whether the BH-bulge mass relation evolves with redshift, but such studies are complicated by the inability to measure bulge masses, rather than total stellar masses. Furthermore, although many studies find that high redshifts quasars are powered by SMBHs more massive than those at $z = 0$ at fixed stellar mass, this can be caused by a selection bias (Lauer et al. 2007).

A complementary way to study galaxies at high redshift is by using large-scale cosmological simulations. These simulations give a detailed representation of the formation and evolution of the large-scale structures in large volumes of $(100 - 300)^3$ Mpc^3. The initial conditions of these galaxies are based on the power spectrum of density fluctuations in the Early Universe. Then simulations follow the collapse of dark matter into halos, the flow of gas into these halos, gas cooling and the ensuing star formation, as well as the growth of SMBHs in the galaxies. The observed Universe is closely matched by the representations from the cosmological simulations.

For this work we look at the evolution of the masses of galaxies and their central black holes at redshift range $0 \leq z \leq 5$ from the Illustris, Horizon-AGN, SIMBA, TNG100, TNG300, and EAGLE simulations

[1] LPC2E, CNRS Orleans, France and Station de radioastronomie de Nançay, France
[2] Institut d'Astrophysique de Paris, France
[3] Max Planck Institute für Astronomie (MPIA), Germany and Zentrum für Astronomie (ZAH, ITA), Germany
[4] Università di Milano-Bicocca (INFN), Italy
*`http://www.ipta4gw.org/`

(Habouzit et al. 2021, and references therein). We formulate the evolution of BH-bulge mass relation by tracking the evolution in these simulations.

A brief review of observational parameters of BH-bulge mass relation is given in Section 2. The simulated GWB spectrum as measured PTA using these different observational parameters is also discussed there. Section 3 gives a formulation of evolution of the BH-bulge mass relation with redshift. In Section 4 we investigate the parameters of the BH-bulge mass relation with redshift for the different simulations. And Section 5 provide our conclusions.

2 BH-Bulge Mass Relation

Optical and near infrared imagining photometry allows us to separate the bulge and disc stellar components of a galaxy at very low redshifts. The connection between the mass of galaxies and their central SMBHs is correlated with galactic bulge. The relation between the SMBH mass and the bulge mass of the host galaxy is

$$M_{BH} = \mathcal{N}\left\{\left(\frac{M_{bulge}}{10^{11}M_\odot}\right)^{\alpha} 10^{\beta}, \epsilon\right\}. \tag{2.1}$$

where M_{BH} is the SMBH mass, M_{bulge} is the corresponding galactic bulge mass, α, β and ϵ are the BH-bulge mass parameters. The intrinsic scatter ϵ is associated with the distribution of BH mass around the mean value at fixed bulge mass. $\mathcal{N}$ is the logarithmic normal distribution with standard deviation ϵ and mean defined as

$$\log_{10} M_{BH} = \alpha \log_{10}\left(\frac{M_{bulge}}{10^{11}M_\odot}\right) + \beta. \tag{2.2}$$

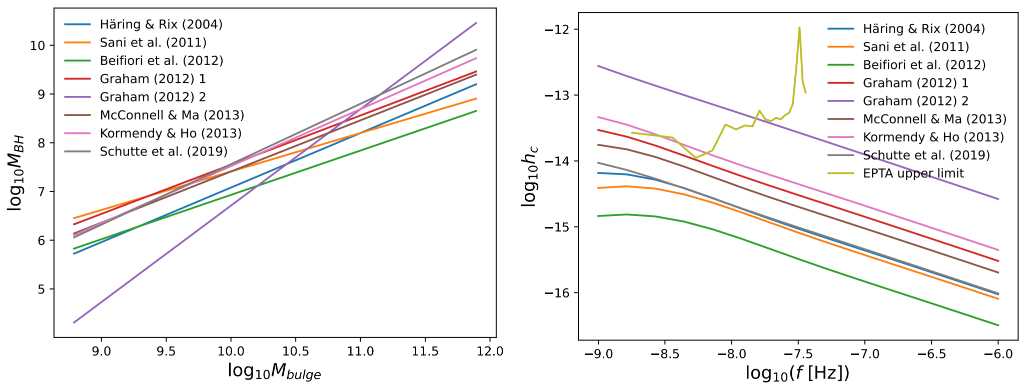

Fig. 1. Left: Plot of equation (2.2) for different BH-bulge mass parameters in the literature. **Right:** The corresponding characteristic strain spectrum of GWB as a function of frequency in the PTA range. The EPTA DR1 upper limit is shown as a reference (Lentati et al. 2015).

Different values of the BH-bulge mass parameters have been observationally determined in the literature (eg. Sesana 2013; Schutte et al. 2019), shown on the left side of Figure 1. The right side of Figure 1 shows the simulated characteristic strain spectrum of the GWB using the corresponding BH-bulge mass parameters computed using equation 1 in Chen et al. (2019). It also shows the importance of the BH-bulge mass relation in predicting the GWB which could be detected with PTAs.

3 Adding Redshift Dependence

We have seen the strong correlation between the mass of a SMBH and the galactic bulge observed in the local Universe. This correlation is anticipated to be seen at higher redshift. It is an indication to link the evolution of SMBH and galactic bulge by a common mechanism. And there is evidence suggesting that galaxy mergers are the possible reason and the correlation is independent of the evolution of the cold gas fraction in the population of galaxies. The strong evolution of the global galaxy merger rate of the Universe with time suggests the evolution of BH-bulge mass relation. The population of SMBHs does not evolve similarly to the bulge and hence the BH-bulge mass relation is compelled to evolve by the evolution in mass of galactic bulge rather than the SMBH. The anticipated correlation does not have a clear picture as some studies claim there is only little evolution in mass of SMBH within the epoch of $z \sim 3$ whereas other studies measured consistent correlation at epoch of $z \sim 2$ for Quasars.

A model for the growth of SMBH which matches with many observations from ($z \lesssim 6$) and local AGN predicted evolution in BH-bulge mass relation as $M_{BH} \propto \zeta(z)^{1/2}(1+z)^{3/2}M_{bulge}$ where $\zeta(z)$ has a weak redshift dependency corresponding with the cosmological parameters. And this is approximated for $z < 2$ as $M_{BH} \sim (1+z)^{1.15}M_{bulge}$ (Wyithe & Loeb 2003). Similar phenomenological model constrained by the evolution of Quasars assuming the growth of SMBHs exclusively through accretion gave $M_{BH} \sim (1+z)^{0.5}M_{bulge}$. The evolution with redshift in this model is weaker comparing with the previous model (Croton 2006, and references therein). Another model for Quasars at $z \gtrsim 6$ gave the BH-bulge mass relation with redshift dependence as (Venemans et al. 2016)

$$\frac{M_{BH}}{M_{bulge}} = \left(\frac{M_{BH}}{M_{bulge}}\right)_{z=0}(1+z)^{\beta} \tag{3.1}$$

where $\beta \approx 0.6$. Using this equation as parametric relation for generic galaxies of six different cosmological simulations (Illustris, Horizon-AGN, SIMBA, TNG100, TNG300, and EAGLE) give inconsistent β parameter for $z \leq 5$, hence we are in need to new formalism. Using the mass of galaxies and their central SMBHs from those six simulations and converting the stellar mass into galactic bulge mass, we formulate a phenomenological BH-bulge mass relation with redshift as the logarithmic normal distribution as equation (2.1) with logarithmic mean of the SMBH mass

$$\log_{10} M_{BH} = \alpha_* \log\left(\frac{M_{bulge}}{10^{11}}\right) + \beta_* + \gamma_* z. \tag{3.2}$$

where γ_* determines the evolution of SMBH mass with redshift, while α_*, β_* and standard deviation ϵ are independent of redshift.

4 BH Mass Parameters for Simulations

We study the masses of galaxies and those of their BHs for $z \leq 5$ in the Illustris, Horizon-AGN, SIMBA, TNG100, TNG300, and EAGLE simulations. These different cosmological simulations use different cosmological parameters and subgrid physics which are described in Habouzit et al. (2021). Many predictions have been made using these simulations on the formation and evolution of galaxies. It is an effective way to understand phenomena at high redshifts which are difficult to observe with current telescopes.

Simulation	α_*	β_*	γ_*	ϵ
Illustris	1.28 ± 0.040	8.38 ± 0.088	$0.18^{+0.046}_{-0.063}$	$0.08^{+0.144}_{-0.058}$
Horizon-AGN	1.03 ± 0.026	8.50 ± 0.036	$0.07^{+0.008}_{-0.020}$	$0.08^{+0.032}_{-0.048}$
SIMBA	1.24 ± 0.046	8.78 ± 0.063	$-0.15^{+0.080}_{-0.064}$	$0.28^{+0.055}_{-0.050}$
TNG100	1.23 ± 0.022	8.91 ± 0.074	$-0.02^{+0.025}_{-0.014}$	$0.16^{+0.078}_{-0.047}$
TNG300	1.29 ± 0.019	8.91 ± 0.050	$-0.02^{+0.007}_{-0.007}$	$0.26^{+0.256}_{-0.115}$
EAGLE	1.39 ± 0.027	8.23 ± 0.039	$0.01^{+0.022}_{-0.035}$	$0.21^{+0.079}_{-0.076}$
Tiamat	1.43 ± 0.185	8.14 ± 0.066	$0.05^{+0.010}_{-0.010}$	$0.18^{+0.140}_{-0.050}$

Table 1. Black hole - bulge mass parameters of the six different simulations from the the fitting process.

The mass of the SMBH and galactic bulge can be fitted using equation (3.2) for the 6 different cosmological simulations individually. The slope of the linear least square fit in the logarithmic scale of the masses from a simulation for all $z \leq 5$ is α_* for that simulation. This slope is taken as the slope for the least square fit of each redshift. The intercept at $z = 0$ is β_* and γ_* can be calculated from the intercept of other redshifts. ϵ is the deviation of mass of SMBH from the phenomenological fit by equation (3.2). The parameters of the BH-bulge mass relation for these different cosmological simulations are given in Table 1.

Figure 2 shows the evolution of SMBH mass with redshift for different simulations using equation (3.2). α, β and ϵ parameters for the Tiamat simulation using equation(2.1) for $z \leq 6$ from Marshall et al. (2020) is

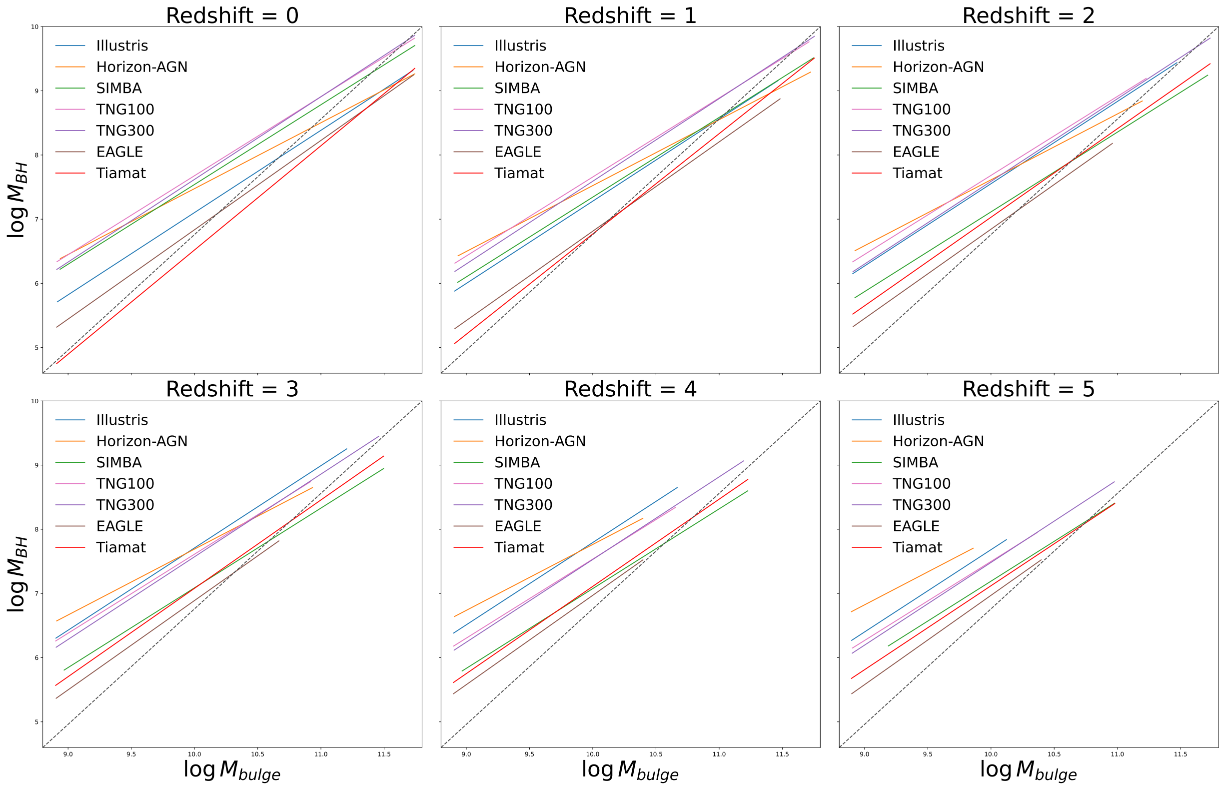

Fig. 2. Fits of SMBH masses using equation (3.2) for redshifts $z = 0, 1, 2, 3, 4$ and 5 for Illustris, Horizon-AGN, SIMBA, TNG100, TNG300, EAGLE and Tiamat simulations. The black dotted reference line is fixed across all panels.

also shown in Figure 2. Converting this BH mass parameters from the Tiamat simulation into parameters of equation (3.2), also gives consistent γ_* value which is given in Table 1.

5 Conclusions

The new formalism for the BH-bulge mass relation is supported by simulations. In the Illustris simulation, SMBH mass increases as we go to higher redshifts in Figure 2 due to the positive value of γ_*. Whereas SMBH mass decreases as we go to higher redshifts in SIMBA because of the negative value of γ_*. The differences found in the redshift evolution of the BH-bulge mass relations likely come from the combination of the different BH and galaxy subgrid physics employed in each simulation (e.g., BH formation, BH accretion rates, AGN feedback, etc.). Current observations, that however may not be unbiased, suggest positive or no evolution with redshift, therefore models with negative evolution are disfavored. The GWB strain in the PTA range we get using the BH-bulge mass parameters with redshift will be different for each simulations similar to Figure 1.

References

Chen, S., Sesana, A., & Conselice, C. J. 2019, MNRAS, 488, 401
Croton, D. J. 2006, Mon. Not. Roy. Astron. Soc., 369, 1808
Habouzit, M., Li, Y., Somerville, R. S., et al. 2021, MNRAS, 503, 1940
Lauer, T. R., Tremaine, S., Richstone, D., & Faber, S. M. 2007, Astrophysical Journal, 670, 249
Lentati, L., Taylor, S. R., Mingarelli, C. M. F., et al. 2015, MNRAS, 453, 2576
Marshall, M. A., Mutch, S. J., Qin, Y., Poole, G. B., & Wyithe, J. S. B. 2020, MNRAS, 494, 2747
Schutte, Z., Reines, A. E., & Greene, J. E. 2019, Astrophysical Journal, 887, 245
Sesana, A. 2013, MNRAS, 433, L1
Venemans, B. P., Walter, F., Zschaechner, L., et al. 2016, Astrophysical Journal, 816, 37
Wyithe, J. S. B. & Loeb, A. 2003, Astrophysical Journal, 595, 614

Session 26

Magnétosphères (exo-)planétaires comparées

CHARGE EXCHANGE X-RAY EMISSION IN THE NEAR-EARTH ENVIRONMENT: SIMULATIONS IN PREPARATION FOR THE SMILE MAGNETOSPHERIC MISSION

Y. Tkachenko[1], D. Koutroumpa[2], R. Modolo[2], H. Connor[3] and S. Sembay[4]

Abstract. Solar Wind Charge exchange X-ray (SWCX) imaging of the Earth's magnetosheath will be the target of the Solar wind Magnetosphere Ionosphere Link Explorer (SMILE), a joined ESA-CAS mission. The mission aims to study the solar wind-magnetosphere coupling through simultaneous X-ray and UV imaging and in situ plasma and magnetic field measurements. We present simulations of the SWCX emission produced in the Earth's magnetosheath, developped in the framework of the Modeling Working Group (MWG, `https://smile.alaska.edu/`) which provides modeling support for the SMILE mission. The goal of the current study is to extend the application of a Test Particle model to input electric and magnetic fields from MHD simulations, and compare the X-ray emissivity maps to the ones from a pure MHD approach.

Keywords: Earth, exosphere, magnetosphere, Solar Wind, charge exchange, soft X-rays

1 Introduction

Generally associated with hot and energetic plasmas, soft X-ray emission was discovered in ROSAT observations of comet Hyakutake (Lisse et al. 1996) and identified as Solar Wind Charge exchange (SWCX; Cravens 1997): highly charged ions from the 1MK solar corona extract electrons from cometary neutrals and the newly created excited ions emit soft X-rays as they de-excite to their ground state. Soon, it became obvious that neutral targets would include the Earth's hydrogen geocorona, other planets' exospheres, and the interplanetary medium (Cox 1998; Cravens 2000; Dennerl 2002).

While an unpredictable nuisance for X-ray astrophysics (e.g., Snowden et al. 1995, 2004; Ezoe et al. 2011), geocoronal SWCX was recognised as a potential diagnostic goldmine for solar-terrestrial interactions (Sibeck et al. 2018). Dedicated space missions, such as SMILE (Branduardi-Raymont et al. 2020), will target this emission as an imaging tool to study the dynamic response of the Earth's magnetosphere to the solar wind (SW) impact in a global manner. The SMILE MWG has been organized to support the mission and in particular the Soft X-ray Imager science (SXI; Sembay et al. 2016). Among other, the MWG's main goals are to provide unified input parameters for magnetohydrodynamic (MHD) models of the SW-magnetosphere interaction and SWCX emission, help define the mission science requirements and potential observation geometries, and investigate magnetopause boundary reconstruction techniques from SXI images (Sun et al. 2020; Connor et al. 2021).

This proceeding focuses on a complementary approach to calculate the geocoronal SWCX emission using a Test-Particle (TP) simulation with electric (E) and magnetic (B) field input from the OpenGGCM (Open Geospace General Circulation Model; Raeder et al. 1998) MHD model. Our aim is to compare the TP X-ray emissivity maps to the ones from a pure MHD model and investigate kinetic effects that the TP approach introduces. We briefly describe the MHD and TP approaches to geocoronal SWCX calculation in section 2. In section 3, we present the simulation results: we discuss the various diagnostics performed for a single reference SW ion (O^{7+}) to estimate input parameter sensitivity in section 3.1, we present total intensity maps of the SWCX emission produced by all highly charged SW ions relevant to the SXI energy range, and subsequent synthetic SXI images in section 3.2. Finally, we offer some conclusions and perspectives in section 4.

[1] Université d'Orléans, Orléans, France
[2] LATMOS, CNRS, UVSQ Paris-Saclay, Sorbonne Université, Guyancourt, France
[3] University of Alaska Fairbanks, Fairbanks AK, USA
[4] University of Leicester, Leicester, UK

2 Model Description

The TP model describes the dynamic of charged particles in a static electromagnetic field environment. It solves the equation of motion with a basic leap-frog pusher and a predictor-corrector scheme to determine the acceleration of the particles. The E and B field description comes from the OpenGGCM MHD model simulation with SW input of $n_p = 12.5\ cm^{-3}$, $v_p = 400\ km/s$, and $T = 20,000\ K$, the IMF input of $(B_x, B_y, B_z) = (0, 0-5)\ nT$, and no dipole tilt. For the TP simulation, we used a uniform cartesian grid covering the spatial domain $0 \leq X_{GSE} \leq 20R_E$, $-10R_E \leq Y_{GSE}, Z_{GSE} \leq +10R_E$ with an adaptable spatial resolution $ds = 0.05$ or $0.1\ R_E$. For each simulation, 37.5M test-particles representing a given ion species X^{q+} are launched from the entry face of the simulation ($X_{GSE} = 20R_E$) with plasma properties corresponding to the SW characteristics of the OpenGGCM MHD simulation.

During the motion of the particle, at each time step, we compute the SWCX production associated with the reaction

$$X^{q+} + H \longrightarrow X^{(q-1)+} + H^+ \tag{2.1}$$

with X^{q+} the parent solar wind ions, H geocoronal targets, $X^{(q-1)+}$ the produced ions and H^+ the newly born planetary protons. The number of produced ions is determined by the number of parent ions lost at a particular position in space and as a function of time, according to the equation:

$$\frac{\partial N_{X^{q+}}}{\partial t} = -N_{X^{q+}} \times \sigma_{X^{q+},H} \times v_{X^{q+}} \times n_H \tag{2.2}$$

with $N_{X^{q+}}$ the number of physical ions, $\sigma_{X^{q+},H}$ the CX cross-section between parent ions and H atoms, $v_{X^{q+}}$ the speed of the parent ions (the neutral atoms' speed is negligible), and n_H the geocoronal neutral density. The n_H density distribution is given by Cravens et al. (2001). To obtain the total SWCX production rate for an ion species (proportional to the SWCX emissivity), we sum the production rate contributed by each test-particle in the cartesian grid. The emissivity $Q_{TP}^{X^{q+}}$, is then calculated by multiplying by the relative abundance of the ion species, and their characteristic soft X-ray emission line probabilities (in eV). Simulations have been performed for 21 parent ion species ($C^{5,6+}$, $O^{7,8+}$, $N^{6,7+}$, $Ne^{8,9+}$, $Mg^{8,9,10,11+}$, $Si^{8,9,10+}$, $S^{8,9+}$, $Fe^{8,9,10,11+}$), producing main SWCX emission lines in the SXI energy range (0.2 - 2.0 keV). The total TP emissivity Q_{TP} in the SXI bandpass is then calculated as the sum of individual $Q_{TP}^{X^{q+}}$ emissivities.

In the pure MHD approach, the total emissivity Q_{MHD} is calculated as in Cravens et al. (2001): $Q_{MHD} = \alpha \times n_p \times v_p \times n_H$, where $n_p \times v_p$ is the MHD SW proton flux, and α combines all cross-section, ion abundance and line emission probability information for the list of ions above.

3 Results

3.1 O^{7+} SWCX Emissivity

We performed several TP simulations for reference ion O^{7+} to estimate the sensitivity of the results to input parameters. First we test velocity-dependent CX cross-sections, and conclude that they do not have a significant impact in the specific SW velocity regime considered here. Fig.1 shows a side view of the TP results on the O^{7+} SWCX emissivity for different spatial and time-step resolutions (panels b, c, d, e & f), in comparison with MHD results for the same ion (panel a). The single-fluid MHD shows a continuous emissivity gradient, while the TP simulations exhibit small scale structures due to kinetic effects, such as streamlines that ions follow due to the superposition of the gyromotion and the bulk flow, as well as regions of re-acceleration of the ion plasma flow just above and below the subsolar region. A finer spatial resolution (panel c) also highlights a ripple effect due to magnetic overshoot at the bow shock crossing (marked by a white arrow in the zoomed-in panels of the subsolar bow-shock; Masters et al. 2013). Nevertheless, once all the TP results of individual ions (with different gyroradii) are combined in the projected SWCX intensity maps (see section 3.2 and Fig.2), this effect does not seem quite as conspicuous. On the other hand, a higher temporal resolution seems decisive. As the time step becomes smaller, the description of the charged particles penetration into the cusps improves (compare panels d, e & f) and simulations show that charged particles stay in the cusps longer producing higher X-ray emission.

3.2 Total Intensity maps and SXI Synthetic Images

The total SWCX intensity maps (from all 21 ions) were then calculated with the MHD and TP approaches in various observation geometries (Fig.2). Columns (a) and (b) present emission maps integrated along the main

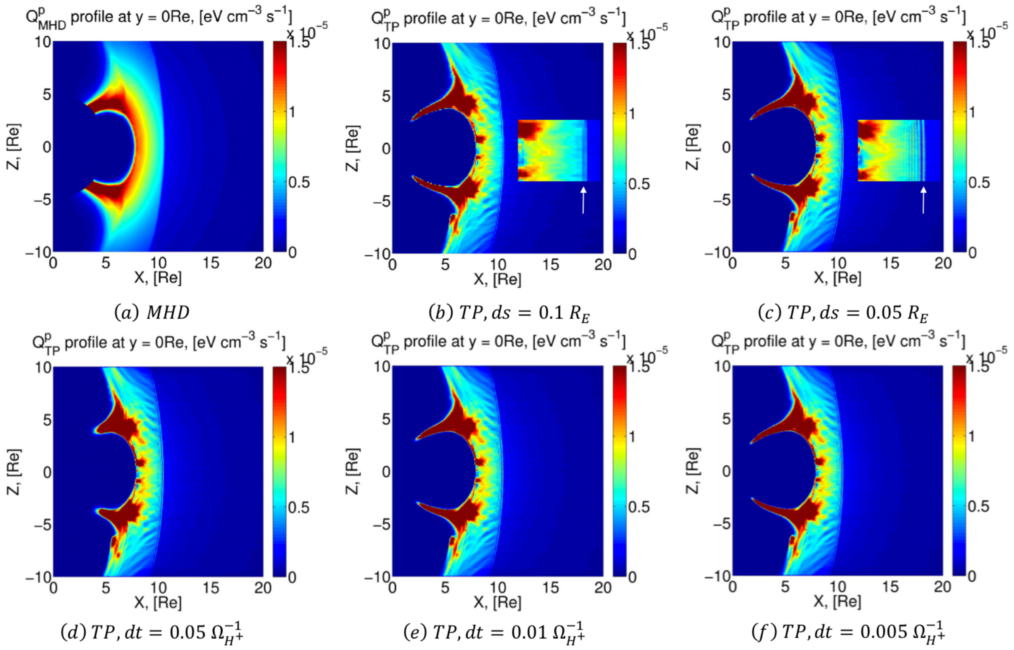

Fig. 1. MHD-calculated (a) and TP-calculated (b, c, d, e & f) production rate (emissivity) cuts along the noon meridian (XZ plane, at Y = 0 R_E) for emission lines produced by SWCX of the reference ion O^{7+}. For the TP-calculated cuts, (b) & (c) compare simulation results for two different spatial resolutions (zoomed-in panels of the subsolar bow-shock highlight the magnetic overshoot), and (d), (e) & (f) compare simulation results for different time step resolutions.

simulation axes. The location of the magnetopause in the two models is consistent and its distance to the Earth along the X-axis is about 7 - 7.5 R_E, where the MHD maximum emission drops in both XY and XZ planes (top a-, b-panels). In the TP case, moving from +X to -X, the emission starts rising around the same region as the MHD, but in the XY plane (bottom a-panel) the cusps intense emission (integrated along Z) widens the emission region even inward from the magnetopause (< 7 R_E). In the XZ plane (Fig.2 - b), the TP emission starts and drops around the same regions as the MHD, except that the kinetic effects give more structure and higher intensity along the magnetopause in the re-acceleration regions close to the X-axis. Also the pre-cusp regions are much brighter in the TP results.

The produced MHD and TP total ion data cubes were then used as input to the SXI instrument simulation software to produce a realistic SXI observation from orbit (Fig. 2 - c, d). The SMILE spacecraft was positioned at $\vec{r} = (3.76,\ 7.46,\ 17.97)$ R_E, the SXI field of view was aimed at $\vec{p} = (8.04,\ 0.00,\ 0.00)$ R_E and the Earth limb angle was 20.48°. Column (c) plots show the projected simulation maps and column (d) plots show the synthetic detector images for a typical exposure time of 300 s with simulated noise sources included. Despite the synthetic observations' noise, it is obvious that the TP simulations yield higher intensity over a wider region.

4 Conclusions and Perspectives

We have performed TP simulations of the SWCX emission in the Earth's geocorona, compared the results to equivalent MHD simulations, and produced realistic synthetic images through the SMILE/SXI instrument simulator. The TP simulations are consistent with the existing MHD model. At the same time, TP results exhibit more complex structure, highlighting kinetic effects such as re-acceleration regions, while also generating more intense soft X-ray emissivity in general.

We have also tested the sensitivity of TP results to several parameters (dynamic cross-sections, spatial and temporal resolution), of which the temporal resolution was the most crucial for the proper description of ion trajectories in the cusps. An advance on this parameter would be to use an adaptive time step through the simulation grid. This would potentially help optimize the required numerical ressources.

Future work includes TP simulations for different E & B configurations and SW conditions, like ICMEs (Interplanetary Coronal Mass Ejections). Such events may push the magnetosheath boundaries inward where

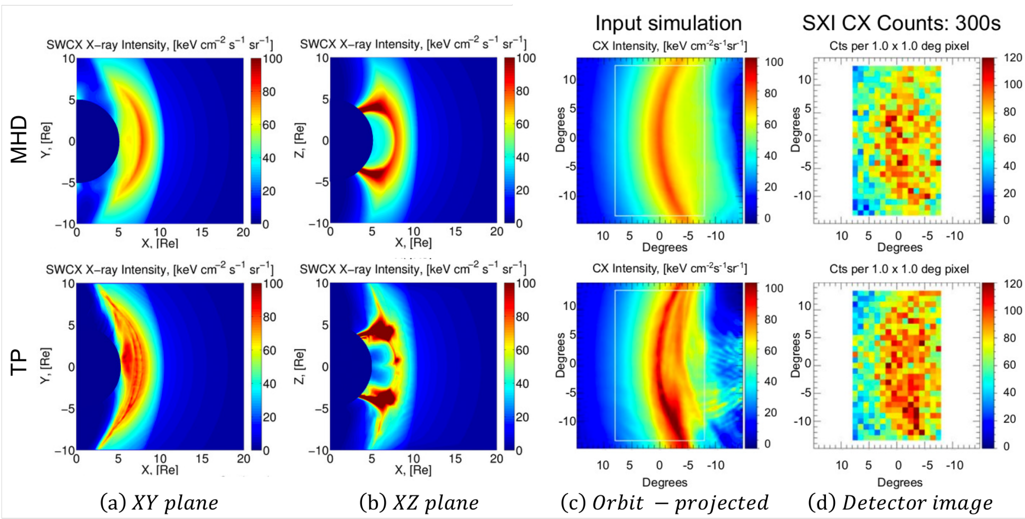

Fig. 2. X-ray intensity maps for MHD (top) and TP (bottom) simulations integrated along the simulation box main axes Z (a) and Y (b), and from a simulated SMILE orbit (c - the white rectangle represents the SXI field-of-view). Column (d) shows the corresponding synthetic SXI images for a typical 300 s exposure. See text for details.

neutral H density is larger while high energy SW particles may penetrate through the magnetopause as well as deeper into the cusps. In addition, changes in SW ion thermal velocities and SW elemental composition (and thus relative SWCX spectral line strength) may require the use of TP simulations where the consideration of each ion separately may prove to be an advantage over MHD models.

Finally, we will produce synthetic SXI observations for different geometry configurations (including the highly emissive cusp regions), to be tested with the boundary tracing methods developed by the SMILE MWG.

This work is supported by CNES. To process the SWCX test-particle simulations data, this study benefited from the IPSL mesocenter ESPRI facility which is supported by CNRS, UPMC, Labex L-IPSL, CNES and Ecole Polytechnique. H. K. Connor gratefully acknowledges support from the NASA grants 80NSSC18K1043, 80NSSC20K1670, and 80MSFC20C0019. The SXI simulation software is supported by UKSA.

References

Branduardi-Raymont, G., Wang, C., Escoubet, C. P., et al. 2020, in EGU General Assembly Conference Abstracts, EGU General Assembly Conference Abstracts, 10783

Connor, H. K., Sibeck, D. G., Collier, M. R., et al. 2021, Journal of Geophysical Research (Space Physics), 126, e28816

Cox, D. P. 1998, Modeling the Local Bubble, ed. D. Breitschwerdt, M. J. Freyberg, & J. Truemper, Vol. 506, 121–131

Cravens, T. E. 1997, Geophys. Res. Lett., 24, 105

Cravens, T. E. 2000, Advances in Space Research, 26, 1443

Cravens, T. E., Robertson, I. P., & Snowden, S. L. 2001, Journal of Geophysical Research: Space Physics, 106, 24883

Dennerl, K. 2002, A&A, 394, 1119

Ezoe, Y., Miyoshi, Y., Yoshitake, H., et al. 2011, PASJ, 63, S691

Lisse, C. M., Dennerl, K., Englhauser, J., et al. 1996, Science, 274, 205

Masters, A., Slavin, J. A., Dibraccio, G. A., et al. 2013, Journal of Geophysical Research (Space Physics), 118, 4381

Raeder, J., Berchem, J., & Ashour-Abdalla, M. 1998, J. Geophys. Res., 103, 14787

Sembay, S., Branduardi-Raymont, G., Drumm, P., et al. 2016, in AGU Fall Meeting Abstracts, SM44A–04

Sibeck, D. G., Allen, R., Aryan, H., et al. 2018, Space Sci. Rev., 214, 79

Snowden, S. L., Collier, M. R., & Kuntz, K. D. 2004, ApJ, 610, 1182

Snowden, S. L., Freyberg, M. J., Plucinsky, P. P., et al. 1995, ApJ, 454, 643

Sun, T., Wang, C., Connor, H. K., Jorgensen, A. M., & Sembay, S. 2020, Journal of Geophysical Research (Space Physics), 125, e28169

SF2A 2021
A. Siebert, K. Baillié, E. Lagadec, N. Lagarde, J. Malzac, J.-B. Marquette, M. N'Diaye, J. Richard, O. Venot (eds)

THE SEARCH FOR RADIO EMISSION FROM EXTRASOLAR PLANETS USING LOFAR BEAM FORMED OBSERVATIONS

J.-M. Grießmeier[1,2], J. D. Turner[3,4] and P. Zarka[2,5]

Abstract. Observing planetary auroral radio emission is the most promising method to detect exoplanetary magnetospheres and magnetic fields, the knowledge of which will provide valuable insights into the planet's interior structure, atmospheric escape, and habitability. We present LOFAR (LOw-Frequency ARray) Low Band Antenna (LBA: 10-90 MHz) circularly polarized beamformed observations of three exoplanetary systems which are usually considered to be among the best candidates for exoplanetary radio emission. We tentatively detect circularly polarized bursty emission from the τ Boötis system in the range 14-21 MHz with a statistical significance of 3 σ. Assuming the detected signal is real, we discuss its potential origin. A possible explanation is radio emission from the exoplanet τ Boötis b via the cyclotron maser mechanism. Assuming a planetary origin, we derived limits for the planetary polar surface magnetic field strength, finding values compatible with theoretical predictions. Follow-up observations will allow to confirm this possible first detection of an exoplanetary radio signal. We will discuss such follow-up observations that have recently been performed on LOFAR-LBA, NenuFAR and UTR-2.

Keywords: Planets and satellites: magnetic fields, Radio continuum: planetary systems, Magnetic fields, Planet-star interactions, Planets and satellites: aurorae, planets and satellites: gaseous planets

1 Introduction

This proceeding article is a summary of recent work. The full article (Turner et al. 2021) contains more details on the observational setup, data processing, and the interpretation of the observations.

All the planets in our Solar System (except Venus), have or used to have a magnetic field, and many exoplanets are expected to have magnetic fields as well. Measuring the magnetic field of an exoplanet would give valuable information to constrain its interior structure, its atmospheric escape, and the nature of any star-planet interaction (e.g. Grießmeier et al. 2007; Hess & Zarka 2011; Zarka et al. 2015; Grießmeier 2015, 2017; Lazio 2018; Grießmeier 2018; Zarka 2018). For these reasons, many methods have been proposed to study the magnetic fields of exoplanets. By contrast to all other suggested methods, radio observation can constrain the magnetic field amplitude directly without invoking complex model assumptions, and is much less susceptible to false positives (Grießmeier 2015). Still, despite decades of search, the direct detection of exoplanetary magnetic fields has so far remained elusive (e.g. Grießmeier 2017).

2 LOFAR beamformed observation campaign

We have performed beam-formed observations with LOFAR (van Haarlem et al. 2013), observing three planets which were selected based on theoretical predictions: 55 Cancri, υ Andromedae, and τ Boötis. The available observing time (between 20 and 45h per target) was spread as evenly as possible over the planetary orbital period. We used multiple beams (at least one 'ON' beam and two 'OFF' beams) to allow to search for rapid bursts. The pipeline has been tested and calibrated with Jupiter data (Turner et al. 2017; Turner et al. 2019).

[1] Laboratoire de Physique et Chimie de l'Environnement et de l'Espace (LPC2E) Université d'Orléans/CNRS, Orléans, France
[2] Station de Radioastronomie de Nançay, Observatoire de Paris, PSL Research University, CNRS, Univ. Orléans, OSUC, 18330 Nançay, France
[3] Department of Astronomy and Carl Sagan Institute, Cornell University, Ithaca, NY, USA
[4] Department of Astronomy, University of Virginia, Charlottesville, VA, USA
[5] LESIA, Observatoire de Paris, CNRS, PSL, Meudon, France

3 A radio burst from τ Bootis b?

For one or the observations of the τ Bootis system, our analysis found an excess of circularly polarized bursts of a duration of the order of 1 second in the ON beam. The frequency range of the emission was 14-21 MHz. This detection is significant at 3.2 σ. The most likely cause for this emission is the planet τ Bootis b, via cyclotron maser emission. For this, the planet requires a surface magnetic field strength of 5-11 G, which is roughly comparable to Jupiter's magnetic field. With a measured intensity of 900 mJy, the emission would be 4-5 orders of magnitude stronger than Jupiter's emission, which is be consistent with current models. Figure 1 compares the observed emission to Jupiter's emission and upper limits derived during other observation campaigns.

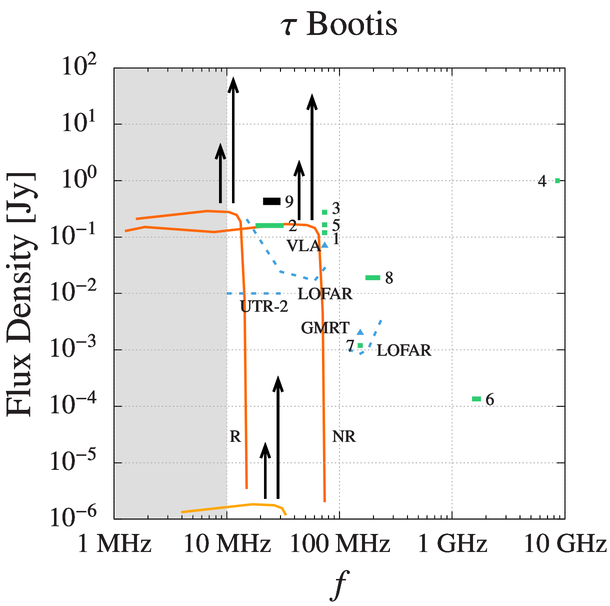

Fig. 1. Predictions and observations for the exoplanet τ Boötis b. Grey area: Emission below 10 MHz is not detectable for ground-based observations (ionospheric cut-off). Lower solid line (light orange): Typical spectrum of Jupiter's radio emissions at 15.6 pc distance. Two upper solid lines (orange): Jupiter's radio emission scaled for values expected for τ Boötis b according to models R (left) and NR (right) from Grießmeier (2017). For Jupiter, the radio flux increases by up to two order of magnitude during periods of high activity. The same variability is assumed for exoplanetary emission, as indicated by the vertical black arrows. Dashed lines and triangles show the theoretical sensitivity limit of the radio-telescopes UTR-2, LOFAR (low band), VLA, LOFAR (high band), and GMRT (for 1 h of integration time and a bandwidth of 4 MHz). Black line (9): this study. Other numbered lines and points: upper limits derived in previous observations of τ Bootis. See Turner et al. (2021) for details.

4 Conclusions

While promising, the result if not yet fully conclusive. In particular, we cannot rule out stellar flares as the source of the emission. In order to confirm that the source of the detected signal is indeed the planet τ Boötis b, we have performed a follow-up campaign using four different radio telescopes (LOFAR, LWA, UTR-2 and NenuFAR). We have increased the number of observations, with an improved orbital coverage. The data of this follow-up campaign are currently under analysis.

References

Grießmeier, J.-M. 2015, in Astrophysics and Space Science Library, Vol. 411, Characterizing stellar and exoplanetary environments, ed. H. Lammer & M. Khodachenko (Springer), 213–237

Grießmeier, J.-M. 2017, in Planetary Radio Emissions VIII, ed. G. Fischer, G. Mann, M. Panchenko, & P. Zarka (Austrian Academy of Sciences Press, Vienna)

Grießmeier, J.-M. 2018, in Handbook of Exoplanets, ed. H. J. Deeg & J. A. Juan Antonio Belmonte (Springer)

Grießmeier, J.-M., Zarka, P., & Spreeuw, H. 2007, Astron. Astrophys., 475, 359

Hess, S. L. G. & Zarka, P. 2011, Astron. Astrophys., 531, A29

Lazio, T. J. W. 2018, in Handbook of Exoplanets, ed. H. J. Deeg & J. A. Juan Antonio Belmonte (Springer)

Turner, J. D., Grießmeier, J.-M., Zarka, P., & Vasylieva, I. 2017, in Planetary Radio Emissions VIII, ed. G. Fischer, G. Mann, M. Panchenko, & P. Zarka (Austrian Academy of Sciences Press, Vienna), 301–313

Turner, J. D., Grießmeier, J.-M., Zarka, P., & Vasylieva, I. 2019, Astron. Astrophys., 624, A40

Turner, J. D., Zarka, P., Grießmeier, J.-M., et al. 2021, Astron. Astrophys., 645, A59

van Haarlem, M. P., Wise, M. W., Gunst, A. W., et al. 2013, Astron. Astrophys., 556, A2

Zarka, P. 2018, in Handbook of Exoplanets, ed. H. J. Deeg & J. A. Juan Antonio Belmonte (Springer)

Zarka, P., Lazio, J., & Hallinan, G. 2015, Advancing Astrophysics with the Square Kilometre Array (AASKA14), 120

Author Index